



**VYSOKÉ UČENÍ TECHNICKÉ V BRNĚ**  
BRNO UNIVERSITY OF TECHNOLOGY

**STŘEDOEVROPSKÝ TECHNOLOGICKÝ INSTITUT**  
CENTRAL EUROPEAN INSTITUTE OF TECHNOLOGY

**RENTGENOVÁ POČÍTAČOVÁ TOMOGRAFIE VE  
VĚDNÍCH OBORECH**  
X-ray computed tomography in scientific fields

**HABILITAČNÍ PRÁCE**  
**HABILITATION THESIS**

**AUTOR PRÁCE**  
**AUTHOR**

**Ing. Tomáš Zikmund, Ph.D.**

**BRNO 2021**

*"It is strange that only extraordinary men make the discoveries, which later appear so easy and simple."*

Georg C. Lichtenberg

## ACKNOWLEDGMENT

I would especially like to thank prof. Ing. Jozef Kaiser, Ph.D. who gave me the chance to be part of the laboratory and who has taught and supervised me for most of my carrier. Many thanks also belong to all the members of the CT research group at CEITEC, who were always working as a team which made me believe we could get further.

I would like to thank my colleagues from various research fields who contributed to this work in any way and inspired me in doing the research.

Finally, I would like to thank my family for all the support and patience not only during the writing of this thesis but also during my whole professional life. Many thanks belong to my wife Mgr. Eva Zikmundová, Ph.D., who was the first opponent of this thesis and whose contribution improved this work a lot.

## ABSTRACT

This work deals with the implementation of the laboratory-based X-ray micro and nano computed tomography technique in various fields related to the author's postgraduate research activities. It gives a brief overview of the computed tomography terminology and it is partially focused on clarifying the basic terms which usually have several meanings or can be misinterpreted in the literature. The second part introduces the author's contributions to selected scientific publications in the form of concise comments. These are divided into methodology focused publications which extend the capabilities of this imaging technique and application related publications where computed tomography acts as a tool to answer specific questions in varied research fields.

## KEY WORDS

*X-ray computed tomography, development biology, soft tissue, quantitative CT, voxel resolution, correlation of techniques, image processing, analysis*

## TABLE OF CONTENTS

1. Introduction .....	5
2. Aims of the habilitation thesis .....	7
3. Brief overview of X-ray computed tomography .....	8
4. Extending of the CT imaging capabilities .....	17
5. Applications in various research fields .....	22
6. Conclusions .....	28
7. Commented papers .....	30
8. References .....	33
9. List of abbreviations.....	36
Printed versions of commented papers .....	37

## 1. INTRODUCTION

My doctoral study was primarily focused on the processing of image data of carcinoma cells from a holographic microscope developed under the leadership of prof. Radim Chmelík at the Department of Optics and Precise Mechanics, Institute of Physical Engineering, Brno University of Technology. Thanks to his good relationship with prof. Alan Boyde from the Dental Physical Sciences unit, Institute of Dentistry at Queen Mary University of London I was given a great opportunity of a foreign internship. At that time, prof. Boyde obtained an older X-ray computed tomography (CT) system Scanco Medical  $\mu$ CT 40 and asked me to perform a CT analysis of a rat femur as a part of a drug experiment. This was my first encounter with the basics of tomography and the first experience with CT measurements and CT data processing. Although it was a different technique than the holographic microscopy it was still connected to my Ph.D. topic through the image processing methods. Nevertheless, I became so fascinated by tomography that I decided to deal with it further.

By a lucky chance, when I came back from the internship in 2013, the laboratory of X-ray computed tomography was just being built in the frame of a newly emerging CEITEC BUT Research Centre as an initiative of prof. Jozef Kaiser who had previously worked with tomography in the Elettra Synchrotron Trieste (Trieste, Italy). The industrial CT system from General Electric Company (GE, Waygate Technologies today) equipped with a microfocus X-ray tube, a large protection cabinet and a flexible manipulation system was installed in Brno with the idea to create a complementary system to a synchrotron device. Therefore, I met with prof. Kaiser to express my enthusiasm for the tomographic technique and he gave me the opportunity to become a part of the laboratory as an assistant of the first measurements. After finishing my Ph.D. studies in 2014, I have finally started to work full time in the CT laboratory, while establishing the first research activities and building a team of experts around them.

The new technology has raised big expectations from the point of its introduction into the research and development. However, a new laboratory that is being established from zero needs to find its user community first. This was a challenging task since, at that time, the capabilities and utilization possibilities of the CT system were not very well known yet. Approaching potential users has been a completely new role for me and it took me on a long journey of a CT possibilities presentation with the need to understand the problematics from other scientific fields and to constantly adapt the analysis for their purposes.

A non-destructivity and a visualization of an internal structure make CT a very attractive technique for unique samples and unusual topics. I have encountered a variety of exciting and interesting studies from a wide spectrum of research fields. I believe there is no other technology which provides such an application diversity and that is also why I have become completely absorbed in this work. Furthermore, thanks to the biological projects our laboratory managed to establish the international cooperation, e.g., with Karolinska Institute (Sweden), Pasteur Institute (France) or University of British Columbia (Canada) and it successfully fulfilled the expectations of the CEITEC consortium to interconnect life and material sciences.

Nevertheless, the laboratory is devoted to address both the basic and the applied research [1]. Therefore, besides developing a cooperation in the scientific sphere, I have also strived to

establish a cooperation with industry in the form of a contractual research. For this purpose, I started to build a special team of experts working in a regime driven by the industrial needs, like flexibility and a rapid operation. In several years, we have managed to build a highly professional expertise and a long-term cooperation with many national companies and international corporations. This helped not only with the financial sustainability of the laboratory, but above all it brought us an extensive experience of a daily use of CT and of working on various specific tasks. Nowadays, the laboratory often figures as a strategical partner of various companies in the development of the CT systems and as a co-applicant in national technological grants (like TAČR TREND).

Another mission of the laboratory is to keep up with innovations, a constant improvement of the technology knowledge and a modernization of current devices. For this reason, we have wanted to collaborate with world's leading CT system producers via a joint development. This was very hard since the big producers usually already cooperate with renowned institutions and us being a new small research group basically had no confidence at the beginning. We have managed to achieve this only thanks to a long-term cooperation and also by building a sufficiently strong team capable to offer some innovations to the producers. Having the titles such as Application Laboratory of Rigaku, Application Laboratory of Thermo Fisher Scientific and Testing Laboratory of Waygate Technologies, the laboratory is now participating on a development of the tools improving the data quality, a verification of metrological properties or a testing of the latest beta software.

All these activities, which we considered necessary to keep the equipment at a high level and to build an excellent expertise at the beginning of the new laboratory, thus, also directed my scientific career and they are reflected in the publishing activities. This work aims to introduce and summarize my publications in the form of a commentary. I have divided the scientific papers into two groups. The first one is dedicated to the methodological papers improving the CT technology or imaging capabilities which are the results of cooperation with the CT producers or of our own development. The second group refers to various applications of CT motivated mainly by studies or projects coming from different research areas. I have also aimed for an introduction of the basic terms of X-ray computed tomography and for a determination of the categories of lab-based systems. This should help readers to become well informed about the current state of lab-based systems and also with the clarification of the terms which are often discussed, or the meaning of which is often interchanged. The explanation of the tomographic reconstruction principle is not included as it is very well described elsewhere in the literature [2-6].

## 2. AIMS OF THE HABILITATION THESIS

- Development of advanced methods of the CT imaging, the sample preparation, the data interpretation, and the quantitative analysis which extends the possibilities of the CT use.
- Implementation of the CT technique into various research fields using the state-of-the-art commercial CT devices and data analysis software.
- Alignment of the CT imaging implementation and development in the biology field

### 3. BRIEF OVERVIEW OF X-RAY COMPUTED TOMOGRAPHY

#### *Terminology*

Tomography is an imaging technique which is connected with two main merits – a non-destructivity and a three-dimensional (3D) imaging - which establish its indispensable position in many scientific and engineering fields. The word tomography is derived from Greek words *tomos*, 'slice', and *graphō*, 'to write', and it simply means 'a description in sections'. In the literature, tomography, thus, denotes a set of multiple techniques regardless of using different principles to obtain the sections.

For example, the focused-ion beam tomography (FIB) [7] uses a beam of ions to sequentially mill the specimen while the newly exposed surface is scanned by electron microscopes. The final output is a series of surface images. On the contrary, the optical coherence tomography (OCT) is based on the phenomenon of a white light interferometry [8-10], recording the reflection properties of the sample. The cross-sectional images are then collected in various scanning depths. Another technique, which should not be forgotten, is the magnetic resonance tomography [11] rather known under the shortcut MRI which stands for the magnetic resonance imaging. This technique uses an external magnetic field and the radiofrequency to realign protons. By acquiring the time of the realignment and the amount of energy released the difference between tissues is defined in each section of the magnetic field.

However, tomography is historically linked with methods based on the principle of Radon transform [12] meaning that a two-dimensional (2D) section of the object is mathematically computed from a set of radiographic images (projections) acquired around the sample. To prevent the confusion and to clearly separate these methods, this type of tomography should always be called a computed tomography or a computerized tomography (both abbreviated as CT). The second expression resulted from the development of a modern computer technology which made computed tomography feasible and enabled its development and practical use.

Projection images can be obtained by different source-detector systems and this fact is usually highlighted by another additional word in the name of the technique. Among such systems there are: the electron tomography (ET) utilising a beam of electrons passing through an incrementally rotated sample [13], the ultrasound computed tomography (ultrasound CT) based on acoustic waves [14], the optical projection tomography (OPT) [15-17] using the light transmitting through a transparent object, the X-ray computed tomography (XCT) [2], the positron emission tomography (PET) [18, 19] or the single-photon emission computed tomography (SPECT) [20, 21] detecting gamma rays generated by a radioactive tracer injected into a body of a living organism.

#### *X-ray computed tomography*

The scope of this work is reserved for the X-ray computed tomography which I dare to separate into two groups according to the utilisation and the construction, i.e. medical and industrial. The medical CT is driven by the needs of a human patient, which means to decrease the exposure time, to reduce the X-ray dosage and to minimize the blurring caused by the patient's motion especially due to breathing or the cardiac activity. The construction of the

system is designed for a high-speed rotation of the detector and the source around the patient's body. The patient is usually positioned into the system in the direction of the rotation axis to get a complete volumetric imaging. The fixed detector-source distance and the given size of the patient limit the resulting accuracy and detectability properties which are, however, still sufficient for clinical purposes.

Compared to that, the industrial CT is meant to inspect lifeless and shape-stable objects, therefore, basically the dosage is not limited, and the construction of the systems is adapted to higher accuracy and stability. This is achieved by a fixation of detector and source positions during the acquisition process and by a rotation of the sample. The resolution and accuracy are then adjusted by positioning the object in a given cone beam geometry. These devices use a geometrical magnification, which means that positioning the object closer to the source gives a higher magnification, but a smaller field of view while positioning it closer to the detector provides a bigger field of view with a lower magnification (see Fig. 1).

Flat panels consisting of a straight 2D array of pixels are the most widely used detectors. They are often based on amorphous silicon photodiode arrays positioned behind X-ray scintillators that convert X-rays into the visible light. The standard commercial flat panels have the dimensions of 410 mm × 410 mm with a pixel size of 200 μm × 200 μm (2048 pixels × 2048 pixels) and commonly withstand powers up to about 250 keV [22]. Nowadays even 16 mega pixels panels with 4096 pixels × 4096 pixels at a pixel size of 100 μm × 100 μm are offered on the market and optimized for even higher energies than 250 keV.

In comparison with the medical CT, the industrial systems use high intensity X-ray sources and rather long scanning times. The accelerating voltage and the current of an X-ray tube control the X-rays that are produced. The voltage (tens – hundreds kV) determines the X-ray spectrum and the current (hundreds μA – a few mA) influences the X-ray intensity without changing the X-ray spectrum. Both parameters determine the finite focal spot size of the X-ray which is important for high magnification settings to avoid blurred images and the degradation of resolution. Generally speaking, the focal spot size is smaller when a lower power is applied, however, it limits the usage for denser materials such as metals.

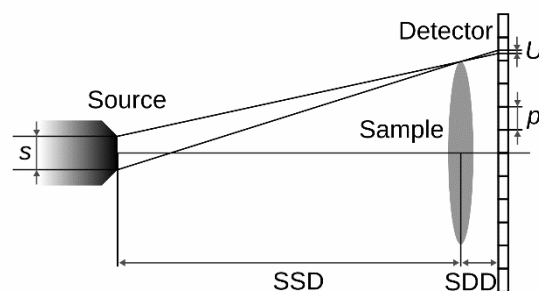


**Fig. 1:** Typical industrial system consists of a stationary X-ray source, a flat panel detector and a rotatory table. SSD stands for the source–sample distance, SDD stands for the sample–detector distance. U shows a geometrical unsharpness at the detector with a linear pixel size p due to a finite focal spot size s (adapted from [23]).

### CT in industry

Even though actual CT devices exist from 1960s, this technology only started getting into the industry at the turn of the millennium. This is thanks to the development of their main components which makes the system capable of a high-level accuracy of measurements and

an acceptably low scanning time (approx. an hour). CT has emerged in the industry as a powerful solution both for the dimensional and the material quality control in a single scan. Gradually it has found its place in the non-destructive testing, the material analysis, the dimensional metrology and the defect analysis both in the research laboratories and the industrial companies within the last decade and the market is still growing [24].

The automotive industry where CT is mainly involved in dimensional measurements, the research and the development, simulations of the reaction tests and the understanding of car component failures is the leading segment with 52% of the market share [25]. The aerospace and aviation industry, which mainly inspects electronic sensors and rotor blades is the second biggest segment with a 25% market share. The electronics industry shares 9% of the market using CT for the inspection of solder joints, bond wires, small motors, batteries and electrical connectors. 7.4% of the market is shared by life-critical medical devices, i.e. the surgical needles and implants checking. The remaining 6.6% is shared by other industrial areas, such as foundry castings, and power generation. The global market registers more than 10 key manufacturers of industrial CTs [26]: Waygate Technologies (former GE Inspection Technologies), Carl Zeiss Industrial Metrology, Wenzel Group, YXLON International, Nikon Metrology, North Star Imaging, Diondo – X-ray systems and services, Werth Messtechnik, Bruker Corporation, RayScan Technologies, RX Solutions, Rigaku Corporation, Shimadzu Corporation.

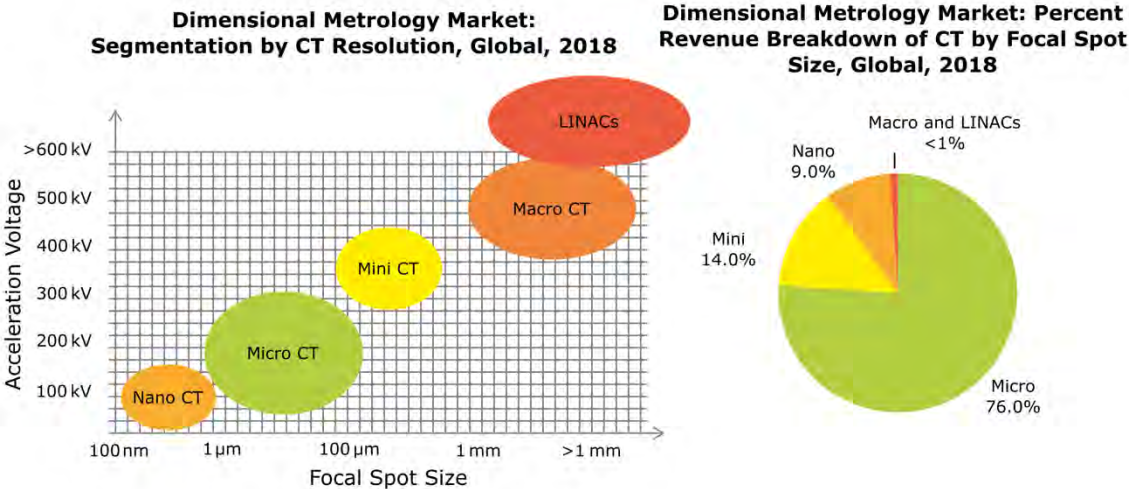


Fig. 2: Classification of industrial CT (adapted from [26]).

**Classification**

The industrial CT systems are usually marked by a specific term to enable a direct identification of the system and its capabilities (e. g. micro-CT). While the classification given by Kastner [27], perhaps a more complex and user-friendly one, helps to understand what spatial resolution can be reached and what object size can be addressed by a particular system, there is another option of the classification. It is strictly related to the parameters of the X-ray source [26], i. e. the focal spot size and the accelerating voltage, as the focal spot size of an X-ray tube is particularly important to determine the spatial resolution and the accelerating voltage determines the maximum penetrable material thickness. However, such a sorting of the CT

systems is approximate with no clear definition which is often abused by the producers to increase the attractiveness of the product on the market (see Fig. 2).

Nano-CT systems are equipped with X-ray tubes with a spot size smaller than 1  $\mu\text{m}$ . They can reach the resolution of hundreds of nanometres and they are characterized by a small field of view. To provide the appropriate spot size small energies of the X-ray source (acceleration voltage in the range 50 – 160 kV) are used. Nano-CT systems are suitable only for small samples (less than 1 mm in diameter) and light materials, such as polymers or carbon composites. These systems can also use detectors with a small pixel size (CCD or CMOS technology) and add optical lenses (Rigaku Nano3DX) for magnifying the image onto the detector plane (see Fig. 3). The term “nano-CT” is often criticized by the scientific community, since in nanotechnologies the dimensions considered nano usually range from a few to hundreds of nanometres maximum, nevertheless, this term is historically established in commercial or industrial CT systems. To avoid misinterpretation the term “submicron-CT” may be used. There are some systems providing a resolution in tens of nanometres, however, they are connected with the synchrotron source and they are usually marked respectively (e. g. sCT or SRCT) [27]. Among the lab-based systems, the ZEISS XRadia system is the only exception providing a resolution under 100 nanometres by using a zonal plate [28].

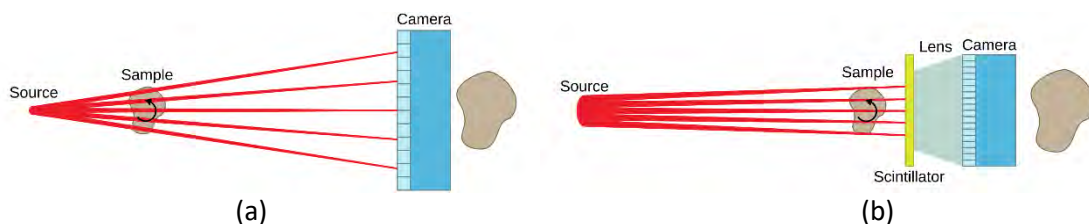


**Fig. 3:** CT components arrangement: (a) Conventional geometry using a geometrical magnification, (b) near-parallel beam geometry (adapted from RIGAKU marketing materials).

Regarding the availability and applicability, micro-CT (or  $\mu\text{CT}$ ) is the most widespread type of the industrial CT systems with up to a 76% market share which made revenue of \$76.7 million in 2017 [26]. It has a focal spot size between 1 and 100  $\mu\text{m}$  and an acceleration voltage of 80 kV – 300 kV. X-ray tubes with a tungsten anode and an adjustable acceleration voltage enable penetrating most of the used non-metal and metal materials such as plastics and glass or aluminium alloys, cast iron and steel, respectively.

Mini-CT systems have the X-ray focus spot size in the range from 100  $\mu\text{m}$  to 1 mm and an acceleration voltage of 320kV - 450kV. It is characterized by a high stability and wide beam angles. Key applications include electronics, food, pharmaceutical inspections, and the industrial non-destructive testing.

The macro-CT uses X-ray tubes with a spot size above 1 mm and an acceleration voltage above 450 kV. These tubes are usually composed of two single X-ray tubes positioned opposite each other (see Fig. 4), which doubles the acceleration voltage of the used tube, i. e. to 450 kV ( $2 \times 225$  kV) or 600 kV ( $2 \times 300$  kV). Such sources are used to analyse big steel castings, nickel alloys and concrete. However, due to a big spot size (above 1 mm) they do not provide a very good resolution.

The last group of the systems uses a linear accelerator (linac-CT) with the acceleration voltage of 1 MeV – 24 MeV and a focal point above 1 mm. With such parameters, the technique is

applicable mainly in the analysis of large objects and dense materials, e. g. engine blocks and big products of additive manufacturing.

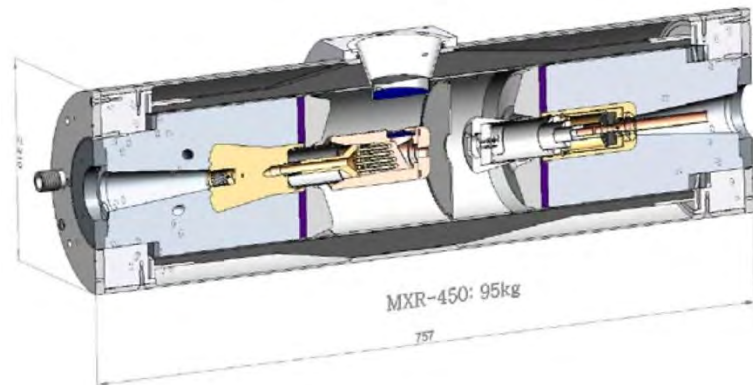


*Fig. 4: Scheme of a bipolar minifocus X-ray tube (adapted from[29]).*

### *Voxel resolution vs spatial resolution*

Among the characteristics expressing the accuracy of CT machines and the quality of the CT data, the resolution is the main used parameter. If it is not specified, the term resolution usually refers to the voxel resolution which, in tomography, is mainly given as a linear dimension of the voxels. A voxel is a volume element in a regular grid of a 3D space. It is an analogy to a pixel representing the value in a 2D space. Although a voxel is a volume element and volumetric units (e. g.,  $\mu\text{m}^3$ ) should be, thus, used, also one-dimensional units (e. g.,  $\mu\text{m}$ ) are often used in the literature. In such case, a cubical shape of the voxel is assumed and its dimension is defined by the dimension of the edge.

The voxel resolution characterizes the possibilities of a machine. It is calculated only from the machine geometry, i.e.  $V_x = P/M$ , where  $V_x$  is a voxel size,  $P$  is a linear pixel size and  $M$  is a magnification given by a ratio of the source-detector to the source-object distance (Fig. 1). Thus, it does not reflect the possibilities of the machine regarding the detection of microscopic features of the object or their detectability in the data. For this purpose, the spatial resolution is being determined by various approaches. One of them uses a QRM (Quality Assurance in Radiology and Medicine GmbH) Micro-CT Bar Pattern Phantom [30] which consists of two perpendicular silicon chips with a bar and a point pattern with the diameters ranging from 5 to 150  $\mu\text{m}$  (Fig. 6(a)). The resolution is then determined based on the smallest distinguishable pattern in the real CT data. Another option is to proceed according to the American Standard Test Method - ASTM E1695-95 [31] and determine the resolution as a percentage from a module transfer function of a measured circular object. The resolution depends on the used method or the reference phantom and the details of its determination should always be included.

The influence of the voxel resolution is demonstrated by the imaging of an aluminium alloy turbine wheel which contains a crack in one of the blades. This blade was scanned with three different voxel resolutions. Although the defect is less than 10  $\mu\text{m}$  wide, it could be captured even with a three times worse resolution (see Fig. 5).

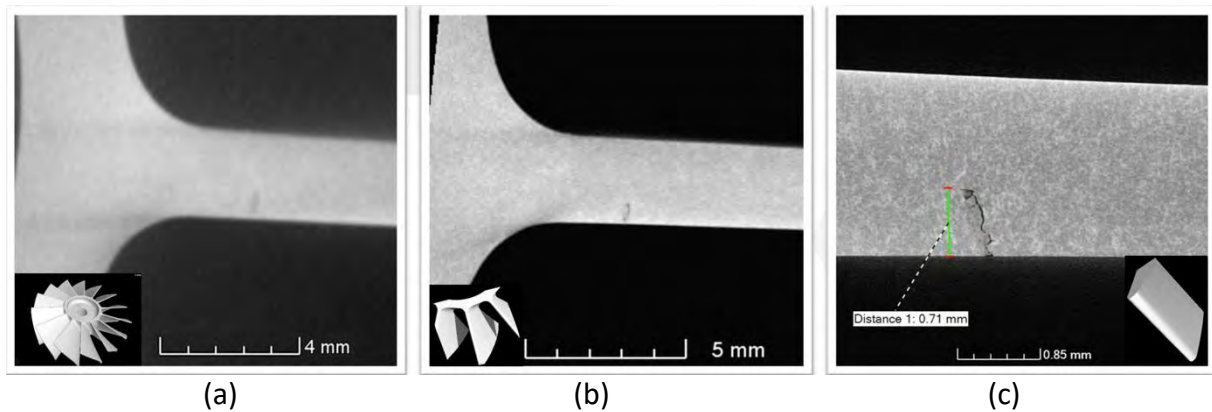


**Fig. 5:** Aluminium turbine blade CT scans at (a)  $70\ \mu\text{m}$ , (b)  $30\ \mu\text{m}$ , (c)  $7\ \mu\text{m}$  voxel resolution. Performed by GE phoenix v|tome|x L240 and visualized by enhanced contrast in Volume graphics software. 3D render in the bottom corner shows scanned areas of the turbine.

### Quantitative CT

With the possibility to digitise both the inner and the outer structure of the object, one of the aims of the CT analysis is to provide quantitative information, i. e. to numerically describe the analysed object, to measure its dimensions, to define its inner structure or to quantify its material composition. Due to different calibration approaches and the information obtained, I would like to divide the quantitative CT (QCT) into a density-based QCT and dimensional-based QCT in the following paragraphs.

The density-based QCT deals with the determination of the volumetric mass density of an object from the CT numbers. This was first mentioned in relation with a medical examination where it was used, e. g. to measure a 3D bone mineral density in a spine and a hip [32], or to separately analyse a cortical and a trabecular bone [33]. For this purpose, the intensities (or so-called CT numbers) in medical systems are given in the Hounsfield units (HU) defined by the X-ray attenuation coefficient of water which is contained in the vast majority of every organic tissue. It means that the water has a value of 0 HU, the air has -1000 HU, and bones have a value in the range of several hundreds to several thousand HU [3].

The micro-CT systems do not utilize the HU scale because, unlike medical CT, they are designed for variable materials, using a wide range of voltages and spectra filters which makes the system calibration very demanding. Furthermore, a micro-CT equipped with a large-area detector uses a cone beam of X-rays introducing variabilities in CT numbers across the whole dataset [34]. It means that the same material of an object appears with a slightly different greyscale values depending on its position in the dataset. However, for example in the micro-CT analysis of laboratory animal bones or in a mechanical stress simulation on bones the knowledge of the material density is required. Thus, the micro-CT systems are calibrated by a phantom including cylindrical inserts (Fig. 6(b)) of a known calcium hydroxyapatite concentration and the CT numbers are recalculated to a  $\text{g}/\text{cm}^3$  scale.

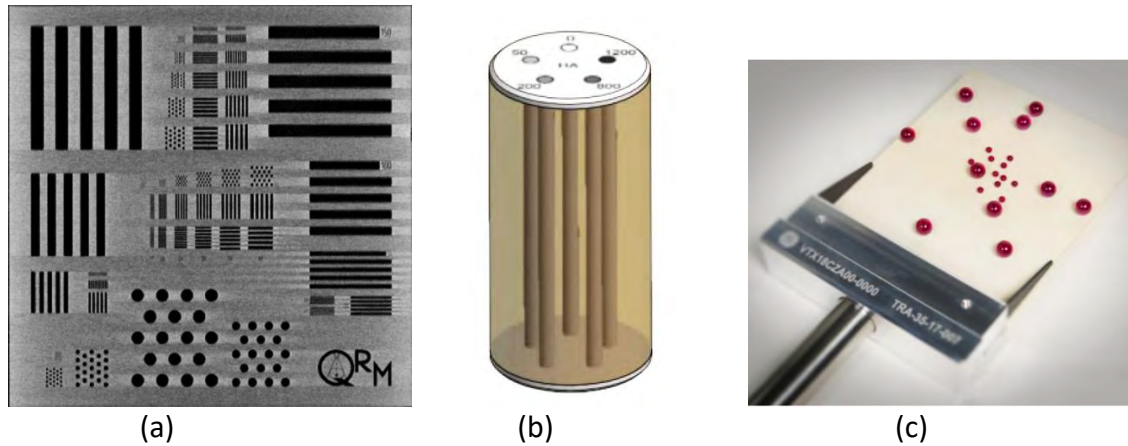


**Fig. 6:** CT phantoms: (a) CT slice of a bar pattern (adapted from [35]), (b) Hydroxyapatite composite for a bone density calibration (adapted from [35]), (c) Ruby plate from Waygate Technologies (adapted from [36]).

The dimensional-based QCT refers to the industrial micro-CT applications associated mainly with dimensional measurement [37, 38], the porosity [39], the fibre orientation [40] or other morphological analyses. This type of QCT demands for knowledge of the voxel size true value and for the suppression of the variability of all factors influencing CT measurements (see Fig. 7). Nowadays, commercially available metrological systems can be found with their properties verified in accordance with the only respected VDI/VDE 2630-1.3:2011 guideline [41].

Such a CT system needs to be both consistent and accurate [2]. The consistency implies that the CT data do not change if the same object is scanned over time and the measurement is repeatable. Therefore, these devices work under strict air-conditioning conditions and voxel size calibrations are performed regularly by reference phantoms. The calibrations, thus, provide the traceability of the metric scale through the distances of ruby balls (Fig. 6(c)) measured by a tactile coordinate measurement machine. The accuracy is improved by corrections of mechanical imperfections of CT components, e. g., by a precise determination of the source-detector distance or by software corrections of the detector large-area curvature [42].

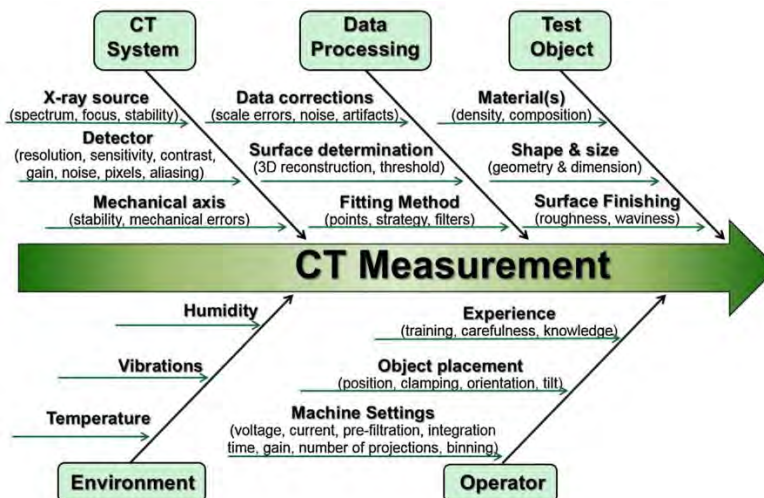


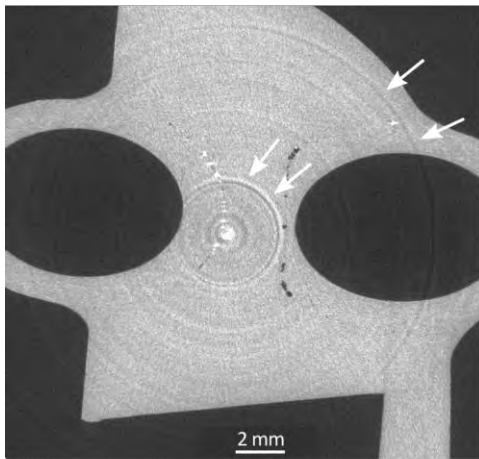
**Fig. 7:** Main factors influencing the uncertainty of CT measurements (adapted from [43]).

### *CT artefacts*

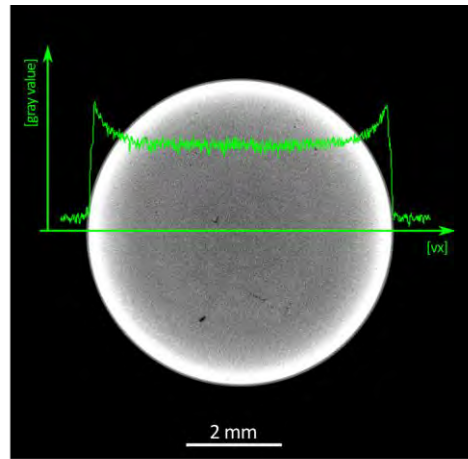
Despite all the effort to make a mechanically precise machine, the CT data are still influenced by the presence of tomographic artefacts [44, 45] which distort the reconstructed CT data by streaks, shading rings and bands. It brings errors both to the density and the dimensional quantification. Among the most frequently mentioned artefacts there are ring artefacts, beam hardening artefacts, cone beam artefacts, metal artefacts and scatter radiation artefacts [37, 46].

Ring artefacts appear as concentric ring-like features superimposed on the displayed scene and they degrade the resulting image (see Fig. 8(a)). They are caused by uncalibrated or imperfect responses of individual pixels of the detector. Artefacts which are presented by a non-uniform distribution of the intensities of a homogenous material, a so-called cupping effect (see Fig. 8(b)), or by shadings between two dense objects are the demonstration of the beam hardening. It is related to the use of a polychromatic X-ray beam which passes through an object and gets attenuated at a different rate depending on a photon energy, i.e. low-energy photons attenuate at a faster rate than high-energy photons. The use of a cone beam negatively influences the structural information by blurring the edges of horizontal flat structures. This phenomenon becomes more significant with the increase of the cone angle. For this reason, it can usually be seen mainly at the top and the bottom of the reconstructed volume (see Fig. 8(c)). This occurs because the cone-beam CT systems with a circular acquisition trajectory do not fulfil conditions for an exact tomographic reconstruction, except for the central plane of the cone. Scatter artefacts result in a high background signal and in a general loss of contrast (see Fig. 8(d)). X-ray photons interacting with objects can deflect from the original path. These scattered photons alter the detected signals which deviate from an ideal measurement of the X-ray absorption. Metal artefacts are visible as dark stripes in between the metal parts, and as bright stripes on the non-metal material (see Fig. 8(e)). They occur when the signal from behind the highly absorbent parts recorded by the detector is close to zero.

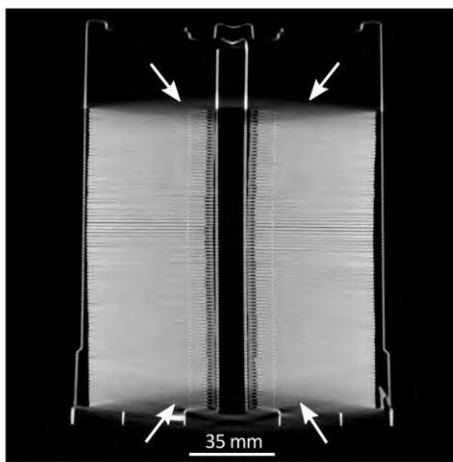
The recognition of the artefact type is one of the necessary skills of every CT operator. In some cases, hardware strategies are applied to prevent or at least minimize artefacts occurrences in the CT data. These strategies are based on a suitable sample orientation, the right settings of the X-ray tube with the filter, the detector calibration, or a proper tomographic acquisition process. They are adopted with regard to the specific composition, size and shape of the object and also to the task of the analysis. The other artefact-eliminating approaches are based on a post-processing of the reconstructed data, which means that mathematical or image processing methods are implemented on the projection or the CT data to get rid of the rings, streaks, double edges, non-uniformity or noise in the cross-sections.



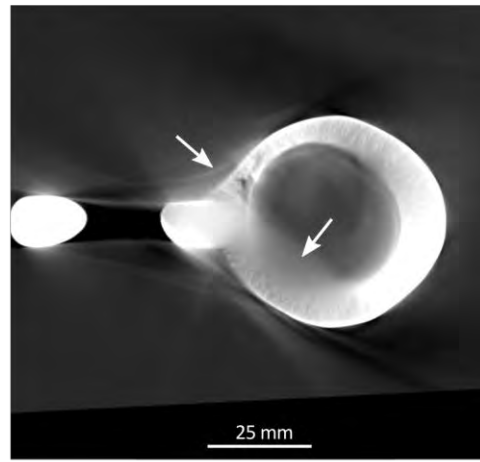
(a)



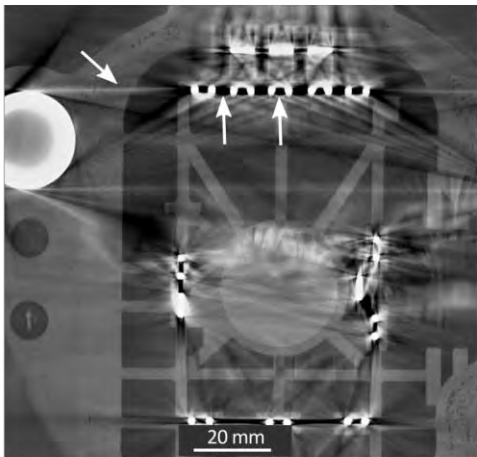
(b)



(c)



(d)



(e)

**Fig. 8:** Tomographic artefacts marked by arrows and a grayscale profile in equalized images: (a) plastic parts with ring artefacts, (b) a steel tensile test sample with beam hardening artefacts, (c) a pack of CD discs with cone beam artefacts, (d) a bronze vase with scattering artefacts, (e) a plastic part including metal pins with metal artefacts - bright stripes in plastic and dark regions among the pins.

## 4. EXTENDING OF THE CT IMAGING CAPABILITIES

This part of the work is dedicated to the commentaries of papers focusing on the improvement of the X-ray micro- and nano-CT systems performance and their imaging regime. It discusses advanced techniques which do not use an altered hardware of the CT station but which move the limits of the scanning of challenging samples or enhance special applications based on innovative sample preparations, special acquisition procedures or image post-processing methods.

One of the advanced techniques is the phase contrast imaging (PCI) which is used for the imaging of X-ray low absorbing samples, such as fine polymeric structures, light material composites or organic soft tissues. This phenomenon is very well known from synchrotron devices [47, 48] using the X-ray coherency, a high flux and long sample-detector distances. Despite employing polychromatic and much less coherent X-ray sources, the PCI has become available on the lab-based CT systems in the form of the propagation-based imaging. This method is the simplest implementation of PCI which does not require any additional components such as Talbot-Lau grating [49] and which only requires a sufficiently prolonged source-detector distance. The change of a phase is detected in the intensity image in the form of an edge enhancement. The amount of the phase change is then calculated by a phase retrieval algorithm [50] which practically removes the edge enhancement and increases the contrast in the CT data.

This phenomenon was studied on a Rigaku Nano3DX nano-CT system which is a part of the CT laboratory portfolio at CEITEC. This device is a unique system using optical magnification, a small effective pixel size (270 nm) of CCD, a high flux X-ray tube with a rotatory target and a selectable X-ray spectrum of Cr, Cu or Mo material. It uses a near-parallel geometry (see Fig. 3). This arrangement is close to the properties of a synchrotron device and PCI is, thus, reachable more easily than with the standard lab-based systems. In this article [I] we have formulated a combination of three criteria to theoretically evaluate any system capability to get a propagation-based PCI. These criteria serve to check the near-field imaging regime, the degree of coherence of the system and the avoidance of the geometrical unsharpness. We determined specific settings to enable the Nano3DX to reach PCI and these settings were consequently verified by real measurements performed at given critical settings. A carbon fibre-reinforced polymer with a fine structural composition was chosen for this experiment. The quantitative evaluation of the PCI impact was performed on the original edge-enhanced data as well as on the data processed by the phase retrieval algorithm.

Nevertheless, to a lesser extent PCI is also reachable on standard CT devices equipped with a flat panel detector and a polychromatic micro-focus X-ray tube. We tested these properties by a HeliScan MK1 micro-CT device from Thermo Fisher Scientific [51]. When using this system, PCI is even more challenging since it uses a wide cone ( $>60^\circ$  angle) to obtain a higher flux of the X-ray beam. On the other hand, it uses an iterative reconstruction with an auto-focus algorithm [52] which improves the quality of the reconstructed data by correcting the geometrical distortion of the projection images [53]. Although this system does not allow increasing the source-detector distance too much which is one the assumptions to reach the PCI, a small edge-enhancement phenomenon has been recorded in the data. In the article [III], we tested the selected configurations of the system on real measurements of a similar carbon

fibre-reinforced polymer as in the previous work. The image improvement before and after the phase retrieval was quantified. These experiments were used for an implementation of PCI on Heliscan to visualize the polymeric hydrogel and to analyse its spongy structure in 3D.

Another trend in CT is to correlate the 3D data with 2D images acquired by surface imaging or analytical techniques. The correlation is used for a standardization of the CT data post-processing, a combination of structural and material information to get a more complex sample description or a verification of the CT data information. In this area, we presented a method combining the micro-CT data with an elemental map to acquire the spatial distribution of selected materials and their volume [III]. This perfectly fits the needs of a geological analysis. The elemental map was performed by the laser-induced breakdown spectroscopy (LIBS) [54] which offers the benefits of an on-line analysis in the air at the atmospheric pressure, with little or no need of a sample preparation and virtually with no limitations regarding the sample size. The published method connected the data acquired by both techniques through one appropriate flat surface created by cutting and grinding of the sample. At first, the sample was digitised by CT and LIBS was then applied on the surface. This procedure ensures that the top CT slice of the object corresponds to the LIBS map, thus, no advanced techniques for seeking the right section in 3D are needed. Several image processing steps were suggested to unify the different data character enabling the assignment of the elemental map to the grayscale CT slice. The assumption for this approach is that all the materials present in the sample are contained in the mechanically prepared surface. This procedure was applied to copper–nickel ores from the northwest flank of the Triassic basalt trap formation of Siberia because of their chemical heterogeneity and their different X-ray absorption properties.

The correlative approach was also used for a porosity analysis of metal samples presented in [IV]. In additive manufacturing (AM) the quality of the process and final products needs to be checked because the internal defects often appear and worsen the mechanical properties of the parts. The porosity analysis by CT indicates the quality of the sample and helps to optimize the production process. However, the porosity values may vary due to the CT data quality fluctuation among individual scans and inconsistent procedures in the data processing. Our method uses the microscopic image as reference data to choose the right pore segmentation strategy for the CT data. The segmentation is based on a global thresholding and either an automatic or a manual selection of the threshold value is influenced by several aspects, such as the voxel size, the noise in the CT data, the operator's experience, the visualization setup and the character of the defects (shrinkage cavities, cracks, or an unmelted powder). The microscopic image provides a higher resolution and a higher pore-material contrast than the CT data and pores can be reliably segmented. By using the top CT section which corresponds to the microscopic image of the sample surface the threshold selection for the CT data can be determined. This way of the CT porosity calculation is then reproducible and enables an objective comparison among the samples measured in a different time, CT systems or laboratories.

Thanks to a non-destructive imaging of a complete volume of animal tissues at a micrometer resolution, micro-CT has found an indispensable role also in biology. The accurate visualization of 3D structures is used for comparative, functional, and developmental studies of the animal morphology [55]. These studies are often performed on laboratory rodents such as mice or

rats which have become a convenient model for studying various human diseases, treatment procedures, injury regenerations or the embryonic development. The size of these animals (tens of millimetres) also fits the micro-CT device well and allows reaching a sufficient resolution (micrometre level) for an internal structure study. CT is a widely used technique in the analysis of mineralised tissues like bones or teeth [56, 57] as they have a sufficient absorption to reduce the intensity of the X-ray radiation generated by micro-CT systems. Soft tissues like muscles, fat, tendons, blood or ligaments have a low absorption and they are practically invisible in the CT data. This is usually solved by applying a contrast-enhancement agent into the samples which, however, limits their use only to ex-vivo experiments. The advantage is that various tissues can be differentiated in the CT data because they are differently impacted by the contrast substances. Several contrast agents mostly based on iodine, osmium or phosphotungstic acid (PTA) are used [55].

The tissue differentiation contrast is crucial for an organ recognition or a visualization of specific structures within the organ. However, the result of contrasting depends on the concentration of the substances, the application time, the sample fixation, storage media and the age of the sample. We have been experimentally optimizing a contrasting protocol **[V]** for a visualization of mouse brain structures. This was motivated by several studies involving CT as a crucial tool, e. g. a brain tumour research [58], a study of the Alzheimer's disease [59] and a research focused on the damages caused by a stroke [60]. The tested protocols showed a big variability in the resulting contrast of the image. The most contrasting and sharp edges of anatomical structures were obtained by the iodine solution which also provided a fast preparation of the sample. The micro-CT data were confronted with post-mortem data obtained by MRI which is a widely used technique in this field. In the comparison of several corresponding coronal sections the micro-CT data showed a considerably stronger tissue contrast and a higher resolution. An isotropic voxel (in our case  $6\ \mu\text{m} \times 6\ \mu\text{m} \times 6\ \mu\text{m}$ ) in micro-CT unlike a rectangular cuboid voxel (in our case  $27\ \mu\text{m} \times 27\ \mu\text{m} \times 500\ \mu\text{m}$ ) produced in MRI enables an arbitrarily oriented section view. These benefits together with a 5 times faster scanning time bring the micro-CT technique closer to a routine use in neurobiological experiments.

The main advantage of the CT imaging is an ability to check the individual organs morphology. Firstly, the organ must be segmented and extracted from over a thousand grey-scaled slices while the method of segmentation needs to be set according to the presentation of the organ tissue in the CT data. We have established a complete workflow **[VI]** for a 3D reconstruction of a mouse embryo nasal capsule. This work was motivated by a craniofacial development research (Laboratory of Prof. Adameyko, Karolinska Institute) which deals with shape changes during initial skeletal formation and growth. The workflow contains the PTA-based staining protocol and introduces the segmentation process and the advanced data processing for creating a 3D model. Furthermore, the nasal capsule was printed up to an appropriately scaled physical object using additive manufacturing. This allows an intuitive exploration and extends observation possibilities of the samples by enabling, e. g. to view them from all sides, or to sense the surface roughness and wall thickness. This feasibility study demonstrates that a combination of CT and 3D printing presents a new dimension of the perception in biology.

Once the virtual 3D model is created, the question how to share and communicate it with others usually comes up. It is challenging for all common computers and free software

platforms. Micro-CT files usually in the size of gigabytes cannot easily be transferred on the internet and the 3D rendering requires a specific licenced software. For this reason, we have provided a pipeline [VII] for an interactive visualisation and interpretation of the 3D micro-CT data based on a 3D portable document format (PDF). This \*.pdf file can be sent via an email (having the size of a couple of megabytes), is readable across all operational systems using a free PDF reader and it allows the operator to adjust the view of the 3D model using a computer mouse. The pipeline is built on an accessible software which transforms a 3D surface from the CT data into the 3D mesh geometry format. The 3D PDF document then allows fundamental operations in the 3D space known from CAD programs, such as the magnification, rotation, movement or visibility adjustment of individual parts. This approach has completely changed not only the communication with the cooperative biologists, but it has also enabled sharing a 3D content online via the data clouds of scientific journals.

The future of CT in the development biology is in obtaining a complete structural information from a single measurement. This information helps for example to unravel the connections of bones and muscles which are both part of the growth process of the animal. Another considerable effort in the utilisation of CT in biology is to improve its resolution capability at the level of cells. Both trends were dealt with in our methodological paper [VIII] focused on the analysis of a re-developing salamander limb which is a key model organism for vertebrate regeneration studies. A micro-CT measurement with a 2.5  $\mu\text{m}$  voxel resolution was used to map the limb muscle sizes and shape together with a joint cartilage of three different stages. The resolution was then pushed down to 1  $\mu\text{m}$  using the phase-contrast synchrotron X-ray computed tomography (SYRMEP beamline, Elettra Synchrotron Trieste, Italy). This allowed us to distinguish individual cells (so called chondrocytes) in the cartilage of the developing limb. Open-source software such as ImageJ or Pore3D as well as professional industrial modules like fibre orientation analysis were proposed for the processing procedure. The cell number, the density of occurrence, their polarization and zonal distribution were evaluated. For the first time a complex view including muscles, the cells polarity and the cartilage geometry together was obtained in a single 3D volume. The comparison of the synchrotron and the micro-CT data suggests that with a further development such experiments should be feasible using the conventional laboratory CT systems in the near future.

The improvement of the data quality by a correction of the tomographic artefacts is another topic in the CT research. Ring artefacts are one of the most common type of the artefacts discussed in nano-CT systems. Although the flat-field correction is commonly realized, many of these artefacts remain. The micro-CT systems, thus, randomly shift the flat panel detectors for each angular position during the acquisition. However, this is hardly applicable in the nano-CT systems which are using detector pixels of a small size and the arrangement of an exact detector shift is demanding. Therefore, an image-based processing method is the only option of the artefacts correction. For this purpose, we have introduced a novel ring artefacts reduction procedure [IX] which promises a complete removal of rings in the nano-CT systems with a maximum image sharpness preservation. The procedure differentiates between two types of ring artefacts in the image. Both the detection and the correction are then adapted based on the appearance and the pattern of each type of the artefacts. Each type is addressed separately in the sinogram domain which is beneficial for two reasons. The ring artefacts are displayed in the form of stripes, which are easily detectable, and the detection procedure is

not negatively influenced by the tomographic reconstruction. The proposed procedure was optimized and tested on different types of data (real, simulated), detectors (CCD and CMOS cameras), and samples (polymer, glass) as well.

## 5. APPLICATIONS IN VARIOUS RESEARCH FIELDS

In this part of the work, papers where CT was mainly applied as a means for answering questions from other research fields are commented. This does not exclude the use of innovative methods, however, in this case the methodology is not the main focus of the publications. Each paper is commented by a brief description of the research context, the motivation and highlights of the CT implementation, and my contribution.

### *Developmental biology*

The CT analysis was first included in the biological research in a collaboration with the laboratory of Prof. Igor Adameyko (Karolinska Institute, Stockholm). The laboratory was exploring the developmental processes responsible for the shaping of the face which is defined in the embryonic stage and it depends on the clonal dynamics and the coordinated and directional cells behaviour. Any defects in such cellular processes can affect the developmental program leading to congenital defects. These processes are studied by a clonal analysis, computer simulations, mouse mutants, and a microscopic imaging. Despite the CT capabilities being far from looking at the cell dynamics, CT was involved in showing morphological differences of the digitised faces by comparing the mutant (an organism with a “knock out” gene, which is primarily used to understand how a specific gene influences the general shape) with a wildtype embryo. These experiments were performed on mice as model organisms for humans. In the study [X], the heads of 15.5 days old mice embryos were contrasted by the PTA solution and scanned with a 5  $\mu\text{m}$  voxel resolution. Simple measurements of the face dimensions were performed in the micro-CT sections to quantify its proportions. These proportions indicate that in comparison with the wildtype littermates the mutant embryos have a short snout and a wider face which is also clearly visible in the 3D reconstructions of the heads. This first contribution of our CT expertise in such a study lead to numerous cooperations in the field of biology and initiated the development of an advanced data analysis.

During the growth and shaping of the face cartilaginous structures are formed before the bone itself. The lateral expansion of curved cartilaginous sheets and the control of cartilage thickness are not connected in the growth mechanism [XI]. The geometry and the positioning of the overall facial shape are mainly driven by the shape of the nasal capsule. Its formation in the face is controlled by signals from the brain and olfactory epithelium [XII]. In both studies, micro-CT analyses of multiple mouse mutants were used to assess changes in the complete 3D anatomy of the face. The key point of a 3D reconstruction of the face is a segmentation of the cartilaginous structure, which is distinguishable, however, not sufficiently to enable an automatic segmentation. Therefore, in this case the segmentation was performed manually by processing thousands of slices which was supervised by a skilled anatomist. To quantify the reconstructed 3D models, a commercial software tool originally designed for the industry was implemented to calculate the cartilage thickness in the overall structure. Using another industrial tool, the actual-nominal comparison, the differences between the mutant and the wildtypes were revealed and growth increments between individual developmental stages were determined. To perform a correct shape comparison, a strategy of a 3D model alignment was defined.

Along with the cartilage, muscles and tendons which ensure the movement of organs are also formed in the embryonic stage. To differentiate the muscle tissue from the other tissues of the internal structure, the PTA-based staining protocol was used. Thanks to this procedure, a CT analysis could be performed to investigate the shape development of extraocular muscles [XIII], which are crucial for a coordinated movement of the eyeballs and for a visual acuity. The insight into the development of the muscle functional unit was gained by the comparison of a wildtype and mutants with an ocular perturbation. All six muscles moving the eyeball were segmented out. The segmentation had to be performed manually with the support of anatomists as the fuzzy edges of muscles did not allow using any automatic procedure. The reconstruction of a muscle group 3D model provided an overview of the muscle position and their quantification. In comparison with the standard confocal microscopy which images only muscles, the main benefit of CT is the imaging possibility of all tissues in one analysis. Therefore, we could examine the attachment points of individual extraocular muscles to the nasal capsule. Moreover, by also imaging the eyeball, the lens and the optic nerve in the 3D context of the head, it was discovered that the eye of a mutant is in a lower position than that of a wildtype sample. To quantify this difference, a software pipeline based on the fitting of geometrical objects was invented.

#### *Biology – diseases*

The quantification of an internal structure of organs can serve to explore the manifestation of a disease or to help its early detection. Our contrast enhanced CT technique was applied to rodent models of Alzheimer's disease [XIV]. This disease is associated with amyloid plaques, small ( $\sim 50 \mu\text{m}$ ), dense aggregates of proteins in the brain tissue which are supposed to be playing a key role in the diagnostics and the evaluation of the disease progress. It was found out that the iodine-based brain tissue contrasting provides a precise CT imaging of the plaques. In our study, the CT measurement was focused on an isolated part of a rat brain (3 mm in diameter) to reach the best possible resolution (a  $3 \mu\text{m}$  voxel size). The occurrence of the plaques (represented by dark spots in the CT data) in the brain tissue of the diseased animal was confirmed in comparison with a healthy brain. These spots were further validated by a standard histological method. In order to precisely correlate the CT slice with a histological section, we used the brain, which had previously been scanned on CT. In addition to a common quantification such as the number, volumes and shapes of the plaques, we quantified also their relation to blood vessels and the mutual distance of the plaques using commercial software tools to understand their patterning.

Another of our works related to a disease study dealt with Alagille syndrome which is a genetic disorder that damages liver. The disease is manifested by abnormalities in the bile duct system which are studied on animal models of diseases. A technique called double resin casting micro-CT was developed for the purposes of this study [XV] which allows the insight into the architecture of bile ducts together with blood vessels. The technique is based on filling both tubular systems with radiopaque resins, creating a cast of the entire tree structure. One type of the resin is injected into the bile ducts, and another one into the blood vessels. Thanks to the different types of the resins, they show up differently in the CT data which makes them easier to distinguish. A 3D analysis of both individual tree systems was designed to determine branching points and to specify individual tubular segments according to the number of

a branching generation. Each segment was quantified by its diameter, volume, length, and tortuosity. To quantify the mutual interactions of these two tree systems several parameters such as their surface proximity, the corresponding branching point distances and the length ratios of the branches were proposed.

### *Animal physiology*

In biology, CT is a widely used technique thanks to the analysis of bones and teeth, where no special preparation is needed and their natural X-ray absorption contrast is used. This was utilized in the exploration of a chameleon dentition [XVI] which is characterized by a unique fusion of teeth with the jaw bone and their junction along the jaw. This makes the dentition very stable, and it prevents individual teeth from falling out. CT was used to study age-related changes in a hard-tissue morphology with a focus on the tooth–bone fusion area during the first days of the chameleon’s life. Special tools of a commercial software were used for the detailed exploration of the teeth. With these tools, the 3D jaw model was clipped following the curvature of the jaw for the purpose of visualizing all teeth together in a cross-section. They also allowed picking a transverse cross-section of each tooth plane perpendicular to this curvature to keep the same view on the teeth. The 3D rendering also showed a varied shape of the teeth along the jaw in accordance with their different functions of food processing. Lastly, the internal tooth cavities were visualized in 3D. This showed that the dental channel sizes and distribution decrease with the increasing age until they completely disappear.

### *Analytical chemistry*

In our work focused on a LIBS depth profiling method [XVII] which enables the investigation of the interface of multi-layered samples, micro-CT served as a calibration tool. Without further destructive sampling, the most critical and challenging task in LIBS depth profiling is to convert the number of applied laser pulses into the depth of the created crater. With this knowledge, it is possible to determine the depth of the interface and the thickness of individual layers. The LIBS depth profiling was performed on a glazed fragment of archaeological ceramics where the glaze layer (containing lead) was easily distinguishable from the ceramic matrix (lead-free) by micro-CT. Several ablation craters were created with a pre-defined increasing number of pulses to determine its relation to the depth of the created craters and the ablation rate. The crater area was scanned with a resolution at a micrometre level, and both the glaze layer thickness and the total depth of the narrow craters of a conical shape were measured. Enabling the measurement of these two characteristics is an added value of CT in contrast with commonly used methods such as the optical profilometry, the confocal microscopy or the contact profilometry.

### *Meteorology*

CT has also proved its important role in a non-destructive exploration of extra-terrestrial materials, the appearance of which is rare on Earth. Meteorites falling through the Earth’s atmosphere are the example of such a material. The CT measurement of three meteorites found in a predicted area of Žďár nad Sázavou (Czech Republic) in 2014 was performed [XVIII]. The common task for CT is to characterize the internal structure, to digitise the shape for the

meteorite flight simulation and to specify the volume of the piece which is important for a bulk and grain density calculation. One of the meteorites was cut in half for the purposes of a scanning electron microscopy analysis (SEM), which created an opportunity to show the structural and material resolution of the state-of-the-art micro-CT based on the correlation with SEM images. Furthermore, the natural porosity of the meteorite was distinguished from the cracks related to erosion processes which helped to discuss the weathering changes after the impact of the meteorite.

### *Geology*

Another of our scientific contributions was motivated by the need of the civil engineering industry to examine limestone as an important raw material of lime and cement. In the process of limestone firing volumetric changes occur and cause a loss of compactness. This phenomenon can be explained by the presence of fluid inclusions which are common in natural minerals. The CT characterisation of the inner structure of limestone [XIX] focused on the amount and the distribution of fluid inclusions determination was applied which could help to predict the limestone behaviour during firing. To digitise the fine structure of the limestone and to detect air cavities and fluid inclusions down to 1.3  $\mu\text{m}$  in diameter the nano-CT system was used. The 3D render of these features was verified by the light microscopy as a standard technique of fluid inclusions imaging. To understand the chemical composition of the inclusions, a 3D material analysis was performed by SEM. Regarding SEM analyses, the CT data were used to define the area also containing inhomogeneities such as Mg and Fe-rich areas, in addition to the inclusions.

### *Restoration*

The non-destructivity of a micro-CT analysis also makes it a very helpful tool for restorers. Our laboratory was involved in an exploration of a 19<sup>th</sup> century treasure chest [XX] which was subjected to a conservation and restoration intervention. As the chest was locked and the key was missing, the inspection of a lock mechanism was necessary. The micro-CT measurement of such a heavy object (60 kg) made of steel with the dimensions of 580 x 392 x 410 mm was very challenging. A complete CT scan of the lock mechanism area situated on the lid of the chest was performed. Although generally, massive steel parts introduce a low quality into the CT data due to tomographic artefacts, in this case it was possible to read the edges of each component and to reconstruct a 3D virtual model of the lock mechanism. A consequent exploration of this model revealed damages of the mechanism and helped to understand the procedure of the chest opening and to obtain the dimensions required for a new key copy manufacturing.

### *Food industry*

The mechanically separated meat (MSM) is often used as a raw material of meat products. It reduces the price of the products, but its presence often degrades their quality as MSM is acquired by cutting off a bone using machines, therefore, it contains a considerable amount of a bone marrow, cartilages and bones. In our paper, CT was introduced as a new detection method of mechanically separated meat based on the detection of bone fragments [XXI] on

the example of a cooked meat product (a salami) containing 50% of MSM. Bone fragments are easily identifiable thanks to their high contrast compared to the soft tissues. This was validated by the comparison with a histological analysis. For a feasible correlation of a microscopy image with a corresponding CT slice a small piece of salami embedded in paraffin was scanned, a 4 µm top layer of which was sliced for the histological analysis. This comparison demonstrated the advantages of CT, e. g., a short analysis time and a non-destructivity, which suggest its potential use for the common examination of final products.

### *Additive manufacturing*

Additive manufacturing, or 3D printing, is a unique technique of producing parts with internal cavities or lattice structures which are impossible to produce with the standard techniques such as machining or casting. CT has become an established method of testing and analysing the additively manufactured parts. Our team was involved in a study dealing with a fabrication strategy of aluminium alloy thin struts made by a laser powder bed fusion technique [XXII]. The struts are part of the lattice structures the use of which leads to the reduction of the weight of the final product, the energy and the manufacturing time needed. However, the effort to minimize the strut diameter puts more demands on the quality in terms of surface roughness and porosity because these can significantly change the mechanical properties of the whole lattice structure. In this work, CT was incorporated to the quality control by using a 3D porosity analysis, which also revealed the distribution of pores, their sizes, and shapes. This information helped to understand the formation of pores and to evaluate the process parameters such as the laser speed, the laser power, and the input energy to the current layer.

### *Tissue engineering*

The CT porosity measurement is also valuable for the characterization of foamlike porous structures. They are characterized by an open, interconnected network of pores. In tissue engineering, these structures are called scaffolds and they serve as a complex temporary cell-supporting material. They mimic both the biological and the mechanical properties of the original extracellular matrix. The scaffolds should fulfil the requirements not only for a suitable porous morphology, but also for the biocompatibility and the degradability in a biological environment. Our laboratory was involved in several studies with such a design using CT as a morphological analytical tool. Various materials with various purposes, e. g., a hydroxyapatite scaffold for bone regeneration [XXIII], a hydrogel for a cultivation of human oral mucosa stem cells [XXIV], and a cryogel as a support for a proliferation of human dental pulp stem cells [XXV] were studied. The CT scanning strategy was adapted for each experiment to reach a sufficient resolution. In the case of hydrogel and cryogel, nano-CT with a phase contrast imaging was applied and the sample size was reduced (down to 1 mm in diameter) for the visualization of such a fine structure. Moreover, the sample was lyophilized to achieve a better tissue contrast and to prevent any movement due to the drying process. The digitised 3D structure was carefully characterised by the total open porosity, the count of the pores, the wall thickness or the specification of the most frequent pore size and interconnecting pore window size. All these analyses were adapted from commercial software tools of Volume Graphics or Avizo softwares.

To better understand the behaviour of cells while interacting with 3D biomaterials soft biopolymeric scaffolds seeded with stem cells were examined [XXVI]. The lab-based nano-CT was introduced as a tool capable of visualizing stem cells in the whole volume of a porous collagen scaffold in one measurement. By using a special staining protocol with osmium tetroxide, a high resolution (a 540 nm voxel size) and a phase contrast imaging, it was possible to see not only the cells on the scaffold surface but also those integrated in the inner structure. These findings were validated by correlating a SEM surface image with a CT 3D render. However, the segmentation of the scaffold and the cells CT data is sensitive to the selection of optimal thresholding and it still makes the quantitative analysis challenging.

Last but not least, our laboratory also contributed to several studies only by digitising inner or outer structure of samples without a further participation in the analysis. These studies demanded an inventive approach in terms of, e. g., a sample preparation for the CT measurement, a secure fastening of a valuable and unique sample or tricky CT machine settings. The quality of the micro-CT data plays a big role in the assessment of a bone-implant biomechanical interaction performance [XXVII]. In the case of this study, our laboratory performed a measurement of a hydroxyapatite phantom simultaneously with a human cranium sample. The phantom images were used to determine the bone mineral density, which is an important input to create finite element models of a bone interacting with the fixation-screw of a cranial implant. The simultaneous CT measurement of both guarantees the same quality of the density calibration. Moreover, a mounting procedure of six long bones together was come up with to make the scanning of a large amount of them cost and time effective [XXVIII]. The mounting was made of a light material to preserve the original contrast of the bone in the data. This procedure was used to digitise 86 non-adult femora and to estimate the error of the methods in deriving periosteal and endosteal contours from mid-shaft cross-sections.

## 6. CONCLUSIONS

The habilitation thesis provides an overview of a scientific research work in the field of X-ray computed tomography from the last 8 years. The work reflects the activities within the laboratory at CEITEC Brno University of Technology (BUT), which was established from zero, simultaneously with the establishment of the CEITEC infrastructure. The laboratory is using the state-of-the-art CT systems of global manufacturers and the top professional computational tools with the aims for a deeper insight into the principle of the CT devices. It combines participating in the development of the devices through the position of an application laboratory and gaining practical experience with CT measurements and the data analysis via a daily-based cooperation with the industry. Students of various study fields and degrees are involved in the research projects. All these aspects brought a unique set of experience and knowledge which impacted the solutions of the research projects presented in this work.

The CT technique is specific in its applicability in any scientific field, where the imaging of the internal structure of the object is needed. Working with CT is, thus, predisposed to a constant interdisciplinary cooperation, where it is necessary to understand the topic and synchronize the possibilities of the imaging with the demands of the sample analysis. In this work, the implementation of CT as a new technique is demonstrated in several areas. The obtained data were mostly compared with standard microscopic techniques, which also allowed the validation of the CT data. In some of the cases, the correlation of the data was directly used to specify the region of interest or to obtain complex information about the sample. For this purpose, the wide range of the in-house equipment of CEITEC BUT was used. Although CT has no ambition to completely replace existing analytical techniques, it brings new important information and the visualization of the internal structure. Therefore, it has established itself very quickly among the commonly used tools.

The initial ideas of CT imaging improvement came from the work on these individual applications and also from the cooperation with the CT manufacturers. The improvement methods were mostly focused on achieving a high resolution, a better contrast, or on enabling an automatic segmentation of the structure. Due to the impossibility of interfering in the hardware of commercial systems, the effort was put into the influenceable steps, e. g., the sample preparation, the scanning method and the data processing. These steps were most successfully connected in the field of biology, in which I see the greatest focus and impact of my work. In my opinion, the success is based on a combination of mastering the preparation of biological tissues (the contrasting protocol of soft tissues) and skilfully using professional industrial tools (the CT device, the software, computing stations), which are two attributes that usually do not occur together. In this sense, we managed to take advantage of the potential of CEITEC's multidisciplinary background and the environment of a university city of Brno.

In conclusion, the goals of the habilitation thesis were completely fulfilled. Within a few years, our laboratory has earned an international reputation and the CEITEC BUT can be classified as one of the major institutions in Europe involved in the development of the X-ray computed tomography.

In my future work I would like to focus on the current trends in the field of CT, i.e., the characterization and improvement of CT devices for the metrology, the battery cells analysis, the development of a dual-target CT method and the involvement of a high-energy CT based on a linear accelerator in the industry and the material research.

## 7. COMMENTED PAPERS

- [I] D. Kalasova, T. Zikmund, L. Pina, Y. Takeda, M. Horvath, K. Omote, J. Kaiser. Characterization of a Laboratory-Based X-Ray Computed Nanotomography System for Propagation-Based Method of Phase Contrast Imaging, *IEEE Transactions on Instrumentation and Measurement*, 69 (2020) 1170-1178.
- [II] D. Kalasová, A. Břínek, M. Šlouf, M. Dušková-Smrčková, T. Zikmund, Z. Patáková, J. Kaiser. Wide-cone angle phase-contrast X-ray computed tomography of synthetic polymer materials, *IEEE Transactions on Instrumentation and Measurement*, (2020) 1-1.
- [III] D. Prochazka, T. Zikmund, P. Porizka, A. Brinek, J. Klus, J. Salplachta, J. Kynicky, J. Novotny, J. Kaiser. Joint utilization of double-pulse laser-induced breakdown spectroscopy and X-ray computed tomography for volumetric information of geological samples, *Journal of Analytical Atomic Spectrometry*, 33 (2018) 1993-1999.
- [IV] T. Zikmund, J. Salplachta, A. Zatocilova, A. Brinek, L. Pantelejev, R. Stepanek, D. Koutny, D. Palousek, J. Kaiser. Computed tomography based procedure for reproducible porosity measurement of additive manufactured samples, *Ndt & E International*, 103 (2019) 111-118.
- [V] T. Zikmund, M. Novotna, M. Kavkova, M. Tesarova, M. Kaucka, B. Szarowska, I. Adameyko, E. Hrubá, M. Buchtova, E. Drazanova, Z. Starcuk, J. Kaiser. High-contrast differentiation resolution 3D imaging of rodent brain by X-ray computed microtomography, *Journal of Instrumentation*, 13 (2018) 14.
- [VI] M. Tesarova, T. Zikmund, M. Kaucka, I. Adameyko, J. Jaros, D. Palousek, D. Skaroupka, J. Kaiser. Use of micro computed-tomography and 3D printing for reverse engineering of mouse embryo nasal capsule, *Journal of Instrumentation*, 11 (2016).
- [VII] M. Tesarova, E. Heude, G. Comai, T. Zikmund, M. Kaucka, I. Adameyko, S. Tajbakhsh, J. Kaiser. An interactive and intuitive visualisation method for X-ray computed tomography data of biological samples in 3D Portable Document Format, *Scientific Reports*, 9 (2019).
- [VIII] M. Tesarova, L. Mancini, A. Simon, I. Adameyko, M. Kaucka, A. Elewa, G. Lanzafame, Y. Zhang, D. Kalasova, B. Szarowska, T. Zikmund, M. Novotna, J. Kaiser. A quantitative analysis of 3D-cell distribution in regenerating muscle-skeletal system with synchrotron X-ray computed microtomography, *Scientific Reports*, 8 (2018).
- [IX] J. Salplachta, T. Zikmund, M. Zemek, A. Brinek, Y. Takeda, K. Omote, J. Kaiser. Complete Ring Artifacts Reduction Procedure for Lab-Based X-ray Nano CT Systems, *Sensors*, 21 (2021).
- [X] M. Kaucka, E. Ivashkin, D. Gyllborg, T. Zikmund, M. Tesarova, J. Kaiser, M. Xie, J. Petersen, V. Pachnis, S.K. Nicolis, T. Yu, P. Sharpe, E. Arenas, H. Brismar, H. Blom, H. Clevers, U. Suter, A.S. Chagin, K. Fried, A. Hellander, I. Adameyko. Analysis of neural crest-derived clones reveals novel aspects of facial development, *Science Advances*, 2 (2016).
- [XI] M. Kaucka, T. Zikmund, M. Tesarova, D. Gyllborg, A. Hellander, J. Jaros, J. Kaiser, J. Petersen, B. Szarowska, P.T. Newton, V. Dyachuk, L. Li, H. Qian, A.S. Johansson, Y. Mishina, J.D. Currie, E.M. Tanaka, A. Erickson, A. Dudley, H. Brismar, P. Southam, E. Coen, M. Chen, L.S. Weinstein, A. Hampl, E. Arenas, A.S. Chagin, K. Fried, I. Adameyko. Oriented clonal cell dynamics enables accurate growth and shaping of vertebrate cartilage, *Elife*, 6 (2017) 37.
- [XII] M. Kaucka, J. Petersen, M. Tesarova, B. Szarowska, M.E. Kastriti, M. Xie, A. Kicheva, K. Annusver, M. Kasper, O. Symmons, L. Pan, F. Spitz, J. Kaiser, M. Hovorakova, T. Zikmund, K.

- Sunadome, M.P. Matisse, H. Wang, U. Marklund, H. Abdo, P. Ernfors, P. Maire, M. Wurmser, A.S. Chagin, K. Fried, I. Adameyko. Signals from the brain and olfactory epithelium control shaping of the mammalian nasal capsule cartilage, *Elife*, 7 (2018).
- [XIII] G.E. Comai, M. Tesarova, V. Dupe, M. Rhinn, P. Vallecillo-Garcia, F. da Silva, B. Feret, K. Exelby, P. Dolle, L. Carlsson, B. Pryce, F. Spitz, S. Stricker, T. Zikmund, J. Kaiser, J. Briscoe, A. Schedl, N.B. Ghyselinck, R. Schweitzer, S. Tajbakhsh. Local retinoic acid signaling directs emergence of the extraocular muscle functional unit, *Plos Biology*, 18 (2020).
- [XIV] M. Kavkova, T. Zikmund, A. Kala, J. Salplachta, S.L.P. Pena, J. Kaiser, K. Jezek. Contrast enhanced X-ray computed tomography imaging of amyloid plaques in Alzheimer disease rat model on lab based micro CT system, *Scientific Reports*, 11 (2021).
- [XV] S. Hankeova, J. Salplachta, T. Zikmund, M. Kavkova, N. Van Hul, A. Brinek, V. Smekalova, J. Laznovsky, F. Dawit, J. Jaros, V. Bryja, U. Lendahl, E. Ellis, A. Nemeth, B. Fischler, E. Hannezo, J. Kaiser, E.R. Andersson. DUCT reveals architectural mechanisms contributing to bile duct recovery in a mouse model for Alagille syndrome, *eLife*, 10 (2021) e60916.
- [XVI] H. Dosedelova, K. Stepankova, T. Zikmund, H. Lesot, J. Kaiser, K. Novotny, J. Stembirek, Z. Knotek, O. Zahradnicek, M. Buchtova. Age-related changes in the tooth-bone interface area of acrodont dentition in the chameleon, *Journal of Anatomy*, 229 (2016) 356-368.
- [XVII] M. Novotna, E. Zikmundova, P. Porizka, T. Zikmund, K. Novotny, J. Kaiser. X-ray micro computed tomography-aided calibration of laser-induced breakdown spectroscopy depth profiling for archaeological ceramics examination, *Spectrochimica Acta Part B-Atomic Spectroscopy*, 172 (2020).
- [XVIII] D. Kalasova, T. Zikmund, P. Spurny, J. Haloda, J. Borovicka, J. Kaiser. Chemical and physical properties of Zr nad Sazavou L chondrite and porosity differentiation using computed tomography, *Meteoritics & Planetary Science*, 55 (2020) 1073-1081.
- [XIX] D. Kalasova, K. Dvorak, M. Slobodnik, D. Vsiansky, T. Zikmund, J. Dluhos, R. Vana, J. Bures, J. Kaiser. Characterization of inner structure of limestone by X-ray computed sub-micron tomography, *Construction and Building Materials*, 174 (2018) 693-700.
- [XX] E. Zikmundova, T. Zikmund, V. Sladek, J. Kaiser. Non-destructive lock-picking of a historical treasure chest by means of X-ray computed tomography, *Plos One*, 15 (2020).
- [XXI] M. Pospiech, T. Zikmund, Z. Javurkova, J. Kaiser, B. Tremlova. An Innovative Detection of Mechanically Separated Meat in Meat Products, *Food Analytical Methods*, 12 (2019) 652-657.
- [XXII] R. Vrana, D. Koutny, D. Palousek, L. Pantelejev, J. Jaros, T. Zikmund, J. Kaiser. Selective Laser Melting Strategy for Fabrication of Thin Struts Usable in Lattice Structures, *Materials*, 11 (2018).
- [XXIII] P. Stastny, Z. Chlup, D. Kalasova, T. Zikmund, J. Kaiser, M. Trunec. Epoxy-based gelcasting of machinable hydroxyapatite foams for medical applications, *Journal of the American Ceramic Society*, 101 (2018) 3317-3327.
- [XXIV] C. Oliver-Urrutia, R.R. Ibanez, M.V. Flores-Merino, L. Vojtova, J. Salplachta, L. Celko, J. Kaiser, E.B. Montufar. Lyophilized Polyvinylpyrrolidone Hydrogel for Culture of Human Oral Mucosa Stem Cells, *Materials*, 14 (2021).

[XXV] T. Sedlacik, O.K. Acar, H. Studenovska, I. Kotelnikov, J. Kucka, Z. Konecna, T. Zikmund, J. Kaiser, G.T. Kose, F. Rypacek. Chondrogenic potential of macroporous biodegradable cryogels based on synthetic poly(alpha-amino acids), *Soft Matter*, 14 (2018) 228-238.

[XXVI] L. Vojtova, T. Zikmund, V. Pavlinakova, J. Salplachta, D. Kalasova, E. Prosecka, J. Brtnikova, J. Zidek, D. Pavlinak, J. Kaiser. The 3D imaging of mesenchymal stem cells on porous scaffolds using high-contrasted x-ray computed nanotomography, *Journal of Microscopy*, 273 (2019) 169-177.

[XXVII] P. Marcián, L. Borák, T. Zikmund, L. Horáčková, J. Kaiser, M. Joukal, J. Wolff. On the limits of finite element models created from (micro)CT datasets and used in studies of bone-implant-related biomechanical problems, *Journal of the Mechanical Behavior of Biomedical Materials*, 117 (2021) 104393.

[XXVIII] V. Sladek, V. Sabolova, O. Sebesta, T. Zikmund, J. Kaiser, S. Cerevkova. Effect of deriving periosteal and endosteal contours from microCT scans on computation of cross-sectional properties in non-adults: the femur, *Journal of Anatomy*, 233 (2018) 381-393.

## 8. REFERENCES

- [1] M. Gulbrandsen, S. Kyvik, Are the concepts basic research, applied research and experimental development still useful? An empirical investigation among Norwegian academics, *Science & Public Policy - SCI PUBLIC POLICY*, 37 (2010) 343-353.
- [2] J. Hsieh, *Computed Tomography: Principles, Design, Artifacts, and Recent Advances*, SPIE Press, 2003.
- [3] W.A. Kalender, *Computed Tomography: Fundamentals, System Technology, Image Quality, Applications*, Wiley, 2011.
- [4] A.C. Kak, M. Slaney, *Principles of Computerized Tomographic Imaging*, Society for Industrial and Applied Mathematics, 2001.
- [5] S.R. Stock, *MicroComputed Tomography: Methodology and Applications*, CRC Press, 2008.
- [6] P. Grangeat, *Tomography*, Wiley, 2013.
- [7] L. Holzer, M. Cantoni, Review of FIB tomography, in: *Nanofabrication using focused ion and electron beams: principles and applications*, Oxford University Press, New York, 2012.
- [8] M. Singh, A. Nair, T. Vedakkan, V. Piazza, R. Udan, M.V. Frazier, T. Janecek, M.E. Dickinson, K.V. Larin, Comparison of Optical Projection Tomography and Optical Coherence Tomography for Assessment of Murine Embryonic Development, in: *Conference on Optical Methods in Developmental Biology III*, San Francisco, CA, 2015.
- [9] W. Drexler, J.G. Fujimoto, *Optical Coherence Tomography: Technology and Applications*, Springer International Publishing, 2015.
- [10] M.E. Brezinski, *Optical Coherence Tomography: Principles and Applications*, Elsevier Science & Technology Books, 2013.
- [11] M.F. Reiser, W. Semmler, H. Hricak, *Magnetic Resonance Tomography*, Springer Berlin Heidelberg, 2007.
- [12] J. Radon, ON THE DETERMINATION OF FUNCTIONS FROM THEIR INTEGRAL VALUES ALONG CERTAIN MANIFOLDS, *Ieee Transactions on Medical Imaging*, 5 (1986) 170-176.
- [13] P.A. Midgley, R.E. Dunin-Borkowski, Electron tomography and holography in materials science, *Nature Materials*, 8 (2009) 271-280.
- [14] R.M. Schmitt, *Ultrasound Computed Tomography: From the Past to the Future*, in: R.G. Maev (Ed.) *Acoustical Imaging*, Springer US, Boston, MA, 2002, pp. 25-35.
- [15] J. Sharpe, *Optical Projection Tomography*, in: C.W. Sensen, B. Hallgrímsson (Eds.) *Advanced Imaging in Biology and Medicine: Technology, Software Environments, Applications*, Springer Berlin Heidelberg, Berlin, Heidelberg, 2009, pp. 199-224.
- [16] R. Bryson-Richardson, S. Berger, P. Currie, Chapter 2 - Methodology and Interpretation of the Atlas, in: R. Bryson-Richardson, S. Berger, P. Currie (Eds.) *Atlas of Zebrafish Development*, Academic Press, San Diego, 2012, pp. 3-6.
- [17] J. Sharpe, U. Ahlgren, P. Perry, B. Hill, A. Ross, J. Hecksher-Sørensen, R. Baldock, D. Davidson, *Optical Projection Tomography as a Tool for 3D Microscopy and Gene Expression Studies*, *Science*, 296 (2002) 541.
- [18] D.L. Bailey, D.W. Townsend, P.E. Valk, M.N. Maisey, *Positron Emission Tomography: Basic Sciences*, Springer London, 2006.
- [19] W.-H.G. Wong, J. Uribe, *Principles of Single Photon Emission Computed Tomography and Positron Emission Tomography*, in: E.E. Kim, D.J. Yang (Eds.) *Targeted Molecular Imaging in Oncology*, Springer New York, New York, NY, 2001, pp. 19-29.
- [20] B.Y. Croft, *Single-photon emission computed tomography*, *Year Book Medical Pub*, 1986.
- [21] P. Herscovitch, *Single-Photon Emission Computed Tomography (SPECT)*, in: M.J. Aminoff, R.B. Daroff (Eds.) *Encyclopedia of the Neurological Sciences (Second Edition)*, Academic Press, Oxford, 2014, pp. 173-178.
- [22] J.P. Kruth, M. Bartscher, S. Carmignato, R. Schmitt, L. De Chiffre, A. Weckenmann, *Computed tomography for dimensional metrology*, *CIRP Annals*, 60 (2011) 821-842.

- [23] D. Kalasova, T. Zikmund, L. Pina, Y. Takeda, M. Horvath, K. Omote, J. Kaiser, Characterization of a Laboratory-Based X-Ray Computed Nanotomography System for Propagation-Based Method of Phase Contrast Imaging, *Ieee Transactions on Instrumentation and Measurement*, 69 (2020) 1170-1178.
- [24] Frost&Sullivan, Global Non-destructive Test Equipment Market, Forecast 2022, in, 2017.
- [25] Frost&Sullivan, Global Computed Tomography (CT) in Dimensional Metrology Market, Forecast to 2022, in, 2018.
- [26] Frost&Sullivan, Frost Radar in the Industrial Computed Tomography Solutions Industry, in, 2019.
- [27] L. De Chiffre, S. Carmignato, J.P. Kruth, R. Schmitt, A. Weckenmann, Industrial applications of computed tomography, *CIRP Annals*, 63 (2014) 655-677.
- [28] T. Andrei, F. Michael, C. Hongtao, D. Fred, C. Hauyee, Y. Wenbing, High-resolution x-ray tomography using laboratory sources, in: *Proc.SPIE*, 2006.
- [29] J. Schulz, Innovation in X-Ray technology, *Matéria (Rio de Janeiro)*, 16 (2010) 868-876.
- [30] Q.A.i.R.a.M. GmbH, <https://www.qrm.de/en/>, in, 2021.
- [31] A.S.T. Method, <https://www.astm.org/DATABASE.CART/HISTORICAL/E1695-95.htm>, in, Accessed 2021.
- [32] K. Engelke, Quantitative Computed Tomography-Current Status and New Developments, *Journal of Clinical Densitometry*, 20 (2017) 309-321.
- [33] J.E. Adams, Quantitative computed tomography, *European Journal of Radiology*, 71 (2009) 415-424.
- [34] W. De Vos, J. Casselman, G.R.J. Swennen, Cone-beam computerized tomography (CBCT) imaging of the oral and maxillofacial region: A systematic review of the literature, *International Journal of Oral and Maxillofacial Surgery*, 38 (2009) 609-625.
- [35] Q.A.i.R.a.M. GmbH, <https://www.qrm.de/en/>, in, Accessed 2021.
- [36] W. Technologies, <https://www.bakerhughesds.com/waygate-technologies>, in, Accessed 2021.
- [37] H. Villarraga-Gomez, E.L. Herazo, S.T. Smith, X-ray computed tomography: from medical imaging to dimensional metrology, *Precision Engineering-Journal of the International Societies for Precision Engineering and Nanotechnology*, 60 (2019) 544-569.
- [38] A. Kraemer, G. Lanza, Assessment of the measurement procedure for dimensional metrology with X-ray computed tomography, *14th Cirp Cat 2016 - Cirp Conference on Computer Aided Tolerancing*, 43 (2016) 362-367.
- [39] A. du Plessis, B.J. Olawuyi, W.P. Boshoff, S.G. le Roux, Simple and fast porosity analysis of concrete using X-ray computed tomography, *Materials and Structures*, 49 (2016) 553-562.
- [40] T.B.N. Thi, M. Morioka, A. Yokoyama, S. Hamanaka, K. Yamashita, C. Nonomura, Measurement of fiber orientation distribution in injection-molded short-glass-fiber composites using X-ray computed tomography, *Journal of Materials Processing Technology*, 219 (2015) 1-9.
- [41] Duesseldorf, VDI/VDE 2617 Part 13 Accuracy of Coordinate Measuring Machines – Characteristics and their Testing – Guideline for the Application of DIN EN ISO 10360 for Coordinate Measuring Machines with CT-sensors, in, 2011.
- [42] M. Lüthi, B. Bircher, F. Meli, A. Küng, R. Thalmann, X-ray flat-panel detector geometry correction to improve dimensional computed tomography measurements, *Measurement Science and Technology*, 31 (2019).
- [43] H. Villarraga-Gómez, C. Lee, S.T. Smith, Dimensional metrology with X-ray CT: A comparison with CMM measurements on internal features and compliant structures, *Precision Engineering*, 51 (2018) 291-307.
- [44] J. Barrett, N. Keat, Artifacts in CT: Recognition and Avoidance, *Radiographics : a review publication of the Radiological Society of North America, Inc*, 24 (2004) 1679-1691.
- [45] F. Boas, D. Fleischmann, CT artifacts: Causes and reduction techniques, *Imaging in Medicine*, 4 (2012) 229-240.
- [46] S. Carmignato, W. Dewulf, R. Leach, *Industrial X-Ray Computed Tomography*, Springer International Publishing, 2017.
- [47] A. Momose, Recent Advances in X-ray Phase Imaging, *Japanese Journal of Applied Physics*, 44 (2005) 6355-6367.

- [48] J. Kastner, B. Plank, G. Requena, Non-destructive characterisation of polymers and Al-alloys by polychromatic cone-beam phase contrast tomography, *Materials Characterization*, 64 (2012) 79-87.
- [49] F. Pfeiffer, T. Weitkamp, O. Bunk, C. David, Phase retrieval and differential phase-contrast imaging with low-brilliance X-ray sources, *Nature Physics*, 2 (2006) 258-261.
- [50] A. Burvall, U. Lundström, P.A.C. Takman, D.H. Larsson, H.M. Hertz, Phase retrieval in X-ray phase-contrast imaging suitable for tomography, *Optics Express*, 19 (2011) 10359-10376.
- [51] D. Kalasová, A. Břínek, M. Šlouf, M. Dušková-Smrčková, T. Zikmund, Z. Patáková, J. Kaiser, Wide-cone angle phase-contrast X-ray computed tomography of synthetic polymer materials, *IEEE Transactions on Instrumentation and Measurement*, (2020) 1-1.
- [52] A. Kingston, A. Sakellariou, T. Varslot, G. Myers, A. Sheppard, Reliable automatic alignment of tomographic projection data by passive auto-focus, *Medical physics*, 38 (2011) 4934-4945.
- [53] T. Varslot, A. Kingston, G. Myers, A. Sheppard, High-resolution helical cone-beam micro-CT with theoretically-exact reconstruction from experimental data, *Medical physics*, 38 (2011) 5459.
- [54] W.H.a.N.O. David, Laser-Induced Breakdown Spectroscopy (LIBS), Part II: Review of Instrumental and Methodological Approaches to Material Analysis and Applications to Different Fields, *Appl. Spectrosc.*, 66 347--419.
- [55] B. Metscher, MicroCT for comparative morphology: simple staining methods allow high-contrast 3D imaging of diverse non-mineralized animal tissues, *BMC Physiol*, (2009).
- [56] F. Neues, M. Epple, X-ray Microcomputer Tomography for the Study of Biomineralized Endo- and Exoskeletons of Animals, *Chemical Reviews*, 108 (2008) 4734-4741.
- [57] M.L. Bouxsein, S.K. Boyd, B.A. Christiansen, R.E. Guldborg, K.J. Jepsen, R. Muller, Guidelines for Assessment of Bone Microstructure in Rodents Using Micro-Computed Tomography, *Journal of Bone and Mineral Research*, 25 (2010) 1468-1486.
- [58] J.F. Hainfeld, H.M. Smilowitz, M.J. O'Connor, F.A. Dilmanian, D.N. Slatkin, Gold nanoparticle imaging and radiotherapy of brain tumors in mice, *Nanomedicine*, 8 (2013) 1601-1609.
- [59] L. Massimi, I. Bukreeva, G. Santamaria, M. Fratini, A. Corbelli, F. Brun, S. Fumagalli, L. Maugeri, A. Pacureanu, P. Cloetens, N. Pieroni, F. Fiordaliso, G. Forloni, A. Uccelli, N.K. de Rosbo, C. Balducci, A. Cedola, Exploring Alzheimer's disease mouse brain through X-ray phase contrast tomography: From the cell to the organ, *Neuroimage*, 184 (2019) 490-495.
- [60] N. Hayasaka, N. Nagai, N. Kawao, A. Niwa, Y. Yoshioka, Y. Mori, H. Shigeta, N. Kashiwagi, M. Miyazawa, T. Satou, H. Higashino, O. Matsuo, T. Murakami, In Vivo Diagnostic Imaging Using Micro-CT: Sequential and Comparative Evaluation of Rodent Models for Hepatic/Brain Ischemia and Stroke, *Plos One*, 7 (2012).

## 9. LIST OF ABBREVIATIONS

CEITEC – Central European Institute of Technology  
BUT – Brno University of Technology  
CT – Computed Tomography  
TAČR - Technology Agency of the Czech Republic  
3D – Three Dimensions  
GE – General Electric  
FIB – Focused-ion Neam  
OCT – Optical Coherence Tomography  
MRI – Magnetic Resonance Imaging  
ET – Electron Tomography  
OPT – Optical Projection Tomography  
XCT – X-ray Computed Tomography  
PET – Positron Emission Tomography  
SPECT – Single-photon Emission Computed Tomography  
Linac-CT – Linear accelerator-based Computed Tomography  
SRCT – Synchrotron-based Computed Tomography  
QRM – Quality Assurance in Radiology and Medicine  
ASTM – American Standard Test Method  
QCT – Quantitative Computed Tomography  
 $\mu$ CT – Micro Computed Tomography  
PDF – Portable Document Format  
HU – Hounsfield Unit  
CAD – Computer-Aided Design  
PCI – Phase Contrast Imaging  
SYRMEP - Synchrotron Radiation for Medical Physics  
PTA – Phosphotungstic Acid  
LIBS – Laser-induced Breakdown Spectroscopy  
SEM – Scanning Electron Microscopy  
MSM – Mechanically Separated Meat  
AM – Additive Manufacturing

PRINTED VERSIONS OF COMMENTED PAPERS

PAPER [I]

# Characterization of a Laboratory-Based X-Ray Computed Nanotomography System for Propagation-Based Method of Phase Contrast Imaging

Dominika Kalasová, Tomáš Zikmund, Ladislav Pína, Yoshihiro Takeda, Martin Horváth, Kazuhiko Omote, and Jozef Kaiser<sup>IB</sup>

**Abstract**—Phase contrast imaging (PCI) is used to extend X-ray computed nanotomography (nCT) technique for analyzing samples with a low X-ray contrast, such as polymeric structures or soft tissues. Although this technique is used in many variations at synchrotrons, along with the development of X-ray tubes and X-ray detectors, a PCI becomes available also for laboratory systems. This paper is focused on determining the conditions for propagation-based PCI in laboratory nCT systems based on three criteria. It is mostly employed in near-field imaging regime, which is quantified via the Fresnel number. X-rays must reach a certain degree of coherence to form edge enhancement. Finally, the setup of every computed tomography (CT) measurement has to avoid geometrical unsharpness due to the finite focal spot size. These conditions are evaluated and discussed in terms of different properties and settings of the CT machine. Propagation-based PCI is tested on a sample of carbon fibers reinforced polyethylene and the implementation of the Paganin phase retrieval algorithm on the CT data is shown.

**Index Terms**—Characterization of computed tomography (CT) system, laboratory-based X-ray computed nanotomography (nCT), phase contrast imaging (PCI), propagation-based imaging (PBI), X-ray nCT.

## I. INTRODUCTION

X-RAY computed nanotomography (nCT) is a nondestructive, 3-D imaging method used for analyses of the inner structure of materials. This term is used for devices that reach spatial resolution below  $1\ \mu\text{m}$  [1], [2]. Unlike X-ray computed microtomography, these devices often have highly

precise mechanical parts, advanced X-ray detectors with additional optical units after scintillator and chips based on charge-coupled device (CCD) or scientific complementary metal-oxide-semiconductor (sCMOS) technology. Consequently, they are able to process special examination protocols while maintaining a high resolution [3].

Phase contrast X-ray computed tomography (CT) imaging methods [phase contrast imaging (PCI)] make possible the imaging of samples with a low X-ray contrast, e.g., polymers, biological soft tissues, or scaffolds [4]. PCI is utilized in various fields in biology and medicine for imaging of small animals and soft tissues [5]–[8] and in material science as well, for example, in imaging of material discontinuities in polymer composites composed of light materials with similar attenuation coefficient [9]–[11].

The phase of an X-ray beam transmitted through material is shifted due to its interaction with the electron shells of atoms [12]. There are several ways of recording this phase shift and obtaining phase contrast. X-ray interferometry technique is based on the interference of a reference beam with a beam transmitted through the sample [13], [14]. Analyzer-based methods involve the reflection on the Bragg crystals, which filter different X-rays based on their angle [15], [16]. Talbot–Lau grating interferometry uses the self-imaging property of gratings to make the phase changes visible [17]–[19]. Phase contrast can also be achieved by using X-ray optics in X-ray microscopes [20]–[22].

When X-rays diffracted on inner structures of material propagate through a certain distance, their wavefronts interfere and form an inline phase contrast [23]. If a tomographic setup is modified just by increasing the distance between the sample and the detector, this phase contrast becomes visible in the form of edge enhancement [24]. This approach is called propagation-based imaging (PBI). For large sample–detector distances (SDDs), multiple interference fringes appear, which shifts the imaging toward the holographic regime. The imaging regime is described via the Fresnel number, as discussed in Section II-A.

In PBI, phase changes caused by radiation passing through the object are transformed to variations of measured intensity.

Manuscript received October 30, 2018; revised March 15, 2019; accepted March 16, 2019. Date of publication April 11, 2019; date of current version March 10, 2020. This research was carried out under the Project CEITEC 2020 (LQ1601) with financial support from the Ministry of Education, Youth and Sports of the Czech Republic under the National Sustainability Programme II. Part of the work was carried out with the support of CEITEC Nano Research Infrastructure (Ministry of Education, Youth and Sports of the Czech Republic, 2016–2019). The Associate Editor coordinating the review process was Shutao Li. (Corresponding author: Jozef Kaiser.)

D. Kalasová, T. Zikmund, and J. Kaiser are with the Central European Institute of Technology (CEITEC), Brno University of Technology, 612 00 Brno, Czech Republic (e-mail: dominika.kalasova@ceitec.vutbr.cz; tomas.zikmund@ceitec.vutbr.cz; jozef.kaiser@ceitec.vutbr.cz).

L. Pína and M. Horváth are with Rigaku Innovative Technologies Europe s.r.o., 14221 Prague, Czech Republic (e-mail: ladislav.pina@rigaku.com; martin.horvath@rigaku.com).

Y. Takeda and K. Omote are with Rigaku Corporation, Tokyo 196-8666, Japan (e-mail: y-takeda@rigaku.co.jp; omote@rigaku.co.jp).

Digital Object Identifier 10.1109/TIM.2019.2910338

The task of retrieving information about the phase change is solved by phase retrieval algorithms [25]–[27]. In [28], phase retrieval approaches taking into account polychromaticity of laboratory-based X-ray source are shown. Nevertheless, also techniques developed for monochromatic radiation would still be appropriate if an average X-ray energy or the main characteristic peak was considered [28], [29]. From an image processing point of view, the application of phase retrieval algorithm is necessary to obtain data with less noise and multimodal histogram, which would be easier to segment [24], [30].

PBI requires a high degree of coherence of X-ray beam; therefore, the method is not only used with the synchrotron radiation [31] but also with laboratory polychromatic sources [32]. Development of materials, precise mechanics, and electron focusing systems in laboratory X-ray sources made the propagation-based imaging available on many CT devices. Examples of edge enhancement via PBI with a laboratory, polychromatic X-ray source have been reported on various examples of fibers in the polymer matrix [33]–[35], mouse lungs [36], liver tissue [37] or cochlea [38], or leaves and insects [39].

Tomographic setup in laboratory-based PBI requires certain conditions to be fulfilled [40]–[43]. Tomographic PBI is usually done in a near-field regime to avoid the formation of multiple fringes in larger SDDs, where the direct morphology information is lost (this is referred to as a holographic or far-field regime). This condition on SDD is quantified via the Fresnel number [36], [44]. To observe edge enhancement on structures of certain dimensions, an X-ray beam must reach a sufficient degree of coherence. The coherence requirements on the X-ray beam can be evaluated by the ratio of shearing and lateral coherence length [23] (these terms are explained in Section II-B). Laboratory-based X-ray tubes produce an X-ray cone beam with a finite focal spot size. When a proper geometrical arrangement of components is not set, the unsharpness from the finite focal spot size causes blurring of edges of the sample [45].

Laboratory-based X-ray CT devices without additional X-ray optics mostly employ geometrical magnification by the cone-beam shape of X-rays: the sample is placed close to the X-ray tube and projected to the large-area detector placed at a longer distance [Fig. 1(a)] [46]. The small voxel size is restricted by focal spot size, and therefore, for small voxel sizes, small focal spot sizes are necessary. In another approach, so-called inverse geometry [47]–[49], the sample is not placed directly in front of the X-ray tube but the source–sample distance is fixed at a relatively large distance compared to the sample size. The detector is placed close to the sample, so only a small part of the cone beam at the sample position is used; therefore, it is considered semiparallel [Fig. 1(b)]. The image is magnified by an optical system after scintillator. The small voxel size is achieved by small pixels at the detector, therefore, in this case, a high-power source with a large focal spot size is acceptable.

In this paper, PBI with a laboratory-based nCT system is studied. Theoretical conditions for PBI are stated. Based on these theoretical assumptions, the limits of the nCT machine for PBI are discussed and tested on several measurements

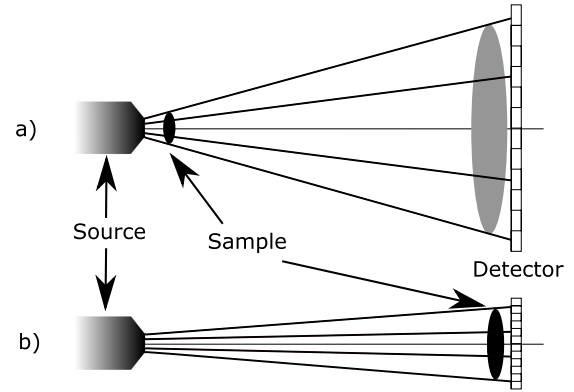


Fig. 1. Different approaches in nCT systems. (a) Geometrical magnification is reached by use of cone-beam X-ray. (b) Long source–sample distance is used to achieve semiparallel X-ray beam at sample position and the image is magnified by optical system after scintillator.

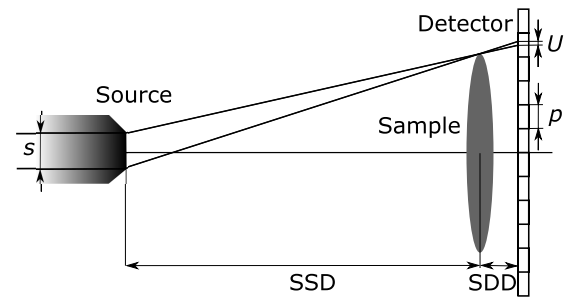


Fig. 2. Formation of geometrical unsharpness  $U$  at the detector with LPS  $p$  due to finite focal spot size  $s$ . SSD stands for source–sample distance and SDD stands for sample–detector distance.

of carbon fibers reinforced polyethylene (CFRP) sample. Moreover, the application of phase retrieval algorithm is shown as a suitable postprocessing method for data acquired by PBI.

## II. THEORY

X-ray wavefronts passing through the sample are distorted on samples' structures proportionally to the phase shift imposed by the sample. After propagating through a given distance, they interfere to form Fresnel diffraction fringes [32], [34]. In the image, this is visible in the form of edge enhancement. The interference is influenced by the sample to detector distance (e.g., imaging regime) and the degree of X-ray coherence. These factors, together with limitations following from finite focal spot size, are discussed in this section.

### A. Imaging in Near-Field Regime

For propagation-based phase-contrast imaging in paraxial approximation, the imaging regime is characterized by the Fresnel number  $N_F$

$$N_F = \frac{a^2}{\lambda z_{\text{eff}}} \quad (1)$$

where  $a$  is the size of a feature of interest,  $\lambda$  is the wavelength, and the effective propagation distance  $z_{\text{eff}} = \text{SSD} \times \text{SDD} / (\text{SSD} + \text{SDD})$ , where SSD is the source–sample distance and SDD is the sample–detector distance (Fig. 2).

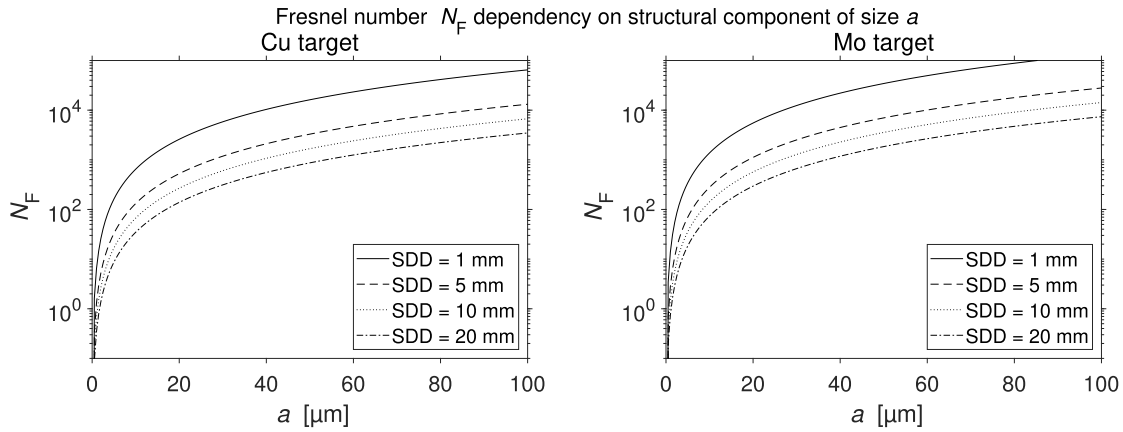


Fig. 3. Analysis of conditions for near-field imaging for different SDDs according to (1). The imaging is not in near-field regime for  $N_F \ll 1$ .

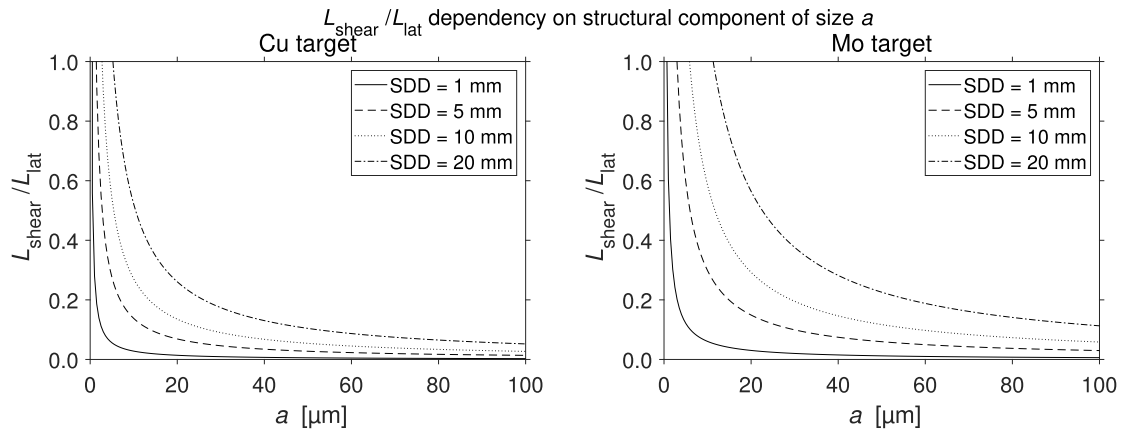


Fig. 4. Analysis of coherence requirements and for different SDDs according to (2). The degree of X-ray coherence is high enough to observe phase effects at structures of given size  $a$  for  $L_{\text{shear}}/L_{\text{lat}} < 1$ .

The edge enhancement for the given feature size is pronounced when  $N_F \approx 1$  [36], [44], and from the obtained images, it is possible to directly extract the morphological information about the sample. For  $N_F \ll 1$ , not only edge enhancement but also multiple fringes appear, and the real structure is no longer recognizable. This is a so-called holographic, or for very low  $N_F$  far-field regime.

To have the structures of the sample directly recognizable, the holographic regime, e.g., large sample–detector distances, should be avoided. In such case, in order to stay in the near-field regime,  $N_F > 1$  should be fulfilled for every structure visible in the image. At the same time, the Fresnel number should not be too large ( $N_F \gg 1$ ) since for small SDDs, the propagation effects are negligible and the results are only absorption images.

### B. Degree of X-Ray Coherence

The superposition of wavefronts for the formation of edge enhancement occurs only if waves are coherent. In case of X-rays emitted from the finite focal spot size, the spatial coherence is given by lateral coherence length  $L_{\text{lat}} = \lambda \times \text{SSD}/s$ , where  $s$  is the focal spot size. Phase contrast is formed between interfering waves from positions separated by a shearing length  $L_{\text{shear}} = \lambda \times \text{SDD}/(Ma)$ , where  $M = (\text{SSD} + \text{SDD})/\text{SSD}$  stands for magnification. The wave

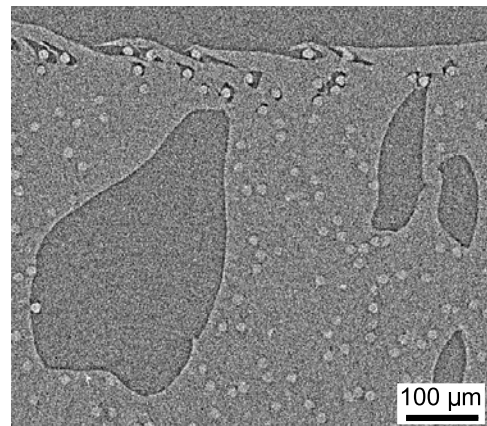


Fig. 5. Tomographic slice of CFRP sample measured with LPS (0.54  $\mu\text{m}$ ) at source–detector distance 1.5 mm with Mo target.

has to have a sufficiently high degree of coherence over this length to make phase contrast visible. Visibility of phase contrast is, therefore, characterized by ratio  $L_{\text{shear}}/L_{\text{lat}}$  [23], [29].

The X-ray beam is almost fully coherent if the ratio  $L_{\text{shear}}/L_{\text{lat}} \ll 1$ . In practice, the phase contrast fringes occur also when the X-rays are partially coherent and their visibility is improved with an increasing degree of coherence.

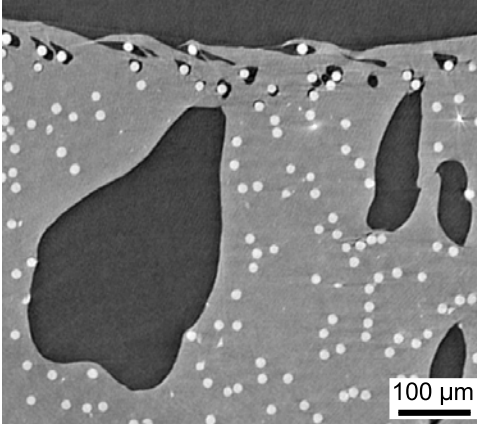


Fig. 6. Tomographic slice of the CFRP sample. Phase retrieval is applied on the data measured with Cu target at the SDD 1.5 mm [reconstruction without phase retrieval is in Fig. 7(b)].

The criterion for partial coherence can, therefore, be stated as

$$\frac{L_{\text{shear}}}{L_{\text{lat}}} = \frac{s \times \text{SDD}}{a(\text{SSD} + \text{SDD})} < 1. \quad (2)$$

### C. Geometrical Unsharpness due to Focal Spot Size

In X-ray tubes, X-rays are always emitted from a finite area called the focal spot. The resolution is restricted by the focal spot size because at a given sample–detector distance, the X-rays from the whole area of the focal spot start to form an unsharpened spot of size  $U$  on the detector larger than pixel size  $p$  (Fig. 2). To avoid this unsharpness, the condition  $U < p$  must be fulfilled. From the geometry of the system, this means

$$\frac{\text{SDD}}{\text{SSD}} \times s < p. \quad (3)$$

## III. MATERIALS AND METHODS

### A. CT Equipment

PBI was studied on a laboratory-based nCT system RIGAKU Nano3DX (Japan). The machine employs a geometrical arrangement based on a long SSD [Fig. 1(b)]: the SSD is fixed at 260 mm, the SDD can be varied between 0 and 50 mm. In this paper, two materials of rotating anode were used: Cu and Mo, working at acceleration voltage 40 and 50 kV, respectively, with the focal spot size 73 and 150  $\mu\text{m}$ , respectively, measured according to EN 125435 norm. For further calculations, such as an X-ray wavelength, the corresponding Cu  $K\alpha$  line 8 keV or Mo  $K\alpha$  line 17 keV was taken. The machine is equipped with an XSight Micron X-ray CCD camera with dimensions of 3300 px  $\times$  2500 px and 0.27  $\mu\text{m}$  pixel size. To achieve a larger pixel size, a binning parameter  $b$  of value 1, 2, 3, 4, or 8 can be used (signal from  $(b \times b)$  px<sup>2</sup> is summed, thus the effective pixel size is larger).

### B. CT Measurement

A light-element composite made of polyethylene matrix reinforced with 15 %–20 % of carbon fibers (CFRP) was chosen to demonstrate PBI.

TABLE I

SUMMARY OF EXPERIMENTAL CONDITIONS OF CFRP MEASUREMENT FOR A DEMONSTRATION OF PBI EFFECT AND VERIFICATION OF GEOMETRICAL UNSHARPNESS RULE DESCRIBED BY (3). SDD STANDS FOR SAMPLE–DETECTOR DISTANCE AND LPS STANDS FOR LINEAR PIXEL SIZE

Target material	SDD [mm]	Bin	LPS [ $\mu\text{m}$ ]	Projections	Exposure time [s]
Cu	0.8	1	0.27	1600	25
Cu	1.5	2	0.54	800	9
Cu	3.1	4	1.08	600	2
Cu	6.2	8	2.16	400	0.5
Cu	7.7	2	0.54	800	9
Mo	1.5	2	0.54	800	9

To show the varying amount of edge enhancement, the sample was measured at four different SDDs (Table I). For larger distances, bigger pixel sizes were used to avoid geometrical unsharpness. In this way, images for larger SDD are less sharp but allow to decrease the exposure time and storage place. For each pixel size, 80 % (determined to reflect possible variations of real instrument conditions) of the maximum allowed SDD calculated by (3) was used. Other acquisition parameters (number of projections and exposure time) were adapted according to specified CT machine rules to achieve optimum transmission and to avoid low signal and undersampling. A measurement with linear pixel size (LPS) 0.54  $\mu\text{m}$  was also performed at 400 % of the maximum allowed SDD in order to show the geometrical unsharpness effect. For comparison of different X-ray wavelengths and, therefore, different degrees of coherence, the sample was also measured with Mo target under the same conditions as with Cu target for SDD 1.5 mm. Projections were reconstructed using VGStudio MAX 3.1 reconstruction module.

### C. Data Processing

The Paganin phase retrieval algorithm [50] implemented in the ANKPhase software [51] was used on the data measured with Cu target at the SDD 1.5 mm. The  $\delta/\beta$  ratio of values in the index of refraction  $n$  ( $n = 1 - \delta + i\beta$ ) was chosen as 780 for polyethylene [52].

The edge enhancement was evaluated on an averaged line profile (pixels in 8  $\mu\text{m}$  area above and below the line were averaged to reduce noise). It was specifically evaluated on the edge of air and polymer matrix by calculating absorption contrast value  $C_{\text{ABS}}$  and phase contrast value  $C_{\text{PHC}}$  according to [33]

$$C_{\text{ABS}} = \frac{I_{\text{mat}} - I_{\text{bcg}}}{(I_{\text{mat}} + I_{\text{bcg}})/2}$$

$$C_{\text{PHC}} = \frac{I_{\text{max}} - I_{\text{min}} - (I_{\text{mat}} - I_{\text{bcg}})}{(I_{\text{max}} + I_{\text{min}})}$$

where  $I_{\text{mat}}$ ,  $I_{\text{bcg}}$ ,  $I_{\text{max}}$ , and  $I_{\text{min}}$  are the mean gray values of material and background and maximum and minimum gray values in the line profile, respectively.

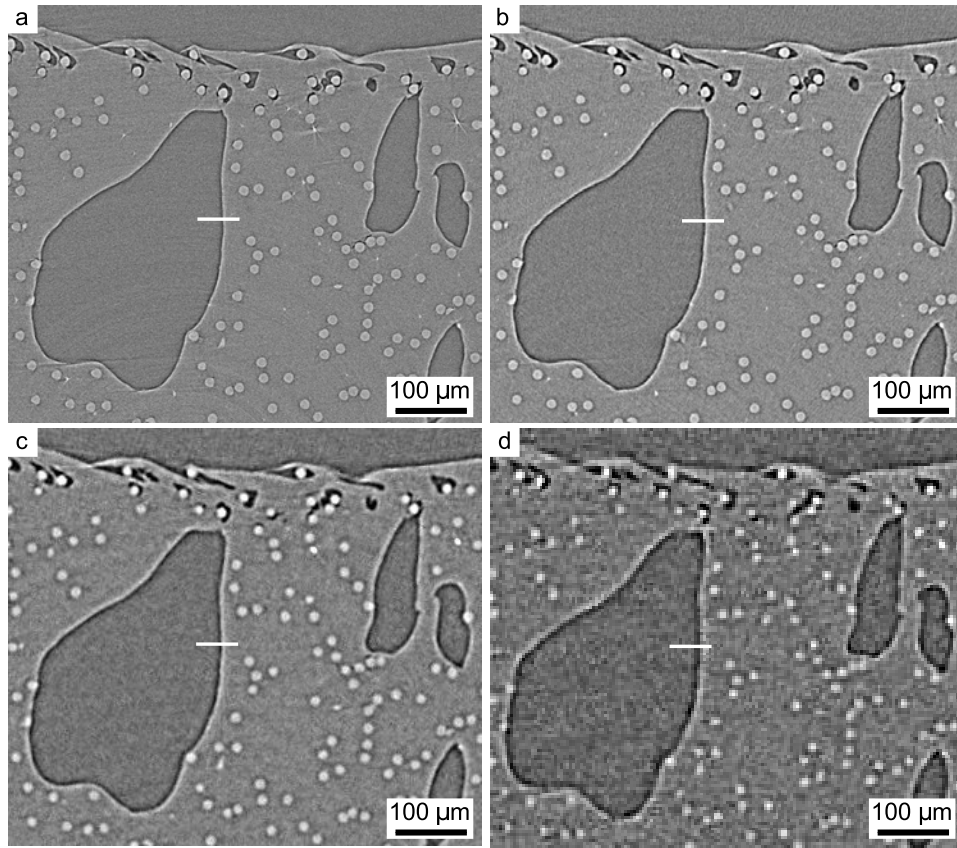


Fig. 7. Tomographic slice of CFRP sample measured at different SDDs with different LPSs according to Table I. (a) SDD 0.8 mm, LPS 0.27  $\mu\text{m}$ . (b) SDD 1.5 mm, LPS 0.54  $\mu\text{m}$ . (c) SDD 3.1 mm, LPS 1.08  $\mu\text{m}$ . (d) SDD 6.2 mm, LPS 2.16  $\mu\text{m}$ . The line was used for generation of edge profiles in Fig. 9.

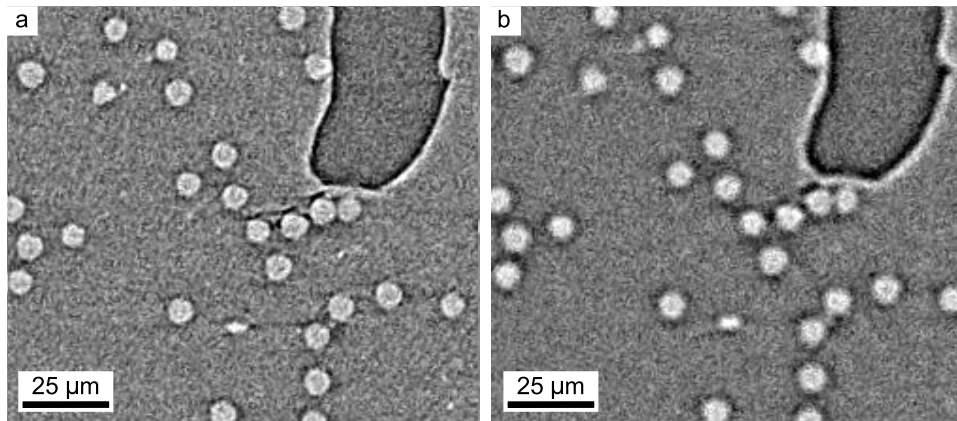


Fig. 8. Tomographic slice of CFRP sample measured with LPS (0.54  $\mu\text{m}$ ) at source–detector distances (SDD). (a) 1.5 mm. (b) 7.7 mm. For this LPS, SDD 7.7 mm does not fulfill (3) and in contrast with SDD 1.5 mm, the structures are blurred.

#### IV. RESULTS AND DISCUSSION

##### A. Theoretical Evaluation of Conditions for PBI

When performing tomographic experiments in laboratory conditions, change of values of  $s$ ,  $\lambda$ ,  $p$  usually requires altering a hardware setup, whereas positions of the source, the sample, and the detector can be adjusted more easily. In the case of Nano3DX, it is possible to change the target material. SSD is fixed and only the SDD value can be changed. Therefore,

in the following paragraphs, the results of calculations are given for different SDDs and target materials.

For identification of the imaging regime, the graph plotting  $N_F$  dependence on a feature of interest of size  $a$  (Fig. 3) gives information about the approximate size of the structure at which edge effect is pronounced at a given sample–detector distance.

By substituting (1) into  $N_F > 1$  and modifying the equation, we obtain  $\text{SDD} (a^2 - \lambda \text{SSD}) > -a^2 \text{SSD}$ . From here, for

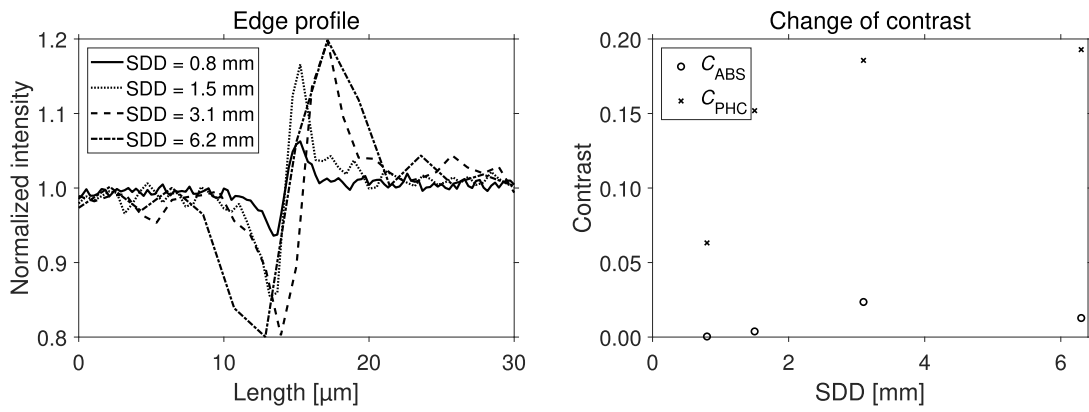


Fig. 9. Averaged line profiles normalized by mean value over air-polymer edge marked in Fig. 7 and absorption ( $C_{ABS}$ ) and phase contrast ( $C_{PHC}$ ) for different SDDs.

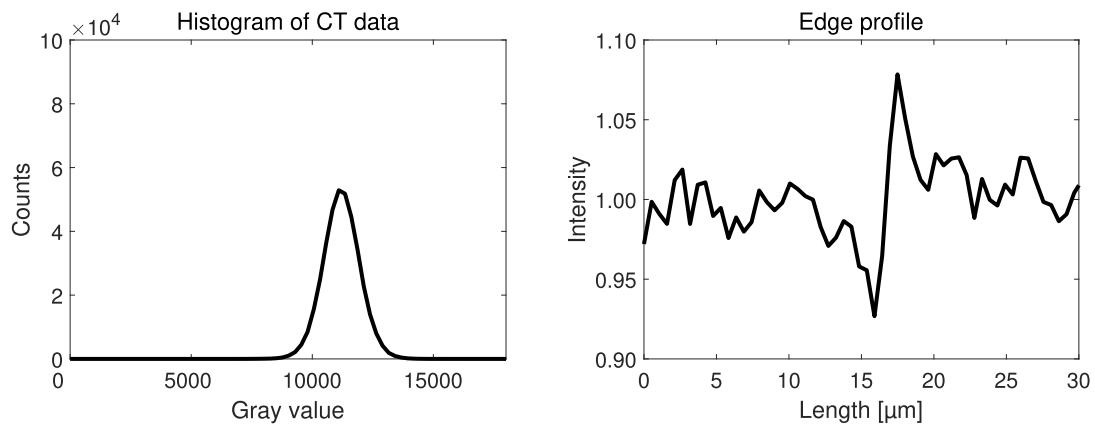


Fig. 10. Image evaluation of a tomographic slice of the CFRP sample from Fig. 5: averaged edge profile and histogram.

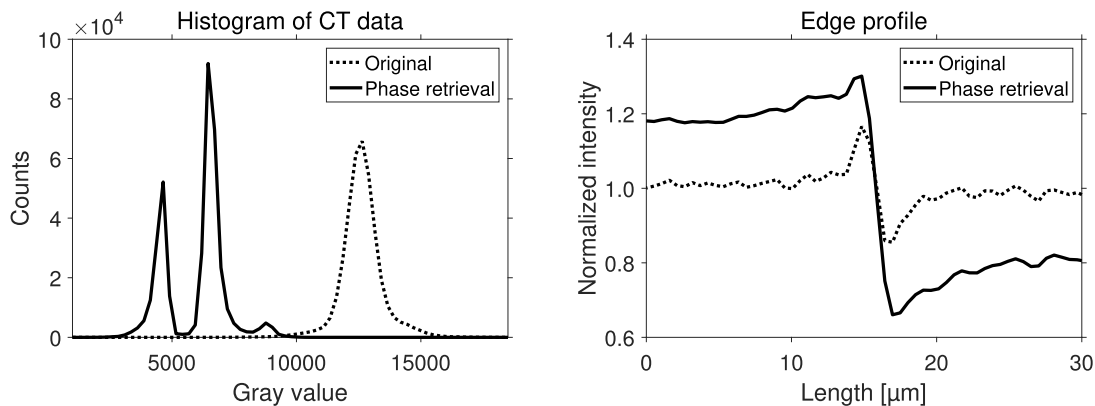


Fig. 11. Image evaluation of tomographic slices of the CFRP sample from Figs. 6 and 7(b). Averaged edge profile and histogram are used to show the influence of phase retrieval on CT data.

$a > (\lambda SSD)^{1/2}$ , the condition is always fulfilled since the right side of the equation is negative. Value of  $(\lambda SSD)^{1/2}$  is 6 μm for Cu and 4 μm for Mo target. The smallest features that can be distinguished must have a minimum size of two pixels, which is 0.54 μm for the smallest pixel size, or larger. Therefore, the imaging can be considered almost always in the near-field regime, except the very small details measured with the highest possible resolution. For large structures, where  $N_F \gg 1$ , the effect of X-ray propagation becomes

insignificant and the resulting images reflect only the absorption of the sample.

The ratio  $L_{shear}/L_{lat}$  determining the coherence degree of X-ray is plotted in Fig. 4. The coherence requirements have a high restriction on PBI since (2) is strictly fulfilled only for structures larger than about 5 μm for Cu and 10 μm for Mo target, depending on SDD. For rather small structures, the degree of coherency is decreased and phase effects will be less pronounced.

TABLE II  
CALCULATION OF MAXIMUM SDDs (IN MM) WHICH  
ARE ALLOWED TO AVOID GEOMETRICAL  
UNSHARPNESS FOR DIFFERENT  
LPSs ACCORDING TO (3)

Target \ LPS [ $\mu\text{m}$ ]	0.27	0.54	1.08	2.16
Cu	1.0	1.9	3.8	7.7
Mo	0.4	0.9	1.8	3.6

The maximum values of SDD to avoid the unsharpness according to (3) are shown in Table II for different LPSs. For example, in case of measuring with LPS 0.27  $\mu\text{m}$ , SDD should not exceed 1.0 mm for Cu and 0.4 mm for Mo. This condition must be verified before the beginning of every measurement. To improve contrast between materials, it is possible to increase the SDD to get a more pronounced phase contrast effect even at the cost of the reduced resolution.

Using (1)–(3), it is always possible to determine the highest possible SDD and estimate which structure sizes will have edge enhancement fringes visible.

### B. Imaging of CFRP Samples

In general, tomographic slices of CFRP (Fig. 7) show a strong edge enhancement at borders between the sample and the air. It might also be observed at carbon fibers to a much lesser extent. When the SDD increases, the edge enhancement becomes stronger and phase contrast increases, while absorption contrast does not change so rapidly (Fig. 9). Since an increase of SDD is possible only with an increase of the pixel size to fulfill the condition on geometrical unsharpness given by (3), the resolution becomes lower and some small details of the sample are no longer visible. Therefore, the calculated increase in phase contrast is slightly underestimated.

For all SDDs, the imaging is in near-field regime according to Fig. 3. The fibers have a diameter of 6–8  $\mu\text{m}$ . The lateral dimension of the whole sample is about 600  $\mu\text{m}$  and the size of air voids in the sample is in the range of 50–200  $\mu\text{m}$ . For all these intervals  $N_F > 1$ , so none of those features is in a holographic regime.

When SDD is set too big and therefore it does not fulfill the condition of geometrical unsharpness (3), the image is blurred. For example, CFRP measured with LPS 0.54  $\mu\text{m}$  at 400 % of the maximum allowed SDD [Fig. 8(b)] is more blurred than the same sample at 80 % of the maximum SDD [Fig. 8(a)]. This confirms that the geometrical unsharpness must be taken into account whenever a laboratory cone-beam X-ray source is used.

Measurement of CFRP with a different target material, and therefore the characteristic wavelength, was made with Mo target (Fig. 5). In the applied setup, Mo target has a larger spot size than Cu target; therefore, the maximum allowed distances due to geometrical unsharpness are, in general, lower. Although in this case, the SDD exceeds this distance, it was used for the experiment to have the comparison with Cu target under the same conditions [Fig. 7(b)].

The histograms of both data have a similar shape (Figs. 10 and 11) exhibiting only one peak. The contrast

between structures with similar density (polyethylene matrix and C fibers) is worse for the Mo target. Naturally, this is an expected result since higher energy was used resulting in lower contrast for such light materials. Edge enhancement at matrix/air interface is still present, but to a lesser extent (edge profiles at Fig. 10 compared to Fig. 11). This is evident also from values of calculated phase contrast:  $C_{\text{PHC}} = 0.152$  for Cu target and  $C_{\text{PHC}} = 0.071$  for Mo target. It can be explained by the lower degree of partial coherence of X-rays emitted from Mo target than from Cu target.

By an application of the phase retrieval on tomographic data (Fig. 6), the edge enhancement was reduced compared to the original data [Fig. 7(b)] as it is shown on the edge profile (Fig. 11). The absorption contrast increased ( $C_{\text{ABS}} = 0.004$  for original data and  $C_{\text{ABS}} = 0.366$  with phase retrieval) and the phase contrast decreased ( $C_{\text{PHC}} = 0.152$  for original data and  $C_{\text{PHC}} = 0.139$  with phase retrieval), which is very convenient for material segmentation.

The histogram (Fig. 11) contains several peaks corresponding to different structures and allowing the segmentation of different parts (air, matrix, and carbon fibers). Without the phase retrieval, the histogram of data has only one peak which makes segmentation very challenging. This is the reason why it is sometimes useful to apply the algorithm also on data without any strong visible edge enhancement, a further analysis is easier on these data from the image processing point of view.

## V. CONCLUSION

PCI extends possibilities of X-ray nCT to imaging of materials consisting of light elements with low X-ray absorption, such as biological or polymeric samples. The propagation-based imaging is a very popular method of PCI because it does not demand any extra hardware setup and it is easily available on laboratory-based CT systems.

In this paper, a method for evaluation of the capability of a laboratory-based CT system of PBI is summarized. It is based on a combination of three criteria—an imaging regime, a degree of coherency, and geometrical unsharpness. By using these principles, it is possible to determine specific settings of the CT system where PBI regime is available.

The method is demonstrated on measurements of carbon fiber reinforced polymer by the nCT system. A capability of the system for PBI was tested at various critical settings. The quality of results is evaluated based on edge enhancement analysis. A phase retrieval was applied to the measured data to emphasize the advantages of the propagation-based imaging for image quality improvement.

This evaluation method proved capable of estimating the suitability of a CT device for PBI using knowledge of machine parameters. It is a useful tool for researchers developing X-ray PCI techniques with a laboratory-based CT system.

## REFERENCES

- [1] P. J. Withers, "X-ray nanotomography," *Mater. Today*, vol. 10, no. 12, pp. 26–34, 2007.
- [2] L. De Chiffre, S. Carmignato, J.-P. Kruth, R. Schmitt, and A. Weckenmann, "Industrial applications of computed tomography," *CIRP Ann.*, vol. 63, no. 2, pp. 655–677, 2014.

- [3] M. Kampschulte *et al.*, “Nano-computed tomography: Technique and applications,” *RöFo-Fortschritte auf dem Gebiet der Röntgenstrahlen und der bildgebenden Verfahren*, vol. 188, no. 2, pp. 146–154, 2016.
- [4] S.-A. Zhou and A. Brahme, “Development of phase-contrast X-ray imaging techniques and potential medical applications,” *Phys. Medica*, vol. 24, no. 3, pp. 129–148, 2008.
- [5] O. Betz *et al.*, “Imaging applications of synchrotron X-ray phase-contrast microtomography in biological morphology and biomaterials science. I. General aspects of the technique and its advantages in the analysis of millimetre-sized arthropod structure,” *J. Microsc.*, vol. 227, no. 1, pp. 51–71, 2007.
- [6] P. Miao *et al.*, “Synchrotron radiation X-ray phase-contrast tomography visualizes microvasculature changes in mice brains after ischemic injury,” *Neural Plasticity*, vol. 2016, Jun. 2016, Art. no. 3258494.
- [7] J. J. Socha, M. W. Westneat, J. F. Harrison, J. S. Waters, and W.-K. Lee, “Real-time phase-contrast X-ray imaging: A new technique for the study of animal form and function,” *BMC Biol.*, vol. 5, no. 1, p. 6, 2007.
- [8] J. Kaiser *et al.*, “Investigation of the microstructure and mineralogical composition of urinary calculi fragments by synchrotron radiation X-ray microtomography: A feasibility study,” *Urological Res.*, vol. 39, no. 4, pp. 259–267, Aug. 2011.
- [9] F. Cosmi, A. Bernasconi, and N. Sodini, “Phase contrast microtomography and morphological analysis of a short carbon fibre reinforced polyamide,” *Compos. Sci. Technol.*, vol. 71, no. 1, pp. 23–30, 2011.
- [10] B. Yu, R. S. Bradley, C. Soutis, and P. J. Withers, “A comparison of different approaches for imaging cracks in composites by X-ray microtomography,” *Philos. Trans. Roy. Soc. A, Math., Phys. Eng. Sci.*, vol. 374, no. 2071, 2016, Art. no. 20160037.
- [11] S. C. Garcea, Y. Wang, and P. J. Withers, “X-ray computed tomography of polymer composites,” *Compos. Sci. Technol.*, vol. 156, pp. 305–319, Mar. 2018.
- [12] J. Baruchel, Ed., *X-Ray Tomography in Material Science*. Paris, France: Hermès, 2000.
- [13] A. Yoneyama *et al.*, “Large-area phase-contrast X-ray imaging using a two-crystal X-ray interferometer,” *J. Synchrotron Radiat.*, vol. 9, no. 5, pp. 277–281, 2002.
- [14] A. Momose, T. Takeda, Y. Itai, A. Yoneyama, and K. Hirano, “Phase-contrast tomographic imaging using an x-ray interferometer,” *J. Synchrotron Radiat.*, vol. 5, no. 3, pp. 309–314, 1998.
- [15] T. J. Davis, D. Gao, T. E. Gureyev, A. W. Stevenson, and S. W. Wilkins, “Phase-contrast imaging of weakly absorbing materials using hard X-rays,” *Nature*, vol. 373, no. 6515, pp. 595–598, 1995.
- [16] D. Chapman *et al.*, “Diffraction enhanced X-ray imaging,” *Phys. Med. Biol.*, vol. 42, no. 11, pp. 2015–2025, 1997.
- [17] Z. Wang *et al.*, “Quantitative coherence analysis with an X-ray Talbot–Lau interferometer,” *Anal. Bioanal. Chem.*, vol. 397, no. 6, pp. 2091–2094, 2010.
- [18] J. Tanaka *et al.*, “Cadaveric and *in vivo* human joint imaging based on differential phase contrast by X-ray Talbot–Lau interferometry,” *Zeitschrift für Medizinische Physik*, vol. 23, no. 3, pp. 222–227, 2013.
- [19] Z. Wang *et al.*, “Grating-based X-ray phase contrast imaging using polychromatic laboratory sources,” *J. Electron Spectrosc. Rel. Phenomena*, vol. 184, nos. 3–6, pp. 342–345, 2011.
- [20] A. Tkachuk, F. Diewer, H. Cui, M. Feser, S. Wang, and W. Yun, “X-ray computed tomography in Zernike phase contrast mode at 8 keV with 50-nm resolution using Cu rotating anode X-ray source,” *Zeitschrift für Kristallographie-Crystalline Mater.*, vol. 222, no. 11, pp. 650–655, 2007.
- [21] M. D. de Jonge *et al.*, “Quantitative phase imaging with a scanning transmission X-ray microscope,” *Phys. Rev. Lett.*, vol. 100, no. 16, 2008, Art. no. 163902.
- [22] A. S. Kumar, P. Mandal, Y. Zhang, and S. Litster, “Image segmentation of nanoscale Zernike phase contrast X-ray computed tomography images,” *J. Appl. Phys.*, vol. 117, no. 18, 2015, Art. no. 183102.
- [23] X. Wu and H. Liu, “Clarification of aspects in in-line phase-sensitive X-ray imaging,” *Med. Phys.*, vol. 34, no. 2, pp. 737–743, 2007.
- [24] S. Mohammadi *et al.*, “Quantitative evaluation of a single-distance phase-retrieval method applied on in-line phase-contrast images of a mouse lung,” *J. Synchrotron Radiat.*, vol. 21, no. 4, pp. 784–789, 2014.
- [25] A. Burvall, U. Lundström, P. A. C. Takman, D. H. Larsson, and H. M. Hertz, “Phase retrieval in X-ray phase-contrast imaging suitable for tomography,” *Opt. Express*, vol. 19, no. 11, pp. 10359–10376, 2011.
- [26] R. C. Chen, L. Rigon, and R. Longo, “Comparison of single distance phase retrieval algorithms by considering different object composition and the effect of statistical and structural noise,” *Opt. Express*, vol. 21, no. 6, pp. 7384–7399, 2013.
- [27] M. Langer, P. Cloetens, J.-P. Guigay, and F. Peyrin, “Quantitative comparison of direct phase retrieval algorithms in in-line phase tomography,” *Med. Phys.*, vol. 35, no. 10, pp. 4556–4566, 2008.
- [28] R. S. Bradley, A. McNeil, and P. J. Withers, “An examination of phase retrieval algorithms as applied to phase contrast tomography using laboratory sources,” *Proc. SPIE*, vol. 7804, Sep. 2010, Art. no. 780404.
- [29] X. Wu, H. Liu, and A. Yan, “Phase-contrast X-ray tomography: Contrast mechanism and roles of phase retrieval,” *Eur. J. Radiol.*, vol. 68, no. 3, pp. S8–S12, 2008.
- [30] M. Töpperwien, M. Krenkel, F. Quade, and T. Salditt, “Laboratory-based X-ray phase-contrast tomography enables 3D virtual histology,” *Proc. SPIE*, vol. 9964, Sep. 2016, Art. no. 996401.
- [31] A. Momose, “Recent advances in X-ray phase imaging,” *Jpn. J. Appl. Phys.*, vol. 44, no. 9A, pp. 6355–6367, 2005.
- [32] S. W. Wilkins, T. E. Gureyev, D. Gao, A. Pogany, and A. W. Stevenson, “Phase-contrast imaging using polychromatic hard X-rays,” *Nature*, vol. 384, p. 335, Nov. 1996.
- [33] J. Kastner, B. Plank, and G. Requena, “Non-destructive characterisation of polymers and Al-alloys by polychromatic cone-beam phase contrast tomography,” *Mater. Characterization*, vol. 64, pp. 79–87, Feb. 2012.
- [34] S. C. Mayo, A. W. Stevenson, and S. W. Wilkins, “In-line phase-contrast X-ray imaging and tomography for materials science,” *Materials*, vol. 5, no. 5, pp. 937–965, 2012.
- [35] S. Mayo *et al.*, “X-ray phase-contrast tomography for quantitative characterisation of self-healing polymers,” *Mater. Sci. Forum*, vols. 654–656, pp. 2322–2325, Jun. 2010.
- [36] M. Krenkel, M. Töpperwien, C. Dullin, F. Alves, and T. Salditt, “Propagation-based phase-contrast tomography for high-resolution lung imaging with laboratory sources,” *AIP Adv.*, vol. 6, no. 3, 2016, Art. no. 035007.
- [37] C. M. Laperle *et al.*, “Low density contrast agents for X-ray phase contrast imaging: The use of ambient air for X-ray angiography of excised murine liver tissue,” *Phys. Med. Biol.*, vol. 53, no. 23, pp. 6911–6923, 2008.
- [38] M. Bartels, V. H. Hernandez, M. Krenkel, T. Moser, and T. Salditt, “Phase contrast tomography of the mouse cochlea at microfocus X-ray sources,” *Appl. Phys. Lett.*, vol. 103, no. 8, 2013, Art. no. 83703.
- [39] Y. S. Kashyap, P. S. Yadav, T. Roy, P. S. Sarkar, M. Shukla, and A. Sinha, “Laboratory-based X-ray phase-contrast imaging technique for material and medical science applications,” *Appl. Radiat. Isot.*, vol. 66, no. 8, pp. 1083–1090, 2008.
- [40] A. Pogany, D. Gao, and S. W. Wilkins, “Contrast and resolution in imaging with a microfocus X-ray source,” *Rev. Sci. Instrum.*, vol. 68, no. 7, pp. 2774–2782, 1997.
- [41] Y. I. Nesterets, S. W. Wilkins, T. E. Gureyev, A. Pogany, and A. W. Stevenson, “On the optimization of experimental parameters for X-ray in-line phase-contrast imaging,” *Rev. Sci. Instrum.*, vol. 76, no. 9, 2005, Art. no. 093706.
- [42] T. E. Gureyev, Y. I. Nesterets, A. W. Stevenson, P. R. Miller, A. Pogany, and S. W. Wilkins, “Some simple rules for contrast, signal-to-noise and resolution in in-line X-ray phase-contrast imaging,” *Opt. Express*, vol. 16, no. 5, pp. 3223–3241, 2008.
- [43] A. Balles, S. Zabler, T. Ebensperger, C. Fella, and R. Hanke, “Propagator based formalism for optimizing in-line phase contrast imaging in laboratory X-ray setups,” *Rev. Sci. Instrum.*, vol. 87, no. 9, 2016, Art. no. 093707.
- [44] D. Paganin, *Coherent X-Ray Optics*. London, U.K.: Oxford Univ. Press, 2006.
- [45] F. Ouandji, E. Potter, W. R. Chen, and H. Liu, “Impact of focal spot size on the spatial resolution of a digital X-ray imaging system for small-animal studies,” *Proc. SPIE*, vol. 4615, pp. 109–117, May 2002.
- [46] E. L. Ritman, “Micro-computed tomography—Current status and developments,” *Annu. Rev. Biomed. Eng.*, vol. 6, no. 1, pp. 185–208, 2004.
- [47] B. D. Arhatari and A. G. Peele, “Optimisation of phase imaging geometry,” *Opt. Exp.*, vol. 18, no. 23, pp. 23727–23739, 2010.
- [48] M. Reichardt *et al.*, “Nanoscale holographic tomography of heart tissue with X-ray waveguide optics,” *Proc. SPIE*, vol. 10391, Sep. 2017, Art. no. 1039105.
- [49] M. Töpperwien *et al.*, “Three-dimensional mouse brain cytoarchitecture revealed by laboratory-based X-ray phase-contrast tomography,” *Sci. Rep.*, vol. 7, Feb. 2017, Art. no. 42847.

- [50] D. Paganin, S. Mayo, T. E. Gureyev, P. R. Miller, and S. W. Wilkins, "Simultaneous phase and amplitude extraction from a single defocused image of a homogeneous object," *J. Microsc.*, vol. 206, no. 1, pp. 33–40, 2002.
- [51] T. Weitkamp, D. Haas, D. Wegrzynek, and A. Rack, "ANKAphase: Software for single-distance phase retrieval from inline X-ray phase-contrast radiographs," *J. Synchrotron Radiat.*, vol. 18, no. 4, pp. 617–629, 2011.
- [52] J. Taylor. (2015). X-ray complex refraction coefficient. CSIRO CSS eToolbox Home. [Online]. Available: <https://ts-imaging.net/Services/Simple/ICUtilXdata.aspx>



**Dominika Kalasová** was born in 1992. She received the M.Sc. degree from the Brno University of Technology, Brno, Czech Republic, in 2016, where she is currently pursuing the Ph.D. degree, under the supervision of Prof. J. Kaiser.

Her current research interests include imaging of soft materials by X-ray computed tomography.



**Tomáš Zikmund** was born in 1984. He received the M.Sc. and Ph.D. degrees from the Brno University of Technology (BUT), Brno, Czech Republic, in 2008 and 2014, respectively.

He is the Head of the Laboratory of X-ray Micro and Nano Computed Tomography, Central European Institute of Technology (CEITEC), BUT. His current research interests include X-ray computed tomography and image processing of soft tissue (cartilage tissue, mouse brain, bile duct system in the liver, bio-degradable composites, stem cells), and

correlations of 2-D imaging techniques with 3-D data of X-ray computed tomography.



**Ladislav Pína** was born in 1946. He received the M.Sc. and Ph.D. degrees from the Faculty of Nuclear Sciences and Physical Engineering, Czech Technical University, Prague, Czech Republic, in 1972 and 1978, respectively.

From 1980 to 1981, he was on a study stay with the Department of Pure and Applied Physics, Queen's University of Belfast, Belfast, U.K., which included experimental work using ion and X-ray diagnostics of laser plasma in the Rutherford Appleton Laboratory. In 1983, he joined the Department of

Physical Electronics, Czech Technical University, as an Associate Professor and has been teaching electricity and magnetism, quantum electronics, and X-ray physics. He supervises M.Sc. and Ph.D. students. His current research interests include physics of generation, detection, and imaging in extreme ultraviolet to X-ray radiation bands.

Dr. Pína is a member of SPIE.



**Yoshihiro Takeda** was born in 1979. He received the B.Sc. and M.Sc. degrees from Osaka Prefecture University, Osaka, Japan, in 2002 and 2004, respectively, and the Ph.D. degree from Tsukuba University, Tsukuba, Japan, in 2007.

From 2007 to 2008, he was a Post-Doctoral Fellow with the Graduate School of Frontier Sciences, The University of Tokyo, Tokyo, Japan. In 2008, he was a Specially Appointed Assistant Professor with the Keio University School of Medicine, Tokyo. He is currently a Researcher with the X-ray Research Laboratory, Rigaku Corporation, Tokyo. His current research interests include X-ray phase imaging and X-ray computed tomography.



**Martin Horváth** was born in 1970. He received the M.Sc. and Ph.D. degrees from the Charles University, Prague, Czech Republic, in 1994 and 2002, respectively.

From 1999 to 2008, he was a Development Scientist with Reflex s.r.o., Prague. Since 2008, he has been a Development Scientist with Rigaku Innovative Technologies Europe, s.r.o., Prague. His current research interests include design and development of X-ray detectors.



**Kazuhiko Omote** received the Ph.D. degree in engineering from the University of Nagoya, Nagoya, Japan, in 1991.

He was a General Manager with the X-Research Laboratory, Rigaku Corporation, Tokyo, Japan. He has developed a lot of instruments and software for X-ray analysis of Rigaku Corporation. His current research interests include structural analysis of thin films and nanomaterials, X-ray diffraction/scattering theory, and X-ray optics.



**Jozef Kaiser** was born in 1974. He received the M.Sc. and Ph.D. degrees from the Brno University of Technology, Brno, Czech Republic, in 1997 and 2001, respectively.

He absolved long-term internships with the University of Pécs, Pécs, Hungary, from 1998 to 2001; the University of Orléans, Orléans, France, in 2003; and the University of L'Aquila, L'Aquila, Italy, in 2006; and several short-term research stays with Synchrotron Elettra, Trieste, Italy, from 2005 to 2014. In 2013, he was a Professor with the Brno

University of Technology. He is currently a Research Group Leader of the Materials Characterization and Advanced Coatings Group, Central European Institute of Technology, Brno University of Technology. His current research interests include laser-based analytical methods [Laser-Induced Breakdown Spectroscopy (LIBS) and Laser Ablation Inductively Coupled Plasma methods, and Raman spectroscopy] and X-ray computed tomography, especially on the development of high-end LIBS instrumentation and the technology transfer of LIBS technology to industry.

PAPER [II]

# Wide-Cone Angle Phase-Contrast X-Ray Computed Tomography of Synthetic Polymer Materials

Dominika Kalasová<sup>1</sup>, Adam Břínek<sup>1</sup>, Miroslav Šlouf<sup>1</sup>, Miroslava Dušková-Smrčková<sup>1</sup>,  
Tomáš Zikmund<sup>1</sup>, Zuzana Patáková<sup>1</sup>, and Jozef Kaiser<sup>1</sup>

**Abstract**—X-ray phase-contrast imaging (PCI) is sensitive to the phase shift of X-rays induced by the sample. This is advantageous for low X-ray absorption samples, such as polymers, biomaterials, tissues, and scaffolds. We show propagation-based phase-contrast X-ray computed tomography (CT) imaging [propagation-based imaging (PBI)] in a specific configuration with the wide-cone angle ( $>50^\circ$ ), polychromatic X-ray source, and a flat-panel detector. We demonstrate PBI on measurements with a polymer composite. The experiments show a tradeoff between high signal-to-noise ratio (SNR) acquisition at very large cone angles and low-SNR acquisition at large propagation distances. The degree of data quality improvement by phase retrieval increases for high propagation distances. We show the application of PBI on macroporous synthetic hydrogels, which represents an important type of material with a complex 3-D morphology in the field of polymer science. With the use of the above-described experimental configuration, it is possible to visualize the hydrogels and segment the structure of the sample in tomographic data. The segmented sample can be used for morphology characterization, such as the description of internal space or determination of specific surface area (SSA).

**Index Terms**—Phase-contrast imaging (PCI), propagation-based imaging (PBI), synthetic polymer materials, wide-cone angle X-ray computed tomography (CT), X-ray CT.

## I. INTRODUCTION

X-RAY phase-contrast imaging (PCI) is a great imaging modality for X-ray computed tomography (CT) systems [1]. It is sensitive to the phase shift of X-rays induced by the sample, so the image contrast does not rely only on X-ray absorption. This is advantageous for low-absorbing samples, such as polymers, biomaterials, tissues, or scaffolds [2]–[6].

The phase shift induced by the interaction of X-rays transmitted through the material with electron shells of atoms can be used for contrast enhancement in several techniques of PCI.

Manuscript received February 3, 2020; accepted May 7, 2020. Date of publication May 18, 2020; date of current version October 9, 2020. This work was supported by the Project TA CR under Grant TN01000008. The Associate Editor coordinating the review process was Shutao Li. (Corresponding author: Jozef Kaiser.)

Dominika Kalasová, Adam Břínek, Tomáš Zikmund, and Jozef Kaiser are with the Central European Institute of Technology (CEITEC), Brno University of Technology, 61200 Brno, Czech Republic (e-mail: dominika.kalasova@ceitec.vutbr.cz; adam.brinek@ceitec.vutbr.cz; tomas.zikmund@ceitec.vutbr.cz; jozef.kaiser@ceitec.vutbr.cz).

Miroslav Šlouf and Miroslava Dušková-Smrčková are with the Institute of Macromolecular Chemistry, Czech Academy of Sciences, 16206 Prague 6, Czech Republic (e-mail: slouf@imc.cas.cz; m.duskova@imc.cas.cz).

Zuzana Patáková is with Thermo Fisher Scientific, 62700 Brno, Czech Republic (e-mail: zuzana.patakova@thermofisher.com).

Color versions of one or more of the figures in this article are available online at <http://ieeexplore.ieee.org>.

Digital Object Identifier 10.1109/TIM.2020.2995232

Interferometric techniques use beam splitters (crystals or gratings) to divide the beam into two beams, an undisturbed reference one and a one passing through the sample. When these beams meet, they create interference patterns, from which the phase shift can be retrieved [7], [8]. Alternatively, analyzer crystals can be used to filter X-rays diffracted at different angles [9], [10]. These methods require a high degree of X-ray coherence. For this reason, they are mostly employed with synchrotron X-ray sources.

However, PCI can be employed with polychromatic, much less coherent X-ray sources emerging in the form of cone beam from the finite focal spot. A very popular form of PCI is Talbot–Lau grating interferometry [11], [12]. The setup uses a self-imaging property of a diffraction grating. Disturbances in the image of the grating induced by the sample can be used to calculate the image of the sample. Laboratory setups equipped with two masks with slits can be used for edge illumination technique [13], [14]. The first mask is placed so that only a part of the incident beam is used for sample illumination. The intensity of the beam incident on the second mask in front of a detector is attenuated, and its spatial position is shifted. By scanning the sample with these masks, an image of the sample is calculated. Phase contrast can also be observed in X-ray microscopes with zonal plates [15]. Nevertheless, these methods require the usage of X-ray optics additionally to the original CT setup.

Propagation-based, or in-line, imaging (PBI) is the simplest implementation of PCI and can also be implemented easily for laboratory X-ray sources [16]–[18]. It does not require any additional optical components in the setup, only the change of the detector position to a longer distance than for absorption contrast imaging. The phase of radiation passing through the sample is varied with different thicknesses and refractive index of a material. As the X-rays propagate after the sample, the change of phase is transferred to the change of intensity in the form of edge enhancement, which is recorded at the detector. Amount of edge enhancement is higher as the Laplacian and gradient of phase shift  $\phi$  increases. The relationship between intensity  $I(x, y)$  and phase  $\phi(x, y)$  of a monochromatic wave of wavelength  $\lambda$  propagating along the  $z$ -axis is described via the transport of intensity equation [19]

$$\nabla_{\perp}[I(x, y)\nabla_{\perp}\phi(x, y)] = -\frac{2\pi}{\lambda} \frac{\partial}{\partial z} I(x, y)$$

where  $\nabla_{\perp}$  is applied in the plane  $x$  and  $y$  perpendicular to the direction of propagation. This relation can be generalized

for polychromatic spectrum, cone-beam setup, and optical response of the detector [17], but the principal relation between phase and intensity remains the same. This implies a stronger phase contrast for higher propagation distances.

Data from PBI are processed with phase retrieval algorithms to calculate the amount of the phase change the X-rays developed during the interaction with the sample [20], [21]. In case of the above-described experimental setup for PBI at a single distance in laboratory conditions, we use the frequently applied Paganin algorithm [22]. It filters the image intensity image in Fourier domain  $u, v$  and it depends on  $\delta$  and  $\beta$  values of index of refraction  $n = 1 - \delta + i\beta$

$$\pi(x, y) = \frac{\delta}{2\beta} \ln \left( \mathcal{F}^{-10} \left( \frac{\mathcal{F}(I(x, y))}{\frac{\lambda\delta}{4\pi\beta}(u^2 + v^2) + 1} \right) \right).$$

In a rough approximation, the strength of the filter increases linearly with  $z_p$ .

PBI is influenced and limited by several factors on a physical or mechanical basis. The formation of interference fringes depends on the degree of X-ray coherence [17], [23]. Amount and appearance of the fringes are influenced by the detector position [24]. At the same time, the intensity of X-rays emerging from the focal spot follows the inverse-square law:  $I(x, y) \propto 1/z_p^2$  for the propagation distance  $z_p$ . The intensity, and therefore the signal on the detector, decreases with distance. Thus, more noise can be expected in data. The resolution of laboratory-based CT systems is limited by the source focal spot of size [25]. All these factors influence the possibilities of PBI of a given CT device [26].

Research on macroporous synthetic hydrogels is an important field of polymer science. In biology, the porous water-swollen hydrogels are used as so-called 3-D scaffolds for the cultivation of cellular tissues [27], [28]. In technical applications, the porosity in gels is highly demanded because of gels sorption capability, an increase of gel's internal surface, and providing permeability to materials. Porous hydrogels are used as well-defined substrates in chromatography in analytical chemistry [29], [30] and as substrates in the removal of water pollutants in waste-water treatment [31]. The specially designed porous hydrogel particles serve, for example, as heavy metals scavengers from water, as the substrate for enzyme immobilization in enzymatic pollutant degradation technology, but recently also as the selective sorbents for hormone disruptors removal. A very promising are the emerging applications of hydrogels in water recovery [32].

In 2-hydroxyethyl methacrylate (HEMA)-based systems, the phase separation induced during polymerization leads to a special particulate morphology of nearly uniform, evenly distributed, and connected hydrogel spheres spanning throughout the whole sample volume [33]–[35]. Such particulate structure is well known in the area of phase separation of hydrogels and is sometimes called “spongy morphology.” The size of spheres in water-swollen gels is approximately 4–8  $\mu\text{m}$ , and the 2-D micrographs from scanning electron microscopy (SEM) techniques suggest that the structure is bicontinuous [36]. However, despite many studies on the morphology of the phase-separated spongy hydrogel mostly done

with SEM or light microscopy (LM) techniques [37], [38], little is known about the precise structural arrangement in the space of the fused hydrogel spheres. Also, imaging methods to obtain quantitative information on the pore volume fraction, size and shape distribution of pores, or the internal surface area in the spongy gels are still not available.

The visualization of morphology of synthetic polymer hydrogels by microscopic techniques is a challenging task in both 2-D and 3-D, despite all recent progress in microscopic techniques. As the hydrogels can contain more than 90 wt.% of water, their morphology breaks down completely when they are dried without any special treatment at room temperature. In principle, microscopy of polymer hydrogels can be carried out in the swollen state, frozen state, or dried state.

From the point of view of image artifact (incorrect visualization) minimization, the best option is the microscopy of polymer hydrogels in their native, swollen state, when they are fully submerged in water [33], [39], [40]. This can be achieved by classical, wide-field LM, laser scanning confocal microscopy (LSM), scanning probe microscopy (SPM), environmental scanning electron microscopy (ESEM), or phase-contrast X-ray CT. Nevertheless, all the techniques mentioned earlier have their limitations; LM yields just 2-D micrographs, which suffer from low resolution and low depth of focus. LSM has slightly better resolution in  $xy$  plane and gives 3-D-images, but the  $Z$ -range is quite limited. SPM microscopy is unsuitable due to the limited range of the probe in both  $xy$ - and  $z$ -directions. ESEM microscopy (also referred to as variable pressure SEM or VP-SEM) of polymer hydrogels is quite demanding, not completely free from image artifacts, and yields just 2-D-micrographs. CT of polymer hydrogels in the swollen state is extremely difficult if not impossible due to the very low contrast between swollen hydrogel and water.

Observation of the hydrogels in a dried or frozen state is possible by means of SEM and cryogenic scanning electron microscopy (Cryo-SEM) techniques [41], [42]. Both techniques have sufficient resolution and improved depth of focus in comparison with LM but yield just 2-D-images of the 3-D structure. It might seem possible to employ some of the 3-D-SEM microscopy techniques. However, both serial block-face SEM (SBF-SEM: physical slicing of a specimen in the microscopic chamber) and focused ion beam SEM (FIB-SEM: observation of the inner structure of a specimen after etching with ion beam) fail due to unsuitable mechanical properties of dried and/or frozen hydrogels (brittle, porous structures). Therefore, the CT phase-contrast technique with improved resolution represents an interesting alternative to the SEM methods, as far as the visualization of complex 3-D-morphologies of dried synthetic polymer hydrogels is concerned. The resolution of CT methods may be still below the resolution of modern SEM microscopes, but the possibility of 3-D-visualization is a significant advantage. In general, freezing or drying of the hydrogels can cause serious image artifacts, but according to our experience, in dried particulate hydrogels (i.e., the hydrogels with spongy morphology formed by interconnected spherical particles), the artifacts are not

TABLE I

EXPERIMENTAL SETUP OF PBI EXPERIMENTS—TWO MEASUREMENTS AT TWO DIFFERENT PROPAGATION DISTANCES  $z_p$  (SAMPLE–DETECTOR DISTANCE).  $z_p = y_D - y_S$  ( $y_S$  IS THE SOURCE–SAMPLE DISTANCE AND  $y_D$  IS THE SOURCE–DETECTOR DISTANCE)

$y_S$ [mm]	$y_D$ [mm]	$z_p$ [mm]
5	300	$295 \approx 300$
11	719	$708 \approx 710$

critical, and the overall morphology is qualitatively preserved although the structure may be isotropically shrunk [39].

In this article, PBI in configuration with wide-cone angle, the polychromatic X-ray source, and a flat-panel detector is shown. We demonstrate the phenomena on measurements with polymer composite at different propagation distances and apply a modified phase retrieval algorithm to improve data quality. We discuss relations and tradeoffs between different image evaluation parameters. The CT in configuration for PBI and with high magnification is used for imaging of polymeric hydrogel samples, where we show advantages of CT as a 3-D imaging technique. Measurement of hydrogels is complemented with and SEM to compare the CT results with the results of commonly employed methods.

## II. MATERIALS AND METHODS

### A. Testing of Propagation-Based Imaging

Experiments with PBI were performed on a laboratory-based CT system HeliScan microCT (Thermo Fisher Scientific) with a tungsten filament and a wide-cone angle X-ray beam. Helical space-filling trajectory with iterative reconstruction developed by Thermo Fisher Scientific was used [43]. To test different settings of PBI, a polymer composite with carbon fibers (CFPC) was used. The carbon hollow rod with fibers with approximately 2-mm diameter was filled with glue and attached to the sample holder. The cracks in the rod create a lot of air-sample boundaries, where edge enhancement is visible. Different kinds of polymers in the sample have a similar density. The small difference in densities of such light materials results in low absorption contrast and high phase contrast.

The main variable in the PBI is the distance between the sample and the detector. Two CT scans were made at two propagation distances  $z_p$  (sample–detector distance) to record and evaluate the edge enhancement (see Table I) while maintaining the voxel resolution. Both measurements were recorded with 50-kV tube voltage, 100- $\mu$ A tube current, 4-s exposure time, 1800 projections per revolution, and the same linear voxel size 2  $\mu$ m. The phase retrieval suggested by Paganin ([22], commented in Section I) was applied to the data.

Image evaluation was performed in MATLAB (The MathWorks, Inc.) on a representative slice from the data set (see Fig. 1). The edge enhancement was evaluated on an averaged line profile on the edge of air and polymer (five pixels above and below the line were averaged to reduce noise). The following parameters, signal-to-noise ratio (SNR), absorption contrast value  $C_{ABS}$ , and phase-contrast value  $C_{PHC}$ , were used

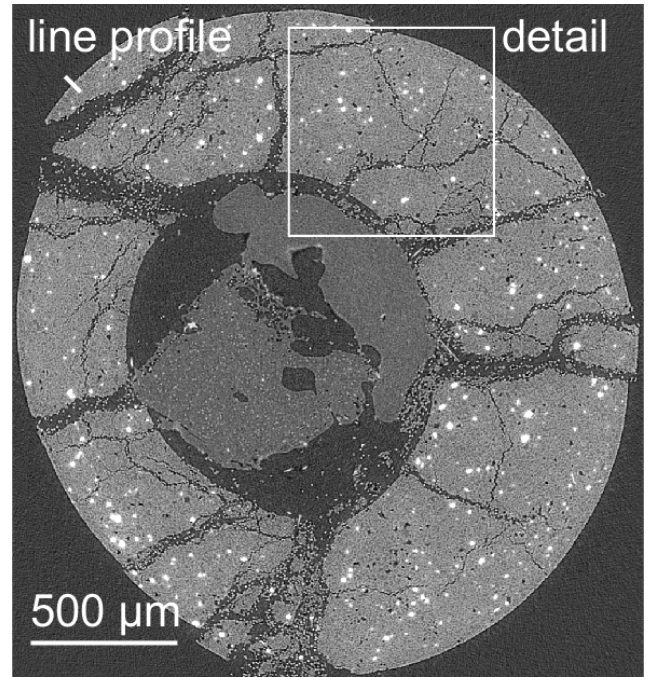


Fig. 1. Slice of carbon fibers polymer composite obtained via PBI. The rectangle marks the area used in Fig. 2. The line was used for the generation of edge profiles in Fig. 3.

as a figure of merit [24]:

$$\text{SNR} = \frac{I_{\text{mat}}}{\text{std}(I_{\text{bcg}})}$$

$$C_{\text{ABS}} = \frac{I_{\text{mat}} - I_{\text{bcg}}}{(I_{\text{mat}} + I_{\text{bcg}})/2}$$

$$C_{\text{PHC}} = \frac{I_{\text{max}} - I_{\text{min}} - (I_{\text{mat}} - I_{\text{bcg}})}{(I_{\text{max}} + I_{\text{min}})}$$

where  $I_{\text{mat}}$ ,  $I_{\text{bcg}}$ ,  $I_{\text{max}}$ , and  $I_{\text{min}}$  are the mean gray values of material and background and the maximum and minimum gray values in the line profile, respectively. The ratio of the values in phase retrieved and original images is called the gain.

### B. Imaging of Hydrogels

Polymeric hydrogel scaffold was used to demonstrate the advantages of PBI CT for characterization of material's structure. The sample was prepared by free-radical crosslinking polymerization of 2-HEMA monomer initiated by a redox system composed of ammonium persulphate (APS) and N,N,N,N-tetramethylethylenediamine (TEMED) at ambient conditions in the presence of water as diluent. HEMA contained 0.07% diethylene glycol dimethacrylate (DEGDMA) (bifunctional cross linker) and 0.44% of di(ethylene glycol) monomethacrylate. The water was used as diluent at a level of 80 vol.-%, the rest of polymerization mixture was composed of HEMA monomer, the crosslinker ethylenglycol dimethacrylate (EDMA) at a level 0.1 and 4 molar % with respect to both monomers (HEMA + EDMA), and the initiator (APS/TEMED). The sample was then dried by lyophilization (freeze drying) in the lyophilizer Gregor.

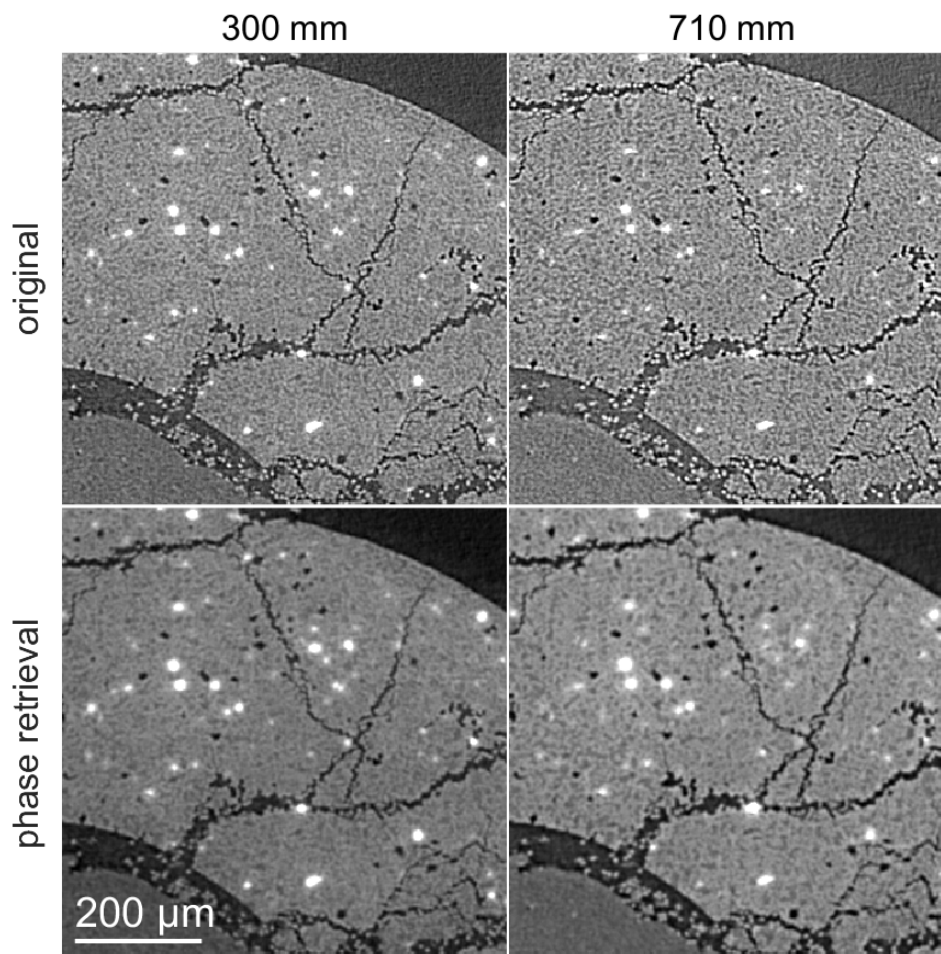


Fig. 2. Two measurements of carbon fibers polymer composite at different propagation distances  $z_p$  (300 and 710 mm), original and with phase retrieval. The images depict detail indicated in Fig. 1.

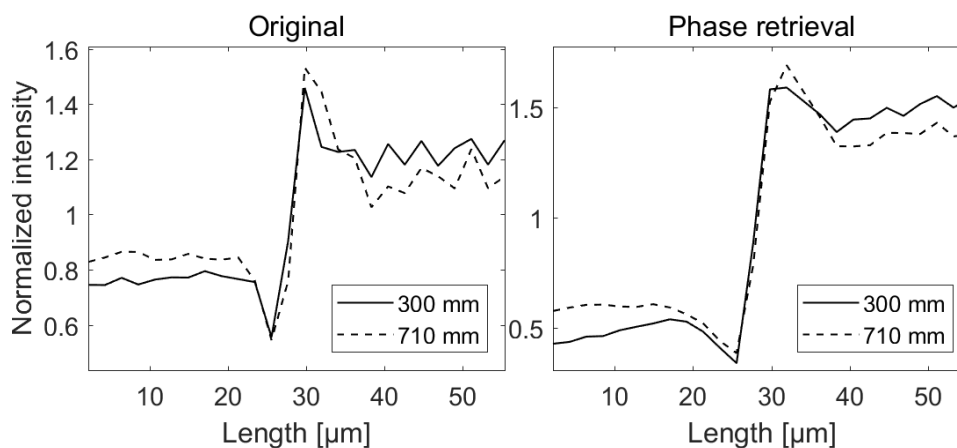


Fig. 3. Line profiles (along the line in Fig. 1) for two measurements of carbon fibers polymer composite at different propagation distances  $z_p$  (300 and 710 mm), original and with phase retrieval.

The sample was measured with the HeliScan microCT device with space-filling helical trajectory. Based on the results from previous PBI testing, the strategy for measurement of the hydrogel was to exploit PBI as much as possible. This means

the long propagation distance  $\approx 727$  mm (source–sample distance was 4.101 mm and source–detector distance was 731.568 mm). This is also the setup with big magnification—the voxel size is  $0.78 \mu\text{m}$ . Other imaging parameters are tube

voltage 50 kV, tube current 100  $\mu\text{A}$ , exposure time 16 s, and 1800 projections per revolution. The phase retrieval suggested by Paganin [22] was applied to the data. The visualization and pore space analysis were performed in VGStudio MAX software.

For comparison, the sample was also imaged with the LM DM 6000 M (Leica, Austria) and SEM Maia3 (Tescan, Czech Republic). Final LM micrographs were acquired with an extended depth of focus, and the final image was composed of a series of images taken at different Z-positions of the microscopic stage. The images were combined into the final micrograph by means of dedicated software for automatic image acquisition (Leica Application Suite (LAS) Multifocus module; Leica, Austria).

### III. RESULTS AND DISCUSSION

#### A. Testing of Propagation-Based Imaging

The CFPC sample contains several kinds of polymers with different densities (see Fig. 1). For the detailed view, a region containing multiple materials, including the fibers in the outer layer, is shown for all measurements in Fig. 2. The line profile was evaluated on both data without and with phase retrieval in Fig. 3.

The phase-contrast enhancement is visible in both measurements. The data recorded at higher propagation distance exhibit higher edge enhancement (higher  $C_{\text{PHC}}$ ) and lower absorption contrast ( $C_{\text{ABS}}$ ) than at lower propagation distance. This is supported by the supposed increase of phase effects with increasing Laplacian and gradient of phase shift introduced by the transport of intensity equation.

The SNR is, on the other hand, lower for high  $z_p$  (high cone angle). This is understandable since the flux remains the same for both measurements and the intensity naturally decreases with the distance. Thus, the noise is more pronounced at high  $z_p$ .

Application of phase retrieval on data increases SNR about 35%–45% and  $C_{\text{ABS}}$  about 120%–170%. The phase retrieval transforms the phase contrast into “absorption” contrast in the image, which is convenient for segmentation and further processing (for each image, there is increased  $C_{\text{ABS}}$  and decreased  $C_{\text{PHC}}$ ). Materials with similar densities are more easily recognizable from each other. The differences should be more significant at high propagation distances. Indeed, a degree of data quality improvement by phase retrieval, expressed by gain, increases for high  $z_p$ .

In general, data obtained at small  $z_p$  have higher SNR and absorption contrast than data obtained at larger  $z_p$ , which exhibit more phase contrast. Since the intensity decreases with the square of the distance and using the simplification that phase-contrast increases approximately linearly with distance, we can deduce that there is an optimal imaging distance for each type of sample.

For a very absorbing object, high-SNR acquisition at small  $z_p$  is suitable. However, samples composed of light materials, such as various polymer structures, have a different optimal strategy. The phase shift of X-rays that they induce is much more significant than their absorption compared with heavy

TABLE II  
IMAGE EVALUATION PARAMETERS FOR TWO MEASUREMENTS OF CARBON FIBERS POLYMER COMPOSITE AT DIFFERENT PROPAGATION DISTANCES  $z_p$

$z_p$		300 mm	710 mm
SNR	original	17	11
	phase retrieval	23	27
	gain	1.36	2.45
$C_{\text{ABS}}$	original	0.48	0.30
	phase retrieval	1.05	0.80
	gain	2.19	2.67
$C_{\text{PHC}}$	original	0.21	0.33
	phase retrieval	0.11	0.25

materials. Using PBI and processing with phase retrieval will give data with good quality for long propagation distances. There are two main limitations to increasing the propagation distance. The decreasing intensity means the need for higher exposure times, and thus, the measurements will take a longer time. Second, with high distance, the blurring due to finite focal spot size can occur. With phase retrieval also lowering the resolution, we must consider what resolution will be sufficient for a specific case.

#### B. Imaging of Hydrogels

The polymer hydrogel sample was visualized via multiple techniques to compare the CT imaging with methods that are commonly used for this kind of samples—LM and SEM (see Fig. 4). The communicating pores of size on the order of  $10^1$ – $10^2$   $\mu\text{m}$  serve as channels to support the growth of multicellular structure through the hydrogel, while the hydrogel matrix provides a biomimetic environment that enables the transfer of nutrition and metabolites through a much finer network of fine communicating pores on the order of  $10^0$ – $10^{-1}$   $\mu\text{m}$ . The comparison of 2-D LM and 2-D SEM micrographs suggested that the swollen microsized spheres of the investigated hydrogel do shrink, but the overall morphology and topology (i.e., mutual connectivity between the domains) seems to be preserved.

The applied techniques provide the images of the sample, but they have some limitations. LM is only a 2-D image of the sample. The sample has to be prepared in a form similar to a thin plate, so it is transparent enough for light. At the same time, it suffers from a low depth of focus, so only a thin part of the sample is in focus. In comparison with LM, the SEM has improved focal depth and resolution. Although SEM microscopy visualizes the 3-D structure of the sample quite well, the outcome is still a 2-D image, where analysis in 3-D cannot be performed.

A significant advantage of CT measurements is a big volume of samples it can visualize, while the maximal field of view in LM and SEM is usually limited to a few millimeters. Moreover, during the LM/SEM observations of microscale structures, the field of view is further decreased as we have to increase the magnification in order to achieve sufficient resolution. In the case of polymer hydrogels, the typical LM and SEM fields of view are in the range of tens of micrometers. In contrast, the diameter of the sample measured by CT with applied resolution can be up to 2 mm, and with the use of helical trajectory, it can have up to 10 cm in height.

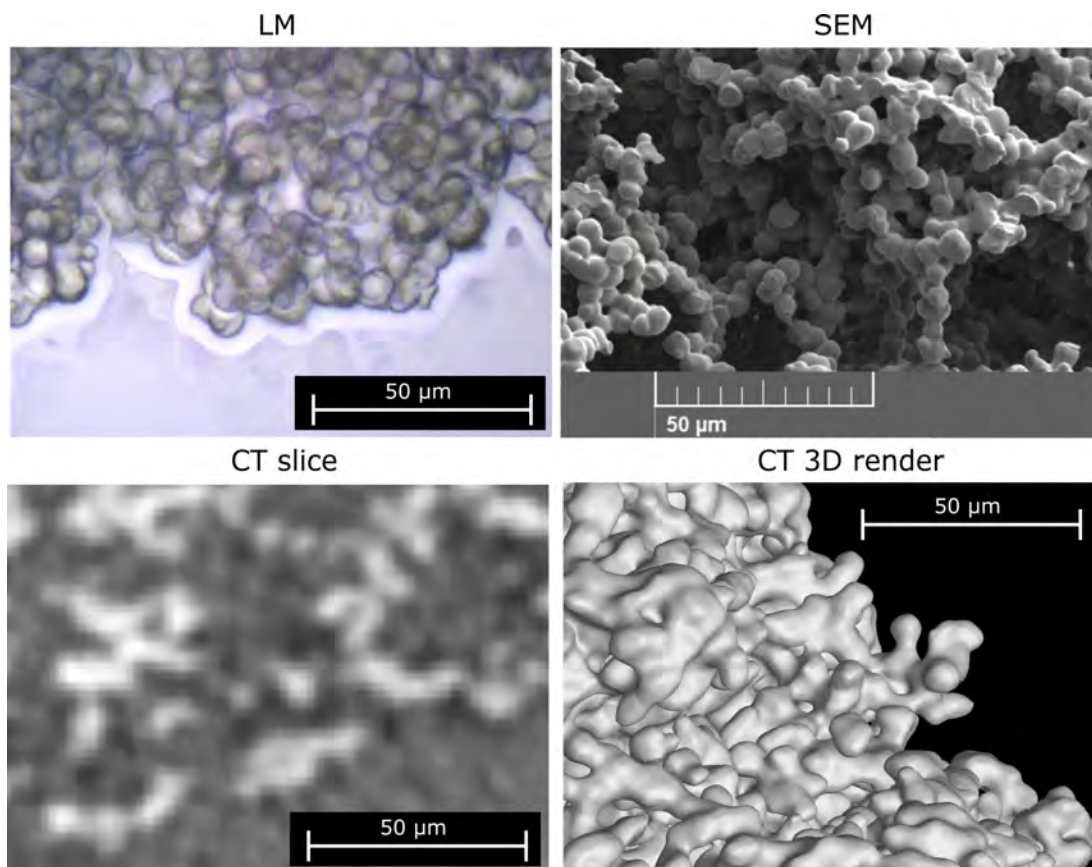


Fig. 4. Polymer hydrogel sample visualized by different techniques: (LM, extended depth of focus), SEM, slice from X-ray CT, and 3-D render from CT data.

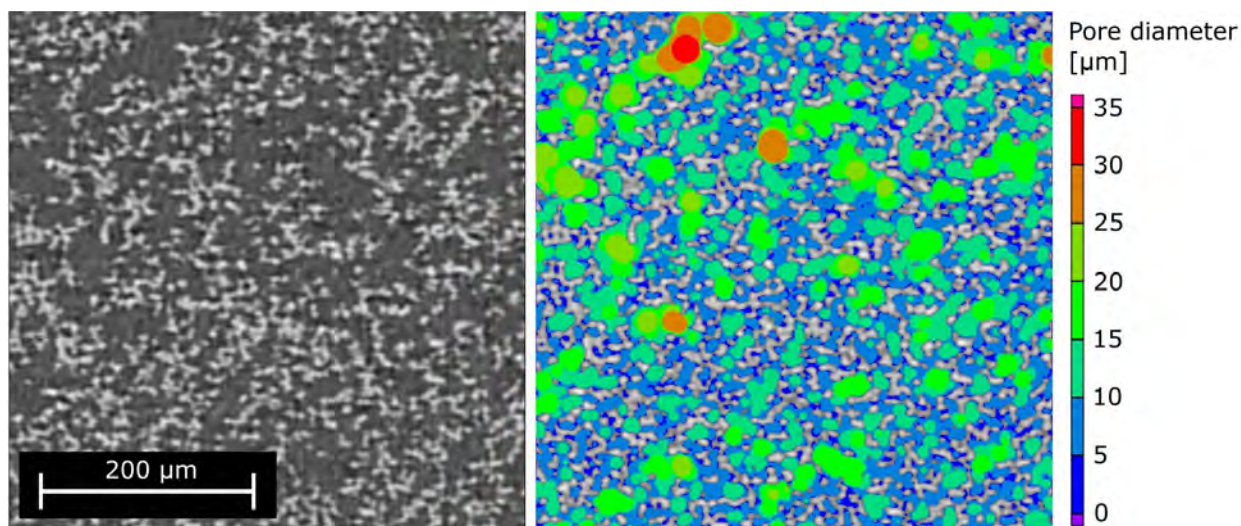


Fig. 5. CT slice of polymeric hydrogel sample. Left: clusters of white balls represent the structure of the polymer hydrogel. Right: size of internal space is color-coded by the size of the pore.

The CT data in the form of a slice through the sample exhibit lower spatial resolution in comparison with LM and SEM, but they still allow the segmentation of the structure. The 3-D render of segmented structure results in a similar image as from SEM, but it provides true 3-D information. Once the structure is segmented in a given volume of sample, it is easy to calculate the parameters describing the structure: sample volume ( $0.052 \text{ mm}^3$ ), sample surface ( $25.22 \text{ mm}^2$ ),

bulk volume ( $0.125 \text{ mm}^3$ ), or specific surface area (SSA; ratio between the sample surface and the bulk volume, in this case, it is  $201.76 \text{ mm}^{-1}$ ). The measurements of SSA by CT can be compared to measurements using gas adsorption [44].

The CT data can also be used for quantification and morphology characterization of internal space within the hydrogel structure (see Fig. 5, colors characterize dimensions of the inner space). It is possible to evaluate the passability through

the structure, i.e., to determine the size of the largest particle that can travel through the structure. In this case, it is  $8.96 \mu\text{m}$ . These key characteristics of the bicontinuous porous structures cannot be obtained with any 2-D imaging method.

#### IV. CONCLUSION

Phase-contrast propagation-based X-ray CT is no longer used only at synchrotron facilities but also in laboratories in CT devices equipped with X-ray tubes. A significant limitation in these setups for PBI is mostly an X-ray source, which produces polychromatic, cone-beam X-rays from the finite focal spot.

Here, we showed a laboratory propagation-based imaging with wide-cone X-ray angle and a flat-panel detector. The phenomenon was demonstrated on measurements of a polymer composite at two different propagation distances. The phase retrieval was applied to improve the data by removing the edge enhancement and increase the SNR about 35%–45% and the contrast about 120%–170%. The phase contrast increases with the distance between the sample and the detector, but SNR decreases with this distance. Therefore, the optimal propagation distance to achieve good contrast is application-dependent. The advantages and disadvantages of absorption/phase contrast setups were discussed.

Based on these demonstration experiments, we show the measurements of a polymeric hydrogel. It is an example of light material with a complex 3-D morphology. With PBI, it is possible to visualize the structure and reveal morphology characteristics, which would be inaccessible with 2-D imaging methods.

Demonstration of PBI as a useful tool for examination of polymer materials can encourage scientists to perform their experiments with laboratory CT devices.

#### ACKNOWLEDGMENT

The authors would like to thank Trond Varslot for helpful discussions, and Benjamin Young and David Prokop who helped with CT measurements.

#### REFERENCES

- [1] S.-A. Zhou and A. Brahme, "Development of phase-contrast X-ray imaging techniques and potential medical applications," *Phys. Medica*, vol. 24, no. 3, pp. 129–148, Sep. 2008.
- [2] O. Betz *et al.*, "Imaging applications of synchrotron X-ray phase-contrast microtomography in biological morphology and biomaterials science. I. General aspects of the technique and its advantages in the analysis of millimetre-sized arthropod structure," *J. Microsc.*, vol. 227, no. 1, pp. 51–71, Jul. 2007.
- [3] J. J. Socha, M. W. Westneat, J. F. Harrison, J. S. Waters, and W.-K. Lee, "Real-time phase-contrast X-ray imaging: A new technique for the study of animal form and function," *BMC Biol.*, vol. 5, no. 1, pp. 1–15, Dec. 2007. [Online]. Available: <https://www.ncbi.nlm.nih.gov/pmc/articles/PMC1831761/>
- [4] F. Cosmi, A. Bernasconi, and N. Sodini, "Phase contrast microtomography and morphological analysis of a short carbon fibre reinforced polyamide," *Composites Sci. Technol.*, vol. 71, no. 1, pp. 23–30, Jan. 2011.
- [5] S. C. Garcea, Y. Wang, and P. J. Withers, "X-ray computed tomography of polymer composites," *Composites Sci. Technol.*, vol. 156, pp. 305–319, Mar. 2018.
- [6] B. Yu, R. S. Bradley, C. Soutis, and P. J. Withers, "A comparison of different approaches for imaging cracks in composites by X-ray microtomography," *Phil. Trans. Roy. Soc. Math., Phys. Eng. Sci.*, vol. 374, no. 2071, Jul. 2016, Art. no. 20160037.
- [7] A. Momose, T. Takeda, Y. Itai, A. Yoneyama, and K. Hirano, "Phase-contrast tomographic imaging using an X-ray interferometer," *J. Synchrotron Radiat.*, vol. 5, no. 3, pp. 309–314, May 1998.
- [8] A. Yoneyama *et al.*, "High-energy phase-contrast X-ray imaging using a two-crystal X-ray interferometer," *J. Synchrotron Radiat.*, vol. 12, no. 4, pp. 534–536, Jul. 2005.
- [9] D. Chapman *et al.*, "Diffraction enhanced X-ray imaging," *Phys. Med. Biol.*, vol. 42, no. 11, pp. 2015–2025, 1997.
- [10] P. Coan, J. Mollenhauer, A. Wagner, C. Muehleman, and A. Bravin, "Analyzer-based imaging technique in tomography of cartilage and metal implants: A study at the ESRF," *Eur. J. Radiol.*, vol. 68, no. 3, pp. S41–S48, Dec. 2008.
- [11] F. Pfeiffer, T. Weitkamp, O. Bunk, and C. David, "Phase retrieval and differential phase-contrast imaging with low-brilliance X-ray sources," *Nature Phys.*, vol. 2, no. 4, pp. 258–261, Apr. 2006.
- [12] M. Bech, T. H. Jensen, R. Feidenhans, O. Bunk, C. David, and F. Pfeiffer, "Soft-tissue phase-contrast tomography with an X-ray tube source," *Phys. Med. Biol.*, vol. 54, no. 9, pp. 2747–2753, May 2009.
- [13] P. C. Diemoz, C. K. Hagen, M. Endrizzi, and A. Olivo, "Sensitivity of laboratory based implementations of edge illumination X-ray phase-contrast imaging," *Appl. Phys. Lett.*, vol. 103, no. 24, Dec. 2013, Art. no. 244104.
- [14] C. K. Hagen *et al.*, "Theory and preliminary experimental verification of quantitative edge illumination X-ray phase contrast tomography," *Opt. Express*, vol. 22, no. 7, p. 7989, 2014.
- [15] A. Tkachuk, F. Duewer, H. Cui, M. Feser, S. Wang, and W. Yun, "X-ray computed tomography in Zernike phase contrast mode at 8 keV with 50-nm resolution using Cu rotating anode X-ray source," *Zeitschrift für Kristallographie Crystalline Mater.*, vol. 222, no. 11, pp. 650–655, 2007.
- [16] S. W. Wilkins, T. E. Gureyev, D. Gao, A. Pogany, and A. W. Stevenson, "Phase-contrast imaging using polychromatic hard X-rays," *Nature*, vol. 384, no. 6607, pp. 335–338, Nov. 1996.
- [17] X. Wu and H. Liu, "Clarification of aspects in in-line phase-sensitive X-ray imaging," *Med. Phys.*, vol. 34, no. 2, pp. 737–743, Jan. 2007.
- [18] S. C. Mayo, A. W. Stevenson, and S. W. Wilkins, "In-line phase-contrast X-ray imaging and tomography for materials science," *Materials*, vol. 5, no. 12, pp. 937–965, May 2012.
- [19] M. Töpperwien, M. Krenkel, F. Quade, and T. Salditt, "Laboratory-based X-ray phase-contrast tomography enables 3D virtual histology," in *Advances in Laboratory-Based X-Ray Sources, Optics, and Applications V*, vol. 9964, A. M. Khounsary and G. E. van Dorssen, Eds. San Diego, CA, USA: SPIE, 2016.
- [20] A. Burvall, U. Lundström, P. A. C. Takman, D. H. Larsson, and H. M. Hertz, "Phase retrieval in X-ray phase-contrast imaging suitable for tomography," *Opt. Express*, vol. 19, no. 11, p. 10359, 2011.
- [21] R. S. Bradley, A. McNeil, and P. J. Withers, "An examination of phase retrieval algorithms as applied to phase contrast tomography using laboratory sources," *Develop. X-Ray Tomogr. VII*, vol. 7804, no. 6, 2010, Art. no. 780404.
- [22] D. Paganin, S. C. Mayo, T. E. Gureyev, P. R. Miller, and S. W. Wilkins, "Simultaneous phase and amplitude extraction from a single defocused image of a homogeneous object," *J. Microsc.*, vol. 206, no. 1, pp. 33–40, Apr. 2002.
- [23] X. Wu, H. Liu, and A. Yan, "Phase-contrast X-ray tomography: Contrast mechanism and roles of phase retrieval," *Eur. J. Radiol.*, vol. 68, no. 3, pp. S8–S12, Dec. 2008.
- [24] J. Kastner, B. Plank, and G. Requena, "Non-destructive characterisation of polymers and Al-alloys by polychromatic cone-beam phase contrast tomography," *Mater. Characterization*, vol. 64, pp. 79–87, Feb. 2012.
- [25] F. Ouanji, E. Potter, W. R. Chen, and H. Liu, "Impact of focal spot size on the spatial resolution of a digital X-ray imaging system for small-animal studies," in *Proc. Int. Symp. Biomed. Opt.*, San Jose, CA, USA, 2002, pp. 109–116.
- [26] D. Kalasova *et al.*, "Characterization of a laboratory-based X-ray computed nanotomography system for propagation-based method of phase contrast imaging," *IEEE Trans. Instrum. Meas.*, vol. 69, no. 4, pp. 1170–1178, Apr. 2020.
- [27] H. Macková *et al.*, "Reductively degradable poly(2-hydroxyethyl methacrylate) hydrogels with oriented porosity for tissue engineering applications," *ACS Appl. Mater. Interfaces*, vol. 9, no. 12, pp. 10544–10553, 2017.

- [28] S. Woerly, R. Marchand, and G. Lavallée, "Interactions of copolymeric poly(glyceryl methacrylate)-collagen hydrogels with neural tissue: Effects of structure and polar groups," *Biomaterials*, vol. 12, no. 2, pp. 197–203, Mar. 1991.
- [29] B. Beiler, Á. Vincze, F. Svec, and Á. Sáfrány, "Poly(2-hydroxyethyl acrylate-co-ethyleneglycol dimethacrylate) monoliths synthesized by radiation polymerization in a mold," *Polymer*, vol. 48, no. 11, pp. 3033–3040, May 2007.
- [30] C. G. Gomez, G. Pastrana, D. Serrano, E. Zuzek, M. A. Villar, and M. C. Strumia, "Macroporous poly(EGDMA-co-HEMA) networks: Morphological characterization from their behaviour in the swelling process," *Polymer*, vol. 53, no. 14, pp. 2949–2955, Jun. 2012.
- [31] P. Mohammadzadeh Pakdel and S. J. Peighambaroust, "A review on acrylic based hydrogels and their applications in wastewater treatment," *J. Environ. Manage.*, vol. 217, pp. 123–143, Jul. 2018.
- [32] L. Arens *et al.*, "Energy consumption for the desalination of salt water using polyelectrolyte hydrogels as the separation agent," *Macromole. Chem. Phys.*, vol. 218, no. 24, Dec. 2017, Art. no. 1700237.
- [33] E. Karpushkin, M. Dušková-Smrčková, M. Šlouf, and K. Dušek, "Rheology and porosity control of poly(2-hydroxyethyl methacrylate) hydrogels," *Polymer*, vol. 54, no. 2, pp. 661–672, Jan. 2013.
- [34] L. Šprincl, J. Kopeček, and D. Lím, "Effect of porosity of heterogeneous poly(glycol monomethacrylate) gels on the healing-in of test implants," *J. Biomed. Mater. Res.*, vol. 5, no. 5, pp. 447–458, Sep. 1971.
- [35] E. Karpushkin, M. Dušková-Smrčková, T. Remmler, M. Lapčíková, and K. Dušek, "Rheological properties of homogeneous and heterogeneous poly(2-hydroxyethyl methacrylate) hydrogels," *Polym. Int.*, vol. 61, no. 2, pp. 328–336, Feb. 2012.
- [36] M. Dušková-Smrčková, Z. Sadakbayeva, M. Steinhart, and K. Dušek, "The manifold varieties of poly(2-hydroxyethyl methacrylate) hydrogels-IPNs," *Macromole. Symposia*, vol. 372, no. 1, pp. 28–42, Apr. 2017.
- [37] T. V. Chirila, Y.-C. Chen, B. J. Griffin, and I. J. Constable, "Hydrophilic sponges based on 2-hydroxyethyl methacrylate. I. Effect of monomer mixture composition on the pore size," *Polym. Int.*, vol. 32, no. 3, pp. 221–232, 1993.
- [38] S. M. Paterson, Y. S. Casadio, D. H. Brown, J. A. Shaw, T. V. Chirila, and M. V. Baker, "Laser scanning confocal microscopy versus scanning electron microscopy for characterization of polymer morphology: Sample preparation drastically distorts morphologies of poly(2-hydroxyethyl methacrylate)-based hydrogels," *J. Appl. Polym. Sci.*, vol. 127, no. 6, pp. 4296–4304, Mar. 2013.
- [39] M. Přádny *et al.*, "Macroporous 2-hydroxyethyl methacrylate hydrogels of dual porosity for cell cultivation: Morphology, swelling, permeability, and mechanical behavior," *J. Polym. Res.*, vol. 21, no. 11, p. 579, Nov. 2014.
- [40] B. Strachota, K. Oleksyuk, A. Strachota, and M. Šlouf, "Porous hybrid poly(N-isopropylacrylamide) hydrogels with very fast volume response to temperature and pH," *Eur. Polym. J.*, vol. 120, Nov. 2019, Art. no. 109213.
- [41] K. Depa, A. Strachota, M. Šlouf, J. Brus, and V. Cimrová, "Synthesis of conductive doubly filled poly(N-isopropylacrylamide)-polyaniline-SiO<sub>2</sub> hydrogels," *Sens. Actuators B, Chem.*, vol. 244, pp. 616–634, Jun. 2017.
- [42] B. Strachota *et al.*, "Insight into the cryopolymerization to form a poly(N-isopropylacrylamide)/clay macroporous gel: Structure and phase evolution," *Soft Matter*, vol. 13, no. 6, pp. 1244–1256, 2017.
- [43] A. M. Kingston, G. R. Myers, S. J. Latham, B. Recur, H. Li, and A. P. Sheppard, "Space-filling X-ray source trajectories for efficient scanning in large-angle cone-beam computed tomography," *IEEE Trans. Comput. Imag.*, vol. 4, no. 3, pp. 447–458, Sep. 2018.
- [44] M. Kerbrat, B. Pinzer, T. Huthwelker, H. W. Gäggeler, M. Ammann, and M. Schneebeli, "Measuring the specific surface area of snow with X-ray tomography and gas adsorption: Comparison and implications for surface smoothness," *Atmos. Chem. Phys.*, vol. 8, no. 5, pp. 1261–1275, Mar. 2008.



**Dominika Kalasová** was born in 1992. She received the M.Sc. and Ph.D. degrees from the Brno University of Technology, Brno, Czech, in 2016 and 2019, respectively.

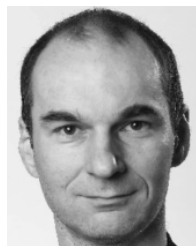
She absolved long term internships with Sinchrotrone Elettra, Trieste, Italy, in 2015, University of Jyväskylä, Jyväskylä, Finland, in 2018, and Rigaku Corporation, Tokyo, Japan, in 2018. Since 2020, she has been the Scientist with Rigaku Innovative Technologies Europe s.r.o. Her main focus is imaging of soft materials by X-ray computed tomography.



**Adam Břínek** was born in 1991. He received the M.Sc. degree from the Brno University of Technology, Czech, in 2016. He is currently pursuing the Ph.D. degree with CEITEC BUT under the supervision of Dr. Tomas Zikmund.

His study is focused on the image processing and mainly on the interface analysis in the X-ray computed tomography. He is currently doing his Internship with the Thermo Fisher Scientific company working on the CT system and mainly on multimodal and multidimensional correlative workflows.

He has coauthored several articles where he focuses on image processing analysis mainly for material characterization.



**Miroslav Šlouf** was born in 1973. He received the B.Sc., M.Sc., and Ph.D. degrees in chemistry specialized on X-ray diffraction of single crystals from Charles University, Prague, Czech, in 1994, 1996, and 2001, respectively.

Since 1998, he has been working with the Laboratory of Electron Microscopy, Institute of Macromolecular Chemistry, Prague, Czech. In 2002, he became the Head of the Laboratory, since 2010, he has been a Leader of the Department of Polymer Morphology. In 2013, he was promoted to

an Associate Professor with the Faculty of Chemistry, Brno University of Technology, Brno, Czech, where he is currently working with the Institute of Macromolecular Chemistry. His research focuses on biodegradable polymer blends for local release of antibiotics, ultrahigh molecular weight polyethylene for total joint replacements, and relations between morphology, macro- and micromechanical properties of polymer systems.



**Miroslava Dušková-Smrčková** received the M.Sc. and Ph.D. degrees from the Institute of Chemical Technology, Prague, in 1991 and 1997, respectively.

From 1997 to 1998, she was a Post-Doctoral Fellow with the Pulp and Paper Research Center, McGill University, Montreal, Canada. She is currently leading the Department of Polymer Networks and Gels, Institute of Macromolecular Chemistry, Czech Academy of Sciences, Prague. Her research interests include high-performance organic coatings, hydrogels for biomedical applications, and reactive systems for hydrogel additive manufacturing.



**Tomáš Zikmund** was born in 1984. He received the M.Sc. and Ph.D. degrees from the Brno University of Technology, Brno, Czech, in 2008 and 2014, respectively.

He is currently the Head of the Laboratory of X-ray Micro and Nano Computed Tomography (CT), CEITEC BUT. His research interest is focused on X-ray CT and image processing of soft tissue (cartilage tissue, mouse brain, bile duct system in liver, biodegradable composites, stem cells) and correlations of 2-D imaging techniques with 3-D data of X-ray CT.



**Zuzana Patáková** received the master's degree from Czech Technical University in Prague in 2015.

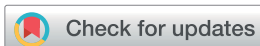
She currently leads the development of X-ray CT technologies within ThermoFisher Scientific in Brno with the main focus on helical acquisition and reconstruction.



**Jozef Kaiser** was born in April 1974. He received the M.Sc. and Ph.D. degrees from the Brno University of Technology, Brno, Czech, in 1997 and 2001, respectively.

In 2013, he was promoted to a Professor with the Brno University of Technology. He absolved long term internships with the University of Pécs, Hungary from 1998 to 2001, University of Orleans, France, in 2003, University of L'Aquila, Italy, in 2006 and several short term research stays at Synchrotron Elettra, Trieste, Italy from 2005 to 2018. He is currently the Research Group Leader of Materials Characterization and Advanced Coatings Group. His research activity is aimed at laser-based analytical methods (laser-induced breakdown spectroscopy (LIBS) and Raman spectroscopy) and X-Ray computed tomography. He is also focused on the development of high-end LIBS instrumentation and the technology transfer of LIBS technology to industry.

PAPER [III]



Cite this: *J. Anal. At. Spectrom.*, 2018, **33**, 1993

## Joint utilization of double-pulse laser-induced breakdown spectroscopy and X-ray computed tomography for volumetric information of geological samples

D. Prochazka,<sup>ab</sup> T. Zikmund,<sup>a</sup> P. Pořízka,<sup>ab</sup> A. Břínek,<sup>a</sup> J. Klus,<sup>ab</sup> J. Šalplachta,<sup>a</sup> J. Kynický,<sup>c</sup> J. Novotný<sup>ab</sup> and J. Kaiser<sup>\*ab</sup>

The purpose of this study is to present a novel algorithm to combine high-resolution X-ray Computed Tomography (HRXCT) and Double-Pulse Laser-Induced Breakdown Spectroscopy (DP LIBS) for geological samples' analysis. The ability to reveal the elemental composition of the internal structure is demonstrated on a rare geological sample from a unique Talnakh PGE–Cu–Ni sulfide deposit. The main point of the suggested approach is to assign the DP LIBS elemental maps to the different densities of the HRXCT data. This assignment is based on the coordinates of the HRXCT data (top-cross section) and DP LIBS elemental maps of the surface. The resolution and orientation of these two images are aligned in order to enable a comparison. Moreover, the volumetric information about individual materials within the sample was estimated.

Received 11th July 2018  
Accepted 3rd September 2018

DOI: 10.1039/c8ja00232k

rsc.li/jaas

### Introduction

Information about the spatial distribution and the volume of elements and materials is highly demanded in many areas of science and industrial applications. One of the areas where this information is of high importance is geology. A decision about the economic viability of a deposit can be done only based on the knowledge about the volume distribution of selected minerals within the ore. Moreover, the 3D structure of minerals can help to understand the processes of formation of geological deposits.

High-resolution X-ray computed tomography (HRXCT) could be considered as the most common tool for an effective, powerful and nondestructive 3D inspection of geological materials.<sup>1</sup> State of the art HRXCT systems enable a complete visualization and quantification of the internal structure of geological materials at scales down to the sub-micron level.<sup>2–6</sup> Consequently, HRXCT becomes an extension technique and an inseparable part to the traditional petrographic analysis. It is applied in many disciplines of geoscience,<sup>7</sup> such as 3D pore characterisation,<sup>8,9</sup> 3D grain analysis,<sup>10,11</sup> fracture analysis,<sup>12,13</sup> multi-scale imaging,<sup>14</sup> ore analysis,<sup>15,16</sup> monitoring structural dynamic processes,<sup>17,18</sup> and fluid flow analysis.<sup>19,20</sup>

Despite the fact that the X-ray attenuation is proportional to the atomic number of the element, the HRXCT data don't show right away the chemical composition. In order to get some information not only about the internal structure but also about the chemical composition of each distinguished mineral phase, a certain analytical chemistry method has to be employed.

Some conventionally used methods for a chemical analysis of geological samples are X-ray photoelectron spectroscopy (XPS),<sup>21,22</sup> Auger electron spectroscopy (AES),<sup>23</sup> secondary ion mass spectroscopy (SIMS),<sup>24</sup> Raman spectroscopy<sup>25</sup> and scanning electron microscopy-energy dispersive X-ray spectroscopy (SEM-EDX).<sup>26</sup> Despite certain advantages of these techniques, most of them present some drawbacks such as: need for some sample preparation (*e.g.*, polishing, conductive surface treatment, *etc.*), requirement for vacuum conditions, analyzed volume limitation, long acquisition time and high operational costs. Laser-Induced Breakdown Spectroscopy (LIBS) is a good alternative to the above-mentioned methods. LIBS enables us to perform on-line analyses with a short turn-around time in air at atmospheric pressure, with little or no need for sample preparation and with no limitations in sample size. The basic principles and data processing of LIBS are described in greater detail in ref. 27–29.

LIBS is able to provide a depth-resolved elemental analysis of samples by applying repetitively a laser pulse onto the same spot, and therefore the composition of layers under the surface can be determined. The ablation depth and thus the thickness of different layers can also be estimated<sup>30,31</sup> (so-called depth-profiling analysis). Moreover, it is possible to get a 3D

<sup>a</sup>Central European Institute of Technology, Brno University of Technology, Purkyňova 123, CZ-61200 Brno, Czech Republic. E-mail: jozef.kaiser@ceitec.vutbr.cz

<sup>b</sup>AtomTrace a.s., Kolejní 9, 61200 Brno, Czech Republic

<sup>c</sup>Mendel University in Brno, Faculty of Agronomy, Department of Chemistry and Biochemistry, Zemědělská 1/1665, 613 00 Brno, Czech Republic

composition of a sample by combining the depth-profiling and surface mapping. Analogously to the HRXCT data, each slice of the LIBS 3D chemical map is composed of volume elements. The size of a volume element in a LIBS 3D map is given by the diameter and depth of an ablation crater, giving spatial and depth resolution.

The 3D elemental mapping using LIBS was demonstrated in solar cell applications.<sup>32,33</sup> The solar cells were ablated layer by layer to provide a 3D spatial distribution of titanium, carbon, silver and silicon<sup>32</sup> and aluminum respectively.<sup>33</sup> In ref. 34, this approach was adopted for a 3D analysis of screen-printed electrodes. In ref. 35, LIBS and LA-ICP-MS were combined to obtain the chemical composition of a bastnäsite mineral sample. The utilization of femtosecond LIBS with the aim of getting a 3D multi-elemental map of a Li-ion solid-state electrolyte material was presented in ref. 36. In ref. 37 the authors employed double-pulse micro LIBS in order to acquire both higher sensitivity and spatial distribution of chemical maps. The measurement was presented in three different samples – homogeneous, heterogeneous and layered metallic samples. A different procedure of a 3D analysis was used in ref. 38. Catalytic converters were cut into several slices obtaining maps of palladium and rhodium distribution in each slice. The 2D chemical maps were then combined to get 3D information.

Analyses from all the above-mentioned studies dealing with 3D LIBS elemental mapping achieved a satisfactory spatial and depth resolution for mineral analysis. However, the reach of the used methods is only several micrometers under the surface. The only exception is the analysis described in ref. 38 where the sample was sectioned. Moreover, all the above-mentioned measurements lead to significant sample damage, or even a complete destruction, which is in many cases undesirable. Therefore we propose to connect techniques providing both structural and elemental analysis. Similarly, in ref. 39 a double-pulse LIBS (DP LIBS) chemical map and HRXCT data were used to investigate the osteitis deformans phases in snake vertebrae. The data from both techniques were not directly combined in order to obtain 3D chemical information. In contrast, they were investigated separately to study the decalcification and deformation of healthy and pathological snake vertebrae.

This paper presents a possibility to utilize together the HRXCT data and DP LIBS elemental map in order to acquire the spatial distribution of selected minerals and their volume. To the best of our knowledge, a combination of these two techniques has never been used for obtaining this kind of complete (structural and elemental) information.

## Materials and methods

### Sample

The studied sample is originated from the unique Talnakh PGE–Cu–Ni sulfide deposit that is located on the northwest flank of the Triassic basalt trap formation of Siberia. All metals entered the basalts due to a remobilization (recycling) of ore elements. The discovery of the Talnakh deposits with high-grade sulfide ores confined to the base of Early Triassic thin (150 m in average) sill-shaped bodies of the giant Siberian traps

significantly influenced the concepts of the origin of magmatic copper–nickel ores. The world's leading scientists are interested in the Talnakh as well as in the associated Norilsk deposits due to the uniquely giant sizes of ore bodies, their assumed association with the young Mesozoic basalt traps, and the fact that all other large known deposits of copper–nickel and platinum ore deposits in the world are much older and associated with giant Proterozoic ultramafic-mafic intrusions.

The sample was chosen not only because of its heterogeneity from the chemical point of view (the sample comprises different elements and minerals) but also because of X-ray radiation attenuation. The sample comprises four separate rocks which were placed into resin and polished for the subsequent geological analysis (see Fig. 1).

### High-resolution X-ray computed tomography

The 3D tomographic data result from a set of X-ray images (projections) of the sample. These projections, acquired from different angles of view over a 360° turn, are used in tomographic reconstruction to generate virtual cross-sections of the sample (slices).<sup>40</sup> Each tomographic slice represents a certain sample thickness and is composed of voxels (volume elements). The gray levels in a HRXCT slice correspond to X-ray attenuation which reflects the proportion of X-rays scattered or absorbed as they pass through each voxel.<sup>41</sup> X-ray attenuation primarily depends on the X-ray energy of the source as well as on the density and atomic number of the material.

The HRXCT analysis was performed using a GE phoenix|X-ray tomography system v|tome|x s, equipped with a 240 kV/320 W maximum power microfocus X-ray tube. To achieve the smallest tube spot size, it was necessary to keep X-ray energy as small as possible. For this reason, no filter was installed in the beam path. The HRXCT scan was carried out at 220 kV acceleration voltage and 65  $\mu$ A X-ray tube current. The linear voxel size of the obtained volume was 14.8  $\mu$ m. A total number of 2400 projections were taken over a 360° range at an integration time of 1000 ms. The images were projected onto a high contrast digital array detector DXR250 with 2048  $\times$



Fig. 1 The rocks were placed into resin to form a sample, and its surface was polished.

2048 pixels and  $200 \times 200 \mu\text{m}$  pixel size. The HRXCT scan was carried out in an air-conditioned X-ray cabinet ( $21^\circ\text{C}$ ).

The tomographic reconstruction was realized by using GE phoenix datos|x 2.0 with a sample drift correction, beam hardening correction and no noise filtration. The 2D-cross section imaging and 3D visualizations were performed with VG Studio MAX 3.1 software.

### Laser-induced breakdown spectroscopy (LIBS)

The orthogonal DP LIBS measurements were performed on a commercially available device (Sci-Trace, AtomTrace, CZ) equipped with an ablation laser (LQ529a, SOLAR, BY), operating at the second harmonic (532 nm, pulse duration  $\sim 10$  ns) focused with a 32 mm focal length glass triplet (Sill optics, DE). The beam of the second laser (Brilliant b, Quantel, FR), operating at the fundamental wavelength (1064 nm, pulse duration  $\sim 4$  ns), was directed to the plasma using mirrors and a plano-convex lens with a 40 mm focal length (Thorlabs, US). Both the above-mentioned lasers are Q-switched Nd:YAG lasers operating at 10 Hz. The energy of the primary/ablation laser pulse was 30 mJ per pulse, and the energy of the secondary/re-excitation laser pulse was 110 mJ per pulse.

The LIBS plasma radiation was collected with a UV-NIR achromatic collimating reflective system, CC52 (ANDOR, UK), and transported by a fiber optic system ( $25 \mu\text{m}$ , Thorlabs, US) onto the entrance of a spectrometer in echelle configuration (Mechelle 5000,  $\lambda/\Delta\lambda > 5000$ , ANDOR, UK) equipped with an iCCD detector (iStar 734i, ANDOR, UK).

All devices were triggered with a delay generator (DG535, Stanford Research System, US) and a specially developed electronic switch. They were controlled *via* a computer equipped with control software. The time-resolved studies were performed by controlling the gate width  $t_w$ , the gate delay  $t_d$  and the delay between the two pulses  $\Delta t$ . All these parameters were optimized for the highest signal to noise ratio first and then held constant throughout the measurement ( $t_w = 16 \mu\text{s}$ ,  $t_d = 1.5 \mu\text{s}$ , and  $\Delta t = 1.5 \mu\text{s}$ ).

The sample was mounted on the stage with precision movements inside an ablation chamber (AtomTrace, CZ).<sup>42</sup> The size of the ablation spot was  $50 \mu\text{m}$ , determined by using an optical profilometer (MicroProf FRT, DE). Therefore, the spatial resolution in both directions was set to  $100 \mu\text{m}$ . The measurement was performed under ambient conditions at atmospheric pressure.

## Results and discussion

### High-resolution X-ray CT sections

In the HRXCT data, Fig. 2, there are three easily differentiated materials, *i.e.* acrylic glass (darker areas) embedding the sample, a dominant mineral (middle gray level) and a metallic constituent (the brightest areas). These materials' densities and atomic constituents are significantly divergent, and therefore they are represented by a good grey level contrast and they can be segmented by a simple thresholding.<sup>20</sup> However, the data are distorted by metal artefacts,<sup>43</sup> which are presented by brighter and/or darker stripes in the surroundings of the metal pieces. This phenomenon brings about a big overlap of the material peaks in the histogram and makes the segmentation procedure more challenging as it might lead to a data misinterpretation.

### DP LIBS elemental mapping

The strategy of LIBS elemental mapping is to maintain information about the coordinates (relative or absolute) of each measurement. Then each pixel of the chemical map corresponds to the intensity of the selected spectral line which is represented by a color on the selected scale. The most common case of elemental map patterns is a rectangular grid of equidistant points. The lateral resolution and the size of the elemental map are given by the laser spot size and the number of shots in each direction. The lateral resolution is limited solely by the ablation crater diameter.

It is noteworthy that the LIBS measurement comprises 62 500 ( $250 \times 250$ ) spectra with an effective spectral range from

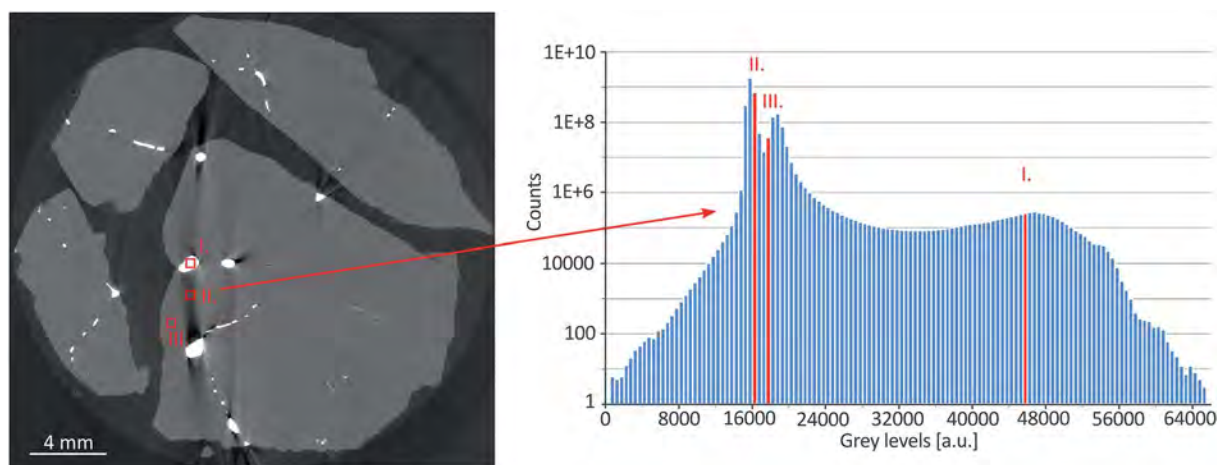


Fig. 2 CT top cross-section showing three different intensities in the sample and their position in the histogram of the CT data, *i.e.* I. region = 45 400, II. region = 16 483, and III. region = 17 781 (averaged values from an area of  $0.14 \text{ mm}^2$ ).

200 to 850 nm. Manual identification of each element in such a dataset is tedious. Hence, the spectra were automatically divided into four groups, and only one representative from each group was studied. The procedure of automatic spectra classification is described in detail in ref. 44 and 45 and also in our previous work.<sup>46</sup> One group was identified as resin and this group was omitted from the further analysis. Three remaining groups were searched for significant spectral lines representing specific elements in each group; the respective elements were copper, nickel and lead. The representative spectra for each respective group are depicted in Fig. 3.

### HRXCT and DP LIBS data combination

Since DP LIBS is a quasi-nondestructive method, the HRXCT analysis has to be performed first. Then, the most significant

plane for an analysis is identified for a consecutive chemical mapping. To assign corresponding information from the chemical map to the 16-bit grayscale HRXCT data, it is necessary to find a HRXCT slice corresponding to the chemically analyzed plane. We simplified the process for the purpose of our feasibility study. Therefore the sample was cut prior to a HRXCT scan. Consequently, we were able to relate the sample surface used for the elemental analysis to the first cross-section obtained from the reconstructed HRXCT data.

During a tomographic measurement the sample was tilted in order to avoid the cone beam artefacts<sup>37</sup> in the HRXCT data. For this reason, the obtained data were registered into a new stack of cross sections according to the plane of the sample surface. Then, the first top cross section of this stack was considered as the image corresponding to the 2D elemental map. The chemical image and HRXCT top cross section were aligned in terms

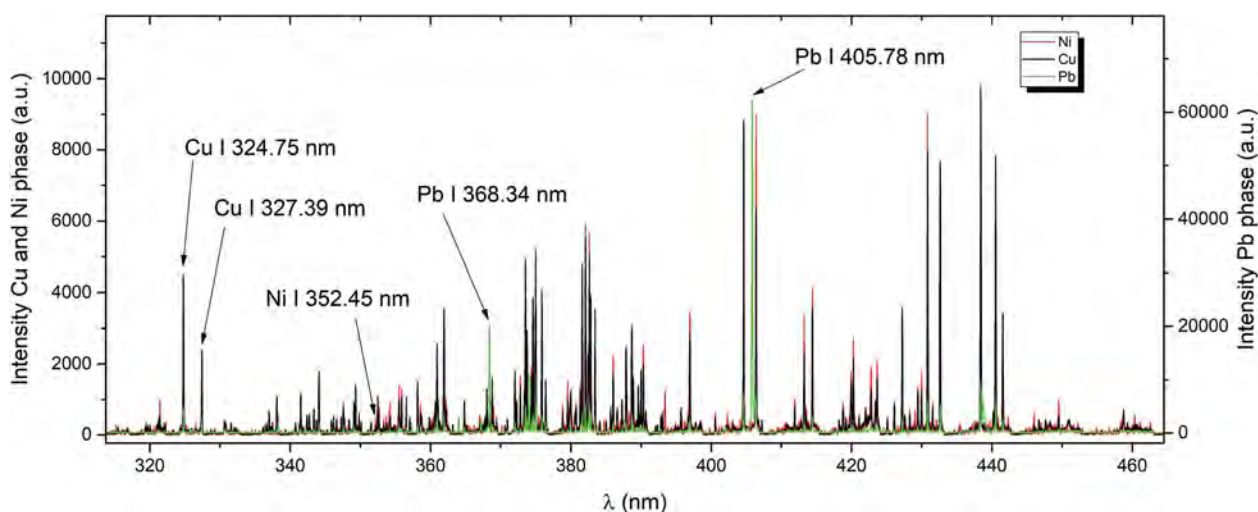


Fig. 3 Typical DP LIBS spectrum with the description of selected spectral lines (Cu I 324.75 nm and 327.39 nm; Ni I 352.45 nm and Pb I 368.34 nm and 405.78 nm).

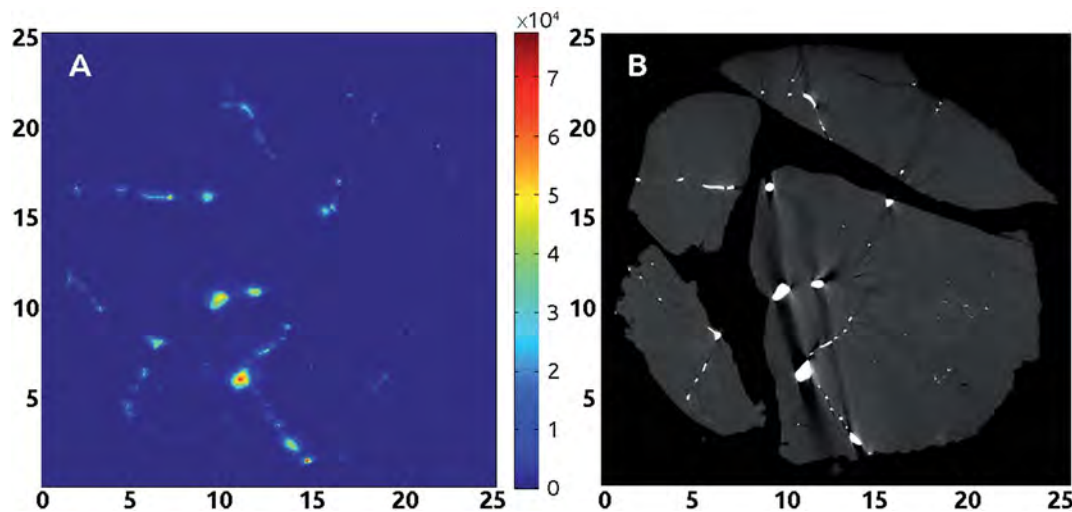


Fig. 4 (A) Chemical map of lead – spectral line 405.78 nm and (B) tomogram top cross section. The orientation and size were adjusted. The spots on the tomogram with higher density are white. The X and Y axes in both images are in millimeters and the intensities in the elemental map represented in the color bar are in arbitrary units.

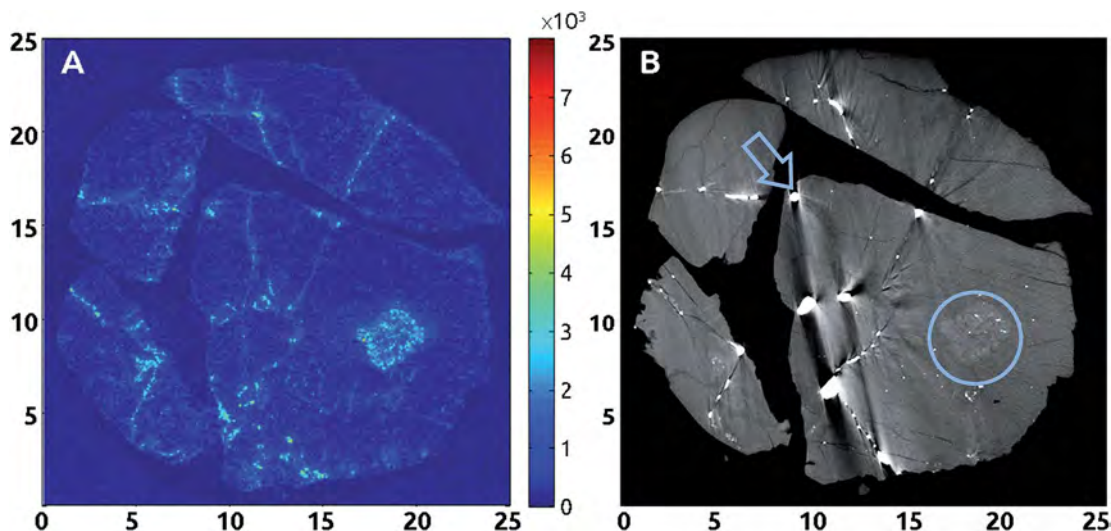


Fig. 5 (A) Chemical map of nickel – spectral line 352.45 nm and (B) tomogram top cross section with contrast enhancement. The orientation and size were adjusted. The HRXCT image (B) shows a damage of the sample boundary due to metal artefacts (by an arrow) and the significant area including nickel (circled area). The X and Y axes in both images are in millimeters and the intensities in the elemental map represented in the color bar are in arbitrary units.

Table 1 Volume of selected mineral phases within the sample

Mineral	Volume [mm <sup>3</sup> ]
The mineral phase containing Pb	32
The mineral phase containing Cu + Ni	1538
Total sample volume	1570

of rotation, scale and translation. The mismatch in the resolution and size of both 2D images (elemental map and HRXCT cross section) was adjusted. The dimensions of the HRXCT

cross section (1690 × 1690 pixels) were compressed by a simple recalculation to fit the dimensions of the DP LIBS map (250 × 250 pixels). The distribution of lead, which is clearly presented in both images, was used for this kind of alignment, see Fig. 4. Finally, when both images were overlapped, the elements from chemical images could be assigned to the grey scale of the tomogram.

In Fig. 5A, the elemental image of nickel and in Fig. 5B, the HRXCT top cross section with enhanced contrast is depicted. Both images are already in the common coordinate system (the

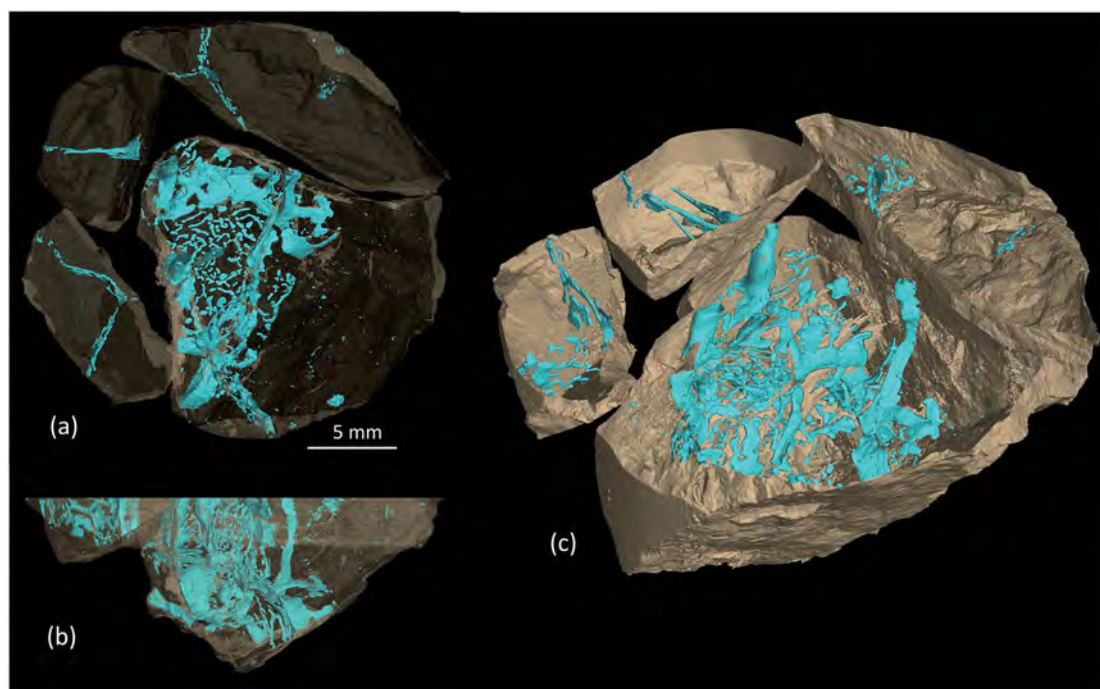


Fig. 6 3D distribution of the mineral phase containing lead within the sample. (a) Top-view; (b) side-view; (c) front-top view.

same transformation as in the previous case was applied). The distribution of nickel is clearly visible by a simple comparison of both images – the position highlighted by a circle in Fig. 5B can be used as an example. However, in some positions of the HRXCT top cross section the nickel is hidden by the metal artefacts caused by the presence of lead (see the position marked by an arrow in Fig. 5B). These artefacts make an automatic segmentation of the associated mineral phase nearly impossible.

### Volumetric information

The contrast level of HRXCT data allowed us to segment all pieces of rock and the lead-containing mineral phase based on global thresholding. However, the boundary of the sample had to be corrected in areas where metal artefacts worsened the quality of the obtained HRXCT data. The segmented data were used to determine the volume (see Table 1) and 3D visualization (see Fig. 6). The volume of the mineral phase containing lead in the investigated sample was roughly 2%, excluding the epoxy embedding. Although, the mineral phase containing nickel was visible in HRXCT data (see Fig. 5B), this element could not be determined correctly using global thresholding methods because of a low contrast to the dominant surrounding mineral.

## Conclusion

In this work, we demonstrated a possibility of the joint utilization of HRXCT and DP LIBS in order to provide volumetric information about the element distribution within a geological sample. The DP LIBS elemental map of lead was manually aligned and overlapped with the HRXCT top cross section. Afterwards, elements from DP LIBS elemental maps were assigned to the grey scale of HRXCT data. Then, the volume of each mineral phase was calculated from all HRXCT slices. As a final result, the total content of the mineral phase containing lead was estimated to be roughly 2% within all four rocks. Despite the encountered challenges in the sample analysis and data processing, the results obtained from our feasibility study are promising for further implementation of both techniques in the 3D elemental imaging of investigated samples.

Despite some limitations in the contrast of mineral phases in HRXCT, the joint implementation with DP LIBS provides more complex information about the geological sample. Even though the tomographic data are influenced by artefacts (dark/light stripes and dissimilarities between consecutive slices), the elemental composition depicted in the chemical map helps to reveal some initially unnoticed structures. Moreover, a preliminary HRXCT mineral study could help to select the most advantageous plane for the consecutive cutting and LIBS 2D elemental mapping.

## Conflicts of interest

There are no conflicts to declare.

## Acknowledgements

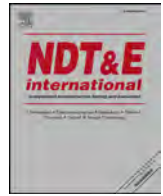
This research was carried out under the project CEITEC 2020 (LQ1601) with financial support from the Ministry of Education, Youth and Sports of the Czech Republic under the National Sustainability Programme II and CEITEC Nano Research Infrastructure (MEYS CR, 2016–2019). J. Ka and J. Kl acknowledge the support of the Brno University of Technology through grant FSI-S-17-4506.

## References

- 1 D. R. Baker, L. Mancini, M. Polacci, M. Higgins, G. Gualda, R. Hill and M. Rivers, *Lithos*, 2012, **148**, 262–276.
- 2 S. J. Barnes, G. A. Osborne, D. Cook, L. Barnes, W. D. Maier and B. Godel, *Econ. Geol.*, 2011, **106**, 1083–1110.
- 3 W. D. Carlson, C. Denison and R. A. Ketcham, *Visual Geosciences*, 2000, **4**, 1–14.
- 4 R. A. Ketcham, *J. Struct. Geol.*, 2005, **27**, 1217–1228.
- 5 M. Polacci, D. R. Baker, L. Mancini, G. Tromba and F. Zanini, *Geophys. Res. Lett.*, 2006, **33**, L13312.
- 6 M. Voltolini, D. Zandomenoghi, L. Mancini and M. Polacci, *J. Volcanol. Geotherm. Res.*, 2011, **202**, 83–95.
- 7 V. Cnudde and M. N. Boone, *Earth-Sci. Rev.*, 2013, **123**, 1–17.
- 8 O. Rozenbaum, *Science of the total environment*, 2011, **409**, 1959–1966.
- 9 I. U. Bhuiyan, J. Mouzon, F. Forsberg, S. Forsmo, M. Sjö Dahl and J. Hedlund, *Powder Technol.*, 2013, **233**, 312–318.
- 10 V. Cnudde, J. Dewanckele, W. De Boever, L. Brabant and T. De Kock, in *Quantitative Mineralogy and Microanalysis of Sediments and Sedimentary Rocks*, Mineralogical Association of Canada (MAC), 2012, vol. 42, pp. 99–113.
- 11 G. A. Gualda, A. S. Pamukcu, L. L. Claiborne and M. L. Rivers, *Geosphere*, 2010, **6**, 782–792.
- 12 Z. Kalam, T. Al Dayyani, A. Grader and C. Sisk, *World Oil*, 2011, **232**, 85–90.
- 13 R. A. Ketcham, D. T. Slotke and J. M. Sharp Jr, *Geosphere*, 2010, **6**, 499–514.
- 14 R. M. Sok, M. A. Knackstedt, T. Varslot, A. Ghous, S. Latham and A. P. Sheppard, *Petrophysics*, 2010, **51**(6), 379–387.
- 15 J. R. Kyle, A. S. Mote and R. A. Ketcham, *Miner. Deposita*, 2008, **43**, 519–532.
- 16 Y. Ghorbani, M. Becker, J. Petersen, S. H. Morar, A. Mainza and J.-P. Franzidis, *Miner. Eng.*, 2011, **24**, 1249–1257.
- 17 S. Peth, J. Nellesen, G. Fischer and R. Horn, *Soil Tillage Res.*, 2010, **111**, 3–18.
- 18 S. Hall, M. Bornert, J. Desrues, Y. Pannier, N. Lenoir, G. Viggiani and P. Bésuelle, *Géotechnique*, 2010, **60**, 315–322.
- 19 D. Wildenschild and A. P. Sheppard, *Adv. Water Resour.*, 2013, **51**, 217–246.
- 20 R. A. Ketcham and G. J. Iturrino, *J. Hydrol.*, 2005, **302**, 92–106.
- 21 K. Laajalehto, I. Kartio and E. Suoninen, *Int. J. Miner. Process.*, 1997, **51**, 163–170.
- 22 R. G. Acres, S. L. Harmer and D. A. Beattie, *Int. J. Miner. Process.*, 2010, **94**, 43–51.

- 23 M. M. Hyland and G. M. Bancroft, *Geochim. Cosmochim. Acta*, 1990, **54**, 117–130.
- 24 C. LaFlamme, L. Martin, H. Jeon, S. M. Reddy, V. Selvaraja, S. Caruso, T. H. Bui, M. P. Roberts, F. Voute, S. Hagemann, D. Wacey, S. Littman, B. Wing, M. Fiorentini and M. R. Kilburn, *Chem. Geol.*, 2016, **444**, 1–15.
- 25 K. Sasaki, Y. Nakamuta, T. Hirajima and O. H. Tuovinen, *Hydrometallurgy*, 2009, **95**, 153–158.
- 26 B. J. Williamson, I. Mikhailova, O. W. Purvis and V. Udachin, *Sci. Total Environ.*, 2004, **322**, 139–154.
- 27 D. A. Cremers and L. J. Radziemski, *Handbook of Laser-Induced Breakdown Spectroscopy*, Wiley, 2nd edn, 2013.
- 28 D. W. Hahn and N. Omenetto, *Appl. Spectrosc.*, 2010, **64**, 335a–366a.
- 29 D. W. Hahn and N. Omenetto, *Appl. Spectrosc.*, 2012, **66**, 347–419.
- 30 K. Novotný, T. Vaculovič, M. Galiová, V. Otruba, V. Kanický, J. Kaiser, M. Liška, O. Samek, R. Malina and K. Páleníková, *Appl. Surf. Sci.*, 2007, **253**, 3834–3842.
- 31 T. Canel, P. Demir, E. Kacar, B. Genc Oztoprak, E. Akman, M. Gunes and A. Demir, *Opt. Laser Technol.*, 2013, **54**, 257–264.
- 32 J. M. Vadillo, S. Palanco, M. D. Romero and J. J. Laserna, *Fresenius. J. Anal. Chem.*, 1996, **355**, 909–912.
- 33 D. Romero and J. J. Laserna, *Spectrochim. Acta, Part B*, 2000, **55**, 1241–1248.
- 34 J. Amador-Hernández, J. M. Fernández-Romero and M. D. Luque de Castro, *Anal. Chim. Acta*, 2001, **435**, 227–238.
- 35 J. R. Chirinos, D. D. Oropeza, J. J. Gonzalez, H. Hou, M. Morey, V. Zorba and R. E. Russo, *J. Anal. At. Spectrom.*, 2014, **29**, 1292–1298.
- 36 H. Hou, L. Cheng, T. Richardson, G. Chen, M. Doeff, R. Zheng, R. Russo and V. Zorba, *J. Anal. At. Spectrom.*, 2015, **30**, 2295–2302.
- 37 R. Grassi, E. Grifoni, S. Gufoni, S. Legnaioli, G. Lorenzetti, N. Macro, L. Menichetti, S. Pagnotta, F. Poggialini, C. Schiavo and V. Palleschi, *Spectrochim. Acta, Part B*, 2017, **127**, 1–6.
- 38 P. Lucena and J. J. Laserna, *Spectrochim. Acta, Part B*, 2001, **56**, 177–185.
- 39 M. Galiová, J. Kaiser, K. Novotný, M. Ivanov, M. Nývltová Fišáková, L. Mancini, G. Tromba, T. Vaculovič, M. Liška and V. Kanický, *Anal. Bioanal. Chem.*, 2010, **398**, 1095–1107.
- 40 W. A. Kalender, *Computed Tomography: Fundamentals, System Technology, Image Quality, Applications*, John Wiley & Sons, 2011.
- 41 J. R. Kyle and R. A. Ketcham, *Ore Geol. Rev.*, 2015, **65**, 821–839.
- 42 J. Novotný, M. Brada, M. Petrilak, D. Prochazka, K. Novotný, A. Hrdička and J. Kaiser, *Spectrochim. Acta, Part B*, 2014, **101**, 149–154.
- 43 J. F. Barrett and N. Keat, *Radiographics*, 2004, **24**, 1679–1691.
- 44 S. Pagnotta, M. Lezzerini, B. Campanella, G. Gallelo, E. Grifoni, S. Legnaioli, G. Lorenzetti, F. Poggialini, S. Raneri, A. Safi and V. Palleschi, *Spectrochim. Acta, Part B*, 2018, **146**, 9–15.
- 45 S. Pagnotta, M. Lezzerini, L. Ripoll-Seguer, M. Hidalgo, E. Grifoni, S. Legnaioli, G. Lorenzetti, F. Poggialini and V. Palleschi, *Appl. Spectrosc.*, 2017, **71**, 721–727.
- 46 J. Klus, P. Porizka, D. Prochazka, P. Mikysek, J. Novotny, K. Novotny, M. Slobodnik and J. Kaiser, *Spectrochim. Acta, Part B*, 2017, **131**, 66–73.

PAPER [IV]



## Computed tomography based procedure for reproducible porosity measurement of additive manufactured samples

Tomáš Zikmund<sup>a</sup>, Jakub Šalplachta<sup>a,\*</sup>, Aneta Zatočilová<sup>b</sup>, Adam Břínek<sup>a</sup>, Libor Pantělejev<sup>c</sup>, Roman Štěpánek<sup>c</sup>, Daniel Koutný<sup>b</sup>, David Paloušek<sup>b</sup>, Jozef Kaiser<sup>a</sup>

<sup>a</sup> CEITEC – Central European Institute of Technology, Brno University of Technology, Purkyňova 656/123, 612 00, Brno, Czech Republic

<sup>b</sup> Institute of Machine and Industrial Design, Faculty of Mechanical Engineering, Brno University of Technology, Technická 2, 616 69, Brno, Czech Republic

<sup>c</sup> Institute of Materials Science and Engineering, Faculty of Mechanical Engineering, Brno University of Technology, Technická 2, 616 69, Brno, Czech Republic

### ARTICLE INFO

#### Keywords:

Porosity measurement  
SLM sample  
Metallography  
Micro tomography  
Automatic pores segmentation

### ABSTRACT

Metallic parts made by selective laser melting technology are evaluated for internal porosity. The non-standardized pores segmentation is one of the key aspects to apply in order to achieve a precise porosity measurement using X-ray computed micro tomography. In this work, we present a new porosity analysis procedure which is based on the global thresholding and the correlation with metallographic image data. The procedure is independent on the obtained voxel resolution and makes an analysis reproducible. The novelty of this work is that the computed tomography is used for a comparative porosity analysis of samples from separate measurements. The functionality of proposed procedure is demonstrated on a test sample of aluminium alloy and is compared to standardly used procedures.

### 1. Introduction

Additive Manufacturing (AM) is considered to be a technology with a high potential for the industrial production of high-value engineered products. The high potential is especially seen in manufacturing metallic parts by means of selective laser melting technology (SLM) [1]. This technology provides an alternative solution to the casting or forming of the metallic parts. Together with the shape optimization, SLM technique can produce lightweight, structured and complex parts with a significant weight reduction [2–4]. Currently, there are about 20 dissimilar materials that can be processed by SLM [5]. SLM parts' mechanical properties are usually comparable to the properties of conventionally produced parts from bulk materials, although the tensile and fatigue characteristics are usually worse [6–10]. The presence of internal defects has a negative effect on the fatigue life and ultimate tensile strength (UTS). Therefore, one of the major challenges in the production of SLM parts is minimizing their internal porosity [11–18].

Currently, there are several possible ways to measure porosity, such as mass measurement, Archimedes method, metallography, and X-ray computed tomography. All these methods are based on different principles and incomparable in terms of getting the absolute value of the porosity for one sample [19–23]. For this reason, it is necessary to keep one technique with the same measurement settings in order to evaluate

the samples among each other by their relative values of porosity.

In order to improve the SLM production quality, it is also very important to know the character of internal defects and to distinguish the shrinkage cavities, cracks, and bulk material [24]. This information is given only by the image-based methods like metallography and CT. Besides the porosity number, these methods determine also complex information about the distribution of defects and their morphological parameters [13,17,18,21]. Such an analysis is usually performed on testing samples which have a reasonably small size regarding the field of view of used imaging system or requested resolution [18].

Metallography is the most frequently used image-based method for the porosity analysis of SLM parts thanks to a high resolution that can be achieved and also to the fact that light or electron microscopes are accessible [5–12,15,16]. The weakness of this method is the evaluation of the total porosity (i.e. for the whole sample volume) as a mean value of several surfaces measurements. This approach requires a perfect preparation of a sample surface including wet grinding and polishing for every surface imaging. The final porosity value is then affected by the limited number of the evaluated planar sections (i.e. missing a certain number of irregular distributed defects) [17].

In comparison to metallography, CT technique has some undisputed benefits. CT technique enables to visualize the inner structure non-destructively, in three dimensions, and at one measurement process [17].

\* Corresponding author.

E-mail address: [Jakub.Salplachta@ceitec.vutbr.cz](mailto:Jakub.Salplachta@ceitec.vutbr.cz) (J. Šalplachta).

<https://doi.org/10.1016/j.ndteint.2019.02.008>

Received 22 June 2018; Received in revised form 31 January 2019; Accepted 22 February 2019

Available online 27 February 2019

0963-8695/ © 2019 Elsevier Ltd. All rights reserved.

However, the final resolution is limited by the sample size [18]. For this reason, the size of SLM testing samples is usually several millimetres, which enables to reach the CT data resolution of about tens micrometres [7,8,13,17–20,25,26]. Particular CT machines having different properties, there is no standard methodology for CT measurement implementation that would enable to generate uniform data in terms of resolution, quality, and contrast.

Another aspect contributing to the porosity calculation uncertainty is the absence of a standard for CT image processing. It means that the result is influenced by the variabilities in user's behaviour and by different segmentation approaches [27–30]. The only exception is a standard VW 50097/50093 (defined by the German Association of Foundry Specialists or Volkswagen AG) [31,32] based on a manual evaluation of selected 2D cross-section and it is not convenient for three dimensional character of CT data.

The porosity  $P$  from image data is calculated using following expression:

$$P = \left( \frac{N_p}{N_m + N_p} \right) \cdot 100 \quad [\%] \quad (1)$$

where  $N_m$  is the total number of material pixels and  $N_p$  is the total number of pores pixels. Before the actual porosity calculation, pixels of an image must be divided into two categories: material and pores. This is realized by the image segmentation. The simplest and the most commonly used segmentation method is thresholding [33] that in case of two-dimensional data creates a binary image  $g$  by following definition [33]:

$$g(x, y) = \begin{cases} 1, & \text{if } f(x, y) \geq T \\ 0, & \text{if } f(x, y) < T \end{cases} \quad (2)$$

where  $f(x,y)$  is an intensity value of the input two-dimensional image  $f$ ,  $g(x,y)$  is a binary value of the output binary image  $g$ , both at corresponding spatial coordinates  $x$ ,  $y$ , and  $T$  is a threshold value. For the porosity calculation (Eq. (1)), the number of material pixels  $N_m$  is defined by stated equation (2) as a number of pixels represented in an analysed image data  $f$ , by the intensity which is equal or greater than threshold  $T$ . Number of pores pixels  $N_p$  is a number of pixels represented by an intensity which is lesser than threshold  $T$ . In case the constant threshold value is used in the whole image volume (e.g. in every CT cross-section), this method is called global thresholding [34].

The crucial point of the porosity calculation is then the selection of a correct threshold value  $T$ , which is usually done automatically by some software. The most widely used automatic methods are based on the intensity histogram shape evaluation, where the peaks, valleys and curvatures are analysed [34]. A study done by Iassonov [28] compared several methods used for the pores segmentation based on CT data. According to this study, the most reliable automatic segmentation methods are Otsu [35] and Ridler [36] global thresholding methods which work very well for the bimodal shape of histogram.

However, CT images of SLM samples are usually presented by a histogram with a shape close to the unimodal distribution. Thus, the automatic methods (including Otsu and Ridler) fail [23]. This is the case mainly when the number of small pores makes the peak of pores very low and the histogram is then presented only by one dominant peak of material. Another possible situation is when the peaks of pores and material are so close that they overlap. This might happen in the following cases: low material contrast, tomographic artefacts, noise or presence of bulk material (typically unmelted or partially melted powder particles) in the cavities. If the bimodal histogram absence is assumed, it is more suitable to select the threshold manually by the operator's visual evaluation of one representative CT image. However, this approach is highly subjective and gives variable results depending on the operator's experience, knowledge of the studied sample and even on the way CT data are displayed on an ordinary monitor. These aspects rule out any trustworthy results coming from a comparative porosity

measurement of two samples scanned in different laboratories and also of two samples measured in different times within one CT system. Consequently, some published studies dealing with image-based porosity calculation did not even present the methodology of used pores segmentation [9,11,12,16,19,21]. As an example, threshold selection in case of thresholding [11,21] which makes the porosity analysis un-reproducible, was not even mentioned.

In this paper, we propose a new porosity analysis procedure for X-ray computed tomography measurement using the benefits of metallography (i.e. the high material-pores contrast and high resolution). The porosity analysis uses the simple global thresholding with an automatic threshold selection based on a correlation of corresponding computed tomography (CT) and light microscope (LM) images. This procedure provides a reliable and traceable porosity value with respect to the obtained voxel resolution. This enables to compare objectively the porosity of the samples measured even by different CT systems or laboratories.

## 2. Materials and methods

### 2.1. SLM sample

The sample was fabricated by a SLM 280HL machine equipped with a 400 W ytterbium fibre laser. The laser operational beam focus was 82  $\mu\text{m}$  in diameter with Gaussian profile and a wavelength of 1.06 mm. The real temperature of building platform was 80 °C. A block specimen of size 13 mm  $\times$  13 mm  $\times$  8 mm ( $x$ ,  $y$ ,  $z$ ) was used. The sample was built in nitrogen inert atmosphere while the oxygen level was kept below 0.2% during the process. The following SLM processing parameters were used: layer thickness = 50  $\mu\text{m}$ , laser power = 200 W, laser scanning speed = 200 mm/s, hatching distance was set to 110  $\mu\text{m}$  (optimum value according to previous study [38]). The specimen was fabricated with the meander scanning strategy, with a rotation of hatching direction in each follow up layer about 79°. The block was fabricated on the supports to enable a manual removal from the building platform. The supports were fabricated with following process parameters: laser power at 400 W, laser scanning speed at 1150 mm/s, support hatch at 0.9 mm.

### 2.2. Metallographic analysis

Six images of the SLM specimen were acquired and separately evaluated for porosity using the Otsu's thresholding method. A light metallographic microscope Olympus GX 51 at the total magnification of 50 $\times$  (pixel size: 2.5  $\mu\text{m}$ ) was used for imaging. Except for the first image (referring to the sample surface), all images were acquired after the micro tomography measurement. The inter layer distance of evaluated cross-sections was approximately 0.3 mm. The sample was prepared by the standard metallographic technique at each depth level, using wet grinding and polishing with a diamond paste in order to achieve mirror-like surface quality. The overall sample porosity was then calculated as the mean of all particular porosity values.

### 2.3. Micro CT

A system GE phoenix v|tome|x L 240 equipped with a 180 kV/15 W nanofocus X-ray tube and a flat panel detector DXR 250 was used for the tomographic measurement with following parameters: 125 kV accelerating voltage, 55  $\mu\text{A}$  tube current, 300 ms detector exposure time, 3500 number of projections. The X-ray spectrum was filtered by a 0.2 mm thick copper filter. The detector was used in a special regime which consisted in switching the position horizontally and extending the field of view. By using the special regime it was possible to obtain a voxel resolution of 6  $\mu\text{m}$ . The object was positioned to a small tilt in order to avoid the Feldkamp artefacts [37].

The tomographic reconstruction was done using a GE phoenix

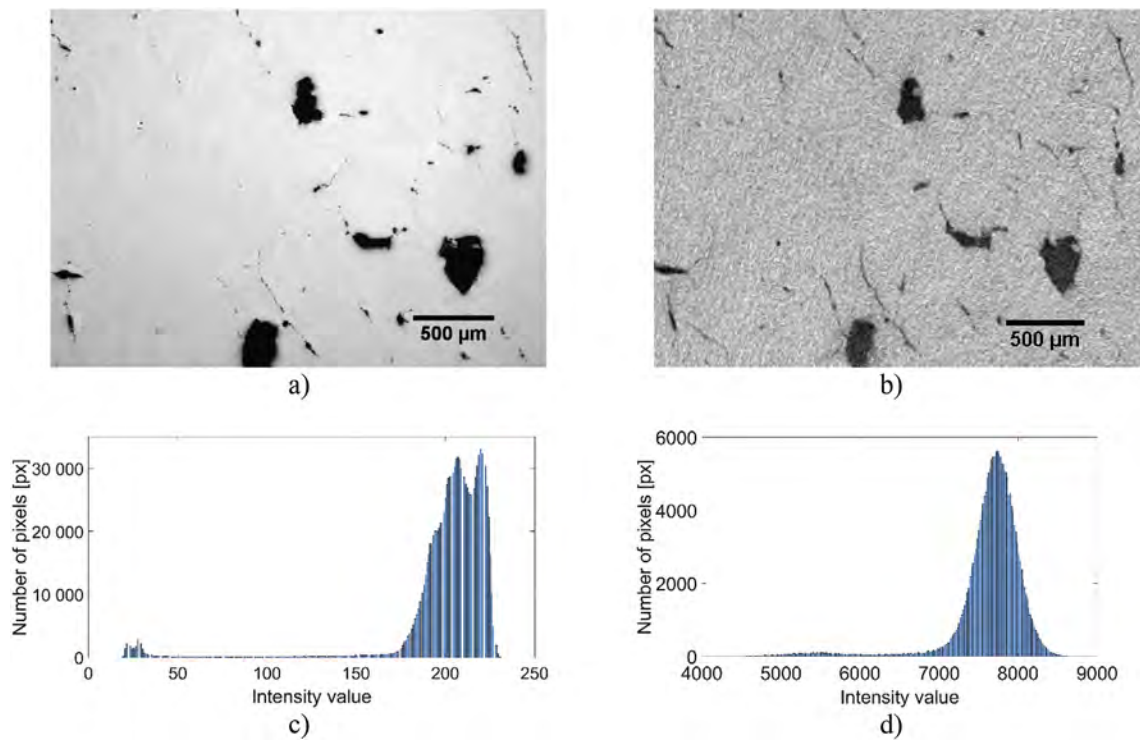


Fig. 1. Comparison of corresponding section of sample surface cross-sections of analysed SLM sample: (a) 8-bit LM image; (b) 16-bit CT image; (c) histogram of LM image; (d) histogram of CT image.

datos|x 2.0 with the sample drift correction, beam hardening correction, and no noise filtration. Based on the top cross-section of the sample, the registration of the object was conducted using a VG Studio MAX 3.0. Consequently, a new stack of cross-sections were generated. The first top cross-section of this stack was considered as a corresponding image to the sample surface image acquired by means of metallography.

### 3. Porosity measurement

#### 3.1. Subjectivity in manual threshold selection

The inner structure of SLM samples is usually presented with small pores and cracks. In case of micro CT data (Fig. 1b), this is described by a histogram of inconvenient shape for standardly used automatic threshold selection methods (see Fig. 1d). However, as for the selection, the manual selection is almost the only possible way in a common software. There are several factors that can influence the manual threshold selection process. These factors are related to the operators' experience with image processing, their familiarity with SLM inner structures and the way they can visualize the data (e.g. a type of monitor etc.):

- uncalibrated monitors presented by different colours/contrast,
- the way of 16-bit data display on 8-bit monitor,
- image modifications (e.g. zooming, contrast enhancement),
- the method of binary mask display in CT image.

We examined the variability of operators' behaviour while carrying out the manual threshold selection process. Our experiment involved twenty experts with knowledge of image analysis and porosity measurement. The task for participants was to select the most appropriate threshold for the pores-material binarization on one representative CT image (see Fig. 1b). Participants independently chose a threshold value based on their visual opinion about the binary mask copying the pores. The users estimated the threshold values in the range  $6700 \pm 439$  (see

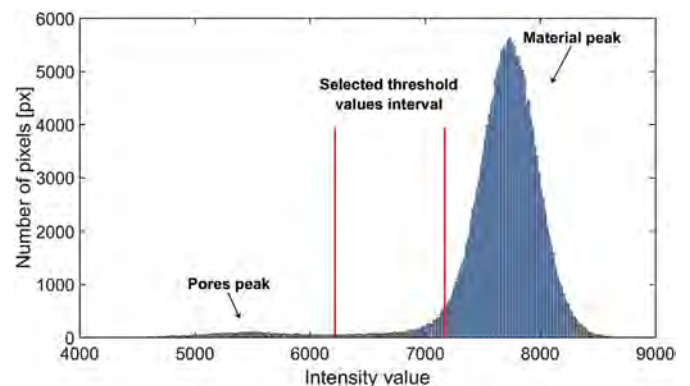


Fig. 2. Histogram of testing CT image with marked interval of selected threshold values and labelled pores and material peaks.

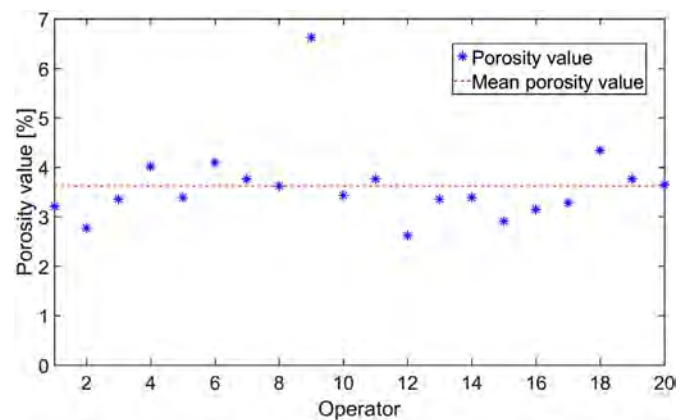


Fig. 3. Graphical dependence of porosity value of testing image based on thresholds selected by operators.

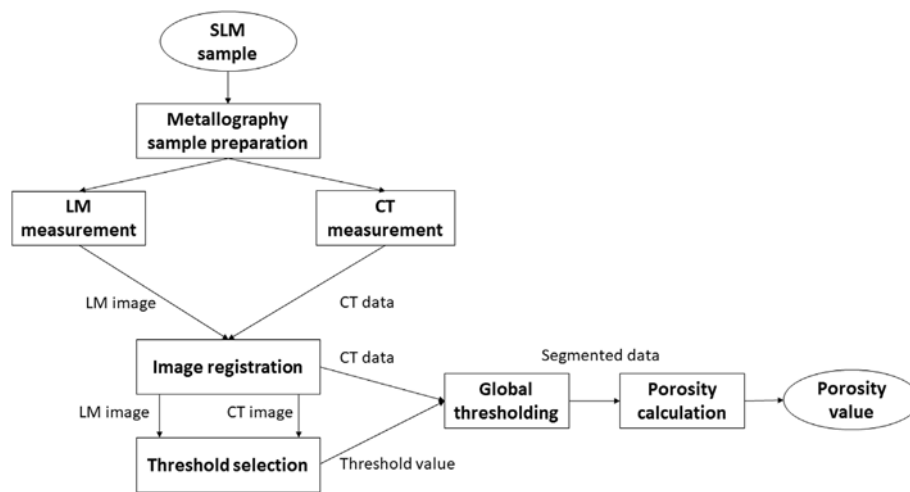


Fig. 4. Diagram of proposed porosity analysis procedure.

Fig. 2) and this resulted in the porosity values from 2.6 [%] to 6.6 [%] (see Fig. 3). This inter-participants variability brings a significant uncertainty to the porosity measurement in terms of the SLM production quality evaluation. Moreover, it doesn't allow comparing more samples among themselves.

### 3.2. Reproducible porosity analysis (RPA)

The proposed procedure was designed with a respect to the crucial points of tomographic data processing. These aspects are the user independence, correct pores segmentation, reproducibility, and adaptation for different resolution. The workflow of proposed procedure is described by the diagram in Fig. 4. The method is based on a correlation between CT data and metallographic data. The characteristics of metallographic analysis using microscopy are the high resolution and easy pores segmentation. Therefore, the metallographic analysis complies with the task of the reference and the calibration for the CT porosity analysis.

The correlation of these techniques is based on an alignment of corresponding images, i.e. a light microscopic image of the sample surface (LM image) and a CT top cross-section (CT image). Getting such corresponding images can be guaranteed only when the CT measurement is performed on a sample whose surface was already analysed by metallography.

The acquisition of LM and CT images is followed by an image registration which aims to unify both images to the same size and orientation. This is done by a geometric transformation of LM image because the LM reaches higher resolution than micro CT does. The transformation including the scaling, rotation and translation is determined automatically by the phase correlation [39]. Then the LM image and CT data are trimmed around the sample centre (see Fig. 6) in order to avoid distorted areas of the image caused by a mechanical preparation of the sample surface. The prepared surface is not absolutely flat and it results in blurry sample corners and edges in case of LM images. This effect is even more obvious in CT top cross-section by darker regions (see Fig. 6). Moreover, removing these edges simplifies the porosity calculation as there is no need to distinguish the background pixels (outer sample space) from the pores pixels presented by the same grey values.

The threshold selection is implemented on these registered corresponding images. The reference porosity value is determined from LM image using global thresholding with Otsu's automatic threshold selection for pores segmentation. This method works reliably on LM images because of a high pores/material contrast. The reference porosity value is subsequently used for the selection of an optimal

threshold value for CT data. This selection is realized using a brute-force search [40] during the optimization process. In this process, the porosity from CT image is calculated for a series of threshold values (from minimum to maximum CT image intensity value). A criterion function is expressed for each porosity value. This function is defined as Euclidean distance from the reference LM image porosity value and the CT image porosity value for a particular threshold. The optimal threshold for global thresholding of CT data is then selected as a threshold where the criterion function reaches its minimum.

This threshold is subsequently applied to the trimmed CT data volume using the global thresholding. The porosity value is then calculated on segmented data by Eq. (1). In order to express the estimation of repeatability in porosity calculation, a 1% variation on both sides of the selected threshold value is taken in account (inspired by: [41]).

## 4. Results and discussion

The proposed procedure was applied on 6  $\mu\text{m}$  voxel resolution CT data coming from a SLM sample made from aluminium alloy of AlCu2Mg1.5Ni. The inner structure of this sample included both larger cavities and cracks, making it the best example for a demonstration of advantages of proposed procedure. The porosity was also calculated using automatic-based thresholding methods (Otsu and Ridler) and manually-defined thresholding in order to simulate the actual behaviour of the software available for us. Furthermore, the porosity numbers were consequently compared with a standardly used metallographic approach.

### 4.1. RPA implementation

The polished side of the sample embedded in a cylindrical acrylic block was imaged with a light microscope. The CT measurement of this sample was conducted in a tilt position to avoid cone beam artefacts [37]. The obtained tomographic data were registered to align into the coordinate system according to the polished plane. Then, the top cross-section was taken as a corresponding section to LM image. The LM image resolution was scaled down according to the CT cross-section (see Fig. 5) using the bicubic interpolation method. This meant down-scaling from 2.5  $\mu\text{m}$  to 6  $\mu\text{m}$  which had no significant effect on the porosity analysis (difference of porosity value in original and down-scaled image was 0.0107%). Subsequently, both LM image and CT cross-section were trimmed (see Fig. 6) to avoid the influence of sample boundaries.

To confirm the similarity between the LM image and CT cross-section, the Structural Similarity Index (SSIM) [42] was analysed. Binary

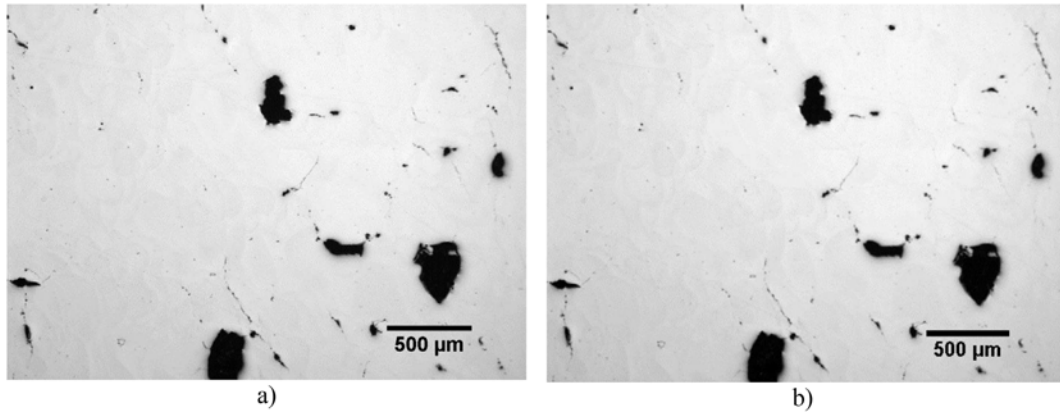


Fig. 5. Effect of used downscaling on LM image: a) section from original image (pixel size: 2.5 μm) and b) corresponding section from image after downscaling to correspond CT image (pixel size: 6 μm).

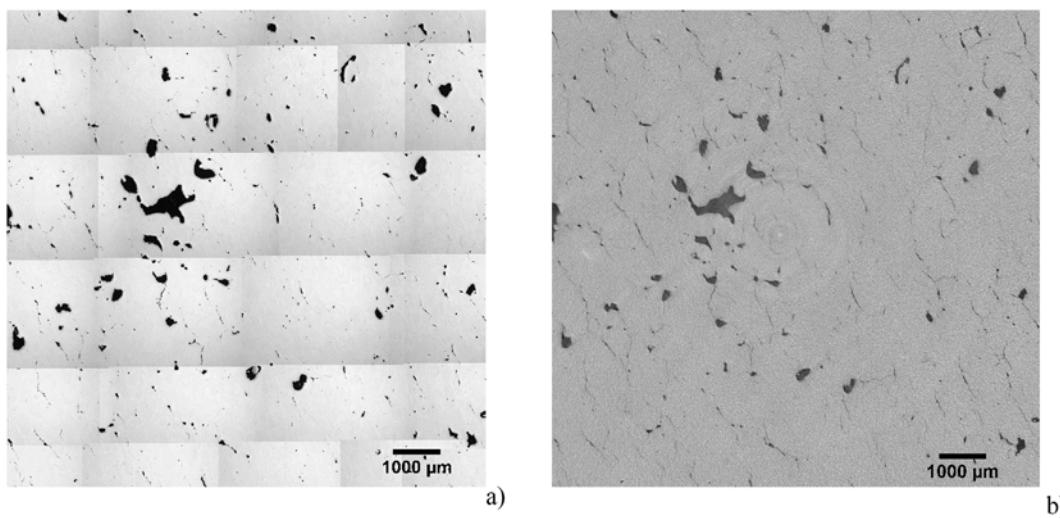


Fig. 6. Aligned corresponding surface LM image and CT top image after trimming.

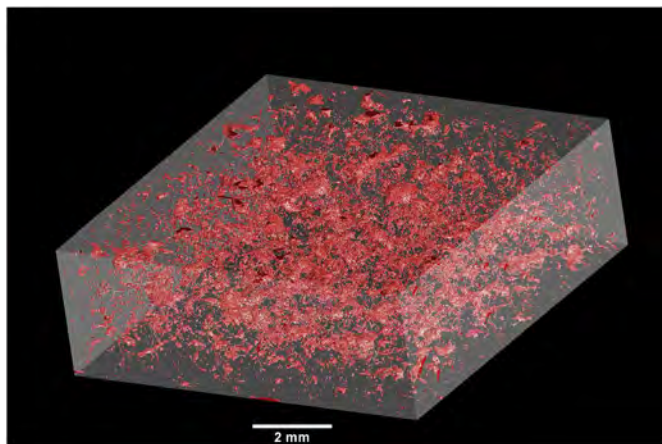


Fig. 7. 3D pores distribution in analysed sample volume – achieved from CT data with use of proposed thresholding procedure.

masks and an after pores segmentation of Fig. 1 a) and Fig. 1 b) were used for this evaluation. Otsu thresholding was used in case of LM image and RPA selected threshold was applied for the CT image segmentation. The binary masks were used rather than original images in order to evaluate the true structural similarity between these images. This way, the possible influence of different noise and textural

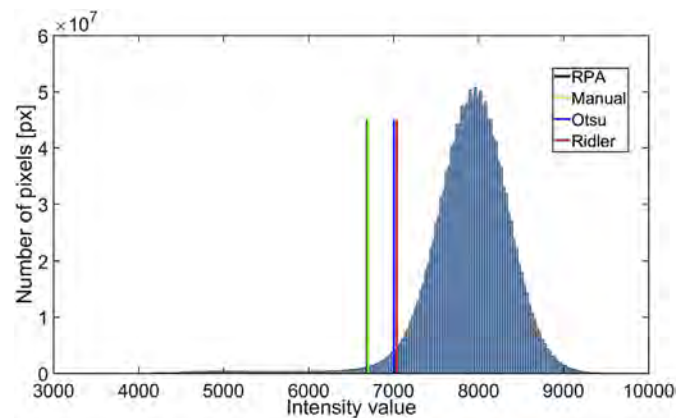


Fig. 8. Histogram of all CT data volume with marked positions of threshold values selected by studied methods.

properties was avoided. Moreover, there was no influence of the intensity variations of original images that are related to the imaging character of the used modalities. The SSIM index values lie in the interval from -1 to +1, where SSIM = 1 reflects identical images. In our case, SSIM value for analysed images was equal to 0.91. This result really confirmed that the analysed images had a high degree of structural similarity.

**Table 1**  
Comparison of total porosity results calculated by different approaches.

	Metallographic analysis	CT porosity analysis			
		Manual thresholding	Proposed method	Otsu thresholding	Ridler thresholding
Total porosity [%]	2.62 ± 0.02	1.92 ± 0.16	1.90 ± 0.15	3.27 ± 0.56	3.56 ± 0.56

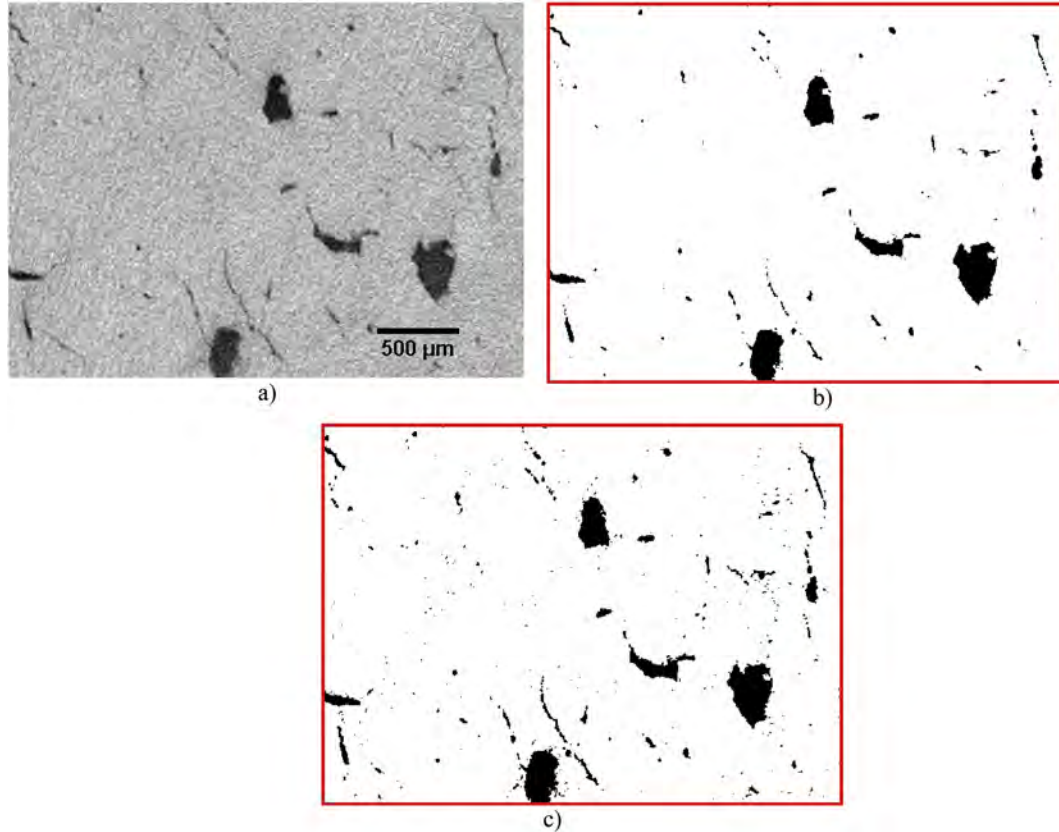


Fig. 9. Comparison of binary masks of CT image detail: a) Input; b) RPA method; c) Otsu method.

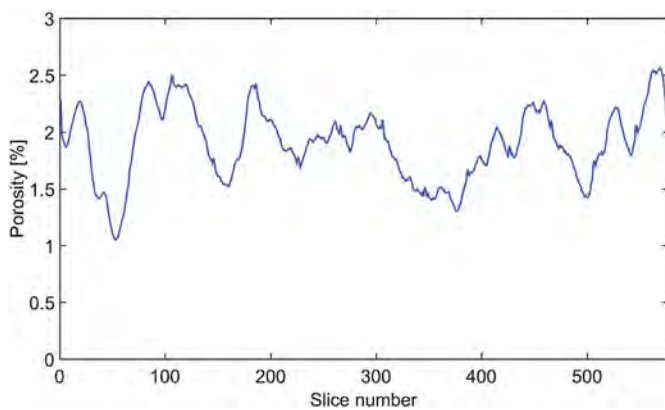


Fig. 10. Pores distribution in analysed sample– studied by proposed CT porosity analysis for all sample cross-sections.

The porosity in LM image was then calculated based on the Otsu's global thresholding for  $2.2855 \pm 0.02\%$ . This number became the reference number for the automatic selection of threshold value for the CT image. The resulting threshold value (i.e. 6689) was then applied for the pores segmentation in all CT cross-sections by means of the global thresholding. The porosity of the sample was  $1.90 \pm 0.16\%$ .

#### 4.2. Comparison with standard methods

To imitate the actual use of available software, the porosity analysis was performed on the whole sample's CT data volume using Otsu's and also Ridler global thresholding methods. Although the CT data (Fig. 7) showed a relatively high distribution of pores, it was presented by a low material-pores contrast and a small overall number of dark voxels. Consequently, the resulting histogram was almost unimodal. None of the methods (Otsu and Ridler) was successful in distinguishing the peak of pores. The methods only determined thresholds in the peak of material (Fig. 8), which resulted in a high porosity numbers (see Table 1) because non-pores pixels were considered as pores (see Fig. 9).

The porosity value was also calculated based on the manually selected threshold. This is usually the second option when the applied automatic method is not successful. The threshold value was taken from the study of manual threshold selection (section 3.1). Selected threshold values were averaged so that the participants' variability was eliminated and the value represented the whole group's opinion. This averaged value was close to the RPA method threshold (Fig. 9) giving also similar porosity number (Table 1). This means that the results of the proposed method are in compliance with the major opinion of a group of experts. This experiment also showed that a measurement done by a group of people could reduce the deviations in manual thresholding. However, involving many operators in working on the threshold selection process at the same time is a challenging task in

practice.

For the purpose of metallographic analysis, six cut-off surfaces of the analysed sample were imaged by using LM. A porosity value for each of the images was calculated with the use of Otsu's global thresholding method. The overall sample porosity was then expressed as the mean of all individual porosity values. When we compared the porosity results of our method and the results coming from the metallographic analysis for the sample top surface, our method reached only 0.0001% difference from the metallographic result. However, the difference reached 0.72% for the total sample porosity value. The difference between the porosity number resulting from the metallographic analysis and the one from RPA method might be caused by acquiring a small number of cuts where the pores concentration was higher than in the rest of the sample. The variability of pores distribution was confirmed by the porosity calculation done with every CT cross-section using the RPA selected threshold. This showed that the porosity value varied from  $1.05 \pm 0.15\%$  to  $2.57 \pm 0.15\%$  over all the CT cross-sections (see Fig. 10). In practice, however, there are technical and time constraints that prevent from increasing the number of sample mechanical cutting. Another aspect explaining the difference might be the fact that the resolution was higher in LM than in CT. However, this aspect is not so significant since only cracks and very tiny cavities were revealed. They represented a negligible number of pixels compared to total number of material pixels.

## 5. Conclusion

For the purpose of a SLM production quality inspection, only small test samples are made and analysed for the internal porosity using X-ray micro computed tomography method. The porosity analysis is commonly based on the global thresholding. However, the threshold selection becomes a critical point influencing the final result. In this paper, it was demonstrated that the automatic threshold selection depends on the character of the material inner structure. Moreover, the way an operator influences a variability while carrying out the manual threshold selection was also discussed. As a result, a new porosity analysis procedure on CT data was designed. It is based on a correlation with the metallographic image of the sample surface which is obtained with higher resolution and pore contrast than the CT data. For this reason, the metallographic image is used as a reference image for the threshold selection. The procedure respects the given voxel resolution of CT data and it is objective and reproducible. These properties enable a comparative porosity analysis of samples from separate measurements which are even performed on different CT machines. The proposed procedure was tested on a sample of aluminium alloy including all possible defects related to additive manufacturing. Based on a comparison with manual and standard automatic techniques, the RPA method showed a reliable determination of pores and a good agreement with the value determined by a group of experienced CT users.

## Acknowledgments

This work is an output of GACR project 15-23274S: Design of advanced materials using selective laser melting.

## References

- Levy GN, Schindel R, Kruth JP. Rapid manufacturing and rapid tooling with layer manufacturing (lm) technologies, state of the art and future perspectives. *CIRP Ann - Manuf Technol* 2003;52(2):589–609.
- Kruth JP, Vandenbroucke B, van Vaerenbergh J, Mercelis P. Benchmarking of different SLS/SLM processes as rapid manufacturing techniques. Proceedings of the international conference on polymers & moulds innovations (PMI); 2005 20-24 April. 2005. p. 1–7. Gent, Belgium; paper 525. Gent (Belgium).
- Santos EC, Shiomi M, Osakada K, Laoui T. Rapid manufacturing of metal components by laser forming. *Int J Mach Tool Manuf* 2006;46(12–13):1459–68.
- Yadroitsev I, Smurov I. Selective laser melting technology: from the single laser melted track stability to 3D parts of complex shape. *Phys Procedia* 2010;2010(5B):551–60.
- Manfredi D, Calignano F, Krishnan M. Additive manufacturing of Al alloys and aluminium matrix composites (AMCs). In: Monteiro Waldemar A, editor. *Light Metal Alloys Applications*. InTech; 2014. p. 3–34.
- Kruth JP, Badrossamay M, Yasa E, Deckers J, Thijs L, van Humbeeck J. Part and material properties in selective laser melting of metals. Proceedings of the 16th international symposium on electromachining; 2010 April 19-23. 2010. p. 1–12. Shanghai, China. Shanghai (China).
- Koukal O, Koutný D, Paloušek D, Vrána R, Zikmund T, Pantělejev L. Research about the influence of process parameters of selective laser melting on material EN AW 2618. *Euro PM2015 proceedings*; 2015. 2015. p. 1–6. Reims, France. Reims (France).
- Ilčík J, Koutný D, Paloušek D. Geometrical accuracy of the metal parts produced by selective laser melting: initial tests. Proceedings of 54th international conference of machine Design departments. 1; 2013. Liberec (Czech Republic): Springer: Technical University of Liberec, Liberec, Czech Republic; 2014. p. 477–86.
- Brandl E, Heckenberger U, Holzinger V, Buchbinder D. Additive manufactured AlSi10Mg samples using Selective Laser Melting (SLM): microstructure, high cycle fatigue, and fracture behavior. *Mater Des* 2012;34:159–69.
- Olakanmi EO. Selective laser sintering/melting (SLS/SLM) of pure Al, Al–Mg, and Al–Si powders. *J Mater Process Technol* 2013;213(8):1387–405.
- Yasa E, Deckers J, Kruth JP. The investigation of the influence of laser re-melting on density, surface quality and microstructure of selective laser melting parts. *Rapid Prototyp J* 2011;17(5):312–27.
- Aboulkhair NT, Everitt NM, Ashcroft I, Tuck Ch. Reducing porosity in AlSi10Mg parts processed by selective laser melting. *Addit Manuf* 2014;1–4(5):77–86.
- du Plessis A, le Roux SG, Booysen G, Els J. Directionality of cavities and porosity formation in powder-bed laser additive manufacturing of metal components investigated using X-ray tomography. *3D Print Addit Manuf* 2016;3(1):48–55.
- Spierings AB, Levy G. Comparison of density of stainless steel 316L parts produced with selective laser melting using different powder grades. Paper presented at: proceedings of the annual international solid freeform fabrication symposium. 2009. August 3-5, Austin, TX, USA.
- Xia M, Gu D, Yu G, Dai D, Chen H, Shi Q. Porosity evolution and its thermodynamic mechanism of randomly packed powder-bed during selective laser melting of Inconel 718 alloy. *Int J Mach Tool Manuf* 2017 May;116:96–106.
- Choi JP, Shin GH, Yang S, Yang DY, Lee JS, Brochu M, Yu JH. Densification and microstructural investigation of Inconel 718 parts fabricated by selective laser melting. *Powder Technol* 2017 April;310:60–6.
- Maskery I, Aboulkhair NT, Corfield MR. Quantification and characterisation of porosity in selectively laser melted Al–Si10–Mg using X-ray computed tomography. *Mater Char* 2016;111:193–204.
- Cai X, Malcolm AA, Wong BS, Fan Z. Measurement and characterization of porosity in aluminium selective laser melting parts using X-ray CT. *Virtual Phys Prototyp* 2015;10(4):195–206.
- Spierings AB, Schneider M, Eggenberger R. Comparison of density measurement techniques for additive manufactured metallic parts. *Rapid Prototyp J* 2011;17(5):380–6.
- Slotwinski JA, Garboczi EJ, Keith M. Porosity measurements and analysis for metal additive manufacturing process control. *J Res Natl Inst Stand Technol* 2014 September 16;119:494–528.
- Nicoletto G, Anzelotti G, Konečná R. X-ray computed tomography vs. metallography for pore sizing and fatigue of cast Al-alloys. *Procedia Eng* 2010;2(1):547–54.
- Zou Y, Malzbender J. Development and optimization of porosity measurement techniques. *Ceram Int* 2016;42(2):2861–70.
- Robin V, Sardini P, Mazurier A, Regnault O, Descostes M. Effective porosity measurements of poorly consolidated materials using non-destructive methods. *Eng Geol* 2016;205:24–9.
- Olakanmi EO, Cochrane RF a, Dalgarno KW. A review on selective laser sintering/melting (SLS/SLM) of aluminium alloy powders: processing, microstructure, and properties. *Prog Mater Sci* 2015;74:401–77.
- Rueckel J, Stockmar M, Pfeiffer F, Herzen J. Spatial resolution characterization of a X-ray microCT system. *Appl Radiat Isot* 2014;94:230–4.
- Lee Ch, Baek J. A new method to measure directional modulation transfer function using sphere phantoms in a cone beam computed tomography system. *IEEE Trans Med Imaging* 2015;34(4):902–10.
- Taud H, Martinez-Angeles R, Parrot JF, Hernandez-Escobedo L. Porosity estimation method by X-ray computed tomography. *J Petrol Sci Eng* 2005;47(3–4):209–17.
- Iassonov P, Gebrenegus T, Tuller M. Segmentation of X-ray computed tomography images of porous materials: a crucial step for characterization and quantitative analysis of pore structures. *Water Resour Res* 2009;45(9).
- Papa JP, Nakamura RYM, de Albuquerque VHC, Falcão AX, Tavares JMRS. Computer techniques towards the automatic characterization of graphite particles in metallographic images of industrial materials. *Expert Syst Appl* 2013;40(2):590–7.
- Zatočilová A, Zikmund T, Kaiser J, Paloušek D, Koutný D. Measurement of the porosity of additive-manufactured Al–Cu alloy using X-ray computed tomography. *Solid State Phenom* 2016;258:448–51.
- Volkswagen. VDG P201/VW 50097: porosity of metal castings. Germany: Volkswagen; 2007. p. 7.
- Volkswagen. VDG P201/VW 50097: porosity of metal castings. Germany: Volkswagen; 2012. p. 7.
- Jan J. Medical image processing, reconstruction, and restoration: concepts and methods. Boca Raton, FL: CRC Press; 2005 November 2. p. 760.
- Sankur B. Survey over image thresholding techniques and quantitative performance evaluation. *J Electron Imag* 2004;13(1):146–68.

- [35] Otsu NA. Threshold selection method from gray-level histograms. *IEEE Trans Syst Man Cybern* 1979;9(1):62–6.
- [36] Ridler TW. Picture thresholding using an iterative selection method. *IEEE Trans Syst Man Cybern* 1978;8(8):630–2.
- [37] Davis GR, Elliott JC. Artefacts in X-ray microtomography of materials. *Mater Sci Technol* 2013;22(9):1011–8.
- [38] Koukal O, Koutný D, Paloušek D, Vrána R, Zikmund T, Pantělejev L. Research about the influence of process parameters of selective laser melting on material EN AW 2618. *Euro PM2015 proceedings*; 2015, Reims, France. Reims (France). 2015. p. 1–6.
- [39] Reddy BS, Chatterji BN. An FFT-based technique for translation, rotation, and scale-invariant image registration. *IEEE Trans Image Process* 1996;5(8):1266–71.
- [40] Cormen TH, Leiserson ChC, Rivest RL, Stein C. *Introduction to algorithms*. third ed. Cambridge: The MIT Press; 2009. p. 1180.
- [41] Kumar Jagadeesha, Abulrub Abdul Hadi G, Attridge a Alex, Williams Mark A. Effect of X-ray computed tomography scanning parameters on the estimated porosity of foam specimens. *Appl Mech Mater* 2011;110–116:808–15.

## PAPER [V]

**OPEN ACCESS**

# High-contrast differentiation resolution 3D imaging of rodent brain by X-ray computed microtomography

To cite this article: T. Zikmund *et al* 2018 *JINST* **13** C02039

View the [article online](#) for updates and enhancements.

INTERNATIONAL WORKSHOP ON IMAGING II  
4–8 SEPTEMBER 2017  
VARENNA, ITALY

## High-contrast differentiation resolution 3D imaging of rodent brain by X-ray computed microtomography

T. Zikmund,<sup>a</sup> M. Novotná,<sup>a</sup> M. Kavková,<sup>a</sup> M. Tesařová,<sup>a</sup> M. Kaucká,<sup>b,c</sup> B. Szarowská,<sup>c</sup>  
I. Adameyko,<sup>b,c</sup> E. Hrubá,<sup>d</sup> M. Buchtová,<sup>d</sup> E. Dražanová,<sup>e</sup> Z. Starčuk<sup>e</sup> and J. Kaiser<sup>a,1</sup>

<sup>a</sup>Central European Institute of Technology, Brno University of Technology, CEITEC - BUT,  
Purkyňova 123, 612 00 Brno, Czech Republic

<sup>b</sup>Department of Physiology and Pharmacology, Karolinska Institutet,  
Nanna Svartz väg 2, Stockholm 17177, Sweden

<sup>c</sup>Department of Molecular Neurosciences, Center for Brain Research, Medical University of Vienna,  
Spitalgasse 4, Vienna, Austria 1090

<sup>d</sup>Laboratory of Molecular Morphogenesis, Institute of Animal Physiology and Genetics AS CR,  
v. v. i., Brno, Czech Republic

<sup>e</sup>Institute of Scientific Instruments of the CAS, v. v. i., Brno, Czech Republic

E-mail: [jozef.kaiser@ceitec.vutbr.cz](mailto:jozef.kaiser@ceitec.vutbr.cz)

**ABSTRACT:** The biomedically focused brain research is largely performed on laboratory mice considering a high homology between the human and mouse genomes. A brain has an intricate and highly complex geometrical structure that is hard to display and analyse using only 2D methods. Applying some fast and efficient methods of brain visualization in 3D will be crucial for the neurobiology in the future. A post-mortem analysis of experimental animals' brains usually involves techniques such as magnetic resonance and computed tomography. These techniques are employed to visualize abnormalities in the brains' morphology or reparation processes. The X-ray computed microtomography (micro CT) plays an important role in the 3D imaging of internal structures of a large variety of soft and hard tissues. This non-destructive technique is applied in biological studies because the lab-based CT devices enable to obtain a several-micrometer resolution. However, this technique is always used along with some visualization methods, which are based on the tissue staining and thus differentiate soft tissues in biological samples. Here, a modified chemical contrasting protocol of tissues for a micro CT usage is introduced as the best tool for *ex vivo* 3D imaging of a post-mortem mouse brain. This way, the micro CT provides a high spatial resolution

<sup>1</sup>Corresponding author.

of the brain microscopic anatomy together with a high tissue differentiation contrast enabling to identify more anatomical details in the brain. As the micro CT allows a consequent reconstruction of the brain structures into a coherent 3D model, some small morphological changes can be given into context of their mutual spatial relationships.

**KEYWORDS:** Computerized Tomography (CT) and Computed Radiography (CR); MRI (whole body, cardiovascular, breast, others), MR-angiography (MRA)

---

## Contents

<b>1</b>	<b>Introduction</b>	<b>1</b>
<b>2</b>	<b>Materials and methods</b>	<b>2</b>
2.1	Sample preparation for micro CT measurement	2
2.2	Micro CT measurement and data processing	2
2.3	MRI measurement	3
<b>3</b>	<b>Results and discussion</b>	<b>3</b>
<b>4</b>	<b>Conclusion</b>	<b>9</b>

---

## 1 Introduction

Computed tomography is widely applied in the human medicine especially to monitor bone injuries, to diagnose head, lung and chest conditions or to detect cancer. In the last decades, this non-destructive imaging technique has been evolved and therefore is able to provide high-resolution *ex vivo* analyses of biological samples. The micro CT brings unique possibilities concerning the imaging of complex biological systems, such as the following cases: a description of a mouse knee cartilage development [1]; a formation of 3D models of mouse chondrocranium, an analysis of the ossification onset and morphological changes in various transgenic mice [2–4]; a noninvasive observation of a human embryo [5].

The principle of the X-ray micro CT imaging is based on taking series of 2D projection radiographs from different angles and their subsequent processing. In each projection, the information about radiographic density is recorded. A mathematical process called tomographic reconstruction forms a 3D matrix which represents a map of volume density. The spatial resolution of the system is determined by the geometry of a cone beam. The achievable resolution is down to 1  $\mu\text{m}$  for lab-based machines. This method has proven to be an effective tool for imaging of native bone tissues [6, 7], since the hydroxyapatite is dense enough to be easily detected. In the case of biological samples and soft tissues *ex vivo*, the micro CT imaging requires an application of some X-ray absorbing contrast agents, e. g. phosphotungstic acid (PTA), iodine or osmium [8]. If the contrast is sufficient, it is possible to segment different structures within the 3D tomographic data by using an appropriate software.

The major advantage of the CT method is the ability to image a bone, soft tissues and blood vessels at the same time. In some cases, it is advantageous to combine the CT method with some other techniques for *in vivo* imaging to visualize better various soft tissues. Especially in the case of cancer diagnosis, the computed tomography is combined with the positron emission tomography (PET/CT) [9].

In biomedical research, the rodent brain attracts a lot of attention because of some human-related pathologies that can be modelled in transgenic animals and also because of the high homology between the human and mouse genome, which causes numerous fundamental neurobiological questions [10]. To take advantage of the information gained from mouse brain research, it is necessary to systematically collect the phenotype information at all biological levels. Conventionally used 2D analysis methods — histology, immunochemistry or transmission electron microscopy — show a high resolution within the plane in which the tissue is sectioned. However, these methods are destructive and two dimensional in their nature.

In the case of post-mortem 3D imaging of mouse brain, the micro CT is not the only method that could be applied. The magnetic resonance imaging (MRI) could be used for a similar purpose as well. In the past, the micro CT was used as an accessory technique to MRI for the imaging of the mouse brain. The micro CT was employed for the imaging of the skull [6, 7] or for the visualization of vascular system of mouse brain filled with radio-opaque silicone rubber Microfil [11–17]. With the recent progress in development of chemical contrasting protocols for brain tissue [6, 18–22] or application of micro CT imaging as a tool for location of cerebral ischemia [22, 23] or brain tumors [21, 24], micro CT imaging is becoming a vital research tool for mouse brain imaging in general.

In this article, we will focus on the mouse brain 3D imaging with a high-resolution laboratory micro CT system combined with an optimization of sample staining. We use different staining protocols based on iodine solution and phosphotungstic acid. The benefits of such approaches will be specified. We will summarize the comparison of the different staining procedures and we will also compare the gained data with the corresponding magnetic resonance data. Furthermore, the power of presented method will be demonstrated by a number of 3D models of selected brain structures with specifically complex 3D geometries that we have reconstructed and analyzed.

## 2 Materials and methods

### 2.1 Sample preparation for micro CT measurement

An adult mouse was sacrificed with isoflurane overdose. The brain was dissected from skull and collected into ice-cold PBS. Subsequently, the sample was fixed in freshly prepared 4% paraformaldehyde (PFA). The sample was dehydrated in ethanol grade (12 h) and stained in 1% iodine solution in 90% methanol. After 24 hours in the solution, the sample was rinsed in ethanol rehydration series to end up in sterile distilled water. For the sake of micro CT measurement, the brain was embedded in 1% agarose gel and placed in a plastic tube. All animal (mouse) concerned work had been approved and permitted by the Ethical Committee on Animal Experiments (Norra Djurförsöksetiska Nämnd, ethical permit N226/15 and N5/14) and was conducted according to The Swedish Animal Agency's Provisions and Guidelines for Animal Experimentation recommendations.

### 2.2 Micro CT measurement and data processing

Micro CT measurement was performed with a GE Phoenix v|tome|x L 240 (GE Sensing & Inspection Technologies GmbH, Germany), equipped with a nanofocus X-ray tube with maximum power of 180 kV/15 W. The data were acquired using a high contrast flat panel detector DXR250 with 2048 px × 2048 px, 200 μm × 200 μm pixel size. The micro CT scan was carried out in an air-conditioned cabinet (21°C) at 60 kV acceleration voltage and 200 μA tube current. Exposure

time was 900 ms and 3 images were averaged for reducing the noise. Two different measurement procedures were performed. The first one was used for the evaluation of staining protocol. The brains contrasted by various techniques were scanned with a voxel resolution of  $18\ \mu\text{m}$ . After the evaluation, the second measurement procedure was applied for one brain with a voxel resolution of  $6.5\ \mu\text{m}$ . 2200 projections were taken over  $360^\circ$  in this case. A tomographic reconstruction was realized by software GE phoenix datavision 2.0 (GE Sensing & Inspection Technologies GmbH, Germany). Reconstructed slices were imported into a VG Studio MAX 3.1 (Volume Graphics GmbH, Germany). In this software, the 3D data were aligned so that orthogonal slices matched the horizontal ( $xy$ ), coronal ( $yz$ ) and sagittal plane ( $xz$ ) resulting in series of 1700 coronal, 1090 sagittal and 680 horizontal tomographic sections of the brain. These data were compared with an anatomical atlas, and 3D models of anatomical structures were obtained by a segmentation based on the global thresholding.

### 2.3 MRI measurement

The post-mortem mouse brain within the skull was measured by a high-resolution MRI scanner Bruker Avance 9.4 T (Bruker Biospin MRI, Ettlingen, Germany). The resolution of the obtained data was  $0.027 \times 0.027\ \text{mm}$  (matrix  $512 \times 512$  pixels).  $T_1$ -weighted anatomical images of 25 parallel 2D slices were taken using the FLASH sequence with slice thickness 0.5 mm, interslice distance 0.5 mm, repetition time (TR) 461.3 ms, effective echo time (TE) 6.1 ms, 50 averages, flip angle  $35.0^\circ$ , echo spacing 6.1 ms. The total measurement time was 9 hours and 25 images were obtained.

## 3 Results and discussion

For a comprehensive visualization of the mouse brain structures done by a conventional micro CT, a chemical contrasting step is usually required. The differentiation of soft tissues by an imaging method delivers the biologically-relevant information only if the contrasting is sufficient. Our priority in this research was achieving the ultimate differential contrast enabling the identification of all major cell types or the tissue modes.

Inorganic iodine and phosphotungstic acid (PTA) are the most broadly used agents in the field of post-mortem tissue contrasting for the following X-ray investigation [25]. Previously, it was suggested to use alcohol solutions containing these compounds to enable a rapid diffusion into the sample [8]. If iodine is compared to PTA, PTA appears as a larger molecule with much slower tissue penetration rates [8]. Ten different staining protocols were tested to visualize mouse brain structures by micro CT imaging (table 1). Samples were stained in PTA, iodine or combination of both of solutions for various periods of time.

In order to compare the contrast among these samples, we analyzed all of them in the same condition. The voxel resolution of obtained CT data was  $18\ \mu\text{m}$ , which turned out to be enough to compare the quality of different contrasting protocols (figure 1). In summary, the staining in iodine exhibited more clear contours of fibres than in the case of PTA-stained samples. Fixation of samples in 4% PFA demonstrated higher contrast to tissues fixed in 10% PFA. The best resolution was obtained in 1% iodine in 90% methanol solution. As this staining showed the most contrastive and sharp edges of anatomical structures at coronal brain sections, we selected the sample stained with this protocol for further analysis.

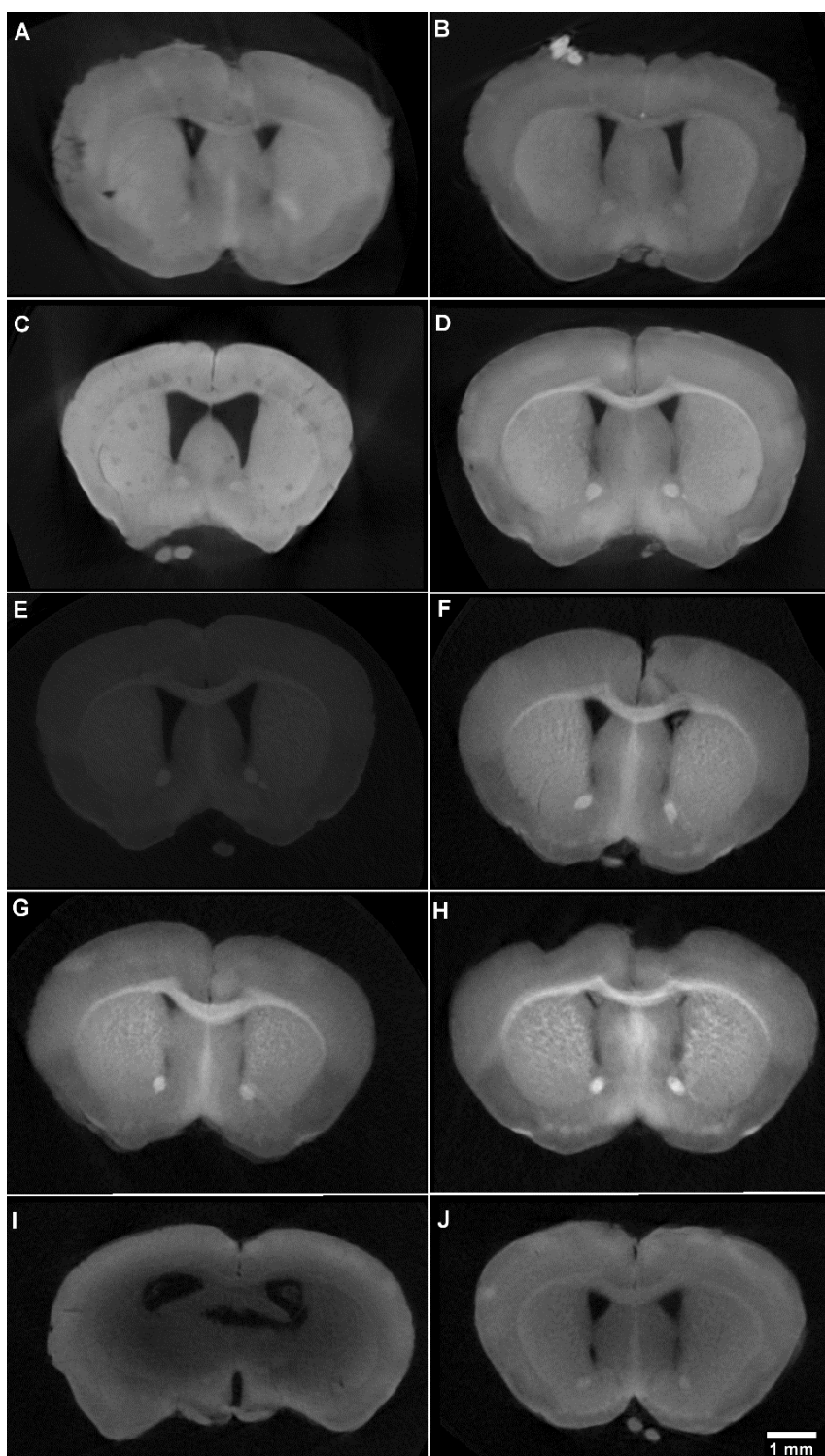


**Figure 1.** Comparison of the coronal sections of samples following different staining protocols. (A) 1% PTA in 90% MeOH for 21 days, (B) 1% PTA in 90% MeOH for 14 days, (C) 1% PTA in 100% MeOH for 16 days, (D) 1% PTA for 10 days + 1% iodine in 90% MeOH for additional 24h, (E) 1% iodine in 100% EtOH for 24h, (F) 1% iodine in 100% EtOH for 48h, (G) 1% iodine in 100% EtOH for 7 days, (H) 1% iodine in 90% MeOH for 24h, (I) 1% iodine in 100% EtOH overnight, (J) 1% iodine in 100% EtOH for 24h.

**Table 1.** List of different processing and staining protocols for brain visualization in micro CT.

	Pre-fixation	Post-fixation	Dehydration	Staining	Time
<b>A</b>	4% PFA	4% PFA (24h)	EtOH / 12h	1% PTA in 90% MeOH	21 days
<b>B</b>	/	4% PFA (24h)	EtOH / 12h	1% PTA in 90% MeOH	14 days
<b>C</b>	10% PFA	10% PFA (24h)	EtOH / 12h	1% PTA in 100% MeOH	16 days
<b>D</b>	4% PFA	4% PFA (24h)	EtOH / 12h	1% PTA + 1% iodine in 90% MeOH	10 days PTA/24h iodine
<b>E</b>	4% PFA	4% PFA (24h)	EtOH / 12h	1% iodine in 100% EtOH	24h
<b>F</b>	4% PFA	4% PFA (24h)	EtOH / 12h	1% iodine in 100% EtOH	48h
<b>G</b>	4% PFA	4% PFA (24h)	EtOH / 12h	1% iodine in 100% EtOH	7 days
<b>H</b>	4% PFA	4% PFA (24h)	EtOH / 12h	1% iodine in 90% MeOH	24h
<b>I</b>	10% PFA	10% PFA (12h)	EtOH / 2h	1% iodine in 100% EtOH	overnight
<b>J</b>	10% PFA	10% PFA (12h)	EtOH / 2h	1% iodine in 100% EtOH	24h

Four coronal sections (figure 2) from different parts of the mouse brain demonstrate the extent of resolution quality of contrasting protocol as captured by a micro CT scan. Identification of the

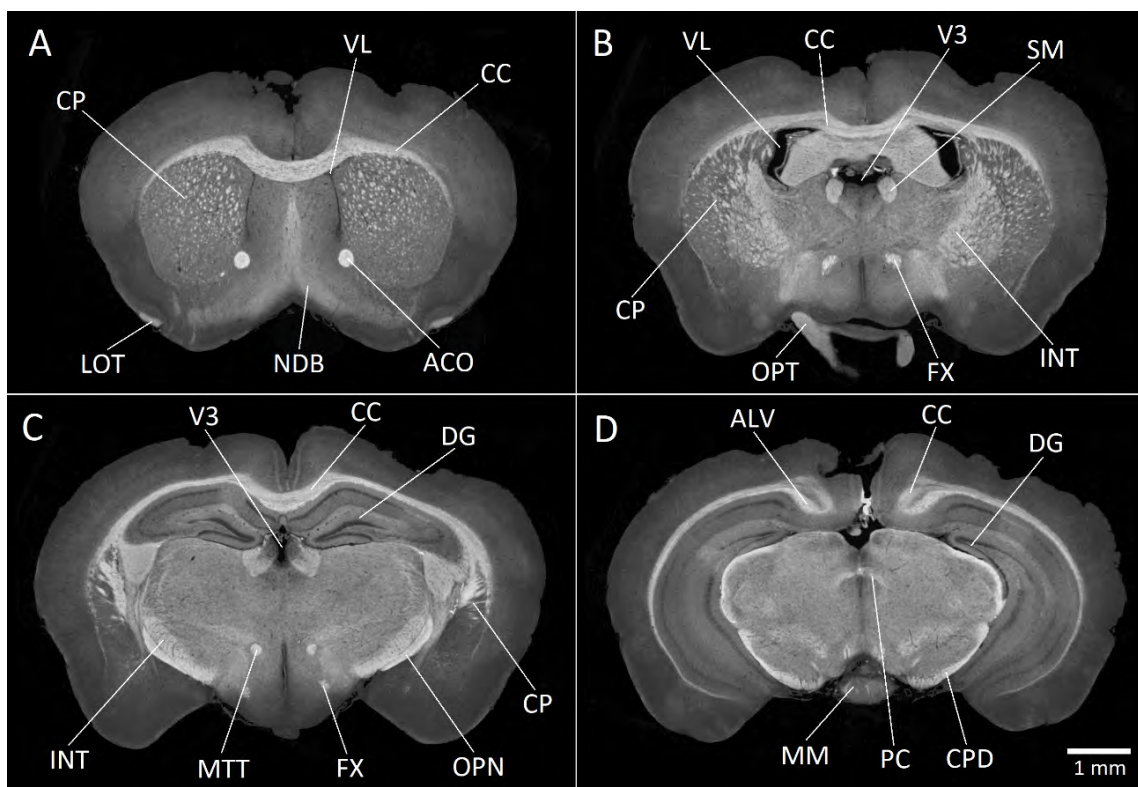


**Figure 2.** Visualization of the internal brain structures as shown on CT images in the coronal sections. (A) ACO anterior commissure, CC corpus callosum, CP caudoputamen, LOT lateral olfactory tract, NDB nucleus of diagonal band, VL lateral ventricle. (B) CC corpus callosum, CP caudoputamen, FX fornix, INT internal capsule, OPT optic tract, SM stria medullaris (thalamus), V3 third ventricle, VL lateral ventricle. (C) CC corpus callosum, CP caudoputamen, DG dentate gyrus, FX fornix, INT internal capsule, MTT mamillothalamic tract, OPN olivary pretectal nucleus, V3 third ventricle. (D) ALV alveus, CC corpus callosum, CPD cerebral crus, DG dentate gyrus, MM medial mammillary nucleus, PC posterior commissure.

described structures in the coronal sections was based on the annotation from Allen Mouse Brain Atlas [26]. For instance, corpus callosum, cerebral peduncle and anterior commissure appeared among the most contrasted and easily identifiable structures. Furthermore, the smaller and finer structures such as mamillothalamic tract, column of the fornix or caudoputamen were successfully recognized as well. Because of the grey matter's high contrast, the ventricles (e.g. lateral ventricle and third ventricle) were also evident.

Although both micro CT and MRI belong to the category of methods providing 3D imaging of the internal structures, the character of the output data including the resolution quality is rather different. The geometry of the data element called voxel has a cubic shape (the same dimensions in all three axes) in the CT and a rectangular cuboid shape in the MRI. The MRI data voxel is defined by the pixel size and slice thickness, which is typically significantly larger than pixel dimensions, i.e. the lateral and axial resolution are different. Isotropic 3D imaging is feasible by both methods, however the length of such experiments needed for achieving a good signal-to-noise ratio is limiting. Consequently, the brain structures were analyzed in detail on 1900 coronal CT slices (with voxel size  $6.5 \mu\text{m} \times 6.5 \mu\text{m} \times 6.5 \mu\text{m}$ ) and 25 coronal MRI slices (with voxel size  $27 \mu\text{m} \times 27 \mu\text{m} \times 500 \mu\text{m}$ ). From this point of view, CT data provided enhanced opportunities to study the arbitrary cross-sections within one dataset and also demonstrated an accurate 3D modelling of internal structures.

The voxel values are defined by greyscale values depending on different properties of the material. CT greyscale values are defined by the X-ray absorption properties in relation to the atomic number of the sample material and to the accelerated voltage of the X-ray source [27, 28]. Based on this fact, brighter tissues refer to denser materials. In the case of anatomical T1 weighted MRI, the amount of the obtained signal depends on the time needed for realigning proton spins in main magnetic field (realigned to Boltzmann equilibrium) [29, 30]. For instance, the fat realigns its spins quickly, and therefore it appears bright on a  $T_1$  weighted image [29, 30]. Water realigns much slower, and therefore it has a lower signal and is represented by darker values.

As for the measurement time, it depends on the particular method. Considering *ex vivo* approach plus the highest possible resolution of both systems, the typical brain measurement took approx. 9 hours for the MRI and 2 hours for the CT.

To compare corresponding MRI and micro CT data (figure 3, table 2), we selected four pairs of corresponding coronal slices of the adult mouse brain. Corpus callosum, anterior commissure, medial mammillary nucleus, posterior commissure and cerebral peduncle were clearly recognizable on both micro CT and MRI images. All the mentioned structures demonstrated well-defined edges in micro CT data. Lateral ventricle, lateral olfactory bulb, optic tract, stria medullaris, internal capsule and cerebral peduncle were also detectable in both micro CT and MRI data. However, unlike the micro CT images, MRI pictures did not display a clear identification of above mentioned structures. The structures such as myelinated fibres in caudoputamen, third ventricle, column of the fornix, dentate gyrus, mamillothalamic tract and other locations were clearly distinguished in the micro CT. Moreover, the compartmentation of dorsal hippocampal commissure from corpus callosum and alveus was possible only in micro CT images.

As the next step, we selected several structures for segmentation to demonstrate possible outputs from micro CT data (figure 4, figure 5, figure 6). Tissue segmentation and construction of accurate

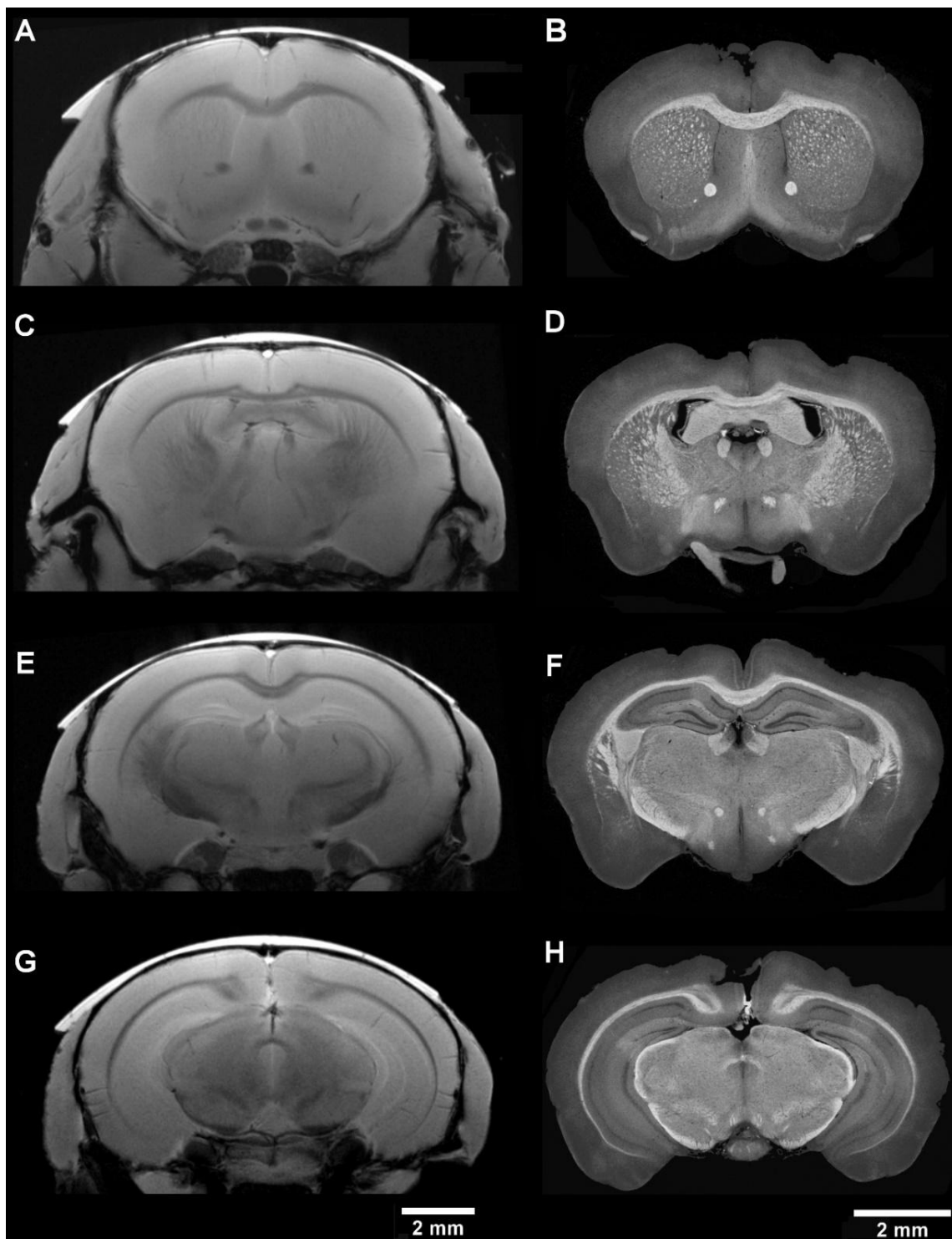


**Figure 3.** Comparison between corresponding coronal sections in MRI (A, C, E, G) and contrasted (1% iodine in 90% methanol) micro CT (B, D, F, H) of mouse brain.

**Table 2.** Identification of anatomical structures in mouse brain in micro CT and MRI images (\*not suitable for segmentation, hard to detect).

structure	micro CT	MRI
corpus callosum	✓	✓
anterior commissure	✓	✓
medial mammillary nucleus	✓	✓
posterior commissure	✓	✓
cerebral peduncle	✓	✓
lateral ventricle	✓	✓*
lateral olfactory bulb	✓	✓*
optic tract	✓	✓*
stria medullaris	✓	✓*
internal capsule	✓	✓*
cerebral peduncle	✓	✓*
myelinated fibres in caudoputamen	✓	×
third ventricle	✓	×
column of the fornix	✓	×
dentate gyrus	✓	×
mamillothalamic tract	✓	×

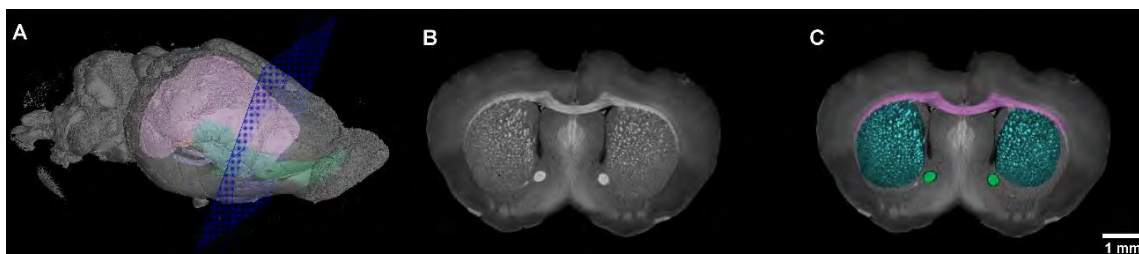


**Figure 4.** Visualization of steps during segmentation. (A) Area of the coronal section in the 3D model of the adult mouse brain, (B) Unmarked tomographic section, (C) Tomographic section with manually segmented corpus callosum (pink), myelinated fibres in caudoputamen (light blue) and anterior commissure (green).

3D models was possible thanks to high-resolution tomographic sections in all coronal, sagittal and horizontal planes and also, a fine contrast was implied by the improved staining protocol. Such a precise 3D visualization could be useful in future for variety of structural analyses in developmental biology and pathological studies. Above that, such data can be used for the educational purposes as they may be utilized for a subsequent 3D printing [31].

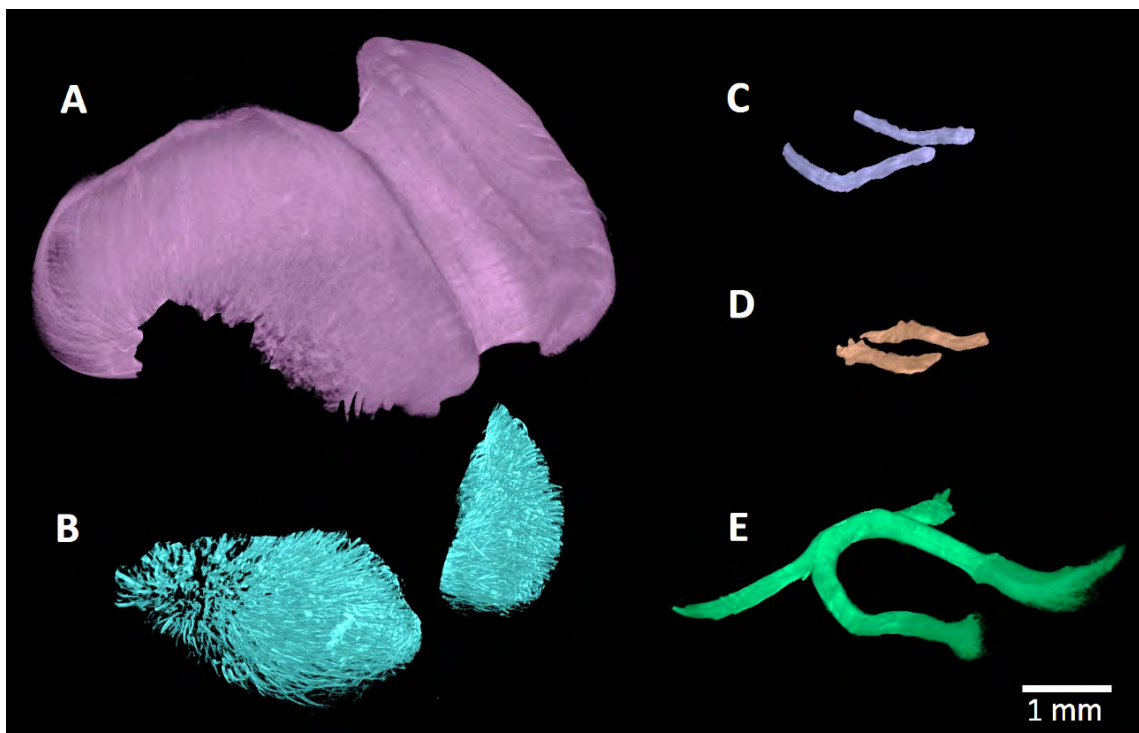


**Figure 5.** Structures segmented from micro CT images. (A) Complex of corpus callosum, dorsal hippocampal commissure and alveus (pink), (B) Myelinated fibres in caudoputamen (light blue), (C) Column of the fornix (purple), (D) Mamillothalamic tract (orange), (E) Anterior commissure (green).

#### 4 Conclusion

Three-dimensional imaging of the rodent brain plays an important role in modern neurobiology and biomedicine research. This kind of imaging enables a precise analysis of developmental changes, tissue damage and tumor recognition with a focus on fine morphological modifications. We worked with several chemical contrasting protocols and compared their ability to visualize brain tissues by a laboratory micro CT device. Our results proved this method to be a powerful tool for a high-resolution *ex vivo* 3D imaging of the rodent soft tissues. The state of the art of the laboratory CT systems together with a staining protocol based on iodine solution enabled to reveal an intricate and geometrically complex internal brain structures in a high resolution. Tissue contrast was found to be considerably stronger in the micro CT images in comparison to the commonly used post-mortem MRI. Consequently, CT data enabled an easier segmentation and 3D reconstruction of internal brain structures. Generally, the 24 hours sample processing together with a two-hour-long CT measurement can provide a quick and complete visualization of the brain's internal and external morphology with a simultaneous and semi-automated identification of the major neural tracks, nuclei and other delicate details. Thanks to all these benefits, the micro CT systems have their place in a routine use in various types of neurobiological experiments.

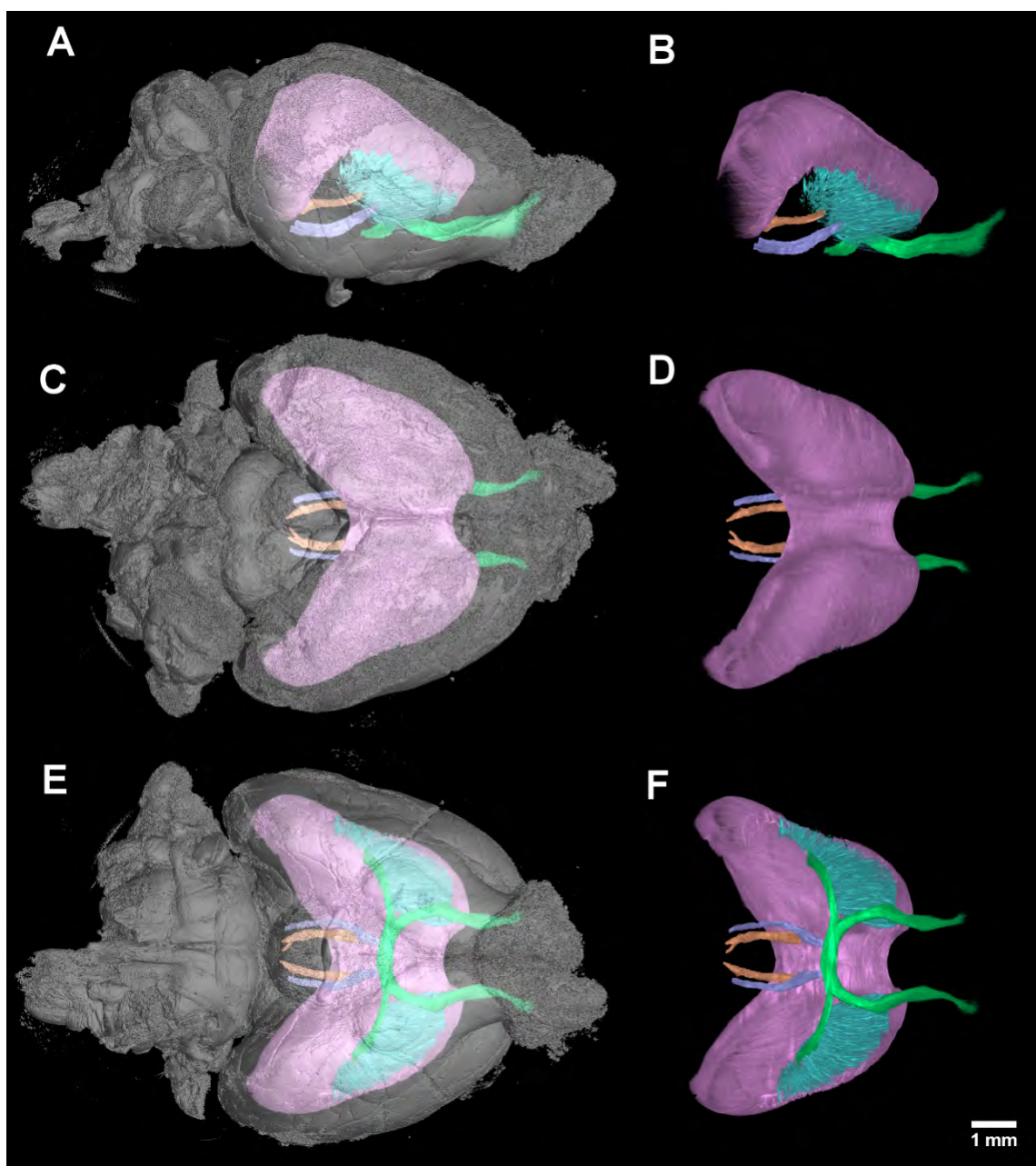


**Figure 6.** Segmented brain structures micro CT images. (A, B) Sagittal view, (C, D) dorsal view, (E, F) ventral views on dorsal hippocampal commissure and alveus (pink), column of the fornix (purple), mamillothalamic tract (orange), myelinated fibres in caudoputamen (light blue), anterior commissure (green) and complex of corpus callosum, dorsal hippocampal commissure and alveus (pink), in context of the whole adult mouse brain.

### Acknowledgments

This research was carried out under the project CEITEC 2020 (LQ1601) with financial support from the Ministry of Education, Youth and Sports of the Czech Republic under the National

Sustainability Programme II and CEITEC Nano Research Infrastructure (MEYS CR, 2016–2019). JK acknowledges the support of the Brno University of Technology on the frame of grant FSI-S-17-4506 (Application of Advanced Optical Methods II). The MR part was supported by the Czech-BioImaging infrastructure grant LM2015062 (MEYS CR, 2016-2019) and NSP II grant LO1212 (MEYS CR, 2014–2018). MB lab was supported by the Ministry of Education, Youth and Sports of the Czech Republic (CZ.02.1.01/0.0/0.0/15\_003/0000460) and Czech Science Foundation (14-37368G). MK was supported by SSMF fellowship.

## References

- [1] L. Li, P. T. Newton, T. Boudierlique, M. Sejnohova, T. Zikmund, E. Kozhemyakina et al., *Superficial cells are self-renewing chondrocyte progenitors, which form the articular cartilage in juvenile mice*, *The FASEB Journal* **31** (2017) 1067.
- [2] M. Kaucka, T. Zikmund, M. Tesarova, D. Gyllborg, A. Hellander, J. Jaros et al., *Oriented clonal cell dynamics enables accurate growth and shaping of vertebrate cartilage*, *eLife* **6** (apr, 2017) e25902.
- [3] M. Kaucka, E. Ivashkin, D. Gyllborg, T. Zikmund, M. Tesarova, J. Kaiser et al., *Analysis of neural crest-derived clones reveals novel aspects of facial development*, *Sci. Adv.* **2** (2016) e1600060.
- [4] P. Cela, M. Hampl, N. Shylo, K. Christopher, M. Kavkova, M. Landova et al., *Ciliopathy protein *tmem107* plays multiple roles in craniofacial development*, *J. Dent. Res.* **97** (2017) 108.
- [5] K. Vymazalová, L. Vargová, T. Zikmund and J. Kaiser, *The possibilities of studying human embryos and fetuses using micro-CT: a technical note*, *Anat. Sci. Int.* **92** (2016) 299.
- [6] B.J. Nieman, A.M. Flenniken, S.L. Adamson, R.M. Henkelman and J.G. Sled, *Anatomical phenotyping in the brain and skull of a mutant mouse by magnetic resonance imaging and computed tomography*, *Physiol. Genom.* **24** (2006) 154.
- [7] M. Aggarwal, J. Zhang, M. Miller, R. Sidman and S. Mori, *Magnetic resonance imaging and micro-computed tomography combined atlas of developing and adult mouse brains for stereotaxic surgery*, *Neuroscience* **162** (2009) 1339.
- [8] B.D. Metscher, *MicroCT for comparative morphology: simple staining methods allow high-contrast 3d imaging of diverse non-mineralized animal tissues*, *BMC Physiol.* **9** (2009) 11.
- [9] R. Bar-Shalom et al., *Clinical performance of PET/CT in evaluation of cancer: additional value for diagnostic imaging and patient management*, *J. Nucl. Med.* **44** (2003) 1200.
- [10] W.W. Wasserman, M. Palumbo, W. Thompson, J.W. Fickett and C.E. Lawrence, *Human-mouse genome comparisons to locate regulatory sites*, *Nat. Genet.* **26** (2000) 225.
- [11] E. Stolz, M. Yeniguen, M. Kreisel, M. Kampschulte, S. Doenges, D. Sedding et al., *Angioarchitectural changes in subacute cerebral venous thrombosis. a synchrotron-based micro- and nano-CT study*, *NeuroImage* **54** (2011) 1881.
- [12] S. Heinzer, T. Krucker, M. Stampanoni, R. Abela, E. P. Meyer, A. Schuler et al., *Hierarchical microimaging for multiscale analysis of large vascular networks*, *NeuroImage* **32** (2006) 626.
- [13] S. Ghanavati, L.X. Yu, J.P. Lerch and J.G. Sled, *A perfusion procedure for imaging of the mouse cerebral vasculature by x-ray micro-CT*, *J. Neurosci. Meth.* **221** (2014) 70.
- [14] A.C. Langheinrich, M. Yeniguen, A. Ostendorf, S. Marhoffer, M. Kampschulte, G. Bachmann et al., *Evaluation of the middle cerebral artery occlusion techniques in the rat by in-vitro 3-dimensional micro- and nano computed tomography*, *BMC Neurol.* **10** (2010) .

- [15] B.P. Chugh, J.P. Lerch, L.X. Yu, M. Pienkowski, R.V. Harrison, R.M. Henkelman et al., *Measurement of cerebral blood volume in mouse brain regions using micro-computed tomography*, *NeuroImage* **47** (2009) 1312.
- [16] B. Xie, P. Miao, Y. Sun, Y. Wang and G.-Y. Yang, *Micro-computed tomography for hemorrhage disruption of mouse brain vasculature*, *Transl. Stroke Res.* **3** (2012) 174.
- [17] A. Dorr, J. Sled and N. Kabani, *Three-dimensional cerebral vasculature of the CBA mouse brain: A magnetic resonance imaging and micro computed tomography study*, *NeuroImage* **35** (2007) 1409.
- [18] R. Anderson and A.M. Maga, *A novel procedure for rapid imaging of adult mouse brains with MicroCT using iodine-based contrast*, *PLOS ONE* **10** (2015) e0142974.
- [19] A. de Crespigny, H. Bou-Reslan, M.C. Nishimura, H. Phillips, R.A. Carano and H.E. D’Arceuil, *3d micro-CT imaging of the postmortem brain*, *J. Neurosci. Meth.* **171** (2008) 207.
- [20] S. Saito and K. Murase, *Ex vivo imaging of mouse brain using micro-CT with non-ionic iodinated contrast agent: a comparison with myelin staining*, *Br. J. Radiol.* **85** (2012) e973.
- [21] N.S. Bautista, A. Martínez-Dávalos, M. Rodríguez-Villafuerte, T. Murrieta-Rodríguez, J. Manjarrez-Marmolejo, J. Franco-Pérez et al., *Ex vivo micro-CT imaging of murine brain models using non-ionic iodinated contrast*, *AIP Conf. Proc.* **1626** (2014) 19.
- [22] M. Dobrivojević, I. Boháček, I. Erjavec, D. Gorup and S. Gajović, *Computed microtomography visualization and quantification of mouse ischemic brain lesion by nonionic radio contrast agents*, *Croat. Med. J.* **54** (2013) 3.
- [23] N. Hayasaka, N. Nagai, N. Kawao, A. Niwa, Y. Yoshioka, Y. Mori et al., *In vivo diagnostic imaging using micro-CT: Sequential and comparative evaluation of rodent models for hepatic/brain ischemia and stroke*, *PLoS ONE* **7** (2012) e32342.
- [24] J.F. Hainfeld, H.M. Smilowitz, M.J. O’Connor, F.A. Dilmanian and D.N. Slatkin, *Gold nanoparticle imaging and radiotherapy of brain tumors in mice*, *Nanomedicine* **8** (2013) 1601.
- [25] B.D. Metscher, *MicroCT for developmental biology: A versatile tool for high-contrast 3d imaging at histological resolutions*, *Dev. Dynam.* **238** (2009) 632.
- [26] *Allen Mouse Brain Atlas*, Allen Institute for Brain Science © 2004, <http://mouse.brain-map.org/static/atlas>.
- [27] J. Hsieh, *Computed tomography: principles, design, artifacts, and recent advances*, SPIE, Bellingham, WA (2009).
- [28] A.C. Kak and M. Slaney, *Principles of computerized tomographic imaging*, Society for Industrial and Applied Mathematics (2001).
- [29] B.M. Dale, M.A. Brown and R.C. Semelka, *MRI: basic principles and applications*, John Wiley & Sons (2015).
- [30] P. Tofts ed., *Quantitative MRI of the brain: measuring changes caused by disease*, John Wiley & Sons (2005).
- [31] M. Tesařová et al., *Use of micro computed-tomography and 3D printing for reverse engineering of mouse embryo nasal capsule*, *2016 JINST* **11** C03006.

PAPER [VI]

## Use of micro computed-tomography and 3D printing for reverse engineering of mouse embryo nasal capsule

This content has been downloaded from IOPscience. Please scroll down to see the full text.

2016 JINST 11 C03006

(<http://iopscience.iop.org/1748-0221/11/03/C03006>)

View [the table of contents for this issue](#), or go to the [journal homepage](#) for more

Download details:

IP Address: 147.229.85.86

This content was downloaded on 16/05/2016 at 19:14

Please note that [terms and conditions apply](#).

INTERNATIONAL WORKSHOP ON IMAGING  
7–10 SEPTEMBER 2015  
VARENNA, ITALY

## Use of micro computed-tomography and 3D printing for reverse engineering of mouse embryo nasal capsule

M. Tesařová,<sup>a,b</sup> T. Zikmund,<sup>a</sup> M. Kaucká,<sup>c,d</sup> I. Adameyko,<sup>c,d</sup> J. Jaroš,<sup>e,f</sup> D. Paloušek,<sup>b</sup>  
D. Škaroupka<sup>b</sup> and J. Kaiser<sup>a,b,1</sup>

<sup>a</sup>CEITEC — BUT, Brno University of Technology,  
Technická 3058/10, 616 00 Brno, Czech Republic

<sup>b</sup>Faculty of Mechanical Engineering, Brno University of Technology,  
Technická 2896/2, 616 69 Brno, Czech Republic

<sup>c</sup>Department of Physiology and Pharmacology, Karolinska Institutet,  
Nanna Svartz väg 2, Stockholm 17177, Sweden

<sup>d</sup>Department of Molecular Neurosciences, Center for Brain Research, Medical University of Vienna,  
Spitalgasse 4, Vienna 1090, Austria

<sup>e</sup>Department of Histology and Embryology, Faculty of Medicine, Masaryk University,  
Kamenice 3, 625 00 Brno, Czech Republic

<sup>f</sup>International Clinical Research Center — Center of Biomolecular and Cellular Engineering,  
St. Anne's University Hospital Brno, Pekařská 53, 656 91, Brno, Czech Republic

E-mail: [jozef.kaiser@ceitec.vutbr.cz](mailto:jozef.kaiser@ceitec.vutbr.cz)

**ABSTRACT:** Imaging of increasingly complex cartilage in vertebrate embryos is one of the key tasks of developmental biology. This is especially important to study shape-organizing processes during initial skeletal formation and growth. Advanced imaging techniques that are reflecting biological needs give a powerful impulse to push the boundaries of biological visualization. Recently, techniques for contrasting tissues and organs have improved considerably, extending traditional 2D imaging approaches to 3D. X-ray micro computed tomography ( $\mu$ CT), which allows 3D imaging of biological objects including their internal structures with a resolution in the micrometer range, in combination with contrasting techniques seems to be the most suitable approach for non-destructive imaging of embryonic developing cartilage. Despite there are many software-based ways for visualization of 3D data sets, having a real solid model of the studied object might give novel opportunities to fully understand the shape-organizing processes in the developing body. In this feasibility study we demonstrated the full procedure of creating a real 3D object of mouse embryo nasal capsule, i.e. the staining, the  $\mu$ CT scanning combined by the advanced data processing and the 3D printing.

**KEYWORDS:** Computerized Tomography (CT) and Computed Radiography (CR); Image reconstruction in medical imaging; Multi-modality systems

<sup>1</sup>Corresponding author.



---

## Contents

<b>1</b>	<b>Introduction</b>	<b>1</b>
<b>2</b>	<b>Materials and methods</b>	<b>3</b>
2.1	Preparation of samples for micro CT measurements, staining	3
2.2	CT measurement and gathering data for 3D printing	3
2.3	Additive manufacturing — 3D printing	4
<b>3</b>	<b>Results</b>	<b>5</b>
<b>4</b>	<b>Discussions and ongoing work</b>	<b>6</b>
<b>5</b>	<b>Conclusions</b>	<b>9</b>

---

## 1 Introduction

Despite the long-standing investigation of craniofacial development, this process is still not fully understood [1]. It is partially because of significant complexity of the structures in the head. These structures play an important role for vital functions through the whole life. The primary research of craniofacial development is often done on mouse embryos [2, 3]. Differences between the samples are usually investigated at craniofacial parts. Typical size of the mouse embryo nasal capsule at day 15 of embryonic development is in the range of few millimetres. There is a wide variety between different developmental stages or mutations that are manifested by small differences in the shape or thickness of the nasal capsule. In order to compare these fine details, high-resolution imaging techniques are needed.

For decades imaging has relied on optical and then also on electron microscopy of histological sections, which provides high resolution 2D data. Over time confocal microscopy enabled collection of optical sections through thicker samples [4]. Episcopic fluorescence image capturing is another technology for generating high-resolution 3D datasets. This method is based on capturing the autofluorescence of each of the histological slices. However, all above mentioned technologies are costly and time-consuming [5]. Optical projection tomography [6] is another approach for 3D imaging, but it is rather limited by sample size. The same accounts for light sheet microscopy (SPIM). Moreover, the sample preparation is rather complicated. Magnetic resonance imaging (MRI) currently represents an universal tool for different needs of soft tissue morphology [7]. This method uses magnetic field and radio waves in order to map various internal structures. MRI is suitable for imaging soft tissues such as internal organs, but it does not provide sufficient resolution for cartilage imaging [5].

One of the most convenient tools for imaging mouse embryonic samples from 12 to 17 days of embryonic development is X-ray computed tomography [3]. It is the oldest tomography imaging technique [8]. X-ray micro computed-tomography ( $\mu$ CT), i.e. X-ray computed-tomography with high spatial-resolution down to  $1\ \mu\text{m}$ , has the same principle as CT machines used for medical scanning. The sample that is placed between the X-ray source and the detector is rotated by  $360^\circ$  around its axis perpendicular to the line connecting the source and the detector. In every rotation step a two dimensional projection is taken. The sequence of obtained projections is subsequently processed by tomographic reconstruction based on inverse Radon transform [8]. In this way different X-ray absorption at each sample point is visualized and the 3D volume map of object density is created. Due to the cone shape of the X-ray beam, geometric magnification can be used to reach high-resolution [8].

X-ray tomography imaging has been limited by low contrast of soft un-mineralized tissues. Phase contrast can be the solution for enhancement of image quality of the X-ray projections [9]. However, this method is not much convenient for industrial and laboratory  $\mu$ CTs, where the image reconstruction rely predominantly on absorption contrast. Phase contrast is more applicable for monochromatic radiation used at synchrotrons [9, 10]. In the case of lab-based  $\mu$ CT systems it is necessary to use contrasting agents for increasing X-ray absorption of soft tissues. There are various methods that are using contrasting agents for staining of biological samples [11]. Phosphotungstic acid (PTA) was utilized as standard histological technique for light and electron microscopy due to its capability to increase the contrast of soft versus mineralized tissues or different type of soft tissues [12–14]. PTA also confers strong X-ray contrast when attached to the collagens and fibrils [12, 13], and to various other proteins. It is considered to be suitable for visualizing soft connective tissue in general [15]. Here we found that cartilage is stained significantly weaker in comparison to surrounding tissue, therefore we took the advantage of that for discriminating and outlining cartilage in  $\mu$ CT analysis.

Another step important for successful  $\mu$ CT is the mounting of the biological sample. It is crucial to have the sample fixed appropriately during the  $\mu$ CT scanning. Even a minuscule movement destroys the tomographic measurement and results in artefacts in the reconstructed tomographic cross-sections. It happens if samples are floating in aqueous or alcohol surrounding. Minimization of background can be reached by mounting the samples to hydrogels based on agarose, gelatine or alginate and by mechanical fixation of samples in standard laboratory equipment, like plastic tubes or polyimide tubes that are not very contrasting for X-rays.

If the contrast is sufficient, it is straightforward to visualize the 3D volume rendering of different features of the sample using proper tomographic software. The differentiation of these features is simply based on setting the appropriate gray values or gray value intervals in image histogram. However, it is difficult to set threshold for cartilage. As it was mentioned above, the cartilage is stained significantly weaker in comparison with surrounding tissue, so only its border is detectable (figure 1). In this case, data processing cannot be fully automated yet, but using suitable software tools enable relatively fast and precise manual segmentation of the craniofacial cartilage.

Here we present the whole process of reverse engineering of mouse embryo nasal capsule including staining and tomographic measurement combined with the advanced data processing for creating 3D model and its printing.

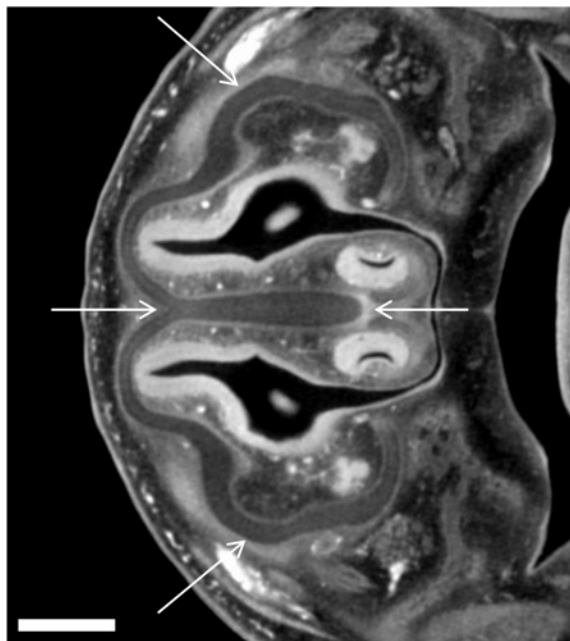


**Figure 1.** Reconstructed tomographic cross section of mouse embryo. Arrows show cartilage of nasal capsule. The length of the scale bar is 0.4 mm.

## 2 Materials and methods

### 2.1 Preparation of samples for micro CT measurements, staining

Our staining protocol has been modified from protocol developed by Brian Metscher [15]. After excision, the 15.5 days old C57BL strain mouse embryos were fixed with 4% formaldehyde in phosphate buffer saline (PBS) for 24 hours at +4°C. Samples were then washed with PBS and dehydrated by ethanol grade (30%, 50%, 70%), each concentration for 1 day.

We experimentally found out the best tissue contrast and penetration with PTA (10026-AP0, Lach-Ner, Czech Republic) dissolved in 90% methanol (21190-11000, Ing. Petr Švec-PENTA, Czech Republic). Therefore we transferred the samples from 70% ethanol (71250-11000, Ing. Petr Švec-PENTA, Czech Republic) to ethanol-methanol-water mixture (4:4:3) and then into 80% and 90% methanol, each bath for 1 hour. After that, 0.7% PTA-methanol solution was used to stain the samples for 6 days and exchanged every day with the fresh one.

The staining was followed by rehydration of the samples in methanol grade series (90%, 80%, 70%, 50% and 30%) to end up in sterile distilled water. After that, rehydrated embryos were embedded in 0.5% agarose gel (A5304, Sigma-Aldrich) and placed in 1.5 ml polypropylene tubes to avoid the movement artefacts during X-ray computer tomography scanning.

### 2.2 CT measurement and gathering data for 3D printing

The polypropylene tube was fixed on a plastic rod by a silicone gun. The rod was mounted in the chuck which provides the position of the sample in rotation axis (figure 2). The  $\mu$ CT scanning was performed using laboratory system GE Phoenix v|tome|x L 240 (GE Sensing & Inspection

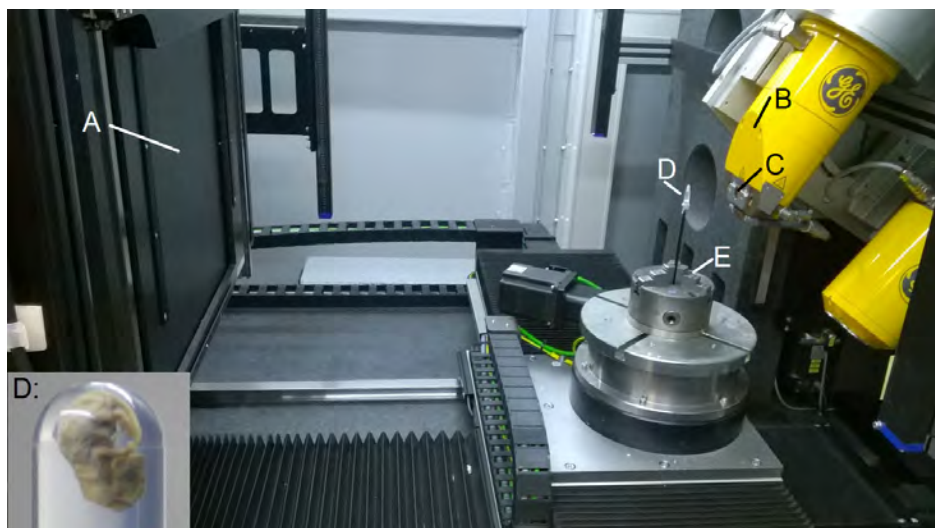


**Figure 2.** Fixing the sample for  $\mu$ CT measurement. A — flat panel detector; B — X-ray tube; C — aluminium filter; D — embryo embedded in agarose gel in the tube; E — chuck.

Technologies GmbH, Germany), equipped with a 180 kV/15 W maximum power nanofocus X-ray tube and high contrast flat panel detector DXR250 with  $2048 \times 2048$  pixel<sup>2</sup>,  $200 \times 200 \mu\text{m}^2$  pixel size. The exposure time was 900 ms in every of the 2200 positions. The utilized acceleration voltage and X-ray tube current were 60 kV and  $200 \mu\text{A}$ , respectively. The beam was filtered by the beryllium window of the X-ray housing and by 0.2 mm of aluminium filter. The voxel size of obtained volume was  $5 \mu\text{m}$ . The tomographic reconstruction was realized using 3D computed tomography software GE phoenix datos|x 2.0 (GE Sensing & Inspection Technologies GmbH, Germany). The data processing was realized in software VG Studio MAX 2.2 (Volume Graphics GmbH, Germany). Segmentation of nasal capsule was completed manually (approx. 8 hours of segmentation). The “smoothing” tool, with strength 20 was used to smooth the virtual 3D model in order to get rid of inaccuracies.

### 2.3 Additive manufacturing — 3D printing

The Parts have been manufactured by ZPrinter 650 (Peak Solutions, U.S.A.). Building volume is  $254 \times 381 \times 203$  mm and layer thickness was established to 0.1016 mm. Color printing resolution in  $x$  and  $y$  directions is  $600 \times 540$  dots per inch (DPI) and the minimum feature size is also 0.1016 mm. All data were adjusted in the 3D printing software ZPrint 7.15 (Peak Solutions, U.S.A.).

The STL data generated from  $\mu$ CT measurements were scaled 50 times directly in the 3D printing software. Monochromatic green color, the same color that was used as a virtual color in VG studio MAX 2.2 software, was chosen. The printer spread 716 layers of plaster based powder, where each layer was bound by five Hewlett Packard print heads (CMYK binders + one Clear binder) with the resolution of  $600 \times 540$  DPI. After 6 hours and 15 minutes the printing was finished and the printer dried up the part still surrounded by the powder in the building chamber. Dry part was carefully removed from the powder by vacuumer and brush and depowdered by compressed air in the post-processing unit. It was infiltrated by cyanoacrylate using drizzle method to give it additional strength, durability, and color vibrancy.

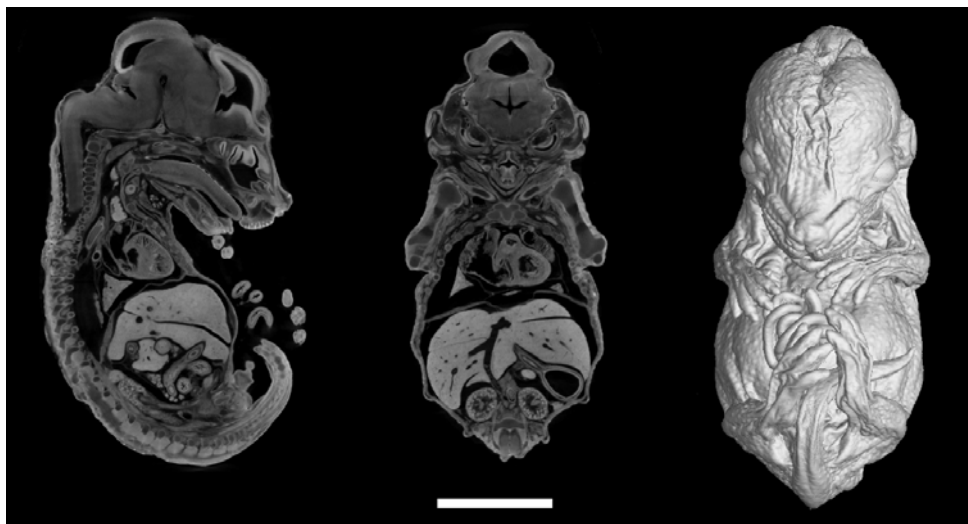


**Figure 3.** The obtained data from the  $\mu$ CT measurement. The cross section in two perpendicular planes and the 3D render of the whole 15.5 days old embryo. The length of the scale bar is 3 mm.

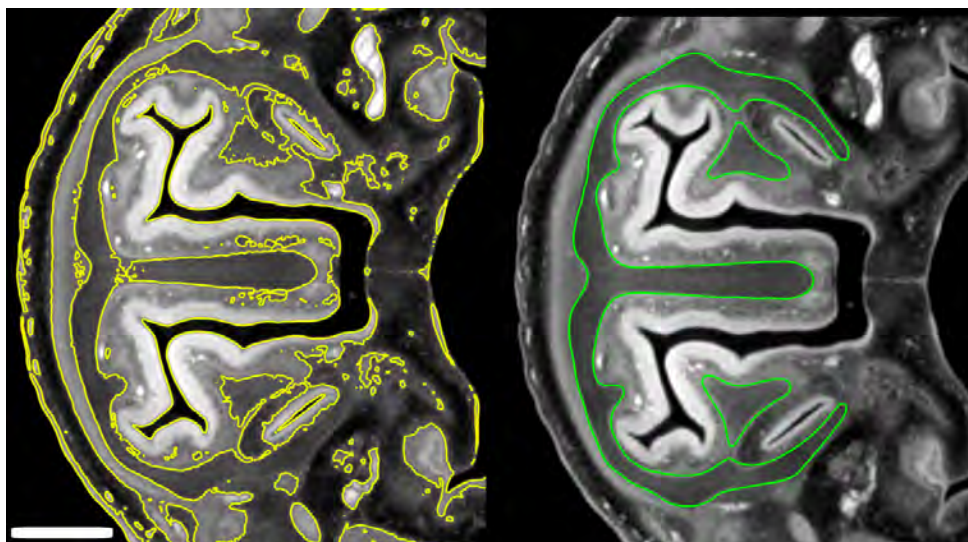


**Figure 4.** Comparison between automatic (yellow) and manual (green) segmentation. The length of the scale bar is 0.5 mm.

### 3 Results

The overall procedure is demonstrated on a representative 15.5 days old mouse embryo stained by PTA. The  $\mu$ CT measurement had a satisfactory contrast for the overall 3D render of the mouse embryo (figure 3).

Gray value intervals for border of the cartilage was not sufficiently pronounced for automatic segmentation (figure 4). The manual segmentation was realized in one direction across the sample, along the cross section shown in figures 1 and 5, denoted  $x$ ,  $y$  in figure 5. Using manual segmentation, a 3D model of a nasal capsule was created (figure 6).

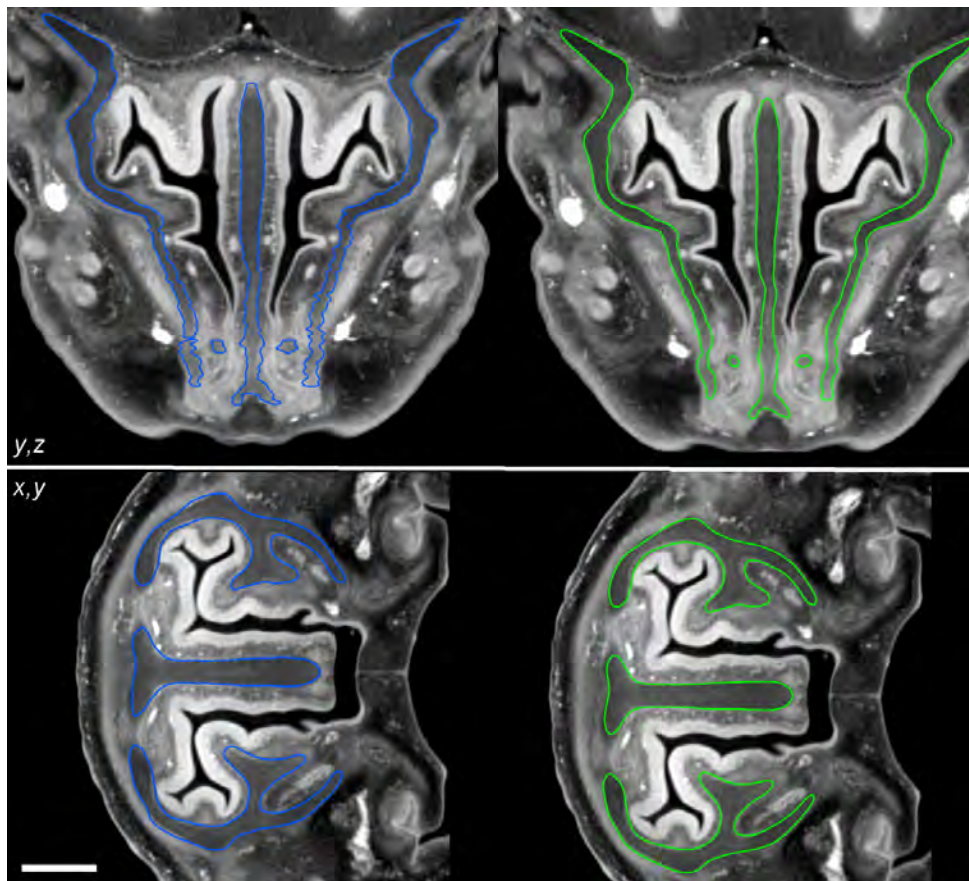


**Figure 5.** Using the “smoothing” tool. Blue line — before the application of the tool, green line — after the smoothing. The upper part shows the cross section  $y, z$ , perpendicular to the cross section  $x, y$  in which the segmentation was realized. The smoothing was controlled in the cross section  $x, y$  (bottom image) by comparing the segmented and smoothed data. The length of the scale bar is 0.35 mm.

Segmentation along one cross section caused disfluencies in the perpendicular cross section  $y, z$  (figure 5). After the segmentation these visible distinct inaccuracies were smoothed and fluent model was obtained. The smoothing parameter was optimized that way to preserve the small details. This was controlled by comparison with the original tomographic cross sections  $x, y$  (figure 5 and 6).

The finished virtual 3D model was exported to STL format for 3D printing. The printed 3D model is compared with the STL model in figure 7.

Figure 8 shows the comparison of the printed 3D model of an olfactory system with the human hand.

#### 4 Discussions and ongoing work

Even if the proper combination of different techniques may represent a breakthrough with clinical significance, the use of advanced techniques in multi-disciplinary biological research is nowadays still a challenge [16]. Using  $\mu$ CT, stereolithography computer-aided design (STL CAD) modeling and matrix-assisted laser desorption-ionisation — time of flight mass spectrometry (MALDI-TOF

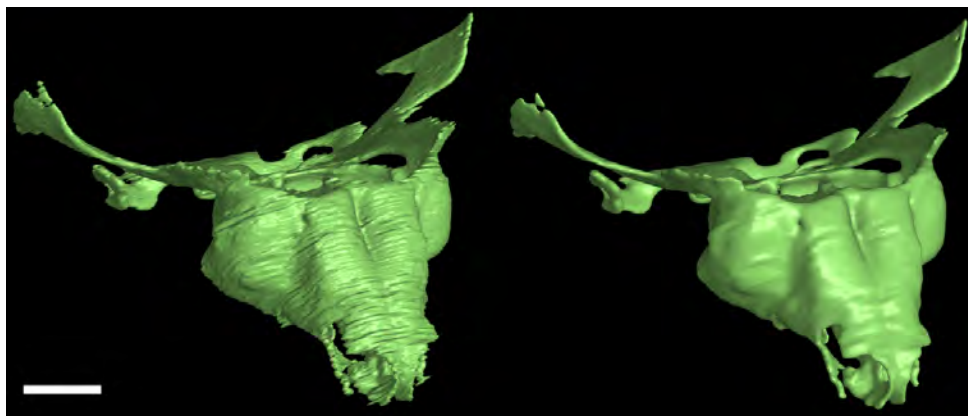


**Figure 6.** Segmented models without smoothing (left) and with smoothing (right). The length of the scale bar is 0.5 mm.

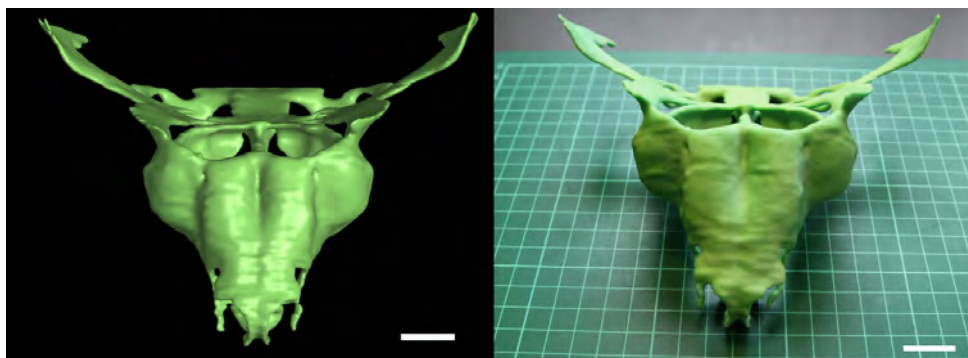


**Figure 7.** Comparison of the STL model (left) with the 50:1 upscaled model from 3D print (right). The scale bar is 0.4 mm (left) and 2 cm (right).



**Figure 8.** Comparison of the object from 3D print with human hand.

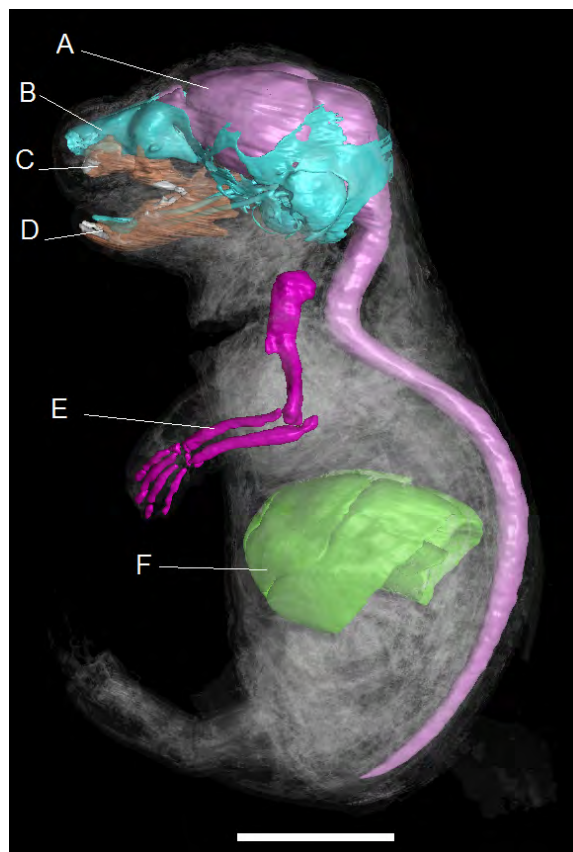


**Figure 9.** Segmented parts of 17.5 days old mouse embryo by using  $\mu$ CT. A — brain with spinal cord; B — cranium; C — upper jaw; D — lower jaw; E — upper limb; F — liver. The length of the scale bar is 4 mm.

MS) we recently confirmed the causative role of absorbable suture material in the pathogenesis of hollow channel structures in some canine compound uroliths [17]. The straightforward combination of  $\mu$ CT with 3D printing is however more common in medical practice [18–20]. In [18] the medical uses of 3D printing are reviewed, with the main emphasis on surgical training, special surgical planning and prosthetics applications. The overview of the main requirements for medical imaging affected needs of additive manufacturing (AM) formerly known as rapid prototyping is reviewed in [19]. It is shown that successful clinical cases of AM rely heavily in multi-disciplinary approach, i.e. on efficient collaboration between various disciplines, as operating surgeons, radiologists and engineers. The review also intends to narrow the potential communication gap between radiologists and engineers who work with projects involving AM by showcasing the overlap between the two disciplines. The possibilities to apply 3D printers in veterinary medicine are explored and illustrated in review [20]. It is stated that the increased use of this technology in human medicine together with the decreasing cost are making 3D printing more affordable also for veterinary use.

Combining the  $\mu$ CT imaging, and 3D printing with tissue staining, the possibilities of reverse engineering are very broad. Here we created the real 3D cartilage model of the 15.5 days old mouse embryo to show that these techniques are suitable for demonstrating the complexity of biological structures (figure 9).

Using 3D printers, the physical exploration is extending observation of the samples by viewing from all sides, sensing surface roughness and wall thickness. Simple visualization of images on a computer does not allow all of these qualities for research, demonstrations and educational purposes.

Definitely, it is not easy to orient in such sophisticated geometry using only imagination even empowered by visualizing software. Researchers also may focus on developmental shape transformations of spine, limbs etc. The inner ear with its complex structure could be another part of the cartilaginous tissue suitable for such reverse engineering.

With sufficient resolution allowing the segmentation, one  $\mu$ CT scan lasts about 2 hours. The relatively short scanning time gives an opportunity for creating entire real anatomical atlases or databases allowing researchers to browse in different structures, mutants etc. In addition, after one scan, objects can be printed in different scales or colors, which can also be used for educational purposes [18]. 3D print is a rapidly evolving technology and several methods exist like STL, digital light processing (DLP), laser sintering and laser melting, extrusion of thermoplastic material etc. Using this technology it is affordable to make such a collection.

$\mu$ CT also enables to display another soft tissues — liver, heart, gray matter i.e. brain and spinal cord (figure 7).  $\mu$ CT so can complete other techniques that can image 3D structures (e.g. MRI, optical projection tomography [18] or high resolution episcopic microscopy). Using the specific advantages of each of these methods a complex and sophisticated 3D structure can be visualized and subsequently printed on 3D printers.

## 5 Conclusions

Here we have demonstrated the comprehensive process of the reverse engineering of mouse embryo nasal capsule. For this feasibility study a 15.5 days old mouse embryo was chosen as a representative sample that was contrasted by phosphotungstic acid. It was shown that the combination of micro computed-tomography with 3D printing brings new possibilities for exploring and understanding the processes in craniofacial development. Combination of these two methods can be also useful for various studies in developmental, comparative and quantitative biology.

## Acknowledgments

This work is an output of cooperation between CEITEC — Central European Institute of Technology (CZ.1.05/1.1.00/02.0068) and NETME Centre, regional R&D centre built with the financial support from the Operational Programme Research and Development for Innovations within the project NETME Centre (New Technologies for Mechanical Engineering), Reg. No. CZ.1.05/2.1.00/01.0002 and, in the follow-up sustainability stage, supported through NETME CENTRE PLUS (LO1202) by financial means from the Ministry of Education, Youth and Sports under the National Sustainability Programme I. JJ acknowledge the support by FNUSA-ICRC Project (No. CZ.1.05/1.1.00/02.0123) from the European Regional Development Fund. JK acknowledge the support of Brno University of Technology on the frame of grant FSI-S-14-2494 (Application of Advanced Optical Methods). MK was supported by EMBO long-term fellowship.

## References

- [1] B. Hallgrímsson, D.E. Lieberman, W. Liu, A.F. Ford-Hutchinson and F.R. Jirik, *Epigenetic interactions and the structure of phenotypic variation in the cranium*, *Evol. Dev.* **9** (2007) 76.
- [2] T.E. Parsons et al., *Phenotypic variability and craniofacial dysmorphology: increased shape variance in a mouse model for cleft lip*, *J. Anat.* **212** (2008) 135.
- [3] K. Degenhardt, A.C. Wright, D. Horng, A. Padmanabhan and J.A. Epstein, *Rapid 3D phenotyping of cardiovascular development in mouse embryos by micro-CT with iodine staining*, *Circ. Cardiovasc. Imaging* **3** (2010) 314.
- [4] W.J. Weninger et al., *High-resolution episcopic microscopy: a rapid technic for high detailed 3D analysis of gene activity in the context of tissue architecture and morphology*, *Anat. Embryol.* **211** (2006) 213.
- [5] F.C. Norris et al., *A coming of age: advanced imaging technologies for characterising the developing mouse*, *Trends Genet.* **29** (2013) 700.
- [6] J. Kerwin et al., *3 dimensional modelling of early human brain development using optical projection tomography*, *BMC Neurosci.* **5** (2004) 27.
- [7] S.W. Ruffins et al., *Digital three-dimensional atlas of quail development using high-resolution MRI*, *Sci. W. J.* **7** (2007) 592.
- [8] W.A. Kalender, *Computed tomography: fundamentals, system technology, image, quality, applications*, 3<sup>rd</sup> edition, Wiley (2005).
- [9] J. Kaiser et al., *Investigation of the microstructure and mineralogical composition of urinary calculi fragments by synchrotron radiation X-ray microtomography: a feasibility study*, *Urol. Res.* **39** (2011) 259.
- [10] E. Ettl et al., *X-ray phase-contrast tomography with a compact laser-driven synchrotron source*, *Proc. Natl. Acad. Sci. USA* **112** (2015) 5567.
- [11] B.D. Metscher, *Micro-CT for comparative morphology: simple staining methods allow high contrast 3D imaging of diverse non-mineralized animal tissues*, *BMC Phys.* **9** (2009) 11.
- [12] V.S. Constantine and R.W. Mowry, *Selective staining of human dermal collagen*, *J. Inv. Derm.* **50** (1968) 419.
- [13] T. Nemetschek, H. Riedl and R. Jonak, *Topochemistry of the binding of phosphotungstic acid to collagen*, *J. Mol. Biol.* **133** (1979) 67.
- [14] R.N. Rao, P.M. Fallman, D. Greer Falls and S.N. Meloan, *A comparative study of PAS-phosphotungstic acid-Diamine Supra Blue FGL and immunological reactions for type I collagen*, *Histochemistry* **91** (1989) 283.
- [15] B.D. Metscher, *MicroCT for developmental biology: a versatile tool for high-contrast 3D imaging at histological resolutions*, *Dev. Dynam.* **238** (2009) 632.
- [16] H.G. Elmendorf and A.G. Rosenwald, *Biology of global health: preparing students for multi-disciplinary group work*, in *Proceedings of the 2014 ASCB/IFCB Meeting*, Philadelphia U.S.A., 6–10 Dec 2014.
- [17] J. Kaiser et al., *Determination of the cause of selected canine urolith formation by advanced analytical methods*, *J. Small Anim. Pract.* **53** (2012) 646.

- [18] F. Rengier et al., *3D printing based on imaging data: review of medical applications*, *Int. J. Comput. Assist. Radiol. Surg.* **5** (2010) 335.
- [19] E. Huotilainen et al., *Imaging requirements for medical applications of additive manufacturing*, *Acta Radiol.* **55** (2014) 78.
- [20] A.M. Hespel, R. Wilhite and J. Hudson, *Applications for 3D printers in veterinary medicine*, *Vet. Radiol. Ultrasoun.* **55** (2014) 347.

2016 JINST 11 C03006

PAPER [VII]

OPEN

# An interactive and intuitive visualisation method for X-ray computed tomography data of biological samples in 3D Portable Document Format

Markéta Tesařová<sup>1</sup>, Eglantine Heude<sup>2,3,4</sup>, Glenda Comai<sup>3,4</sup>, Tomáš Zikmund<sup>1</sup>, Markéta Kaucká<sup>5,6</sup>, Igor Adameyko<sup>5,6</sup>, Shahragim Tajbakhsh<sup>3,4</sup> & Jozef Kaiser<sup>1\*</sup>

3D imaging approaches based on X-ray microcomputed tomography (microCT) have become increasingly accessible with advancements in methods, instruments and expertise. The synergy of material and life sciences has impacted biomedical research by proposing new tools for investigation. However, data sharing remains challenging as microCT files are usually in the range of gigabytes and require specific and expensive software for rendering and interpretation. Here, we provide an advanced method for visualisation and interpretation of microCT data with small file formats, readable on all operating systems, using freely available Portable Document Format (PDF) software. Our method is based on the conversion of volumetric data into interactive 3D PDF, allowing rotation, movement, magnification and setting modifications of objects, thus providing an intuitive approach to analyse structures in a 3D context. We describe the complete pipeline from data acquisition, data processing and compression, to 3D PDF formatting on an example of craniofacial anatomical morphology in the mouse embryo. Our procedure is widely applicable in biological research and can be used as a framework to analyse volumetric data from any research field relying on 3D rendering and CT-biomedical imaging.

One of the formidable phenomena in developmental biology is how the shape diversity observed among living organisms is defined and controlled during development and growth. Embryonic patterning is a highly dynamic process implicating multiple molecular mechanisms and cell interactions at the basis of organ formation. In the human embryo, defects in such cellular processes can affect the developmental program leading to congenital disorders. Congenital defects have an incidence of 3% in the human population<sup>1</sup> and they are causal for up to one-quarter of all reported neonatal deaths<sup>2</sup>. Thus, contextual visualisation of embryonic development is critical to elucidate the origins of malformations.

Multi-disciplinary collectives composed of clinical doctors, biologists, engineers and imaging experts are currently pushing forward the understanding of biological questions using three dimensional (3D) approaches. While the analysis of histological sections remains a mainstay in developmental biology, the reconstruction of 3D volumes from 2D slices has provided important information to understand morphogenesis in mouse and human embryos<sup>3-6</sup>. Non-destructive technologies such as 3D imaging by confocal microscopy and light sheet methods<sup>7-9</sup>, optical projection tomography (OPT)<sup>10-12</sup> and micro-computed tomography (microCT)<sup>13-16</sup> constitute emerging powerful methods to analyse the topography of developing structures in 3D context, to gain insight into the pathogenesis of congenital disorders. However, one major challenge of 3D approaches is sharing of complex datasets effectively and intuitively between colleagues from different fields for discussion, and ultimately

<sup>1</sup>Central European Institute of Technology, Brno University of Technology, Brno, Czech Republic. <sup>2</sup>Department Adaptation du Vivant, Museum national d'Histoire naturelle, CNRS UMR 7221, Paris, France. <sup>3</sup>Department of Developmental and Stem Cell Biology, Stem Cells and Development Unit, Institut Pasteur, Paris, France. <sup>4</sup>CNRS UMR, 3738, Paris, France. <sup>5</sup>Department of Physiology and Pharmacology, Karolinska Institutet, Solna, Sweden. <sup>6</sup>Department of Molecular Neurosciences, Medical University of Vienna, Vienna, Austria. \*email: [kaiser@fme.vutbr.cz](mailto:kaiser@fme.vutbr.cz)

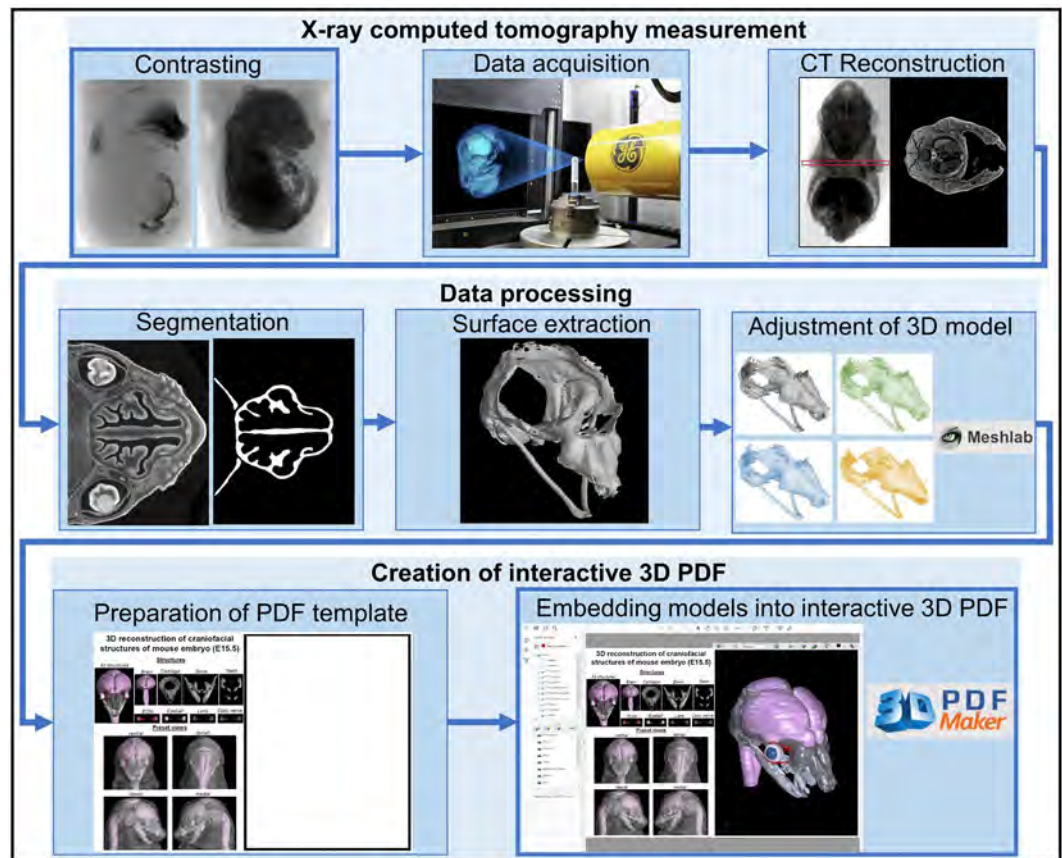


**Figure 1.** Overview of the method pipeline described in this study.

presenting them in a publication format. Generally, 3D datasets need special software for visualisation or are reduced to 2D pictures in which important information might be lost.

The study of the developing head constitutes a good example of the need for 3D approaches given its complex anatomy. The craniofacial region is built of diverse embryonic cell types giving rise to hard and soft tissues including skeletal, muscular and nervous components<sup>17</sup>. The final shape of the face strongly depends on the geometry of the skeletal elements and their interaction with adjacent soft tissues such as muscles and the nervous system<sup>15,16</sup>. Numerous congenital craniofacial abnormalities affect the form and function of the face and explanations of these malformations still await the fundamental understanding of the underlying failure of morphogenesis<sup>18</sup>. The microCT approach followed by 3D reconstruction has enabled high-quality information of the complex morphological aspects of head and face development<sup>15,16</sup>.

To facilitate assimilation and visualisation of microCT datasets, interactive 3D Portable Document Format (PDF) has been used in different field including in developmental biology<sup>6,19,20</sup>, in human physiology and anatomy<sup>4,21–23</sup>, in entomology<sup>24</sup> and marine biology<sup>25,26</sup>. However, a major limitation of previously published methods is the requirement of advanced programming skills and/or installation of further prepaid software packages<sup>21</sup>. Most of these approaches depend on the use of Adobe Acrobat Pro Extended software<sup>4,6,19,23–28</sup> or JavaScript programming language<sup>20,27</sup>.

Here, we provide an alternative, user-friendly way to create interactive 3D PDF files from microCT datasets taking the complexity of mouse craniofacial anatomy as a model example. Our innovative and efficient pipeline comprises microCT data acquisition, segmentation and final establishment of a 3D PDF using a combination of free and pre-paid software. The resulting file can be viewed with standard PDF viewers and offers an interactive interface for microCT data sharing, analysis and presentation.

### Pipeline for the Creation of Interactive 3D PDF

To create an interactive 3D PDF from microCT data, the critical steps are: (i) chemical contrasting of biological samples if soft tissues are to be visualized, (ii) data acquisition and (iii) CT virtual reconstruction (Fig. 1). This is followed by data processing, the most critical step consisting of segmentation, surface extraction, adjustment of segmented 3D models, and conversion into a final interactive PDF file. Here, we provide a detailed description of each step of the pipeline (see also Supplementary Material 1).

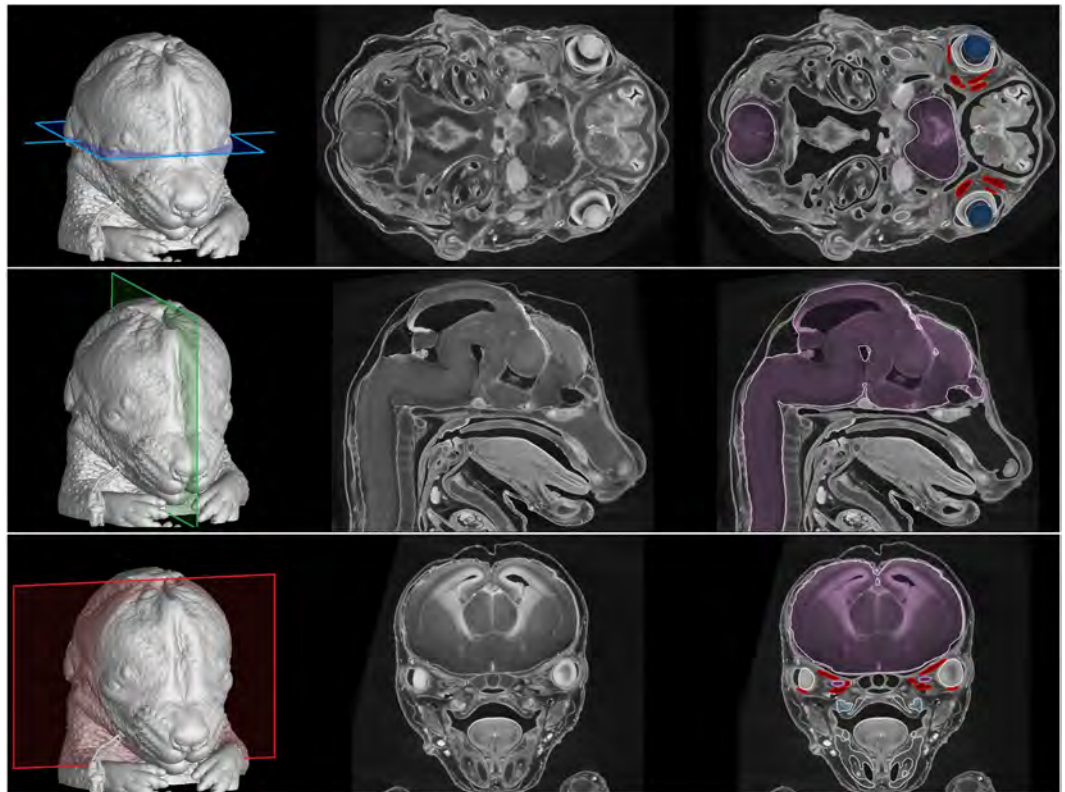


**Figure 2.** Tomographic measurements and segmentation of craniofacial structures in a mouse embryo 15 days post-fertilisation. Colour planes on 3D models (left panels) indicate the position of the raw tomographic slices (middle panels) and some segmented structures (right panels) including the central nervous system (purple), the lens (dark blue), the dental placodes (light blue) and extraocular muscles (red).

### X-Ray Microtomography Measurement

MicroCT is an established technology for imaging mineralized tissues in animal specimens. However, its use in comparative morphology has been limited by the low intrinsic X-ray contrast of non-mineralised soft tissues. To overcome this problem, methods have been developed to increase tissue contrast, including chemical treatment with contrasting agents<sup>29,30</sup>, phase-contrast imaging<sup>31–36</sup> or dual-energy computed tomography (DECT)<sup>37</sup>.

Chemical contrasting treatments have mostly been applied for the characterization of musculoskeletal tissues on small fixed samples. For *in vivo* CT imaging including clinical diagnoses, non-toxic iodine-based contrast agents (e.g. iohexol or hexabrix) are used for the analysis of the cardiovascular system and cavities, but not for direct analysis of muscle tissues<sup>38,39</sup>. Clinical CT imaging of the musculoskeletal system is commonly performed without a contrasting agent, thereby limiting the analysis to discrete soft organs<sup>40</sup>. Therefore, on small fixed samples, multiple contrasting protocols have been used, each with its own advantages and limitations<sup>41,42</sup>. The stainings based on iodine, osmium or the toxic phosphotungstic acid (PTA) are the most commonly used<sup>29,30</sup>. For the pipeline proposed here on the study of craniofacial mouse development, we propose the use of PTA contrasting treatment that permits high contrast imaging of a wide variety of soft and mineralised tissues composing the mouse head (Fig. 2). However, microCT data obtained with other contrasting agents or in their absence, such as clinical data or data from non-biological specimens, will be equally amenable for the subsequent steps of the 3D PDF pipeline.

### Data Processing

Following the acquisition of high-contrast tomographic slices, the segmentation of complex craniofacial structures constitutes a major challenge. Fully-automatic approaches have been tried and were generally unsuccessful<sup>43</sup>. Thus, the manual approach is usually the only method available to achieve precise and accurate segmentations<sup>44</sup>. However, some semi-automatic methods such as local segmentation or interpolation between manually segmented slices can be used<sup>45,46</sup>. For verification of the accuracy of manually segmented structures, Fig. 2 shows both original and segmented tomographic slices. This approach permitted the segmentation of soft tissues such as eyeballs, extraocular muscles and the central nervous system, as well as of hard tissues including the chondrocranium, bones and future teeth (dental placodes) (Fig. 3).

For 3D volume rendering, it is then more convenient to use 3D mesh formats rather than a stack of 2D images. 3D mesh formats represent a series of 2D polygons (typically triangles or quadrangles) linked together to recreate the surface of a 3D object<sup>28</sup>. It encodes the 3D model's geometry, colours, textures, etc. For further work, the segmented masks need to be transferred to the meshes. Most software can transfer the mask into a wide range of

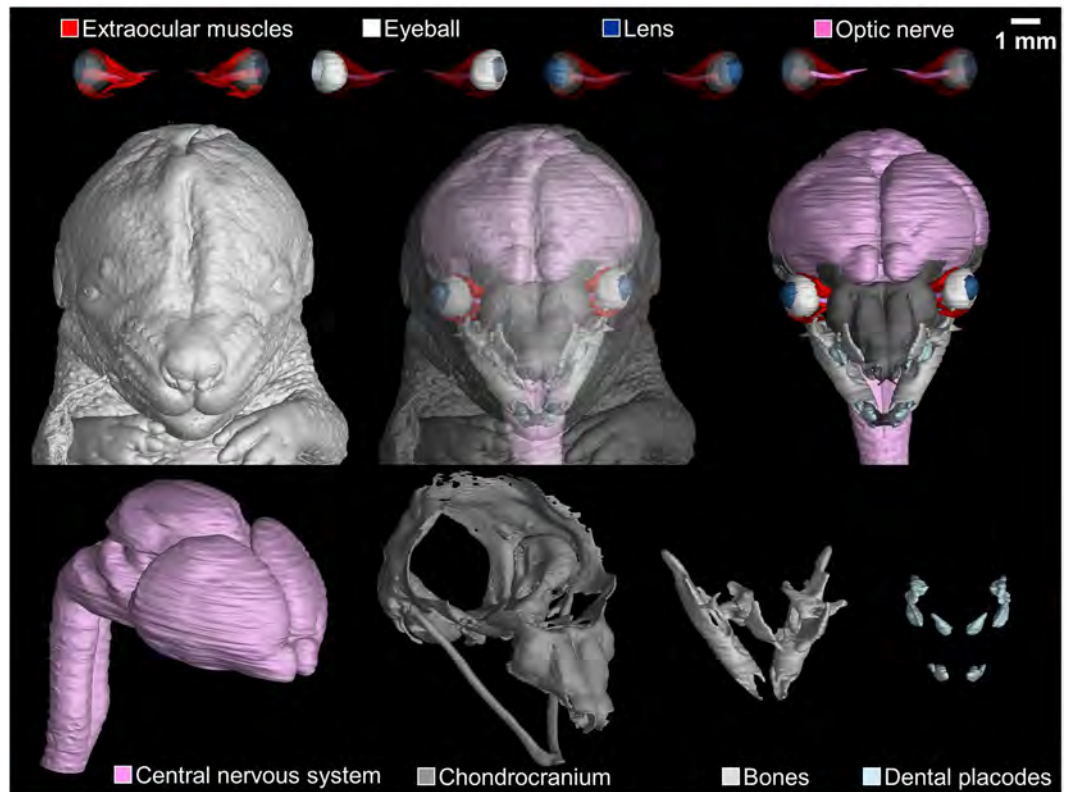


**Figure 3.** Surface rendering of segmented structures in a mouse embryo 15 days post-fertilisation. Structures of interest are colour-coded.

equivalent formats. However, only some of the formats contain information about the colour (e.g. OBJ, VRML and STEP) which is important for the visualisation of several structures in one model. Other formats represent only the mesh (e.g. STL and Matlab m-file).

Another problem to be solved is the size of the model (i.e. the number of faces in the mesh). When transferring the segmented mask into the mesh, an unnecessarily large number of faces can be created. Comparison of a different number of faces and corresponding size can be found in Fig. 4. Surprisingly, reducing by four times the number of faces does not significantly compromise details in the 3D models. Simple shapes such as the eyeball do not show notable errors besides the slight deformation of the sphere. However, further simplification of complex shapes, such as the chondrocranium and extraocular muscles (EOM), reduces the model quality and some details are lost (Fig. 4, red arrows). Thus, depending on the structures analysed and the resolution needed, different face reductions should be tested and validated before further analysis. Therefore, the compression of the data should be customised according to the complexity of the model and the resolution of tomographic slices.

Among the 3D printing software, some free software enable colour modifications or mesh simplification. Here, we made use of the Meshlab<sup>47</sup> and Blender<sup>48</sup> packages for this purpose. Notably, the latter allows unifying different sub-models into one mesh preserving the individuality of each object (see Supplementary Material 1 for more details).

### Creation of an Interactive 3D PDF

Once the models are colour-labelled and simplified, they are then converted into an interactive file. We exploited 3D PDF Maker Standalone<sup>49</sup> taking advantage of the pre-prepared model that provides an interactive window in the PDF file by clicking on Add 3D button. Before embedding the model into an interactive file, the user can prepare an ordinary PDF file using standard software (e.g. Microsoft Office, Apache OpenOffice etc.). This file is used as a template showing, for example, individual structures or predefined views. These areas (i.e. images or signs) are taken into life in 3D PDF Maker by assigning whatever area in the page to specific view/structure (see for more details Supplementary Materials 1 and 2).

The model document presented here (Supplementary Material 3) consists of four predefined views (ventral, dorsal, lateral and medial) and a possibility of showing individual craniofacial structures (brain, cartilage, bone and teeth). It helps to manipulate the 3D model and can be set according to the areas/views of interest that are important to show. For example, for better visualisation, some structures can be set to the semi-transparent mode, or structures can be switched on/off individually in the model tree. The interactive 3D PDF also allows the user to rotate, turn and pan the model, change the pre-defined 3D-rendering, change the lights and background colour or add a virtual cross-section on the model.

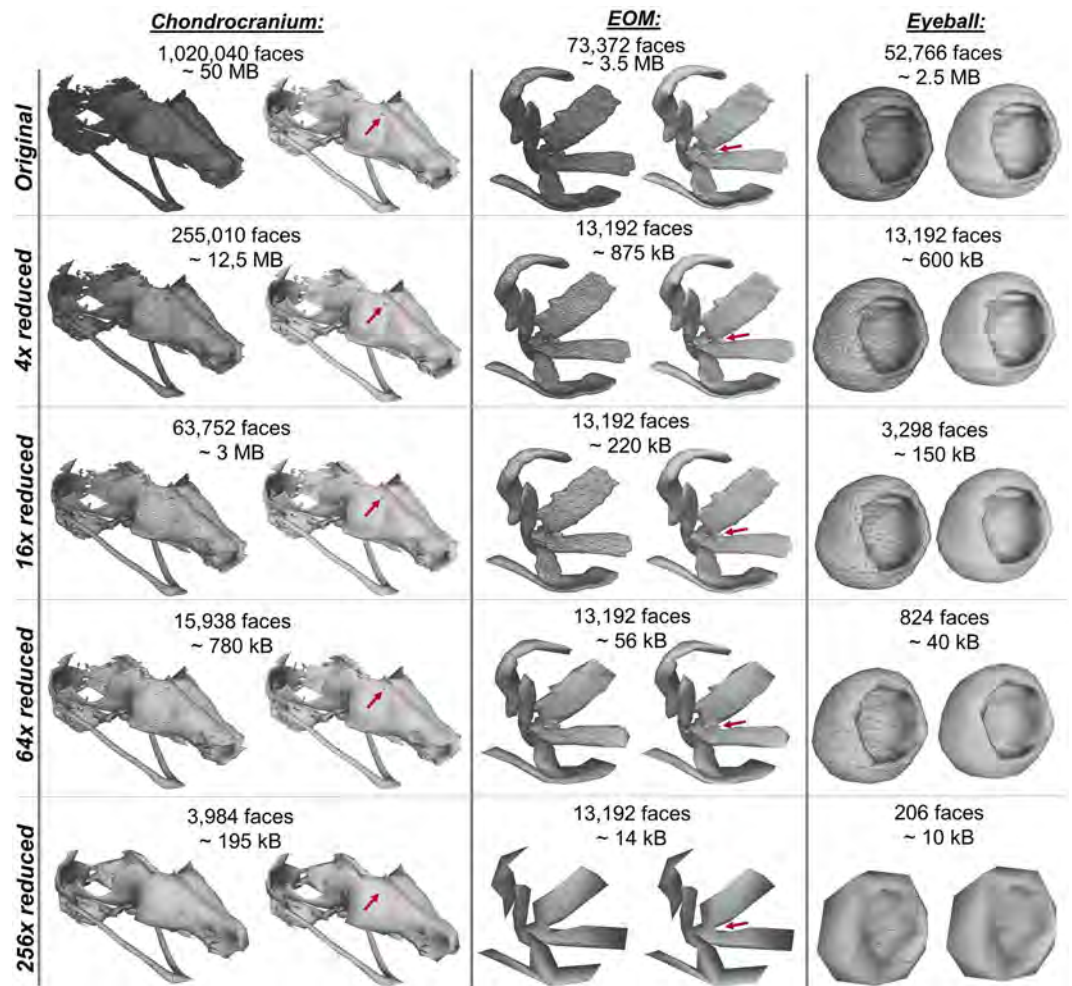


**Figure 4.** The number of faces affects the detection of details in chondrocranium, extraocular muscles (EOM) and eyeball models. Red arrows indicate details in the 3D model that disappear with model simplification.

## Discussion and Conclusion

Comparative morphological studies in the field of developmental biology have been challenging, but contrast-enhanced X-ray computed tomography has brought new possibilities of high-resolution 3D visualisation<sup>15,16,50</sup>. In this study, we present a detailed, user-friendly protocol for the surface rendering of craniofacial structures including soft tissues (muscles, eyeballs, central nervous system) as well as of hard tissues (cartilages, bones and teeth), with a step-by-step procedure from sample collection to the creation of an interactive 3D PDF. The final PDF is readable on all operating systems with the free standard AdobeReader®/AcrobatReaderDC (Adobe Inc., California USA).

Our 3D reconstruction methodology has already shown its utility and strength for visualisation and phenotypic analysis of complex structures such as the neck musculoskeletal system<sup>50</sup> and nasal capsules of control and mutant mouse embryos<sup>16</sup>. Therefore, a user-friendly method for creating such files will be of great utility for biologists. In addition, our procedure can be used as a framework to analyse volumetric data for any field of research that relies on 3D rendering, e.g. for visualisation of volumetric information of geological samples by laser-induced breakdown spectroscopy<sup>51</sup>.

The use of interactive 3D PDF files has a great potential for data sharing, communication and publications<sup>21</sup>, but is still sparsely used. We believe that our work will inspire researchers working with 3D imaging to present their data in such a user-friendly format.

## Methods

**Use of experimental animals.** All animal work was approved and permitted by the Local Ethical Committee on Animal Experiments (North Stockholm Animal Ethics Committee) and conducted according to The Swedish Animal Agency's Provisions and Guidelines for Animal Experimentation recommendations. Mice were sacrificed with isoflurane (Baxter KDG9623) overdose or cervical dislocation, and embryos were collected into ice-cold PBS. Subsequently, tissue samples were fixed into freshly prepared 4% paraformaldehyde (PFA) in PBS solution for 24 hours at +4°C with slow rotation and washed in PBS.

**Tissue contrasting.** Staining protocol has been adapted and modified from the original protocol developed by Brian Metscher laboratory<sup>33,34</sup>. After fixation, the samples were dehydrated in increasing concentration of ethanol series (30%, 50%, 70%, 90%), one day in each concentration to minimise the shrinkage of tissues. For tissue contrasting, samples were then transferred into 1% PTA (phosphotungstic acid) in 90% methanol for three weeks. The PTA-methanol solution was changed every two days. Subsequently, the samples were rehydrated by ethanol series (90%, 70%, 50% and 30%) and shipped to the CT-laboratory for scanning.

**X-ray microCT measurements.** After fixation and contrasting treatments, samples were fully rehydrated in distilled water, embedded in 1.0% agarose gel and placed in a polypropylene tube to avoid movement artefacts during tomography scanning. The polypropylene tube was fixed on a plastic rod by a silicone gun. The rod was put in the centre of the rotation stage axis. The microCT scanning was performed using the laboratory system GE Phoenix v|tome|x L 240 (GE Sensing & Inspection Technologies GmbH, Germany) with a 180 kV/15 W maximum power nanofocus X-ray tube and flat panel dynamic 41|100 with 4000 × 4000 px and a pixel size of 100 × 100 μm. The exposure time was 600 ms in each of the 2200 projections acquired over a total angle of 360°. Three projections were acquired and averaged in every position to reduce the noise in the tomographic data. Thus, the scanning time was 73 minutes. The acceleration voltage and current of the X-ray tube were 60 kV and 200 μA, respectively. The beam was filtered by a 0.2 mm-thick aluminium filter. The linear voxel resolution of the measurement was set to 4.2 μm in all dimensions. The tomographic reconstruction was conducted using the software GE phoenix datos|x 2.0 (GE Sensing & Inspection Technologies GmbH, Germany).

**Data processing and analysis.** Segmentation of craniofacial structures was performed semi-manually in Avizo (Thermo Fisher Scientific, USA). We used some automatic tools using a region growing method and thresholding on 2D slices. Segmentations were done on one of three to five slices, and the mask was interpolated. Subsequently, the segmented models were smoothed in VG Studio MAX 3.2 (Volume Graphics GmbH, Germany) according to<sup>45</sup>. The segmented mask was then exported into a mesh (\*.OBJ format) and was colour-labelled and adjusted in Meshlab<sup>47</sup> and Blender software<sup>48</sup>. The colour-coded models were transferred into a pre-prepared PDF file in 3D PDF Maker Standalone<sup>49</sup>. The detailed manual can be found in Supplementary Material 1. The use of the interactive 3D PDF is available in Supplementary Material 2.

### Data availability

The datasets generated during and/or analysed during the current study are available from the corresponding author on reasonable request.

Received: 20 May 2019; Accepted: 25 September 2019;

Published online: 17 October 2019

### References

- World Health Organization. Congenital anomalies, Fact sheet No. 370. <https://www.who.int/news-room/fact-sheets/detail/congenital-anomalies> (2016).
- World Health Organization. Birth defects: report by the Secretariat, Executive board 125th session EB125/7. <http://www.who.int/iris/handle/10665/2271> (2009).
- Weninger, W. *et al.* High-resolution episcopic microscopy: a rapid technique for high detailed 3D analysis of gene activity in the context of tissue architecture and morphology. *Anat Embryol* **211**, 213–221, <https://doi.org/10.1007/s00429-005-0073-x> (2006).
- De Bakker, B. *et al.* An interactive three-dimensional digital atlas and quantitative database of human development. *Science* **354**, 1019–1028, <https://doi.org/10.1126/science.aag0053> (2016).
- De Bakker, B., De Jong, K., Hagoort, J., Oostra, R. & Moorman, A. Towards a 3-dimensional atlas of the developing human embryo: The Amsterdam experience. *Reproductive Toxicol* **34**, 225–236, <https://doi.org/10.1016/j.reprotox.2012.05.087> (2012).
- De Boer, B., Van den Berg, G., De Boer, P., Moorman, A. & Ruijter, J. Growth of the developing mouse heart: An interactive qualitative and quantitative 3D atlas. *Dev Biol* **368**, 203–213, <https://doi.org/10.1016/j.ydbio.2012.05.001> (2012).
- Belle, M. *et al.* Tridimensional Visualization and Analysis of Early Human Development. *Cell* **169**, 161–173, <https://doi.org/10.1016/j.cell.2017.03.008> (2017).
- Renier, N. *et al.* iDISCO: A Simple, Rapid Method to Immunolabel Large Tissue Samples for Volume Imaging. *Cell* **159**, 896–910, <https://doi.org/10.1016/j.cell.2014.10.010> (2014).
- Ragazzi *et al.* G. Fluorescence confocal microscopy for pathologists. *Mod Pathol* **27**, 460–471, <https://doi.org/10.1038/modpathol.2013.158> (2014).
- Dickinson, M. *et al.* High-throughput discovery of novel developmental phenotypes. *Nature* **537**, 508–514, <https://doi.org/10.1038/nature19356> (2016).
- Sharpe, J. Optical Projection Tomography as a Tool for 3D Microscopy and Gene Expression Studies. *Science* **296**, 541–545, <https://doi.org/10.1126/science.1068206> (2002).
- Sharpe, J. Optical projection tomography as a new tool for studying embryo anatomy. *J Anat* **202**, 175–181, <https://doi.org/10.1046/j.1469-7580.2003.00155.x> (2003).
- Wong, M., Dorr, A., Walls, J., Lerch, J. & Henkelman, R. A novel 3D mouse embryo atlas based on micro-CT. *Dev* **139**, 3248–3256, <https://doi.org/10.1242/dev.082016> (2012).
- Hsu, C. *et al.* Three-dimensional microCT imaging of mouse development from early post-implantation to early postnatal stages. *Dev Biol* **419**, 229–236, <https://doi.org/10.1016/j.ydbio.2016.09.011> (2016).
- Kaucka, M. *et al.* Oriented clonal cell dynamics enables accurate growth and shaping of vertebrate cartilage. *elife* **6**, e25902, <https://doi.org/10.7554/eLife.25902> (2017).
- Kaucka, M. *et al.* Signals from the brain and olfactory epithelium control shaping of the mammalian nasal capsule cartilage. *eLife* **7**, e34465, <https://doi.org/10.7554/eLife.34465> (2018).
- Noden, D. & Trainor, P. Relations and interactions between cranial mesoderm and neural crest populations. *J Anat* **207**, 575–601, <https://doi.org/10.1111/j.1469-7580.2005.00473.x> (2005).
- Buchanan, E., Xue, A. & Hollier, L. Craniofacial Syndromes. *Plast Reconstr Surg* **134**, 128e–153e, <https://doi.org/10.1097/PRS.0000000000000308> (2014).

19. De Boer, B. *et al.* The interactive presentation of 3D information obtained from reconstructed datasets and 3D placement of single histological sections with the 3D portable document format. *Dev* **138**, 159–167, <https://doi.org/10.1242/dev.051086> (2010).
20. De Laurier, A. *et al.* The Mouse Limb Anatomy Atlas: An interactive 3D tool for studying embryonic limb patterning. *BMC Dev Biol* **8**, 1–7, <https://doi.org/10.1186/1471-213x-8-83> (2008).
21. Neue, A. & Becker, L. Three-Dimensional Portable Document Format (3D PDF) in Clinical Communication and Biomedical Sciences: Systematic Review of Applications, Tools, and Protocols. *JMIR Med Inform* **6**, e10295, <https://doi.org/10.2196/10295> (2018).
22. Danz, J. & Katsaros, C. Three-dimensional portable document format: A simple way to present 3-dimensional data in an electronic publication. *Am J Orthod Dentofac Orthop* **140**, 274–276, <https://doi.org/10.1016/j.ajodo.2011.04.010> (2011).
23. Valera-Melé, M. *et al.* A Novel and Freely Available Interactive 3d Model of the Internal Carotid Artery. *J Med Syst* **42**, 6, <https://doi.org/10.1007/s10916-018-0919-4> (2018).
24. Van de Kamp, T. *et al.* Three-Dimensional Reconstructions Come to Life – Interactive 3D PDF Animations in Functional Morphology. *PLoS ONE* **9**, e102355, <https://doi.org/10.1371/journal.pone.0102355> (2014).
25. Ruthensteiner, B. & Heß, M. Embedding 3D models of biological specimens in PDF publications. *Microsc Res Techn* **71**, 778–786, <https://doi.org/10.1002/jemt.20618> (2008).
26. Ruthensteiner, B., Baeumlner, N. & Barnes, D. Interactive 3D volume rendering in biomedical publications. *Micron* **41**, 886.e1–886.e17, <https://doi.org/10.1016/j.micron.2010.03.010> (2010).
27. Menn, J. & Seliger, G. Increasing Knowledge and Skills for Assembly Processes through Interactive 3D-PDFs. *Procedia CIRP* **48**, 454–459, <https://doi.org/10.1016/j.procir.2016.02.093> (2016).
28. Semple, T., Peakall, R. & Tatarinic, N. A comprehensive and user-friendly framework for 3D-data visualisation in invertebrates and other organisms. *J Morphol* **280**, 223–231, <https://doi.org/10.1002/jmor.20938> (2019).
29. Metscher, B. D. MicroCT for comparative morphology: simple staining methods allow high-contrast 3D imaging of diverse non-mineralized animal tissues. *BMC Physiol* **9**, 11, <https://doi.org/10.1186/1472-6793-9-11> (2009).
30. Metscher, B. D. MicroCT for developmental biology: A versatile tool for high-contrast 3D imaging at histological resolutions. *Dev Dyn* **238**, 632–640, <https://doi.org/10.1002/dvdy.21857> (2009).
31. Wilkins, S., Gureyev, T., Gao, D., Pogany, A. & Stevenson, A. Phase-contrast imaging using polychromatic hard X-rays. *Nature* **384**, 335–338, <https://doi.org/10.1038/384335a0> (1996).
32. Baran, P. *et al.* High-Resolution X-Ray Phase-Contrast 3-D Imaging of Breast Tissue Specimens as a Possible Adjunct to Histopathology. *IEEE Trans Med Imaging* **37**, 2642–2650, <https://doi.org/10.1109/TMI.2018.2845905> (2018).
33. Wagner, W. *et al.* Towards synchrotron phase-contrast lung imaging in patients – a proof-of-concept study on porcine lungs in a human-scale chest phantom. *J Synchrotron Rad* **25**, 1827–1832, <https://doi.org/10.1107/S1600577518013401> (2018).
34. Momose, A., Takeda, T., Itaj, Y. & Hirano, K. Phase-contrast X-ray computed tomography for observing biological soft tissues. *Nat. Med.* **2** (1996).
35. Saccomano, M. *et al.* Synchrotron inline phase contrast  $\mu$ CT enables detailed virtual histology of embedded soft-tissue samples with and without staining. *J Synchrotron Radiat* **25**, <https://doi.org/10.1107/S1600577518005489> (2018).
36. Larsson, D. H., Vågberg, W., Yaroshenko, A., Yildirim, A. Ö. & Hertz, H. M. High-resolution short-exposure small-animal laboratory x-ray phase-contrast tomography. *Sci. Rep.* **6**, <https://doi.org/10.1038/srep39074> (2016).
37. Yang, M. *et al.* Theoretical variance analysis of single- and dual-energy computed tomography methods for calculating proton stopping power ratios of biological tissues. *Phys Med Biol* **55**, 1343–1362, <https://doi.org/10.1088/0031-9155/55/5/006> (2010).
38. Yan, D., Zhang, Z., Luo, Q., Yang, X. & Chen, C. A Novel Mouse Segmentation Method Based on Dynamic Contrast Enhanced Micro-CT Images. *PLoS ONE* **12**, <https://doi.org/10.1371/journal.pone.0169424> (2017).
39. Lusic, H. & Grinstaff, M. W. X-Ray Computed Tomography Contrast Agents. *Chem Rev* **3**, 113, <https://doi.org/10.1021/cr200358s> (2013).
40. Heude, E., Rivals, I., Couly, G. & Levi, G. Masticatory muscle defects in hemifacial microsomia: A new embryological concept. *Am J Med Genet Part A* **155**, 1991–1995, <https://doi.org/10.1002/ajmg.a.34095> (2011).
41. de Bournonville, S., Vangrunderbeeck, S. & Kerckhofs, G. Contrast-Enhanced MicroCT for Virtual 3D Anatomical Pathology of Biological Tissues: A Literature Review. *Contrast Media Mol. Imaging* **2019**, 1–9, <https://doi.org/10.1155/2019/8617406> (2019).
42. Zikmund, T. *et al.* High-contrast differentiation resolution 3D imaging of rodent brain by X-ray computed microtomography. *J Instrum* **13**, C02039–C02039, <https://doi.org/10.1088/1748-0221/13/02/C02039> (2018).
43. Weinhardt, V. *et al.* Quantitative morphometric analysis of adult teleost fish by X-ray computed tomography. *Sci Rep* **8**, 16531, <https://doi.org/10.1038/s41598-018-34848-z> (2018).
44. Boccardi, M. *et al.* Survey of Protocols for the Manual Segmentation of the Hippocampus: Preparatory Steps Towards a Joint EADC-ADNI Harmonized Protocol. *J Alzheimers Dis* **26**, 61–75, <https://doi.org/10.3233/JAD-2011-0004> (2011).
45. Tesařová, M. *et al.* Use of micro computed-tomography and 3D printing for reverse engineering of mouse embryo nasal capsule. *J Instrum* **11**, C03006–C03006, <https://doi.org/10.1088/1748-0221/11/03/C03006> (2016).
46. Tesařová, M. *et al.* A quantitative analysis of 3D-cell distribution in regenerating muscle-skeletal system with synchrotron X-ray computed microtomography. *Sci Rep* **8**, 14145, <https://doi.org/10.1038/s41598-018-32459-2> (2018).
47. Cignoni, P. *et al.* MeshLab: an Open-Source Mesh Processing Tool. <http://vcg.isti.cnr.it/Publications/2008/CCCDGR08/MeshLabEGIT.final.pdf> (2008).
48. Hess, R. *The essential Blender: guide to 3D creation with the open source suite Blender* (ed. Roosendaal, T.) (No Starch Press, 2007).
49. 3D PDF Maker [software] [www.3dpdfmaker.com](http://www.3dpdfmaker.com) (2019).
50. Heude, E. *et al.* Unique morphogenetic signatures define mammalian neck muscles and associated connective tissues. *eLife* **7**, e40179, <https://doi.org/10.7554/eLife.40179> (2018).
51. Prochazka, D. *et al.* Joint utilization of double-pulse laser-induced breakdown spectroscopy and X-ray computed tomography for volumetric information of geological samples. *J Anal Atom Spectrom* **33**, 1993–1999, <https://doi.org/10.1039/c8ja00232k> (2018).

## Acknowledgements

This research was carried out under the project CEITEC 2020 (LQ1601) with financial support from the Ministry of Education, Youth and Sports of the Czech Republic under the National Sustainability Programme II, CEITEC Nano Research Infrastructure (MEYS CR, 2016–2019) and) and Ceitec Nano+ project, CZ.02.01/0.0./0.0./16\_013/0001728 under the program OP RDE. We acknowledge support by grant AFM Telethon 21853. J.K. and M.T. acknowledge the support of the Brno University of Technology through grant FSI-S-17-4506. M.T. was financially supported by grant CEITEC VUT-J-19-5764 and by the Brno City Municipality as a Brno Ph.D. Talent Scholarship Holder.

## Author contributions

M.T., E.H. and G.C. worked on the data analysis and methodology. M.K. prepared the samples and stained them for CT measurement. M.T. and T.Z. performed CT measurements. I.A., S.T. and J.K. designed the experiments. M.T., T.Z. and J.K. wrote the manuscript. All authors reviewed the manuscript.

## Competing interests

The authors declare no competing interests.

## Additional information

**Supplementary information** is available for this paper at <https://doi.org/10.1038/s41598-019-51180-2>.

**Correspondence** and requests for materials should be addressed to J.K.

**Reprints and permissions information** is available at [www.nature.com/reprints](http://www.nature.com/reprints).

**Publisher's note** Springer Nature remains neutral with regard to jurisdictional claims in published maps and institutional affiliations.



**Open Access** This article is licensed under a Creative Commons Attribution 4.0 International License, which permits use, sharing, adaptation, distribution and reproduction in any medium or format, as long as you give appropriate credit to the original author(s) and the source, provide a link to the Creative Commons license, and indicate if changes were made. The images or other third party material in this article are included in the article's Creative Commons license, unless indicated otherwise in a credit line to the material. If material is not included in the article's Creative Commons license and your intended use is not permitted by statutory regulation or exceeds the permitted use, you will need to obtain permission directly from the copyright holder. To view a copy of this license, visit <http://creativecommons.org/licenses/by/4.0/>.

© The Author(s) 2019

PAPER [VIII]

# SCIENTIFIC REPORTS

OPEN

## A quantitative analysis of 3D-cell distribution in regenerating muscle-skeletal system with synchrotron X-ray computed microtomography

Markéta Tesařová<sup>1</sup>, Lucia Mancini<sup>2</sup>, Andras Simon<sup>3</sup>, Igor Adameyko<sup>4,5</sup>, Markéta Kaucká<sup>4,5</sup>, Ahmed Elewa<sup>3</sup>, Gabriele Lanzafame<sup>2</sup>, Yi Zhang<sup>4,6</sup>, Dominika Kalasová<sup>1</sup>, Bára Szarowská<sup>4</sup>, Tomáš Zikmund<sup>1</sup>, Marie Novotná<sup>1</sup> & Jozef Kaiser<sup>1</sup>

One of the greatest enigmas of modern biology is how the geometry of muscular and skeletal structures are created and how their development is controlled during growth and regeneration. Scaling and shaping of vertebrate muscles and skeletal elements has always been enigmatic and required an advanced technical level in order to analyse the cell distribution in 3D. In this work, synchrotron X-ray computed microtomography ( $\mu$ CT) and chemical contrasting has been exploited for a quantitative analysis of the 3D-cell distribution in tissues of a developing salamander (*Pleurodeles waltl*) limb – a key model organism for vertebrate regeneration studies. We mapped the limb muscles, their size and shape as well as the number and density of cells within the extracellular matrix of the developing cartilage. By using tomographic approach, we explored the polarity of the cells in 3D, in relation to the structure of developing joints. We found that the polarity of chondrocytes correlates with the planes in joint surfaces and also changes along the length of the cartilaginous elements. Our approach generates data for the precise computer simulations of muscle-skeletal regeneration using cell dynamics models, which is necessary for the understanding how anisotropic growth results in the precise shapes of skeletal structures.

Several experimental techniques have recently been used for the visualization of cells in three dimensions (3D). These techniques usually use electromagnetic radiation with wavelengths of visible light or X-rays (wavelength  $10^{-6}$ – $10^{-10}$  m). Mainly due to the shape and composition of the investigated samples, all imaging methods have their own advantages and limitations. The 3D biological structures, in their natural shape, may be thick and highly scattering, preventing e.g. light from penetrating them without significant distortion. Advanced light microscopy techniques can image thicker biological specimens at a high spatial resolution such as confocal microscopy, multiphoton microscopy, and optical coherence tomography<sup>1</sup>.

Confocal microscopy is considered to be one of the most convenient techniques for imaging cells in 3D. Moreover, this method has also been used specifically for the study of cell columns in the articular cartilage of rats<sup>2</sup>. Also, an *in vivo* study of the collagen matrix was performed by high-resolution fluorescence confocal microscopy<sup>3</sup>. However, *in vivo*, fluorescence imaging or the immunostaining of labelled specific cells<sup>4</sup> have high requirements for the sample preparation. Moreover, fluorescence-based techniques are used to visualize a fluorescent marker that was targeted to the structure of interest. The auto-fluorescent properties of the cells can provide sufficient contrast to allow for the identification of the desired structures<sup>1</sup>. However, they cannot be used for all types of tissues, which can limit the utilization of this technique.

Additionally, imaging techniques based on the scattering of light are not suitable for imaging larger samples, e.g. the whole limbs of vertebrates. The penetration depth of confocal microscopy is limited to less than  $100\ \mu\text{m}$ <sup>5,6</sup>.

<sup>1</sup>Central European Institute of Technology, Brno University of Technology, Brno, Czech Republic. <sup>2</sup>Elettra-Sincrotrone Trieste S.C.p.A., Basovizza, Trieste, Italy. <sup>3</sup>Department of Cellular and Molecular Biology, Karolinska Institutet, Solna, 171777, Stockholm, Sweden. <sup>4</sup>Department of Physiology and Pharmacology, Karolinska Institutet, Solna, 171777, Stockholm, Sweden. <sup>5</sup>Department of Molecular Neurosciences, Medical University Vienna, Vienna, Austria. <sup>6</sup>Department of Orthopaedics, Xiangya Hospital, Central South University, Changsha, Hunan Province, China. Correspondence and requests for materials should be addressed to J.K. (email: [kaiser@fme.vutbr.cz](mailto:kaiser@fme.vutbr.cz))

Surface imaging microscopy has been compared to confocal microscopy imaging in order to visualize larger samples, such as whole embryos<sup>7</sup>. Despite the high spatial resolution for the whole body of an embryo, the method is destructive and highly demanding in terms of sample preparation.

A deeper sample penetration for 3D imaging can be achieved by multi-photon microscopy. This technique provides deep penetration mainly because of a scattered signal of photons which results from localized nonlinear signal generation. It can allow for optical sectioning in samples on a millimeter thickness scale, depending on the tissue type<sup>8</sup>. Such a thickness is comparable with the size of the skeletal elements of some embryonic vertebrates. However, this method cannot be applied to biological samples in general. The three-dimensional resolution of a two-photon excitation microscope is identical to that achieved in an ideal confocal microscope, i.e. hundreds of nanometers<sup>9</sup>.

Optical coherence tomography is a technique, which is capable of obtaining images from even thicker tissue samples<sup>10</sup>. On the other hand, the spatial resolution is lower (of the order of 5–10  $\mu\text{m}$ )<sup>11,12</sup>, which is not sufficient for a quantitative analysis of single cell distribution in vertebrates.

A number of improvements have developed in X-ray-based methods for cellular imaging. X-rays can penetrate cells and thick tissues (from millimeter- to centimeter-sized samples) without the need for sectioning the sample and it is possible to generate quantitative 3D data with spatial resolution of up to several dozen nanometers on the selected regions of interest<sup>13–15</sup>. Soft X-ray microscopy or tomography and coherent diffractive imaging are techniques that examine even the subcellular structures. The soft X-ray microscopes usually use wavelengths in the so-called water window – the region of the spectrum between the K shell absorption edges of carbon and oxygen, which are the typical components for biological tissues. Carbon and nitrogen compounds absorb these X-rays more than water<sup>12,16</sup>. However, visualizing an entire organ or a developing limb would generate an inhibitive amount of data. The feasible approach must allow for the 3D imaging of a large field of view (millimeter scale) with the eventual possibility of zooming into areas of interest<sup>17</sup>.

X-ray computed microtomography ( $\mu\text{CT}$ ) is a non-destructive imaging method that provides high spatial resolution (from micron to sub-micron scale) of 3D data for samples with the size ranging from sub-millimeter to several millimeters. The result is a map of the X-ray attenuation coefficient within the sample volume and, if certain experimental conditions are fulfilled, then also phase changes can be detected<sup>18,19</sup>. Recent developments of this method have significantly advanced biological imaging.

In synchrotron facilities, the small angular source size, the high intensity and the nearly-parallel geometry of the X-ray beam makes it possible to obtain not only a high spatial resolution on the macroscopic samples, but also to exploit the transverse coherence properties of the X-ray beam. This allows a very simple experimental approach to be used in the propagation-based phase-contrast imaging (PCI)<sup>20,21</sup>. By using synchrotron radiation,  $\mu\text{CT}$  measurements of the different regions of the large-scale objects (centimeter range) can be imaged at high spatial resolution (on the micron scale)<sup>22–28</sup>. Furthermore, the application of PCI techniques could allow different tissues with similar chemical compositions and radioscopic density, to be distinguished<sup>29,30</sup>.

Staining with heavy elements such as iodine, tungsten or osmium-based compounds<sup>31,32</sup> also enhances the contrast within the various types of tissues using advanced  $\mu\text{CT}$  instruments (either laboratory or synchrotron-based). A PCI of biological samples can be employed even for unstained samples<sup>33–35</sup>. However, the combination of phase-contrast with the increasing X-ray absorption contrast by staining gives excellent image quality with better voxel resolution than absorption  $\mu\text{CT}$  setups<sup>25,26</sup>.

The patterning of skeletal elements during limb development in salamanders differs from other tetrapods<sup>36</sup>. Salamanders show an anterior or preaxial dominance in the order of formation and ossification of the zeugopodial and autopodial elements. Moreover, some proximal elements condense later than proximal ones<sup>37</sup>, which is definitely isolated from the familiar order of proximal to distal limb development in other tetrapods. In contrast with mammals, salamanders have a remarkable ability to regenerate their extraordinary range of body structures such as limbs, tails, retina, and spinal cord, along with some sections of the heart and brain<sup>38</sup>. Limb regeneration depends on the formation of a blastema, which is a pool of progenitor cells that arise after amputation. Blastema cells redifferentiate, proliferate and then restore the structured limbs<sup>39</sup>. The basic anatomy of the salamander joints, with the apposed, articular surfaces between the adjacent long bones, encapsulated by the connective tissues, is very similar to mammals<sup>40–42</sup>.

In many cases, the oriented cell dynamics and proliferation play an essential role in shaping and scaling, but the directional deposition of the matrix in the bone and cartilage is not very well understood. The majority of work so far has concentrated mainly on the analysis of the epithelial or migratory mesenchymal populations during limb or facial development, which has produced important knowledge on the asymmetric proliferation of mesenchyme and convergent extension processes in shape-making, in general<sup>43–45</sup>. However, the sculpting of precise and highly complex cartilaginous structures has not been recently focused upon except for several published works<sup>46–50</sup>. Despite attention to the cartilage shape, current works do not provide any comprehensive explanation for shape-making, but rather focuses on the importance of a multitude of factors for different aspects of cartilage and mesenchyme development with some general impact on shape.

Muscle is a tissue that lies immediately next to the developing cartilage tissue in the embryo and remains in close proximity to the cartilage template after birth<sup>51,52</sup>. On the one hand, the mechanical forces, induced by muscle contraction, seem to directly influence the morphogenesis regulation. Animal models, where muscle contractions have been removed or altered, and mouse mutants, without forming skeletal muscles, have led to the underdeveloped and misshapen skeletal elements<sup>53</sup>. Similar to humans, a short stature and scoliosis are common features in children with Duchenne Muscular Dystrophy<sup>54</sup>. Moreover, the immobilized muscle can also lead to joint structures loosening, such as a cavity, articular surfaces and patella<sup>53</sup>. On the other hand, muscle cells can release biochemical signals to regulate the cartilage gene expression indirectly<sup>55</sup>. It is still unknown how the precise, three-dimensional shape of skeletal elements is established, scaled up and what is the interaction in muscle and cartilage development. Finding a way to visualize and analyse cell distribution in 3D would be a

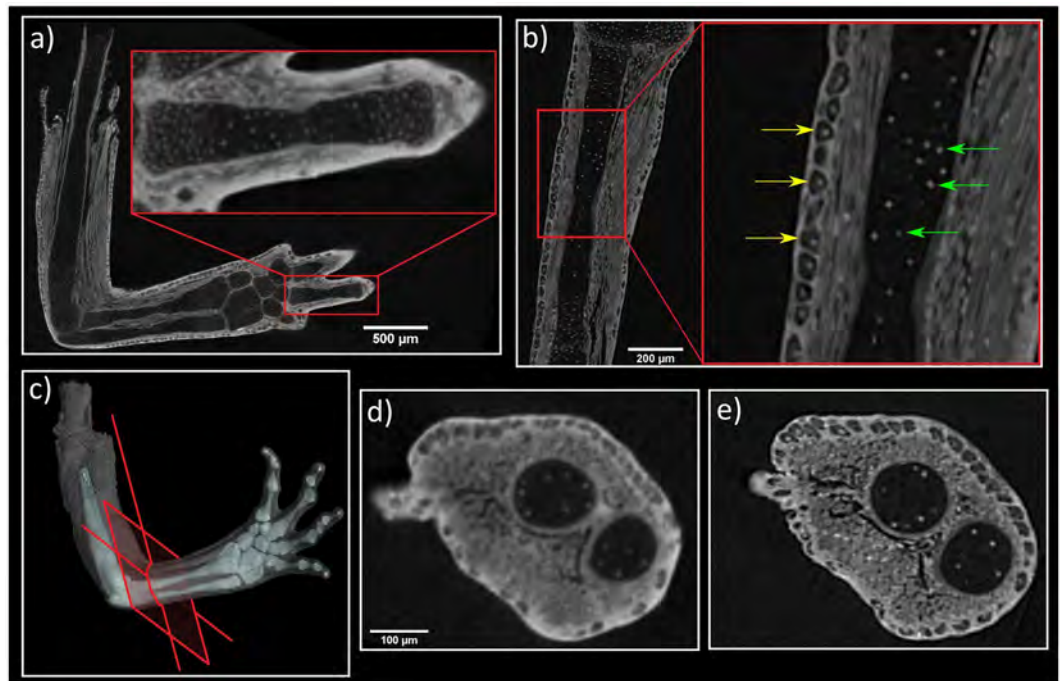


**Figure 1.** Comparison of the tomographic slices of a *P. waltl* forearm obtained by conventional and synchrotron  $\mu$ CT. Despite near-cellular resolution, the employed conventional  $\mu$ CT setup does not provide sufficient resolution for the automatic counting of cells with necessary accuracy. (a) Tomographic slice of the limb, the red area shows detail of one finger, (b) reconstructed slice obtained by phase-contrast  $\mu$ CT at the SYRMEP beamline of the Elettra synchrotron facility, yellow arrows show cells of skin epithelium, green arrows show nuclei of cartilage, (c) 3D visualization of a limb with red plane representing the same plane of interest of tomographic slices: (d) Data obtained by conventional  $\mu$ CT and (e) by synchrotron  $\mu$ CT.

great step forward to answering these biological issues. 3D morphological characterization at cellular resolution using synchrotron-generated X-rays has already been successfully demonstrated. Furthermore, the spatial distribution of single cells inside the articular cartilage has been proven on stained<sup>56</sup> and unstained samples<sup>57</sup>. Other tissues, such as Purkinje cells in the brain, were quantified using automated cell counting<sup>58</sup>. However, previous approaches did not suffice in analysing cell polarization and the complex organization of multiple tissue types simultaneously with other 3D-analysis.

Here, we took advantage of the synchrotron-based X-ray  $\mu$ CT technique in combination with chemical contrasting in mapping the actual cells, their orientation and extracellular matrix distribution in 3D, during salamander (*Pleurodeles waltl*) limb development in the simultaneous analysis of cartilage and muscles. We decided to use the larval limb of a Spanish ribbed newt because it is a promising emerging model of limb regeneration and development<sup>59</sup>. The developing cartilages of *P. waltl* limbs are of the suitable size and are in the active growing and shaping phase. Our results demonstrated how the cell density and polarization within individual cartilaginous elements can be measured highlighting the localized accumulations of the extracellular matrix and changes in cell distribution and polarization during cartilage development. The method allowed for the mapping and 3D-reconstruction of several different tissue types at the same time, which is essential for understanding the development of a muscle-skeletal system. This study is a proof of the principle which shows the opportunity to use this type of analysis for exploring and modeling the development of skeletal structures with single-cell resolution.

## Results

**X-ray microtomography measurements.** The conventional X-ray  $\mu$ CT was exploited for overview experiments and the 3D visualization of developing *P. waltl* limbs stained with phosphotungstic acid (PTA). Here, we achieved an exceptional quality in chemical contrasting of the samples. However, the employed, conventional  $\mu$ CT instruments, did not provide sufficient resolution for a quantitative analysis and counting every single cell. Nevertheless, the resolution delivered by conventional  $\mu$ CT, gave basic information about qualitative cell distribution in the cartilage element (Fig. 1a,d). Though the information was only near-cellular, it was possible to detect some cell nuclei inside the limb.

The high photon flux, X-ray beam geometry and high spatial resolution (down to 1  $\mu$ m) of synchrotron  $\mu$ CT achieved the cellular resolution for a quantitative analysis of cell distribution (see Fig. 1b,e). Moreover, the possibility to perform PCI experiments allowed the borders of cells in cartilaginous elements to be distinguished. A comparison of the same slice from conventional and synchrotron X-ray  $\mu$ CT is reported in Fig. 1. A video of raw tomographic slices obtained by synchrotron  $\mu$ CT measurement is in Supplementary Material 1.

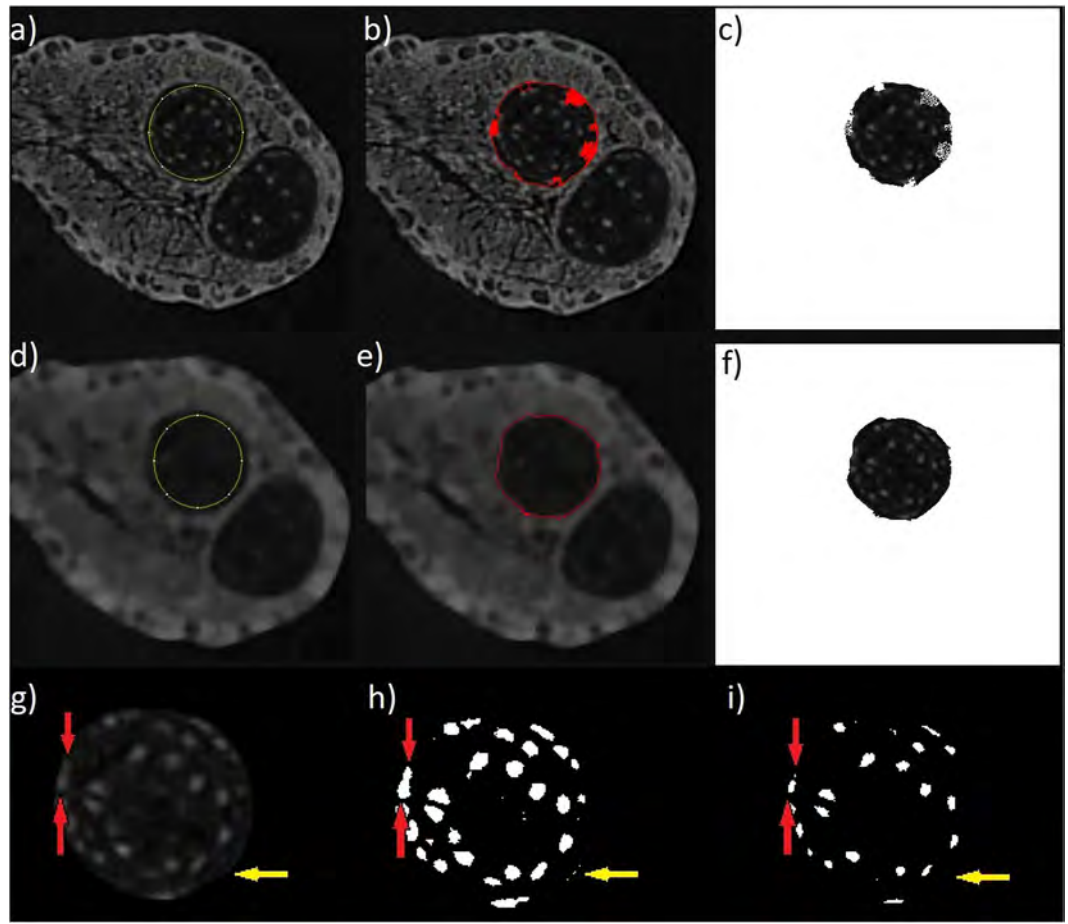


**Figure 2.** Automatic segmentation of skeletal elements performed by ABSnake<sup>65,66</sup>. (a–c) Shows the contour applied to non-filtered tomographic slices; however, rough borders caused errors. (d–f) Shows the contour applied to a filtered image. The mask was obtained without any errors and the shape of the resulting data appears almost perfect. (g–i) *Blob analysis* in the *Pore3D* software<sup>67</sup>. (g) One of the reconstructed slices used for the analysis, after the application of the 3D K-means clustering algorithm. (h) the results of the *blob analysis*, (i) the eroded segmented image. Red arrows indicate two nuclei of the cells that were connected within the *blob analysis*. The erosion of the binary image splits the blob into two parts. Yellow arrows show the light border of the cartilaginous element which should not be counted in the analysis. The erosion of the image also solved this problem.

**Data processing and analysis.** Obtaining high-contrast tomographic data is the first step in 3D analysis. By chemical contrasting, the cartilage is significantly less stained in comparison to the surrounding tissue, which leads to easier discrimination and outline of cartilage in  $\mu$ CT data<sup>48–50,60</sup>. The reason is that PTA provides a strong X-ray contrast as it is attached to proteins such as collagens and fibrils<sup>61,62</sup>. Another important part is the data processing and analysis of the reconstructed tomographic volumes. Post-reconstruction data treatment requires segmentation of the investigated cartilage or bone elements by applying the appropriate algorithms for distinguishing every single cell in the desired area and then its quantitative analysis.

First, the detection and separation of a cartilaginous element is needed with segmentation. Conventional segmentation algorithms using the region growing method<sup>63</sup> are not suitable, due to the white spots inside the cartilage. These spots represent cell nuclei. Here, we applied the freeware image analysis software ImageJ<sup>64</sup> with its plug-in ABSnake<sup>65,66</sup>. The next steps are to determine the starting contour for segmentation, the gradient threshold to be used in edge detection and the number of iterations of the segmentation cycles. Nevertheless, by applying a contour on the non-filtered tomographic slices, the iteration process does not converge to the border of the cartilage (Fig. 2a–c). This is due to the light spots (cell nuclei) in the cartilage body. Thus, the segmentation is not precise enough for the analysis. To avoid this problem, the contour is applied on the 3D median-filtered images. By filtering, the iteration procedure converges and the result of the process is the definition of the cartilage border. The final contour is smooth and perfectly copies the border of the cartilage body (Fig. 2d–f). The segmented data (cartilage element) can then be utilized for further analysis.

The next step for the quantification of cells was to count the cell nuclei represented by light spots in the image. For this purpose, the *Pore3D* software library<sup>67</sup> developed at Elettra, was employed. The 3D K-means clustering algorithm was used to sort data into three classes. The K-means algorithm converts an input image into vectors of

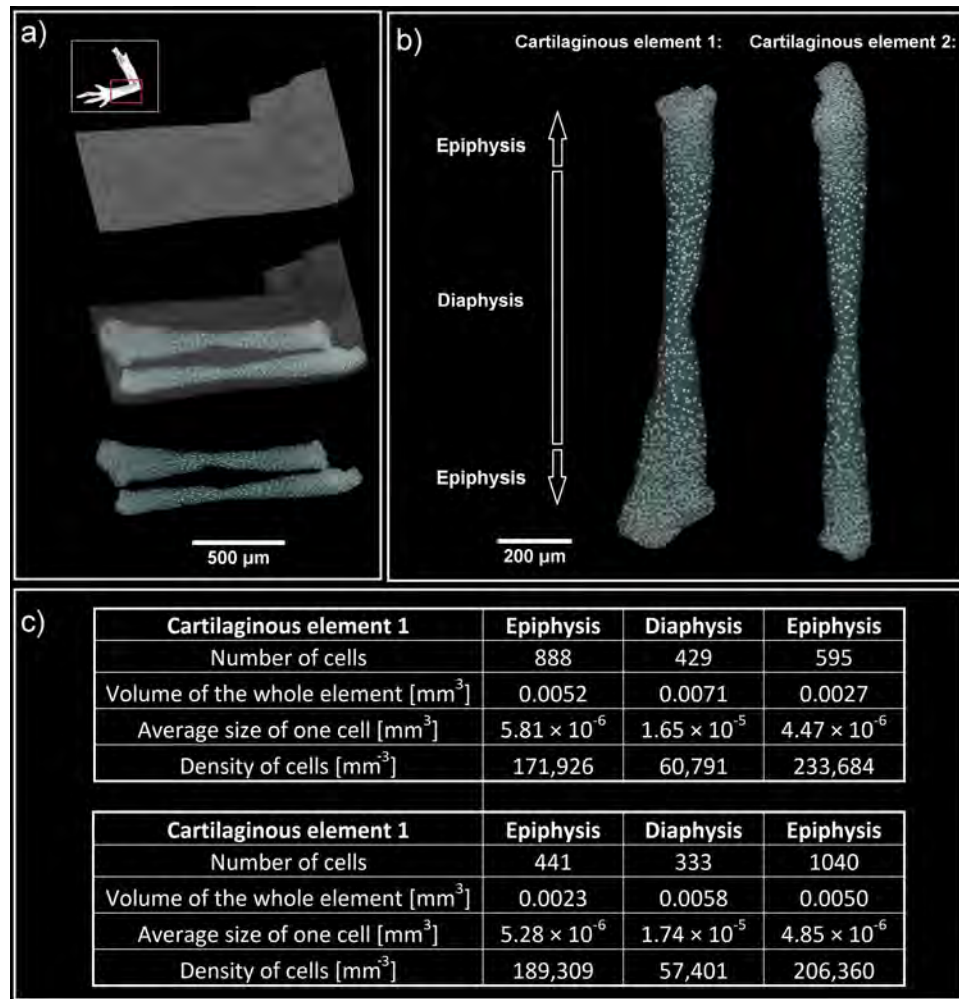


**Figure 3.** (a,b) 3D visualization of cartilaginous elements from a developing *P. waltl* limb forearm. White spots represent cell nuclei. c) Quantitative analysis allowed the determination of cell number, average size (given by ratio of volume of the whole element and number of cells), density and the volume of each cartilaginous element. The difference between diaphysis and epiphysis is evident: the density of cells in the diaphysis is half in comparison with the density in the epiphysis.

equal size and then by minimizing the sum of the squared distances from all points in a class to the class center<sup>68</sup>. This way, the binary images were obtained for the nuclei of cells, extracellular matrix and the background. The binary image for the class, representing the cell nuclei (binary large object – blob) is shown in Fig. 2h.

By comparing Fig. 2g,h, it is evident that some nuclei are connected into one blob. This example is shown by the red arrows in Fig. 2. Moreover, some border segments of the cartilage are miss-detected as blobs (yellow arrows in Fig. 2). To correct these analytical issues, the erosion of the 3D data is the next step. After this step, the data is well suited to determine the number of cells (Fig. 2i). To obtain the final number of cells, the binary data of cell nuclei after erosion (Fig. 2i) was implemented for further blob analysis<sup>69</sup>.

Basically, the limit of this type of analysis is determined by the resolution (spatial and contrast) of the system and by the size of the analysed structure. The spatial resolution of the detection system and the detectability of the given features of interest can be further influenced by working in phase-contrast mode<sup>70</sup>. In our 3D image processing and analysis, the objects considered as cells and included in the computations, were those with size larger than 3 pixels = 27 voxels (=27 μm<sup>3</sup> per blob). The video of segmented data is shown in Supplementary Material 2.

**Biological results.** Our analysis of developing ulna and radius cartilages from a *P. waltl* limb demonstrated zonation that included a wide central region inhabited by the chondrocytes submerged in much larger amounts of extracellular matrix as compared to developing epiphyseal regions defined based on the instant changes of a cell density on a histogram. The cell number of these sparse chondrocytes in the central regions of both the ulna and the radius appeared low, which could reflect the reduction of cell number by decreased proliferation and acquisition of a hypertrophic stage. According to a classical model, epiphyseal chondrocytes continue proliferation longer than chondrocytes in a central region of a cartilaginous element and, consequently, show much higher density according to our data (Fig. 3).

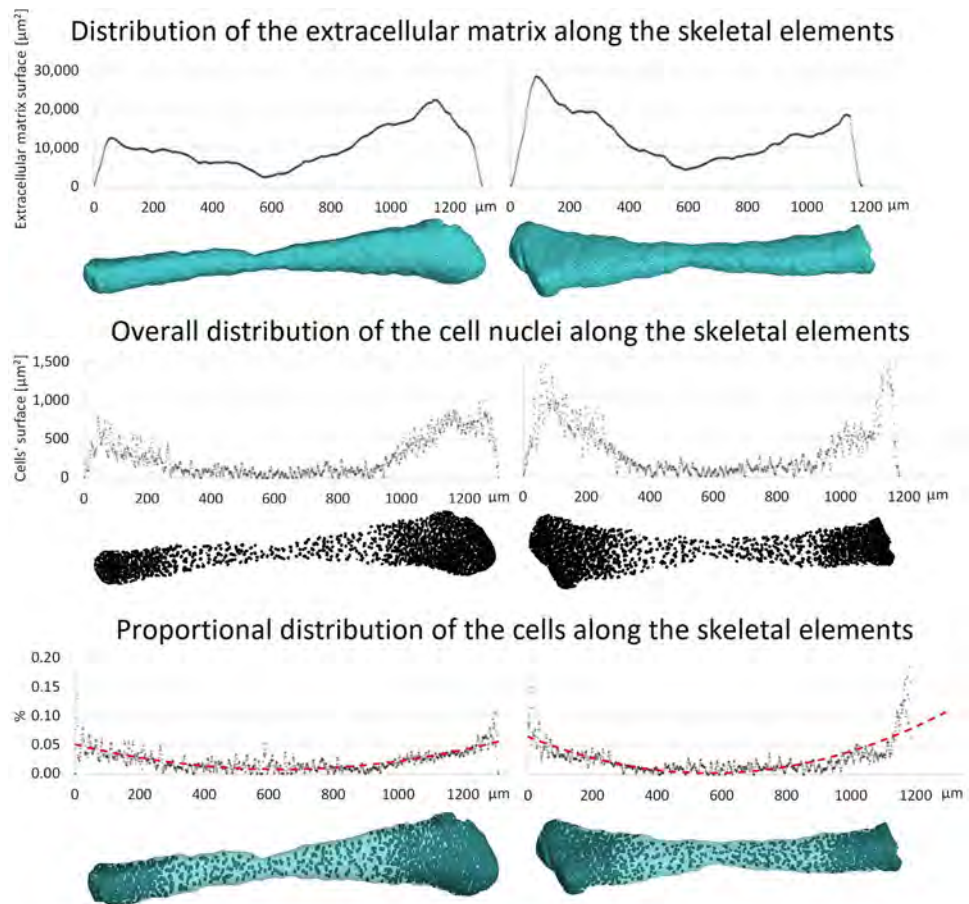


**Figure 4.** Distribution of extracellular matrix and cell nuclei along skeletal elements. Top: distribution of the area of extracellular matrix along the element. Middle: distribution of number of cells represented by the area of cell nuclei. Bottom: ratio between the area of cell nuclei and the area of extracellular matrix; the red-dotted line fits the data by a second order polynomial. The minimum of the parabola sits in the centre of the diaphyseal regions.

Further analysis showed more detailed distribution of cartilage along the growing skeletal element. For each slice, the area of the cell nuclei and area of the whole extracellular matrix were computed. Both structures showed uneven distribution in the distal direction. Interestingly, the ratio between cell nuclei and extracellular matrix areas changes (from approx. 0.1% to 0.01% - Fig. 4). The determined density of cells corresponds to the literature, which records estimated values for the cell density in cartilage between 30,000 and 110,000 cells  $\text{mm}^{-3}$  by confocal imaging<sup>71</sup> or digital volumetric imaging by Jadin *et al.*<sup>72</sup>. However, the distribution in epiphyseal and diaphyseal regions has not been further discussed.

A key advantage of synchrotron X-ray  $\mu$ CT measurements enhanced by PTA staining is the large variety of tissues that can be detected simultaneously. Information from all structures in a sample is included in one dataset obtained by a single measurement, which determines the position of each structure within the sample (Fig. 5, Supplementary Material 3). Efficient analysis can be done for a wide spectrum of tissues. This allows to reveal connections between muscles and cartilage development simultaneously. The muscles showed incremental growth during the regeneration process in coordination with expanding cartilage and also appeared with their corresponding attachment points at different timing. The development of muscles then might guide cartilage and joint formation<sup>73</sup>. Three developmental stages were observed in muscle-skeletal point of view. At the youngest analyzed stage (41–42), only one small group of muscle around the elbow joint was found. However, different muscle group (*biceps brachii*, *triceps brachii*, *brachioradialis* and *flexor carpi radialis*) were recognized in the next two stages (Fig. 6b). Meanwhile, the elbow joint angle was decreasing with the development of muscle. Interestingly, the decreasing angle between *ulna* and *humerus* was observed with increasing developmental stages (Fig. 6a). Beyond question, the development of *biceps brachii* and *brachioradialis* may contribute to the decreasing elbow joint directly (the physical function of *biceps brachii* and *brachioradialis* is to bend the elbow joint). Another important finding is shape and position of the developing muscles. Surprisingly, there is no muscle splitting at the youngest analysed stage (41–42). The muscle splitting occurs later together with shaping of the cartilaginous joint. Furthermore, there is a correlation between the cell polarity inside the cartilage and splitting of the muscles (Fig. 7). The chondrocytes next to the muscles attachment points have a higher cell polarity. In another word, there is a correlation between the cell polarity inside cartilage and muscle attachment point. It is natural to speculate the mechanical force from muscle stretch may be delivered to attach point and then influence

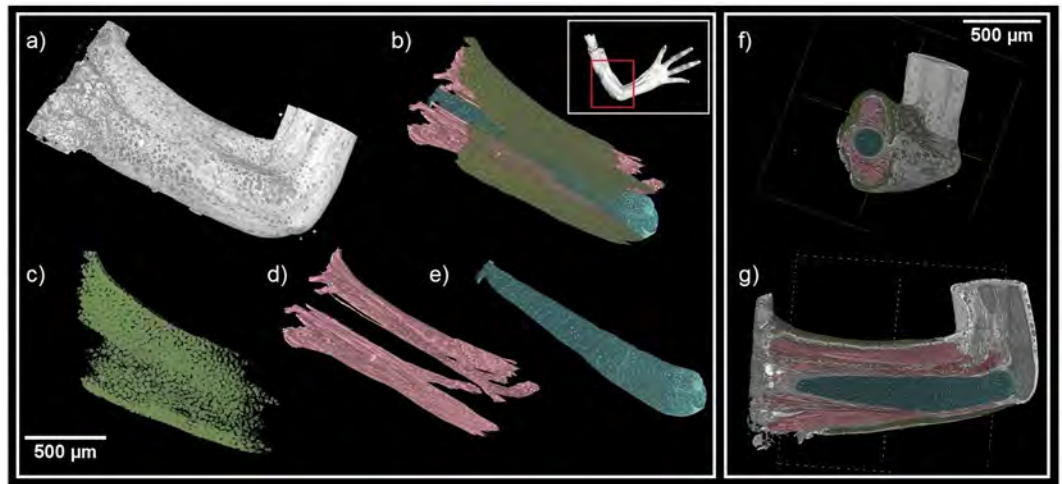


**Figure 5.** (a,b) 3D visualization of soft tissues showing other structures in the sample. (c–e) Sample segmentation showing cartilage (light blue), muscle fibers (red) and skin epithelium (yellow). (f–g) Clipping planes on the 3D model showing segmented structures inside the sample.

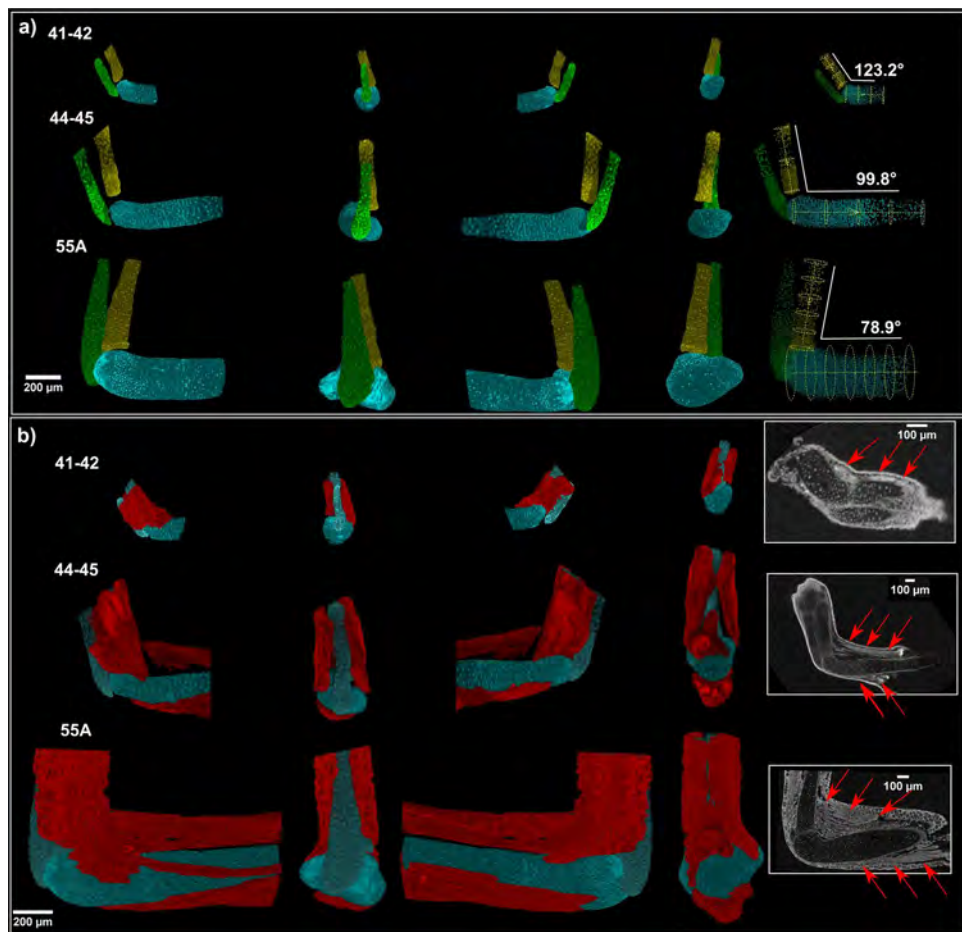


**Figure 6.** (a) Development of cartilage of the joint for three different developmental stages. The angle between *ulna* and *humerus* is decreasing with increasing developmental stage. (b) Visualization of joint simultaneously with developing muscles for three developmental stages. There is a correlation between decreasing angle and splitting of the muscles.

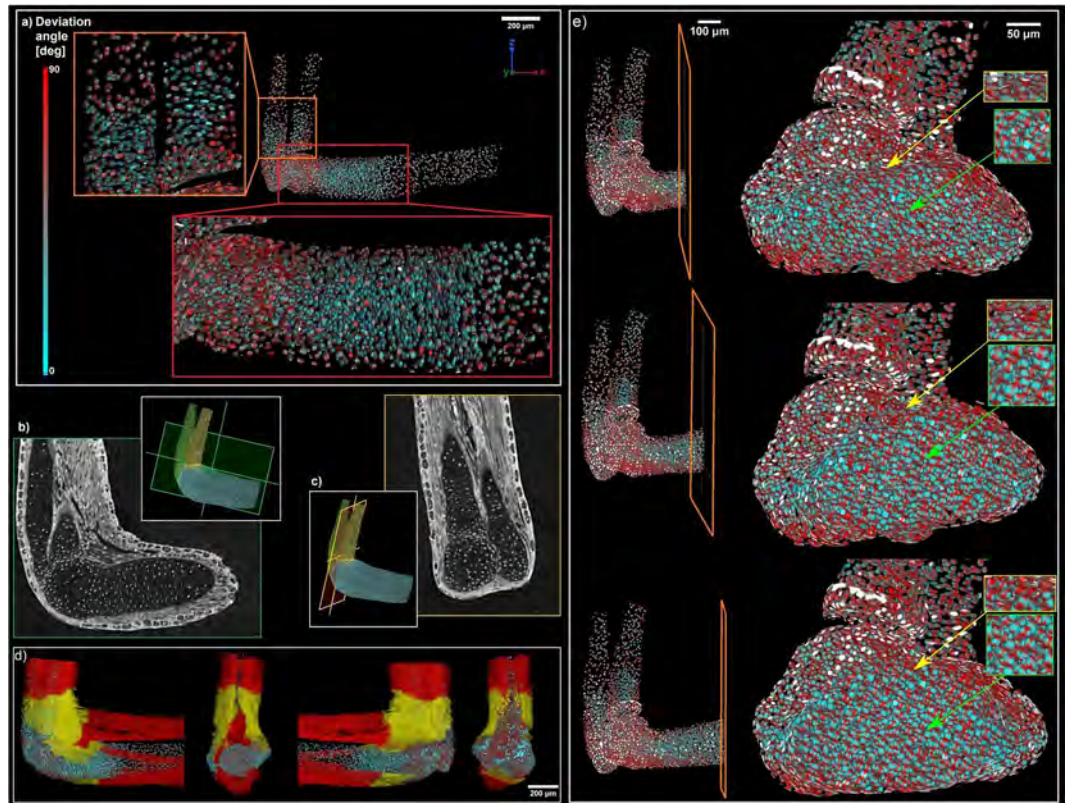


**Figure 7.** (a) Polarization of the cells inside cartilage. There are polarized zones between diaphysis and epiphysis for all cartilaginous elements: *ulna*, *radius* and *humerus*. Deviation angle  $0^\circ$  for *ulna* and *radius* was set to the plane  $x, y$  and for *humerus* was set to the plane  $y, z$ ; (b,c) Corresponding tomographic slices verifying the computation of polarization; (d) Muscle attachment points in correlation with cell polarization; (e) Detail of orientation of the cells: Superficial chondrocytes near surface (yellow arrow) are aligned with the developing surface of the cartilage in the contrary of chondrocytes in the middle of the cartilage (green arrow).

local chondrocytes polarity (Fig. 7d). It gives rise to a thought that a hitherto unknown mechanism controls the location and the density of chondrocytes together with cell polarity and muscle attachment points.

Our visualizations provided detailed information about developing joint surfaces at cellular resolution in 3D in the regenerating salamander limb. Development of surface geometry correlated in time with the formation of attached striated muscles. Orientation of chondrocytes in the developing joint, measured for the first time in the entire 3D volume by using X-ray computed tomography, correlated with the changing curvatures of joint surfaces. More generally, the resolution and differential contrast were sufficient to map the orientation of all chondrocytes within the cartilage, which provided important foundation for future inference of the oriented cell behaviour during cartilage shaping. Our results demonstrated that the predominant orientation of chondrocytes in epiphyseal regions was different from rather central regions of the cartilage, where the cell density appeared low. In addition to this, superficial chondrocytes in epiphyseal regions were aligned with the developing surface of the cartilage (Fig. 7e).

Taken together, our biological results show that development of cartilage geometry (including forming joints) correlates in time with developing skeletal muscles, which may influence the orientation of chondrocytes in epiphyseal regions, and through this, and in accordance with previously published data<sup>73</sup>, regulate morphogenesis and fine shaping of specific regions in cartilage.

## Discussion and Conclusion

In this study, we have demonstrated a novel, technical approach allowing for the quantitative analysis of polarization and 3D cell distribution inside the whole developing muscle-cartilaginous units from a regenerative animal model. This approach is based on the chemical contrasting of samples with PTA, followed by a high-resolution X-ray microtomography ( $\mu$ CT) measurement and the subsequent 3D data-processing and analysis. The polarization of the cell is determined by analysing the shape of cells in the matrix or the shape of their nuclei within other soft tissues. The best results, suitable for the quantitative analysis, with a single cell resolution and qualified for the computer simulations, were achieved by the phase-contrast synchrotron X-ray  $\mu$ CT analyses performed at the SYRMEP beamline of the Elettra facility. On the other hand, by using a conventional X-ray  $\mu$ CT instrument, the resolution turned out to be near-cellular, whereas the quantitative analysis faced a number of additional problems.

Nevertheless, the data obtained by the conventional setup delivered important complementary information and allowed the visualization of many well-resolved internal structures.

Unexpectedly, our biological results show that the orientation of cells in the cartilage changes with cell density and position along the cartilaginous element and also in relation to the general position of the muscle attachment points and forming joint surfaces. The polarity of a cell may reflect so-called oriented cell behaviour, which might include oriented cell divisions, cell migration or other asymmetric processes important for shaping the structure<sup>74</sup>. Geometrical signs of cell polarisation in the cartilage, obtained from tomographic data, suggest the potential role of mechanical forces in cartilage geometry formation via the control of the chondrocyte cell orientation within the extracellular matrix. The polarity of chondrocytes and perichondrial cells in the attachment point areas may result from tension in the developing muscles, which we mapped in terms of geometry and volume. Previous findings already established the role of the developing muscles in cartilage shaping<sup>73</sup>. Brunt and co-authors<sup>73</sup> demonstrated that muscles are important for the morphogenesis of joints by using zebrafish as a model system together with computer simulations. The authors of the study concluded that the mechanical strain created by the muscles, influences cell orientation in the developing jaw joint of a fish<sup>73</sup>, which goes along with our findings in the regenerative model system, where we provide 3D information of cell orientation suitable for further 3D-modeling efforts. On the other hand, according to our data, the muscles also expand in the direction following the attachment points that change their relative position in the growing cartilage with time.

In general, the obtained data, including the number of cells in 3D volume, their density, polarization, zonal distribution and the total volume of the skeletal elements, are important to understand growth, shaping, scaling and the regeneration of muscle and cartilaginous structures in the developing and regenerating vertebrates. Here, we have delivered proof of the principle study to show the possibility of visualizing and counting the individual chondrocytes in the cartilage of a vertebrate model system, suitable for both the developmental biology and the regenerative research. This approach can provide precise information about the incremental growth of a structure in terms of changes in cell polarity, cell numbers and simultaneously with the transforming shape. We envision that in the near future conventional laboratory  $\mu$ CT setups will gain similar imaging capabilities to the synchrotron beamlines, opening new possibilities of studying biological structures in 3D with single-cell resolution. Hereby, the use of such conventional  $\mu$ CT measurements in combination with open-source software for 3D image analysis, will enable new opportunities for the community of biologists and biomedical specialists, investigating the development and regeneration of skeletal and non-skeletal tissues.

## Methods

**Sample preparation.** The *Pleurodeles waltl* (Spanish ribbed newt) colony was established from fertilized eggs produced in a laboratory colony located in Madrid, Spain. Animals originating from a wild population in the Doñana National Park (Spain) were obtained for research purposes by Agustin Gonzalez. The animals, used to prove the concept study were 4th/5th generation, developmental stage 41–42, 44–45 and 55 A (approximate length of the whole larva was 3.7 cm). Staging of the larva was performed according to Joven *et al.*<sup>75</sup>. The frontal amputated limbs were briefly washed in PBS and fixed in freshly mixed 4% PFA for 12 hours at +4 degrees. A contrasting of the developing limbs was performed as follows: the samples were dehydrated in increasing ethanol grade (30%, 50%, 70%, 90%) at room temperature, 2 hours for each step, using a slow rotation of the samples. The samples were transferred into a solution of 0.7% PTA (phosphotungstic acid) in 90% methanol and incubated at +4 degrees for 5 days using slow rotation and the PTA-contrasting solution was changed after every 24 hours for a fresh one. The samples were washed with 90% methanol overnight at +4 degrees and then rehydrated in a decreasing ethanol grade (90%, 70%, 50%, 30%) at room temperature, 2 hours for each step and slow rotation.

**Use of experimental animals.** All procedures on newts were approved by local ethics committee (Stockholms Djurförsöksetiska Nämnd) and were performed in accordance with national regulations issued by the Swedish Board of Agriculture.

**Conventional X-ray  $\mu$ CT measurements.** The contrast of the stained samples was checked by a conventional X-ray  $\mu$ CT. Following that, the developing limbs were embedded in 1.0% of agarose gel and placed in polypropylene tubes to avoid movement artefacts during tomography scanning. A polypropylene tube was fixed on a plastic rod by a silicone gun. The rod, containing the sample, was put in the centre of the rotation stage axis. A  $\mu$ CT scanning was performed using the laboratory system GE Phoenix v|tome|x L 240 (GE Sensing & Inspection Technologies GmbH, Germany) with a 180 kV/15 W maximum power nanofocus X-ray tube and a high contrast, flat panel detector DXR250 with 2048 × 2048 px<sup>2</sup> and a pixel size of 200 × 200  $\mu$ m<sup>2</sup>. Exposure time was 900 ms in each of the 2200 projections acquired over a total angle of 360°. The utilized acceleration voltage and the current of the X-ray tube were 60 kV and 200  $\mu$ A, respectively. The beam was filtered by a 0.2 mm-thick aluminium filter to reduce beam-hardening artefacts. The tomographic reconstruction was done using the software GE phoenix datos|x 2.0 (GE Sensing & Inspection Technologies GmbH, Germany) with an isotropic voxel size of 2.5  $\mu$ m.

**Synchrotron X-ray  $\mu$ CT measurements.** Phase-contrast synchrotron X-ray  $\mu$ CT measurements were performed at the SYRMEP beamline of the Italian synchrotron radiation facility Elettra with the white beam mode. The X-ray spectrum of the beam was filtered with 1.5 mm of silicon and 0.025 mm of molybdenum. The sample-detector distance was set at 100 mm. The experiments were conducted with an isotropic voxel size of 1.05  $\mu$ m. The exposure time per projection was 1.0 s with 1000 projections acquired over a total scan angle of 180°. Thus, the total scanning time was about 17 minutes. The tomographic slices were reconstructed using the SYRMEP Tomo Project (STP) software developed at Elettra<sup>76</sup>.

**Data processing and analysis.** Reconstructed slices were further analysed using the freeware ImageJ<sup>62</sup> and the *Pore3D* software library<sup>65,67</sup>. Firstly, the segmentation of cartilaginous elements was carried out using the

plugin ABSnake<sup>63,64</sup> with a gradient threshold of 30 and a setting of 50 iterations. This plugin was applied to the dataset filtered by a Median 3D filter with a radius of 10 in all three dimensions. The final cartilaginous element (i.e. developing *P. waltl* forearm) was obtained in ImageJ by using the segmented slices as a transparent-zero mask on the original, non-filtered dataset. Further analyses were carried out by using *Pore3D*. To separate the background, the extracellular matrix and the bright cell nucleus, a 3D K-means clustering algorithm was applied to divide the data into three classes. The binary image of the class represented by the cell nuclei was consequently processed by the *erosion* and the *blob analysis* modules of *Pore3D*, which allowed for the determination of the number of *blobs*, i.e. the number of cells. Cell polarization was determined using the software, VGStudio Max 3.1, with its module *Fiber orientation analysis*. The different tissues such as the skin epithelium and muscles were segmented semi-automatically in combination with the software Avizo and VGStudio Max 2.2 according to Tesarova *et al.*<sup>60</sup>.

## Data Availability

The datasets generated and/or analysed during the current study are available in the Image Data Resource repository.

## References

- Graf, B. W. & Boppart, S. A. Imaging and Analysis of Three-Dimensional Cell Culture Models. *Methods Mol Biol.* **591**, 211–227, [https://doi.org/10.1007/978-1-60761-404-3\\_13](https://doi.org/10.1007/978-1-60761-404-3_13) (2010).
- Hedlund, H., Brismar, H., Widholm, M. & Svensson, O. Studies of cell columns of articular cartilage using UV-Confoal scanning laser microscopy and 3D image processing. *J. Musculoskelet. Res.* **3**, 93–98 (1994).
- Artym, V. V. & Matsumoto, K. Imaging Cells in Three-Dimensional Collagen Matrix. in *Curr. Protoc Cell Biol.* Chapter 10: Unit10.18.1–20 <https://doi.org/10.1002/0471143030.cb1018s48> (2010).
- Morgan, F., Barbarese, E. & Carson, J. H. Visualizing cells in three dimensions using confocal microscopy, image reconstruction and isosurface rendering: application to glial cells in mouse central nervous system. *Scanning Microsc.* **6**, 345–56 (1992).
- Pawley, J. *Handbook of Biological Confocal Microscopy*. (Springer, 1995).
- Reihani, S. N. S. & Oddershede, L. B. Confocal microscopy of thick specimens. *J Biomed. Opt.* **14**, 030513, <https://doi.org/10.1117/1.3156813> (2009).
- Ewald, A. J., McBride, H., Reddington, M., Fraser, S. E. & Kerschmann, R. Surface imaging microscopy, an automated method for visualizing whole embryo samples in three dimensions at high resolution. *Dev Dyn.* **225**, 369–375, <https://doi.org/10.1002/dvdy.10169> (2002).
- Helmchen, F. & Denk, W. Deep tissue two-photon microscopy. *Nat. Methods* **2**, 932–940, <https://doi.org/10.1038/nmeth818> (2005).
- Ustione, A. & Piston, D. W. A simple introduction to multiphoton microscopy: A simple introduction to multiphoton microscopy. *J Microsc.* **243**, 221–226, <https://doi.org/10.1111/j.1365-2818.2011.03532.x> (2011).
- Schmitt, J. M. Optical coherence tomography (OCT): a review. *IEEE J. Quantum Electron.* **5**, 1205–1215, <https://doi.org/10.1109/2944.796348> (1999).
- Fercher, A. F., Drexler, W., Hitzinger, C. K. & Lasser, T. Optical coherence tomography—principles and applications. *Rep.Prog. Phys.* **66**, 239, <https://doi.org/10.1088/0034-4885/66/2/204> (2003).
- Campbell, J. P. *et al.* Detailed Vascular Anatomy of the Human Retina by Projection-Resolved Optical Coherence Tomography Angiography. *Sci. Rep.* **7**, 42201, <https://doi.org/10.1038/srep42201> (2017).
- Le Gros, M. A., McDermott, G. & Larabell, C. A. X-ray tomography of whole cells. *Curr Opin Struct Biol.* **15**, 593–600, <https://doi.org/10.1016/j.sbi.2005.08.008> (2005).
- Larabell, C. A. & Nugent, K. A. Imaging cellular architecture with X-rays. *Curr Opin Struct Biol.* **20**, 623–631, <https://doi.org/10.1016/j.sbi.2010.08.008> (2010).
- Langer, M. *et al.* Assessment of imaging quality in magnified phase CT of human bone tissue at the nanoscale. *Proc.SPIE.* 10391, <https://doi.org/10.1117/12.2272561> (SPIE, 2017).
- Attwood, D. T. *Soft X-rays and extreme ultraviolet radiation: Principles and application.* (Cambridge University press, 1999).
- Krenkel, M. *et al.* Phase-contrast zoom tomography reveals precise locations of macrophages in mouse lungs. *Sci. Rep.* **5**, 9973, <https://doi.org/10.1038/srep09973> (2015).
- Snigirev, A., Snigireva, I., Kohn, V., Kuznetsov, S. & Schelokov, I. On the possibilities of x-ray phase contrast microimaging by coherent high-energy synchrotron radiation. *Rev. Sci. Instrum.* **66**, 5486–5492, <https://doi.org/10.1063/1.1146073> (1995).
- Wilkins, S. W., Gureyev, T. E., Gao, D., Pogany, A. & Stevenson, A. W. Phase-contrast imaging using polychromatic hard X-rays. *Nature* **384**, 335, <https://doi.org/10.1038/384335a0> (1996).
- Baruchel, J., Buffière, J. Y., Maire, E., Merle, P. & Peix, G. X-ray tomography in material science, general principles. (Hermes Science Publications, 2000).
- Cloetens, P., Barrett, R., Baruchel, J., Guigay, J. P. & Schlenker, M. Phase objects in synchrotron radiation hard X-ray imaging. *J PhysD Appl Phys* **29**, 133–146 (1996).
- Kaiser, J. *et al.* Investigation of the microstructure and mineralogical composition of urinary calculi fragments by synchrotron radiation X-ray microtomography: a feasibility study. *Urol Res.* **39**, 259–267, <https://doi.org/10.1007/s00240-010-0343-9> (2011).
- Astolfo, A. *et al.* In vivo visualization of gold-loaded cells in mice using x-ray computed tomography. *Nanomedicine* **9**, 284–292, <https://doi.org/10.1016/j.nano.2012.06.004> (2013).
- Larsson, D. H., Vågberg, W., Yaroshenko, A., Yildirim, A. Ö. & Hertz, H. M. High-resolution short-exposure small-animal laboratory x-ray phase-contrast tomography. *Sci. Rep.* **6**, <https://doi.org/10.1038/srep39074> (2016).
- Dullin, C. *et al.*  $\mu$ CT of *ex-vivo* stained mouse hearts and embryos enables a precise match between 3D virtual histology, classical histology and immunochemistry. *PLoS one* **12**, e0170597, <https://doi.org/10.1371/journal.pone.2017> (2017).
- Saccomano M. *et al.* Synchrotron inline phase contrast  $\mu$ CT enables detailed virtual histology of embedded soft-tissue samples with and without staining. *J. Synchrotron Radiat.* **25**, <https://doi.org/10.1107/S1600577518005489> (2018).
- Albers J. *et al.* X-ray-Based 3D Virtual Histology—Adding the Next Dimension to Histological Analysis. *Mol Imaging Biol.* <https://doi.org/10.1007/s11307-018-1246-3> (2018).
- Albers J. *et al.* X-ray based virtual histology allows guided sectioning of heavy ion stained murine lungs for histological analysis. *Sci. Rep.* **8**, <https://doi.org/10.1038/s41598-018-26086-0> (2018).
- Momose, A., Takeda, T., Itai, Y. & Hirano, K. Phase-contrast X-ray computed tomography for observing biological soft tissues. *Nat. Med.* **2** (1996).
- Beltran, M. A., Paganin, D. M., Uesugi, K. & Kitchen, M. J. 2D and 3D X-ray phase retrieval of multi-material objects using a single defocus distance. *Opt Express* **18**, 6423–36, <https://doi.org/10.1364/OE.18.006423> (2010).
- Metscher, B. D. MicroCT for comparative morphology: simple staining methods allow high-contrast 3D imaging of diverse non-mineralized animal tissues. *BMC Physiol* **9**, 11, <https://doi.org/10.1186/1472-6793-9-11> (2009).
- Metscher, B. D. MicroCT for developmental biology: A versatile tool for high-contrast 3D imaging at histological resolutions. *Dev Dyn.* **238**, 632–640. [10.1002/dvdy.21857](https://doi.org/10.1002/dvdy.21857) (2009).

33. Shinohara, M. *et al.* Atherosclerotic plaque imaging using phase-contrast X-ray computed tomography. *Am J Physiol Heart Circ Physiol* **294**, H1094–H1100 (2008).
34. Zanette, I. *et al.* Holotomography versus X-ray grating interferometry: A comparative study. *Applied Physics Letters* **103**, 244105 (2013).
35. Lang, S. *et al.* Experimental comparison of grating- and propagation-based hard X-ray phase tomography of soft tissue. *Journal of Applied Physics* **116**, 154903, <https://doi.org/10.1152/ajpheart.01149.2007> (2014).
36. Kumar A. *et al.* An orphan gene is necessary for preaxial digit formation during salamander limb development. *Nat Commun.* **6** <https://doi.org/10.1038/ncomms9684> (2015).
37. Frobisch, N. B. & Shubin, N. H. Salamander limb development: integrating genes, morphology, and fossils. *Dev. Dyn.* **240**, 1087–1099 (2011).
38. Godwin, J. W. *et al.* Macrophages are required for adult salamander limb regeneration. *Proc Natl Acad Sci USA* **23**, 9415–20, <https://doi.org/10.1073/pnas.1300290110> (2013).
39. Yun, M. H. *et al.* Regulation of p53 is critical for vertebrate limb regeneration. *Proc Natl Acad Sci USA* **43**, 17392–7 (2013).
40. Cosden, R. S. *et al.* Intrinsic repair of full-thickness articular cartilage defects in the axolotl salamander. *Osteoarthritis Cartilage* **19**, 200–205 (2011).
41. Khan, I. M. *et al.* The development of synovial joints. *Curr. Top. Dev. Biol.* **79**, 1–36 (2007).
42. Cosden-Decker, R. S. *et al.* Structural and functional analysis of intra-articular interzone tissue in axolotl salamanders. *Osteoarthritis Cartilage* **20**, 1347–1356, <https://doi.org/10.1016/j.joca.2012.07.002> (2012).
43. Adameyko, I. & Fried, K. The Nervous System Orchestrates and Integrates Craniofacial Development: A Review. *Front. Physiol.* **7**, 49, <https://doi.org/10.3389/fphys.2016.00049> (2016).
44. Davidson, L. A. Epithelial machines that shape the embryo. *Trends Cell Biol.* **22**, 82–87, <https://doi.org/10.1016/j.tcb.2011.10.005> (2012).
45. Boehm, B. *et al.* The Role of Spatially Controlled Cell Proliferation in Limb Bud Morphogenesis. *PLoS Biol.* **8**, e1000420, <https://doi.org/10.1371/journal.pbio.1000420> (2010).
46. Abzhanov, A. & Tabin, C. J. Shh and Fgf8 act synergistically to drive cartilage outgrowth during cranial development. *Dev Biol.* **273**, 134–148, <https://doi.org/10.1016/j.ydbio.2004.05.028> (2004).
47. Gros, J. & Tabin, C. J. Vertebrate Limb Bud Formation Is Initiated by Localized Epithelial-to-Mesenchymal Transition. *Science* **343**, 1253–1256, <https://doi.org/10.1126/science.1248228> (2014).
48. Kaucza, M. *et al.* Oriented clonal cell dynamics enables accurate growth and shaping of vertebrate cartilage. *Elife* **6**, e25902, <https://doi.org/10.7554/eLife.25902> (2017).
49. Li, L. *et al.* Superficial cells are self-renewing chondrocyte progenitors, which form the articular cartilage in juvenile mice. *FASEB J.* **31**, 1067–1084, <https://doi.org/10.1096/fj.201600918R> (2017).
50. Kaucza, M. *et al.* Signals from the brain and olfactory epithelium control shaping of the mammalian nasal capsule cartilage. *eLife* **7**, e34465, <https://doi.org/10.7554/eLife.34465> (2018).
51. Buckingham, M. *et al.* The formation of skeletal muscle: from somite to limb. *J Anat.* **202**, 59–68 (2003).
52. Stockdale, F. E. *et al.* Molecular and cellular biology of avian somite development. *Dev Dyn.* **219**, 304–21 (2000).
53. Roddy, K. A. *et al.* Mechanical Influences on Morphogenesis of the Knee Joint Revealed through Morphological, Molecular and Computational Analysis of Immobilised Embryos. *PLoS One* **6**, e17526, <https://doi.org/10.1371/journal.pone.0017526> (2011).
54. Rapaport, D. *et al.* Short stature in Duchenne muscular dystrophy. *Growth Regul.* **1**, 11–5 (1991).
55. Cairns, D. M. *et al.* The role of muscle cells in regulating cartilage matrix production. *J Orthop Res* **28**, 529–536 (2010).
56. Zehbe, R. *et al.* Characterization of oriented protein-ceramic and protein-polymer-composites for cartilage tissue engineering using synchrotron m-CT. *Int. J. Mater. Res.* **98**, 562–568, <https://doi.org/10.3139/146.101509> (2007).
57. Zehbe, R. *et al.* Going beyond histology. Synchrotron micro-computed tomography as a methodology for biological tissue characterization: from tissue morphology to individual cells. *J R Soc Interface* **7**, 49–59, <https://doi.org/10.1098/rsif.2008.0539> (2010).
58. Hieber, S. *et al.* Tomographic brain imaging with nucleolar detail and automatic cell counting. *Sci. Rep.* **6**, 32156, <https://doi.org/10.1038/srep32156> (2016).
59. Elewa, A. *et al.* Reading and editing the Pleurodeles waltl genome reveals novel features of tetrapod regeneration. *Nat. Commun.* **8**, 9, <https://doi.org/10.1038/s41467-017-01964-4> (2017).
60. Tesařová, M. *et al.* Use of micro computed-tomography and 3D printing for reverse engineering of mouse embryo nasal capsule. *JINST* **11**, C03006–C03006, <https://doi.org/10.1088/1748-0221/11/03/C03006> (2016).
61. Constantine, V. S. & Mowry, R. W. Selective staining of human dermal collagen. *J. Invest Dermatol.* **50**, 414–418 (1968).
62. Nemetschek, T., Riedl, H. & Jonak, R. Topochemistry of the binding of phosphotungstic acid to collagen. *J. Mol. Biol.* **133**, 67–83 (1979).
63. Adams, R. & Bischof, L. Seeded region growing. *IEEE Trans. Pattern Anal. Mach. Intell.* **16**, 641–647, <https://doi.org/10.1109/34.295913> (1994).
64. Schneider, C. A., Rasband, W. S. & Eliceiri, K. W. NIH Image to ImageJ: 25 years of image analysis. *Nat. methods* **9**, 671, <https://doi.org/10.1038/nmeth.2089> (2012).
65. Boudier, T. Elaboration d'un modèle de déformation pour la détection de contours aux formes complexes. *Innov. Techn. Biol. Med.* **18**, 1 (1997).
66. Andrey, P. & Boudier, T. Adaptive active contours (snakes) for the segmentation of complex structures in biological images. in *Centre de Recherche Public Henri Tudor Copyright Notice* 181 (2006).
67. Brun, F. *et al.* Pore3D: A software library for quantitative analysis of porous media. *Nucl. Instr. Meth. Phys. Res.* **615**, 326–332, <https://doi.org/10.1016/j.nima.2010.02.063> (2010).
68. Hartigan, J. A. & Wong, M. A. Algorithm AS 136: A K-Means Clustering Algorithm. *Applied Statistics* **28**, 100 (1979).
69. Zandomenighi, D. *et al.* Quantitative analysis of X-ray microtomography images of geomaterials: Application to volcanic rocks. *Geosphere* **6**, 793–804, <https://doi.org/10.1130/GES00561.1> (2010).
70. Viani, A. *et al.* Microstructural characterization of dental zinc phosphate cements using combined small angle neutron scattering and microfocus X-ray computed tomography. *Dent Mater* **4**, 402–417, <https://doi.org/10.1016/j.dental.2017.01.008> (2017).
71. Wong, M. *et al.* Zone-specific cell biosynthetic activity in mature bovine articular cartilage: a new method using confocal microscopic stereology and quantitative autoradiography. *J. Orthop. Res.* **14**, 424–432, <https://doi.org/10.1002/jor.1100140313> (1996).
72. Jadin, K. D. *et al.* Depth-varying density and organization of chondrocytes in immature and mature bovine articular cartilage assessed by 3D imaging and analysis. *J. Histochem. Cytochem.* **53**, 1109–1119, <https://doi.org/10.1369/jhc.4A6511.2005> (2005).
73. Brunt, L. H. *et al.* Finite element modelling predicts changes in joint shape and cell behaviour due to loss of muscle strain in jaw development. *J Biochem* **48**, 3112–22, <https://doi.org/10.1016/j.jbiomech.2015.07.017> (2015).
74. Kaucza, M. *et al.* Analysis of neural crest-derived clones reveals novel aspects of facial development. *Science Advances* **2**, e1600060, <https://doi.org/10.1126/sciadv.1600060> (2016).
75. Joven, A., Kirkham, M. & Simon, A. Husbandry of Spanish Ribbed Newts (Pleurodeles waltl). *Methods Mol Biol.* 47–70 [https://doi.org/10.1007/978-1-4939-2495-0\\_4](https://doi.org/10.1007/978-1-4939-2495-0_4) (2015).
76. Brun, F. *et al.* Enhanced and Flexible Software Tools for X-ray Computed Tomography at the Italian Synchrotron Radiation Facility Elettra. *Fundamenta Informaticae* **141**, 233–243, <https://doi.org/10.3233/FI-2015-1273> (2015).

## Acknowledgements

This research was carried out under the project CEITEC 2020 (LQ1601) with financial support from the Ministry of Education, Youth and Sports of the Czech Republic under the National Sustainability Programme II and CEITEC Nano Research Infrastructure (MEYS CR, 2016–2019). M.K. was funded by the SSMF fellowship. The authors acknowledge Elettra for access to synchrotron radiation computed microtomography facilities. J.K. and M.T. acknowledge the support of the Brno University of Technology with the grant FSI-S-17–4506. D.K. acknowledges the support of CEITEC Brno University of Technology with the grant FSI/STI-J-18–5337. We are grateful to the staff of SYRMEP for the experimental support during the experiments and to Adam Břínek who helped with the experiments at the synchrotron facility.

## Author Contributions

A.S., I.A., and J.K. designed the experiments. M.K., A.E. and B.S. prepared the samples and stained them for  $\mu$ CT measurement. Conventional  $\mu$ CT experiments were performed by M.T., M.N. and D.K., synchrotron  $\mu$ CT experiments were performed by M.T., L.M., D.K. and T.Z. Data analysis was done by M.T., L.M. and G.L. Biological part was discussed by I.A. and Y.Z. The manuscript was written by M.T., L.M., I.A. and J.K. All authors reviewed the manuscript.

## Additional Information

**Supplementary information** accompanies this paper at <https://doi.org/10.1038/s41598-018-32459-2>.

**Competing Interests:** The authors declare no competing interests.

**Publisher's note:** Springer Nature remains neutral with regard to jurisdictional claims in published maps and institutional affiliations.



**Open Access** This article is licensed under a Creative Commons Attribution 4.0 International License, which permits use, sharing, adaptation, distribution and reproduction in any medium or format, as long as you give appropriate credit to the original author(s) and the source, provide a link to the Creative Commons license, and indicate if changes were made. The images or other third party material in this article are included in the article's Creative Commons license, unless indicated otherwise in a credit line to the material. If material is not included in the article's Creative Commons license and your intended use is not permitted by statutory regulation or exceeds the permitted use, you will need to obtain permission directly from the copyright holder. To view a copy of this license, visit <http://creativecommons.org/licenses/by/4.0/>.

© The Author(s) 2018

PAPER [IX]

Article

# Complete Ring Artifacts Reduction Procedure for Lab-Based X-ray Nano CT Systems

Jakub Šalplachta <sup>1</sup>, Tomáš Zikmund <sup>1</sup>, Marek Zemek <sup>1</sup>, Adam Břínek <sup>1</sup>, Yoshihiro Takeda <sup>2</sup>, Kazuhiko Omote <sup>2</sup> and Jozef Kaiser <sup>1,\*</sup>

<sup>1</sup> CEITEC—Central European Institute of Technology, Brno University of Technology, Purkyňova 656/123, 612 00 Brno, Czech Republic; jakub.salplachta@ceitec.vutbr.cz (J.Š.); tomas.zikmund@ceitec.vutbr.cz (T.Z.); marek.zemek@ceitec.vutbr.cz (M.Z.); adam.brinek@ceitec.vutbr.cz (A.B.)

<sup>2</sup> Rigaku Corporation, 3-9-12, Matsubara-cho, Akishima-shi, Tokyo 196-8666, Japan; y-takeda@rigaku.co.jp (Y.T.); omote@rigaku.co.jp (K.O.)

\* Correspondence: jozef.kaiser@ceitec.vutbr.cz

**Abstract:** In this article, we introduce a new ring artifacts reduction procedure that combines several ideas from existing methods into one complex and robust approach with a goal to overcome their individual weaknesses and limitations. The procedure differentiates two types of ring artifacts according to their cause and character in computed tomography (CT) data. Each type is then addressed separately in the sinogram domain. The novel iterative schemes based on relative total variations (RTV) were integrated to detect the artifacts. The correction process uses the image inpainting, and the intensity deviations smoothing method. The procedure was implemented in scope of lab-based X-ray nano CT with detection systems based on charge-coupled device (CCD) and scientific complementary metal-oxide-semiconductor (sCMOS) technologies. The procedure was then further tested and optimized on the simulated data and the real CT data of selected samples with different compositions. The performance of the procedure was quantitatively evaluated in terms of the artifacts' detection accuracy, the comparison with existing methods, and the ability to preserve spatial resolution. The results show a high efficiency of ring removal and the preservation of the original sample's structure.

**Keywords:** ring artifacts reduction; CCD detector; sCMOS detector; high-resolution X-ray computed tomography; relative total variation



**Citation:** Šalplachta, J.; Zikmund, T.; Zemek, M.; Břínek, A.; Takeda, Y.; Omote, K.; Kaiser, J. Complete Ring Artifacts Reduction Procedure for Lab-Based X-ray Nano CT Systems. *Sensors* **2021**, *21*, 238. <https://doi.org/10.3390/s21010238>

Received: 7 December 2020

Accepted: 23 December 2020

Published: 1 January 2021

**Publisher's Note:** MDPI stays neutral with regard to jurisdictional claims in published maps and institutional affiliations.



**Copyright:** © 2021 by the authors. Licensee MDPI, Basel, Switzerland. This article is an open access article distributed under the terms and conditions of the Creative Commons Attribution (CC BY) license (<https://creativecommons.org/licenses/by/4.0/>).

## 1. Introduction

In the field of high-resolution X-ray computed tomography (CT) with a micron and submicron spatial resolution, reconstructed CT data are often affected by severe ring artifacts. They appear as concentric ring-like features superimposed on the imaged scene and are centered on the object's center of rotation creating either full rings (full scan over 360°) or half rings (half scan over 180°) [1]. Ring artifacts are mainly caused by imperfect detector pixels, where a perfect pixel's response should be linearly proportional to the amount of photons incident on the detector. There are many different underlying causes for individual pixels to have imperfect responses. These include defects in the scintillator, the detector itself, and the readout electronics [2]. Moreover, the detector responses may vary due to numerous time-dependent drifts, such as thermal drifts, and also due to changes in the X-ray spectrum [2]. No matter the cause, ring artifacts degrade the resulting image quality. Therefore, it is desirable to remove or at least significantly reduce the presence of ring artifacts in CT data.

Ring artifacts reduction methods can be divided into three approaches. The first is based on a flat-field correction of a detector [3]. The proper flat-field correction should ideally remove all the detector sensitivity variations [4]. However, ring artifacts may persist after this correction due to the detector pixels intensity dependencies and non-linear

response functions, or due to time-dependent non-uniformities of the incident beam [5]. To overcome these issues, advanced flat-field correction approaches were proposed in several recent works [2,4,6,7]. However, such sophisticated flat-field methods are not easily applicable in practice, because they require specific CT acquisition scenarios, and precise knowledge of used detection system is needed.

Second approach is the hardware-based ring artifacts reduction method. This method is based on moving the detector system in defined horizontal steps during the CT acquisition so that the object is projected on different regions of the detector during a CT scan [8]. Through this, the effect of non-uniform detector responses is suppressed. Although the practical functionality of this method was reported in [9] and [10], this procedure's disadvantage is reducing the spatial resolution of the CT data if the detector shifts are not accurately known [2] or the movement precision is worse than the used detector pixel size. In general, this method is hardly applicable in nano CT systems due to such demanding requirements on the movement precision.

The third approach for the ring artifacts reduction are the image-based processing methods. These methods can be further divided, based on the domain of processed data, to sinogram-based (sinogram pre-processing) and tomogram-based (CT data post-processing) methods [11]. Sinogram-based methods work directly with the sinogram data, where the ring artifacts appear as straight lines in a vertical direction and are therefore easier to detect and to process. Some of these methods assume the presence of a specific high-frequency component that is directly related to the ring artifacts. Therefore, they aim to filter out the artifacts using low pass filters [12–15]. Most of these, however, fail to remove the strong artifacts related to dead detector elements or damaged areas on the scintillator, in which case they create an extra band around the original ring [10]. To overcome this, other methods first detect the ring artifacts elements and then correct them using various approaches: image inpainting [1,16–18] moving average and weighted moving average filters [19–21], sensitivity equalization [22]. However, even these methods have their limitations. Most of these methods are only suitable for suppressing a certain type of stripe. Moreover, they are generally difficult to use in practice due to many parameters needing to be adjusted when a wrong selection of parameters significantly affects the resulting quality. However, the work of Anas [16] can be pointed out because it introduced a novel idea for classifying rings based on their statistical properties and for addressing each type separately.

On the contrary, the tomogram post-processing methods work with CT data after the tomographic reconstruction. These methods often use a conversion of the data from Cartesian to the polar coordinate system. After this conversion, the ring artifacts appear as stripes that can be further processed using similar assumptions and strategies as for sinogram-based methods [23–27]. One method from these can be pointed out, Liang [26] proposed a novel ring artifacts reduction approach integrating benefits of an efficient iterative framework together with relative total variations (RTV) algorithm for the texture extraction. However, this method uses a simple mean values analysis to detect and correct the artifacts, which is insufficient in the case of dead detector elements or damaged areas on the scintillator. Moreover, tomogram-based methods are, in general, strongly dependent on the quality of the used tomographic reconstruction because some extra artifacts might be created [20]. Therefore, a novel class of methods lying between sinogram-based and tomogram-based approaches has been recently developed. The ring artifacts reduction is addressed directly during the reconstruction process using specific forms of regularizations (e.g., [11,28,29]). Such regularizations can, however, be highly computationally demanding, which limits the practical applicability of those methods.

In this article, we present a new ring artifacts reduction procedure that combines several selected ideas from image-based processing methods into one complex sinogram-based method with a goal to overcome all previously mentioned limitations. The ring artifacts are classified into two types based on their cause and actual appearance in the CT data. We prefer to separate the detection and correction schemes for each type of artifact

for their effective removal. We propose a two-step iterative correction scheme that deals with all the artifact types in the sinogram domain. Consequently, a significant influence of tomographic reconstruction on the efficiency of artifacts reduction is avoided. The reduction strategy was optimized for each artifact type separately to preserve the spatial resolution and sample's structural information, which are the most important factors in the field of nano-tomography. Practical functionality of the proposed method was verified on both synthetic data and real CT data. It shows a high efficiency of ring artifacts removal, and a robustness to character of input data and used detection system in context of other tested ring artifacts correction techniques.

## 2. Materials and Methods

In this article, a two-step ring artifacts reduction scheme is proposed. This scheme was developed for the artifacts' reduction in the sinogram domain and is based on a categorization of ring artifacts into two types. The ring artifacts are categorized based on the observation of responses from different kinds of deficiencies in sinograms and on their specific hardware causes (see Figure 1). In the proposed reduction scheme, each of these classes is then addressed separately using dedicated detection and reduction procedures. In the first step, the most prominent ring artifacts (high-level artifacts) are corrected, and subsequently weak artifacts (low-level artifacts) are corrected in the second step.

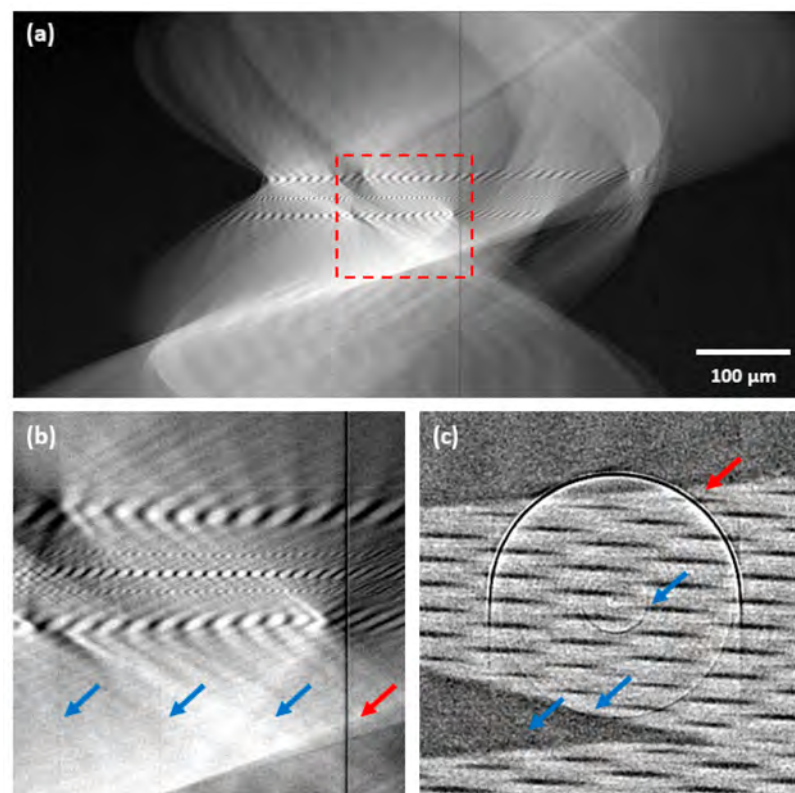


**Figure 1.** Example of ring artifacts affected data—glass capillary sample acquired with a charge-coupled device (CCD)-based camera: (a) sinogram; (b) detail of sinogram central area; (c) central area of corresponding tomogram. Red arrows indicate the high-level ring artifacts and blue arrows the low-level ring artifacts.

### 2.1. High-Level Ring Artifacts

The class of high-level ring artifacts (HRA) is represented by the most prominent stripes in the sinograms (see Figure 1). The actual cause of such artifacts is two-fold. One cause originates from entirely dead detector pixels or damaged areas on the scintillator. The behavior of these pixels then does not follow the pattern of responses of adjacent

non-defective elements. Their responses are close or equal to the saturation level of the detector (maximum of the dynamic range) or the minimum of the dynamic range. The second cause is related to so-called “hot pixels”, which may be considered as a type of fixed pattern noise [30]. They are defined as pixels with the dark current values significantly above the average. They follow the responses of the adjacent non-defective pixels but with significant deviations that do not vary in time. In the sinograms, they appear as prominent stripes, but they do not reach the extremes of the dynamic range.

### High-Level Ring Artifacts Removal

The reduction in high-level ring artifacts is divided into two parts: first, the artifacts' positions are detected, and second, the input sinogram is corrected at these positions. For the artifacts' detection, an iterative detection scheme was designed. This detection procedure consists of 5 steps (see Figure 2) that are iteratively repeated until any of 4 stopping conditions is fulfilled. These steps are:

#### 1. Texture extraction

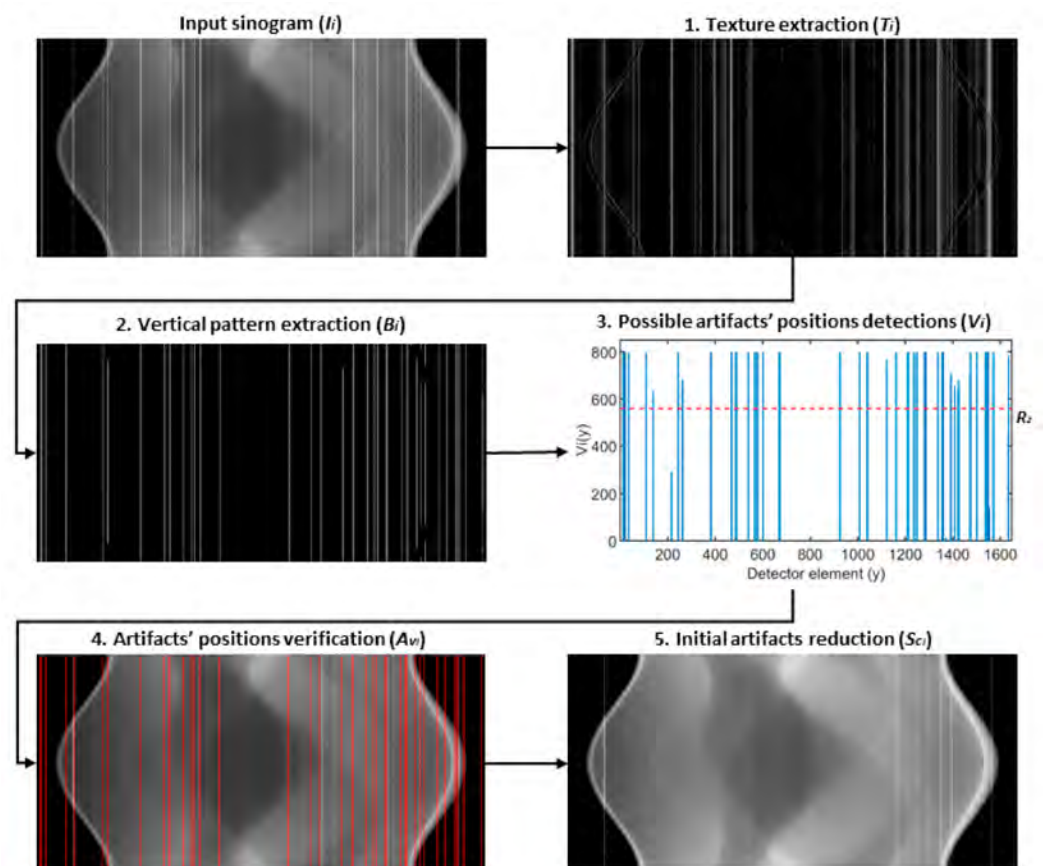


**Figure 2.** Illustrative scheme of proposed high-level ring artifacts detection scheme—as example images, the outputs from the first iteration are shown.

Ring artifacts, together with the structural details, are considered as a texture of sinogram. Therefore, textural information is first extracted using the subtraction of input sinogram and its smoothed version (i.e., image after texture removal):

$$T_i = I_i - S_{s,i}, \quad (1)$$

where  $T_i$  is extracted texture image in the current iteration  $i$ ,  $I_i$  is input sinogram in the current iteration  $i$  and  $S_{s,i}$  is input sinogram after the texture removal. For texture removal, an algorithm based on relative total variation (RTV) is used (for more details see the

Appendix A section). After the texture extraction in the current iteration, the first stopping condition (SC 1) is evaluated:

$$\frac{\|T_i - T_{i-1}\|_2}{\|T_1\|_2} \leq R_1, \quad (2)$$

where  $T_i$  is extracted texture image in the current iteration  $i$ ,  $T_{i-1}$  is extracted texture image in the previous iteration,  $T_1$  is extracted texture image in the first iteration, and  $R_1$  is a selected threshold value. Using this stopping condition, the iteration is stopped when the normalized L2 norm of the difference between two sequential extracted textures is equal or lower than the set value  $R_1$ .

## 2. Vertical pattern extraction

The extracted texture image from the previous step is further convolved:

$$P_i = T_i * k, \quad (3)$$

with a convolution kernel  $k$  that corresponds to one-dimensional (1D) vertical mean filter with the length  $l$ . This is done to highlight a vertical stripe pattern (e.g., ring artifacts) and to blur remaining non-vertical structures. Then, the first derivative is approximated by finite differences in the horizontal direction, and the result is binarized row-by-row by thresholding with a threshold value set to a double of the calculated standard deviation of a given row:

$$B_i(x, y) = \begin{cases} 1, & \text{if } \Delta_x P_{ix}(y) > 2 \cdot \sigma_{\Delta_x P_{ix}} \\ 0, & \text{otherwise} \end{cases}, \quad (4)$$

where  $B_{i(x,y)}$  corresponds to the value of resulting binary mask in the current iteration  $i$  at coordinates  $x, y$  and  $\sigma$  is used notation for standard deviation.

## 3. Possible artifacts' positions detections

The binary mask is then summed in the column direction:

$$V_i(y) = \sum_{x=1}^M B_i(x, y), \quad (5)$$

where  $V_{i(y)}$  refers to value of the resulting vector at position  $y$  and  $M$  refers to number of rows in the binary mask  $B_i$ ,  $x$  and  $y$  refer to vertical and horizontal indices, respectively. In the resulting vector, only elements with values above threshold  $R_2$  are considered as possible candidates for positions of ring artifacts  $A_p$ :

$$A_{pi}(y) = \begin{cases} 1, & \text{if } V_i(y) > R_2 \\ 0, & \text{otherwise} \end{cases} \quad (6)$$

However, the inevitable RTV smoothing errors may negatively affect this detection. To avoid this, the distances between possible detected artifacts are also analyzed. When the distance between two neighboring possible artifacts' positions is below threshold  $R_3$ , the intermediate positions are also considered as the possible artifacts' positions. In this step, the second stopping condition (SC 2) is evaluated, the iteration is stopped when no possible artifacts' positions are detected.

## 4. Artifacts' positions verification

Verification of detected possible artifacts' positions  $A_p$  is achieved by the analysis of mean column vector  $L_{T_i}$  of extracted textural information  $T_i$  in the current iteration  $i$ . Possible artifact positions  $A_p$  are considered as verified  $A_v$ , if they meet the following condition:

$$A_{vi}(y) = \begin{cases} 1, & \text{if } |L_{T_i}(A_{pi}(y)) - L_{T_i}(A_{pi}(y_x))| > 2 \cdot \sigma_{\Delta L_{T_i}} \\ 0, & \text{otherwise} \end{cases} \quad (7)$$

where  $A_{p_i}(y_x)$  is the nearest artifact-free position to analyzed possible artifacts' position  $A_{p_i}(y)$  and the threshold value corresponds to twice the standard deviation value of the first derivative of  $L_{T_i}$ , which is approximated by finite differences. If no possible artifacts' positions are considered as verified, the iteration is stopped (the third stopping condition—SC 3). On the other hand, when certain positions are verified in the current iteration  $i$ , they are then compared to the verified positions from previous iterations and if no new verified artifacts' position is detected, the iteration is stopped (the fourth stopping condition—SC 4).

### 5. Initial artifacts reduction

In each iteration, the sinogram is corrected at new verified artifacts' positions. This is achieved by filling the sinogram at artifacts' positions by means of image inpainting. In our work, this is completed by using a partial differential equation (PDE)-based approach, where Laplace equation is solved with the Dirichlet boundary condition:

$$S_{C_i} = \begin{cases} \nabla^2 u = 0, & \text{for } A_{v_i} \\ u(x, y) = I_i(x, y), & \text{on } \partial A_{v_i} \end{cases} \quad (8)$$

where  $S_{C_i}$  corresponds to corrected sinogram in the current iteration  $i$ .

After the termination of the detection procedure, the final artifacts reduction is conducted. In this step, the previously described inpainting scheme is used again, and the input sinogram is corrected at the detected ring artifacts' positions  $A_v$ . The implementation details and used parameters can be found in Appendix C (Table A3).

### 2.2. Low-Level Ring Artifacts

Low-level ring artifacts (LRA) are caused by miscalibrated detector pixels. Their sensitivity deviations result from higher or lower dark current values compared to the non-defected pixels. They follow the responses of the adjacent non-defective pixels but with certain deviations. In the sinogram (see Figure 1), their presence is not distinct from the non-defective pixels as the HRA, but they still negatively affect the data quality.

#### Low-Level Ring Artifacts Removal

The main idea of the proposed algorithm for LRA removal is that column-wise neighboring homogenous areas (i.e., areas at same vertical positions of two adjacent columns) from extracted texture should ideally (without any artifact) have the same average values. To achieve this, an iterative procedure was proposed (see Figure 3), consisting of these steps:

#### 1. Texture extraction

For the texture extraction, the same procedure as in high-level ring artifacts removal (Equation (1)) is used with the same stopping condition (Equation (2)) set to the threshold value  $R_1$ . To reduce the presence of noise and its negative effect on the subsequent analysis, the extracted texture is further filtered with a 1D pixel-wise adaptive low-pass Wiener filter in column-wise direction:

$$T_{f_i} = T_i * w, \quad (9)$$

where  $T_i$  is extracted texture in current iteration  $i$ ,  $w$  is kernel of 1D Wiener filter with the length  $l$  and  $T_{f_i}$  is the noise reduced texture, which is used only within steps 2 and 3.

#### 2. Homogenous areas detection

Homogenous texture areas are detected column-wise using the following formula:

$$H_i(x, y) = \begin{cases} 1, & \text{if } T_{f_i}(x, y) \leq \overline{T_{f_i}(1 : M, y)} \\ 0, & \text{otherwise} \end{cases}, \quad (10)$$

where  $y$  is the coordinate of analyzed column,  $H_i(x, y)$  corresponds to the value of resulting binary mask in the current iteration  $i$  at coordinates  $x, y$  and  $M$  is the number of sinogram rows.

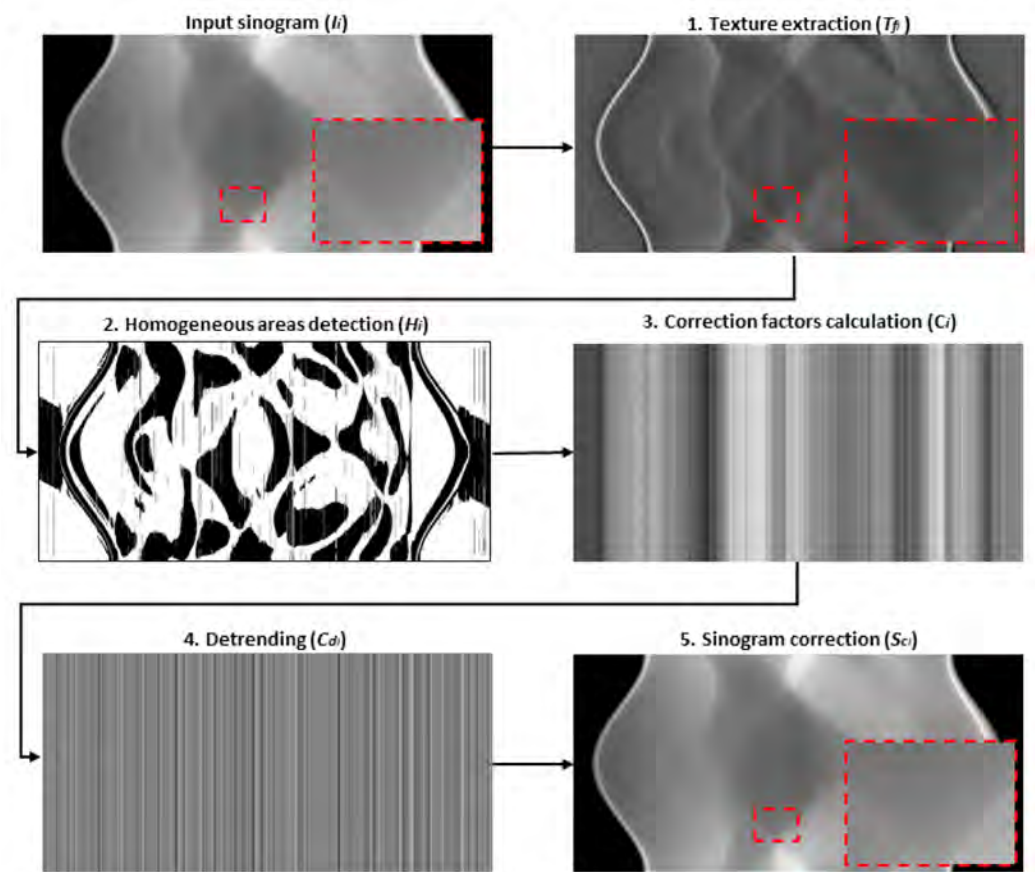


**Figure 3.** Illustrative scheme of the proposed low-level ring artifacts removal procedure—the outputs from the first iteration are shown as examples.

### 3. Correction factors calculation

Correction factors for sinogram columns are calculated from extracted texture  $T_{fi}$  by comparing two neighboring columns in terms of average intensity values of their neighboring homogenous areas. The column with smaller index is always taken as a reference, and other column is then corrected using the following equation:

$$T_{fi}(1 : M, y) = T_{fi}(1 : M, y) + C_i(y), \quad (11)$$

where  $C_i(y)$  is a correction factor for column  $y$  in the current iteration  $i$ :

$$C_i(y) = \left( \frac{\sum_{j=1}^{N_h} T_{fi}(h, y-1)}{N_h} - \frac{\sum_{j=1}^{N_h} T_{fi}(h, y)}{N_h} \right), \quad (12)$$

where  $h$  is  $x$  coordinates of neighboring homogenous areas in analyzed columns (at coordinates  $y$  and  $y-1$ ),  $h$  is those coordinates where  $H_y = 1 \wedge H_{y-1} = 1$ , and  $N_h$  is the number of those positions. If  $N_h = 0$ , the correction factor for the previous column ( $C_{y-1}$ ) is used.

### 4. Detrending

Calculated correction factors in the previous step can successfully reduce the artifacts, but the overall structural trend of the extracted texture is also lost. To avoid this, the Savitzky-Golay filter [31] is used to extract this trend from the calculated correction factor values:

$$t = C_i * s, \quad (13)$$

where  $s$  is the 1D kernel of the Savitzky-Golay filter with polynomial order  $r$  and frame length  $f$ . The value of this parameter  $f$  is decreasing with each iteration by power of two—by this the over-smoothing effect is avoided. Subsequently, this trend is subtracted from the calculated correction factors:

$$C_{d_i} = C_i - t, \quad (14)$$

to ensure that only the artifacts are reduced while the overall structural pattern of the textural information is preserved.

### 5. Sinogram correction

In each iteration  $i$ , the corrected sinogram  $S_C$  is calculated as the sum of the smoothed sinogram  $S_s$  (i.e., sinogram after texture removal) and the extracted texture after an artifact reduction:

$$S_{C_i} = S_{s_i} + (T_i + C_{d_i}). \quad (15)$$

These steps are repeated until the stopping condition described by Equation (2) is fulfilled. The implementation details and used parameters can be found in Appendix C (Table A4).

### 2.3. Real CT Data Acquisition

A laboratory-based CT system Rigaku nano3DX [32] was used for CT measurements. For purposes of our study, this CT system was equipped with a Rigaku's scientific X-ray CDD camera (XSight™ Micron LC X-ray CCD camera [33]) and a scientific X-ray scientific complementary metal-oxide-semiconductor (sCMOS) camera (XSight™ Micron LC X-ray sCMOS camera [34]), nominal parameters of used cameras are stated in Table A2 in Appendix B. As it was shown in our previous study [35], radiographic data acquired by tested charge-coupled device (CCD) and sCMOS cameras mainly differ in projection domain in terms of the population of hot pixels that mostly correspond to high-level ring artifacts. As samples, a glass capillary array (pores diameter: 3 μm) and a ruby ball (diameter: 300 μm) were selected. They were scanned using circular trajectory with an angular range from 0 to 180 degrees with an acquisition of 800 projection images for one CT scan. Molybdenum rotatory target was used (50 kV and 24 mA) for all the measurements. Exposure times for X-ray projection data were selected following the manufacturer's recommendations (based on the level of detected signal). Specifically, the exposure times for glass capillary array measurements were 16 s (CCD) and 6 s (sCMOS), and they were 13 s (CCD) and 4.5 s (sCMOS) for ruby ball measurements. Acquired projection data were only flat-field corrected before the ring artifacts reduction was applied. Subsequently, CT data were reconstructed using ASTRA toolbox [36]—filtered back projection (FBP) reconstruction with cosine filter. Then, all the data were normalized so that the minimum and maximum values were 0 and 1 arbitrary units, respectively. The achieved linear voxel size values for binning 2 × 2 were 0.53 μm and 0.63 μm for the CCD and sCMOS cameras, respectively.

### 2.4. Synthetic Data Creation

Three synthetic images were used in this work, representing various levels of data complexity—a ball phantom (single material sample), a Shepp-Logan phantom (multi material sample) and a Siemens star phantom (highly complex sample). Phantom images were generated in tomogram domain (see Figure 4) and then transformed by Radon transform to sinogram domain, using the ASTRA Tomography Toolbox [36]. The sinograms were simulated to have similar parameters as those acquired by nano3DX device equipped with a CCD camera, specifically to have a linear voxel size of 0.53 μm, a detector width of 1648 pixels and to follow the acquisition of 800 projection angles from an angular range of 0° to 180°. Gaussian distributed noise with a standard deviation of 0.01 (reflects noise properties of real projection data) was also added to generated sinograms.

The ring artifacts were simulated (see Figure 5) and added to the sinograms (see Figure 6). In total, 25% of detector elements were affected by artifacts: 5% HRA and

20% LRA. The artifacts' positions were generated randomly without any recurrences. As for high-level artifacts, one fifth of affected positions was assigned the intensity value (referring to detector response) equal to the maximum of used dynamic range (16bit), which corresponds to dead, unresponsive detector pixels. The remaining high-level artifacts' positions were assigned the intensity deviations generated as uniformly distributed random numbers from the interval from 10% to 60% of maximum sinogram intensity value. The intensity deviations of low-level artifacts were generated similarly but from the interval  $\pm 1\%$  of maximum sinogram intensity value. Such deviations were then added to the original responses at given artifacts' positions. Using such parameters, an extreme case of ring artifacts presence in sinogram was simulated.



**Figure 4.** Synthetic data used for testing and validation of all tested methods: (a) ball phantom; (b) Shepp-Logan phantom; (c) Siemens star phantom.

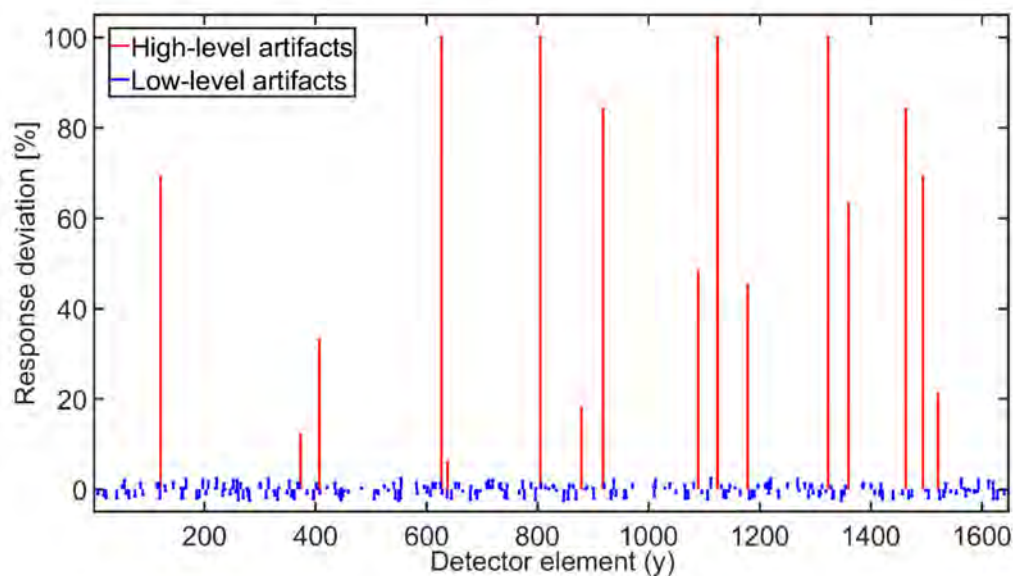


**Figure 5.** Example of simulated response deviations of detector elements representing the ring artifacts.

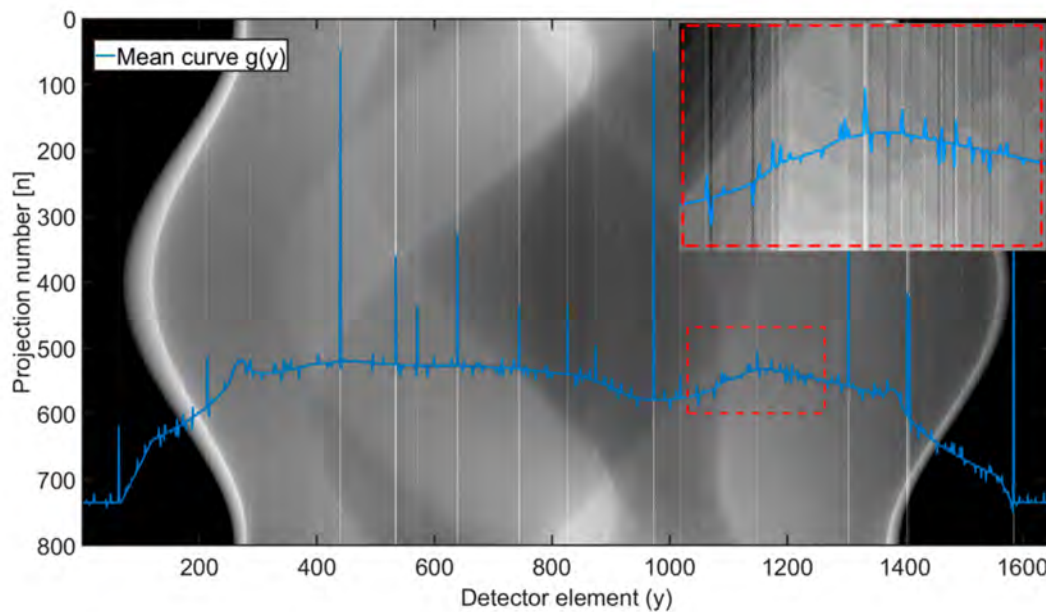


**Figure 6.** Shepp-Logan phantom sinogram affected by simulated ring artifacts presented in Figure 5. Blue curve shows mean column values—the highest peaks belong to high-level ring artifacts (HRA). In the red labelled image, the magnified area affected by low-level ring artifacts (LRA) is shown.

### 2.5. Other Methods

The performance of the proposed method was compared to three other selected approaches from the class of sinogram-based methods: the wavelet-Fourier-transform-based method by Münch [13], correction vector-based method by Eldib [15] and complex correction technique by Vo [21]. For notational simplicity, these methods are further called M1, M2 and M3, respectively. Since the performance of all the methods is highly dependent on specific settings, the optimal parameters for each method were selected to ensure a relevant and fair comparison. This was completed based on the suggestions in the original works and also based on the practical testing on synthetic data using a combination of both qualitative and quantitative evaluation (brute-force search with structural similarity index (SSIM) [37] as a validation metric). To test the consistency of these parameters within various test samples, only one specific setting was used for each of the methods (see Table A5).

### 2.6. Evaluated Criteria and Metrics

The proposed method was tested on both synthetic and real high-resolution CT data. Three criteria were considered for the evaluation. First, the proposed method was tested in terms of artifacts detection accuracy focused on the HRA detection. For this evaluation, three statistical metrics were used: true positive rate (TPR—ratio of correctly detected artifacts' positions to all positions labelled as artifacts) [38], positive predictive value—precision (PPV—percentage of artifacts' positions that were correctly detected) [39] and Dice similarity coefficient (DSC) [40].

Then, the overall performance of the proposed method was evaluated in context of other ring artifacts correction methods. This was completed both quantitatively using synthetic data with ground truth images and qualitatively on real CT data. For the quantitative performance evaluation, two metrics were used: the peak signal-to-noise ratio (PSNR), and structural similarity index (SSIM) [37]. These were calculated between the corrected tomogram (tomogram reconstructed from the ring artifacts corrected sinogram) and the ground truth tomogram (tomogram reconstructed from the corresponding sinogram without ring artifacts). The resulting tomogram data were first standardized to Z-scores, i.e., mean value was subtracted from the data and the result was divided by the corresponding standard deviation. This was completed so that the possible effect of intensity shifts on

corrected data could be eliminated. It was possible to precisely evaluate the functionality of ring artifacts reduction and also the effect of distortion on the data.

The lastly considered criterion focused on the robustness of the proposed ring artifacts reduction procedure to the used detection system, and on its effect on achieved spatial resolution. For the spatial resolution calculation, the modulation transfer function (MTF) analysis [41] was used following the procedure defined in ASTM E1695-95(2013) standard [42]. CT data of the ruby ball sample, acquired by both CCD- and sCMOS- based cameras, were used for this analysis.

### 3. Results

#### 3.1. HRA Detection Accuracy of Proposed HRA Detection Scheme

The accuracy of the proposed HRA detection scheme was evaluated on the synthetic data with known artifacts' positions. The results are stated in Table 1. For all the phantom images, the proposed method was able to classify all the artifacts' positions with a precision above 95%. However, a certain amount of artifacts' positions, out of total 82 artifacts' positions, was not detected in all the cases: two artifacts' positions for Shepp-Logan and Siemens star phantoms, and three positions in the case of ball phantom. For Siemens star phantom, a higher number of falsely classified artifacts' positions led to a PPV score of 84.21% and DSC of 90.40%. On the contrary, for Shepp-Logan phantom, all the positions classified as artifacts were correct (PPV = 100%).

**Table 1.** Proposed HRA detection scheme accuracy—evaluated for synthetic data.

	Ball	Shepp-Logan	Siemens Star
TPR [%]	96.34	97.56	97.56
PPV [%]	96.34	100.0	84.21
DSC [%]	96.34	98.77	90.40

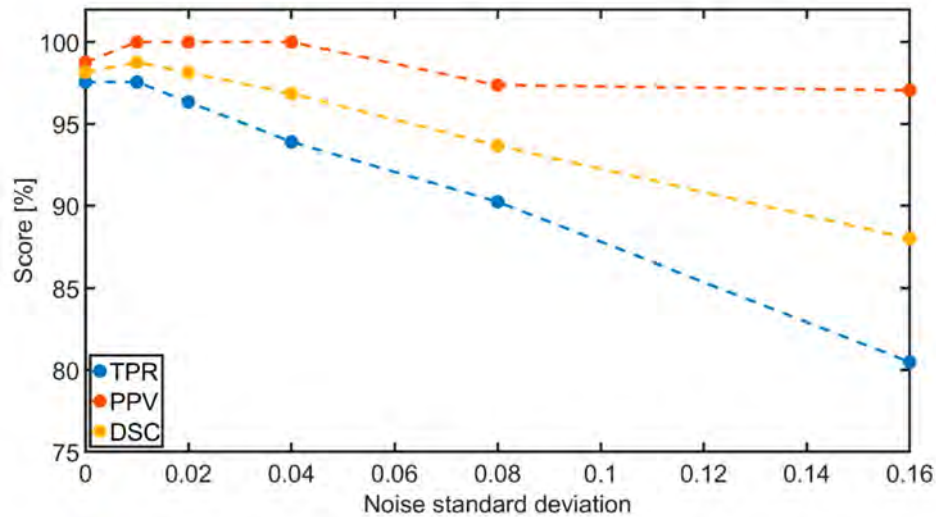
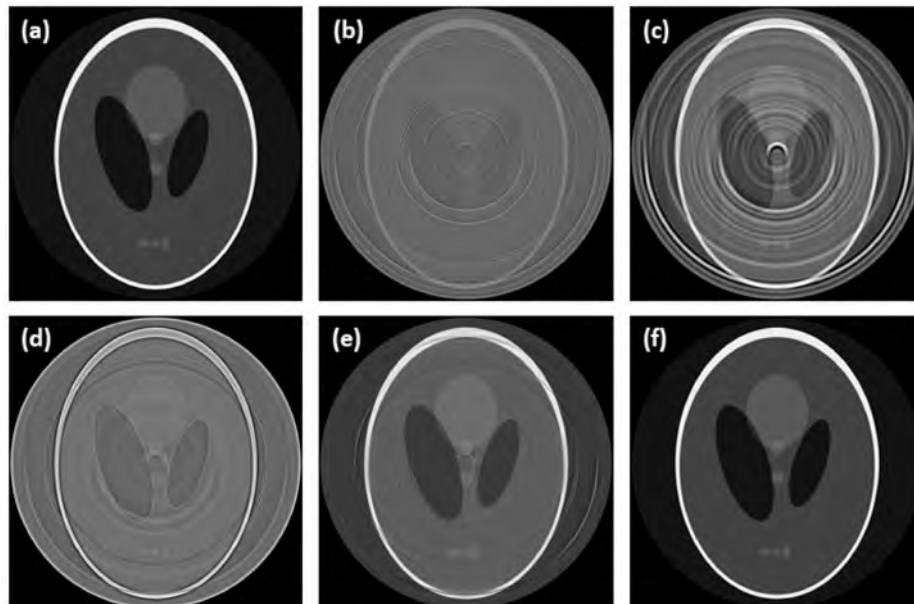
We further evaluated the effect of noise level in the data on the detection accuracy of proposed HRA detection scheme (tested on Shepp-Logan phantom). Results of this analysis are shown in Figure 7. The precision of artifacts' detection was found almost independent of the noise presence, reaching values above 95% for all tested cases. However, a direct proportion was found between the noise level and the number of artifacts' positions that were not detected. This tendency is expressed by both the TPR and DSC metrics. Despite this tendency, the proposed HRA detection scheme resulted in scores of both metrics above 80% even for cases with a severe noise presence.

#### 3.2. Overall Performance Evaluation in Context of Other Tested Methods

A high ring artifacts presence in the synthetic data made their correction very challenging, which is reflected by the poor results of the tested methods (Table 2). Apart from the proposed method, all the tested methods failed to successfully reduce the artifacts, especially the population of HRA, and to preserve the structural information (see Figure 8). The overall worst results were achieved by the M2 method. Especially in case of the ball phantom, the M2 method failed to distinguish the artifacts and sample structure. It led to an almost complete suppression of structural information (see Figure 9), which is further represented by a negative SSIM value (Table 2). In the case of the M1 method, a poor correction led to wide rings and blurring the overall image structures (see Figure 8). The M3 method results were visually good, and most of the artifacts were successfully reduced (see Figure 8). However, the quantitative evaluation (Table 2) revealed a poor input data preservation in terms of structural information and intensity values. This effect is further demonstrated in Figure 10 by histogram analysis of the Shepp-Logan phantom tomogram. Unlike the proposed method, the M3 method led to a significant transformation of histogram shape and Z-score range compared to the reference data. Compared to all other methods, the proposed method obtained the best results, as all the artifacts were reduced, and the sample structure was fully preserved (see Figures 8–10).

**Table 2.** Quantitative performance evaluation of tested methods.

	Ball		Shepp-Logan		Siemens-Star	
	PSNR [dB]	SSIM	PSNR [dB]	SSIM	PSNR [dB]	SSIM
M1	7.59	0.39	3.95	0.29	3.66	0.22
M2	1.03	−0.03	1.81	0.27	3.21	0.21
M3	11.39	0.47	1.91	0.22	3.30	0.20
Proposed	27.48	0.97	28.45	0.97	11.17	0.72

**Figure 7.** Dependence of the accuracy of the proposed HRA detection scheme on the noise level—evaluated for Shepp-Logan phantom.**Figure 8.** Comparison of tomograms after ring artifacts reduction by tested methods—simulated data of Shepp-Logan phantom: (a) reference; (b) original (without any correction); (c) M1; (d) M2; (e) M3; (f) proposed. For visualization, the same contrast setting was used for all the images.

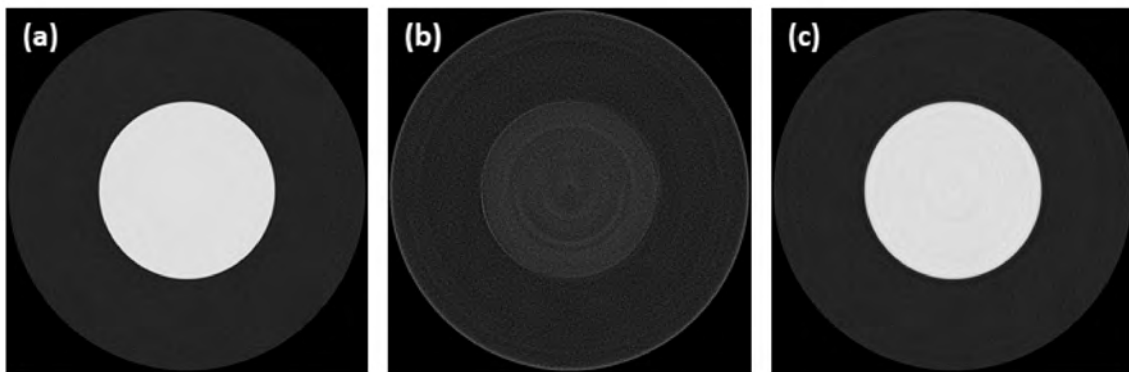


**Figure 9.** Comparison of data distortion between the proposed method and M2 method—tomograms of ball phantom: (a) reference; (b) M2 method; (c) proposed. For visualization, the same contrast setting was used for all the images.

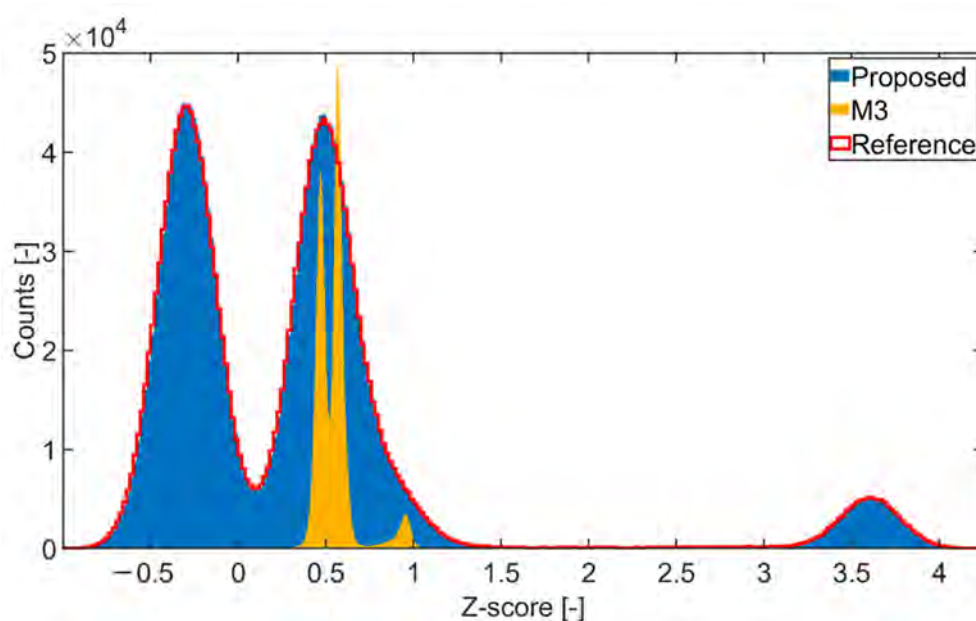


**Figure 10.** Comparison of data distortion between the proposed method and M3 method—histogram analysis of standardized tomogram values.

The overall performance of the tested methods was further evaluated on real CT data. From the resulting tomograms, the effectiveness of the tested methods was evaluated qualitatively using visual perception. For visualization purposes, the glass capillary array data acquired by a CCD camera were selected due to the presence of prominent HRA in the central area (see Figure 11). Apart from the proposed method, the other methods only reduced the HRA to a certain degree, leaving the artifacts still detectable after the correction. Moreover, in the case of the M3, some extra artifacts were created during the correction (see Figure 11e).

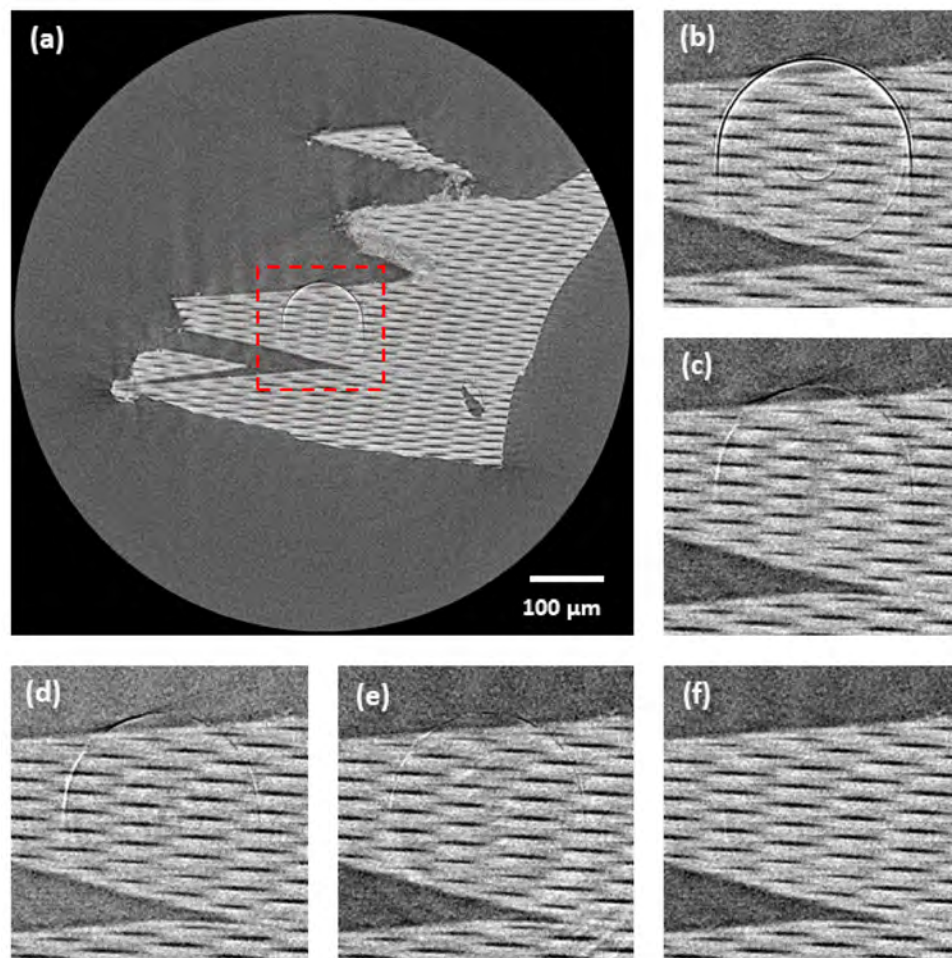


**Figure 11.** Comparison of tomograms after ring artifacts reduction by tested methods—real computed tomography (CT) data of glass capillary array acquired with a CCD-based camera: (a) original tomogram (without any correction)—red labelled area marks central area visualized in following images; (b) original; (c) M1; (d) M2; (e) M3; (f) proposed. For visualization, the same contrast setting was used for all the images.

### 3.3. Spatial Resolution Preservation and Robustness to Used Detection System

The results of the spatial resolution evaluation are stated in Table 3. The proposed method was able to preserve the spatial resolution within the accuracy limit of the used standard for both used detection systems. The robustness is further visually demonstrated in Figure 12. The proposed method in this example reduced all the ring artifacts without any negative effect or distortion on the data regardless of the used detection system.

**Table 3.** Results of spatial resolution evaluation.

	CCD	sCMOS
Original	$0.62 \mu\text{m} \pm 0.03 \mu\text{m}$	$0.85 \mu\text{m} \pm 0.04 \mu\text{m}$
Proposed	$0.62 \mu\text{m} \pm 0.03 \mu\text{m}$	$0.82 \mu\text{m} \pm 0.04 \mu\text{m}$

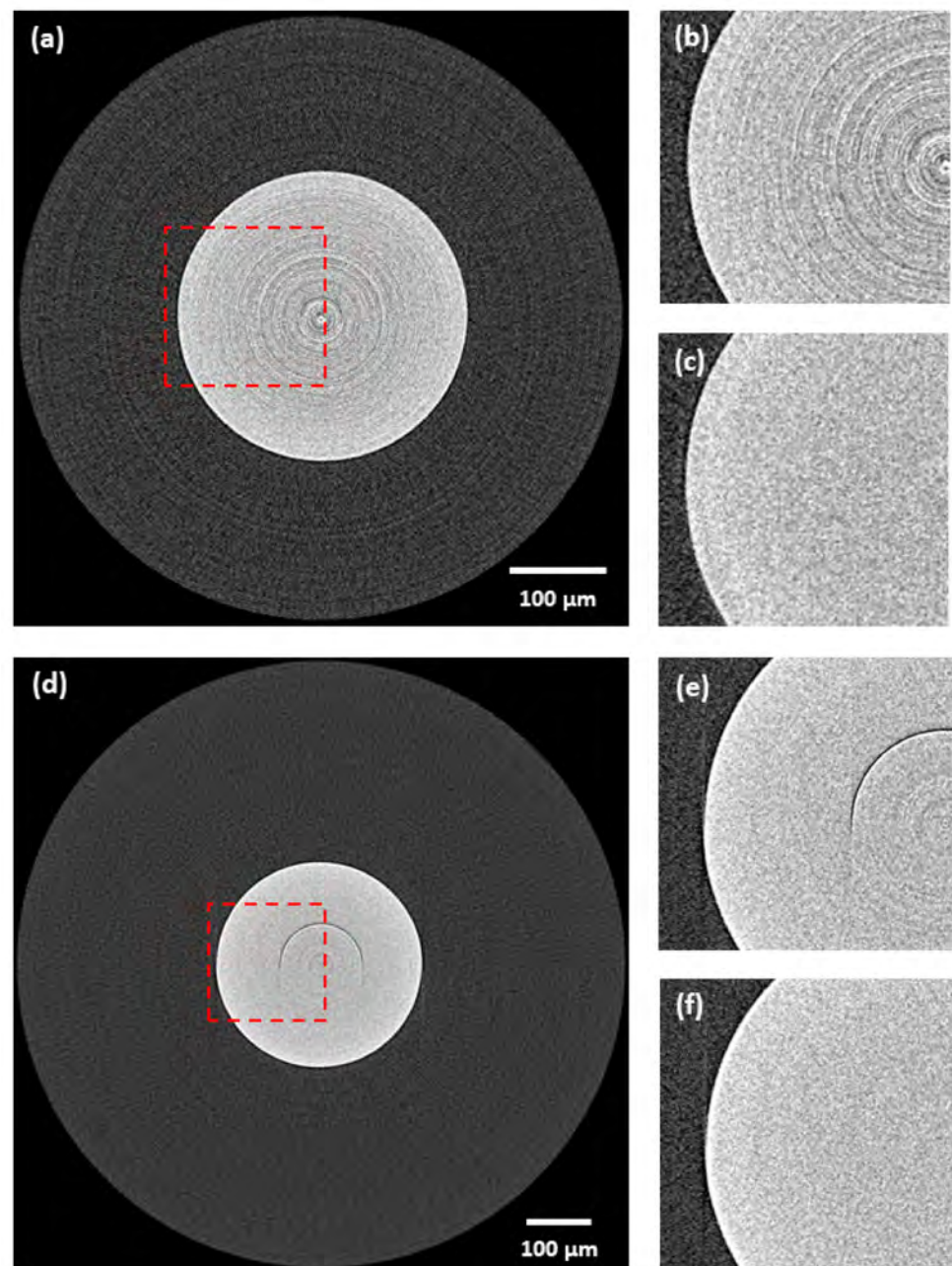


**Figure 12.** Demonstration of robustness of the proposed method to the used detection system—real CT data of ruby ball: (a) original tomogram (scientific complementary metal-oxide-semiconductor (sCMOS), without any correction)—red labelled area marks the central area visualized in following images; (b) detail (sCMOS)—original; (c) detail (sCMOS)—corrected by proposed method; (d) original tomogram (CCD, without any correction)—red labelled area marks the central area visualized in following images; (e) detail (CCD)—original; (f) detail (CCD)—corrected by proposed method. For visualization, the same contrast setting was used for all the images.

#### 4. Discussion

The practical testing demonstrated that the proposed ring artifacts reduction procedure, compared to other methods, can achieve superior results in the following criteria: artifacts detection accuracy, overall performance, robustness to detection system, and the ability to preserve the spatial resolution. First, the method was tested in terms of HRA detection accuracy. It was found that for all the tested data, the proposed HRA detection scheme achieved a precision higher than 95% (see Table 1), even for the increasing noise

level present in the data (see Figure 7). However, for all data, a certain amount of artifacts' positions was not detected. Moreover, a direct proportion was found between the number of HRA positions that were not detected and the noise level. However, this amount was found to be negligible in terms of the total number of artifacts' positions, as both the TPR and DSC metrics scored above 80% even for cases with a severe noise presence.

Although the proposed method did not detect all the HRA positions, the overall quantitative and qualitative results were superior to other tested methods. This was achieved by the proposed two-step correction scheme, when the HRA reduction algorithm and LRA reduction algorithm are working in tandem reducing all the artifacts effectively. A high ring artifacts presence in the case of the synthetic data made their correction very challenging, which was reflected by poor results of the M1, M2 and M3 methods (see Table 2). As for the M1 method, residual rings persisted after the correction for all the tested data resulting in unusable data for further analysis. However, the worst overall results were achieved with the M2 method, as it failed to reduce all the artifacts and preserve the structural information of the input data. Specifically, in the case of ball phantom, the method failed to distinguish the artifacts and sample structure leading to an almost complete suppression of structural information (see Figure 9), which is further represented by a negative SSIM value (Table 2). The M3 method achieved visually acceptable results, but the quantitative evaluation on synthetic data revealed that the method had led to a poor preservation of structural information and intensity range of the input data (see Figure 10). All these findings were further confirmed by testing on the real CT data. The acquired results corresponded to those from testing on the synthetic data. Compared to all other methods, the proposed method obtained the best results, as all the artifacts were reduced, and the sample structures were fully preserved.

The lastly considered criterion focused on the robustness of the proposed ring artifacts reduction procedure to the used detection system and its effect on the spatial resolution. In this analysis, the proposed method proved itself to preserve the spatial resolution within the accuracy limit of the regular standard for both detection systems (see Table 3). Moreover, the proposed method was functional regardless of the detection system without the need for any settings' optimization.

All the beforehand discussed aspects restrict the application of the M1, M2 and M3 methods in nano-tomography, where preservation of quality and structural information of input data are of key importance. Moreover, these methods were found highly dependent on the used parameters and the character of input data. Even following the original authors' recommendations and optimization, the methods did not achieve acceptable results with one setting for all the tested data. This showed a limited robustness and applicability of these methods in practice. Only the proposed method achieved acceptable results for all the conducted tests and showed a high robustness to the character of input data in terms of structure complexity and also the used detection system.

## 5. Conclusions

The small size of detector pixels used in nano CT devices does not enable an application of any hardware-based method for removing ring artifacts, leaving image-based processing methods as the most promising way for an effective ring artifacts removal. Several approaches from this class exist but each with some deficiencies, such as the degradation of data quality and spatial resolution, which is inconsistent with the core purpose of nano-tomography. The procedure presented in this paper is based on a smart implementation of several ideas from existing methods and utilization of their advantages.

The ring artifacts are classified into two types based on their cause and actual appearance in the CT data. Each artifact class is then handled separately since it is impossible for a single approach to remove all of them. In our procedure, we applied novel iterative RTV-based algorithms in the sinogram domain to avoid any negative influence of tomographic reconstruction. The proposed procedure was optimized and tested on different types of data, cameras, and samples as well.

In confrontation with other advanced ring artifacts reduction methods, it proved its supremacy during practical tests, being robust regarding the character of input data and used detection system. Moreover, the method was able to fully preserve the input data, structural information and spatial resolution. Such features show a high potential of the proposed procedure for practical use in the field of synchrotron- or lab-based nano CT systems.

**Author Contributions:** Conceptualization, J.Š.; methodology, J.Š. and M.Z.; software, J.Š.; validation, J.Š. and T.Z.; formal analysis, T.Z.; investigation, J.Š.; resources, J.K. and K.O.; data curation, J.Š.; writing—original draft preparation, J.Š.; writing—review and editing, J.Š., T.Z., M.Z., Y.T. and A.B.; visualization, J.Š.; supervision, T.Z., Y.T. and K.O.; project administration, J.K.; funding acquisition, J.K. All authors have read and agreed to the published version of the manuscript.

**Funding:** This research was carried out under the project CEITEC 2020 (LQ1601) with financial support from the Ministry of Education, Youth and Sports of the Czech Republic under the National Sustainability Programme II and CzechNanoLab Research Infrastructure supported by MEYS CR (LM2018110) and the internal grant agency of Brno University of Technology (STI-J-18-5494).

**Institutional Review Board Statement:** Not applicable.

**Informed Consent Statement:** Not applicable.

**Data Availability Statement:** The data and the code used for the manuscript are available for researchers on request from the corresponding author.

**Conflicts of Interest:** The authors declare no conflict of interest.

## Appendix A

In this work, a relative total variation (RTV)-based algorithm proposed by Xu et al. [43] is used for the texture extraction. Objective function of this algorithm can be expressed as:

$$\operatorname{argmin}_S \sum_p (S_p - I_p)^2 + \lambda \cdot \left( \frac{D_x(p)}{L_x(p) + \varepsilon} + \frac{D_y(p)}{L_y(p) + \varepsilon} \right). \quad (\text{A1})$$

The data term  $(S_p - I_p)^2$  makes the input  $I$  and result  $S$  not extensively deviate, where  $p$  corresponds to pixel indices. The second part of the objective function,  $\lambda \cdot ((D_x(p))/(L_x(p) + \varepsilon) + (D_y(p))/(L_y(p) + \varepsilon))$ , corresponds to the RTV measure, where  $\lambda$  is a weight controlling the degree of smoothing, and  $\varepsilon$  is a small positive number to avoid division by zero and also controlling the sharpness of the image  $S$ .  $D_x(p)$  and  $D_y(p)$  are windowed total variations in the  $x$  and  $y$  directions for pixel  $p$ :

$$D_x(p) = \sum_{q \in R(p)} g_{p,q} \cdot |(\partial_x S)_q|, \quad (\text{A2})$$

$$D_y(p) = \sum_{q \in R(p)} g_{p,q} \cdot |(\partial_y S)_q|, \quad (\text{A3})$$

which count the absolute spatial difference within the rectangular window  $R(p)$  centered at pixel  $p$ . Pixel  $q$  belongs to  $R(p)$ . The term  $g_{p,q}$  refers to a weighting function defined according to spatial affinity:

$$g_{p,q} \propto \exp\left(-\frac{(x_p - x_q)^2 + (y_p - y_q)^2}{2\sigma^2}\right), \quad (\text{A4})$$

where  $\sigma$  controls the spatial scale of the window corresponding to the size of textural elements. To help distinguish the prominent structures from the texture elements, the RTV

measure also contains windowed inherent variations  $L_x(p)$  and  $L_y(p)$  in the directions  $x$  and  $y$ , defined as:

$$L_x(p) = \left| \sum_{q \in \mathcal{R}(p)} g_{p,q} \cdot (\partial_x S)_q \right|, \quad (\text{A5})$$

$$L_y(p) = \left| \sum_{q \in \mathcal{R}(p)} g_{p,q} \cdot (\partial_y S)_q \right|. \quad (\text{A6})$$

The objective function defined in Equation (A1) is non-convex and can be solved using the linear optimization process with the penalty of quadratic measure proposed by Xu et al. [43]. For a practical implementation, the available Matlab<sup>®</sup> code by Xu et al. [43] was used with the settings stated in Table A1. These settings were selected by an extensive practical testing where the overall functionality of both HRA and LRA removal algorithms was evaluated and optimized using described synthetic data by a combination of both qualitative and quantitative evaluation (brute-force search with SSIM [37] as a validation metric).

**Table A1.** Relative total variation (RTV) texture extraction settings used within HRA and LRA removal algorithms.

Parameter	HRA Removal	LRA Removal
$\Delta$	0.005	0.050
$E$	0.020	0.030
$\Sigma$	6	1

## Appendix B

**Table A2.** Nominal parameters of both used cameras without a lens unit.

Technical Features	CCD Camera	sCMOS Camera
Array size	3320(H) × 2500(V)	2048(H) × 2048(V)
Pixel size	5.4 μm	6.5 μm
Sensor diagonal	22.5 mm	18.8 mm
Nonlinearity	<1%	0.2%
Dynamic range	2300: 1	21,400: 1
Acquisition gain	0.45 e-/ADU	0.52 e-/ADU
Readout noise	11 e-rms	1.4 e-rms
Readout rate	8 Mpix./s (approx. 1 fps)	40 fps (@ 16 bit)
Dark current	0.001 e-/pix./s −35 °C	0.14 e-/pix./s @ 0 °C
Binning	Independent on-chip binning in x, y	2 × 2, 3 × 3, 4 × 4, 8 × 8
Peak quantum efficiency	56% @ 540 nm	82% @ 550 nm
Shutter type	Electromechanical	Rolling shutter
Data interface	USB 2.0	USB 3.0

## Appendix C

### Appendix C.1. Proposed Method—Used Settings

These settings were selected by an extensive practical testing where the overall functionality of the algorithms was evaluated and optimized using synthetic data by a combination of both qualitative and quantitative evaluation (brute-force search with SSIM [37] as a validation metric).

**Table A3.** HRA removal algorithm settings.

Parameter	Value
$L$	10% of sinogram rows
$R_1$	0.05
$R_2$	70% of sinogram rows
$R_3$	0.25% of sinogram columns

**Table A4.** LRA removal algorithm settings.

Parameter	Value
$F$	129
$L$	10% of sinogram rows
$R_1$	0.02
$R$	6

### Appendix C.2. Other Methods—Used Settings

**Table A5.** List of the other methods and used settings (notations of the parameters are adopted from the original works).

Method	Notation	Settings
Münch [13]	M1	Wavelet: DB7; Decomposition level: 4; Damping factor: 1.3
Eldib [15]	M2	Filter size: 15; Standard deviation: 10
Vo [21]	M3	Algorithms sequence: 6, 5, 3; $R = 7$ ; Filter size for algorithms 5 and 6: 81; Filter size for algorithm 3: 31

## References

1. Yousuf, M.; Asaduzzaman, M. An Efficient Ring Artifact Reduction Method Based on Projection Data for Micro-CT Images. *J. Sci. Res.* **2009**, *2*, 37–45. [\[CrossRef\]](#)
2. Lifton, J.; Liu, T. Ring artefact reduction via multi-point piecewise linear flat field correction for X-ray computed tomography. *Opt. Express* **2019**, *27*, 3217–3228. [\[CrossRef\]](#) [\[PubMed\]](#)
3. Seibert, J.; Dobbins, J., III; Boone, J.; Boone, J.; Lindfors, K. Flat-field correction technique for digital detectors. In *Medical Imaging 1998: Physics of Medical Imaging, Proceedings of the SPIE, San Diego, CA, USA, 21–26 February 1998*; International Society for Optics and Photonics: Bellingham, WA, USA, 1998; Volume 1998, pp. 348–354.
4. Vågberg, W.; Larsson, J.; Hertz, H. Removal of ring artifacts in microtomography by characterization of scintillator variations. *Opt. Express* **2017**, *25*, 23191–23198. [\[CrossRef\]](#) [\[PubMed\]](#)
5. Boin, M.; Haibel, A. Compensation of ring artefacts in synchrotron tomographic images. *Opt. Express* **2006**, *14*, 12071–12075. [\[CrossRef\]](#)
6. Croton, L.; Ruben, G.; Morgan, K.; Paganin, D.; Kitchen, M. Ring artifact suppression in X-ray computed tomography using a simple, pixel-wise response correction. *Opt. Express* **2019**, *27*, 14231–14245. [\[CrossRef\]](#)
7. Van Nieuwenhove, V.; De Beenhouwer, J.; De Carlo, F.; Mancini, L.; Marone, F.; Sijbers, J. Dynamic intensity normalization using eigen flat fields in X-ray imaging. *Opt. Express* **2015**, *23*, 27975–27989. [\[CrossRef\]](#)
8. Davis, G.; Elliott, J. X-ray microtomography scanner using time-delay integration for elimination of ring artefacts in the reconstructed image. *Nucl. Instrum. Methods Phys. Res. Sect. A Accel. Spectrom. Detect. Assoc. Equip.* **1997**, *394*, 157–162. [\[CrossRef\]](#)
9. Doran, S.; Koerkamp, K.; Bero, M.; Jenneson, P.; Morton, E.; Gilboy, W. A CCD-based optical CT scanner for high-resolution 3D imaging of radiation dose distributions: Equipment specifications, optical simulations and preliminary results. *Phys. Med. Biol.* **2001**, *46*, 3191–3213. [\[CrossRef\]](#)
10. Jenneson, P.; Gilboy, W.; Morton, E.; Gregory, P. An X-ray micro-tomography system optimised for the low-dose study of living organisms. *Appl. Radiat. Isot.* **2003**, *58*, 177–181. [\[CrossRef\]](#)
11. Ji, D.; Qu, G.; Hu, C.; Liu, B.; Jian, J.; Guo, X. Anisotropic total variation minimization approach in in-line phase-contrast tomography and its application to correction of ring artifacts. *Chin. Phys. B* **2017**, *26*, 060701. [\[CrossRef\]](#)
12. Raven, C. Numerical removal of ring artifacts in microtomography. *Rev. Sci. Instrum.* **1998**, *69*, 2978–2980. [\[CrossRef\]](#)
13. Münch, B.; Tirtik, P.; Marone, F.; Stampanoni, M. Stripe and ring artifact removal with combined wavelet—Fourier filtering. *Opt. Express* **2009**, *17*, 8567–8591. [\[CrossRef\]](#) [\[PubMed\]](#)
14. Sadi, F.; Lee, S.; Hasan, M. Removal of ring artifacts in computed tomographic imaging using iterative center weighted median filter. *Comput. Biol. Med.* **2010**, *40*, 109–118. [\[CrossRef\]](#) [\[PubMed\]](#)

15. Eldib, M.; Hegazy, M.; Mun, Y.; Cho, M.; Cho, M.; Lee, S. A Ring Artifact Correction Method: Validation by Micro-CT Imaging with Flat-Panel Detectors and a 2D Photon-Counting Detector. *Sensors* **2017**, *17*, 269. [CrossRef]
16. Anas, E.; Lee, S.; Kamrul Hasan, M. Classification of ring artifacts for their effective removal using type adaptive correction schemes. *Comput. Biol. Med.* **2011**, *41*, 390–401. [CrossRef]
17. Anas, E.; Kim, J.; Lee, S.; Hasan, M. High-quality 3D correction of ring and radiant artifacts in flat panel detector-based cone beam volume CT imaging. *Phys. Med. Biol.* **2011**, *56*, 6495–6519. [CrossRef]
18. Rashid, S.; Lee, S.; Hasan, M. An improved method for the removal of ring artifacts in high resolution CT imaging. *EURASIP J. Adv. Signal Process.* **2012**, *2012*, 93. [CrossRef]
19. Anas, E.; Lee, S.; Hasan, M. Removal of ring artifacts in CT imaging through detection and correction of stripes in the sinogram. *Phys. Med. Biol.* **2010**, *55*, 6911–6930. [CrossRef]
20. Ashrafuzzaman, A.; Lee, S.; Hasan, M. A Self-Adaptive Approach for the Detection and Correction of Stripes in the Sinogram: Suppression of Ring Artifacts in CT Imaging. *EURASIP J. Adv. Signal Process.* **2011**, *2011*, 1–8. [CrossRef]
21. Vo, N.; Atwood, R.; Drakopoulos, M. Superior techniques for eliminating ring artifacts in X-ray micro-tomography. *Opt. Express* **2018**, *26*, 28396–28412. [CrossRef]
22. Kim, Y.; Baek, J.; Hwang, D. Ring artifact correction using detector line-ratios in computed tomography. *Opt. Express* **2014**, *22*, 13380–13392. [CrossRef] [PubMed]
23. Wei, Z.; Wiebe, S.; Chapman, D. Ring artifacts removal from synchrotron CT image slices. *J. Instrum.* **2013**, *8*, C06006. [CrossRef]
24. Sijbers, J.; Postnov, A. Reduction of ring artefacts in high resolution micro-CT reconstructions. *Phys. Med. Biol.* **2004**, *49*, N247–N253. [CrossRef] [PubMed]
25. Kyriakou, Y.; Prell, D.; Kalender, W. Ring artifact correction for high-resolution micro CT. *Phys. Med. Biol.* **2009**, *54*, N385–N391. [CrossRef]
26. Liang, X.; Zhang, Z.; Niu, T.; Yu, S.; Wu, S.; Li, Z.; Zhang, H.; Xie, Y. Iterative image-domain ring artifact removal in cone-beam CT. *Phys. Med. Biol.* **2017**, *62*, 5276–5292. [CrossRef]
27. Yan, L.; Wu, T.; Zhong, S.; Zhang, Q. A variation-based ring artifact correction method with sparse constraint for flat-detector CT. *Phys. Med. Biol.* **2016**, *61*, 1278–1292. [CrossRef]
28. Paleo, P.; Mirone, A. Ring artifacts correction in compressed sensing tomographic reconstruction. *J. Synchrotron Radiat.* **2015**, *22*, 1268–1278. [CrossRef]
29. Titarenko, S.; Withers, P.; Yagola, A. An analytical formula for ring artefact suppression in X-ray tomography. *Appl. Math. Lett.* **2010**, *23*, 1489–1495. [CrossRef]
30. Yu, J.; Imai, F.; Sampat, N.; Collins, D.; Yasan, A.; Xiao, F.; Bae, S.; Ramaswami, S. Hot pixel reduction in CMOS image sensor pixels. In Proceedings of the SPIE 7537: Digital Photography VI 2010, San Jose, CA, USA, 18–19 January 2010.
31. Savitzky, A.; Golay, M. Smoothing and Differentiation of Data by Simplified Least Squares Procedures. *Anal. Chem.* **1964**, *36*, 1627–1639. [CrossRef]
32. Rigaku Corporation: Nano3DX—X-ray Microscope. Available online: <https://www.rigaku.com/en/products/xrm/nano3dx> (accessed on 21 August 2019).
33. Rigaku Corporation: Compact Two-Dimensional CC Detector. Available online: <https://www.rigaku.com/en/products/detectors/micron> (accessed on 21 August 2019).
34. Rigaku Corporation: Compact Two-Dimensional sCMOS Detector. Available online: <https://www.rigaku.com/en/products/detectors/micron-cmos> (accessed on 21 August 2019).
35. Šalplachta, J.; Zikmund, T.; Horváth, M.; Takeda, Y.; Omote, K.; Pína, L.; Kaiser, J. CCD and scientific-CMOS detectors for submicron laboratory based X-ray Computed tomography. In Proceedings of the 9th Conference on Industrial Computed Tomography (iCT), Padova, Italy, 13–15 February 2019.
36. Van Aarle, W.; Palenstijn, W.; Cant, J.; Janssens, E.; Bleichrodt, F.; Dabrvolski, A.; De Beenhouwer, J.; Joost Batenburg, K.; Sijbers, J. Fast and flexible X-ray tomography using the ASTRA toolbox. *Opt. Express* **2016**, *24*, 25129–25147. [CrossRef]
37. Wang, Z.; Bovik, A.; Sheikh, H.; Simoncelli, E. Image Quality Assessment: From Error Visibility to Structural Similarity. *IEEE Trans. Image Process.* **2004**, *13*, 600–612. [CrossRef] [PubMed]
38. Altman, D.; Bland, J. Statistics Notes: Diagnostic tests 1. *BMJ* **1994**, *308*, 1552. [CrossRef] [PubMed]
39. Altman, D.; Bland, J. Statistics Notes: Diagnostic tests 2. *BMJ* **1994**, *309*, 102. [CrossRef] [PubMed]
40. Zou, K.; Warfield, S.; Bharatha, A.; Tempany, C.; Kaus, M.; Haker, S.; Wells, W.; Jolesz, F.; Kikinis, R. Statistical validation of image segmentation quality based on a spatial overlap index1. *Acad. Radiol.* **2004**, *11*, 178–189. [CrossRef]
41. Friedman, S.; Fung, G.; Siewerdsen, J.; Tsui, B. A simple approach to measure computed tomography (CT) modulation transfer function (MTF) and noise-power spectrum (NPS) using the American College of Radiology (ACR) accreditation phantom. *Med. Phys.* **2013**, *40*, 051907. [CrossRef]
42. ASTM E1695-95: Standard Test Method for Measurement of Computed Tomography (CT) System Performance 2013. Available online: <https://compass.astm.org/Standards/HISTORICAL/E1695-95R13.htm> (accessed on 1 December 2020).
43. Xu, L.; Yan, Q.; Xia, Y.; Jia, J. Structure extraction from texture via relative total variation. *ACM Trans. Graph.* **2012**, *31*, 1–10. [CrossRef]

PAPER [X]

# Analysis of neural crest–derived clones reveals novel aspects of facial development

Marketa Kaucka,<sup>1\*</sup> Evgeny Ivashkin,<sup>1,2\*</sup> Daniel Gyllborg,<sup>3</sup> Tomas Zikmund,<sup>4</sup> Marketa Tesarova,<sup>4</sup> Jozef Kaiser,<sup>4</sup> Meng Xie,<sup>1</sup> Julian Petersen,<sup>5</sup> Vassilis Pachnis,<sup>6</sup> Silvia K. Nicolis,<sup>7</sup> Tian Yu,<sup>8</sup> Paul Sharpe,<sup>8</sup> Ernest Arenas,<sup>3</sup> Hjalmar Brismar,<sup>9</sup> Hans Blom,<sup>9</sup> Hans Clevers,<sup>10</sup> Ueli Suter,<sup>11</sup> Andrei S. Chagin,<sup>1</sup> Kaj Fried,<sup>12</sup> Andreas Hellander,<sup>13†‡</sup> Igor Adameyko<sup>1,5†‡</sup>

2016 © The Authors, some rights reserved; exclusive licensee American Association for the Advancement of Science. Distributed under a Creative Commons Attribution NonCommercial License 4.0 (CC BY-NC). 10.1126/sciadv.1600060

Cranial neural crest cells populate the future facial region and produce ectomesenchyme-derived tissues, such as cartilage, bone, dermis, smooth muscle, adipocytes, and many others. However, the contribution of individual neural crest cells to certain facial locations and the general spatial clonal organization of the ectomesenchyme have not been determined. We investigated how neural crest cells give rise to clonally organized ectomesenchyme and how this early ectomesenchyme behaves during the developmental processes that shape the face. Using a combination of mouse and zebrafish models, we analyzed individual migration, cell crowd movement, oriented cell division, clonal spatial overlapping, and multilineage differentiation. The early face appears to be built from multiple spatially defined overlapping ectomesenchymal clones. During early face development, these clones remain oligopotent and generate various tissues in a given location. By combining clonal analysis, computer simulations, mouse mutants, and live imaging, we show that facial shaping results from an array of local cellular activities in the ectomesenchyme. These activities mostly involve oriented divisions and crowd movements of cells during morphogenetic events. Cellular behavior that can be recognized as individual cell migration is very limited and short-ranged and likely results from cellular mixing due to the proliferation activity of the tissue. These cellular mechanisms resemble the strategy behind limb bud morphogenesis, suggesting the possibility of common principles and deep homology between facial and limb outgrowth.

## INTRODUCTION

The facial compartment is arguably the most sophisticated and heterogeneous part of our body. Despite the keen attention to the biology of facial development, the functional and adaptive placement and spatial integration of sensory organs, skeletal structures, nervous system, and feeding apparatus are still not well understood. Numerous congenital craniofacial abnormalities affect the form and function of the face. These may result in, for instance, deformities, distractions, elongations, shortenings, asymmetries, and generally aberrant structures. Explanations to these malformations still await the fundamental understanding of the underlying failure of morphogenesis (1). Cells of the facial compartment arise from four main sources: neural crest stem cells, paraxial mesoderm, epidermis, and endoderm. The nonepithelial tissues in the facial region originate from migratory neural crest stem cells and the paraxial mesoderm

(2). Embryonic epidermis and endoderm generate epithelialized structures, including covering tissues, various glands, epithelial compartments of the hair follicles, and teeth (3, 4). The paraxial mesoderm produces progenitors of striated muscles and endothelial cells and forms the vascular tree in the face and the head in general (5, 6). The neural crest, the largest contributor to the developing face, gives rise to cartilage, bone, dentin and pulp of the teeth, dermal papillae of hair follicles, smooth muscles of the vessel walls, ligaments, fascia, adipose tissue, dermis, pericytes in the forebrain, epithelial cells in the ear, pigment cells, peripheral glial cells, subpopulation of sensory neurons in trigeminal ganglia, sympathetic and parasympathetic neurons, and some other cell types found in the head (7). Neural crest cells have long been considered to be multipotent within the neural tube and later during their active migration (8–11). However, current evidence has suggested that early cell fate restrictions in the neural crest may already exist at the level of the neural tube (12, 13). Still, a very recently performed clonal analysis of neural crest populations in the trunk has supported the concept of multipotency of the premigratory and migratory neural crest (14). Despite this, questions concerning neural crest heterogeneity, multipotency, and progressive specification are far from resolved. This is especially evident when considering the intrinsic differences between neural crest populations that delaminate from different parts along the anterioposterior axis and also along the time scale. For example, only cranial neural crest cells give rise to the ectomesenchyme as an intermediate embryonic cell type that, in turn, will produce most of the structures in a developing face (7, 15). These neural crest–derived early ectomesenchymal cells are the main focus of this study. Little is known about their behavior before the formation of bones, cartilages, and other tissues in the face.

<sup>1</sup>Department of Physiology and Pharmacology, Karolinska Institutet, Stockholm SE-171 77, Sweden. <sup>2</sup>Research Center of Neurology, 125367 Moscow, Russia. <sup>3</sup>Unit of Molecular Neurobiology, Department of Medical Biochemistry and Biophysics, Karolinska Institutet, Stockholm SE-171 77, Sweden. <sup>4</sup>Central European Institute of Technology, Brno University of Technology, 616 00 Brno, Czech Republic. <sup>5</sup>Department of Molecular Neurosciences, Medical University of Vienna, Vienna 1190, Austria. <sup>6</sup>Division of Molecular Neurobiology, Medical Research Council National Institute for Medical Research, London NW7 1AA, UK. <sup>7</sup>Department of Biotechnology and Biosciences, University of Milano-Bicocca, 20126 Milano, Italy. <sup>8</sup>Department of Craniofacial Development and Stem Cell Biology, King's College London Dental Institute, Guy's Hospital, London SE1 9RT, UK. <sup>9</sup>Science for Life Laboratory, Royal Institute of Technology, Solna 17121, Sweden. <sup>10</sup>Hubrecht Institute of the Royal Netherlands Academy of Arts and Sciences, Princess Maxima Centre and University Medical Centre Utrecht, 3584 Utrecht, Netherlands. <sup>11</sup>Department of Biology, Institute of Molecular Health Sciences, ETH Zurich, Zurich CH-8093, Switzerland. <sup>12</sup>Department of Neuroscience, Karolinska Institutet, Stockholm SE-171 77, Sweden. <sup>13</sup>Department of Information Technology, Uppsala University, Uppsala SE-751 05, Sweden.

\*These authors contributed equally to this work.

†Co-senior authors.

‡Corresponding author. Email: igor.adameyko@ki.se (I.A.); andreas.hellander@it.uu.se (A.H.)

In the limb bud, similar mesenchymal cells of a different origin also play a major role in tissue morphogenesis and shape development (16). Previous studies have demonstrated that elongation and shape formation of the embryonic limb are achieved mostly as a result of directional cell activities that include oriented cell divisions, cell allocation, and migration. The shaping largely results from orientation signals and their interpretation in the tissue, rather than only from local differences in proliferation speed (17, 18). The directional activities are regulated by Wnt5a/JNK (c-Jun N-terminal kinase), whereas continuous rearrangements of mesenchymal cells are controlled by the FGF (fibroblast growth factor)/MAPK (mitogen-activated protein kinase) pathway (17). Planar cell polarity (PCP) pathway members (including Wnt5a) are well known to control orientation of cells (19) and are heavily involved in coordinated outgrowth and shape development of multiple embryonic structures (20). As an example, knockout and overexpression of Wnt5a result in the shortening and widening of both the limbs and the face (21–23).

After the arrival of neural crest cells to the face, the embryo is still very small, and significant growth and expansion of the cranial structures will follow. Very little is known about the role of clonal dynamics and the coordinated and directional cell behavior in the ectomesenchyme that eventually shape the face. Here, we attempted to address questions concerning the process of face morphogenesis after the stage of migratory neural crest: How do the newly arrived individual neural crest cells occupy and build different regions of the face? Are there any defined regions occupied by unique clones? Is there a somatotopical mapping at the level of the dorsal neural tube, and what is the degree of cell and tissue polarization, clonal mixing, and migratory behavior of ectomesenchymal cells? Using a variety of methods, we demonstrated that the early outgrowth and shaping of the face are driven by oriented cell divisions and allocations of daughter cells, as well as organized relocations of large cellular groups with minimal individual migration. These are features shown to be of utmost importance in limb shaping, and our findings might support the concept of conserved programs in limb and facial outgrowth.

## RESULTS

### The early face is organized by well-defined overlapping ectomesenchymal clones

To understand clonal arrangements in relation to facial shape and outgrowth, we took advantage of genetic tracing with the help of *Sox10-CreERT2* and *PLP-CreERT2* mouse strains coupled to an *R26Confetti* reporter (24). Both *Sox10-CreERT2* (25) and *PLP-CreERT2* (26, 27) recombine in the cranial neural crest when the pregnant females are injected with tamoxifen at embryonic day 8.5 (E8.5), whereas the *R26Confetti* reporter enables efficient color coding of individual cells by 10 individual color combinations suitable for clonal analysis. There are unequal chances of activating different color combinations (14). For example, clones with activated yellow fluorescent protein (YFP) + red fluorescent protein (RFP), RFP + cyan fluorescent protein (CFP), RFP + YFP, and green fluorescent protein (GFP) are rare compared to clones expressing only YFP, RFP, or CFP and are always significantly underrepresented as compared to these single-color clones. Clones carrying GFP together with another fluorescent protein were never detected. For details about proportions of recombined color combinations, see Baggiolini *et al.* (14). *Sox10-*

*CreERT2* and *PLP-CreERT2* demonstrate different recombination efficiencies and can be selectively used to achieve the desired tracing outcomes and to confirm the specificity of neural crest recombination in cross-comparisons.

With the help of the *Sox10-CreERT2* line, we focused on single-color solitary clones in the whole head, which we successfully achieved by titrating the amount of the injected tamoxifen (28). First, we induced genetic recombination in the neural crest at E8.5 and analyzed the progeny 24 to 36 hours later, using three-dimensional (3D) imaging and analysis. The results showed that genetically traced neural crest cells give rise to spatially defined clonal patches of early ectomesenchyme (“clonal envelopes”) after arrival to the facial region (Figs. 1, A and B, and 2A). A clonal envelope can be strictly defined as a region of 3D space demarcated by a graph connecting all cells belonging to one neural crest–derived clone. Such a clonal envelope occupies only a local portion of the face. Together with the identification of clonal envelopes, we could assess the amount of mixing or overlapping of several clones in a particular location that was analyzed. In cases of rare recombination events, we observed a single compact group of cells in one solitary facial location. We termed this an ectomesenchymal neural crest–derived clone (Fig. 1A). Such single clones, from multiple embryos, were analyzed in detail for cell number, occupied volume, clonal density, and variation of distances between individual cells comprising the clone (Figs. 1 and 2). Observations of such single compact clones in the whole embryo head allowed us to rule out the possibility of a long-range migration of individual early ectomesenchymal cells.

For clonal analysis, with the help of the *PLP-CreERT2* line, we focused on the rare double color combination–labeled clones in the front part of the head to clearly distinguish individual regions occupied by single clones (fig. S1). Results obtained from rare double-colored and GFP<sup>+</sup> clones in *PLP-CreERT2/R26Confetti* embryos and from clonally titrated recombination events in *Sox10-CreERT2/R26Confetti* were in agreement with each other.

The cells inside the defined clonal envelopes appeared sparse at all investigated developmental stages and, as a result, we observed a high degree of clonal overlapping between the progenies of individual neural crest cells in any given location (Fig. 1, C and E to H). Despite such an extensive overlapping of the clones, all clones appeared to be spatially distinct with recognizable borders (Fig. 1, A to I).

Next, we looked into the cellular structure of ectomesenchyme clones at E10 to address their compactness, spatial heterogeneity, and size. The results showed that the cellular density in a typical clone drops from the center to the periphery of the clone. This was analyzed through measuring minimum and maximum distances between all neighboring cells of the same clone and plotting such distances in 3D space as attributes of every cell (Fig. 2). In terms of compactness, we observed a natural variation within clones. Still, they were rather similar to each other in wild-type embryos (Fig. 2, A to C and F). However, we managed to challenge the clonal arrangements, compactness, and heterogeneity by treating the embryos with cyclopamine 1 day before analysis. Facial development is known to be affected by cyclopamine, and the effects have been extensively studied in the past (29). In treated embryos, the clones were smaller and often dissimilar from each other, especially when compared to the control (Fig. 2, D to E and G). We often observed spatially distinct or even connected rare clonal patches of the same color code located in close proximity to each other in E9.5 to E10 embryonic heads (see Fig. 1B,

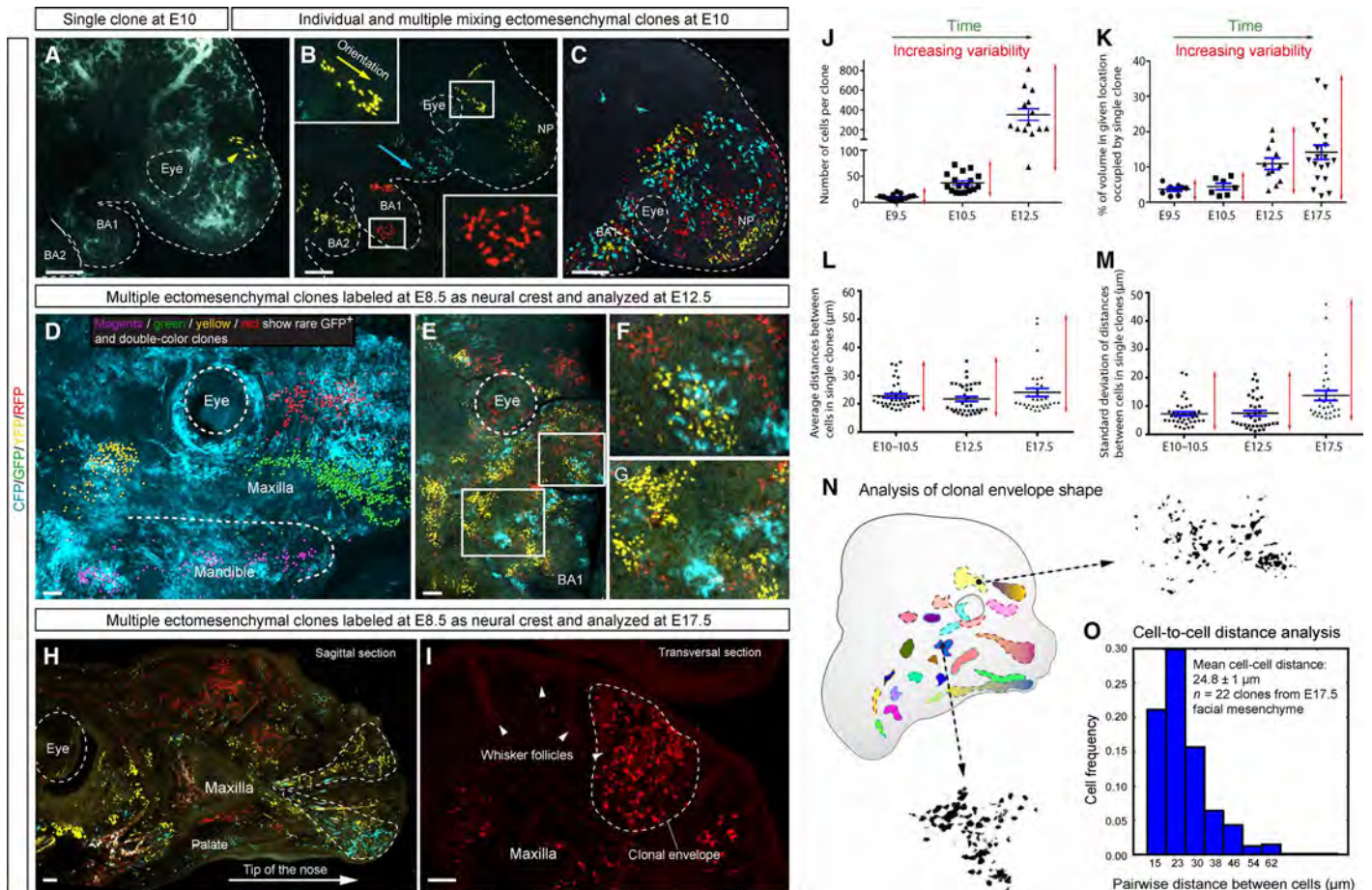


**Fig. 1. Size, shape, and distribution of neural crest–derived ectomesenchymal clones.** (A to C) Genetic tracing of neural crest cells and their progenies induced at E8.5 in *Sox10-CreERT2/R26Confetti* embryos and analyzed at E9.5 to E10. (A) Head of the E10 embryo with single YFP<sup>+</sup> ectomesenchymal clone. Note the compact structure of the clone. (B) Multiple separated clones in different regions of embryo face. Yellow and blue arrowheads show the orientation of cellular groups. (C) Example of multiple overlapping clones in the early developing face. Note the intense local clonal mixing. (D to I) Genetic tracing of neural crest cells and their progenies induced at E8.5 in *PLP-CreERT2/R26Confetti* embryos and analyzed at E12.5. (D) Reconstruction of rare (RFP+CFP, YFP+CFP, RFP+YFP, and GFP-expressing) individual clones in the facial region of an E12.5 embryo. Note that some clones are markedly stretched in the anterior facial region. (E to G) Distribution of ectomesenchymal single-color–labeled clones in the periocular posterior maxillary region. Note the irregular geometry of clonal envelopes and their well-defined borders. (F and G) Magnified regions outlined in (E). (H) Sagittal section through the head of a genetically traced embryo starting from E8.5 and analyzed at E17.5. Area of the maxilla and frontonasal prominence with individual traced clones acquiring conical shape (dotted line) in the anteroposterior direction. (I) Transversal section through the upper jaw of the genetically traced E17.5 embryo. Note the compact shape and defined borders of the RFP<sup>+</sup> clone (outlined by the dotted line). Arrowheads point at whisker follicles. (J) Graph showing the increasing size and variability of individual ectomesenchymal clones during facial development. (K) Graph showing the proportional occupied clonal volume and related variability of individual ectomesenchymal clones at different developmental stages. (L and M) Graphs visualizing developmental dynamics of clonal density (L) and its heterogeneity (M) measured as an average distance between cells of one clone (closest-neighbor approach) and SD of this parameter per clone, respectively. Bars show mean (black) and SEM (blue). (N) Examples of ectomesenchymal clonal envelopes from an E12.5 embryo with traced neural crest–derived progenies. Note the isotropic structure of clones and well-defined borders with irregular curvature. (O) Histogram showing spatial isotropy based on pairwise distances between cells sharing a common clonal origin in experimentally obtained ectomesenchymal clones at E17.5. All images are maximum-intensity projections of confocal stacks, except (C) and (D) with volume rendering of isosurfaces. BA1 and BA2, the first and the second branchial arches; NP, nasal prominence. The eye is outlined by the dashed line. Scale bars, 200 μm (A to C and E to O) and 30 μm (D).

next to the arrows). This suggests the presence of a dividing migratory neural crest cell producing progenies in a few neighboring locations within a restricted facial region.

In contrast to the arrangements in the face, migrating neural crest in the trunk did not show a similar clonal compact clustering with resolvable clonal borders (fig. S2, A to C). This suggests extensive mixing due to intense migration of individual cells.

Regardless of the significant increase in the number of cells in each clone in the growing face (Fig. 1J), the borders of the clonal envelopes remained visually defined (Fig. 1, A, I, and N), and the average distances between cells in the clone remained largely stable (Fig. 1L). However, 4 days after tamoxifen-induced genetic tracing of neural crest progenies, at E12.5 and onward, we observed an increasing variability in the size of the analyzed clones and in the proportional volume occupied by the

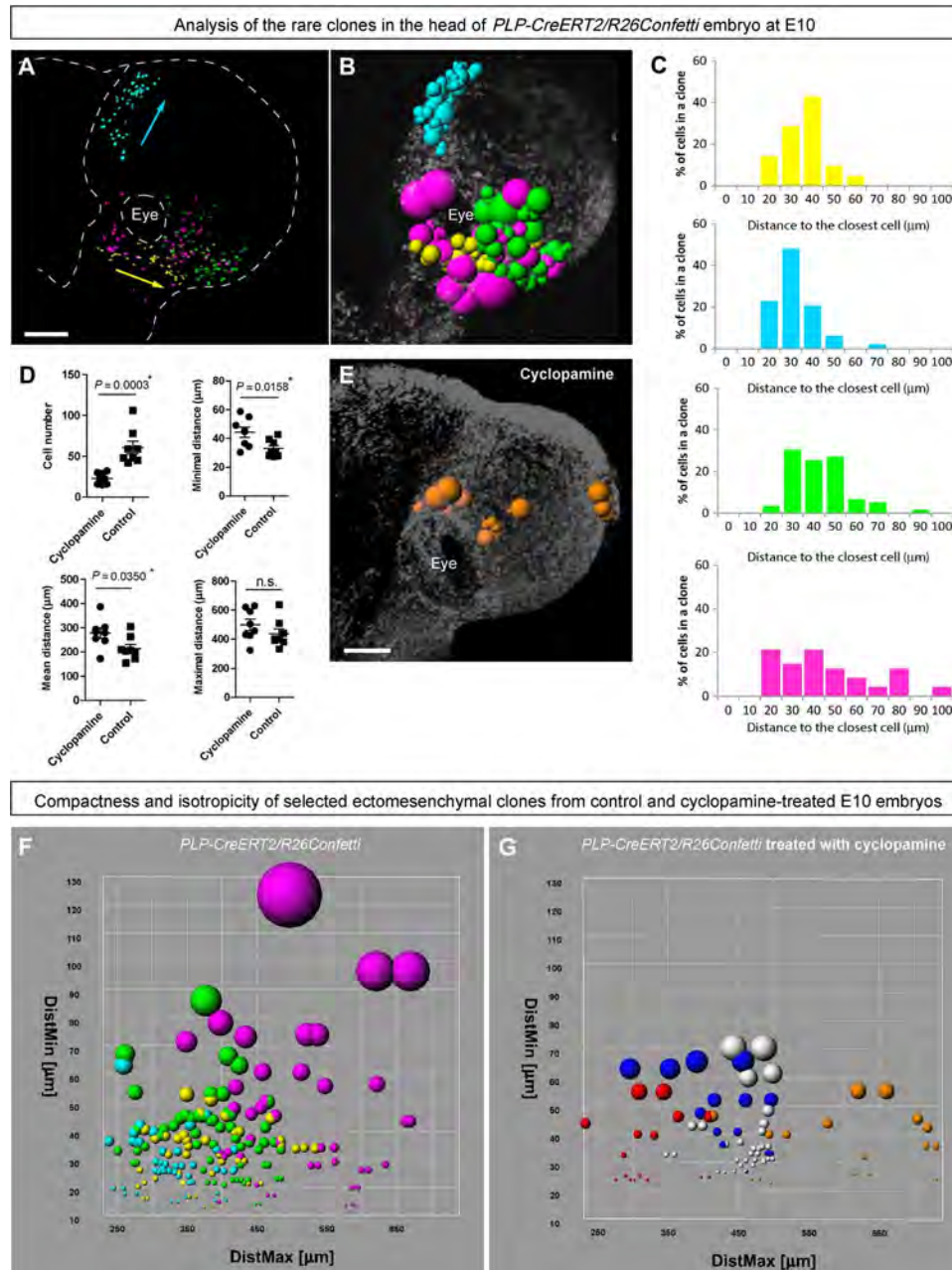


**Fig. 2. Analysis of clonal structure in the faces of E10 control and cyclopamine-treated embryos.** (A) Distribution of analyzed clones from *PLP-CreERT2/R26Confetti* head. Purple, yellow, and green colors mark different rare dual-color clones, whereas cyan represents the rare  $GFP^+$  clone. (B) Spatial structure of clones: Radiuses of colored spheres (representing single cells) correspond to minimal distances to the closest neighbors. When all cells in a clone are analyzed, this parameter reflects the compactness of the clone. (C) Histograms showing distances to the closest neighbor for every cell in the clone. (D) Graphs showing differences between wild-type and cyclopamine-treated ectomesenchymal clones in the faces of E10 embryos. Each point represents the average of the following parameters determined for each cell within a single clone: minimal distance, distance to the closest cell; mean distance, mean distance between one cell and all other cells in the clone; and maximal distance, distance to the furthest cell in the same clone. (E) Spatial structure of a clone from a cyclopamine-treated embryo. Radiuses of colored spheres (representing single cells) correspond to minimal distances to the closest neighbors. (F and G) Plots reflecting the compactness and clonal structure of analyzed clones from control (left) and cyclopamine-treated (right) E10 embryos. Colored spheres on these plots correspond to individual cells. Color defines a clone. The radius of spheres reflects the distance to the most proximal neighbor cell (DistMin) in a clone. DistMax is the maximal distance between a given cell and the most distal cell from the same clone. When the entire clone is analyzed, this parameter describes the spatial dimension of the clone. Scale bars, 200  $\mu m$  (A and E). n.s., not significant.

cells of the clone within the clonal envelope (showing proportional contribution of this clone to the location) (Fig. 1, J and K). We also observed an increase in dispersion of the individual intercellular distances within a clone over time (Fig. 1M). Furthermore, the clones tended to attain a stretched asymmetric shape in regions with extensive growth in the head, which suggests a mechanism of directional clonal expansion in such locations (Fig. 1, D, H, and N). Surprisingly, the clonal progenies of labeled neural crest cells retained a compact structure even at later developmental stages, such as E17.5, as visualized on sagittal and transversal sections (Fig. 1, H, I, and O).

Clonal arrangements in the branchial arches did not differ from the nasal prominence and other facial locations in terms of defined clonal envelopes and clonal overlapping (fig. S2, D to F). Analysis of heart neural crest also showed a high degree of clonal overlapping that simultaneously occurs with clonal clustering of individual neural crest progenies (fig. S2, E and F, arrowheads).

### Coexistence of neural crest–derived ectomesenchyme and mesodermal derivatives in the early face

The existence of well-defined clonal envelopes is supported by the manifestation of the border between neural crest– and mesoderm-derived mesenchymal derivatives that persists to postnatal stages. To visualize this border at postnatal stages, we used conditional knockout of *Sox2* (30) in neural crest cells, using *Wnt1-Cre* (31).

The results of this experiment showed that only facial follicles corresponding to *Sox2*-deficient areas demonstrated a change in hair color shade—instead of black, it became brownish, which highlighted the border between neural crest– and mesoderm-derived dermis in young postnatal animals (fig. S3, A to Q). This border between neural crest– and mesoderm-derived mesenchyme was also observed during embryonic stages (fig. S3, R to T). Expression of dopachrome tautomerase (DCT) showed that melanocytes survived well in the targeted tissue and that the pigment-producing pathway was in place in both wild-type and *Sox2*-deficient melanocytes. The melanocytes did not express *Sox2*, as opposed to dermal papilla cells (fig. S3, B to Q). This is in line with the fact that expression of *Sox2* is generally incompatible with melanocyte fate (32). Therefore, the outcome of *Sox2* deficiency in skin must result from an interplay between melanocytes and dermal papilla cells. Indeed, melanocytes communicate with dermal papilla cells to adjust the amounts and the ratio of different pigments (33), which involves the *Agouti* pathway and explains how animals dynamically change pigmentation patterns (34). Because dermal papilla cells in the head are produced from neural crest cells and the mesoderm, and loss of *Sox2* affected only the neural crest–derived dermal papillae, we were able to detect the border between numerous ectomesenchyme (NCC)– and mesoderm-derived dermal papillae in head skin. We suggest that the presence of such visual border is an interesting and important observation, especially because the dermis is organized by fibroblast-like cells that presumably are capable of long-range migration during late embryonic development and afterward.

Both neural crest and paraxial head mesoderm contribute to a range of mesenchyme-derived structures, including skeletal elements that fuse without signs of different cellular origin. This indicates that clonal behavior and morphogenetic cell dynamics in paraxial mesoderm derivatives are similar to the clonal dynamics in neural crest–derived tissues. We used *Mesp1-Cre/R26Confetti* animals in 2D and 3D imaging to trace the progeny of paraxial mesoderm in the face (35). Mesoderm-derived mesenchyme showed a high degree of clonal overlapping not only in

branchial arches but also in the dorsolateral aspects of maxillary and occipital regions (fig. S4, A to I). Additionally, local angiogenic progenitors in multiple places demonstrated an impressive diversity of clonal origins based on their color code (fig. S4, J and K). Numerous mesoderm-derived mesenchymal domains sharing the same color code appeared compact and local, similar to ectomesenchymal clones in the face (fig. S4, E to I; see arrowheads). These data point toward the possibility that similar morphogenetic mechanisms operate in neural crest– and mesoderm-derived mesenchymal tissues.

Next, we wanted to investigate the volume proportions occupied by the mesoderm and the neural crest, respectively, in different localities in the developing face. We also wanted to calculate the number of neural crest–derived clones that contribute to a given location within selected regions of interest (ROIs). For this, we made 3D analyses of the traced mesodermal (high efficiency of recombination) and neural crest (low efficiency) progenies in various facial regions, including the nasal prominence and branchial arches. The analyses showed that mesodermal derivatives occupied  $21.01 \pm 3.46\%$  of ROI volume (mean and SEM;  $n = 9$ ) in the face at E10.5 (fig. S4, L to P). Furthermore, we calculated that single neural crest–derived clones contributed to  $4.465 \pm 0.8844\%$  of ROI volume (mean and SEM;  $n = 7$ ) at the same stage (see Fig. 1K). Thus, we concluded that up to 17 neural crest clones may contribute to one ROI location.

### Modeling ectomesenchymal cell dynamics in 2D and 3D confirms the minimal role of individual cell migration in clonal overlapping

As seen from above, most of the observed ectomesenchyme-derived clones in the face show complex clonal envelope shapes (Fig. 1N), with the borders representing sharp drops of cellular density at the periphery of the clone (Figs. 1O and 2C). Highly variable and complex shapes of the clonal envelopes cannot be explained without the assumption that complex morphogenetic processes operate in the tissue.

Given that the ectomesenchyme is a potentially migratory tissue, we asked whether migratory behavior contributes to the development of facial shape and, if this is the case, how the selectivity and directionality of cell migration can be achieved. On the basis of our previous results, we wanted to understand how the experimentally observed sharp borders of clonal envelopes can be maintained in the case of migratory behavior of facial neural crest–derived cells. To address this issue, we devised a mathematical model that operates virtual cells in 3D space plus time. We tested a group of variables, such as cell division speed, migration, and allocation of daughter cells in random or defined directions, as well as pushing of newborn mitotic products during proliferation. We compared the readouts from the series of *in silico* simulations to the results of our experimental clonal analyses. We looked for parameter combinations in the model that gave rise to dynamics with degrees of overlapping and clonal shapes that were compatible with those observed in the experiments. Unexpectedly, the 2D version of the model showed that proliferation-driven cell pushing/place-exchanging and related short-distance movements are sufficient to achieve efficient clonal overlapping over time (Fig. 3, A and B). In this model, we assumed (based on the biological data including live imaging experiments described below) that products of cell divisions would push neighboring cells to obtain space. Alternatively, they could intermingle with close neighboring cells by exchanging positions with them, as a way of accommodating the pushing forces in the growing tissue. Such short-ranged spatial rearrangements require some dynamics of

cell shape. This can be rendered as a very short range migratory behavior. Indeed, simulations in 3D space confirmed that clonal overlapping is compatible with zero or minimal individual migratory behavior, whereas proliferation appeared to be the main driving force for the mixing of the cell division products. Moreover, well-defined clonal envelopes were maintained only when individual migration (in relation to neighboring cells) was minimal in the simulated system. An *in silico* model, while showing defined clonal patches, also demonstrated a drop in clonal compactness from the center of the clone to the periphery in agreement with experimental data (Fig. 2, B, C, and F). Together, this strongly suggests that clonal overlap in authentic facial development may occur owing to the spatial allocations and mingling of daughter cells that result from cell divisions exclusively. In such a case, the products of mitoses will push and blend in the directions of surrounding domains, and through this, the clonal progenies will intermix.

### Oriented divisions and crowd movements of ectomesenchymal cells participate in facial shaping

The modeling of fine borders of clonal envelopes remained imperfect as compared to the experimental data, unless the concept of polarizing morphogen gradients was considered. Therefore, we introduced a local radial gradient that affects the directionality of cell division and allocation of daughter cells in 3D space into the *in silico* model. The results of these simulations demonstrated that the oriented cell divisions (or controlled allocations of the progeny after mitosis) together with minimal individual migratory behavior are the keys to achieving the distribution of virtual clonal progenies that resemble the actual clonal patterns in facial development (Figs. 3, C to H, and 4). Experimental data on the stretched geometry of clonal envelopes in the most outgrowing parts of the face additionally point toward oriented cell divisions during progressive shape development (consistent with Fig. 1, D and H). At the same time, the distribution

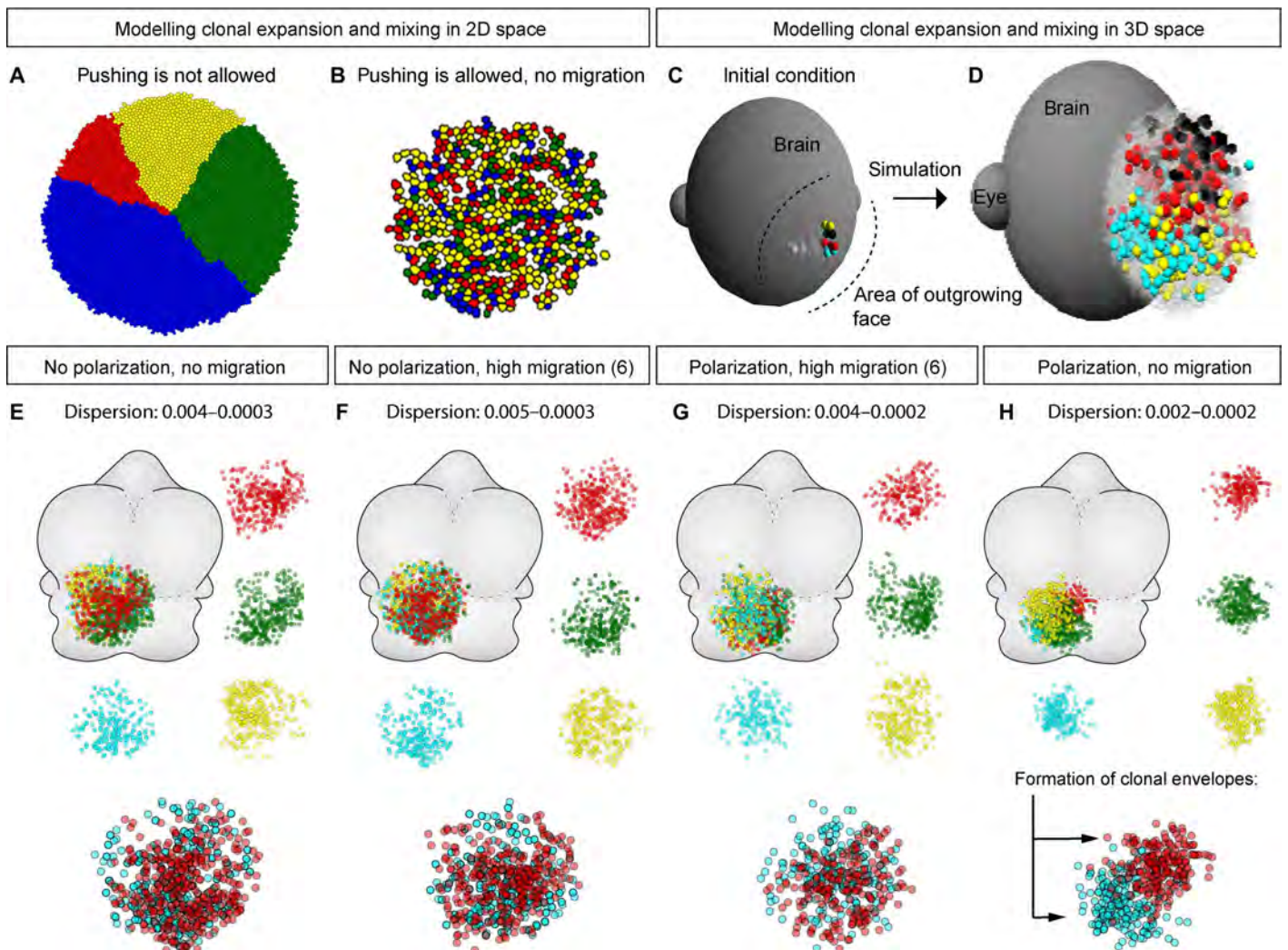


**Fig. 3. Mathematical modeling of clonal expansion and overlapping in 3D space.** (A and B) 2D modeling of cell dynamics; initially traced clones are labeled by different colors. Note that in the condition where cell pushing is allowed (B), clonal overlapping is efficiently achieved without any migratory behavior. (C and D) Visualization of initial conditions and example of *in silico* cell dynamics simulation in 3D space. (E to H) Results of *in silico* cell dynamics simulation in 3D space performed with different settings. Note the formation of defined clonal envelopes under the condition where polarization probabilistically directs oriented cell divisions with minimal individual cell migration (H).

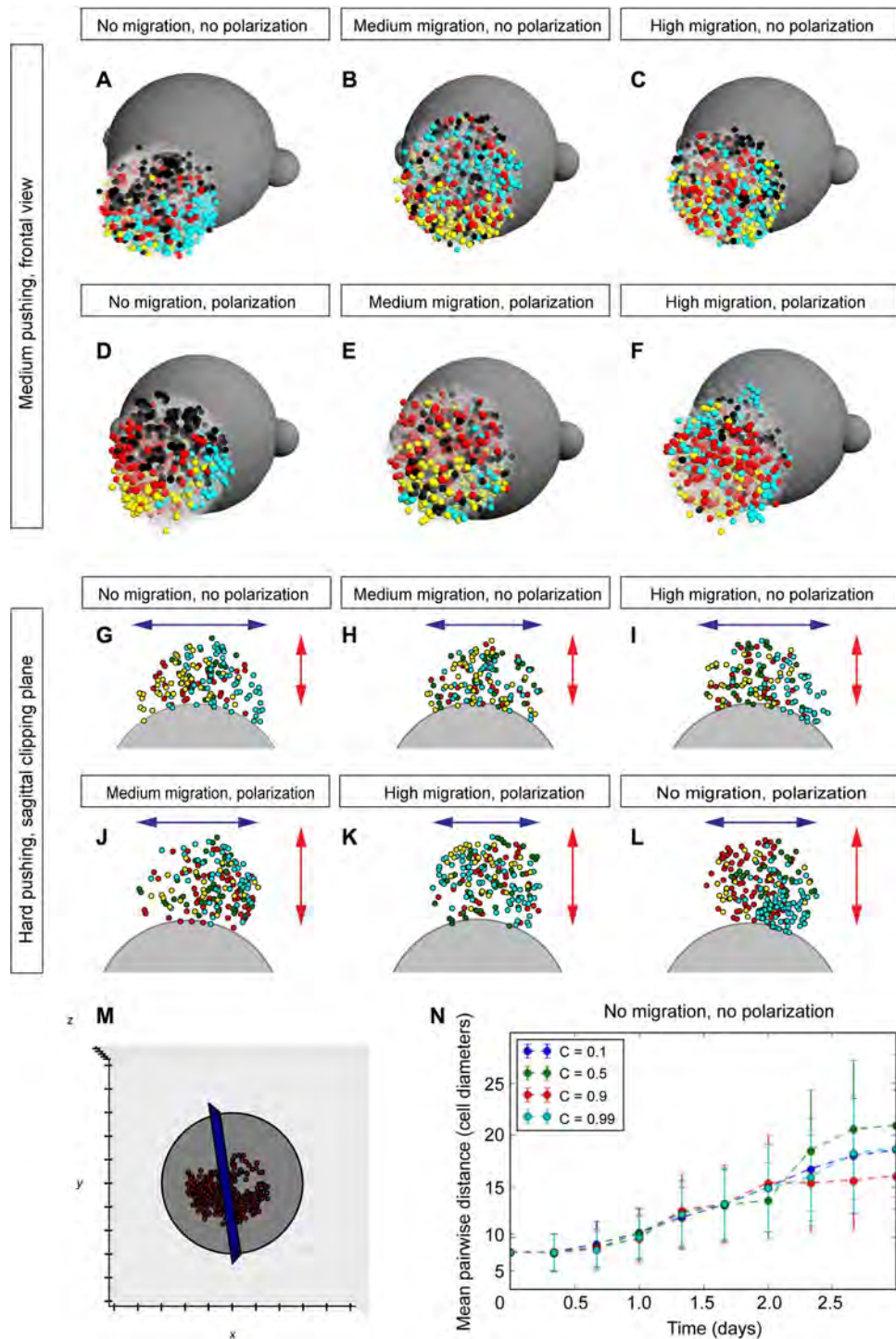


**Fig. 4. Mathematical model predicts widening versus elongation strategies of in silico facial development depending on the conditions. (A to F)** Simulations of cell dynamics in a 3D environment with medium pushing power (technical value in a model  $c = 0.5$ ). **(G to L)** Clipping planes, view from the top on simulations of facial development. Note how different conditions lead to widening or elongation of the cellular cluster with clonal envelopes. The technical value for high pushing power in a model was  $c = 0.9$ . **(M)** Example of the clipping plane, frontal view. **(N)** Graph showing the changes in the spatial homogeneity (isotropicity) of simulated clones during rounds of simulation.

of cells within the analyzed clonal envelope appeared to be relatively uniform as defined by variation in individual cell-to-cell distances (measured as a distance to the closest neighbor) (Figs. 1O and 2C).

This was similar to the *in silico* simulations, where we found that polarization (and no migration) was characterized by the lowest dispersion of distances between the cells (Fig. 3H). *In silico* simulations demonstrated a clear difference in elongation versus widening of the modeled facial structure, depending on the presence of an anterioposterior polarizing gradient (Fig. 4, G to L).

To conclude, the mathematical model predictions pointed toward the likelihood of locally controlled allocations of daughter cells after mitosis. Such allocations can result from oriented cell divisions and controlled spindle orientation following anterioposterior polarization cues in the tissue.

In such a case, most of the allocations of newborn cells occur predominantly in one direction. This reduces the “lateral” clonal mixing because the pushing power of clonal mitotic products that invade lateral clonal domains during proliferation is eased. This should lead to reduced clonal blending and to the efficient maintenance of defined clonal envelope borders while having an impact on the resulting shape in terms of widening versus elongation (Fig. 4, especially G to L).

To directly test the predictions from the model, we analyzed *Wnt5a* knockout mouse embryos (36). *Wnt5a* is a noncanonical Wnt and a member of the PCP pathway that is involved in polarizing epithelial and mesenchymal tissues. Indeed, the knockout of *Wnt5a* leads to massive shortening and widening of the face, starting from preskeletogenic time points (Fig. 5, A to J). The lower jaw appeared much shorter and wider. At the same time, our data showed that the volume of the lower jaw was not reduced as compared to the control (Fig. 5, F and H). This indicates that there was no deficit in proliferation and in the number of cells that formed the face. This is similar to the modeling predictions shown in Fig. 4 (G to L). Moreover, this phenotype does not influence the induction of all necessary facial structures, including cartilages, bones, sensory compartments, muscles, glands, and developing teeth, as monitored by x-ray micro-computed tomography ( $\mu$ -CT) scans and visualizations (Fig. 5, E to P). Additionally, we did not observe any changes in the general position of major anisotropic proliferative zones, as analyzed with ethynyl deoxyuridine (EdU) incorporation assay at E12.5 (Fig. 6, Q and R). Strikingly, when we examined the orientation of cell divisions using an antibody against phospho-histone 3 (PH3; commonly used to visualize metaphase plate) in the anterior face, we found that the predominant anterioposterior orientations of mitotic products were no longer prevalent in *Wnt5a* mutants at E12.5 (Fig. 5, S to V). This result is in full accordance with the *in silico* simulations (Figs. 3 and 4, G to L).

### Live imaging in zebrafish reveals oriented crowd movements of large cellular groups

To directly observe the dynamics of early shape development in the facial region, and to connect it with individual cellular behavior, we used live imaging of genetically traced zebrafish larvae. For this, we took advantage of the *Sox10-CreERT2/Ubi:zebrabow* fish line, which is suitable for clonal color coding and inducible lineage tracing in neural crest cells. The nonrecombined cells express RFP, whereas cells after recombination can acquire stable YFP or CFP expression in the lineage. Because of imaging constraints, we followed mostly YFP<sup>+</sup> neural crest-derived clones during early craniofacial development.

First, the results of this experiment demonstrated that neural crest cells labeled at clonal density give rise to spatially separate and compact groups of cells. These groups are analogous to the ectomesenchymal clones that we observed in mouse embryos (fig. S5, A to D, arrows). Second, live imaging clearly demonstrated that individual ectomesenchymal cells do not migrate significant distances but rather rearrange their shape and accommodate their position within their local microdomain (Fig. 6 and movies S1 to S4). This complies with the theoretical prediction from the mathematical model (see Fig. 4). As a result, the labeled cellular clusters change their shape over time (Fig. 6A) but do not alter their basic cellular structure. This structure includes cell density and coordinated orientation of cell divisions that may change over time (Fig. 6, B to L, and especially E).

The progenies of dividing ectomesenchymal cells remain in close proximity to each other in most of the cases (see tracks of the progeny in Fig. 6, J to L). In agreement with the inference from the mathematical model, these ectomesenchymal cells mostly divide in certain orientations within spatial microdomains, as observed in live imaging (Fig. 6, B to E). This, too, is consistent with the results obtained in the mouse model (see Fig. 5, S to V).

At the same time, ectomesenchymal cells relocate to new distant positions in the embryonic head in synchronized crowd movements (Fig. 6, J to L, and fig. S5, E to P). These movements stem from pushing activities in major proliferative centers, located in, for example, branchial arches, as evident from EdU analysis (Fig. 6, M to Q, and movie S5) and direct live observations (movies S1 to S4). Anisotropic proliferation is apparent in larval ectomesenchyme. This is reflected in results from an acute EdU incorporation experiment (Fig. 6, M and N) as well as in EdU label-retaining analysis in ectomesenchyme-derived cranial cartilage (Fig. 6, O to Q). Application of EdU for 15 min at 48 hours and analysis at 4 dpf showed an uneven, symmetrical, and specific pattern of EdU incorporation and retention in skeletal structures that form after 48 hours of development from ectomesenchymal cells. Note that the translocating groups of ectomesenchymal cells behave similarly to viscous liquid (fig. S5, E to P, and movies S1 to S4). Such morphogenetic movements may account for specific distortions and complex geometries of clonal envelopes, as shown in Fig. 1N.

To sum up, these results agree with computer simulations and are consistent with observations of clonal patterns in mouse embryos. Together, they suggest that crowd movements, anisotropic proliferation, and cell divisions with natural-like variation of the cell cycle length and phase play a significant role in facial morphogenesis, whereas long-range individual migration is limited in the face after neural crest cells transform into neuroglial and ectomesenchymal components.

### Early ectomesenchymal cells are oligopotent within a given locality

The establishment of facial structures by ectomesenchymal clones raises the question whether each clone displays restricted and defined competence to generate only specific cell types. Hypothetically, overlapping clones may have committed to distinct fates and later give rise to different derivatives within a single locality. We tested this assumption using lineage tracing and fate analysis of rare double-colored and single-colored clones (Fig. 7). The results instead demonstrated that multiple fates are often generated within one compact clone. Thus, an individual clone may contribute to, for example, local mesenchyme and to dermal papillae of whisker follicles (Fig. 7, A and B). In other

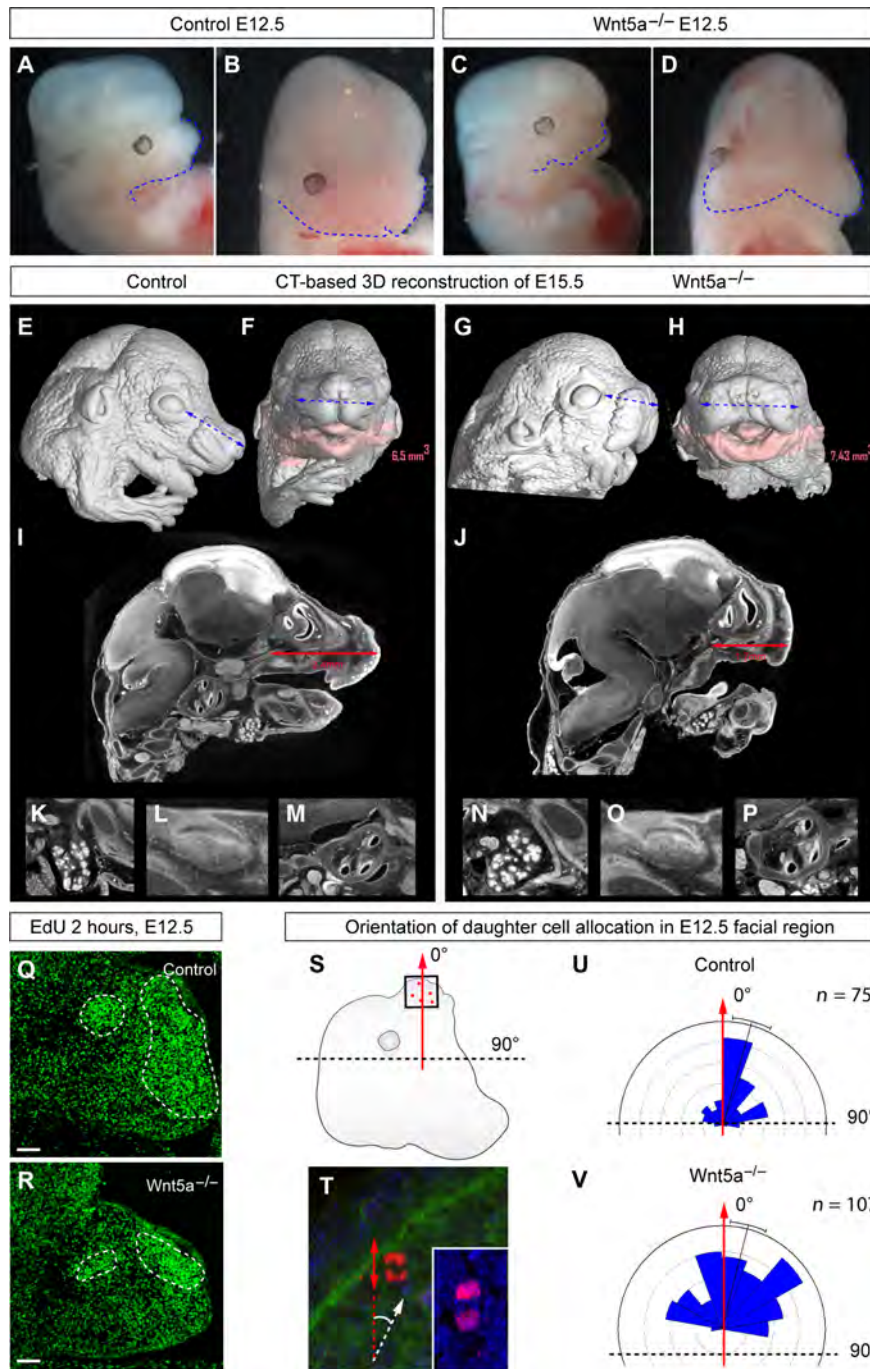


**Fig. 5. Disruption of Wnt/PCP-driven cell polarization and subsequent changes in facial shape.** (A to D) Representative images of E12.5 embryos: littermate controls (A and B) and *Wnt5a* full knockout embryos (C and D). (E to H)  $\mu$ -CT-based 3D reconstructions of the E15.5 embryonic heads: littermate controls (E and F) and *Wnt5a* full knockout (G and H). Note the short snout and wider face of the mutant embryos as compared to the control littermates. Pink color code shows the mandible and its volume calculated for control and mutant embryos. (I to P)  $\mu$ -CT-based sagittal section through the head of the control (I and K to M) and mutant (J and N to P) embryos with the measurements of the length between the posterior part of the olfactory system and the anterior tip of the snout. (K to P) Tomographic slices through the salivary gland, developing the molar and the inner ear from control (K to M) and *Wnt5a* mutant (N to P) embryos. (Q and R) Distribution of high proliferation zones in control (Q) and *Wnt5a* knockout mutant (R) E12.5 embryonic mandibles that were treated with EdU for 2 hours before analysis. Dotted lines outline stereotypic, highly proliferative zones. (S) Scheme of the ROIs where the oriented cell divisions were quantified in the head of E12.5 embryos. (T) Example of chromosome PH3-based staining on the section of an E12.5 embryonic head; the white arrow points toward the outgrowing part of nasal prominence, whereas the red arrows show the orientation of cell division and the allocation of daughter cells. (U and V) Rose diagram of quantified orientations of cell divisions in the anterior face of E12.5 control (U) and *Wnt5a* knockout mutant (V) embryos. Note the disruption of the directionality of cell divisions in the mutant embryo as compared to the control littermate. Scale bars, 200  $\mu$ m (Q and R).

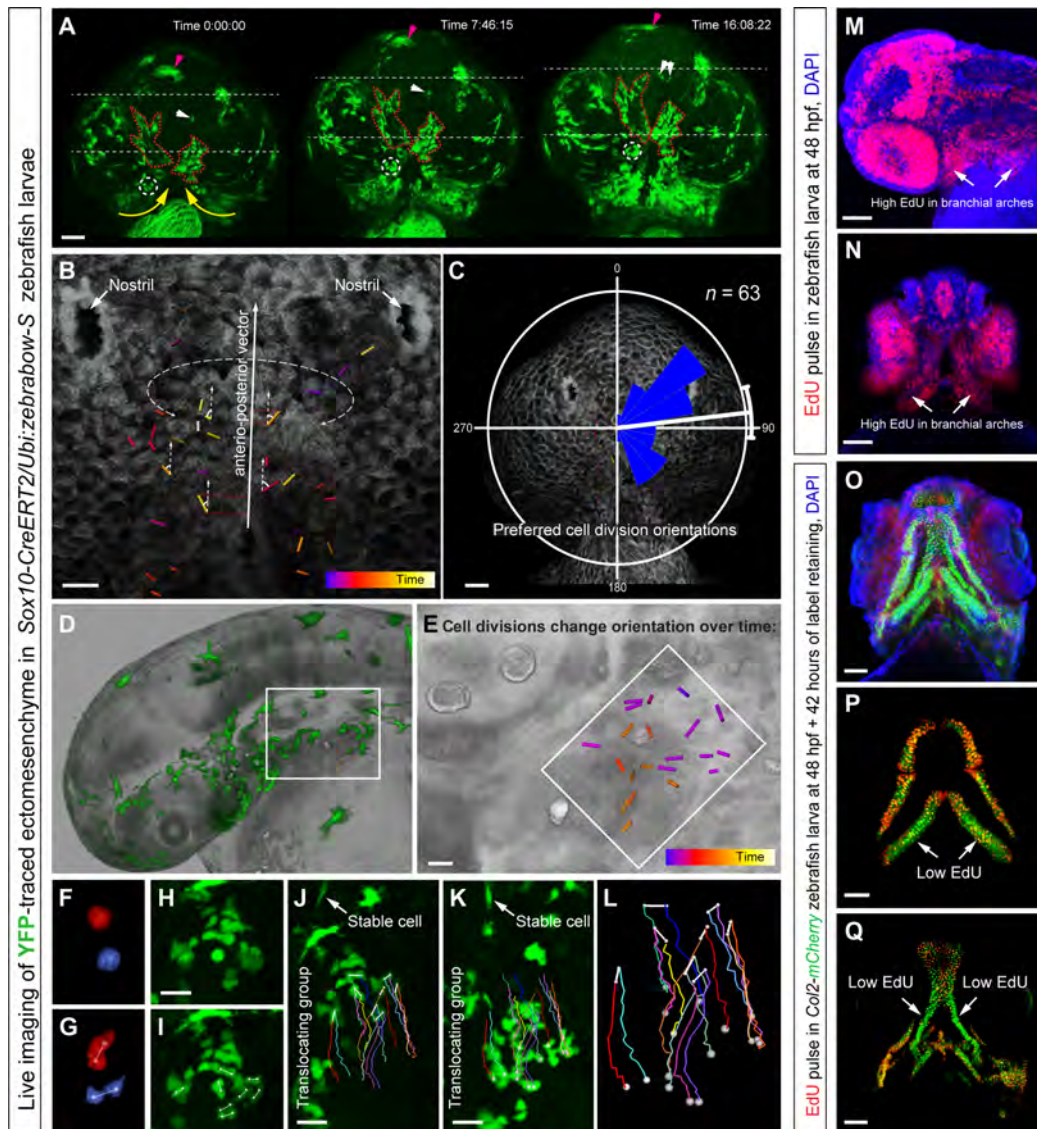


**Fig. 6. Live imaging of early zebrafish craniofacial development.** (A to L) Live imaging of genetically traced neural crest-derived progenies in *Sox10-CreERT2/Ubi:zebrabow-S* zebrafish larvae between 30 and 56 high-power field (hpf) (A to C) and 30 and 42 hpf (D to L). (A) Ventral view on zebrafish larva head with genetically labeled groups of YFP<sup>+</sup> cells. Note the spatial stability of translocating labeled groups during organized cell movements in the regions of expanding branchial arches and around the stomodeum. The dotted circle and white arrows show small defined trackable groups of cells. Purple arrows point at the melanocyte. The red dotted line shows how the borders of YFP<sup>+</sup> groups change over time. Yellow arrows demonstrate the major direction of crowd movement. (B and C) Analysis of oriented cell divisions during live imaging of developing zebrafish head, ventral view. (B) Bars show orientations of individual cell divisions and color code corresponds to the timing of cell division. (C) Rose diagram of orientations of cell divisions. (D to L) Cell divisions in the branchial arch of zebrafish at 30 to 42 hpf, side view. (E) Magnified region from (D). Note that cell divisions change the predominant orientation over time. (F to L) Analysis of the group of cells from the region outlined by the white rectangle in (D). (F and G) Frames from time lapse with two dividing cells from the branchial arch. (H and I) Frame before (H) and immediately after (I) mitosis of several ectomesenchymal cells in the region, side view on the branchial arch. (J to L) Tracking of dividing ectomesenchymal cells and their progeny in the forming branchial arch. (J) First frame of tracking. (K) Final frame of tracking (12 hours). Arrows in (J) and (K) point at the stable YFP<sup>+</sup> cell that does not change the position in the embryo and serves as a stable orientation anchor for measuring translocation/crowd movement of the labeled group of ectomesenchymal cells. Note that during the displacement of the entire group, most of the cell division products stay proximally close to each other with some rare exceptions [dark brown track in (L)]. Despite this, high intensity of local cellular mixing is achieved owing to proliferation in accordance with modeling results presented in Fig. 2 (A to C). (M and N) EdU incorporation shows proliferation rates in different parts of the developing zebrafish head. Note that a 5-min EdU pulse at 48 hpf immediately followed by the analysis showed high proliferation rates in branchial arches (arrows). (O to Q) Transgenic *Col2a1BAC:mCherry* zebrafish larva's entire head (O) and skeletal elements (P and Q) at 4 days postfertilization (dpf) with incorporated EdU, administered at 48 hpf for 5 min. Note that this EdU label-retaining experiment highlights uneven proliferation in ectomesenchymal chondrogenic progenitors at 48 hpf (5-min pulse). Arrows point at low EdU-retaining regions in the facial cartilages. Scale bars, 50  $\mu$ m (A, C, M to O, and Q) and 20  $\mu$ m (B, E, and H to K).



situations, single clones contributed to the dental mesenchymal compartment and the surrounding osteogenic tissue (Fig. 7, C to E). We often observed that perichondrial cells, chondrocytes, and neighboring mesenchymal patches shared the same clonal origin (Fig. 7, F to K). Osteogenic cells of membranous bones and neighboring mesenchyme also showed clonal relationships (Fig. 7, L and M).

None of the analyzed unique ectomesenchymal clones showed any progeny in the neuroglial compartment (Fig. 7O). Consistently, several rare analyzed clones in the neuroglial compartment did not appear to share the same color code with cells in the ectomesenchymal domain (Fig. 7P).

Embryonic ectomesenchyme-derived pericytes (marked by NG2) were found to spread clonally by dividing along the vessels. This is similar to how glial cells clonally spread along nerve fibers (Fig. 7, Q to S). To conclude, labeled neural crest cells give rise to oligopotent clonal local patches of ectomesenchyme that generate different fates that are necessary in a specific location.

## DISCUSSION

The facial region is largely composed of neural crest-derived progenies. The purpose of the present study was to investigate how those progenies dynamically build the face. Previously, an elegant clonal analysis has been performed in the trunk neural crest derivatives that include neurons, glial cells, and melanocytes. Many important questions related to both trunk crest multipotency and techniques concerning Confetti multicolor tracing were resolved in that study (14). However, trunk neural crest and cranial neural crest are different in their ability to give rise to mesenchymal structures. Consequently, knowledge of the clonal structure and cell behavior in relation to early morphogenesis of the face has remained obscure.

We addressed this question with clonal analysis using a multicolor Confetti reporter and found that neural crest cells give rise to well-defined clonal patches (clonal envelopes) of ectomesenchymal tissue in the prospective facial compartment. They demonstrate conspicuous borders and consist of clonal progeny formed from a single labeled neural crest cell. Once formed, these clonal patches persist until at least late embryonic development and most likely postnatally: They occupy certain locations in the face and retain recognizable borders. The patches do not dissolve with developmental time despite some growing heterogeneity inside the clone in terms of intercellular distances. The cells within the clonal envelope are loosely packed and mix locally with the progenies of other neural crest cells. Developmental robustness of the facial compartment might be rooted in a high degree of clonal overlapping in any given locality that is populated by the progenies of at least several individual neural crest cells. Hypothetically, negative somatic mutations occurring in a single migrating neural crest cell or at the level of the neural tube can be compensated by other unaffected neural crest-derived local clonal progenies. Moreover, the intense clonal overlapping among neural crest progenies argues against any somatopic mapping (37) at the level of the neural tube. The increasing variability in geometrical shape and size of the clones might reflect directional cell behavior unique for a given locality, with different proliferation rates in various compartments of the outgrowing face.

We took advantage of mathematical modeling to sort out these potential mechanisms of clonal behavior. The 3D *in silico* simulations of cell dynamics showed that highly efficient clonal overlapping can be

achieved without migration of individual cells, solely due to the pushing and mingling force of cells as a result of multiple cell divisions in the area. Moreover, the model predicted the existence of a chemical gradient that controls the orientation of cell divisions, to achieve defined clonal envelopes. We set out to test the suggestions from the model regarding both the minor migratory behavior and the directional cell dynamics related to cell divisions with subsequent allocations of daughter cells. Live imaging experiments in zebrafish confirmed our computer model predictions that ectomesenchymal cells do not perform extensive individual migrations and predominantly divide in few orientation planes within a local microdomain. Moreover, similar to the situation in the developing limb (17), we discovered that ectomesenchymal cells execute large-scale, collective, coordinated morphogenetic movements, where the cellular arrangements of microdomains remain well preserved. Such crowd movements, reminiscent of the behavior of viscous fluid, have been previously described (17, 38). The viscous fluid approach was previously used for analyses of biological systems on cellular and organismal levels (39). According to our results, the ectomesenchymal cells in the zebrafish lower jaw translocate or perform crowd movement in relation to the eyes and the brain. This takes place while the stomodeum is displaced anteriorly, presumably as a result of lower jaw mesenchyme outgrowth. The massive relocation of ectomesenchymal cells occurs because of proliferation in the lateral regions of the branchial arches and does not involve independent migration of each cell. This is supported by the fact that differentiating chondrocytes are still moving forward together with the surrounding tissue during lower jaw extension (see movie S3). Thus, it seems that individual ectomesenchymal clones mix and overlap as cells are added because of cell divisions. This causes subsequent mingling with the neighbors without obvious middle- or long-range individual cell migration. However, translocations of large groups of cells (that is, crowd movements) might be responsible for the changes in clonal envelope 3D geometry during critical morphogenetic rearrangements.

The individual shape of clonal envelopes reflects the anisotropic growth of the structure (40, 41) following local orientation cues. Our results show that the cues that orient the plane of cell divisions in the face, at least in part, are represented by the gradient of Wnt5a, which influences the allocation of daughter cells after mitosis and, through this, the general shape. The idea of a Wnt5a gradient is strongly supported by the similarity of the phenotypes resulting from full Wnt5a knockout and overexpression of Wnt5a (21–23). In both cases, the gradient is erased from the tissue, which is phenotypically manifested by the shortening and widening of the face and limbs. Thus, the molecular mechanisms controlling the emission, detection, and interpretation of polarity signals (including noncanonical Wnts) can be partly responsible for the early body plans as well as for the developmental origins of facial diversity (42), especially during early preskeletogenic stages. Despite the strong phenotype in Wnt5a and in other PCP mutants, many parameters related to the shape and placement of different structures are not seriously affected. Therefore, there must be other mechanisms unrelated to directional cell divisions that control the facial shape. Anisotropic proliferation rates in different facial compartments and resulting crowd movements/translocations of cells can provide an alternative way of governing the shape.

Progressively, ectomesenchymal cells that belong to the same clone adopt different fates following odontogenic, chondrogenic, osteogenic, adipogenic, and other directions of differentiation within a spatial

microdomain. Therefore, single neural crest–derived ectomesenchymal early progenitors are oligopotent in the face. Our data do not support the fact that different pools of neural crest cells contribute to prespecified ectomesenchymal populations restricted in their fate potential within the mesenchymal spectrum of fates. However, the results may partly support previously described early fate restrictions in the cranial neural crest and the existence of an early choice between neuroglial and mesenchymal directions of differentiation (15). This renders cranial neural crest cells different in early fate restrictions as compared to cells of the trunk neural crest (14).

Various early embryonic mesenchymal populations, similar to neural crest–derived ectomesenchyme, give rise to multiple differentiated cell types that organize muscle, connective, and skeletal tissues in the head and other compartments, including limbs. Our results show that cellular mechanisms of early facial shaping seem to be very similar to those operating in the limb. Furthermore, recent discoveries of epithelial-to-mesenchymal transition (EMT), a classical property of neural crest (43), in limb bud initiation (16) suggest that similarities between limb and face development are stronger than previously thought. Moreover, a recent study demonstrated that cranial neural crest cells that give rise to mesenchymal derivatives in the head may undergo EMT from a neural fold domain that might not express neural markers (15). If true, it can be defined as a non-neural ectoderm and is possibly similar to analogous sites in regions of future limb buds. For instance, it is widely accepted that facial growth and patterning are regulated by the frontonasal ectodermal zone (FEZ), which includes SHH and FGF8 expression domains (44, 45). The roles of BMPs, endothelins, and other soluble factors in facial development and outgrowth have been thoroughly investigated (44, 46). Variation of signals that affect cartilage and bone development may also influence shaping programs at later stages. This is suggested, for example, by studies on BMP3 mutations associated with the size and varying geometry of the vertebrate skull (47). Apparently, these key signals, including SHH, FGFs, and BMPs, play critical instructive roles in both facial and limb development. It could be speculated that the apical ectodermal ridge secreting FGF8 and the zone of polarizing activity emitting SHH in limb buds might be considered to be deeply homologous to the FEZ in the face. Thus, a blueprint of the cellular and molecular logics that operate in the mesenchyme of the anterior head could become a starting point for the induction of appendages in the more posterior parts of the ancestral body. Some evidence suggest that the origin of paired appendages involved redeployment of genetic programs from the paraxial to the lateral mesoderm (48, 49). Our data highlight a great degree of similarity in clonal dynamics between neural crest– and paraxial mesoderm–derived mesenchyme in the face and branchial arches. Together, our results support a profound similarity between vertebrate face and limb development and, in turn, raise questions concerning a deep homology (50) between these seemingly unrelated structures.

## MATERIALS AND METHODS

### Experimental design

This study heavily relied on clonal density genetic tracing and on the investigation of clonal envelopes in facial ectomesenchyme both as a series of static pictures and as a dynamic live imaging of mouse and zebrafish embryos, respectively. In silico modeling of clonal envelopes in developing ectomesenchyme helped to visualize and define princi-

ples of clonal overlapping in 3D envelope border formation and other important aspects leading to the prediction of a gradient that orients cell divisions. Investigation of a Wnt5a mouse mutant with deficient polarizing signals confirmed the importance of oriented cell dynamics in facial development.

### Mouse strains and animal information

All animal work was approved and permitted by the Ethical Committee on Animal Experiments (Norra Djurförsöksetiska Nämnd; [www.djurforsok.info/lagar-regler/](http://www.djurforsok.info/lagar-regler/)) and conducted according to the Swedish Animal Agency's Provisions and Guidelines for Animal Experimentation, and international guidelines and regulations were followed (Institutional Review Board/Institutional Animal Care and Use Committee). Glia-specific genetic tracing mouse strains *PLP-CreERT2* and *Sox10-CreERT2* were previously described (25, 26). Both *PLP-creERT2* and *Sox10-creERT2* strains were coupled to *R26Confetti* mice that were received from the laboratory of H. Clevers (24). To induce genetic recombination of adequate efficiency, pregnant females were injected intraperitoneally with tamoxifen (Sigma, T5648) dissolved in corn oil (Sigma, C8267). Tamoxifen concentration ranged from 1 to 5 mg per animal to obtain a range of recombination efficiency. Wnt5a full knockout embryos were obtained from *Wnt5a<sup>+/-</sup>* mice (36) at the expected Mendelian proportions. Mesodermal tracing was obtained using *Mesp1-Cre* mouse strain (35) coupled to *R26Confetti* reporter strain. *Sox2<sup>fl/fl</sup>* mice have been previously described (30) and were coupled to *Wnt1-Cre* (31) that were ordered from the Jackson Laboratory (stock number 003829). For embryo analyses, heterozygous mice of the relevant genotype were mated overnight, and by noon, the plug was considered to be E0.5. Mice were sacrificed by isoflurane (Baxter, KDG9623) overdose, and embryos were dissected and collected into ice-cold phosphate-buffered saline. Subsequently, the samples were placed on freshly prepared 4% paraformaldehyde and, depending on the developmental stage, were fixed for 3 to 6 hours at 4°C on a roller. Afterward, the embryos were cleared in Scale-A2 reagent [4 M urea, 0.1% (w/v) Triton X-100, 10% (w/w) glycerol, distilled water] for 6 hours and imaged in whole-mount mode or, alternatively, the embryos, after fixation, were cryopreserved in 30% sucrose (VWR, C27480) overnight at 4°C, embedded in optimal cutting temperature medium (Histolab, 45830), and cut into 14- to 150- $\mu$ m sections on a cryostat (Microm), depending on the subsequent application.

For cyclopamine treatments, three time-mated *PLP-CreERT2/R26Confetti* females were injected with cyclopamine (LC Laboratories) solution that was administered in corn oil via double intraperitoneal injections (30 mg/kg in each injection; days 8 and 9 of gestation). On gestation day 10, we took out and analyzed more than 16 individual embryos.

### $\mu$ -CT analysis

We used a GE Phoenix v|tome|x L 240 equipped with a 180-kV/15-W maximum-power nanofocus x-ray tube and a high-contrast flat panel detector DXR 250 with 2048  $\times$  2048 pixels and a 200  $\times$  200  $\mu$ m pixel size. The exposure time was 900 ms for every 2000 positions. The  $\mu$ -CT scan was carried out at an acceleration voltage of 60 kV and at an x-ray tube current of 200  $\mu$ A. The voxel size of the obtained volumes was in the range of 4 to 6  $\mu$ m, depending on the size of the embryo head. The tomographic reconstruction was realized using GE Phoenix datos|x 2.0 3D computed tomography software. The 3D and 2D cross section visualizations were performed with VGStudio

MAX 2.2 software. The histogram of the images was adjusted to reach a better contrast of soft tissues.

### Fish in vivo experiments

For genetic tracing in the zebrafish model, we used heterozygous hybrids obtained from crossings between *Sox10:ERT<sup>2</sup>* (51) and *ubi:ZebraBow-S* (52) transgenic fish strains. The recombination was induced by application of 1  $\mu$ M 4-hydroxytamoxifen (Sigma-Aldrich) into E3 medium at 16 hpf, and embryos were incubated for 12 hours at 28.5°C. All other manipulations with embryos were performed according to the standard methods described by Westerfield (53). Live imaging was performed using a Zeiss LSM 780 (Carl Zeiss) confocal microscope through existing protocols with minor modifications (54). For further image processing and calculations, we used ZEN 2012 (Carl Zeiss) and Imaris software (Bitplane). For EdU analysis in developing zebrafish, we applied EdU to E3 medium at a concentration of 1.5 mg/ml for 5 min. We used *Col2a1aBAC:mCherry* transgenic fishes to visualize a cartilage in EdU-stained individuals.

### Computational model

Individual cells were represented by their location on an underlying unstructured lattice, such as those typically used in finite element computations. The lattice resolution was chosen such that the average cell size is close to the desired biological cell size. Cell division and migration events were executed by inserting a new cell at a lattice site adjacent to the mother cell (division) or by swapping location with an adjacent cell (migration). Unlike many similar implementations of multicellular on-lattice models, we accounted for cell pushing; that is, if a dividing cell attempts to place its progeny at an occupied site, there is a probability that the occupying cell gets pushed to make room for the daughter cell. This means that cells can continue to divide even if all neighboring sites become occupied, rather than becoming quiescent. Because we are interested in capturing naturally occurring variations in the process, our model is stochastic. Stochasticity enters by letting the cell division time and the migration time become normally distributed random variables where the mean and variances are parameters that can be tuned to vary the degree of noise in those processes. The division direction and the migration direction are, in the absence of a polarizing field, uniformly distributed random variables. The degree of randomness in the cell division directions can be modulated by introducing a polarizing field and by tuning via a parameter how strongly the cells respond to this field, allowing us to vary the cell division direction from being completely random to becoming highly directionalized. The model is simulated as an event-driven system by a kinetic Monte Carlo algorithm, where the event with the shortened sampled waiting time is executed in each iteration. Detailed information about the mathematical model is provided in the Supplemental Materials.

### Microscopy

Frozen samples were sectioned at 14 to 50  $\mu$ m, and the sections were stored at -20°C after drying for 1 hour at room temperature. Confocal microscopy was performed with Zeiss LSM 710 CLSM and Zeiss LSM 780 CLSM instruments. The settings for the imaging of Confetti fluorescent proteins were as previously described (24). The imaging of the confocal stacks was performed using a Zeiss LSM 780 CLSM, Plan-Apochromat 10 $\times$ /0.45 M27 Zeiss air objective, with 23 to 79 optical slices of 12  $\mu$ m each with a z-axis shift of 9  $\mu$ m for every step. Before whole-mount imaging, the embryos (from E9.5 to E12.5) were cleared

in Scale-A2 reagent for 6 hours. For basic image processing and analysis, we used ZEN 2012 software.

### Immunohistochemistry, tissue stains, and EdU analysis

The following primary antibodies were used: goat anti-GFP (fluorescein isothiocyanate) (Abcam; 1:500), goat anti-Sox10 (Santa Cruz Biotechnology; 1:500), anti-neurofilament 2H3 (generated by Developmental Studies Hybridoma Bank; 1:100), Tuj1 (Promega, G712A; 1:1000), NG2 (Millipore, AB5320; 1:200), anti-PH3 (Millipore, clone MC463; 1:1000), 4',6-diamidino-2-phenylindole (DAPI; with Vectashield mounting medium for fluorescence; H-1200, Vector Laboratories Inc.), DCT (gift from V. Hearing; 1:1000), and rabbit anti-Sox2 (Abcam, AB97959; 1:1000). For the detection of the abovementioned primary antibodies, we used secondary antibodies produced in donkey conjugated with Alexa Fluor 405, 488, 555, or 647 (Invitrogen; 1:1000). Slices were mounted with 87% glycerol mounting medium (Merck). EdU (Life Technologies) was injected 2 hours before the embryos were harvested at a concentration of 65  $\mu$ g/g. Cells with incorporated EdU were visualized using a Click-iT EdU Alexa Fluor 647 Imaging Kit (Life Technologies). For von Kossa staining of the bone, we submerged the cryosections into silver solution (50 g/liter of silver nitrate in distilled water). Then, we exposed sections to white light from the laboratory lamp for 20 to 50 min. Next, silver nitrate was extensively removed with distilled water during three 7-min washes. After the washes, we placed cryosections into thiosulfate solution (50 g/liter in distilled water) for 5 min. Finally, we performed three sequential 5-min washes in distilled water and mounted microscopic slides with glycerol for imaging. For Alcian blue staining of the cartilage, we used Alcian blue solution (pH 2.5; 1 g of Alcian blue 8GX in 100 ml of 3% glacial acetic acid). Cryoslides were hydrated in distilled water and then kept in 3% acetic acid for 3 min. Then, the slides were transferred to Alcian blue solution and microwaved for 30 s. Afterward, depending on the strength of the signal, the slides were left with Alcian blue solution or were immediately washed in water twice for 5 min and mounted with glycerol.

### Image analysis and statistics

All statistical data in the figures are represented as means  $\pm$  SEM. Every dot on the graphs in Fig. 1 corresponds to one analyzed clone. The unpaired version of Student's *t* test was used to calculate the statistics (*P* value). All results were replicated in at least three different animals. We used Bitplane Imaris software for volume rendering and digital quantifications of occupied clonal volumes, measuring intercellular distances, automated cell counting, and producing maximum intensity projection images. For example, in Fig. 1 and fig. S1, rare double-colored clones in E9.5 and E10.5 and rare green clones in E17.5 were identified, segmented, and visualized in Imaris. For every clone on the graphs in Fig. 1 (M and N), we calculated 6 to 22 intercellular distances depending on the clonal size in a particular location from several embryos. For analysis of the percentage of occupied clonal volume in Fig. 1L and fig. S4P, we used a 150  $\times$  150  $\times$  200  $\mu$ m ROI volume (except for the locations where mesenchymal cells represented a narrow layer between the developing brain and the ectoderm; in such cases, one dimension of the ROI volume was reduced accordingly), where we segmented the clonal surfaces using Imaris, calculated total volume encapsulated in cells of the clone, and then subtracted such volume from the total volume of the ROI for every analyzed clone or in different anatomical positions for all color-coded mesodermal derivatives. In Fig. 2, the distances between cells

in single clones were measured using Spots to Spots Closest Distance Xtension in Imaris.

For the analysis of oriented cell divisions in *Wnt5a* mutants with corresponding controls, we performed immunohistochemistry with PH3 antibody on frozen sagittal sections of embryonic heads. Angle of the cell division was calculated as an angle between the cell division axis and the vector drawn through the basisphenoid toward developing nostrils. At least three individual *Wnt5a* mutant embryos were assessed together with higher numbers of littermate wild-type controls. In zebrafish live imaging experiments, dividing cells were tracked manually through the time series. Coordinates of each cell center after cell division were determined. Angle of the cell division in 3D was calculated as an angle between the cell division axis and the vector drawn through the fish body midline from the mouth to the midpoint between nostrils. We performed the actual calculations using vector coordinates derived from 3D space in Imaris. We counted orientations of cell divisions in three fishes between 30 and 52 hpf.

## SUPPLEMENTARY MATERIALS

Supplementary material for this article is available at <http://advances.sciencemag.org/cgi/content/full/2/8/e1600060/DC1>

fig. S1. Identification of rare double-color and GFP<sup>+</sup> clones in neural crest ectomesenchyme in E9.5 to E10.5 embryonic faces.

fig. S2. Clonal mixing and distribution of NCC-derived clones in the embryonic trunk and head through the development.

fig. S3. Defined borders between mesoderm- and neural crest-derived progenies at postnatal and embryonic stages.

fig. S4. Genetic tracing of mesoderm-derived mesenchymal progenies reveals similarities with the neural crest-derived ectomesenchyme.

fig. S5. Live imaging of ectomesenchymal clones and progenitors in the eye shows difference between organized crowd movements and individual migrations.

movie S1. Live imaging of genetically traced neural crest-derived progenies in *Sox10-CreERT2/Ubi:zebraflow-S* zebrafish larvae between 30 and 56 hpf, ventral view.

movie S2. Live imaging of translocating ectomesenchymal clusters in *Sox10-CreERT2/Ubi:zebraflow-S* zebrafish larvae between 39 and 52 hpf, ventral view.

movie S3. Live imaging of genetically traced neural crest-derived progenies in *Sox10-CreERT2/Ubi:zebraflow-S* zebrafish larvae between 30 and 88hpf, ventral view.

movie S4. Live imaging of translocating ectomesenchymal clusters in *Sox10-CreERT2/Ubi:zebraflow-S* zebrafish larvae between 39 and 52 hpf, ventral view.

movie S5. 3D EdU analysis of *Col2a1aBAC:mCherry* zebrafish larva's entire head at 4 dpf corresponding to Fig. 5 (O to Q).

Supplementary Materials and Methods

## REFERENCES AND NOTES

1. E. P. Buchanan, A. S. Xue, L. H. Hollier Jr., Craniofacial syndromes. *Plast. Reconstr. Surg.* **134**, 128e–153e (2014).
2. P. A. Trainor, P. P. Tam, Cranial paraxial mesoderm and neural crest cells of the mouse embryo: Co-distribution in the craniofacial mesenchyme but distinct segregation in branchial arches. *Development* **121**, 2569–2582 (1995).
3. V. Franklin, P. L. Khoo, H. Bildsoe, N. Wong, S. Lewis, P. P. L. Tam, Regionalisation of the endoderm progenitors and morphogenesis of the gut portals of the mouse embryo. *Mech. Dev.* **125**, 587–600 (2008).
4. J. Pispal, I. Thesleff, Mechanisms of ectodermal organogenesis. *Dev. Biol.* **262**, 195–205 (2003).
5. R. C. Mootoosamy, S. Dietrich, Distinct regulatory cascades for head and trunk myogenesis. *Development* **129**, 573–583 (2002).
6. G. Couly, P. Coltey, A. Eichmann, N. M. Le Douarin, The angiogenic potentials of the cephalic mesoderm and the origin of brain and head blood vessels. *Mech. Dev.* **53**, 97–112 (1995).
7. A. Achilleos, P. A. Trainor, Neural crest stem cells: Discovery, properties and potential for therapy. *Cell Res.* **22**, 288–304 (2012).
8. M. C. McKinney, K. Fukatsu, J. Morrison, R. McLennan, M. E. Bronner, P. M. Kulesa, Evidence for dynamic rearrangements but lack of fate or position restrictions in premigratory avian trunk neural crest. *Development* **140**, 820–830 (2013).

9. M. Bronner-Fraser, S. E. Fraser, Cell lineage analysis reveals multipotency of some avian neural crest cells. *Nature* **335**, 161–164 (1988).
10. A. Baroffio, E. Dupin, N. M. Le Douarin, Clone-forming ability and differentiation potential of migratory neural crest cells. *Proc. Natl. Acad. Sci. U.S.A.* **85**, 5325–5329 (1988).
11. C. V. Baker, M. Bronner-Fraser, N. M. Le Douarin, M. A. Teillet, Early- and late-migrating cranial neural crest cell populations have equivalent developmental potential in vivo. *Development* **124**, 3077–3087 (1997).
12. E. Nitzan, S. Krispin, E. R. Pfaltzgraff, A. Klar, P. A. Labosky, C. Kalcheim, A dynamic code of dorsal neural tube genes regulates the segregation between neurogenic and melanogenic neural crest cells. *Development* **140**, 2269–2279 (2013).
13. S. Krispin, E. Nitzan, Y. Kassem, C. Kalcheim, Evidence for a dynamic spatiotemporal fate map and early fate restrictions of premigratory avian neural crest. *Development* **137**, 585–595 (2010).
14. A. Baggolini, S. Varum, J. M. Mateos, D. Bettosini, N. John, M. Bonalli, U. Ziegler, L. Dimou, H. Clevers, R. Furrer, L. Sommer, Premigratory and migratory neural crest cells are multipotent in vivo. *Cell Stem Cell* **16**, 314–322 (2015).
15. R. T. H. Lee, H. Nagai, Y. Nakaya, G. Sheng, P. A. Trainor, J. A. Weston, J. P. Thiery, Cell delamination in the mesencephalic neural fold and its implication for the origin of ectomesenchyme. *Development* **140**, 4890–4902 (2013).
16. J. Gros, C. J. Tabin, Vertebrate limb bud formation is initiated by localized epithelial-to-mesenchymal transition. *Science* **343**, 1253–1256 (2014).
17. J. Gros, J. K.-H. Hu, C. Vinegoni, P. F. Feruglio, R. Weissleder, C. J. Tabin, WNT5A/JNK and FGF/MAPK pathways regulate the cellular events shaping the vertebrate limb bud. *Curr. Biol.* **20**, 1993–2002 (2010).
18. B. Boehm, H. Westerberg, G. Lesnicar-Pucko, S. Raja, M. Rautschka, J. Cotterell, J. Swoger, J. Sharpe, The role of spatially controlled cell proliferation in limb bud morphogenesis. *PLoS Biol.* **8**, e1000420 (2010).
19. J. A. Zallen, Planar polarity and tissue morphogenesis. *Cell* **129**, 1051–1063 (2007).
20. R. S. Gray, I. Roszko, L. Solnica-Krezel, Planar cell polarity: Coordinating morphogenetic cell behaviors with embryonic polarity. *Dev. Cell* **21**, 120–133 (2011).
21. R. van Amerongen, C. Fuerer, M. Mizutani, R. Nusse, Wnt5a can both activate and repress Wnt/β-catenin signaling during mouse embryonic development. *Dev. Biol.* **369**, 101–114 (2012).
22. E. R. M. Bakker, L. Raghoebir, P. F. Franken, W. Helvensteijn, L. van Gorp, F. Meijlink, M. A. van der Valk, R. J. Rottier, E. J. Kuipers, W. van Veelen, R. Smits, Induced Wnt5a expression perturbs embryonic outgrowth and intestinal elongation, but is well-tolerated in adult mice. *Dev. Biol.* **369**, 91–100 (2012).
23. H.-Y. H. Ho, M. W. Susman, J. B. Bickoff, Y. K. Ryu, A. M. Jonas, L. Hu, R. Kuruvilla, M. E. Greenberg, Wnt5a-Ror-Dishevelled signaling constitutes a core developmental pathway that controls tissue morphogenesis. *Proc. Natl. Acad. Sci. U.S.A.* **109**, 4044–4051 (2012).
24. H. J. Snippet, L. G. van der Flier, T. Sato, J. H. van Es, M. van den Born, C. Kroon-Veenboer, N. Barker, A. M. Klein, J. van Rheenen, B. D. Simons, H. Clevers, Intestinal crypt homeostasis results from neutral competition between symmetrically dividing Lgr5 stem cells. *Cell* **143**, 134–144 (2010).
25. C. Laranjeira, K. Sandgren, N. Kessar, W. Richardson, A. Potocnik, P. Vanden Berghe, V. Pachnis, Glial cells in the mouse enteric nervous system can undergo neurogenesis in response to injury. *J. Clin. Invest.* **121**, 3412–3424 (2011).
26. D. P. Leone, S. Genoud, S. Atanoski, R. Grausenburger, P. Berger, D. Metzger, W. B. Macklin, P. Chambon, U. Suter, Tamoxifen-inducible glia-specific Cre mice for somatic mutagenesis in oligodendrocytes and Schwann cells. *Mol. Cell. Neurosci.* **22**, 430–440 (2003).
27. L. Hari, I. Miescher, O. Shakhova, U. Suter, L. Chin, M. Taketo, W. D. Richardson, N. Kessar, L. Sommer, Temporal control of neural crest lineage generation by Wnt/β-catenin signaling. *Development* **139**, 2107–2117 (2012).
28. F. Lescroart, S. Chabab, X. Lin, S. Rulands, C. Paulissen, A. Rodolose, H. Auer, Y. Achouri, C. Dubois, A. Bondué, B. D. Simons, C. Blanpain, Early lineage restriction in temporally distinct populations of *Mesp1* progenitors during mammalian heart development. *Nat. Cell Biol.* **16**, 829–840 (2014).
29. T. Nagase, M. Nagase, N. Osumi, S. Fukuda, S. Nakamura, K. Ohsaki, K. Harii, H. Asato, K. Yoshimura, Craniofacial anomalies of the cultured mouse embryo induced by inhibition of sonic hedgehog signaling: An animal model of holoprosencephaly. *J. Craniofac. Surg.* **16**, 80–88 (2005).
30. R. Favaro, M. Valotta, A. L. M. Ferri, E. Latorre, J. Mariani, C. Giachino, C. Lancini, V. Tosetti, S. Ottolenghi, V. Taylor, S. K. Nocolis, Hippocampal development and neural stem cell maintenance require *Sox2*-dependent regulation of *Shh*. *Nat. Neurosci.* **12**, 1248–1256 (2009).
31. P. S. Danielian, D. Muccino, D. H. Rowitch, S. K. Michael, A. P. McMahon, Modification of gene activity in mouse embryos in utero by a tamoxifen-inducible form of Cre recombinase. *Curr. Biol.* **8**, 1323–1326 (1998).
32. I. Adameyko, F. Lallemand, A. Furlan, N. Zinin, S. Aranda, S. S. Kitambi, A. Blanchart, R. Favaro, S. Nocolis, M. Lübke, T. Müller, C. Birchmeier, U. Suter, I. Zaitoun, Y. Takahashi, P. Ernfor, *Sox2* and *Mif* cross-regulatory interactions consolidate progenitor and melanocyte lineages in the cranial neural crest. *Development* **139**, 397–410 (2012).

33. D. Enshell-Seiffers, C. Lindon, E. Wu, M. M. Taketo, B. A. Morgan,  $\beta$ -Catenin activity in the dermal papilla of the hair follicle regulates pigment-type switching. *Proc. Natl. Acad. Sci. U.S.A.* **107**, 21564–21569 (2010).
34. D. M. Dinulescu, R. D. Cone, Agouti and agouti-related protein: Analogies and contrasts. *J. Biol. Chem.* **275**, 6695–6698 (2000).
35. Y. Saga, S. Miyagawa-Tomita, A. Takagi, S. Kitajima, J. i. Miyazaki, T. Inoue, MesP1 is expressed in the heart precursor cells and required for the formation of a single heart tube. *Development* **126**, 3437–3447 (1999).
36. T. P. Yamaguchi, A. Bradley, A. P. McMahon, S. Jones, A Wnt5a pathway underlies outgrowth of multiple structures in the vertebrate embryo. *Development* **126**, 1211–1223 (1999).
37. M. H. Schieber, Constraints on somatotopic organization in the primary motor cortex. *J. Neurophysiol.* **86**, 2125–2143 (2001).
38. E. Méhes, T. Vicsek, Collective motion of cells: From experiments to models. *Integr. Biol.* **6**, 831–854 (2014).
39. R. David, O. Luu, E. W. Damm, J. W. H. Wen, M. Nagel, R. Winklbauer, Tissue cohesion and the mechanics of cell rearrangement. *Development* **141**, 3672–3682 (2014).
40. O. Kanca, E. Caussinus, A. S. Denes, A. Percival-Smith, M. Affolter, Raeppli: A whole-tissue labeling tool for live imaging of *Drosophila* development. *Development* **141**, 472–480 (2014).
41. M. I. Worley, L. Setiawan, I. K. Hariharan, TIE-DYE: A combinatorial marking system to visualize and genetically manipulate clones during development in *Drosophila melanogaster*. *Development* **140**, 3275–3284 (2013).
42. N. M. Young, D. Hu, A. J. Lainoff, F. J. Smith, R. Diaz, A. S. Tucker, P. A. Trainor, R. A. Schneider, B. Hallgrímsson, R. S. Marcucio, Embryonic bauplans and the developmental origins of facial diversity and constraint. *Development* **141**, 1059–1063 (2014).
43. E. Theveneau, R. Mayor, Neural crest delamination and migration: From epithelium-to-mesenchyme transition to collective cell migration. *Dev. Biol.* **366**, 34–54 (2012).
44. M. Minoux, F. M. Rijli, Molecular mechanisms of cranial neural crest cell migration and patterning in craniofacial development. *Development* **137**, 2605–2621 (2010).
45. D. Hu, N. M. Young, X. Li, Y. Xu, B. Hallgrímsson, R. S. Marcucio, A dynamic *Shh* expression pattern, regulated by SHH and BMP signaling, coordinates fusion of primordia in the amniote face. *Development* **142**, 567–574 (2015).
46. S. Foppiano, D. Hu, R. S. Marcucio, Signaling by bone morphogenetic proteins directs formation of an ectodermal signaling center that regulates craniofacial development. *Dev. Biol.* **312**, 103–114 (2007).
47. J. J. Schoenebeck, S. A. Hutchinson, A. Byers, H. C. Beale, B. Carrington, D. L. Faden, M. Rimbault, B. Decker, J. M. Kidd, R. Sood, A. R. Boyko, J. W. Fondon III, R. K. Wayne, C. D. Bustamante, B. Ciruna, E. A. Ostrander, Variation of *BMP3* contributes to dog breed skull diversity. *PLOS Genet.* **8**, e1002849 (2012).
48. M. Tanaka, Evolution of vertebrate limb development, in *Encyclopedia of Life Sciences (eLS)* (John Wiley & Sons Ltd., Chichester, UK, 2009), p. 1–9.
49. R. Freitas, G. Zhang, M. J. Cohn, Evidence that mechanisms of fin development evolved in the midline of early vertebrates. *Nature* **442**, 1033–1037 (2006).
50. N. Shubin, C. Tabin, S. Carroll, Deep homology and the origins of evolutionary novelty. *Nature* **457**, 818–823 (2009).
51. A. Mongera, A. P. Singh, M. P. Levesque, Y.-Y. Chen, P. Konstantinidis, C. Nüsslein-Volhard, Genetic lineage labeling in zebrafish uncovers novel neural crest contributions to the head, including gill pillar cells. *Development* **140**, 916–925 (2013).
52. Y. A. Pan, T. Freundlich, T. A. Weissman, D. Schoppik, X. C. Wang, S. Zimmerman, B. Ciruna, J. R. Sanes, J. W. Lichtman, A. F. Schier, Zebrow: Multispectral cell labeling for cell tracing and lineage analysis in zebrafish. *Development* **140**, 2835–2846 (2013).
53. M. Westerfield, *The Zebrafish Book: A Guide for the Laboratory Use of Zebrafish (Danio rerio)* (University of Oregon Press, Eugene, OR, ed. 4, 2000).
54. G. S. O'Brien, S. Rieger, S. M. Martin, A. M. Cavanaugh, C. Portera-Cailliau, A. Sagasti, Two-photon axotomy and time-lapse confocal imaging in live zebrafish embryos. *J. Vis. Exp.* (2009).

**Acknowledgments:** We thank A. Schier, A. Pan, and C. Nüsslein-Volhard for the fish strains; S. Warner for excellent technical support; M. Karlen and O. Kharchenko for the illustrations; and J. Jaros for technical support with  $\mu$ -CT. We also thank V. Dyachuk for essential help with mouse experiments. **Funding:** M.K. was supported by the European Molecular Biology Organization Long-Term Fellowship. The work of E.I. was supported by the Russian Fund for Basic Research (grants 14-04-32027, 15-04-07573, and 15-29-02650). K.F., A.S.C., and I.A. were supported by grants from the Swedish Research Council and Karolinska Institutet. I.A. is supported by the Hällsten Research Foundation and the Åke Wiberg Foundation. T.Z. and J.K. were supported by the Ministry of Education, Youth and Sports of the Czech Republic under the project Central European Institute of Technology 2020 (LQ1601). The laboratory of P.S. was supported by grants from the Medical Research Council and the National Institute of Dental and Craniofacial Research. The laboratory of U.S. was supported by the Swiss National Science Foundation. A.H. was supported by the Swedish strategic research program eSENCE, Vetenskapsrådet (VR), and the NIH under award number R01-EB014877-01. This work is solely the responsibility of the authors and does not necessarily reflect the views of the NIH. H. Brismar and H. Blom acknowledge funding support from VR and the Science for Life Laboratory. **Author contributions:** M.K., A.H., and I.A. designed the study and wrote the paper. M.K., D.G., T.Z., M.T., E.I., M.X., A.H., T.Y., J.P., and I.A. performed the experiments and analyzed the data. K.F., J.K., V.P., S.K.N., P.S., E.A., H. Brismar, H. Blom, H.C., U.S., and A.S.C. contributed to the experimental work and study design. All authors read and approved the paper. **Competing interests:** The authors declare that they have no competing interests. **Data and materials availability:** All data needed to evaluate the conclusions in the paper are present in the paper and/or the Supplementary Materials. Additional data related to this paper may be requested from the authors.

Submitted 13 January 2016

Accepted 29 June 2016

Published 3 August 2016

10.1126/sciadv.1600060

**Citation:** M. Kaucka, E. Ivashkin, D. Gyllborg, T. Zikmund, M. Tesarova, J. Kaiser, M. Xie, J. Petersen, V. Pachnis, S. K. Nicolis, T. Yu, P. Sharpe, E. Arenas, H. Brismar, H. Blom, H. Clevers, U. Suter, A. S. Chagin, K. Fried, A. Hellander, I. Adameyko, Analysis of neural crest-derived clones reveals novel aspects of facial development. *Sci. Adv.* **2**, e1600060 (2016).

PAPER [XI]

# Oriented clonal cell dynamics enables accurate growth and shaping of vertebrate cartilage

Marketa Kaucka<sup>1,2</sup>, Tomas Zikmund<sup>3</sup>, Marketa Tesarova<sup>3</sup>, Daniel Gyllborg<sup>4</sup>, Andreas Hellander<sup>5</sup>, Josef Jaros<sup>6</sup>, Jozef Kaiser<sup>3</sup>, Julian Petersen<sup>2</sup>, Bara Szarowska<sup>2</sup>, Phillip T Newton<sup>1</sup>, Vyacheslav Dyachuk<sup>7</sup>, Lei Li<sup>1</sup>, Hong Qian<sup>8</sup>, Anne-Sofie Johansson<sup>8</sup>, Yuji Mishina<sup>9</sup>, Joshua D Currie<sup>10</sup>, Elly M Tanaka<sup>10</sup>, Alek Erickson<sup>11</sup>, Andrew Dudley<sup>11</sup>, Hjalmar Brismar<sup>12</sup>, Paul Southam<sup>13</sup>, Enrico Coen<sup>13</sup>, Min Chen<sup>14</sup>, Lee S Weinstein<sup>14</sup>, Ales Hampl<sup>6</sup>, Ernest Arenas<sup>4</sup>, Andrei S Chagin<sup>1,15</sup>, Kaj Fried<sup>7\*</sup>, Igor Adameyko<sup>1,2\*</sup>

<sup>1</sup>Department of Physiology and Pharmacology, Karolinska Institutet, Stockholm, Sweden; <sup>2</sup>Center for Brain Research, Medical University Vienna, Vienna, Austria; <sup>3</sup>Central European Institute of Technology, Brno University of Technology, Brno, Czech Republic; <sup>4</sup>Unit of Molecular Neurobiology, Department of Medical Biochemistry and Biophysics, Karolinska Institutet, Stockholm, Sweden; <sup>5</sup>Department of Information Technology, Uppsala University, Uppsala, Sweden; <sup>6</sup>Department of Histology and Embryology, Medical Faculty, Masaryk University, Brno, Czech Republic; <sup>7</sup>Department of Neuroscience, Karolinska Institutet, Stockholm, Sweden; <sup>8</sup>Department of Medicine, Karolinska Institutet, Stockholm, Sweden; <sup>9</sup>Department of Biologic and Materials Sciences, University of Michigan School of Dentistry, Ann Arbor, United States; <sup>10</sup>Center for Regenerative Therapies, Technische Universität Dresden, Dresden, Germany; <sup>11</sup>Department of Genetics, Cell Biology and Anatomy, University of Nebraska Medical Center, Omaha, United States; <sup>12</sup>Science for Life Laboratory, Royal Institute of Technology, Solna, Sweden; <sup>13</sup>John Innes Centre, Norwich, United Kingdom; <sup>14</sup>National Institute of Diabetes and Digestive and Kidney Diseases, National Institutes of Health, Bethesda, United States; <sup>15</sup>Institute for Regenerative Medicine, Sechenov First Moscow State Medical University, Moscow, Russia

\*For correspondence: kaj.fried@ki.se (KF); igor.adameyko@ki.se (IA)

**Competing interests:** The authors declare that no competing interests exist.

**Funding:** See page 28

**Received:** 09 February 2017

**Accepted:** 16 April 2017

**Published:** 17 April 2017

**Reviewing editor:** Marianne Bronner, California Institute of Technology, United States

© This is an open-access article, free of all copyright, and may be freely reproduced, distributed, transmitted, modified, built upon, or otherwise used by anyone for any lawful purpose. The work is made available under the [Creative Commons CC0 public domain dedication](https://creativecommons.org/licenses/by/4.0/).

**Abstract** Cartilaginous structures are at the core of embryo growth and shaping before the bone forms. Here we report a novel principle of vertebrate cartilage growth that is based on introducing transversally-oriented clones into pre-existing cartilage. This mechanism of growth uncouples the lateral expansion of curved cartilaginous sheets from the control of cartilage thickness, a process which might be the evolutionary mechanism underlying adaptations of facial shape. In rod-shaped cartilage structures (Meckel, ribs and skeletal elements in developing limbs), the transverse integration of clonal columns determines the well-defined diameter and resulting rod-like morphology. We were able to alter cartilage shape by experimentally manipulating clonal geometries. Using in silico modeling, we discovered that anisotropic proliferation might explain cartilage bending and groove formation at the macro-scale.

DOI: [10.7554/eLife.25902.001](https://doi.org/10.7554/eLife.25902.001)

## Introduction

Cartilage is an essential skeletal and supportive tissue in our body. The shape and size of each cartilage element results from complex developmental processes; mesenchymal cells initially condensate, differentiate into chondrocytes, and then an orchestrated growth of the entire structure occurs (*Goldring et al., 2006*). Often, cartilage plays an important role as a developmental intermediate, such as during the endochondral growth of the long-bones (*Mackie et al., 2008*). Cartilage elements vary widely in their shapes: they may be simple shapes like rods or bars (Meckel, cartilage templates of the future long bones and ribs) or sheet-like structures (in the head), but can be extremely complicated with a huge number of irregular shapes (for instance, in the inner ear or pelvis). The geometrical properties of cartilage elements must be fine-tuned during the growth because cartilage provides indispensable structural support to the body during development. Yet, how this is achieved despite drastic changes in size is unclear.

After early cartilage forms from mesenchymal condensations, growth typically occurs in all dimensions. However, the diversity of cell dynamics controlling precise early growth and shaping is not well studied. At the same time, the late growth of long rod-shaped cartilage elements in limbs is achieved through a mechanism of endochondral ossification that includes oriented cell dynamics in growth plate-like zones (*Vortkamp et al., 1996*). In the germinal zone of a growth plate, chondrocytes proliferate and produce progenies that form long streams oriented along the main axis of the forming skeletal element. Inside such streams, chondrocytes undergo flattening, oriented cell divisions and hypertrophy before dissipating and giving place to the forming bone (*Nilsson et al., 2005*), a process which is controlled by many signals (*Kronenberg, 2003*). This cell dynamic enables efficient extension of the skeletal element in a specific direction that coincides with the orientation of cell divisions in the proliferative zone (*Abad et al., 2002*). Growth plate disorders may result in dwarfism and other illnesses (*De Luca, 2006*).

Some parts of the cartilaginous skull (e.g. the basisphenoid of the chondrocranium) also undergo endochondral ossification in synchondroses, and significant growth of the cranial base is achieved through a similar mechanism (*Hari et al., 2012; Wealhall and Herring, 2006*).

Synchondroses are mirror-image growth plates arising in the cranial base, which primarily facilitate growth in the antero-posterior direction (*Kettunen et al., 2006; Laurita et al., 2011; Nagayama et al., 2008; Young et al., 2006*). Disorders in the development of synchondroses severely impact the elongation of the cranial base and often result in short-faced mutants and a general decrease of the cranial length (*Ford-Hutchinson et al., 2007; Ma and Lozanoff, 1999*). Insufficient or abnormal development of a cartilage element is one of the reasons for human craniofacial pathologies, providing a connection between the chondrocranium and facial bone geometry, size and placement (*Wang et al., 1999*).

The growth mechanism operating in growth plates and synchondroses involves the transformation of the cartilage into the bone. Since growth plates or synchondroses are oriented towards a specific direction, the expansion of a cartilage in other dimensions is not clear from the mechanistic point of view and requires further investigation. For example, although it is well known that the mouse chondrocranium develops as 14 independent pairs of cartilage elements that form one united structure, the logic behind further shaping and scaling remains unclear (*Hari et al., 2012*). How these initially separated large cartilaginous elements form, grow and fine-tune their geometry, thickness and smoothness during development is still not completely understood. We hypothesized that accurate cartilage growth might require alternative cell dynamics that do not involve hypertrophy, ossification or growth plates.

Such alternative cell dynamics may also contribute to the accuracy of scaling during cartilage growth. Scaling is a process of growth that maintains both the shape and the proportions of the overall structure. In nature, scaling often involves sophisticated principles of directional growth and a number of feedback mechanisms (*Green et al., 2010*). For instance, during bird development, the diversity in beak shape is constrained by the dynamics of proliferative zones in the anterior face (*Fritz et al., 2014*). Furthermore, scaling variations of beaks with the same basic shape result from signaling that controls the growth of the pre-nasal cartilage and the pre-maxillary bone (*Mallarino et al., 2012*). Indeed, in order to accurately scale a pre-shaped 3D-cartilaginous template both local isotropic and anisotropic cell dynamics may be required.

To assess changes in the complete 3D anatomy of the face following cellular-level mechanistic studies we used a variety of approaches including micro-computed tomography ( $\mu$ -CT), genetic tracing with multicolor reporter mouse strains, multiple mutants and mathematical modelling.

Most importantly, we reveal here how oriented clonal behavior in the chondrogenic lineage controls the overall geometry of the cartilage elements, and show that this geometry can be manipulated with molecular tools at various levels.

## Results

Cartilage elements form and grow in all parts of the vertebrate body. The developing face provides a remarkable variety of cartilage geometries and sizes and, therefore, may serve as a sophisticated model system to study the induction of complex cartilaginous structures.

The developing cartilaginous skull, the chondrocranium, displays a very complex geometry of mostly sheet-like cartilages that result from coordinated anisotropic growth in all dimensions. Such expansion of sheet-like cartilaginous tissue during embryonic development involves several mechanisms that were proposed in the past, including the formation and growth of cartilage at synchondroses, as well as at the apical growth zone.

To understand the changes in dimensions of chondrocranium growth at major developmental stages, we took advantage of 3D reconstructions using  $\mu$ -CT enhanced with soft tissue contrasting (**Figure 1**). This approach enables the identification of various tissues and cell types in the embryo based on differential uptake of tungsten ions. We validated the  $\mu$ -CT visualization of embryonic cartilage by directly aligning stained histological sections with the 3D models (**Figure 1—figure supplements 1 and 2**).

We analyzed the expansion of the chondrocranium due to synchondroses and found that despite a significant antero-posterior elongation, synchondroses cannot entirely explain the growth dynamics in all directions: antero-posterior, latero-medial and dorso-ventral vectors of growth (**Figure 1A–C**). Specifically, we found a complete absence of synchondroses and other endochondrial ossifications in the growing nasal capsule, even at the earliest postnatal stages, while membranous ossifications appeared well developed. The stereotypical clonal cell dynamics found in synchondroses (**Figure 1D–I**) did not appear during the development of the nasal capsule. Therefore, during the entire embryonic development, chondrocranium growth and shaping is largely aided by additional and unknown mechanisms of growth.

To investigate another possible mechanism of growth, we examined the apical growth zone of the nasal capsule. To understand growth dynamics there, we birth-dated different regions of the facial cartilage using genetic tracing in *Col2a1-CreERT2/R26Confetti* and *Sox10-CreERT2/R26Confetti* embryos (**Figure 2—figure supplement 1**). Both *Col2a1-CreERT2* and *Sox10-CreERT2* lines recombine in committed chondrocyte progenitors and in mature chondrocytes. 3D analysis following tamoxifen injections at different developmental stages allowed us to identify the parts of the cartilage that develop from pre-existing chondrocytes and the regions generated from other cellular sources (**Figure 2, Figure 2—figure supplement 1**). As an example, after genetic recombination induced at E12.5, locations with high amount of traced cells show structures that come from pre-existing cartilage, whereas areas comprising from non-traced cells present structures originating from de novo mesenchymal condensations. We discovered that important and relatively large geometrical features are produced from waves of fresh mesenchymal condensations induced directly adjacent to larger pre-laid cartilage elements between E13.5 and E17.5: this includes the frontal nasal cartilage, nasal concha, labyrinth of ethmoid and, consistent with previous suggestions, cribriform plate (**Figure 2C and Figure 2—figure supplement 1A–K**). These results cannot be safely inferred from 2D traditional histological atlases because of the complex geometry. Our results are complementary to the findings of McBratney-Owen and Morris-Key with coworkers, who demonstrated that the complete chondrocranium (including skull base) develops from 14 pairs of early independently induced large cartilaginous elements that fuse together during later development (**McBratney-Owen et al., 2008**). Here, we demonstrated how new adjacent mesenchymal condensation can increase the geometrical complexity of a single solid cartilaginous element.

To substantiate our results, we took advantage of *Ebf2-CreERT2/R26Tomato* transgenic mouse line that can genetically label only a few selected patches of early mesenchyme in the cranial region. We wanted to test if some of these labelled mesenchymal patches can undergo chondrogenesis

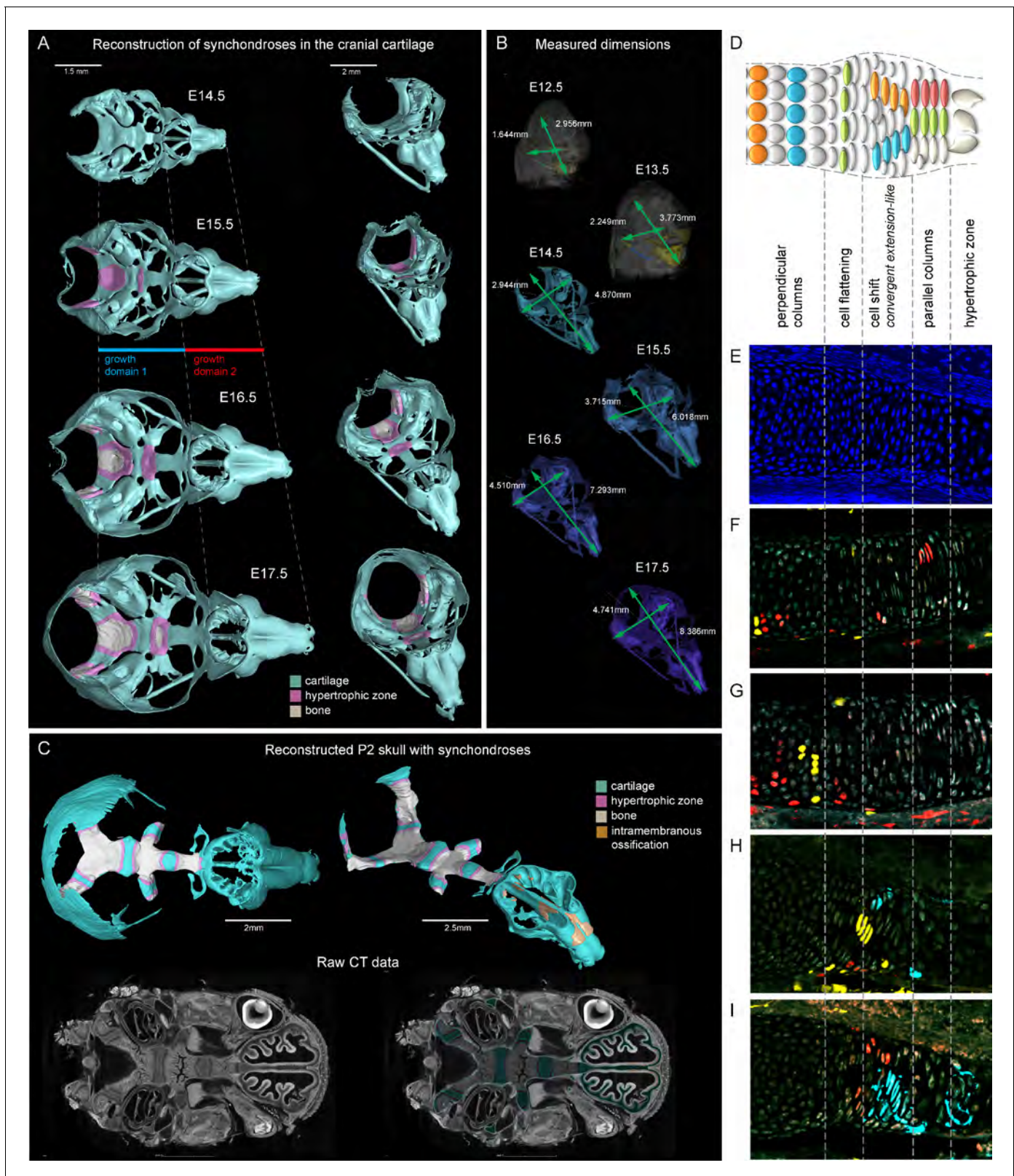


**Figure 1.** Visualizations of endochondrial ossifications in the chondrocranium during development. (A) 3D models of chondrocrania with visualized bone and hypertrophic cartilage. Note the absence of endochondrial ossifications in the nasal capsule between E14.5–17.5. Intramembraneous ossifications are not shown. (B) Width and length of the chondrocranium in E12.5–17.5 stages. (C) P2 stage model with visualized bone formation, hypertrophic zones and intramembraneous ossification in the nasal capsule. Clipping planes are applied for better visualizations of synchondroses. *Figure 1 continued on next page*

Figure 1 continued

Corresponding raw CT data are presented in the lower part. (D–I) Clonal genetic tracing in synchondroses with *Sox10CreERT2/R26Confetti*; injected at E12.5 and collected at E17.5. (D) Schematic of synchondroses, (E) DAPI stained nuclei, (F–I) different clonal arrangements in various zones of progressing synchondroses.

DOI: [10.7554/eLife.25902.002](https://doi.org/10.7554/eLife.25902.002)

The following figure supplements are available for figure 1:

**Figure supplement 1.** Histological confirmation of  $\mu$ -CT results.

DOI: [10.7554/eLife.25902.003](https://doi.org/10.7554/eLife.25902.003)

**Figure supplement 2.** Immuno- and histological validation of cartilage contrasting obtained from  $\mu$ -CT analysis and subsequent 3D modelling.

DOI: [10.7554/eLife.25902.004](https://doi.org/10.7554/eLife.25902.004)

independently and much later than most of the chondrocranium structure. If that would be the case, we could expect the formation of very sharp borders between the labelled and non-labelled cartilage due to the fusion of newly produced labelled cartilage with the old unlabeled one. If the local cartilage would form from labelled and unlabeled mesenchyme at the same time, the border would not form due to mesenchymal clone mixing that we observe when we label early neural crest. We injected *Ebf2-CreERT2/R26Tomato* animals with tamoxifen at E12.5 and analyzed the embryos at E17.5 (**Figure 2—figure supplement 2**). As a result, we discovered that the cartilage element connecting the inner ear with the basisphenoid was genetically traced, and demonstrated a very sharp border with non-traced cartilage (**Figure 2—figure supplement 2C–D**).  $\mu$ -CT data confirmed that this element develops entirely after E14.5 from newly formed mesenchymal condensations adjoining the chondrocranium (**Figure 2—figure supplement 2A–B**), and this might be related to differential regulation at the neural crest-mesodermal border (*McBratney-Owen et al., 2008; Thompson et al., 2012*). At the same time, the main structure of the chondrocranium is expanded in a very precise and symmetrical way due to unknown cellular and molecular mechanisms that cannot be explained by the freshly induced condensations, the apical growth zone, or even cell dynamics in synchondroses. Our  $\mu$ -CT results (**Figure 2**) show that various parts of the chondrocranium develop due to the growth of pre-existing cartilage not involving ossifications, while only additional features are induced in waves as de novo mesenchymal condensations that fuse with the main element during their maturation or expand in the process of ossification.

We further focused on the developing nasal capsule because its growth does not involve synchondroses while the apical growth zone and adjoining mesenchymal condensation only partly provide for the growth and shaping modifications.

The results obtained from comparisons of cartilaginous nasal capsules from different developmental stages showed that the shape of the structure is generally established by E14.5 (**Figure 3, Figure 3—figure supplement 1, Figure 3—figure supplement 2, Video 1**). Nevertheless, from E14.5 until E17.5 the cartilaginous nasal capsule is accurately scaled up with significant geometrical tuning (**Figure 3A–B**). Previous knowledge suggests that the underlying growth mechanism should be based on appositional growth of the cartilage during its transition to bone (*Hayes et al., 2001; Li et al., 2017*), however, numerous facial cartilages never ossify, but continue to grow.

Tomographic reconstructions of sheet-shaped cartilage elements in the nasal capsule revealed extensive expansion of the cartilage surface area and overall volume (**Figure 3E–F**). Surprisingly, the thickness of the cartilaginous sheets did not change as much as the other dimensions during nasal capsule growth (**Figure 3C–F, Figure 3—figure supplement 1, Video 1**). Thus, the sheet-shaped cartilage expands mostly laterally (within the plane) during directional growth. Therefore, we expected that clonal analysis of the neural crest progeny (with *Plp1-CreERT2/R26Confetti*) and of early chondrocytes (with *Col2a1-CreERT2/R26Confetti* or *Sox10-CreERT2/R26Confetti*) would reveal clonal units (so called clonal envelopes) oriented longitudinally along the axis of the lateral expansion of the cartilage. Surprisingly, and contrary to this, clonal color-coding and genetic tracing demonstrated transversely oriented clones represented by mostly perpendicular cell columns or clusters formed by traced chondrocytes (**Figure 4, especially A–C, Figure 4—figure supplement 1**).

To understand this process more in depth, we started with genetic tracing of the neural crest cells and their progeny in the facial cartilage with *Plp1-CreERT2/R26Confetti* (tamoxifen injected at E8.5). Clonal analysis and color-coding of neural crest-derived chondrogenic and non-chondrogenic ectomesenchyme showed intense mixing of neural crest-derived clones in any given location (**Figure 4A–**

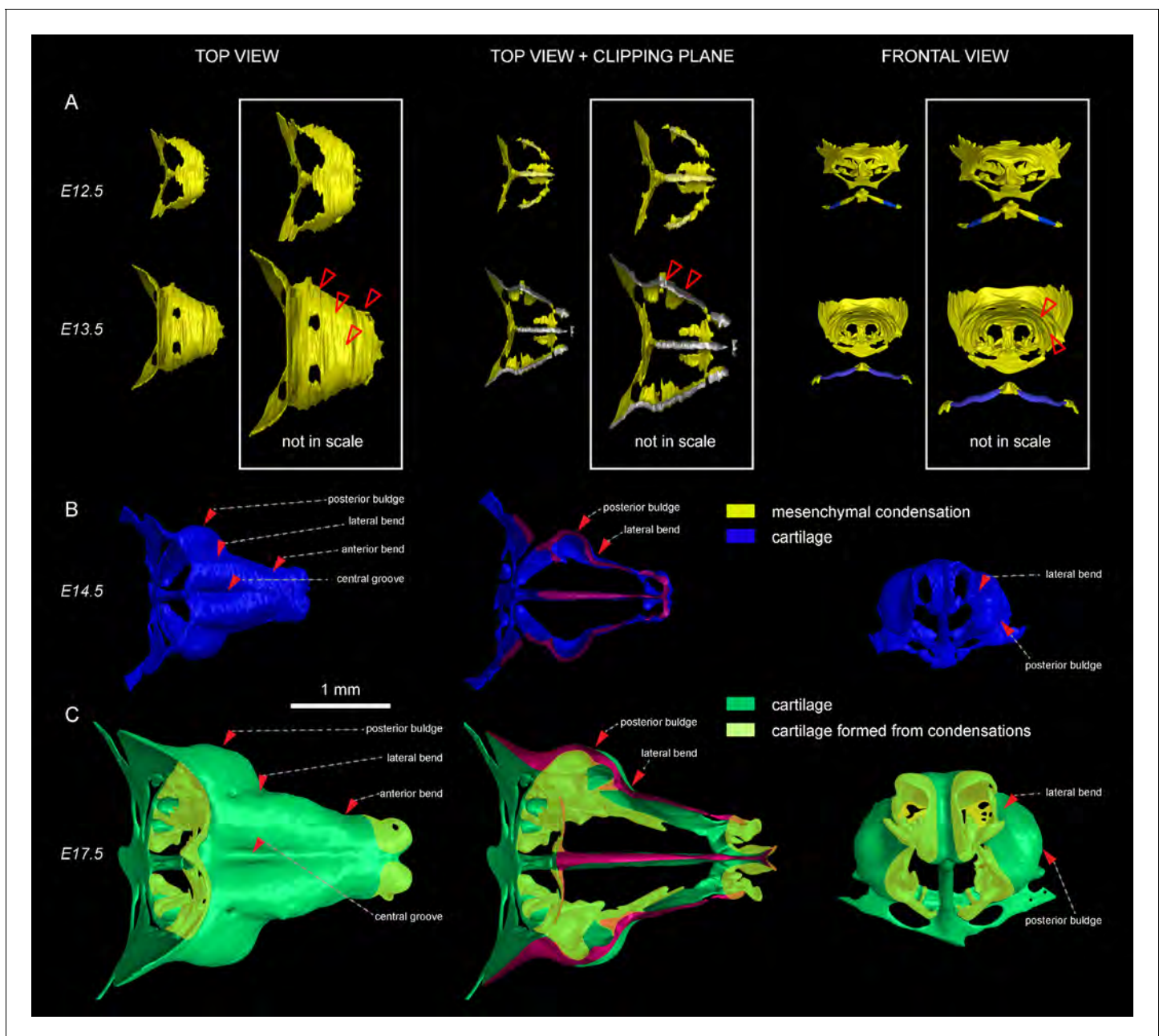


**Figure 2.** Induction of initial shape and geometrical transformations of the facial chondrocranium. (A–C)  $\mu$ -CT-based 3D reconstruction of chondrogenic mesenchymal condensations and cartilage in the face of E12.5, E13.5, E14.5 and E17.5 embryos. (A) Mesenchymal condensations (yellow) segmented from E12.5 and E13.5 embryos and presented in frontal and top projections. Note that the basics of the facial chondrocranium are already established at the stage of mesenchymal condensations during the early development, while general geometry and fine details are tuned during further transformations. (B–C) Top, clipping plane + top and frontal projections of E14.5 (B) and E17.5 (C) developing facial chondrocranium. (C) Yellow color highlights the results of cartilage birth-dating experiments and shows the areas produced from de novo mesenchymal condensations that appear in successional waves after the primary cartilage (shown in green) is produced at previous stages (E14.5). Note that the shape of the facial chondrocranium develops as a result of incremental formation and additive fusion of new mesenchymal condensation with pre-existing cartilage. Red arrows indicate areas of cartilage which bend at later developmental stages (B,C) and red-outlined arrows indicate the same areas within the mesenchymal condensations at E13.5, prior to bending (A, bottom).

DOI: [10.7554/eLife.25902.005](https://doi.org/10.7554/eLife.25902.005)

The following figure supplements are available for figure 2:

**Figure supplement 1.** Genetic tracing serves as a tool for birth-dating of the cartilage during the embryonic development.

DOI: [10.7554/eLife.25902.006](https://doi.org/10.7554/eLife.25902.006)

Figure 2 continued on next page

Figure 2 continued

**Figure supplement 2.** Genetic tracing based on Ebf2-CreERT2/R26Tomato serves as an indicator for structures developed from late mesenchymal condensations.

DOI: [10.7554/eLife.25902.007](https://doi.org/10.7554/eLife.25902.007)

*C*, **Figure 4—figure supplement 1D–G** (Kaucka et al., 2016). At the same time, chondrogenic ectomesenchyme demonstrated the presence of transversely oriented doublets of genetically traced and also EdU-labeled cells already at E13.5 (**Figure 4—figure supplement 1G** (inserts) and H). Next, analysis of neural crest progeny in established cartilage highlighted the presence of perpendicularly oriented clonal doublets and columns (**Figure 4A–C**). Further analysis of EdU incorporation and genetic tracing with chondrocyte-specific *Col2a1-CreERT2/R26Confetti* and *Sox10-CreERT2/R26Confetti* lines confirmed the existence of transversely oriented products of cell proliferation in the mature (E14.5–E17.5) cartilage (**Figure 4D–F** for EdU, **Figure 4G,H–L** and **Figure 4—figure supplement 2** for lineage tracing). These results imply that cells in the sheet-shaped cartilage do not allocate daughter cells in lateral (longitudinal) dimensions as would be intuitively expected.

Thus, simple lateral or unidirectional proliferation cannot account for the accurate scaling of the sheet-shaped cartilage in the face. Instead, the cartilage development from chondrogenic condensations is achieved by a cellular mechanism that involves intercalation of columnar clonal units.

It was unclear to us why column-like structures, and no other shapes, are integrated into the sheet-shaped cartilage and how the fine surface is maintained during this mechanism of growth. To better understand possible mechanisms of accurate sheet-shaped cartilage surface development we modelled individual cell dynamics, in silico in 4D (3D + time) (**Figure 5**) (Hellander, 2015). We used this modelling to address two questions: firstly, under what conditions are clonal columns observed? Secondly, how is the sheet-like shape achieved by polarized or non-polarized cell divisions of single-cell thick layers and what are the controlling mechanisms? We tested a group of variables including: cell division speed, allocation of daughter cells in random- or defined directions, orientation cues in the tissue (equivalent to molecule gradients), as well as pushing/intercalating of the daughter cells during proliferation. We qualitatively compared the results from in silico simulations to our experimental clonal analysis from various genetic tracing experiments, in order to identify conditions in the model that were compatible with patterns observed in vivo.

The results of the mathematical modelling suggested that the clonal dynamics observed in natural conditions requires polarity cues in the system, specifically, a two-sided gradient of signals would be required to precisely fine-tune cartilage thickness (**Figure 5A–J**). At the same time, some yet to be identified mechanism controls the average number of cell divisions in a column, further controlling columnar height and undoubtedly regulating the local thickness of the cartilage. Combined with the observed introduction of the transverse clonal columns, oriented cell proliferation can provide fine surface generation and scaling (**Figure 4—figure supplement 2**). Moreover, the model highlighted the elegance of cartilage design involving transverse columnar clones in the sheet-shaped elements: this logic enables the uncoupling of thickness control (depends on cell numbers within a clone) and lateral expansion (depends on the number of initiated clones), which are likely two molecularly unrelated processes in vivo. The absence of a gradient during in silico simulations led to the generation of 3D asymmetrical clusters instead of straight columns (even in conditions of highly synchronized cell divisions, and starting from a laterally space-constrained initial configuration - suggesting the promotion of vertical growth due to space-exclusion in the lateral direction) (**Figure 5I,J**). This, in turn, led to the formation of surface irregularities in the cartilage with subsequent loss of local flatness (heat-map diagram in **Figure 5I,J**).

Importantly, lineage tracing also showed that for cartilaginous structures in the head with asymmetrical or complex irregular geometries, such as areas where several sheet-shaped cartilage elements were merged, clones were not constructed to perpendicular columns. In such locations, we identified irregular clonal clusters or randomly oriented clonal doublets, in accordance with the modelling results (**Figure 6A–J**). Thus, the shape and orientation of clones corresponds to the local geometry of the cartilage element.

Next, we attempted to target a molecular mechanism that controls the flatness and sheet-like shape of the facial cartilaginous sheets. We discovered that activation of ACVR1 (BMP type one receptor, ALK2) in developing cartilage leads to a phenotype with targeted clonal micro-geometries

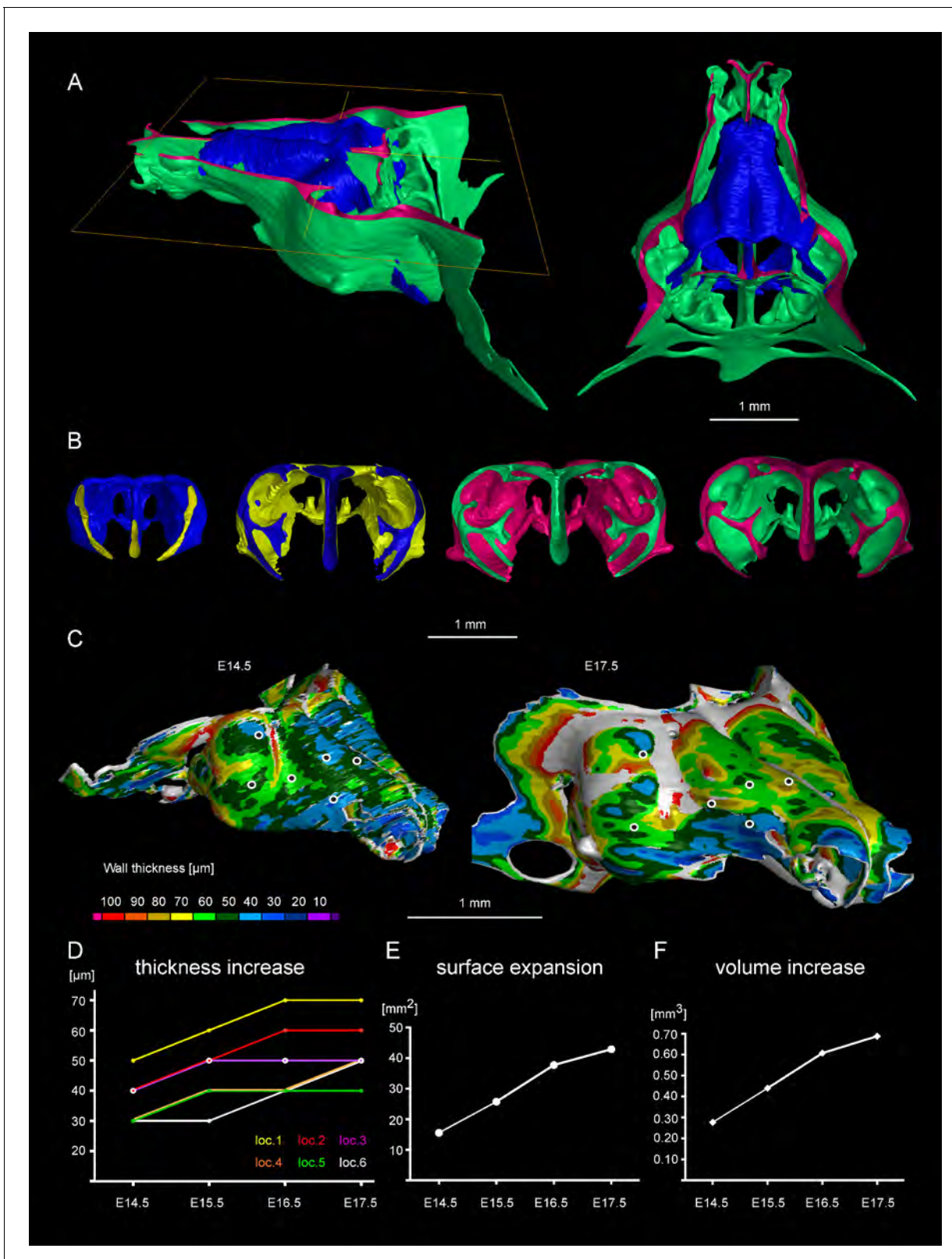


**Figure 3.** Facial chondrocranium undergoes major lateral expansion without extensive thickening during growth. (A) The 3D-model of E14.5 nasal capsule (blue) is placed onto the E17.5 model (green) for better presentation of growth-related changes. (B) Frontal clipping planes of 3D-models of nasal capsules at E14.5, E15.5, E16.5 and E17.5 (from left to right). Notice the mild changes in cartilage thickness as compared to the lateral expansion of the whole structure during growth. (C) Cartilage thickness heat-maps at E14.5 and E17.5 developmental stages. Less thick locations (color-coded in Figure 3 continued on next page

Figure 3 continued

blue) correspond to intense growth zones shown in **Figure 11**. Dots show individual positions selected for precise measurements and demonstration on the graph shown in **(D)**. Note that after E16.5 cartilage thickness remains relatively stable. **(E–F)** Cartilage surface area **(E)** and volume **(F)** expansion has been measured and compared between above mentioned stages. Note that there is a much greater increase in surface and volume (approximately 3-fold) than in thickness of the cartilage (less than 50%).

DOI: [10.7554/eLife.25902.008](https://doi.org/10.7554/eLife.25902.008)

The following figure supplements are available for figure 3:

**Figure supplement 1.** 3D models and wall thickness analysis of chondrocraniums at different developmental stages.

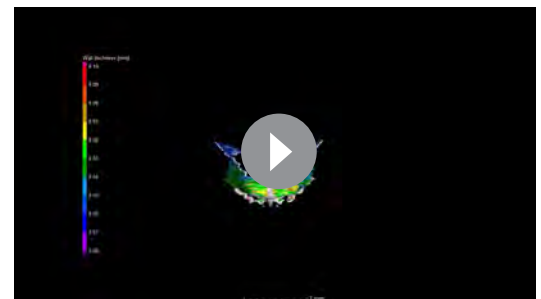
DOI: [10.7554/eLife.25902.009](https://doi.org/10.7554/eLife.25902.009)

**Figure supplement 2.** Comparisons of the shape and size differences between developmental stages and Wnt/PCP mutants.

DOI: [10.7554/eLife.25902.010](https://doi.org/10.7554/eLife.25902.010)

**(Figure 6K–P,R)**. We utilized a constitutively activated caALK2 transgene (*Fukuda et al., 2006*) together with genetic tracing in a way that every GFP-expressing cell is carrying constitutively active ACVR1. This experiment revealed a dramatic change of the shape of clonal envelopes, changing from straight perpendicular columns to disorganized spherical clusters inside the sheet-shaped cartilages of transgenic *Sox10-CreERT2/R26caALK2-IRES-GFP* embryos (**Figure 6K–N**). The ectopically activated ACVR1 resulted in the presence of clonal spherical clusters that interfered with the cartilage borders and caused the formation of ectopic bumps, swellings and other abnormal local shapes - in accordance with the mathematical modelling predictions (substantially resembling the condition with no gradient, see **Figure 5I**) (**Figure 6O–P**). All recombined cells in this caALK2 experiment became Sox9<sup>+</sup> chondrocytes. There were no other cell types found to be GFP<sup>+</sup>, including perichondrial cells. This result indicates that BMP family ligands either produce the gradient that directs the orientated behavior of chondrocytes inside of the cartilage or, alternatively, that an experimental increase of BMP signaling renders the cells insensitive to the gradient established by other molecules. In any case, ACVR1 mutation can be used as a tool to change columnar arrangements into clusters (**Figure 6N,R**). The activation of ACVR1 by *Sox10-CreERT2* starting from E12.5 occurred both in perichondrial cells and in chondrocytes (based on our genetic tracing results using *Sox10-CreERT2/R26Confetti*). This later coincided with clonal bumps and bulging regions positioned mainly at the surface of sheet-shaped cartilaginous sheets (**Figure 6L,N,P**). These data also support the hypothesis that integration of clonal chondrocyte clusters into existing cartilaginous sheets likely depends on clonal shape and originates from the periphery of the cartilage. When this column-inserting process fails, the progeny of cells at the periphery of the cartilage forms ectopic bumps outside of the normal cartilage borders, and disrupts the flatness and straightness of cartilage surfaces.

Next, we attempted to block the planar cell polarity (PCP) pathway to challenge the system and disrupt the formation of perpendicular columns in the flat or curved cartilaginous sheets. To do this we performed  $\mu$ -CT and EdU-incorporation analysis on Wnt/PCP mutants. Wnt/PCP pathway is well known for driving the cell and tissue polarity, and distinct facial phenotypes have appeared in *Ror2*, *Vangl2* and *Wnt5a* homozygous mutants (**Figure 7A**). When EdU was administered 24 hr before embryo harvest, subsequent analysis showed no differences in the EdU-positive perpendicular clonal columns which formed within sheet-shaped facial cartilage of



**Video 1.** 3D-models based on segmentation of mesenchymal condensations and mature cartilage from  $\mu$ -CT tomographic data. The first sequence illustrates wall thickness analysis results represented as a heat-map, starting from E12.5 (facial mesenchymal condensation) until E17.5 (facial cartilage). Cartilages and other soft tissues shrink during contrasting with phosphotungstic acid, and, thus, the reported metrics cannot be directly compared with biological samples treated in a different way. The following sequence shows facial chondrocranium models of Wnt/PCP mutants in comparison to the wild type. The last sequence shows the full chondrocranium at different embryonic stages, followed by 3D models of both the control embryo and *Wnt5a* mutant embryo at E17.5. DOI: [10.7554/eLife.25902.011](https://doi.org/10.7554/eLife.25902.011)

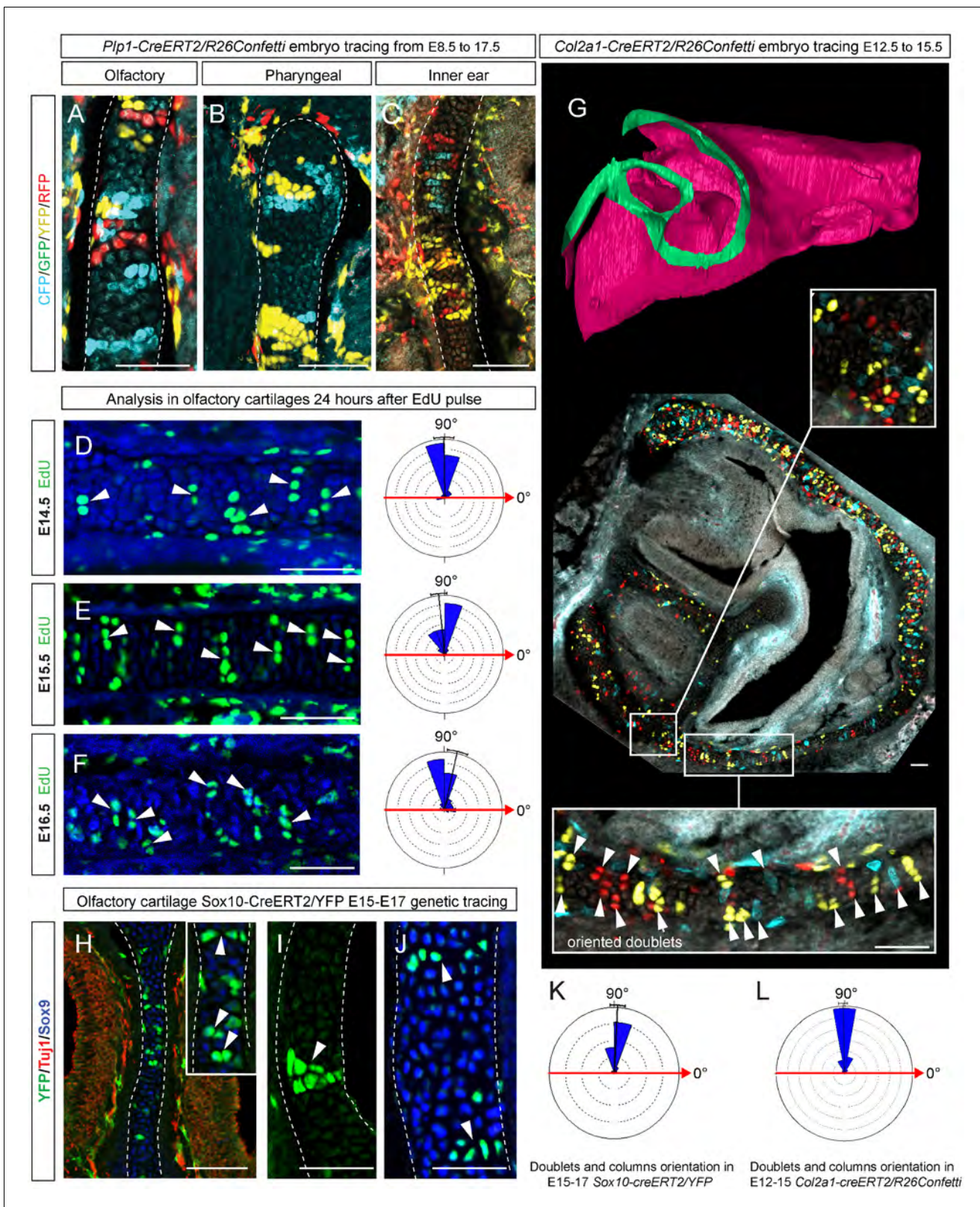


**Figure 4.** Clones of chondrocytes show transversely oriented columnar structure in sheet-shaped facial cartilage. (A–C) Chondrocyte clones at E17.5 were genetically traced from neural crest cells (E8.5), sagittal sections. The cartilage is outlined with white dashed line. (D–F) Analysis of EdU incorporation (24 hr after the pulse) into growing cartilage at different stages. Arrowheads indicate sparse columnar arrangements of EdU<sup>+</sup> cells. Rose diagrams show orientation of EdU<sup>+</sup> clusters in the cartilage of embryos at E14.5 (D), E15.5 (E) and E16.5 (F). (G) Genetic tracing of chondrocytes

Figure 4 continued on next page

Figure 4 continued

initiated at 12.5 and analyzed at 15.5. The clipping plane of a 3D-model (side projection) is shown for better orientation in the analyzed region. Note the transverse orientation of clonal doublets and columns (arrowheads). (H–J) Genetic tracing induced at E15.5 and analyzed two days later in embryos of *Sox10-CreERT2/R26YFP* mouse strain. Arrowheads indicate clonal columns of chondrocytes that formed inside of the growing cartilage between E15.5 and E17.5. The orientations of clonal arrangements are shown in the rose diagram in (K). (L) Orientation of clonal doublets and columns in genetically traced cartilage (from E12 to E15) of *Col2a1-CreERT2/R26Confetti* embryos. Scale bars = 100  $\mu\text{m}$ .

DOI: [10.7554/eLife.25902.012](https://doi.org/10.7554/eLife.25902.012)

The following figure supplements are available for figure 4:

**Figure supplement 1.** Oriented clonal dynamics in chondrogenic mesenchymal condensations.

DOI: [10.7554/eLife.25902.013](https://doi.org/10.7554/eLife.25902.013)

**Figure supplement 2.** Clonal oriented clusters of chondrocytes contain closely associated perichondrial cell in flat facial cartilages.

DOI: [10.7554/eLife.25902.014](https://doi.org/10.7554/eLife.25902.014)

Wnt5a knockout mutants or wild type controls (**Figure 7B–D**).  $\mu$ -CT analysis at early developmental stages showed that as early as at E12.5, Wnt5a mutants had abnormal shape and placement of the mesenchymal condensations that create a template for future cartilaginous structures (**Figure 7E–F**). Although  $\mu$ -CT analysis of Wnt5a, Ror2 and Vangl2 homozygous mutants at later developmental stages confirmed that chondrocranium shape was heavily affected (with generally shortened nasal capsules as compared to both wild-type and heterozygous controls) (**Figure 7A**), we did not detect any defects in cartilage micro-geometry, including thickness or surface organization. Altogether, these results indicate that Wnt5a, Ror2 and Vangl2 do not control cartilage growth and shaping per se (via the insertion of perpendicular columns). Instead, they influence the position and shape of chondrogenic condensations, which define the future geometry of the facial chondrocranium (**Figure 7E,F**).

Following the prediction from our mathematical model that the thickness of the cartilage can be controlled by the number of cells in the inserted clonal column, we searched for the molecular mechanisms which control this. Knowing from our results that proliferation rate drops in the mature cartilage, we hypothesized that chondrocyte maturation speed may influence the number of cell divisions within a column. To test this suggestion, we analyzed G-protein stimulatory  $\alpha$ -subunit ( $Gs\alpha$ ) knockout embryos (**Figure 8**). Inactivation of  $Gs\alpha$ , encoded by *Gnas*, is known to lead to accelerated differentiation of columnar chondrocytes, without affecting other aspects of cartilage biology (**Chagin et al., 2014**). We analyzed three different locations in the developing chondrocrania, and observed a significant reduction of cartilage thickness in absolute metrics (**Figure 8A,B,J**), as well as in terms of the number of cells within each column (**Figure 8B–H**). Thus, the  $Gs\alpha$  knockout is a perfect tool to test whether the modulation of differentiation speed can be used to create a variation of local cartilage thickness. The result of this experiment demonstrated that sheet-shaped cartilages in  $Gs\alpha$  knockout embryos are thinner than that of littermate controls, while other parameters (including general size and shape of nasal capsule and other locations in the head together with the transverse orientation of chondrocyte columns) remain largely unaffected (**Figure 8A,B,I**). Thus, these data experimentally validated mathematical predictions and confirmed that the thickness of cartilage is determined by the number of cell divisions within a transverse clone, and that this is uncoupled from lateral expansion.

Next, we wanted to know how clonal cell dynamics accounts for the shape development in rod-shaped cartilages. For this we investigated the clonal dynamics in Meckel, rib and limb cartilages with the help of Confetti-based genetic tracing as well as EdU incorporation. The clonal arrangements appeared highly oriented and strongly resembled the clonal columns we observed in the facial cartilage. The columnar clones were oriented mostly transversally in the plane of a rod diameter and could not explain the early growth along the main axis of the skeletal element (**Figure 9**). These tracing results suggested that longitudinal extension is based on continuous development of chondrogenic mesenchymal condensations on the distal tip and is followed by the transverse proliferation of chondrocytes, which accounts for the proper diameter of a cartilaginous rod. The logic of oriented cell dynamics in sheet-shaped and rod-shaped cartilages is summarized in **Figure 10**.

Since the integration of clonal units is likely to be uneven in the cartilage, we questioned how the anisotropy of local proliferation can impact the shaping processes on a macro-scale. Starting from E14.5, the olfactory capsule is already formed of mature chondrocytes. Indeed, in this structure,

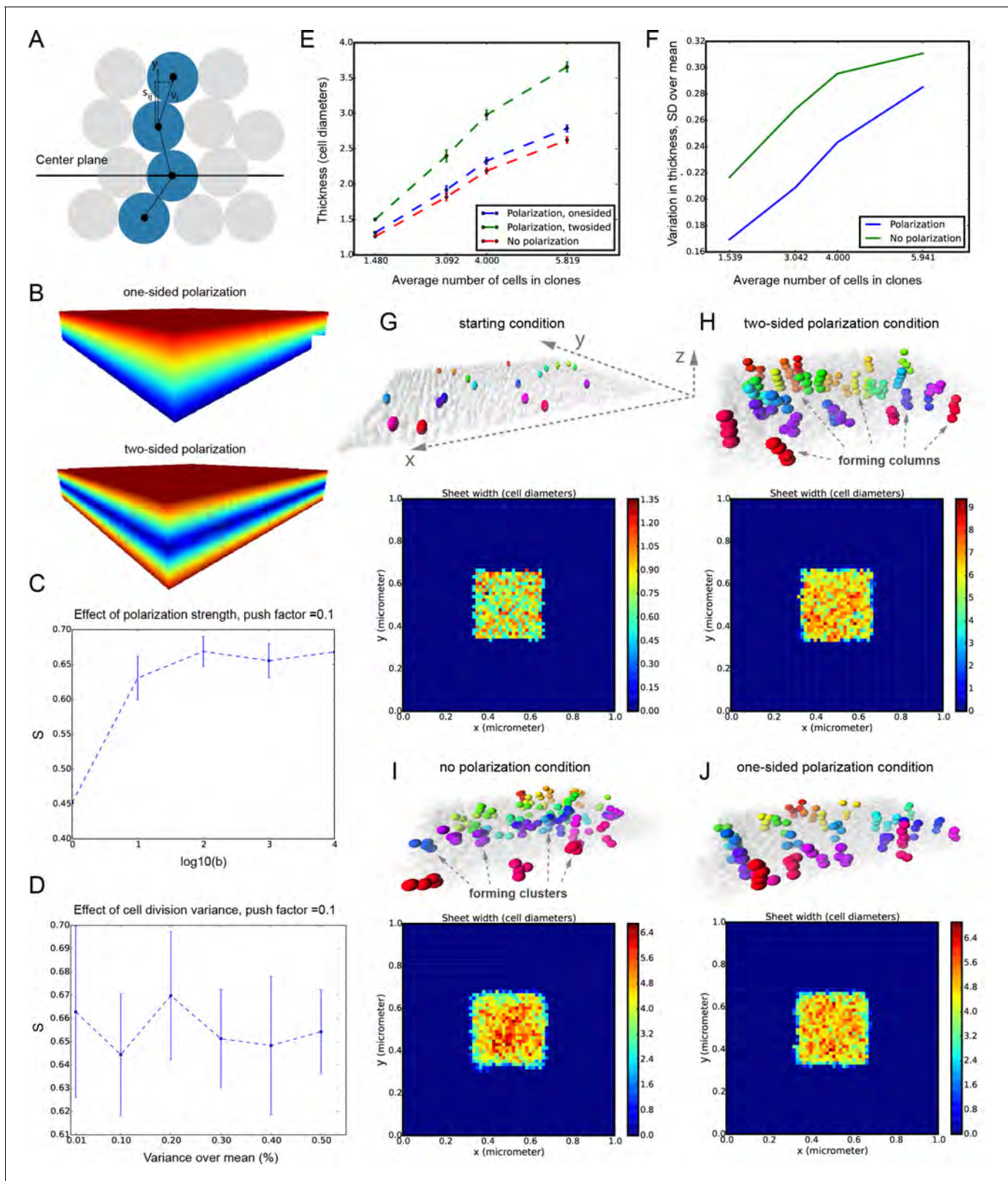


**Figure 5.** Mathematical model of cell dynamics during sheet-shaped cartilage development and growth. (A) Transversal (along z-axis) clipping plane showing conceptual arrangements of modelled cells within the layer as a result of a typical simulation. The degree of microstructure order,  $S$ , is measured by the sum of orthogonal projections on the unit vector in the z-direction, normalized by the number of cells. (B) Visualized and modelled one- and two-sided gradients used to direct oppositional growth of the clonal columns during computer simulations. (C) The degree of determinacy in Figure 5 continued on next page

Figure 5 continued

the response to the external gradient is modeled by a parameter,  $b$ , where a high value results in near perfectly polarized cell divisions (pushing may still introduce randomness in the eventually chosen site) and where the limit  $b$  tends to zero results in completely random division directions. As can be seen, the degree of microstructure order, and hence columnar growth, increases with the strength of the polarization response. (D) For a strongly polarized cell, the model predicts that even a large variation in the individual cell division times results in only a moderate decrease in the columnar order. (E) Graph showing the dependence of cartilage thickness on the absence or presence of one- and two-sided polarizing gradients. (F) Graph showing how the regularity of the thickness depends on the presence of a polarizing gradient. Note that, based on (E–F), the conditions with polarization demonstrate higher regularity and thickness over multiple locations. (G–I) Snapshots of typical *in silico* simulations of cell dynamics during sheet-shaped cartilage development: layers of chondrogenic cells demonstrated in 3D before (G) or after simulations (H–J) shown together with 2D heatmap diagrams of cell layer thickness irregularity (below) represented as a view from above ( $x,y$  dimensions). Clonal progeny is represented as individually color-coded cellular clusters or columns in 3D visualizations. Note the high degree of thickness irregularity that corresponds to the variety of differently oriented clonal shapes in condition with no polarizing gradient (I). The highest geometrical regularity of the modelled cartilaginous sheet together with stereotypical columnar clonal arrangement is achieved in the condition with two-sided polarizing gradient (H).

DOI: [10.7554/eLife.25902.015](https://doi.org/10.7554/eLife.25902.015)

proliferation was localized to specific regions, but remained generally low elsewhere (Figure 11A–B) according to the analysis of EdU incorporation. As we demonstrated above, proliferative regions expand due to the active integration of new clonal columns and clusters. We projected the low- and high proliferative zones onto the 3D structure of the nasal capsule at E13.5–E15.5 to understand not only the dynamics of lateral expansion, but also to see how the local expansion of cartilage may influence bending and geometrical changes on a large scale (Figure 11C–F). Since proliferative zones in nasal capsule are restricted and have defined edges, they inevitably induce tension and bending of the surrounding cartilage sheet.

In order to address the logic of distributed proliferative zones and its role in shape transitions between stages we took advantage of the mathematical model developed by the Enrico Coen and Andrew Bangham laboratories. This model has been efficiently validated and applied for advanced simulations of complex 4D plant organ development (Green *et al.*, 2010; Kennaway *et al.*, 2011). To simulate *in silico* nasal capsule shape transition from E13.5 to E14.5, we generated a basic E13.5-like shape by converting a sheet-shaped growing trapezoid into a corresponding 3D structure (Figure 12A, central part and Video 2). The result was considered as a simplified starting condition for further simulations. Next, two lateral zones with a low rate of proliferation were introduced according to their original position in E13.5 nasal capsule. Further simulations of the growth showed that these low proliferative zones impose a characteristic bending on the sides of the simulated structure. This bending corresponds to the lateral transformations observed in embryonic development of the nasal capsule between E13.5 and E14.5 (Figure 12B–C). This characteristic lateral bending did not depend on antero-posterior polarity in the cartilage or formation of the groove at the midline (Figure 12D). According to the model, the polarity only affected the potential for the anterior elongation due to the anisotropic growth of the entire cartilaginous structure. Our results also suggested that the nasal septum functions as a slower proliferating anchoring point to the roof of the nasal capsule, which is necessary for the formation of the midline groove at E14.5. A simulated groove at the midline provided for the general bend and flattened shape of the *in silico* cartilage, similar to the native E14.5 nasal capsule and contrary to the model without the simulated midline groove (Figure 12C–D).

To validate the general rules of *in silico* transformations, we performed material modelling using plastic film to simulate anisotropic expansion and bending due to integration of local growing zones with attached borders. This simple material modeling demonstrated that growth zones/local expansions in the flat planes generate mechanical tensions which bend the structure (Figure 12E). We then performed another material modelling experiment using isotropic thermal expansion/constriction of a plastic film. For this purpose, we drew black regions (analogous to the lateral low proliferative zones in E13.5 nasal capsule) onto white plastic film that was cut in a shape of a trapezoid capable of transforming into a nasal capsule-like dome. Under the heating provided by a thermal infrared lamp, the black zones received more heat and isotropically shrunk. Shrinkage of the black zones created physical tensions that eventually bent the structure in a way similar to the original nasal capsule geometry at E14.5 (Figure 12F). The model with shrinking zones is comparable to the real growth conditions as the nasal capsule expands faster than spatially distributed slow

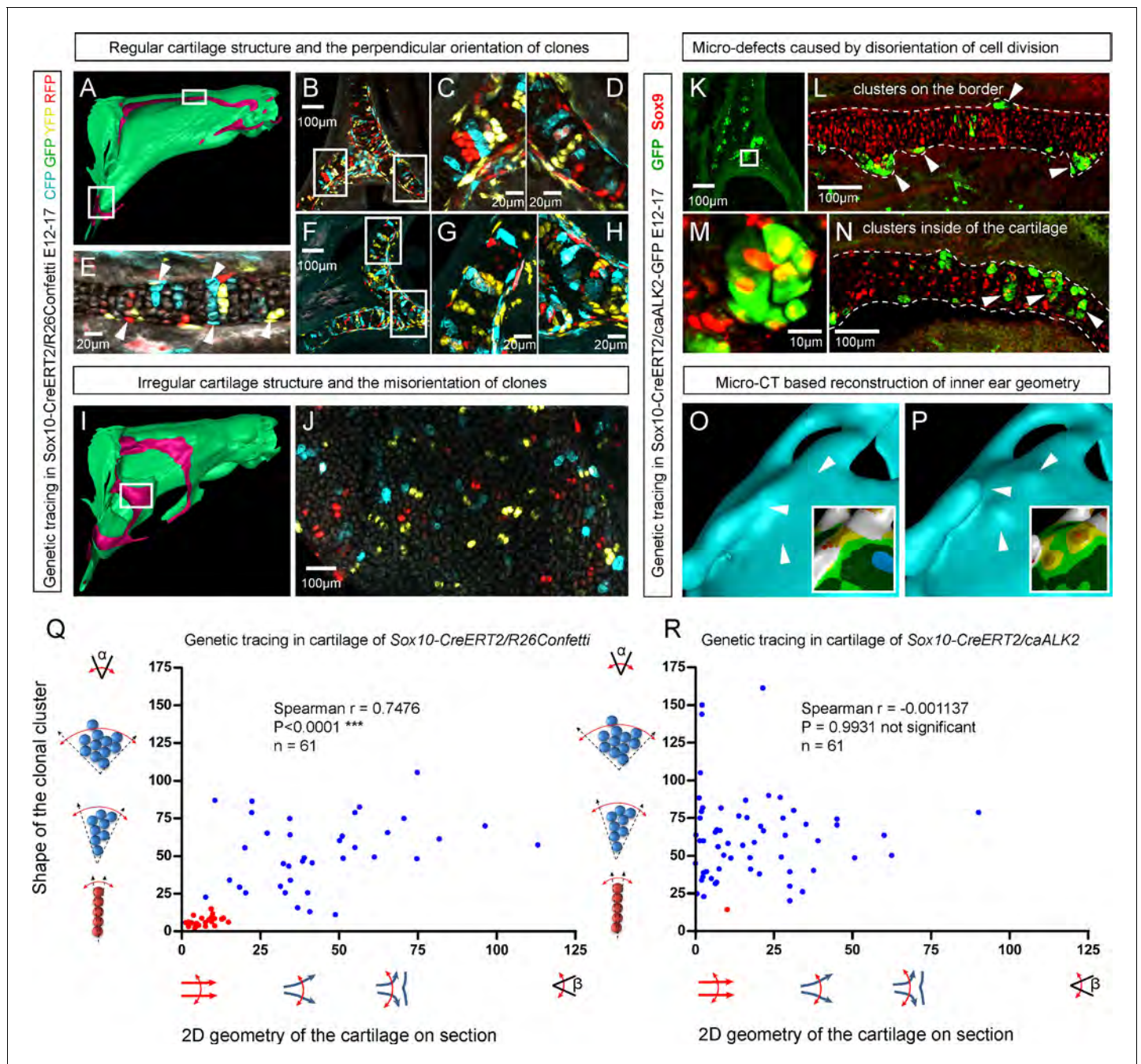


**Figure 6.** Clonal arrangements of chondrocytes influence local geometry and cartilage surface. (A–H) Columnar clonal arrangements in sheet-shaped cartilages of facial chondrocranium visualized with genetic tracing in *Sox10-CreERT2/R26Confetti* embryos. (A) 3D-model with a clipping plane shown as a side projection. White frames show locations analyzed in (B–H). Panels (C,D) and (G,H) represent magnified areas outlined in (B) and (F), respectively. (E) Traced perichondrial cells at the base of chondrocyte columns that share a clonal origin and are indicated by arrowheads. Note that rich tracing in the perichondrium correlates with highly efficient tracing in the cartilage (compare, for example, (B–D and E)). (I–J) Clonal clusters show no columnar structure in geometrically irregular elements such as junctions and fusion points of several cartilaginous elements (highlighted in 3D-model with frame). (K–P) Cre-based activation of ACVR1 in facial sheet-shaped cartilage elements of *Sox10-CreERT2/stop<sup>flxed/flxed</sup>caAlk2-IRES-GFP* embryos induced at E12.5 and analyzed at E17.5. Locations are the same as highlighted in (A). (K–N) Green clusters are sparse and clonal and show successful activation of ACVR1. Note the formation of spherical clusters of chondrocytes instead of transversely oriented columns. Spherical clusters bulging from the sheet-shaped cartilage are indicated by arrowheads in (L). Amorphous clusters caught inside of the structure are indicated by arrowheads in (N). The cartilage surface is outlined with a dotted line. (O–P) Despite low efficiency of Cre-based ACVR1 activation, the local disruptions of cartilage 3D geometry (analyzed with  $\mu$ -CT) take place: the inner ear capsule is affected by bulges and the connecting junction is destroyed as indicated by arrowheads. Thickness heatmaps of analyzed location show local thickening of the cartilage as a result of non-oriented placement of chondrocytes with disrupted

Figure 6 continued on next page

Figure 6 continued

BMP signaling. (Q–R) Graphs showing how the regularity of the cartilage (flatness) correlates with orientation of clonal envelopes in the cartilage of *Sox10-CreERT2/R26Confetti* (Q) and *Sox10-CreERT2/stop<sup>floxed/floxed</sup>caAlk2-IRES-GFP* (R) embryos. The angle  $\alpha$  characterizes the elongation of a clonal cluster consisting of multiple cells, as shown in a legend of a corresponding graph axis. Small values of  $\alpha$  correspond to highly oriented clonal envelopes such as vertical clonal columns. Angle  $\beta$  is the angle between two opposite cartilage surfaces framing cartilage tissue in this locality. Sheet-shaped cartilages have almost parallel surfaces and angle  $\beta$  values are normally set between zero and 20 degrees. Note that the population of clonal columns (red dots) is almost completely eradicated from the cartilage when ACVR1 is activated in (R).

DOI: 10.7554/eLife.25902.016

proliferative regions (simulated as shrinking zones inside of the non-expanding plastic material). These results, combined with analysis of proliferation and 3D visualizations, strongly suggest that the distribution of uneven proliferative zones plays an important role in the shaping of the facial chondrocranium during embryonic development.

Taken together, we reveal a set of principles contributing to the accurate scaling and shaping of cartilage tissue during growth. The reverse engineering of this process highlights the involvement of highly specialized systems that control the directional growth at the levels of micro- (clonal shapes) and macro-geometries (proliferative regions in nasal capsule). Our results show that allometric growth of complex 3D cartilage elements is not achieved by simple, evenly distributed and/or unidirectional proliferation, but is sculpted by precisely localized proliferation.

## Discussion

Here we report the discovery of how oriented cell behavior and molecular signals control cartilage growth and shaping. Previously, the use of chimeric avian embryos demonstrated the competence of facial mesenchyme in producing species-specific shapes and sizes of cartilage elements (Eames and Schneider, 2008), while facial epithelium and brain provided the instructive signals guiding generalized shaping of the face (Chong et al., 2012; Foppiano et al., 2007; Hu et al., 2015). Knowledge of how the facial cartilaginous elements are shaped has been rather restricted, and mainly concerned with the correct formation of chondrogenic mesenchymal condensations.

The accurate expansion of the chondrogenic condensation or cartilage during growth is no trivial matter. The general shape should be both preserved and modified at the same time. We show that anisotropic proliferation and oriented clonal cell dynamics are implemented to achieve the necessary outcome. The reverse engineering of this process highlighted the involvement of highly specialized systems that control the directional growth at the levels of micro- (clonal shapes) and macrogeometries (proliferative regions).

Allometric growth of complex 3D structures requires certain cellular logics and cannot efficiently proceed with equally distributed and/or unidirectional proliferation inside of the mesenchymal condensation or cartilage element. On the other hand, we did not observe the formation of growth plate-like zones in early sheet-shaped (nasal capsule) or rod-shaped cartilages, nor uniform expansion of cartilage in all directions. Thus, the underlying growth and shaping mechanisms required an explanation.

To test various strategies of cellular behavior during cartilage growth we devised a model simulating different aspects of multicellular dynamics in 3D together with lineage tracing of individual clones. Most of the currently existing models of cell dynamics and tracing operate in 2D space, which often limits the predictions (Jarjour et al., 2014). Our model suggested that a gradient-controlled orientation of clonal expansion can explain the biological observations (i.e. it is consistent with ordered columnar growth and its disruption results in spherical microdomains rather than columns), and showed the relation between the geometries of clonal domains (envelopes), the overall shape and the fineness of the surface. We confirmed the predictions from the model in a series of experiments involving tracing with multicolor reporters and manipulating the cartilage with mutations. Our results showed that the formation of oriented clones of chondrocytes with clonal envelope shape corresponds to the geometry of the analyzed locality. The sheet-shaped cartilage elements consisted of transversely oriented clonal columns, while asymmetric complex geometries revealed a variety of clonal shapes ranging from spherical to particularly oriented.

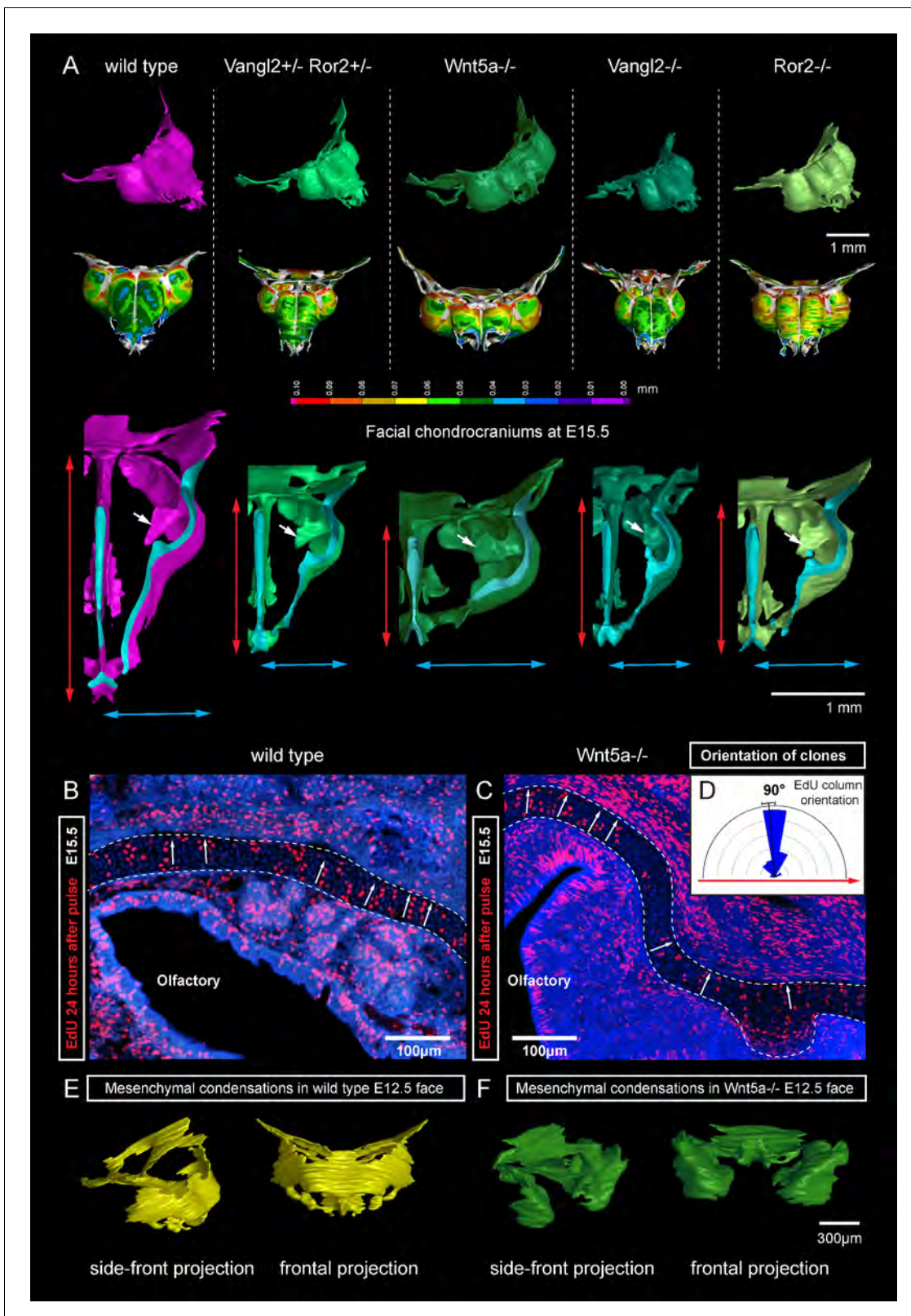


**Figure 7.** Deficiencies in Wnt/PCP pathway reshape the chondrocranium. (A)  $\mu$ -CT-based reconstructions of the facial chondrocranium of wild type control, *Wnt5a*<sup>-/-</sup>, *Vangl2*<sup>+/-</sup>/*Ror2*<sup>+/-</sup> and *Vangl2*<sup>-/-</sup>/*Ror2*<sup>-/-</sup> embryos at E15.5, with wall-thickness analysis (the row below). Clipping planes in the top projections show that all major- and fine structures (indicated by white arrows) are in place in the Wnt/PCP mutants. Red and blue arrows help to compare the width and the length of the chondrocranium. (B–D) Analysis of EdU incorporation in the facial sheet-shaped cartilage, 24 hr after the pulse. (E–F) Analysis of mesenchymal condensations in wild type and *Wnt5a*<sup>-/-</sup> E12.5 faces. *Figure 7 continued on next page*

Figure 7 continued

pulse: control (B) and *Wnt5a*<sup>-/-</sup> mutant (C) embryos. Sparse clusters and columns of EdU<sup>+</sup> cells correspond to clonal arrangements previously shown with genetic tracing in the same locations. Note that the orientation of chondrocyte placement in the cartilage is not affected in the mutant embryos. Quantification is presented in a rose diagram in (D). For control, we refer to the rose diagrams in Figure 3. (E, F)  $\mu$ -CT-based 3D reconstruction of mesenchymal condensations at the developmental stage E12.5 in control (E) and *Wnt5a*<sup>-/-</sup> mutant (F) embryos shows their misplacement in a mutant. DOI: 10.7554/eLife.25902.017

Genetic tracing initiated during transition of condensations into cartilage resulted in clonal columns within both sheet- and rod-shaped cartilage elements. This confirms that chondrogenic condensations undergo complex oriented cell dynamics during their development. Importantly, tracing of chondrocranium cartilage showed formation of transverse clonal columns as growth proceeded. Intercalation of newly born columns into pre-existing cartilage provided for the expansion potential in the sheet-shaped cartilage. This growth mechanism is very original and is not reported elsewhere so far.

A few studies have demonstrated how clonal envelopes form in accordance with the general shape of the structure. These were mainly conducted on *Drosophila* imaginal wing disc or growing flower petals. In all cases the authors highlighted that the shape of clonal geometries correlates with the major vector of expansion in the growing structure (Green et al., 2010; Repiso et al., 2013; Strutt, 2005). This implies the presence of polarized activity that directs the shaping of the tissue. Here, we provided the first experimental evidence of how the control of the directional clonal expansion influences the shape of a vertebrate tissue on a large scale. Moreover, in the sheet-shaped cartilage the orientation of clonal domains, i.e. the columns, does not correspond to the vectors of major expansion, but rather serves for uncoupling lateral expansion control and thickness tuning. In line with that, the number of chondrocytes comprising the clonal column or cluster depends on Gs $\alpha$ -mediated signals. Variations in this number do not significantly affect the lateral dimensions of the whole sheet-shaped cartilage structure: the thickness of the cartilage becomes less while the general geometry and size stay preserved. Additionally, the shape and orientation of clonal envelopes in cartilage is partially controlled by BMP signaling, since micro-geometries of clones depend on activation of ACVR1. Based on these results, we assume that BMP ligands (because of cAlk2/ACVR1 phenotype affected clonal orientation) expressed around the regularly shaped cartilages may play a role similar to the in silico predicted gradients. Indeed, the expression of INHBA, BMP5 and BMP3 fit this expression profile quite well (according to Allen Developing Mouse Brain Atlas (<http://developingmouse.brain-map.org>) and Eurexpress (<http://www.eurexpress.org>) in situ public databases). At least, BMP5 is clearly expressed at the cartilage periphery and has been shown to affect the cartilage shape by David Kingsley lab (Guenther et al., 2008).

Our experimental manipulations of planar cell polarity (PCP) pathway did not affect microgeometries and clonal domains, but strongly affected the chondrocranium shape on the macroscopical scale in several different ways. These phenotypes appeared to be rooted in pre-chondrogenic or early chondrogenic stages, and are based on distorted placement of mesenchymal condensations in the very early head. These experiments with *Wnt*/PCP mutants may potentially provide a better understanding of species-specific mechanisms of control and evolution of the facial shape on a macro scale.

Regular shapes require regular cellular arrangements and clonal cell dynamics. It is not only sheet-shaped cartilage in the head that demonstrate geometric regularity; rod-shaped cartilage (Meckel, embryonic ribs and long cartilages in limbs) also has a regular shape. Regular clonal patterns, conceptually similar to those found in sheet-shaped cartilage, explain conservative tissue dynamics during formation and growth of cartilaginous rods. Indeed, genetic tracing experiments suggested that formation of clonal columns is important for the diameter control, while chondrogenic condensations at the very tip of the rod-shaped growing structures enable elongation. Similar to the cell dynamics in the sheet-shaped cartilage, this mechanism may provide for uncoupling of length versus diameter control. Such uncoupling may generally enable developmental and evolutionary plasticity of cartilage size and shape.

The mechanism controlling the thickness or diameter of sheet-shaped and rod-shaped cartilage elements not only includes spatially orientated behavior, but also involves the regulation of cell number within each chondrogenic clone. Immature chondrocytes are proliferatively active, while more

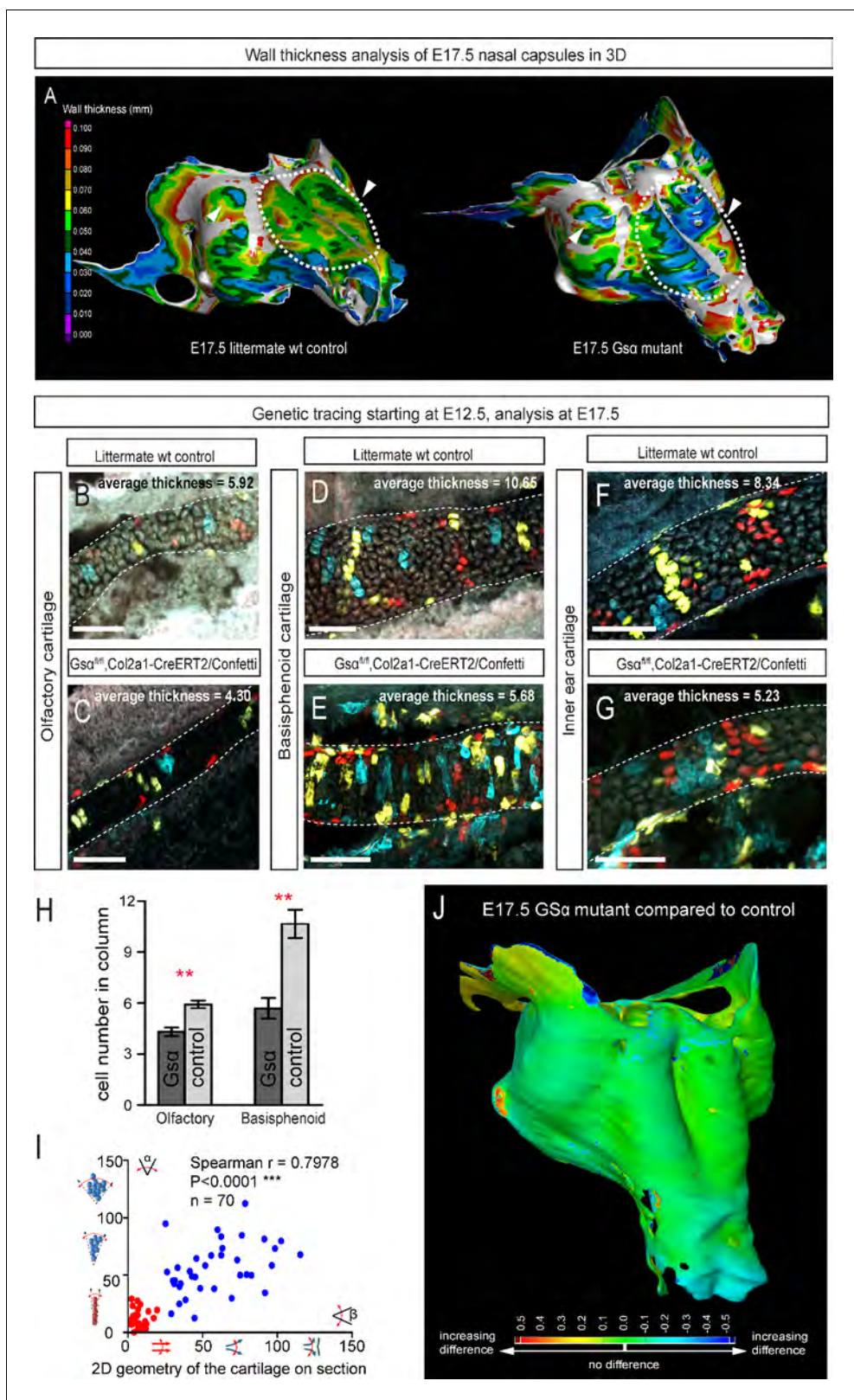


**Figure 8.** Manipulation of cartilage thickness in *GSα* mutant embryos. (A) Wall thickness was analysed in the  $\mu$ -CT segmented olfactory system of control (left) and *GSα* (*G*-protein subunit alpha) mutant (right). Large areas with decreased cartilage thickness are highlighted with a dashed line and white arrows. (B–G) Clonal genetic tracing of chondrocyte progenitors and chondrocytes induced by tamoxifen injection at E12.5 in *Col2a1-CreERT2/R26Confetti/GSα<sup>fl/fl</sup>* embryos (C,E,G) and littermate controls (B,D,F) at E17.5. (H) Quantification of cartilage thickness in the olfactory system and

Figure 8 continued on next page

Figure 8 continued

basisphenoid from three independent experiments. Note the significant decrease of cartilage thickness in all analyzed locations. Oriented organization of the chondrocyte clones was not affected by  $GS\alpha$  ablation. The difference between control (mean = 5.9, sem =  $\pm 0.23$ , n = 4) and mutant (mean = 4.3, sem =  $\pm 0.25$ , n = 3) olfactory cartilage thickness is significant ( $p=0.0053$ ). The difference between control (mean = 10.6, sem =  $\pm 0.83$ , n = 3) and mutant (mean = 5.7, sem =  $\pm 0.61$ , n = 3) basisphenoid cartilage thickness is significant ( $p=0.0087$ ). Scale bars = 100  $\mu\text{m}$ . (I) Graph showing that the regularity (straightness) of the cartilage correlates with the orientation of chondrocyte clones in the cartilage of *Col2a1-CreERT2/R26Confetti/GS $\alpha$ <sup>flxed/flxed</sup>* embryos. Angle  $\alpha$  characterizes the orientation of chondrocyte clones consisting of multiple cells as shown in a legend of a corresponding graph axis (y). Small values of  $\alpha$  correspond to highly oriented chondrocyte clones such as transverse clonal columns. Angle  $\beta$  is the angle between two opposite cartilage surfaces. Since sheet-shaped cartilage elements have almost parallel surfaces the angle  $\beta$  was normally set between zero and 20 degrees. (J) GOM Inspect software was used to compare the shape of the nasal capsule between  $GS\alpha$  mutant and control embryo at E17.5.

DOI: 10.7554/eLife.25902.018

mature chondrocytes show decreased proliferation. Therefore, differentiation speed emerges as a concept which could regulate the organ shape by impinging on clone size, thereby altering the thickness or diameter of the cartilage. This concept is known to operate in the brain and other tissues with classical stem cell/transiently amplifying cell arrangements (*Díaz-Flores et al., 2006*).

Clonal genetic tracing and EdU labeling experiments suggested that the origin of clonal columns and clusters might be represented by the cells located at the periphery of forming cartilage. The spherical clusters of chondrocytes forming at the periphery of the cartilage in *cALK2* mutant mice may suggest that the cell source is also located at the periphery and might be a perichondrial cell. Clonal relationships between perichondrial cells and columns of chondrocytes also support the hypothesis of perichondrial cells acting as a stem population during cartilage expansion. In general, the heterogeneity and multipotency of perichondrial cells is still unclear, although there are multiple studies showing the perichondrium as a source of chondrocytes and osteoblasts (*Kobayashi et al., 2011; Li et al., 2017; Maes et al., 2010*).

In addition to this, the perichondrium might mediate non-autonomous effects in the cartilage in case of *cALK2* and  $GS\alpha$  experiments. Genetic tracing shows that some perichondrial cells always recombine with *Sox10-*, *Plp1-* and *Col2a1-CreERT2* lines, and, in case of functional experiments, may indirectly control some evens in more mature layers. Also, it is not clear how the fine border of the cartilage is set, and whether the perichondrial layer may play a key border-setting role during development and regeneration. This should be investigated further.

Next, our results show that tuning of macro-geometries on a large scale can be achieved through a stage-specific placement of proliferative hot zones where new clonal domains intercalate into the main cartilage structure. Anisotropic heterogeneous proliferation is a powerful tool, which, together with polarity in the tissue and local patterning, can drive the organ shape development (*Ben Amar and Jia, 2013; Campinho and Heisenberg, 2013*). The localized growth zones provide for the general expansion and also bend the cartilage by creating local tensions that require mechanical relaxation and influence further development of the overall shape (*Schötz et al., 2013*). For probing such transformations of the sheet-shaped facial cartilage we applied an *in silico* model that was already successfully validated in a number of growth, shaping and scaling tasks (*Green et al., 2010; Kennaway et al., 2011*). Such a model was necessary to understand why the high and low proliferation zones are positioned in such a specific way. Indeed, the discovered distribution of proliferative zones in the whole nasal capsule did not help us *per se* with intuitive explanations of geometrical changes on the macro-scale. Despite this counter-intuitive dataset, the mathematical model provided an insight into the logic of the high and low proliferation zones in relation to a transition between investigated cartilage shapes.

For example, it turned out that the position of lateral slow proliferation zones enables the generation of the symmetrical bends at the sides of the nasal capsule during transition from E13.5 to E14.5 developmental shapes. Furthermore, real material modelling confirmed the results predicted by the mathematical model, and generated lateral bends similarly to the native structure. The molecular mechanism controlling the dynamic distribution (patterning) of fast/slow proliferative zones in the cartilage is still unknown. It is likely linked to developmental signals from other tissues such as the olfactory epithelium or the mesenchyme surrounding the cartilage. Identification and validation of these signals will be essential in future studies and would involve a substantial combination of screening and functional approaches with transgenic animal models.

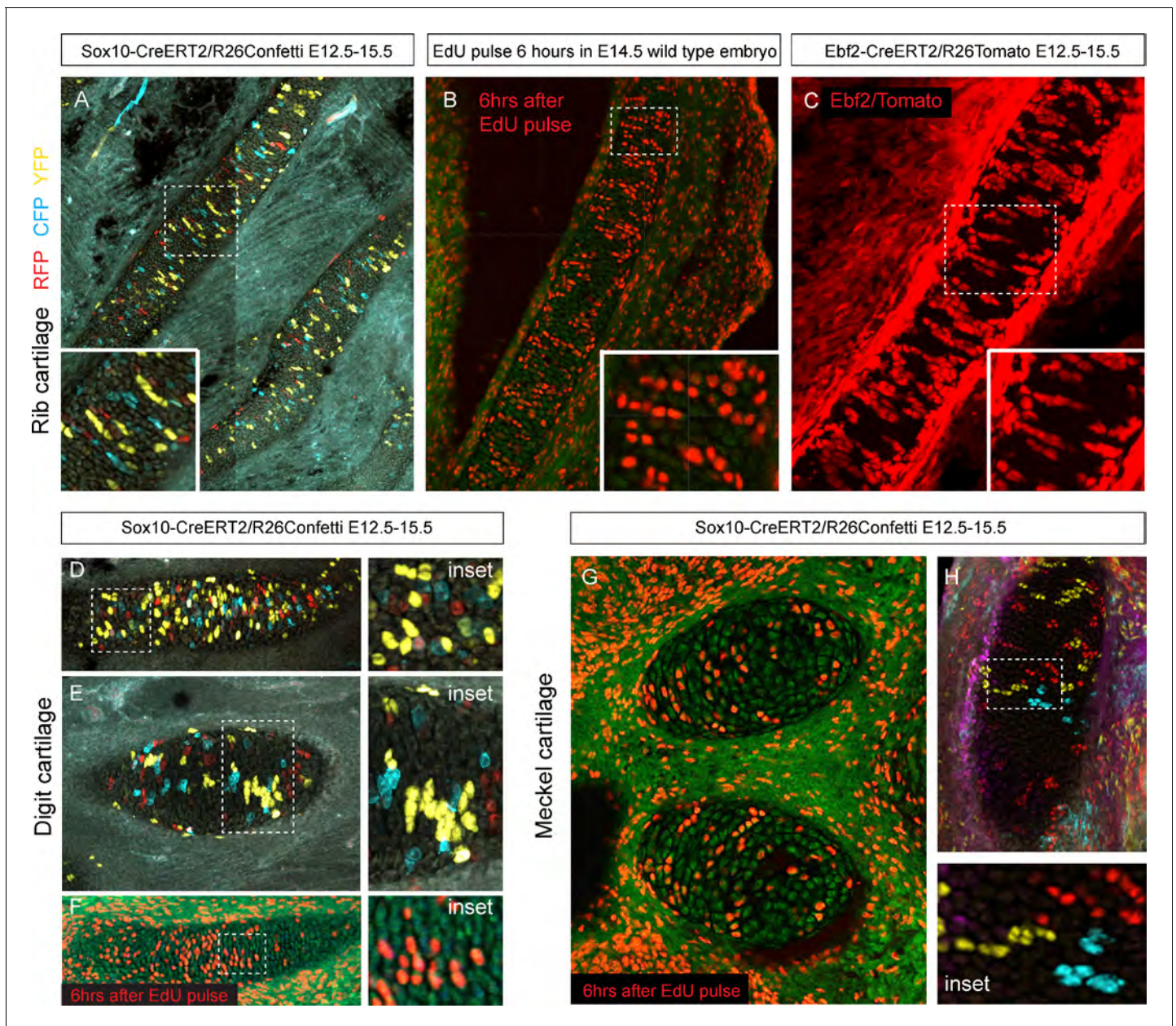


**Figure 9.** Oriented cell dynamics during development of rod-shaped cartilage elements. (A) Genetic tracing in developing rib cartilage. Note the transverse pattern of chondrocyte clones. Dotted rectangle shows the area of magnified inset on bottom left. (B) 6 hr after EdU pulse in E14.5 embryo, transverse patterns were observed in ribs. Dotted rectangle shows the areas of magnified inset in bottom right corner. (C) Genetic tracing in developing rib cartilage shows transverse patterns. Dotted line represents area magnified in inset on the bottom right. (D–F) Genetic tracing (D,E) and 6 hr after EdU pulse (F) in developing digit cartilage of the upper limb. The areas of magnified insets (located on the right side) are outlined by dotted lines. (G) Transverse patterns in developing Meckel cartilage resulting from EdU pulse and analysis 6 hr after administration. (H) Genetic tracing shows transverse orientation of clonal chondrocytic columns in the Meckel cartilage. Dotted line shows the area magnified in the inset on the right.

DOI: [10.7554/eLife.25902.019](https://doi.org/10.7554/eLife.25902.019)

The anisotropic proliferation can be an important evolutionary mechanism that is directly responsible for the differences in snout geometry in a variety of phylogenetic groups. Additionally, it might be important for understanding the development of the facial shape variation in humans (Sheehan and Nachman, 2014) as well as numerous pathologies (Afsharpaiman et al., 2013).

One alternative way to fine-tune macro-geometry of a cartilage element is to continuously add on pre-shaped chondrogenic mesenchymal condensations from the pool of competent progenitors that

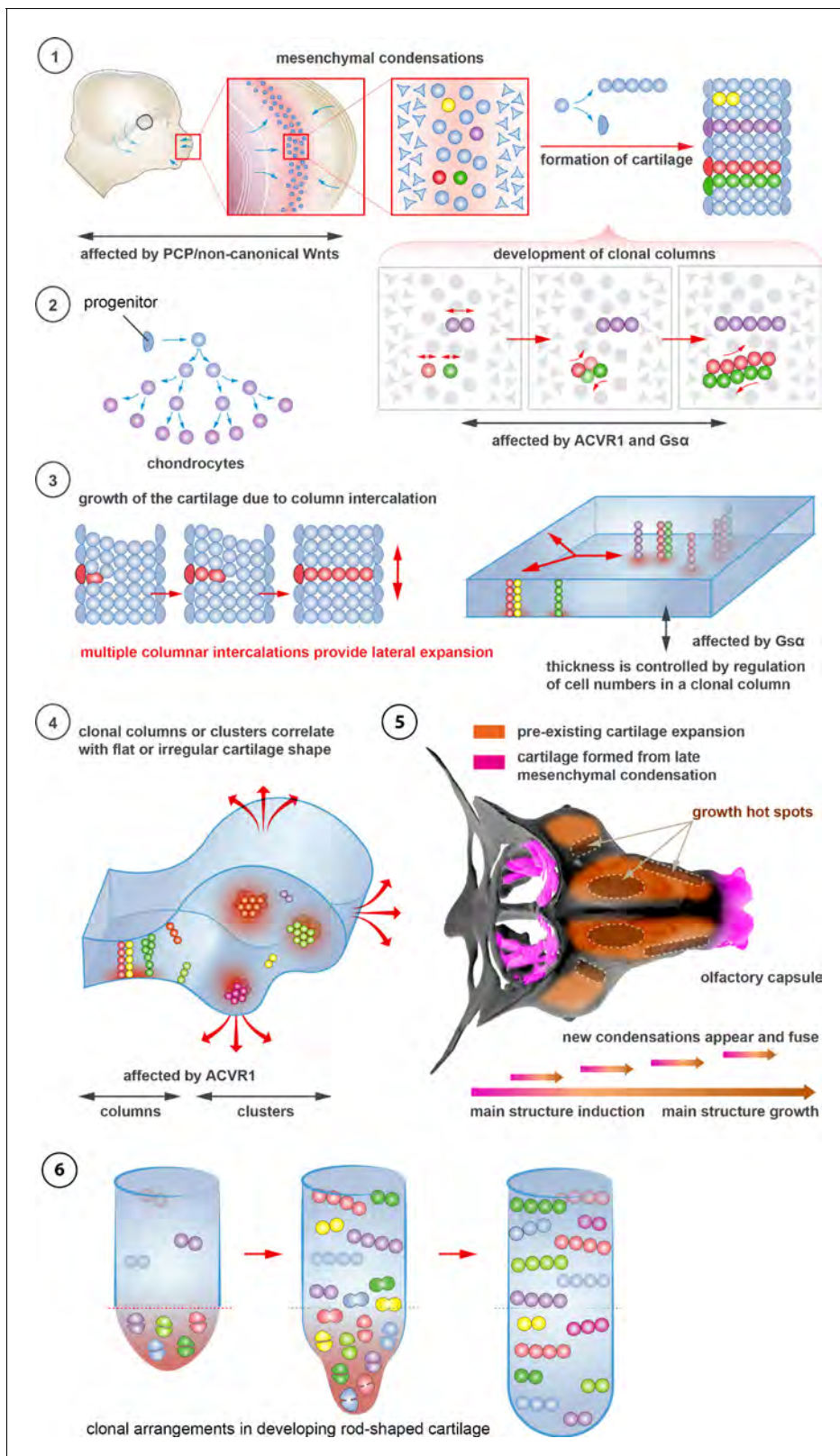


**Figure 10.** Schematic overview of cartilage shaping and scaling processes. (1) Oriented cell divisions in the mesenchymal condensations give rise to the transverse columnar clones of chondrocytes. (2) Perichondrial cells may potentially give rise to chondrocytes. (3) Formation of new clonal columns and their integration into pre-existing cartilage leads to directed lateral expansion of the cartilage. The thickness of the sheet-shaped cartilage depends on the number of cells comprising the column, while the lateral expansion depends on the number of clonal columnar units engaged. (4) Geometry of the

*Figure 10 continued on next page*

Figure 10 continued

clonal unit corresponds to the overall macro-geometry of the cartilage. Regular clonal units correspond to regular shapes of the cartilage.

(5) Chondrogenic mesenchymal condensations are sequentially induced to provide fine details and shape modifications during chondrocranium growth. Upon their maturation, they fuse with the main structure of the chondrocranium. Anisotropic proliferation and specifically positioned proliferative zones further assist the shaping process by imposing physical tensions and curves. (6) Rod-shaped cartilage elements also show the regular clonal patterns that result from the transverse orientation of cell divisions and daughter cell allocations that account for the diameter regulation.

DOI: 10.7554/eLife.25902.020

are retained until late developmental stages. As we demonstrated, the formation of adjoining mesenchymal condensations occurs in sheet-shaped cranial cartilage. In the developing face, new chondrogenic condensations are responsible for introducing geometrically complicated fine details. Such mechanisms may also operate during amphibian metamorphosis, when most of the postmetamorphic cranial cartilage develops *de novo* and not from the pre-metamorphic cartilaginous elements (Kerney *et al.*, 2012).

Taken together, we discovered important novel principles explaining the growth and shaping of cartilaginous structures. Further studies should focus, amongst other things, on the soluble signals emanating from other embryonic structures which influence the oriented behavior or proliferation of chondrogenic clones.

## Materials and methods

### Mouse strains and animal information

All animal (mouse) work has been approved and permitted by the Ethical Committee on Animal Experiments (Norra Djurförsöksetiska Nämnd, ethical permit N226/15 and N5/14) and conducted according to The Swedish Animal Agency's Provisions and Guidelines for Animal Experimentation recommendations. Genetic tracing mouse strains *Plp1-CreERT2* (RRID:MGI:4837112) and *Sox10-CreERT2* were previously described (Laranjeira *et al.*, 2011; Leone *et al.*, 2003; Yu *et al.*, 2013). *Plp1-creERT2*, *Sox10-creERT2* and *Col2a1-CreERT2* (RRID:IMSR\_JAX:006774) (Nakamura *et al.*, 2006) (obtained from laboratory of S. Mackem, NIH) strains were coupled to *R26Confetti* (RRID:IMSR\_JAX:017492) mice that were received from the laboratory of Professor H. Clevers (Snippert *et al.*, 2010). The *Stop<sup>flxed/flxed</sup>caAlk2-IRES-GFP* strain from the laboratory of Y. Mishina (Fukuda *et al.*, 2006) was coupled to *Sox10-CreERT2*. The *Ebf2-CreERT2* (RRID:MGI:4421811) strain was obtained from the laboratory of H. Qian, KI, and was coupled to *R26Tomato*. The *Gsα<sup>flxed/flxed</sup>* strain was obtained from the laboratory of L. Weinstein (Sakamoto *et al.*, 2005). Female mice which were homozygous for the reporter allele [*Gt(ROSA)26Sortm4(ACTB-tdTomato,-EGFP)Luo/J*; Jackson Laboratories] (Muzumdar *et al.*, 2007) were coupled to homozygous *Col2a1::creER<sup>T</sup>* males [FVB-Tg(*Col2a1-cre/ERT*)KA3Smac/J; Jackson Laboratories] (Feil *et al.*, 1997; Nakamura *et al.*, 2006). To induce genetic recombination to adequate efficiency, pregnant females were injected intraperitoneally with tamoxifen (Sigma Aldrich, St.Louis, MO, T5648) dissolved in corn oil (Sigma Aldrich, C8267). Tamoxifen concentration ranged from 1.5 to 5.0 mg per animal in order to obtain a range of recombination efficiencies. *Wnt5a*, *Vangl2* and *Ror2* full knock-out embryos were obtained from heterozygous parents (Gao *et al.*, 2011; Yamaguchi *et al.*, 1999) at the expected Mendelian proportions.

### Immunohistochemistry

For embryo analyses, heterozygous mice of the relevant genotype were mated overnight, and noon of the day of plug detection was considered E0.5. Mice were sacrificed with isoflurane (Baxter, Deerfield, IL, KDG9623) overdose, and embryos were dissected out and collected into ice-cold PBS. Subsequently, the samples were placed into freshly prepared 4% paraformaldehyde (PFA) and depending on the developmental stage they were fixed for 3–6 hr at +4°C on a roller. Embryos were subsequently cryopreserved in 30% sucrose (VWR, Radnor, PA, C27480) overnight at +4°C, embedded in OCT media (HistoLab, Serbia, 45830) and sections cut of between 14 μm to 200 μm on a cryostat (Microm International, Germany), depending on the following application. If needed, sections were stored at –20°C after drying for 1 hr at room temperature, or processed immediately

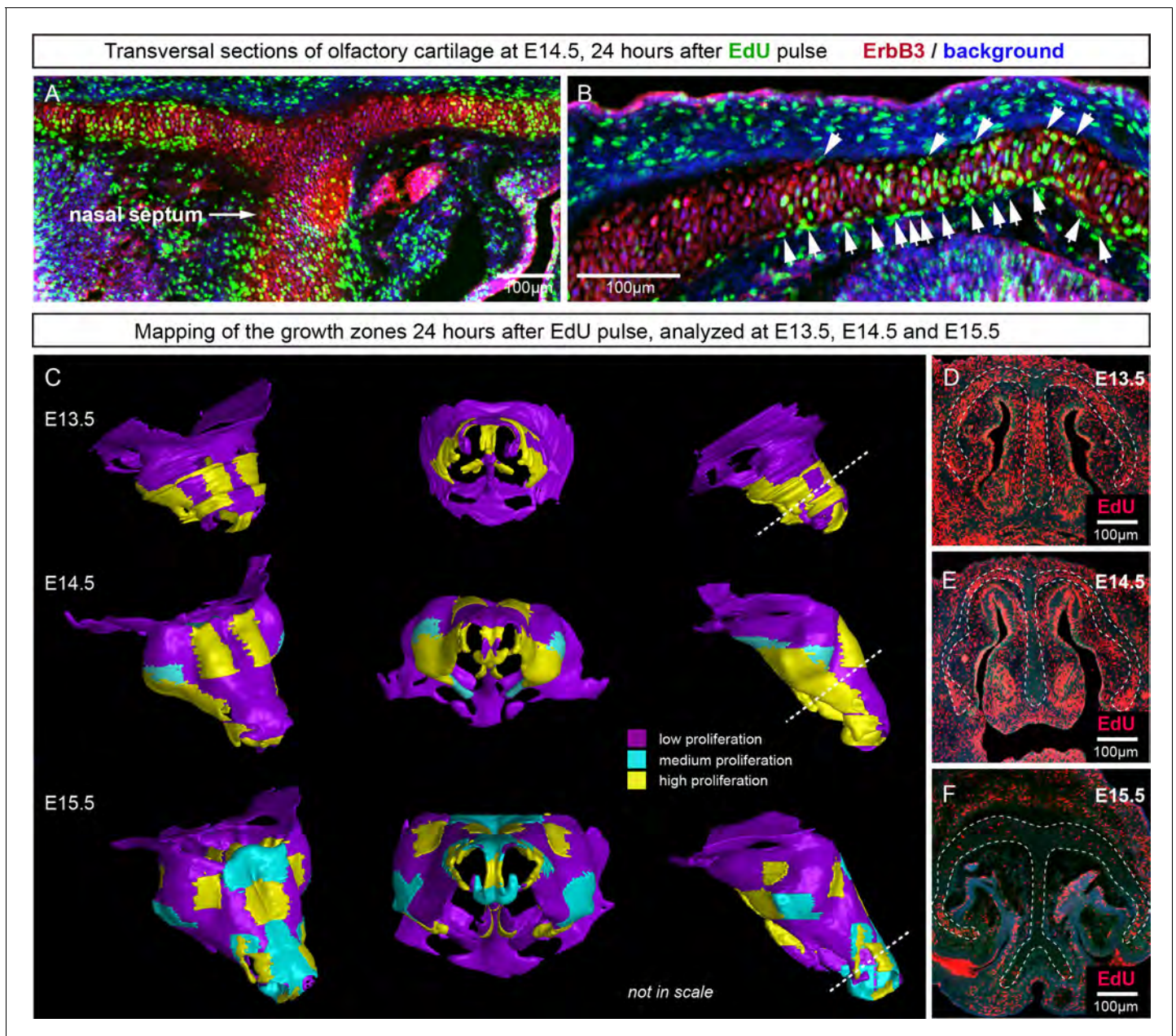


**Figure 11.** Analysis of proliferation identifies specific proliferative regions in nasal capsule. (A–B) Analysis of EdU incorporation 24 hr after the pulse on a transversal section of the facial chondrocranium at E14.5. Notice the distinct proliferative zones in the cartilage that correlate with intense EdU labelling in perichondrial locations shown by arrowheads in (B). (C) Mapping of distinct growth zones onto 3D models of mesenchymal condensations (E13.5) and cartilage (E14.5–E15.5) in the developing face. (D–F) Frontal transversal sections at different developmental stages include proliferative zones within the chondrocranium with EdU incorporation. Scale bars = 100 μm.  
DOI: [10.7554/eLife.25902.021](https://doi.org/10.7554/eLife.25902.021)

after sectioning. Primary antibodies used were: goat anti-GFP (FITC) (Abcam, UK, 1:500, RRID:AB\_305635), rabbit anti-Sox9 (Sigma Aldrich, 1:1000, RRID:AB\_1080067), rabbit anti-Sox5 (Abcam, 1:500, RRID:AB\_10859923), sheep anti-ErbB3 (RnD Systems, Minneapolis, MN, 1:500, RRID:AB\_2099728). For detection of the above-mentioned primary antibodies we utilized 405, 488, 555 or 647-conjugated Alexa-fluor secondary antibodies produced in donkey (Invitrogen, Carlsbad, CA, 1:1000, RRID:AB\_162543, RRID:AB\_141788, RRID:AB\_141708, RRID:AB\_142672, RRID:AB\_2536183, RRID:AB\_141844,). Sections were mounted with 87% glycerol mounting media

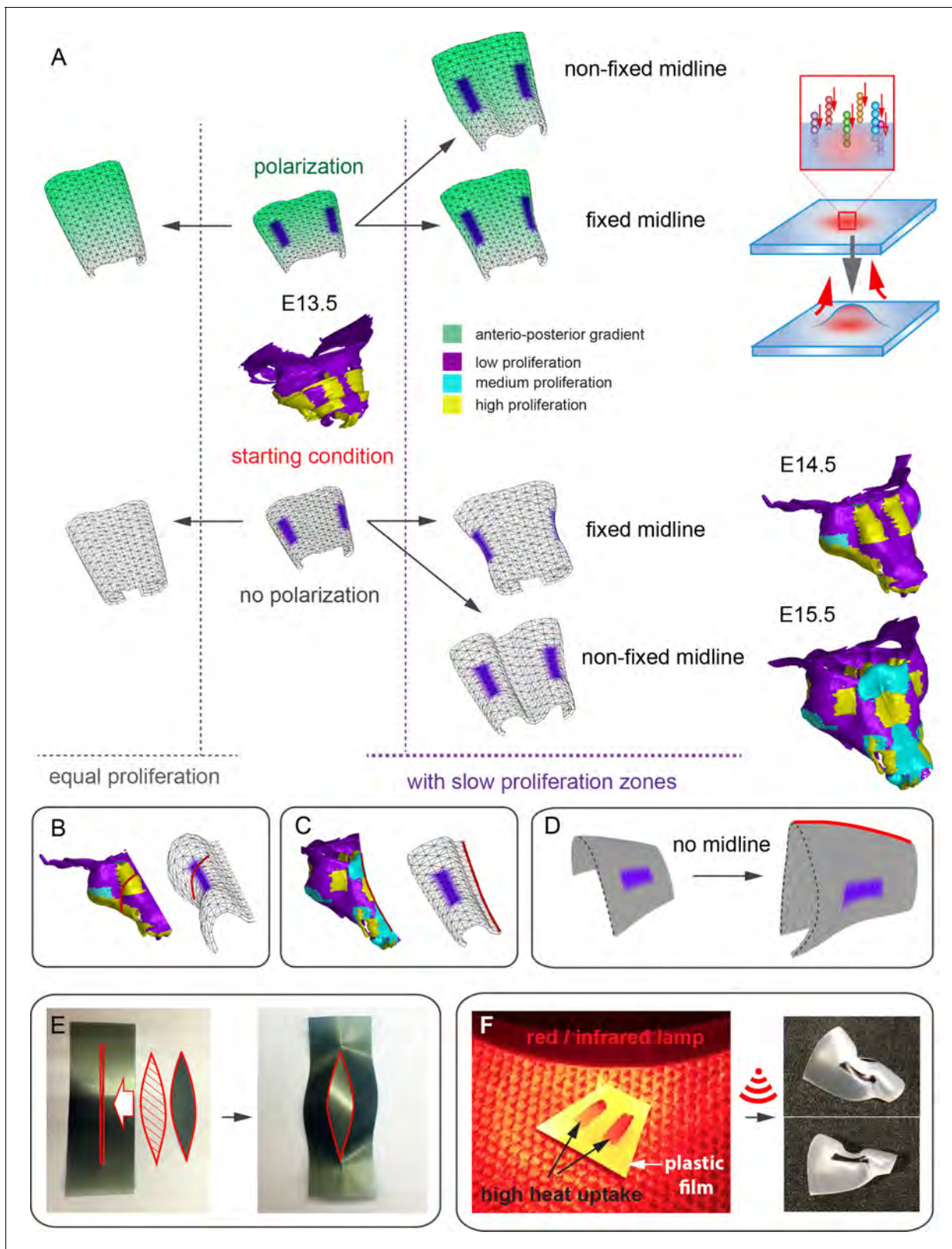


**Figure 12.** Modeling of uneven growth in the shaping of the nasal capsule. (A) In silico geometrical transformations of the nasal capsule-like anlage at E13.5 following various scenarios including: anisotropic oriented growth (following polarization introduced by the anterio-posterior gradient shown in green), non-polarized isotropic growth (no anterio-posterior gradient), the presence of fixed midline (simulation of septum and central groove), condition with the unfixed midline (only central groove), conditions with or without slowly growing lateral regions (shown in purple). Note that in Figure 12 continued on next page

Figure 12 continued

condition with polarized antero-posterior growth the anterior elongation of the structure is more prominent and faster as compared to the condition with non-polarized isotropic growth. The lateral bends are induced by slow proliferating lateral regions. In the center and on the right, the real nasal capsules are shown with mapped fast and slow growing regions. (B) In the condition with isotropic growth and introduced slowly growing regions, we observe the formation of lateral bends (red line) analogous to the lateral bends in the real nasal capsule at E14.5 (shown on the left). In this condition the midline is fixed, and the ventral groove forms straight. (C) In conditions with no fixed midline we observe the formation of the central groove, correct bending of the central groove (red line) and overall flattening of the simulated structure similar to the real object (on the left). (D) Simulation with no midline and central groove. Note the inverted bend (red line) and the absence of the correct flattening of the structure. Despite the absence of the midline, the lateral bends are successfully induced by the slow growing regions (purple), analogous to the real nasal capsule. (E) Material elastic modelling shows how the third dimension (bending) emerges from changes and tensions in plain 2D structure during imitated anisotropic growth. (E, left panel) Initial modelling conditions: completely flat X-ray film with the cut slot in the middle for fitting the imitated flat growth zone, which is also made from X-ray film. (E, right panel) When the growth zone is inserted into the slit, the whole structure bends to accommodate the tensions. (F) Real material (plastic film)-based simulation of isotropic growth was based on uneven shrinking during intense heating. Black painted regions uptake heat more efficiently and shrink faster. The attached edges of the shrinking zone cause bending of the entire structure. Two lateral black stripes were painted on top of the trapezoid as an analog to lateral slowly proliferating zones in nasal capsule. Note the similarity of resulting bends to the lateral bends in real nasal capsule at E14.5.

DOI: [10.7554/eLife.25902.022](https://doi.org/10.7554/eLife.25902.022)

(Merck, Germany) or in Vectashield Antifade Mounting Medium with DAPI (Vector Laboratories, Burlingame, CA, RRID:AB\_2336790).

### EdU incorporation analysis

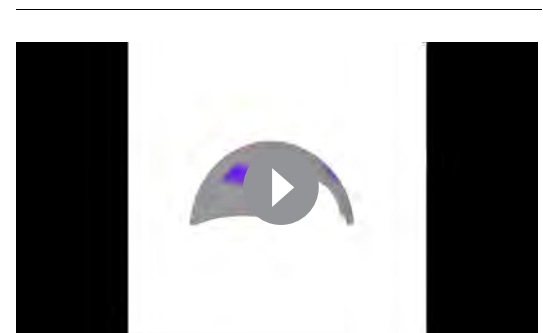
EdU (Life Technologies, Carlsbad, CA) was injected intraperitoneally into the pregnant females (65 µg per gram of body mass) either 6- or 24 hr before the embryos were harvested. Cells with incorporated EdU were visualized using Click-iT EdU Alexa Fluor 647 Imaging Kit (Life Technologies) according to the manufacturer's instructions.

### Microscopy, volume rendering, image analysis and quantifications

Confocal microscopy was performed using Zeiss LSM710 CLSM, Zeiss LSM780 CLSM and Zeiss LSM880Airyscan CLSM instruments. The settings for the imaging of Confetti fluorescent proteins were previously described (*Snippert et al., 2010*). The imaging of the confocal stack was done with a Zeiss LSM780 CLSM, Plan-Apochromat 3 10x/0.45 M27 Zeiss air objective.

### Histological staining

Slides were stained for mineral deposition using von Kossa calcium staining: 5% silver nitrate solution was added to the sections at a room temperature and exposed to strong light for 30 min. After that the silver nitrate solution was removed, and slides were washed with distilled water for three times during 2 min. 2.5% sodium thiosulphate solution (w/v) was added to the sections and incubated for 5 min. Slides were again rinsed for three times during 2 min in distilled water. The sections were then counterstained using Alcian blue. Alcian blue solution (0.1% alcian blue 8GX (w/v) in 0.1 M HCl) was added to the tissue for 3 min at room temperature and then rinsed for three times during 2 min in distilled water. Slides were then transferred rapidly into incrementally increasing ethanol concentrations (20%, 40%, 80%, 100%) and incubated in 100% ethanol for 2 min. Finally, the slides were incubated in two xylene baths (for 2 min and then for 5 min) before mounting and analysis.



**Video 2.** Simulations of shape transitions of the nasal capsule-like 3D object under different growth conditions. Notice the formation of the lateral bends corresponding to the real nasal capsule shape development from E13.5 to E14.5 occur only in the condition with slow growing purple zones. These bends form independently from isotropic or anisotropic modality of growth.

DOI: [10.7554/eLife.25902.023](https://doi.org/10.7554/eLife.25902.023)

## Statistics

Statistical data are represented as mean  $\pm$  s.e.m. Unpaired version of Student's t-test was used to calculate the statistics (*P* value). All results were replicated at least in three different animals. Statistical analysis and graphs were produced in GraphPad Prism (La Jolla, CA, RRID:SCR\_002798) or Oriana Software (Kovach Computing Services, UK). Spearman coefficient was used for correlation assessment of microgeometries corresponding to different locations in the cartilage.

In **Figure 8** the difference between control (mean = 5.9, sem =  $\pm$ 0.23, n = 4) and mutant (mean = 4.3, sem =  $\pm$ 0.25, n = 3) olfactory cartilage thickness is significant ( $p=0.0053$ ). The difference between control (mean = 10.6, sem =  $\pm$ 0.83, n = 3) and mutant (mean = 5.7, sem =  $\pm$ 0.61, n = 3) basisphenoid cartilage thickness is significant ( $p=0.0087$ ).

## Tissue contrasting for $\mu$ -CT scanning

Our staining protocol has been modified from the original protocol developed by Brian Metscher laboratory (University of Vienna, Austria). After dissection, the embryos were fixed with 4% aqueous solution of formaldehyde in PBS for 24 hr at +4°C, with slow rotation. Samples were then dehydrated by incubation in incrementally increasing concentrations of ethanol in PBS (30%, 50%, 70%); samples were incubated at +4°C for two days in each concentration to minimize the tissue shrinkage.

We found that the best signal to noise ratio on scans results from contrasting the samples with 0.5–1.0% PTA (Phosphotungstic acid, Sigma Aldrich) in 90% methanol. After sample dehydration, the tissue-contrasting PTA solution was added to the samples and then changed every day with the fresh solution. E12.5 embryos were contrasted with 0.5% PTA for four days while E15.5 embryos were stained in 0.7% PTA for six days. E16.5 and E17.5 embryos were decapitated, and the contrasting procedure was extended to 9–15 days in 1% PTA to ensure the best penetration of the contrasting agent. Subsequently, tissues were rehydrated through a methanol gradient (90%, 80%, 70%, 50% and 30%), to sterile distilled water. After that, rehydrated embryos were embedded in 0.5% agarose gel (A5304, Sigma-Aldrich) and placed in polypropylene conical tubes (0.5, 1.5 or 15 ml depending on the sample size) to minimize the amount of surrounding agarose gel, and to avoid movement artifacts during X-ray computed tomography scanning.

## $\mu$ -CT analysis (micro computed tomography analysis)

The  $\mu$ -CT analysis of the embryos was performed using laboratory system GE phoenix v|tome|x L 240, equipped with a 180 kV/15W maximum power nanofocus X-ray tube and high contrast flat panel detector DXR250 with 2048  $\times$  2048 pixel, 200  $\times$  200  $\mu$ m pixel size. The exposure time was 900 ms in all 2000 positions. The  $\mu$ -CT scan was carried out at 60 kV acceleration voltage and with 200  $\mu$ A X-ray tube current. The voxel size of obtained volumes appeared in the range of 4  $\mu$ m - 6  $\mu$ m depending on a size of an embryo. The tomographic reconstructions were performed using GE phoenix datos|x 2.0 3D computed tomography software.

The cartilage of the olfactory system was segmented manually using Avizo - 3D image data processing software (FEI, Hillsboro, OR). The volumetric data of a segmented region were transformed to a polygonal mesh that describes the outer boundary of the region. The polygonal mesh consisting of triangles is a digital geometrical representation of the real object. The polygonal mesh of the olfactory system was imported to VG Studio MAX 2.2 software (Volume Graphics, Germany) for surface smoothing. The analysis of wall thickness at different embryonic stages was performed in order to show the differences or similarities in the thickness of the cartilage structures (Tesařová *et al.*, 2016). The results are shown on the polygonal mesh by a colour map. The growth zones in facial chondrocranium at different stages were outlined on top of the 3D polygonal mesh based on the EdU analysis and confocal microscopy results.

## Computer simulations of shape transitions of nasal capsule structure

Models were developed using the growing polarised tissue (GPT) framework and implemented in the MATLAB application GFtbox (Kennaway *et al.*, 2011; Kuchen *et al.*, 2012) (RRID:SCR\_001622). In this method, an initial finite element mesh, also termed the canvas, is deformed during growth. The pattern of deformation depends on growth-modulating factors, whose initial distribution was established during setup. Factors have one value for each vertex and values between vertices are linearly interpolated across each finite element. In the models described here, the initial canvas is

oriented with regard to the external xy-coordinate system such that the canvas base is parallel to the x-axis and the midline is parallel to the y-axis. The initial nasal capsule-line canvas consists of 1800 elements. Elements were not subdivided during the simulations.

Each model has two interconnected networks: the Polarity Regulatory Network (PRN) specifies tissue polarity and hence specified orientations of growth, and the Growth-rate Regulatory Network (KRN) determines how factors influence specified growth rates. In total, growth interactions are specified by three equations, one for the PRN and two for the KRN. These networks determine the specified polarity and growth fields across the canvas. Growth rates are influenced by factors distributed across the canvas. Growth can be promoted in a region by the pro function or inhibited by the inh function as follows:

$$\text{pro}(n, x) = 1 + nx$$

$$\text{inh}(n, x) = 1/(1 + nx)$$

Due to the connectedness of the canvas, this specified growth differs from the resultant growth by which the system is deformed.

### Fixed midline models

These models question how the structure can transform given that the septum actively anchors the midline and the central groove.

#### Setup

The initial set-up phase runs from 0 to 12 time steps and during this phase the canvas deforms from a square sheet into the starting shape for the nasal capsule-like structure. Factor MID is expressed along the proximal-distal midline and used to anchor the midline vertices in the z-plane. Factor CHEEKS is expressed either side of the midline.

#### PRN

A proximo-distal polarity field is set up and used to define the orientations of growth. This field is specified as being oriented parallel to the midline throughout growth by the gradient of a polarity factor, POLARISER (POL). POL has a linear gradient across the canvas with the highest level of one at the proximal base and zero at the distal tip.

#### KRN

The growth phase occurs after the initial setup phase at time step 13. During this phase there are options for specifying either isotropic growth or anisotropic growth.

During isotropic growth, the growth rate K was set to:

$$K = 0.05 \cdot \text{inh}(100, \text{iCHEEKS})$$

During anisotropic growth the specified growth rate parallel to the polarity field,  $K_{\text{par}}$ , was defined as:

$$K_{\text{par}} = 0.05 \cdot \text{inh}(100, \text{iCHEEKS})$$

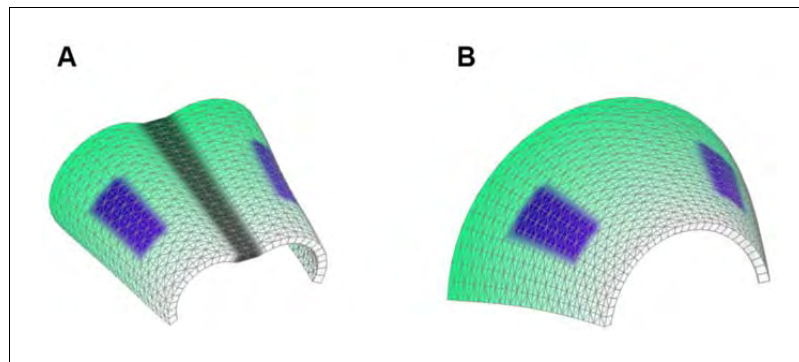
while growth perpendicular to the polarity field,  $K_{\text{per}}$ , was set to zero.

### Non - Fixed midline models

These models are aiming to simulate what happens to the shape transition when the midline and corresponding central groove are not fixed in space (and can bend or change in any other way) following tensions in the whole simulated structure. We used this approach to question how much the roof of the nasal capsule is anchored by the nasal septum.

#### Setup

As with the Fixed-midline model, an initial setup phase runs for 0–12 time-steps in which a square sheet is deformed into an alternative starting shape for the nasal capsule-like structure. In this model the proximo-distal midline was allowed to deform in the z-plane. Factor CHEEKS is expressed either side of the midline and offset slightly distally.



**Scheme 1.** Starting shapes for the Fixed mid-ridge model (A) and Non-Fixed mid-ridge model (B). Green colour indicates the values of POL which is highest at the proximal end. CHEEKS are shown in purple and MID is shown in grey.

DOI: [10.7554/eLife.25902.024](https://doi.org/10.7554/eLife.25902.024)

### PRN

A proximo-distal polarity field is set up as in the Fixed mid-ridge model.

### KRN

The growth regulatory network is defined as in the Fixed mid-ridge model.

## Mathematical model

For detailed description, please see the Appendix, **Appendix 1—figure 1** and **2** and also (Kaucka et al., 2016)

## Acknowledgements

We would like to thank to Olga Kharchenko for illustrations. We are grateful to Prof. Susan Mackem from NIH for the *Col2a1-CreERT2* strain and to Prof. Hans Clevers for the *R26Confetti* strain. M K was supported by EMBO Long-term Fellowship and SSMF (Svenska Sällskapet för Medicinsk Forskning) fellowship. IA and KF were supported by grants from the Swedish Research Council and Karolinska Institutet. IA received support from The Hållsten Research Foundation and Åke Wiberg Foundation. T Z and J K were supported by the Ministry of Education, Youth and Sports of the Czech Republic under the project CEITEC 2020 (LQ1601). J J and A Ha. were supported by the Ministry of Education, Youth and Sports of the Czech Republic (project LQ1605). A He. was supported by the Swedish strategic research programme eSENCE, the Swedish Research Council (grant #2015–03964) and National Institute of Health under Award Number 1R01EB014877-01. ASC, and PN were supported by the Swedish Research Council (grant # 2016–02835) and Karolinska Institutet. A Deo lumen, ab amicis auxilium. The contents are solely the responsibility of the authors and do not necessarily represent the official views of the National Institute of Health. All authors declare no conflict of interest.

## Additional information

### Funding

Funder	Grant reference number	Author
European Molecular Biology Organization	ALTF 216-2013	Marketa Kaucka
Svenska Sällskapet för Medicinsk Forskning		Marketa Kaucka
National Institutes of Health		Andreas Hellander

Svenska Forskningsrådet For-  
masPhillip T Newton  
Andrei S Chagin  
Kaj Fried  
Igor Adameyko

Karolinska Institutet

Phillip T Newton  
Andrei S Chagin  
Kaj Fried  
Igor AdameykoBertil Hållstens Forskningsstif-  
telse

Igor Adameyko

Åke Wiberg Stiftelse

Igor Adameyko

---

The funders had no role in study design, data collection and interpretation, or the decision to submit the work for publication.

---

### Author contributions

MK, Conceptualization, Data curation, Formal analysis, Supervision, Validation, Investigation, Visualization, Methodology, Writing—original draft, Project administration, Writing—review and editing; TZ, Software, Formal analysis, Visualization, Methodology, Writing—review and editing; MT, Software, Formal analysis, Validation, Visualization, Methodology, Writing—review and editing; DG, Investigation, Methodology, Writing—review and editing, Responsible for obtaining all Wnt/PCP mutants, sample preparation and help with their analysis; AHe, Resources, Software, Supervision, Validation, Investigation, Methodology, Writing—original draft, Writing—review and editing; JJ, Methodology, JJ has been responsible for tissue contrasting and preparation of the samples for uCT. JJ participated on the review and editing of the manuscript; JK, Supervision, Funding acquisition, Investigation, Writing—original draft, Project administration; JP, PS, Software, Validation, Investigation, Methodology, Writing—review and editing; BS, Validation, Methodology, Project administration, Writing—review and editing, BS has been responsible for preparation of the samples for uCT (tissue contrasting). Participated on data acquiring (confocal microscopy, cryosectioning, staining); PTN, Investigation, Writing—original draft, Writing—review and editing, PTN has been responsible for EdU pulse embryos and for the GSalph mouse strain. Made very significant contribution to the editing of manuscript (language correction); VD, Investigation, Writing—review and editing, Has been responsible for the production, preparation and analysis of caALK2 embryos; LL, Methodology, Has been responsible for sample preparation, cryosectioning and confocal microscopy; HQ, Conceptualization, Resources, Supervision, Methodology, Writing—review and editing, Preparation of EBF2-GFP/Tomato embryos; A-SJ, Investigation, Methodology, ASJ was responsible for the EBF2-GFP/Tomato strain, injections and sample preparation; YM, Resources, Supervision, Investigation, Writing—review and editing, Responsible for Sox10CreERT2 mouse line; JDC, Data curation, Software, Investigation, Visualization, Methodology, Writing—review and editing; EMT, Resources, Supervision, Funding acquisition, Investigation, Project administration, Writing—review and editing; AE, Software, Investigation, Visualization, Methodology, Writing—review and editing; AD, Software, Supervision, Funding acquisition, Validation, Investigation, Methodology, Writing—review and editing; HB, Resources, Supervision, Funding acquisition, Methodology, Project administration, Writing—review and editing; EC, Resources, Software, Supervision, Funding acquisition, Validation, Investigation, Methodology, Writing—review and editing; MC, Investigation, Methodology, Created and validated the GSa mouse strain; LSW, Resources, Supervision, Project administration, Writing—review and editing; AHa, Resources, Validation, Methodology; EA, Resources, Supervision, Investigation, Writing—review and editing; ASC, Conceptualization, Resources, Formal analysis, Supervision, Investigation, Writing—original draft, Writing—review and editing; KF, Conceptualization, Resources, Supervision, Investigation, Writing—original draft, Writing—review and editing; IA, Conceptualization, Resources, Formal analysis, Supervision, Funding acquisition, Investigation, Writing—original draft, Project administration, Writing—review and editing

### Author ORCIDs

Marketa Kaucka,  <http://orcid.org/0000-0002-8781-9769>Hjalmar Brismar,  <http://orcid.org/0000-0003-0578-4003>Enrico Coen,  <http://orcid.org/0000-0001-8454-8767>

Andrei S Chagin, <http://orcid.org/0000-0002-2696-5850>

Igor Adameyko, <http://orcid.org/0000-0001-5471-0356>

### Ethics

Animal experimentation: All animal (mouse) work has been approved and permitted by the Ethical Committee on Animal Experiments (Norra Djurförsöksetiska Nämnd, ethical permit N226/15 and N5/14) and conducted according to The Swedish Animal Agency's Provisions and Guidelines for Animal Experimentation recommendations.

## References

- Abad V**, Meyers JL, Weise M, Gafni RI, Barnes KM, Nilsson O, Bacher JD, Baron J. 2002. The role of the resting zone in growth plate chondrogenesis. *Endocrinology* **143**:1851–1857. doi: [10.1210/endo.143.5.8776](https://doi.org/10.1210/endo.143.5.8776), PMID: [11956168](https://pubmed.ncbi.nlm.nih.gov/11956168/)
- Afsharpaiman S**, Saburi A, Waters KA. 2013. Respiratory difficulties and breathing disorders in achondroplasia. *Paediatric Respiratory Reviews* **14**:250–255. doi: [10.1016/j.prrv.2013.02.009](https://doi.org/10.1016/j.prrv.2013.02.009), PMID: [23523391](https://pubmed.ncbi.nlm.nih.gov/23523391/)
- Ben Amar M**, Jia F. 2013. Anisotropic growth shapes intestinal tissues during embryogenesis. *PNAS* **110**:10525–10530. doi: [10.1073/pnas.1217391110](https://doi.org/10.1073/pnas.1217391110), PMID: [23754398](https://pubmed.ncbi.nlm.nih.gov/23754398/)
- Campinho P**, Heisenberg CP. 2013. The force and effect of cell proliferation. *The EMBO Journal* **32**:2783–2784. doi: [10.1038/emboj.2013.225](https://doi.org/10.1038/emboj.2013.225), PMID: [24097062](https://pubmed.ncbi.nlm.nih.gov/24097062/)
- Chagin AS**, Vuppapalapati KK, Kobayashi T, Guo J, Hirai T, Chen M, Offermanns S, Weinstein LS, Kronenberg HM. 2014. G-protein stimulatory subunit alpha and  $gq/11\alpha$  G-proteins are both required to maintain quiescent stem-like chondrocytes. *Nature Communications* **5**:3673. doi: [10.1038/ncomms4673](https://doi.org/10.1038/ncomms4673), PMID: [24781502](https://pubmed.ncbi.nlm.nih.gov/24781502/)
- Chong HJ**, Young NM, Hu D, Jeong J, McMahon AP, Hallgrímsson B, Marcucio RS. 2012. Signaling by SHH rescues facial defects following blockade in the brain. *Developmental Dynamics* **241**:247–256. doi: [10.1002/dvdy.23726](https://doi.org/10.1002/dvdy.23726), PMID: [22275045](https://pubmed.ncbi.nlm.nih.gov/22275045/)
- De Luca F**. 2006. Impaired growth plate chondrogenesis in children with chronic illnesses. *Pediatric Research* **59**:625–629. doi: [10.1203/01.pdr.0000214966.60416.1b](https://doi.org/10.1203/01.pdr.0000214966.60416.1b), PMID: [16627871](https://pubmed.ncbi.nlm.nih.gov/16627871/)
- Díaz-Flores L**, Madrid JF, Gutiérrez R, Varela H, Valladares F, Alvarez-Argüelles H, Díaz-Flores L. 2006. Adult stem and transit-amplifying cell location. *Histology and Histopathology* **21**:995–1027. doi: [10.14670/HH-21.995](https://doi.org/10.14670/HH-21.995), PMID: [16763950](https://pubmed.ncbi.nlm.nih.gov/16763950/)
- Eames BF**, Schneider RA. 2008. The genesis of cartilage size and shape during development and evolution. *Development* **135**:3947–3958. doi: [10.1242/dev.023309](https://doi.org/10.1242/dev.023309), PMID: [18987028](https://pubmed.ncbi.nlm.nih.gov/18987028/)
- Feil R**, Wagner J, Metzger D, Chambon P. 1997. Regulation of cre recombinase activity by mutated estrogen receptor ligand-binding domains. *Biochemical and Biophysical Research Communications* **237**:752–757. doi: [10.1006/bbrc.1997.7124](https://doi.org/10.1006/bbrc.1997.7124), PMID: [9299439](https://pubmed.ncbi.nlm.nih.gov/9299439/)
- Fletcher AG**, Osborne JM, Maini PK, Gavaghan DJ. 2013. Implementing vertex dynamics models of cell populations in biology within a consistent computational framework. *Progress in Biophysics and Molecular Biology* **113**:299–326. doi: [10.1016/j.pbiomolbio.2013.09.003](https://doi.org/10.1016/j.pbiomolbio.2013.09.003), PMID: [24120733](https://pubmed.ncbi.nlm.nih.gov/24120733/)
- Foppiano S**, Hu D, Marcucio RS. 2007. Signaling by bone morphogenetic proteins directs formation of an ectodermal signaling center that regulates craniofacial development. *Developmental Biology* **312**:103–114. doi: [10.1016/j.ydbio.2007.09.016](https://doi.org/10.1016/j.ydbio.2007.09.016), PMID: [18028903](https://pubmed.ncbi.nlm.nih.gov/18028903/)
- Ford-Hutchinson AF**, Ali Z, Lines SE, Hallgrímsson B, Boyd SK, Jirik FR. 2007. Inactivation of Pten in osteochondroprogenitor cells leads to epiphyseal growth plate abnormalities and skeletal overgrowth. *Journal of Bone and Mineral Research* **22**:1245–1259. doi: [10.1359/jbmr.070420](https://doi.org/10.1359/jbmr.070420), PMID: [17456009](https://pubmed.ncbi.nlm.nih.gov/17456009/)
- Fritz JA**, Brancale J, Tokita M, Burns KJ, Hawkins MB, Abzhanov A, Brenner MP. 2014. Shared developmental programme strongly constrains beak shape diversity in songbirds. *Nature Communications* **5**:3700. doi: [10.1038/ncomms4700](https://doi.org/10.1038/ncomms4700), PMID: [24739280](https://pubmed.ncbi.nlm.nih.gov/24739280/)
- Fukuda T**, Scott G, Komatsu Y, Araya R, Kawano M, Ray MK, Yamada M, Mishina Y. 2006. Generation of a mouse with conditionally activated signaling through the BMP receptor, ALK2. *Genesis* **44**:159–167. doi: [10.1002/dvg.20201](https://doi.org/10.1002/dvg.20201), PMID: [16604518](https://pubmed.ncbi.nlm.nih.gov/16604518/)
- Gao B**, Song H, Bishop K, Elliot G, Garrett L, English MA, Andre P, Robinson J, Sood R, Minami Y, Economides AN, Yang Y. 2011. Wnt signaling gradients establish planar cell polarity by inducing Vangl2 phosphorylation through Ror2. *Developmental Cell* **20**:163–176. doi: [10.1016/j.devcel.2011.01.001](https://doi.org/10.1016/j.devcel.2011.01.001), PMID: [21316585](https://pubmed.ncbi.nlm.nih.gov/21316585/)
- Golding MB**, Tsuchimochi K, Ijiri K. 2006. The control of chondrogenesis. *Journal of Cellular Biochemistry* **97**:33–44. doi: [10.1002/jcb.20652](https://doi.org/10.1002/jcb.20652), PMID: [16215986](https://pubmed.ncbi.nlm.nih.gov/16215986/)
- Graner F**, Glazier JA. 1992. Simulation of biological cell sorting using a two-dimensional extended Potts model. *Physical Review Letters* **69**:2013–2016. doi: [10.1103/PhysRevLett.69.2013](https://doi.org/10.1103/PhysRevLett.69.2013), PMID: [10046374](https://pubmed.ncbi.nlm.nih.gov/10046374/)
- Green AA**, Kennaway JR, Hanna AI, Bangham JA, Coen E. 2010. Genetic control of organ shape and tissue polarity. *PLoS Biology* **8**:e1000537. doi: [10.1371/journal.pbio.1000537](https://doi.org/10.1371/journal.pbio.1000537), PMID: [21085690](https://pubmed.ncbi.nlm.nih.gov/21085690/)
- Guenther C**, Pantalena-Filho L, Kingsley DM. 2008. Shaping skeletal growth by modular regulatory elements in the Bmp5 gene. *PLoS Genetics* **4**:e1000308. doi: [10.1371/journal.pgen.1000308](https://doi.org/10.1371/journal.pgen.1000308), PMID: [19096511](https://pubmed.ncbi.nlm.nih.gov/19096511/)

- Hari L**, Miescher I, Shakhova O, Suter U, Chin L, Taketo M, Richardson WD, Kessar N, Sommer L. 2012. Temporal control of neural crest lineage generation by wnt/ $\beta$ -catenin signaling. *Development* **139**:2107–2117. doi: [10.1242/dev.073064](https://doi.org/10.1242/dev.073064), PMID: [22573620](https://pubmed.ncbi.nlm.nih.gov/22573620/)
- Hayes AJ**, MacPherson S, Morrison H, Dowthwaite G, Archer CW. 2001. The development of articular cartilage: evidence for an appositional growth mechanism. *Anatomy and Embryology* **203**:469–479. doi: [10.1007/s004290100178](https://doi.org/10.1007/s004290100178), PMID: [11453164](https://pubmed.ncbi.nlm.nih.gov/11453164/)
- Hellander A**. 2015. multicell. Github. e7edeef. <https://github.com/ahellander/multicell>
- Hu D**, Young NM, Xu Q, Jamniczky H, Green RM, Mio W, Marcucio RS, Hallgrímsson B. 2015. Signals from the brain induce variation in avian facial shape. *Developmental Dynamics : An Official Publication of the American Association of Anatomists*. doi: [10.1002/dvdy.24284](https://doi.org/10.1002/dvdy.24284), PMID: [25903813](https://pubmed.ncbi.nlm.nih.gov/25903813/)
- Jarjour M**, Jorquera A, Mondor I, Wienert S, Narang P, Coles MC, Klauschen F, Bajénoff M. 2014. Fate mapping reveals origin and dynamics of lymph node follicular dendritic cells. *The Journal of Experimental Medicine* **211**: 1109–1122. doi: [10.1084/jem.20132409](https://doi.org/10.1084/jem.20132409), PMID: [24863064](https://pubmed.ncbi.nlm.nih.gov/24863064/)
- Kaucka M**, Ivashkin E, Gyllborg D, Zikmund T, Tesarova M, Kaiser J, Xie M, Petersen J, Pachnis V, Nicolis SK, Yu T, Sharpe P, Arenas E, Brismar H, Blom H, Clevers H, Suter U, Chagin AS, Fried K, Hellander A, et al. 2016. Analysis of neural crest-derived clones reveals novel aspects of facial development. *Science Advances* **2**: e1600060. doi: [10.1126/sciadv.1600060](https://doi.org/10.1126/sciadv.1600060), PMID: [27493992](https://pubmed.ncbi.nlm.nih.gov/27493992/)
- Kennaway R**, Coen E, Green A, Bangham A. 2011. Generation of diverse biological forms through combinatorial interactions between tissue polarity and growth. *PLoS Computational Biology* **7**:e1002071. doi: [10.1371/journal.pcbi.1002071](https://doi.org/10.1371/journal.pcbi.1002071), PMID: [21698124](https://pubmed.ncbi.nlm.nih.gov/21698124/)
- Kerney RR**, Brittain AL, Hall BK, Buchholz DR. 2012. Cartilage on the move: cartilage lineage tracing during tadpole metamorphosis. *Development, Growth & Differentiation* **54**:739–752. doi: [10.1111/dgd.12002](https://doi.org/10.1111/dgd.12002), PMID: [23036161](https://pubmed.ncbi.nlm.nih.gov/23036161/)
- Kettunen P**, Nie X, Kvinnsland IH, Luukko K. 2006. Histological development and dynamic expression of Bmp2-6 mRNAs in the embryonic and postnatal mouse cranial base. *The Anatomical Record. Part A, Discoveries in Molecular, Cellular, and Evolutionary Biology* **288**:1250–1258. doi: [10.1002/ar.a.20402](https://doi.org/10.1002/ar.a.20402), PMID: [17066377](https://pubmed.ncbi.nlm.nih.gov/17066377/)
- Kobayashi S**, Takebe T, Zheng YW, Mizuno M, Yabuki Y, Maegawa J, Taniguchi H. 2011. Presence of cartilage stem/progenitor cells in adult mice auricular perichondrium. *PLoS One* **6**:e26393. doi: [10.1371/journal.pone.0026393](https://doi.org/10.1371/journal.pone.0026393), PMID: [22039478](https://pubmed.ncbi.nlm.nih.gov/22039478/)
- Kronenberg HM**. 2003. Developmental regulation of the growth plate. *Nature* **423**:332–336. doi: [10.1038/nature01657](https://doi.org/10.1038/nature01657), PMID: [12748651](https://pubmed.ncbi.nlm.nih.gov/12748651/)
- Kuchen EE**, Fox S, de Reuille PB, Kennaway R, Bensmihen S, Avondo J, Calder GM, Southam P, Robinson S, Bangham A, Coen E. 2012. Generation of leaf shape through early patterns of growth and tissue polarity. *Science* **335**:1092–1096. doi: [10.1126/science.1214678](https://doi.org/10.1126/science.1214678), PMID: [22383846](https://pubmed.ncbi.nlm.nih.gov/22383846/)
- Laranjeira C**, Sandgren K, Kessar N, Richardson W, Potocnik A, Vanden Berghe P, Pachnis V. 2011. Glial cells in the mouse enteric nervous system can undergo neurogenesis in response to injury. *Journal of Clinical Investigation* **121**:3412–3424. doi: [10.1172/JCI58200](https://doi.org/10.1172/JCI58200), PMID: [21865647](https://pubmed.ncbi.nlm.nih.gov/21865647/)
- Laurita J**, Koyama E, Chin B, Taylor JA, Lakin GE, Hankenson KD, Bartlett SP, Nah HD. 2011. The Muenke syndrome mutation (Fgfr3P244R) causes cranial base shortening associated with growth plate dysfunction and premature perichondrial ossification in murine basicranial synchondroses. *Developmental Dynamics* **240**:2584–2596. doi: [10.1002/dvdy.22752](https://doi.org/10.1002/dvdy.22752), PMID: [22016144](https://pubmed.ncbi.nlm.nih.gov/22016144/)
- Leone DP**, Genoud S, Atanasoski S, Grausenburger R, Berger P, Metzger D, Macklin WB, Chambon P, Suter U. 2003. Tamoxifen-inducible glia-specific cre mice for somatic mutagenesis in oligodendrocytes and schwann cells. *Molecular and Cellular Neuroscience* **22**:430–440. doi: [10.1016/S1044-7431\(03\)00029-0](https://doi.org/10.1016/S1044-7431(03)00029-0), PMID: [12727441](https://pubmed.ncbi.nlm.nih.gov/12727441/)
- Li L**, Newton PT, Boudierlique T, Sejnovhova M, Zikmund T, Kozhemyakina E, Xie M, Krivanek J, Kaiser J, Qian H, Dyachuk V, Lassar AB, Warman ML, Barenus B, Adameyko I, Chagin AS. 2017. Superficial cells are self-renewing chondrocyte progenitors, which form the articular cartilage in juvenile mice. *The FASEB Journal* **31**: 1067–1084. doi: [10.1096/fj.201600918R](https://doi.org/10.1096/fj.201600918R)
- Ma W**, Lozanoff S. 1999. Spatial and temporal distribution of cellular proliferation in the cranial base of normal and midfacially retrusive mice. *Clinical Anatomy* **12**:315–325. doi: [10.1002/\(SICI\)1098-2353\(1999\)12:5<315::AID-CA2>3.0.CO;2-2](https://doi.org/10.1002/(SICI)1098-2353(1999)12:5<315::AID-CA2>3.0.CO;2-2), PMID: [10462729](https://pubmed.ncbi.nlm.nih.gov/10462729/)
- Mackie EJ**, Ahmed YA, Tatarczuch L, Chen KS, Mirams M. 2008. Endochondral ossification: how cartilage is converted into bone in the developing skeleton. *The International Journal of Biochemistry & Cell Biology* **40**: 46–62. doi: [10.1016/j.biocel.2007.06.009](https://doi.org/10.1016/j.biocel.2007.06.009), PMID: [17659995](https://pubmed.ncbi.nlm.nih.gov/17659995/)
- Maes C**, Kobayashi T, Selig MK, Torrekens S, Roth SI, Mackem S, Carmeliet G, Kronenberg HM. 2010. Osteoblast precursors, but not mature osteoblasts, move into developing and fractured bones along with invading blood vessels. *Developmental Cell* **19**:329–344. doi: [10.1016/j.devcel.2010.07.010](https://doi.org/10.1016/j.devcel.2010.07.010), PMID: [20708594](https://pubmed.ncbi.nlm.nih.gov/20708594/)
- Mallarino R**, Campàs O, Fritz JA, Burns KJ, Weeks OG, Brenner MP, Abzhanov A. 2012. Closely related bird species demonstrate flexibility between beak morphology and underlying developmental programs. *PNAS* **109**:16222–16227. doi: [10.1073/pnas.1206205109](https://doi.org/10.1073/pnas.1206205109), PMID: [22988109](https://pubmed.ncbi.nlm.nih.gov/22988109/)
- McBratney-Owen B**, Iseki S, Bamforth SD, Olsen BR, Morriss-Kay GM. 2008. Development and tissue origins of the mammalian cranial base. *Developmental Biology* **322**:121–132. doi: [10.1016/j.ydbio.2008.07.016](https://doi.org/10.1016/j.ydbio.2008.07.016), PMID: [18680740](https://pubmed.ncbi.nlm.nih.gov/18680740/)
- Muzumdar MD**, Tasic B, Miyamichi K, Li L, Luo L. 2007. A global double-fluorescent cre reporter mouse. *Genesis* **45**:593–605. doi: [10.1002/dvg.20335](https://doi.org/10.1002/dvg.20335), PMID: [17868096](https://pubmed.ncbi.nlm.nih.gov/17868096/)

- Nagayama M**, Iwamoto M, Hargett A, Kamiya N, Tamamura Y, Young B, Morrison T, Takeuchi H, Pacifici M, Enomoto-Iwamoto M, Koyama E. 2008. Wnt/beta-catenin signaling regulates cranial base development and growth. *Journal of Dental Research* **87**:244–249. doi: [10.1177/154405910808700309](https://doi.org/10.1177/154405910808700309), PMID: [18296608](https://pubmed.ncbi.nlm.nih.gov/18296608/)
- Nakamura E**, Nguyen MT, Mackem S. 2006. Kinetics of tamoxifen-regulated cre activity in mice using a cartilage-specific CreER(T) to assay temporal activity windows along the proximodistal limb skeleton. *Developmental Dynamics* **235**:2603–2612. doi: [10.1002/dvdy.20892](https://doi.org/10.1002/dvdy.20892), PMID: [16894608](https://pubmed.ncbi.nlm.nih.gov/16894608/)
- Nilsson O**, Marino R, De Luca F, Phillip M, Baron J. 2005. Endocrine regulation of the growth plate. *Hormone Research in Paediatrics* **64**:157–165. doi: [10.1159/000088791](https://doi.org/10.1159/000088791), PMID: [16205094](https://pubmed.ncbi.nlm.nih.gov/16205094/)
- Radszweit M**, Block M, Hengstler JG, Schöll E, Drasdo D. 2009. Comparing the growth kinetics of cell populations in two and three dimensions. *Physical Review E* **79**:051907. doi: [10.1103/PhysRevE.79.051907](https://doi.org/10.1103/PhysRevE.79.051907)
- Repiso A**, Bergantiños C, Serras F. 2013. Cell fate respecification and cell division orientation drive intercalary regeneration in *Drosophila* wing discs. *Development* **140**:3541–3551. doi: [10.1242/dev.095760](https://doi.org/10.1242/dev.095760), PMID: [23903186](https://pubmed.ncbi.nlm.nih.gov/23903186/)
- Sakamoto A**, Chen M, Kobayashi T, Kronenberg HM, Weinstein LS. 2005. Chondrocyte-specific knockout of the G protein G(s)alpha leads to epiphyseal and growth plate abnormalities and ectopic chondrocyte formation. *Journal of Bone and Mineral Research* **20**:663–671. doi: [10.1359/JBMR.041210](https://doi.org/10.1359/JBMR.041210), PMID: [15765186](https://pubmed.ncbi.nlm.nih.gov/15765186/)
- Schötz EM**, Lanio M, Talbot JA, Manning ML. 2013. Glassy dynamics in three-dimensional embryonic tissues. *Journal of the Royal Society Interface* **10**:20130726. doi: [10.1098/rsif.2013.0726](https://doi.org/10.1098/rsif.2013.0726), PMID: [24068179](https://pubmed.ncbi.nlm.nih.gov/24068179/)
- Sheehan MJ**, Nachman MW. 2014. Morphological and population genomic evidence that human faces have evolved to signal individual identity. *Nature Communications* **5**:4800. doi: [10.1038/ncomms5800](https://doi.org/10.1038/ncomms5800), PMID: [25226282](https://pubmed.ncbi.nlm.nih.gov/25226282/)
- Snippert HJ**, van der Flier LG, Sato T, van Es JH, van den Born M, Kroon-Veenboer C, Barker N, Klein AM, van Rheenen J, Simons BD, Clevers H. 2010. Intestinal crypt homeostasis results from neutral competition between symmetrically dividing Lgr5 stem cells. *Cell* **143**:134–144. doi: [10.1016/j.cell.2010.09.016](https://doi.org/10.1016/j.cell.2010.09.016), PMID: [20887898](https://pubmed.ncbi.nlm.nih.gov/20887898/)
- Strutt D**. 2005. Organ shape: controlling oriented cell division. *Current Biology* **15**:R758–R759. doi: [10.1016/j.cub.2005.08.053](https://doi.org/10.1016/j.cub.2005.08.053), PMID: [16169474](https://pubmed.ncbi.nlm.nih.gov/16169474/)
- Tesařová M**, Zikmund T, Kaucká M, Adameyko I, Jaroš J, Paloušek D, Škaroupka D, Kaiser J. 2016. Use of micro computed-tomography and 3D printing for reverse engineering of mouse embryo nasal capsule. *Journal of Instrumentation* **11**:C03006. doi: [10.1088/1748-0221/11/03/C03006](https://doi.org/10.1088/1748-0221/11/03/C03006)
- Thompson H**, Ohazama A, Sharpe PT, Tucker AS. 2012. The origin of the stapes and relationship to the otic capsule and oval window. *Developmental Dynamics* **241**:1396–1404. doi: [10.1002/dvdy.23831](https://doi.org/10.1002/dvdy.23831), PMID: [22778034](https://pubmed.ncbi.nlm.nih.gov/22778034/)
- Van Liedekerke P**, Palm MM, Jagiella N, Drasdo D. 2015. Simulating tissue mechanics with agent-based models: concepts, perspectives and some novel results. *Computational Particle Mechanics* **2**:401–444. doi: [10.1007/s40571-015-0082-3](https://doi.org/10.1007/s40571-015-0082-3)
- Vortkamp A**, Lee K, Lanske B, Segre GV, Kronenberg HM, Tabin CJ. 1996. Regulation of rate of cartilage differentiation by indian hedgehog and PTH-related protein. *Science* **273**:613–622. doi: [10.1126/science.273.5275.613](https://doi.org/10.1126/science.273.5275.613), PMID: [8662546](https://pubmed.ncbi.nlm.nih.gov/8662546/)
- Wang Y**, Spatz MK, Kannan K, Hayk H, Avivi A, Gorivodsky M, Pines M, Yayon A, Lonai P, Givol D. 1999. A mouse model for achondroplasia produced by targeting fibroblast growth factor receptor 3. *PNAS* **96**:4455–4460. doi: [10.1073/pnas.96.8.4455](https://doi.org/10.1073/pnas.96.8.4455), PMID: [10200283](https://pubmed.ncbi.nlm.nih.gov/10200283/)
- Wealthall RJ**, Herring SW. 2006. Endochondral ossification of the mouse nasal septum. *The Anatomical Record Part A: Discoveries in Molecular, Cellular, and Evolutionary Biology* **288**:1163–1172. doi: [10.1002/ar.a.20385](https://doi.org/10.1002/ar.a.20385), PMID: [17031811](https://pubmed.ncbi.nlm.nih.gov/17031811/)
- Yamaguchi TP**, Bradley A, McMahon AP, Jones S. 1999. A Wnt5a pathway underlies outgrowth of multiple structures in the vertebrate embryo. *Development* **126**:1211–1223. PMID: [10021340](https://pubmed.ncbi.nlm.nih.gov/10021340/)
- Young B**, Minugh-Purvis N, Shimo T, St-Jacques B, Iwamoto M, Enomoto-Iwamoto M, Koyama E, Pacifici M. 2006. Indian and sonic hedgehogs regulate synchondrosis growth plate and cranial base development and function. *Developmental Biology* **299**:272–282. doi: [10.1016/j.ydbio.2006.07.028](https://doi.org/10.1016/j.ydbio.2006.07.028), PMID: [16935278](https://pubmed.ncbi.nlm.nih.gov/16935278/)
- Yu K**, McGlynn S, Matisse MP. 2013. Floor plate-derived sonic hedgehog regulates glial and ependymal cell fates in the developing spinal cord. *Development* **140**:1594–1604. doi: [10.1242/dev.090845](https://doi.org/10.1242/dev.090845), PMID: [23482494](https://pubmed.ncbi.nlm.nih.gov/23482494/)

## Appendix 1

### Individual based model (IBM) for cartilage dynamics

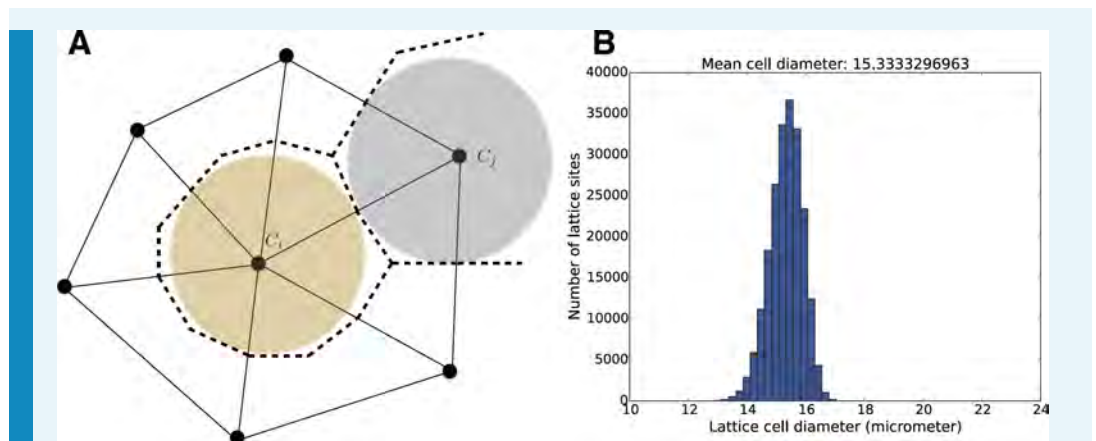
In order to model and illustrate the growth of the cartilage on the cellular level, we developed an individual-based model incorporating cell proliferation (including displacement of surrounding cells via pushing) (Hellander, 2015). The model is stochastic because we want to be able to capture effects of e.g. synchronicity in cell division and the degree of determinism needed to achieve an ordered columnar growth of the structure. We do this by letting the cell division times, direction of allocation of daughter cells after cell division, etc., be random variables. This document describes the details of the model and its implementation.

There are several popular modeling frameworks for simulating interacting cells. In the cellular Potts model (Graner and Glazier, 1992) a single biological cell can be composed of multiple lattice sites making it possible to use a more detailed description of cell shape and include more detailed description of more mechanical properties. In off-lattice center based models cells are often modeled as spheres with pair-wise interactions and a force-based description to evolve the system dynamics, for an overview see (Van Liedekerke et al., 2015). Vertex models can offer even more realistic models of cell mechanics (Fletcher et al., 2013) but become expensive and complicated in three space dimensions.

Rather than these more comprehensive mechanical models, we use a simplistic rule-based, on-lattice stochastic cellular automaton (CA). In the language of a recent review (Van Liedekerke et al., 2015) our model falls into the category of a Type B CA. These types of models are widely used in e.g. cancer tumor modeling and for simulation of monolayers and spheroids (Radszweit et al., 2009). The simulation code is written in Python, relies on the PyURDME package for spatial stochastic simulations ([www.pyurdme.org](http://www.pyurdme.org)) and it is freely available for download from [www.github.com/ahellander/multicell](https://github.com/ahellander/multicell) (Hellander, 2015) under the GPLv3 license. A copy is archived at <https://github.com/elifesciences-publications/multicell>.

The basic entities in our simulation are Agents and Events. An Agent is a model (implemented as a Python class) of an individual (cell). Events simulate discrete state changes involving one or several agents. They occur at a certain time (assuming no other event involving the same agents occurs first). They rely on rules that specify how and under what conditions the event is to be executed. A simulation is initialized by creating the initial population of agents and events, and then creating a priority queue (in our case implemented using a heap data structure using the Python module 'heapq'). In each iteration of the algorithm, the event with the shortest time is popped from the queue and executed (assuming that all of its rules and conditions can be satisfied), the system time updated, new events derived from any newly created agents are created and inserted into the queue, and all existing events affected by changes in the agents or the system state are updated.

Each agent occupies one voxel of a tessellation of 2D or 3D space, and each lattice site can only accommodate one agent. Following the recommendation in (Radszweit et al., 2009) a Delaunay triangulation is used. The mesh resolution is chosen such that the average voxel size is close to the desired cell size (~7  $\mu\text{m}$  radius) taken from the experiments. Being a lattice model, the shape and volume of the cells are a lattice property and are given by the dual grid (Voronoi cells in the case of a Delaunay triangulation). This is illustrated in **Appendix 1—figure 1A**. The interpretation is that individual agents occupy the dual elements (dashed lines) of an unstructured triangular (2D) or tetrahedral primal mesh (3D) (solid lines).



**Appendix 1—figure 1.** (A) Individual cells are modeled by a number of properties such as their color and distributions for cell division times. The positions of cells in space are tracked on an underlying unstructured lattice, or grid. The edges in the primary mesh (solid lines) connect vertices (black dots). A biological cell is modeled by the volume made up of the dual elements (dashed lines), connecting triangle (2D) or tetrahedral (3D) centers and edge or face centers. For visualization purposes, in 3D space, we plot cell individuals as colored spheres with radius equal to the sphere with equal volume as the dual element. (B) Size distribution for the mesh elements for the geometry and mesh used in the simulations in the **Figure 5**.

DOI: [10.7554/eLife.25902.025](https://doi.org/10.7554/eLife.25902.025)

## The individual agents – colored coded cells

Each individual cell is modeled as an individual agent with the following properties:

- Color (a label used to track the lineage).
- Mean cell division time,  $\mu_p$ .
- Variance in cell division time,  $\sigma_p^2$ .

When visualized in 2D, we draw cells as polygons (the actual dual cells) and in 3D for practical reasons we visualize them as spheres centered on the vertices of the primal mesh, with radius chosen such that the volume corresponds to the volume of the corresponding dual element. On the unstructured mesh, there will be a size distribution for the mesh elements, i.e. there will be a small variation in the size associated with each lattice site, see **Appendix 1— figure 1B**.

## Cell proliferation

### Cell division time

The time until a cell, or individual, divides, is assumed to be a random variable. Although a multi-stage model of cell division can give rise to an Erlang distribution (**Radszuweit et al., 2009**) which is found to match experimental data for another system, we are not calibrating our model to experimental data on cell division time distributions. The dividing cell (referred to as the mother cell) create a daughter cell after a normally distributed waiting time  $\tau_D$ .

$$\tau_D \sim N(\mu_d, \sigma_d^2) \quad (1)$$

where the mean division time  $m$  and the variance  $\sigma^2$  are parameters of the model to be supplied as input to the simulation. As a measure of the degree of variability in cell division times, we use the standard deviation over the mean,

$$f = \frac{\sigma_d}{\mu_d} \quad (2)$$

The smaller value of  $f$ , the more deterministic and synchronized the cell cycles of individual cells are. The way our model is set up, there are no events that leads to the recalculation of a cell's division time. A cell gets assigned a time to division at creation and each cell then divide according to its internal clock irrespective of if it gets pushed etc.

After division, the daughter cell needs to be deposited on the grid. The division direction, or receiving voxel, is sampled according to a discrete distribution. In the simplest case, all directions of division are equally probable and the direction distribution is uniform. In the general case, weights are assigned according to an external, deterministic gradient.

### Cell division direction

The division direction is also a random variable and the number of possible directions are given by the connections to the neighbors on the grid. Each individual has a property that sets its polarization, represented by a normalized vector  $p$  pointing in the preferred direction of division. With no polarization, each possible division direction is equally probable. With polarization, the probability to divide in a certain direction is biased by the gradient. The weights for sampling the division direction are taken to be

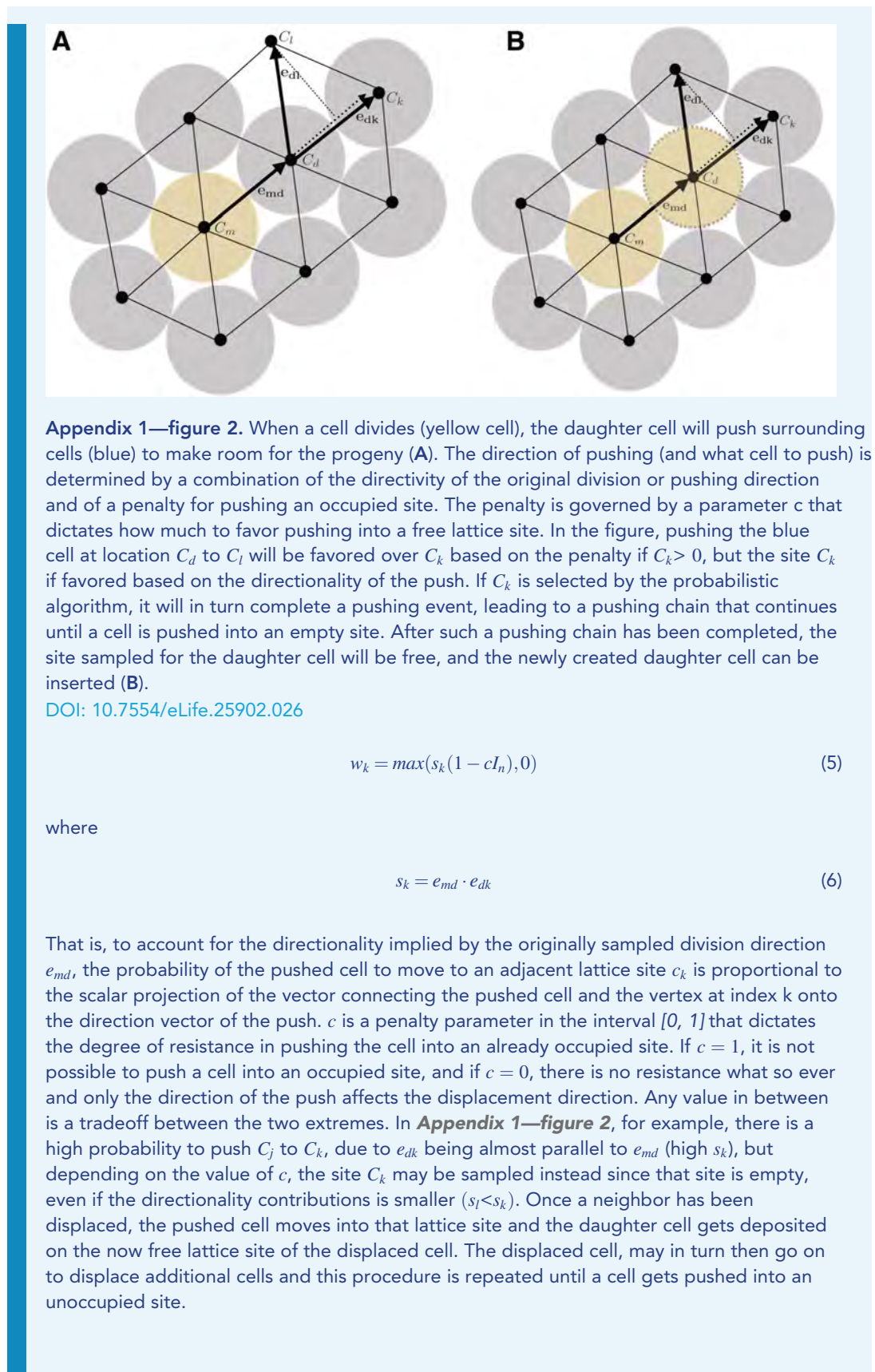
$$w_{ij} = \left( \frac{d_{ij}}{\max_j(d_{ij})} \right)^b, \quad (3)$$

$$d_{ij} = \frac{g(x_j) - g(x_i)}{h_{ij}} \quad (4)$$

where  $x_i$  is the position of the vertex in the grid for which the agent resides, and  $h_{ij}$  is the length of the edge connecting grid points  $x_i$  and  $x_j$  and  $g(x)$  is a given concentration profile. The parameter  $b \geq 0$  dictates how perfectly the cells become polarized by the concentration profile  $g(x)$ . A value  $b = 0$  leads to equal probabilities for all directions, and very large value of  $b$  means that the division direction will always be in the direction of the maximal value of the gradient (the division direction becomes deterministic in the direction of the maximal gradient in the limit  $b \rightarrow \infty$ ). Values in between the extremes describes an increasing precision in polarization axis alignment with the gradient field.

### Cell pushing

If the receiving lattice for the daughter cell site is empty (i.e. occupied by matrix), it is simply deposited there. When the daughter cell cannot be placed on a free lattice site, there is an attempt to reorganize the structure by pushing neighboring cells to make room for it. The procedure is illustrated in **Appendix 1—figure 2**. The probability for the displaced cell to move to a given neighboring grid point depends on the direction of pushing. Let  $e_{md}$  be the vector along the edge connecting the mother cell  $C_m$  and the daughter cell  $C_d$ , pointing towards the daughter cell. Let  $e_{dk}$  be the unit vector along the edge connecting the daughter cell  $C_d$  and one of its neighbors,  $C_k$ . The weight for moving the displaced cell to the neighbor with index  $n$  is given by



## Measure of order in the cartilage model

We are interested in assessing what factors are the main determinants to the degree of ordered columnar growth in the cartilage sheet patches. To that end, we postulate that a perfectly ordered structure consists of clonal columns growing straight and directed along the axis perpendicular to the initial condition starting plane (**Figure 5G**). We then use the following metric to quantify the degree of order in the structure

$$S = \frac{1}{C} \sum_{j=1}^C \frac{1}{N_j} \sum_{i=1}^{N_j} s_{ij} \quad (7)$$

with  $s_{ij}$

$$s_{ij} = |v_i \bullet y| \quad (8)$$

where  $y$  is a unit vector perpendicular to the initial condition plane, and  $v_i$  are normalized vectors joining two consecutive points (sorted by  $y$ -coordinate) in clones with the same color.  $N_j$  is the number of cells of a given color minus one (the number of vectors), and  $C$  is the number of unique clones tracked. This is illustrated graphically in **Figure 5A**. With this metric, a score of  $S = 1$  would mean that all columns are perfectly aligned to the main growth axis and a score of  $S = 0$  would mean that they are all perpendicular to it. We use this metric to score realizations of the process either in the absence of a gradient, or when the gradient is uniform in planes parallel to the center plane, so that in the case of a perfect polarization, cells should all deposit their daughter cells perpendicular to the center plane.

PAPER [XII]

# Signals from the brain and olfactory epithelium control shaping of the mammalian nasal capsule cartilage

Marketa Kaucka<sup>1,2†</sup>, Julian Petersen<sup>1,2†</sup>, Marketa Tesarova<sup>3</sup>, Bara Szarowska<sup>2</sup>, Maria Eleni Kastriti<sup>1,2</sup>, Meng Xie<sup>1</sup>, Anna Kicheva<sup>4</sup>, Karl Annusver<sup>5,6</sup>, Maria Kasper<sup>5,6</sup>, Orsolya Symmons<sup>7</sup>, Leslie Pan<sup>8</sup>, Francois Spitz<sup>8,9</sup>, Jozef Kaiser<sup>3</sup>, Maria Hovorakova<sup>10</sup>, Tomas Zikmund<sup>3</sup>, Kazunori Sunadome<sup>1</sup>, Michael P Matise<sup>11</sup>, Hui Wang<sup>11</sup>, Ulrika Marklund<sup>12</sup>, Hind Abdo<sup>12</sup>, Patrik Ernfors<sup>12</sup>, Pascal Maire<sup>13</sup>, Maud Wurmser<sup>13</sup>, Andrei S Chagin<sup>1,14</sup>, Kaj Fried<sup>15</sup>, Igor Adameyko<sup>1,2\*</sup>

<sup>1</sup>Department of Physiology and Pharmacology, Karolinska Institutet, Stockholm, Sweden; <sup>2</sup>Department of Molecular Neurosciences, Medical University Vienna, Vienna, Austria; <sup>3</sup>Central European Institute of Technology, Brno University of Technology, Brno, Czech Republic; <sup>4</sup>Institute of Science and Technology IST Austria, Klosterneuburg, Austria; <sup>5</sup>Department of Biosciences and Nutrition, Karolinska Institutet, Stockholm, Sweden; <sup>6</sup>Center for Innovative Medicine, Karolinska Institutet, Huddinge, Sweden; <sup>7</sup>Department of Bioengineering, University of Pennsylvania, Philadelphia, United States; <sup>8</sup>Developmental Biology Unit, European Molecular Biology Laboratory, Heidelberg, Germany; <sup>9</sup>Genomics of Animal Development Unit, Institut Pasteur, Paris, France; <sup>10</sup>Department of Developmental Biology, Institute of Experimental Medicine, The Czech Academy of Sciences, Prague, Czech Republic; <sup>11</sup>Department of Neuroscience & Cell Biology, Rutgers-Robert Wood Johnson Medical School, Piscataway, United States; <sup>12</sup>Department of Medical Biochemistry and Biophysics, Karolinska Institutet, Stockholm, Sweden; <sup>13</sup>Department of Development, Reproduction and Cancer, Institute Cochin, Paris, France; <sup>14</sup>Institute for Regenerative Medicine, Sechenov First Moscow State Medical University, Moscow, Russia; <sup>15</sup>Department of Neuroscience, Karolinska Institutet, Stockholm, Sweden

\*For correspondence:  
igor.adameyko@ki.se

†These authors contributed  
equally to this work

**Competing interests:** The  
authors declare that no  
competing interests exist.

**Funding:** See page 22

**Received:** 19 December 2017

**Accepted:** 12 June 2018

**Published:** 13 June 2018

**Reviewing editor:** Richard M  
White, Memorial Sloan Kettering  
Cancer Center, United States

© Copyright Kaucka et al. This  
article is distributed under the  
terms of the [Creative Commons  
Attribution License](#), which  
permits unrestricted use and  
redistribution provided that the  
original author and source are  
credited.

**Abstract** Facial shape is the basis for facial recognition and categorization. Facial features reflect the underlying geometry of the skeletal structures. Here, we reveal that cartilaginous nasal capsule (corresponding to upper jaw and face) is shaped by signals generated by neural structures: brain and olfactory epithelium. Brain-derived Sonic Hedgehog (SHH) enables the induction of nasal septum and posterior nasal capsule, whereas the formation of a capsule roof is controlled by signals from the olfactory epithelium. Unexpectedly, the cartilage of the nasal capsule turned out to be important for shaping membranous facial bones during development. This suggests that conserved neurosensory structures could benefit from protection and have evolved signals inducing cranial cartilages encasing them. Experiments with mutant mice revealed that the genomic regulatory regions controlling production of SHH in the nervous system contribute to facial cartilage morphogenesis, which might be a mechanism responsible for the adaptive evolution of animal faces and snouts.

DOI: <https://doi.org/10.7554/eLife.34465.001>

## Introduction

The shape of a face strongly depends on the geometry of skeletal elements directly under the skin, adipose tissue and muscles. Our adult cranial and, in particular, facial skeleton consists mostly of bony elements. Cartilaginous parts are rather minor. However, during embryonic development bone forms after the cartilage, and the initial phases of facial and skull shaping proceed with the cartilaginous skeleton only. The entire functional and evolutionary meaning of the chondrocranium, that is, the early cartilaginous elements of the embryonic skull, is not clear. Some parts of the chondrocranium will undergo endochondral ossification (for example, pre-sphenoid and basisphenoid, cribriform plate, Meckel's cartilage, olfactory septum, nasal concha, labyrinth of ethmoid, vomer and tympanic bulla). However, the majority of the bones, especially in a facial compartment, will form in a close spatial association with the chondrocranium independently through dermal membranous ossifications (Carson, 1999). Many questions, including how and from where molecular signals control the complex chondrocranial shape, and whether the geometry of the chondrocranium directs the shape of facial bones, are still unanswered.

Achondroplasia, a rare disease due to cartilage insufficiency, includes craniofacial malformations such as protruding forehead, low nasal bridge, maxillary hypoplasia, problems in the otolaryngeal system and macrocephaly as well as foramen magnum stenosis (Shirley and Ain, 2009). Prominent human and mouse achondroplasia phenotypes based on *Fgfr3* mutations suggest that a correctly shaped chondrocranium is essential for proper facial bone geometry and general facial outgrowth. However, *Fgfr3* is expressed also at membranous ossification sites (please see *Fgfr3*(mRNA) expression at E15, <http://developingmouse.brain-map.org/>), as well as in sutural osteogenic fronts (Ornitz and Marie, 2002). Therefore, models involving *Fgfr3* do not allow for precise discrimination of cartilage or bone-dependent parts of the phenotype in affected subjects. Still, these effects strongly suggest that chondrocranium shape might be truly important for producing initial facial geometry and for influencing the formation of membranous bone on top of the cartilaginous template.

The facial chondrocranium is built by neural crest cells that populate the frontal part of the head and undergo multilineage differentiation. They give rise to cartilage, bone, fascia, adipose tissue, smooth muscle, pericytes, glia and neurons (Snider and Mishina, 2014; Baggiolini et al., 2015). Paraxial mesoderm also contributes to the chondrocranium in posterior basicranial and occipital locations. Collective behavior and differentiation of the neural crest and neural crest-derived ectomesenchyme is largely responsible for the future shape of the face (Minoux and Rijli, 2010). However, the precise mechanisms governing this collective behavior, cartilage induction and shape-making are not fully understood, despite significant progress in the research field of cartilage and bone formation.

McBratney-Owen and Morris-Key with coworkers demonstrated that the complete chondrocranium (including the base of the skull) develops from 14 pairs of independently induced large cartilaginous elements that fuse together during later development (McBratney-Owen et al., 2008). Sculpting perfect geometries of such cartilaginous elements is a key developmental and regenerative process that accounts for the shape and integrity of our body. Current opinion holds that cartilage forms from condensing mesenchymal cells that are destined to become chondrocytes (Ornitz and Marie, 2002). Mesenchymal condensations emerge in specific locations. Here, they somehow become shaped, grow and turn into cartilage that later expands until the initiation of endochondral or membranous ossification.

The frontonasal prominence and other facial regions are enriched in signaling systems. Activity in these systems leads to progressive induction and shaping of craniofacial structures, including chondrogenic mesenchymal condensations that turn into cartilage (Minoux and Rijli, 2010). The signaling center located in the most anterior face, the so called FEZ (Frontonasal Ectodermal Zone), produces Sonic Hedgehog (SHH) and Fibroblast growth factor 8 (FGF8), which play important roles in facial shaping. FGF8, SHH and Bone Morphogenetic Proteins (BMPs) produced by FEZ regulate the behavior of ectomesenchymal tissue and participate in positioning of chondrogenic condensations inside of the embryonic face (Foppiano et al., 2007; Hu et al., 2015b; Young et al., 2014). The mechanisms of facial cartilage induction that involve these molecules have received particular attention during recent years (Gros and Tabin, 2014; Abzhanov and Tabin, 2004; Bhullar et al., 2015; Griffin et al., 2013).

Another recent breakthrough brought up the fact that the brain itself can emit signals that influence facial shaping. Expression of *Shh* in the forebrain turned out to be important for the correct formation of FEZ and early steps of facial shaping in general (Hu et al., 2015a; Chong et al., 2012).

Still, how these and other signaling centers synchronize in order to build the 3D shape of facial cartilaginous elements is not understood. The cartilaginous nasal capsule is the most anterior part of the chondrocranium. Together with Meckel's cartilage in the lower jaw, it constitutes an excellent model system to address questions concerning cartilage induction and shaping.

Here, using mild ablations of cartilage with tightly controlled genetic tools, we revealed that the shape of the nasal capsule is a key for the geometry and positioning of the facial bones and overall facial shape. Subsequently, with the help of numerous mouse mutants, specific contrasting techniques and micro-CT, we demonstrated that signaling centers in the developing brain and olfactory epithelium jointly and independently enable the induction of the nasal capsule in the embryonic face. Various genomic regulatory regions that direct the expression of *Shh* to the developing nervous system participate in the fine-tuning of the shape of the facial cartilaginous skeleton.

## Results

Taking into account known achondroplasia facial phenotypes, we hypothesized that even minor changes in the facial cartilaginous template may lead to significant or even major changes in the overlying membranous bone geometry and the overall facial shape. Thus, we performed mild time-controlled genetic ablation of early chondrocytes employing *Col2a1-CreERT2/R26DTA* mice and analyzed their facial development (Figure 1). We used a dose of 2.5 mg of tamoxifen administered at E12.5 and, in an alternative experiment, double injection at E13.5-E14.5 to avoid a strong phenotype with dramatic face shortening and brain shape distortion, and we analyzed the mutant embryos at E17.5 and E15.5 correspondingly (Figure 1). *Col2a1-CreERT2* is a well-established tool to target facial chondrocytes and their immediate progenitors. Tamoxifen was administered at early stages of facial development where no bone is present. Also, this *CreERT2* line does not recombine in osteoblasts or their progenitors in membranous ossification sites and, thus, cannot directly impinge on them (Figure 1A–D). Despite only mild cartilage reduction (mean 30,7% of the cartilage surface decrease at E15.5 and mean 35,2% at E17.5), the facial compartment of the *Col2a1-CreERT2<sup>+/-</sup>/R26DTA<sup>+/-</sup>* embryos appeared massively affected with short snout and distorted membranous ossifications (Figure 1E–R). Interestingly, the forming mandibular bone appeared shortened and widened at the same time, which cannot be explained only by the shortening of Meckel's cartilage (Figure 1—figure supplement 1). This fact suggests an interplay between cartilage and membranous bone that might involve signal-guided rearrangements in skeletogenic tissues. Thus, genetic ablations of COL2A1-producing pre-chondrocytes and chondrocytes revealed a different degree of cartilage loss in the nasal capsule and Meckel's cartilage, together with corresponding incremental dysmorphologies of membranous bones and face in general. These slight differences in the strength of the phenotype are likely attributed to the fine diversity of developmental stages within one litter receiving tamoxifen during a single injection into a mother (Figure 1Q–R and Figure 1—figure supplement 1). Thus, the geometry of the face and corresponding bony structures depend on the correct induction and shaping of a facial cartilage. This, in turn, is largely established at the level of chondrogenic mesenchymal condensations, as we recently demonstrated (Kaucka et al., 2017). It is worth emphasizing that according to our previous study, the chondrogenic condensations are induced being pre-shaped (Kaucka et al., 2017).

Consequently, we decided to analyze the molecular signals and their sources that induce these geometrically complex condensations. Several molecules were reported to have an impact on the cartilage induction, either on the condensation placement or on proper timing of cartilage-forming events (Goldring et al., 2006). Among those, SHH was shown to play a key role in the spatio-temporal induction of chondrogenic mesenchymal condensations (Abzhanov and Tabin, 2004; Billmyre and Klingensmith, 2015; Park et al., 2010). We analyzed the expression of *Shh* in early and late developing mouse face with the help of the *Shh-Cre/GFP* (*B6.Cg-Shhtm1(EGFP/cre)Cjt/J*) model, and found that *Shh* is expressed in very discrete regions of the face between E11.5 and E14.5 at the time of induction of facial cartilages (Figure 2 and Figure 2—figure supplement 1). At the early stages (E11.5 and E12.5, see Figure 2A–B), the SHH + regions included forming olfactory epithelium (magenta), dental and oral epithelium (red), eyes (cyan) and brain (yellow). Interestingly,

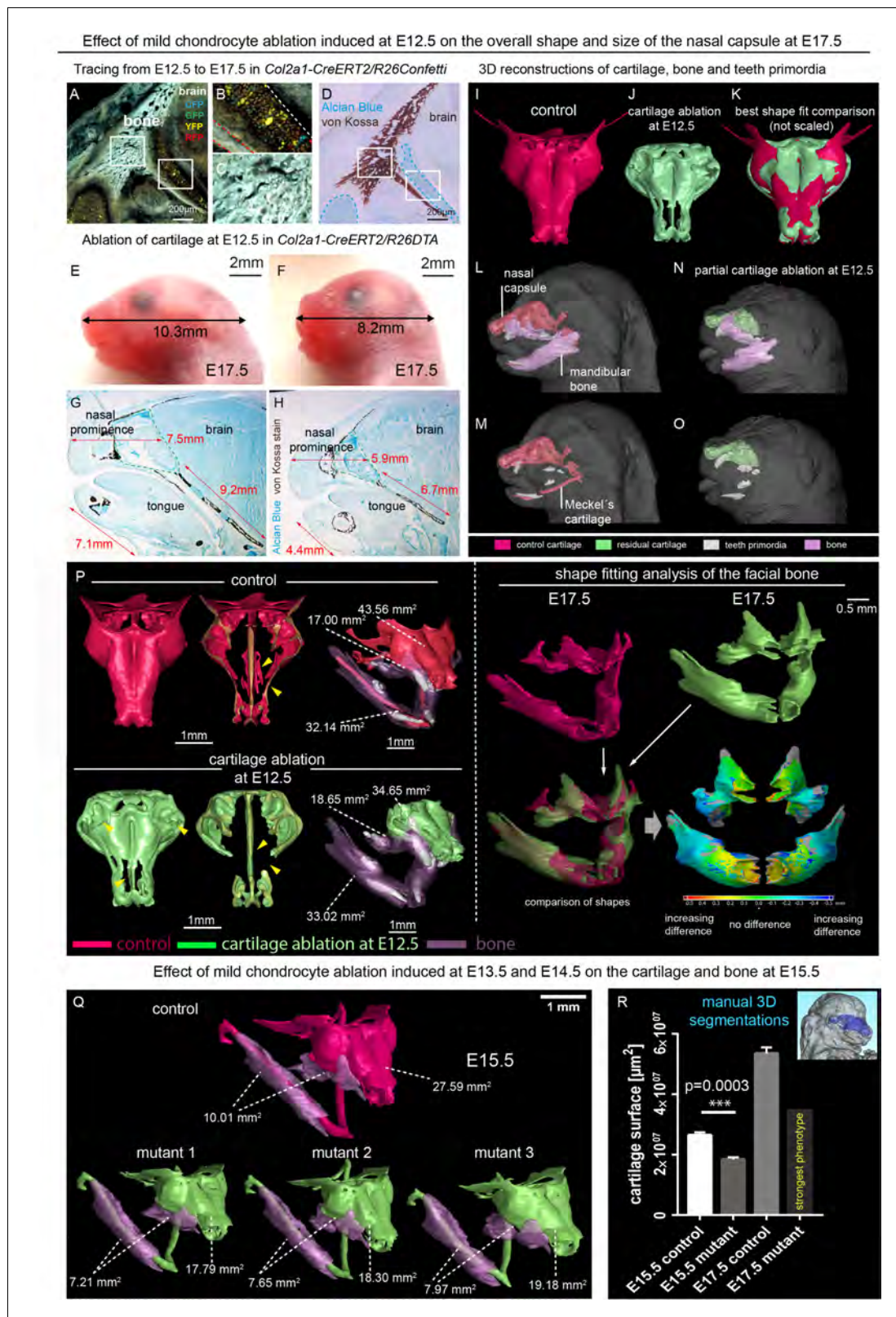


**Figure 1.** Correct chondrocranium development is essential for shaping the embryonic face. (A–C) Genetic tracing induced at E12.5 in *Col2a1-CreERT2/R26Confetti* shows recombination in chondrocytes (B) only and not in a lineage of membranous bone osteoblasts and their progenitors (C), 25  $\mu\text{m}$  cryo-sections (A–D, G–H) were imaged with a confocal microscope (A–C) or phase contrast microscope (D, G–H). (D) Traced sections have been stained using Alcian Blue (cartilage, blue) and von Kossa (brown, mineralized tissue). (E–F) Wild type (E) and *Col2a1-CreERT2/R26DTA* (F) embryos with Figure 1 continued on next page

Figure 1 continued

cartilage being partially ablated as a result of tamoxifen injection (2.5 mg) at E12.5, both analyzed at E17.5. (G–H) Sagittal sections of the anterior head from wild type (G) and *Col2a1-CreERT2/R26DTA* (H) embryos stained with Alcian Blue (blue, stains for cartilage) and von Kossa staining (black, stains for mineralized bone tissue). Olfactory system is outlined by green dashed line for better orientation. Note that physiological growth of the cartilage sets the proper size of the facial compartment. (I–O) 3D-reconstructions of frontal chondrocranium together with bone and teeth primordia in control (I, L, M) and cartilage-ablated (J, N, O) embryos. (K) Best fit comparison of control (red) and cartilage-ablated (light green) 3D chondrocranium models. (P) 3D-reconstruction of frontal chondrocranium and formed cartilage including GOM Inspect software analysis of the mutant bone (Q) overview of analyzed mutants (injected with low dose of tamoxifen (2.5 mg) at both E13.5 and E14.5 and analyzed at E15.5) and formed bone in one representative control and three mutants (R) Bar-graphs showing the manual 3D segmentation of the surface area of cartilage. Data are obtained from three control samples and three mutant mice for (E15.5) and three control samples and one mutant sample with the most pronounced phenotype for (E17.5). The error bars show mean and standard deviation (SD). For the comparison, we used unpaired Student t-test (95% confidence interval –9974138 to –6056665). Raw data are available in **Figure 1—source data 1**.

DOI: <https://doi.org/10.7554/eLife.34465.002>

The following source data and figure supplement are available for figure 1:

**Source data 1.** Raw values of cartilage surface measurements corresponding to Graph in **Figure 1R**.

DOI: <https://doi.org/10.7554/eLife.34465.004>

**Figure supplement 1.** Mild ablation of cartilage using *Col2a1-CreERT2/R26DTA*.

DOI: <https://doi.org/10.7554/eLife.34465.003>

only certain regions of olfactory epithelium were SHH+ (see stained cryosections under the 3D models in **Figure 2**). Later on (at E13.5 and E14.5 – **Figure 2—figure supplement 1**), we detected additional SHH-producing structures such as whiskers (blue-green), tongue (not segmented) and salivary

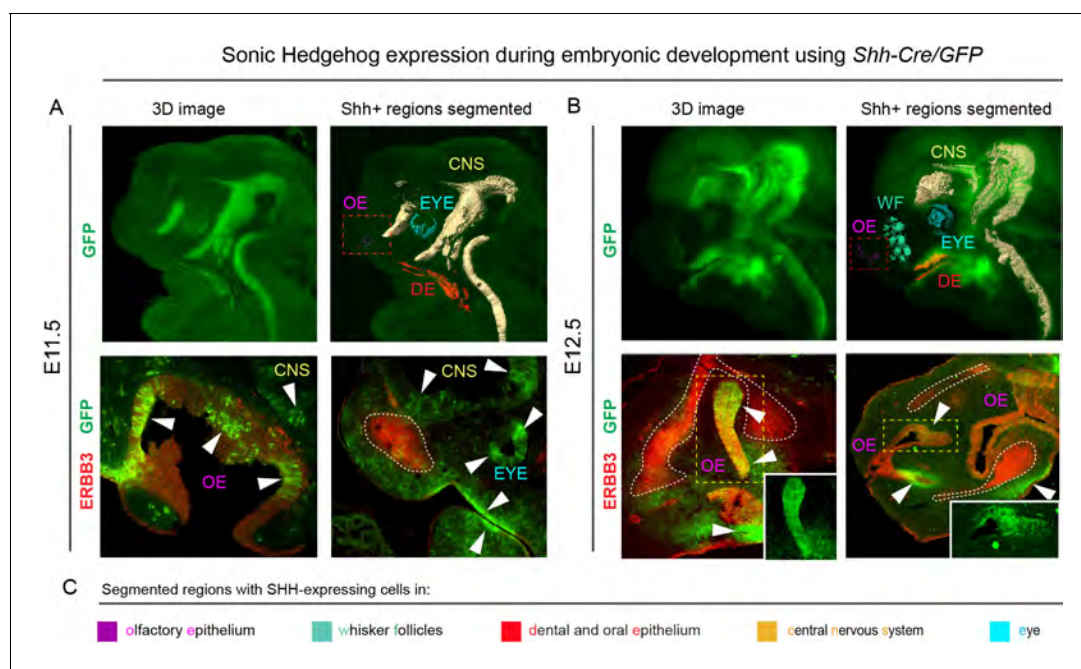


**Figure 2.** *Shh* is expressed through the early facial development in distinct regions of the head. The expression pattern of *Shh* during developmental stages E11.5 (A) and E12.5 (B) in *B6.Cg-Shhtm1(EGFP/cre)Cjt/J*, segmented *Shh*-expression regions are color-coded and clarified in legend (C). Immunohistochemical (IHC) staining shows olfactory neuroepithelium and newly formed mesenchymal condensation as ERBB3 positive. White arrows point at GFP-expressing parts of various tissues. Red rectangle in (A) and (B) upper panel mark the olfactory neuroepithelium, yellow rectangle in (B) shows area magnified in the right bottom corner. White dotted line outlines the shape of mesenchymal condensation. IHC staining was performed on 20  $\mu$ m cryosections and imaged using a confocal microscope.

DOI: <https://doi.org/10.7554/eLife.34465.005>

The following figure supplement is available for figure 2:

**Figure supplement 1.** *Shh* is expressed through the later facial development in distinct regions of the head.

DOI: <https://doi.org/10.7554/eLife.34465.006>

gland (blue). We assumed that there is a prerequisite for a certain minimal distance between *Shh*-expressing structures and forming cartilage of nasal capsule that enables the secreted molecule to reach the target and impose chondrogenic stimuli on mesenchymal cells. According to our results, the most probable pro-chondrogenic SHH-emitting structures in the face were the olfactory epithelium and the forebrain.

To test if SHH emitted by these structures controls nasal capsule induction or influences its geometrical features, we analyzed a series of mouse mutants with a micro-CT-based 3D-visualization approach. To perform these 3D visualizations of the mesenchymal chondrogenic condensations, cartilage and bone, we utilized a soft tissue contrasting with phosphotungstic acid (PTA) followed by micro-CT scanning. Chelation of tungsten is uneven in various cell types and creates reliable contrast highlighting different tissues.

Firstly, to address whether the induction of distinct elements of the facial chondrocranium is not only timely regulated, but also has a discrete spatial aspect related to various sources of inductive signals, we genetically ablated *Shh* in the brain to test its role in facial cartilage induction. For this, we took advantage of *Nkx2.2-Cre/Shh<sup>floxed/floxed</sup>* animals to delete *Shh* in the floor plate cells since the beginning of central nervous system (CNS) development and patterning. We analyzed two different stages: E12.5 as a stage of condensations of cartilaginous mesenchyme (**Figure 3** and **Figure 3—figure supplement 1** 'Interactive PDF') and E15.5 as a later stage of nearly fully formed chondrocranium with its rather final shape (**Figure 3** and **Figure 3—figure supplement 1** 'Interactive PDF'). This experiment resulted in an unexpected phenotype. It included a selective loss of a nasal septum together with heavily affected posterior part of the nasal capsule as detected at E12.5 (**Figure 3B–C, E–F**). The chondrogenic condensation corresponding to a forming septum failed completely, whereas the condensation of the posterior part of nasal capsule appeared incompletely induced. Additional changes were detected in the facial cartilage at E15.5, mainly represented by the missing midline groove (**Figure 3G–H**) and the absence of the very anterior part of nasal cartilage (**Figure 3H**). Additional changes included various malpositioned parts, fused nerve foramina and variations in shaping and bending of cartilage elements, as summarized in **Figure 3**. Notably, the mutant embryos analyzed at E12.5 and E15.5 presented with cleft palate. This could indicate that some clinical cleft palate cases might have their origin in disturbed brain-derived signaling (**Figure 3—figure supplement 2**).

At the same time, the general geometry of the frontal part of facial chondrocranium remained almost unperturbed, thus, supporting the spatial modularity of cartilage induction in the face. The microstructure of the cartilage stayed normal, with fine borders defining bent cartilaginous sheets forming the major structure of the nasal capsule. The thickness of the cartilaginous sheets forming the capsule also remained comparable to that found in littermate controls (**Figure 3J**). These observations strongly suggested that the early stages of cartilage induction must be affected.

We also investigated bone formation in the area of the nasal capsule at E15.5 (**Figure 3I**). We observed missing parts in maxillary bones from mutants, and malpositioned incisors that were found more posteriorly on top of instead of being in the anterior part of the maxilla. At this stage and in this particular location, there was no endochondral ossification ongoing. However, according to micro-CT data, the bone was forming in the proximity and on top of the existing cartilaginous shape template. Thus, the facial chondrocranium is important for the correct formation of the membranous facial bones.

Recently it has been shown that the brain can influence facial shaping via *Shh*, acting presumably on the frontonasal ectodermal signaling zone (abbreviated as FEZ) (**Hu et al., 2015a; Chong et al., 2012**). It is currently believed that FGF8, SHH and BMPs produced by FEZ regulate the behavior of ectomesenchymal tissue and participate in positioning of chondrogenic condensations inside of the embryonic face (**Foppiano et al., 2007; Hu et al., 2015b; Young et al., 2014**). However, our data show that SHH emitted from the forebrain mostly affects the basicranial, posterior and septal parts of the facial chondrocranium without strong effects on the most anterior nasal capsule (including other soft tissues in general), which could be expected if the effects of a brain-derived SHH are entirely mediated by FEZ. Importantly, the major geometric structure of the mutant brain stays largely unchanged although it appears reduced in size. Thus, changes in brain shape are not likely to cause very selective influences on forming facial structures due to mere mechanical interactions (**Figure 3—figure supplement 3**).

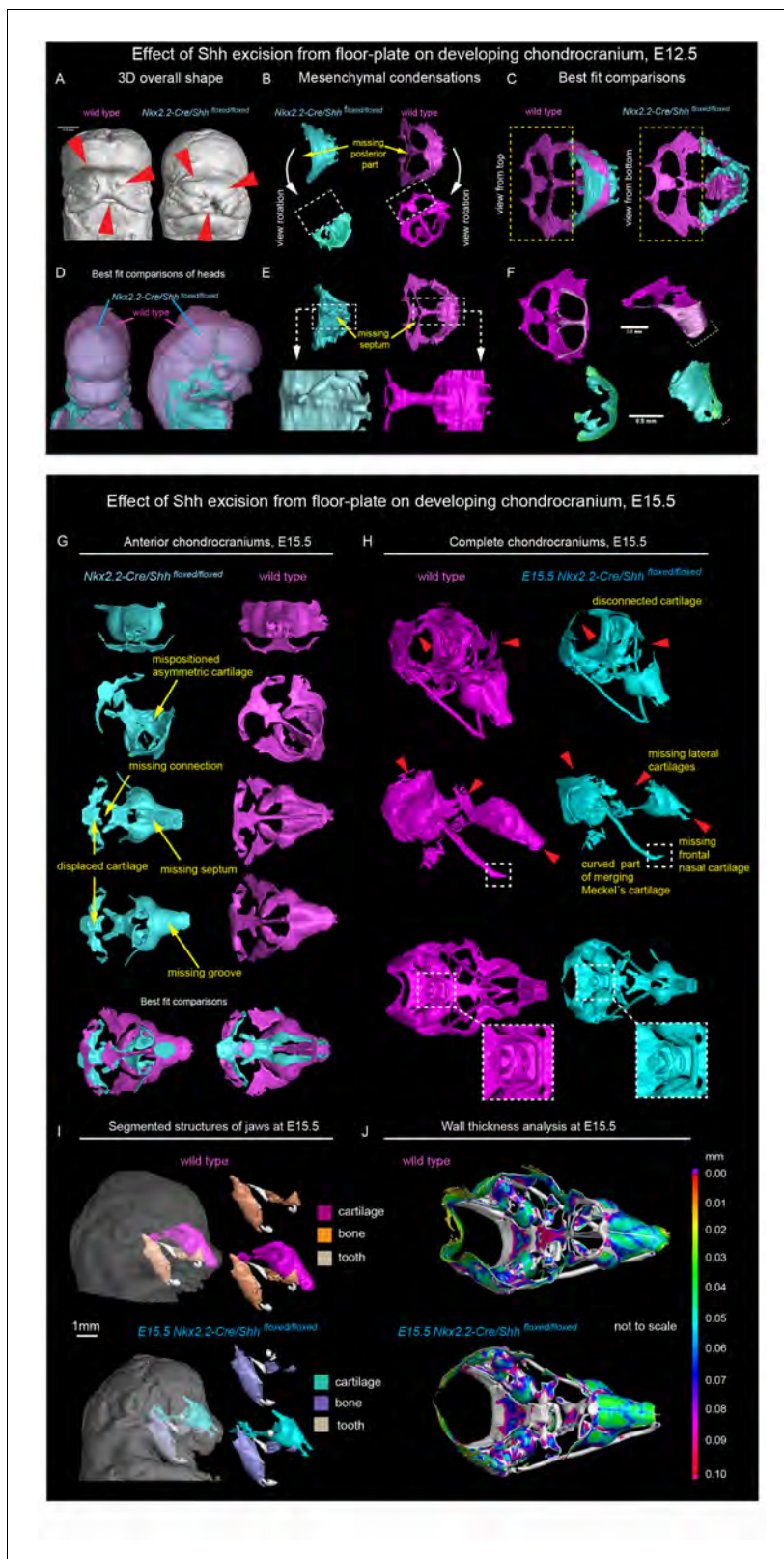


**Figure 3.** *Shh* signal from the brain induces a posterior part of a nasal capsule. (A) Model of overall shape resulting from the excision of *Shh* from the floor plate using *Nkx2.2-Cre/Shh<sup>flxed/flxed</sup>* shows visible phenotype in the E12.5 mutant embryo comprising, for instance, from the cleft of upper lip, non-prominent or missing nasal vestibule and diminished curvature of the snout. (B–C, E–F) micro-CT scans-based 3D reconstructions of chondrogenic mesenchymal condensations in E12.5 mutant and control embryos. Note the missing posterior part of the developing nasal capsule and the missing Figure 3 continued on next page

Figure 3 continued

septum in the mutant. (D) best-fit computed comparison of the overall shape and size of mutant and control embryo. (G–H) 3D models of chondrocrania of mutant ( $Nkx2.2-Cre/Shh^{floxed/floxed}$ ) and control embryo, analyzed at E15.5. Among the main differences are missing frontal part of nasal cartilage, missing lateral parts of developing nasal capsule, malpositioned asymmetric cartilage, not fully closed foramina for pervading nerves and vasculature and various disconnected cartilaginous segments. (I) Segmented cartilage and bones projected in the overall shape of the head of mutant (bottom) and control (upper) embryo. Note the malpositioned incisors in the maxilla of the mutant and missing part of the frontal nasal capsule formed by the bone. (J) Wall thickness analysis of the cartilages in the E15.5 head of mutant (bottom) and control (upper) embryo show no evident differences in the thickness of formed cartilage.

DOI: <https://doi.org/10.7554/eLife.34465.007>

The following figure supplements are available for figure 3:

**Figure supplement 1.** 'Interactive PDF'.

DOI: <https://doi.org/10.7554/eLife.34465.008>

**Figure supplement 2.** Ablation of *Shh* from the floor plate results in the cleft palate.

DOI: <https://doi.org/10.7554/eLife.34465.009>

**Figure supplement 3.** Brain volume and overall anatomy in mutants with *Shh* genetically deleted from the floor plate of the developing CNS.

DOI: <https://doi.org/10.7554/eLife.34465.010>

**Figure supplement 4.** Phenotypic manifestation of *Shh* genetic ablation from the floor-plate, analyzed at E15.5 upper part of spine.

DOI: <https://doi.org/10.7554/eLife.34465.011>

Finally, we analyzed the spinal column of the mutants and control embryos and found localized shape defects in the cervical vertebrae represented by incomplete transverse foramina (*foramina transversariae*) (Figure 3—figure supplement 4). Notably, the defects in the nasal septum stayed confined only to the cartilage as a tissue. The septal chondrogenic condensations and cartilage were missing as apparent E12.5 and E15.5, whereas the soft tissues of the septum stayed in place (Figure 3—figure supplement 4). Similarly, despite the cartilage defects clearly identified in spinal column, the other tissue types that were in close proximity to the defects did not show any difference from control. For instance, the vertebral arteries traversing the distorted cartilage of the transverse foramina appeared unaffected in  $Nkx2.2-Cre/Shh^{floxed/floxed}$  animals (Figure 3—figure supplement 4).

Next, we determined the *Shh* expression in the forming olfactory epithelium and tested the role of the forming olfactory epithelium and olfactory neurons in the process of nasal capsule induction. The possibility that olfactory epithelium controls cartilage shaping is supported by the fact that the conchae of nasal labyrinth geometrically correlate with the folded structure of the olfactory epithelium, which they mechanically support.

A desired experimental setup that would allow us to target and genetically delete *Shh* from the olfactory epithelium does not exist. To define the importance of any signal derived from the olfactory epithelium we utilized *Six1* and *Six4* double knockout to specifically ablate the development of the olfactory epithelium (Ikeda et al., 2007; Kobayashi et al., 2007). We analyzed *Six1/4* double mutant embryos at E18.5, that showed no olfactory structures, using the micro-CT method and performed a thorough comparison to wildtype littermates (Figure 4 and Figure 3—figure supplement 1 'Interactive PDF'). In these mutants which had markedly shortened noses, the roof of the nasal capsule was entirely missing. However, the septum and the posterior part of the capsule were relatively well-preserved (Figure 4B–D). An earlier analysis at E12.5, a stage when the majority of facial chondrogenic condensations come into place, showed that in double knockouts, the chondrogenic condensation corresponding to the nasal capsule roof is missing. The chondrogenic condensation corresponding to the nasal septum appeared non-fused at this stage and fused only later, as evident from E17.5 reconstructions. At the same time, the roof of the nasal capsule was never induced (Figure 4—figure supplement 1A–D). This is consistent with the prediction that a lack of the olfactory epithelium will prevent the induction of olfactory cartilages. Analyses of the bones showed a major change in the overall geometry, with prominent shortening along the anterior-posterior axis (brachycephalic-like appearance). Furthermore, we noticed a lack of mandibular incisors and an obvious asymmetry between left and right parts of the maxilla (Figure 4E,J).

In addition to the expression in olfactory placodes, *Six1* and *Six4* are expressed in different parts of early facial mesenchyme (Kobayashi et al., 2007; Grifone et al., 2005). The full knockout of *Six4* does not show any phenotype according to previously published data (Ozaki et al., 2001). We

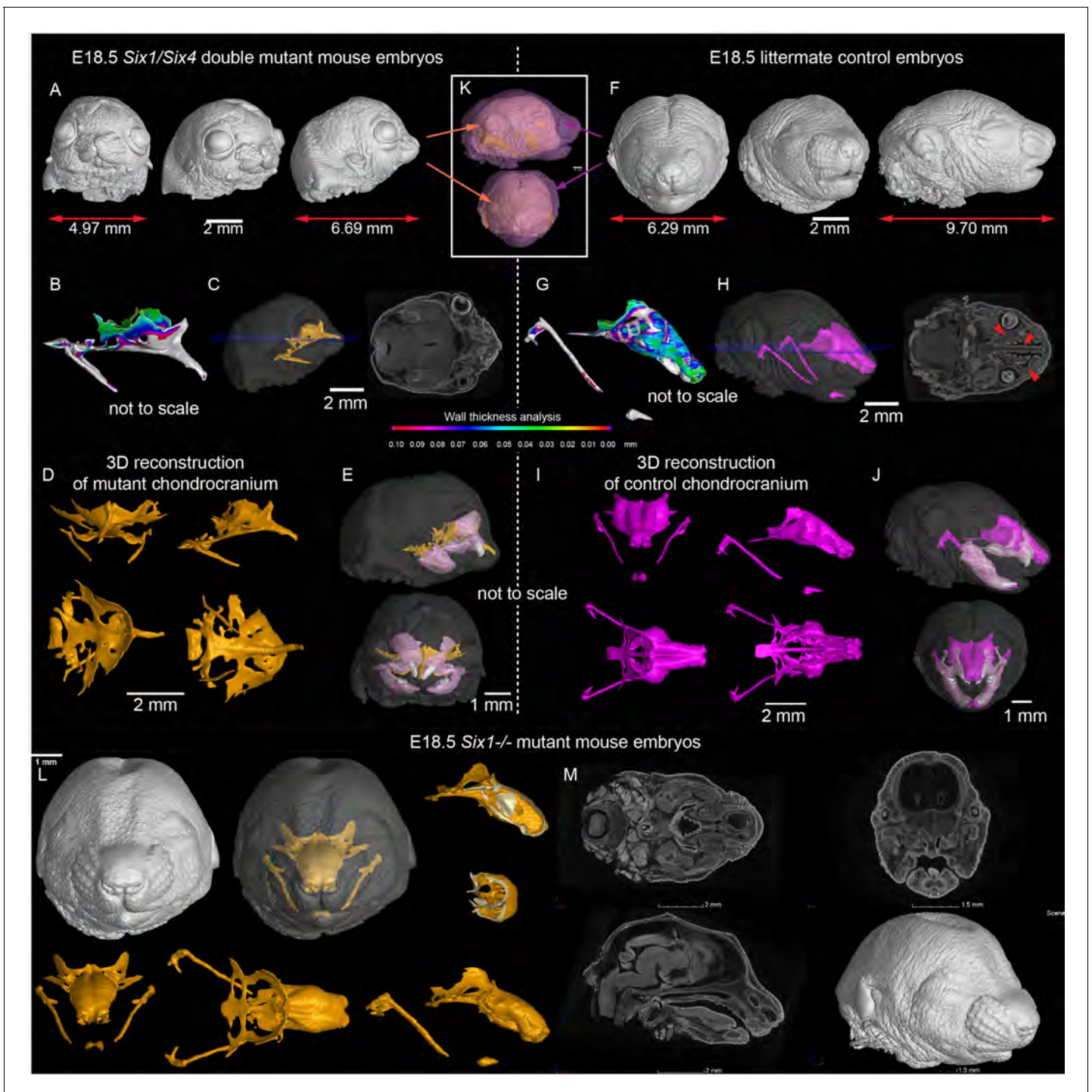


**Figure 4.** Signals from the olfactory epithelium induce the anterior part of the nasal capsule. (A–J) *Six1/Six4* double knock out mouse embryo compared to littermate control and analyzed at E18.5 using micro-CT and 3D-reconstruction. (A, E, K) overall shape and size of the mutant head is different from the control head, showing brachycephalic phenotype, bulging eyes, misshaped earlobes positioned more frontal and lower than the control embryo (F, J, K). Note also the left-right asymmetry of the snout of the mutant. (B, G) Wall thickness analysis of mutant (B) and control (G) embryo. (C, H) single plane from raw CT data shows missing olfactory neuroepithelium in the *Six1/Six4* double mutant and control. Note also missing nasal capsule but retained septum in the mutant. (D–E, I–J) various views on segmented 3D model of chondrocranium of mutant (D–E) and control (I–J) embryo. Among the obvious differences are missing roof and lateral parts of nasal capsule while the septum is preserved. (L) *Six1* single knock out mouse embryo analyzed at E18.5 using micro-CT 3D reconstruction (M) single plane cross-sections from raw CT of *Six1* single knock out E18.5 embryo. DOI: <https://doi.org/10.7554/eLife.34465.012>

Figure 4 continued on next page

Figure 4 continued

The following figure supplements are available for figure 4:

**Figure supplement 1.** Analysis of mesenchymal condensations in *Six1/Six4* double knock out embryos at E12.5.

DOI: <https://doi.org/10.7554/eLife.34465.013>

**Figure supplement 2.** *Ascl1* knockout embryo analyzed at E16.5 does not show any significant changes in formed nasal capsule.

DOI: <https://doi.org/10.7554/eLife.34465.014>

therefore analyzed the full knockout of *Six1*, in which the olfactory epithelium is present, to see whether it will show a mesenchyme-driven phenotype in the nasal capsule roof. The analysis of E18.5 *Six1*<sup>-/-</sup> embryos demonstrated the presence of the nasal capsule roof as well as a septum. The phenotype in *Six1*<sup>-/-</sup> embryos mostly included a narrowing of the posterior nasal capsule with mild septal defects (**Figure 4L–M** and **Figure 4—figure supplement 1E**).

This experiment provided a complementary, non-overlapping phenotype to the one with a nasal capsule resulting from the excision of *Shh* from the floor plate (*Nkx2.2-Cre/Shh*<sup>floxed/floxed</sup>). This suggests that solid cartilage elements in the forming face depend on joint activities of multiple regulatory zones (sources of SHH) during their induction and shaping.

To investigate if sensory neurons in the olfactory neuro-epithelium might be potential sources of SHH, we utilized *Ascl1* (*Mash1*) knock-out embryos (**Figure 4—figure supplement 2**). In these animals, major neurogenic transcriptional factor essential for olfactory neuron formation are missing, and very few olfactory sensory neurons are generated (**Guillemot et al., 1993; Cau et al., 1997**). We analyzed craniofacial structures in these mutants and found out that they did not demonstrate any gross abnormality despite their inability to develop large amounts of olfactory neurons. Hence, the sensory olfactory neurons are not critical cartilage-inducing sources, while the early olfactory epithelium, before the neurogenesis, is important for the formation of chondrogenic mesenchymal condensations.

To check if SHH from the brain and presumably from the olfactory epithelium acts directly on facial mesenchyme inducing chondrogenic differentiation or during cartilage growth, we analyzed embryos carrying a SHH-activity reporter *GBS-GFP* (**Balaskas et al., 2012**) at different developmental stages ranging from E9 to E14.5. The GFP signal was detectable as expected in the forming palate, brain, spinal cord and tissues that are known to receive SHH input. However, we did not observe *GBS-GFP* activity in the chondrogenic mesenchymal condensations from the earliest chondrogenic stages E11.5–E12.5 onwards (**Figure 5A**). Consistently with this, lineage tracing in *Gli1-CreERT2/R26Tomato* mice injected with tamoxifen at E11.5 and analyzed at E17.5 showed sporadic patches of traced chondrocytes in the facial cartilages (**Figure 5B**). If the injection of tamoxifen was performed at E12.5 or later, these sporadic patches of labeled chondrocytes disappeared; that is we observed only very rarely scattered chondrocytes in other locations (**Figure 5B–C**). Analysis of the rare individual clones of chondrocytes resulting from labeling at E11.5 in *Gli1-CreERT2/R26Confetti* demonstrated that mesenchymal cells turn into chondroprogenitors that divide several times to generate clonal clusters of mature chondrocytes (**Figure 5C–D**). At later stages of tamoxifen administration, this was not observed, which is consistent with analysis of *Gli1-LacZ* embryos at E12.5, where the X-gal staining was confined to whisker pads and other peripheral locations. In situ hybridization (RNAscope) for other components of the Hedgehog pathway (including *Ptch1*(mRNA), *Ptch2*(mRNA), *Gli1*(mRNA), *Gli2*(mRNA)) showed no enrichment within potential and actual chondrogenic areas (**Figure 5—figure supplement 1**). To functionally test if inhibition of SHH at chondrogenic stages will affect the development of facial cartilage, we administered SHH-inhibitor vismodegib (**LoRusso et al., 2011**) at either E11.5, E12.5, or E13.5 and analyzed the embryos at E15.5. In line with predictions from expression analysis and SHH-activity reporter, we did not find striking abnormalities in nasal and Meckel's cartilages from all treated and analyzed embryos (n = 4) (**Figure 6A**). At the same time, we observed the absence of palate and concomitant abnormalities in whiskers distributions in E11.5-to-E15.5 and E12.5-to-E15.5 stages of treatment, but not in E13.5-to-E15.5 stages. Indeed, in embryos treated between E11.5 and E12.5, the palatal shelves were severely reduced or missing (**Figure 6A–C**). This showed that SHH signaling in these embryos was inhibited to significant extents and also suggested that the action of SHH on patterning of the nasal capsule precedes the stage of chondrogenic condensations.

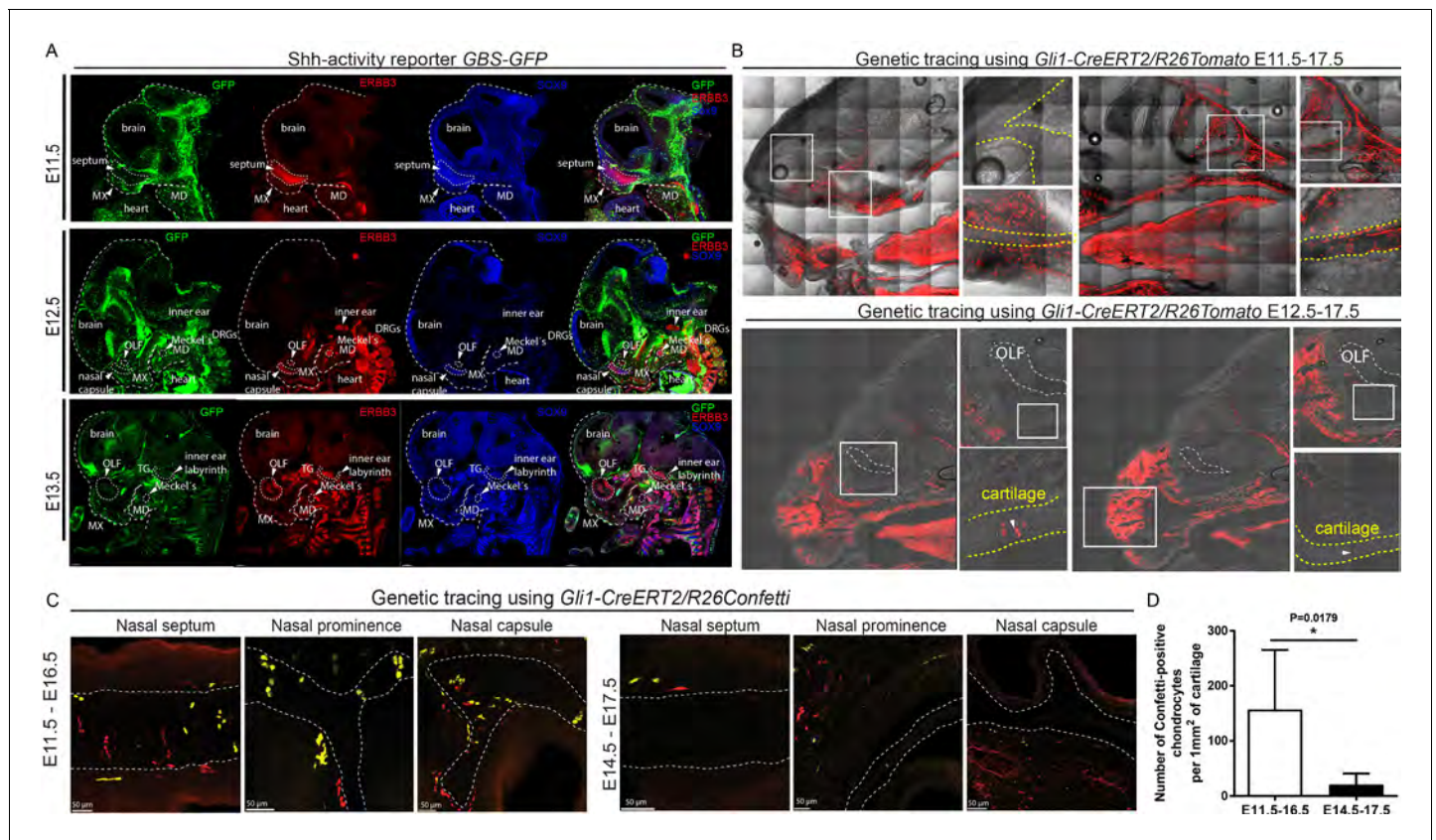


**Figure 5.** Mapping of the expression of *Gli1* and *Shh* signaling activity in mouse embryonic head. (A) Mapping of the activity of the SHH signaling in mouse embryonic head at E11.5, E12.5 and E13.5 prechondrogenic and early chondrogenic stages using *GBS-GFP* activity reporter. (B) Genetic tracing using *Gli1-CreERT2/R26Tomato* induced at E11.5 (upper panel) and E12.5 (bottom panel) and analyzed at E17.5. Dotted line outlines cartilaginous structures within the nasal capsule. White squares outline the magnified area. DRG = dorsal root ganglion, OLF = Olfactory system, MX = maxillary prominence, MD = mandibular prominence. TG = trigeminal ganglion. (C) Genetic tracing using *Gli1-CreERT2/R26Confetti*, induced at E11.5 and analyzed at E16.5 (left panel) and induced at E14.5 and analyzed at E17.5 (right panel) shows the contribution of *Gli1*-traced positive cells to the cartilaginous structures in the embryonic head. (D) Quantification of the contribution of *Gli1*-traced positive cells to the cartilage. (A–C) 20  $\mu$ m cryosections were used for the IHC staining and analysis. A confocal microscope has been used for imaging.

DOI: <https://doi.org/10.7554/eLife.34465.015>

The following figure supplement is available for figure 5:

**Figure supplement 1.** Mapping of the presence of major SHH signaling components in the E12.5 embryo.

DOI: <https://doi.org/10.7554/eLife.34465.016>

Consistent with these results, which suggest an early pre-chondrogenic role of SHH signaling on nasal capsule patterning, the analysis of embryos homozygous for a hypomorphic *Shh* allele (*Shh-GFP*, here referred to as *Shh<sup>HyPo</sup>*), in which SHH signaling is constitutively reduced (Zagorski et al., 2017; Chamberlain et al., 2008), revealed severe abnormalities in the facial cartilage (Figure 6D and Figure 6—figure supplement 3). The results of all genetic perturbations and treatments with drugs as well as their comparative phenotypes are summarized in Figure 7. Taken together, the effects of SHH on chondrogenic differentiation in the facial region are early and precede the first wave of chondrocyte differentiation that occurs between E11.5 and E14.5. These results are also consistent with the phenotype of *Six1/Six4* double knockout embryos at E12.5 (Figure 4), and corroborate the notion of an early pre-cartilage onset of the phenotype.

Tissue-specific expression of *Shh* is known to be controlled by multiple enhancers. Some, which may regulate *Shh* expression in the cranial region, have been characterized (Yao et al., 2016; Jeong et al., 2006; Sagai et al., 2009). To modulate *Shh* expression in different craniofacial regions, we analyzed mutant mice carrying different rearrangements (deletions or inversions) with impacts on the distal regulatory landscape of *Shh* (Symmons et al., 2016). We paid specific attention to

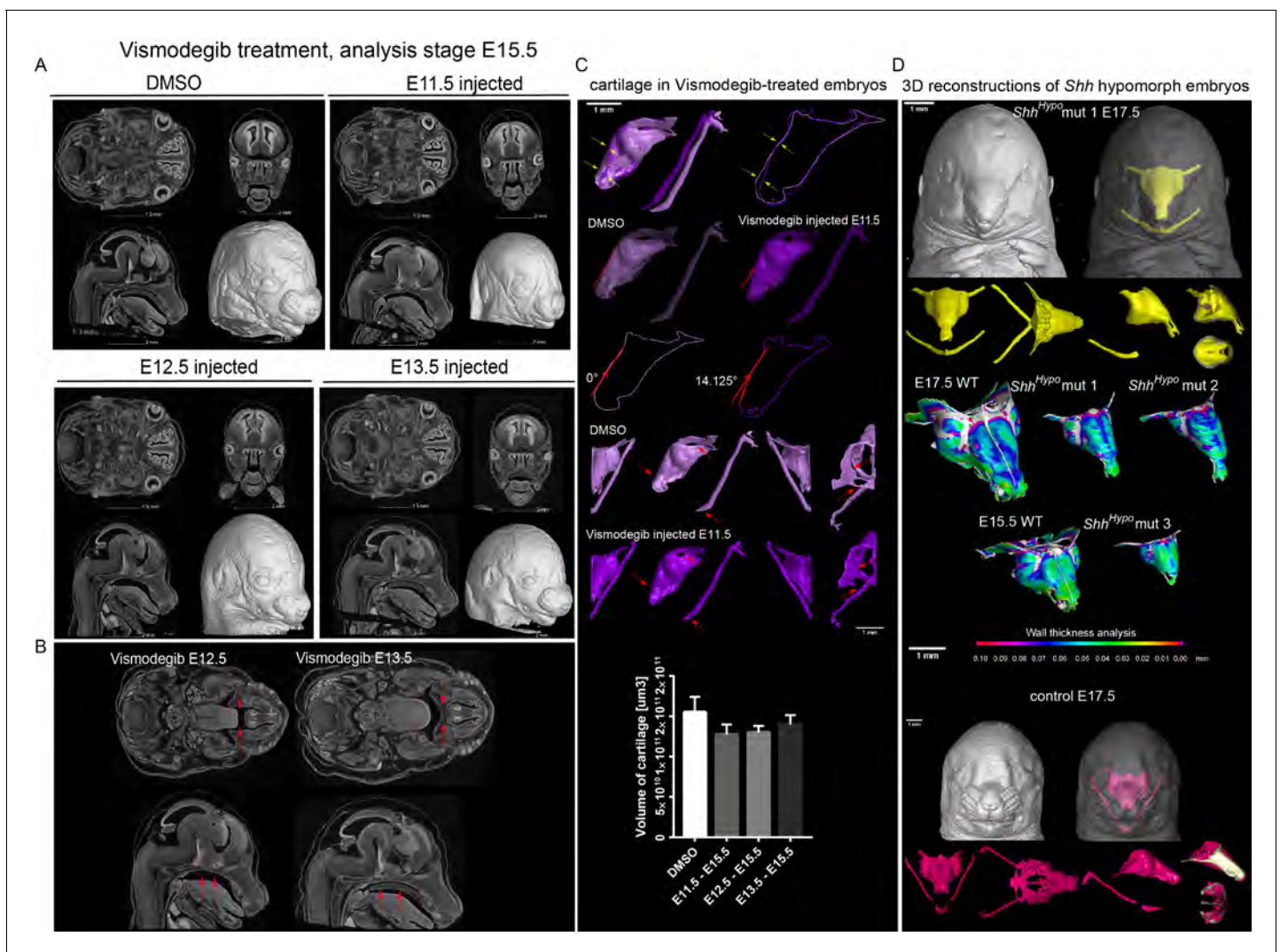


**Figure 6.** Effect of Vismodegib treatment on the size and structure of nasal cartilage. (A) Panel shows raw CT data, cross-sections from various planes from DMSO (control treatment), Vismodegib inhibitor administered at E11.5, E12.5 or E13.5, all analyzed at E15.5 (B) Raw CT cross-sections show absent/disrupted cartilaginous structures in Vismodegib-treated embryos (C) 3D reconstruction and comparison of inhibitor-treated (Vismodegib E11.5-E15.5) and control (DMSO-treated) embryos and their nasal capsules. Arrows point at differences in anatomy and overall geometry of the nasal capsule. Graph representation of overall cartilage change of inhibitor-treated embryos. Raw data are available in **Figure 6—source data 1**. (D) 3D-reconstruction of the nasal capsule of *Shh* hypomorph (analyzed at E15.5 and E17.5) including wall thickness analysis.

DOI: <https://doi.org/10.7554/eLife.34465.017>

The following source data and figure supplements are available for figure 6:

**Source data 1.** Raw values of cartilage measurements corresponding to Graph in **Figure 6C**.

DOI: <https://doi.org/10.7554/eLife.34465.021>

**Figure supplement 1.** Mutations of various regulatory regions controlling expression of *Shh*, their positions and effect on chondrogenesis.

DOI: <https://doi.org/10.7554/eLife.34465.018>

**Figure supplement 2.** Mutated genomic regions containing regulatory sequences controlling expression of *Shh* show a variety of similar and dissimilar phenotypes.

DOI: <https://doi.org/10.7554/eLife.34465.019>

**Figure supplement 3.** The effect of reduced SHH signaling on chondrogenesis at E15.5 and E17.5.

DOI: <https://doi.org/10.7554/eLife.34465.020>

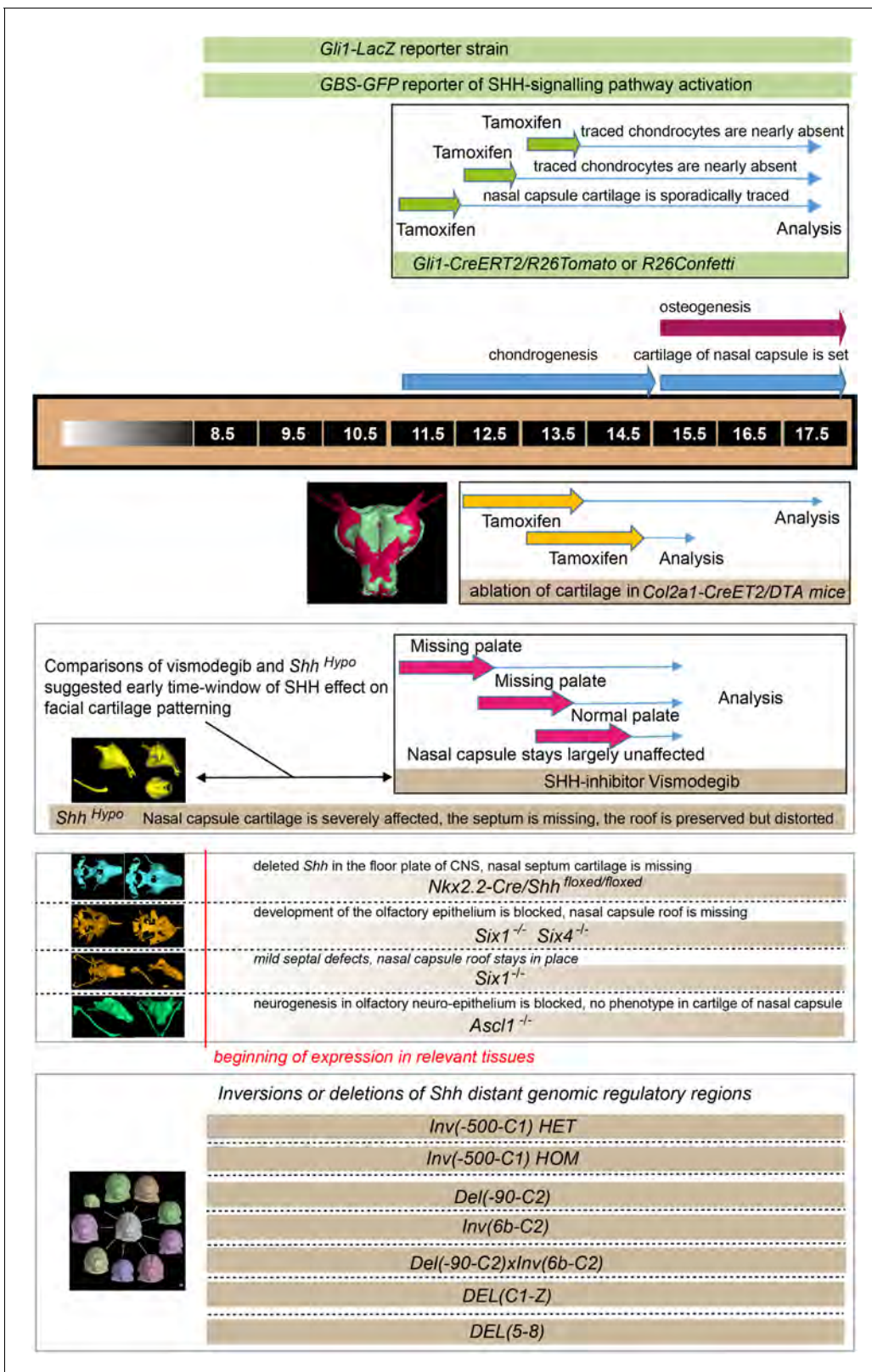


**Figure 7.** Illustration depicting the timeline of all experiments and the beginning of effects. The results of all genetic perturbations and treatments with drugs as well as their comparative phenotypes are summarized.

DOI: <https://doi.org/10.7554/eLife.34465.022>

genomic regions where known and potentially unknown brain-specific enhancers (SBE, Shh Brain Enhancers) are located (Jeong et al., 2006; Sagai et al., 2009). Currently known SBEs (SBE2, SBE3, SBE4) localize between the *Shh* coding region and *mark 6b* (Irimia et al., 2012) (see scheme in **Figure 6—figure supplement 1**). Animals carrying an allele with the inversion of a large genomic region including known SBEs, *INV(-500 C1)*, demonstrated selectively localized mild defects in the nasal septum and also in the tips of Meckel's cartilage, but not in the roof of nasal capsule. This septum-specific phenotype appeared more pronounced in a homozygous *INV(-500 C1)* as compared to the heterozygous genotype. Interestingly, this allele does not change the relative position to *Shh* of most known enhancers that could be responsible for SHH-dependent facial skeletal development. The phenotype observed in this experiment showed that septal cartilage is sensitive to minor changes in SHH patterning signals that result from either removal of regulatory sequences distal to the C1 position, or indirect effects affecting distant enhancer-promoter-communications.

*INV(6b-C2)*, which removes additional enhancers required for ventral forebrain expression of *Shh* in E10.5 embryos (**Figure 6—figure supplement 1A–C**), showed much stronger phenotypes.

Such strong phenotypes are most likely due to disruption of the *Shh* TAD (Topologically Associating Domain), and displacement of major regulatory elements at a position which prevent their interaction with *Shh* (Symmons et al., 2016). Accordingly, *Shh* expression is much reduced in the forebrain of mutant embryos at E10.5 as evident from the results of in situ hybridization for *Shh* (**Figure 6—figure supplement 1A–C**).

Heterozygote *INV(6b-C2)* did cause minor defects in septum, while the same inversion over a full *Shh* deficiency (*DEL(-90 C2)*) led to a strong holoprosencephaly similar to *Shh*<sup>Hyp<sup>o</sup></sup> (**Figure 6 and Figure 6—figure supplement 2**). However, it was not as strong as a full *Shh* knockout, where only a proscis is left.

In the mutants *INV(6b-C2) x DEL(-90 C2)*, the nasal septum did not develop at all, and the rest of the nasal capsule (roof) was present although severely disturbed in shape. The gradual increase in severity of the malformations from *INV(-500 C1)* to *INV(6b-C2)* may indicate the presence of several distinct enhancers related to face morphology distal to position 6b (which likely includes yet uncharacterized enhancers). It could also mean that the efficiency of the interactions of the known enhancers (SBE2-4) with the *Shh* promoter is modulated by the presence of distal elements, which may contribute to organize the *Shh* TAD (Symmons et al., 2016). Both scenarios suggest the existence of other regulatory regions important for facial development including new potential SBEs based on the reduction of the LacZ-based *Shh*-expression reporter signal in the forebrain of mutant embryos at E10.5 (**Figure 6—figure supplement 1**).

*DEL(5-8)* showed a powerful phenotype similar to the homozygous *INV(6b-C2)*. This, in a combination with previous phenotypes, reveals that the key regulatory regions essential for the facial cartilage patterning are located between marks 6b and C1. These regulatory regions are likely SBEs since the LacZ expression disappears from the forebrain of reporter embryos at E12.5 according to previous results (Symmons et al., 2016). *DEL(C1-Z)* did not show any gross abnormalities in the nasal capsule cartilage. Embryos carrying this mutation showed abnormal Meckel's cartilage and a generally affected mandible.

Taken together, local tuning of SHH expression by various enhancers (including brain-specific regulatory elements) seemingly controls discrete steps of chondrocranial patterning, which may represent a key evolutionary mechanism shaping animal snouts and faces.

## Discussion

In addition to the obvious functional aspects, facial shape is important in many ways. For example, recognition of individual facial features assists social interaction and affects numerous important aspects of our everyday life (Vernon et al., 2014). Pathological conditions include a very wide spectrum of deficiencies, and may involve eating, breathing and speech impairments, emotional problems and low quality of life in general (Forbes, 2010). Here, we demonstrated that even fine and selective manipulations of a facial cartilage geometry and size (performed in *Col2-CreERT2<sup>+/-</sup>/R26DTA<sup>+</sup>* embryos) result in significant changes of adjacent membranous bones and facial shape. In turn, the facial cartilage geometry is controlled by the signals coming from neurosensory structures such as brain and olfactory epithelium. Altogether, these results might provide a new explanatory

framework revealing how the integrated development of neural and non-neural tissues results in the precise and evolutionary adapted shape of the bony cranium and corresponding facial appearance.

Previously, Marcucio and Hallgrímsson laboratories demonstrated the co-variation of brain and face as well as the impact of brain-emitted SHH on avian facial development (*Hu and Marcucio, 2009; Marcucio et al., 2011; Parsons et al., 2011; Petryk et al., 2015*). Yet, the role of such brain-derived signals in cartilage and bone shaping has not been extensively investigated. According to our results, SHH, a key signal enabling cartilage induction, arrives from the floorplate of the brain, and the selective ablation of *Shh* in that area by non-inducible *Nkx2.2-Cre* causes a highly selective loss of the nasal septum cartilage. The soft non-cartilaginous tissue of the nasal septum, however, remains intact, rendering this part of the phenotype highly cartilage-specific. The roof of the nasal capsule stays nearly unaffected. The analysis at E12.5 stage suggested that this phenotype must be related to pre-chondrogenic, early SHH-dependent patterning signals enabling cartilage formation.

This reasoning is further supported by the line of experiments involving 'early on action' *Shh<sup>HypO</sup>* embryos, which demonstrated a profound phenotype in the nasal capsule cartilage. This was in contrast to wild type embryos treated with the SHH-inhibitor Vismodegib strictly between chondrogenic stages (E11.5-E13.5). These embryos showed no significant phenotype in the nasal capsule cartilage. Correspondingly, lineage tracing with *Gli1-CreERT2* and expression analysis of SHH pathway members starting from E11.5 did not show any association with development of facial cartilages.

These cartilage-related results, where SHH-activity was not associated with facial chondrogenic differentiation, were dramatically different from those observed in palate-forming mesenchymal cells in the same experimental embryos. Unlike cartilage, the developing palate showed strong activity of the SHH-signaling reporter *GBS-GFP*. We also found high expression levels of SHH pathway members, including numerous traced progeny in *Gli1-CreERT2/R26Tomato* animals. As expected, in embryos treated with Vismodegib between E11.5-E12.5, the palate was almost missing, in contrast to contrary to the nasal capsule cartilage that stayed virtually intact. The presence of abnormal palate clefts in Vismodegib-treated and also in *Nkx2.2-Cre/Shh<sup>floxex/floxex</sup>* embryos agrees with previous findings, which have established a general role of SHH in the patterning of the face and in development of pathological midfacial clefts (*Hu and Helms, 1999*). Accordingly, ciliopathies and their animal models often demonstrate similar defects (*Brugmann et al., 2010; Chang et al., 2016*).

Thus, according to our results, SHH is not involved into facial chondrogenesis at stages when chondrogenic condensations form and convert into mature cartilage. Hence, the role of SHH is most likely indirect. Presumably, it is involved in the early patterning of facial ectomesenchyme, to create proper conditions for the sophisticated facial chondrogenesis that will start at later developmental stages. In line with this reasoning, the mode of action of SHH on chondrogenesis in non-facial locations, for example, during the development of axial skeleton, is indirect and based on SHH-dependent alterations of cell responses to BMPs in potentially pre-chondrogenic mesenchymal cells. Murtaugh et al. demonstrated that even a transient SHH signal was able to ensure the competent chondrogenic response of mesenchymal cells to BMPs (*Murtaugh et al., 1999*). In the case of the axial skeleton, such competence-changing action of SHH depends on the initiated and sustained expression of the transcriptional repressor *Nkx3.2*, which renders cells responsive to pro-chondrogenic actions of BMPs (*Murtaugh et al., 2001*). As shown by Zeng et al., expression of *Nkx3.2* is sufficient to induce SOX9, a major chondrogenic master regulator, and in the presence of BMPs, *NKX3.2* and SOX9 could induce the expression of each other (*Zeng et al., 2002*). Finally, the sequential action of SHH and BMPs could induce SOX9. According to the public in situ database Allen Developmental Mouse Brain Atlas (<http://developingmouse.brain-map.org>), *Nkx3.2* shows distinct expression in a range of cranial cartilages or their future locations at pre-chondrogenic (E11.5) and chondrogenic (E13.5) stages. The knockout of *Nkx3.1* and *Nkx3.2* yields changes in the facial shape, as evident from **Figure 1** in Herbrand et al. (*Herbrand et al., 2002*). Similar patterning effects of SHH in relation to chondrogenesis have previously been demonstrated during the development of serial tracheal rings reinforced with cartilage. SHH inactivation in ventral trachea resulted in a lack of tracheal segmentation which coincided with the loss of cartilage, while the upregulation of *Shh* resulted in cartilage overproduction and similar segmentation defects (*Sala et al., 2011*). Altogether, this may suggest an analogous or similar mechanism of an indirect action of SHH on craniofacial chondrogenesis, especially in light of our results showing only minor and sporadic activity of SHH-signaling reporter in facial chondrogenic condensations or cartilage. Determination of the mechanisms behind SHH action in facial chondrogenesis, with a special focus on the position of the SHH-

signal in the hierarchy of events leading to chondrogenic differentiation, is a key future direction. We anticipate that Single cell transcriptomics approaches (*Picelli et al., 2013*) will be applied to facial mesenchymal populations prior and during chondrogenesis. This should resolve cell signaling cascades with high precision along the developmental timeline, in similarity to pioneering studies utilizing this methodology in other tissue types (*Furlan et al., 2017*).

Complementary to the ablation of *Shh* by *Nkx2.2-Cre*, the loss of the olfactory epithelium in *Six1/Six4* double knockout mutants leads to the absence of the nasal capsule roof, while the nasal septum cartilage stays largely in place. Our data indicate that the loss of a nasal capsule roof in the double knockout condition is driven by the loss of nasal placodes (requiring both *SIX1* and *SIX4*), which causes a collapse of olfactory epithelium. Despite the specific loss of nasal capsule roof, other cartilages appeared intact in locations corresponding to the expression sites of *Six1* and *Six4* (including Meckel's cartilage). The perfect match between the shape of cartilaginous olfactory turbines and the epithelium, as well as the coordinated time course of their development (*Kaucka et al., 2017*), additionally support the notion that signals from the developing olfactory epithelium might enable the induction of adjacent cartilage. Still, these arguments cannot completely rule out the possibility that co-expressed *Six1* and *Six4* may have early roles during neural crest migration and early post-neural crest stages that might be important for the nasal roof formation. Taken together, our results provide strong support for the idea that a single solid cartilaginous element such as the nasal capsule can be induced by the combinatorial action of signals derived from several, in the present case, neural and neurosensory, locations. Notably, facial chondrogenic condensations are induced being 'pre-shaped'. Already at the earliest steps, they are laid down as highly complex 3D-geometries (*Kaucka et al., 2017*). The induction of such 3D-shapes is unlikely to be achieved by signals from a single site and might require more sources including spatially opposed brain and olfactory structures. Since we were unable to validate that SHH from the olfactory placode or epithelium is the key factor that induces a nasal capsule roof, we cannot exclude that other signaling molecules participate during critical steps of facial cartilage induction. This will require further investigations.

During evolution of vertebrates, cartilages forming the neurocranium and the future upper jaw appear before Meckel's cartilage attains a function of a lower jaw skeleton, and the animals acquire articulated hinged jaws (*Shimeld and Donoghue, 2012*). Therefore, one of the primeval functions of the neurocranial and frontal cartilages could be the encasement and protection of the neural and sensory compartments such as brain, eyes, ears and olfactory neurons. If that is the case, it is logical to reason that these neurosensory structures could emit cartilage-inducing signals and coordinate cartilage growth and shaping. Our experimental results reveal the key role of SHH from the developing brain in enabling the induction of a nasal capsule and basicranial cartilages, and, thus, support the aforementioned evolutionary hypothesis. The capacity of the developing olfactory epithelium to shape the cartilaginous support also favors this reasoning. Genetics-based prevention of neuronal differentiation in the olfactory epithelium (via *Ascl1* knockout) does not interfere with shaping of the nasal capsule and confines the shaping role of presumably olfactory progenitors to the developmental period before their differentiation into the mature olfactory neurons. Alternatively, other cell types in the olfactory epithelium may play a cartilage-inducing role (olfactory glia, non-neurogenic epithelium).

In addition to the evolutionary aspect, the role of different neurosensory structures (mainly the brain) in coordinated cartilage induction may suggest a new connection between neurological and craniofacial symptoms in numerous genetic syndromes. Examples of such conditions are Williams syndrome, Down syndrome and others that are manifested by behavioral and morphological abnormalities in the central nervous system (*Starbuck et al., 2017; Weisman et al., 2017; Vincent et al., 2014; Antshel et al., 2008*) (and reviewed by [*Marcucio et al., 2011*]). Based on this reasoning, it is possible to envision a mechanistic connection between the fine aspects of a facial geometry and individual features of the human brain. An enormous facial variability is found among humans, which poses a question regarding the molecular and cellular mechanisms that underlie this variability. In difference to humans, non-human primates generally use variations in colored facial hairs to express their species, social status and sex in addition to body movements, voice expressions and scent (*Santana et al., 2012; Allen and Higham, 2015*). This brings us to speculate whether the loss of dense facial hairs during evolution of humans led to the development of a very broad range of various facial tissue-related features in order to compensate for the loss of facial hair-related communication and individual recognition. We hypothesize that one of those shape-tuning mechanisms could

include flexible and individual modulation of SHH, an important patterning and shaping agent during the embryonic development that comes from different spatial sources including the developing brain.

Previous research has established the existence and position of some of the specific regulatory elements that direct the expression of *Shh* in the craniofacial epithelial linings (*MRC51* and *MFCS4*, see (Sagai et al., 2009) for details) as well as in the floor plate and anterior forebrain (*SBE2* ((*Shh* Brain Enhancer 2)), *SBE3* and *SBE4* [Yao et al., 2016; Jeong et al., 2006]). In order to find out fine effects in facial cartilages as a result of activity by site-specific enhancers, we analyzed a variety of mutants with deleted and inverted genomic regions containing such regulatory elements (mutants created by François Spitz' laboratory [Symmons et al., 2016]). The inversion of the  $-500$  C1 genomic region including known CBEs showed localized defects within the nasal septum that incrementally increased from heterozygous to homozygous state without influencing nasal capsule roof shape. Similarly, the inversion of (*6b-C2*) region in a heterozygous state caused minor defects in septum, whereas the same inversion on the background of deletion of the entire regulatory region ( $-90$  C2) appeared similar to *Shh*<sup>HypO</sup> or even *Shh* knock out. This is explained by the translocation of TAD (see (Symmons et al., 2016) for details) and resulting 'isolation' of *Shh* coding part from head-specific regulatory regions located between positions six and C2. In this latter case (*INV(6b-C2)*), *Shh* expression was dramatically reduced in the anterior forebrain as compared to the control (Symmons et al., 2016).

Further analysis of more restricted *Shh* regulatory regions revealed that brain-specific and facial cartilage-related enhancers are confined within the region (5-8) and are at least partly responsible for the expression of *Shh* in the forebrain according to the loss of in situ hybridization signal in the forebrain of (*DEL(5-8)*) compared to controls. The deletion of this (*DEL(5-8)*) region resulted in severe facial malformation and collapse of the nasal capsule shape to the state resembling *Shh*<sup>HypO</sup>. Despite that we clearly observed the misshaped nasal capsule roof in these embryos, the septum was completely gone similarly to (*DEL(-90 C2) x INV(6b-C2)*) mutants. Taken together, these results provide strong support to the discrete role of genomic regulatory regions directing the expression of *Shh* to the forebrain and, through this, affecting the patterning of septal, basicranial and other cartilages in the head.

Importantly, all analyzed embryos carrying mutated regulatory regions never demonstrated missing nasal capsule roof including severe (*DEL(-90 C2) x INV(6b-C2)*), (*DEL(5-8) HOMO*) and *Shh*<sup>HypO</sup>. This might mean that we still do not know about the position of the corresponding regulatory regions targeting the expression of *Shh* to the olfactory epithelium or FEZ in the frontal face. The loss or inversion of regulatory regions resulting in mild septal defects did not affect the anterior nasal capsule, which might be independently patterned by FEZ. Similarly, the morphology of the anterior nasal capsule stayed relatively stable when septal cartilage disappeared in *Nkx2.2-Cre/Shh<sup>floxex/floxex</sup>* animals. This suggests that the most anterior face including frontal facial cartilages might be indeed patterned by FEZ together with olfactory placodes independently from brain-derived signals. These results point towards the possibility that mouse FEZ can form and act independently of the CNS signaling center contrary to chick embryonic development (Hu and Marcucio, 2009).

To summarize, it is possible that enhancer-dependent spatial and temporal regulations of *Shh* expression could be evolutionary tools to achieve the impressive variety of facial cartilage shapes in humans - a basis for facial individuality. Indeed, much attention has been focused on the role of enhancers in craniofacial evolution. Recently, by applying a combination of morphometry, molecular biology and mouse genetics, Attanasio et al. described numerous enhancers that are differentially active and take part in the development of a facial shape (Attanasio et al., 2013). In line with this, mutations in the enhancers that control the expression of *Fgf8*, another cartilage-inducing factor (Abzhanov and Tabin, 2004), also result in geometrical abnormalities of the nasal capsule (Marinić et al., 2013). It seems that many genes and pathways are involved in shaping the face (Young et al., 2014; Hu et al., 2015a; Foppiano et al., 2007; Hu et al., 2015b). This is not surprising, since the facial shaping includes many stages that are pre-chondrogenic, chondrogenic (including induction, growth, remodeling of the cartilage) and osteogenic. Processes of isotropic and anisotropic growth of the skeletal structures also play important roles in achieving the final geometry of the facial region (Kaucka et al., 2017). Despite such complexity and the enormous degree of spatio-temporal integration, the initial induction of cartilage guided by the brain and olfactory epithelium represents a key moment of facial skeleton formation. It may well also be an evolutionary

substrate driving the diversity of faces and snouts. Consequently, the fine-tuning of patterning and cartilage-inducing signals in neurosensory structures deserves further attention, including explorations of the diversity of corresponding genetic regulatory regions in human and animal genomes.

## Materials and methods

### Key resources table

Reagent type species or resource	Designation	Source or reference	Identifiers	Additional information
Strain	<i>Col2a1-CreERT2</i>	<b>Nakamura et al. (2006)</b>		Received from S. Mackem
Strain	<i>R26Confetti</i>	<a href="https://www.jax.org/strain/013731">https://www.jax.org/strain/013731</a>		Received from H. Clevers
Strain	<i>R26DTA</i>	<b>Voehringer et al. (2008)</b>		Received from Jackson
Strain	<i>Six1 KO</i>	<b>Grifone et al. (2005)</b>		Received from P. Maire
Strain	<i>Six1/4 double KO</i>	<b>Grifone et al. (2005)</b>		Received from P. Maire
Strain	<i>Nkx2.2-Cre/Shhflx/flx</i>	<b>Yu et al., 2013</b>		Received from M. Matisse
Strain	<i>Ascl1 (Mash1)</i>	<b>Cau et al. (1997)</b>		Received from U. Marklund
Strain	<i>B6.Cg-Shhtm1EGFP/creCjt/J</i>	<b>Harfe et al. (2004)</b>		Received from M. Hovorakova
Strain	<i>Gli1-CreERT2</i>	<a href="https://www.jax.org/strain/007913">https://www.jax.org/strain/007913</a>		Received from M.Kasper
Strain	<i>Gli1-lacZ</i>	<a href="https://www.jax.org/strain/008211">https://www.jax.org/strain/008211</a>		Received from M.Kasper
Strain	<i>Shh-GFP</i>	<a href="https://www.jax.org/strain/008466">https://www.jax.org/strain/008466</a> ( <b>Chamberlain et al., 2008</b> )		Received from Jackson
Strain	<i>TgGBS-GFP</i>	<b>Balaskas et al. (2012)</b>		Received from A. Kicheva
Strain	<i>Rosa-CAG-LSL-tdTomato-WPRE</i>	<a href="https://www.jax.org/strain/007914">https://www.jax.org/strain/007914</a>		Received from M. Kasper
Strain	<i>INV-500-C1</i>	F. Spitz ( <b>Symmons et al., 2016</b> )		Received from F. Spitz
Strain	<i>INV6b-C2</i>	F. Spitz ( <b>Symmons et al., 2016</b> )		Received from F. Spitz
Strain	<i>Del-90-C2</i>	F. Spitz ( <b>Symmons et al., 2016</b> )		Received from F. Spitz
Strain	<i>DEL1-Z</i>	F. Spitz ( <b>Symmons et al., 2016</b> )		Received from F. Spitz
Strain	<i>DEL5-8</i>	F. Spitz ( <b>Symmons et al., 2016</b> )		Received from F. Spitz
Antibody	SOX9	Sigma Aldrich, HPA001758		one to 1000 in PBS-T over night at RT
Antibody	ERBB3	RnD Systems, AF4518		one to 500 in PBS-T over night at RT
Drug	Vismodegib	<b>LoRusso et al. (2011)</b>		0.1 mg/kg
Software	IMARIS	<a href="http://www.bitplane.com/">http://www.bitplane.com/</a>		
Software	GOM Inspect	<a href="https://www.gom.com/de/3d-software/gom-inspect.html">https://www.gom.com/de/3d-software/gom-inspect.html</a>		
Software	VGStudio Max	<a href="https://www.volumegraphics.com/en/products/vgstudio-max.html">https://www.volumegraphics.com/en/products/vgstudio-max.html</a>		

Continued on next page

Continued

Reagent type species or resource	Designation	Source or reference	Identifiers	Additional information
RNAScope probes	Gli1 (311001), Gli2 (405771), Gli3 (445511), Smo (318411), Ptch1 (402811) and Ptch2 (435131)	<a href="https://acdbio.com/rnascope%C2%AE-technology-novel-rna-situ-hybridization-research-platform">https://acdbio.com/rnascope%C2%AE-technology-novel-rna-situ-hybridization-research-platform</a>		

## Mouse strains and animal information

All animal work were approved and permitted by the Local Ethical Committee on Animal Experiments (North Stockholm Animal Ethics Committee) and conducted according to The Swedish Animal Agency's Provisions and Guidelines for Animal Experimentation recommendations. Genetic tracing mouse strain *Nkx2.2-Cre* was described previously (Yu et al., 2013). *Col2a1-CreERT2* (Ozaki et al., 2001) (obtained from the laboratory of S. Mackem, NIH) strains (Nakamura et al., 2006) were coupled to *R26Confetti* mice that were received from the laboratory of Professor H. Clevers (Snippert et al., 2010). *DTA* strain (Voehringer et al., 2008) (*B6.129P2-Gt(ROSA)26Sortm1(DTA)Lky/J*, The Jackson Laboratory) was coupled to *Col2a1-CreERT2*. *Six1* and *Six1/4* double KO embryos were generated as described already (Grifone et al., 2005; Laclef et al., 2003). *Nkx2.2-Cre/Shh<sup>flx/flx</sup>* embryos were received from the laboratory of Michael Matisse. *Ascl1* (*Mash1*) KO embryos were received from the laboratory of Ulrika Marklund. *B6.Cg-Shhtm1(EGFP/cre)Cjt/J* (Harfe et al., 2004) embryos were received from the laboratory of Maria Hovorakova (CAS). *Gli1-CreERT2* and *Gli1-lacZ* strains were obtained from the laboratory of Maria Kasper (Karolinska Institutet). *Gli1-CreERT2* was coupled with *R26Confetti* and *R26Tomato*.

The following strains were previously described: *Tg(GBS-GFP)* (Balaskas et al., 2012), *Shh-GFP* (JAX stock #008466 (Chamberlain et al., 2008)). *Shh<sup>Hypo</sup>* embryos are homozygous for *Shh-GFP* and their morphological phenotypes are not affected by the presence or absence of the *Tg(GBS-GFP)* transgene. Strains were bred and maintained on 129/Sv background, in accordance with license BMWFW-66.018/0006-WF/V/3b/2016 granted by the Austrian BMWFW.

*Gli1-LacZ* (<https://www.jax.org/strain/008211>), *Gli1-CreERT2* (<https://www.jax.org/strain/007913>) and *Rosa-CAG-LSL-tdTomato-WPRE* (<https://www.jax.org/strain/007914>) were used under the ethical permit: number S40/13, granted by South Stockholm Animal Ethics Committee.

Mice of the relevant genotype were mated overnight, and noon of the day of the plug was considered as E0.5. To induce genetic recombination of adequate efficiency, pregnant females of relevant couplings were injected intraperitoneally with tamoxifen (Sigma T5648) dissolved in corn oil (Sigma C8267). Tamoxifen concentration ranged from 1.5 to 5.0 mg per animal to obtain a range of recombination efficiency. Mice were sacrificed with isoflurane (Baxter KDG9623) overdose or cervical dislocation, and embryos were dissected out and collected into ice-cold PBS. Subsequently, the samples were placed into freshly prepared 4% paraformaldehyde (PFA) and depending on the developmental stage and the application they were fixed for 3–24 hr at 4°C on a roller. Subsequently, for the purpose of microscopy analysis, the embryos were cryopreserved in 30% sucrose (VWR C27480) overnight at 4°C, embedded in OCT media (HistoLab 45830) and cut into 18 µm to 30 µm sections on a cryostat (Microm). Embryos designated for CT analysis were then stained according to the protocol described beneath.

## Inhibition of hedgehog signaling

In order to inhibit SHH during embryonic development (stages E11.5 to E13.5), the pharmacological inhibitor Vismodegib (LoRusso et al., 2011) was injected intraperitoneally at a dosage of 0.1 mg per g of bodyweight of the pregnant mouse. Embryos were collected at E15.5 and fixed in 4% formaldehyde in PBS solution for 24 hr at +4°C with slow rotation.

## Histological staining

Slides were stained for mineral deposition using von Kossa calcium staining: 5% silver nitrate solution was added to the sections at a room temperature and exposed to strong light for 30 min. After that the silver nitrate solution was removed, and slides were washed with distilled water for 3 times during 2 min. 2.5% sodium thiosulphate solution (w/v) was added to the sections and incubated for five

mins. Slides were again rinsed for 3 times during 2 min in distilled water. The sections were then counterstained using Alcian blue. Alcian blue solution (0.1% alcian blue 8GX (w/v) in 0.1 M HCl) was added to the tissue for 3 min at room temperature and then rinsed for 3 times during 2 min in distilled water. Slides were then transferred rapidly into incrementally increasing ethanol concentrations (20%, 40%, 80%, 100%) and incubated in 100% ethanol for 2 min. Finally, the slides were incubated in two xylene baths (for 2 min and then for 5 min) before mounting and analysis.

### Immunohistochemistry, histological staining and EdU analysis

Frozen samples were sectioned at 18–30  $\mu\text{m}$  depending on specific experiment. If needed, sections were stored at  $-20^{\circ}\text{C}$  after drying 1 hr at room temperature, or processed immediately after sectioning. Primary antibodies used were: chicken anti-GFP (Abcam, 1:500, ab13970), rabbit anti-SOX9 (Sigma Aldrich, 1:1000, HPA001758), sheep anti-ERBB3 (RnD Systems, 1:500, AF4518). For detection of above-mentioned primary antibodies, we utilized 405, 488, 555 or 647-conjugated Alexa secondary antibodies produced in donkey (Invitrogen, 1:1000). Slices were mounted with 87% glycerol mounting media (Merck).

### Fluorescent in situ hybridization (RNAscope)

E12.5 and E13.5 embryos were collected, embedded immediately in OCT and snap frozen on dry ice. Tissue blocks were stored at  $-20^{\circ}\text{C}$  until further use. 8- $\mu\text{m}$ -thick cryosections were collected on Superfrost Plus slides and stored at  $-20^{\circ}\text{C}$  until further use. Fluorescent in situ hybridization was performed for the genes *Gli1* (311001), *Gli2* (405771), *Gli3* (445511), *Smo* (318411), *Ptch1* (402811) and *Ptch2* (435131) using the RNAscope 2.0 Assay, reagents and probes according to manufacturer's instructions (Wang *et al.*, 2012). RNAscope probes were designed commercially by the manufacturer and are available from Advanced Cell Diagnostics, Inc. being protected by patent.

### X-gal staining

E11.5, E12.5 and E13.5 embryos were fixed in 4% formaldehyde in PBS solution for 2–3 hr at  $+4^{\circ}\text{C}$  with slow rotation. Following washes with PBS, embryos were incubated in X-gal staining solution (1 mg/ml X-gal; 2 mM  $\text{MgCl}_2$ ; 0.5 M potassium ferrocyanide; 0.5 M potassium ferricyanide in PBS) at  $37^{\circ}\text{C}$ , overnight, with gentle agitation. Samples were washed twice, 20 min each time at room temperature in PBS and imaged whole mount. When necessary, we proceeded to cryoprotection in 30% sucrose in PBS and embedding in OCT medium.

### Microscopy, volume rendering, image analysis and quantifications

Confocal microscopy was performed using Zeiss LSM880 Airyscan CLSM instruments. The settings for the imaging of Confetti fluorescent proteins were previously described (Snippert *et al.*, 2010). Image analysis has been performed using IMARIS Software (Bitplane, Zurich, Switzerland). Before performing manual segmentations of cartilages and mesenchymal chondrogenic condensations on all representative samples, we assessed the phenotype and the stability of the phenotype using analysis of multiple embryos (typically 3–5 per condition) on histological sections as well as whole-mount assessments of facial morphology and including usage of tomographic slices. In case the phenotype was stable, the representative embryos underwent 3D segmentation process, otherwise we manually segmented facial cartilage and bone from all experimental embryos (in case of *Col2a1-CreERT2/R26DTA* or *Shh<sup>Hypo</sup>*, please see Figure 1—figure supplement 1 and Figure 6—figure supplement 3). For embryonic day E17.5 *Col2a1-CreERT2/R26DTA*, we performed segmentations of the most affected embryo from the litter (Figure 1I–P and graph in R). Other litter mates were analyzed using cryo-sections only (Figure 1E–H). Since we did not investigate fine differences in shape of the nasal capsule and rather concentrated on missing structures (septum or nasal capsule roof), we did not analyze fine shape differences morphometrically in a quantitative way. In special cases, where relevant, we utilized shape fitting analysis using GOM Inspect tool. We did not use any special randomization or masking of embryos during experimental and control group allocations.

### Tissue contrasting for $\mu\text{-CT}$ scanning

Staining protocol has been adapted and modified from the original protocol developed by Brian Metscher laboratory (Metscher, 2009). After embryo dissection in ice-cold PBS, the samples were

fixed in 4% formaldehyde in PBS solution for 24 hr at +4°C with slow rotation. Subsequently, samples were dehydrated in incrementally increasing ethanol concentrations (30%, 50%, 70%), 1 day in each concentration to minimize the shrinkage of the tissue. Samples were transferred, depending on the embryonic stage, into 1.0–1.5% PTA (phospho-tungstic acid) in 90% methanol for tissue contrasting. The PTA-methanol solution was changed every 2–3 days. E12.5 embryos were stained for 7 days, E15.5 embryos for 3 weeks and E18.5 embryos for 7 weeks. The contrasting procedure was followed by rehydration of the samples by incubation in ethanol series (90%, 70%, 50% and 30%) and shipped to the CT-laboratory for scanning. There the rehydrated embryos were embedded in 0.5% agarose gel (A5304, Sigma-Aldrich) and placed in polypropylene conical tubes (0.5, 1.5 or 15 ml depending on the sample size to minimize the amount of medium surrounding it) and to avoid the movement artifacts during X-ray computer tomography scanning.

### **μ-CT analysis (micro computed tomography analysis) and 3D analysis**

The μ-CT analysis of the embryos was conducted using the laboratory system GE phoenix v|tome|x L 240 (GE Sensing and Inspection Technologies GmbH, Germany), equipped with a 180 kV/15W maximum power nanofocus X-ray tube and flat panel detector DXR250 with 2048 × 2048 pixel, 200 × 200 μm pixel size. The embryos were fixed in polyimide tubes by 1% agarose gel to prevent tomographic movement artifacts. The exposure time of the detector was 900 ms in every of 2000 positions. Three projections were acquired and averaged for reduction of the noise in μ-CT data. The utilized power of the tube was 11 W given by acceleration voltage of 60 kV and tube current of 200 μA. X-ray spectrum was filtered by 0.1 mm of aluminium plate. The voxel size of obtained volumes (depending on a size of an embryo head) appeared in the range of 5 μm - 7 μm. The tomographic reconstructions were performed using GE phoenix datos|x 2.0 3D computed tomography software (GE Sensing and Inspection Technologies GmbH, Germany). The cartilage in the embryo head was segmented by an operator with semi-automatic tools within Avizo - 3D image data processing software (FEI, USA). The 3D segmented region was transformed to a polygonal mesh as a STL file. The mesh of the embryo head was imported to VG Studio MAX 2.2 software (Volume Graphics GmbH, Germany) for consequent modification of the mesh, like a surface smoothing, and 3D visualization. The software GOM Inspect V8 (GOM, Braunschweig, Germany) was implemented for comparisons of full shapes of the head. The triangular meshes of the surface of the heads represented by STL models were imported into the software, aligned and compared with parameters of maximum searching distance 1 mm and maximum opening angle 30°. All raw STL files are freely accessible via the following Dryad link: <https://doi.org/10.5061/dryad.f1s76f2>

The STL format can be opened with Paint 3D or Print 3D software.

### **Light sheet microscopy and sample clearing**

Whole heads from *Shh-GFP* embryos at E11.5, E12.5, E13.5 and E14.5 were cleared using a modified CUBIC protocol ([Susaki et al., 2014](#)). In brief, embryos were fixed by using 4% PFA in PBS for 4 hr at four degrees before incubating in CUBIC one solution (25% urea, 25% N,N,N',N'-tetrakis-(2-hydroxypropyl) ethylenediamine and 15% Triton X-100) at 37°C under shaking conditions for 3 days. Subsequently, the samples were washed in PBS at RT. Next, samples were immersed in CUBIC two solution (50% sucrose, 25% urea, 10% 2,2',2''-nitrilotriethanol, and 0.1% Triton X-100) and left shaking at RT for an additional 2–3 days before image acquisition.

Whole embryo head (E11.5–E14.5) GFP fluorescence images were acquired on a Light sheet Z.1 microscope (Zeiss) using a × 5 (EC Plan Neofluar 5×/0.16) detection objective, ×5/0.1 illumination optics, and laser excitation at 488 nm. Samples were imaged in CUBIC two solution with a measured refractory index of 1.45. Each plane was illuminated from a single side of the sample. Whole images were obtained through tile scanning. 3D-rendered images were visualized with Arivis Vision4D for Zeiss (v. 2.11) or Imaris (v. 7.4.2, Bitplane).

Bitplane IMARIS software was subsequently used for 3D visualization and analysis of the light sheet tiles. By using the surface option in IMARIS the different parts of *Shh-GFP* have been highlighted.

## Acknowledgements

We would like to thank to Prof. Susan Mackem for the *Col2a1-CreERT2* mouse strain. MKau was supported by the SSMF fellowship (Svenska sällskapet för medicinsk forskning). IA was supported by Bertil Hållsten Research Foundation, Åke Wiberg Foundation, Vetenskapsrådet (VR), ERC Consolidator grant (STEMMING-FROM-NERVE, Project ID: 647844; ERC-2014-CoG), EMBO Young Investigator Program and Karolinska Institutet. JP was supported by a VR grant. KF was supported by VR MT, JK and TZ have been financially supported by the Ministry of Education, Youth and Sports of the Czech Republic under the project CEITEC 2020 (LQ1601) and by the project CEITEC Nano Research Infrastructure (MEYS CR, 2016–2019). MKas was supported by Cancerfonden, Swedish Foundation for Strategic Research and Ragnar Söderberg Foundation. KA was supported by Karolinska Institutet. FS lab was supported by EMBL. MEK was supported by the NovoNordisk Fonden Postdoctoral Stipend (Ref No NNF17OC0026874). MH was supported by Grant Agency of Czech Republic (14–37368G). Work in the AK lab is supported by the European Research Council under European Union Horizon 2020 research and innovation program grant 680037.

## Additional information

### Funding

Funder	Grant reference number	Author
Vetenskapsrådet		Julian Petersen Andrei S Chagin Igor Adameyko
Svenska Sällskapet för Medicinsk Forskning		Marketa Kaucka
Bertil Hållstens Forskningsstiftelse		Igor Adameyko
Åke Wibergs Stiftelse		Igor Adameyko
Karolinska Institutet		Ulrika Marklund Andrei S Chagin Kaj Fried Igor Adameyko
Ministerstvo Vnitřní České republiky		Marketa Tesarova Tomas Zikmund
Central European Institute of Technology		Marketa Tesarova Tomas Zikmund
Grantová Agentura České republiky		Maria Hovorakova
H2020 European Research Council	680037	Anna Kicheva

The funders had no role in study design, data collection and interpretation, or the decision to submit the work for publication.

### Author contributions

Marketa Kaucka, Julian Petersen, Conceptualization, Data curation, Supervision, Validation, Investigation, Visualization, Methodology, Writing—original draft, Writing—review and editing; Marketa Tesarova, Data curation, Supervision, Investigation, Visualization, Methodology, Writing—review and editing; Bara Szarowska, Maria Eleni Kastriiti, Jozef Kaiser, Resources, Data curation, Supervision, Methodology, Writing—review and editing; Meng Xie, Data curation, Writing—review and editing; Anna Kicheva, Conceptualization, Resources, Data curation, Supervision, Writing—original draft, Writing—review and editing; Karl Annusver, Data curation, Investigation, Methodology, Writing—review and editing; Maria Kasper, Resources, Data curation, Supervision, Methodology, Writing—original draft, Writing—review and editing; Orsolya Symmons, Resources, Data curation, Investigation; Leslie Pan, Resources, Data curation, Investigation, Writing—original draft, Writing—review and editing; Francois Spitz, Data curation, Supervision, Methodology, Writing—review and editing; Maria

Hovorakova, Conceptualization, Resources, Data curation, Supervision, Investigation, Writing—review and editing; Tomas Zikmund, Resources, Investigation, Methodology, Writing—review and editing; Kazunori Sunadome, Resources, Data curation, Investigation, Methodology, Writing—original draft, Writing—review and editing; Michael P Matise, Conceptualization, Resources, Data curation, Investigation, Methodology, Writing—original draft, Writing—review and editing; Hui Wang, Pascal Maire, Conceptualization, Resources, Data curation, Investigation, Methodology, Writing—review and editing; Ulrika Marklund, Hind Abdo, Patrik Ernfors, Andrei S Chagin, Kaj Fried, Igor Adameyko, Conceptualization, Resources, Data curation, Formal analysis, Supervision, Funding acquisition, Investigation, Methodology, Writing—original draft, Writing—review and editing; Maud Wurmser, Conceptualization, Resources, Data curation, Supervision, Investigation, Methodology, Writing—original draft, Writing—review and editing

### Author ORCIDs

Marketa Kaucka  <https://orcid.org/0000-0002-8781-9769>

Julian Petersen  <http://orcid.org/0000-0002-7444-0610>

Ulrika Marklund  <https://orcid.org/0000-0003-1426-1271>

Andrei S Chagin  <https://orcid.org/0000-0002-2696-5850>

Igor Adameyko  <https://orcid.org/0000-0001-5471-0356>

### Ethics

Animal experimentation: All animal work was approved and permitted by the Local Ethical Committee on Animal Experiments (North Stockholm Animal Ethics Committee) and conducted according to The Swedish Animal Agency's Provisions and Guidelines for Animal Experimentation recommendations. Permit numbers S40/13 and N226/15, granted by South Stockholm Animal Ethics Committee. The part, which was done in Austria at the Medical University of Vienna and IST was performed in accordance with license BMWFW-66.018/0006-WF/V/3b/2016 and BMWFW-66.009/0163-WF/V/3b/2016 granted by the Austrian BMWFW.

### Decision letter and Author response

Decision letter <https://doi.org/10.7554/eLife.34465.027>

Author response <https://doi.org/10.7554/eLife.34465.028>

## Additional files

### Supplementary files

- Transparent reporting form

DOI: <https://doi.org/10.7554/eLife.34465.023>

### Data availability

All data obtained including tomographic reconstructions will be freely available upon request since some datasets are considerably large (1TB and more) and depositing the full data is unfeasible. We have made a subset of the datasets available on the Dryad Digital Repository (<http://dx.doi.org/10.5061/dryad.f1s76f2>).

The following dataset was generated:

Author(s)	Year	Dataset title	Dataset URL	Database, license, and accessibility information
Kaucka M, Petersen J, Tesarova M, Szarowska B, Kas-triti ME, Xie M, Kicheva A, Annus-ver K, Kasper M, Symmons O, Pan L, Spitz F, Kaiser J, Hovorakova M, Zik-	2018	Data from: Signals from the brain and olfactory epithelium control shaping of the mammalian nasal capsule cartilage	<a href="http://dx.doi.org/10.5061/dryad.f1s76f2">http://dx.doi.org/10.5061/dryad.f1s76f2</a>	Available at Dryad Digital Repository under a CC0 Public Domain Dedication

mund T, Sunadome K, Matisse MP, Wang H, Marklund U, Abdo H, Ernfors P, Maire P, Wurmser M, Chagin AS, Fried K, Adameyko I

## References

- Abzhanov A**, Tabin CJ. 2004. Shh and Fgf8 act synergistically to drive cartilage outgrowth during cranial development. *Developmental Biology* **273**:134–148. DOI: <https://doi.org/10.1016/j.ydbio.2004.05.028>, PMID: 15302603
- Allen WL**, Higham JP. 2015. Assessing the potential information content of multicomponent visual signals: a machine learning approach. *Proceedings of the Royal Society B: Biological Sciences* **282**:20142284. DOI: <https://doi.org/10.1098/rspb.2014.2284>, PMID: 25652832
- Antshel KM**, Fremont W, Kates WR. 2008. The neurocognitive phenotype in velo-cardio-facial syndrome: a developmental perspective. *Developmental Disabilities Research Reviews* **14**:43–51. DOI: <https://doi.org/10.1002/ddr.7>, PMID: 18636636
- Attanasio C**, Nord AS, Zhu Y, Blow MJ, Li Z, Liberton DK, Morrison H, Plajzer-Frick I, Holt A, Hosseini R, Phouanavong S, Akiyama JA, Shoukry M, Afzal V, Rubin EM, FitzPatrick DR, Ren B, Hallgrímsson B, Pennacchio LA, Visel A. 2013. Fine tuning of craniofacial morphology by distant-acting enhancers. *Science* **342**:1241006. DOI: <https://doi.org/10.1126/science.1241006>, PMID: 24159046
- Baggiolini A**, Varum S, Mateos JM, Bettosini D, John N, Bonalli M, Ziegler U, Dimou L, Clevers H, Furrer R, Sommer L. 2015. Premigratory and migratory neural crest cells are multipotent in vivo. *Cell Stem Cell* **16**:314–322. DOI: <https://doi.org/10.1016/j.stem.2015.02.017>, PMID: 25748934
- Balaskas N**, Ribeiro A, Panovska J, Dessaud E, Sasai N, Page KM, Briscoe J, Ribes V. 2012. Gene regulatory logic for reading the Sonic Hedgehog signaling gradient in the vertebrate neural tube. *Cell* **148**:273–284. DOI: <https://doi.org/10.1016/j.cell.2011.10.047>, PMID: 22265416
- Bhullar BA**, Morris ZS, Sefton EM, Tok A, Tokita M, Namkoong B, Camacho J, Burnham DA, Abzhanov A. 2015. A molecular mechanism for the origin of a key evolutionary innovation, the bird beak and palate, revealed by an integrative approach to Major transitions in vertebrate history. *Evolution* **69**:1665–1677. DOI: <https://doi.org/10.1111/evo.12684>, PMID: 25964090
- Billmyre KK**, Klingensmith J. 2015. Sonic hedgehog from pharyngeal arch 1 epithelium is necessary for early mandibular arch cell survival and later cartilage condensation differentiation. *Developmental Dynamics* **244**:564–576. DOI: <https://doi.org/10.1002/dvdy.24256>, PMID: 25626636
- Brugmann SA**, Powder KE, Young NM, Goodnough LH, Hahn SM, James AW, Helms JA, Lovett M. 2010. Comparative gene expression analysis of avian embryonic facial structures reveals new candidates for human craniofacial disorders. *Human Molecular Genetics* **19**:920–930. DOI: <https://doi.org/10.1093/hmg/ddp559>, PMID: 20015954
- Carson B**. 1999. *Human Embryology & Developmental Biology*. Mosby.
- Cau E**, Gradwohl G, Fode C, Guillemot F. 1997. Mash1 activates a cascade of bHLH regulators in olfactory neuron progenitors. *Development* **124**:1611–1621. PMID: 9108377
- Chamberlain CE**, Jeong J, Guo C, Allen BL, McMahon AP. 2008. Notochord-derived Shh concentrates in close association with the apically positioned basal body in neural target cells and forms a dynamic gradient during neural patterning. *Development* **135**:1097–1106. DOI: <https://doi.org/10.1242/dev.013086>, PMID: 18272593
- Chang CF**, Chang YT, Millington G, Brugmann SA. 2016. Craniofacial ciliopathies reveal specific requirements for GLI proteins during development of the facial midline. *PLoS Genetics* **12**:e1006351. DOI: <https://doi.org/10.1371/journal.pgen.1006351>, PMID: 27802276
- Chong HJ**, Young NM, Hu D, Jeong J, McMahon AP, Hallgrímsson B, Marcucio RS. 2012. Signaling by SHH rescues facial defects following blockade in the brain. *Developmental dynamics : an official publication of the American Association of Anatomists* **241**:247–256. DOI: <https://doi.org/10.1002/dvdy.23726>, PMID: 22275045
- Foppiano S**, Hu D, Marcucio RS. 2007. Signaling by bone morphogenetic proteins directs formation of an ectodermal signaling center that regulates craniofacial development. *Developmental Biology* **312**:103–114. DOI: <https://doi.org/10.1016/j.ydbio.2007.09.016>, PMID: 18028903
- Forbes BJ**. 2010. Congenital craniofacial anomalies. *Current Opinion in Ophthalmology* **21**:367–374. DOI: <https://doi.org/10.1097/ICU.0b013e32833cd422>, PMID: 20634697
- Furlan A**, Dyachuk V, Kastriti ME, Calvo-Enrique L, Abdo H, Hadjab S, Chontorotzea T, Akkuratova N, Usoskin D, Kamenev D, Petersen J, Sunadome K, Memic F, Marklund U, Fried K, Topilko P, Lallemand F, Kharchenko PV, Ernfors P, Adameyko I. 2017. Multipotent peripheral glial cells generate neuroendocrine cells of the adrenal medulla. *Science* **357**. DOI: <https://doi.org/10.1126/science.aal3753>, PMID: 28684471
- Goldring MB**, Tsuchimochi K, Ijiri K. 2006. The control of chondrogenesis. *Journal of Cellular Biochemistry* **97**:33–44. DOI: <https://doi.org/10.1002/jcb.20652>, PMID: 16215986

- Griffin JN**, Compagnucci C, Hu D, Fish J, Klein O, Marcucio R, Depew MJ. 2013. Fgf8 dosage determines midfacial integration and polarity within the nasal and optic capsules. *Developmental Biology* **374**:185–197. DOI: <https://doi.org/10.1016/j.ydbio.2012.11.014>, PMID: 23201021
- Grifone R**, Demignon J, Houbron C, Souil E, Niro C, Seller MJ, Hamard G, Maire P. 2005. Six1 and Six4 homeoproteins are required for Pax3 and Mrf expression during myogenesis in the mouse embryo. *Development* **132**:2235–2249. DOI: <https://doi.org/10.1242/dev.01773>, PMID: 15788460
- Gros J**, Tabin CJ. 2014. Vertebrate limb bud formation is initiated by localized epithelial-to-mesenchymal transition. *Science* **343**:1253–1256. DOI: <https://doi.org/10.1126/science.1248228>, PMID: 24626928
- Guillemot F**, Lo LC, Johnson JE, Auerbach A, Anderson DJ, Joyner AL. 1993. Mammalian achaete-scute homolog 1 is required for the early development of olfactory and autonomic neurons. *Cell* **75**:463–476. DOI: [https://doi.org/10.1016/0092-8674\(93\)90381-Y](https://doi.org/10.1016/0092-8674(93)90381-Y), PMID: 8221886
- Harfe BD**, Scherz PJ, Nissim S, Tian H, McMahon AP, Tabin CJ. 2004. Evidence for an expansion-based temporal Shh gradient in specifying vertebrate digit identities. *Cell* **118**:517–528. DOI: <https://doi.org/10.1016/j.cell.2004.07.024>, PMID: 15315763
- Herbrand H**, Pabst O, Hill R, Arnold HH. 2002. Transcription factors Nkx3.1 and Nkx3.2 (Bapx1) play an overlapping role in sclerotomal development of the mouse. *Mechanisms of Development* **117**:217–224. DOI: [https://doi.org/10.1016/S0925-4773\(02\)00207-1](https://doi.org/10.1016/S0925-4773(02)00207-1), PMID: 12204261
- Hu D**, Helms JA. 1999. The role of sonic hedgehog in normal and abnormal craniofacial morphogenesis. *Development* **126**:4873–4884. PMID: 10518503
- Hu D**, Marcucio RS. 2009. A SHH-responsive signaling center in the forebrain regulates craniofacial morphogenesis via the facial ectoderm. *Development* **136**:107–116. DOI: <https://doi.org/10.1242/dev.026583>, PMID: 19036802
- Hu D**, Young NM, Li X, Xu Y, Hallgrímsson B, Marcucio RS. 2015b. A dynamic shh expression pattern, regulated by SHH and BMP signaling, coordinates fusion of primordia in the amniote face. *Development* **142**:567–574. DOI: <https://doi.org/10.1242/dev.114835>, PMID: 25605783
- Hu D**, Young NM, Xu Q, Jamniczky H, Green RM, Mio W, Marcucio RS, Hallgrímsson B. 2015a. Signals from the brain induce variation in avian facial shape. *Developmental dynamics : an official publication of the American Association of Anatomists*. DOI: <https://doi.org/10.1002/dvdy.24284>, PMID: 25903813
- Ikeda K**, Ookawara S, Sato S, Ando Z, Kageyama R, Kawakami K. 2007. Six1 is essential for early neurogenesis in the development of olfactory epithelium. *Developmental Biology* **311**:53–68. DOI: <https://doi.org/10.1016/j.ydbio.2007.08.020>, PMID: 17880938
- Irimia M**, Royo JL, Burguera D, Maeso I, Gómez-Skarmeta JL, Garcia-Fernandez J. 2012. Comparative genomics of the hedgehog loci in chordates and the origins of shh regulatory novelties. *Scientific Reports* **2**:433. DOI: <https://doi.org/10.1038/srep00433>, PMID: 22666536
- Jeong Y**, El-Jaick K, Roessler E, Muenke M, Epstein DJ. 2006. A functional screen for sonic hedgehog regulatory elements across a 1 Mb interval identifies long-range ventral forebrain enhancers. *Development* **133**:761–772. DOI: <https://doi.org/10.1242/dev.02239>, PMID: 16407397
- Kauka M**, Zikmund T, Tesarova M, Gyllborg D, Hellander A, Jaros J, Kaiser J, Petersen J, Szarowska B, Newton PT, Dyachuk V, Li L, Qian H, Johansson AS, Mishina Y, Currie JD, Tanaka EM, Erickson A, Dudley A, Brismar H, et al. 2017. Oriented clonal cell dynamics enables accurate growth and shaping of vertebrate cartilage. *eLife* **6**:e25902. DOI: <https://doi.org/10.7554/eLife.25902>, PMID: 28414273
- Kobayashi H**, Kawakami K, Asashima M, Nishinakamura R. 2007. Six1 and Six4 are essential for gdnf expression in the metanephric mesenchyme and ureteric bud formation, while Six1 deficiency alone causes mesonephric-tubule defects. *Mechanisms of Development* **124**:290–303. DOI: <https://doi.org/10.1016/j.mod.2007.01.002>, PMID: 17300925
- Laclef C**, Hamard G, Demignon J, Souil E, Houbron C, Maire P. 2003. Altered myogenesis in Six1-deficient mice. *Development* **130**:2239–2252. DOI: <https://doi.org/10.1242/dev.00440>, PMID: 12668636
- LoRusso PM**, Rudin CM, Reddy JC, Tibes R, Weiss GJ, Borad MJ, Hann CL, Brahmer JR, Chang I, Darbonne WC, Graham RA, Zerivitz KL, Low JA, Von Hoff DD. 2011. Phase I trial of hedgehog pathway inhibitor vismodegib (GDC-0449) in patients with refractory, locally advanced or metastatic solid tumors. *Clinical Cancer Research* **17**:2502–2511. DOI: <https://doi.org/10.1158/1078-0432.CCR-10-2745>, PMID: 21300762
- Marcucio RS**, Young NM, Hu D, Hallgrímsson B. 2011. Mechanisms that underlie co-variation of the brain and face. *Genesis* **49**:177–189. DOI: <https://doi.org/10.1002/dvg.20710>, PMID: 21381182
- Marinić M**, Aktas T, Ruf S, Spitz F. 2013. An integrated holo-enhancer unit defines tissue and gene specificity of the Fgf8 regulatory landscape. *Developmental Cell* **24**:530–542. DOI: <https://doi.org/10.1016/j.devcel.2013.01.025>, PMID: 23453598
- McBratney-Owen B**, Iseki S, Bamforth SD, Olsen BR, Morriss-Kay GM. 2008. Development and tissue origins of the mammalian cranial base. *Developmental Biology* **322**:121–132. DOI: <https://doi.org/10.1016/j.ydbio.2008.07.016>, PMID: 18680740
- Metscher BD**. 2009. MicroCT for comparative morphology: simple staining methods allow high-contrast 3D imaging of diverse non-mineralized animal tissues. *BMC Physiology* **9**:11. DOI: <https://doi.org/10.1186/1472-6793-9-11>, PMID: 19545439
- Minoux M**, Rijli FM. 2010. Molecular mechanisms of cranial neural crest cell migration and patterning in craniofacial development. *Development* **137**:2605–2621. DOI: <https://doi.org/10.1242/dev.040048>, PMID: 20663816

- Murtaugh LC**, Chyung JH, Lassar AB. 1999. Sonic hedgehog promotes somitic chondrogenesis by altering the cellular response to BMP signaling. *Genes & Development* **13**:225–237. DOI: <https://doi.org/10.1101/gad.13.2.225>, PMID: 9925646
- Murtaugh LC**, Zeng L, Chyung JH, Lassar AB. 2001. The chick transcriptional repressor Nkx3.2 acts downstream of Shh to promote BMP-dependent axial chondrogenesis. *Developmental Cell* **1**:411–422. DOI: [https://doi.org/10.1016/S1534-5807\(01\)00039-9](https://doi.org/10.1016/S1534-5807(01)00039-9), PMID: 11702952
- Nakamura E**, Nguyen MT, Mackem S. 2006. Kinetics of tamoxifen-regulated Cre activity in mice using a cartilage-specific CreER(T) to assay temporal activity windows along the proximodistal limb skeleton. *Developmental dynamics : an official publication of the American Association of Anatomists* **235**:2603–2612. DOI: <https://doi.org/10.1002/dvdy.20892>, PMID: 16894608
- Ornitz DM**, Marie PJ. 2002. FGF signaling pathways in endochondral and intramembranous bone development and human genetic disease. *Genes & Development* **16**:1446–1465. DOI: <https://doi.org/10.1101/gad.990702>, PMID: 12080084
- Ozaki H**, Watanabe Y, Takahashi K, Kitamura K, Tanaka A, Urase K, Momoi T, Sudo K, Sakagami J, Asano M, Iwakura Y, Kawakami K. 2001. Six4, a putative myogenin gene regulator, is not essential for mouse embryonal development. *Molecular and Cellular Biology* **21**:3343–3350. DOI: <https://doi.org/10.1128/MCB.21.10.3343-3350.2001>, PMID: 11313460
- Park J**, Zhang JJ, Moro A, Kushida M, Wegner M, Kim PC. 2010. Regulation of Sox9 by sonic hedgehog (Shh) is essential for patterning and formation of tracheal cartilage. *Developmental Dynamics* **239**:514–526. DOI: <https://doi.org/10.1002/dvdy.22192>, PMID: 20034104
- Parsons TE**, Schmidt EJ, Boughner JC, Jamniczky HA, Marcucio RS, Hallgrímsson B. 2011. Epigenetic integration of the developing brain and face. *Developmental Dynamics* **240**:2233–2244. DOI: <https://doi.org/10.1002/dvdy.22729>, PMID: 21901785
- Petryk A**, Graf D, Marcucio R. 2015. Holoprosencephaly: signaling interactions between the brain and the face, the environment and the genes, and the phenotypic variability in animal models and humans. *Wiley Interdisciplinary Reviews: Developmental Biology* **4**:17–32. DOI: <https://doi.org/10.1002/wdev.161>, PMID: 25339593
- Picelli S**, Björklund ÅK, Faridani OR, Sagasser S, Winberg G, Sandberg R. 2013. Smart-seq2 for sensitive full-length transcriptome profiling in single cells. *Nature Methods* **10**:1096–1098. DOI: <https://doi.org/10.1038/nmeth.2639>, PMID: 24056875
- Sagai T**, Amano T, Tamura M, Mizushima Y, Sumiyama K, Shiroishi T. 2009. A cluster of three long-range enhancers directs regional Shh expression in the epithelial linings. *Development* **136**:1665–1674. DOI: <https://doi.org/10.1242/dev.032714>, PMID: 19369396
- Sala FG**, Del Moral PM, Tiozzo C, Alam DA, Warburton D, Grikscheit T, Veltmaat JM, Bellusci S. 2011. FGF10 controls the patterning of the tracheal cartilage rings via Shh. *Development* **138**:273–282. DOI: <https://doi.org/10.1242/dev.051680>, PMID: 21148187
- Santana SE**, Lynch Alfaro J, Alfaro ME. 2012. Adaptive evolution of facial colour patterns in neotropical primates. *Proceedings of the Royal Society B: Biological Sciences* **279**:2204–2211. DOI: <https://doi.org/10.1098/rspb.2011.2326>
- Shimeld SM**, Donoghue PC. 2012. Evolutionary crossroads in developmental biology: cyclostomes (lamprey and hagfish). *Development* **139**:2091–2099. DOI: <https://doi.org/10.1242/dev.074716>, PMID: 22619386
- Shirley ED**, Ain MC. 2009. Achondroplasia: manifestations and treatment. *The Journal of the American Academy of Orthopaedic Surgeons* **17**:231–241. DOI: <https://doi.org/10.5435/00124635-200904000-00004>, PMID: 19307672
- Snider TN**, Mishina Y. 2014. Cranial neural crest cell contribution to craniofacial formation, pathology, and future directions in tissue engineering. *Birth Defects Research Part C: Embryo Today: Reviews* **102**:324–332. DOI: <https://doi.org/10.1002/bdrc.21075>, PMID: 25227212
- Snippert HJ**, van der Flier LG, Sato T, van Es JH, van den Born M, Kroon-Veenboer C, Barker N, Klein AM, van Rheenen J, Simons BD, Clevers H. 2010. Intestinal crypt homeostasis results from neutral competition between symmetrically dividing Lgr5 stem cells. *Cell* **143**:134–144. DOI: <https://doi.org/10.1016/j.cell.2010.09.016>, PMID: 20887898
- Starbuck JM**, Cole TM, Reeves RH, Richtsmeier JT. 2017. The influence of trisomy 21 on facial form and variability. *American Journal of Medical Genetics Part A* **173**:2861–2872. DOI: <https://doi.org/10.1002/ajmg.a.38464>, PMID: 28941128
- Susaki EA**, Tainaka K, Perrin D, Kishino F, Tawara T, Watanabe TM, Yokoyama C, Onoe H, Eguchi M, Yamaguchi S, Abe T, Kiyonari H, Shimizu Y, Miyawaki A, Yokota H, Ueda HR. 2014. Whole-brain imaging with single-cell resolution using chemical cocktails and computational analysis. *Cell* **157**:726–739. DOI: <https://doi.org/10.1016/j.cell.2014.03.042>, PMID: 24746791
- Symmons O**, Pan L, Remeseiro S, Aktas T, Klein F, Huber W, Spitz F. 2016. The shh topological domain facilitates the action of remote enhancers by reducing the effects of genomic distances. *Developmental Cell* **39**:529–543. DOI: <https://doi.org/10.1016/j.devcel.2016.10.015>, PMID: 27867070
- Vernon RJ**, Sutherland CA, Young AW, Hartley T. 2014. Modeling first impressions from highly variable facial images. *PNAS* **111**:E3353–3361. DOI: <https://doi.org/10.1073/pnas.1409860111>, PMID: 25071197
- Vincent M**, Collet C, Verloes A, Lambert L, Herlin C, Blanchet C, Sanchez E, Drunat S, Vigneron J, Laplanche JL, Puechberty J, Sarda P, Geneviève D. 2014. Large deletions encompassing the TCOF1 and CAMK2A genes are responsible for Treacher Collins syndrome with intellectual disability. *European journal of human genetics : EJHG* **22**:52–56. DOI: <https://doi.org/10.1038/ejhg.2013.98>, PMID: 23695276

- Voehringer D**, Liang HE, Locksley RM. 2008. Homeostasis and effector function of lymphopenia-induced "memory-like" T cells in constitutively T cell-depleted mice. *The Journal of Immunology* **180**:4742–4753. DOI: <https://doi.org/10.4049/jimmunol.180.7.4742>, PMID: 18354198
- Wang F**, Flanagan J, Su N, Wang LC, Bui S, Nielson A, Wu X, Vo HT, Ma XJ, Luo Y. 2012. RNAscope: a novel in situ RNA analysis platform for formalin-fixed, paraffin-embedded tissues. *The Journal of Molecular Diagnostics* : **JMD** **14**:22–29. DOI: <https://doi.org/10.1016/j.jmoldx.2011.08.002>, PMID: 22166544
- Weisman O**, Feldman R, Burg-Malki M, Keren M, Geva R, Diesendruck G, Gothelf D. 2017. Comparing the broad socio-cognitive profile of youth with williams syndrome and 22q11.2 deletion syndrome. *Journal of Intellectual Disability Research* **61**:1083–1093. DOI: <https://doi.org/10.1111/jir.12424>, PMID: 28990288
- Yao Y**, Minor PJ, Zhao YT, Jeong Y, Pani AM, King AN, Symmons O, Gan L, Cardoso WV, Spitz F, Lowe CJ, Epstein DJ. 2016. Cis-regulatory architecture of a brain signaling center predates the origin of chordates. *Nature Genetics* **48**:575–580. DOI: <https://doi.org/10.1038/ng.3542>, PMID: 27064252
- Young NM**, Hu D, Lainoff AJ, Smith FJ, Diaz R, Tucker AS, Trainor PA, Schneider RA, Hallgrímsson B, Marcucio RS. 2014. Embryonic bauplans and the developmental origins of facial diversity and constraint. *Development* **141**:1059–1063. DOI: <https://doi.org/10.1242/dev.099994>, PMID: 24550113
- Yu K**, McGlynn S, Matise MP. 2013. Floor plate-derived sonic hedgehog regulates glial and ependymal cell fates in the developing spinal cord. *Development* **140**:1594–1604. DOI: <https://doi.org/10.1242/dev.090845>, PMID: 23482494
- Zagorski M**, Tabata Y, Brandenberg N, Lutolf MP, Tkačik G, Bollenbach T, Briscoe J, Kicheva A. 2017. Decoding of position in the developing neural tube from antiparallel morphogen gradients. *Science* **356**:1379–1383. DOI: <https://doi.org/10.1126/science.aam5887>, PMID: 28663499
- Zeng L**, Kempf H, Murtaugh LC, Sato ME, Lassar AB. 2002. Shh establishes an Nkx3.2/Sox9 autoregulatory loop that is maintained by BMP signals to induce somitic chondrogenesis. *Genes & Development* **16**:1990–2005. DOI: <https://doi.org/10.1101/gad.1008002>, PMID: 12154128

PAPER [XIII]

## RESEARCH ARTICLE

# Local retinoic acid signaling directs emergence of the extraocular muscle functional unit

Glenda Evangelina Comai<sup>1,2\*</sup>, Markéta Tesařová<sup>3</sup>, Valérie Dupé<sup>4</sup>, Muriel Rhinn<sup>5</sup>, Pedro Vallecillo-García<sup>6</sup>, Fabio da Silva<sup>7,8</sup>, Betty Feret<sup>5</sup>, Katherine Exelby<sup>9</sup>, Pascal Dollé<sup>5</sup>, Leif Carlsson<sup>10</sup>, Brian Pryce<sup>11</sup>, François Spitz<sup>12</sup>, Sigmar Stricker<sup>6</sup>, Tomáš Zikmund<sup>3</sup>, Jozef Kaiser<sup>3</sup>, James Briscoe<sup>9</sup>, Andreas Schedl<sup>7</sup>, Norbert B. Ghyselinck<sup>5</sup>, Ronen Schweitzer<sup>11</sup>, Shahragim Tajbakhsh<sup>1,2\*</sup>

**1** Stem Cells & Development Unit, Institut Pasteur, Paris, France, **2** CNRS UMR 3738, Institut Pasteur, Paris, France, **3** Central European Institute of Technology, Brno University of Technology, Brno, Czech Republic, **4** Université de Rennes, CNRS, IGDR, Rennes, France, **5** IGBMC-Institut de Génétique et de Biologie Moléculaire et Cellulaire, Illkirch, France, **6** Institute for Chemistry and Biochemistry, Freie Universität Berlin, Berlin, Germany, **7** Université Côte d'Azur, INSERM, CNRS, iBV, Nice, France, **8** Division of Molecular Embryology, German Cancer Research Center (DKFZ), Heidelberg, Germany, **9** The Francis Crick Institute, London, United Kingdom, **10** Umeå Center for Molecular Medicine, Umeå University, Umeå, Sweden, **11** Research Division, Shriners Hospital for Children, Portland, United States of America, **12** Genomics of Animal Development Unit, Institut Pasteur, Paris, France

\* [comai@pasteur.fr](mailto:comai@pasteur.fr) (GEC); [shaht@pasteur.fr](mailto:shaht@pasteur.fr) (ST)



## OPEN ACCESS

**Citation:** Comai GE, Tesařová M, Dupé V, Rhinn M, Vallecillo-García P, da Silva F, et al. (2020) Local retinoic acid signaling directs emergence of the extraocular muscle functional unit. *PLoS Biol* 18(11): e3000902. <https://doi.org/10.1371/journal.pbio.3000902>

**Academic Editor:** Simon M. Hughes, King's College London, UNITED KINGDOM

**Received:** January 7, 2020

**Accepted:** October 1, 2020

**Published:** November 17, 2020

**Peer Review History:** PLOS recognizes the benefits of transparency in the peer review process; therefore, we enable the publication of all of the content of peer review and author responses alongside final, published articles. The editorial history of this article is available here: <https://doi.org/10.1371/journal.pbio.3000902>

**Copyright:** © 2020 Comai et al. This is an open access article distributed under the terms of the [Creative Commons Attribution License](https://creativecommons.org/licenses/by/4.0/), which permits unrestricted use, distribution, and reproduction in any medium, provided the original author and source are credited.

**Data Availability Statement:** All relevant data are within the paper and its [Supporting Information](#) files.

## Abstract

Coordinated development of muscles, tendons, and their attachment sites ensures emergence of functional musculoskeletal units that are adapted to diverse anatomical demands among different species. How these different tissues are patterned and functionally assembled during embryogenesis is poorly understood. Here, we investigated the morphogenesis of extraocular muscles (EOMs), an evolutionary conserved cranial muscle group that is crucial for the coordinated movement of the eyeballs and for visual acuity. By means of lineage analysis, we redefined the cellular origins of periocular connective tissues interacting with the EOMs, which do not arise exclusively from neural crest mesenchyme as previously thought. Using 3D imaging approaches, we established an integrative blueprint for the EOM functional unit. By doing so, we identified a developmental time window in which individual EOMs emerge from a unique muscle anlage and establish insertions in the sclera, which sets these muscles apart from classical muscle-to-bone type of insertions. Further, we demonstrate that the eyeballs are a source of diffusible all-trans retinoic acid (ATRA) that allow their targeting by the EOMs in a temporal and dose-dependent manner. Using genetically modified mice and inhibitor treatments, we find that endogenous local variations in the concentration of retinoids contribute to the establishment of tendon condensations and attachment sites that precede the initiation of muscle patterning. Collectively, our results highlight how global and site-specific programs are deployed for the assembly of muscle functional units with precise definition of muscle shapes and topographical wiring of their tendon attachments.

**Funding:** We acknowledge funding support from the Institut Pasteur, Association Française contre le Myopathies, Agence Nationale de la Recherche (Laboratoire d'Excellence Revive, Investissement d'Avenir; ANR-10-LABX-73) and the Centre National de la Recherche Scientifique. We gratefully acknowledge the UtechS Photonic Bioluminescence (Imagopole), C2RT, Institut Pasteur, supported by the French National Research Agency (France Bioluminescence; ANR-10-INSB-04; Investments for the Future). MT, TZ and JK acknowledge the project CEITEC 2020 (LQ1601) with financial support from the Ministry of Education, Youth and Sports of the Czech Republic under the National Sustainability Programme II and Ceitec Nano+ project CZ.02.01/0.0/0.0/16\_013/0001728 under the program OP RDE. MT was financially supported by the Brno City Municipality as a Brno Ph.D. Talent Scholarship Holder. The funders had no role in study design, data collection and analysis, decision to publish, or preparation of the manuscript.

**Competing interests:** The authors have declared that no competing interests exist.

**Abbreviations:** ADH, alcohol dehydrogenase; ATRA, all-trans retinoic acid; ALDH1A1, Aldehyde Dehydrogenase 1 Family Member A1; ALDH1A3, Aldehyde Dehydrogenase 1 Family Member A3; E, embryonic day; EOM, extraocular muscle; GFP, green fluorescent protein; KO, knock-out; LHX2, LIM Homeobox 2; Mesp1, mesoderm posterior BHLH transcription factor 1; mGFP, membrane tagged GFP; micro-CT, micro-computed tomography; MYF5, myogenic factor 5; MYOD, myogenic differentiation 1; MYOG, Myogenin; MyHC, myosin heavy chain; NCC, neural crest cell; PAX6, Paired Box 6; PAX7, Paired Box 7; PITX2, Paired-like homeodomain transcription factor 2; POM, periocular mesenchyme; RAR, retinoic acid receptor; RARE, retinoic acid response element, RDH, retinol dehydrogenase; RPE, retinal pigmented epithelium; RXR, retinoid X receptor; Scx, scleraxis; Shh, Sonic Hedgehog; SMA, alpha smooth muscle actin; SOX9, SRY-box containing gene 9; TCF4, Transcription factor 4; Tom, tdTomato; WMIF, whole-mount immunofluorescence; Wnt1, Wnt Family Member 1.

## Introduction

Acquisition of shape and pattern during development depends on the orchestrated crosstalk between a variety of tissues and cell types. Although significant knowledge on the mechanisms of differentiation and patterning within individual tissues has been attained, much less is known on how patterning of different adjacent tissues is integrated. The vertebrate musculoskeletal system serves as an ideal model to study these processes as different tissues including muscle, tendon and their attachments need to be articulated in 3D for proper function [1,2].

Among the craniofacial muscles, the morphological configuration of the extraocular muscles (EOMs) has been a longstanding challenge in comparative anatomy and evolutionary biology. Besides specialized adaptations, the basic EOM pattern is shared among all vertebrate classes [3–5] and includes 4 recti muscles (the superior rectus, the medial rectus, the inferior rectus, and the lateral rectus) and 2 oblique muscles (superior oblique and inferior oblique) for movement of the eyeball. Most vertebrates have also accessory ocular muscles that serve to retract the eye (the retractor bulbi) or control eyelid elevation (the levator palpebrae superioris) [3,6]. As such, the EOMs constitute an archetypal and autonomous functional unit for the study of how muscles, tendons, and tendon attachments are integrated with the development of the eyeball, their target organ.

Craniofacial muscles are derived from cranial paraxial and prechordal head mesoderm [3,7]. The corresponding connective tissues, i.e., tendons, bones, cartilages, and muscle connective tissue, were reported to be derived from cranial neural crest cells (NCCs) [7,8]. Although early myogenesis is NCC independent, NCCs later regulate the differentiation and segregation of muscle precursors, dictate the pattern of muscle fiber alignment, and that of associated skeletal and tendon structures [9–14]. Moreover, deletion of several genes in NCCs demonstrated their non-cell-autonomous roles in muscle morphogenesis at the level of the jaw [12,15,16], extraocular [17,18], and somitic-derived tongue muscles [19]. However, the full series of events driving morphogenesis of craniofacial musculoskeletal functional units is unexplored to date, in part because of the anatomical complexity of their configuration in the head. Moreover, understanding the developmental mechanisms that allow musculoskeletal connectivity is essential to understand the anatomical diversification that took place during the evolution of the vertebrate head. Yet, proximate factors that allow cross-tissue communication for coordinated emergence of the individual muscle masses with that of their tendons and attachment sites are poorly defined.

Much of our understanding of musculoskeletal development and integration into functional units comes from studies in the limb. Lateral plate mesoderm-derived muscle connective tissue cells and tendon primordia establish a pre-pattern that determines the sites of myogenic differentiation and participate in splitting of the muscle masses in the limb [20–22]. Tendons connect muscles to the skeleton and are formed by scleraxis (Scx)-expressing mesenchymal progenitors [23,24]. Although some features of tendon development are autonomous, key stages rely on signals emanating from muscle or cartilage, according to their positioning in the limb [2]. Bone superstructures, which provide anchoring points for tendons to the skeleton, are initiated independently of muscle, but their maintenance and growth depend on cues from both tendon and muscle [2]. Given the distinct gene regulatory networks governing cranial muscle development [25,26], and embryonic origins of connective tissues in the head [7,8], it is unclear if this logic of musculoskeletal integration is conserved in the head and how structures that do not integrate bones, such as EOMs, are established.

All-trans retinoic acid (ATRA), the biologically active metabolite of retinol (vitamin A), is a critical morphogen with widespread roles in craniofacial development [27,28]. ATRA acts as a ligand for nuclear retinoic acid receptors (RARs), which are ligand-dependent transcriptional

regulators that work as heterodimers with retinoid X receptors (RXRs) [28,29]. ATRA is synthesized from retinol through 2 oxidation steps by specific retinol/alcohol dehydrogenases (RDH/ADH) and retinaldehyde dehydrogenases (ALDH1A1, ALDH1A2, and ALDH1A3) [28,29]. ATRA is critical for early eye development in several species [30–32], in which ATRA metabolic enzymes are expressed in the early retina with tight spatiotemporal patterns [33]. As such, the developing eye acts as a signaling center nucleating anterior segment morphogenesis, with paired-like homeodomain transcription factor 2 (PITX2) being the potential major downstream ATRA effector in periocular NCCs [30,34–36]. Whether ATRA is required for morphogenesis of the EOMs and associated connective tissues remains unexplored.

Here, we reassessed the embryological origins of the connective tissues of the periocular region and present the first integrative blueprint for morphogenesis of the EOM functional unit. We provide genetic evidence for the existence of a retinoic acid signaling module that coordinates the emergence of individual EOMs, their tendons, and insertion sites. We show that the action of retinoic acid signaling in muscle patterning is mainly non-cell-autonomous, through its action on the NCC-derived periocular mesenchyme. We propose that the interactions between muscles, tendons, and their attachments are similar to those observed in the limb, yet they exhibit specific hallmarks that are characteristic of this anatomical location.

## Results

### Genetic fate mapping of mouse periocular tissues

Given the complex anatomical disposition of the EOMs, we first set out to map morphological landmarks and cell relationships during patterning of these muscles. The periocular mesenchyme (POM) is a heterogeneous cell population surrounding the optic cup that gives rise to specialized structures of the anterior segment of the eye and connective tissues associated with the EOMs [37]. With exception of the EOMs and endothelial lining of ocular blood vessels (choroid), all connective tissues of the POM (cartilage, muscle connective tissue, tendons) were reported to be derived from NCCs in zebrafish, chicken, and mouse embryos [38–43]. The 4 recti EOMs originate deep in the orbit, at the level of a fibrous ring called the annulus of Zinn, and insert into the scleral layer of the eye [44]. Because information on EOM tendons and attachment sites is scarce, we used genetic fate mapping to reassess the embryological origins of the tissues interacting with EOMs during their morphogenesis. We simultaneously traced the contribution of NCC (Fig 1A–1B", S1A, and S1B Fig) and mesodermal (Fig 1C–1D", S1C and S1D Fig) derivatives using *Tg:Wnt1<sup>Cre</sup>* and *Mesp1<sup>Cre</sup>* mice, respectively [45,46], in combination with the *R26<sub>Tom</sub>* reporter [74].

As expected, connective tissues at the EOM insertion level were derived from NCCs as assessed by tdTomato expression (*Tg:Wnt1<sup>Cre</sup>;R26<sup>Tom</sup>*, Fig 1A–1A", S1A Fig). Surprisingly, we found that lineage contributions differed in dorsal sections, where connective tissues at the EOM origin level were derived from the cranial mesoderm (*Mesp1<sup>Cre</sup>;R26<sup>Tom</sup>*, Fig 1D–1D", S1D Fig). To characterize in more detail the cell populations arising from these derivatives, we used transcription factor 4 (TCF4) as muscle connective tissue marker [47], and a *Scx* reporter line (*Tg:Scx-GFP+*) to mark tendons and their early progenitors with green fluorescent protein (GFP) [24,48]. TCF4 was expressed robustly in muscle connective tissue fibroblasts in both NCC- and mesoderm-derived regions (S1E–S1F' Fig). Similarly, *Tg:Scx-GFP* (Fig 1A–1D", S1A–S1D Fig) strongly labeled the future EOM tendons at the origin and insertion sites residing respectively in mesoderm- and NCC-derived domains. Additionally, *Tg:Scx-GFP* (Fig 1A1, 1D1, S1G and S1H Fig) and *Scx* mRNA (S1I and S1J Fig) marked muscle connective tissue fibroblasts that were widely distributed among the muscle masses and overlapped with TCF4 (S1G and S1H Fig), as described in other regions of the early embryo [49,50]. Altogether, these

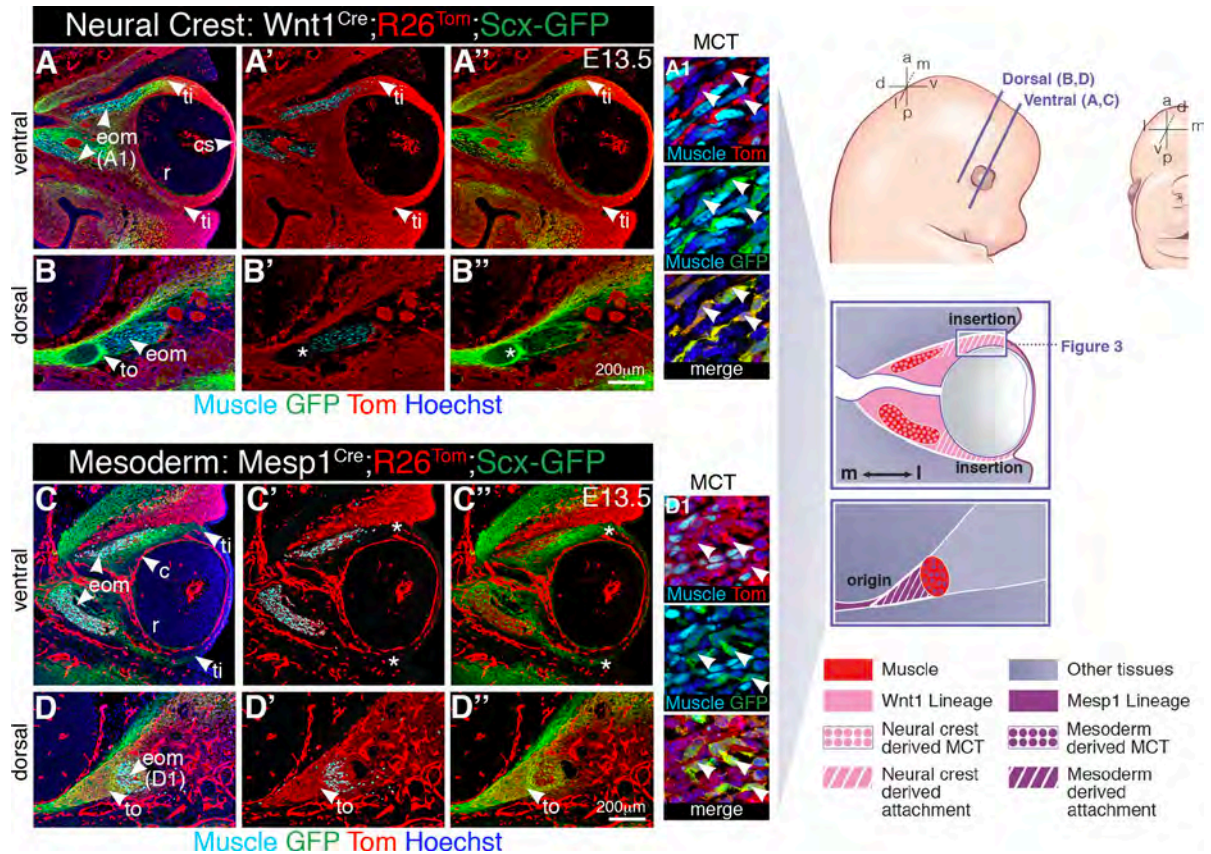


**Fig 1. Lineage contributions to the EOM functional unit.** (A–B'') Neural crest (*Tg:Wnt1<sup>Cre</sup>;R26<sup>Tom</sup>;Scx-GFP*) and (C–D'') mesodermal (*Mesp1<sup>Cre</sup>;R26<sup>Tom</sup>;Scx-GFP*) lineage contributions to the periocular region of E13.5 embryos, combined with immunostaining for tdTomato (Tom), GFP (*Tg:Scx-GFP* reporter), and muscle (PAX7/MYOD/MYOG, myogenic markers). Coronal sections at ventral (A–A'', C–C'') and dorsal (B–B'', D–D'') levels. Asterisks in B', B'' denote Tom negativity at the tendon origin. Asterisks in C', C'' denote Tom negativity at the tendon insertion site. (A1, D1) High-magnification views of muscle areas in panels A and D. (*n* = 3 per condition). a, anterior; c, choroid; cs, corneal stroma; d, dorsal; E, embryonic day; eom, extraocular muscle; l, lateral; m, medial; MCT, muscle connective tissue; p, posterior; r, retina; ti, tendon insertion; to, tendon origin; v, ventral.

<https://doi.org/10.1371/journal.pbio.3000902.g001>

findings indicate that the EOMs develop in close association with connective tissues of 2 distinct embryonic origins: neural crest laterally (at the EOM insertion) and mesoderm medially (at the EOM origin).

### Development of the EOMs and their insertions overlap spatiotemporally

Patterning of the EOMs and their insertions is understudied because of the difficulty in interpreting a complex 3D tissue arrangement from tissue sections alone. Therefore, we established an imaging pipeline that includes whole-mount immunofluorescence (WMIF) of the periocular region, tissue clearing, confocal microscopy, and reconstructions of the obtained images into 3D objects. To visualize the developing EOMs, we used antibodies against myogenic differentiation 1 (MYOD), myogenin (MYOG), and Desmin as myogenic commitment and differentiation markers and myosin heavy chain (MyHC) to label myofibers (Fig 2A–2C' and S1 Video). At embryonic day (E)11.75, the EOMs were present as a single anlage (Fig 2A and 2A') medial to the eyeball. By E12.5, the EOM anlage split towards the eyeball into submasses corresponding to the future 4 recti, 2 oblique muscles, and the accessory retractor bulbi muscle (Fig 2B and 2B'). Fully individuated muscles were evident by E13.5 (Fig 2C and 2C'). Thus, we

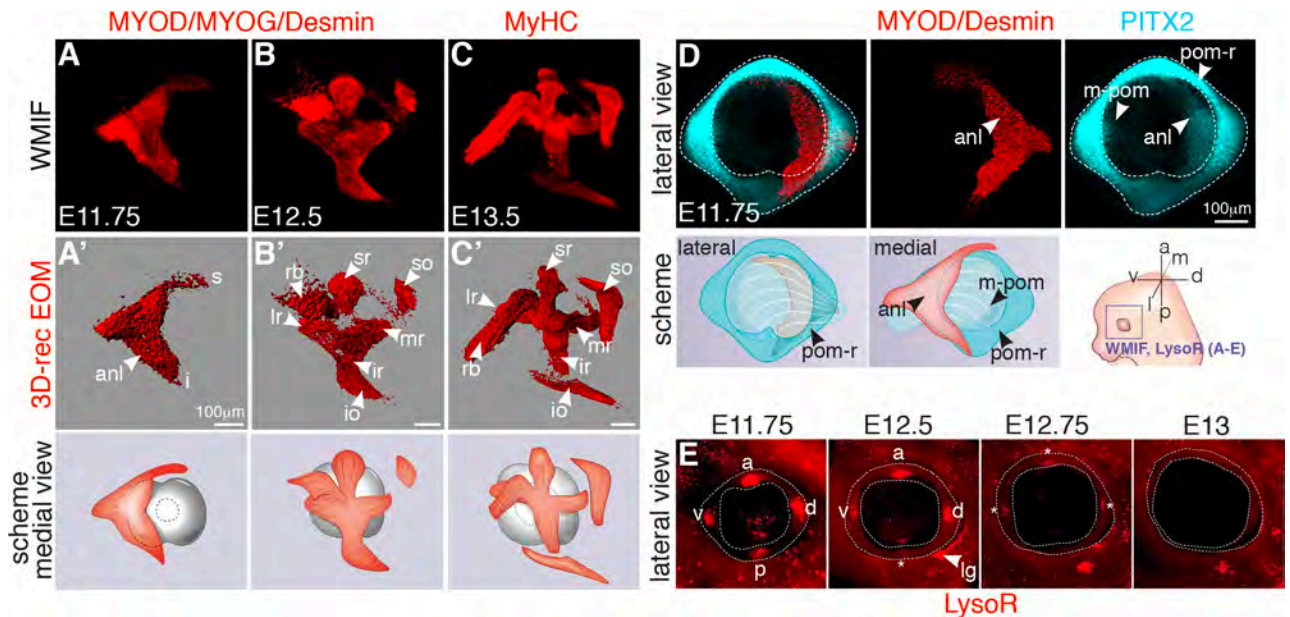


**Fig 2. Developmental time course of EOM development.** (A–C) WMIF for MYOD/MYOG/Desmin (myogenic differentiation markers) (A, B) and MyHC (myofibers) (C) at the indicated embryonic stages. EOMs were segmented from adjacent head structures and 3D-reconstructed in Imaris (Bitplane). (A'–C') EOMs are shown as isosurfaces for clarity of visualization. Medial views as schemes (left eye). (D) WMIF for MYOD/Desmin (labeling the EOM anlage, isosurface) and PITX2 (labeling the POM and EOM anlage) on E11.75 embryos (left eye). Lateral and medial views as schemes. (E) Whole-mount LysoTracker Red (LysoR) staining of the periocular region at the indicated stages (left eye). The POM is delimited with dashed lines. Asterisks indicate apoptotic foci with reduced intensity from E12.5 onwards. anl, anlage; a, anterior; d, dorsal; 3D-rec, 3D reconstruction; E, embryonic day; i, inferior EOM anlage projection; io, inferior oblique; ir, inferior rectus; l, lateral; lg, lacrimal gland sulcus; lr, lateral rectus; m, medial; m-pom, medial periocular mesenchyme; mr, medial rectus; p, posterior; pom, periocular mesenchyme; pom-r, periocular mesenchyme ring; rb, retractor bulbi; s, superior EOM anlage projection; so, superior oblique; sr, superior rectus; v, ventral; WMIF, whole-mount immunofluorescence.

<https://doi.org/10.1371/journal.pbio.3000902.g002>

conclude that EOM patterning in the mouse occurs by splitting from a single mass of myogenic progenitors that target the eyeball, with the most dramatic morphogenetic changes taking place between E11.75 and E12.5.

The EOMs insert into the sclera, a dense fibrous layer derived from the POM [40,44]. PITX2 is a well-established marker of both the POM and EOM progenitors ([40], S2A–S2C Fig), and foci of cell death in the POM were suggested to label the tendon attachment positions of the 4 recti muscles [51]. To better understand the development of the EOM insertions, we first performed whole-mount immunostaining for the POM marker PITX2 and LysoTracker Red staining to detect programmed cell death on live embryos [52]. WMIF for PITX2 at E11.75 revealed a ring of POM cells expressing high levels of PITX2 that formed a continuum with low-expressing cells extending towards the base of the EOM anlage (Fig 2D and S2 Video). The pattern of LysoTracker Red staining in the POM-ring was highly dynamic, where 4 foci of apoptosis were present at E11.75 at the horizons of the eye but regressed progressively from E12.5 onwards (Fig 2E). To confirm that these foci define tendon attachment positions in the POM, we performed whole-mount immunostaining for myogenic and tendon progenitors on LysoTracker-stained embryos. Surprisingly, we observed that even before muscle splitting initiated, *Scx-GFP*<sup>+</sup> condensations bridged the edges of the EOM anlage and the 4 LysoTracker Red<sup>+</sup> foci in the POM (E11.75, S3 Video), presaging the attachment sites of the future 4 recti muscles (E12.5, S4 Video).

We next wanted to understand the relationship between foci of apoptosis in the POM and the establishment of the tendon insertion sites per se. In the developing limb and jaw, bone superstructures or ridges, generated by a unique set of progenitors that co-express *Scx* and

SRY-box containing gene 9 (SOX9), provide a stable anchoring point for muscles via tendons [53–56]. Although EOMs insert into a non-bone NCC-derived structure, early markers of pre-committed cartilage, such as SOX9, are expressed in the POM [57]. To examine the time course of development of EOM insertions in greater detail, we immunostained *Tg:Scx-GFP* and *Tg:Wnt1<sup>Cre</sup>;R26<sup>Tom</sup>;Scx-GFP* coronal (Fig 3A–3J” and S3A–S3F” Fig) and transverse (S3G–S3H” Fig) sections for PITX2 and SOX9. Between E11.5 and E13.5, PITX2 marked all cells of the lateral-most NCC-derived POM between the surface ectoderm and retina (Fig 3B and 3F, and S2A–S2B” Fig), which corresponds to the POM-ring observed in 3D views (Fig 2D). In this region, *Scx-GFP* expression was initially detected in a salt-and-pepper pattern (Fig 3C and S3E Fig) but became progressively limited to the forming tendon tips (Fig 3G and S3F Fig). SOX9 expression overlapped with that of PITX2 (Fig 3D, 3H, S3E’ and S3F’ Fig) but became more restricted to the insertion site by E13.5 and with a pattern complementary to *Scx-GFP*+ (Fig 3G and S3F Fig). Notably, *Scx-GFP*+ SOX9+ cells could be detected between E11.5 and E13.5 at the interface between mutually exclusive *Scx-GFP*+ and SOX9+ cells (S3A–S3C” Fig), resembling what was observed during tendon-to-bone attachment formation in other regions in the embryo [53–56].

At the putative insertion site, the tdTomato staining in the NCC-derived lateral POM initially appeared as punctate (Fig 3A), and reminiscent of the apoptotic domains observed in 3D views (Fig 2E). LysoTracker Red and TUNEL staining confirmed cell death of SOX9+ PITX2 + POM cells (Fig 3I–3J””, S3E, S3E’ and S3G–S3H” Fig) that were at a higher density than the more medial POM cells (Fig 3K, S1 Data). Given that LysoTracker Red+ cells could not longer be seen at E13.5 (S3F and S3F’ Fig), these data suggest that at the insertion sites of the recti muscles in the POM, foci of apoptosis mark the places where cell compaction and refinement of the SOX9 expression pattern will take place.

Major POM remodeling events could be detected by E14.5. EOM tendons co-expressed *Scx-GFP*, Tenascin, and PITX2, but surprisingly, SOX9 expression became restricted to the thin scleral layer and retinal pigmented epithelium (RPE) (Fig 3L–N’ and S3D–S3D” Fig). Altogether, these results show that development of the EOMs, their tendons and insertion sites overlap spatiotemporally and thus, might be regulated in a coordinated manner. Moreover, similarly to other locations in the body, *Scx* and SOX9 show dynamic expression patterns at the insertion site, but additional specific hallmarks, notably the presence of cell compaction and apoptotic foci, seem to be characteristic of this anatomical location.

### Abnormal EOM morphogenesis in mutants with ocular malformations

Having assessed how morphogenesis of EOMs and their insertion sites is coordinated, we set out to investigate the role of the target organ, the eyeball, on the establishment of the EOM functional unit. To this end, we performed micro-computed tomography (micro-CT) scans in mouse mutants with a spectrum of ocular perturbations. First, we examined *small eye* (Sey) *Pax6* (Paired box 6) mutant embryos (*Pax6<sup>Sey/Sey</sup>*), in which eye development is arrested at the optic vesicle stage [58–60]. EOM patterning in *Pax6<sup>Sey/+</sup>* embryos proceeded normally (S4A and S4B Fig), whereas in the *Pax6<sup>Sey/Sey</sup>* mutant, the EOMs appeared as a single mass on top of a rudimentary optic vesicle (S4C Fig). As *Pax6* is expressed in the optic vesicle and overlying ectoderm that forms the lens and cornea [58], but not in EOMs, these observations suggest a non-cell-autonomous role in EOM patterning. Similarly, in LIM homeobox 2 (*Lhx2*) mutant embryos (*Tg:Lhx2<sup>Cre</sup>;Lhx2<sup>fl/fl</sup>*) embryos, in which inactivation of the *Lhx2* gene in eye committed progenitor cells leads to a degeneration of the optic vesicle at E11.5 [61], EOM patterning was severely affected, and few EOM submasses were observed (S4D–S4E’ Fig). Finally, in cyclopic embryos resulting from inversion of Sonic hedgehog (Shh) regulatory regions, EOMs

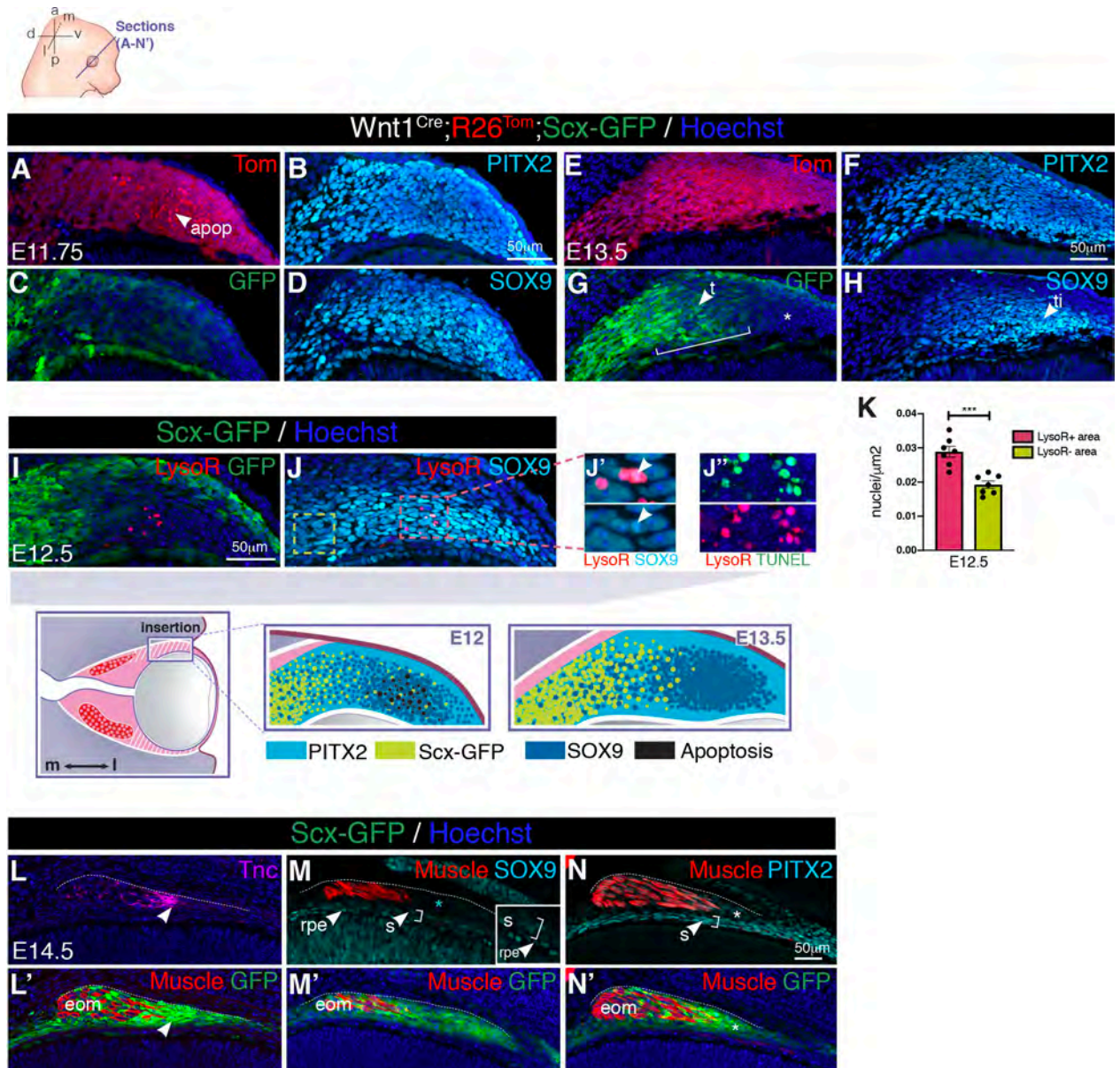


**Fig 3. Developmental time course of EOM insertions in the POM.** (A-D) Immunostaining of lateral POM in coronal sections of E11.75 *Tg:Wnt1<sup>Cre</sup>;R26<sup>Tom</sup>;Scx-GFP* embryos for the indicated markers. B, Immunostaining of section adjacent to the one shown in (A, C, D; channels split for clarity). (E-H) Immunostaining of lateral POM in coronal sections of E13.5 *Tg:Wnt1<sup>Cre</sup>;R26<sup>Tom</sup>;Scx-GFP* embryos for the indicated markers. G, Immunostaining of section adjacent to the one shown in (E, F, H; channels split for clarity). Bracket show overlap between *Scx-GFP* and *SOX9* expression domains (high-magnification views in *S3C* Fig). The asterisk in G points to *Scx-GFP*-negative *SOX9*+ lateral-most POM at the insertion site. (I,J) Immunostaining of lateral POM in coronal sections of E12.5 *Tg:Scx-GFP* embryos pretreated with LysoR. Arrowheads in J' point to LysoR + *SOX9*+ cells. (J'') TUNEL and LysoR staining of a section adjacent to the one shown in (I,J). (K) Quantification of the total number of *SOX9*+ cells per square-micrometer in LysoR+ regions (red square, J) and more medial LysoR-negative regions (yellow square, J). Mann-Whitney test. Cell density was 33% higher in the LysoR+ area compared with the more medial POM. See *S1 Data* for individual values. (L-N') Immunostaining on coronal sections of E14.5 *Tg:Scx-GFP* embryos. (L,L') *Tnc* and *Scx-GFP* co-localize in tendons at level of insertion (arrowhead). (M,M') *SOX9* expression in the POM is greatly reduced at the insertion site and no longer overlaps with *Scx-GFP* (asterisk, cyan). Low levels of *SOX9* expression in the RPE and sclera. (N,N') *PITX2* remains expressed in the POM at the insertion site overlapping with *Scx-GFP* (asterisk) and in the sclera. MyHC (L') and SMA (M-N') were used to label EOM muscle. Dashes in L-N were drawn according to GFP labeling in L'-N'. Images in A-N' correspond to insertion site of superior rectus muscle in the POM as shown in the scheme. (*n* = 3 per condition). a, anterior; apop, apoptosis spots; d, dorsal; E, embryonic day; eom, extraocular muscle; l, lateral; LysoR, LysoTracker Red; m, medial; p, posterior; POM, periorcular mesenchyme; rpe, retinal pigmented epithelium; s, sclera; t, tendon; ti, tendon insertion, v, ventral.

<https://doi.org/10.1371/journal.pbio.3000902.g003>

underwent splitting and projected towards the centrally located ectopic eye, although with an abnormal 3D arrangement as reported for human cyclopia conditions (S4F–S4F” Fig) [7]. Together with previous studies in which surgical removal of the eye at specific timepoints of development results in smaller EOMs [9,62], our observations point to the eye as a critical organizer of EOM patterning.

### Muscle patterning depends on retinoic acid signaling of neural origin

To study the role of target organ derived cues in EOM patterning, we investigated the role of retinoic acid signaling, which plays multiple paracrine roles during embryonic eye development [33]. As ALDH1A1-3 are rate-limiting enzymes in the production of ATRA [63], we characterized their expression in the periocular region at the time of EOM patterning. Between E10.5 and E12.5, *Aldh1a1* was expressed strongly in the dorsal retina and lens, *Aldh1a2* was expressed in the temporal mesenchyme, and *Aldh1a3* was most strongly expressed in the ventral retina and RPE (S5A–S5A” Fig) [34,36]. At the protein level, ALDH1A3 was detected on tissue sections in the surface ectoderm, presumptive corneal epithelium, retina, and RPE (Fig 4A). Interestingly, ALDH1A3 was also expressed in the optic stalk between E10.5 and E12.5 and thus centrally positioned with respect to EOM development (Fig 4A). To target the retinoic signaling pathway (Fig 4B), we used *Aldh1a3*<sup>-/-</sup> [64] and *Rdh10*<sup>-/-</sup> [65] mutants. We also administered the BMS493 inhibitor (pan-RAR inverse agonist) to pregnant females every 10–12 hours between E10.5 and E11.75, i.e., preceding the initiation of muscle splitting (Fig 2A–2C), and once NCC migration to the POM was finalized [66,67]. Micro-CT analysis showed that *Aldh1a3*<sup>-/-</sup> and BMS493-treated embryos displayed eye ventralization and a shortened optic nerve when compared with controls (S5B Fig), but they retained the overall organization of the nasal capsule and orbit (S5C Fig). Ventral and lateral views of the 3D-reconstructed EOMs (Fig 4C–4E), showed that *Aldh1a3*<sup>-/-</sup> and BMS493-treated embryos lacked the standard 3D arrangement of 4 recti and 2 oblique muscles observed at E13.5 in control embryos. Nevertheless, in all cases, EOMs originated medially from the hypochiasmatic cartilages of the pre-sphenoid bone, indicating that the overall orientation of the EOMs was preserved (Fig 4D”). Given that the EOMs are more affected at their insertion than their origin level upon ATRA deficiency, this finding suggests that EOM patterning is, in part, modular.

To analyze EOM and tendon patterning with higher resolution, we performed whole-mount immunostainings for differentiated myofibers and tendon with MyHC and Tnc (Tenascin) antibodies (Fig 4F–4H”). On medial and lateral views of 3D-reconstructed EOMs, only the retractor bulbi and superior rectus could be clearly identified among the non-segregated muscle fibers in *Aldh1a3*<sup>-/-</sup> embryos (Fig 4G and 4G”). As expected from global invalidation of retinoic acid signaling, EOM perturbation was more severe in BMS493-treated embryos (Fig 4H and 4H”). The superior oblique was absent or continuous with the anterior part of the anlage, and the medial portion of the retractor bulbi was thicker and less clearly isolated from the rest of the anlage (Fig 4H). In both conditions of ATRA deficiency, Tenascin and *Scx*-GFP+ cells were present at the tips of the individual, though mispatterned, muscles at this stage (Fig 4G’, 4H’, and S5 Video). Analysis of *Aldh1a3*<sup>-/-</sup> and BMS493-treated embryos revealed, on average, a 26% reduction in the EOM volume compared with controls (Fig 4I, S2 Data). However, MyHC+ myofibers were present in *Aldh1a3*<sup>-/-</sup> and BMS493-treated embryos (Fig 4G and 4H), suggesting that EOM differentiation was not overtly affected in these conditions. Instead, these observations suggest that EOM fiber alignment and segregation of the muscle masses are dependent on retinoic acid signaling.

As dose and temporal control are critical in the context of retinoic acid signaling [27,32,68], we performed other BMS493 injection regimes between E10.5 and E12.5 (S1 Table). EOM

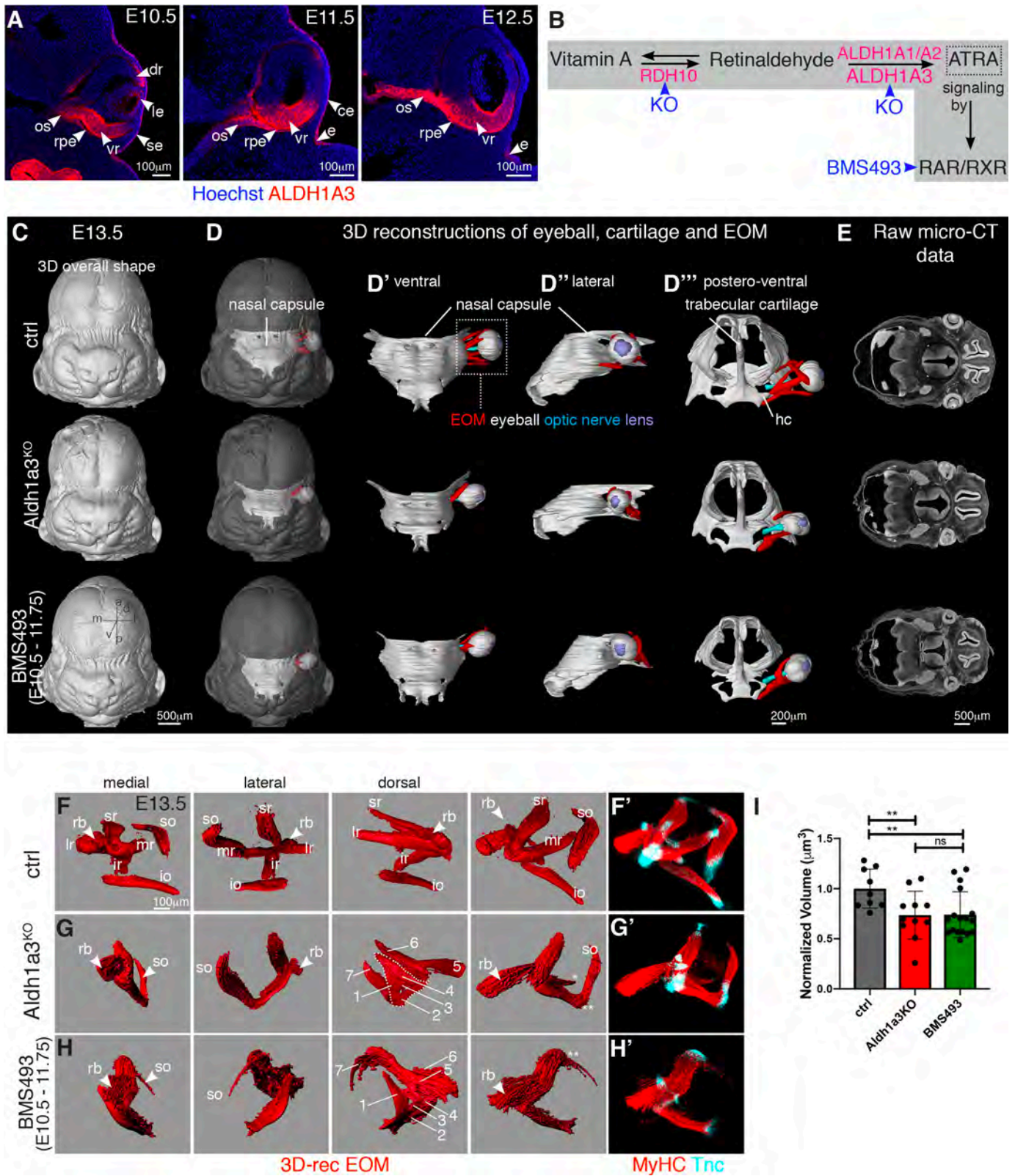


**Fig 4. Extraocular muscle morphogenesis is dependent on ATRA.** (A) Immunostaining for ALDH1A3 on coronal sections of E10.5, E11.5, and E12.5 control embryos ( $n = 3$ ). (B) Scheme of retinoic acid signaling pathway with key enzymes for oxidation of retinol (Vitamin A) and retinaldehyde (pink) and mutants/inhibitors used in this study (blue). (C-D''') Micro-CT-based 3D-reconstruction of chondrogenic mesenchymal condensations of nasal capsule, trabecular

cartilage, EOM, eyeball, optic nerve, and lens in E13.5 control, *Aldh1a3*<sup>KO</sup> and BMS493-treated embryos. EOM visualization in context of whole head (D), nasal capsule (D'-D''), trabecular cartilage (D'''). (E) Raw micro-CT data ( $n = 2$ ). (F-H) 3D-reconstructions of WMIF for MyHC of E13.5 control (F), *Aldh1a3*<sup>KO</sup> (G) and BMS493-treated embryos (H) ( $n > 9$ ). EOMs were segmented from adjacent head structures and 3D-reconstructed in Imaris (Bitplane). EOMs are shown as isosurfaces for clarity of visualization. (1-7) denote non-segregated muscle masses with differential fiber orientation (see also S5D Fig). Raw immunostaining data for MyHC (myofibers) and Tnc (tendon) are shown in panels F'-H'. Double asterisk in G,H indicate fused muscle masses. Asterisk in G indicate misoriented medial rectus. (I) Relative EOM volume (compared with control) of WMIF in F-H. Each dot represents an individual embryo ( $n > 9$ ). Mann-Whitney test. See S2 Data for individual values. a, anterior; ATRA, all-trans retinoic acid; ce, presumptive corneal epithelium; ctrl, control; d, dorsal; dr, dorsal retina; 3D-rec, 3D-reconstruction; e, eyelid groove; E, embryonic day; EOM, extraocular muscle; hc, hypochiasmatic cartilage; io, inferior oblique; ir, inferior rectus; l, lateral; le, lens; lr, lateral rectus; m, medial; mr, medial rectus; micro-CT, micro computed tomography; os, optic stalk; p, posterior; rb, retractor bulbi; rpe, retinal pigmented epithelium; RAR, retinoic acid receptor; RXR, retinoid X receptor; se, surface ectoderm; so, superior oblique; sr, superior rectus; v, ventral; vr, ventral retina.

<https://doi.org/10.1371/journal.pbio.3000902.g004>

patterning phenotypes categorized as strong or severe at E13.5 were only obtained when an E10.75 time point of injection (8 PM of day E10.5) was included in the regime (experiment type I-III, S1 Table, and S5D Fig). Surprisingly, even a single injection at this time point resulted in strong phenotypes (experiment type IV, S1 Table, and S5D Fig), whereas exclusion of this time point (experiment type V, S1 Table, and S5D Fig) resulted in only mild phenotypes at best. Therefore, we identified an early and restricted temporal window in which ATRA activity, prior to any sign of muscle splitting, impacts correct muscle patterning 36–48 hours later. Given the critical action of RDH10 in generating retinaldehyde, the intermediate metabolite in the biosynthesis of ATRA, we examined EOM development in *Rdh10* mutant embryos. *Rdh10* is normally expressed in the optic vesicle and RPE [69], and in *Rdh10*<sup>-/-</sup> embryos, eyes develop intracranially, close to the diencephalon with a very short ventral retina [65]. WMIF analysis of *Rdh10* mutant EOMs revealed that the anlage was specified but lacked any sign of segmentation, in agreement with an upstream role in ATRA synthesis (S5E and S5F Fig). Taken together, our data show that retinoic acid signaling is essential for the correct myofiber alignment and segregation of EOM masses in a dose- and time dependent manner.

### ATRA-responsive cells drive muscle patterning in the periocular mesenchyme

In all body regions, muscle connective tissue plays a central role in muscle patterning [22]. Moreover, this process appears to be tightly coupled to development of tendons and tendon attachment sites [15,70–72]. To determine whether the role of retinoic acid signaling in EOM patterning is direct in myogenic cells or indirect, through action in adjacent connective tissues, we tracked cells that are responsive to ATRA using a novel retinoic acid transgenic Cre reporter line [73]. This transgenic line comprises 3 retinoic acid response elements (*RARE*) from the *Rarb* gene fused to the *Hspa1b* minimal promoter driving expression of a tamoxifen-inducible *Cre-ERT2* recombinase (*Tg:RARE-Hspa1b-Cre/ERT2*, designated as *Tg:RARE-CreERT2* for simplicity). By crossing this line with the *R26*<sup>mTmG</sup> or *R26*<sup>Tom</sup> reporter mice [74,75] (Fig 5A), we permanently labeled ATRA-responsive cells and their descendants with membrane-tagged GFP or tdTomato. Different tamoxifen regimes showed that a greater number of responsive cells were present in the periocular region when tamoxifen was administered between E9.75–E10.5 (S6A–S6C Fig). This finding is in agreement with BMS493 treatments identifying E10.75 as a critical time point for the action of ATRA (S1 Table and S5D Fig) and the fact that maximal recombination efficiency can be achieved between 12–24 hours upon tamoxifen induction [76,77].

To assess whether myogenic cells and adjacent POM cells respond to retinoic acid signaling, we microdissected the periocular region of *Tg:RARE-CreERT2;R26*<sup>mTmG</sup> embryos and subjected it to mild digestion in bulk. Cells were allowed to attach to culture dishes, immunostained, and scored for co-expression of GFP and myogenic markers (MYOD, MYOG). Notably, the great majority of reporter positive-responsive cells were not myogenic (Fig 5B and 5C,

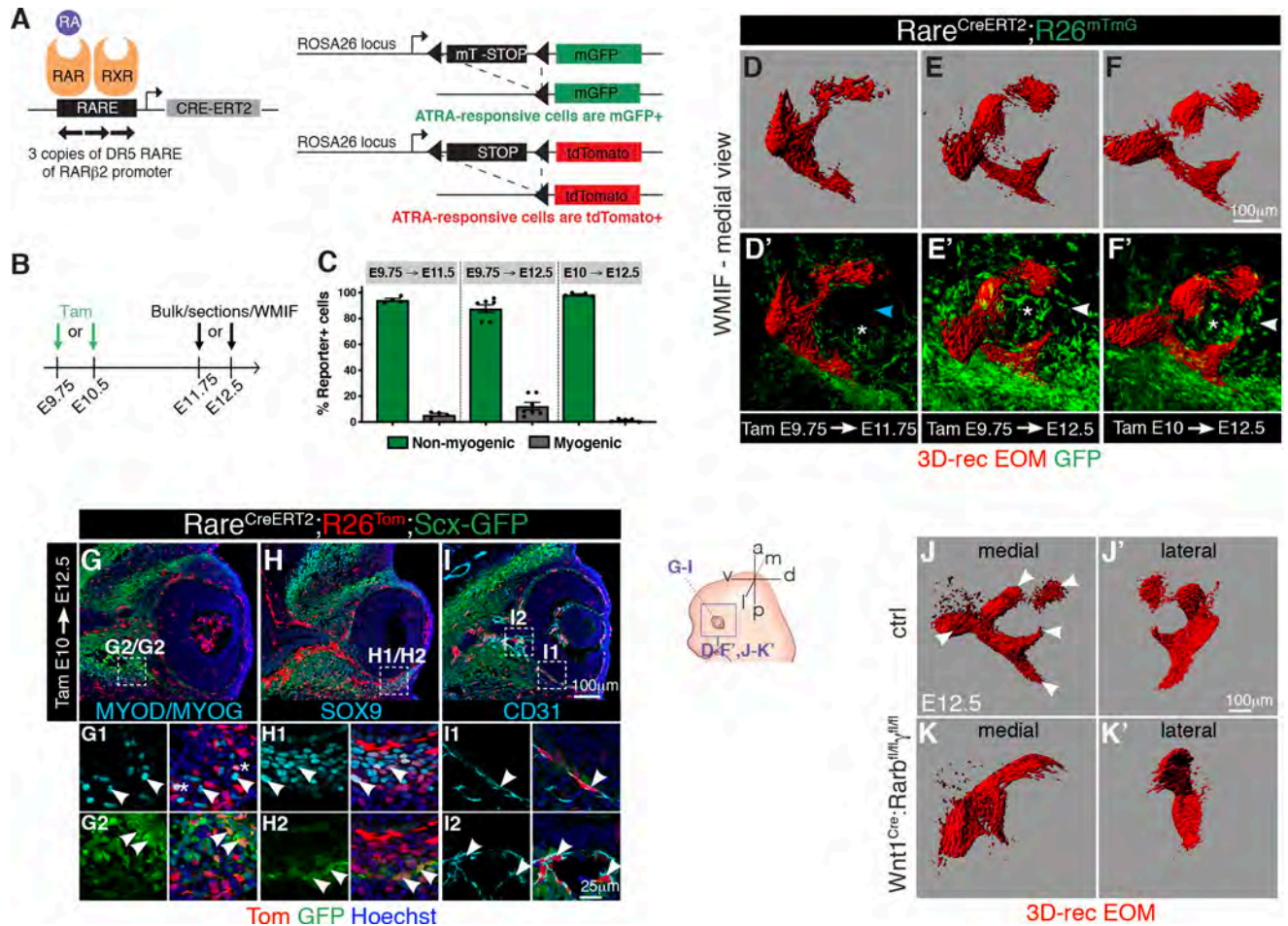


**Fig 5. Periocular connective tissues are responsive to retinoic acid signaling.** (A) Scheme of mouse alleles used. (B) Strategy used to determine cell types responsive to retinoic acid signaling in *Tg:RARE-CreERT2;R26<sup>mTmG</sup>* embryos. Tamoxifen was injected to pregnant females at E9.75 or E10.5 and analysis performed (bulk, sections or WMIF) at E11.75 or E12.5. (C) The percentage of recombined (GFP+) cells within the non-myogenic or myogenic populations (PAX7+, MYOD+, MYOG+) was assessed by immunostaining on bulk cell preparations of the periocular region of *Tg:RARE-CreERT2;R26<sup>mTmG</sup>* embryos following different tamoxifen treatments. Each dot represents an individual embryo (*n* > 4 embryos/condition). See [S3 Data](#) for individual values. (D-F) WMIF of *Tg:RARE-CreERT2;R26<sup>mTmG</sup>* embryos for SMA (differentiated muscle) and GFP (ATRA-responsive cells) at the indicated embryonic stages. The number of reporter positive cells at the place where the developing medial rectus muscle will project increases from E11.75 (blue arrowhead) to E12 (white arrowheads). Asterisks mark the optic nerve (*n* = 3). (G-I) Coronal sections of E12.5 *Tg:RARE-CreERT2;R26<sup>mTmG</sup>;Scx-GFP* embryos immunostained for GFP, Tom (ATRA-responsive cells), MYOD/MYOG (muscle), and CD31 (endothelial cells). Higher-magnification views as insets. Asterisks in G1 indicate sporadic labeling in myogenic cells (*n* = 3). (J-K') WMIF for MyHC (myofibers) of E12.5 control (*Tg:Wnt1Cre;Rarb<sup>fl/+</sup>;Rarg<sup>fl/+</sup>*) and mutant (*Tg:Wnt1Cre;Rarb<sup>fl/fl</sup>;Rarg<sup>fl/fl</sup>*) EOM. Medial and lateral views are shown. Note absence of splitting in mutant EOM. Arrowheads indicate split EOM in controls (*n* = 2 per genotype). In D-F' and J-K' EOMs were segmented from adjacent head structures and 3D-reconstructed in Imaris (Bitplane). EOMs are shown as isosurfaces for clarity of visualization. a, anterior; ATRA or RA, all trans retinoic acid; ctrl, control; d, dorsal; 3D-rec, 3D-reconstruction; E, embryonic day; EOM, extraocular muscle; l, lateral; m, medial; mGFP, membrane-tagged GFP; p, posterior; RAR, retinoic acid receptor; RXR, retinoid X receptor; SMA, alpha smooth muscle actin; Tam, Tamoxifen; v, ventral; WMIF, whole-mount immunofluorescence.

<https://doi.org/10.1371/journal.pbio.3000902.g005>

S6D Fig and [S3 Data](#)). We next performed immunostaining in whole-mount to assess the spatial distribution of ATRA-responsive cells in periocular connective tissues ([Fig 5D–5F'](#)). This analysis revealed that the mesenchyme around the optic nerve in close proximity to the developing EOMs was positive for the reporter. Interestingly, the number of POM GFP+ cells increased from E11.75 to E12 ([Fig 5D'–5F'](#)), which is the temporal window corresponding to EOM splitting ([Fig 2A and 2B](#)). Inactivation of downstream retinoic acid signaling with BMS493, prior and subsequent to the induction of *Tg:RARE-CreERT2;R26<sup>mTmG</sup>* mice with

tamoxifen (S6E Fig), greatly reduced the responsiveness of the reporter in the POM compared with non-treated controls (S6F–S6I Fig, S6 and S7 Videos).

As with experiments on isolated cells, the great majority of tdTomato positive-responsive cells on tissue sections of *Tg:RARE-CreERT2;R26<sup>Tom</sup>* embryos were not myogenic at ventral (Fig 5G) and dorsal levels (S6J Fig). tdTomato positive-responsive cells co-expressed *Scx-GFP* (Fig 5G and 5H), Sox9 (Fig 5H) or the endothelial cell marker CD31 along the choroid (vascular layer of the eye) and ciliary arteries around the optic nerve (Fig 5I). Together, these results are in agreement with previous studies [34–36] showing that despite a sophisticated pattern of ATRA metabolism in the developing retina, retinoic acid signaling exerts its action mostly non-cell autonomously. We show that ATRA targets various connective tissue types of the POM within a temporal window that is crucial for EOM patterning.

As ATRA-responsive cells were found in NCC- (ventral POM) and mesoderm-derived cell compartments (dorsal POM, choroid, and a fraction of myogenic progenitors), we performed more selective perturbations of retinoic acid signaling with available genetic tools. Expression of a dominant negative nuclear retinoid receptor isoform in myogenic cells (*Myod<sup>fCre</sup>; R26<sup>RAR403</sup>*, [78,79]) did not result in noticeable EOM patterning defects (S6K–S6L' Fig). We then inactivated the RAR $\beta$  and RAR $\gamma$  receptors in the NCC-derived POM, which respond to ATRA synthesized by the retina [80,81], using the *Tg:Wnt1<sup>Cre</sup>* driver (*Tg:Wnt1<sup>Cre</sup>;Rarb<sup>fl/fl</sup>; Rarg<sup>fl/fl</sup>*, [35]). WMIF for muscle in *Tg:Wnt1<sup>Cre</sup>;Rarb<sup>fl/fl</sup>;Rarg<sup>fl/fl</sup>* embryos showed absence of muscle splitting (Fig 5J–5K'), and this was as severe as that observed in fully ATRA-deficient *Rdh10<sup>-/-</sup>* embryos (S5F Fig). Altogether, these data suggest that synthesis of ATRA from neural derivatives (retina, optic nerve, RPE) is crucial for EOM patterning, through its action on NCC-derived periocular connective tissues at earlier stages.

## Defective organization of EOM insertions in embryos deficient in retinoic acid signaling

Having addressed a major role of ATRA in NCC-derived cells of the POM for EOM patterning, we set out to assess which specific connective tissue subpopulations, including the EOM insertions in the POM, were affected in *Aldh1a3<sup>-/-</sup>* and BMS493-treated embryos. First, we examined the distribution of Collagen XII (Fig 6A–6C'), a marker of the sclera and corneal stroma [82], on tissue sections at E12. We observed a marked reduction of Collagen XII (Col XII) at the level of the medial-POM that gives rise to the sclera, upon ATRA deficiency (Fig 6B–6C'). In addition, although PITX2 was expressed continuously in the entire POM and corneal stroma in controls (Fig 6D and 6D'), expression in the medial-POM was selectively lost upon ATRA deficiency (Fig 6E–6F'). This observation is in agreement with *Pitx2* being a retinoic acid signaling target in the NCC-derived POM [34–36] and the sclera being absent at fetal stages in *Rarb/Rarg*-NCC mutants [35]. Interestingly, POM organization was unaffected in *Myf5<sup>nlacZ/nlacZ</sup>* mutants (Fig 6G and 6G'), in which the initial EOM anlage forms but myogenesis is aborted from E11.5 [83].

To understand whether the abnormal distribution of POM markers translates into EOM insertion defects and how EOM development and insertion sites are coordinated, we examined the organization of the POM-ring in control, *Aldh1a3<sup>-/-</sup>*, and BMS493-treated embryos. We systematically compared E11.75 and E12 embryos to visualize the organization of these tissues prior to and during muscle splitting (Fig 6H–6P and S7A–S7N Fig). Control embryos showed the presence of overlapping SOX9 and PITX2 POM-ring domains, together with 4 foci of apoptosis labeling the prospective tendon attachment points of the 4 recti muscles (Fig 6H–6J, S7A–S7C', S7E and S7F Fig). As expected, ATRA deficiency perturbed these patterns in a dose-dependent manner. At the level of the POM-ring, *Aldh1a3<sup>-/-</sup>* embryo heads displayed

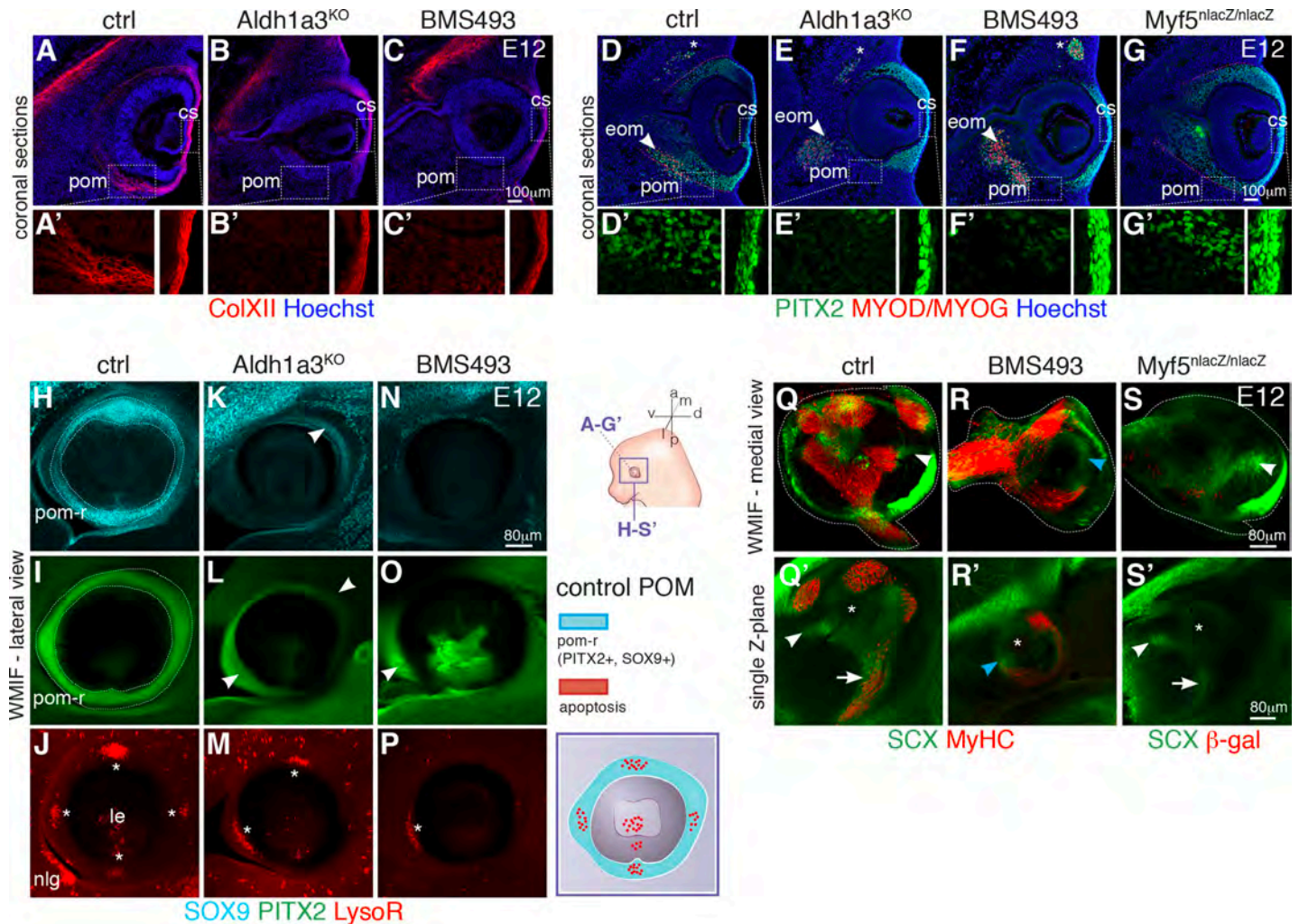


**Fig 6. Altered EOM insertions in the POM upon ATRA deficiency.** (A-C') Immunostaining for ColXII on E12 coronal sections. ColXII expression is lost in the medial POM (future sclera) but not in the corneal stroma of *Aldh1a3*<sup>KO</sup> (B,B') and BMS493-treated embryos (C,C'). Higher magnification of ColXII staining as insets in (A'-C'). (D-G) Immunostaining for PITX2 (muscle progenitors, POM) and MYOD/MYOG (myogenic cells) on E12 coronal sections. Asterisks indicate superior oblique muscle. Red dashed lines delimitate the POM in controls (D) and *Myf5*<sup>nlacZ/nlacZ</sup> (G) embryos. Higher magnification of PITX2 staining as insets in (D'-G'). Note absence of PITX2 expression in medial-POM of *Aldh1a3*<sup>KO</sup> (E,E') and BMS493-treated embryos (F,F'). (H-P) WMIF for SOX9 and PITX2 of E12 control (H-J), *Aldh1a3*<sup>KO</sup> (K-M) and BMS493-treated (N-P) embryos preincubated with LysoR (left eyes). *Aldh1a3*<sup>KO</sup> and BMS493 embryos do not show a complete POM-ring as controls (dashed lines in H,I). Arrowheads mark remaining expression of SOX9/PITX2 in the POM of *Aldh1a3*<sup>KO</sup> (K,L) or inhibitor-treated (O) embryos. Asterisks in (J, M, P) mark apoptosis spots in POM. (Q-R) WMIF for MyHC (myofibers) and GFP on E12 control (Q) and BMS493-treated *Tg:Scx-GFP* embryos (R). WMIF for  $\beta$ -gal (myogenic progenitors) and GFP on E12 *Tg:Scx-GFP;Myf5*<sup>nlacZ/nlacZ</sup> E12 embryos (S) (left eyes). The periocular area was segmented from adjacent structures for ease on visualization (dashed lines). White arrowheads in Q and S highlight correct position of tendon condensations for medial rectus muscle. Blue arrowhead in R marks a diffuse *Scx-GFP*+ pattern at the position of the mispatterned medial rectus muscle. (Q'-S') Single Z-section of the segmented volume. White arrowheads in Q',S' show tendon tips and white arrows correct *Scx-GFP*+ connective tissue pattern along with muscle (Q') or prospective muscle masses (S'). Blue arrowhead in R' marks a *Scx-GFP*+ condensation at the muscle tip. Asterisks mark position of the optic nerve. (*n* = 3 per condition). a, anterior; ATRA, all-trans retinoic acid; cs, corneal stroma; ctrl, control; d, dorsal; eom, extraocular muscles; l, lateral; le, lens; LysoR, LysoTracker red; m, medial; nlg, nasolacrimal gland; p, posterior; pom, periocular mesenchyme; pom-r, periocular mesenchyme ring; v, ventral; WMIF, whole-mount immunofluorescence.

<https://doi.org/10.1371/journal.pbio.3000902.g006>

narrower SOX9 and PITX2 expression domains than controls (Fig 6K–6L, S7G and S7H Fig). In BMS493-treated embryos, expression of these genes in the POM-ring (Fig 6N, 6O, S7D, S7D', S7I and S7J Fig) was further reduced to a minority of cells. Accordingly, foci of apoptosis were lost or disorganized in both cases of ATRA deficiency with a single LysoTracker Red spot almost invariably present in the ventral POM in both conditions (Fig 6M, 6P, S7H and S7J Fig). In medial views of reconstructed 3D volumes, PITX2 showed continuous expression

from the POM-ring to the medial-POM in control embryos (Fig 2D, S7K Fig and S2 Video), whereas we noticed loss of PITX2 expression in both cases of ATRA deficiency (S7M and S7N Fig, blue arrowheads) as observed on tissue sections (Fig 6E' and 6F'). Consistent with these results, the *Tg:RARE-CreERT2;R26<sup>mTmG</sup>* reporter showed a marked reduction of ATRA-responsive cells in the medial POM and POM-ring of *Aldh1a3<sup>-/-</sup>* and BMS493-treated embryos when compared with controls (S7O–S7Q' Fig and S8–S10 Videos). Thus, as seen in other body regions, where development of muscles and bone superstructures into which they insert are tightly coordinated [70], the development of the EOMs is tightly coupled to development of their insertion sites in the soft tissues of the POM.

As tendons were present at muscle tips in E13.5 *Aldh1a3<sup>-/-</sup>* and BMS493-treated embryos but located ectopically with respect to a wild-type configuration (Fig 4F'–4J'), we suspected that the initial 3D organization of *Scx-GFP+* tendon and connective tissue progenitors might also be affected. We performed WMIF for differentiated muscle (MyHC) and tendon progenitors (*Tg:Scx-GFP*) and segmented the reconstructed 3D volume. In control embryos at E12.5, *Scx-GFP+* condensations projected from the tips of the future 4 recti muscles toward the POM-ring (Fig 6Q and S11 Video), facing the 4 foci of apoptosis (Fig 6J and S4 Video). Moreover, as observed in tissue sections (Fig 1A1, 1D1, and S1G–S1H' Fig), *Scx-GFP+* and TCF4+ cells were also present in POM connective tissues presaging the final locales of the recti muscles (Fig 6Q' and S7R Fig). In BMS493-treated embryos at E12, *Scx-GFP* and TCF4 expression were less organized and diffuse (Fig 6R and 6R', and S7S Fig), yet *Scx-GFP+* condensations started to form at the tips of ectopic muscle masses (Fig 6R' and S12 Video). Altogether, these results show that ATRA is required for the proper specification/organization of NCC-derived POM connective tissues, which includes the muscle connective tissue, tendons, and their insertion sites.

In stark contrast with what we observed upon ATRA deficiency, *Scx-GFP* and TCF4 patterning in POM connective tissues was preserved in muscle-less *Myf5<sup>nlacZ/nlacZ</sup>* mutants (Fig 6S and 6S', and S7T Fig). Moreover, *Scx-GFP+* tendon condensations formed at the tips of prospective (albeit absent) recti muscles (Fig 6S and 6S'). This situation is similar to the specification of individual tendons on muscle-less limbs [20,84] and branchial arches [41]. However, at later stages, tendons did not continue their maturation in the absence of EOMs (S7V and S7V' Fig, S13 and S14 Videos), reinforcing the notion that, as in most other anatomical locations [2], tendon differentiation and maintenance ultimately rely on muscle–tendon interactions.

In summary, ATRA produced by the developing eye influences the organization of the entire NCC-derived POM, allowing integration of these tissues into a musculoskeletal functional unit (S8 Fig).

## Discussion

The striking differences in embryological origins, function, and susceptibility to disease among cranial and somite-derived muscles [26] provides impetus to study in detail the morphogenesis of different muscle groups and their integration as part of the musculoskeletal system. Here, we focused on EOMs, an evolutionary conserved group of muscles that are precisely engineered for fine displacement of the eyeball and thus, crucial for visual acuity. Using genetic and 3D imaging approaches, we analyzed EOM development from their emergence as a unique anlage to the establishment of a fully formed functional unit with insertions in the sclera, which sets it apart from classical muscle-to-bone insertions studied to date. We identified a spatiotemporal window in which retinoic acid signaling from the target organ is required for patterning of NCC-derived soft tissues of the POM. These findings provide insights into the deployment of site-specific programs for the establishment of anatomically

distinct muscle functional units, with precise definition of muscle shapes and topographical wiring of their tendon attachments.

### Dual origin of EOM insertions

The connective tissues of the rostral cranium (bone, cartilage, tendon, and muscle connective tissue) were reported to be derived from the neural crest [3,7,8]. However, the hypochiasmatic cartilages, from which the recti muscles originate in mammals, are an exception to this rule as they are mesoderm derived [85]. Here, we found that at this location, tendon and muscle connective tissue are also of mesodermal origin. As such, EOMs originate in mesoderm-derived bone and insert in NCC-derived fibrous tissue of the sclera with muscle connective tissue following the embryonic origins of the respective attachments, as observed in other anatomical locations [86]. Taken together, our observations redefine a novel boundary for NCC contribution to the connective tissues of the periocular region and suggest that at their origin in the base of the skull, the EOMs and their associated connective tissues might have evolved neomorphically in situ from the same mesodermal source.

### RA responsiveness on the POM

Previous studies showed that NCCs have a critical role in the acquisition of cranial muscle morphology [9,13–16]. Our data using the *Tg:RARE-CreERT2* reporter and following invalidation of *Rarb/Rarg* in NCC derivatives suggest that the action of retinoic acid signaling on EOM patterning is also indirect, through its action on periocular connective tissues.

The observation that BMS493 treatments to impair ATRA signaling results in a more severe phenotype than that observed in *Aldh1a3* mutants could have several explanations. First, BMS493 is not a RAR antagonist but pan-RAR inverse agonist, which is capable of repressing RAR basal activity by favoring the recruitment of corepressors and promoting chromatin compaction [87]. Second, additional sources of ATRA could signal to the POM and be inhibited by the BMS493 treatment. Candidates include *Aldh1a1* (retina), *Aldh1a2* (temporal mesenchyme), and *Cyp11B1*, a member of the cytochrome p450 family of monooxygenases that can generate ATRA in the retina in a retinaldehyde dehydrogenase-independent manner [88]. Noneless, the severe patterning phenotypes observed in the *Aldh1a3* single mutant suggest that the local synthesis of ATRA in the RPE, optic stalk, and ventral retina at early stages (around E10.5) cannot be fully compensated by the action of other retinaldehyde dehydrogenases in adjacent tissues (this study, [31,64]).

Interestingly, although the constitutive *RARE-hsp68-lacZ* transgene displays strong reporter activity in the retina and RPE [34,89], we observed a strong ATRA response in the choroid and in POM connective tissues with the *Tg:RARE-CreERT2;R26<sup>Tom</sup>* reporter. However, one needs to consider that this type of reporter provides an off/on readout whose threshold level of response might depend on Cre levels, accessibility of the locus to recombination, and stochastic epigenetic mechanisms [90–93]. Given the difficulties in invalidating retinoic acid signaling in a cell-type-specific fashion and on cells perceiving a certain level of ATRA activity, it remains unclear how a gradient-like signaling system transitions to defined territories of transcription factor activity that will ultimately govern morphogenesis at a local level. We foresee that advances in single-cell transcriptomic approaches will help resolve the consecutive steps of musculoskeletal patterning in this and other anatomical locations.

### EOM and tendon patterning are concerted processes under RA control

We identified a short temporal window (E10.5–E11.75) in which ATRA is essential for the precise morphogenesis of several elements of the POM, including the formation of tendon

condensations and insertion sites in the POM-ring. These phenotypes are already evident from E11.75, a stage in which the EOM still figures as a muscle anlage. Interestingly, analysis of chick and mouse limb development also identified a short time window in which limb mesenchyme perturbations result later in muscle and tendon patterning defects [71,94]. Moreover, concomitant muscle and tendon defects have been observed in the chick limb and zebrafish jaw upon retinoic acid signaling misregulation [15,95]. Altogether, these results suggest that at certain anatomical locations, including the EOMs, endogenous local variations in the concentration of retinoids contribute to the establishment of *Scx-GFP+* condensations, a critical step in muscle functional unit assembly.

### Role of RA in the integration of EOM patterning and insertion site formation

The EOMs insert into the sclera, a non-bone structure in mammals. The generation of 4 attachment points that precisely mirror the position of the 4 recti muscles is a morphogenesis conundrum, as details on their specification are scarce. Four mesenchymal condensations have been described at the periphery of the developing optic cup in cat and human embryos, in positions facing the locations of the recti muscles [96,97]. In the mouse, at equivalent developmental timepoints (E11.5-E12.5) and homologous positions, apoptotic foci were observed and suggested to provide attachment for the recti muscles [51]. Using 3D imaging, we showed that at E11.75, the apoptotic foci are aligned with *Scx-GFP+* condensations that project medially, before any sign of splitting of the EOM anlage. As the apoptotic foci decrease in size from E12.5 onwards concomitant with ongoing muscle splitting and tendon formation, it is possible that they initially presage the POM for future tendon insertions but are not required for attachment per se. These foci appear in condensed SOX9+ PITX2+ cell domains of the future sclera; however, to our knowledge, their presence has not been reported in superstructures at other anatomical locations.

In agreement with the role of RA in the induction of cell death in other locations in the embryo [64], our study shows that upon perturbation of RA signaling, the apoptotic foci in the POM are absent or severely reduced. However, it is also possible that the loss of apoptotic foci upon RA inhibition is secondary to loss or mispatterning of the SOX9+ PITX2+ POM-ring. Thus, it will be of interest to determine whether null or NCC-specific mutations in PITX2 affect the patterns or amount of naturally occurring cell death in the periocular condensations. Although our work sheds light on the genetic mechanisms that regulate EOM insertion, the cellular mechanisms underlying this process remain undefined. It is tempting to speculate that the apoptotic foci are related to the disappearance of signaling centers [98,99] or compaction-mediated cell death and extrusion [100]. Future experiments directed towards modifying the amount or timing of cell death will be informative.

Few reports have demonstrated that mispatterning of specific muscles is coupled with aberrant superstructures [13,70,72] or removal of the prospective tendon attachment sites [95]. Our results are in agreement with that model, given that EOM mispatterning is concomitant with aberrant EOM insertions. As mammals do not develop a cartilage layer within the sclera [57,101], transient expression of SOX9 in the POM-ring of mouse embryos at the time of EOM patterning is intriguing. In the developing limb and jaw, tendon and bone are attached by a transitional connective tissue that develops from bipotent progenitors that co-express *Scx* and SOX9 [53–56], before progenitors are allocated to either cartilage or tendon lineages. Similarly, we observed a transient population of *Scx-GFP/SOX9* double-positive cells at the insertion sites in the POM. In this context, our data suggest that SOX9 expression may represent a redeployment of the developmental module for tendon attachment, despite the fact that there

is no definitive cartilage in the mammalian sclera. Genetic studies will be required to ultimately assess the functional relevance of this population in EOM attachment.

Finally, transcriptome analysis revealed the existence of global and regional regulatory modules for superstructure patterning in the limb bones, offering a mechanism to induce variations in attachment sites without having to rewrite the entire skeletogenic program [102]. As several markers of the POM (*Pitx2*, *Foxc1/2*) and retinoic acid signaling modulators (*Cyp26a1/b1*) were identified as part of specific limb superstructure signatures [102], it is tempting to speculate that those genes also play a conserved role in the generation of the attachment module of the EOMs.

## Conclusion

The developing eye has been proposed to be key organizer of craniofacial development, independent of its role in vision [103]. This notion is based on the role of the eye for proper NCC migration to the periocular region [104], the common association of ocular and craniofacial developmental abnormalities [105] and the initial development of an eye in blind vertebrate species [103,106,107]. Moreover, as the appearance of a "camera-type" eye is a vertebrate innovation [108], and the EOM are already present in lamprey [4], it is possible that muscles and their target tissue might have co-evolved. Here, by characterizing coordinated patterning of the EOMs, their respective tendons and insertions, our findings illustrate further the role of the developing eye as a signaling center allowing integration of the EOM functional unit in the POM. Our results show that the tissue interactions during the development of this craniofacial muscle unit share features with those described in the limb but with additional regional properties (e.g., cell death, specification of attachments in the sclera) that seem to have been specifically incorporated into this group. Moreover, the capacity to instruct muscle patterning through variations in connective tissue derivatives provides a mechanism to explain the plasticity of the musculoskeletal system, at the anatomical and interspecies levels, while ensuring functional integration during evolution. These findings also imply that the generation of musculoskeletal units do not require major restructuring of the developmental programs of all the tissues implicated. Instead, co-option of a general program and simultaneous addition of local features appear to elaborate musculoskeletal diversity.

## Materials and methods

### Mouse strains and animal information

Animals were handled as per European Community guidelines, and the ethics committee of the Institut Pasteur (CETEA) approved protocols (Licence 2015–0008). The following strains were previously described: *Aldh1a3*<sup>KO</sup> [64], *Mesp1*<sup>Cre</sup> [46], *Tg(RARE-Hspa1b-cre/ERT2)*, designated here as *Tg:RARE-CreERT2* [73], *R26*<sup>Tom</sup> (Ai9; [74]), *R26*<sup>mTmG</sup> [75], *Tg:Scx-GFP* [48], *Myf5*<sup>nlacZ</sup> [109], *Myod*<sup>iCre</sup> ([79,110]), *Rarb*<sup>flox</sup> [111], *Rarg*<sup>flox</sup>, [112], *Rdh10*<sup>KO</sup> [65], *Pax6*<sup>Sey/Sey</sup> [59], and *Tg:Wnt1*<sup>Cre</sup> [45]. *R26*<sup>RAR403</sup> ([78]) mice contain a loxP-flanked STOP sequence upstream of a mutated human RAR alpha gene, which behaves as a dominant negative receptor for all nuclear receptors upon Cre-mediated recombination. *Rdh10*<sup>KO</sup> embryos were received from the laboratory of Pascal Dollé. *Tg:Wnt1Cre;Rarb*<sup>f/f</sup>; *Rarg*<sup>f/f</sup> embryos were received from the laboratory of Valérie Dupé. *Pax6*<sup>Sey/Sey</sup> and control embryos were received from the laboratory of James Briscoe. *Tg:Lhx2*<sup>Cre</sup>; *Lhx2*<sup>f/f</sup> [61] were received from the laboratory of Leif Carlsson. *Shh(invC-6)2* embryos were received from the laboratory of François Spitz.

To generate experimental embryos for *Mesp1*<sup>Cre</sup> or *Tg:Wnt1*<sup>Cre</sup> together with *Tg:Scx-GFP* and *R26*<sup>Tom</sup> lineage tracings, Cre/+ males were crossed with *Tg:Scx-GFP;R26*<sup>Tom/Tom</sup> females. Mice were kept on a mixed genetic background C57BL/6J and DBA/2J (B6D2F1, Janvier

Labs). Mouse embryos and fetuses were collected between E10 and E18.5, with noon on the day of the vaginal plug considered as E0.5. Pregnant females were euthanized by cervical dislocation.

To induce recombination with the *Tg:RARE-CreERT2;R26<sup>mTmG</sup>* line, 5 mg of tamoxifen (Sigma #T5648) were administered by gavage to pregnant females. A 25 mg/ml stock solution in 5% ethanol and 95% sunflower seed oil was prepared by thorough resuspension with rocking at 4°C.

To inhibit retinoic acid signaling, pregnant females of relevant genotypes were injected intraperitoneally with 10 mg/kg of BMS493 (Tocris, 3509), a pan-RAR inverse agonist. A 5-mg/ml BMS493 stock solution in DMSO (SIGMA, D2650) was prepared and stored in single use aliquots at -20°C in tight cap tubes. At the time of injection, the aliquot was thawed, 200  $\mu$ l of sterile PBS was added per 50 $\mu$ l aliquot and injected immediately.

### Immunofluorescence, detection of cell death, and in situ hybridization

Embryos were fixed for 2.5 hours in 4% paraformaldehyde (PFA; 15710, Electron Microscopy Sciences) in PBS with 0.2–0.5% Triton X-100 (according to the embryonic stage) at 4°C and washed overnight at 4°C in PBS. For cryosectioning, embryos were equilibrated in 30% sucrose in PBS overnight at 4°C and embedded in OCT. Cryosections (16–18  $\mu$ m) were allowed to dry at RT for 30 minutes and washed in PBS. Immunostaining was performed as described in [113]. An anti-DsRed antibody (rabbit) was used to enhance the *R26<sup>Tom</sup>* signal except when co-staining was performed with antibodies raised in rabbit. In this case, the endogenous reporter signal was used. An anti-GFP antibody (chicken) was used to enhance the *R26<sup>mTmG</sup>* and *Tg:Scx-GFP* signal in whole-mount and section immunostainings.

*Scx* in situ hybridization was performed as per manufacturer instructions using the RNA-scope Multiplex Fluorescent V2 Assay [113] and RNAscope Probe-Mm-Scx probe (Cat No. 439981). Sample pre-treatments were performed as described in [113]. Signal development was carried out using Opal 570 Reagent Pack (FP1488001KT, Perkin Elmer) diluted 1:1,500 in the ACD-provided TSA buffer and followed up by immunostaining.

TUNEL staining, which marks double-strand breaks, was performed with the In Situ Cell Death Detection Kit/Fluorescein (Roche, 11 684 795 910). Slides were first pretreated with a 2:1 mix of Ethanol:Acetic Acid for 5 minutes at -20°C, washed twice for 20 minutes with PBS at RT, and processed for TUNEL staining as described by the manufacturer.

For whole-mount immunostaining, embryos were fixed and washed as described here and dehydrated in 50% Methanol in PBS and twice in 100% Methanol, 30 minutes each at RT and kept at -20°C till needed. Heads were rehydrated, the periocular region was microdissected in PBS, and immunostaining performed as described in [113]. For embryos older than E13.5, the alternative pretreatment (containing 0.1% Tween-20, 0.1% TritonX100, 0.1% Deoxycholate, 0.1% NP40, 20% DMSO in PBS) and primary antibody immunolabeling steps of the idisco protocol (<https://idisco.info/idisco-protocol/>) were generally used. In all cases, secondary antibodies were applied in blocking buffer as described in [113] for >4 days at 4°C with rocking. After immunolabelling, samples washed in 0.1% Tween/PBS, dehydrated in 50% Methanol in PBS and 100% Methanol 10 minutes each at RT, cleared with a mix benzyl alcohol and benzyl benzoate (BABB), and mounted for imaging as described in [114].

LysoTracker Red staining was used for detection of cell death in whole-mount live tissues as it reveals lysosomal activity correlated with increased cell death [52,115]. Embryos were quickly dissected in HBSS (Invitrogen, 14025–092), incubated in 2-ml tubes containing 5  $\mu$ M of LysoTracker Red DND-99 (Molecular Probes, L7528) 45 minutes at 37°C with rocking in

the dark, washed twice in PBS, fixed and processed for cryosections or whole-mount immunostaining as described previously.

### Antibodies

Primary and secondary antibodies used in this study are listed in [S2 Table](#). To detect differentiating EOMs, we used  $\alpha$ -smooth muscle actin (SMA), which is transiently expressed in differentiating myoblasts and myotubes [116–118]; Desmin, an early cytoskeletal muscle protein expressed in myoblasts, myotubes, and myofibers [116,119]; and myosin heavy chain (MyHC) to label sarcomeric myosin [120].

### Static imaging

A Zeiss SteREO Discovery V20 microscope was used for imaging the endogenous fluorescence of whole embryos at the time of dissection. For tissue sections and whole-mount immunostaining of cleared embryos, a LSM700 and a LSM800 laser-scanning confocal microscope with ZEN software (Carl Zeiss, [www.zeiss.com](http://www.zeiss.com)) were used.

All images were assembled in Adobe Photoshop and InDesign (Adobe Systems). Volume-3D rendering of the Z-stack series was performed in Imaris (version 7.2.1) software (Bitplane). For ease of EOM visualization, the Z-stack volumes were first manually segmented to define the EOM or the whole POM area using the Isosurface Imaris function. The signal outside the isosurface was set to zero, the corresponding channel duplicated, and subsequently, a new isosurface was created using automatic thresholding on the new channel. This new isosurface was used to calculate the corresponding EOM volumes.

### In situ hybridization

Whole-mount in situ hybridization with digoxigenin-labeled antisense mRNA probes was performed as described previously in [90]. The Aldh1a1, Aldh1a2, and Aldh1a3 probes were previously described in [34,36].

### micro-CT analysis

The tissue contrasting protocol has been adapted from the original protocol developed by [121] and applied to mouse embryos as described in [122] and [86]. For tissue contrasting, E13.5 embryos were stained in 0.5% phospho-tungstic acid (PTA) in 90% methanol for 4 days, E15.5 embryos were stained in 0.7% PTA in 90% methanol for 1 week.

The micro-CT analysis of the embryos was conducted using the GE phoenix v|tome|x L 240 (GE Sensing and Inspection Technologies GmbH, Germany), equipped with a 180 kV/15W maximum power nanofocus X-ray tube and flat panel detector DXR250 with 2048 × 2048 pixel, 200 × 200  $\mu$ m pixel size. The exposure time of the detector was 900 milliseconds in every position over 360°. Three projections were acquired and averaged in every position for reduction of the noise in micro-CT data. The acceleration voltage was set to 60 kV and tube current to 200  $\mu$ A. The radiation was filtered by 0.2 mm of aluminium plate. The voxel size of obtained volumes (depending on a size of an embryo) appeared in the range of 2–6  $\mu$ m. The tomographic reconstructions were performed using GE phoenix datos|x 2.0 3D CT software (GE Sensing and Inspection Technologies GmbH, Germany). The EOM, eye, and cartilages in the embryo head were segmented by an operator with semiautomatic tools within Avizo - 3D image data processing software (FEI, USA). The 3D segmented region was transformed to a polygonal mesh as an STL file and imported to VG Studio MAX 2.2 software (Volume Graphics GmbH, Germany) for surface smoothing and 3D visualization.

## Cell isolation from the periocular region and bulk cell cultures

The periocular region of *Tg:RARE-CreERT2;R26<sup>mTomG</sup>* embryos (including the eye itself) was microdissected and minced with small scissors inside a 2-ml Eppendorf tube. Samples were incubated with 1 ml of TrypLE Express (Invitrogen, 12604013) for 15 minutes at 37°C with agitation. Samples were resuspended by gently pipetting up and down 10–15 times using a P1000 pipette. Upon addition of 1 ml of culture media containing (10 µg/ml) DNaseI (Roche, 11284932001), samples were spun 15 minutes at 500g at RT, pellet resuspended in 400 µl of culture media containing of 20% fetal bovine serum (FBS, Gibco), 1% Penicillin-Streptomycin (15140, Gibco), and 2% Ultrosor G (15950–017, Pall Biosepra) in 50:50 DMEM:F12 (31966 and 31765, Gibco) and plated on individual wells of 8-well glass-bottom dishes (Ibidi, 80826) coated with 1 mg/ml of Matrigel (354234, BD Biosciences). Cells were allowed to attach for 8 hours at 37°C 5% CO<sub>2</sub>, washed with PBS, and fixed for 15 minutes at RT with 4% PFA in PBS. After fixation, cells were washed in PBS and permeabilized with 0.5% Triton X-100 in PBS for 5 minutes at RT. After 3 washes in PBS (5 minutes each), cells were blocked with 20% goat serum in PBS 1 hour at RT. Primary antibodies were added to cells in 2% goat serum in PBS for 2 h at RT or ON at 4°C. Cells were washed 3 times with PBS, incubated with secondary antibodies for 1 hour at RT, washed in PBS, and kept in PBS for imaging.

## Statistics

The number of embryos of each genotype used for analysis is indicated in the figure legends and [S1 Table](#). The graphs were plotted, and statistical analyses were performed using Prism8 (GraphPad Software, Inc). All data points are presented as mean ± SEM (error bars). Individual values can be found in S1, S2 and S3 Data files. Statistical tests used for analysis are indicated on the respective figure legends. *p*-values less than 0.05 were considered significant (\**p* < 0.05; \*\**p* < 0.01; \*\*\**p* < 0.001).

## Supporting information

**S1 Fig. Lineage contributions to the EOM functional unit. (A–D)** NCC (*Tg:Wnt1<sup>Cre</sup>;R26<sup>Tom</sup>;Scx-GFP*) and mesoderm (*Mesp1<sup>Cre</sup>;R26<sup>Tom</sup>;Scx-GFP*) lineage contributions to the periocular region on coronal cryosections of E17.5 embryos, combined with immunostaining for tendon (GFP) and muscle (Tnnt3, Troponin T Type 3, differentiated muscle). Sections at ventral (A, C) and dorsal (B, D) levels. Note that tendon insertions at the level of the orbit are NCC-derived (A), whereas the tendon origin (D) is mesoderm-derived. Higher-magnification views at the level of the tendon insertion (A1, C1) and origin (B1, D1) are shown as insets. Asterisk in D1 indicates *Scx-GFP*<sup>+</sup> cells in the perichondrium of the hypochiasmatic cartilage. (E–F') NCC (*Tg:Wnt1<sup>Cre</sup>;R26<sup>Tom</sup>*) and mesoderm (*Mesp1<sup>Cre</sup>;R26<sup>Tom</sup>*) lineage contributions to the periocular region on coronal cryosections of E13.5 embryos, combined with immunostaining for TCF4 and muscle (PAX7/MYOD/MYOG, myogenic markers). Note that TCF4 is expressed robustly in connective tissue fibroblasts and at lower levels in myogenic cells. White arrowheads in (E', F') mark Tom<sup>+</sup>, TCF4<sup>+</sup>, myogenic marker-negative connective tissue cells in the NCC- and mesoderm-derived areas. Pink arrowheads in (E', F') mark myogenic cells (TCF4<sup>low</sup>). (G–H') Coronal cryosections of E13.5 *Tg:Scx-GFP* embryos, combined with immunostaining for TCF4 (connective tissue, myogenic progenitors) and muscle (PAX7/MYOD/MYOG). White arrowheads in (G', H') mark Tom<sup>+</sup>, TCF4<sup>+</sup>, myogenic marker-negative connective tissue cells in the NCC and mesoderm-derived areas. Pink arrowheads in (G', H') mark myogenic cells (TCF4<sup>low</sup>). (I, J) In situ hybridization on E12.5 (I) and E13.5 (J) coronal cryosections for *Scx* combined with immunofluorescence for muscle (PAX7/MYOD/MYOG). High levels of *Scx* mRNA are seen at the tendon origin and insertion but also in the bulk of the

muscle masses (I',J', insets). a, anterior; d, dorsal; l, lateral; m, medial; MCT, muscle connective tissue; E, embryonic day; eom, extraocular muscle; NCC, neural crest cell; p, posterior; ti, tendon insertion; to, tendon origin; v, ventral.

(TIF)

**S2 Fig. Expression of PITX2 in the POM.** (A-C) Immunostaining on E11.5 (A), E12.5 (B) and E13.5 (C) coronal sections of control embryos for PITX2 (EOM myogenic progenitors, POM) and SMA (differentiated muscle). Arrowheads mark the EOM masses and asterisks point to PITX2 expression in the medial POM. Note thinning of the lateral POM as development proceeds (brackets). ( $n = 3$  per stage). E, embryonic day; EOM, extraocular muscle; POM, periocular mesenchyme.

(TIF)

**S3 Fig. Developmental timing of EOM functional unit components.** (A-D') Immunostaining for the indicated markers on coronal sections of E11.5 (A), E12.5 (B, E, F), E13.5 (C) and E14.5 (D) *Tg:Scx-GFP* embryos. (A'-D'') Higher-magnification views of the anterior tendon insertions (superior rectus) in the POM. White arrowheads mark SOX9+ *Scx-GFP*+ cells up to E13.5. Asterisks in A'-C'' point to SOX9+ *Scx-GFP*-negative areas. Double asterisk in D'' mark *Scx-GFP*+ SOX9-negative tendon tips at E14.5. SOX9 expression remains at the sclera. (E-F') Immunostaining for the indicated markers on coronal sections of E11.75 and E13.5 *Tg:Scx-GFP* embryos preincubated with LysoR. Arrowheads in E,E' indicate SOX9+ LysoR+ cells in the E11.75 POM. (G-H'') Immunostaining for the indicated markers on transversal sections of E12.5 *Tg:Scx-GFP* embryos. (G'-H'') Higher magnification views of the lateral tendon insertions (lateral rectus) showing SOX9+ or PITX2+ LysoR+ areas. MYOD/MYOG (myogenic markers) in A-D and MyHC (myofibers) in G-H were used to identify the EOMs. ( $n = 3$  per stage). a, anterior; d, dorsal; E, embryonic day; EOM, extraocular muscle; l, lateral; LysoR, LysoTracker Red; m, medial; p, posterior; POM, periocular mesenchyme; s, sclera; v, ventral.

(TIF)

**S4 Fig. EOM morphogenesis in mutants with eye defects.** (A-C) Micro-CT-based 3D reconstruction of EOM, eyeball, optic nerve, and lens in E13.5 control (A), *Pax6<sup>Sey/+</sup>* (B), and *Pax6<sup>Sey/Sey</sup>* embryos (C). Note that in heterozygote embryos, EOM patterning proceeds normally despite having a smaller retina and lens ( $n = 3$ ). (D-E) Micro-CT-based 3D-reconstruction of EOM and eyeball in E18.5 control (A) and *Tg:Lhx2<sup>Cre</sup>;Lhx2<sup>fl/fl</sup>* (B) embryos. Arrowheads highlight some extent of EOM segregation in the mutant. (D'-E') Coronal sections of control (D') and mutant (E') embryos stained with MyHC (differentiated muscle). Arrowheads indicate individual EOM masses ( $n = 2$ ). (F-F'') Analysis of EOM patterning in E15.5 embryos containing inversions of *Shh* genomic regulatory regions (Inv(6-C2)). (F) Skeletal preparation of mutant embryos displaying cyclopia. (F'-F'') Micro-CT-based 3D-reconstruction of EOM and eyeball of mutant embryos ( $n = 2$ ). a, anterior; ctrl, control; d, dorsal; E, embryonic day; EOM, extraocular muscle; l, lateral; m, medial; micro-CT, micro-computed tomography; p, posterior; v, ventral.

(TIF)

**S5 Fig. EOM morphogenesis is dependent retinoic acid signaling.** (A) Whole-mount in situ hybridization for *Aldh1a1*, *Aldh1a2*, and *Aldh1a3* in E10.5, E11.5, and E12.5 wildtype embryos ( $n = 3$ ). (A'-A'') In situ hybridization for *Aldh1a2* (A') and immunostaining for ALDH1A2 and MyHC (differentiated muscle) (A'') on E12.5 coronal sections. ALDH1A2 is expressed in the temporal mesenchyme and adjacent connective tissues ( $n = 3$ ). (B) Micro-CT-based 3D-reconstruction of eyeball, optic nerve and lens of E13.5 control, *Aldh1a3<sup>KO</sup>* and BMS493-treated embryos ( $n = 2$  each genotype). The lower row is a scheme of a sphere fitting the

eyeball and lens, and a cylinder for the optic nerve. Note ventralization of the eyeball in *Aldh1a3<sup>KO</sup>* and BMS493-treated embryos. (C) Micro-CT-based 3D-reconstruction of the mesenchymal condensations of the nasal capsule and trabecular cartilage of E13.5 control (white), *Aldh1a3<sup>KO</sup>* (yellow) and BMS493-treated (green) embryos. (D–D') MyHC WMIF of E13.5 BMS493-treated embryos as described in S1 Table. The most severe phenotype obtained in each condition is shown as an isosurface. Two different examples of the phenotype observed upon treatment VI (a,b) are shown (most and least severe). An *Aldh1a3<sup>KO</sup>* embryo is shown as comparison. Asterisk denotes ectopic duplicated SO muscle. (D') Higher-magnification views from D (dashed squares) with examples of adjacent, nonsplit muscle masses (1,2) depicted by differential fiber orientation. (E–F) MyHC WMIF of E13.5 control (E) and *Rdh10<sup>KO</sup>* (F) embryos. Note total absence of muscle splitting in mutant ( $n = 3$  per condition). EOMs in D–F were segmented from adjacent head structures and 3D-reconstructed in Imaris (Bitplane). ctrl, control; dr, dorsal retina; 3D-rec, 3D-reconstruction; e, eyelid groove; E, embryonic day; EOM, extraocular muscle; io, inferior oblique; ir, inferior rectus; le, lens; lgb, lacrimal gland bud; lr, lateral rectus; micro-CT, micro-computed tomography; mr, medial rectus; nlg, nasolacrimal groove; np, nasal pit; os, optic stalk; rb, retractor bulbi; rpe, retinal pigmented epithelium; so, superior oblique; sr, superior rectus; tm, temporal mesenchyme; vr, ventral retina, WMIF, whole-mount immunofluorescence. (TIF)

**S6 Fig. Retinoic acid signaling responsiveness in the periocular region.** (A–C) Macroscopic views of endogenous GFP fluorescence of *Tg:RARE-CreERT2;R<sup>26mTomG</sup>* embryos. Tam was injected into pregnant females and embryos analyzed at indicated time points. Arrowheads indicate labeling in POM ( $n > 3$  per condition). (D) Immunostaining on cells isolated from the periocular region of *Tg:RARE-CreERT2;R<sup>26mTomG</sup>* embryos for GFP and myogenic markers (MYOD/MYOG). (E) Strategy used to determine responsiveness of *Tg:RARE-CreERT2* reporter in presence of BMS493. BMS493 was injected to pregnant females every 10–12 hours between E10 and E11.75. Recombination was induced by tamoxifen at E10.5 (2 hours after the first BMS injection). (F–I) WMIF for MyHC (differentiated muscle) and GFP (ATRA-responsive cells) of control (F,G) and BMS493-treated embryos (H,I). BMS493 treatment before and after tamoxifen induction reveals a drastic decrease in GFP+ cells in the periocular region (I) compared with controls (G). Asterisks mark the location of the optic nerve ( $n = 3$ ). (J) Coronal sections (dorsal, EOM origin) of E12.5 *Tg:RARE-CreERT2;R26<sup>Tom</sup>;Scx-GFP* embryos immunostained for GFP, Tom (ATRA-responsive cells) and MYOD/MYOG (muscle). Higher magnification views as insets. Arrowheads in J1 mark Tom-negative myogenic cells, and asterisks indicate sporadic labeling in myogenic cells. Arrowheads in J2 mark Tom+ *Scx-GFP*+ cells ( $n = 3$ ). (K–L) WMIF for SMA (differentiated muscle) of *Myod<sup>iCre</sup>* (control, K, K') and *Myod<sup>iCre</sup>;R26<sup>RAR403</sup>* (mutant embryos, L, L') ( $n = 3$ ). EOMs in F–I and K–L' were segmented from adjacent head structures and 3D-reconstructed in Imaris (Bitplane). a, anterior; ATRA, all-trans retinoic acid; ctrl, control; d, dorsal; E, embryonic day; EOM, extraocular muscle; l, lateral; m, medial; p, posterior; POM, periocular mesenchyme; Tam, tamoxifen; v, ventral; WMIF, whole-mount immunofluorescence. (TIF)

**S7 Fig. EOM insertions in the POM are altered upon ATRA deficiency.** (A–D') Immunostaining for the indicated markers on coronal E12 sections of control (A,C,C') and BMS493-treated (B,D,D') *Tg:Scx-GFP* embryos pre-incubated with LysoTracker Red (LysoR). (C',D') Higher-magnification views of the POM region. In BMS493-treated embryos, LysoR and SOX9 staining are absent in the POM (D', asterisk) and SOX9 staining also missing in the RPE (D', double asterisk). (E–N) WMIF for the indicated markers of E11.75 control (E,F,K),

*Aldh1a3*<sup>KO</sup> (G,H,M) and BMS493-treated (I,J,N) embryos pre-incubated with LysoR (right eyes). In lateral views, neither *Aldh1a3*<sup>KO</sup> or BMS493-treated embryos (H,J) show a full PITX2+ POM-ring as the controls (F). Arrowheads in (G,H) mark remaining expression of SOX9/PITX2 in the POM of mutant or inhibitor treated embryos. Asterisks in (F,H,J) mark apoptosis spots in the POM. (K-N) Segmented medial views of periocular region of control, *Aldh1a3*<sup>KO</sup> or BMS493-treated embryos. Volumes were truncated in Z for clarity. Full view as schemes below. The PITX2+ POM-ring is continuous with the medial-POM in control embryos (K). In mutant and BMS493-treated embryos, residual PITX2 expression in POM is discontinuous with the medial-POM (blue arrowheads) (M,N). (O-Q') WMIF for SMA (differentiated muscle), GFP (ATRA-responsive cells) and PITX2 (muscle progenitors, POM) of *Tg:RARE-CreERT2;R26<sup>mTmG</sup>* control (O,O'), *Aldh1a3*<sup>KO</sup> (P,P') and BMS493-treated (Q,Q') embryos. Blue arrowheads in P and Q show reduction or loss of ATRA-responsive cells in the periocular region. (O'-Q') Single Z-planes of the segmented volume. White arrowhead in O shows correct PITX2+ connective tissue pre-pattern in the prospective muscle areas and arrow marks PITX2 expression along the muscle masses. Blue arrowheads in P' and Q' show reduction or loss of ATRA-responsive cells and PITX2 pre-pattern in the medial periocular mesenchyme. (R-T) Single cell plane of WMIF of E12 control (R), BMS493-treated (S) and *Myf5<sup>nlacZ/nlacZ</sup>* embryos (T) (right eyes) for TCF4 (muscle connective tissue) and SMA (differentiated muscle). Asterisks mark position of the optic nerve. White arrowheads in R,T show correct TCF4+ connective tissue pre-pattern in the prospective muscle areas and white arrow marks TCF4 expression along the muscle masses (R). (U-V) WMIF for GFP and  $\beta$ -gal (myogenic progenitors) of E14.5 *Tg:Scx-GFP;Myf5<sup>nlacZ/+</sup>* (U, control) and *Tg:Scx-GFP;Myf5<sup>nlacZ/nlacZ</sup>* (V, mutant) embryos (left eyes). Asterisk indicates few remaining  $\beta$ -gal+ cells in mutant. (U', V') split GFP channel. Arrowheads in (V) indicate the correct position of tendon condensations for the 4 recti muscles although these are absent in the mutant. Lower panel, higher-magnification views. a, anterior; ATRA, all-trans retinoic acid; anl, anlage; apop, apoptosis; ctrl, control; d, dorsal; E, embryonic day; eom, extraocular muscle; l, lateral; m, medial; m-pom, medial periocular mesenchyme; l-pom, lateral periocular mesenchyme; POM, periocular mesenchyme; pom-r, periocular mesenchyme ring; p, posterior; rpe, retinal pigmented epithelium; v, ventral; WMIF, whole-mount immunofluorescence.

(TIF)

**S8 Fig. Illustration depicting the timeline of EOM and POM development in relation to ATRA signaling.** Summary of the most relevant genetic perturbations and drug treatments of this study. ATRA, all-trans retinoic acid; EOM, extraocular muscle; POM, periocular mesenchyme.

(TIF)

**S1 Table. BMS493 injection regimes.** The same BMS493 concentration (Conc BMS) was used across injection regimes, from I to VI. Pink cases mark injection time points in the morning (mo), midday (mid) or evening (eve) between E10.5 and E12.5. The number of embryos with different muscle phenotype severity at E13.5 are shown: (no), no altered phenotype; mild (+), muscle mispatterning but overall organization retained; strong (++) , strong mispatterning but with a minimum of 2 muscles split; severe (+++), no or almost absent splitting. n is the total number of embryos analyzed for a certain treatment type ( $n = 38$  embryos analyzed in total); N exp, number of times the experiment was repeated. E, embryonic day; EOM, extraocular muscle.

(XLSX)

**S2 Table. Antibodies and resources used in this study.**

(XLSX)

**S1 Data. Excel table containing individual values to generate the histogram in Fig 3K.**

For each tissue section, a rectangular ROI (region of interest) was defined in Fiji (Image J) in the LysoTracker Red-positive and adjacent LysoTracker Red-negative areas. The number of SOX9+ cells was scored in each ROI. Individual values were represented by the ratio of N° cells/ROI area ( $\mu\text{m}^2$ ).

(XLSX)

**S2 Data. Excel table containing individual values to generate the histogram in Fig 4I.** For each embryo, the EOM volume was calculated as described in the methods section. The normalized EOM volume is the ratio of the individual volume value/average of the control values. EOM, extraocular muscle.

(XLSX)

**S3 Data. Excel table containing individual values to generate the histogram in Fig 5C.** Each data point represents the percentage of myogenic and non-myogenic GFP+ cells isolated by bulk digestion of the periocular area of a single *Tg:RARE-CreERT2;R26<sup>mTmG</sup>* reporter embryo.

(XLSX)

**S1 Video. Temporal sequence of EOM patterning.** Whole-mount immunostaining for MYOD/MYOG/Desmin (E11.5 to E12.5) or MyHC (E13.5 to E14.5) on the developing EOM of control embryos. EOMs were segmented from adjacent head structures and 3D-reconstructed in Imaris (Bitplane). E, embryonic day; EOM, extraocular muscle.

(MOV)

**S2 Video. Organization of the EOM functional unit at E11.75.** Whole-mount immunostaining for MyHC (myofibers, Red) and PITX2 (POM and myogenic progenitors, Cyan) on control embryo. EOMs were segmented from adjacent head structures and 3D-reconstructed in Imaris (Bitplane). E, embryonic day; EOM, extraocular muscle; POM, periocular mesenchyme.

(MOV)

**S3 Video. Organization of the EOM functional unit at E11.75.** Whole-mount immunostaining for MyHC (myofibers, Cyan) and GFP (tendon progenitors, Green) on *Tg:Scx-GFP* embryo. EOMs were segmented from adjacent head structures and 3D-reconstructed in Imaris (Bitplane). Apoptotic foci are visualized by LysoTracker Red staining. A clipping plane was added for clarity of visualization. Note that tendon condensations start to organize radially and towards the apoptotic foci in the POM. E, embryonic day; EOM, extraocular muscle; POM, periocular mesenchyme.

(MOV)

**S4 Video. Organization of the EOM functional unit at E12.5.** Whole-mount immunostaining for MyHC (myofibers, Cyan) and GFP (tendon progenitors, Green) on *Tg:Scx-GFP* embryo. EOMs were segmented from adjacent head structures and 3D-reconstructed in Imaris (Bitplane). Apoptotic foci are visualized by LysoTracker Red staining. A clipping plane was added for clarity of visualization. Note how tendon condensations of the recti muscles are more refined at this stage and project towards the apoptotic foci in the POM. E, embryonic day; EOM, extraocular muscle; POM, periocular mesenchyme.

(MOV)

**S5 Video. Organization of the EOM functional unit of E13.5 BMS493-treated (E10.5 → E11.75) *Tg:Scx-GFP* embryos.** Whole-mount immunostaining for MyHC (myofibers, Red) and GFP (tendon progenitors, Green). EOMs were segmented from adjacent head structures

and 3D-reconstructed in Imaris (Bitplane). Note the presence of tendon condensations at the tips of mispatterned muscle masses. E, embryonic day; EOM, extraocular muscle.

(MOV)

**S6 Video. ATRA-responsiveness in the periocular region of E13.5 *Tg:RARE-CreERT2*; *R26<sup>mTmG</sup>* control embryos (Tamoxifen induction at E10.5).** Whole-mount immunostaining for MyHC (myofibers, Red), and GFP (ATRA-responsive cells, Green). EOMs were segmented from adjacent head structures and 3D-reconstructed in Imaris (Bitplane). EOMs are shown as isosurfaces for clarity of visualization. ATRA, all-trans retinoic acid; E, embryonic day; EOM, extraocular muscle.

(MOV)

**S7 Video. ATRA-responsiveness in the periocular region of E13.5 BMS493-treated *Tg:RARE-CreERT2*; *R26<sup>mTmG</sup>* embryos (BMS493 treatment: E10 → E11.75; Tamoxifen induction at E10.5).** Whole-mount immunostaining for MyHC (myofibers, Red) and GFP (ATRA-responsive cells, Green). EOMs were segmented from adjacent head structures and 3D-reconstructed in Imaris (Bitplane). EOMs are shown as isosurfaces for clarity of visualization.

ATRA, all-trans retinoic acid; E, embryonic day; EOM, extraocular muscle.

(MOV)

**S8 Video. ATRA-responsiveness in the periocular region of E12.5 *Tg:RARE-CreERT2*; *R26<sup>mTmG</sup>* control embryos (Tamoxifen induction at E10.5).** Whole-mount immunostaining for GFP (ATRA-responsive cells, Green), PITX2 (POM and myogenic progenitors, Cyan) and SMA (differentiated muscle, Red). Z-planes from medial to lateral levels. ATRA, all-trans retinoic acid; E, embryonic day; POM, periocular mesenchyme.

(MOV)

**S9 Video. ATRA-responsiveness in the periocular region of E12.5 *Tg:RARE-CreERT2*; *R26<sup>mTmG</sup>*; *Aldh1a3<sup>KO</sup>* embryos (Tamoxifen induction at E10.5).** Whole-mount immunostaining for GFP (ATRA-responsive cells, Green), PITX2 (POM and myogenic progenitors, Cyan), and SMA (differentiated muscle, Red). Z-planes from medial to lateral levels. ATRA, all-trans retinoic acid; E, embryonic day; POM, periocular mesenchyme.

(MOV)

**S10 Video. ATRA-responsiveness in the periocular region of E12.5 *Tg:RARE-CreERT2*; *R26<sup>mTmG</sup>* BMS493-treated embryos (BMS493 treatment: E10 → E11.75; Tamoxifen induction at E10.5).** Whole-mount immunostaining for GFP (ATRA-responsive cells, Green), PITX2 (POM and myogenic progenitors, Cyan) and SMA (differentiated muscle, Red). Z-planes from medial to lateral levels. ATRA, all-trans retinoic acid; E, embryonic day; POM, periocular mesenchyme.

(MOV)

**S11 Video. Organization of the EOM insertions of E12.5 *Tg:Scx-GFP* control embryos.** Whole-mount immunostaining for MyHC (myofibers, Red) and GFP (tendon progenitors, Green). EOMs were segmented from adjacent head structures and 3D-reconstructed in Imaris (Bitplane). A clipping plane has been added for clarity of visualization. E, embryonic day; EOM, extraocular muscle.

(MOV)

**S12 Video. Organization of the EOM insertions of E12.5 BMS493-treated (E10.5 → E11.75) *Tg:Scx-GFP* embryos.** Whole-mount immunostaining for MyHC (myofibers, Red) and GFP (tendon progenitors, Green). EOMs were segmented from adjacent head structures

and 3D-reconstructed in Imaris (Bitplane). A clipping plane has been added for clarity of visualization. Note that distribution of *Scx-GFP*<sup>+</sup> cells is more diffuse than for controls (Video 11), but an *Scx-GFP*<sup>+</sup> condensation is present at the tip of the inferior muscle mass. E, embryonic day; EOM, extraocular muscle.

(MOV)

**S13 Video. Organization of the EOM insertions of E14.5 *Tg:Scx-GFP;Myf5<sup>nlacZ/+</sup>* embryos.**

Whole-mount immunostaining for  $\beta$ -gal (myogenic progenitors, Red) and GFP (tendon, Green). EOMs were segmented from adjacent head structures and 3D-reconstructed in Imaris (Bitplane). E, embryonic day; EOM, extraocular muscle.

(MOV)

**S14 Video. Organization of the EOM insertions of E14.5 *Tg:Scx-GFP;Myf5<sup>nlacZ/nlacZ</sup>* embryos.**

Whole-mount immunostaining for  $\beta$ -gal (myogenic progenitors, Red) and GFP (tendon, Green). E, embryonic day; EOM, extraocular muscle.

(MOV)

## Acknowledgments

We gratefully acknowledge the UtechS Photonic BioImaging (Imagopole), C2RT, Institut Pasteur. We thank Robert Kelly (IBDM, Marseille, France) for kindly providing *R26<sup>RAR403</sup>* mice.

## Author Contributions

**Conceptualization:** Glenda Evangelina Comai, Shahragim Tajbakhsh.

**Data curation:** Glenda Evangelina Comai.

**Formal analysis:** Glenda Evangelina Comai, Markéta Tesařová.

**Funding acquisition:** Shahragim Tajbakhsh.

**Investigation:** Glenda Evangelina Comai.

**Methodology:** Glenda Evangelina Comai, Markéta Tesařová, Tomáš Zikmund, Jozef Kaiser.

**Project administration:** Glenda Evangelina Comai, Shahragim Tajbakhsh.

**Resources:** Glenda Evangelina Comai, Valérie Dupé, Muriel Rhinn, Pedro Vallecillo-García, Fabio da Silva, Betty Feret, Katherine Exelby, Pascal Dollé, Leif Carlsson, Brian Pryce, François Spitz, Sigmar Stricker, James Briscoe, Andreas Schedl, Norbert B. Ghyselinck, Ronen Schweitzer, Shahragim Tajbakhsh.

**Supervision:** Jozef Kaiser, Ronen Schweitzer, Shahragim Tajbakhsh.

**Validation:** Glenda Evangelina Comai.

**Visualization:** Glenda Evangelina Comai, Markéta Tesařová.

**Writing – original draft:** Glenda Evangelina Comai.

**Writing – review & editing:** Glenda Evangelina Comai, Markéta Tesařová, Valérie Dupé, Muriel Rhinn, Pedro Vallecillo-García, Fabio da Silva, Leif Carlsson, Sigmar Stricker, Tomáš Zikmund, Jozef Kaiser, James Briscoe, Andreas Schedl, Norbert B. Ghyselinck, Ronen Schweitzer, Shahragim Tajbakhsh.

## References

1. Hasson P. "Soft" tissue patterning: muscles and tendons of the limb take their form. *Developmental dynamics: an official publication of the American Association of Anatomists*. 2011; 240(5):1100–7. <https://doi.org/10.1002/dvdy.22608> PMID: 21438070
2. Huang AH. Coordinated development of the limb musculoskeletal system: Tendon and muscle patterning and integration with the skeleton. *Developmental biology*. 2017; 429(2):420–8. <https://doi.org/10.1016/j.ydbio.2017.03.028> PMID: 28363737; PubMed Central PMCID: PMC5581688.
3. Noden DM, Francis-West P. The differentiation and morphogenesis of craniofacial muscles. *Developmental dynamics: an official publication of the American Association of Anatomists*. 2006; 235(5):1194–218. <https://doi.org/10.1002/dvdy.20697> PMID: 16502415.
4. Suzuki DG, Fukumoto Y, Yoshimura M, Yamazaki Y, Kosaka J, Kuratani S, et al. Comparative morphology and development of extra-ocular muscles in the lamprey and gnathostomes reveal the ancestral state and developmental patterns of the vertebrate head. *Zoological Lett*. 2016; 2:10. <https://doi.org/10.1186/s40851-016-0046-3> PMID: 27081572; PubMed Central PMCID: PMC4831119.
5. Young GC. Number and arrangement of extraocular muscles in primitive gnathostomes: evidence from extinct placoderm fishes. *Biology letters*. 2008; 4(1):110–4. <https://doi.org/10.1098/rsbl.2007.0545> PMID: 18077236.
6. Spencer RF, Porter JD. Biological organization of the extraocular muscles. *Progress in brain research*. 2006; 151:43–80. Epub 2005/10/14. [https://doi.org/10.1016/S0079-6123\(05\)51002-1](https://doi.org/10.1016/S0079-6123(05)51002-1) PMID: 16221585.
7. Ziermann JM, Diogo R, Noden DM. Neural crest and the patterning of vertebrate craniofacial muscles. *Genesis*. 2018; 56(6–7):e23097. <https://doi.org/10.1002/dvg.23097> PMID: 29659153.
8. Nassari S, Duprez D, Fournier-Thibault C. Non-myogenic Contribution to Muscle Development and Homeostasis: The Role of Connective Tissues. *Front Cell Dev Biol*. 2017; 5:22. <https://doi.org/10.3389/fcell.2017.00022> PMID: 28386539; PubMed Central PMCID: PMC5362625.
9. Bohnsack BL, Gallina D, Thompson H, Kasprick DS, Lucarelli MJ, Dootz G, et al. Development of extraocular muscles requires early signals from periocular neural crest and the developing eye. *Archives of ophthalmology*. 2011; 129(8):1030–41. Epub 2011/04/13. <https://doi.org/10.1001/archophthalmol.2011.75> PMID: 21482859; PubMed Central PMCID: PMC3248700.
10. Ericsson R, Cerny R, Falck P, Olsson L. Role of cranial neural crest cells in visceral arch muscle positioning and morphogenesis in the Mexican axolotl, *Ambystoma mexicanum*. *Developmental dynamics: an official publication of the American Association of Anatomists*. 2004; 231(2):237–47. <https://doi.org/10.1002/dvdy.20127> PMID: 15366001.
11. Noden DM. The role of the neural crest in patterning of avian cranial skeletal, connective, and muscle tissues. *Developmental biology*. 1983; 96(1):144–65. [https://doi.org/10.1016/0012-1606\(83\)90318-4](https://doi.org/10.1016/0012-1606(83)90318-4) PMID: 6825950.
12. Rinon A, Lazar S, Marshall H, Buchmann-Moller S, Neufeld A, Elhanany-Tamir H, et al. Cranial neural crest cells regulate head muscle patterning and differentiation during vertebrate embryogenesis. *Development*. 2007; 134(17):3065–75. <https://doi.org/10.1242/dev.002501> PMID: 17652354.
13. Tokita M, Schneider RA. Developmental origins of species-specific muscle pattern. *Developmental biology*. 2009; 331(2):311–25. <https://doi.org/10.1016/j.ydbio.2009.05.548> PMID: 19450573; PubMed Central PMCID: PMC2726847.
14. von Scheven G, Alvares LE, Mootoosamy RC, Dietrich S. Neural tube derived signals and Fgf8 act antagonistically to specify eye versus mandibular arch muscles. *Development*. 2006; 133(14):2731–45. <https://doi.org/10.1242/dev.02426> PMID: 16775000.
15. McGurk PD, Swartz ME, Chen JW, Galloway JL, Eberhart JK. In vivo zebrafish morphogenesis shows Cyp26b1 promotes tendon condensation and musculoskeletal patterning in the embryonic jaw. *PLoS Genet*. 2017; 13(12):e1007112. <https://doi.org/10.1371/journal.pgen.1007112> PMID: 29227993; PubMed Central PMCID: PMC5739505.
16. Shimizu M, Narboux-Neme N, Gitton Y, de Lombares C, Fontaine A, Alfama G, et al. Probing the origin of matching functional jaws: roles of Dlx5/6 in cranial neural crest cells. *Scientific reports*. 2018; 8(1):14975. <https://doi.org/10.1038/s41598-018-33207-2> PMID: 30297736; PubMed Central PMCID: PMC6175850.
17. Evans AL, Gage PJ. Expression of the homeobox gene Pitx2 in neural crest is required for optic stalk and ocular anterior segment development. *Human molecular genetics*. 2005; 14(22):3347–59. Epub 2005/10/06. <https://doi.org/10.1093/hmg/ddi365> PMID: 16203745.
18. Heude E, Bellessort B, Fontaine A, Hamazaki M, Treier AC, Treier M, et al. Etiology of craniofacial malformations in mouse models of blepharophimosis, ptosis and epicanthus inversus syndrome. *Human molecular genetics*. 2015; 24(6):1670–81. <https://doi.org/10.1093/hmg/ddu579> PMID: 25416281.

19. Iwata J, Suzuki A, Pelikan RC, Ho TV, Chai Y. Noncanonical transforming growth factor beta (TGFbeta) signaling in cranial neural crest cells causes tongue muscle developmental defects. *The Journal of biological chemistry*. 2013; 288(41):29760–70. <https://doi.org/10.1074/jbc.M113.493551> PMID: 23950180; PubMed Central PMCID: PMC3795273.
20. Kardon G. Muscle and tendon morphogenesis in the avian hind limb. *Development*. 1998; 125(20):4019–32. Epub 1998/09/15. PMID: 9735363.
21. Kardon G, Harfe BD, Tabin CJ. A Tcf4-positive mesodermal population provides a prepattern for vertebrate limb muscle patterning. *Developmental cell*. 2003; 5(6):937–44. [https://doi.org/10.1016/s1534-5807\(03\)00360-5](https://doi.org/10.1016/s1534-5807(03)00360-5) PMID: 14667415.
22. Sefton EM, Kardon G. Connecting muscle development, birth defects, and evolution: An essential role for muscle connective tissue. *Current topics in developmental biology*. 2019; 132:137–76. <https://doi.org/10.1016/bs.ctdb.2018.12.004> PMID: 30797508; PubMed Central PMCID: PMC6449175.
23. Murchison ND, Price BA, Conner DA, Keene DR, Olson EN, Tabin CJ, et al. Regulation of tendon differentiation by scleraxis distinguishes force-transmitting tendons from muscle-anchoring tendons. *Development*. 2007; 134(14):2697–708. <https://doi.org/10.1242/dev.001933> PMID: 17567668.
24. Schweitzer R, Chyung JH, Murtaugh LC, Brent AE, Rosen V, Olson EN, et al. Analysis of the tendon cell fate using Scleraxis, a specific marker for tendons and ligaments. *Development*. 2001; 128(19):3855–66. PMID: 11585810.
25. Diogo R, Kelly RG, Christiaen L, Levine M, Ziermann JM, Molnar JL, et al. A new heart for a new head in vertebrate cardiopharyngeal evolution. *Nature*. 2015; 520(7548):466–73. Epub 2015/04/24. <https://doi.org/10.1038/nature14435> PMID: 25903628.
26. Sambasivan R, Kuratani S, Tajbakhsh S. An eye on the head: the development and evolution of craniofacial muscles. *Development*. 2011; 138(12):2401–15. <https://doi.org/10.1242/dev.040972> PMID: 21610022.
27. Gitton Y, Heude E, Vieux-Rochas M, Benouaiche L, Fontaine A, Sato T, et al. Evolving maps in craniofacial development. *Seminars in cell & developmental biology*. 2010; 21(3):301–8. <https://doi.org/10.1016/j.semcd.2010.01.008> PMID: 20083217.
28. Rhinn M, Dolle P. Retinoic acid signalling during development. *Development*. 2012; 139(5):843–58. <https://doi.org/10.1242/dev.065938> PMID: 22318625.
29. Cunningham TJ, Duester G. Mechanisms of retinoic acid signalling and its roles in organ and limb development. *Nature reviews Molecular cell biology*. 2015; 16(2):110–23. <https://doi.org/10.1038/nrm3932> PMID: 25560970; PubMed Central PMCID: PMC4636111.
30. Bohnsack BL, Kasprick DS, Kish PE, Goldman D, Kahana A. A zebrafish model of axenfeld-rieger syndrome reveals that pitx2 regulation by retinoic acid is essential for ocular and craniofacial development. *Investigative ophthalmology & visual science*. 2012; 53(1):7–22. <https://doi.org/10.1167/iov.11-8494> PMID: 22125274; PubMed Central PMCID: PMC3292384.
31. Harding P, Moosajee M. The Molecular Basis of Human Anophthalmia and Microphthalmia. *J Dev Biol*. 2019; 7(3):16. <https://doi.org/10.3390/jdb7030016> PMID: 31416264; PubMed Central PMCID: PMC6787759.
32. See AW, Kaiser ME, White JC, Clagett-Dame M. A nutritional model of late embryonic vitamin A deficiency produces defects in organogenesis at a high penetrance and reveals new roles for the vitamin in skeletal development. *Developmental biology*. 2008; 316(2):171–90. <https://doi.org/10.1016/j.ydbio.2007.10.018> PMID: 18321479.
33. Cvekl A, Wang WL. Retinoic acid signaling in mammalian eye development. *Exp Eye Res*. 2009; 89(3):280–91. <https://doi.org/10.1016/j.exer.2009.04.012> PMID: 19427305; PubMed Central PMCID: PMC2756743.
34. Matt N, Dupe V, Garnier JM, Dennefeld C, Chambon P, Mark M, et al. Retinoic acid-dependent eye morphogenesis is orchestrated by neural crest cells. *Development*. 2005; 132(21):4789–800. Epub 2005/10/07. <https://doi.org/10.1242/dev.02031> PMID: 16207763.
35. Matt N, Ghyselinck NB, Pellerin I, Dupe V. Impairing retinoic acid signalling in the neural crest cells is sufficient to alter entire eye morphogenesis. *Developmental biology*. 2008; 320(1):140–8. Epub 2008/06/10. <https://doi.org/10.1016/j.ydbio.2008.04.039> PMID: 18539269.
36. Molotkov A, Molotkova N, Duester G. Retinoic acid guides eye morphogenetic movements via paracrine signaling but is unnecessary for retinal dorsoventral patterning. *Development*. 2006; 133(10):1901–10. Epub 2006/04/14. <https://doi.org/10.1242/dev.02328> PMID: 16611695; PubMed Central PMCID: PMC2833011.
37. Williams AL, Bohnsack BL. Neural crest derivatives in ocular development: discerning the eye of the storm. *Birth defects research Part C, Embryo today: reviews*. 2015; 105(2):87–95. <https://doi.org/10.1002/bdrc.21095> PMID: 26043871; PubMed Central PMCID: PMC5262495.

38. Couly GF, Coltey PM, Douarin NML. The developmental fate of the cephalic mesoderm in quail-chick chimeras. *Development*. 1992; 114:1–15. PMID: [1576952](#)
39. Creuzet S, Couly G, Le Douarin NM. Patterning the neural crest derivatives during development of the vertebrate head: insights from avian studies. *J Anat*. 2005; 207(5):447–59. <https://doi.org/10.1111/j.1469-7580.2005.00485.x> PMID: [16313387](#); PubMed Central PMCID: PMC1571568.
40. Gage PJ, Rhoades W, Prucka SK, Hjalt T. Fate maps of neural crest and mesoderm in the mammalian eye. *Investigative ophthalmology & visual science*. 2005; 46(11):4200–8. Epub 2005/10/27. <https://doi.org/10.1167/iovs.05-0691> PMID: [16249499](#).
41. Grenier J, Teillet MA, Grifone R, Kelly RG, Duprez D. Relationship between neural crest cells and cranial mesoderm during head muscle development. *PLoS ONE*. 2009; 4(2):e4381. <https://doi.org/10.1371/journal.pone.0004381> PMID: [19198652](#).
42. Johnston MC, Noden DM, Hazelton RD, Coulombre JL, Coulombre AJ. Origins of avian ocular and periocular tissues. *Exp Eye Res*. 1979; 29(1):27–43. [https://doi.org/10.1016/0014-4835\(79\)90164-7](https://doi.org/10.1016/0014-4835(79)90164-7) PMID: [510425](#).
43. Noden DM. The embryonic origins of avian cephalic and cervical muscles and associated connective tissues. *Am J Anat*. 1983; 168:257–76. <https://doi.org/10.1002/aja.1001680302> PMID: [6650439](#)
44. Sevel D. The origins and insertions of the extraocular muscles: development, histologic features, and clinical significance. *Trans Am Ophthalmol Soc*. 1986; 84:488–526. PMID: [3590478](#); PubMed Central PMCID: PMC1298748.
45. Danielian PS, Muccino D, Rowitch DH, Michael SK, McMahon AP. Modification of gene activity in mouse embryos in utero by a tamoxifen-inducible form of Cre recombinase. *Curr Biol*. 1998; 8(24):1323–6. [https://doi.org/10.1016/s0960-9822\(07\)00562-3](https://doi.org/10.1016/s0960-9822(07)00562-3) PMID: [9843687](#).
46. Saga Y, Miyagawa-Tomita S, Takagi A, Kitajima S, Miyazaki J, Inoue T. MesP1 is expressed in the heart precursor cells and required for the formation of a single heart tube. *Development*. 1999; 126(15):3437–47. PMID: [10393122](#).
47. Mathew SJ, Hansen JM, Merrell AJ, Murphy MM, Lawson JA, Hutcheson DA, et al. Connective tissue fibroblasts and Tcf4 regulate myogenesis. *Development*. 2011; 138(2):371–84. Epub 2010/12/24. <https://doi.org/10.1242/dev.057463> PMID: [21177349](#); PubMed Central PMCID: PMC3005608.
48. Pryce BA, Brent AE, Murchison ND, Tabin CJ, Schweitzer R. Generation of transgenic tendon reporters, ScxGFP and ScxAP, using regulatory elements of the scleraxis gene. *Developmental dynamics: an official publication of the American Association of Anatomists*. 2007; 236(6):1677–82. Epub 2007/05/15. <https://doi.org/10.1002/dvdy.21179> PMID: [17497702](#).
49. Deries M, Schweitzer R, Duxson MJ. Developmental fate of the mammalian myotome. *Developmental dynamics: an official publication of the American Association of Anatomists*. 2010; 239(11):2898–910. <https://doi.org/10.1002/dvdy.22425> PMID: [20865781](#).
50. Stricker S, Mathia S, Haupt J, Seemann P, Meier J, Mundlos S. Odd-skipped related genes regulate differentiation of embryonic limb mesenchyme and bone marrow mesenchymal stromal cells. *Stem Cells Dev*. 2012; 21(4):623–33. <https://doi.org/10.1089/scd.2011.0154> PMID: [21671783](#).
51. Sulik KK, Dehart DB, Johnson CS, Ellis SL, Chen SY, Dunty WC Jr., et al. Programmed cell death in extraocular muscle tendon/sclera precursors. *Molecular vision*. 2001; 7:184–91. Epub 2001/08/15. PMID: [11503002](#).
52. Fogel JL, Thein TZ, Mariani FV. Use of LysoTracker to detect programmed cell death in embryos and differentiating embryonic stem cells. *J Vis Exp*. 2012; (68). <https://doi.org/10.3791/4254> PMID: [23092960](#); PubMed Central PMCID: PMC3490301.
53. Blitz E, Sharir A, Akiyama H, Zelzer E. Tendon-bone attachment unit is formed modularly by a distinct pool of Scx- and Sox9-positive progenitors. *Development*. 2013; 140(13):2680–90. <https://doi.org/10.1242/dev.093906> PMID: [23720048](#).
54. Blitz E, Viukov S, Sharir A, Shwartz Y, Galloway JL, Pryce BA, et al. Bone ridge patterning during musculoskeletal assembly is mediated through SCX regulation of Bmp4 at the tendon-skeleton junction. *Developmental cell*. 2009; 17(6):861–73. <https://doi.org/10.1016/j.devcel.2009.10.010> PMID: [20059955](#); PubMed Central PMCID: PMC3164485.
55. Roberts RR, Bobzin L, Teng CS, Pal D, Tuzon CT, Schweitzer R, et al. FGF signaling patterns cell fate at the interface between tendon and bone. *Development*. 2019; 146(15). <https://doi.org/10.1242/dev.170241> PMID: [31320326](#); PubMed Central PMCID: PMC6703712.
56. Sugimoto Y, Takimoto A, Akiyama H, Kist R, Scherer G, Nakamura T, et al. Scx+/Sox9+ progenitors contribute to the establishment of the junction between cartilage and tendon/ligament. *Development*. 2013; 140(11):2280–8. <https://doi.org/10.1242/dev.096354> PMID: [23615282](#).
57. Thompson H, Griffiths JS, Jeffery G, McGonnell IM. The retinal pigment epithelium of the eye regulates the development of scleral cartilage. *Developmental biology*. 2010; 347(1):40–52. <https://doi.org/10.1016/j.ydbio.2010.08.006> PMID: [20707994](#); PubMed Central PMCID: PMC2977850.

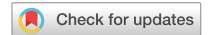
58. Grindley JC, Davidson DR, Hill RE. The role of Pax-6 in eye and nasal development. *Development*. 1995; 121(5):1433–42. PMID: [7789273](#).
59. Roberts RC. Small eyes—a new dominant eye mutant in the mouse. *Genet Res, Cam*. 1967; 9:121–2. <https://doi.org/10.1017/S0016672300010387>
60. Kaufman MH, Chang HH, Shaw JP. Craniofacial abnormalities in homozygous Small eye (Sey/Sey) embryos and newborn mice. *J Anat*. 1995; 186(Pt 3):607–17. PMID: [7559133](#); PubMed Central PMCID: PMC1167018.
61. Hagglund AC, Dahl L, Carlsson L. Lhx2 is required for patterning and expansion of a distinct progenitor cell population committed to eye development. *PLoS ONE*. 2011; 6(8):e23387. <https://doi.org/10.1371/journal.pone.0023387> PMID: [21886788](#); PubMed Central PMCID: PMC3158764.
62. Twitty VC. Influence of the eye on the growth of its associated structures, studied by means of heteroplastic transplantation. *Journal of Experimental Zoology*. 1932; 61:333–74. <https://doi.org/10.1002/jez.1400610302>
63. Duester G. Keeping an eye on retinoic acid signaling during eye development. *Chem Biol Interact*. 2009; 178(1–3):178–81. <https://doi.org/10.1016/j.cbi.2008.09.004> PMID: [18831967](#); PubMed Central PMCID: PMC2646828.
64. Dupe V, Matt N, Garnier JM, Chambon P, Mark M, Ghyselinck NB. A newborn lethal defect due to inactivation of retinaldehyde dehydrogenase type 3 is prevented by maternal retinoic acid treatment. *Proceedings of the National Academy of Sciences of the United States of America*. 2003; 100(24):14036–41. <https://doi.org/10.1073/pnas.2336223100> PMID: [14623956](#); PubMed Central PMCID: PMC283541.
65. Rhinn M, Schuhbauer B, Niederreither K, Dolle P. Involvement of retinol dehydrogenase 10 in embryonic patterning and rescue of its loss of function by maternal retinaldehyde treatment. *Proceedings of the National Academy of Sciences of the United States of America*. 2011; 108(40):16687–92. <https://doi.org/10.1073/pnas.1103877108> PMID: [21930923](#); PubMed Central PMCID: PMC3189044.
66. Osumi-Yamashita N, Ninomiya Y, Doi H, Eto K. The contribution of both forebrain and midbrain crest cells to the mesenchyme in the frontonasal mass of mouse embryos. *Developmental biology*. 1994; 164(2):409–19. <https://doi.org/10.1006/dbio.1994.1211> PMID: [8045344](#).
67. Serbedzija GN, Bronner-Fraser M, Fraser SE. Vital dye analysis of cranial neural crest cell migration in the mouse embryo. *Development*. 1992; 116(2):297–307. PMID: [1283734](#).
68. Chawla B, Schley E, Williams AL, Bohnsack BL. Retinoic Acid and Pitx2 Regulate Early Neural Crest Survival and Migration in Craniofacial and Ocular Development. *Birth Defects Res B Dev Reprod Toxicol*. 2016; 107(3):126–35. <https://doi.org/10.1002/bdrb.21177> PMID: [27175943](#).
69. Sandell LL, Sanderson BW, Moiseyev G, Johnson T, Mushegian A, Young K, et al. RDH10 is essential for synthesis of embryonic retinoic acid and is required for limb, craniofacial, and organ development. *Genes & development*. 2007; 21(9):1113–24. <https://doi.org/10.1101/gad.1533407> PMID: [17473173](#); PubMed Central PMCID: PMC1855236.
70. Colasanto MP, Eyal S, Mohassel P, Bamshad M, Bonnemann CG, Zelzer E, et al. Development of a subset of forelimb muscles and their attachment sites requires the ulnar-mammary syndrome gene Tbx3. *Dis Model Mech*. 2016; 9(11):1257–69. <https://doi.org/10.1242/dmm.025874> PMID: [27491074](#); PubMed Central PMCID: PMC5117227.
71. Hasson P, DeLaurier A, Bennett M, Grigorieva E, Naiche LA, Papaioannou VE, et al. Tbx4 and tbx5 acting in connective tissue are required for limb muscle and tendon patterning. *Developmental cell*. 2010; 18(1):148–56. <https://doi.org/10.1016/j.devcel.2009.11.013> PMID: [20152185](#); PubMed Central PMCID: PMC3034643.
72. Swinehart IT, Schlientz AJ, Quintanilla CA, Mortlock DP, Wellik DM. Hox11 genes are required for regional patterning and integration of muscle, tendon and bone. *Development*. 2013; 140(22):4574–82. <https://doi.org/10.1242/dev.096693> PMID: [24154528](#); PubMed Central PMCID: PMC3817943.
73. Chassot AA, Le Rolle M, Jolivet G, Stevant I, Guignon JM, Da Silva F, et al. Retinoic acid synthesis by ALDH1A proteins is dispensable for meiosis initiation in the mouse fetal ovary. *Sci Adv*. 2020; 6(21):eaaz1261. Epub 2020/06/05. <https://doi.org/10.1126/sciadv.aaz1261> PMID: [32494737](#); PubMed Central PMCID: PMC7244317.
74. Madisen L, Zwingman TA, Sunkin SM, Oh SW, Zariwala HA, Gu H, et al. A robust and high-throughput Cre reporting and characterization system for the whole mouse brain. *Nature neuroscience*. 2010; 13(1):133–40. Epub 2009/12/22. <https://doi.org/10.1038/nn.2467> PMID: [20023653](#); PubMed Central PMCID: PMC2840225.
75. Muzumdar MD, Tasic B, Miyamichi K, Li L, Luo L. A global double-fluorescent Cre reporter mouse. *Genesis*. 2007; 45(9):593–605. <https://doi.org/10.1002/dvg.20335> PMID: [17868096](#).
76. Nakamura E, Nguyen MT, Mackem S. Kinetics of tamoxifen-regulated Cre activity in mice using a cartilage-specific CreER(T) to assay temporal activity windows along the proximodistal limb skeleton.

- Developmental dynamics: an official publication of the American Association of Anatomists. 2006; 235(9):2603–12. <https://doi.org/10.1002/dvdy.20892> PMID: 16894608.
77. Nguyen MT, Zhu J, Nakamura E, Bao X, Mackem S. Tamoxifen-dependent, inducible Hoxb6CreERT recombinase function in lateral plate and limb mesoderm, CNS isthmus organizer, posterior trunk neural crest, hindgut, and tailbud. *Developmental dynamics: an official publication of the American Association of Anatomists*. 2009; 238(2):467–74. <https://doi.org/10.1002/dvdy.21846> PMID: 19161221; PubMed Central PMCID: PMC3483870.
  78. Rajaii F, Bitzer ZT, Xu Q, Sockanathan S. Expression of the dominant negative retinoid receptor, RAR403, alters telencephalic progenitor proliferation, survival, and cell fate specification. *Developmental biology*. 2008; 316(2):371–82. <https://doi.org/10.1016/j.ydbio.2008.01.041> PMID: 18329011.
  79. Wood WM, Etemad S, Yamamoto M, Goldhamer DJ. MyoD-expressing progenitors are essential for skeletal myogenesis and satellite cell development. *Developmental biology*. 2013; 384(1):114–27. Epub 2013/09/24. <https://doi.org/10.1016/j.ydbio.2013.09.012> PMID: 24055173; PubMed Central PMCID: PMC3838901.
  80. Kastner P, Grondona JM, Mark M, Gansmuller A, LeMeur M, Decimo D, et al. Genetic analysis of RXR alpha developmental function: convergence of RXR and RAR signaling pathways in heart and eye morphogenesis. *Cell*. 1994; 78(6):987–1003. [https://doi.org/10.1016/0092-8674\(94\)90274-7](https://doi.org/10.1016/0092-8674(94)90274-7) PMID: 7923367.
  81. Mori M, Ghyselinck NB, Chambon P, Mark M. Systematic immunolocalization of retinoid receptors in developing and adult mouse eyes. *Investigative ophthalmology & visual science*. 2001; 42(6):1312–8. PMID: 11328745.
  82. Oh SP, Griffith CM, Hay ED, Olsen BR. Tissue-specific expression of type XII collagen during mouse embryonic development. *Developmental dynamics: an official publication of the American Association of Anatomists*. 1993; 196(1):37–46. <https://doi.org/10.1002/aja.1001960105> PMID: 8334298.
  83. Sambasivan R, Gayraud-Morel B, Dumas G, Cimper C, Paisant S, Kelly R, et al. Distinct regulatory cascades govern extraocular and pharyngeal arch muscle progenitor cell fates. *Developmental cell*. 2009; 16(6):810–21. <https://doi.org/10.1016/j.devcel.2009.05.008> PMID: 19531352.
  84. Huang AH, Riordan TJ, Pryce B, Weibel JL, Watson SS, Long F, et al. Musculoskeletal integration at the wrist underlies the modular development of limb tendons. *Development*. 2015; 142(14):2431–41. <https://doi.org/10.1242/dev.122374> PMID: 26062940; PubMed Central PMCID: PMC4510863.
  85. McBratney-Owen B, Iseki S, Bamforth SD, Olsen BR, Morriss-Kay GM. Development and tissue origins of the mammalian cranial base. *Developmental biology*. 2008; 322(1):121–32. <https://doi.org/10.1016/j.ydbio.2008.07.016> PMID: 18680740; PubMed Central PMCID: PMC2847450.
  86. Heude E, Tesarova M, Sefton EM, Jullian E, Adachi N, Grimaldi A, et al. Unique morphogenetic signatures define mammalian neck muscles and associated connective tissues. *Elife*. 2018;7. <https://doi.org/10.7554/eLife.40179> PMID: 30451684; PubMed Central PMCID: PMC6310459.
  87. Germain P, Gaudon C, Pogenberg V, Sanglier S, Van Dorsselaer A, Royer CA, et al. Differential action on coregulator interaction defines inverse retinoid agonists and neutral antagonists. *Chem Biol*. 2009; 16(5):479–89. <https://doi.org/10.1016/j.chembiol.2009.03.008> PMID: 19477412.
  88. Chambers D, Wilson L, Maden M, Lumsden A. RALDH-independent generation of retinoic acid during vertebrate embryogenesis by CYP1B1. *Development*. 2007; 134(7):1369–83. <https://doi.org/10.1242/dev.02815> PMID: 17329364.
  89. Rossant J, Zirngibl R, Cado D, Shago M, Giguere V. Expression of a retinoic acid response element-hsplacZ transgene defines specific domains of transcriptional activity during mouse embryogenesis. *Genes & development*. 1991; 5(8):1333–44. <https://doi.org/10.1101/gad.5.8.1333> PMID: 1907940.
  90. Comai G, Sambasivan R, Gopalakrishnan S, Tajbakhsh S. Variations in the efficiency of lineage marking and ablation confound distinctions between myogenic cell populations. *Developmental cell*. 2014; 31(5):654–67. Epub 2014/12/10. <https://doi.org/10.1016/j.devcel.2014.11.005> PMID: 25490270.
  91. Liu J, Willet SG, Bankaitis ED, Xu Y, Wright CV, Gu G. Non-parallel recombination limits Cre-LoxP-based reporters as precise indicators of conditional genetic manipulation. *Genesis*. 2013; 51(6):436–42. Epub 2013/02/27. <https://doi.org/10.1002/dvg.22384> PMID: 23441020; PubMed Central PMCID: PMC3696028.
  92. Long MA, Rossi FM. Silencing inhibits Cre-mediated recombination of the Z/AP and Z/EG reporters in adult cells. *PLoS ONE*. 2009; 4(5):e5435. <https://doi.org/10.1371/journal.pone.0005435> PMID: 19415111; PubMed Central PMCID: PMC2672169.
  93. Ma Q, Zhou B, Pu WT. Reassessment of Isl1 and Nkx2-5 cardiac fate maps using a Gata4-based reporter of Cre activity. *Developmental biology*. 2008; 323(1):98–104. Epub 2008/09/09. <https://doi.org/10.1016/j.ydbio.2008.08.013> PMID: 18775691; PubMed Central PMCID: PMC2655699.
  94. Chevallier A, Kieny M. On the role of the connective tissue in the patterning of the chick limb musculature. *Wilehm Roux Arch Dev Biol*. 1982; 191(4):277–80. <https://doi.org/10.1007/BF00848416> PMID: 28305059.

95. Rodriguez-Guzman M, Montero JA, Santesteban E, Ganan Y, Macias D, Hurle JM. Tendon-muscle crosstalk controls muscle bellies morphogenesis, which is mediated by cell death and retinoic acid signaling. *Developmental biology*. 2007; 302(1):267–80. <https://doi.org/10.1016/j.ydbio.2006.09.034> PMID: 17070795.
96. Gilbert P. The origin and development of the human extrinsic ocular muscles. 1957. *Carnegie Inst. Wash. Publ.* 611, *Contrib. Embryol.* 36: 59–78.
97. Gilbert PW. The origin and development of the extrinsic ocular muscles in the domestic cat. *Journal of morphology*. 1947; 81(2):151–93. Epub 1947/09/01. PMID: 20258884.
98. Jernvall J, Aberg T, Kettunen P, Keranen S, Thesleff I. The life history of an embryonic signaling center: BMP-4 induces p21 and is associated with apoptosis in the mouse tooth enamel knot. *Development*. 1998; 125(2):161–9. PMID: 9486790.
99. Nonomura K, Yamaguchi Y, Hamachi M, Koike M, Uchiyama Y, Nakazato K, et al. Local apoptosis modulates early mammalian brain development through the elimination of morphogen-producing cells. *Developmental cell*. 2013; 27(6):621–34. <https://doi.org/10.1016/j.devcel.2013.11.015> PMID: 24369835.
100. Moreno E, Valon L, Levillayer F, Levayer R. Competition for Space Induces Cell Elimination through Compaction-Driven ERK Downregulation. *Curr Biol*. 2019; 29(1):23–34 e8. <https://doi.org/10.1016/j.cub.2018.11.007> PMID: 30554899; PubMed Central PMCID: PMC6331351.
101. Franz-Odenaal TA, Vickaryous MK. Skeletal elements in the vertebrate eye and adnexa: morphological and developmental perspectives. *Developmental dynamics: an official publication of the American Association of Anatomists*. 2006; 235(5):1244–55. <https://doi.org/10.1002/dvdy.20718> PMID: 16496288.
102. Eyal S, Kult S, Rubin S, Krief S, Felsenthal N, Pineault KM, et al. Bone morphology is regulated modularly by global and regional genetic programs. *Development*. 2019; 146(14). <https://doi.org/10.1242/dev.167882> PMID: 31221640; PubMed Central PMCID: PMC6679367.
103. Kish PE, Bohnsack BL, Gallina D, Kasprick DS, Kahana A. The eye as an organizer of craniofacial development. *Genesis*. 2011; 49(4):222–30. Epub 2011/02/11. <https://doi.org/10.1002/dvg.20716> PMID: 21309065; PubMed Central PMCID: PMC3690320.
104. Langenberg T, Kahana A, Wszalek JA, Halloran MC. The eye organizes neural crest cell migration. *Developmental dynamics: an official publication of the American Association of Anatomists*. 2008; 237(6):1645–52. <https://doi.org/10.1002/dvdy.21577> PMID: 18498099; PubMed Central PMCID: PMC2762319.
105. Zein WM, Lewanda AF, Traboulsi EI, Jabs EW. Ocular Manifestations of Syndromes with Craniofacial Abnormalities. In: Traboulsi EI, editor. *Genetic Diseases of the Eye* (2nd ed). New York: Oxford University Press; 2012. p. 174–89
106. Durand JP. Ocular development and involution in the European cave salamander, *Proteus anguinus laurenti*. *Biol Bull*. 1976; 151(3):450–66. <https://doi.org/10.2307/1540499> PMID: 1016662.
107. Yamamoto Y, Stock DW, Jeffery WR. Hedgehog signalling controls eye degeneration in blind cavefish. *Nature*. 2004; 431(7010):844–7. <https://doi.org/10.1038/nature02864> PMID: 15483612.
108. Lamb TD, Collin SP, Pugh EN Jr. Evolution of the vertebrate eye: opsins, photoreceptors, retina and eye cup. *Nature reviews Neuroscience*. 2007; 8(12):960–76. <https://doi.org/10.1038/nrn2283> PMID: 18026166; PubMed Central PMCID: PMC3143066.
109. Tajbakhsh S, Rocancourt D, Buckingham M. Muscle progenitor cells failing to respond to positional cues adopt non-myogenic fates in myf-5 null mice. *Nature*. 1996; 384:266–70. <https://doi.org/10.1038/384266a0> PMID: 8918877
110. Yamamoto M, Shook NA, Kanisicak O, Yamamoto S, Wosczyzna MN, Camp JR, et al. A multifunctional reporter mouse line for Cre- and FLP-dependent lineage analysis. *Genesis*. 2009; 47(2):107–14. <https://doi.org/10.1002/dvg.20474> PMID: 19165827.
111. Chapellier B, Mark M, Bastien J, Dierich A, LeMeur M, Chambon P, et al. A conditional floxed (loxP-flanked) allele for the retinoic acid receptor beta (RARbeta) gene. *Genesis*. 2002; 32(2):91–4. <https://doi.org/10.1002/gene.10073> PMID: 11857787.
112. Chapellier B, Mark M, Garnier JM, Dierich A, Chambon P, Ghyselinck NB. A conditional floxed (loxP-flanked) allele for the retinoic acid receptor gamma (RARgamma) gene. *Genesis*. 2002; 32(2):95–8. <https://doi.org/10.1002/gene.10072> PMID: 11857788.
113. Comai G, Heude E, Mella S, Paisant S, Pala F, Gallardo M, et al. A distinct cardiopharyngeal mesoderm genetic hierarchy establishes antero-posterior patterning of esophagus striated muscle. *Elife*. 2019; 8. <https://doi.org/10.7554/eLife.47460> PMID: 31535973; PubMed Central PMCID: PMC6752947.
114. Yokomizo T, Yamada-Inagawa T, Yzaguirre AD, Chen MJ, Speck NA, Dzierzak E. Whole-mount three-dimensional imaging of internally localized immunostained cells within mouse embryos. *Nat*

- Protoc. 2012; 7(3):421–31. <https://doi.org/10.1038/nprot.2011.441> PMID: 22322215; PubMed Central PMCID: PMC3629302.
115. Zucker RM, Hunter ES, 3rd, Rogers JM. Apoptosis and morphology in mouse embryos by confocal laser scanning microscopy. *Methods*. 1999; 18(4):473–80. <https://doi.org/10.1006/meth.1999.0815> PMID: 10491277.
  116. Babai F, Musevi-Aghdam J, Schurch W, Royal A, Gabbiani G. Coexpression of alpha-sarcomeric actin, alpha-smooth muscle actin and desmin during myogenesis in rat and mouse embryos I. *Skeletal muscle*. *Differentiation*. 1990; 44(2):132–42. <https://doi.org/10.1111/j.1432-0436.1990.tb00546.x> PMID: 2283002.
  117. Li L, Miano JM, Cserjesi P, Olson EN. SM22 alpha, a marker of adult smooth muscle, is expressed in multiple myogenic lineages during embryogenesis. *Circulation research*. 1996; 78(2):188–95. <https://doi.org/10.1161/01.res.78.2.188> PMID: 8575061.
  118. Sawtell NM, Lessard JL. Cellular distribution of smooth muscle actins during mammalian embryogenesis: expression of the alpha-vascular but not the gamma-enteric isoform in differentiating striated myocytes. *The Journal of cell biology*. 1989; 109(6 Pt 1):2929–37. <https://doi.org/10.1083/jcb.109.6.2929> PMID: 2687290; PubMed Central PMCID: PMC2115902.
  119. Li Z, Marchand P, Humbert J, Babinet C, Paulin D. Desmin sequence elements regulating skeletal muscle-specific expression in transgenic mice. *Development*. 1993; 117(3):947–59. PMID: 8325245.
  120. Bader D, Masaki T, Fischman DA. Immunochemical analysis of myosin heavy chain during avian myogenesis in vivo and in vitro. *The Journal of cell biology*. 1982; 95(3):763–70. <https://doi.org/10.1083/jcb.95.3.763> PMID: 6185504; PubMed Central PMCID: PMC2112936.
  121. Metscher BD. MicroCT for developmental biology: a versatile tool for high-contrast 3D imaging at histological resolutions. *Developmental dynamics: an official publication of the American Association of Anatomists*. 2009; 238(3):632–40. <https://doi.org/10.1002/dvdy.21857> PMID: 19235724.
  122. Kaucka M, Petersen J, Tesarova M, Szarowska B, Kastriti ME, Xie M, et al. Signals from the brain and olfactory epithelium control shaping of the mammalian nasal capsule cartilage. *Elife*. 2018;7. <https://doi.org/10.7554/eLife.34465> PMID: 29897331; PubMed Central PMCID: PMC6019068.

PAPER [XIV]



OPEN

## Contrast enhanced X-ray computed tomography imaging of amyloid plaques in Alzheimer disease rat model on lab based micro CT system

Michaela Kavkova<sup>1</sup>✉, Tomas Zikmund<sup>1</sup>, Annu Kala<sup>2</sup>, Jakub Salplachta<sup>1</sup>,  
Stephanie L. Proskauer Pena<sup>2</sup>, Josef Kaiser<sup>1</sup> & Karel Jezek<sup>2</sup>✉

Amyloid plaques are small (~ 50 μm), highly-dense aggregates of amyloid beta (Aβ) protein in brain tissue, supposed to play a key role in pathogenesis of Alzheimer's disease (AD). Plaques' in vivo detection, spatial distribution and quantitative characterization could be an essential marker in diagnostics and evaluation of AD progress. However, current imaging methods in clinics possess substantial limits in sensitivity towards Aβ plaques to play a considerable role in AD screening. Contrast enhanced X-ray micro computed tomography (micro CT) is an emerging highly sensitive imaging technique capable of high resolution visualization of rodent brain. In this study we show the absorption based contrast enhanced X-ray micro CT imaging is viable method for detection and 3D analysis of Aβ plaques in transgenic rodent models of Alzheimer's disease. Using iodine contrasted brain tissue isolated from the Tg-F344-AD rat model we show the micro CT imaging is capable of precise imaging of Aβ plaques, making possible to further analyze various aspects of their 3D spatial distribution and other properties.

Alzheimer's disease (AD) is the most common cause of dementia worldwide, extensively interfering with personal, social, and health care levels of human society. AD progression is characterized by a gradual deterioration of cognitive abilities, starting with often unnoticed declarative memory impairment, followed by problems with spatial orientation, and ending with an inability to cope with daily life routine. The rare early onset form can affect individuals in their 40 s or 50 s, but the AD risk rapidly increases after the age of 65. While the etiology of AD remains still unclear, there are several hypothesized mechanisms reflecting molecular changes observed in brain tissue of AD patients, mainly the deposits of amyloid beta and hyperphosphorylated tau protein<sup>1-3</sup>. The classical "amyloid cascade hypothesis"<sup>4</sup> states that the amyloid beta (Aβ) plaques are the causative agent of Alzheimer's pathology. The Aβ plaques are small (~ 50 μm), dense objects composed of clumped fibrils of amyloid β (Aβ), a peptidic product of the amyloid precursor protein. Their formation induces a local inflammation resulting in progressive cellular loss and related cognitive inability. It has been therefore assumed that the reduction of Aβ deposits might help to control the AD course. Numerous approaches have been designed to reduce the Aβ content in the brain tissue<sup>5</sup>. In order to test the effectiveness of such an AD therapy, there is a substantial need of a non-invasive, precise, and reproducible imaging method to analyze the location and size of the Aβ plaques in the brain.

In the large majority of studies on mouse and rat models, the amyloid plaques were quantified histologically in sliced and stained brain tissue. While the histology and immunohistochemistry still remain important routines for characterizing the plaque properties, imaging techniques represent a powerful tool for a precise 3D analysis of plaque distribution.

So far all the attempts to image the amyloid plaques in rodent brain by Computed Tomography (CT) have been performed on mouse brain (*mus musculus*). The experiments were performed with synchrotron X-ray sources using variations of phase contrast imaging to visualize the Aβ plaques<sup>6-11</sup>. Overall, in all published

<sup>1</sup>Central European Institute of Technology, Brno University of Technology, Brno, Czech Republic. <sup>2</sup>Faculty of Medicine in Pilsen, Charles University, Pilsen, Czech Republic. ✉email: michaela.kavkova@ceitec.vutbr.cz; karel.jezek@lfp.cuni.cz

papers on the topic of A $\beta$  plaques detection, the authors were able to identify the A $\beta$  plaques in the mouse brain using phase contrast imaging, some even performing quantitative analyses<sup>11</sup>. However, imaging at synchrotron facilities is often limited by the narrow field of view resulting in a need of several scans for the imaging of one brain. Also, the access to synchrotron facilities is very limited and burdened by the high price of the CT scans.

Absorption based contrast enhanced X-ray micro CT imaging utilizing a lab based industrial micro CT devices is an emerging imaging technique which uses the staining solutions with high proton number elements to employ the contrast in soft tissues of biological samples which are in their native state invisible to X-rays<sup>12,13</sup>. Contrast enhanced micro CT imaging has been previously proved to be a promising method for a precise 3D analysis of wide variety of samples such as the developing cartilage of nasal capsule of mice<sup>14–17</sup>, development of palate<sup>18,19</sup>, complex tooth shape in reptiles<sup>20</sup>, research of congenital heart and kidneys defects<sup>21</sup>, formation of mammalian neck muscles<sup>22</sup> and even a noninvasive observation of a human embryo<sup>23</sup>. One of the advantages of micro CT imaging is the possibility to translate a micro CT generated 3D model into a 3D pdf format, which enables an easier communication of obtained data<sup>24</sup>.

The main advantage of absorption based contrast enhanced X-ray micro CT imaging is the possibility to obtain precise 3D information about inner structures of the entire brain without sectioning (which might induce artifacts related to brain deformation or missing tissue due to the sectioning). The micro CT imaging of rodent brain has been previously used for the visualization of vascular system of mouse brain filled with radio-opaque silicone rubber Microfil<sup>25–31</sup>, as a tool for localization of cerebral ischemia<sup>32,33</sup> to test the efficiency of different micro CT contrasting agents<sup>24–38</sup>, and even for the analysis of specific structures of the brain<sup>39</sup>.

However, it has not been previously determined whether the absorption based contrast enhanced X-ray micro CT imaging is capable of detecting and quantifying amyloid plaques in the brains of rodents. In this study, we optimized the mouse brain staining protocol<sup>40</sup> for the staining of a much larger rat brain. The lab based industrial micro CT device GE Phoenix v|tome|x L 240 was utilized to scan the contrast enhanced brains of a recent rat AD model to determine whether amyloid plaques could be detected by contrast enhanced micro CT imaging. Further, the exploration of the possibilities of A $\beta$  plaque analyses provided by obtained high resolution micro CT data was pursued. This experimental setup promises a faster, more precise and accessible alternative to the synchrotron based micro CT imaging of the A $\beta$  plaque deposits.

## Results

We used brains from three 18 months old female rats (two transgenic TgF-344 AD animals and one wild type control). The micro CT scan slices of iodine stained brains from transgenic and wild type samples are shown in the Fig. 1a (for an animated movie see the [Supplementary material](#)). Besides the basic anatomical structures visualized equally across both brains, the transgenic brain expressed a large amount of dark grey spots—most likely suspect A $\beta$  plaques that were condensed widely in cortical (neocortex, hippocampus) and some subcortical areas.

Beta amyloid is the main component of amyloid plaques. Because of their dense protein content, we expected the applied iodine based contrasting protocol would preferably stain the tissue around the amyloid plaques, resulting in their “negative” highlight in the micro CT data. The golden standard for beta amyloid detection is its immunostaining by binding to a specific antibody tagged by fluorescent probe. Here, we used this approach to validate the identity of lower density loci detected by micro CT in the transgenic samples. To confirm the identity of the suspect plaques, the iodine stained brain samples were washed in ethanol solution after the micro CT scanning, cut into histological sections and finally specifically stained for the amyloid protein. For selected histological slices we identified their respective sections in the micro CT data. The resulting comparison is displayed in Fig. 1b which shows the corresponding slice as a micro CT image (1b) and as a histological section (Fig. 1c, detailed view in Fig. 1d). The placements of the suspect A $\beta$  plaques overlapped with the immunodetected A $\beta$  plaques positions (arrows in Fig. 1d). This match strongly supports the fact that the introduced micro CT protocol sufficiently detects individual amyloid plaques in ex vivo whole brain.

In the industrial micro CT setups that use the cone beam geometry, the dimension of the sample is one of the main factors that determine the resulting voxel size of the obtained dataset. To acquire a 3D distribution of A $\beta$  plaques in the best possible details, we decided to image an isolated part of the brain and to scan it again with a smaller voxel size. We focused on the dorsal hippocampus as this structure is severely impaired by the amyloid accumulation and cellular loss in AD. The dissected dorsal part of the hippocampus is showed in Fig. 2a,b. While the whole brain scan delivered a voxel size of 9  $\mu\text{m}$  (Fig. 2c), in the case of isolated hippocampus we achieved a voxel dimension of 3  $\mu\text{m}$  (Fig. 2d). The comparison of both scans convincingly shows that the readability of the large amyloid plaques’ borders and especially the visibility of small plaques was compromised, even though they were distinguishable in the whole brain scan. On the contrary, the dissected sample yielded a considerably higher level of detail, enabling to detect a large amount of plaques of various sizes.

The next step was designed to assess the sensitivity of amyloid plaques detection using micro CT in contrast to the standard immunohistological staining. After the CT measurement, we sliced the isolated hippocampal tissue sample. Despite the dehydrated and iodine stained tissue turned out to be highly fragile while slicing, we were able to select four well preserved tissue sections and immunostained them for the A $\beta$  presence. Then the corresponding micro CT sections were identified and their match was evaluated (Fig. 3a,b). The areas of A $\beta$  deposit cross sections were marked by different observers. Each of the micro CT/histology image pairs was treated as independent. We obtained the plaque area median value of 597.9  $\mu\text{m}^2$  (IQR 862.3  $\mu\text{m}^2$ ) from CT data, whereas only 28.9  $\mu\text{m}^2$  (IQR 105.4  $\mu\text{m}^2$ ) from the histological sections, respectively. The plaque size histograms are depicted in Fig. 3c. This showed a considerable sensitivity difference between both methods, as the immunodetection returned more than one order higher amount of A $\beta$  plaque sections in the lowest size category (0–500  $\mu\text{m}^2$ ), accounting for its low median values. Besides the invisibility of smallest deposits on the scans, the comparison of the detailed images in Fig. 3a,b showed that the plaque border was harder to read in the micro CT

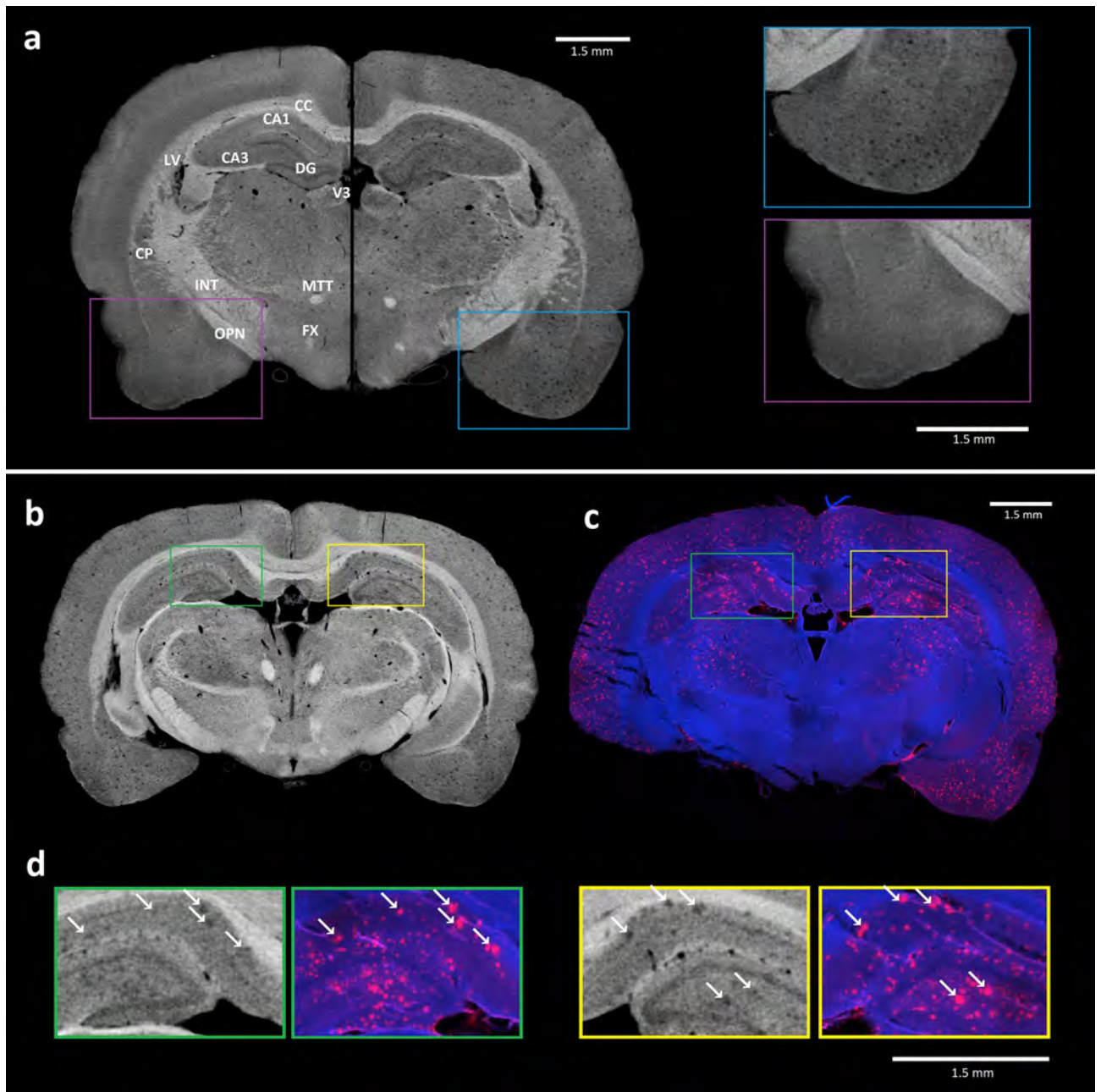


**Figure 1.** Confirmation of plaques identity in micro CT data: **(a)** Composed picture of the micro CT scan sections from control (left side) and transgenic (right side) rat brain. The transgenic tissue exhibits a large amount of suspect amyloid plaques (right part of the brain). Selected detail image of corresponding areas that are shown in pink and blue frames. Basic anatomical structures visualized in micro CT scan: *CA1* and *CA3* cornu Ammonis 1 and 3 of hippocampus, *CC* corpus callosum, *CP* caudoputamen, *DG* dentate gyrus, *FX* fornix, *INT* internal capsule, *LV* lateral ventricle, *MTT* mammillothalamic tract, *OPN* olivary pretectal nucleus, *V3* third ventricle. Micro CT image **(b)** and immunohistology section with detected plaques **(c)** of corresponding coronal brain sections from the transgenic rat no. 60 confirms the presence of plaques in micro CT scan. Selected plaques are indicated by white arrows in enlarged slice windows **(d)**<sup>41</sup>.

data. This also might have caused an overestimation of the sizes of some of the smallest deposits. Consequently, they might have been marked as larger and so they were scored within the category of 501–1000  $\mu\text{m}^2$ .

The data obtained from the micro CT scan of the dissected hippocampus was chosen for a subsequent 3D analysis. Since the  $\text{A}\beta$  plaques had similar contrast values as other tissue structures, they could not be detected with global thresholding methods. Hence, a manual segmentation of the plaques was performed. After defining the region of interest, all segmented plaques were counted and measured. In the dissected hippocampus (total volume = 13.88  $\text{mm}^3$ ) we identified in total 1666 individual plaques. The volume of the smallest individual deposit was 895  $\mu\text{m}^3$ , indicating the lower limit for amyloid plaque identification in the present micro CT data. The biggest identified  $\text{A}\beta$  plaque had a volume of 721,552  $\mu\text{m}^3$ , the dataset of measured volumes was characterized

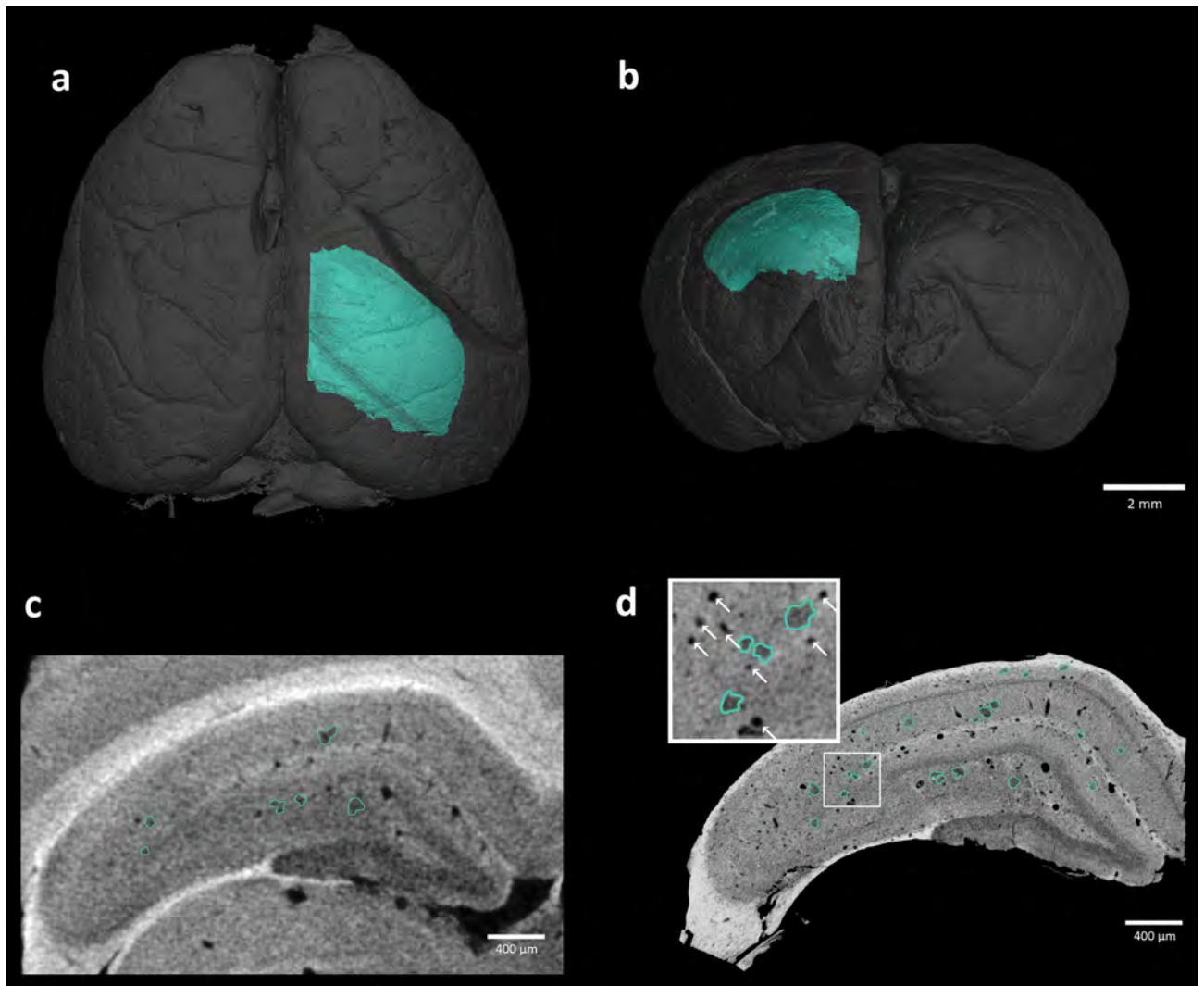


**Figure 2.** Detailed scan of the dissected dorsal hippocampus: Horizontal (a) and coronal (b) reconstructed view of the brain with dissected right dorsal hippocampus (green) used for the isolated scan. The same hippocampal tissue sample imaged by two different micro CT approaches (c,d) where the suspect plaques are highlighted in green. Panel (c) shows the section taken from the whole brain scan. Panel (d) depicts the same area after the isolated scanning that achieved smaller voxel size, in the magnified image the blood vessels are labeled by white arrows<sup>41,42</sup>.

by median value  $38,423 \mu\text{m}^3$  and IQR of  $57,512 \mu\text{m}^3$ . The distribution of the  $\text{A}\beta$  plaques in 3D space with their color coded volumes is shown in Fig. 4a. Next, we assessed the shapes' variability of  $\text{A}\beta$  plaques by measuring their compactness. The volume of the plaque was divided by the volume of the sphere circumscribed to the plaque. The values ranged between 0–1 where score of one represented a perfect sphere (Fig. 4b). The identified plaques had median of compactness at 0.396 with interquartile range 0.135. To alleviate supposed bias that could be caused by an eventual imperfection in defining boundaries in the smaller plaques, we additionally restricted the measurement to subset of plaques with volume larger than its median value (50% of the population). The corresponding compactness had a comparable median of 0.383 and IQR of 0.149.

A precise 3D model of the plaque occurrence in the hippocampal sample allowed to quantify their spatial distribution including the relation to other labeled structures. We evaluated the distances of plaques to the nearest blood vessel and the inter-plaque distance (Fig. 5). The reconstructed 3D model returned the median distance between the plaques and the nearest vessel of  $64.5 \mu\text{m}$  with IQR  $62.3 \mu\text{m}$  (Fig. 5a). We then investigated whether their relation followed a non-random pattern. For each of the 1666 plaques we generated a random coordinate within the dissected part of hippocampus, leaving out the detected blood vessels. We measured the respective distances of generated “plaques” to a nearest vessel with median of  $89.1 \mu\text{m}$  and IQR  $103 \mu\text{m}$ . The comparison between the sets of experimental and randomly generated data returned the plaque-vessel distance significantly shorter in experimental data than in the random sample ( $Z = 10.95$ ,  $p < 0.001$ , Mann Whitney U test), indicating the plaques tended to appear closer to the blood vessels than if their distribution was random. Finally we tested whether the plaques aggregated together irrespectively of the vessels. The same method of generating dataset with random positions was applied, and the distances between the two closest plaques were measured within the

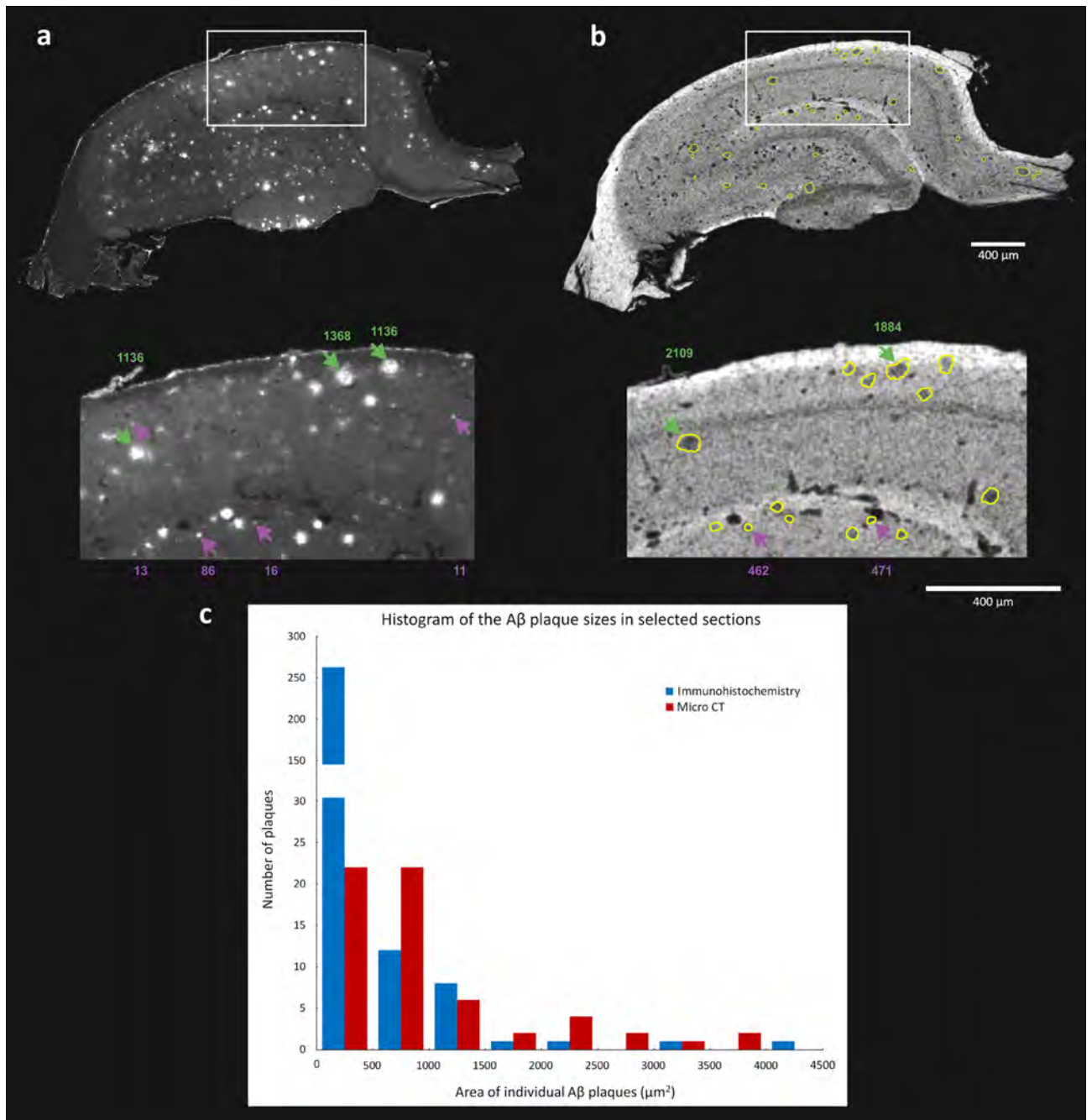


**Figure 3.** Comparison of the precision in identification of plaques in micro CT data versus the immunohistological detection: Comparison of corresponding sections from the same rat brain showing immunodetected A $\beta$  plaques (a) and the micro CT data where the yellow line represents the manually selected plaque boundaries (b). The purple arrows indicate examples of the plaque cross sections corresponding to the smallest fraction (0–500  $\mu\text{m}^2$ ) while the green arrows mark the larger size cases. The corresponding area values in  $\mu\text{m}^2$  are reported in proper colors above and under both pictures. The histogram (c) depicts the size interval distribution of detected A $\beta$  plaque sections in the selected slices using immunohistochemistry and micro CT imaging, respectively<sup>41–43</sup>.

experimental and the random positions datasets, respectively (Fig. 5b). The median of distances from the tissue sample data was 101.1  $\mu\text{m}$  with IQR = 46.5  $\mu\text{m}$ , whereas the randomly generated dataset returned a distribution shift towards larger values (median distance 123.4  $\mu\text{m}$  and IQR 62.7  $\mu\text{m}$ ). The Mann Whitney U test confirmed a statistically significant difference between the both measurements ( $Z = 11.97$ ,  $p < 0.001$ ).

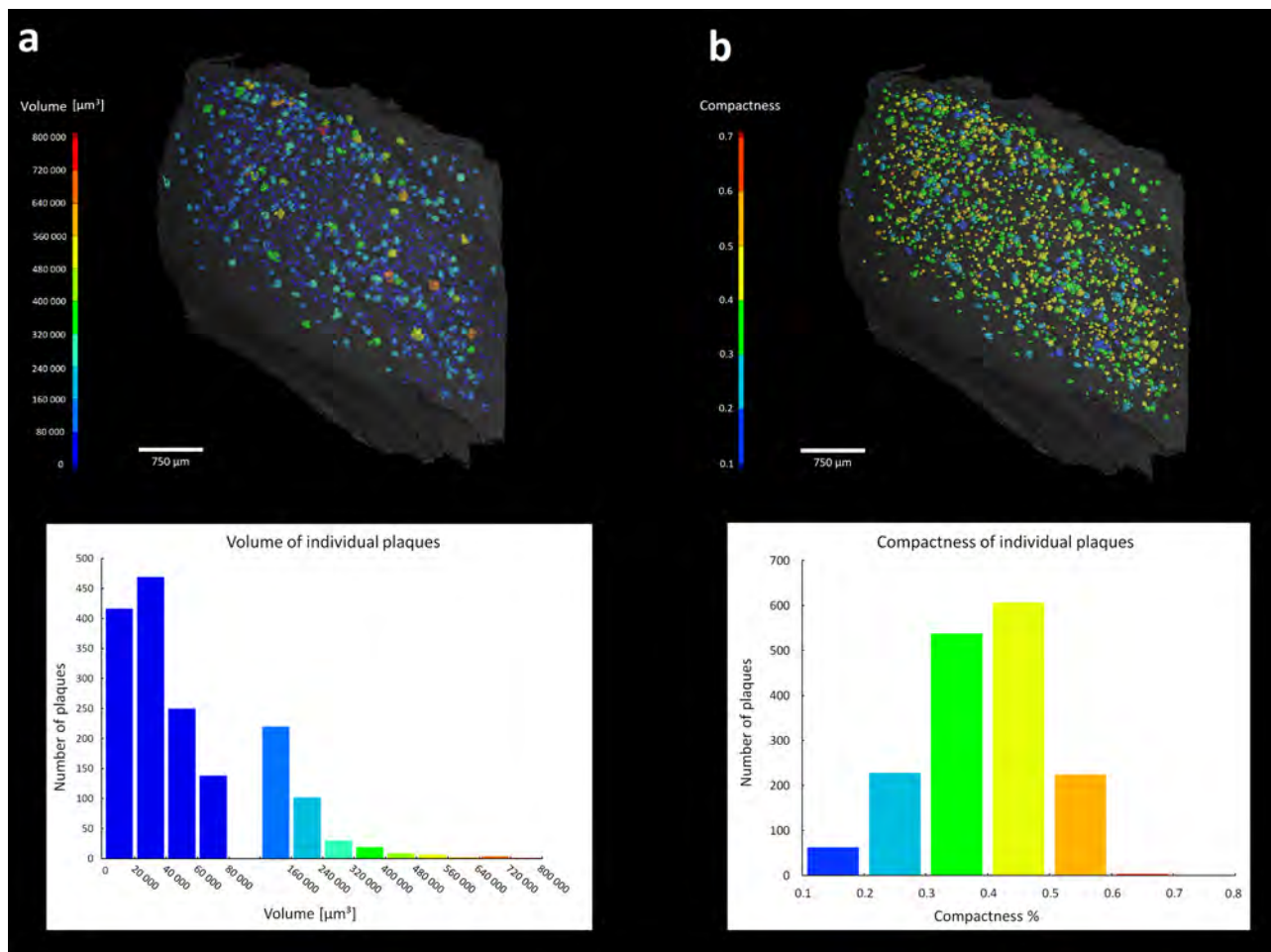


**Figure 4.** 3D quantitative analysis of the A $\beta$  plaques size and shape in hippocampus: Panel (a) shows the plaques 3D distribution color coded respective to their size, with the corresponding histogram in the same color scale on the right. Panel (b) illustrates the same plaques color scaled according their compactness (red codes for higher similarity to a sphere) with the respective histogram (right)<sup>41,42</sup>.

## Discussion

In this paper, we present the absorption based contrast enhanced X-ray micro CT imaging performed on the industrial lab based CT system as an imaging tool for a 3D analysis of A $\beta$  plaques of transgenic rat brains used as a model in Alzheimer disease research.

The detection of amyloid plaques in rodent brain by Computed Tomography (CT) has been attempted so far by using the mouse brain (*mus musculus*) and the experiments have been performed with synchrotron X-ray sources using variations of phase contrast imaging to visualize the A $\beta$  plaques in a brain. TOMCAT beamline of the Swiss Light Source, Astolfo et al.<sup>6</sup> demonstrated that synchrotron-based X-ray phase contrast imaging can be used for the 3D visualization and basic quantification of A $\beta$  plaques in the mouse brain. At the same synchrotron facility the Pinzer et al.<sup>7</sup> analyzed the neocortex of mouse brain via differential phase contrast imaging and accompanied their findings with complementary thioflavin S staining of the brain to confirm the presence of the A $\beta$  plaques in brain in CT data. The diffraction enhanced imaging phase contrast X-ray imaging technique was applied by the Connor et al.<sup>8</sup> at National Synchrotron Light Source, Brookhaven National Laboratory, USA. In that study, several scans of the one brain were needed in order to obtain a full scan of the brain. A comparison of the affected and wild type mouse brain was shown and the identity of A $\beta$  plaques was confirmed by applying specific immunostaining on the A $\beta$  plaques. The X-ray phase contrast tomography was applied for the purpose of the amyloid plaque imaging specifically to describe the microenvironment of the A $\beta$  plaque at European Synchrotron Radiation Facility, Grenoble, France<sup>9</sup>. Finally, the research group of Noda-Saita et al.<sup>10</sup> at High Energy Accelerator Research Organization, Ibaraki, Japan used phase-contrast X-ray CT imaging to describe the density of A $\beta$  plaques supporting their findings with a complementary immunodetection of A $\beta$  plaques in the mouse brain and with scans of control brains.

Unfortunately, the synchrotron facilities are not readily available for general use since the complicated imaging setups imply higher costs of equipment, its service and its maintenance. Moreover, the multiple scans have to be acquired to retrieve the information from the whole brain sample because of the sample's size limitations. This restricts a wide use of synchrotron based CT imaging in the Alzheimer's disease research, despite the obvious advantages for the quantification of amyloid plaques.

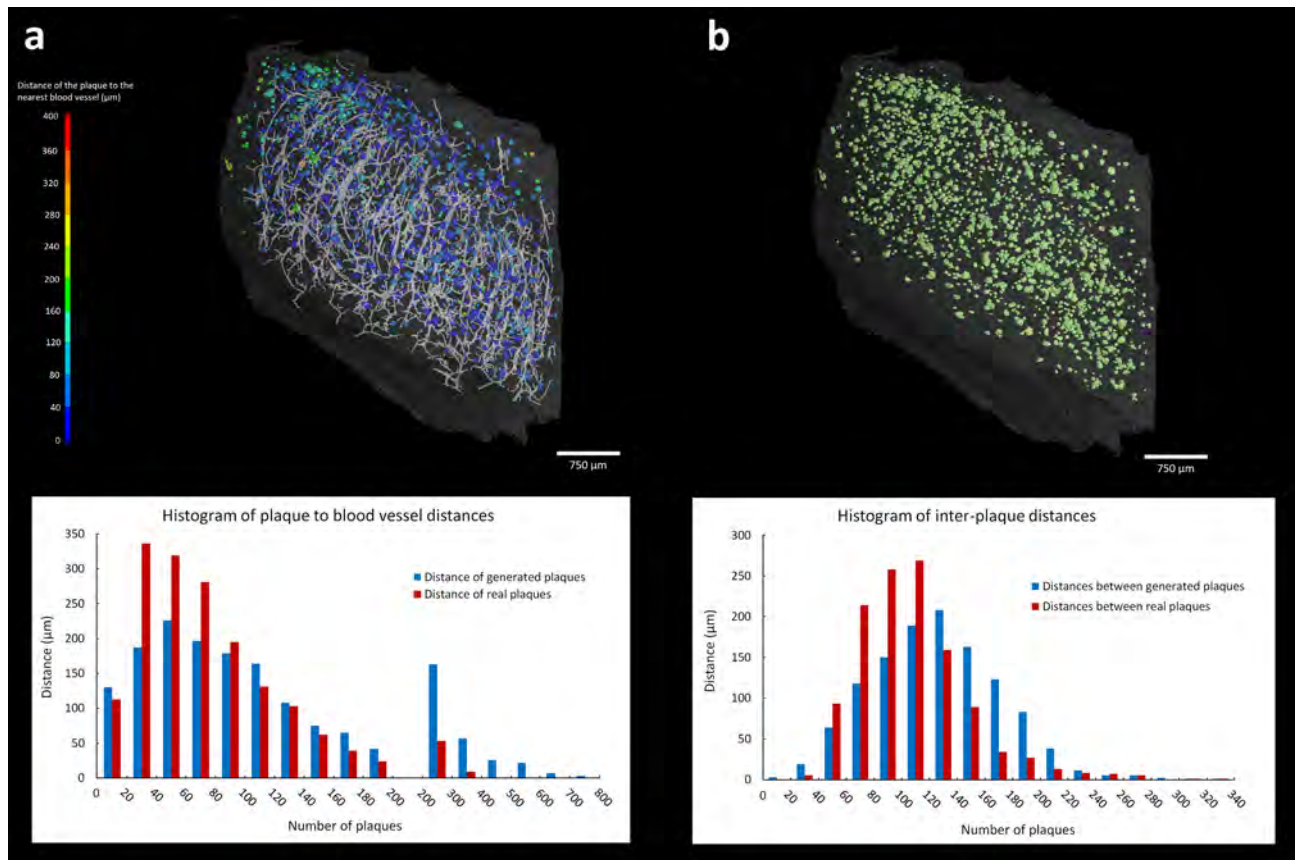


**Figure 5.** 3D quantitative analysis of the plaques distribution in hippocampus: Horizontal view of the hippocampus with color coded distances of individual plaques to the nearest blood vessel (a) and the corresponding histogram showing the distances to the nearest blood vessel of randomly generated (in blue) and the real (in red) plaques, respectively. Horizontal view of the hippocampus depicting the distribution of the plaques inside the hippocampus (b) and the corresponding histogram showing the distribution of randomly generated plaques (in blue), and the distribution of real plaques (in red)<sup>41,42</sup>.

This fact led us to the idea of developing an imaging method for detection of amyloid plaques in the rat brain applicable to easily accessible industrial X-ray lab-based devices. Absorption based contrast enhanced X-ray micro CT imaging as an alternative to the synchrotron based phase contrast imaging techniques retrieves not only a 3D distribution of amyloid plaques with decent voxel resolution, but also provides valuable data for quantitative analysis of the amyloid plaques (total number, volume, shape).

The immunodetection of amyloid plaques performed on histological slices is the golden standard of identification of plaques in the brain tissue. In this paper, we used this method to validate our findings. In order to precisely correlate the micro CT data with the immunodetection of the plaques, we used the brain which had been previously scanned on micro CT. Then, we performed a classical histological sectioning and carried out the immunodetection of the plaques. The comparison of data from the same brain analyzed by both techniques showed a good agreement between immunodetection and micro CT imaging. Even though the immunodetection is indisputably more sensitive in detection of smaller plaques, it lacks a convenient approach to the 3D analysis across large brain volumes. This comparison thus highlights the advantages of contrast enhanced micro CT imaging. The immunostaining based affirmation of plaque identity detected by micro CT shows that the absorption-based contrast enhanced micro CT imaging is robust in detection of amyloid plaques. While its applicability as described in this report is not suitable for *in vivo* experiments for the staining protocol toxicity or because of the high irradiation dose, we believe the CT brain imaging approach in the context of Alzheimer's disease research has a considerable potential for further development.

## Materials and methods

**Animals.** Brains from three 18 months old female rats (two transgenic TgF-344 AD animals and one wild type control) obtained from the local breeding colony at Faculty of Medicine in Pilsen, Charles University, were used to collect the data. All protocols followed in this study were approved by the Ethical Committee of the Ministry of Education, Youth and Sports of the Czech Republic (approval no. MSMT-12048/2019-14) according to the Guide for the Care and Use of Laboratory Animals (Protection of Animals from Cruelty Law Act No. 246/92, Czech Republic).

Sample	Rat brain F60 +	Rat brain F61-	Rat brain F87 +	Hippocampus F87 +
Voltage [kV]	60	60	60	60
Current [ $\mu$ A]	200	200	200	200
Timing [ms]	600	600	600	700
Source spot size [ $\mu$ m]	5	5	5	5
Sample/source distance [mm]	40.8	40.8	40.8	11.9
Sample/detector distance [mm]	864.9	864.9	864.9	785.4
Images	2200	2200	2200	2400
Time [min.]	80	80	80	100
Voxel size [ $\mu$ m <sup>3</sup> ]	9	9	9	3

**Table 1.** Micro CT scan settings.

**Micro CT staining.** At the beginning of the experiments the rats were overdosed with pentobarbital and intracardially perfused with saline, followed by 4% PFA. Then the brains were manually extracted and post-fixed in 4% PFA for another 3 h. Afterwards, the samples were dehydrated in ethanol solutions of different concentrations which increased: 30%, 50%, 70%, 80% and 90%. The process lasted 12 h for each concentration. After the dehydration, samples were submerged in a staining solution consisting of 1% iodine in 90% methanol for 72 h, where the staining solution was refreshed after the first 24 h. Then the samples were washed in 50% ethanol and embedded in 1% agarose gel. In one of the transgenic animals, after the whole brain scan, the dorsal hippocampus was dissected and embedded in 1% agarose gel for another scan.

**Micro CT measurement.** Before scanning, all samples were embedded in 1% agarose gel in 15 ml Falcon tubes in order to prevent movement during the imaging procedure. The micro CT scanning was performed using a laboratory system GE Phoenix v|tome|x L 240 (GE Sensing & Inspection Technologies GmbH, Germany), equipped with a 180 kV/15 W maximum power nanofocus X-ray tube and a high contrast flat panel detector dynamic 41|100 (number of pixels: 4048 × 4048 px, pixel size 100  $\mu$ m). The measurements were carried out in an air-conditioned cabinet (21 °C). The parameters for each scan are indicated in the Table 1. The tomographic reconstruction was realized by software GE phoenix datos|x 2.0 (GE Sensing & Inspection Technologies GmbH).

**Micro CT data processing.** All 3D visualizations and measurements were performed in VG Studio MAX 3.4 software (Volume Graphics GmbH)<sup>41</sup>. The segmentation of plaques in the hippocampus sample was carried out using Avizo 9.5 software (Thermo Fisher Scientific)<sup>42</sup>. In the first step we isolated the hippocampus from the background by creating the corresponding region of interest (ROI). Blood vessels were segmented by global thresholding based on the grey level (vessels appeared as the darkest part since they did not contain any iodine), continuity, and their resulting prolonged and branched 3D shape. The amyloid plaques were segmented manually in Avizo 9.5 software by selecting the plaque areas across the sections under the following criteria: the area of the plaque should be distinguishably darker than the surrounding tissue and its volume should extend across at least 3 following sections. The boundaries of smaller plaques were selected section by section, in bigger plaques (some were spread over more than 30 sections) we interpolated between every other slice while any inconsistencies were additionally manually corrected.

For the analysis of A $\beta$  distribution we generated datasets of plaques coordinates (Matlab R2020a). First, the coordinates of plaques centroids were extracted from the segmented 3D binary data to represent the experimental dataset. Then the random dataset of “plaque’s” centroids was created within the volume of the sample leaving out its vascular system. The resulting coordinates then represented centroids of randomly distributed A $\beta$  plaques with total amount corresponding to the experimental dataset. The analysis of A $\beta$  plaque position in relation to the blood vessels was carried out in VG studio. Both real plaques centroid positions and simulated plaques centroid positions were imported in form of binary image data. The distance of the centroid to the nearest blood vessel was measured via pore analysis module. Subsequently, the intra-plaques distances were analyzed separately in simulated plaque centroids and real plaque centroids. The nearest neighboring centroid of each centroid was found using 3D Euclidean distances analysis in Matlab R2020a. Repeating combinations of the nearest neighbors were excluded from the subsequent analysis.

**Statistical analysis.** The non-parametric Mann–Whitney test was applied to compare the detected and random datasets ([https://www.statskingdom.com/170median\\_mann\\_whitney.html](https://www.statskingdom.com/170median_mann_whitney.html)).

**Histology and immunohistochemical labeling.** After the CT measurements, the sample tissue was embedded in a paraffin block and cut into 10 $\mu$  thick sections using an Automated Microtome (Leica RM2255). The slices were then deparaffinized and rehydrated. Phosphate buffer saline (PBS, 0.1 M) was applied for washing. To block the non-specific binding, normal goat serum (ab138478, Abcam) was used. The sections were then incubated overnight at 4 °C with the primary antibody (ab2539, Abcam, 1:200, 1 mg/ml) against amyloid beta. Next day, the sections were washed with 1X PBS (0.01 M) thrice (5', 10' and 15') to remove the unbound anti-

body remnants. Staining was visualized with an Alexa Fluor 647-conjugated goat anti-rabbit antibody (Jackson ImmunoResearch Laboratories) applied in 1:500 dilution at 37 °C for 4 h. All the sections were then counterstained with DAPI to label the nuclei and glass mounted using fluoroshield mounting medium (Merck). The Amyloid beta plaques were visualized using fluorescent microscopy (Olympus), and quantified in open source Fiji image analysis software<sup>43</sup>.

## Data availability

Datasets used in this publication are available on request at corresponding authors.

Received: 3 December 2020; Accepted: 18 February 2021

Published online: 16 March 2021

## References

- Hardy, J. & Selkoe, D. J. The amyloid hypothesis of Alzheimer's disease: Progress and problems on the road to therapeutics. *Science* **297**(5580), 353–356 (2002).
- Kametani, F. & Hasegawa, M. Reconsideration of amyloid hypothesis and tau hypothesis in Alzheimer's disease. *Front. Neurosci.* **12**, 25 (2018).
- Zempel, H. & Mandelkow, E. Lost after translation: Missorting of Tau protein and consequences for Alzheimer disease. *Trends Neurosci.* **37**(12), 721–732 (2014).
- Hardy, J. A. & Higgins, G. A. Alzheimer's disease: The amyloid cascade hypothesis. *Science* **256**(5054), 184–186 (1992).
- Cao, J., Hou, J., Ping, J. & Cai, D. Advances in developing novel therapeutic strategies for Alzheimer's disease. *Mol. Neurodegen.* **13**(1), 64 (2018).
- Astolfo, A., Lathuiliere, A., Laversenne, V., Schneider, B. & Stampanoni, M. Amyloid- $\beta$  plaque deposition measured using propagation-based X-ray phase contrast CT imaging. *J. Synchr. Radiat.* **23**(3), 813–819 (2016).
- Pinzer, B. R. *et al.* Imaging brain amyloid deposition using grating-based differential phase contrast tomography. *Neuroimage.* **61**(4), 1336–1346 (2012).
- Connor, D. M. *et al.* Computed tomography of amyloid plaques in a mouse model of Alzheimer's disease using diffraction enhanced imaging. *Neuroimage.* **46**(4), 908–914 (2009).
- Massimi, L. *et al.* Exploring Alzheimer's disease mouse brain through X-ray phase contrast tomography: From the cell to the organ. *NeuroImage.* **184**, 490–495 (2019).
- Noda-Saita, K. *et al.* Quantitative analysis of amyloid plaques in a mouse model of Alzheimer's disease by phase-contrast X-ray computed tomography. *Neuroscience* **138**(4), 1205–1213 (2006).
- Massimi, L. *et al.* Assessment of plaque morphology in Alzheimer's mouse cerebellum using three-dimensional X-ray phase-based virtual histology. *Sci. Rep.* **10**(1), 1–10 (2020).
- Metscher, B. D. MicroCT for developmental biology: A versatile tool for high-contrast 3D imaging at histological resolutions. *Dev. Dyn.* **238**(3), 632–640 (2009).
- Metscher, B. D. MicroCT for comparative morphology: Simple staining methods allow high-contrast 3D imaging of diverse non-mineralized animal tissues. *BMC Physiol.* **9**(1), 11 (2009).
- Li, L. *et al.* Superficial cells are self-renewing chondrocyte progenitors, which form the articular cartilage in juvenile mice. *FASEB J.* **31**(3), 1067–1084 (2017).
- Kaucka, M. *et al.* Oriented clonal cell dynamics enables accurate growth and shaping of vertebrate cartilage. *Elife.* **6**, e25902 (2017).
- Kaucka, M. *et al.* Analysis of neural crest-derived clones reveals novel aspects of facial development. *Sci. Adv.* **2**(8), e1600060 (2016).
- Kaucka, M. *et al.* Signals from the brain and olfactory epithelium control shaping of the mammalian nasal capsule cartilage. *Elife.* **7**, e34465 (2018).
- Celá, P. *et al.* Ciliopathy protein Tmem107 plays multiple roles in craniofacial development. *J. Dent. Res.* **97**(1), 108–117 (2018).
- Hampel, M. *et al.* Polarized sonic hedgehog protein localization and a shift in the expression of region-specific molecules is associated with the secondary palate development in the veiled chameleon. *Front. Cell Dev. Biol.* **8**, 572 (2020).
- Landova Sulcova, M. *et al.* Developmental mechanisms driving complex tooth shape in reptiles. *Dev. Dyn.* **249**(4), 441–464 (2020).
- Kohoutek, J. *et al.* Mouse model of congenital heart defects, dysmorphic facial features and intellectual developmental disorders as a result of nonfunctional CDK13. *Front. Cell Dev. Biol.* **7**, 155 (2019).
- Heude, E. *et al.* Unique morphogenetic signatures define mammalian neck muscles and associated connective tissues. *Elife.* **7**, e40179 (2018).
- Vymazalová, K., Vargová, L., Zikmund, T. & Kaiser, J. The possibilities of studying human embryos and fetuses using micro-CT: A technical note. *Anat. Sci. Int.* **92**(2), 299–303 (2017).
- Tesařová, M. *et al.* An interactive and intuitive visualisation method for X-ray computed tomography data of biological samples in 3D Portable Document Format. *Sci. Rep.* **9**(1), 1–8 (2019).
- Stolz, E. *et al.* Angioarchitectural changes in subacute cerebral venous thrombosis A synchrotron-based micro- and nano-CT study. *Neuroimage* **54**(3), 1881–1886 (2011).
- Heinzer, S. *et al.* Hierarchical microimaging for multiscale analysis of large vascular networks. *Neuroimage.* **32**(2), 626–636 (2006).
- Ghanavati, S., Lisa, X. Y., Lerch, J. P. & Sled, J. G. A perfusion procedure for imaging of the mouse cerebral vasculature by X-ray micro-CT. *J. Neurosci. Methods* **221**, 70–77 (2014).
- Langheinrich, A. C. *et al.* Evaluation of the middle cerebral artery occlusion techniques in the rat by in-vitro 3-dimensional micro- and nano computed tomography. *BMC Neurol.* **10**(1), 36 (2010).
- Chugh, B. P. *et al.* Measurement of cerebral blood volume in mouse brain regions using micro-computed tomography. *Neuroimage.* **47**(4), 1312–1318 (2009).
- Xie, B., Miao, P., Sun, Y., Wang, Y. & Yang, G. Y. Micro-computed tomography for hemorrhage disruption of mouse brain vasculature. *Transl. Stroke Res.* **3**(1), 174–179 (2012).
- Dorr, A., Sled, J. G. & Kabani, N. Three-dimensional cerebral vasculature of the CBA mouse brain: A magnetic resonance imaging and micro computed tomography study. *Neuroimage.* **35**(4), 1409–1423 (2007).
- Hayasaka, N. *et al.* In vivo diagnostic imaging using micro-CT: sequential and comparative evaluation of rodent models for hepatic/brain ischemia and stroke. *PLoS ONE* **7**(2), e32342 (2012).
- Dobrivojević, M., Boháček, I., Erjavec, I., Gorup, D. & Gajović, S. Computed microtomography visualization and quantification of mouse ischemic brain lesion by nonionic radio contrast agents. *Croatian Med. J.* **54**(1), 3–11 (2013).
- Anderson, R. & Maga, A. M. A novel procedure for rapid imaging of adult mouse brains with microCT using iodine-based contrast. *PLoS ONE* **10**(11), e0142974 (2015).
- de Crespigny, A. *et al.* 3D micro-CT imaging of the postmortem brain. *J. Neurosci. Methods* **171**(2), 207–213 (2008).

36. Saito, S. & Murase, K. Ex vivo imaging of mouse brain using micro-CT with non-ionic iodinated contrast agent: A comparison with myelin staining. *Br. J. Radiol.* **85**(1019), e973–e978 (2012).
37. Bautista, N. S. *et al.* Ex vivo micro-CT imaging of murine brain models using non-ionic iodinated contrast. *Am. Inst. Phys. Conf. Proc.* **1**(1626), 197–200 (2014).
38. Hainfeld, J. F. *et al.* Gold nanoparticle imaging and radiotherapy of brain tumors in mice. *Nanomedicine.* **8**(10), 1601–1609 (2013).
39. Kastriti, M. E. *et al.* Ablation of CNTN2+ pyramidal neurons during development results in defects in neocortical size and axonal tract formation. *Front. Cell. Neurosci.* **13**, 454 (2019).
40. Zikmund, T. *et al.* High-contrast differentiation resolution 3D imaging of rodent brain by X-ray computed microtomography. *J. Instrum.* **13**(02), C02039 (2018).
41. Volume Graphics. <https://www.volumegraphics.com> 2020 (accessed 30 October 2020).
42. Thermo Fisher Scientific. <https://www.fei.com/software/avizo3d/>.
43. Fiji. <https://imagej.net/Fiji>.

## Acknowledgements

This research was carried out under the project CEITEC 2020 (LQ1601) with financial support from the Ministry of Education, Youth and Sports of the Czech Republic under the National Sustainability Programme II and CzechNanoLab Research Infrastructure supported by MEYS CR (LM2018110), projects PRIMUS 27051, Progres Q39, FIND No. CZ.02.1.01/0.0/0.0/16\_019/0000787 provided by the Ministry of Education, Youth and Sports of the Czech Republic, and GAUK 12539. We are grateful to Marketa Slajerova for help with processing the samples.

## Author contributions

M.K., T.Z., J.K. and K.J. designed the study, M.K. performed the CT scanning and staining, M.K. and J.S. analyzed the CT data, A.K. and S.L.P.P. processed and analyzed the histology, M.K. and K.J. wrote the manuscript.

## Competing interests

The authors declare no competing interests.

## Additional information

**Supplementary Information** The online version contains supplementary material available at <https://doi.org/10.1038/s41598-021-84579-x>.

**Correspondence** and requests for materials should be addressed to M.K. or K.J.

**Reprints and permissions information** is available at [www.nature.com/reprints](http://www.nature.com/reprints).

**Publisher's note** Springer Nature remains neutral with regard to jurisdictional claims in published maps and institutional affiliations.



**Open Access** This article is licensed under a Creative Commons Attribution 4.0 International License, which permits use, sharing, adaptation, distribution and reproduction in any medium or format, as long as you give appropriate credit to the original author(s) and the source, provide a link to the Creative Commons licence, and indicate if changes were made. The images or other third party material in this article are included in the article's Creative Commons licence, unless indicated otherwise in a credit line to the material. If material is not included in the article's Creative Commons licence and your intended use is not permitted by statutory regulation or exceeds the permitted use, you will need to obtain permission directly from the copyright holder. To view a copy of this licence, visit <http://creativecommons.org/licenses/by/4.0/>.

© The Author(s) 2021

PAPER [XV]

# DUCT reveals architectural mechanisms contributing to bile duct recovery in a mouse model for Alagille syndrome

Simona Hankeova<sup>1,2†</sup>, Jakub Salplachta<sup>3†</sup>, Tomas Zikmund<sup>3‡</sup>, Michaela Kavkova<sup>3‡</sup>, Noémi Van Hul<sup>1‡</sup>, Adam Brinek<sup>3</sup>, Veronika Smekalova<sup>3</sup>, Jakub Laznovsky<sup>3</sup>, Feven Dawit<sup>4</sup>, Josef Jaros<sup>5</sup>, Vítězslav Bryja<sup>2</sup>, Urban Lendahl<sup>6</sup>, Ewa Ellis<sup>4</sup>, Antal Nemeth<sup>7</sup>, Björn Fischler<sup>4</sup>, Edouard Hannezo<sup>8</sup>, Jozef Kaiser<sup>3\*</sup>, Emma Rachel Andersson<sup>1,6\*</sup>

<sup>1</sup>Department of Biosciences and Nutrition, Karolinska Institutet, Solna, Sweden; <sup>2</sup>Department of Experimental Biology, Masaryk University, Brno, Czech Republic; <sup>3</sup>CEITEC – Central European Institute of Technology, Brno University of Technology, Brno, Czech Republic; <sup>4</sup>Department of Pediatrics, Clinical Science, Intervention and Technology (CLINTEC), Karolinska Institutet and Karolinska University Hospital, Solna, Sweden; <sup>5</sup>Department of Histology and Embryology, Masaryk University, Brno, Czech Republic; <sup>6</sup>Department of Cell and Molecular Biology, Karolinska Institutet, Solna, Sweden; <sup>7</sup>Department of Laboratory Medicine, Karolinska Institutet, Solna, Sweden; <sup>8</sup>Institute of Science and Technology, Klosterneuburg, Austria

## \*For correspondence:

Jozef.Kaiser@ceitec.vutbr.cz (JK); emma.andersson@ki.se (ERA)

†These authors contributed equally to this work

‡These authors also contributed equally to this work

**Competing interests:** The authors declare that no competing interests exist.

**Funding:** See page 26

**Received:** 09 July 2020

**Accepted:** 14 January 2021

**Published:** 26 February 2021

**Reviewing editor:** Anna Mae Diehl, Duke University School of Medicine, United States

© Copyright Hankeova et al. This article is distributed under the terms of the [Creative Commons Attribution License](https://creativecommons.org/licenses/by/4.0/), which permits unrestricted use and redistribution provided that the original author and source are credited.

**Abstract** Organ function depends on tissues adopting the correct architecture. However, insights into organ architecture are currently hampered by an absence of standardized quantitative 3D analysis. We aimed to develop a robust technology to visualize, digitalize, and segment the architecture of two tubular systems in 3D: double resin casting micro computed tomography (DUCT). As proof of principle, we applied DUCT to a mouse model for Alagille syndrome (*Jag1<sup>Ndr/Ndr</sup>* mice), characterized by intrahepatic bile duct paucity, that can spontaneously generate a biliary system in adulthood. DUCT identified increased central biliary branching and peripheral bile duct tortuosity as two compensatory processes occurring in distinct regions of *Jag1<sup>Ndr/Ndr</sup>* liver, leading to full reconstitution of wild-type biliary volume and phenotypic recovery. DUCT is thus a powerful new technology for 3D analysis, which can reveal novel phenotypes and provide a standardized method of defining liver architecture in mouse models.

## Introduction

The correct three-dimensional (3D) architecture of lumenized structures in our bodies is essential for function and health. The cardiovascular system, lungs, kidneys, liver, and other organs depend on precisely patterned tubular networks. Several diseases are caused by, or result in, alterations in the 3D architecture of lumenized structures. Vascular architecture defects contribute to Alzheimer's disease (Klohs et al., 2014), opportunistic infections cause narrowing of bile ducts in liver (De Angelis et al., 2009), and branching morphogenesis defects in the renal urinary system cause hypertension (Short and Smyth, 2016). In some pathologies, several lumenized structures are affected at once. Visualizing multiple tubular systems in tandem in 3D, in animal disease models, is necessary to allow investigation of how these systems interact in vivo in development, homeostasis, and disease.

**eLife digest** Many essential parts of the body contain tubes: the liver for example, contains bile ducts and blood vessels. These tubes develop right next to each other, like entwined trees. To do their jobs, these ducts must communicate and collaborate, but they do not always grow properly. For example, babies with Alagille syndrome are born with few or no bile ducts, resulting in serious liver disease. Understanding the architecture of the tubes in their livers could explain why some children with this syndrome improve with time, but many others need a liver transplant.

Visualising biological tubes in three dimensions is challenging. One major roadblock is the difficulty in seeing several tubular structures at once. Traditional microscopic imaging of anatomy is in two dimensions, using slices of tissue. This approach shows the cross-sections of tubes, but not how the ducts connect and interact. An alternative is to use micro computed tomography scans, which use X-rays to examine structures in three dimensions. The challenge with this approach is that soft tissues, which tubes in the body are made of, do not show up well on X-ray. One way to solve this is to fill the ducts with X-ray absorbing resins, making a cast of the entire tree structure. The question is, can two closely connected tree structures be distinguished if they are cast at the same time?

To address this question, Hankeova, Salplachta et al. developed a technique called double resin casting micro computed tomography, or DUCT for short. The approach involved making casts of tube systems using two types of resin that show up differently under X-rays. The new technique was tested on a mouse model of Alagille syndrome. One resin was injected into the bile ducts, and another into the blood vessels. This allowed Hankeova, Salplachta et al. to reconstruct both trees digitally, revealing their length, volume, branching, and interactions. In healthy mice, the bile ducts were straight with uniform branches, but in mice with Alagille syndrome ducts were wiggly, and had extra branches in the centre of the liver.

This new imaging technique could improve the understanding of tube systems in animal models of diseases, both in the liver and in other organs with tubes, such as the lungs or the kidneys. Hankeova, Salplachta et al. also lay a foundation for a deeper understanding of bile duct recovery in Alagille syndrome. In the future, DUCT could help researchers to see how mouse bile ducts change in response to experimental therapies.

2D histological sections remain the standard practice for all types of tissues. Recent advances in tissue clearing (*Chung et al., 2013; Susaki et al., 2014; Renier et al., 2016*) carbon ink injections (*Kaneko et al., 2015*) and high-end microscopy begin to address the need for, and benefits of, whole organ analysis. Importantly, organ systems often interact with one another and almost always are connected to blood supply. In order to study tissue spatial organization in development, disease, and regeneration, a 3D analysis of multiple networks is indispensable. A lack of markers, suitable antibodies, tissue autofluorescence and/or organ size often preclude the possibility for whole organ analysis. Radiopaque resin casting is an alternative approach that enables micro computed tomography ( $\mu$ CT) scanning, digitalization with full rotation and the possibility for both qualitative and quantitative analyses compatible with multiple imaging softwares.

In this study, we focused on establishing a simple, robust, antibody-free and inexpensive method for whole organ visualization of lumenized structures. We built on previous work to image a single network using resin (*Masyuk et al., 2003; Kline et al., 2011; Walter et al., 2012*) and imaging with  $\mu$ CT. First, in order to visualize multiple structures, we tested different radiopaque substances to enhance the resin contrast, resulting in mixing of two MICROFIL resins with distinctive radiopacity. As proof of principle, we focused on studying the hepatic vascular and biliary systems of wild type and *Jagged1* Nodder (*Jag1<sup>Ndr/Ndr</sup>*) (*Andersson et al., 2018*) mice, which are challenging to image by other methods due to liver size and autofluorescence (*Renier et al., 2016*). We devised double resin-casting micro computed tomography (DUCT) to inject, image and digitalize two systems in tandem in 3D to gain a deeper insight into the organ recovery process. The subsequent analysis is performed using a custom-written MATLAB pipeline (available and deposited in <https://github.com/JakubSalplachta/DUCT>; *Hankeova, 2021* copy archived at [swh:1:rev:6b0b0eb88bbaf9bfc4f8ee42cafa4c122866fbba](https://swh.1:rev:6b0b0eb88bbaf9bfc4f8ee42cafa4c122866fbba)) as well as with ImageJ.

Alagille syndrome (ALGS) is a congenital disorder affecting multiple organs, including the hepatic and cardiovascular systems (Spinner et al., 1993; Mašek and Andersson, 2017). The disease is usually caused by mutations in the Notch ligand *JAGGED1* (*JAG1*, OMIM: ALGS1 [Oda et al., 1997; Li et al., 1997; Gilbert et al., 2019]) or, less frequently, in the receptor *NOTCH2* (OMIM: ALGS2 [Spinner et al., 1993; McDaniel et al., 2006]), and is chiefly characterized by intrahepatic peripheral bile duct paucity (Alagille et al., 1975; Riely et al., 1979). Importantly, bile duct development is regulated by portal vein mesenchyme (Hofmann et al., 2010), implying that the architectural relationship between liver cells and the vasculature affects opportunities for signaling cross-talk between these systems in liver. Some patients with ALGS spontaneously recover a biliary system (Riely et al., 1979; Fujisawa et al., 1994). Ductular reaction, aberrant biliary growth and/or trans-differentiation from hepatocytes can contribute to biliary recovery in ALGS and other cholestatic disorders (Schaub et al., 2018; Fabris et al., 2007). Furthermore, it has been reported that liver vascular architecture is affected in ALGS (previously also known as arteriohepatic dysplasia or syndromic paucity of bile ducts [Hadchouel et al., 1978]). It is thus clear that understanding and defining both biliary and vascular intrahepatic defects is essential for ALGS.

DUCT is a versatile, reliable tool allowing standardized architecture analysis and definition of multiple lumenized trees on a whole organ level, facilitating systems insights. We demonstrated the applicability of DUCT by revealing the distinct morphological features that allow the de novo generated *Jag1<sup>Ndr/Ndr</sup>* adult biliary system to achieve wild-type biliary volume: (1) an increase in the number of central low generation branches and (2) profound tortuosity in the liver periphery. We confirmed these 3D findings in 2D sections from *Jag1<sup>Ndr/Ndr</sup>* mice and patients with ALGS, demonstrating that the new phenotypes identified with DUCT in the mouse model are representative of patient pathology. Using DUCT we also discovered novel phenotypes such as bile duct bridging between two portal veins, which would be misinterpreted as bile duct proliferation in 2D histological sections. Hence, 2D histological sections are not sufficient to understand the structural abnormalities of tubular networks.

## Results

### DUCT revealed that *Jag1<sup>Ndr/Ndr</sup>* adult mice generate a full-volume biliary system

In order to define and quantify the adaptive process resulting in a de novo generated biliary system in adult *Jag1<sup>Ndr/Ndr</sup>* mice, we investigated the spatial relationship of portal venous and biliary systems in normal and diseased liver in 3D. First, we compared double carbon ink injection (Kaneko et al., 2015) and whole mount immunofluorescence staining combined with tissue clearing using iDISCO+ (Renier et al., 2016) to assess the 3D architecture of the liver (Figure 1—figure supplement 1A and B). Neither carbon ink injection nor iDISCO+ (due to poor labeling of vascular network) were suitable for dual 3D analysis of vascular and biliary networks. We therefore developed an alternative approach for 3D analysis: DUCT (Figure 1A, Figure 1—figure supplement 1C) followed by semi-automated segmentation generating 3D binary masks of these two systems. The binary masks were used directly for DUCT data volume analysis. For further quantification of the architectural parameters the binary masks were skeletonized and analyzed (Figure 1B) using a custom-written MATLAB pipeline, ImageJ, or qualitative visual assessment.

DUCT outperformed ink injection and immunofluorescence in most aspects (Figure 1—figure supplement 1D), from 3D analysis (not possible with ink) to analysis of lumenization (not possible with immunofluorescence). One limitation, however, is that DUCT cannot visualize lumens smaller than 5  $\mu\text{m}$ . Finally, to test whether DUCT can be applied to other organ systems, we visualized lung architecture by injecting the airways (via the trachea) and the vasculature (via the pulmonary artery) and 3D reconstructed the respiratory and vascular systems (Figure 1—figure supplement 1E). In lungs, as in liver, the two lumenized systems can be clearly distinguished using DUCT. In all the DUCT liver experiments in this manuscript, we applied DUCT to the right medial lobe, and used the other lobes for sample-matched quality control (Figure 1—figure supplement 2).

Our previous work revealed that *Jag1<sup>Ndr/Ndr</sup>* bi-potential hepatoblasts did not differentiate into cholangiocytes during embryonic development. Newborn *Jag1<sup>Ndr/Ndr</sup>* mice were jaundiced and displayed intrahepatic bile duct paucity. However, by adulthood *Jag1<sup>Ndr/Ndr</sup>* livers exhibited mature

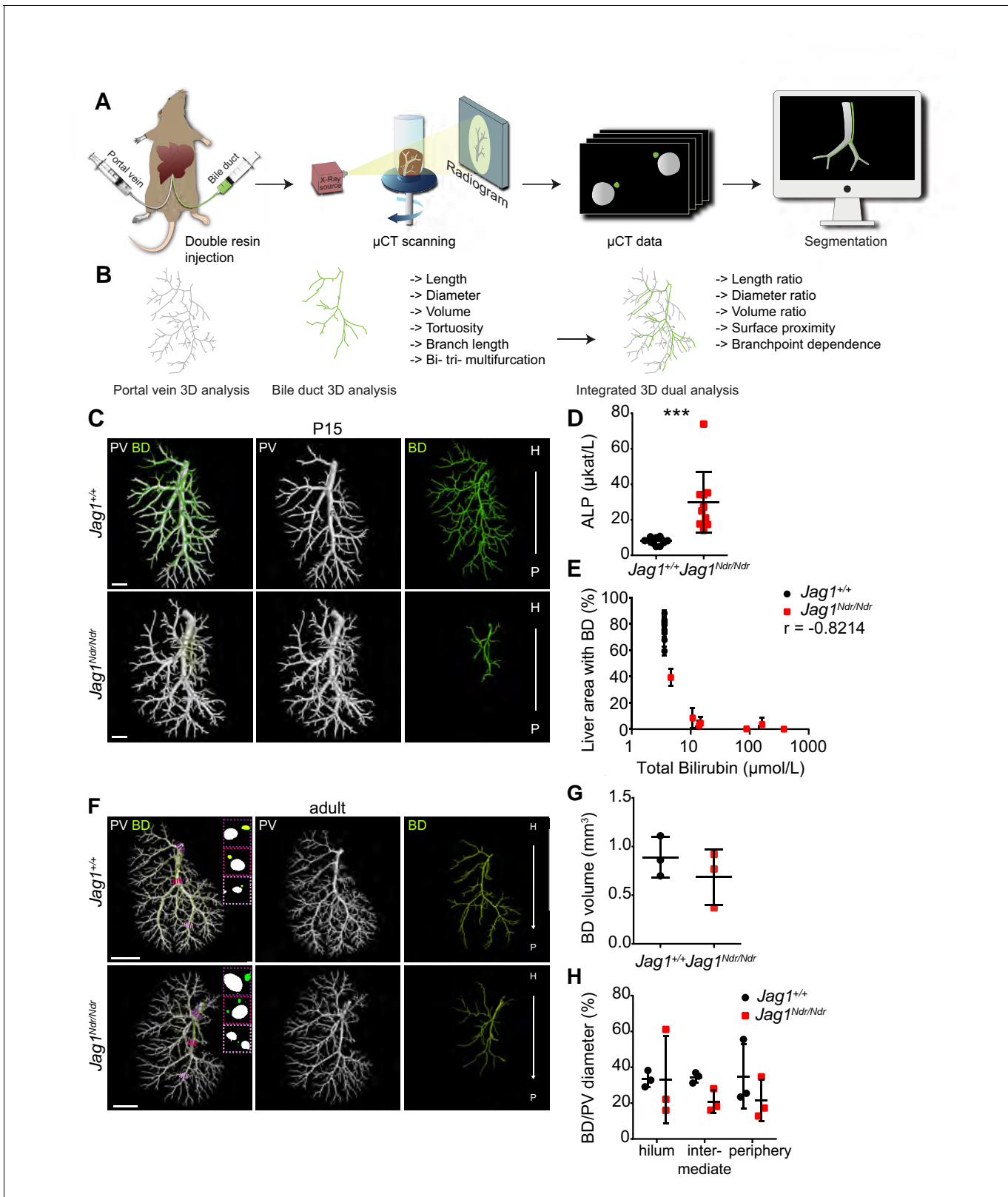


**Figure 1.** DUCT revealed that *Jag1<sup>Ndr/Ndr</sup>* bile ducts recover a full-volume biliary system. (A) The DUCT pipeline encompasses resin injection into two systems (portal venous and biliary), micro computed tomography ( $\mu$ CT) scanning of the organ, or individual lobes, and segmentation of  $\mu$ CT data (tomographs) into 3D binary masks. (B) The image analysis pipeline creates 3D skeletons from the binary masks, to quantify architectural parameters in individual or combined systems. (C) 3D rendering of BD and PV structures using DUCT in postnatal day 15 (P15) *Jag1<sup>+/+</sup>* (top panel) and *Jag1<sup>Ndr/Ndr</sup>* (bottom panel). Figure 1 continued on next page

Figure 1 continued

livers (bottom panel). Scale bar = 1 mm. (D) Alkaline phosphatase (ALP) serum levels at P15. Each dot represents one animal; lines show mean value  $\pm$  standard deviation. Statistical test – unpaired t-test,  $p=0.0008$ . (E) Correlation analysis between total bilirubin levels and liver area with resin-injected BD. Each dot represents one animal; lines show mean value  $\pm$  standard deviation (measured in right medial and left lateral lobe). Statistical test – non-parametric Spearman correlation,  $p=0.0341$ ,  $r = -0.8214$ . (F) 3D rendering of BD and PV structures using DUCT in adult (4.5–6.5 months old)  $Jag1^{+/+}$  (top panel) and adult de novo generated  $Jag1^{Ndr/Ndr}$  livers (bottom panel). Boxed regions highlight 2D sections of hilar, intermediate and peripheral regions identified with dotted lines in matched colors. Scale bar = 4 mm. (G) BD system volume is similar in adult  $Jag1^{+/+}$  and  $Jag1^{Ndr/Ndr}$  mice. Each dot represents one animal; lines show mean value  $\pm$  standard deviation, unpaired t-test,  $p=0.3730$  (H) BD/PV diameter ratio in  $Jag1^{+/+}$  and  $Jag1^{Ndr/Ndr}$  mice in hilar, intermediate and peripheral regions. Each dot represents one animal; lines show mean value  $\pm$  standard deviation. Two-way ANOVA,  $p=0.2496$ . 3D, three dimensional; ALP, alkaline phosphatase; BD, bile duct; DUCT, double resin casting micro computed tomography; H, hilar; P, peripheral. PV, portal vein.

The online version of this article includes the following source data and figure supplement(s) for figure 1:

**Figure supplement 1.** DUCT outperforms other state of the art techniques to visualize mouse liver in 3D.

**Figure supplement 2.** Resin injection quality control of the left lateral lobe.

**Figure supplement 3.** Liver cast of P15  $Jag1^{+/+}$  showing bile duct (green) and portal vein (white) together (top panel) or separately (bottom panels).

**Figure supplement 3—source data 1.** 3D interactive liver cast shown in **Figure 1—figure supplement 3**.

**Figure supplement 4.** Liver cast of P15  $Jag1^{Ndr/Ndr}$  showing bile duct (green) and portal vein (white) together (top panel) or separately (bottom panels).

**Figure supplement 4—source data 1.** 3D interactive liver cast shown in **Figure 1—figure supplement 4**.

**Figure supplement 5.**  $Jag1^{Ndr/Ndr}$  bile ducts displayed heterogeneous de novo growth.

**Figure supplement 6.** Liver cast of adult  $Jag1^{+/+}$  showing bile duct (green) and portal vein (white) together (top panel) or separately (bottom panels).

**Figure supplement 6—source data 1.** 3D interactive liver cast shown in **Figure 1—figure supplement 6**.

**Figure supplement 7.** Liver cast of adult  $Jag1^{+/+}$  showing bile duct (green) and portal vein (white) together (top panel) or separately (bottom panels).

**Figure supplement 7—source data 1.** 3D interactive liver cast shown in **Figure 1—figure supplement 7**.

**Figure supplement 8.** Liver cast of adult  $Jag1^{+/+}$  showing bile duct (green) and portal vein (white) together (top panel) or separately (bottom panels).

**Figure supplement 8—source data 1.** 3D interactive liver cast shown in **Figure 1—figure supplement 8**.

**Figure supplement 9.** Liver cast of adult  $Jag1^{Ndr/Ndr}$  showing bile duct (green) and portal vein (white) together (top panel) or separately (bottom panels).

**Figure supplement 9—source data 1.** 3D interactive liver cast shown in **Figure 1—figure supplement 9**.

**Figure supplement 10.** Liver cast of adult  $Jag1^{Ndr/Ndr}$  showing bile duct (green) and portal vein (white) together (top panel) or separately (bottom panels).

**Figure supplement 10—source data 1.** 3D interactive liver cast shown in **Figure 1—figure supplement 10**.

**Figure supplement 11.** Liver cast of adult  $Jag1^{Ndr/Ndr}$  showing bile duct (green) and portal vein (white) together (top panel) or separately (bottom panels).

**Figure supplement 11—source data 1.** 3D interactive liver cast shown in **Figure 1—figure supplement 11**.

**Figure supplement 12.** Overview of 3D reconstructed bile duct and portal vein systems, their branching skeletons and volume.

bile ducts, but with abnormal apical polarity (Andersson et al., 2018). Using DUCT, we first investigated to what degree  $Jag1^{Ndr/Ndr}$  mice can grow a biliary tree by postnatal day 15 (P15). We examined the biliary system in 7  $Jag1^{Ndr/Ndr}$  P15 pups and discovered a rudimentary or absent biliary tree in  $Jag1^{Ndr/Ndr}$  pups, while there was a fully developed biliary tree in  $Jag1^{+/+}$  mice (Figure 1C). The 3D reconstruction of both systems can be explored in separate channels or in tandem with rotation (interactive PDFs, Figure 1—figure supplements 3 and 4). We noted high variability in biliary outgrowth between the right medial lobe (RML) and the left lateral lobe (LLL) in  $Jag1^{Ndr/Ndr}$  livers (illustration of liver lobes Figure 1—figure supplement 5A). In the RML of five  $Jag1^{Ndr/Ndr}$  pups, the biliary tree covered >5% of liver area, whereas in LLL only 1  $Jag1^{Ndr/Ndr}$  pup displayed >5% biliary tree coverage, while four  $Jag1^{Ndr/Ndr}$  pups had no lumenized bile ducts. In  $Jag1^{+/+}$  pups the biliary network covered on average 75% of the liver area in both RML and LLL (Figure 1—figure supplement 5B and C). The P15  $Jag1^{Ndr/Ndr}$  pups were cholestatic, and manifested increased levels of alkaline phosphatase (ALP) (Figure 1D), aspartate aminotransferase (AST), alanine aminotransferase (ALT) and decreased levels of albumin (Figure 1—figure supplement 5D). Interestingly, two different groups were noted in  $Jag1^{Ndr/Ndr}$  pups with regard to the total bilirubin levels, that is, 50% of the animals had highly increased and 50% had mildly increased total bilirubin ( $p=0.0079$ ), while all  $Jag1^{+/+}$  mice displayed bilirubin levels below detection limits (Figure 1—figure supplement 5D). We correlated the total bilirubin amount with the liver area covered by lumenized bile ducts and detected a strong negative correlation between these two factors (Figure 1E,  $r = -0.8214$ ). We further sectioned the resin injected P15 liver and stained for the early biliary marker SOX9 (SRY-Box

transcription factor 9) (note remaining resin in some portal veins). In *Jag1<sup>+/+</sup>* central liver, lumenized bile ducts were clearly detected, whereas in all four *Jag1<sup>Ndr/Ndr</sup>* central livers no lumenized bile ducts were visible and the number of SOX9 positive cells varied between animals, poorly reflecting the total bilirubin levels (**Figure 1—figure supplement 5E**).

Next, we aimed to characterize and quantify the biliary architecture of the *Jag1<sup>Ndr/Ndr</sup>* de novo generated biliary system in adult mice (**Figure 1F**). The 3D reconstruction of both systems can be explored in separate channels or in tandem (interactive PDFs, **Figure 1—figure supplement 6–11**). While *Jag1<sup>+/+</sup>* mice demonstrated a stereotyped vascular and biliary architecture (**Figure 1—figure supplement 12A, B and C**), *Jag1<sup>Ndr/Ndr</sup>* livers exhibited greater architectural variability (**Figure 1—figure supplement 12D, E and F**). To quantify the degree of de novo biliary formation, we extracted the volume (using the binary masks) and diameters of the portal venous and biliary systems (using the binary masks and skeletons). The total volume of the vascular and biliary trees was similar in *Jag1<sup>Ndr/Ndr</sup>* and *Jag1<sup>+/+</sup>* mice (**Figure 1G, Figure 1—figure supplement 12H**). There was a tendency toward a larger portal venous volume and smaller biliary volume in *Jag1<sup>Ndr/Ndr</sup>* mice, resulting in a trend toward a reduced BD:PV (bile duct, portal vein) volume ratio in *Jag1<sup>Ndr/Ndr</sup>* mice (**Figure 1—figure supplement 12H**,  $p=0.0594$ ). Next, we investigated portal vein and bile duct diameters along the main branch. There was a tendency to an increase in the *Jag1<sup>Ndr/Ndr</sup>* portal vein diameter and a decrease in biliary diameter as a function of distance compared with *Jag1<sup>+/+</sup>* mice (**Figure 1—figure supplement 12I**). However, there was high variability in venous and bile duct diameter in the *Jag1<sup>Ndr/Ndr</sup>* hilar region. In *Jag1<sup>+/+</sup>* liver, the BD:PV diameter ratio was consistently 1:3 in hilar and intermediate regions (**Figure 1H**). This BD:PV diameter ratio was not preserved in the *Jag1<sup>Ndr/Ndr</sup>* livers (**Figure 1H**).

DUCT enabled 3D visualization of postnatal and adult biliary and vascular trees. The biliary network in *Jag1<sup>Ndr/Ndr</sup>* mice appeared postnatally, but with high heterogeneity between liver lobes and animals. Moreover, the liver area with lumenized bile ducts correlated with total bilirubin levels and disease severity at P15. The adult segmented  $\mu$ CT data were analyzed for volume and inner diameter of two injected systems. Comparisons of the portal vein and bile duct diameters demonstrated a conserved portal vein – bile duct architectural relationship with a stereotype BD:PV 1:3 diameter ratio in *Jag1<sup>+/+</sup>* liver. The adult *Jag1<sup>Ndr/Ndr</sup>* mice displayed a heterogeneous phenotype that nevertheless resulted in full restoration of biliary function (**Andersson et al., 2018**) via recovery of a wild-type biliary volume.

## Alagille syndrome human and murine bile ducts end abruptly

The intrahepatic biliary tree forms by a tubulogenic process in which a heterogeneous, hierarchical fine mesh of connected cholangiocytes is refined to single larger conduits of bile ducts, resembling a branching tree (**Ober and Lemaigre, 2018; Tanimizu et al., 2016**). In *Jag1<sup>+/+</sup>* liver, the qualitative analysis of network connectivity revealed that the biliary system formed a continuous tree, branching outwards toward the periphery as expected (**Figures 1C, F and 2A left panel**). In contrast, the *Jag1<sup>Ndr/Ndr</sup>* biliary system displayed some branches oriented from peripheral to hilar, with abrupt endings (**Figure 2A right panels, blue arrowheads**, on average one abruptly ending BD per lobe). We confirmed the abruptly ending bile ducts in *Jag1<sup>Ndr/Ndr</sup>* livers in serial liver sections (**Figure 2B, bottom panels**). The black arrowhead labels a well-formed bile duct, that ended bluntly in the following section (+5  $\mu$ m, blue arrowhead), and disappeared completely in the next section (+10  $\mu$ m).

To determine whether the *Jag1<sup>Ndr/Ndr</sup>* biliary abnormalities were representative of pathology in patients with Alagille syndrome, we evaluated liver serial sections from whole liver explants (patients with severe Alagille syndrome (S-ALGS) that underwent transplantation) and biopsies obtained for clinical reasons in non-transplanted patients (patients with mild Alagille syndrome (M-ALGS)). The liver function tests for individual patients are reported in **Table 1** and representative liver sections are presented in **Figure 2—figure supplement 1**. One patient (M\_ALGS-5) had been biopsied at multiple time points revealing paucity of bile duct at 2.5 months, a regenerating phase with hepatocytes expressing CK7 at 1.3 years and bile duct recovery at 4.7 years (**Figure 2—figure supplement 1D**).

We evaluated liver sections from patients with severe (top panel) and mild (bottom panel) Alagille syndrome for the presence of abruptly terminating bile ducts. A black arrowhead labels a well-formed bile duct that terminated in the subsequent section (+5  $\mu$ m, blue arrowhead), (**Figure 2C**). In conclusion, DUCT facilitated qualitative assessments of the tubular networks, including connectivity

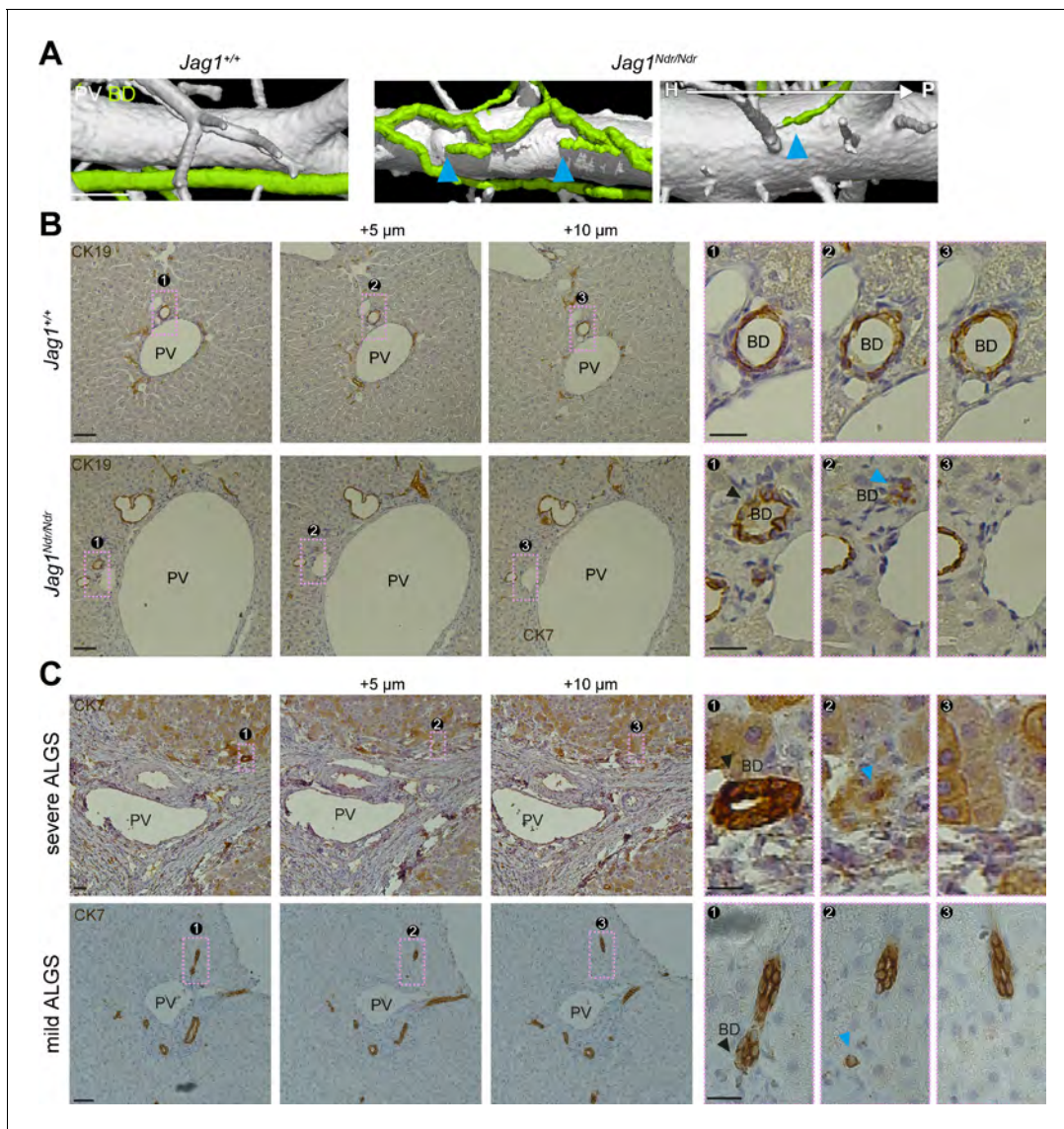


**Figure 2.** Alagille syndrome human and murine bile ducts end abruptly. (A) *Jag1<sup>Ndr/Ndr</sup>* BDs (right panel) terminated randomly and facing toward the hilum (blue arrowheads). (B) 2D histological consecutive liver sections confirmed abruptly terminating BDs in *Jag1<sup>Ndr/Ndr</sup>* liver. Black arrowhead depicts lumenized well-formed BD that ended in the following sections (blue arrowhead). (C) BDs in patients with severe ALGS (top panel) or mild ALGS (bottom panel) terminate abruptly (blue arrowhead) in consecutive liver histological sections. Scale bars (A) 500 μm, (B left panels), (C) 50 μm, (B boxed region) 20 μm. ALGS, Alagille syndrome; BD, bile duct; CK, cytokeratin; H, hilar; P, peripheral. PV, portal vein. The online version of this article includes the following figure supplement(s) for figure 2:

**Figure supplement 1.** Overview of liver samples from patients with Alagille syndrome stained for CK7.

and perfusion. Both the *Jag1<sup>Ndr/Ndr</sup>* and Alagille syndrome biliary systems displayed abruptly ending bile ducts, which may affect bile flow and shear stress.

### Alagille syndrome human and murine de novo generated bile ducts are further from portal veins

During embryonic development, cholangiocytes differentiate from hepatoblasts that are in contact with portal vein mesenchyme expressing *Jag1* (Ober and Lemaigre, 2018). Whether postnatally de novo generated bile ducts arise adjacent to the portal vein, or whether they are less dependent on portal vein proximity has not yet been explored. We therefore analyzed the distance between the biliary and portal venous systems by calculating the surface distances using the MATLAB pipeline.

**Table 1.** Liver function test overview for patients with Alagille syndrome.

M-ALGS stands for patients with mild Alagille syndrome. S-ALGS stands for patients with severe Alagille syndrome.

ID	Age (years)	ALT ( $\mu\text{kat/L}$ )	AST ( $\mu\text{kat/L}$ )	ALP ( $\mu\text{kat/L}$ )	GT ( $\mu\text{kat/L}$ )	Bil Tot ( $\mu\text{mol/L}$ )	BilD ( $\mu\text{mol/L}$ )	Bile acids ( $\mu\text{mol/L}$ )	Sample
Reference value		<0.76	<1	<7.6	<0.76	<22	<4	<10	
S-ALGS_1	1.2	3.29	2.87	23.4	21.8	308	272	665	Explant
S-ALGS_2	1.5	3.09	-	10.8	13.5	274	246	473	Explant
S-ALGS_3	4	4.41	-	9.9	7.5	238	215	246	Explant
S-ALGS_4	6	3.9	-	9.4	8.1	220	193	244	Explant
M-ALGS_1	0.6	1.09	-	4.6	1.2	7	2	-	Biopsy
M-ALGS_2	1.4	0.78	0.96	6.6	1.2	3	<2	33	Biopsy
M-ALGS_3	2.5	1.46	1.44	13.6	7.4	10	6	106	Biopsy
M-ALGS_4	3.4	0.68	0.92	5.2	1.5	14	4	31	Biopsy
M-ALGS_5_1	0.2	1.44	1.77	-	-	46	39	175	Biopsy
M-ALGS_5_2	1.2	1.59	1.8	-	-	3	2	-	Biopsy
M-ALGS_5_3	4.7	0.79	0.93	3.5	0.52	9	<2	2	Biopsy
M-ALGS_6	6.4	1.18	1.44	6.4	3	6	<2	1	Biopsy

Specifically, the surface distance was defined as the shortest length from biliary skeleton to the portal venous skeleton, minus radiuses of these systems at the defined points (**Figure 3A**). *Jag1<sup>+/+</sup>* bile ducts maintained a uniform distance to adjacent portal veins throughout the liver (**Figure 3B** top panel, asterisk, 3C, 3D 100% of BDs within 0.5 mm of a PV). In contrast, *Jag1<sup>Ndr/Ndr</sup>* bile ducts did not maintain a uniform distance to the nearest portal vein (**Figure 3B** bottom panel, double arrow, 3C, 3D 1.5% of BD are placed 0.5–1.26 mm away from a PV) and sometimes traversed the parenchyma to join another portal vein branch (**Figure 3B** bottom right panel, **Figure 1—figure supplement 2** empty arrowheads). Both the increased BD-PV distance and parenchymal bile ducts were validated in histological sections, in which *Jag1<sup>+/+</sup>* bile ducts were in close proximity to, or embedded in portal vein mesenchyme (**Figure 3E** left panel, asterisk). In contrast, *Jag1<sup>Ndr/Ndr</sup>* bile ducts were confirmed to be present outside of the portal vein mesenchyme area (**Figure 3E** middle panel, double arrow) or even in the liver parenchyma close to the edge of the liver (**Figure 3E** right panel). This phenotype, visualized in 2D sections, could resemble biliary proliferation, or ductular reaction, rather than a bridging structure, highlighting the importance of 3D imaging. Parenchymal bile ducts were also detected in liver samples from patients with severe and mild Alagille syndrome (**Figure 3F**) but not in control human liver. In sum, DUCT pipeline together with the MATLAB algorithm, measured the gap between surfaces of two resin injected systems to address the spatial relationship between them. Our data showing biliary cells in the parenchyma and bile ducts far from portal veins in *Jag1<sup>Ndr/Ndr</sup>* liver and liver from patients with Alagille syndrome thus suggest that postnatal bile duct formation does not rely on close proximity to portal vein mesenchyme and may occur independent of signals from portal vein mesenchyme.

### Alagille syndrome human and murine de novo generated bile ducts display branching independent of portal vein branching

Portal vascular and biliary systems are ductal tree-like structures with numerous branches, which function to maximize the area of exchange between the tissue and its lumen. We evaluated portal venous and biliary branching using the DUCT pipeline and the MATLAB script to quantify the total number of vascular or biliary branch points. Branch points were identified using the 3D skeletons of each system, and categorized based on the number of incoming/outgoing branches (classifying as bifurcations, trifurcations, or nodes with more than three branches) (**Figure 1—figure supplement 12D and G**). We did not identify any differences in the absolute numbers of branch points in *Jag1<sup>+/+</sup>* and *Jag1<sup>Ndr/Ndr</sup>* systems, again suggesting that de novo biliary growth generally reconstituted a full-volume, well-branched biliary tree (**Figure 4—figure supplement 1**).

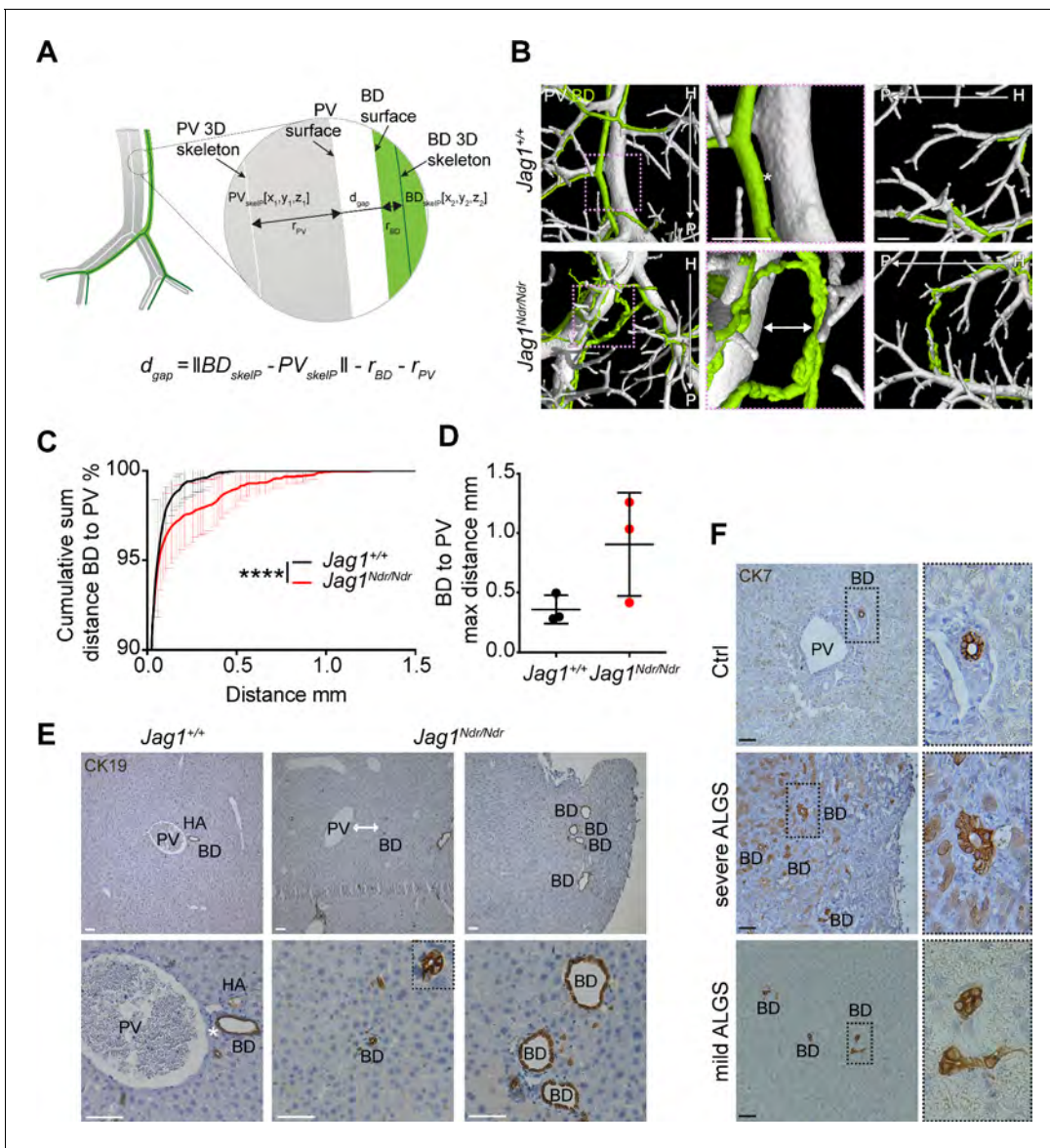


**Figure 3.** Alagille syndrome human and murine de novo generated bile ducts are further from portal veins. (A) Scheme of BD to PV surface distance analysis.  $PV_{skelP}$  = single point on PV skeleton,  $BD_{skelP}$  = single point on BD skeleton,  $r_{PV}$  = radius of PV at  $PV_{skelP}$  (i.e. minimal distance from  $PV_{skelP}$  to PV surface),  $r_{BD}$  = radius of BD at  $BD_{skelP}$  (i.e. minimal distance from  $BD_{skelP}$  to BD surface),  $d_{gap}$  = gap distance, which is derived by subtracting the radii from the skeleton to skeleton distance. (B) 3D rendering shows homogenous distance between a BD and PV in *Jag1<sup>+/+</sup>* livers (asterisk), but a large heterogeneous distance in *Jag1<sup>Ndr/Ndr</sup>* liver (double-headed arrow). Right panel shows a parenchymal bile duct traversing between two PVs at the *Jag1<sup>Ndr/Ndr</sup>* liver edge. Scale bar 500  $\mu$ m. (C) Cumulative sum of percentage of BDs at a given distance from the nearest PV. 3 *Jag1<sup>+/+</sup>* and 3 *Jag1<sup>Ndr/Ndr</sup>* mice were used. Bars represent mean  $\pm$  standard deviation, Kolmogorov - Smirnov test (on raw data),  $p < 0.0001$ , (\*\*\*\*). For individual data points see **Figure 3—source data 1**. (D) Maximum distance between BD and PV. Each dot represents one animal, bars are mean  $\pm$  standard deviation, unpaired t-test,  $p = 0.1041$ , not significant. (E) BD – PV distances confirmed in 2D histological sections. Overview in top panel and magnification in bottom panel. *Jag1<sup>Ndr/Ndr</sup>* PVs can be present in the parenchyma far from (middle panels), or independent of (right panels), the nearest PV. Scale bars 50  $\mu$ m. (F) Healthy human liver with BD close to PV (top panel). Parenchymal CK7+ BDs in histological liver sections from a patient with severe ALGS (middle panel) and distant BDs in a patient with mild ALGS (bottom panel). Magnification shows lumenization of BDs. Scale bar 50  $\mu$ m. ALGS, Alagille syndrome, BD, bile duct; CK, cytokeratin; H, hilar; HA, hepatic artery; P, peripheral; PV, portal vein.

The online version of this article includes the following source data for figure 3:

**Source data 1.** Raw data measuring the distance from the surface of bile duct to a portal vein surface.

During embryonic development, the biliary system is established alongside the portal venous system. This is reflected in the final architecture of the system, with bile ducts in close proximity to portal veins (**Figure 3**). A prediction based on this embryonic process and BD/PV dependency is therefore that bile ducts should invariably branch where portal veins branch. We extracted the coordinates for branch points in the biliary and portal venous systems from the corresponding 3D skeletonized data and calculated 3D Euclidean distances between biliary branch points and their nearest neighboring portal vein branch point (**Figure 4A**). Indeed, *Jag1<sup>+/+</sup>* bile ducts (**Figure 4B** left panel, blue arrowhead) branched adjacent to portal vein branch points (magenta arrowhead, defined as within 0.5 mm). In contrast, *Jag1<sup>Ndr/Ndr</sup>* bile ducts (**Figure 4B** middle panel, blue arrowhead) branched further from portal vein branch points (magenta arrowhead), or independent of portal vein branch points (blue arrow in **Figure 4B**, and data in 4C; independence defined as distance >0.54 mm). On average, 1.3% of *Jag1<sup>+/+</sup>* bile ducts branch points and 8.6% of *Jag1<sup>Ndr/Ndr</sup>* bile duct branch points were further than 0.5 mm from the nearest portal vein branch point (**Figure 4C**). We analyzed consecutive histological liver sections to confirm branching morphology defects discovered using DUCT. *Jag1<sup>+/+</sup>* bile ducts (**Figure 4D** top panel, blue arrowhead) indeed branched at the same point as portal veins branch (magenta arrowhead). In contrast, in *Jag1<sup>Ndr/Ndr</sup>* liver bile ducts might bifurcate in the absence of portal vein branching (**Figure 4D** bottom panel, blue arrow).

We next asked whether similar branching phenotypes were present in healthy human liver or in patients with mild or severe Alagille syndrome. In normal human liver, biliary branching occurred close to portal vein bifurcation (**Figure 4E** top panel, blue arrowheads, PV branching within 25  $\mu$ m in this example, branching not shown). In patients with severe Alagille syndrome, biliary branching could be seen independent of portal vein branching (**Figure 4E** middle panel, blue arrows), the nearest portal vein branch point for this bile duct was 13 sections hilar (circa 65  $\mu$ m earlier). We also detected independent bile duct branching in patients with mild Alagille syndrome (**Figure 4E** bottom panel, blue arrows). In conclusion, DUCT revealed dual system 3D architectural phenotypes: (1) similar numbers of branch points in *Jag1<sup>+/+</sup>* and *Jag1<sup>Ndr/Ndr</sup>* livers but (2) a greater distance between portal vein and bile duct branch points in *Jag1<sup>Ndr/Ndr</sup>* livers. Bile ducts in patients with Alagille syndrome displayed similar branching abnormalities, corroborating the architectural independence from portal vein patterning.

### Strahler analysis of resin casts reveal excess central branching in the *Jag1<sup>Ndr/Ndr</sup>* de novo generated biliary system

Whether de novo bile duct formation occurs evenly throughout the liver or is more extensive in certain regions has not yet been quantitatively defined. One of the mechanisms by which the biliary system can regenerate is via abundant branching of the network (**Vartak et al., 2016; Masyuk et al., 2001**). We therefore employed the DUCT pipeline and ImageJ to perform a Strahler analysis (3D branching analysis based on generation number from the origin, see Material and methods section 'Branching analysis' for details on generation number calculation) to address the branch length, number and distribution in specific liver areas. In order to define anatomy correctly for differently sized livers, the liver lobe data were separated into three equivalent regions using portal vein branch generation number and lengths as a proxy for hilum/intermediate/periphery. These regions were denoted region 1 (R1 enriched for hilar region), 2 (R2, intermediate), and 3 (R3, peripheral-enriched) (**Figure 5A**). The average branch length of the portal vein was shorter in *Jag1<sup>Ndr/Ndr</sup>* livers, resulting in significantly smaller portal vein region sizes (**Figure 5B** middle panel), reflecting the overall smaller size of the mice and livers. Using the regions defined by the portal venous system, biliary region size was similar in the 1st and 2nd region of wild type and *Jag1<sup>Ndr/Ndr</sup>* mice, while region three was smaller in both animal groups due to resin not penetrating ducts < 5  $\mu$ m (**Figure 5B** right panel, **Figure 5—figure supplement 1**). Two out of three *Jag1<sup>Ndr/Ndr</sup>* mice had a marked reduction in biliary region size in R3, while one had an increase, reflecting the somewhat variable phenotype manifested by both the patients and the mouse model.

Branching trees in biological systems have a stereotype structure in which branch lengths shorten with each branching generation from start (R1) to end (periphery, R3) (**Masyuk et al., 2001; Hannezo et al., 2017**). We analyzed the portal vein and biliary branch lengths within each region and found that portal vein segments shortened as expected with each generation in both *Jag1<sup>+/+</sup>* and *Jag1<sup>Ndr/Ndr</sup>* livers (**Figure 5C** middle panel). *Jag1<sup>+/+</sup>* bile ducts followed the same stereotype branching principle, but *Jag1<sup>Ndr/Ndr</sup>* bile ducts branch lengths were significantly shorter in regions 1

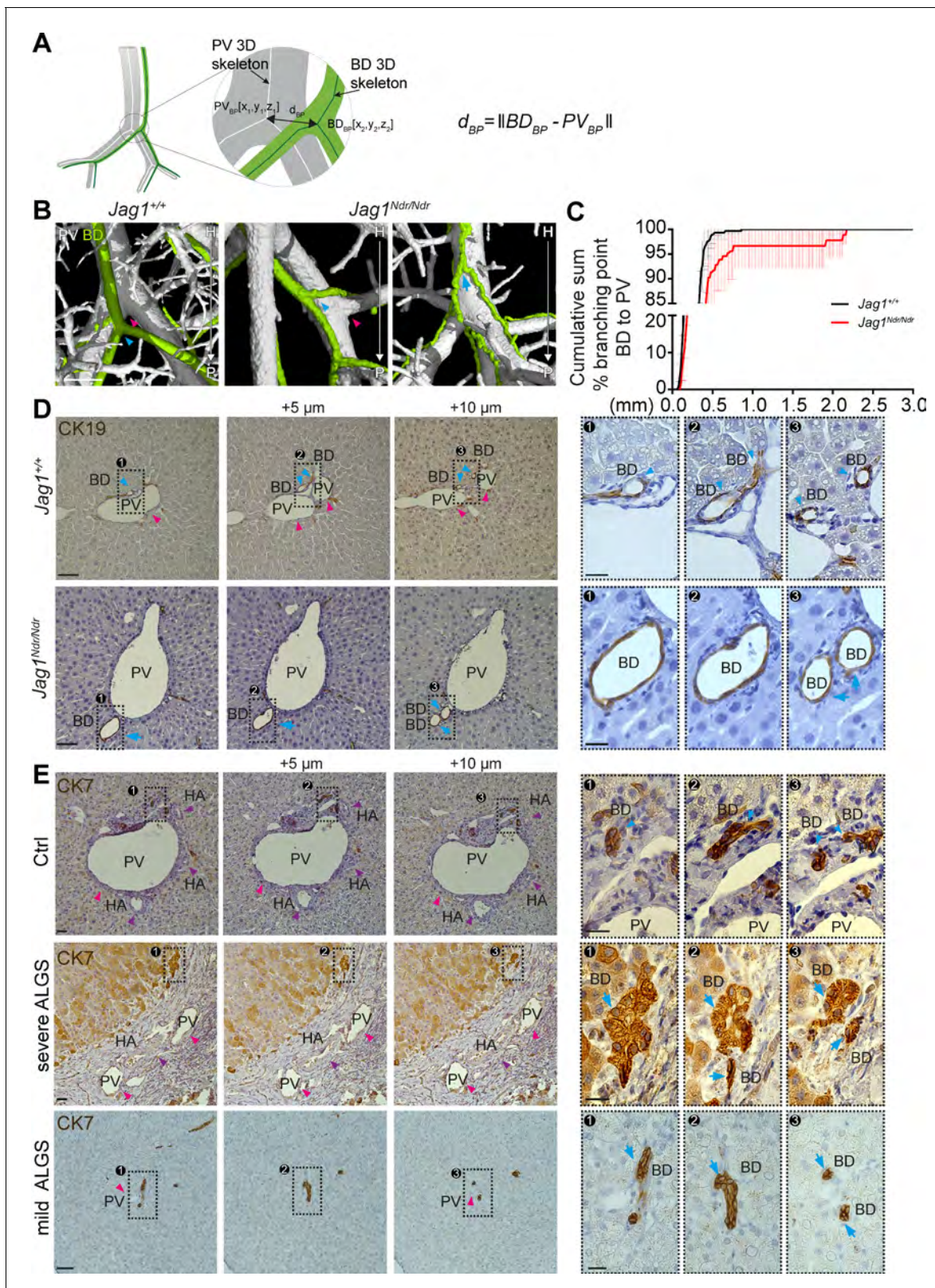


**Figure 4.** Alagille syndrome human and murine de novo generated bile ducts display branching independent of portal vein branching. (A) Scheme representing BD to PV branch point analysis.  $PV_{BP}$  = PV branch point,  $BD_{BP}$  = BD branch point,  $d_{BP}$  = Euclidean 3D distance between branch points. (B) Branching pattern in *Jag1<sup>+/+</sup>* (left panel) and *Jag1<sup>Ndr/Ndr</sup>* liver (middle and right panel). PV branch points (pink arrowheads) were near BD branch points (blue arrowheads) in wild type mice, but further away in *Jag1<sup>Ndr/Ndr</sup>* mice. BD branch points in *Jag1<sup>Ndr/Ndr</sup>* mice also occurred in the absence of PV branch points. (C) Cumulative sum of % branching point BD to PV. (D-F) Histological images of liver sections showing bile duct branching in various conditions. Figure 4 continued on next page

Figure 4 continued

PV branching (blue arrow). Scale bar 500  $\mu\text{m}$ . (C) Cumulative sum of BD branching point percentage at a given distance to the nearest PV branching point. 3  $Jag1^{+/+}$  and 3  $Jag1^{Ndr/Ndr}$  mice were used. 100% of  $Jag1^{+/+}$  bile duct branchpoints were within 1 mm of a PV branchpoint, but only 95% of  $Jag1^{Ndr/Ndr}$  branchpoints were within 1 mm. Bars represent mean  $\pm$  standard deviation, Kolmogorov-Smirnov test (on raw data,  $p=0.9985$ , not significant). For individual data points see **Figure 4—source data 1** (D) Branching analysis in 2D histological consecutive  $Jag1^{+/+}$  and  $Jag1^{Ndr/Ndr}$  liver sections. PV branching (pink arrowheads) was present near BD branching (blue arrowheads) in wild type mice (top panels). In  $Jag1^{Ndr/Ndr}$  mice, BDs branched ectopically in the absence of PV branching (bottom panel). Boxed regions magnified in panels at right. Scale bar 50  $\mu\text{m}$ , boxed region 20  $\mu\text{m}$ . (E) Branching pattern in consecutive human liver histological sections shows BD branching in association with PV (pink arrowhead) branching in controls (top panel), but BD branching in the absence of PV branching in patients with severe ALGS (middle panel) and patients with mild ALGS (bottom panel). Scale bar 50  $\mu\text{m}$ , boxed region 20  $\mu\text{m}$ . ALGS, Alagille syndrome; BD, bile duct; CK, cytokeratin; HA, hepatic artery; H, hilar; P, peripheral; PV, portal vein.

The online version of this article includes the following source data and figure supplement(s) for figure 4:

**Source data 1.** Raw data measuring the distance from the bile duct branching point to a portal vein branching point.

**Figure supplement 1.** De novo grown bile ducts did not show significant differences in the numbers of bifurcations, trifurcations or nodes > 3 branches when normalized to system size.

and 2, and uniform across the hierarchy of branches (**Figure 5C** right panel). We further analyzed the distribution of number of branches in the three regions and discovered that, on average, 9% of  $Jag1^{+/+}$  portal vein branches fell into R1, 66% into R2% and 25% into R3, with a similar distribution in  $Jag1^{Ndr/Ndr}$  livers (**Figure 5D** middle panel). Based on biological tree structure, we would expect fewest biliary branches in R1, an intermediate number in R2, and most branches in R3. However, resin penetration and lumen diameter precluded filling of all terminal portal vein branches in R3. Mirroring the wild type portal venous branch distribution,  $Jag1^{+/+}$  biliary branch distribution was, on average, 16% in R1, 66% in R2% and 18% in R3.  $Jag1^{Ndr/Ndr}$  biliary branch distribution was shifted, with 44% in R1, 44% in R2% and 12% in R3 (**Figure 5D** right panel). The distribution of biliary branches number was highly heterogeneous among the different  $Jag1^{Ndr/Ndr}$  mice. DUCT pipeline is compatible with multiple image analysis software programs. Here, we used ImageJ to address the branching length over branching generations, and our data collectively indicated that low-generation number biliary segments were shorter and more numerous than expected, suggesting that ectopic regenerative branching and/or incorporation of de novo generated biliary cells, occurs in region 1. However, peripheral branching, which may be undetectable if biliary diameters are under 5  $\mu\text{m}$ , cannot be excluded.

### Alagille syndrome human and murine de novo generated bile ducts are tortuous

The biliary system can adapt to excessive amounts of bile by increasing its diameter or length (Vartak et al., 2016; Slott et al., 1990). One means of enlarging length is by duct convolution. We therefore investigated the length and tortuosity of the biliary and portal vascular trees using the DUCT pipeline in combination with the MATLAB algorithm (whole system and main branch quantification) and ImageJ (R1, R2 and R3 analysis). 3D reconstruction of portal vein vasculature and the biliary network revealed straight  $Jag1^{+/+}$  bile ducts (**Figure 6A** top panel), whereas  $Jag1^{Ndr/Ndr}$  bile ducts were tortuous (**Figure 6A** bottom panel), especially in the liver periphery. We confirmed in histological liver sections that the  $Jag1^{Ndr/Ndr}$  BDs were tortuous (**Figure 6B**). We further assessed biliary tortuosity in patients with mild Alagille syndrome and found several tortuous bile ducts (**Figure 6C**); however, we did not detect any tortuous bile ducts in patients with severe Alagille syndrome (data not shown). In order to quantify tortuosity, we calculated the actual (curved) length and theoretical (chord) length (scheme **Figure 6D**). The curved and chord lengths of the entire system, and the main branch alone did not differ for portal venous or biliary systems in  $Jag1^{+/+}$  and  $Jag1^{Ndr/Ndr}$  mice (**Figure 6—figure supplement 1A–G**). The BD:PV ratio was not significantly different for curved (**Figure 6—figure supplement 1H**) or chord length (**Figure 6—figure supplement 1I**). However, there was a 6% increase in overall portal venous tortuosity in  $Jag1^{Ndr/Ndr}$  mice when the entire system was taken into account (**Figure 6E**) and biliary tortuosity was increased by 50%. Biliary tortuosity was greatest in the  $Jag1^{Ndr/Ndr}$  liver periphery, with a 140% increase in R3 (**Figure 6E**). The tortuosity of the main portal vein or main bile ducts branch analyzed alone was not significantly different (**Figure 6—figure supplement 1J and K**), highlighting the importance of analyzing the

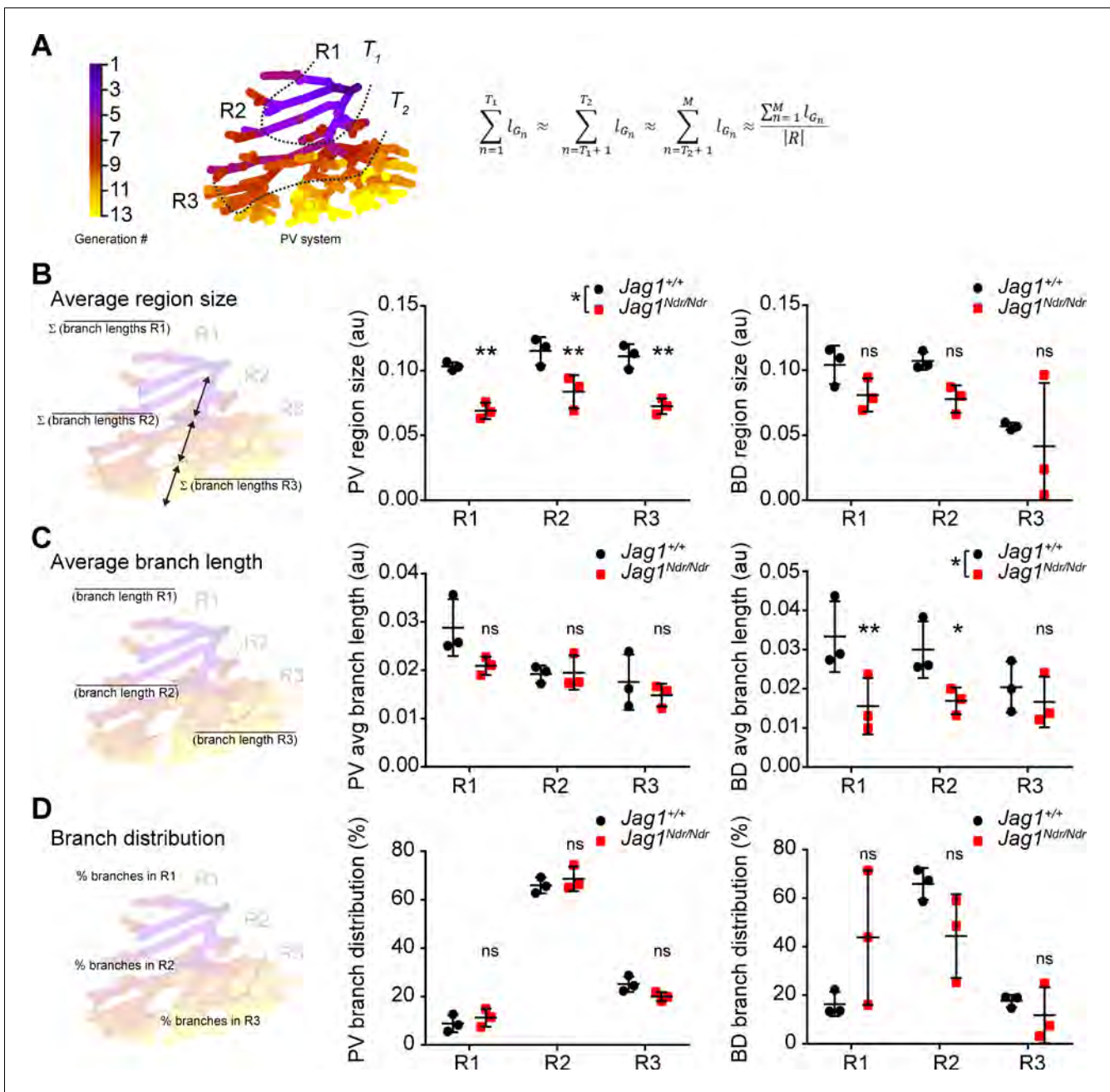


**Figure 5.** Strahler analysis of resin casts reveal excess central branching in the *Jag1<sup>Ndr/Ndr</sup>* de novo generated biliary system. (A) 3D branching analysis based on Strahler number. The branching generations were divided into three equal regions: R1, R2 and R3 based on portal vein average branch length and generation number. Formula:  $R = \{R1, R2, R3\}$ ;  $n \in [1, M] \subset \mathbb{N}$ ;  $T_1, T_2 \subset \mathbb{N}$ ; R, region; G, branch generation; M, maximal branch generation number;  $l_{G_n}$ , average branch length of  $n^{\text{th}}$  generation;  $T_1, T_2$ , borders between regions (specific generation number). (B) Schematic representation of region size calculation, deriving the sum of the average branch lengths within a given region (left). Liver region size for PV (middle panel) and BD (right panel). (C) Schematic representation of average branch length calculation within a region (left panel). Average branch length analysis for PV (middle panel) and BD (right panel) system. (D) Schematic representation of branch distribution, deriving the percentage of branches belonging to each region (left panel). Percentage of branches in each liver region in PV (middle panel) and BD (right panel) systems. Each dot represents one animal, bars represent mean  $\pm$  standard deviation. Two-way ANOVA, (B) middle panel  $p = 0.0289$ , right panel  $p = 0.2029$ ; (C) middle panel  $p = 0.1177$ , right panel  $p = 0.0367$ ; (D) middle panel  $p = 0.4226$ , right panel  $p = 0.8845$ ; followed by Sidak's multiple comparisons test,  $p < 0.05$  (\*),  $p < 0.01$  (\*\*), ns not significant. au, arbitrary units; BD, bile duct; PV, portal vein.

The online version of this article includes the following figure supplement(s) for figure 5:

**Figure supplement 1.** Bile duct branch distribution per region.

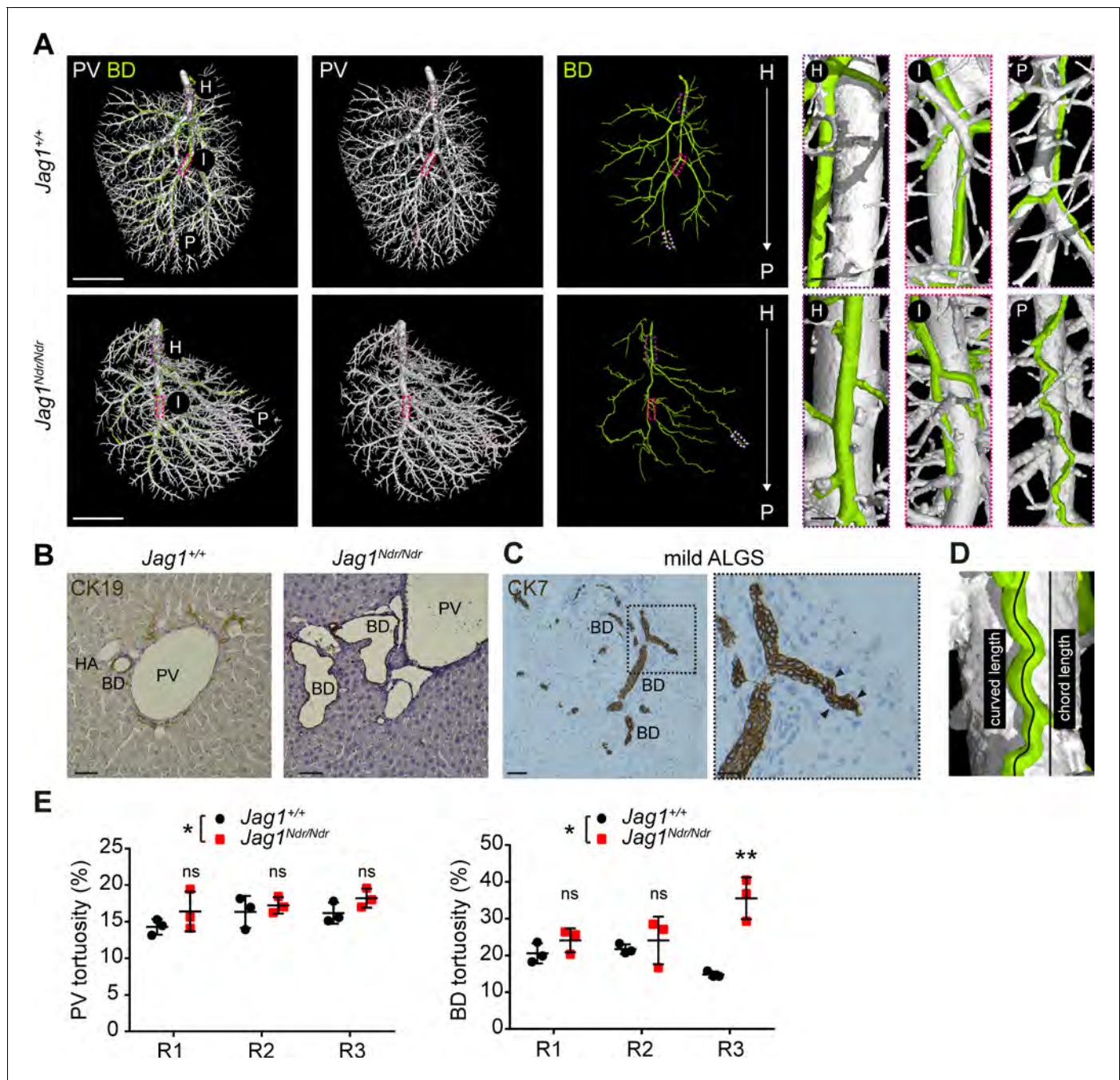


**Figure 6.** Alagille syndrome human and murine de novo generated bile ducts are tortuous. (A) DUCT 3D rendering of BD and PV structures in *Jag1<sup>+/+</sup>* (top panels) and *Jag1<sup>Ndr/Ndr</sup>* liver (bottom panels). Boxed areas magnify the hilar (H), intermediate (I) and peripheral (P) regions. Scale bars left 4 mm, boxed regions 250  $\mu$ m. (B) 2D histological liver sections, show well-formed round CK19+ BDs in *Jag1<sup>+/+</sup>* liver, but aberrantly formed BDs in *Jag1<sup>Ndr/Ndr</sup>* liver. Scale bar 50  $\mu$ m. (C) 2D liver section from patient with mild ALGS revealed tortuous misshaped BDs. Scale bar 50  $\mu$ m, boxed region 20  $\mu$ m. (D) Schematic representing length measurements. Percentage tortuosity was calculated by dividing curved (actual) length by chord (theoretical) length, and subtracting 100% (final value of 0% = not tortuous, perfectly straight). (E) The overall *Jag1<sup>Ndr/Ndr</sup>* PV (left graph) and BD (right graph) systems are more tortuous than wild types, and the *Jag1<sup>Ndr/Ndr</sup>* BD system is particularly tortuous in Region 3 (periphery). Each dot represents one animal, lines show mean value  $\pm$  standard deviation. Statistical test: two-way ANOVA, left panel  $p=0.0141$ , right panel  $p=0.0251$ ; followed by Sidak's multiple comparisons test;  $p<0.05$  (\*),  $p<0.01$  (\*\*). ALGS, Alagille syndrome; BD, bile duct; CK, cytokeratin; DUCT, double resin casting micro computed tomography, H, hilar; HA, hepatic artery, I, intermediate P, peripheral; PV, portal vein.

The online version of this article includes the following figure supplement(s) for figure 6:

**Figure supplement 1.** The adult de novo formed *Jag1<sup>Ndr/Ndr</sup>* and *Jag1<sup>+/+</sup>* biliary systems are similar in length.

entire tree to obtain comprehensive and accurate results. In summary, DUCT allowed analysis of curved and chord length measurements for the entire or defined regions of the injected trees. *Jag1<sup>Ndr/Ndr</sup>* bile ducts recovered wild-type lengths postnatally, with a pronounced increase in peripheral tortuosity.

## Discussion

Precisely defining the three-dimensional (3D) architecture of healthy and diseased organs is a fundamental aspect of biology, and improved imaging methods would allow stricter characterization of animal models for human diseases. Until now, 3D liver analysis has been restricted by a lack of adequate tools and high auto-fluorescence of the tissue. Carbon ink injection is robust, but imaging is 2D, precluding 3D analysis of the architecture. In contrast, immunostaining and clearing allows 3D analysis, but success is variable and highly dependent on tissue fixation, antibody quality, penetrance and tissue autofluorescence. Here, we further advanced organ resin casting, which was previously used to analyze one system at a time (*Masyuk et al., 2003; Kline et al., 2011; Walter et al., 2012*). We developed a simple, robust and inexpensive method (DUCT) for simultaneous visualization and digitalization of two lumenized systems in mouse to analyze organ architecture. DUCT is completely independent of antibody staining, endogenous fluorescent proteins and is not sensitive to tissue fixation. Unlike whole mount immunohistochemistry techniques, DUCT provides information about the lumen, internal diameter, perfusion and connectivity of the injected tree. The most important limitation of DUCT is that it cannot visualize structures with a diameter under 5  $\mu\text{m}$ , due to resin viscosity. We showed that resin casting, segmentation and 3D representation can be used as input for further investigation by visual qualitative assessment, and for in depth analysis by imaging softwares such as ImageJ or custom written MATLAB scripts. The pipeline for imaging and segmentation followed by detailed customized quantification of cellular and architectural mechanisms of two tubular networks could serve as a standard for whole organ analysis in animal models, and can be further adapted for a specific applications.

DUCT is based on radiopaque resin injection into multiple lumenized systems. First, identifying resins with sufficient contrast and low viscosity is crucial for scanning using computed tomography. Combining multiple resins with distinct contrasts can upscale the analysis to several networks simultaneously. In our study, it was imperative to use two fresh MICROFIL resins to obtain sufficiently distinct contrast to separate the two injected systems. Prolonged storage ( $\sim$ 3 months) of the MICROFIL resin leads to resin precipitation and a significant decrease in the resin radiopacity (for details see materials and methods). Future efforts to identify or develop differentially radiopaque substances would further accelerate the analysis pipeline. Second, in order to achieve a successful injection, an appropriate resin injection site for each system must be identified, and a suitable amount of pressure must be applied while avoiding bubble formation. Third, resin segmentation of the scanned sample is straightforward in well-injected, well-contrasted samples, but in samples with bubbles or poor contrast segmentation requires time-consuming manual correction and careful tracing of the resin throughout the whole organ to ensure a coherent network. Minor resin leakage can be digitally excluded during the image segmentation, but artefacts such as air bubbles in resin, non-homogenous resin contrast (in our set up caused by mixing of blue and yellow MICROFIL) and resin leakage due to lumen rupture (probably caused by high pressure during injection) slow down the analyses substantially (**Figure 7B**). Thus, a well-chosen and well-injected resin are a prerequisite for efficient downstream analyses.

Regarding instrumentation, the DUCT pipeline is not restricted to specific CT systems or acquisitions parameters, therefore samples can be imaged on any CT device with sufficient spatial resolution to study selected samples and their morphology. For further qualitative and quantitative analysis of the DUCT  $\mu\text{CT}$  data, robust computational power is necessary – and dedicated workstations with sufficient RAM memory ( $>64$  MB RAM) are recommended, dependent on the volume of acquired data.

Our study describes a complex spatial adaptation of the biliary tree to postnatal BD paucity in a mouse model for Alagille syndrome (ALGS), with validation in samples from patients with ALGS. Based on our data and reported case studies, we propose a model in which *Jag1* mutant intrahepatic bile ducts (IHBDs) did not form during embryonic development (*Andersson et al., 2018; Alessandro et al., 2007*) but in some animals (and some patients, **Figure 2—figure supplement**

1D), bile ducts grew after birth (Dahms et al., 1982). The lumenized bile ducts formed from hilar to peripheral regions with different timings in the different liver lobes and in individual animals. The fully remodeled biliary system was tortuous, exhibited abrupt ends, and was hyper-branched in region 1 (summarized in Figure 8).

Our findings in the mice, using DUCT, may help to explain the poor prognostic value of biopsies in patients with ALGS. Our results suggest that the lack of predictive value between peripheral bile duct paucity, observed in diagnostic biopsies, and phenotype severity in patients with ALGS (Mouzaki et al., 2016) may reflect differences in bile duct growth and presence/absence in hilar versus peripheral regions (Figure 1C, Figure 1—figure supplement 5B,C,E). Mouzaki et al, showed that bile duct density was not predictive of outcome, instead, bilirubin levels, fibrosis, and cholestasis were correlated with disease presentation. In line with this, in the  $Jag1^{Ndr/Ndr}$  pups the total bilirubin levels correlated well with 3D postnatal bile duct growth, which was apparent from 3D resin-injected whole lobe analysis, but did not correlate with bile duct paucity in 2D sections of central



**Figure 7.** Schematic of  $Jag1^{Ndr/Ndr}$  biliary abnormalities in de novo generated bile ducts. Left panel depicts a simplified wild type or healthy human spatial arrangement of portal veins and bile ducts in three liver regions (R1, R2 and R3). Right panel illustrates a simplified adult  $Jag1^{Ndr/Ndr}$  regenerated biliary system displaying morphological abnormalities including (1) increased branching in region 1, (2) branching independent of the portal vein, (3) increased distance from portal vein, (4) abrupt/blunt endings facing the hilum, (5) peripheral tortuosity and (6) bridging between two portal veins. Independently branching, abruptly ending, parenchymal and tortuous bile ducts were confirmed in liver from patients with Alagille syndrome.

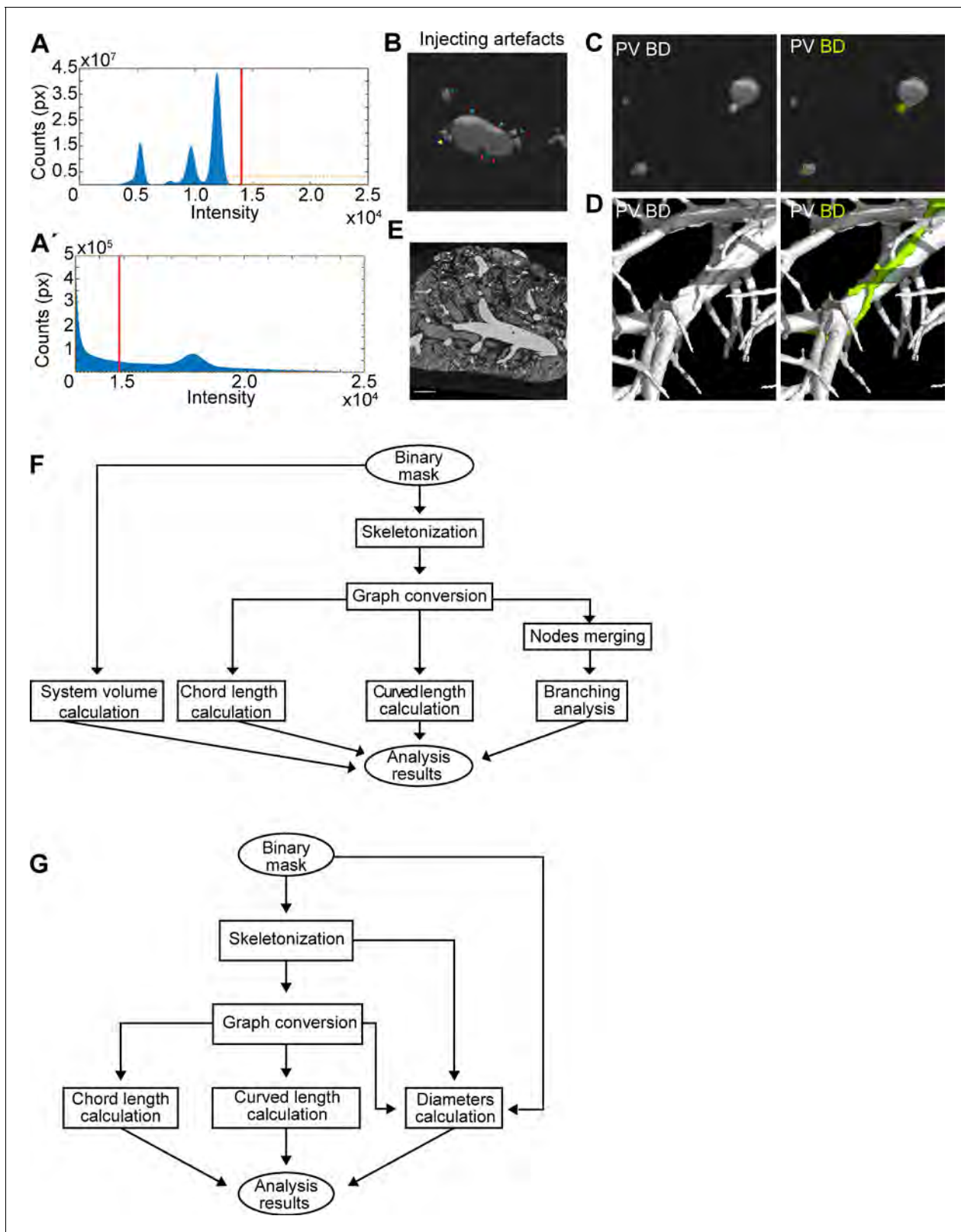


**Figure 8.** Micro computed tomography image processing. (A)  $\mu$ CT scan thresholding. Orange box in (A), magnified in (A'), shows MICROFIL intensity levels. (B) Resin injection artefacts including inadequate mixing of MICROFIL resin (blue arrowheads), bubbles in the resin which require manual correction (magenta arrowheads), and leakage due to excessive injection pressure or vessel/duct weakness (yellow arrowhead). Green arrowheads represent side branches. (C) Global thresholding separates old MICROFIL injected ducts and vessels from background tissue. BD and PV are identified *Figure 8 continued on next page*

Figure 8 continued

manually. (D) 3D visualization of BD and PV after first segmentation (left panel) and after the systems separation. (E) Global thresholding separates fresh MICROFIL injected airways and vessels from each other and the background tissue. (F) Quantification pipeline schematic for the whole lobe (G) or only the main branch analysis.

liver. A 40% regrowth of lumenized bile ducts in *Jag1<sup>Ndr/Ndr</sup>* pup was sufficient to reduce cholestatic burden to almost wild type levels, while not leading to a normal density of bile ducts in the periphery - emphasizing the importance of whole-liver architecture analyses.

Identifying and quantifying architectural defects such as branch length differences, stochastic branching, tortuosity, differences in portal-biliary distance and blunt end bile ducts is very challenging in sections (compare histology and 3D imaging in **Figures 2–6**). We demonstrated here that DUCT is a powerful method for visualization and semi-automated quantitative analysis of two lumenized biological systems in vivo. DUCT could be applied to other tubular networks including blood vessels and bronchi in lung (**Figure 1—figure supplement 1E**) or blood vessels and urinary ducts in kidney (**Wagner et al., 2011; Wei et al., 2006**). DUCT has multiple advantages over ink injections and iDISCO+, as 3D imaging with  $\mu$ CT avoids the drawbacks of tissue autofluorescence or poor antibody penetration. By injecting two resins into a single animal, it is possible to study the relation between these biological systems, which has not been previously reported. While experts in the field are careful to discriminate hilar and peripheral regions of the liver, carefully tracing organ structures for hundreds of micrometers in tissue sections is not standard practice and is a demanding endeavor. DUCT would be a suitable readout for testing drug compounds in mouse models for liver cholestatic diseases. With DUCT, it is now possible to map and quantify architecture of two networks in mouse models, setting the stage for an in depth understanding of how systems interact in health, disease, and regenerative processes.

## Materials and methods

### Key resources table

Reagent type (species) or resource	Designation	Source or reference	Identifiers	Additional information
Antibody	Anti-Cytokeratin 7 (rabbit monoclonal)	Abcam	Cat # ab181598 RRID:AB_2783822	iDISCO+ (1:1000)
Antibody	Anti-Cytokeratin 7 (mouse monoclonal)	Invitrogen/ThermoFisher Scientific	Cat # MA5-11986, clone: OV-TL 12/30 RRID:AB_10989596	IHC (1:200)
Antibody	Anti-Cytokeratin 7 (mouse monoclonal)	Sigma - Aldrich	Cat # C6198 RRID:AB_476856	iDISCO+ (1:2000)
Antibody	Anti-Cytokeratin 19 (rat monoclonal)	DSHB	Cat # TROMA-III RRID:AB_2133570	IHC (1:50)
Antibody	Anti-human SOX9 (goat polyclonal)	RnD Systems	Cat # AF3075 RRID:AB_2194160	IHC (1:100)
Commercial assay or kit	MICROFIL	Flow Tech Inc	Cat # MV120, MV-122	DUCT
Software, algorithm	MATLAB	Mathworks	RRID:SCR_001622	codes available: <a href="https://github.com/JakubSalplachta/DUCT">https://github.com/JakubSalplachta/DUCT</a>

### Experimental mice

All animal experiments were performed in accordance with Stockholm's Norra Djurförsöksetiska nämnd (Stockholm animal research ethics board, ethics approval numbers: N150/14, N61/16, N5253/19, N2987/20) regulations. Animals were maintained with standard day/night cycles, provided with food and water ad libitum, and were housed in cages with enrichment. For postnatal day 15 (P15) experiments, 10 wild type (*Jag1<sup>+/+</sup>*) (eight males and two females) and 10 *Jagged1* Nodder (*Jag1<sup>Ndr/Ndr</sup>*) littermate pups (five males and five females) were used for serum analysis. Within this group, nine *Jag1<sup>+/+</sup>* and seven *Jag1<sup>Ndr/Ndr</sup>* mice were injected with resin. All 16 animals were analyzed in 3D, revealing extensive heterogeneity that would necessitate performing DUCT on a large

number of animals to obtain significant quantitative data, while the bile duct paucity was obvious. 1 *Jag1<sup>+/+</sup>* and 1 *Jag1<sup>Ndr/Ndr</sup>* pair was therefore scanned and rendered in 3D. From this group, four *Jag1<sup>+/+</sup>* and four *Jag1<sup>Ndr/Ndr</sup>* left medial lobes were used for 2D liver sections and staining.

Adult animals were between 4.5 and 6.5 months old. In total, 18 *Jag1<sup>+/+</sup>* and 6 *Jag1<sup>Ndr/Ndr</sup>* animals were injected with resin for  $\mu$ CT. Quality control of injections (**Figure 1—figure supplement 2**) was performed on all livers during method development until surgery and injection technique resulted in well-injected livers. Three *Jag1<sup>+/+</sup>* and three *Jag1<sup>Ndr/Ndr</sup>* animals were used for the DUCT quantifications in adulthood. For liver histology, two *Jag1<sup>+/+</sup>* and three *Jag1<sup>Ndr/Ndr</sup>* mice were used. For ink injections, nine *Jag1<sup>+/+</sup>* mice were used (four males and five females) and for iDISCO+ four *Jag1<sup>+/+</sup>* and four *Jag1<sup>Ndr/Ndr</sup>* mice were used (six males and two females). For lung 3D resin casting five *Jag1<sup>+/+</sup>* mice were used (two males and three females). Samples were not blinded for investigation since the phenotype is overt and the genotype is therefore obvious to the experimenter. The animals were maintained on a mixed C57bl6J/C3HeN background. *Jag1<sup>Ndr/+</sup>* (Nodder) mice were bred and genotyped as previously described (**Andersson et al., 2018**).

## Patient samples

Collection of liver samples and clinical data from patients or donors was approved by the Swedish Ethical Review Authority (2017/269-31, 2017/1394-31). Samples from patients with severe Alagille syndrome (four) were obtained at time of liver transplant from extirpated liver. Samples were obtained with a consent to be used for research according to ethical permit 2017/269-31. Samples were dissociated for primary cell culture e.g. organoids (data not shown), and a matching sample was formalin fixed or fresh-frozen for comparative analyses. Liver tissue samples from patients with mild Alagille syndrome (six) were obtained for clinical follow-up purposes and were retrospectively analyzed. The liver material was obtained within the framework of clinical patient care can be analyzed retrospectively without the need for consent according to ethical permit 2017/1394-31. Healthy controls (two) were left-over donor material, or from organ donation post-mortem. The liver function tests were obtained during routine biochemical analyses.

## MICROFIL injections

MICROFIL (Flow Tech Inc) was prepared as follows. Yellow MICROFIL (Y) cat. #MV-122 was diluted with clear MICROFIL (C) cat. # MV-Diluent in 3:1 (Y:C). Blue MICROFIL (B) cat. #MV-120 was diluted 1:1 (B:C) with clear MICROFIL. Diluted yellow MICROFIL was mixed with diluted blue MICROFIL 1:1 creating a green MICROFIL. Yellow MICROFIL was injected into common bile duct (CBD) or pulmonary artery (PA). Green MICROFIL was injected into portal vein (PV) or trachea (TA). 1 ml of diluted MICROFIL is mixed with 50  $\mu$ l of hardener (supplied by Flow Tech Inc) prior injection.

Postnatal day 15 (P15) mice were sacrificed by decapitation and perfused through the heart with 3 ml of Hanks' Balanced Salt solution (HBSS) (Life Technologies cat. # 14025092). Adult mice were sacrificed by CO<sub>2</sub> inhalation and perfused through the heart with HBSS for 3 min (perfusion rate 5 ml / 1 min). For liver resin injections, the mice were perfused through the left ventricle, for lung resin injections the mice were perfused through the right ventricle.

## Injection into CBD

A small transversal incision was made in inferior vena cava with spring scissor to release the liver vascular pressure. CBD was exposed by moving aside the liver and intestine and cleaned from surrounding tissue in area about 5 mm long. Silk suture (Agnthos AB cat. #14757) was loosely wrapped around the cleaned CBD. A longitudinal CBD incision was made at the spot where CBD enters the pancreas next to sphincter of Oddi by spring scissor. The tubing (PE10, BD Biosciences cat. # 427401) ~15 cm long was prepared by stretching one side of the tube until the diameter becomes thin enough to fit into CBD. Diagonal cut is made at the tip of the tubing while the other side contains needle (27G) connected to the syringe filled with MICROFIL. The tubing connected to a syringe and filled with a yellow MICROFIL was inserted into the CBD, the suture around the CBD can be tightened to secure the tubing in place. Yellow MICROFIL was injected into the CBD until resistance was met or MICROFIL spots were visible on the liver surface. Massaging the liver with cotton swab while injecting helped to disperse the MICROFIL. The tubing was removed and silk suture was tightened around the CBD to prevent leakage.

### Injection into PV

PV was cleaned from surrounded tissue. A small incision was made in PV using spring scissor. Silk suture was loosely wrapped around the cleaned PV above the incision. Tubing (PE10) ~15 cm long connected to (27G) needle was inserted into the PV incision and secured with silk suture. Green MICROFIL was injected into the PV until blood vessels on the surface were filled or resistance was met. Massaging the liver with a cotton swab while injecting helped to introduce the MICROFIL. The tubing was removed and silk suture was tightened around the PV to prevent leakage.

Liver was dissected out and placed at 4°C overnight (ON) for MICROFIL to solidify. The next day the liver was fixed with 3.7% formaldehyde solution (FA) (Sigma-Aldrich cat. #F1635) diluted in Dulbecco's phosphate-buffered saline (DPBS) (Life Technologies cat. # 14190144). After 24 hr, liver was washed and kept in DPBS. Liver was separated into lobes. The left lateral lobe was placed in 50% methanol (Sigma-Aldrich, cat. # 322415) for 4 hr and into 100% methanol ON. Further, the lobe was placed in benzyl alcohol (Sigma-Aldrich, cat. #402834) and benzyl benzoate (Sigma-Aldrich, cat. #B6630) (BA:BB 1:2) solution until transparent. The right medial lobe (only FA fixed) was used for  $\mu$ CT scanning. Liver lobe images of right medial lobe (P15) and left lateral lobe (P15 and adult) were taken using a stereomicroscope Stemi 305 (Carl Zeiss Microscopy) with a PowerShot S3 IS camera (Canon) or iPhone6 connected to a LabCam adapter.

### Injection into lung

The mouse heart was pulled toward the liver to expose the pulmonary artery (PA) and pinned down through the heart apex with a 1 ml empty syringe connected with a needle. A silk suture was wrapped loosely around the PA as close to the heart as possible. A small incision was made in the right ventricle with spring scissors. Tubing (PE50, BD bioscience, cat #427411) ~15 cm long (stretched at the tip) connected to (23G) needle was inserted into the PA through the incision in the right ventricle and tightened with the suture. A total of 1 ml of DPBS was injected into the lung via PA to remove all the remaining blood. Afterwards, to expand the collapsed lung, the trachea was exposed and cleaned from surrounding tissue. A silk suture was loosely wrapped around the trachea and a small incision was made into the trachea with spring scissors. Tubing (PE50) ~15 cm long connected to (23G) needle was inserted into the trachea and tightened with the suture. One ml of DPBS was injected into the lungs via trachea – this inflates the collapsed lungs. A 1 ml syringe filled with yellow MICROFIL was connected to the tubing inserted into the PA, and MICROFIL was injected into the PA vasculature until all the blood vessels were filled. Massaging the lung with a cotton swab while injecting helped to disperse the MICROFIL. After the vasculature was completely filled, the tubing was removed and the suture around the PA tightened to prevent MICROFIL leakage. For airways injection, a 1 ml syringe filled with green MICROFIL was connected to the tubing inserted into the trachea, and MICROFIL was injected into the trachea until the lung was entirely filled with MICROFIL. Massaging the lung with cotton swab while injecting again helped to disperse the MICROFIL. After the lung was completely filled, the tubing was removed and the suture around the trachea tightened to prevent MICROFIL leakage.

Lungs were dissected out and placed at 4°C ON to allow the MICROFIL to solidify. The next day the lung was fixed with 3.7% FA diluted in DPBS. After 24 hr, lungs were washed and kept in DPBS. Lungs were separated into lobes and the right superior lobe was used for  $\mu$ CT scanning.

### Ink injections

Mice were sacrificed by CO<sub>2</sub> inhalation and transcardially perfused with HBSS for 3 min (perfusion rate 5 ml/1 min).

Injection into CBD and PV. CBD and PV were accessed in the same way as described for MICROFIL injections. When injecting with ink, there is no need to tighten the CBD with silk suture as the ink is not leaking out. Black ink (Higgins cat. #44032) was injected into the CBD until BDs on the surface were filled or resistance was met. White ink (Higgins cat. #44032) was injected using PE50 tubing into the PV until blood vessels on the surface were filled or resistance was met. Liver was dissected out and separated into lobes. All lobes were cleared in BABB as described above. Liver ink images of right medial lobe were taken under stereomicroscope Stemi 305 (Carl Zeiss Microscopy) using PowerShot S3 IS camera (Canon).

## Whole mount immunohistochemistry

Mice were anesthetized by isoflurane inhalation (~2%) and transcidentally perfused with HBSS for 3 min (perfusion rate 5 ml/1 min) and 10% neutral buffered formalin (NBF) for 5 min. Liver was dissected out and further immersion fixed with 10% NBF ON at 4°C. The next day liver was washed and kept in DPBS and separated into lobes. Right medial lobe was stained and cleared following the iDISCO+ protocol and imaged by light sheet microscope by Gubra (Denmark).

Fixed and washed samples were dehydrated in methanol/H<sub>2</sub>O gradient: 20%, 40%, 60%, 80% and 2 × 100% methanol, each step 1 hr at room temperature (RT). The samples were bleached in cooled fresh 5% H<sub>2</sub>O<sub>2</sub> in methanol ON at 4°C. The samples were subsequently rehydrated in methanol/PBS series: 80%, 60%, 40%, 20%, with 0.2% Triton X-100, 1 hr each at RT. They were washed in PBS with 0.2% Triton X-100 (PTx.2) for 2 × 1 hr at RT.

## Whole organ immunolabeling (iDISCO+)

Samples were incubated in permeabilization solution at 37°C for 3 days. Blocking is carried out in blocking solution at 37°C for 2 days. The samples were incubated with primary antibody in PTwH/5% DMSO/3% donkey serum at 37°C for 7 days. They were washed in PTwH for 1 × 10 min, 1 × 20 min, 1 × 30 min, 1 × 1 hr, 1 × 2 hr and 1 × 2 days. Samples were incubated with secondary antibody in PTwH/3% donkey serum at 37°C for 7 days, followed by washes in PTwH: 1 × 10 min, 1 × 20 min, 1 × 30 min, 1 × 1 hr, 1 × 2 hr and 1 × 3 days. All steps were performed in tightly closed tubes to minimize evaporation and oxidation.

## Solutions for iDISCO

PTx.2 (1L): 100 ml PBS 10x, 2 ml TritonX-100

PTwH (1L): 100 PBS 10x, 2 ml Tween-20, 1 ml of 10 mg/ml heparin stock solution

Permeabilization solution (500 ml): 400 ml PTx.2, 11.5 g glycine, 100 ml DMSO

Blocking solution (50 ml): 42 ml PTx.2, 3 ml donkey serum, 5 ml DMSO

Secondary antibody: Alexa Fluor 488 (dilution 1:1000, Life technologies)

## Tissue clearing

Tissue was cleared in methanol/H<sub>2</sub>O series: 20%, 40%, 60%, 80%, and 100% for 1 hr each at RT. Samples were incubated for 3 hr (with shaking) in 66%DCM (Dichloromethane)/33% methanol at RT and in 100% DCM 15 min 2x (with shaking) to remove traces of methanol. They were incubated in DiBenzyl Ether (DBE) (without shaking).

## Light sheet microscopy

Tissue samples were imaged using a light sheet microscope (Ultramicroscopell, Miltenyi). DBE was used as clearing agent during data acquisition. Data was collected at room temperature using Lavi-sion ultramicroscope system and MV PLAPO 2X C/0.5 objective with dry lens, RI correction collar using Andor Zyla 4.2 Plus sCMOS camera. CK7 staining was detected with AF790 (Alexa Fluor, Life Technologies). The acquisition software used was ImSpector (LaVision biotech).

## Liver immunohistochemistry

5 μm FFPE-liver (mouse and human) sections were deparafinized and rehydrated through consecutive baths of xylene (cat. #28975.325, VWR) and isopropanol (cat. #K50655934838, Merck). Endogenous peroxidase was blocked by immersion of the slides in methanol (cat. #322415, Sigma-Aldrich) containing 0,3% H<sub>2</sub>O<sub>2</sub> (cat. #H1009, Sigma-Aldrich) for 15 min and rehydration was finalized by rinsing the slides in tap water. Heat-induced epitope retrieval was done using citrate buffer (PH 6.0) for 20 min in a pressure cooker. After blocking of the sections with 2% BSA (cat. #A7906, Sigma-Aldrich) for 20 min, slides were incubated for 1 hr at 37°C with primary antibody (antibodies used are listed in Key resources table). Anti-mouse (cat. #G21040, dilution: 1/1000, Invitrogen) or anti-goat (Impress, cat. #MP7405, Vector), respectively, HRP-coupled secondary antibody was applied for 30 min at 37°C and revealed with DAB for 30 s (cat. #K3468, Dako). After counterstaining with hematoxylin (cat. #HX86014349, diluted 1/5, Merck), the sections were dehydrated in consecutive baths of ethanol (cat. #20821.310, VWR), isopropanol (cat. #K50655934838, Merck), and xylene

(cat. #28975.325, VWR) to finally be mounted with hardening medium (Eukitt, cat. #03989, Sigma-Aldrich).

### Liver section image acquisition

Chromogenic stained images were taken with Axiomager (Carl Zeiss) microscope, Axiocam 503 color camera using Plan-Apochromat 5x/0.16, Plan-Apochromat 10x/0.45 M27, Plan-Apochromat 20x/0.8 M27 and Plan-Apochromat 40x/1.4 Oil DIC (UV) VIS-IR M27 objectives at room temperature. The acquisition software used was Zen Blue (Carl Zeiss).

### Image processing

Whole mount liver images cleared with iDISCO+ were initially processed in ImageJ for maximum z-projection and segmentation. The images were filtered using the unsharp mask and integral image filter function. Images were next processed in Amira. In Amira images were filtered using the Gaussian filter and background detection correlation. Images were manually segmented. The manual segmentation was further traced using the autoskeleton function. The skeletons were further analyzed in Amira for length, volume and branching.

Images of ink injected liver were proceeds for filament tracing. Bile duct and portal vein filament tracing was performed using Amira. The images were filtered using the unsharp mask and mean filter. The signal was manually segmented to remove artificial signal. The manual segmentation was further traced using the autoskeleton function. The skeletons were analyzed in Amira for length, volume and branching. For double ink injection (**Figure 1—figure supplement 1A**) the background was changed for esthetic purposes using the lasso tool in Adobe Photoshop.

DUCT 2D slices were exported from MyVGL (Volumegraphics) and processed in ImageJ for maximum contrast and brightness.

### Liver sections IHC were processed in ImageJ for contrast and brightness

P15 MICROFIL injected and BABB-cleared left lateral and right medial lobe were analyzed in ImageJ. The total liver area was measured followed by the measurement of the liver area covered by MICROFIL injected bile ducts. The percentage of liver containing bile ducts was calculated.

### Blood serum collection and analysis

Blood from P15 pups was collected from the trunk after decapitation into 1.5 ml tubes. The serum was allowed to clot at room temperature. The blood was centrifuged for 15 min at 17,000 g at room temperature. The serum was stored at  $-80^{\circ}\text{C}$  until analyzed. Serum was sent to the Swedish University of Agricultural Sciences for analysis of alanine aminotransferase (ALT), alkaline phosphatase (ALP), aspartate aminotransferase (AST), albumin (Alb), and total bilirubin.

### MicroCT measurement

The system GE Phoenix v|tome|x L 240 (GE Sensing and Inspection Technologies GmbH, Germany) equipped with nanofocus X-ray tube (180 kV/15 W) was used for the tomographic measurements that were carried out in the air-conditioned cabinet (fixed temperature  $21^{\circ}\text{C}$ ). The samples were adapted for this temperature before the measurement to prevent any thermal expansion effect. To prevent any sample motion during the scanning, the samples were placed in 15 ml Falcon tube, filled with 1% agarose gel. The tomographic reconstruction of acquired data was performed using GE phoenix datos|x 2.0 software. The voxel resolution was fixed for all the adult liver samples at  $12\ \mu\text{m}$ , except one (sample #2401,  $8\ \mu\text{m}$ ). For all the P15 liver samples the voxel resolution was fixed at  $6.5\ \mu\text{m}$  and for the lung lobe sample at  $8\ \mu\text{m}$ . Detailed overview of used acquisition parameters is stated in **Table 2**.

### MicroCT data segmentation

The identification and segmentation of both tubular systems (e.g. bile duct (BD) and portal vein (PV) for liver samples and pulmonary artery and airways for lung samples) in each CT cross-section was necessary for further analysis of each system. The segmentation was based on differential contrast between the resin and the soft tissue. Two different resins were used to identify the individual

tubular systems. The differential contrast for system identification was highly dependent on the freshness of the MICROFIL.

The resin segmentation was performed by global thresholding in VG Studio MAX 3.3 (Volume Graphics GmbH, Germany) software together with manual corrections where necessary. The threshold value was determined based on the histogram shape and visual evaluation of a selected cross-section (**Figure 8A,A'**). The resin cast, especially when using an old MICROFIL, could contain artefacts caused by poor contrast, insufficient filling or high injection pressure. These artefacts include air bubbles in resin, non-homogenous resin contrast (caused by mixing of blue and yellow MICROFIL) and resin leakage due to lumen rupture (probably caused by high pressure during injection), (**Figure 8B**). Therefore, the thresholding step was supplemented with manual corrections to create smooth, continuous and solid canal masks. Furthermore, the cut-off for the smallest distal canal included in the mask is considered an area of at least four voxels.

Next, the individual tubular systems were identified in the segmented resin mask (**Figure 1—figure supplement 12D and G**). When fresh MICROFIL was used, it was possible to identify each system by global thresholding with threshold value determined based on histogram shape and visual evaluation of CT data. However, in case of the old MICROFIL (used for adult liver samples) the resin absorption properties were not distinguishable in CT data. In most regions, both tubular systems blended with each other in one continuous region (**Figure 8C, D** left panel). Manual segmentation was therefore necessary to ensure the correct identification of both systems (**Figure 8C, D** right panel). The manual segmentation was performed by outlining the BD regions in every slice of the CT data. VG Studio automatically creates 3D render based on the regions outlined in CT sections.

### MicroCT data analysis

The adult liver was analyzed using a custom-written algorithm and freely available Matlab codes (Version R2017a, The MathWorks Inc, Natick, MA). The algorithm was designed to analyze morphological parameters of the BD and PV systems, and is compatible with the 3D binary masks. Two separate masks of BD and PV system were generated and the analysis was divided in two independent parts. First, the analysis of the entire portal vein and biliary system and second, analysis of the corresponding main branch (=the longest branch) of each system (**Figure 6—figure supplement 1A**). For detailed analysis and comparison of the whole system versus only the main branch, two algorithms, described by the diagrams in **Figure 8F, G**, were developed. They differ in the input data and the evaluated parameters. For both algorithms, the first step is to create a 3D skeleton of the input binary mask.

### Skeletonization of binary masks

The 3D skeleton was derived using the homotopic thinning algorithm described in *Lee et al., 1994* specifically optimized for Matlab implementation by Kollmannsberger (*Kerschnitzki et al., 2013*), (online source: <https://www.mathworks.com/matlabcentral/fileexchange/43400-skeleton3d>).

**Table 2.** Settings parameters of the GE Phoenix v|tome|x L 240 system.

Sample	Voxel size	Acceleration voltage	X-ray tube current	Exposition time	Number of projections
2401	8 $\mu\text{m}$	80 kV	160 $\mu\text{A}$	600 ms*	2500*
2404	12 $\mu\text{m}$	80 kV	160 $\mu\text{A}$	600 ms*	2500*
2405	12 $\mu\text{m}$	80 kV	160 $\mu\text{A}$	600 ms*	2500*
2431	12 $\mu\text{m}$	80 kV	160 $\mu\text{A}$	600 ms*	2500*
2713	12 $\mu\text{m}$	80 kV	160 $\mu\text{A}$	334 ms <sup>†</sup>	1900 <sup>†</sup>
2714	12 $\mu\text{m}$	80 kV	160 $\mu\text{A}$	334 ms <sup>†</sup>	1900 <sup>†</sup>
N864	6.5 $\mu\text{m}$	80 kV	160 $\mu\text{A}$	400 ms <sup>†</sup>	1800 <sup>†</sup>
N865	6.5 $\mu\text{m}$	80 kV	160 $\mu\text{A}$	400 ms <sup>†</sup>	1800 <sup>†</sup>
<i>Jag1</i> <sup>+/+</sup> lung	8 $\mu\text{m}$	80 kV	160 $\mu\text{A}$	400 ms <sup>†</sup>	2000 <sup>†</sup>

\*Flat panel DXR250 (2048 px  $\times$  2048 px, pixel size 200  $\mu\text{m}$ ).

<sup>†</sup>Flat panel dynamic 41|100 (4048 px  $\times$  4048 px, pixel size 100  $\mu\text{m}$  with binning 2).

Calculated 3D medial axis skeleton was subsequently converted to a network graph, using algorithm described in *Kerschnitzki et al., 2013* (online source: <https://www.mathworks.com/matlabcentral/fileexchange/43527-skel2graph-3d>). Resulting network graph is formed by nodes and links between them (**Figure 1—figure supplement 12D and G**).

### Liver region subdivision

Liver was separated into three regions: R1 (approximately hilum), R2 (approx. intermediate) and R3 (approx. periphery). The optimal region size was calculated as a summary of average PV branch lengths per generation and divided by three (detailed branching generation subdivision **Table 3** for PV and **Table 4** for BD). Subsequently the branching generations were assigned to a region by matching the summary of branch length per generation to optimal region size. The same region was applied for both PV and BD analysis with the exception of one *Jag1<sup>Ndr/Ndr</sup>* sample (#1 or 2714) where the bile duct optimal region size was greater than portal vein.

Regions were assigned in order that total average lengths of each generation within each region yielded an equal size of R1, R2, and R3. Each sub-column represents one animal.

The distribution of BD branches within each region were quantified based on regions defined by the PV system (**Table 4**). Each sub-column represents one animal.

### Branching analysis

Branching points analysis was programmed in Matlab to analyze the distance between BD and PV branching point. This parameter was calculated using 3D Euclidean distances between the BD branching points and the nearest branching point from PV system. The data is represented as cumulative sum of percentage of BD branching point at a given distances between BD and PV branching points (from 0.015 mm to 3 mm).

For branch length analysis the structure of BD and PV trees were first reconstructed in 3D, using the Analyze Skeleton toolbox in ImageJ, which provided the three-dimensional coordinates of all branch points for both BD and PV, as well as the connectivity of the graph. Next, we computed for each branch the length along its path to the Euclidean distance between its extremities (branch points). To calculate the generation number of branches (both for the PV and BD structures), we manually defined the origin of the ducts and vessels as generation 1, and computed generation number as the number of generation branches separating a given branch from the origin. To distinguish side branching events, we calculated the angle between a branch and its 'parent' by computing the dot product  $p$  of both their unit vectors. A branch with  $p > 0.95$  with its parent branch was considered to belong to the same generation. We then computed distributions of length for the BD and PV structures as a function of generation number. Each generation was assigned to a region R1, R2, or R3.

The branch distribution in each region was calculated as a summary of number of branches per generation in a given region. The sum of branch numbers of each region is displayed as a proportion of the total number of branches per sample.

The number of bi-furcations (i.e. one input and two outputs), tri-furcations (i.e. one input and three outputs) and quadri- and more-furcations (one input and more than three outputs), were assessed in Matlab based on binary mask skeleton nodes that were divided into endpoints and branching points. Branching points closer than 0.2 mm (this threshold value was derived based on visual assessment and knowledge of the system) were merged together and further represented by one node.

**Table 3.** PV branching generation distribution into liver regions.

PV generation #	<i>Jag1<sup>+/+</sup></i> (3 animals)			<i>Jag1<sup>Ndr/Ndr</sup></i> (3 animals)		
R1	1–4	1–3	1–4	1–4	1–3	1–3
R2	5–10	4–9	5–10	5–8	4–7	4–7
R3	11–18	10–14	11–17	9–15	8–12	8–11

**Table 4.** BD branching generation distribution into liver regions.

BD generation #	<i>Jag1<sup>+/+</sup></i> (3 animals)			<i>Jag1<sup>Ndr/Ndr</sup></i> (3 animals)		
R1	1–4	1–4	1–2	1–4	1–6	1–6
R2	5–7	5–7	3–5	5–9	7–10	7–10
R3	8–12	8–11	6–7	10–16	11	11–12

### Gap analysis between bile duct and portal vein

To evaluate the gap between BD and PV the surface distances were calculated in Matlab for each BD skeleton point by detecting the nearest PV skeleton point and connecting the two points with a line and measuring the non-resin area on this line (zero area in the input binary masks). Surface distance was then calculated using 3D Euclidean distance between the detected non-resin voxel coordinates. The data is represented as cumulative sum of percentage of BD at a given distance from PV (from 0.015 mm to 1.5 mm). The maximum distance between BD and PV for each liver sample was depicted in a separate graph.

### Tortuosity measurements

To quantify length and tortuosity, total (curved) and theoretical (chord) lengths were measured in Matlab for the whole system length and for the corresponding main branch. The curved length was defined as a cumulative sum of 3D Euclidean distances between neighboring graph points (i.e. links forming points) multiplied by voxel size. The chord length was defined as cumulative sum of 3D Euclidean distances between neighboring nodes multiplied by voxel size. The chord length therefore reflects system length where any nodes are connected by links with the shortest possible length. To analyze the relationship between BD and PV a length of the BD was divided by a PV length (curved or chord). Tortuosity was calculated as curved length divided by chord length of the same system and distributed into regions based on the generation number as previously described. Tortuosity was assessed in %, as BD and PV are not straight lines the actual tortuosity measurements were subtracted by 100% (perfectly straight line).

### Volume analysis

Total system volume was calculated in Matlab by multiplying a number of voxels representing PV or BD by volume of one voxel. The relationship between BD and PV volumes was addressed by dividing the BD volume by PV volume.

### Diameter measurements

The main branch diameter was calculated in Matlab every 1.5 mm along the total length of the main branch. The radius was defined as the minimal distance from the skeleton to the segmented area boundary in the input binary mask (i.e. border between background and area of interest). This boundary was calculated using a two-step procedure. In the first step, the input map was eroded using a 3D spherical shaped structural element with one pixel radius. Subsequently, the eroded area was subtracted from the original binary mask. This resulted in a binary mask representing the boundary between the background and the area of interest. One radius value at a given skeleton point was then expressed as the minimum distance from that point to the mask boundary. This was calculated, using the minimal value search in the intersection of the boundary mask and the distance map from that point. The distance map from a given skeleton point was calculated as 3D Euclidean distance of the spatial coordinates. Subsequently the diameter value was calculated as the minimum distance to the boundary area multiplied by 2. To avoid any misrepresentation, the one final diameter value at a given point (every 1.5 mm of branch length) was calculated as a mean value of a diameter at that point and diameters at four neighboring points (two on each side). PV and BD diameters were divided into three areas: hilum, intermediate and periphery. Hilar region represents distance from 0 to 1.5 (sample #2401) or 0–3 mm (other samples), Intermediate region is from 3 to 6 mm (sample #2401) or 4.5 mm – 9 mm (other samples), Periphery is from 7.5 mm – 9 mm (sample #2401) or 10.5–13.5 mm (other samples). BD to PV diameter ratio was calculated by dividing BD diameter at a given region by PV diameter of the same region.

## Statistical analysis

*Jag1<sup>+/+</sup>* and *Jag1<sup>Ndr/Ndr</sup>* data were tested for significant differences using multiple tests based on the type of experiment and data distribution. Student's *t*-test (Figures 1D, G and 3D, Figure 1—figure supplement 12H, Figure 6—figure supplement 1B–E, H–K). Kolmogorov-Smirnov test (on raw data, graph depicts cumulative sum) (Figures 3C and 4C). Mann-Whitney test (Figure 4—figure supplement 1). Wilcoxon test (Figure 1—figure supplement 5D). Two-way ANOVA (Figures 1H and 5B–D, 6E, Figure 1—figure supplements 5C and 12I, Figure 6—figure supplement 1F and G) followed by Sidak's multiple comparisons test. Spearman correlation (Figure 1E). A *p* value below 0.05 was considered statistically significant. The statistical analysis was done in Prism 9 (GraphPad).

## Acknowledgements

Grant support: ERA: Work in ERA lab is supported by the Swedish Research Council, the Center of Innovative Medicine (CIMED) Grant, Karolinska Institutet, and the Heart and Lung Foundation, and the Daniel Alagille Award from the European Association for the Study of the Liver. One project in ERA lab is funded by ModeRNA, unrelated to this project. The funders have no role in the design or interpretation of the work. SH has been supported by a KI-MU PhD student program, and by a Wera Ekström Foundation Scholarship. We are grateful for support from Tornspiran foundation to NVH. JK: This research was carried out under the project CEITEC 2020 (LQ1601) with financial support from the Ministry of Education, Youth and Sports of the Czech Republic under the National Sustainability Programme II and CzechNanoLab Research Infrastructure supported by MEYS CR (LM2018110). UL: The financial support from the Swedish Research Council and ICMC (Integrated CardioMetabolic Center) is acknowledged. JJ: The work was supported by the Grant Agency of Masaryk University (project no. MUNI/A/1565/2018). We thank Kari Huppert and Stacey Huppert for their expertise and help regarding bile duct cannulation and their laboratory hospitality. We also thank Nadja Schultz and Charlotte L Mattsson for their help with common bile duct cannulation. We thank Daniel Holl for his help with trachea cannulation. We thank Nikos Papadogiannakis for his assistance with mild Alagille biopsy samples and discussion. We thank Karolinska Biomedicum Imaging Core, especially Shigeaki Kanatani for his help with image analysis. We thank Jan Masek and Carolina Gutierrez for their scientific input in manuscript writing. We thank Peter Ranefall and the BioImage Informatics (SciLife national facility) for their help writing parts of the MATLAB pipeline. The TROMA-III antibody developed by Rolf Kemler was obtained from the Developmental Studies Hybridoma (DSHB) Bank developed under the auspices of NICHD and maintained by The University of Iowa, Department of Biological Sciences, Iowa City, IA52242. We thank Goncalo M Brito for all illustrations. This work was supported by the European Union (European Research Council Starting grant 851288 to E.H.).

## Additional information

### Funding

Funder	Grant reference number	Author
Karolinska Institutet	2-560/2015-280	Emma Rachel Andersson
Stockholms Läns Landsting	CIMED (2-538/2014-29)	Emma Rachel Andersson
Ragnar Söderbergs stiftelse	Swedish Foundations' Starting Grant	Emma Rachel Andersson
European Association for the Study of the Liver	Daniel Alagille Award	Emma Rachel Andersson
Swedish Heart-Lung Foundation	20170723	Emma Rachel Andersson
Vetenskapsrådet	2019-01350	Emma Rachel Andersson
Ministerstvo Školství, Mládeže a Tělovýchovy	LQ1601	Jozef Kaiser
Ministerstvo Školství, Mládeže	LM2018110	Jozef Kaiser

a Tělovýchovy

---

European Research Council	Starting grant 851288	Edouard Hannezo
---------------------------	-----------------------	-----------------

---

The funders had no role in study design, data collection and interpretation, or the decision to submit the work for publication.

---

### Author contributions

Simona Hankeova, Conceptualization, Data curation, Formal analysis, Validation, Investigation, Visualization, Methodology, Writing - original draft; Jakub Salplachta, Conceptualization, Software, Formal analysis, Investigation, Visualization, Methodology, Writing - original draft; Tomas Zikmund, Conceptualization, Software, Formal analysis, Supervision, Investigation, Visualization, Methodology, Writing - review and editing; Michaela Kavkova, Formal analysis, Investigation, Visualization, Methodology, Writing - review and editing; Noémi Van Hul, Formal analysis, Validation, Investigation, Visualization, Writing - original draft; Adam Brinek, Jakub Laznovsky, Software, Visualization, Writing - review and editing; Veronika Smekalova, Visualization, Writing - review and editing; Feven Dawit, Investigation; Josef Jaros, Validation, Writing - review and editing; Vítězslav Bryja, Urban Lendahl, Funding acquisition, Writing - review and editing; Ewa Ellis, Resources, Writing - review and editing; Antal Nemeth, Björn Fischler, Data curation; Edouard Hannezo, Conceptualization, Investigation, Writing - review and editing; Jozef Kaiser, Conceptualization, Resources, Funding acquisition, Project administration, Writing - review and editing; Emma Rachel Andersson, Conceptualization, Resources, Data curation, Formal analysis, Supervision, Funding acquisition, Methodology, Writing - original draft, Project administration

### Author ORCIDs

Simona Hankeova  <https://orcid.org/0000-0002-7797-3818>  
Jakub Salplachta  <https://orcid.org/0000-0002-0149-7843>  
Noémi Van Hul  <https://orcid.org/0000-0003-1410-8808>  
Vítězslav Bryja  <http://orcid.org/0000-0002-9136-5085>  
Ewa Ellis  <http://orcid.org/0000-0002-3057-5337>  
Edouard Hannezo  <http://orcid.org/0000-0001-6005-1561>  
Emma Rachel Andersson  <https://orcid.org/0000-0002-8608-625X>

### Ethics

Human subjects: Collection of liver samples from patients or donors was approved by the Swedish Ethical Review Authority (2017/269-31, 2017/1394-31). Samples were obtained with a consent to be used for research according to ethical permit 2017/269-31.

Animal experimentation: All animal experiments were performed in accordance with Stockholm's Norra Djurförsöksetiska nämnd (Stockholm animal research ethics board, ethics approval numbers: N150/14, N61/16, N5253/19, N2987/20) regulations.

### Decision letter and Author response

Decision letter <https://doi.org/10.7554/eLife.60916.sa1>

Author response <https://doi.org/10.7554/eLife.60916.sa2>

---

## Additional files

### Supplementary files

- Transparent reporting form

### Data availability

Our MATLAB pipeline is deposited in Github: <https://github.com/JakubSalplachta/DUCT>. Copy archived at <https://archive.softwareheritage.org/swh:1:rev:6b0b0eb88bbaf9bfc4f8ee42cafa4c122866fbba/>. All data generated or analysed during this study are included in the manuscript and supporting files. Source data files have been provided for Figures 3 and 4.

## References

- Alagille D**, Odièvre M, Gautier M, Dommergues JP. 1975. Hepatic ductular hypoplasia associated with characteristic facies, vertebral malformations, retarded physical, mental, and sexual development, and cardiac murmur. *The Journal of Pediatrics* **86**:63–71. DOI: [https://doi.org/10.1016/S0022-3476\(75\)80706-2](https://doi.org/10.1016/S0022-3476(75)80706-2), PMID: 803282
- Alessandro G**, Incerti M, Andreani M. 2007. Alagille syndrome: prenatal sonographic findings. *Journal of Clinical Ultrasound : JCU* **35**:156–158. DOI: <https://doi.org/10.1002/jcu.20292>, PMID: 17295271
- Andersson ER**, Chivukula IV, Hankeova S, Sjöqvist M, Tsoi YL, Ramsköld D, Masek J, Elmansuri A, Hoogendoorn A, Vazquez E, Storvall H, Netušilová J, Huch M, Fischler B, Ellis E, Contreras A, Nemeth A, Chien KC, Clevers H, Sandberg R, et al. 2018. Mouse model of alagille syndrome and mechanisms of Jagged1 missense mutations. *Gastroenterology* **154**:1080–1095. DOI: <https://doi.org/10.1053/j.gastro.2017.11.002>, PMID: 29162437
- Chung K**, Wallace J, Kim SY, Kalyanasundaram S, Andalman AS, Davidson TJ, Mirzabekov JJ, Zalocusky KA, Mattis J, Denisin AK, Pak S, Bernstein H, Ramakrishnan C, Grosenick L, Gradinaru V, Deisseroth K. 2013. Structural and molecular interrogation of intact biological systems. *Nature* **497**:332–337. DOI: <https://doi.org/10.1038/nature12107>, PMID: 23575631
- Dahms BB**, Petrelli M, Wyllie R, Henoch MS, Halpin TC, Morrison S, Park MC, Tavill AS. 1982. Arteriohepatic dysplasia in infancy and childhood: a longitudinal study of six patients. *Hepatology* **2**:350–358. DOI: <https://doi.org/10.1002/hep.1840020311>, PMID: 7076119
- De Angelis C**, Mangone M, Bianchi M, Saracco G, Repici A, Rizzetto M, Pellicano R. 2009. An update on AIDS-related cholangiopathy. *Minerva Gastroenterologica E Dietologica* **55**:79–82. PMID: 19212310
- Fabris L**, Cadamuro M, Guido M, Spirli C, Fiorotto R, Colledan M, Torre G, Alberti D, Sonzogni A, Okolicsanyi L, Strazzabosco M. 2007. Analysis of liver repair mechanisms in alagille syndrome and biliary atresia reveals a role for notch signaling. *The American Journal of Pathology* **171**:641–653. DOI: <https://doi.org/10.2353/ajpath.2007.070073>, PMID: 17600123
- Fujisawa T**, Kage M, Ushijima K, Kimura A, Ono E, Kato H. 1994. Alagille syndrome with a spontaneous appearance of the interlobular bile ducts. *Pediatrics International* **36**:506–509. DOI: <https://doi.org/10.1111/j.1442-200X.1994.tb03235.x>, PMID: 7825452
- Gilbert MA**, Bauer RC, Rajagopalan R, Grochowski CM, Chao G, McEldrew D, Nassur JA, Rand EB, Krock BL, Kamath BM, Krantz ID, Piccoli DA, Loomes KM, Spinner NB. 2019. Alagille syndrome mutation update: comprehensive overview of JAG1 and NOTCH2 mutation frequencies and insight into missense variant classification. *Human Mutation* **40**:2197–2220. DOI: <https://doi.org/10.1002/humu.23879>, PMID: 31343788
- Hadchouel M**, Hugon RN, Gautier M. 1978. Reduced ratio of portal tracts to paucity of intrahepatic bile ducts. *Archives of Pathology & Laboratory Medicine* **102**:402. PMID: 580878
- Hankeova S**. 2021. DUCT. *Software Heritage*. swh:1:rev:6b0b0eb88bbaf9bfc4f8ee42cafa4c122866fbba. <https://archive.softwareheritage.org/swh:1:dir:afbad9c713d7371c41db68b434647c147709600c;origin=https://github.com/JakubSalplachta/DUCT;visit=swh:1:snp:078f3064f3631c5a2055016f6184b774fccacba4;anchor=swh:1:rev:6b0b0eb88bbaf9bfc4f8ee42cafa4c122866fbba/>
- Hannezo E**, Scheele C, Moad M, Drogo N, Heer R, Sampogna RV, van Rheenen J, Simons BD. 2017. A unifying theory of branching morphogenesis. *Cell* **171**:242–255. DOI: <https://doi.org/10.1016/j.cell.2017.08.026>, PMID: 28938116
- Hofmann JJ**, Zovein AC, Koh H, Radtke F, Weinmaster G, Iruela-Arispe ML. 2010. Jagged1 in the portal vein mesenchyme regulates intrahepatic bile duct development: insights into alagille syndrome. *Development* **137**:4061–4072. DOI: <https://doi.org/10.1242/dev.052118>, PMID: 21062863
- Kaneko K**, Kamimoto K, Miyajima A, Itoh T. 2015. Adaptive remodeling of the biliary architecture underlies liver homeostasis. *Hepatology* **61**:2056–2066. DOI: <https://doi.org/10.1002/hep.27685>, PMID: 25572923
- Kerschnitzki M**, Kollmannsberger P, Burghammer M, Duda GN, Weinkamer R, Wagermaier W, Fratzl P. 2013. Architecture of the osteocyte network correlates with bone material quality. *Journal of Bone and Mineral Research* **28**:1837–1845. DOI: <https://doi.org/10.1002/jbmr.1927>, PMID: 23494896
- Kline TL**, Zamir M, Ritman EL. 2011. Relating function to branching geometry: a micro-CT study of the hepatic artery, portal vein, and biliary tree. *Cells Tissues Organs* **194**:431–442. DOI: <https://doi.org/10.1159/000323482>, PMID: 21494011
- Klohs J**, Rudin M, Shimshek DR, Beckmann N. 2014. Imaging of cerebrovascular pathology in animal models of Alzheimer's disease. *Frontiers in Aging Neuroscience* **6**:1–30. DOI: <https://doi.org/10.3389/fnagi.2014.00032>, PMID: 24659966
- Lee TC**, Kashyap RL, Chu CN. 1994. Building skeleton models via 3-D medial surface Axis thinning algorithms. *CVGIP: Graphical Models and Image Processing* **56**:462–478. DOI: <https://doi.org/10.1006/cgip.1994.1042>
- Li L**, Krantz ID, Deng Y, Genin A, Banta AB, Collins CC, Qi M, Trask BJ, Kuo WL, Cochran J, Costa T, Pierpont ME, Rand EB, Piccoli DA, Hood L, Spinner NB. 1997. Alagille syndrome is caused by mutations in human Jagged1, which encodes a ligand for Notch1. *Nature Genetics* **16**:243–251. DOI: <https://doi.org/10.1038/ng0797-243>, PMID: 9207788
- Mašek J**, Andersson ER. 2017. The developmental biology of genetic Notch disorders. *Development* **144**:1743–1763. DOI: <https://doi.org/10.1242/dev.148007>, PMID: 28512196
- Masyuk TV**, Ritman EL, LaRusso NF. 2001. Quantitative assessment of the rat intrahepatic biliary system by three-dimensional reconstruction. *The American Journal of Pathology* **158**:2079–2088. DOI: [https://doi.org/10.1016/S0002-9440\(10\)64679-2](https://doi.org/10.1016/S0002-9440(10)64679-2), PMID: 11395385

- Masyuk TV**, Ritman EL, LaRusso NF. 2003. Hepatic artery and portal vein remodeling in rat liver: vascular response to selective cholangiocyte proliferation. *The American Journal of Pathology* **162**:1175–1182. DOI: [https://doi.org/10.1016/S0002-9440\(10\)63913-2](https://doi.org/10.1016/S0002-9440(10)63913-2), PMID: 12651609
- McDaniell R**, Warthen DM, Sanchez-Lara PA, Pai A, Krantz ID, Piccoli DA, Spinner NB. 2006. NOTCH2 mutations cause alagille syndrome, a heterogeneous disorder of the notch signaling pathway. *The American Journal of Human Genetics* **79**:169–173. DOI: <https://doi.org/10.1086/505332>, PMID: 16773578
- Mouzaki M**, Bass LM, Sokol RJ, Piccoli DA, Quammie C, Loomes KM, Heubi JE, Hertel PM, Scheenstra R, Furuya K, Kutsch E, Spinner NB, Robbins KN, Venkat V, Rosenthal P, Beyene J, Baker A, Kamath BM. 2016. Early life predictive markers of liver disease outcome in an international, multicentre cohort of children with alagille syndrome. *Liver International* **36**:755–760. DOI: <https://doi.org/10.1111/liv.12920>, PMID: 26201540
- Ober EA**, Lemaigre FP. 2018. Development of the liver: insights into organ and tissue morphogenesis. *Journal of Hepatology* **68**:1049–1062. DOI: <https://doi.org/10.1016/j.jhep.2018.01.005>, PMID: 29339113
- Oda T**, Elkahloun AG, Pike BL, Okajima K, Krantz ID, Genin A, Piccoli DA, Meltzer PS, Spinner NB, Collins FS, Chandrasekharappa SC. 1997. Mutations in the human Jagged1 gene are responsible for alagille syndrome. *Nature Genetics* **16**:235–242. DOI: <https://doi.org/10.1038/ng0797-235>, PMID: 9207787
- Renier N**, Adams EL, Kirst C, Wu Z, Azevedo R, Kohl J, Autry AE, Kadiri L, Umadevi Venkataraju K, Zhou Y, Wang VX, Tang CY, Olsen O, Dulac C, Osten P, Tessier-Lavigne M. 2016. Mapping of brain activity by automated volume analysis of immediate early genes. *Cell* **165**:1789–1802. DOI: <https://doi.org/10.1016/j.cell.2016.05.007>, PMID: 27238021
- Riely CA**, Cotlier E, Jensen PS, Klatskin G. 1979. Arteriohepatic dysplasia: a benign syndrome of intrahepatic cholestasis with multiple organ involvement. *Annals of Internal Medicine* **91**:520–527. DOI: <https://doi.org/10.7326/0003-4819-91-4-520>, PMID: 484950
- Schaub JR**, Huppert KA, Kurial SNT, Hsu BY, Cast AE, Donnelly B, Karns RA, Chen F, Rezvani M, Luu HY, Mattis AN, Rougemont AL, Rosenthal P, Huppert SS, Willenbring H. 2018. De novo formation of the biliary system by TGFβ-mediated hepatocyte transdifferentiation. *Nature* **557**:247–251. DOI: <https://doi.org/10.1038/s41586-018-0075-5>, PMID: 29720662
- Short KM**, Smyth IM. 2016. The contribution of branching morphogenesis to kidney development and disease. *Nature Reviews Nephrology* **12**:754–767. DOI: <https://doi.org/10.1038/nrneph.2016.157>, PMID: 27818506
- Slott PA**, Liu MH, Tavoloni N. 1990. Origin, pattern, and mechanism of bile duct proliferation following biliary obstruction in the rat. *Gastroenterology* **99**:466–477. DOI: [https://doi.org/10.1016/0016-5085\(90\)91030-A](https://doi.org/10.1016/0016-5085(90)91030-A), PMID: 1694804
- Spinner NB**, Leonard LD, Krantz ID. 1993. *Alagille Syndrome*: GeneReviews(R).
- Susaki EA**, Tainaka K, Perrin D, Kishino F, Tawara T, Watanabe TM, Yokoyama C, Onoe H, Eguchi M, Yamaguchi S, Abe T, Kiyonari H, Shimizu Y, Miyawaki A, Yokota H, Ueda HR. 2014. Whole-brain imaging with single-cell resolution using chemical cocktails and computational analysis. *Cell* **157**:726–739. DOI: <https://doi.org/10.1016/j.cell.2014.03.042>, PMID: 24746791
- Tanimizu N**, Kaneko K, Itoh T, Ichinohe N, Ishii M, Mizuguchi T, Hirata K, Miyajima A, Mitaka T. 2016. Intrahepatic bile ducts are developed through formation of homogeneous continuous luminal network and its dynamic rearrangement in mice. *Hepatology* **64**:175–188. DOI: <https://doi.org/10.1002/hep.28521>, PMID: 26926046
- Vartak N**, Damle-Vartak A, Richter B, Dirsch O, Dahmen U, Hammad S, Hengstler JG. 2016. Cholestasis-induced adaptive remodeling of interlobular bile ducts. *Hepatology* **63**:951–964. DOI: <https://doi.org/10.1002/hep.28373>, PMID: 26610202
- Wagner R**, Van Loo D, Hossler F, Czymbek K, Pauwels E, Van Hoorebeke L. 2011. High-resolution imaging of kidney vascular corrosion casts with Nano-CT. *Microscopy and Microanalysis* **17**:215–219. DOI: <https://doi.org/10.1017/S1431927610094201>, PMID: 21122193
- Walter TJ**, Sparks EE, Huppert SS. 2012. 3-Dimensional resin casting and imaging of mouse portal vein or intrahepatic bile duct system. *Journal of Visualized Experiments* **1**:e4272. DOI: <https://doi.org/10.3791/4272>
- Wei W**, Popov V, Walocha JA, Wen J, Bello-Reuss E. 2006. Evidence of angiogenesis and microvascular regression in autosomal-dominant polycystic kidney disease kidneys: a corrosion cast study. *Kidney International* **70**:1261–1268. DOI: <https://doi.org/10.1038/sj.ki.5001725>, PMID: 16883324

PAPER [XVI]

# Age-related changes in the tooth–bone interface area of acrodont dentition in the chameleon

Hana Dosedělová,<sup>1,2</sup> Kateřina Štěpánková,<sup>3</sup> Tomáš Zikmund,<sup>4</sup> Herve Lesot,<sup>5,6</sup> Jozef Kaiser,<sup>4</sup> Karel Novotný,<sup>3,4</sup> Jan Štembírek,<sup>2,7</sup> Zdeněk Knotek,<sup>8</sup> Oldřich Zahradníček<sup>9</sup> and Marcela Buchtová<sup>2,10</sup>

<sup>1</sup>Department of Anatomy, Histology and Embryology, University of Veterinary and Pharmaceutical Sciences Brno, Brno, Czech Republic

<sup>2</sup>Institute of Animal Physiology and Genetics, v.v.i., Academy of Sciences of the Czech Republic, Brno, Czech Republic

<sup>3</sup>Department of Chemistry, Faculty of Science, Masaryk University, Brno, Czech Republic

<sup>4</sup>CEITEC – Central European Institute of Technology, Brno, University of Technology, Brno, Czech Republic

<sup>5</sup>INSERM (French National Institute of Health and Medical Research), ‘Osteoarticular and Dental Regenerative NanoMedicine’ Laboratory, Faculté de Médecine, Université de Strasbourg, UMR 1109, Strasbourg, France

<sup>6</sup>Faculté de Chirurgie Dentaire, Université de Strasbourg, Strasbourg, France

<sup>7</sup>Department of Oral and Maxillofacial Surgery, University Hospital Ostrava, Ostrava, Czech Republic

<sup>8</sup>Clinic of Small Animals, University of Veterinary and Pharmaceutical Sciences Brno, Brno, Czech Republic

<sup>9</sup>Department of Teratology, Institute of Experimental Medicine, Academy of Sciences of the Czech Republic, Prague, Czech Republic

<sup>10</sup>Department of Experimental Biology, Masaryk University, Brno, Czech Republic

---

## Abstract

Chameleon teeth develop as individual structures at a distance from the developing jaw bone during the pre-hatching period and also partially during the post-hatching period. However, in the adult, all teeth are fused together and tightly attached to the jaw bone by mineralized attachment tissue to form one functional unit. Tooth to bone as well as tooth to tooth attachments are so firm that if injury to the oral cavity occurs, several neighbouring teeth and pieces of jaw can be broken off. We analysed age-related changes in chameleon acrodont dentition, where ankylosis represents a physiological condition, whereas in mammals, ankylosis only occurs in a pathological context. The changes in hard-tissue morphology and mineral composition leading to this fusion were analysed. For this purpose, the lower jaws of chameleons were investigated using X-ray micro-computed tomography, laser-induced breakdown spectroscopy and microprobe analysis. For a long time, the dental pulp cavity remained connected with neighbouring teeth and also to the underlying bone marrow cavity. Then, a progressive filling of the dental pulp cavity by a mineralized matrix occurred, and a complex network of non-mineralized channels remained. The size of these unmineralized channels progressively decreased until they completely disappeared, and the dental pulp cavity was filled by a mineralized matrix over time. Moreover, the distribution of calcium, phosphorus and magnesium showed distinct patterns in the different regions of the tooth–bone interface, with a significant progression of mineralization in dentin as well as in the supporting bone. In conclusion, tooth–bone fusion in chameleons results from an enhanced production of mineralized tissue during post-hatching development. Uncovering the developmental processes underlying these outcomes and performing comparative studies is necessary to better understand physiological ankylosis; for that purpose, the chameleon can serve as a useful model species.

**Key words:** acrodont dentition; laser-induced breakdown spectroscopy; micro-computed tomography; reptiles.

---

## Correspondence

Dr Marcela Buchtova, Institute of Animal Physiology and Genetics, v.v.i., Academy of Sciences of the Czech Republic, Veverí 97, 602 00, Brno, Czech Republic.

T: + 420 532 290157; E: buchtova@iach.cz

Accepted for publication 6 April 2016

Article published online 12 May 2016

## Introduction

Reptiles show variability in tooth morphology (Edmund, 1969) as well as in the microscopic anatomy of tooth attachment (Osborn, 1984; Gaengler, 1991; Gaengler & Metzler, 1992; Zaher & Rieppel, 1999). Ancestral reptiles generally had teeth inserted in shallow sockets (protothecodont attachment) (Edmund, 1969). Some lizards (e.g. agamas,

chameleons) have teeth ankylosed to the crest of the tooth-bearing bone (acrodont teeth) (Edmund, 1969; Zaher & Rieppel, 1999). However, most lizards and snakes have teeth ankylosed to the inner side of the high labial wall (pleurodont attachment) (Gaengler, 1991; Gaengler & Metzler, 1992). In contrast, the teeth of mammals, including humans, have relatively long cylindrical roots connected by periodontal tissues with a deep bony socket (thecodont attachment). Thecodont attachment is also found in the extant archosaurian lineage of reptiles. The morphology of caiman periodontal attachments represents an intermediate condition between the ankylosis-type of attachment of Lepidosaurian reptiles and the mammalian periodontium (McIntosh et al. 2002).

In the chameleon, there is only one generation of teeth, and all teeth attach firmly to the underlying bone by mineralized attachment tissue (Fig. 1A,B) (Buchtova et al. 2013). Moreover, the adult teeth are attached to each other to form saw-like dentition along the jaw (Fig. 1B,C). Whereas ankylosis represents a pathological condition in humans and leads to serious damage, such as root and surrounding bone tissue resorption (Andersson & Malmgren, 1999), acrodontal ankylosis in the chameleon is a normal and physiological state. Moreover, in juvenile chameleons, the gingiva recedes from the area of the tooth–bone interface and naked bone is revealed (Buchtova et al. 2013) without any obvious health troubles, unlike in humans.

Interestingly, tooth to bone attachment is so firm in chameleons that if injury to the oral cavity occurs, teeth are not lost, as would happen in mammals. Rather, a piece of the jaw with several neighbouring teeth is broken off (Fig. 1C).

Such large injuries to the jaw can happen during incautious feeding with hard metal tools or sexual competition, as male chameleons are known to bite each other during conflict (Stuart-Fox & Whiting, 2005). Moreover, non-receptive females can be bite-aggressive toward the male (Burrage, 1973; Stuart-Fox & Whiting, 2005).

Based on previous findings, we aimed to analyse age-related changes in hard-tissue morphology with a focus on the tooth–bone fusion area during post-hatching stages in the chameleon. First, micro-computed tomography (microCT) imaging was used to evaluate how the fusion between tooth and jaw, as well as between neighbouring teeth, occurs during development. Next, the possible differences in mineral content accompanying these developmental processes were analysed. Calcium and phosphorus are the main matrix elements of hard tissues. In human teeth, enamel contains approximately 96% calcium apatite, as either hydroxyapatite  $[\text{Ca}_{10}(\text{PO}_4)_6(\text{OH})_2]$  or fluorapatite  $[\text{Ca}_{10}(\text{PO}_4)_6\text{F}_2]$  (Young, 1974; Lucas, 1979; Ten Cate, 1994). Magnesium is mostly present during bone and tooth formation, where it regulates calcification (Althoff et al. 1982; Bigi et al. 1992). For these reasons, the changes in composition of these three elements (calcium, phosphorus and magnesium) were analysed in tooth, jaw bone and the fusion areas between tooth and bone using laser-induced breakdown spectroscopy (LIBS) and quantitatively with microprobe analysis at post-hatching stages in the chameleon. In reptiles, LIBS has been previously used only for the analysis of mineral content in snake vertebrae (Galiova et al. 2010), and mineral content in teeth has not been evaluated using this method until now. We hypothesized that mineral

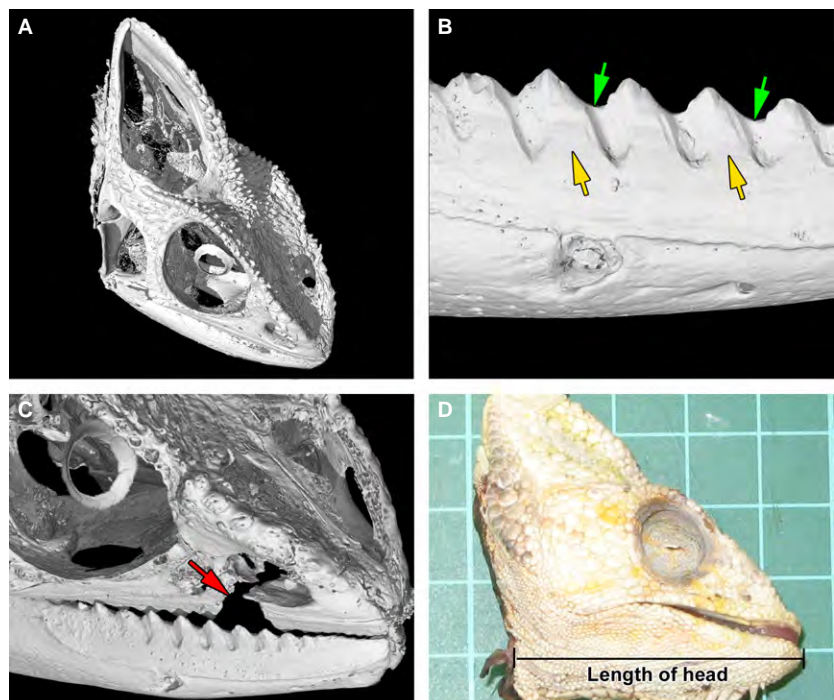


**Fig. 1** Skull morphology in the chameleon. (A) The microCT scanning allowed a visualization of individual skull elements. (B) Detailed view of the tooth–bone fusion area (yellow arrow) as well as the firm adhesion between neighbouring teeth (green arrow). (C) Tooth loss was linked with the fracture of maxillary bone (red arrow). (D) The head length was measured from the most distal tip of the mandible to the mandibular angle.

distribution in post-hatching chameleons might be different than in humans and other previously studied mammalian species, where ankylosis leads to demineralization of the underlying bone.

## Materials and methods

### Animals

Animals were obtained from the University of Veterinary and Pharmaceutical Sciences (Brno, Czech Republic). To demonstrate developmental changes in tooth–bone fusion area and bone morphology, four pre-hatching stages (13, 14, 15 and 16 weeks of incubation) were collected. For mineral content analyses, juvenile and adult post-hatching animals were selected and their lower jaw size measured (Fig. 1D) in a rostral-caudal direction (juvenile 1: 1.4 cm, juvenile 2: 1.9 cm, adult 1: 3.6 cm, adult 2: 4.0 cm). All of the animals died due to non-skeleton-related diseases. All procedures were conducted following a protocol approved by the Laboratory Animal Science Committee of the University of Veterinary and Pharmaceutical Sciences – Brno (Czech Republic).

### Histological analysis

The heads of embryonic and juvenile chameleons were fixed in 4% formaldehyde overnight, and the specimens were decalcified in 5% EDTA with 4% paraformaldehyde at room temperature. The time of the decalcification varied from 2 weeks to 3 months and it was directly related to the age of the animals (e.g. degree of calcification). Adult samples were decalcified in 15% EDTA with 4% paraformaldehyde at room temperature for 3 weeks and subsequently for 1 week at 40 °C. The specimens were embedded in paraffin and cut in the transverse plane. Serial histological sections were prepared (5 µm thickness for pre-hatching stages and 10 µm thickness for post-hatching stages) and stained with haematoxylin-eosin. Images were taken under bright field using a Leica compound microscope (DMLB2) with a Leica camera (DFC480) attached (Leica Microsystems, Wetzlar, Germany).

### Micro-computed tomography analysis

MicroCT analysis of the chameleon jaw was performed using the GE Phoenix v|tome|x L 240 laboratory system equipped with a 240 kV/320 W maximum power microfocal X-ray tube and a high-contrast flat panel detector DXR250 with a resolution of 2048 × 2048 pixels and a pixel size of 200 × 200 µm. The exposure time was 500 ms; three images were averaged and one image was skipped every 2000 positions. The microCT scan was carried out at an acceleration voltage and X-ray tube current of 60 kV and 110 µA, respectively. The voxel size of obtained volumes was in the range of 2–18 µm, depending on the size of the jaw. The tomographic reconstruction was produced using GE Phoenix dataview 2.0 3D computed tomography software. The 3D- and 2D-cross-section visualizations were performed using volume rendering VG STUDIO MAX 2.2 software (Volume Graphics GmbH, Heidelberg, Germany). The 3D jaw model was clipped according to the polyline path, copying the curvature of the jaw for the purpose of visualizing all teeth in cross-section. Two-dimensional transverse cross-sections of the teeth were performed perpendicular to the polyline.

### Laser-induced breakdown spectroscopy

For the element analysis, soft tissues were mechanically removed from the mandible using scissors. The jaws were macerated in water, boiled and dried. Clean samples were embedded in epoxy resin and ground with diamond paste.

LIBS setup was based on a modified laser ablation system UP 266 MACRO (New Wave, USA) equipped with a pulsed Nd:YAG laser operated at a wavelength of 266 nm. The radiation was transported using a fibre optic system onto the entrance slit of a Czerny-Turner monochromator (Jobin Yvon, Triax 320, France) with a PI MAX3 ICCD detector (Princeton Instruments). The detection delay time and gate width were set for phosphorus at 0.1 and 8 µs, for calcium at 0.3 and 12 µs, and for magnesium at 0.7 and 3 µs, respectively. The spectral data were collected in three spectral windows centred at 251, 284 and 456 nm for detection of emission lines P I 253.56 nm, Mg II 280.27/Mg I 285.21 nm and Ca I 452.69 nm, respectively.

The ablation experiments were performed at a pulse energy of 10 mJ. The crater size was set to 120 µm, and the distances from crater to crater in both axes were 150 µm.

### Microprobe

Microprobe measurements were performed using a Magellan™ 400 SEM. To show the surface topography of the samples, a secondary electron detector and EDX detector for analysing the particles were used. A voltage of 5 kV was selected, and the size of the calculated area was 5 × 5 µm.

## Results

### Formation of acrodont attachment in pre-hatching chameleons

The bases of the rostral and middle teeth in the chameleon formed during the pre-hatching period (Fig. 2). The cervical loop elongated towards the bone (Fig. 2A–F). Progressively, small, bony pedicles were directed towards the cervical loop and approached the dentin (Fig. 2D,G). Odontoblasts produced predentin that connected dentin to the supporting bone pedicles (Fig. 2I). This fusion process resulted in the formation of a firm morphological unit (Fig. 2J–L).

At an early stage, the jaw bone had a large amount of bone marrow (Fig. 2). The dental papilla was formed by dense cellular tissue, but later during development, its cellularity decreased to become similar to that found in bone marrow (compare Fig. 2B and K). Bony lamellae formed ahead of lateral bony pedicles and were interposed between the bone marrow and dental pulp cavities (Fig. 2A). The dental papilla remained widely connected to the underlying bony medulla by perforations in the lamella (Fig. 2E,H).

### Progressive initiation of teeth in the caudal part of juvenile jaws

Tooth development and attachment to the bone also proceed during the post-hatching stages (Fig. 3). Growth of

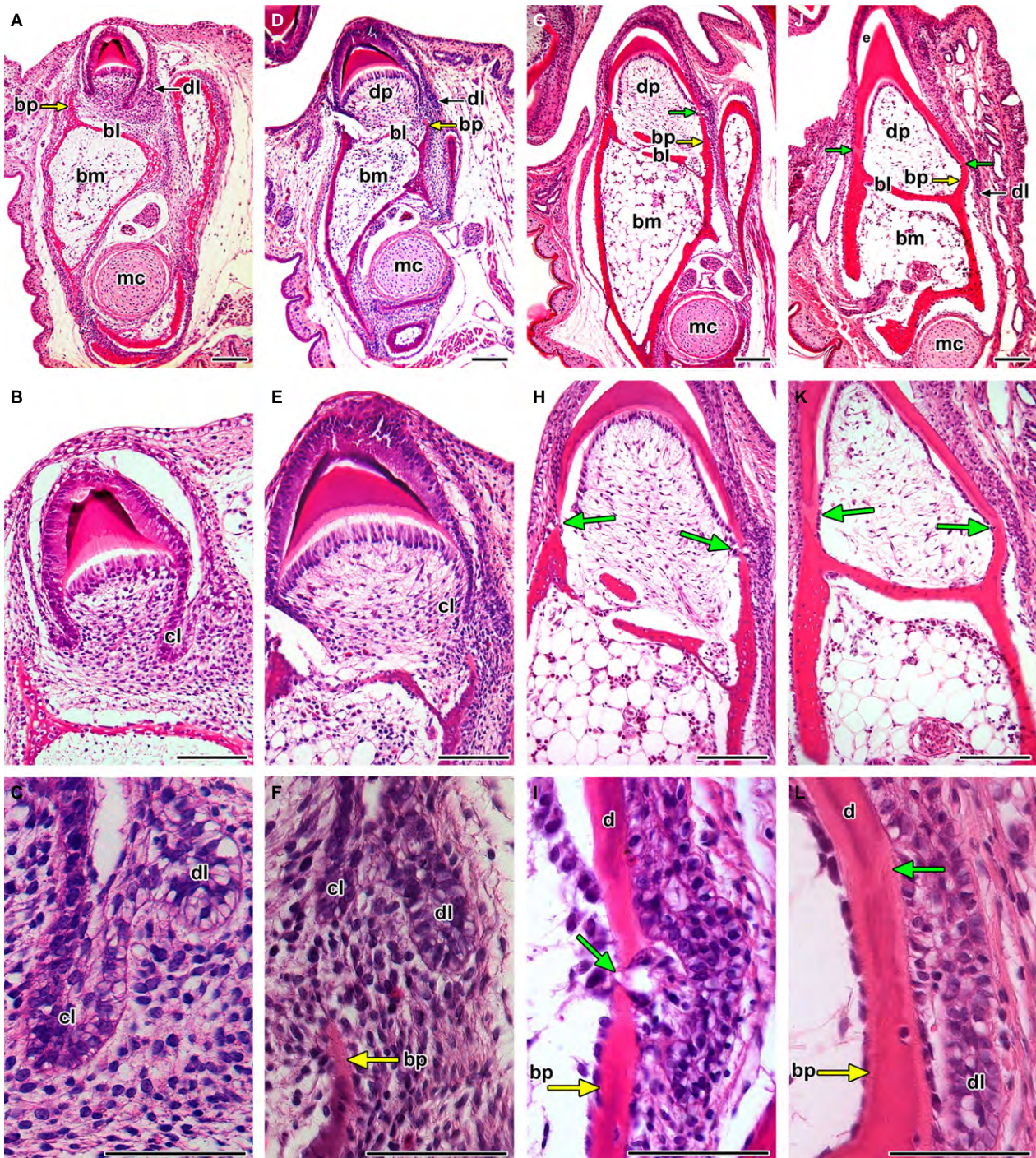


**Fig. 2** Development of the tooth–jaw interface. (A–C) The tooth base forms after mineralization of the crown. Labial bone pedicle (yellow arrow) is formed first while the lingual bone pedicle is behind in development. (D–F) The cervical loop grows deeper into the mesenchyme towards the bone pedicles (yellow arrow). (G–I) Bony pedicles almost in contact with the tooth base formed by dentin. (J–L) The gap between dentin and the underlying bone (green arrow) is filled by a layer of predentin produced by odontoblasts. The tooth base and their surface is formed only by dentin; the enamel did not develop in these areas. bl, bony lamellae; bm, bone marrow; bp, bony pedicle; cl, cervical loop; d, dentin; dl, dental lamina; dp, dental papilla; e, enamel; mc, Meckel cartilage. Haematoxylin–eosin. Scale bar: (A, B, D, E, G, H, J, K) 100  $\mu$ m, (C, F, I, L) 50  $\mu$ m.

the mandible occurred in a caudal direction, such that the most recent teeth were added in the caudal part of the mandible. In the most caudal teeth of juvenile animals, the

fusion between tooth bases and bone pedicles was not yet achieved (Fig. 3A,C).

Computed tomography revealed that bony pedicles grew from the lamellae in a caudal direction and formed round structures in the shape of a future tooth–bone contact area (Fig. 3B,D,E). Moreover, all juvenile teeth were connected by horizontally oriented channels, which joined each dental pulp to its caudal and rostral neighbours (Fig. 3D,E).

The number of teeth increased with age in the chameleon (Fig. 4). In juveniles, there were 11–13 teeth in the lower jaw quadrant (Fig. 4A,D); in adult animals, their number varied from 15 to 21 (Fig. 4G,J).

### Morphological changes in acrodont dentition during post-hatching stages

There were obvious differences in tooth shape in the rostral and caudal areas of the mandible at all analysed stages (Fig. 4). The smaller and more simply shaped teeth were located in the most rostral part of the mandible; more complex teeth appeared caudally (compare Fig. 4B,E with C,F). Moreover, the abrasion of rostral teeth with increasing age caused progressive loss of tooth morphology and therefore it was more difficult to count their exact number in adult animals (Fig. 4I,L).

Tomography allowed for a more detailed analysis of tooth–jaw and tooth–tooth fusion areas. In juvenile animals,

the apical tips of the tooth bases were already connected to the alveolar bone via ankylosis (Fig. 4B,C), and the junctional area between the teeth and jaw bone in the juvenile jaw became almost invisible. An imaginary boundary could be predicted only based on the location of the osteocyte lacunae, as they did not extend to the dental tissue (Supporting Information Fig. S1A,B). In adult specimens, the fusion had progressed so that the exact border between tooth and bone could no longer be localized (Figs 4G–L and S1C–E).

Moreover, firm fusion between neighbouring teeth occurred progressively during post-hatching development. Therefore, differences between the dental and interdental areas were hardly visible on transverse sections, especially in the rostral area where teeth were smaller and abrasions more advanced (Fig. 4I,L).

### The dental cavity is filled in adult animals

In juvenile animals, a large dental pulp cavity was clearly separated from the underlying bone marrow cavity by bony lamellae (Fig. 5A–E, Supporting Information Fig. S2A–G). Numerous large perforations of the lamella were observed in the central and lateral areas (Fig. 5E,J). The size of the dental papilla decreased with the increasing age of the animals (Figs 5F–J and S2H–M).

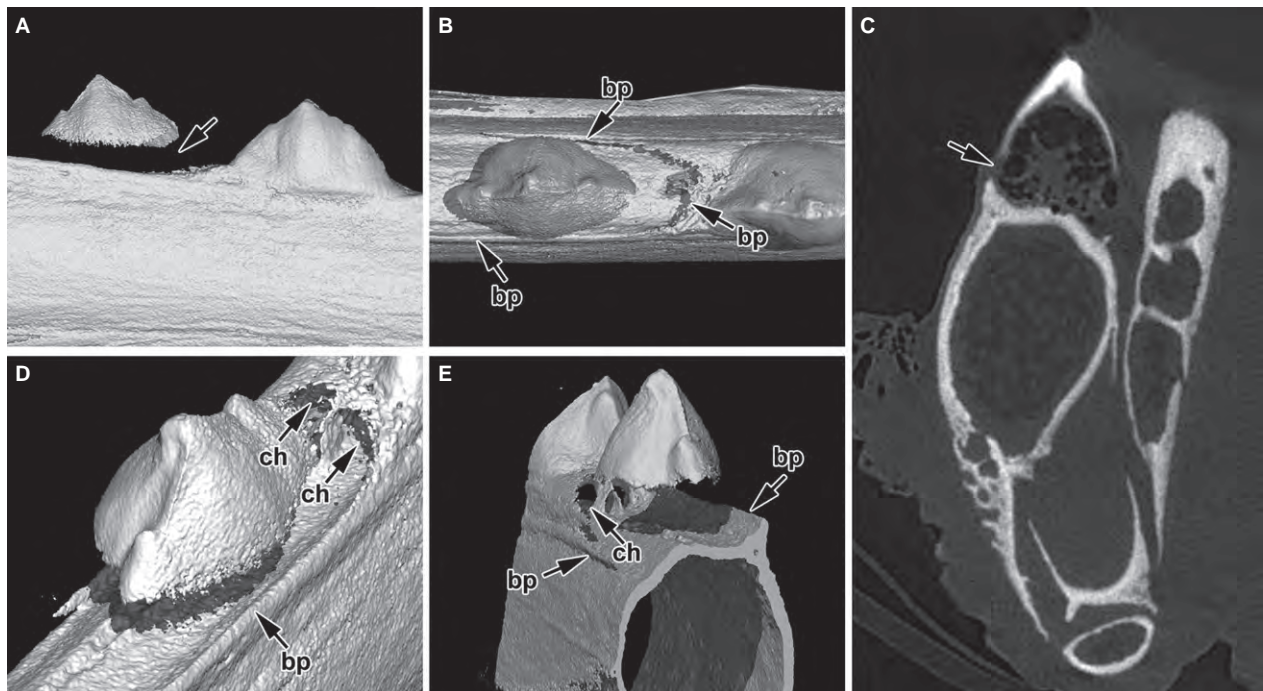


**Fig. 3** Tooth initiation in the caudal part of the jaw. (A) Newly added tooth is seen in the caudal part of the juvenile jaw as tooth initiation occurs continually throughout the chameleon life. (B) There is no contact of hard tissues between tooth and bone as yet; bone pedicles are well formed in the labial and rostral area. (C) The mineralized tooth basis does not reach to the jaw bone on the transverse section in microCT; the tooth is held in its position only by soft tissue. (D) A shallow socket in the jaw bone is formed in the future area of tooth–bone fusion where walls are made up of growing bone pedicles. (E) Detail of bony pedicles (arrows) in the rostral area of the tooth. The bone marrow is separated from the future dental pulp. Channels connecting neighbouring teeth develop in advance of tooth–bone fusion. bp, bony pedicle; ch, channel.

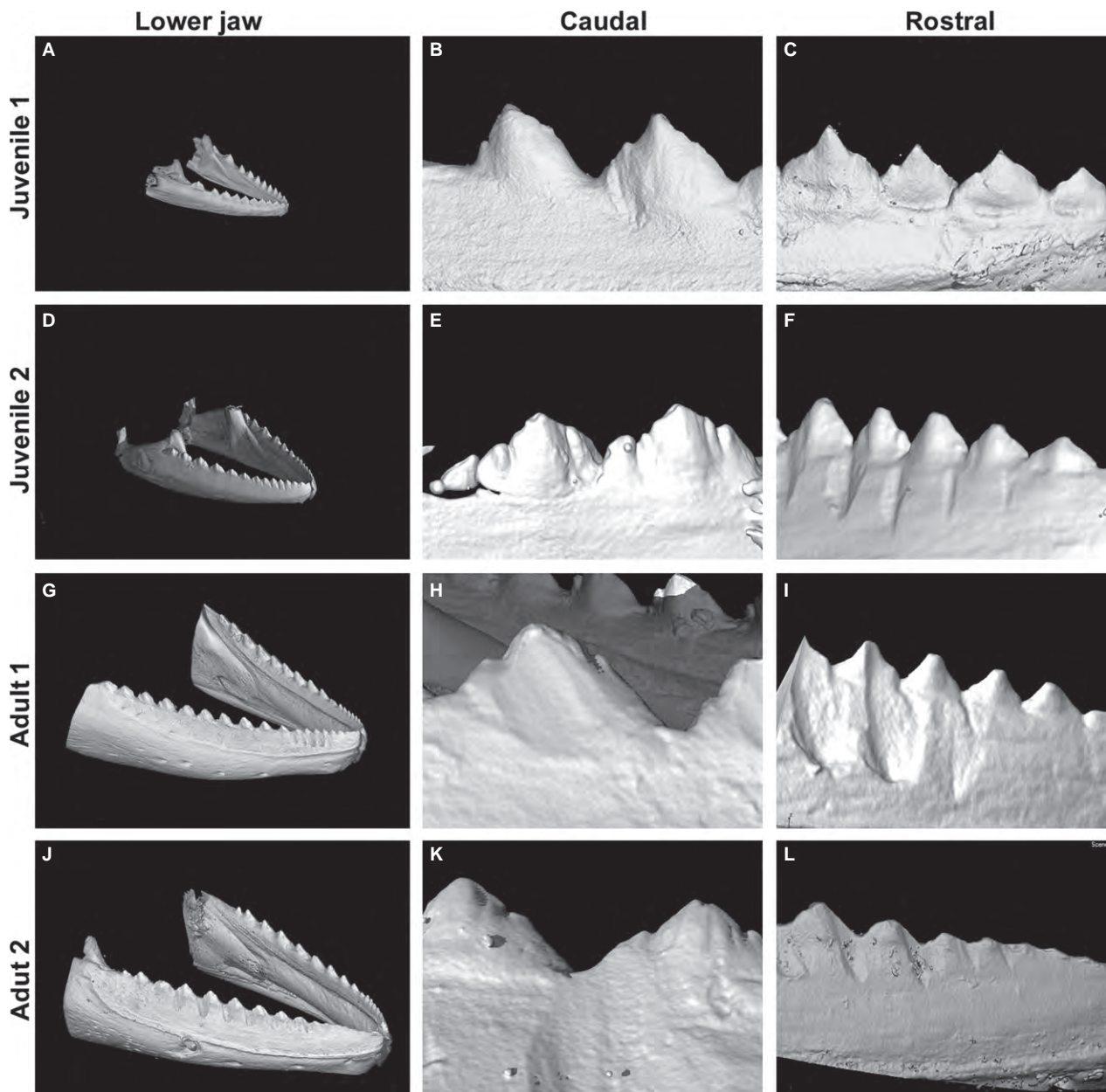


**Fig. 4** Jaw and tooth morphology using microCT. (A) The number of teeth is the smallest in juvenile chameleons. Teeth are well separated from each other. (B) Caudal teeth are larger and exhibit more complex shapes than rostral teeth. (C) Rostral teeth in juvenile chameleons do not have a uniform size, which is based on altered patterns of eruption. The shallow groove is visible in the area between the tooth and jaw. (D) The jaw becomes more robust and the number of teeth increases. (E) Newly mineralized tooth appears in the most caudal part of the jaw. (F) Teeth bases in the rostral part of the jaw fuse firmly to their neighbours. (G) In adult specimens, the number of teeth increased in the lower jaw. (H) The most caudal teeth exhibit a tricuspid shape. (I) Rostral teeth are firmly fused to each other, forming a saw-like appearance. (J) The abrasion and fusion of teeth is progressed in the adult specimen. (K) The lateral cusp of caudal teeth tips in the adult specimen are still visible but with apparent signs of abrasion. (L) Individual rostral teeth in adult specimens are hardly recognizable as the fusion and abrasion of tooth cusps has significantly progressed.

Adult chameleons possessed only a rudimentary dental cavity, which was progressively filled with mineralized tissue (Fig. 5K–O). A narrow channel was oriented caudally, interconnecting the dental pulp and bone marrow cavity (Fig. 5N,O, Supporting Information Fig. S3). The dental papilla was partially replaced by dentin, characterized by

the presence of parallel tubules oriented towards the central area, as well as by bony matrix distinguishable by the presence of osteocytes (Fig. S1).

In the largest animals, the dental pulp cavity was almost fully filled with mineralized tissue (Fig. 5M) and only very small channels remained (Fig. 5S); only some of the animals

had a connection between the dental pulp and bone marrow cavity (Fig. 5Q). In many cases, these channels were no longer even connected to the marrow cavity (Fig. S3G–L). In the rostral teeth, the dental pulp disappeared, and completely filled and unmineralized channels were observed under the bony lamellae (Fig. S3G–I).

### The intensity distribution of elements in the tooth–bone area

Because of the morphological changes in the pulp cavity and junction area between the tooth and bone, we hypothesized that extensive changes in elemental composition may occur in the fusion area during the post-hatching stages to mediate a firm connection between dentin and bone. LIBS analysis was performed with a focus on the key elements contributing to bone and tooth mineralization: calcium (Ca), phosphorus (P) and magnesium (Mg). Intensity maps illustrated the distribution of individual elements (Figs 6 and 7).

The intensity of the calcium line was measured at 452.69 nm and that of the phosphorus line at 253.56 nm. For magnesium, the ionic and atomic lines measured at 280.27 and 285.21 nm, respectively, were chosen because of their expected optical thinness (Le Drogoff et al. 2001). Moreover, the ratio  $MgII/MgI$  is known to be an indicator of hardness, because these lines are not as affected by self-absorption (Abdel-Salam et al. 2007).

The intensity of Ca and P was directly correlated with the age of the specimens (Fig. 6). In juvenile animals, the areas of highest intensity of both of these elements were distributed in the teeth and jaw, which corresponded to ossification centres in the mandible (Fig. 6A,D). The intensity of Ca and P increased when the animals became older, not only in the teeth and jaw bone but also in the junctional area between the two tissues (Fig. 6B,E). In the largest chameleon, the intensity of both elements was attenuated in the area of the lamellar bone, which was thinner than the growing bone of the smaller chameleons (Fig. 6C,F). The highest intensity of Ca and P was concentrated in the area of tooth–bone fusion and also partially in the area of the tooth itself (Fig. 6C,F). The intensity of Mg also increased with the age of the animal (Fig. 7). However, unlike Ca and P, the intensity of Mg in the jaw bone remained relatively low, whereas the intensity

expanded in the area of bone–tooth fusion and the tooth area (Fig. 7A–C).

### Relative quantity of elements in the tooth and jaw areas

To quantify the LIBS measurements, we used the MicroProbe method (Supporting Information Fig. S4) in the two extreme stages (the smallest juvenile and the largest adult animals), and we measured elements in the apical part of the tooth, in the junctional area between tooth and bone and in the lateral part of the jaw bone.

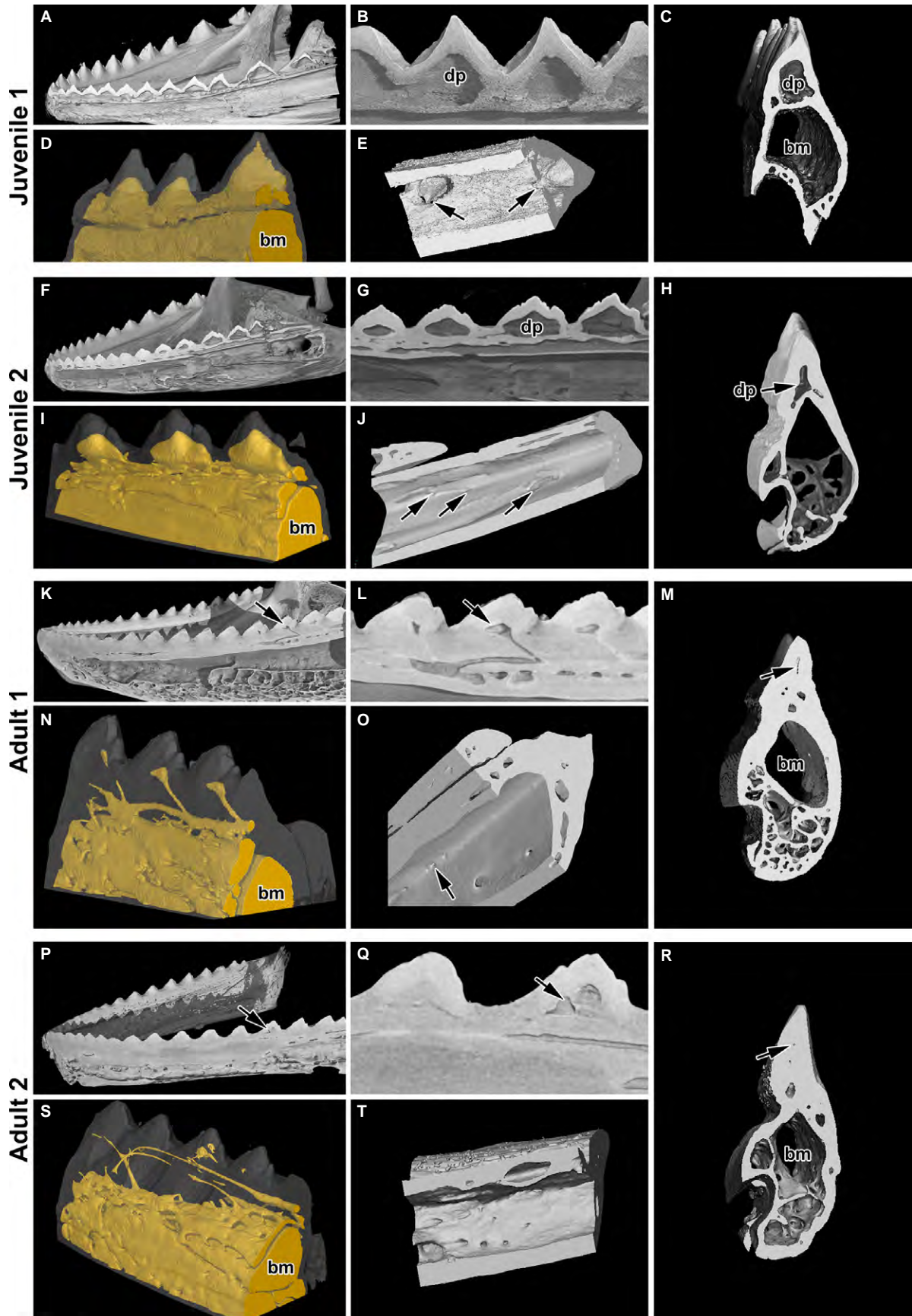
The Ca content did not vary significantly between the tooth and jaw bone areas at any of the analysed stages (Fig. 8A). However, the Ca content was higher at the older stage (Fig. 8A). The amount of P and Mg also increased with age (Fig. 8B,C). When compared with tooth areas, the jaws exhibited significantly lower amounts of Mg at both analysed stages, and the differences between the two stages were statistically significant (Fig. 8C). The P content was significantly lower in the jaw than in the teeth, but only at the juvenile stage (Fig. 8B). Moreover, the comparison of all three areas between stages showed statistically significant differences in P content.

All ratios (Ca/P, P/Mg and Ca/Mg) were higher for each analysed area at juvenile stages in contrast to adult stages (Fig. 8D–F). In juvenile chameleons, although the P/Mg and Ca/Mg ratios in the tooth and tooth–bone fusion area were similar, the ratios of these elements were much higher in the jaw bone (Fig. 8D–F).

### Discussion

The jaw apparatus of the chameleon has a unique morphology and functional adaptation for food processing. Chameleon feeding behaviour is exceptional because of its ballistic tongue projection (Gnanamuthu, 1930; Zoond, 1933; Anderson & Deban, 2010; Herrel et al. 2014) as well as its modified skull and hyoideal skeleton with hyoglossal muscles (Mivart, 1870; Rieppel, 1981; Bell, 1989). Its dentition is characterized by the fusion of tooth bases with the jaw bone and their junction along the jaw, which makes dentition very stable and prevents the teeth from falling out. As teeth cannot be replaced, any loss would lead to starvation and eventual death of the animals. Chameleon teeth are

**Fig. 5** Fusion of teeth to the jaw and neighbouring teeth. (A,B) Sagittal section of the lower jaw in juvenile animals shows fusion of teeth to the bone lamellae as well as tooth to tooth. (C) A distinct dental papilla is separated from the bone marrow by dental lamella on transverse section. (D) Angled view of the cavities, which are labelled in yellow. (E) Ventral view of the perforations connecting bone marrow to dental papilla (arrows). (F,G) The process of deposition of mineralized tissue occurs first in the rostral part of the jaw of juvenile animals. (I) Angled view of smaller dental pulp cavities. (J) Ventral view of reduced perforations connecting bone marrow to dental papilla (arrows). (H,M,R) Transverse sections show reduced dental papilla. (N,S) Remnants of channels and cavities are labelled by yellow filling. (K,L,P,Q) Teeth are firmly connected to the bone. The dental papilla becomes filled by mineralized tissue in adult animals. (O,T) Ventral view of small channels connecting bone marrow to the dental papilla. bm, bone marrow; dp, dental papilla.



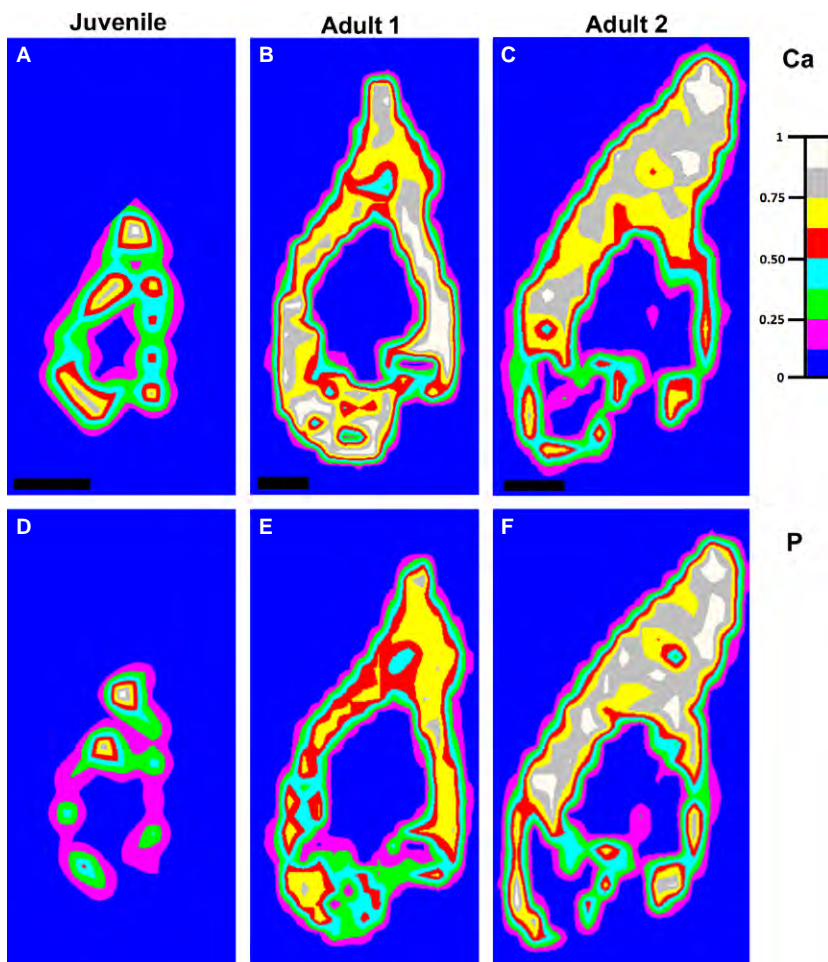


**Fig. 6** Distribution maps of calcium and phosphorus in the lower jaw of chameleons by LIBS analysis. (A–C) Distribution maps of calcium measured at 452.69 nm. (D–F) Distribution maps of phosphorus measured at 253.56 nm.

designed to hold prey and to apply pressure to kill the insect. Food is swallowed whole or partly chewed. A behavioural study revealed several chewing cycles in which the insect was positioned between jaws and crushed several times before it was transported to the oesophagus (So et al. 1992). MicroCT imaging showed that the shape of the teeth varied along the jaw in accordance with their different functions. Smaller rostral teeth contribute to food transport inside the oral cavity, whereas caudal teeth display a more complex tricuspid morphology, which corresponds to their chewing function.

#### Tooth–bone fusion

MicroCT revealed a firm fusion of tooth bases with bony pedicles in adult chameleons. This strong fusion between tooth and bone prevents the loss of individual teeth. Chameleon teeth fuse not only to bone but also with neighbouring teeth, both rostrally and caudally. This phenomenon has also been reported in the tuatara (Edmund, 1969; Zaher & Rieppel, 1999). Similarly to chameleons, tuatara teeth are also not replaced, and newly formed teeth are added caudally during development.

Morphological analysis of bony pedicles development revealed their initiation on the labial side and later development on the lingual side. Furthermore, the bony pedicle developed earlier on the rostral side than the caudal side. While the formation of labial and lingual pedicles has been observed previously (Zaher & Rieppel, 1999; Buchtova et al. 2013), the formation of the rostral pedicle could not be observed without detailed microCT analysis. Therefore, a round socket for the future fusion area is formed ahead of tooth mineralization and is probably based on cellular signalling between the cervical loop and bony pedicles. In the mouse, the formation of the tooth–bone interface is precisely controlled by molecules such as OPG or RANK (Ohazama et al. 2004; Alfaqeeh et al. 2013). However, the detailed signalling ‘cross-talk’ between both structures in the chameleon remains to be investigated in the future.

The structure of pedicles as well as the lamellae between dental pulp and bone marrow cavities appear to have much simpler morphology in comparison with mouse alveolar bones. Alveolar bone in mice arises from several ossification centres (Saffar et al. 1997; Sodek & McKee, 2000), in contrast to chameleon pedicles, which overgrow from the

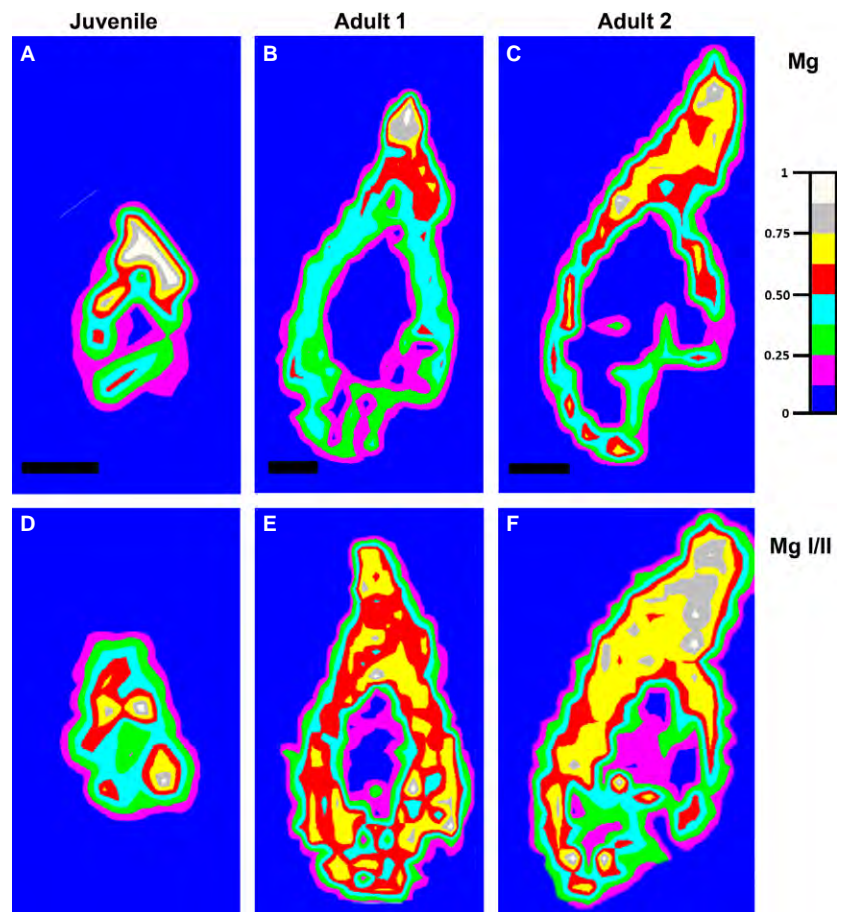


**Fig. 7** Distribution maps of magnesium in the lower jaw of chameleons by LIBS analysis. (A–C) Distribution maps of magnesium measured at 285.21 nm (for Mg I). (D–F) Ratio between distribution maps of magnesium measured at 280.27 nm (Mg II) and 285.21 nm (Mg I).

underlying lamellae. Moreover, mouse alveolar bones are initiated separately from the mandibular bone and fuse together much later during postnatal development. Therefore, differences in developmental processes during chameleon pedicle formation can be expected when compared with the mouse.

#### Dental pulps and bone marrow communication

In juveniles, the cavity of dental pulp is connected with bone marrow by large connections. However, the dental pulp cavity becomes filled over the course of post-hatching development, and only channels connecting dental pulp to the underlying bone marrow remain visible. Later, only remnants of channels are observed in some areas of the jaw. The probable purpose of communication between pulp and bone-marrow chambers is to allow blood vessels and nerves to reach the pulp cavity. Channels connecting teeth to their more caudal neighbours are formed very early during development, before the tooth to bone attachment is finished. Similar neurovascular canals connecting adjacent teeth have previously been described in tuatara (Kieser et al. 2009). It is interesting that teeth in juveniles are horizontally connected by channels and therefore serve together as one functional unit. Tooth anlagen are initially

built as separate elements and then connected to underlying bone, which requires very complex patterning steps to build all of the communications and channels in the correct areas before mineralization occurs.

In the adult chameleon, the filling of the dental pulp cavity leads to the loss of connection to the underlying bone and disappearance of vascular supply in this area. In the largest animals, the connection channels between the bone marrow and the tooth are reduced. Therefore, it seems improbable that tooth tissue remains fully vascularized and innervated, as observed in mammals. Furthermore, odontoblasts in mammals are maintained throughout life, and though they are active for a very long time in a healthy environment, they can also be reactivated to produce reactionary dentin (Smith & Lesot, 2001). However, in the chameleon, not even remnants of a cavity were observed in the most rostral teeth. Here, we focused only on hard bone structures; however, in the future, it will be necessary to investigate dentin ultrastructure in chameleons and possibly the presence of odontoblast processes in this area, including the cellular events involved in dental pulp and channel filling, such as cellular degradation, the fate of odontoblasts and the arrangement or disappearance of vessels and nerves in the pulp cavity.

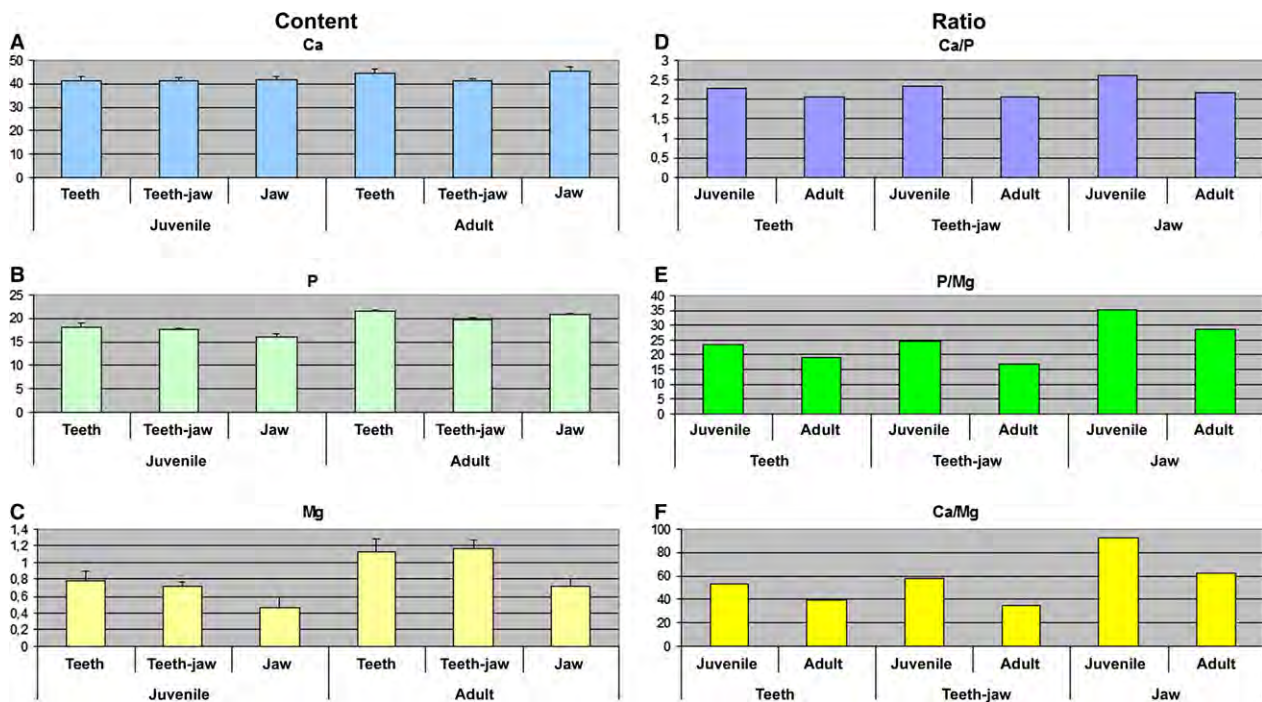


Fig. 8 Microprobe analysis of element content and ratio of elements.

### Mineral content changes during development

To study the progress of mineralization in teeth as well as underlying bone, we analysed the distribution of calcium, phosphorus and magnesium in hard tissues and their changes with age. LIBS was carried out to map the intensity of individual elements in the area of teeth, bone and tooth attachment at three different post-hatching stages. There is a general lack of information about the distribution of elements from comparative points of view and the chemical composition of reptilian teeth. The wavelength-dispersive electron microprobe has been used to evaluate the teeth of recent and fossilized animals (Dauphin & Williams, 2007, 2008). Those authors found an approximately two-fold higher content of calcium in enamel in comparison with dentin, whereas Mg was enriched in dentin (Dauphin & Williams, 2007). In crocodiles, X-ray powder diffraction (XRD) was used to measure mineral content in dentin, enamel and cementum (Enax et al. 2013). The advantage of this method was the evaluation of the exact amount of elements from individual material. Therefore, we combined both analytical approaches to determine mineral content differences, and we also performed quantitative measurements using an EDX detector on juvenile and adult animals, which allowed the determination of element content in selected areas.

Calcium, phosphorus and magnesium have been selected as the most common elements to analyse the degree of mineralization in different areas of dental or bone tissues in developing or experimental mammalian models or even

pathological processes (Steinfort et al. 1991; Aoba et al. 1992a,b; Tjaderhane et al. 1995; Akiba et al. 2006). In the teeth and jaw bone areas of chameleons, the intensity of calcium and phosphorus was low in juvenile animals but significantly increased in adult animals. The borders between tooth and bone areas become invisible with advancing animal age, and the mineral composition confirmed the very firm connections for protection against loss of teeth. Similarly, in humans the calcium and phosphorus content increases during the mineralization of dentin and enamel (Arnold & Gaengler, 2007).

Interestingly, the calcium and phosphorus content was lower in the jaw bone than in the teeth, especially at the juvenile stage. This could explain the broken jaw bones during fights between animals, as the bone is much weaker than the junctional tooth–bone areas.

Magnesium is known to be associated with the mineralization of teeth and bone tissue. It has been proposed that magnesium can replace calcium to bind to phosphate. Magnesium can be involved in the process of biological apatite crystal formation (Bigi et al. 1992) and mineral metabolism through activation of alkaline phosphatase (Althoff et al. 1982). Areas of high magnesium content were found in the newly formed dentin of rat incisors where the calcium/phosphorus ratio was low (Wiesmann et al. 1997). In chameleons, the magnesium content increased with animal age. The jaw bones had a significantly lower magnesium content in comparison with teeth, and differences between the two stages were also statistically significant.

Our recent observations suggest a strictly regulated progression of the mineralization process, both in time and in space. However, future comparative studies between acrodont and pleurodont dentition will be necessary.

## Conclusion

Here, age-related changes in morphology and mineral content were documented in the tooth–bone interface area, which contribute to firm and fully mineralized fusion between two types of tissues as a result of physiological ankylosis in chameleons. However, these results raise two complementary questions: (i) which cell types are involved in the progressive filling of the dental pulp cavity and (ii) what are the regulatory mechanisms specifying the functional differentiation in the junction area? This mineralization of the cavity impairs all possibilities of a later reparative process. Further study will be necessary to analyse the cellular processes involved in filling the dental pulp cavity and increasing mineralization in the underlying tooth–bone junction area. Moreover, a comparison between mammalian and reptilian models may provide new and useful information to study the molecular interactions at the tooth–bone interface during development.

## Acknowledgements

This study was supported by the Grant Agency of the Czech Republic (14-37368G to M.B. lab and O.Z., 14-29273P to J.Š.), Grant Agency of the University of Veterinary and Pharmaceutical Sciences Brno (61/2013/FVL to H.D.) and International Cooperation by Academy of Sciences of the Czech Republic (M200451201). T.Z., J.K. and K.N. acknowledge the CEITEC 2020 (LQ1601) with financial support from the Ministry of Education, Youth and Sports of the Czech Republic under the National Sustainability Programme II. We thank also Jan Hříbal for material support. This contribution is free of conflict of interest.

## References

Abdel-Salam ZA, Galmed AH, Tognoni E, et al. (2007) Estimation of calcified tissues hardness via calcium and magnesium ionic to atomic line intensity ratio in laser induced breakdown spectra. *Spectrochim Acta, Part B* **62**, 1343–1347.

Akiba N, Sasano Y, Suzuki O, et al. (2006) Characterization of dentin formed in transplanted rat molars by electron probe microanalysis. *Calcif Tissue Int* **78**, 143–151.

Alfaqueh SA, Gaete M, Tucker AS (2013) Interactions of the tooth and bone during development. *J Dent Res* **92**, 1129–1135.

Althoff J, Quint P, Krefting ER, et al. (1982) Morphological studies on the epiphyseal growth plate combined with biochemical and X-ray microprobe analyses. *Histochemistry* **74**, 541–552.

Anderson CV, Deban SM (2010) Ballistic tongue projection in chameleons maintains high performance at low temperature. *Proc Natl Acad Sci U S A* **107**, 5495–5499.

Andersson L, Malmgren B (1999) The problem of dentoalveolar ankylosis and subsequent replacement resorption in the growing patient. *Aust Endod J* **25**, 57–61.

Aoba T, Moreno EC, Shimoda S (1992a) Competitive adsorption of magnesium and calcium ions onto synthetic and biological apatites. *Calcif Tissue Int* **51**, 143–150.

Aoba T, Shimoda S, Moreno EC (1992b) Labile or surface pools of magnesium, sodium, and potassium in developing porcine enamel mineral. *J Dent Res* **71**, 1826–1831.

Arnold WH, Gaengler P (2007) Quantitative analysis of the calcium and phosphorus content of developing and permanent human teeth. *Ann Anat* **189**, 183–190.

Bell DA (1989) Functional anatomy of chameleon tongue. *Zool Jb Anat* **119**, 313–336.

Bigi A, Foresti E, Gregorini R, et al. (1992) The role of magnesium on the structure of biological apatites. *Calcif Tissue Int* **50**, 439–444.

Buchtova M, Zahradnické O, Balkova S, et al. (2013) Odontogenesis in the Veiled Chameleon (*Chamaeleo calyptratus*). *Arch Oral Biol* **58**, 118–133.

Burrage BR (1973) Comparative ecology and behaviour of *Chamaeleo pumilis pumilis* (Gemelin) and *C. namaguensis* A. Smith (Sauria: Chamaeleonidae). *Ann S Afr Mus* **61**, 1–158.

Dauphin Y, Williams CT (2007) The chemical compositions of dentine and enamel from recent reptile and mammal teeth – variability in the diagenetic changes of fossil teeth. *Cryst Eng Comm* **9**, 1252–1261.

Dauphin Y, Williams CT (2008) Chemical composition of enamel and dentine in modern reptile teeth. *Mineral Mag* **72**, 247–250.

Edmund AG (1969) Dentition. In: *Biology of the Reptile* (ed. Gans C), pp. 117–200. London: Academic Press.

Enax J, Fabritius HO, Rack A, et al. (2013) Characterization of crocodile teeth: correlation of composition, microstructure, and hardness. *J Struct Biol* **184**, 155–163.

Gaengler P (1991) Evolution of tooth attachment in lower vertebrates to tetrapods. In: *Mechanisms and Phylogeny of Mineralization in Biological Systems* (eds Suga S, Nakahara H), pp. 173–185. Berlin: Springer.

Gaengler P, Metzler E (1992) The periodontal differentiation in the phylogeny of teeth – an overview. *J Periodontol Res* **27**, 214–225.

Galiova M, Kaiser J, Novotny K, et al. (2010) Investigation of the osteitis deformans phases in snake vertebrae by double-pulse laser-induced breakdown spectroscopy. *Anal Bioanal Chem* **398**, 1095–1107.

Gnanamuthu CP (1930) The anatomy and mechanism of the tongue of *Chamaeleon calcaratus*. *Proc Zool Soc Lond* **1930**, 467–486.

Herrel A, Redding CL, Meyers JJ, et al. (2014) The scaling of tongue projection in the veiled chameleon, *Chamaeleo calyptratus*. *Zoology (Jena)* **117**, 227–236.

Kieser JA, Tkatchenko T, Dean MC, et al. (2009) Microstructure of dental hard tissues and bone in the Tuatara dentary, *Sphenodon punctatus* (Diapsida: Lepidosauria: Rhynchocephalia). *Front Oral Biol* **13**, 80–85.

Le Droffoff B, Margot J, Chaker M, et al. (2001) Temporal characterization of femtosecond laser pulses induced plasma for spectrochemical analysis of aluminum alloys. *Spectrochim Acta Part B*, **56**, 987–1002.

Lucas PW (1979) Basic principles of tooth design. In: *Teeth, Form, Function, Evolution*. (ed. Kurten B), pp. 154. New York: Columbia University Press.

- McIntosh JE, Anderton X, Flores-De-Jacoby L, et al.** (2002) Caiman periodontium as an intermediate between basal vertebrate ankylosis-type attachment and mammalian 'true' periodontium. *Microsc Res Tech* **59**, 449–459.
- Mivart SG** (1870) On the myology of *Chamaelon parsonii*. *Proc Zool Soc Lond* **1870**, 850–890.
- Ohazama A, Courtney JM, Sharpe PT** (2004) Opg, Rank, and Rankl in tooth development: co-ordination of odontogenesis and osteogenesis. *J Dent Res* **83**, 241–244.
- Osborn JW** (1984) From reptile to mammals: evolutionary considerations of dentition with emphasis on tooth attachment. *Symp Zool Soc Lond* **52**, 549–574.
- Rieppel O** (1981) The skull and jaw adductor musculature in chameleons. *Rev Suisse Zool* **88**, 433–445.
- Saffar JL, Lasfargues JJ, Cherruau M** (1997) Alveolar bone and the alveolar process: the socket that is never stable. *Periodontol* **2000** **13**, 76–90.
- Smith AJ, Lesot H** (2001) Induction and regulation of crown dentinogenesis: embryonic events as a template for dental tissue repair? *Crit Rev Oral Biol Med* **12**, 425–437.
- So K-KJ, Wainwright PC, Bennett AF** (1992) Kinematics of prey processing in *Chamaeleo jacksonii*: conservation of function with morphological specialization. *J Zool* **226**, 47–64.
- Sodek J, McKee MD** (2000) Molecular and cellular biology of alveolar bone. *Periodontol* **2000** **98**(24), 99–126.
- Steinfort J, Driessens FC, Heijligers HJ, et al.** (1991) The distribution of magnesium in developing rat incisor dentin. *J Dent Res* **70**, 187–191.
- Stuart-Fox DM, Whiting MJ** (2005) Male dwarf chameleons assess risk of courting large, aggressive females. *Biol Lett* **1**, 231–234.
- Ten Cate AR** (1994) *Development of The Tooth and its Supporting Tissue*. In: *Oral histology: development, structure and function*. St. Louis: Mosby-Year Book.
- Tjaderhane L, Hietala EL, Larmas M** (1995) Mineral element analysis of carious and sound rat dentin by electron probe microanalyzer combined with back-scattered electron image. *J Dent Res* **74**, 1770–1774.
- Wiesmann HP, Tkotz T, Joos U, et al.** (1997) Magnesium in newly formed dentin mineral of rat incisor. *J Bone Miner Res* **12**, 380–383.
- Young RA** (1974) Implications of atomic substitutions and other structural details in apatites. *J Dent Res* **53**, 193–203.
- Zaher H, Rieppel O** (1999) Tooth implantation and replacement in squamates, with special reference to mosasaurs lizards and snakes. *Am Mus Novit* **3271**, 1–19.
- Zoond A** (1933) The mechanism of projection of the chameleon's tongue. *J Exp Biol* **10**, 174–185.

## Supporting Information

Additional Supporting Information may be found in the online version of this article:

**Fig. S1.** Transverse sections of the dental pulp cavity in juvenile (A,B) and adult (C–E, E') animals.

**Fig. S2.** Channel formation during the fusion of teeth to the jaw in juvenile animals.

**Fig. S3.** Channel formation during the fusion of teeth to the jaw in adult animals.

**Fig. S4.** Typical emission spectra of the tooth, jaw and transitional area in both analysed stages.

PAPER [XVII]



# X-ray micro computed tomography-aided calibration of laser-induced breakdown spectroscopy depth profiling for archaeological ceramics examination



Marie Novotná<sup>a,\*</sup>, Eva Zikmundová<sup>a,b</sup>, Pavel Pořízka<sup>a,c</sup>, Tomáš Zikmund<sup>a</sup>, Karel Novotný<sup>b</sup>, Jozef Kaiser<sup>a,c</sup>

<sup>a</sup> Central European Institute of Technology, Brno University of Technology (CEITEC BUT), Purkyňova 123, Brno CZ-61200, Czech Republic

<sup>b</sup> Department of Chemistry, Faculty of Science, Masaryk University, Kotlářská 2, Brno CZ-61137, Czech Republic

<sup>c</sup> Department of Optics and Precise Mechanics, Faculty of Mechanical Engineering, Brno University of Technology, Technická 2, Brno CZ-61200, Czech Republic

## ARTICLE INFO

### Keywords:

LIBS  
X-ray  $\mu$ CT  
Depth profiling  
Calibration

## ABSTRACT

The investigation of archaeological samples, such as ancient ceramics, provides more details about the past. In this work, we suggest a new approach for the calibration of a depth profiling of ceramic fragments with glazed layers. X-ray Micro Computed Tomography ( $\mu$ CT) serves as a calibration method for a depth-profile analysis using Laser-Induced Breakdown Spectroscopy (LIBS). In this case,  $\mu$ CT benefits from different contrasts of the glaze layer (containing lead) and the ceramic matrix (lead-free). Non-destructive  $\mu$ CT scans provide a dimensional analysis and a 3D observation of LIBS craters with a resolution at the micrometer level. The LIBS analysis combined with  $\mu$ CT enables a precise depth-wise calibration to the number of laser pulses. Moreover, a visualization of the ablation process allows observing the laser beam as it passes through the glaze, the interface and the ceramic matrix. The ablation rate determined using  $\mu$ CT scans enabled the differentiation of individual phases of the ablation process penetrating the surface layer. As each of these steps is characterized by a different ablation rate, a more precise calibration for the depth calculation is possible. Such an approach is unique and may be further used in a depth profile calibration regardless of the analyzed sample.

## 1. Introduction

Analytical tools used for the characterization of various ceramic artefacts in the archaeological survey are of great importance. New and advanced analytical techniques help to answer many basic archaeological questions, even those that could not be answered in the past. Determining a provenance and a production technology of an artefact is one of these issues which had been hard to solve. A material composition and a structure of the glaze (or ceramic matrix) may help determine the provenance and the production technology. Ancient ceramics are composed dominantly of silicate material with a layer of glaze, a vitrified material. Various oxides, natural minerals and clays were used as glaze materials. For routine chemical and structural analyses of such archaeological objects, different approaches are applied [1]. Optical emission spectrometry methods (OES) play an important role in this field. Currently, the analytical techniques based on laser ablation, especially laser-induced breakdown spectroscopy (LIBS), are powerful tools in the analysis of archaeological ceramic objects [2]. LIBS has

been used for the analyses of a wide range of unique samples (paintings [3,4,5,6], pottery [7,8,9], glass [10]) in archaeology and cultural heritage. Such applications of LIBS were also described in several books and reviews [11,12,13]. Moreover, LIBS serves not only for a determination of the elemental composition but also for the elemental imaging of different types of samples [14,15,16,17].

Archaeological ceramics often occur in the form of fragments which can be analyzed on the cross-section, (usually by Scanning Electron Microscopy with Energy Dispersive Spectroscopy SEM-EDS). However, some ceramic items are preserved as a whole and it is essential to maintain the integrity of the object following the conservation-restoration ethics. For this reason, while analysing layered samples it is necessary to employ a depth profiling technique which is non-destructive or at least micro-destructive with an acceptable sample damage. From this perspective, LIBS technique can be considered as micro-destructive with a potential for depth profiling of archaeological ceramic objects. The ability of LIBS to investigate the depth profile by repeatedly directing laser pulses to the same point has been known and

\* Corresponding author.

E-mail address: [marie.novotna@ceitec.vutbr.cz](mailto:marie.novotna@ceitec.vutbr.cz) (M. Novotná).

<https://doi.org/10.1016/j.sab.2020.105965>

Received 18 May 2020; Received in revised form 19 August 2020; Accepted 22 August 2020

Available online 25 August 2020

0584-8547/ © 2020 Elsevier B.V. All rights reserved.

utilized from the beginning of the LIBS development [18].

In the literature, the depth-profile analysis is performed on various types of samples, especially metal multi-layered materials [19]. During the LIBS analysis of electrolytically deposited brass samples with a nominal thickness of the layers the ablated mass per pulse was found at ng level. Depth profiling of zinc-coated steel in different ablation atmospheres (air, argon, helium) and the influence on zinc and iron emission lines was investigated [20]. Calibration strategies for quantitative LIBS depth-profiling of Al, Fe, and Zn in two galvanized coatings on steel were developed [21]. Depth profiling of tin-coated glass with the standardization to the acoustic signal is described by Kanický et al. [22].

Besides metal layers, some works were also focused on a depth profiling of layered ceramic materials, as well as of archaeological and cultural heritage objects. A depth-resolved analysis of multi-layered model samples of historical easel paintings was performed using LIBS. It was proved to be a suitable method for distinguishing layers of a different material composition and the estimation of their thickness [23]. Characterization of a ceramic multi-layered material performed by using the double-pulse LIBS arrangement is described by Čtvrtníčková et al. After an optimization of double-pulse experimental conditions and the detection time, the depth profiles were evaluated on the basis of various elemental compositions in both layers of ceramic samples [24]. The LIBS technique enables to obtain an in-depth compositional profile, which was demonstrated on Hispanic Terra Sigillata pottery. Moreover, LIBS also enables to distinguish differences between the slip and the body and to characterize the interface between both parts of the sample [25]. Surprisingly, even organic layers can be monitored by LIBS as it was demonstrated on the example of rabbit glue and pigment layers [26]. This technique is also promising as a tool for monitoring of a laser cleaning process [27].

The depth profiling enables an investigation of the interfaces of structured materials. Nevertheless, the most critical and challenging task in LIBS depth profiling is converting the number of laser pulses into the depth. Only after such a conversion, it is possible to determine the depth of the interface and the thickness of individual layers in the case of multi-layered samples. The depth of the ablation crater is often measured by optical methods (optical profilometry, optical microscopy, confocal microscopy) or contact profilometry. However, the performance of optical or contact methods is limited by the shape and the depth of LIBS craters [23,28]. Moreover, crater parameters and a determination of the true layer interface might be distorted by a number of phenomena (instrumental factors, beam-sample interactions and sample characteristics) [13,29,30]. The properties and the profile of the laser beam have a great impact on the crater characteristics and the selection of a suitable laser is essential [30,31]. Depth-profiling process is usually quantified by the depth resolution and the ablation rate [13,32,33]. For example, an *in-situ* optical microscopy was used for a three-dimensional (3D) characterization and observation of laser ablation craters in an aluminium specimen [34]. A typical approach for the characterization of LIBS crater profiles is using the optical profilometry [23,35,31].

Limitations of optical and contact methods create further needs for a more suitable technique. Radiographic methods are the most commonly used for a non-invasive and non-destructive examination of archaeological ceramics. The X-ray micro computed tomography ( $\mu$ CT) allows obtaining a complete 3D information about the studied object [36]. The method is primarily used for a visualization of mineralized tissues, and as a basic tool in skeletal research [37]. Therefore, this method is widely used in archaeology for the investigation of human and/or animal remains, especially bones or teeth [38,39]. Concurrently, this method has an irreplaceable role in the research of inorganic materials including ceramics [40,41].  $\mu$ CT has already been used for the characterization of laser ablation craters or processes [42,43]. The laser ablation craters created in the samples of metal (aluminium) and rock (false gold ore) were also investigated using  $\mu$ CT [42]. The  $\mu$ CT scan

enabled an accurate measurement of the crater volume, width, depth and cone angle comparable to the results obtained from a theoretical simulation model. The  $\mu$ CT method was also applied to observe the progression of the tooth enamel and dentin ablation process [43].

In this work, LIBS depth profiling was performed on an archaeological fragment of glazed ceramics.  $\mu$ CT was employed for the structural observation, and in combination with LIBS it served as a tool for a calibration of the ablation rate and a measurement of laser ablation crater depths.

## 2. Material and methods

### 2.1. Samples

A collection of glazed fragments of modern history archaeological ceramics comes from an archaeological excavation in the locality of Provaznická, (Cheb, Czech Republic) where a complex group of strata from 13th to 20th century has been revealed. A presence of a lead glaze on ten fragments of different hues of yellow was investigated and confirmed by LA-ICP-MS analysis (details in 2.2). Considering the sample requirements in LIBS and  $\mu$ CT, i. e. a flat sample surface and distinguishable materials in X-ray radiation respectively, a yellow-green fragment was chosen for further experiments. It has a triangle shape with dimensions of 1.8 cm  $\times$  1.7 cm  $\times$  2.0 cm, Fig. 1.

### 2.2. LA-ICP-MS measurement

The elemental analysis was carried out by the LA-ICP-MS method. The system consisted of LSX-213 G2+ laser ablation device (Teledyne Cetac Technologies, USA) and Agilent 7900 ICP-MS analyser with an octopole reaction cell (Agilent Technologies, Japan). The laser operates at a wavelength of 213 nm with a pulse duration  $\sim$ 4 ns. Using helium as a carrier gas with a flow rate of 0.9 l min<sup>-1</sup>, the aerosol was washed out a 2-volume ablation cell (HelEx). Then the aerosol was mixed with argon serving as makeup gas with flow rate 1 l min<sup>-1</sup> and transported through a FEP (Fluorinated Ethylene Propylene) tube (i.d. 2 mm, length 1 m) to the ICP-MS. The mass spectrometer operated at the forwarded power of 1550 W and Ar gas flow rate of 15 (outer plasma gas). 60 s line scan ablation was performed through the glaze-ceramic interface, with the spot diameter of 50  $\mu$ m, scan speed of 10  $\mu$ m s<sup>-1</sup>, repetition rate of 10 Hz and fluence of 10 J cm<sup>-2</sup>. Each part of the line scan (glaze and ceramic) was evaluated separately. Seven isotopes representing the major components of the sample were monitored with the total integration time of 0.5 s: <sup>23</sup>Na, <sup>26</sup>Mg, <sup>27</sup>Al, <sup>29</sup>Si, <sup>39</sup>K, <sup>44</sup>Ca, <sup>208</sup>Pb. External calibration was performed using the standard reference materials (SRM) NIST 610. Quantification was based on the sum of oxides of elements to 100 wt% (Table 1).

### 2.3. LIBS measurement

The LIBS measurements were performed using a lab-built LIBS system. A Gaussian beam profile laser pulse from a CFR Ultra laser (Quantel, France) with a pulse energy of 20 mJ, a wavelength of 532 nm, a pulse duration of 10 ns and a repetition rate of 20 Hz was focused onto the sample surface with a 30 mm focal lens forming a spot of 100  $\mu$ m in diameter. The radiation of the laser-induced plasma was collected and delivered through an optical fibre to the detection unit consisting of an echelle spectrometer EMU 65 (Catalina Scientific, USA) equipped with an EMCCD detector Falcon Blue (Raptor Photonics, UK). The gate delay was controlled using a digital pulse generator and custom-developed control electronics. The gate delay was set to 1  $\mu$ s and the integration time was 50  $\mu$ s.

During the LIBS analysis, individual craters were ablated with 5–150 pulses forming a depth profile used for a further calibration. Throughout the whole experiment, a spectrum was acquired per each pulse. LIBS data were evaluated in a lab-made LIBS software. The depth

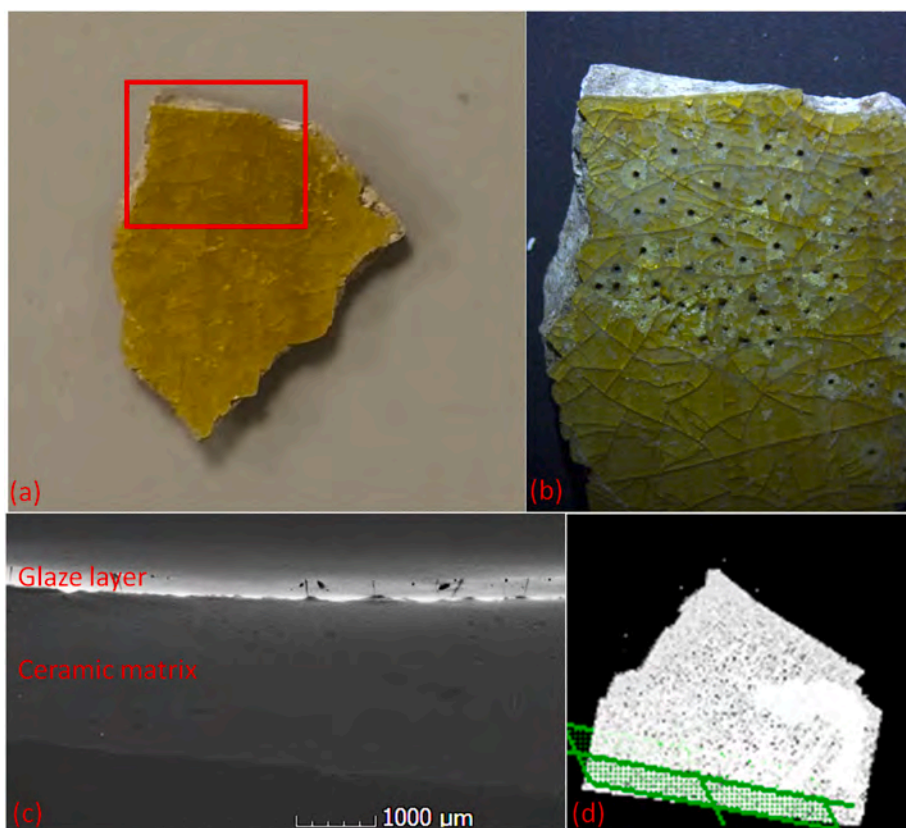


**Fig. 1.** Sample of the yellow-green glazed ceramic fragment (a) with a highlighted corner where LIBS and  $\mu$ CT analyses were performed. (b) Microscopic image of the sample corner after LIBS analysis. (c)  $\mu$ CT slice of the glaze ceramic fragment sample: visualization of the structural defects in the glaze layer. The position of the indicator (green) in the 3D render shows the location of the  $\mu$ CT slice (d). The amount of structural defects increases towards the centre of the ceramic fragment. Therefore, the corner of the sample marked in (a) (red square) was chosen for the LIBS analysis. (For interpretation of the references to colour in this figure legend, the reader is referred to the web version of this article.)

**Table 1**

Content of lead and potassium in glaze and ceramic matrix, results obtained by LA-ICP-MS.

	K [wt%]	Pb [wt%]
Glaze	$0.19 \pm 0.01$	$62.7 \pm 0.7$
Ceramic matrix	$1.19 \pm 0.09$	$3.0 \pm 0.1$

profiling of the investigated layer was carried out using a signal of two elements, lead (Pb I 405.81 nm) and potassium (K I 766.49 nm). These elements were chosen as representatives of the glaze (lead) and the ceramic matrix (potassium).

#### 2.4. $\mu$ CT measurement

The tomographic measurement was performed with a GE phoenix v|tome|x L240 (GE Sensing & Inspection Technologies GmbH, Germany) equipped with a nanofocus X-ray tube with maximum power of 180 kV/15 W. The data were acquired using a high contrast flat panel detector dynamic 41|100 with  $4000 \times 4000$  px and a pixel size of  $100 \mu\text{m}$ . The  $\mu$ CT scan was performed at the current of  $125 \mu\text{A}$  and the voltage of 150 kV. The X-ray intensity was reduced with the 0.4 mm Cu filter and the temperature in the air-conditioned cabinet was  $21^\circ\text{C}$ . The exposure time was 400 ms and two images were averaged for reducing the noise. During the measurement, 2400 projections were taken, and the voxel size was  $6 \mu\text{m}$ . Tomographic reconstruction was realized using the GE phoenix datos|x 2.0 (GE Sensing & Inspection Technologies GmbH, Germany) software with a sample drift correction, a beam hardening correction and no noise filtration. Reconstructed slices were imported into the VGStudio MAX 3.2 (Volume Graphics GmbH, Germany) for a 3D visualization and the  $\mu$ CT data evaluation.

### 3. Results and discussion

After a verification of the high lead content in the glaze by a LA-ICP-MS analysis, an inspection of the ceramic fragment was performed by  $\mu$ CT (Fig. 1 (c)). The aim of this procedure was to investigate the inner structure of the glaze layer and its homogeneity. A  $\mu$ CT slice of the glazed ceramic fragment and a visualization of structural defects in the glaze layer can be seen in Fig. 1 (c). The location of the  $\mu$ CT slice on the 3D render is depicted in the right bottom corner. The corner of the sample (marked by a red square in Fig. 1 (a)) was chosen for the LIBS depth profiling because of the amount of structural defects that increase towards the centre of the fragment. The  $\mu$ CT scanning of the sample also enabled a subsequent determination of the glaze layer thickness (especially in specific places where laser ablation craters had been created). The  $\mu$ CT scanning was performed both before and after the depth-resolved ablation of a layer to calibrate the LIBS ablation rate.

#### 3.1. Laser ablation and depth profiling

A series of ten LIBS depth profiles was measured by focusing 1000 laser pulses to one point, and ablation craters were created in the area with minimal structural defects observed by  $\mu$ CT (see Fig. 1(c)). The measurement points were selected outside the evident cracks in the glaze (shown in Fig. 1 (b)), observable even with the naked eye.

The LIBS spectra (Fig. 2) were measured for each laser pulse in each spot. After the background intensity correction, two wavelength intervals were chosen. The emission line peak area for the interval of 405.59–406.00 nm represents the signal of lead and for the interval of 765.97–767.02 nm represents the signal of potassium. These elements were chosen because the content of lead in the glaze is  $> 60\%$  (see 2.2) while in the ceramic matrix, only a low content is expected. On the other hand, the content of potassium in the glaze is significantly lower in comparison with the ceramic matrix as verified by LA-ICP-MS.

Depth profiles were plotted using the intensities of selected emission

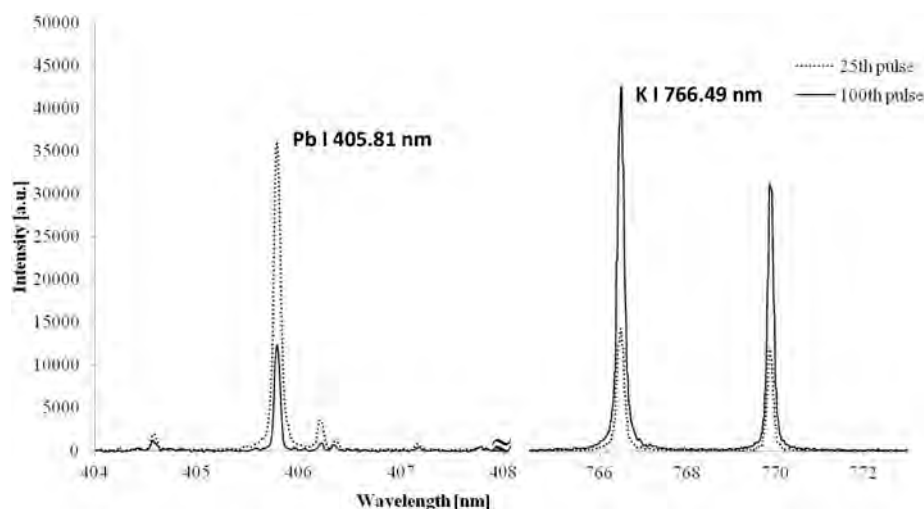


Fig. 2. Selected ranges of LIBS spectra with emission lines of lead (Pb I 405.81 nm) and potassium (K I 766.49 nm) selected from the depth profile; 25th (dashed line) and 100th pulse (solid line).

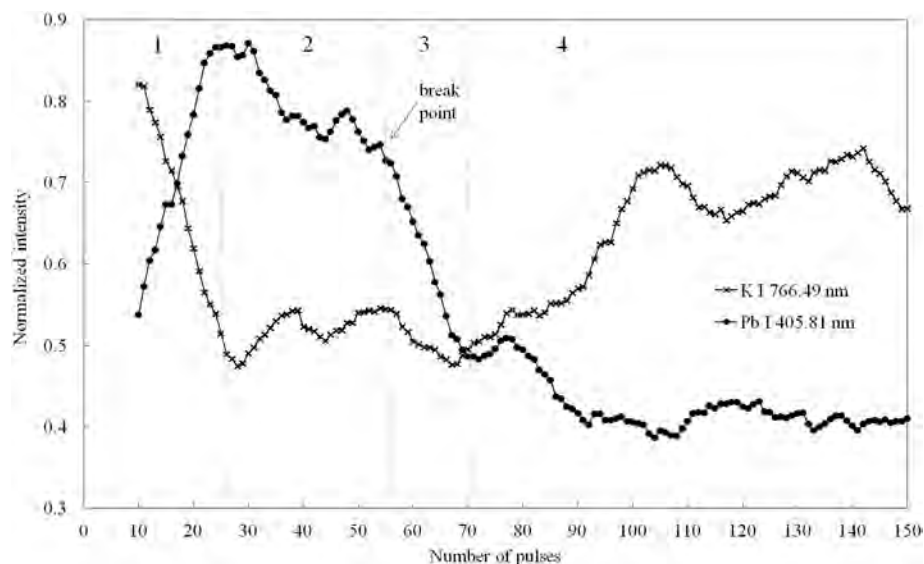


Fig. 3. Normalized LIBS depth profiles of Pb I 405.81 nm and K I 766.49 nm. Four parts of the profile and the break point are marked.

lines for 150 laser pulses in each spot. Signal intensities of both elements were normalized so that the maximal intensity for a particular element in the depth profile was equal to 1. Subsequently, the curves were smoothed so that each point represents a moving average of ten adjacent values. This is the reason why the maximal values of intensities are lower than 1 (see Fig. 3). When more than 150 laser pulses were applied during the ablation of the ceramic matrix, a formation of an irregular crater bottom occurred and the intensities of lead and potassium were not changing significantly (they were constantly decreasing due to increasing crater depths and to a subsequent plasma emission shielding). This signal was analytically useless regarding the depth profiling of the glaze/ceramic matrix intersection and it was not further taken into account.

It was found out that the basic depth-profile pattern was similar for each spot. Although there are differences in the individual course of the profiles and signal intensities for both elements, probably mostly due to the variability of the glaze layer thickness, four different ablation steps were clearly distinguishable in all depth profiles (see Fig. 3).

### 3.1.1. Ablation of the surface layer

During the first 25 pulses, the signal of lead quickly increased while

the potassium signal showed the maximum for the first pulse and then decreased. The results obtained by LA-ICP-MS and  $\mu$ CT indicate that the glaze layer is uniform throughout its whole thickness and therefore this signal profile cannot be attributed to the surface contamination or corrosion. The observed behavior is probably caused by variable plasma parameters or a non-stoichiometric ablation. Such effects were already described in the literature and they are associated with a lower electron temperature in the beginning of the ablation. Correction methods were also developed [44,45,46]. The behavior is also consistent with the lower signal observed for the lead emission line with higher excitation energy while the higher signal corresponds to potassium with lower excitation and ionization energy. On the other hand, the higher ablation rate (see below) is somewhat inconsistent with this effect and a detailed study would be desired. Nevertheless such study is beyond the scope of this work.

### 3.1.2. Ablation of glaze layer bulk

After 25 laser pulses, the lead signal reached its maximum and then slowly decreased while the potassium signal kept constant with more or less periodical fluctuations. This part corresponds with the ablation of the glaze layer bulk and it is characterized by a constant ablation rate

(see below).

### 3.1.3. Penetration through the interface

The most important moment is marked in Fig. 3 at the 55th pulse. There is an evident breakpoint in the lead signal profile. After this point, the signal of lead rapidly decreased because the centre of the crater had reached the bottom of the glaze layer. The slope of this part more or less characterizes the depth resolution of the method. The resolution is lower due to the Gaussian profile of the laser beam [47,48,49]. Moreover, further laser pulses repeatedly ablated the glaze layer from the crater walls although the centre had already reached the layer interface. At that time, the increase of potassium signal was still not evident probably due to a small amount of the ablated ceramic matrix. Consequently, this part can be considered as a penetration through the interface.

### 3.1.4. Ablation of ceramic matrix

The signal of potassium was increasing from 70th pulse, where the laser beam fully reached the ceramic matrix (at the same time the lead signal reached the local minimum). Therefore, it is not possible to consider the intersection of lead and potassium depth profiles the point where the laser beam reached the interface.

The number of laser pulses necessary to penetrate through the glaze layer corresponds to the breakpoint in the lead depth profile after which a rapid decrease in the intensity was observed. In order to verify the above-mentioned conclusions derived only from the LIBS depth profiles of two elements, a technique which allows observing the laser beam passing through the glaze layer was necessary. For the purposes of our study, a detailed inspection of laser ablation craters and monitoring of the ablation process by  $\mu$ CT was chosen.

## 3.2. LIBS craters characterization by $\mu$ CT

After a series of LIBS depth profiling measurements, a  $\mu$ CT scanning of the ceramic fragment was performed again. A slice of an individual LIBS crater (Fig. 4 (a)) shows a specific shape of the crater created by applying 1000 laser pulses: a long, narrow and differently curved in the ceramic matrix. The average overall crater depth passing through the glaze layer into the matrix after applying 1000 laser pulses was 1406  $\mu$ m with 2.8% relative standard deviation (RSD). This statistics was estimated from the measurement of ten craters. The small relative standard deviation can be attributed to a specific saturated ablation process in very deep craters and it does not correspond with standard deviations for the first 150 pulses; see Table 2. With regard to specifically shaped ablation craters, it was not possible to use optical profilometry for in-depth studies. On the other hand, the use of  $\mu$ CT method was very advantageous thanks to the easy observation of the whole craters including not only the glaze layer containing lead but also the ceramic matrix.

To determine the crater depth in the glaze layer corresponding to the thickness of the glaze, the truncated cone-shaped part of the crater in the glaze layer was primarily investigated (Fig. 4 (b)). The software allowed a measurement of required dimensions (the thickness of the glaze layer) and an observation of structural defects. After the LIBS analysis, the depth of the LIBS craters in the glaze layer was measured perpendicularly to the centre of the circle area on the top of the cone. The distance between the point in the centre of the circle area and the bottom of the cone was considered as the thickness of the layer for a given depth profile measurement. The measurement of the layer thickness in the centre of the crater is based on the assumption that a crater with a more or less Gaussian profile is formed during the ablation. Therefore, the interface is first reached by the centre of the crater (in the moment when the breakpoint is observed in the depth profile). This procedure offers a method of glaze layer thickness determination which is compatible with LIBS measurement. The results of the above-mentioned ten craters are shown in the "reference ( $\mu$ CT)" column of

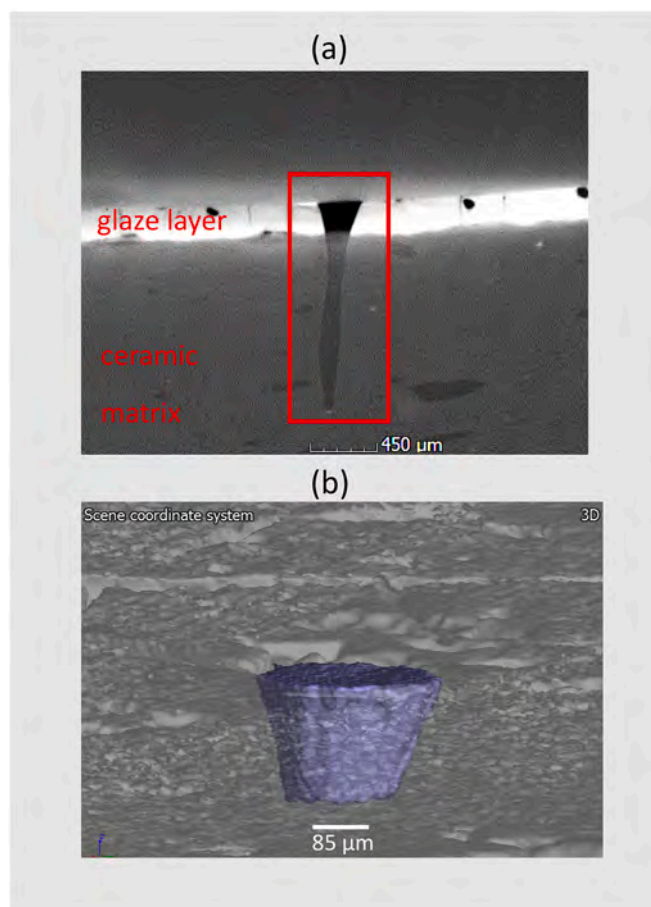


Fig. 4. Visualization of the ceramic fragment with the LIBS crater: (a) a  $\mu$ CT slice of the specific long and narrow crater created by applying 1000 laser pulses, (b) a 3D visualization of the same crater in the glaze structure (inner side view).

Table 2

Comparison of experimental LIBS and  $\mu$ CT values of glaze layer thickness.

Crater No.	Glaze layer interface	Depth of the ablation crater		
		predicted (LIBS)	reference ( $\mu$ CT)	$\Delta$
	number of pulses	[ $\mu$ m]	[ $\mu$ m]	[ $\mu$ m]
1	54	222	237	15
2	54	222	226	4
3	41	204	214	10
4	73	248	266	18
5	59	229	259	30
6	62	233	238	5
7	54	222	205	17
8	51	218	219	1
9	51	218	211	7
10	60	230	234	4
Average	56	225	231	11
SD	8	12	20	
RSD	15%	5%	8%	

Table 2. The RSD of this method was approximately 10% with respect to the  $\mu$ CT scan resolution and a manual procedure.

### 3.3. Calibration of the depth to the number of laser pulses

The aim of this work is an implementation of  $\mu$ CT into the accurate routine LIBS depth calibration. In order to fulfil this aim, the next step was the construction of a proper calibration function. For this reason,

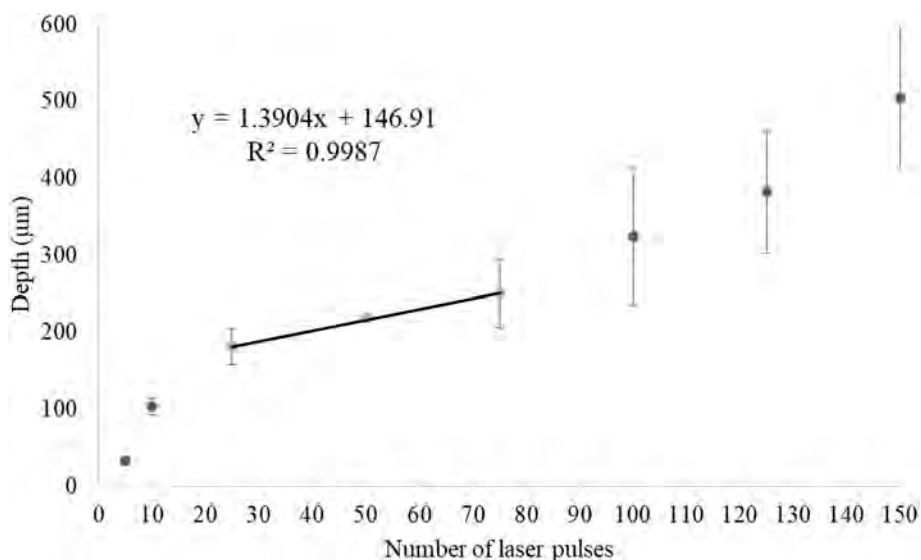


Fig. 5. Function of the laser ablation crater depth on the number of laser pulses with a linear part used for calibration.

series of laser ablation craters were prepared at suitable places of the ceramic fragment. Ablation craters were always created in three repetitions by applying 5, 10, 25, 50, 75, 100, 125 and 150 pulses. The  $\mu$ CT data were then evaluated for each of the three repetitions for a given number of pulses and a function of the depth on the number of laser pulses was constructed. The resulting function is in agreement with LIBS depth profiles (Fig. 3), and the different steps are evident (Fig. 5).

It is clearly visible that the function of the ablation depth is non-linear during the first 25 pulses, and it is characterized by a faster penetration into the glaze layer. The depth of the crater increases rapidly, which is in agreement with the lead signal in the LIBS depth profile (Fig. 3). This corresponds with the considered surface effects (see 3.1.1.) and it can seriously complicate the calibration in thin layers. In our case, the depth of 182  $\mu$ m reached by the 25th pulse is a very significant part in comparison with the entire layer thickness (Fig. 6a). Therefore, it is evident that the influence of physical and chemical conditions of the surface is critical for the reliability of the depth profile evaluation.

In the range from 25 to 75 pulses, the ablation of the glaze layer bulk is expected to occur (see 3.1.2). Linear function is observed in this range of laser pulses which allows a construction of a reliable calibration line. Because this part represents an interval up to the breakpoint in the depth profile (Fig. 3), it also limits the applicability of the calibration. In other words, a thick-layer standard can be used for the

calibration of the measurement of thin layers, but not *vice versa*. In our case, the calibration range is linear from 25 to 75 pulses and it corresponds to a depth range from 182 to 252  $\mu$ m. In this range, the average ablation rate is 1.39  $\mu$ m per pulse. A progressive penetration through the glaze layer is clearly visible in the  $\mu$ CT slices of the craters created by 25, 50 and 75 pulses respectively (see Fig. 6).

Between 75 and 150 pulses, the laser beam passes through the interface into the ceramic matrix and the ablation rate changes again. Although the ablation rate during the penetration through the interface probably changes continuously it is practically impossible to determine its exact value pulse by pulse. At the same time, the increase of the crater depth measurement standard deviation is noticeable (see error bars on the calibration curve). While RSD during the ablation of the glaze layer does not exceed 10%, it increases above 20% after the penetration to the ceramic matrix. It can be attributed to a specific ablation process in ceramics (surprisingly, the uncertainty is compensated for a large number of pulses, see 3.2).

#### 3.4. Determination of glaze layer thickness

Finally, the obtained calibration function was used for a calculation of experimental results of the glaze layer thickness. LIBS experimental values for ten depth profiles (see 3.1) compared to those determined from the  $\mu$ CT data are summarized in Table 2. It should be noted that the results are in a mutual agreement as the variations of the

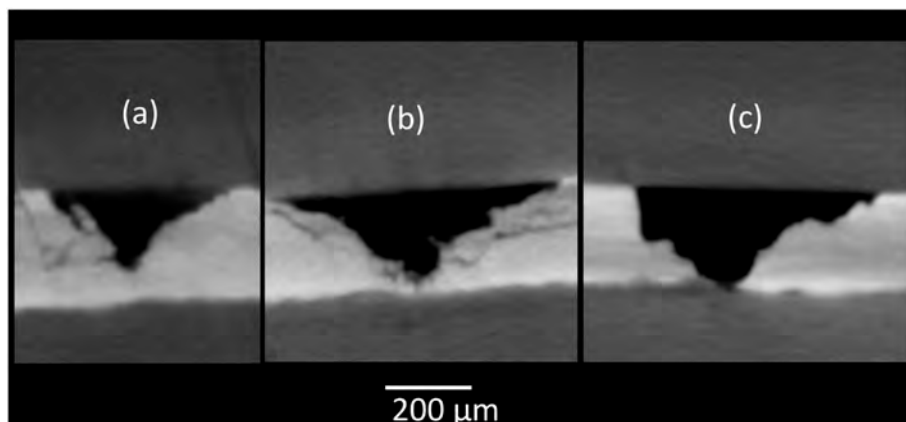


Fig. 6.  $\mu$ CT slices of ablation craters of the linear calibration points: (a) 25 pulses, (b) 50 pulses and (c) 75 pulses.

determined thicknesses are relatively small. The results are characterized by a relatively low RSD which for  $\mu$ CT does not exceed 10% (see 3.2) and for LIBS depth profiling reaches approximately 5%. The uncertainty of the break point was determined from the smoothed depth profile. The calculated RSD (in Table 2) for the series of ten LIBS depth profiles carried out in different points represents the uniformity of the sample glaze layer thickness. It is evident from the results that the uncertainty of this method is comparable to the fluctuations of individual measurements (RSD 5% for LIBS and 8% for  $\mu$ CT). These results indicate that the glaze layer thickness should be considered uniform.

#### 4. Conclusions

In this work, a novel approach in the calibration of LIBS depth profiles using  $\mu$ CT was suggested. The LIBS depth profiling was performed on a glazed fragment of archaeological ceramics where the lead glaze layer was easily distinguishable by  $\mu$ CT. LIBS depth profiles were constructed for Pb I 405.81 nm (high content in glaze layer) and K I 766.49 nm (higher content in the ceramic matrix) emission lines using 150 laser pulses.

It was found out that four different steps can be clearly distinguished in the depth profiles. During the first 25 pulses, the signal was influenced mainly by the surface effects and the ablation was characterized by a rather high ablation rate. After 25 laser pulses, the ablation of the glaze layer bulk occurred, the lead signal reached its maximum and then it was slowly decreasing. In the range from 25 to 75 laser pulses, a constant ablation rate was observed, and this part allowed for a construction of a reliable linear calibration function. The breakpoint in the lead signal profile indicates that the centre of the laser beam reached the bottom of the glaze layer. Therefore, this point is considered a moment of penetration through the interface. After 75 laser pulses, the laser beam thoroughly penetrated into the ceramic matrix.

The visualization of the ablation process by  $\mu$ CT allows observing the laser beam passing through the glaze, the interface and the ceramic matrix. The ablation rate was determined during different steps of the sample ablation. These steps were characterized by a different ablation rate, therefore, a more precise depth profiling calibration was possible. Experimental results of the glaze layer thickness were calculated based on the obtained calibration function.

The received results were in a mutual agreement as the variations of determined thicknesses were relatively small. Based on the results, the analyzed glaze layer thickness was considered to be uniform. The suggested approach is unique and it may be further used in the depth profile calibration regardless of the analyzed sample.

The method is primarily limited to the layers providing a sufficient contrast in  $\mu$ CT which is given by their different X-ray absorption coefficients. The layers should be sufficiently thick with respect to the  $\mu$ CT resolution. On the other hand, as was demonstrated, very narrow and deep ablation craters can also be investigated.

#### Author statement

Marie Novotná – Methodology, Investigation, Writing - original draft, Writing - review & editing.

Eva Zikmundová – Conceptualization, Methodology.

Pavel Pořízka – Supervision, Data curation.

Tomáš Zikmund – Supervision, Data curation.

Karel Novotný – Writing - original draft, Writing - review & editing.

Jozef Kaiser – Supervision.

#### Declaration of Competing Interest

The authors declare no conflict of interest.

#### Acknowledgement

This research was carried out under the project CEITEC 2020 (LQ1601) with financial support from the Ministry of Education, Youth and Sports of the Czech Republic under the National Sustainability Programme II and CzechNanoLab Research Infrastructure supported by MEYS CR (LM2018110). JK acknowledges the support of the Brno University of Technology on the frame of grant FSI-S-20-6353. We highly acknowledge David Prochazka for the help with LIBS measurements, Markéta Tesařová for the help with  $\mu$ CT data evaluation and Markéta Holá for the LA-ICP-MS measurements.

#### References

- [1] A. Pollard, *Analytical Chemistry in Archaeology*, Cambridge University Press, New York, 2007.
- [2] K. Muller, H. Stege, Evaluation of the analytical potential of laser-induced breakdown spectrometry (LIBS) for the analysis of historical glasses, *Archaeometry* 45 (2003) 421–433, <https://doi.org/10.1111/1475-4754.00119>.
- [3] V. Lazic, M. Vadrucchi, R. Fantoni, M. Chiari, A. Mazzinghi, A. Gorghinian, Applications of laser-induced breakdown spectroscopy for cultural heritage: a comparison with X-ray fluorescence and particle induced X-ray emission techniques, *Spectrochim. Acta B At. Spectrosc.* 149 (2018) 1–14, <https://doi.org/10.1016/j.sab.2018.07.012>.
- [4] A. Martínez-Hernández, M. Oujja, M. Sanz, E. Carrasco, V. Detalle, M. Castillejo, Analysis of heritage stones and model wall paintings by pulsed laser excitation of Raman, laser-induced fluorescence and laser-induced breakdown spectroscopy signals with a hybrid system, *J. Cult. Herit.* 32 (2018) 1–8, <https://doi.org/10.1016/j.culher.2018.02.004>.
- [5] M. Alberghina, R. Barraco, M. Brai, D. Fontana, L. Tranchina, LIBS and XRF analysis for a stratigraphic study of pictorial multilayer surfaces, *Periodico Mineral.* 84 (2015) 569–589, <https://doi.org/10.2451/2015PM0024>.
- [6] E. Kaszewska, M. Sylwestrzak, J. Marczak, W. Skrzeczanowski, M. Iwanicka, E. Szmit-Naud, D. Anglos, P. Targowski, Depth-resolved multilayer pigment identification in paintings: combined use of laser-induced breakdown spectroscopy (LIBS) and optical coherence tomography (OCT), *Appl. Spectrosc.* 67 (2013) 960–972, <https://doi.org/10.1366/12-06703>.
- [7] M. Mateo, T. Ctvrtnickova, G. Nicolas, Characterization of pigments used in painting by means of laser-induced plasma and attenuated total reflectance FTIR spectroscopy, *Appl. Surf. Sci.* 255 (2009) 5172–5176, <https://doi.org/10.1016/j.apsusc.2008.08.040>.
- [8] A. Hrdlička, L. Zaorálková, M. Galiová, T. Čtvrtníčková, V. Kanický, V. Otruba, K. Novotný, P. Krásenský, J. Kaiser, R. Malina, K. Páleníková, Correlation of acoustic and optical emission signals produced at 1064 and 532 nm laser-induced breakdown spectroscopy (LIBS) of glazed wall tiles, *Spectrochim. Acta B At. Spectrosc.* 64 (2009) 74–78, <https://doi.org/10.1016/j.sab.2008.10.043>.
- [9] K. Melessanaki, M. Mateo, S. Ferrence, P. Betancourt, D. Anglos, The application of LIBS for the analysis of archaeological ceramic and metal artifacts, *Appl. Surf. Sci.* 197–198 (2002) 156–163, [https://doi.org/10.1016/S0169-4332\(02\)00459-2](https://doi.org/10.1016/S0169-4332(02)00459-2).
- [10] I. Marcaida, M. Maguregui, H. Morillas, N. Prieto-Taboada, M. Veneranda, S. Fdez-Ortiz de Vallejuelo, A. Martellone, B. De Nigris, M. Osanna, J. Madariaga, In situ non-invasive multianalytical methodology to characterize mosaic tesserae from the House of Gilded Cupids, Pompeii, *Heritage Sci.* 7 (2019), <https://doi.org/10.1186/s40494-019-0246-1>.
- [11] F. Fortes, J. Moros, P. Lucena, L. Cabalín, J. Laserna, Laser-induced breakdown spectroscopy, *Anal. Chem.* 85 (2012) 640–669, <https://doi.org/10.1021/ac303220r>.
- [12] A. Botto, B. Campanella, S. Legnaioli, M. Lezzneri, G. Lorenzetti, S. Pagnotta, F. Poggialini, V. Palleschi, Applications of laser-induced breakdown spectroscopy in cultural heritage and archaeology: a critical review, *J. Anal. At. Spectrom.* 34 (2019) 81–103, <https://doi.org/10.1039/C8JA00319J>.
- [13] J.M. Vadillo, J.J. Laserna, A. Miziolek, V. Palleschi, I. Schechter, *Chemical imaging of surfaces using LIBS, Laser-Induced Breakdown Spectroscopy (LIBS): Fundamentals and Applications*, Cambridge University Press, New York, 2006, pp. 254–281.
- [14] L. Jolivet, M. Leprince, S. Moncayo, L. Sorbier, C. Lienemann, V. Motto-Ros, Review of the recent advances and applications of LIBS-based imaging, *Spectrochim. Acta B At. Spectrosc.* 151 (2019) 41–53, <https://doi.org/10.1016/j.sab.2018.11.008>.
- [15] J. Kaiser, K. Novotný, M. Martin, A. Hrdlička, R. Malina, M. Hartl, V. Adam, R. Kizek, Trace elemental analysis by laser-induced breakdown spectroscopy—biological applications, *Surf. Sci. Rep.* 67 (2012) 233–243, <https://doi.org/10.1016/j.surfrep.2012.09.001>.
- [16] P. Modlitbová, P. Pořízka, J. Kaiser, Laser-induced breakdown spectroscopy as a promising tool in the elemental bioimaging of plant tissues, *TrAC Trends Anal. Chem.* 122 (2020) 1–10, <https://doi.org/10.1016/j.trac.2019.115729>.
- [17] O. Syta, B. Wagner, E. Bulska, D. Zielińska, G. Zukowska, J. Gonzalez, R. Russo, Elemental imaging of heterogeneous inorganic archaeological samples by means of simultaneous laser induced breakdown spectroscopy and laser ablation inductively coupled plasma mass spectrometry measurements, *Talanta.* 179 (2018) 784–791, <https://doi.org/10.1016/j.talanta.2017.12.011>.
- [18] D. Anderson, C. McLeod, T. English, A. Smith, Depth profile studies using laser-

- induced plasma emission spectrometry, *Appl. Spectrosc.* 49 (2016) 691–701, <https://doi.org/10.1366/0003702953964516>.
- [19] J. Vadillo, J. Laserna, Depth-resolved analysis of multilayered samples by laser-induced breakdown spectrometry, *J. Anal. At. Spectrom.* 12 (1997) 859–862, <https://doi.org/10.1039/a607622j>.
- [20] K. Novotný, T. Vaculovič, M. Galiova, V. Otruba, V. Kanický, J. Kaiser, M. Liška, O. Samek, R. Malina, K. Páleníková, The use of zinc and iron emission lines in the depth profile analysis of zinc-coated steel, *Appl. Surf. Sci.* 253 (2007) 3834–3842, <https://doi.org/10.1016/j.apsusc.2006.08.047>.
- [21] L. St-Onge, M. Sabsabi, Towards quantitative depth-profile analysis using laser-induced plasma spectroscopy: investigation of galvannealed coatings on steel, *Spectrochim. Acta B At. Spectrosc.* 55 (2000) 299–308, [https://doi.org/10.1016/S0584-8547\(00\)00146-4](https://doi.org/10.1016/S0584-8547(00)00146-4).
- [22] V. Kanický, V. Otruba, J. Mermet, Depth profiling of tin-coated glass by laser ablation inductively coupled plasma emission spectrometry with acoustic signal measurement, *Fresenius J. Anal. Chem.* 366 (2000) 228–233, <https://doi.org/10.1007/s002160050045>.
- [23] E. Pospíšilová, K. Novotný, P. Pořízka, D. Hradil, J. Hradilová, J. Kaiser, V. Kanický, Depth-resolved analysis of historical painting model samples by means of laser-induced breakdown spectroscopy and handheld X-ray fluorescence, *Spectrochim. Acta B At. Spectrosc.* 147 (2018) 100–108, <https://doi.org/10.1016/j.sab.2018.05.018>.
- [24] T. Čtvrtníčková, F. Fortes, L. Cabalín, V. Kanický, J. Laserna, Depth profiles of ceramic tiles by using orthogonal double-pulse laser induced breakdown spectrometry, *Surf. Interface Anal.* 41 (2009) 714–719, <https://doi.org/10.1002/sia.3077>.
- [25] A. López, G. Nicolás, M. Mateo, V. Piñón, M. Tobar, A. Ramil, Compositional analysis of Hispanic Terra Sigillata by laser-induced breakdown spectroscopy, *Spectrochim. Acta B At. Spectrosc.* 60 (2005) 1149–1154, <https://doi.org/10.1016/j.sab.2005.05.009>.
- [26] N. Mendes, I. Osticioli, J. Striava, A. Sansonetti, M. Becucci, E. Castellucci, Versatile pulsed laser setup for depth profiling analysis of multilayered samples in the field of cultural heritage, *J. Mol. Struct.* 924–926 (2009) 420–426, <https://doi.org/10.1016/j.molstruc.2009.01.047>.
- [27] G. Senesi, I. Carrara, G. Nicolodelli, D. Milori, O. De Pascale, Laser cleaning and laser-induced breakdown spectroscopy applied in removing and characterizing black crusts from limestones of Castello Svevo, Bari, Italy: a case study, *Microchem. J.* 124 (2016) 296–305, <https://doi.org/10.1016/j.microc.2015.09.011>.
- [28] B. Chide, S. Maurice, N. Murdoch, J. Lasue, B. Bousquet, X. Jacob, A. Cousin, O. Forni, O. Gasnault, P. Meslin, J. Fronton, M. Bassas-Portús, A. Cadu, A. Sournac, D. Mimoun, R. Wiens, Listening to laser sparks: a link between laser-induced breakdown spectroscopy, acoustic measurements and crater morphology, *Spectrochim. Acta B At. Spectrosc.* 153 (2019) 50–60, <https://doi.org/10.1016/j.sab.2019.01.008>.
- [29] X. Li, Z. Wang, Y. Fu, Z. Li, W. Ni, Wavelength dependence in the analysis of carbon content in coal by nanosecond 266 nm and 1064 nm laser induced breakdown spectroscopy, *Plasma Sci. Technol.* 17 (2015) 621–624, <https://doi.org/10.1088/1009-0630/17/8/02>.
- [30] J. Jia, H. Fu, Z. Hou, H. Wang, Z. Ni, Z. Wang, F. Dong, Z. Zhang, Analysis of element content in cement by Gaussian and flat-top laser-induced breakdown spectroscopy, *J. Phys. D: Appl. Phys.* 52 (2019), <https://doi.org/10.1088/1361-6463/ab3128>.
- [31] E. Pospíšilová, K. Novotný, P. Pořízka, J. Hradilová, J. Kaiser, V. Kanický, Influence of laser wavelength and laser energy on depth profiling of easel painting samples, *Chem. Pap.* 73 (2019) 2937–2943, <https://doi.org/10.1007/s11696-019-00803-z>.
- [32] J. Vadillo, J. Fernandez Romero, C. Rodriguez, J. Laserna, Depth-resolved analysis by laser-induced breakdown spectrometry at reduced pressure, *Surf. Interface Anal.* 26 (1998) 995–1000, [https://doi.org/10.1002/\(SICI\)1096-9918\(199812\)26:1395::AID-SIA4473.0.CO;2-D](https://doi.org/10.1002/(SICI)1096-9918(199812)26:1395::AID-SIA4473.0.CO;2-D).
- [33] L. Cabalín, D. Romero, J. Baena, J. Laserna, Saturation effects in the laser ablation of stainless steel in air at atmospheric pressure, *Fresenius J. Anal. Chem.* 365 (1999) 404–408, <https://doi.org/10.1007/s002160051631>.
- [34] A. Casal, R. Cerrato, M. Mateo, G. Nicolas, 3D reconstruction and characterization of laser induced craters by in situ optical microscopy, *Appl. Surf. Sci.* 374 (2016) 271–277, <https://doi.org/10.1016/j.apsusc.2015.11.249>.
- [35] P. Pořízka, I. Ročňáková, J. Klus, D. Prochazka, L. Sládková, P. Šperka, Z. Spotz, L. Čelko, K. Novotný, J. Kaiser, Estimating the grade of mg corrosion using laser-induced breakdown spectroscopy, *J. Anal. At. Spectrom.* 30 (2015) 2099–2106, <https://doi.org/10.1039/C5JA00257E>.
- [36] W. Kalender, *Computed Tomography: Fundamentals, System Technology, Image Quality, Applications*, 3rd rev., Publicis, Erlangen, 2011.
- [37] S. Rawson, J. Maksimcuka, P. Withers, S. Cartmell, X-ray computed tomography in life sciences, *BMC Biol.* 18 (2020), <https://doi.org/10.1186/s12915-020-0753-2>.
- [38] C. Tuniz, F. Zanini, *Microcomputerized Tomography (MicroCT) in Archaeology*, in: *Encyclopedia of Global Archaeology*, Springer International Publishing, Cham, 2018, pp. 1–7, [https://doi.org/10.1007/978-3-319-51726-1\\_675-2](https://doi.org/10.1007/978-3-319-51726-1_675-2).
- [39] A. Hunt, *The Oxford Handbook of Archaeological Ceramic Analysis*, Oxford University Press, Oxford, 2017.
- [40] J. Baruchel, *X-Ray Tomography in Material Science*, Hermes Science, Paris, 2000.
- [41] M. Sanger, Investigating pottery vessel manufacturing techniques using radiographic imaging and computed tomography: studies from the late archaic American southeast, *J. Archaeol. Sci. Rep.* 9 (2016) 586–598, <https://doi.org/10.1016/j.jasrep.2016.08.005>.
- [42] A. Galmed, A. Du Plessis, S. Le Roux, E. Hartnick, H. Von Bergmann, M. Maaza, Three dimensional characterization of laser ablation craters using high resolution X-ray computed tomography, *Spectrochim. Acta B At. Spectrosc.* 139 (2018) 75–82, <https://doi.org/10.1016/j.sab.2017.11.011>.
- [43] C. Mercer, P. Anderson, G. Davis, Sequential 3D X-ray microtomographic measurement of enamel and dentine ablation by an Er: YAG laser, *Br. Dent. J.* 194 (2003) 99–104, <https://doi.org/10.1038/sj.bdj.4809883>.
- [44] V. Lazić, A. Trujillo-Vazquez, H. Sobral, C. Márquez, A. Palucci, M. Ciaffi, M. Pistilli, Corrections for variable plasma parameters in laser induced breakdown spectroscopy: application on archeological samples, *Spectrochim. Acta B At. Spectrosc.* 122 (2016) 103–113, <https://doi.org/10.1016/j.sab.2016.06.003>.
- [45] U. Panne, C. Haisch, M. Clara, R. Niessner, Analysis of glass and glass melts during the vitrification process of fly and bottom ashes by laser-induced plasma spectroscopy. Part I: Normalization and plasma diagnostics, *Spectrochim. Acta B At. Spectrosc.* 53 (1998) 1957–1968, [https://doi.org/10.1016/S0584-8547\(98\)00238-9](https://doi.org/10.1016/S0584-8547(98)00238-9).
- [46] L. Cabalín, D. Romero, J. Baena, J. Laserna, Effect of surface topography in the characterization of stainless steel using laser-induced breakdown spectrometry, *Surf. Interface Anal.* 27 (1999) 805–810, [https://doi.org/10.1002/\(SICI\)1096-9918\(199909\)27:9<805::AID-SIA576>3.0.CO;2-K](https://doi.org/10.1002/(SICI)1096-9918(199909)27:9<805::AID-SIA576>3.0.CO;2-K).
- [47] J.M. Vadillo, C.C. García, S. Palanco, J.J. Laserna, Nanometric range depth-resolved analysis of coated-steels using laser-induced breakdown spectrometry with a 308 nm collimated beam, *J. Anal. At. Spectrom.* 13 (1998) 793–797, <https://doi.org/10.1039/A802343C>.
- [48] V. Margetic, M. Bolshov, A. Stockhaus, K. Niemax, R. Hergenröder, Depth profiling of multi-layer samples using femtosecond laser ablation, *J. Anal. At. Spectrom.* 16 (2001) 616–621, <https://doi.org/10.1039/B100016K>.
- [49] A. Galmed, A. Kassem, H. Von Bergmann, M. Harith, A study of using femtosecond LIBS in analyzing metallic thin film–semiconductor interface, *Appl. Phys. B Lasers Opt.* 102 (2011) 197–204, <https://doi.org/10.1007/s00340-010-4144-1>.

PAPER [XVIII]

## Chemical and physical properties of Žďár nad Sázavou L chondrite and porosity differentiation using computed tomography

Dominika KALASOVÁ<sup>1</sup>, Tomáš ZIKMUND<sup>1\*</sup>, Pavel SPURNÝ<sup>2</sup>, Jakub HALODA<sup>3</sup>,  
Jiří BOROVIČKA<sup>2</sup>, and Jozef KAISER<sup>1</sup>

<sup>1</sup>CEITEC – Central European Institute of Technology, Brno University of Technology, Purkyňova 123, Brno, Czech Republic

<sup>2</sup>Astronomical Institute of the Czech Academy of Sciences, Fričova 298, 25165 Ondřejov, Czech Republic

<sup>3</sup>Czech Geological Survey, Geologická 6, 152 00 Prague, Czech Republic

\*Corresponding author: E-mail: tomas.zikmund@ceitec.vutbr.cz

(Received 13 May 2019; revision accepted 04 February 2020)

---

**Abstract**—A very bright and long bolide was observed over the eastern part of the Czech Republic during late local evening on December 9, 2014. This bolide was recorded by professional instruments in the Czech part of the European Fireball Network. Three meteorites weighing in total 87 g were found in the predicted area and were named Žďár nad Sázavou. The complete material composition of the meteorite was obtained from one cut-off piece using petrography, mineralogy, and scanning electron microscopy (together with X-ray energy dispersive spectroscopy and wavelength dispersive spectroscopy). X-ray computed tomography (CT) was applied on all pieces for the determination of their grain and bulk density, digitization of shape, and examination of the structural homogeneity. CT has proved its important role for nondestructive exploration of brecciated meteorites formed by distinct lithologies or petrological types. In this article, we discuss its limits in terms of structural and material resolution based on the correlation of state-of-the-art CT data and SEM images. Furthermore, we introduce a new way of air cavity quantification, which distinguishes the natural porosity of meteorite and cracks related to erosion processes. This helps to discuss the presence of weathering products based on comparison of the meteorite pieces found at different times after impact.

---

### INTRODUCTION

On Tuesday, December 9, 2014, at 16:16:45 UT (corresponding to the late local dusk, UT + 1 h), extensive areas of Central Europe, especially in the Czech Republic, western Slovakia, southern Poland, and northern Austria, were illuminated by a very bright fireball. At maximum, it reached –15 absolute magnitude and riveted the attention of thousands of casual witnesses not only in the Czech Republic but also in the whole of Central Europe, where it was clear during its passage. Moreover, it was clear at seven stations in the Czech part of the European Fireball Network (network description in Spurný et al. 2017). Thanks to these circumstances, it was possible to obtain many instrumental records of this spectacular bolide. High-resolution photographic

images and radiometric records proved to be essential for its complex and rigorous description (Spurný 2015; Spurný et al. 2016). Apart from a very precise determination of the atmospheric trajectory and heliocentric orbit, also the impact area of potential meteorites could be computed, and the ground distribution of meteorites could be modeled. This prediction was perfectly confirmed in reality because all three recovered meteorites were found almost exactly in the predicted location for the given meteorite masses (Spurný et al. 2016). In this respect, the Žďár nad Sázavou bolide belongs among the best instrumentally documented bolides connected with recovered meteorites (Spurný et al. 2020).

A description of a meteorite may include petrographic analyses (Hanna and Ketcham 2017; Flynn et al. 2018) such as various types of optical and

electron microscopies (Uesugi et al. 2010; Russell and Howard 2013; Hazeli et al. 2018), chemical and mineralogical analyses, spectroscopies, X-ray diffraction (Uesugi et al. 2013), pycnometry (Friedrich et al. 2013), and thermal and magnetic properties (Bartoschewitz et al. 2017).

X-ray computed tomography (CT) as a 3-D, nondestructive imaging method, is an excellent tool for inner inspection of extra-terrestrial materials (Hanna and Ketcham 2017; Hibiya et al. 2019). The first examined samples were inclusions in the Allende meteorite (Arnold et al. 1983). Distribution and quantification of clasts were studied in impact breccias from the Portales Valley fall (Rubin et al. 2001) and the Bosumtwi impact (Koeberl 2002). Subsurface fluid pathways and 3-D mineralogy were determined for the Martian Nakhla meteorite (Needham et al. 2013). Other CT analyses of some famous chondrites include the determination of bulk/air ratios, abundances of metal and other phases, and distribution and morphology of various inclusions. They are applied, for example, in studies of the Allende CV3ox (Ebel et al. 2016), the CV3.7 and the Mokoia CV3.6 (Hezel et al. 2013), the Renazzo CR2 (Hertz et al. 2003), the Murchison CM (Hanna et al. 2015), the Graves Nunataks 95209 (McCoy et al. 2006), the Mason Gully (Dyl et al. 2016), and the Itokawa regoliths from the Hayabusa mission (Noguchi et al. 2011). Various chondrules can be identified and studied via CT (Hertz et al. 2003). Besides, CT analysis is used for a detailed porosity analysis. Some authors determine the porosity from CT data simply as an amount of air in bulk material (Hanna and Ketcham 2017), but a common method is also to determine grain volume from pycnometry and bulk volume from CT (Friedrich et al. 2008; Wittmann et al. 2011; Dyl et al. 2016). However, cracks and pores connected to the surface are not included in this analysis, although they may constitute a non-negligible amount of the meteorite's total volume (Friedrich and Rivers 2013).

Here, we show an analysis of three fragments from the Žd'ár nad Sázavou meteorite fall which were found at different times after impact. Petrographic and mineralogy analyses are performed to describe the meteorite's composition. Volumes of the bulk of the material, metal, and troilite phases, and air are calculated based on CT data. The plausibility of quantification is verified with a scanning electron microscopy image, and porosity measurement is supplemented with pycnometry. We emphasize the difference between the inner enclosed air voids (natural porosity) and air cracks connected to the surface. We discuss the quantification of weathering and erosion by studying the volume of air cracks after impact.

## MATERIALS

Fast photometers (time resolution 5000 samples/s), which are integrated into each automated bolide camera used in the Czech part of the European Fireball Network (Spurný et al. 2006), took a detailed light curve of the observed bolide. Based on this, it is evident that the initial meteoroid was heavily fragmented in the last third of its luminous atmospheric flight. Consequently, the number of pieces that could reach the ground significantly increased. Naturally, it also increased the probability that at least some small meteorites are recovered.

The impact area is located in the low-populated Bohemian-Moravian Highlands close to the town of Žd'ár nad Sázavou, covered mostly by fields, grasslands, and forests. Two largest fragmentation events occurred at the heights of 40 and 37 km. A very complex model of the impact area comprising a distribution of individual meteorites deposited from each particular breakup directly visible on the light curve was created. It was possible thanks to precise trajectory data, position of individual breakups, and a wind profile which was available from balloon data and meteorological models. The resulting strewn field is very large. The distance between the largest predicted meteorite, whose mass should be slightly more than 1 kg (not recovered yet), and the smallest 1 g meteorites is more than 30 km. Fortunately, the ground was not snow covered when the meteorite fell, nor during the following days. Thanks to these favorable circumstances, the first meteorite (M1, 5.9 g) was found on December 20, 2014, shortly before the snow period. The second meteorite (M2, 39.3 g, Fig. 1) was found on January 12, 2015, after a quick snow melting and this searching window lasted only less than 1 week. The searching activities continued in spring, and the third meteorite (M3, 42.2 g) was found on May 2, 2015. All meteorites were found almost exactly in the location predicted for a given mass.

## METHODS

### Petrographic Analysis

The first piece of meteorite (M1) was subjected to a study of petrography, mineralogy, and microchemical composition. In addition, water loss during the drying process was measured for the second piece of meteorite (M2). The grain volume of all pieces was measured with a gas pycnometer AccuPyc11340, Micromeritics.

The sample was prepared in the form of polished thick and thin sections. Optical features and textural and mineralogical characteristics were studied using a LEICA DMLP petrographic microscope. Subsequently,



Fig. 1. The second piece (M2) of the Žďár nad Sázavou meteorite found on January 12, 2015. (Color figure can be viewed at [wileyonlinelibrary.com](http://wileyonlinelibrary.com).)

thick and thin sections were coated by 30 nm thick conductive layer of carbon for a scanning done with an electron microscope (SEM) TESCAN MIRA 3GMU (Czech Geological Survey in Prague, Czech Republic). This microscope was used for all micro-analytical studies and a collection of backscattered electron images (BSE) and elemental distribution maps.

BSE images were generated using an accelerating voltage of 15 kV and 2–10 nA beam current range. Mineral compositions were determined using Oxford Instruments AZtec Energy Automated analytical system with SDD X-ray energy dispersive detector X-MaxN 80 Premium (EDS) and X-ray wavelength dispersive detector Wave 700 (WDS). Both detectors were used for simultaneous EDS-WDS analysis with the following parameters: accelerating voltage 15 kV, beam current 20 nA, 0.090  $\mu\text{m}$  beam size. Acquisition live time for analysis of major elements by EDS was 60 s, output count rate was 110 kcps. Counting times for analysis of minor and trace elements by WDS system were 15 s, 20 s, or 30 s. A combination of natural and synthetic standards was used for standardization and calibration procedures.

The integrated electron backscattered diffraction system (EBSD), Oxford Instruments AZtec HKL Automated and Nordlys Nano detector, was employed to confirm microstructural characteristics of studied minerals, especially to distinguish alkali-bearing glass and feldspar where similar chemical composition can be expected. Analytical conditions were 15 mm working distance, 20 kV accelerating voltage, and 3.5 nA beam current.

AZtec Energy Automated software was used for a collection of multiple large area elemental distribution

maps covering entire thin and thick section areas in order to achieve most possible representativeness of collected data sets. Each elemental distribution map has a resolution of  $512 \times 512$  pixels, pixel size 1  $\mu\text{m}$  and each pixel represents a saved point X-ray spectrum. All collected X-ray elemental distribution maps were processed using dedicated analytical procedures (TrueMap and Pulse pile-up correction). As a result, peaks' positions were determined by deconvolution and background subtraction. Sets of elemental distribution maps from each sample covering entire areas of studied sections were merged into one data set for future processing. This method was used for the creation of "virtual samples," which allows us to analyze the mineral subsequently and chemical characteristics of the samples within the whole area of thin sections as well as on a micro scale. Mineral modes and average chemical composition of the presented minerals from studied areas were determined from virtual sample data sets by using the AZtec PhaseMap software module.

### X-Ray Computed Tomography

All three samples were scanned on a GE phoenix v|tome|x L240 system, equipped with a 240 kV microfocus X-ray tube and a high-contrast flat panel detector DXR250. The parameters of tomographic measurements were set according to the size of the meteorite piece: the acceleration voltage 150–160 kV, the tube current 110–190  $\mu\text{A}$ , the exposure time 500–750 ms, and 2000–2200 projections. The linear voxel size was 15  $\mu\text{m}$  for M1, 24  $\mu\text{m}$  for M2, and 28  $\mu\text{m}$  for M3. The tomographic reconstruction was realized using GE phoenix datos|x 2.0 software.

To determine which materials correspond to different gray values in CT data, an SEM image was correlated with a CT slice of the same region. First, meteorite M1 was cut and analyzed by SEM. Afterward, a CT scan of the sample was performed. Resulting CT data were oriented so that the slice corresponding to the previously obtained SEM image could be extracted.

The CT data of meteorites were segmented in order to obtain volumes of each distinguishable material component (Fe-Ni [metals], troilite, air cavities). The air cavities were segmented by standard global thresholding and separated to cracks which were connected to the surface, and to closed cavities called here voids. To get rid of the noise influence, the volume of detected cavities was computed only for objects with a volume larger than  $113000 \mu\text{m}^3$  for all samples, which corresponds to a sphere with a diameter of 60  $\mu\text{m}$ . To express the estimation of repeatability in a calculation of porosity, regions with each material were eroded and

dilated by 0.3 px and the porosity values' variation was calculated. The pore analysis was done to express the grain density of the meteorites (the mass was divided by the volume of meteorite without the air volume). Bulk density was calculated as the mass divided by the total volume.

The material phases were segmented by a trainable segmentation (Kalasová et al. 2017) using the random forest algorithm (Breiman 2001). Results of segmentations were processed in pore analysis module within VG Studio MAX 3.2 software (Volume Graphics, Germany).

## RESULTS

### Petrographic Analysis

The first two studied meteorite pieces M1 and M2 look fresh as they were found shortly after the observed fall (11 and 34 days). Only weak veins of weathering products on the surface of fusion crust and surrounding cracks on the surface were visible. The mass of the meteorite M2 was 41.08 g when it was found, and decreased to 39.25 g after drying. This drying, that is, water evaporation, took place in the office under normal conditions, that is, atmospheric pressure and room temperature. The equilibrium weight of 39.25 g was reached about 30 h after first weighing (still in the field) and 25 h after being at the office. The mass difference means that the pore space or the material absorbed 1.83 g of water having a total volume of 1830 mm<sup>3</sup>.

The third piece of meteorite M3 found 144 days after the fall was noticeably more affected by weathering, consequently it showed mostly the products of Fe-Ni phases and troilite oxidation. The weathering products filled a network of thin surface micro-fractures and cracks, and the surface of fusion crust is partially covered by a thin Fe-oxides layer. These observed weathering features indicate weathering grade W0 for the two early found meteorites and W1 grade for the third meteorite according to the classification of Wlotzka (1993).

Meteorites contain clearly visible and sharply defined chondrules and fine-grained matrix (images from SEM and CT in Figs. 2 and 3). Chondrule sizes vary from around 0.4 mm up to 7 mm. Recrystallization of a major part of the fine-grained matrix is visible in the thin section (Fig. 3).

Mineral modes obtained by AZtec Phase Map Analysis were recalculated into weight % and are presented in Table 1. Silicate minerals are represented mainly by olivine, low-Ca pyroxene, plagioclase, and alkalic glass. EBSD data were used for verification of

plagioclase and alkaline glass distinction, where some similarities of silicate minerals' chemical composition can be expected. Observed lack of Kikuchi band diffraction is typical for glass and all amorphous materials. We used it as a supportive criterion to distinguish presented glass and plagioclase grains.

Chondrules consist mainly of olivine (Fa<sub>20-27</sub>) mean Fa<sub>23.8</sub>, PMD-FeO 7.6 %,  $\sigma$ -Fa 3.4 mole%, n = 52; low-Ca pyroxene (Fs<sub>15-23</sub>Wo<sub>0.7-1.6</sub>) mean Fs<sub>19.5</sub> Wo<sub>1.33</sub>, Fs PMD 8.4%, Wo PMD 15.5%, n = 53. Alkali-bearing glass exhibits a wide range of chemical composition. Most of the secondary feldspar grains are <1  $\mu$ m in size; rarely, a few grains >1  $\mu$ m were observed. Other non-silicate minerals are represented by chromite, chlorapatite, troilite, kamacite, and taenite. The average Co amount in kamacite is 1.3 wt%; the mean deviation is 1.8%.

All three studied meteorites represent an L chondrite with average olivine and low-Ca pyroxene composition Fa<sub>23.8</sub>, Fs<sub>19.5</sub> (Bouvier et al. 2017). Based on calculated olivine PMD-FeO (7.6%) and  $\sigma$ -Fa (3.4 mole%) values and the presence of secondary feldspar grains with submicrometer size and isotropic glass, the studied meteorites were classified as the petrologic subtype 3.9 (Bouvier et al. 2017) following published classification criteria for ordinary chondrites (Huss et al. 2006).

Olivine and pyroxene in this L3.9 lithology show weak shock features represented by undulose extinction of olivine and orthopyroxene grains and the presence of irregular fractures corresponding to shock stage S2. The EBSD method did not confirm the presence of plagioclase-maskelynite conversion typical for higher shock stages (Stöffler et al. 1991).

### X-ray Computed Tomography

To assign gray values to individual materials in CT data, an SEM image was correlated with a corresponding CT slice (Figs. 2 and 3). Air voids and cracks are easy to distinguish as they have the same intensity as air, represented by the darkest gray values. Based on different X-ray absorption, Fe-Ni and troilite phases are distinguishable and have enough contrast to be further segmented from the bulk. Moreover, the glass is visible in chondritic parts of meteorite (especially in detailed view in Fig. 3). Throughout the bulk of meteorites, many chondrules are visible. The largest ones are more than 6 mm in diameter.

From CT data, the volumes of meteorite components, bulk and grain density, and derived characteristics were calculated (Table 2). Pore analysis detected air cavities (voids and cracks altogether) and determined the total porosity percentage. The cavities

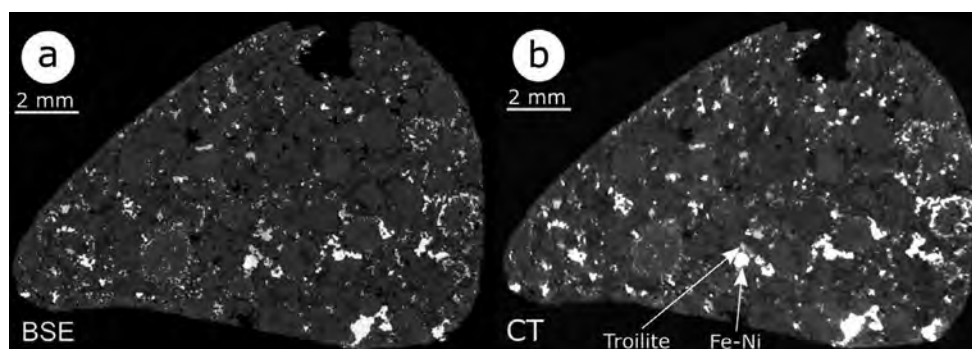


Fig. 2. The comparison of resolution and quality of (a) backscattered electron image (SEM) of studied thin section acquired by scanning electron microscope and (b) appropriate CT section (M1).

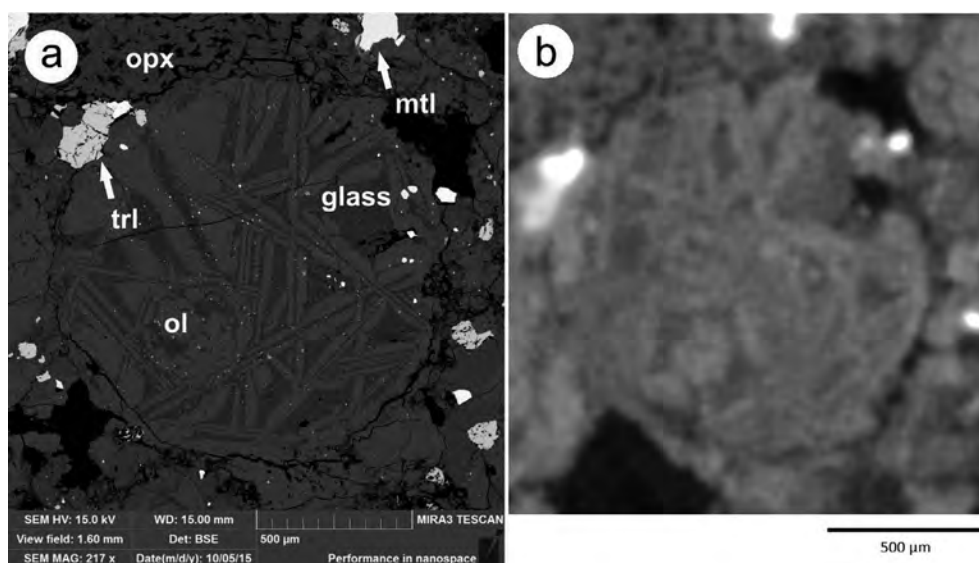


Fig. 3. Chondritic parts of meteorite (M1) with the presence of glass. a) SEM (BSE) image (ol, olivine; opx, low-Ca pyroxene; mtl, metal; trl, troilite), (b) CT image.

Table 1. Modal analysis obtained from thin and thick sections of the Žďár nad Sázavou meteorite M1.

Phase	Mineral modes (wt%)
Olivine	42.7
Low-Ca pyroxene	25.8
High-Ca pyroxene	4.2
Plagioclase	1.7
Glass	9.3
Troilite	6.7
Metal	8.2
Other	1.4

were separated into two groups, voids and cracks, according to the morphological character (Fig. 4). Pycnometric porosity was calculated using bulk volume from the CT measurement. For comparison, according

to Flynn et al. (2018), the average grain density of L chondrites is  $3.58 \pm 0.01 \text{ g/cm}^3$  and the average porosity is  $8.0 \pm 0.3\%$ . However, the porosities of individual samples vary in larger intervals, from 0.7% to 11% (Consolmagno et al. 2006, 2008).

Compact cavities enclosed inside of the inner structure were determined as air voids which represent a natural porosity of the original meteorite structure. The distribution of voids through the entire fragment is mostly uniform except a few clusters.

Long thin cavities connected to the outside surface were labeled as cracks. Detection of cracks is difficult due to their thin shape, and is also limited by the obtained resolution. Therefore, we expect that there are more cracks than it was possible to detect. These cracks are mostly interconnected, and they are found throughout the whole fragment. There are no preferred crack orientations in the samples. In the case of M2,

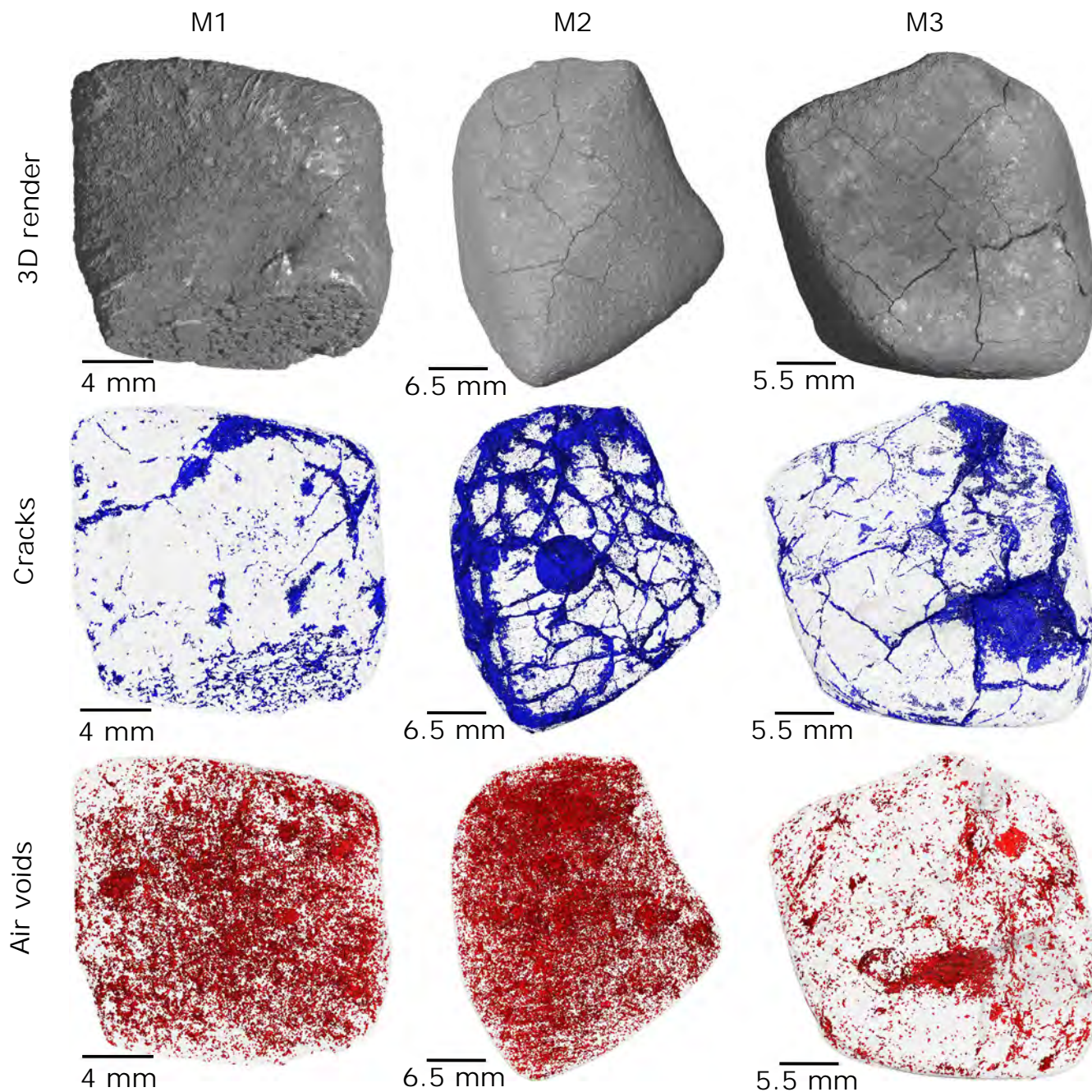


Fig. 4. Volume rendering of CT data of each Žďár nad Sázavou meteorite designated M1–M3. Air cracks connected to the surface are blue; air voids are red. (Color figure can be viewed at [wileyonlinelibrary.com](http://wileyonlinelibrary.com).)

these cavities surround a big spherical chondrule in the middle of the sample, and they represent nearly one continuous region within the entire sample (see Fig. 4 M2 cracks).

### DISCUSSION

It is convenient to compare SEM and CT slices to determine which materials correspond to different gray

values in CT data (Figs. 2 and 3). To do such a correlation, it is necessary first to image a polished section by 2D SEM and then perform the CT measurement and find the corresponding slice in CT data. SEM image identifies different materials in selected CT slices and subsequently, they can be segmented from the whole volume of a meteorite. The resolution of SEM images is generally higher than the one of CT images, but the technique is limited only to

Table 2. The volumes of inner structure components and physical characteristics of the Žďár nad Sázavou meteorite. The porosity of M1 could be affected by residual epoxy that could remain on the meteorite after cutting the section for SEM.

	M1	M2	M3
Sample volume (mm <sup>3</sup> )	1808	12906	13031
Mass (g)	5.60	39.25	41.70
Volume of Fe-Ni (mm <sup>3</sup> )	55	348	261
Volume of Fe-Ni (wt%)	7.37	6.65	4.69
Volume of troilite (mm <sup>3</sup> )	62	311	429
Volume of troilite (wt%)	5.10	3.65	4.74
Volume of other phases (mm <sup>3</sup> )	1673	12064	12274
Volume of cracks (mm <sup>3</sup> )	2.7 ± 1.5	70.4 ± 32.6	44.6 ± 16.3
Volume of cracks (vol%)	0.15 ± 0.08	0.55 ± 0.25	0.34 ± 0.12
Volume of air voids (mm <sup>3</sup> )	15.6 ± 7.5	112.9 ± 53.1	22.6 ± 10.1
Volume of air voids (vol%)	0.86 ± 0.41	0.87 ± 0.41	0.17 ± 0.08
Grain density from CT (g/cm <sup>3</sup> )	3.13	3.09	3.22
Grain density from pycnometry (g/cm <sup>3</sup> )	4.40	3.56	3.55
Bulk density (g/cm <sup>3</sup> )	3.10	3.04	3.20
Porosity—CT (%)	1.01 ± 0.50	1.42 ± 0.66	0.52 ± 0.20
Porosity—pycnometry (%)	7.26 ± 1.31	14.56 ± 0.22	9.73 ± 0.12

one 2-D slice and a small studied area. The resolution of the CT technique is limited mainly by sample size—the voxel size is usually about 1/1000 of the maximum sample's dimension. 3-D CT scans provide more representative data than SEM because they represent a full volume of studied samples. Moreover, a significant advantage of CT lies in the complete preservation of the sample (nondestructive method), a simple sample preparation without cutting, polishing, and coating of the sample.

In this study, only troilite and metal modal abundances (Table 2) were obtained by processing of CT data. It is not possible to recognize the main silicate phases using standard processing methods. We recalculated obtained vol% abundances for metal and troilite from CT data into wt% in order to compare them with modal data calculated from EDS-WDS elemental distribution maps. Obtained modal abundances of metal and troilite reflect higher heterogeneity of their presence for all three studied meteorites, but these data are more representative than modal data obtained from two polished sections.

The porosity calculated from CT data for all three meteorites shows values in a range of 0.5–1.4 vol%. The porosity calculated with grain volume from pycnometry shows higher values in a range of 7–15 vol%. The pycnometry always gives higher numbers of porosity than CT. It is in agreement with other studies where measurements of porosity were performed applying both CT and pycnometry (Friedrich et al. 2008, 2013; Wittmann et al. 2011). This suggests that a large amount of pores is not detected by CT. Nevertheless, CT brings a different perspective to the porosity in

terms of morphology and distribution of air cavities in 3-D. Also, the bulk volume obtained from CT is more precisely determined than with glass beads, Archimedes methods, or 3-D laser scanning (Britt and Consolmagno 2003; Li et al. 2012).

The porosity is contained rather in the voids than in cracks in M1 and M2 (these two were found relatively shortly after the impact, and they are not affected by weathering as much as M3). This suggests that the shock load on meteorites was very low. It is also confirmed by the presence of undulose extinction of olivines, the presence of small microcracks, and the absence of conversion of plagioclase to maskelynite (shock stage S2; Stöffler et al. 1991). The shock load of the impact had only a small influence on the distribution of intergranular space. Although cracks can be generated by the impact, the presence of intergranular spaces, especially in the matrix, is original and was not significantly changed by the impact.

The porosity of M3 is lower than M2. This trend is confirmed by both CT and pycnometry. The M2 and M3 samples are similar in size, shape, and character (both are individual, non-split pieces), but the M2 was found relatively shortly after the impact and the M3 was found about 4 months later. The presence of weathering products on the surface and within visible cracks in M3 indicate that a part of the cracks and air voids could be filled by weathering products and thus explains lower porosity. This statement is supported by CT data (Fig. 4) where a crack network directly connected with the surface allows for a migration of water and a subsequent formation and growth of weathering products. The lower porosity of M1 could

be due to residual epoxy that could remain on the meteorite after cutting the section for SEM.

CT technique also enables a detection of interesting structures or anomalies within the whole meteorite (such as in Bischoff et al. 2013) without destruction. In this study, there is a large chondrule in M2 surrounded by air cracks (Fig. 4 M2 cracks). Besides, the shape of the glass is visually distinguishable in chondrules (Fig. 3), but still too challenging to be segmented automatically. If only a 2-D imaging method of selected sections had been used, many similar anomalies or special occurrences would have been discovered randomly, or they would not have been discovered at all. For this reason, CT should become an important step in meteorite characterization in general.

## CONCLUSION

This work describes a material analysis of three recovered pieces of Žd'ár nad Sázavou meteorite (Czech Republic). The meteorite was classified as a L3.9 ordinary chondrite with a shock stage S2 and a weathering grade W0 (W1 for M3). CT data collected from all three pieces show textures typical for ordinary chondrites. Any other lithologies were not identified. In addition, the studied distribution and modal analysis of metal and troilite and their comparison with EDS data confirm the same class for all three meteorites.

Simultaneously, we demonstrate that state-of-the-art lab-based CT systems have a sufficient resolution and sensitivity to determine material composition by taking advantage of nondestructive testing and 3-D volume information. We show this on a corresponding CT cross section and SEM image of one meteorite piece. CT data show enough contrast between Fe-Ni and troilite inclusions and air cavities for an automatic identification.

Furthermore, we categorized the porosity of studied meteorites into two types. The first is related to closed pores in the inner structure which represent natural porosity of the meteorite. The second concerns the surface, is crack shaped, and shows weathering influence. A distinction between air voids (natural porosity) and cracks (weathering, etc.) is only possible via CT analysis. The difference in the porosity of similar samples found at different times of impact shows a rather strong presence of weathering products in the sample that was found the latest.

CT data and their processing is a unique way to study the internal structure of a meteorite, distribution of selected phases, and porosity and heterogeneity of individual pieces. This method is very important for nondestructive studies of meteorites or their fragments. High-resolution CT studies show a potential of a

nondestructive study of possible newfound meteorites, especially for brecciated meteorites formed by distinct lithologies or petrological types.

*Acknowledgment*—This work was supported by project CEITEC 2020 (LQ1601) with financial support from the Ministry of Education, Youth and Sports of the Czech Republic under the National Sustainability Programme II and Ceitec Nano+ project, CZ.02.01/0.0./0.0./16\_013/0001728 under the program OP RDE. The work of P. Spurný and J. Borovička was supported by Praemium Academiae from the Czech Academy of Sciences. Authors would also like to acknowledge the reviewers, Robert Macke and Jon Friedrich, for their efforts and comments during the review process.

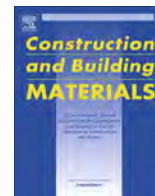
*Editorial Handling*—Prof. Alex Ruzicka

## REFERENCES

- Arnold J. R., Testa J. P., Friedman P. J., and Kambic G. X. 1983. Computed tomographic analysis of meteorite inclusions. *Science* 219:383–384.
- Bartoschewitz R., Appel P., Barrat J.-A., Bischoff A., Caffee M. W., Franchi I. A., Gabelica Z., Greenwood R. C., Harir M., Harries D., Hochleitner R., Hopp J., Laubenstein M., Mader B., Marques R., Morlok A., Nolze G., Prudencio M. I., Rochette P., Ruf A., Schmitt-Kopplin P., Seemann E., Szurgot M., Tagle R., Wach R. A., Welten K. C., Weyrauch M., and Wimmer K., and The Braunschweig Meteorite Consortium. 2017. The Braunschweig meteorite—A recent L6 chondrite fall in Germany. *Geochemistry* 77:207–224.
- Bischoff A., Dyl K. A., Horstmann M., Ziegler K., Wimmer K., and Young E. D. 2013. Reclassification of Villalbeto de la Peña—Occurrence of a winonaite-related fragment in a hydrothermally metamorphosed polymict L-chondritic breccia. *Meteoritics & Planetary Science* 48:628–640.
- Bouvier A., Gattacceca J., Agee C., Grossman J., and Metzler K. 2017. The Meteoritical Bulletin, No. 104. *Meteoritics & Planetary Science* 52:2284.
- Breiman L. 2001. Random forests. *Machine Learning* 45:5–32.
- Britt D. T. and Consolmagno G. J. S. J. 2003. Stony meteorite porosities and densities: A review of the data through 2001. *Meteoritics & Planetary Science* 38:1161–1180.
- Consolmagno G. J., Macke R. J., Rochette P., Britt D. T., and Gattacceca J. 2006. Density, magnetic susceptibility, and the characterization of ordinary chondrite falls and showers. *Meteoritics & Planetary Science* 41:331–342.
- Consolmagno G. J., Britt D. T., and Macke R. J. 2008. The significance of meteorite density and porosity. *Chemie der Erde* 68:1–29.
- Dyl K. A., Benedix G. K., Bland P. A., Friedrich J. M., Spurný P., Towner M. C., O'Keefe M. C., Howard K., Greenwood R., Macke R. J., Britt D. T., Halfpenny A., Thostenson J. O., Rudolph R. A., Rivers M. L., and Bevan A. W. R. 2016. Characterization of Mason Gully (H5): The second recovered fall from the Desert Fireball Network. *Meteoritics & Planetary Science* 51:596–613.

- Ebel D. S., Brunner C., Konrad K., Leftwich K., Erb I., Lu M., Rodriguez H., Crapster-Pregont E. J., Friedrich J. M., and Weisberg M. K. 2016. Abundance, major element composition and size of components and matrix in CV, CO and Acfer 094 chondrites. *Geochimica et Cosmochimica Acta* 172:322–356.
- Flynn G. J., Consolmagno G. J., Brown P., and Macke R. J. 2018. Physical properties of the stone meteorites: Implications for the properties of their parent bodies. *Geochemistry* 78:269–298.
- Friedrich J. M. and Rivers M. L. 2013. Three-dimensional imaging of ordinary chondrite microporosity at 2.6  $\mu\text{m}$  resolution. *Geochimica et Cosmochimica Acta* 116:63–70.
- Friedrich J. M., Macke R. J., Wignarajah D. P., Rivers M. L., Britt D. T., and Ebel D. S. 2008. Pore size distribution in an uncompacted equilibrated ordinary chondrite. *Planetary and Space Science* 56:895–900.
- Friedrich J. M., Ruzicka A., Rivers M. L., Ebel D. S., Thostenson J. O., and Rudolph R. A. 2013. Metal veins in the Kernouvé (H6 S1) chondrite: Evidence for pre- or syn-metamorphic shear deformation. *Geochimica et Cosmochimica Acta* 116:71–83.
- Hanna R. D. and Ketcham R. A. 2017. X-ray computed tomography of planetary materials: A primer and review of recent studies. *Geochemistry* 77:547–572.
- Hanna R. D., Ketcham R. A., Zolensky M., and Behr W. M. 2015. Impact-induced brittle deformation, porosity loss, and aqueous alteration in the Murchison CM chondrite. *Geochimica et Cosmochimica Acta* 171:256–282.
- Hazeli K., El Mir C., Papanikolaou S., Delbo M., and Ramesh K. T. 2018. The origins of Asteroidal rock disaggregation: Interplay of thermal fatigue and microstructure. *Icarus* 304:172–182.
- Hertz J., Ebel D. S., and Weisberg M. K. 2003. Tomographic study of shapes and metal abundances of Renazzo chondrule (abstract #1959). 34th Lunar and Planetary Science Conference. CD-ROM.
- Hezel D. C., Elangovan P., Viehmann S., Howard L., Abel R. L., and Armstrong R. 2013. Visualisation and quantification of CV chondrite petrography using micro-tomography. *Geochimica et Cosmochimica Acta* 116:33–40.
- Hibiya Y., Archer G. J., Tanaka R., Sanborn M. E., Sato Y., Iizuka T., Ozawa K., Walker R. J., Yamaguchi A., Yin Q.-Z., Nakamura T., and Irving A. J. 2019. The origin of the unique achondrite Northwest Africa 6704: Constraints from petrology, chemistry and Re–Os, O and Ti isotope systematics. *Geochimica et Cosmochimica Acta* 245:597–627.
- Huss G. R., Rubin A. E., and Grossman J. N. 2006. Thermal metamorphism in chondrites. In *Meteorites and the early solar system II*, edited by Lauretta D. S. and McSween H. Y. Tucson, Arizona: University of Arizona. pp. 567–586.
- Kalasová D., Mašek J., Zikmund T., Spurný P., Haloda J., Burget R., and Kaiser J. 2017. Segmentation of multi-phase object applying trainable segmentation. *The e-Journal of Nondestructive Testing* 2017.
- Koeberl C. 2002. High-resolution X-ray computed tomography of impactites. *Journal of Geophysical Research* 107:5089.
- Li S., Wang S., Li X., Li Y., Liu S., and Coulson I. M. 2012. A new method for the measurement of meteorite bulk volume via ideal gas pycnometry. *Journal of Geophysical Research: Planets* 117:E10.
- McCoy T. J., Carlson W. D., Nittler L. R., Stroud R. M., Bogard D. D., and Garrison D. H. 2006. Graves Nunataks 95209: A snapshot of metal segregation and core formation. *Geochimica et Cosmochimica Acta* 70:516–531.
- Needham A. W., Abel R. L., Tomkinson T., and Grady M. M. 2013. Martian subsurface fluid pathways and 3D mineralogy of the Nakhla meteorite. *Geochimica et Cosmochimica Acta* 116:96–110.
- Noguchi T., Nakamura T., Kinura M., Zolensky M. E., Tanaka M., Hashimoto T., Konno M., Nakato A., Ogami T., Fujimura A., Abe M., Yada T., Mukai T., Ueno M., Okada T., Shirai K., Ishibashi Y., and Okazaki R. 2011. Incipient space weathering observed on the surface of Itokawa dust particles. *Science* 333:1121–1125.
- Rubin A. E., Ulf-Møller F., Wasson J. T., and Carlson W. D. 2001. The Portales Valley meteorite breccia: Evidence for impact-induced melting and metamorphism of an ordinary chondrite. *Geochimica et Cosmochimica Acta* 65:323–342.
- Russell S. S. and Howard L. 2013. The texture of a fine-grained calcium–aluminium-rich inclusion (CAI) in three dimensions and implications for early solar system condensation. *Geochimica et Cosmochimica Acta* 116:52–62.
- Spurný P. 2015. Instrumentally documented meteorite falls: Two recent cases and statistics from all falls. *Proceedings of the International Astronomical Union* 10:69–79.
- Spurný P., Borovička J., and Shrbený L. 2006. Automation of the Czech part of the European fireball network: Equipment, methods and first results. *Proceedings of the International Astronomical Union* 2:121–130.
- Spurný P., Borovička J., Haloda J., Shrbený L., and Heinlein D. 2016. Two very precisely instrumentally documented meteorite falls: Zdar nad sazavou and stubenberg—Prediction and reality. *Meteoritics & Planetary Science* 51: A591.
- Spurný P., Borovička J., Mucke H., and Svoreň J. 2017. Discovery of a new branch of the Taurid meteoroid stream as a real source of potentially hazardous bodies. *Astronomy & Astrophysics* 605:A68.
- Spurný P., Borovička J., and Shrbený L. 2020. The Žďár nad Sázavou meteorite fall: Fireball trajectory, photometry, dynamics, fragmentation, orbit, and meteorite recovery. *Meteoritics & Planetary Science*. <https://doi.org/10.1111/maps.13444>.
- Stöffler D., Keil K., and Edward R. D. S. 1991. Shock metamorphism of ordinary chondrites. *Geochimica et Cosmochimica Acta* 55:3845–3867.
- Uesugi M., Uesugi K., and Oka M. 2010. Non-destructive observation of meteorite chips using quantitative analysis of optimized X-ray micro-computed tomography. *Earth and Planetary Science Letters* 299:359–367.
- Uesugi M., Uesugi K., Takeuchi A., Suzuki Y., Hoshino M., and Tsuchiyama A. 2013. Three-dimensional observation of carbonaceous chondrites by synchrotron radiation X-ray CT—Quantitative analysis and developments for the future sample return missions. *Geochimica et Cosmochimica Acta* 116:17–32.
- Wittmann A., Friedrich J. M., Troiano J., Macke R. J., Britt D. T., Swindle T. D., Weirich J. R., Rumble D. III, Lasue J., and Kring D. A. 2011. H/L chondrite LaPaz Icefield 031047—A feather of Icarus? *Geochimica et Cosmochimica Acta* 75:6140–6159.
- Wlotzka F. 1993. The Meteoritical Bulletin, No. 74. *Meteoritics* 28:146–153.

PAPER [XIX]



## Characterization of inner structure of limestone by X-ray computed sub-micron tomography

Dominika Kalasová<sup>a,\*</sup>, Karel Dvořák<sup>b</sup>, Marek Slobodník<sup>c</sup>, Dalibor Všíanský<sup>c</sup>, Tomáš Zikmund<sup>a</sup>, Jiří Dluhoš<sup>d</sup>, Rostislav Váňa<sup>d</sup>, Jaroslav Bureš<sup>b</sup>, Jozef Kaiser<sup>a</sup>

<sup>a</sup> CEITEC – Central European Institute of Technology, Brno University of Technology, Purkyňova 123, 612 00 Brno, Czech Republic

<sup>b</sup> Faculty of Civil Engineering, Brno University of Technology, Veveří 331/95, 602 00 Brno, Czech Republic

<sup>c</sup> Department of Geological Sciences, Faculty of Science, Masaryk University, Kotlářská 2, 611 37 Brno, Czech Republic

<sup>d</sup> TESCANA Brno, s.r.o., Libušina třída 1, 62300 Brno, Czech Republic

### HIGHLIGHTS

- X-ray computed tomography (CT) is used to visualize limestone inner structure.
- Limestone containing coarser cement of calcite with fluid inclusions is studied.
- Characterization of material is performed by classical petrographic methods.
- 3D distribution of fluid inclusions and air voids in volume is shown by CT.
- CT data are correlated with light microscopy and 3D EDS analysis using FIB-SEM.

### ARTICLE INFO

#### Article history:

Received 7 November 2017

Received in revised form 16 April 2018

Accepted 17 April 2018

Available online 25 April 2018

#### Keywords:

Limestone

Petrography

X-ray computed tomography

Fluid inclusions

Microthermometry

### ABSTRACT

Limestones are fundamental industrial and building materials. Sparry calcite as a principal petrographic component of limestones can contain fluid inclusions. A certain amount of fluid inclusions directly influences decarboxation which plays an important role in decarbonisation processes.

In this paper, a limestone with a high content of fluid inclusions and carbon was investigated. Presence of chlorine and alcaic elements was confirmed with microthermometry, mineralogical and chemical analyses. X-ray computed tomography with sub-micron resolution (CT) was applied to obtain a 3D distribution of cavities. CT data were correlated with some light microscopy images and also with the same sample's tomography data which were gathered using the 3D X-ray energy dispersive spectroscopy (3D EDS) by a scanning electron microscope equipped with a focused ion beam (FIB-SEM). The latter further determined dolomites and metals in the CT data of limestone.

© 2018 Elsevier Ltd. All rights reserved.

### 1. Introduction

Limestone is a very important industrial rock and a raw material. It is used for the production of lime and cement and also serves as a desulphurization of flue gases of large energy sources. It is also used as a filler in the manufacture of paper with high white balance requirements, in the chemical industry and, last but not least, as a fertilizer. Limestones occur in various sedimentary basin environments, hence they differ in their geological age, crystallinity, petrographic structure, chemical purity and in the porous structure as a result of lithofacial conditions. All of these properties influence not only their behaviour during firing process but also the reactivity with acids in the process of mutual reactions. Many scientific works have been focused on finding and describing the relationship of limestone properties to their behaviour [1–3].

In the process of firing of limestones, some volumetric changes occur, which significantly affects the decarbonation process, especially in shaft kilns. There is only a very small number of publications dealing with this issue and searching for some more general dependence of the limestone properties on their volume changes during firing. Wolter et al. carried out a relatively extensive study in this area on 21 limestone samples [4]. However, the available

\* Corresponding author.

E-mail addresses: [dominika.kalasova@ceitec.vutbr.cz](mailto:dominika.kalasova@ceitec.vutbr.cz) (D. Kalasová), [dvorak.k@fce.vutbr.cz](mailto:dvorak.k@fce.vutbr.cz) (K. Dvořák), [marek@sci.muni.cz](mailto:marek@sci.muni.cz) (M. Slobodník), [dalibor@sci.muni.cz](mailto:dalibor@sci.muni.cz) (D. Všíanský), [tomas.zikmund@ceitec.vutbr.cz](mailto:tomas.zikmund@ceitec.vutbr.cz) (T. Zikmund), [jiří.dluhos@tescan.cz](mailto:jiří.dluhos@tescan.cz) (J. Dluhoš), [rostislav.vana@tescan.cz](mailto:rostislav.vana@tescan.cz) (R. Váňa), [jaroslav.bures@gmail.com](mailto:jaroslav.bures@gmail.com) (J. Bureš), [jozef.kaiser@ceitec.vutbr.cz](mailto:jozef.kaiser@ceitec.vutbr.cz) (J. Kaiser).

works deal mostly with the expansion of pure calcite grains, possibly also with the influence of various impurities on this quantity. This relatively frequently observed phenomenon is related to the volumetric changes of limestone during firing, e.g. a loss of compactness due to the development of net cracks, so called decrepitation.

The process of decrepitation has been investigated by various authors, especially from the viewpoint of the influence of a particle size [5]. This phenomenon makes some types of limestone absolutely unusable for the production of lime. A similar issue was observed in the case of flue gas desulphurization by the fluid combustion technology [6].

The only reasonable way to explain the “decrepitation” of limestones is to take into account the presence of fluid inclusions in sparry carbonate minerals, mostly calcite that is a coarse crystalline component of limestones. Fluid inclusions are common objects in natural minerals. They originate as defects during the growth of crystalline lattice leaving voids which are filled by ambient solution (fluids). Consequently, natural crystal/mineral phases precipitate from this solution. Sparry calcite in most limestones is formed from simple pore-filling cement among allochems (particles forming structural framework of limestones – intraclasts, oolites, fossils and pellets of microcrystalline calcite). The sparry calcite crystallizes from pore solutions and its amount differs according to a particular type of limestones. Thanks to the presence of a particular genetic type of calcite cement, it is possible to observe various properties and behaviour of limestone within industrial processing.

One of standard methods for investigation of nature of fluids trapped inside inclusions is optical microthermometry. This method is based on the phase transitions during temperature changes and also on the interpretation and thermodynamic calculations of fluid properties [7,8]. In studies of micro and nanostructures of rocks, nano-detection methods are applied. The scanning electron microscopy (SEM) is commonly used for obtaining information about the morphology of the sample surface [9]. The transmission electron microscopy (TEM) shows a connection between fluid inclusions and crystal structure defects [10]. A sample can be only observed layer by layer, which are removed by a focused ion beam (FIB). The electron microscopy can be further supported by a quantitative analysis such as energy dispersive X-ray spectroscopy or wavelength dispersive X-ray spectroscopy [10,11]. They provide a good resolution below 1 nm [12], thus they enable the observation of structures in more detail than the previously mentioned petrographic methods.

Density discontinuities in materials have been studied using X-ray computed tomography (CT) [13,14]. CT is a non-destructive method applied for 3D visualizations of materials' inner structure [15,16]. A sample is placed on a rotational table and scanned with the X-ray from many angles of rotation to get X-ray projections [17]. On the basis of these projections, virtual slices through the sample are reconstructed. The slices are stacked together to get 3D data. Gray values in slices correspond to the linear attenuation coefficient of the material. Based on different X-ray attenuations, different materials can be distinguished, segmented and quantified [18,19]. Modern laboratory CT devices are capable of reaching a voxel resolution (voxel is a volumetric element of CT data) of hundreds of nm [20,21]. Nevertheless, an observation with a small voxel size is only possible with adequately small samples due to a smaller field of view.

CT has been applied in various fields in geology, from hydrology, soil science, geodynamics up to planetary science. This technique is used to visualize the distribution and determination of a volume fraction in different phases of rock [22,23]. It has been applied for the detection of nano-inclusions of solids and fluid inclusions in diamonds [24], for the detection of cracks in rocks

[25] and even for the identification of phases inside fluid inclusions [26]. The CT is often combined with various petrographic methods [11,24,25].

This paper introduces a novel approach for investigation of the limestone's inner structure. It is focused on the identification and quantification of air voids and fluid inclusions, which play an important role in the decrepitation of limestone during firing. For this investigation, the laboratory-based X-ray computed tomography that provides a sufficiently high resolution and sensitivity to image fluid inclusions was applied. CT data reveal some parameters (such as the volume fraction of inclusions and their 3D distribution) which have not been determined so far by any other method. This approach was demonstrated on a selected limestone sample which was subjected to both chemical and mineralogical analyses and to microthermometry. To interpret the CT data correctly, also the two following techniques were used. Firstly, the light microscopy (LM) was used to verify the inclusions detected in CT data. Secondly, the serial-sectioning 3D analysis with X-ray energy dispersive spectroscopic analysis (3D EDS) by a scanning electron microscope equipped with a focused ion beam (FIB-SEM) was applied as a supplementary method for the determination of sample composition. As a consequence, this paper presents a unique combination of these three imaging techniques which were implemented on one sample in a special order showing a correlation between the outputs.

## 2. Materials

26 samples of limestones coming from various locations and geological units were collected. They differ in structure, petrographic character and chemical composition. Chemical and mineralogical analyses were made on all samples, the procedures were the same as described further in Section 3.1. The LM was applied on samples which might contain fluid inclusions. For the investigation, a sample which contained coarser cement of calcite (sparry calcite) and plenty of fluid inclusions was selected. The statement was based on the highest amount of chlorine and the LM (Fig. 1).

The examined sample was a hard, compact limestone classified as bioclastic grainstone according to Dunham classification [27]. It had been taken from a limestone deposit near Koněprusy, Czech Republic, from Lower Devonian sedimentary sequence of the Czech Karst area. The sample was prepared in several forms corresponding to the employed methods: homogenized powder of the rock

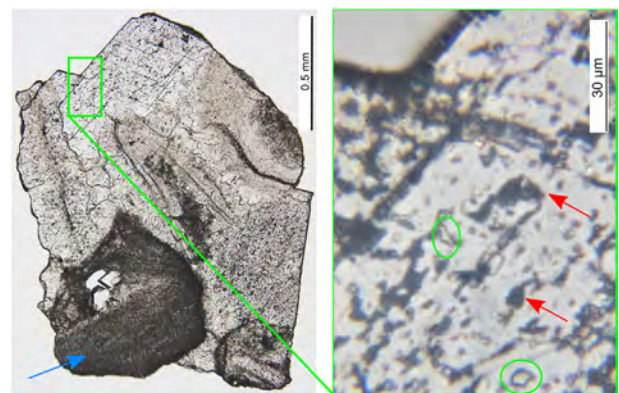


**Fig. 1.** Fragment of the double-sided polished limestone section from LM shows an enormous number of fluid inclusions spread within dotted brighter areas of sparry calcite. Among tiny black dots in calcite (defects in crystal lattice, pointed by red arrow), dominate the fluid inclusions (circled in green). Dark areas (pointed by the blue arrow) present allochems. (For interpretation of the references to colour in this figure legend, the reader is referred to the web version of this article.)

was used for a bulk chemical analysis and a double-sided polished 80  $\mu\text{m}$  thin section for LM, microthermometry and CT.

### 3. Methods

Petrographic, mineralogical and chemical analyses together with microthermometry were performed to achieve a complete petrographic description of the sample. In order to examine the same piece of the sample, one thin section was scanned with the CT and an area rich in fluid inclusions selected with the LM (detail in Fig. 1) was examined with 3D EDS analysis.

#### 3.1. Petrographic, mineralogical and chemical analysis

Fundamental petrographic and mineralogical observations of rocks were performed on thin sections with an optical microscope Olympus BX51. To avoid an inaccurate identification of fluid inclusions in the LM, a statistical evaluation was made followingly: the average number of inclusions was found out based on their counting in several focused planes in sectors  $20 \times 20 \mu\text{m}^2$  throughout the sample and then recalculated to the area of interest  $100 \times 70 \mu\text{m}^2$ .

For the mineralogical analysis, it was necessary to remove  $\text{CaCO}_3$  due to a high purity of the selected limestone. An insoluble residue was obtained by limestone dissolution in acetic acid using a slightly modified method according to Jeppsson and Dalton [28,29]. The total limestone dosage was 1500 g. The acetic acid concentration was 10% and was maintained by a pH measurement throughout the dissolution time. The total dissolution time was 3 months at a stable temperature of 21  $^\circ\text{C}$ . After the limestone dissolution had been finished, the insoluble residue was washed several times with distilled water, dried at room temperature and analysed. A XRD analysis was carried out using a Panalytical Empyrean X-ray diffractometer with a Cu anode (current of 40 mA, voltage of 45 kV),  $0.013^\circ$  2Theta step size, 298.09 s scan step time in continuous scanning mode. Data were processed with the HighScore+ software with PDF 2 and ICSD 2012 databases. Only qualitative analysis was performed.

To calculate the weight percent of major elements or oxides, a chemical analysis of the limestone samples was carried out using several supplementary methods: the gravimetric analysis, atomic absorption spectroscopy (AAS, instrument iCE™ 3500) and X-ray fluorescence spectroscopy (XRF, instrument Panalytical Axios). The method of the determination is always given for the relevant oxide/element in Table 1.

#### 3.2. Microthermometry

Thin sections and doubly polished thin sections (thickness 80  $\mu\text{m}$ ) were prepared for fluid inclusion studies. The only relevant positions for an investigation of fluid inclusions were growth zones, short trails and clusters. Linkam stage THMSG600 mounted on Nikon Eclipse80i was used for microthermometric measurements calibrated by synthetic fluid inclusions. Measured temperatures were  $(0.0 \pm 0.1)^\circ\text{C}$  (melting point of pure  $\text{H}_2\text{O}$ ),  $(-21.2 \pm 0.2)^\circ\text{C}$

$^\circ\text{C}$  (eutectic melting point of  $\text{H}_2\text{O}-\text{NaCl}$ ) and  $(-56.6 \pm 0.2)^\circ\text{C}$  (temperature of  $\text{CO}_2$  melting in  $\text{H}_2\text{O}-\text{CO}_2$  fluid system) of synthetic standards. The estimated accuracy of measurements on samples was within  $\pm 0.1^\circ\text{C}$  during freezing runs. The melting temperature of ice ( $T_m$ ) had to be measured to calculate salinity and also the eutectic temperature ( $T_e$ ) to assess the fluid system composition. The salinity of solutions in aqueous inclusions was calculated according to Bodnar [30]. Programmes of the FLUIDS 1 [31] were used for calculations of fluid density.

#### 3.3. 3D EDS analysis

The serial-sectioning 3D analysis with X-ray energy dispersive spectroscopic analysis (3D EDS) by a scanning electron microscope equipped with a focused ion beam (FIB-SEM) was applied on the area defined by the earlier results from the CT and LM. Then, an analysis using a TESCAN FERA 3  $\text{Xe}^+$  Plasma FIB-SEM [32] equipped with an EDAX Octane Elite energy-dispersive X-ray spectrometer was carried out. The sample had been carbon-coated in order to prevent charging artefacts. The region of interest (ROI) was identified on the basis of the correlative electron and light microscopy. The ROI was cropped by FIB (300 nA at 30 keV) to avoid shadowing and backscattering of analytical signal in the ROI surroundings. The sample surface was protected by placing a thin silicon mask on the top of it. This way, a clean FIB cross section without curtaining artefacts was obtained (Fig. 2).

The ROI was sliced in order to acquire 3D data (using 100 nA FIB current). A volume of  $125 \times 125 \times 50 \mu\text{m}^3$  was gradually sliced off with a step of  $0.5 \times 0.5 \times 0.5 \mu\text{m}^3$ . Afterwards, each slice was analysed as follows: backscattered electron (BSE) image, EDS mapping and full X-ray spectra storage for each voxel. The electron and EDS data acquisition was done at 10 keV and 20 nA SEM beam current. During post-processing, from each slice the individual elemental maps for selected elements were extracted. HyperSpy toolbox [33] was used to obtain 3D elemental maps and then they were correlated with CT data. The 3D correlation was done using ORS Visual SI software.

#### 3.4. X-ray computed tomography

The sample was scanned using the RIGAKU Nano3DX device with Mo target operating at 50 kV,  $3300 \times 2500 \text{ px}^2$  X-ray CCD camera and  $0.27 \times 0.27 \mu\text{m}^2$  pixel size. An exposure time of 20 s was used, the number of projections was 800. Binning 2 was set (information from  $2 \times 2 \text{ px}^2$  area was summed up) to reach the linear voxel size of 0.53  $\mu\text{m}$ . The tomographic reconstruction was realized using RIGAKU software. Data after reconstruction were filtered with nonlocal means filter for noise removal [34]. In CT data, a region of  $456 \times 41 \times 259 \mu\text{m}^3$  (the total volume of area without outer air was  $4.5 \times 106 \mu\text{m}^3$ ) was selected for further analysis in VGStudio Max 3.0. The darkest cavities were segmented by global thresholding, where the threshold was chosen manually by an operator. The minimum volume of cavity was set to 8 voxels. Furthermore, CT data were correlated with the 3D EDS analysis to determine several occurrences of Mg rich regions. These were seg-

**Table 1**

Chemical analysis of the limestone sample (LOI – loss of ignition, GA – gravimetric analysis, AAS – atomic absorption spectroscopy, XRF – X-ray fluorescence microscopy).

Element/oxide	wt [%]	Method	Element/oxide	wt [%]	Method
CaO	55.24	GA	$\text{K}_2\text{O}$	0.0039	GA
$\text{SiO}_2$	0.06	GA	$\text{SO}_3$	0.010	AAS
$\text{Al}_2\text{O}_3$	0.02	GA	Cl	62 [ppm]	GA
MgO	0.47	GA	Others	0.099	GA
$\text{Fe}_2\text{O}_3$	0.04	XRF	LOI (1000 $^\circ\text{C}$ )	44.05	GA
$\text{Na}_2\text{O}$	0.007	GA			

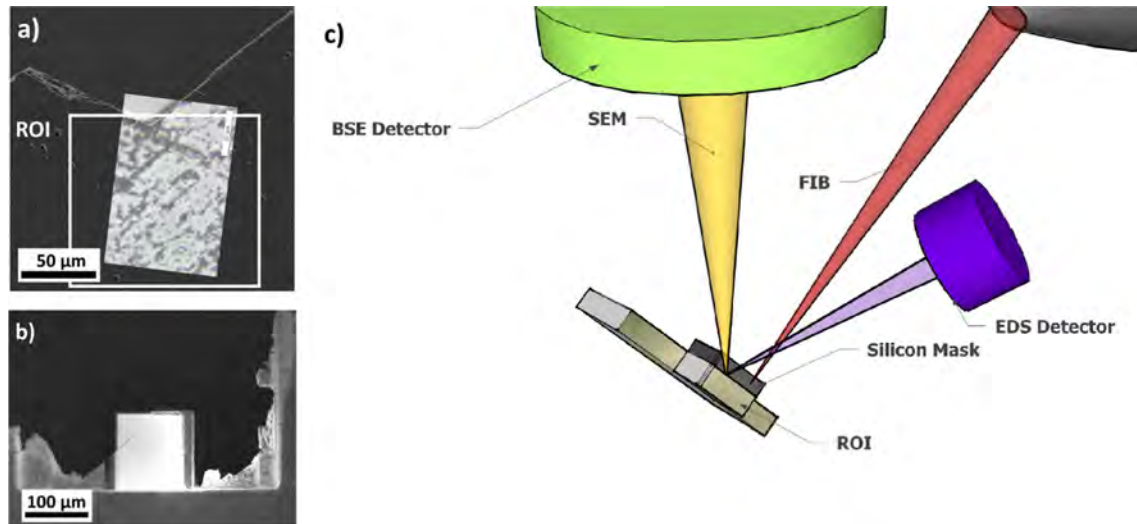


**Fig. 2.** 3D EDS analysis. a) Location of ROI using correlative SEM and LM image, b) preparation of ROI by FIB, c) 3D EDS static-acquisition geometry (ROI in cross section view), BSE means backscattered electrons.

mented by global thresholding, but only large areas were taken into account thanks to their sufficient contrast against surrounding calcite. The thresholding segmentation method was inaccurate in areas around air voids, therefore the region with a high content of Mg was manually corrected based on the correlation with 3D EDS analysis.

## 4. Results

### 4.1. Petrographic, mineralogical and chemical analysis

From LM images (Fig. 1), the number of inclusions in sparry calcite within the sample's investigated region with volume of  $100 \times 70 \times 80 \mu\text{m}^3$  was determined. The number is between 80 and 200 inclusions which corresponds to  $10^8$  inclusions per  $\text{cm}^3$ . The sample contained numerous tiny fluid inclusions with size up to 2–3  $\mu\text{m}$ , only a few inclusions were of a size 5–10  $\mu\text{m}$ . Their shape was rounded or irregular and they were rather randomly distributed. Fluid inclusions were one-phase and two-phase and there

was no difference in distribution and shape of inclusions of these two types.

A mineralogical analysis showed that the prevailing bioclasts in the sample were echinoderms and crinoids. Bryozoans, rugose corals and ostracodes were also common. Rugose corals, as well as the bryozoans, occurred as complete branches. Syntaxial calcite cement overgrowths appeared due to diagenesis. Calcite crystals reached the maximum size of about 2 mm. Depositional setting could be interpreted as shallow-marine, above the fair-weather wave base.

An XRD analysis of insoluble residue (Fig. 3) showed that minerals such as calcite and dolomite had been still presented in the sample after three months of dissolution, however, their content decreased enough to enable an identification of other phases. Common minerals in the samples were quartz, fluorapatite, goethite, illite/mica, kaolinite, orthoclase, gypsum, smectite (vermiculite/chlorite) and also pyrite.

According to the chemical analysis, the predominating chemical component was  $\text{CaCO}_3$ . The content of  $\text{CaCO}_3$  was higher than 98 % (Table 1). A small amount of magnesium in form of  $\text{MgCO}_3$  was

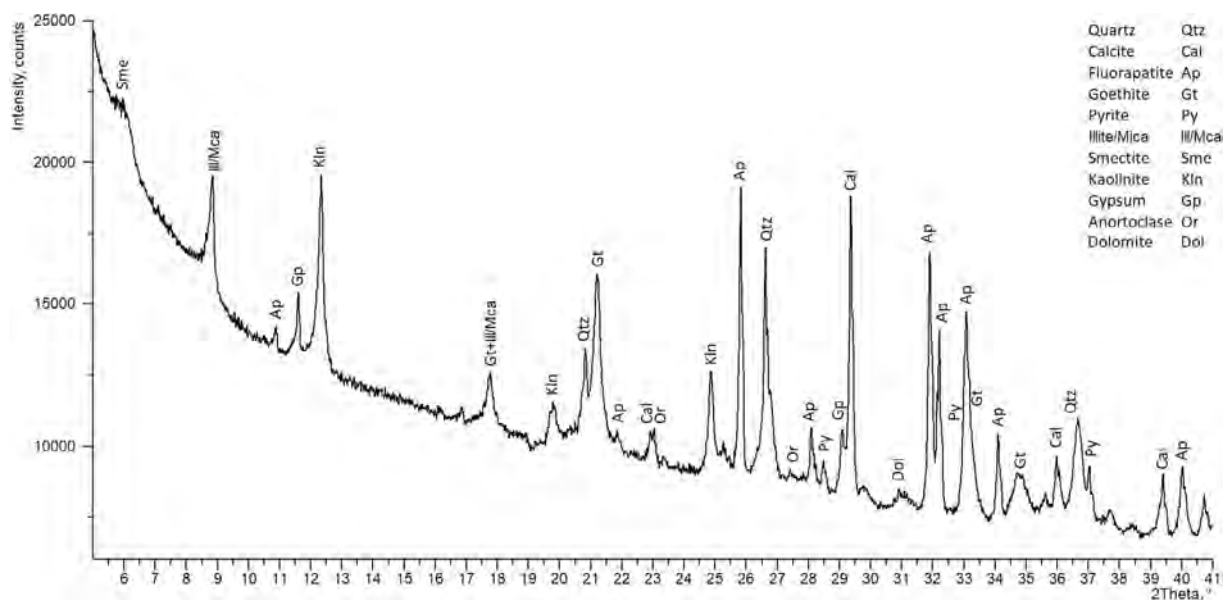


**Fig. 3.** Mineralogical analysis of the insoluble residue.

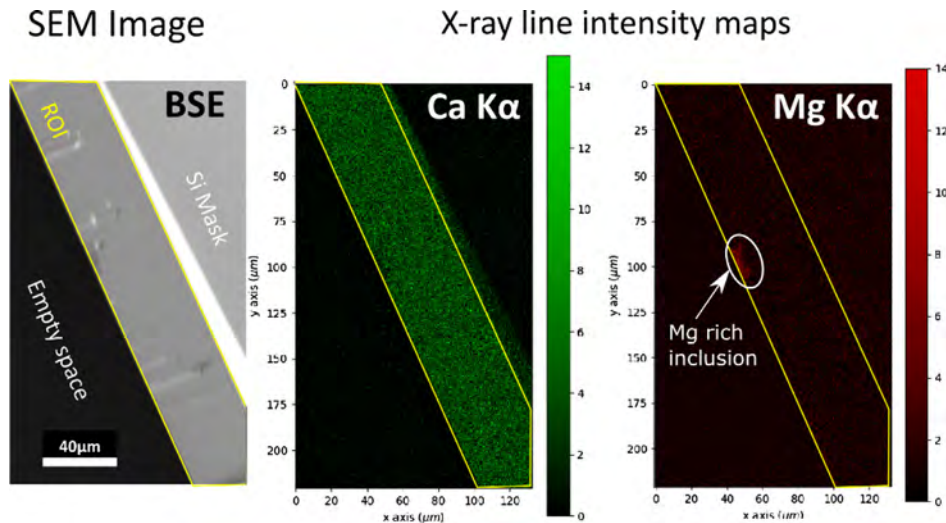


**Fig. 4.** 2D data output for a single FIB slice (ROI cross section): BSE – backscattered electron SEM image, Ca K $\alpha$ , Mg K $\alpha$  – EDS elemental maps extracted from the spectral data cube according to the selected peak intensity.

present as well. Some salt components such as Na<sup>+</sup> and Cl<sup>-</sup> were also detected, pointing out the presence of salt in fluid inclusions. Chemical analyses are in a good agreement with a mineral composition. Fairly pure limestone apparently contained a high amount of CaCO<sub>3</sub> and other minor and accessory mineral phases, as detected by XRD, which were responsible for other elements. A relatively ubiquitous dolomite contained some Mg, however Mg was a component in smectite/vermiculite/chlorite ((Mg, Fe<sup>++</sup>, Al)<sub>3</sub>(Al, Si)<sub>4</sub>O<sub>10</sub>(OH)<sub>2</sub>·4(H<sub>2</sub>O)) as well. Other discovered mineral phases contained also the following elements: quartz (SiO<sub>2</sub>), illite/mica (KAl<sub>2</sub>(Si<sub>3</sub>Al)O<sub>10</sub>(OH,F)<sub>2</sub>), kaolinite (Al<sub>2</sub>Si<sub>2</sub>O<sub>5</sub>(OH)<sub>4</sub>), orthoclase (KAlSi<sub>3</sub>O<sub>8</sub>), gypsum (CaSO<sub>4</sub>), pyrite (FeS<sub>2</sub>) and goethite (Fe<sup>+++</sup>O(OH)). Relatively high contents of chlorine and sodium denoted a presence of salt in the fluid inclusions.

#### 4.2. Microthermometry

The majority of inclusions (80–90 %) contained a one-phase system only, i.e. they contained only liquid. By contrast, two-phase fluid inclusions contained liquid and vapour (L+V type). These facts indicate that fluids, which represent diagenetic conditions of the limestone, were trapped at temperature below +50 °C [7]. Cryothermometry was applied to obtain data on the composition and salinity of the fluids. Eutectic temperatures of the system were around -22 °C and -20 °C which indicates presence of the H<sub>2</sub>O-NaCl and possibly H<sub>2</sub>O-NaCl-KCl system as dominant components [35]. The temperature at which the last solid (ice) melts ranges between -0.3 °C and -0.9 °C which means that the salinity of aqueous fluids is between 0.5 and 1.5 mass% NaCl eq. [30]. In accordance with those salinities, a density of the aqueous solution inside the inclusions is between 1.0020 and 1.0094 g·cm<sup>-3</sup>.

#### 4.3. 3D EDS analysis

The 3D EDS analysis showed presence of some individual Mg rich regions in a small area of the sample (Fig. 4). This method did not enable detection of the salt content of fluid inclusions due to their low salinity. The liquid evaporated immediately after opening of the inclusion and the size of remaining salt crystals was below the resolution limit.

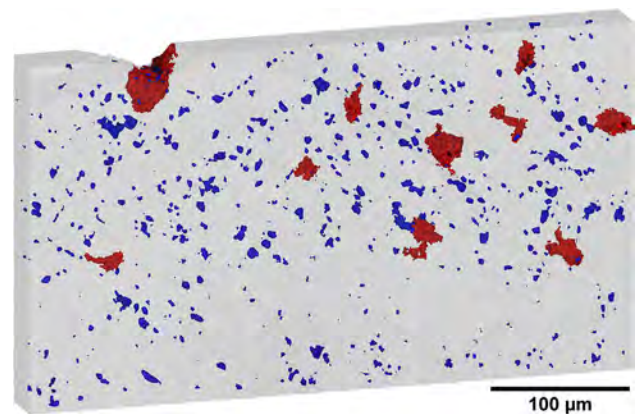


**Fig. 5.** 3D transparent render of CT data. Cavities are labelled by blue colour, magnesium rich regions are labelled by red colour. (For interpretation of the references to colour in this figure legend, the reader is referred to the web version of this article.)

#### 4.4. X-ray computed tomography

The CT data of examined sample showed nearly a uniform distribution of cavities (Fig. 5). It was not possible to distinguish air voids from fluid inclusions, since they have similar gray values in CT data. These cavities were segmented and their total volume was determined in VGStudio MAX as  $19.4 \times 10^3 \mu\text{m}^3$ , resulting in 0.43 vol.% in volume of the examined region.

A stack of LM images was aligned with CT images so that the edges of the samples fitted (Fig. 6). Some fluid inclusions with the same shape and position as seen in LM were recognized in the CT data. According to CT analysis, there were 107 cavities within an area of  $100 \times 70 \mu\text{m}^2$  (indicated in the Fig. 1).

To further verify the presence of fluid inclusions in the limestone sample, the CT data were correlated with the 3D EDS analysis (Fig. 7), but this method failed to show the distribution of inclusions. However, Mg rich regions were recognized in the CT data (Fig. 6d). The total volume of Mg rich area segmented in the CT data was  $23.1 \times 10^3 \mu\text{m}^3$ , resulting in 0.51 vol.%. According to the results from chemical and mineralogical analyses, these areas corresponded to dolomites.

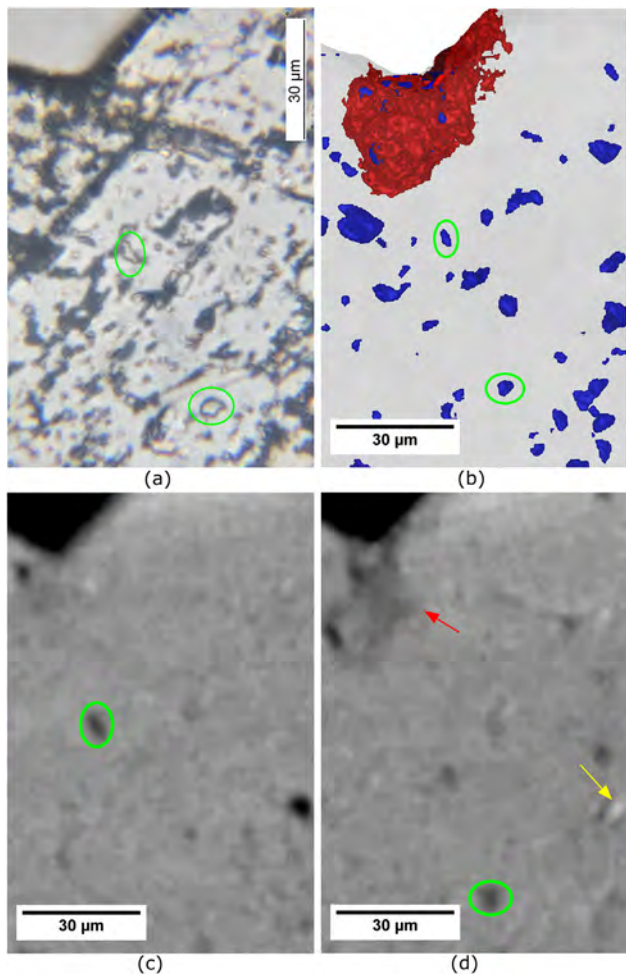


**Fig. 6.** (a) LM image: focused 2D images are stacked together, selected fluid inclusions are circled in green; (b) 3D transparent render of CT data. Blue colour represents air voids and fluid inclusions, red colour represents magnesium rich area; (c), (d) CT slices with selected fluid inclusions, red arrow marks magnesium, yellow arrow marks material with very high density. (For interpretation of the references to colour in this figure legend, the reader is referred to the web version of this article.)

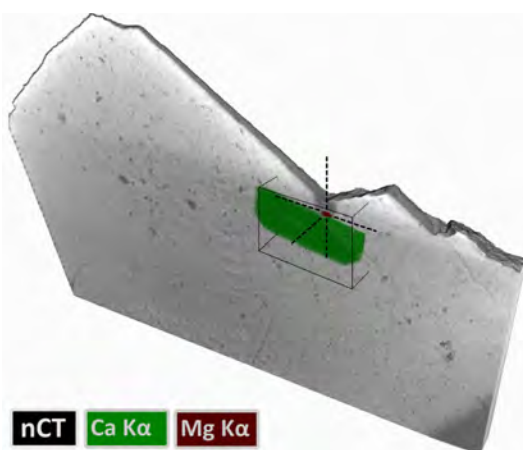


**Fig. 7.** 3D visualization of limestone plate as a correlative CT analysis (grayscale volume rendering) with 3D EDS elemental maps (Ca  $K\alpha$  – green, Mg  $K\alpha$  – red). Location of Mg rich region is marked by the cross. (For interpretation of the references to colour in this figure legend, the reader is referred to the web version of this article.)

Furthermore, some bright regions with significantly higher X-ray absorption were detected (Fig. 6d). These regions might contain some heavy elements (such as Fe), which was confirmed by the results of the chemical analysis.

## 5. Discussion

The number of cavities shown by the CT analysis corresponds to the LM result.  $10^8$  inclusions per  $\text{cm}^3$  in minerals is considered rather high if a reference Roedder [37] is taken –  $10^9$  inclusions per  $\text{cm}^3$  were reported in his study as a high number. Consequently, the volume of cavities derived by CT (0.43 vol.%) could be considered as rather high as well. All presented data explain behaviour of investigated limestone in firing process.

The smallest diameter of inclusion detectable by the CT is 1.3  $\mu\text{m}$  (diameter of sphere with volume of 8 voxels). It is possible to study tiny individual inclusions with synchrotron CT devices [26], but the field of view is restricted to only one inclusion at a time. The larger field of view of laboratory-based CT allows to visualize a 3D distribution of a high amount of inclusions in the sample's volume.

In the proposed procedure, the LM is used as a method to get an overview of the sample and to select the region of interest for further study. But once the CT data are acquired, the selection of the region for further investigation is faster in comparison with the LM. It is because all inclusions, voids, cracks and grains from different materials are visible in 3D data of the sample. In LM, all the inclusions do not have to be visible due to the fractures along cleavage planes in the calcite structure. Besides that, some small fractures or grains may be confused with inclusions and the number of inclusions results in inaccurate number or could be undervalued.

The shape of the sample must be taken into account while planning an experiment as it affects quality of the CT data. For the sake of the experiment, the sample was polished in form of a thin section which was required for the LM analysis. However, such an asymmetric shape leads to an occurrence of artefacts in CT data. The fact that X-rays pass through very different thicknesses of the sample results in some false intensity gradients [36]. This is visible in the CT data in Fig. 7: the top of the sample is significantly brighter than the thicker part at the bottom although there is no big material difference. To avoid these artefacts, it is advisable to shape a sample to a cylinder form with no regular straight planes. However, this recommendation is applicable only for CT measurements. Breaking the sample and picking the most suitable fragment could often be sufficient and useful as it saves time and effort during sample preparation.

The 3D EDS analysis results do not confirm the presence of inclusions, however, the technique was used to identify a Mg rich region. In general, the application of this method helps with a material identification in CT data and with an interpretation of the 3D CT analysis results.

## 6. Conclusion

Fluid inclusions in sparry calcites as cement in limestones have an influence on its behaviour during industrial processing. When firing in shaft kilns, fluids trapped inside of fluid inclusions explode and expand (decrepitation), which results in a dense network of plenty of tiny fissures in rock and hence the limestones undergo some volumetric changes. This process is directly influenced by the amount and distribution of fluid inclusions. A high amount of fluid inclusions increases the decrepitation tendency of the limestone in the process of firing. A visualization and a direct study of fluid inclusions distribution in limestone predict its behaviour

during firing. The light microscopy is a standard technique of fluid inclusions' imaging. Using this technique, the visibility of fluid inclusions is restricted by disturbances of the calcite structure. The aim of this paper is to demonstrate the use of the laboratory-based X-ray computed tomography for a detection of fluid inclusions, a precise determination of their volume and a visualization of 3D distribution of inclusions in the volume of the sample.

A study of a hard, compact limestone from Koněprusy, Czech Republic is shown. The sample of a high purity limestone selected for investigation with CT contained a lot of fluid inclusions, a small amount of dolomite, clay minerals and Fe rich minerals which was confirmed by mineralogical and chemical analyses and microthermometry. To observe the fluid inclusions, one piece of the sample was studied using three methods: the CT, the LM for verification, and the 3D EDS analysis as a supplement method. The sample had to be prepared in the form of a thin section for the LM and the microthermometry although it was a very disadvantageous shape for the CT. The CT data show segmented cavities even though it is not possible to distinguish directly air voids from fluid inclusions. Images and results from all methods were correlated and some of fluid inclusions, dolomites and Fe-rich minerals such as pyrite and goethite were identified in the limestone CT data. Some of these inhomogeneities such as Mg and Fe rich areas were unidentified or only partially identified in the LM. The distribution of cavities and Mg rich areas in the volume was shown in a 3D model and their volume was determined based on the CT data.

This paper shows that the state of the art laboratory-based CT device is capable of a material analysis with the sufficient resolution to describe the fine inner structure of limestone. Unlike the commonly used optical microscopy, the CT requires an easier sample preparation and brings a non-destructive 3D characterization of materials' structure.

## Conflict of interest

There are no known conflicts of interest.

## Acknowledgements

This research was carried out under the project CEITEC 2020 (LQ1601) with financial support from the Ministry of Education, Youth and Sports of the Czech Republic under the National Sustainability Programme II. The work is further supported by National Sustainability Program under Grant LO1401 and by Preamium Academiae from CAS. Also, this work was financially supported by project No. **LO1408 "AdMaS UP" – Advanced Materials, Structures and Technologies**, supported by the Ministry of Education, Youth and Sports under "National Sustainability Programme I" and by project No. 15-08755S: "Study of the effects of samples preparation on the final properties of inorganic binders". Part of the work was carried out with the support of CEITEC Nano Research Infrastructure (MEYS CR, 2016–2019).

## References

- [1] J.J. Wuhler, *Zement-Kalk-Gips Int.* 6 (1953) 354.
- [2] J. Wuhler, G. Rademacher, W. Lahl, *J. TIZ Int.* 80 (100) (1956).
- [3] J. Wuhler, Über den Einfluss der Kristallgröße und von Fehlernungen im Gitter auf die Reaktionsfähigkeit von Kalk, *Schriftenreihe des Bundesverbandes der Deutschen Kalkindustrie* 10 (1970) 119–141.
- [4] A. Wolter, S. Hogewoning, Vorhersage und Beeinflussung der Reaktivität von Branntkalk. 2011. Forschungabericht für die Forschungsgemeinschaft Kalk und Mörtel e.V.: 94 S, TU Clausthal.
- [5] D. Dollimore, J.G. Dunn, Y.F. Lee, B.M. Penrod, The decrepitation of dolomite and limestone, *Thermochim. Acta* 237 (1) (1994) 125–131, [https://doi.org/10.1016/0040-6031\(94\)85191-3](https://doi.org/10.1016/0040-6031(94)85191-3). ISSN 00406031.
- [6] P.M. Crnkovic, W.L. Polito, C.G. da Silva Filho, F.E. Milioli, J.D. Pagliuso, The particle size effect on decrepitation during the thermal decomposition of limestones and coal, *Química Nova* 27 (1) (2004) 58–61, <https://doi.org/10.1590/S0100-40422004000100012>. ISSN 0100-4042.
- [7] R.H. Goldstein, Fluid inclusions in sedimentary and diagenetic systems, *Lithos* 55 (1–4) (2001) 159–193, [https://doi.org/10.1016/S0024-4937\(00\)00044-X](https://doi.org/10.1016/S0024-4937(00)00044-X). ISSN 00244937.
- [8] A. Anderson, D.D. Marshall, I. Samson (Eds.), *Fluid Inclusions: Analysis and Interpretation*, Mineralogical Association of Canada, Ottawa, 2003. ISBN 09-212-9432-8.
- [9] M.R. Lee, C.L. Smith, Scanning transmission electron microscopy using a SEM: Applications to mineralogy and petrology, *Mineral. Mag.* 70 (5) (2006) 579–590, <https://doi.org/10.1180/0026461067050351>. ISSN 0026461x.
- [10] C. Viti, M.-L. Frezzotti, Transmission electron microscopy applied to fluid inclusion investigations, *Lithos* 55 (1–4) (2001) 125–138, [https://doi.org/10.1016/S0024-4937\(00\)00042-6](https://doi.org/10.1016/S0024-4937(00)00042-6). ISSN 00244937.
- [11] M. van Geet, R. Swennen, P. David, Quantitative coal characterisation by means of microfocus X-ray computer tomography, colour image analysis and back-scattered scanning electron microscopy, *Int. J. Coal Geol.* 46 (1) (2001) 11–25, [https://doi.org/10.1016/S0166-5162\(01\)00006-4](https://doi.org/10.1016/S0166-5162(01)00006-4). ISSN 01665162.
- [12] G. Möbus, B.J. Inkson, Nanoscale tomography in materials science, *Mater. Today* 10 (12) (2007) 18–25, [https://doi.org/10.1016/S1369-7021\(07\)70304-8](https://doi.org/10.1016/S1369-7021(07)70304-8). ISSN 13697021.
- [13] V. Cnudde, M.N. Boone, High-resolution X-ray computed tomography in geosciences: a review of the current technology and applications, *Earth-Sci. Rev.* 123 (2013) 1–17, <https://doi.org/10.1016/j.earscirev.2013.04.003>. ISSN 00128252.
- [14] H.S. Barnard, A.A. Macdowell, D.Y. Parkinson, et al., Synchrotron X-ray microtomography at the Advanced Light Source: Developments in high-temperature in-situ mechanical testing, *J. Phys.* 849 (2017), <https://doi.org/10.1088/1742-6596/849/1/012043>. ISSN 1742-6588.
- [15] J. Friml, K. Procházková, G. Melnyk, T. Zikmund, J. Kaiser, Investigation of Cheb relief intarsia and the study of the technological process of its production by micro computed tomography, *J. Cult. Heritage* 15 (6) (2014) 609–613, <https://doi.org/10.1016/j.culher.2013.12.006>. ISSN 12962074.
- [16] M. Kaucka, T. Zikmund, M. Tesarova, et al., Oriented clonal cell dynamics enables accurate growth and shaping of vertebrate cartilage, *ELife* 6 (2017), <https://doi.org/10.7554/eLife.25902>. ISSN 2050-084x.
- [17] J. Hsieh, *Computed tomography: principles, design, artifacts, and recent advances*. 2nd ed. Bellingham, Wash.: SPIE Press, 2009. ISBN 978-0-8194-7533-6.
- [18] F. Mees, R. Swennen, M. Van Geet, P. Jacobs, Applications of X-ray computed tomography in the geosciences, *Geol. Soc. London, Spec. Publ.* 215 (1) (2003) 1–6, <https://doi.org/10.1144/GSL.SP.2003.215.01.01>. ISSN 0305-8719.
- [19] W.D. Carlson, T. Rowe, R.A. Ketcham, M.W. Colbert, Applications of high-resolution X-ray computed tomography in petrology, meteoritics and palaeontology, *Geol. Soc. London, Spec. Publ.* 215 (1) (2003) 7–22, <https://doi.org/10.1144/GSL.SP.2003.215.01.02>. ISSN 0305-8719.
- [20] M. Kampschulte, A. Langheinrich, J. Sender, et al., Nano-computed tomography: technique and applications, *RöFo - Fortschritte auf dem Gebiet der Röntgenstrahlen und der bildgebenden Verfahren*. 188 (02) (2016) 146–154, <https://doi.org/10.1055/s-0041-106541>. ISSN 1438-9029.
- [21] F. Peyrin, P. Dong, A. Pacureanu, M. Langer, Micro- and Nano-CT for the Study of Bone Ultrastructure, *Curr. Osteoporosis Rep.* 12 (4) (2014) 465–474, <https://doi.org/10.1007/s11914-014-0233-0>. ISSN 1544-1873.
- [22] W.D. Carlson, Three-dimensional imaging of earth and planetary materials, *Earth Planet. Sci. Lett.* 249 (3–4) (2006) 133–147, <https://doi.org/10.1016/j.epsl.2006.06.020>. ISSN 0012821x.
- [23] I.A. Taina, R.J. Heck, T.R. Elliot, Application of X-ray computed tomography to soil science: a literature review, *Can. J. Soil Sci.* 88 (1) (2008) 1–19, <https://doi.org/10.4141/CJSS06027>. ISSN 0008-4271.
- [24] D.E. Jacob, R. Wirth, F. Enzmann, A. Kronz, A. Schreiber, Nano-inclusion suite and high resolution micro-computed-tomography of polycrystalline diamond (framesite) from Orapa, Botswana, *Earth Planet. Sci. Lett.* 308 (3–4) (2011) 307–316, <https://doi.org/10.1016/j.epsl.2011.05.056>. ISSN 0012821x.
- [25] S. Zabler, A. Rack, I. Manke, K. Thermann, J. Tiedemann, N. Harthill, H. Riesemeier, High-resolution tomography of cracks, voids and micro-structure in greywacke and limestone, *J. Struct. Geol.* 30 (7) (2008) 876–887, <https://doi.org/10.1016/j.jsg.2008.03.002>. ISSN 01918141.
- [26] K. Yoshida, T. Hirajima, A. Miyake, A. Tsuchiyama, S. Ohi, T. Nakano, K. Uesugi, Combined FIB microsampling and X-ray microtomography: a powerful tool for the study of tiny fluid inclusions, *Eur. J. Mineral.* 28 (2) (2016) 245–256, <https://doi.org/10.1127/ejm/2015/0027-2498>. ISSN 09351221.
- [27] R.J. Dunham, Classification of Carbonate Rocks According to Depositional Texture, In: HAM, William E. Classification of Carbonate Rocks—A Symposium. 1. American Association of Petroleum Geologists, 1962, pp. 108–121.
- [28] L. Jeppsson, R. Anehus, D. Fredholm, The optimal acetate buffered acetic acid technique for extracting phosphatic fossils, *J. Paleontol.* 73 (05) (1999) 964–972, <https://doi.org/10.1017/S0022336000040798>. ISSN 0022-3360.
- [29] L.A. Dalton, T. Bosak, F.A. Macdonald, D.J.G. Lahr, S.B. Pruss, Preservation and morphological variability of assemblages of agglutinated eukaryotes in cryogenian cap carbonates of northern Namibia, *PALAIOS*. 28 (2) (2013) 67–79, <https://doi.org/10.2110/palo.2012.p12-084r>. ISSN 0883-1351.
- [30] R.J. Bodnar, Revised equation and table for determining the freezing point depression of H<sub>2</sub>O-NaCl solutions, *Geochim. Cosmochim. Acta* 57 (3) (1993) 683–684, [https://doi.org/10.1016/0016-7037\(93\)90378-A](https://doi.org/10.1016/0016-7037(93)90378-A). ISSN 00167037.

- [31] R.J. Bakker, Package FLUIDS 1. Computer programs for analysis of fluid inclusion data and for modelling bulk fluid properties, *Chem. Geol.* 194 (1–3) (2003) 3–23, [https://doi.org/10.1016/S0009-2541\(02\)00268-1](https://doi.org/10.1016/S0009-2541(02)00268-1). ISSN 00092541.
- [32] T. Hrncir, et. al. In: 38th ISTFA Conference Proceedings. 2012, s. 26.
- [33] F. de la Pena, et al. 2017, May 27. hyperspy/hyperspy: HyperSpy 1.3. Zenodo. <http://doi.org/10.5281/zenodo.583693>.
- [34] P. Coupe, P. Yger, S. Prima, P. Hellier, C. Kervrann, C. Barillot, An optimized blockwise nonlocal means denoising filter for 3-D magnetic resonance images, *IEEE Trans. Med. Imaging* 27 (4) (2008) 425–441, <https://doi.org/10.1109/TMI.2007.906087>. ISSN 0278-0062.
- [35] D.W. Davis, T.K. Lowenstein, R.J. Spencer, Melting behavior of fluid inclusions in laboratory-grown halite crystals in the systems NaCl-H<sub>2</sub>O, NaCl-KCl-H<sub>2</sub>O, NaCl-MgCl<sub>2</sub>-H<sub>2</sub>O, and NaCl-CaCl<sub>2</sub>-H<sub>2</sub>O, *Geochim. Cosmochim. Acta* 54 (3) (1990) 591–601, [https://doi.org/10.1016/0016-7037\(90\)90355-O](https://doi.org/10.1016/0016-7037(90)90355-O). ISSN 00167037.
- [36] J.P. Kruth, M. Bartscher, S. Carmignato, R. Schmitt, L. De Chiffre, A. Weckenmann, Computed tomography for dimensional metrology, *CIRP Ann.* 60 (2) (2011) 821–842, <https://doi.org/10.1016/j.cirp.2011.05.006>. ISSN 00078506.
- [37] E. Roedder, Fluid Inclusions. Reviews in Mineralogy. Washington D.C.: Mineralogical Society of America, 1984, p. 12.

PAPER [XX]

## RESEARCH ARTICLE

# Non-destructive lock-picking of a historical treasure chest by means of X-ray computed tomography

Eva Zikmundová<sup>1,2</sup>, Tomáš Zikmund<sup>1</sup>, Vladimír Sládek<sup>3</sup>, Jozef Kaiser<sup>1\*</sup>

**1** Central European Institute of Technology, Brno University of Technology (CEITEC BUT), Brno, Czech Republic, **2** Department of Chemistry, Faculty of Science, Masaryk University, Brno, Czech Republic, **3** Department of Anthropology and Human Genetics, Faculty of Science, Charles University, Prague, Czech Republic

\* [jozef.kaiser@ceitec.vutbr.cz](mailto:jozef.kaiser@ceitec.vutbr.cz)

## Abstract

An innovative approach to a non-destructive lock mechanism examination by means of X-ray computed tomography (CT) was involved in a careful opening of a locked 19<sup>th</sup> century chest missing the key, as an interdisciplinary cooperation with the restorers. In regard of the exploration and conservation of such locked objects, their opening is important to the restorers. However, the opening may be complicated, if not impossible, without damaging the object when the key is missing. Moreover, the historical locks might be equipped with protective mechanisms. Despite the exceeding dimensions and the weight of the steel chest, a CT analysis was performed, which enabled a detailed exploration of the lock based on a system of levers and bolts handled by a single key, located in a case on the inside of the chest lid, including the dimensions essential for manufacturing of a new key copy. Moreover, two secret protective mechanisms were revealed, as well as all the damages of the object.

## OPEN ACCESS

**Citation:** Zikmundová E, Zikmund T, Sládek V, Kaiser J (2020) Non-destructive lock-picking of a historical treasure chest by means of X-ray computed tomography. PLoS ONE 15(7): e0235316. <https://doi.org/10.1371/journal.pone.0235316>

**Editor:** Joseph P. R. O. Orgel, Illinois Institute of Technology, UNITED STATES

**Received:** October 30, 2019

**Accepted:** June 8, 2020

**Published:** July 6, 2020

**Peer Review History:** PLOS recognizes the benefits of transparency in the peer review process; therefore, we enable the publication of all of the content of peer review and author responses alongside final, published articles. The editorial history of this article is available here: <https://doi.org/10.1371/journal.pone.0235316>

**Copyright:** © 2020 Zikmundová et al. This is an open access article distributed under the terms of the [Creative Commons Attribution License](https://creativecommons.org/licenses/by/4.0/), which permits unrestricted use, distribution, and reproduction in any medium, provided the original author and source are credited.

**Data Availability Statement:** The whole CT dataset underlying the findings of this study are available on the Open Science Framework repository at DOI: [10.17605/OSF.IO/NXPHY](https://doi.org/10.17605/OSF.IO/NXPHY).

## Introduction

X-ray computed tomography (CT) [1] enables to investigate non-destructively the objects of cultural heritage. The technique is based on a sample scanning using the trans-illuminative X-ray radiation [2], and a 3D model can be obtained as a result [3]. The dense parts of the scanned material reduce the intensity of the radiation, as the X-rays are partly absorbed. The sample projections represented by different intensities for different materials of the sample are then detected and the data acquired over an angular range of 360° are mathematically processed into virtual cross-sections (CT data) [4] including the detailed information about the inner structure of the material up to a micro-level resolution [5]. Moreover, X-rays cannot cause any harm to inanimate objects (unlike biological samples) and the scanning is, therefore, non-invasive. These advantages make CT a promising technique in the study of the cultural heritage objects, such as various wooden artefacts [6–9] including musical instruments [10, 11], pottery [12] and skeletal remains [13]. However, the use of commercially available medical [14] or industrial [15] CT systems is limited due to the achieved resolution or the size of the

**Funding:** This research was carried out under the project CEITEC 2020 (LQ1601) with financial support from the Ministry of Education, Youth and Sports of the Czech Republic under the National Sustainability Programme II, CEITEC Nano Research Infrastructure (MEYS CR, 2016-2019) and Ceitec Nano+ project, CZ.02.01/0.0./0.0./16\_013/0001728 under the program OP RD. J.K. acknowledges the support of the Brno University of Technology through grant FSI-S-17-4506.

**Competing interests:** The authors have declared that no competing interests exist.

objects. Thus, special systems have been developed and used in the analysis of large objects, e. g. in Bologna and Turin, Italy [16, 17] or Ghent, Belgium [11]. In this study, an innovative approach to open a locked historical chest is suggested via a non-destructive exploration of the lock mechanism using CT measurements.

In museum depositories throughout the Czech Republic, there are many locked objects missing the key [18, 19]. Opening of these objects is essential not only for the restoration process but also for the exploration of the inner space and possible content, for the examination of the lock mechanism and its functionality, and eventually for a new key copy manufacturing. A presumably locked steel chest, currently in the property of the South Moravian Museum in Znojmo, Czech Republic, which might have served as a guild or a city treasure chest was used to demonstrate an innovative approach of the lock mechanism exploration by applying CT.

Historical chests were used as early as in the Ancient Egypt [20–22] with a wide range of purposes. With the establishment of guilds, chests were used as vaults to store important documents, valuable objects and also money of the guilds or of the city councils [23, 24]. However, they also served for the ceremonial purposes—the plenary guild meetings used to be initiated by opening of the chest and ended by closing it [25]. The sanctity of the open chest was significant, as the decisions made while the chest was opened were considered legitimate and binding. Disrespectful behaviour was even considered as a violation of the ceremony and was penalized [24]. The chests could also have a social function, when they were carried in a carnival procession during their transportation to a new location or as a part of celebrations and festivals [23]. With the abolition of the guilds in the 19<sup>th</sup> century, the guild chests lost their purpose and became the relics [23, 25].

The chests containing the valuables were highly treasured, therefore, several safety precautions were involved. The treasure chests were made of wood and armoured with steel strips or entirely made of steel. To increase the protection, the chest could have been fastened to the ground [26], e. g. through the holes in the bottom. Thus, it could not be moved without its opening and dismounting. Moreover, the lock mechanisms were used as a protection. The chests used to be equipped with more locks with different keys usually held by the guild masters or councilmen and it was only possible to open the chests when all the keys were present. Hidden keyholes and even false ones or lock bolts directed into three or four sides of the chest were among many devices often present in order to increase the protection of the chest's content [25].

The impossibility of the chest opening may have various causes—the key absence, the damage of the lock mechanism, the presence of the corrosion products, etc. Any destructive technique, including e. g. cutting the bottom of the chest, is, however, barely acceptable by the restorers and it is used only if inevitable.

A possibility of a non-destructive examination of the construction and potential defects of a steel treasure chest lock mechanism by means of CT is introduced in this work. We encountered several challenges, such as the very positioning of the chest in the CT cabinet regarding the large dimensions and weight of the object, a possible data distortion due to the thickness and a high attenuation character of the analysed material, etc. Despite them, the goal is to provide a detailed construction model with precise dimensions to be used for a new key copy manufacturing and for understanding the functionality of the lock mechanism.

## Materials and methods

### Treasure chest

The historical chest investigated in this study currently belongs to the collections of the South Moravian Museum in Znojmo, Czech Republic. Its origin is unknown, but the chest was dated

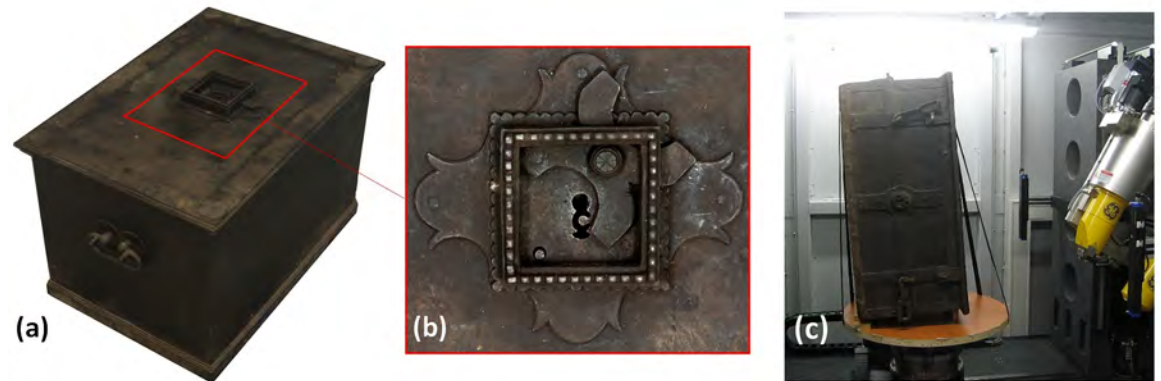


**Fig 1.** (a): Analysed chest; (b): detail of the lock [27] located in the centre of the chest lid; (c): illustration of a chest fixation in the CT system.

<https://doi.org/10.1371/journal.pone.0235316.g001>

to the 1<sup>st</sup> half of the 19<sup>th</sup> century by the art historian PhDr. Jan Mohr [27]. It has the dimensions of 580 x 392 x 410 mm and because it is completely made of steel, its weight is 60 kg. The maximum material thickness of the scanned area is approximately 500 mm, representing the width of the lid, which was a challenge for the CT measurement. It seems plain, without decorations. In the bottom, there are four holes, probably enabling to fasten the chest to the ground. The original key is missing.

The lock mechanism is located in the centre of the lid (Fig 1(a) and 1(b)). The keyhole is framed in a scalloped square-shaped frame, underlaid with one similarly scallop-edged plate and a second bigger plate forming a simple floral motif. An X-shaped cap is attached to the frame as a protection of the keyhole.

### X-ray computed tomography

A CT measurement of the lock mechanism was performed using a GE phoenix v|tome|x L 240 industrial CT system equipped with a 240 kV/300W maximum power X-ray micro focus tube and a high-contrast flat-panel detector DXR250 with a 2048 × 2048 pixel, 200 × 200 μm pixel size [28]. The granite based 7-axis manipulator allows placing a bulky object (see Fig 1(c)). The exposure time was 850 ms in each of 1800 projections. The position of the detector for every X-ray image was randomly shifted during the acquisition process in order to eliminate the ring artefacts [29]. The microCT scan was carried out at the maximum possible acceleration voltage (240 kV) and a 270 μA X-ray tube current, i.e. a power of 64.8 W. The X-ray spectrum of a tungsten target was modified by 0.5 mm Cu and 0.5 mm Sn filters to reduce the beam hardening [30]. The tomographic measurement was performed at the temperature of 21 °C. The detector distance at 1255 mm and the object distance at 639 mm gave the magnification of 1.9 and the angle of a cone beam of 18°. The isotropic linear voxel size of the obtained volume was 102 μm. This defined the field of view of 20 cm × 20 cm, which was focused on the lock area (Fig 2, the scanned area is marked in Fig 4), i.e. region of interest tomography [31]. The tomographic reconstruction was realized using the GE phoenix datos|x 2.0 3D computed tomography software [28] based on the filtered back projection algorithm [4]. Within this software, the object shifting correction and the beam hardening correction in a different material mode (number set to 8.5) was applied [32].

The VG Studio MAX 2.2 [33] software was used for all visualizations of the CT data and the measurement of the key dimensions. Individual parts of the lock mechanism were transformed into geometric objects which were subsequently colour-coded in a 3D visualization. The

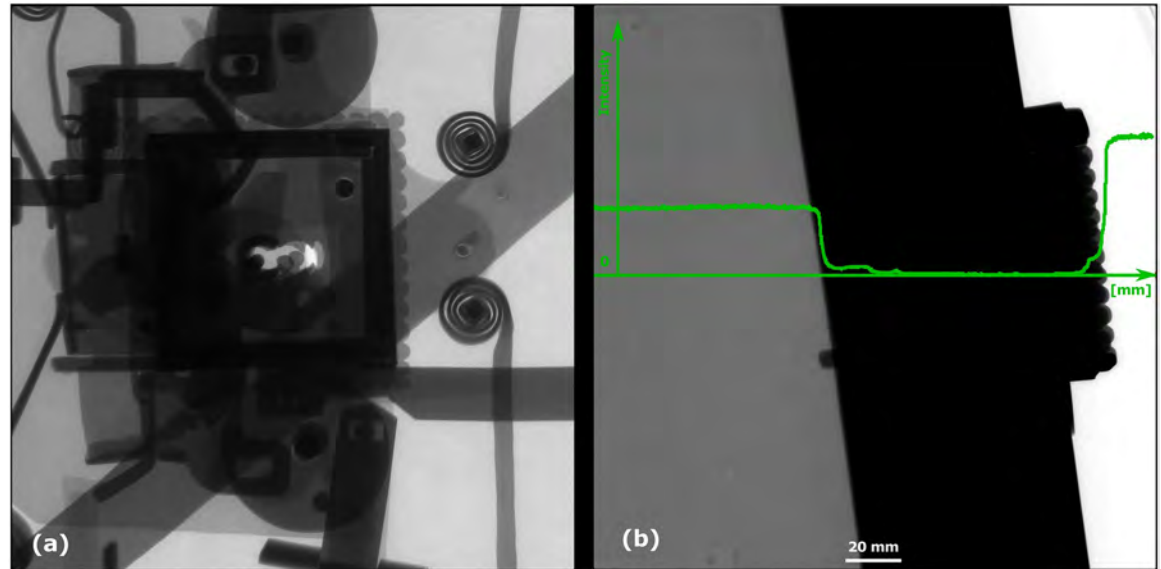


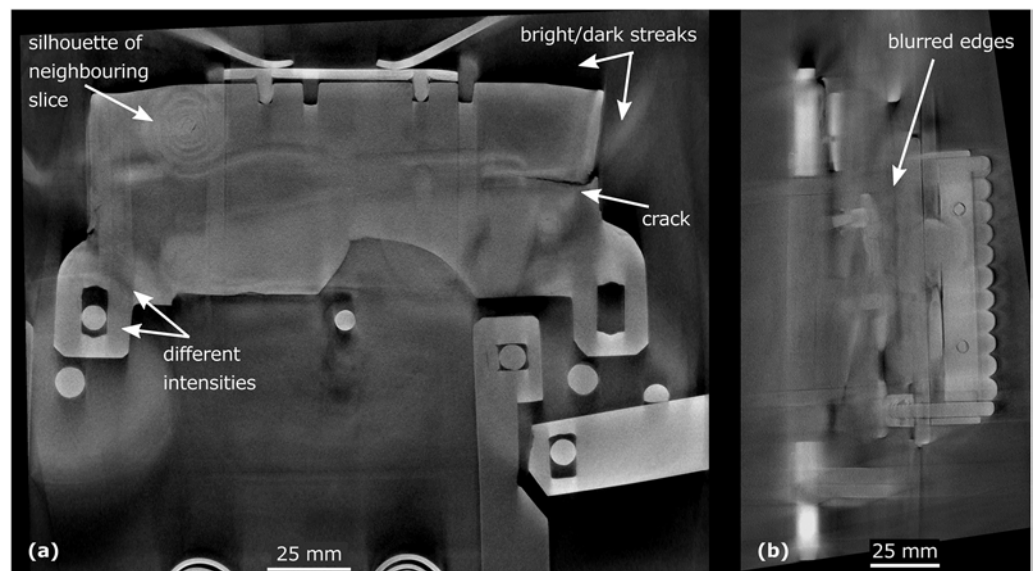
**Fig 2.** Radiographic image in a sample rotation by (a)  $0^\circ$  and (b)  $90^\circ$  with no signal in the dark area; the intensity plot is pictured in green (the black colour is represented by the lowest intensity, the highest intensity corresponds to the white colour).

<https://doi.org/10.1371/journal.pone.0235316.g002>

transformation into geometric objects was done manually. Based on the edges of the lock mechanism parts, polygonal formations were drawn using VG Studio software.

### CT data

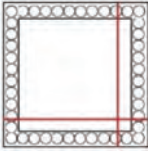
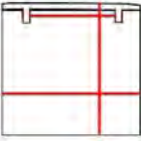
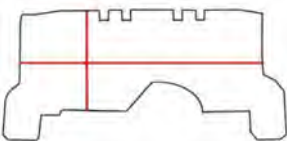
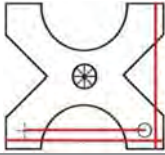
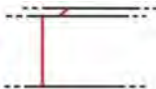
The chest is made of a high attenuation material, which caused the beam hardening and the scattering of the X-ray radiation [29]. This brought various artefacts into the images in the form of bright/dark streaks, variability in the intensities and the silhouettes from the neighbouring slices (see Fig 3(a)). Furthermore, the large dimensions of the chest lid (a projecting



**Fig 3.** Selected transverse (a) and longitudinal (b) cross-section.

<https://doi.org/10.1371/journal.pone.0235316.g003>

**Table 1. An overview of characteristic lock parts; the typical dimensions are marked red in the pictograms (l = length, w = width, th = thickness, Ø = diameter).**

	Lock part	Pictogram	Typical dimension
	Scalloped frame		l: 92 mm w: 92 mm
	Case		l: 440 mm w: 285 mm th: 3 mm
First mechanism	Keyhole		l (key bit): 23.6 mm Ø: 11.5 mm
	Peg		l: 21 mm Ø: 6.2mm
	Catcher		l: 125 mm th: 1.5 mm w: 37 mm
	Arresting plate		l: 68 mm w: 65 mm detents distance: 14 mm th: 6 mm
	Bar		l: 152 mm w: 63 mm th: 6 mm
	Guiding wheels		th: 5 mm Ø: 64mm
	Bolts		w: 20 mm th: 7 mm
Second mechanism	Secret button		l: 15 mm th: 5 mm
	X-shaped cap		l: 81 mm th: 5 mm w: 77 mm peg distance from the rotation axis: 62 mm
	Peg		l: 13 mm Ø: 7 mm
	Bolts		w: 21 mm th: 3 mm

(Continued)

Table 1. (Continued)

	Lock part	Pictogram	Typical dimension
Third mechanism	Cradle		button to axis distance: 40 mm th: 3.5 mm peg to axis distance: 28 mm
	Peg		l: 18 mm Ø: 5 mm

<https://doi.org/10.1371/journal.pone.0235316.t001>

material thickness of about 500 mm in one direction) completely shielded the X-ray radiation in a few rotation positions around 90° (see Fig 2). That led to unclear or blurred edges of the steel sheets (see Fig 3(b)). All of these issues made an automatic segmentation impossible. Nevertheless, the CT images allowed detecting e. g. a 29 mm long crack in the bar (see Fig 3(a)) and they were pictured by enough contrast to distinguish the edges of each component.

## Results

### Lock mechanism exploration

Three different and mutually independent mechanisms, hidden in a case on the inside of the chest lid, were revealed by the CT analysis. An overview of the parts of the lock belonging to individual mechanisms with their typical dimensions is summed up in Table 1.

The first mechanism controlled by the key is a system of bolts and levers (Fig 4). It is necessary to insert a right-shaped key which would pass both through the keyhole and the second aperture (Fig 5(aI) and 5(aII)) respectively) of a slightly different shape hidden inside the lid. In the lock, the hollow key shank is slid onto a peg (Fig 5(aIII)) which serves as a rotation axis

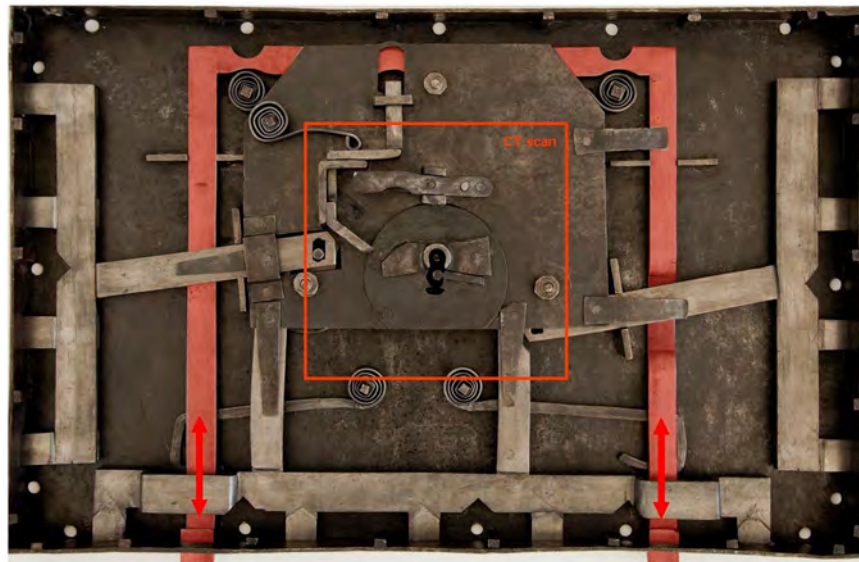
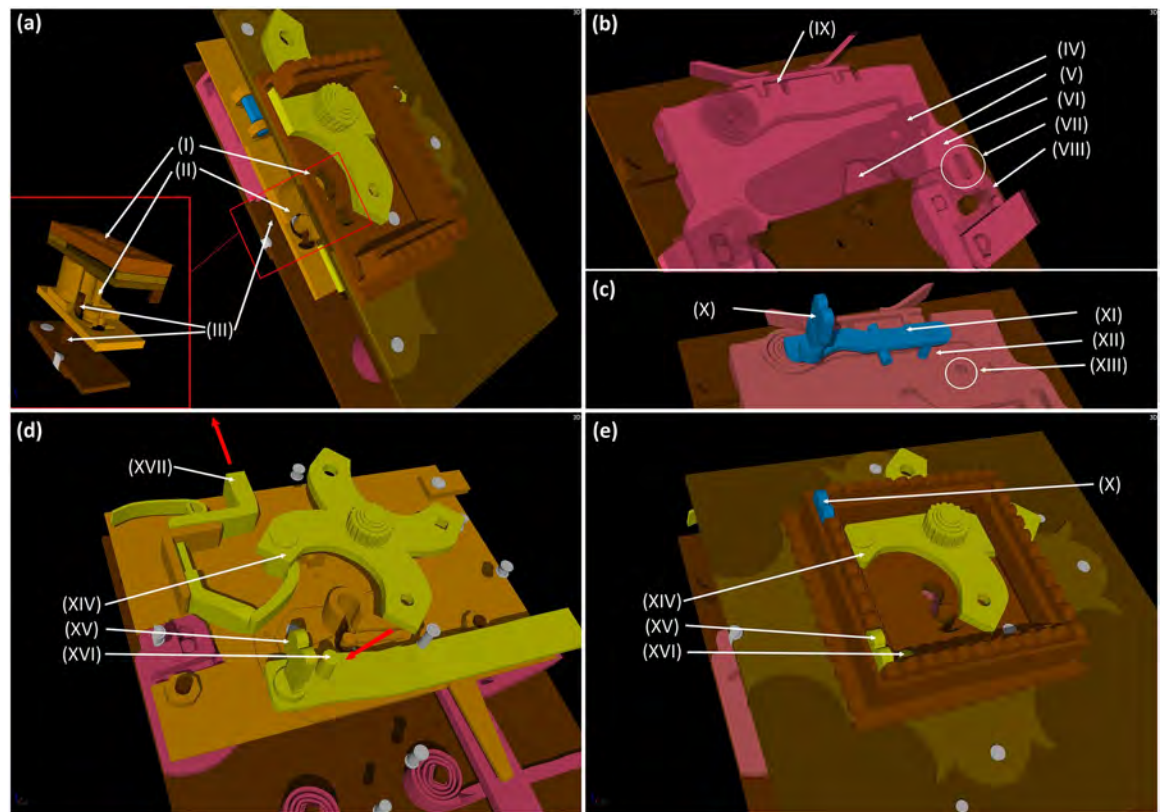


Fig 4. Complete lock mechanism of the chest in the case from below the covering plate (after restoration) [27] including the bolts and levers of the first mechanism; the lever of the second mechanism with the bolts in a locked position is marked red with the direction of their motion indicated by the arrows.

<https://doi.org/10.1371/journal.pone.0235316.g004>



**Fig 5.** A 3D model of the lock mechanism from the CT data; (a): a cross section with a detail of the keyhole depicting: (I) the keyhole, (II) the second aperture of the lock and (III) the peg onto which the key shank is being slid; (b): first mechanism: (IV) the catcher, depicted semi-transparent, (V) the arresting plate, partly hidden by (VI) the bar, (VII) the missing peg that should connect the bar with the (VIII) guiding wheel, (XI) the detents of the bar with the arresting plate fit in the unlocked position; (c): parts of the third mechanism depicted in blue: (X) the secret button, (XI) the cradle, (XII) the peg, which was supposed to fit in (XIII) the hole to block the catcher; (d + e): parts of the second mechanism depicted in yellow as seen on the lid of the chest: (XIV) the X-shaped cap covering the keyhole, (XV) the secret button, (XVI) the peg supposed to fix the cap in the closed position, (XVII) a little lever transferring the motion of the X-shaped cap onto the main lever with the bolts (see Fig 4), direction of the motion to the opened position is marked by the red arrows, (X) the third mechanism secret button depicted in blue.

<https://doi.org/10.1371/journal.pone.0235316.g005>

of the key. By turning the key, the catcher and the arresting plate (Fig 5(bIV) and 5(V) respectively) are lifted and the bar (Fig 5(bVI)) is shifted. This movement is transferred onto the levers with the bolts via two guiding wheels (Fig 5(bVIII)). Thirteen bolts on the three sides of the case are pushed in or out. When the key is fully turned, the arresting plate falls back into the detents of the bar (Fig 5(bIX)) which is held until the key is turned again.

The second mechanism is connected with an X-shaped keyhole cap (Fig 5(d) and 5(eXIV)) which can be hold with a peg (Fig 5(d) and 5(eXV)) in the lower left corner of the lock when turned to hide the keyhole. In order to reveal the keyhole, it is necessary to press a secret button (Fig 5(d) and 5(eXVI)) in the lower left corner of the frame hidden in the decoration. The mechanism connects the cap with the lever ended with two lock bolts on one side of the case (see Figs 4 and 5(dXVII)). The bolts prevent the lid from opening when the keyhole is revealed, and it is necessary to turn the cap back after unlocking.

The third mechanism is controlled by the second secret button hidden in the frame decoration (Fig 5(c) and 5(eX)). By pushing the button, a cradle (Fig 5(cXI)) supported by a spring from the board with the second keyhole is lifted. The cradle is ended with a peg (Fig 5(cXII)) reaching above the catcher. In the catcher, there is a hole (Fig 5(cXIII)) probably for the peg to

fit in and fix it. This mechanism was probably meant to block the catcher under particular circumstances. The peg was supposed to fit in the hole during unlocking and prevent any further movement of the first mechanism. In such case, it would be necessary to push the secret button when turning the key.

## Discussion

### Chest opening and the obstacles

Based on the 3D model, it was found out that the mechanism had actually been unlocked during the analysis. The first mechanism was partly broken, as the connection of one of the guiding wheels and the bar was missing (Fig 5(bVII)). However, this was not an obstacle for the chest opening thanks to a system of levers outside of the scanned area connecting both wheels that transferred the movement of one wheel to the other one. It was not possible to repair this malfunction, probably caused during the manufacturing of the chest, as the parts of the guiding mechanism would have to be rearranged.

The second mechanism was not functional either because it was stuck in the closed position regardless of the cap movement. It was estimated and consequently confirmed that there had been a misplaced spring outside of the scanned area which usually served to push the lever with the bolts back. The misplaced spring was actually the reason why the chest could not be opened.

The intended function of the third mechanism was explained neither by the CT analysis nor after dismantling of the lock during the restoration intervention. It was not possible to lift the catcher enough by turning the key, thus, the trajectory of the hole could not reach the position of the peg in any way (Fig 6). A hypothesis was formed that the mechanism had never

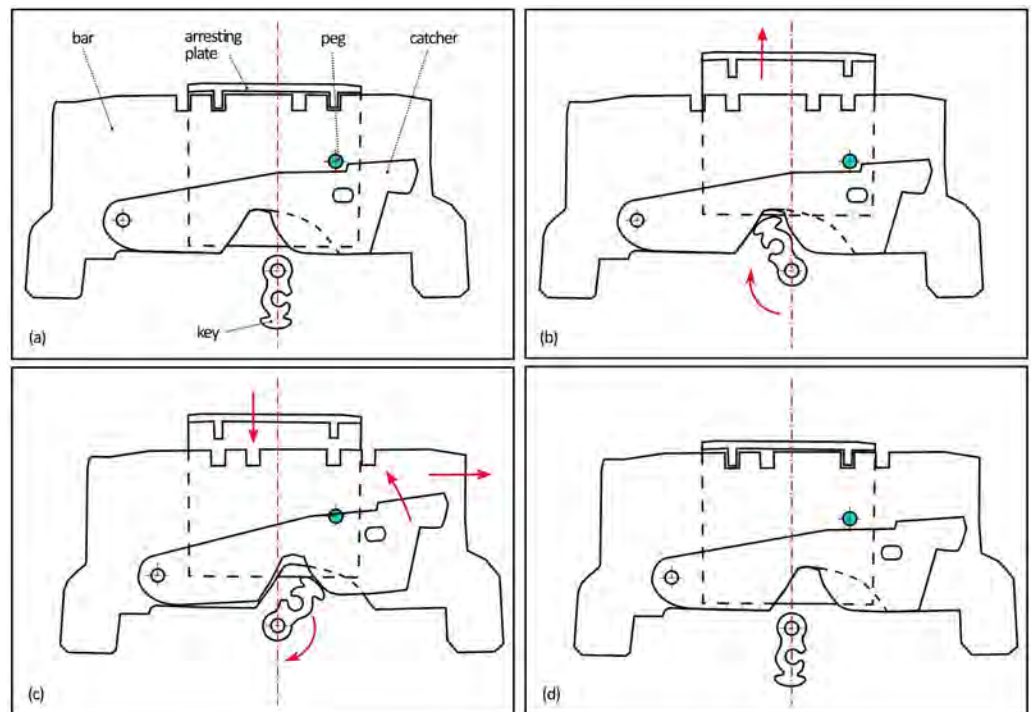


**Fig 6.** The first mechanism motion scheme from the locked position (a) to the unlocked position (d) marked by the arrows, demonstrating the malfunction of the third mechanism; the trajectory of the hole cannot reach the position of the peg (marked blue).

<https://doi.org/10.1371/journal.pone.0235316.g006>

actually been functional, because no signs of damage were indicated, and it was still possible to open the chest despite the non-functionality of the third mechanism.

If the key was not missing and all the mechanisms were fully functional, three steps would be necessary in the opening process. The first secret button (lower left corner of the frame) would have to be pushed to turn the X-shaped cap and would reveal the keyhole. The second step would be inserting the key, pushing the second secret button (upper right corner of the frame) and turning the key. The final step, removing the key and turning the X-shaped cap back to hide the keyhole, would follow. Only after these three steps it would be possible to open the chest.

### Restoration intervention

A temporary key copy was created based on the shape and dimensions (Table 1) acquired from the CT measurement.

The only repairable issue preventing the opening was the loosened spring of the first mechanism. The lock bolt connected to the spring had to be pushed by a long custom-made iron rod inserted into the chest through the hole in its bottom, possibly used to fasten the chest to the ground. After opening the chest, it was found out that the spring had only fallen out from its position and it was possible to repair the mechanism immediately.

After the opening, the whole chest including the lock mechanism was dismantled, there was no content hidden inside. The material of the chest suffered from a corrosion attack and it was polluted by dust and grease. Therefore, all the parts of the chest were cleaned and preserved. An original dark green surface coating in a very good condition was revealed. The corrosion products were removed or stabilized. Several missing minor parts, such as nuts or pegs, were replaced if possible.

The lock mechanism was repaired and it was possible to lock it again. Despite the functionality of the mechanism, it was recommended by the restorer not to lock the chest, because the parts of the mechanisms were worn out and they could be easily broken down again. Such a damage would probably lead to a necessary re-conservation of some of the parts or it could even prevent the chest opening again. As the temporary key copy used to open the chest before the intervention was not esthetical enough, a second copy (see Fig 7) was manufactured for the exhibition purposes [27].

### Conclusions

The non-destructive exploration of the 19<sup>th</sup> century treasure chest lock mechanism by means of X-ray computed tomography was carried out successfully. Despite several restraints, such as the high absorbing material and the size of the chest, the obtained tomographic data were of a sufficient quality and they allowed creating a 3D model of the lock mechanism. Therefore, it was possible to explore all parts of the lock in detail, to reveal the potential damages and to obtain the dimensions required for a new key copy. It was found out that the chest had not been locked and the only issue preventing it from opening was, in fact, a misplaced spring of the second mechanism. Based on the acquired information, it was possible to open the chest non-destructively. A conservation and restoration intervention was performed including the lock mechanism repair and the key manufacturing. Since any destructive approach is always preferably avoided by the restorers, this method might become a useful tool in the cultural heritage preservation practice.



Fig 7. Second manufactured key copy; the key bit is pictured in two different angles.

<https://doi.org/10.1371/journal.pone.0235316.g007>

## Supporting information

**S1 File. Lock mechanism of a historical chest.**  
(PDF)

## Author Contributions

**Conceptualization:** Jozef Kaiser.

**Data curation:** Eva Zikmundová, Vladimír Sládek, Jozef Kaiser.

**Formal analysis:** Eva Zikmundová, Vladimír Sládek.

**Funding acquisition:** Jozef Kaiser.

**Investigation:** Tomáš Zikmund.

**Methodology:** Tomáš Zikmund.

**Project administration:** Jozef Kaiser.

**Resources:** Jozef Kaiser.

**Supervision:** Jozef Kaiser.

**Validation:** Eva Zikmundová, Vladimír Sládek, Jozef Kaiser.

**Visualization:** Eva Zikmundová, Tomáš Zikmund.

**Writing – original draft:** Eva Zikmundová, Tomáš Zikmund, Vladimír Sládek, Jozef Kaiser.

## References

1. Hsieh J. *Computed Tomography: Principles, Design, Artifacts, and Recent Advances*: SPIE Press; 2003.
2. Attwood D. *Soft X-Rays and Extreme Ultraviolet Radiation: Principles and Applications*: Cambridge University Press; 2007.
3. Tesarova M, Zikmund T, Kaucka M, Adameyko I, Jaros J, Palousek D, et al. Use of micro computed-tomography and 3D printing for reverse engineering of mouse embryo nasal capsule. *Journal of Instrumentation*. 2016; 11. <https://doi.org/10.1088/1748-0221/11/03/c03006>
4. Kak A, Slaney M. *Principles of Computerized Tomographic Imaging*: Society for Industrial and Applied Mathematics; 2001. 335 p.
5. Baird E, Taylor G. X-ray micro computed-tomography. *Current Biology*. 2017; 27(8):R289–R91. <https://doi.org/10.1016/j.cub.2017.01.066> PMID: 28441557
6. Friml J, Prochazkova K, Melnyk G, Zikmund T, Kaiser J. Investigation of Cheb relief intarsia and the study of the technological process of its production by micro computed tomography. *Journal of Cultural Heritage*. 2014; 15(6):609–13. <https://doi.org/10.1016/j.culher.2013.12.006>
7. Zhang X, Blaas J, Botha C, Reischig P, Bravin A, Dik J. Process for the 3D virtual reconstruction of a microcultural heritage artifact obtained by synchrotron radiation CT technology using open source and free software. *Journal of Cultural Heritage*. 2012; 13(2):221–5. <https://doi.org/10.1016/j.culher.2011.08.004>
8. Okochi T. A nondestructive dendrochronological study on japanese wooden shinto art sculptures using micro-focus X-ray Computed Tomography (CT) Reviewing two methods for scanning objects of different sizes. *Dendrochronologia*. 2016; 38:1–10. <https://doi.org/10.1016/j.dendro.2016.01.004>
9. Morigi MP, Casali F, Bettuzzi M, Brancaccio R, D'Errico V. Application of X-ray Computed Tomography to Cultural Heritage diagnostics. *Applied Physics a-Materials Science & Processing*. 2010; 100(3):653–61. <https://doi.org/10.1007/s00339-010-5648-6>
10. Stoel BC, Borman TM. A Comparison of Wood Density between Classical Cremonese and Modern Violins. *Plos One*. 2008; 3(7). <https://doi.org/10.1371/journal.pone.0002554> PMID: 18596937
11. Van den Bulcke J, Van Loo D, Dierick M, Masschaele B, Van Hoorebeke L, Van Acker J. Nondestructive research on wooden musical instruments: From macro- to microscale imaging with lab-based X-ray CT systems. *Journal of Cultural Heritage*. 2017; 27:S78–S87. <https://doi.org/10.1016/j.culher.2016.01.010>
12. Karl S, Kazimierski KS, Hauzenberger CA. An interdisciplinary approach to studying archaeological vase paintings using computed tomography combined with mineralogical and geochemical methods. A Corinthian alabastron by the Erlenmeyer Painter revisited. *Journal of Cultural Heritage*. 2018; 31:63–71. <https://doi.org/10.1016/j.culher.2017.10.012>
13. Wilson PF, Smith MP, Hay J, Warnett JM, Attridge A, Williams MA. X-ray computed tomography (XCT) and chemical analysis (EDX and XRF) used in conjunction for cultural conservation: the case of the earliest scientifically described dinosaur *Megalosaurus bucklandii*. *Heritage Science*. 2018; 6:14. <https://doi.org/10.1186/s40494-018-0223-0> PMID: 31258911
14. Kalender WA. *Computed Tomography: Fundamentals, System Technology, Image Quality, Applications*: Wiley; 2011.
15. De Chiffre L, Carmignato S, Kruth JP, Schmitt R, Weckenmann A. Industrial applications of computed tomography. *Cirp Annals-Manufacturing Technology*. 2014; 63(2):655–77. <https://doi.org/10.1016/j.cirp.2014.05.011>
16. Morigi MP, Casali F, Berdondini A, Bettuzzi M, Bianconi D, Brancaccio R, et al. X-ray 3D Computed Tomography of large objects: investigation of an ancient globe created by Vincenzo Coronelli. O3A - Optics for Arts, Architecture, and Archaeology Conference; 2007 Jun 20–22; Munich, GERMANY2007.
17. Re A, Albertin F, Avataneo C, Brancaccio R, Corsi J, Cotto G, et al. X-ray tomography of large wooden artworks: the case study of "Doppio corpo" by Pietro Piffetti. *Heritage Science*. 2014; 2(1):19. <https://doi.org/10.1186/s40494-014-0019-9>
18. Špaček M. Draft restoration plan for a council bench from the exposition of Vlašský dvůr, Kutná Hora (in Czech). 2017.
19. Kos M. Restoration of the objects for the purpose of new expositions at the Rokštejn castle (in Czech). *Museum Factum*. 2018; 8(1):7–8.
20. Boyce C, Butler JT. *Dictionary of Furniture: Second Edition*: Skyhorse; 2014.
21. Piña LA. *Furniture in History, 3000 B.C.-2000 A.D.*: Prentice Hall; 2010.
22. Rivers S, Umney N. *Conservation of Furniture*: Butterworth Heinemann; 2003.
23. Novotný A. *Prague guild chests and standards (in Czech)* Prague: Pražské nakladatelství V. Poláčka; 1948.

24. Kieser A. Organizational, Institutional, and Societal Evolution: Medieval Craft Guilds and the Genesis of Formal Organizations. *Administrative Science Quarterly*. 1989; 34(4):540–64. <https://doi.org/10.2307/2393566>
25. Weir AK. Material Culture of the Guild: A Study of a German Cabinetmakers' Guild Chest. *Studies in Eighteenth-Century Culture*. 1999; 28:173–206. <https://doi.org/10.1353/sec.2010.0102>
26. Večeř A. On construction and manufacturing of European and American locks (in Czech). Prague: I. L. Kober; 1926.
27. Müller V. Restoration Documentation: City Chest (in Czech). Turnov: Střední uměleckoprůmyslová škola a Vyšší odborná škola Turnov, Skálova 373, příspěvková organizace; 2014.
28. GE Phoenix v|tome|x L 240 [cited 2018 12/28]. <http://www.ge-mcs.com/en/radiography-x-ray/ctcomputed-tomography/vtomex-l-240.html>.
29. Boas F, Fleischmann D. CT artifacts: Causes and reduction techniques; 2012.
30. Davis GR, Elliott JC. Artefacts in X-ray microtomography of materials. *Materials Science and Technology*. 2006; 22(9):1011–8. <https://doi.org/10.1179/174328406X114117>
31. Baranowski T, Dobrovolskij D, Dremel K, Holzinger A, Lohfink G, Schladitz K, et al. Local fiber orientation from X-ray region-of-interest computed tomography of large fiber reinforced composite components. *Composites Science and Technology*. 2019; 183:12. <https://doi.org/10.1016/j.compscitech.2019.107786>
32. Fishman EK, Jeffrey RB. *Multidetector CT: Principles, Techniques, and Clinical Applications*: Lippincott Williams & Wilkins; 2004.
33. VG Studio MAX software [cited 2018 12/28]. <https://www.volumegraphics.com/en/products/vgstudio-max.html>.

PAPER [XXI]



# An Innovative Detection of Mechanically Separated Meat in Meat Products

Matej Pospiech<sup>1</sup> · Tomas Zikmund<sup>2</sup> · Zdeňka Javůrková<sup>1</sup> · Jozef Kaiser<sup>2</sup> · Bohuslava Tremlová<sup>1</sup>

Received: 6 May 2018 / Accepted: 1 November 2018  
© Springer Science+Business Media, LLC, part of Springer Nature 2018

## Abstract

In meat products, mechanically separated meat (MSM) is often used as a raw material. Usage of MSM has economic benefit for meat industries and height utilization of animal raw material. In opposite is consumer concern for height quality of meat products. In order to detect MSM, invasive/destructive methods are mainly used and their nature is largely based on demonstrating the accompanying substances or structures. This paper describes a new non-invasive method to detect bone fragments as accompanying structures of MSM and it is based on X-ray micro computed tomography ( $\mu$ CT).  $\mu$ CT method was tested on a cooked meat product containing 50% of MSM. Bone tissue detected based on the higher density via  $\mu$ CT was confirmed by the image analysis and histochemical method using alizarin red staining which is used for detection of bone tissue. The  $\mu$ CT method was verified as a suitable non-destructive method to analyze bone fragments in meat products with the possibility to determine their shape parameters.

**Keywords** Micro computed tomography · Bone fragment · Meat products · Histochemistry · Mechanically separated meat

## Introduction

Meat products represent a broad family of products which differ in composition, degree of processing, production technology, and post-processing storage. Diversity of these factors makes meat products problematic for detection of individual components contained therein. Quality of some meat products is often reduced, in particular due to the pressure of retail chains on the lowest price possible. Also, the issue of meat product adulteration is still topical, and in this context it may be just about the unauthorized use of mechanically separated meat (MSM) in products or incorrect declaration of this raw material in the product. This raw material is still the subject of interest not only to the public but also within the professional sphere. Although MSM is a raw material of animal origin, under current legislation it cannot be considered meat (European Union 2011). MSM represents raw material which

was acquired of meaty bones using machines and the structure of muscle fibers was modified (Josefowitz et al. 2007). Composition of MSM differs from hand deboned meat (HDM). Higher content of connective tissues, bone marrow (Toldrá et al. 2012), cartilage (Pickering et al. 1995), bones (Pickering et al. 1995; Branscheid and Troeger 2012), and the associated higher content of calcium (Branscheid and Troeger 2012) was reported in MSM.

Currently, MSM can be detected using various methods. These methods include chemical methods that can determine the accompanying substance amount of connective tissue (Zarkadas et al. 1995), amount of iron, amount of bone marrow (Toldrá et al. 2012), haem pigments as well as amount of calcium (Branscheid and Troeger 2012).

In case of MSM detection in meat products, however, we face a problem since individual substances contained in MSM in larger quantities can get into meat products from sources different from MSM, for example higher amounts of connective tissue (Zarkadas et al. 1995), haem pigment, and calcium (Branscheid and Troeger 2012). With regard to the above, the histological methods are the most commonly used methods to detect MSM in meat products in the EU. In these methods, however, only a small portion of the sample is analyzed and the result is therefore burdened by error which is of course minimized in case of compliance with the principles of sampling. Given the above facts, MSM demonstration in meat

✉ Zdeňka Javůrková  
javurkovaz@vfu.cz

<sup>1</sup> University of Veterinary and Pharmaceutical Sciences Brno, Palackého tř. 1946/1, 612 42 Brno, Czech Republic

<sup>2</sup> CEITEC—Central European Institute of Technology, Brno University of Technology, Purkyňova 656/123, 612 00 Brno, Czech Republic

products is not easy and often must rely on more than one examination (EFSA 2013).

Analysis of bone tissue may also be performed using non-invasive methods, such as X-ray analysis (Tao and Ibarra 2000). In their work, Tao and Ibarra (2000) describe the proposed imaging method which eliminated the false patterns and enhanced the sensitivity of X-ray in bone fragment detection. The technique tested by them has the potential for non-destructive internal detection of hazardous materials in food products with uneven thickness.

The aim of this work was to demonstrate an entirely new non-invasive detection of MSM utilizing X-ray micro computed tomography ( $\mu$ CT) based on the detection of bone fragments as an indicator of the use of MSM in meat products. Identification of bone tissue in  $\mu$ CT data is performed using correlation of the same  $\mu$ CT slice and histochemical section. Accuracy of the method for detection of individual bone fragments is discussed with regard to classic histochemical examination.

## Material and Methods

A cooked meat product containing 50% of MSM, as declared by the manufacturer, was used for the analysis. The sausage (Masokombinát Plzeň, Plzeň, Czech Republic) was purchased in the market, it was a finely ground sausage with a total weight of 500 g, 19 cm long, and 6.5 cm wide.

Composition of the product: chicken MSM 50%, water, pork 10%, pork skin, potato starch, nitrite salt mixture (edible salt with iodine), preservative E250, soy protein, stabilizer E450, mixture of spices and spice extracts, dextrose, mustard seed, antioxidant E300, pigment E120, smoky aroma, thickener E412, and acidity regulator E500. Basic chemical composition: proteins 10%, carbohydrates 5.2%, fat 17.3%, fiber 1%, and sodium 0.8%.

### MicroCT Analysis

The  $\mu$ CT measurements of the sample were performed using the system of GE phoenix v|tome|x L240 (GE, Phoenix, AZ USA), which is equipped with a 240 kV/320 W maximum power microfocus X-ray tube and flat panel detector GE DXR250 with 2048  $\times$  2048 pixel, 200  $\times$  200  $\mu$ m pixel size. First, half of the sausage with acceleration voltage 120 kV, current 300  $\mu$ A, integration time 500 ms, number of images 2400, and voxel size of 42  $\mu$ m was measured. These measurement was focused to determine the appropriate resolution for the purpose of detecting bone fragments and specify the appropriate place for the sampling area for subsequent region of interest (ROI) analysis. Second, the ROI with acceleration voltage 65 kV, current 170  $\mu$ A, integration time 333 ms, number of images 2200, and voxel size 22  $\mu$ m was measured. The

aim of ROI measurement was to achieve a better resolution for comparing the structure with histochemical analysis, and in particular to digitize the ROI. This step ensured that identical sections in terms of morphology, bone fragments, and their distribution will be compared.

The tomographic reconstruction was realized using GE phoenix datos|x 2.0 3D (GE, Phoenix, AZ USA). The “Only Threshold” algorithm was used for the pore analysis and the threshold value for each data set was chosen based on the visual assessment of a segmented bone tissue in a  $\mu$ CT cross-section. Non-planar view function was used to flatten the image, which corresponds to the physical section analyzed by the histochemical method.

### Quantitative Comparison of Methods’ Results

Results of bone fragments per area unit obtained by the applied methods were compared. For histological examination, the number of bone fragments was counted by the examiner. For image analysis, histological sections were scanned by the film scanner Nikon SuperCool Scan9000 (Nikon, Japan) and automatically evaluated by NIS-elements software (Laboratory Imaging, s.r.o., Prague, Minato, Czech Republic) based on thresholding the HUE parameter (hue, lightness, and chroma of colors). The number of bone fragments with  $\mu$ CT analysis was evaluated based on the brightness intensity.

## Results and Discussion

The study shows a unique approach to the examination of meat product quality using  $\mu$ CT analysis. The method is used to analyze the presence of MSM. Previous studies dealing with the  $\mu$ CT methods are focused rather on describing the relationship between microstructure and texture of foodstuffs (Schoeman et al. 2016). Validating the detection of bone fragments in meat products shows a new option to examine the use of MSM in products. In particular with regard to the non-destructive nature of the method (Léonard et al. 2008), this finding opens the possibility to use X-ray and  $\mu$ CT technologies for the inspection of raw materials used in foods that can also be applied in the quality inspection of meat products. The advantage of these techniques is the possibility to involve them in the production systems of food businesses directly in their production lines due to the non-destructive measurement (Haff and Toyofuku 2008).

### MicroCT Data and Histology Correlation

The level of X-ray transmission depends mainly on the mass density and mass absorption coefficient of the material (Lim and Barigou 2004). Different densities of the material are

shown in the  $\mu$ CT data by means of different pixel intensity in the image. Denser materials, such as bone tissue, appear in lighter pixels (Fig. 1) than adipose tissue, muscle tissue, organs, or plant parts. The darkest areas represent air cavities. Objective of the correlation between the  $\mu$ CT slice and histological image was to confirm that the light areas represent just bone tissue based on the distribution of these areas and the similarity of morphological features of the individual bone fragments. Therefore, the first tomographic slice section of salami (ROI) was selected and compared with the histological section. This guaranteed an adequate comparison of  $\mu$ CT image and histological sections of the sample. Suitability of histological methods for the detection of bone tissue has been validated in numerous studies (Tremlová et al. 2006).

Despite the different resolutions of the two images, equivalence of the two methods in the occurrence of bone fragments was demonstrated on the basis of the images. Different thickness of the histological section and  $\mu$ CT slice is manifested in some cases by greater or smaller area of bone fragments; nevertheless, it is still possible to recognize the identical shapes of the fragments and their relative positions to one another. An accurate analysis of the structure of rather large fragments using histological methods is problematic. This is due to the destructive nature of histological methods.

Density differences for bone tissue and cartilage is also manifested in different pixel intensities (Fig. 2). To set the threshold, a bone fragment was selected (Fig. 1B) which was first confirmed by histological analysis. Objects with lower intensity were excluded from  $\mu$ CT analysis. It is important to set the threshold according to different calcium contents in bone which can be affected by several factors (Field 2000).

To minimize structural changes, the method of paraffin blocks was used because it allows formation of less distorted structure of the sample in comparison with cryosections. An absolute avoidance of changes in the microstructure of this matrix, however, is not possible causing certain deformities of meat product microstructure also in the examined histological sections (Fig. 3). In particular, sections folded, sections

torn apart, and protein matrix collapsed in the slices were observed. Moreover, slicing the sample results in displacement of bone fragments and fragmentation or falling out of them from the histological sections (Fig. 3B). The reason for this phenomenon is different hardness of the bone matrix and the meat product. Falling out of bone fragments was confirmed by the discovery of bone fragments in the neighboring histological sections or its presence over the product matrix (Fig. 3A). Falling out of bone tissue in histological preparations is also accompanied by destruction of the original matrix (Fig. 3D).

## Comparison of Methods

Results of  $\mu$ CT analysis were further compared (in pairs) with histochemical and image analysis (IA). For the comparison, the first  $\mu$ CT slice of ROI and the first following 4  $\mu$ m thick histological section were used. The comparison focused on the number of bone fragments detected by each method per area unit. Results are shown in Table 1.

Using histological analysis and image analysis (Tremlová et al. 2006) to detect the presence of bone tissue was validated as options to demonstrate the use of MSM in meat products. Due to that, these methods were compared with the  $\mu$ CT method, which is being validated. Nearly identical results were achieved in the image and  $\mu$ CT analysis in the total number of bone fragments per square centimeter. This result also confirmed the correctness of the selected threshold for bone segmentation in  $\mu$ CT data. Histological analysis detected more bone fragments than by the image analysis and  $\mu$ CT method. The reason is higher resolution of this method, up to 2.7  $\mu$ m. The disadvantage for routine use, however, is the section area calculation difficulty and time-consuming testing. The section area calculation within the histological method is performed manually with a calibrated ruler with an accuracy of 0.1 mm and converting to the closest geometric shape. Calculation in the case of complex shapes can only be approximate. An option would be a combination with evaluation of

**Fig. 1** Example of verification of morphological structure of bone fragment detection, unequal size is due to the different thickness of sections and  $\mu$ CT slices. (1) Histological analysis section thickness 4  $\mu$ m; (2)  $\mu$ CT analysis slice thickness 22  $\mu$ m

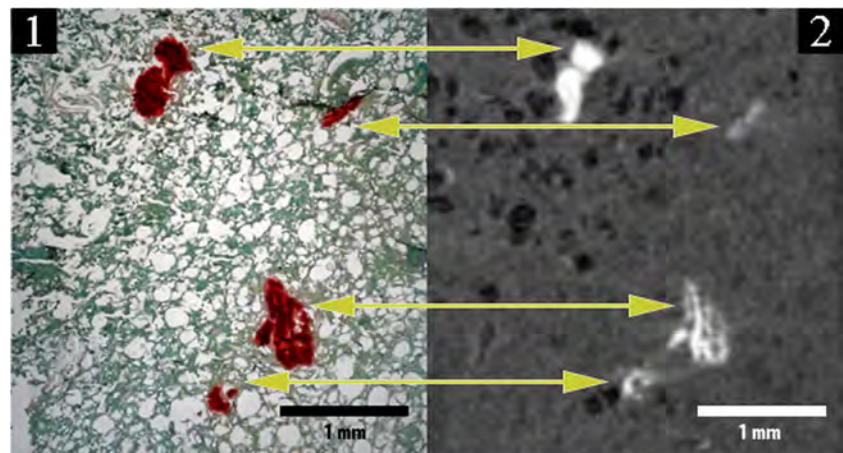
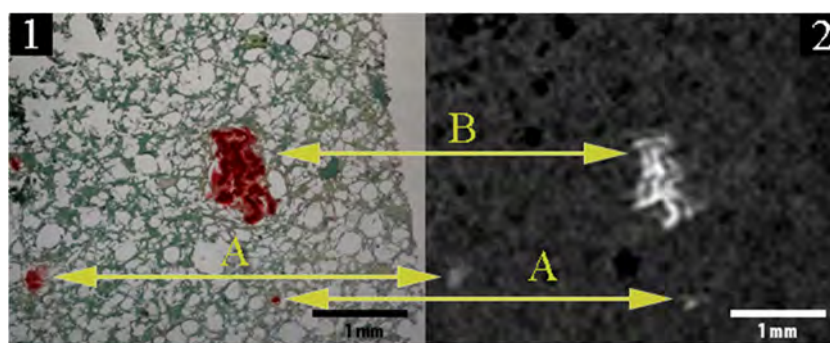


**Fig. 2** Different intensities of cartilage (A) compared with the intensity of bone tissue (B). (1) Histological analysis section thickness 4  $\mu\text{m}$ ; (2)  $\mu\text{CT}$  analysis slice thickness 22  $\mu\text{m}$



histological section area using IA, but that would require more equipment in the histological laboratory and increase the cost of the examination.

To evaluate whether MSM was used in the product, it is still necessary to have defined limits in terms of the number of bone fragments which can be considered positive or negative results regarding the use of MSM. In this work, the limit used by enforcement authorities of the Czech Republic, Slovakia, and Germany was applied. Namely, it is 0–0.2 negative, 0.2–1.5 doubtful, and more than 1.5 positive (Ketteritzsch 2007). These limits apply for histological analysis. For  $\mu\text{CT}$ , this limit may be adjusted, in particular due to the fact that this method can examine a larger volume of products than is the case with histological methods. It is therefore expected that  $\mu\text{CT}$  method will be more accurate.

### MicroCT Analysis

The  $\mu\text{CT}$  analysis visualizes the inner structure according to the material absorption properties. For the purpose of showing bone fragments, there is no need of a sample preparation (except the freezing procedure when the salami is moving) as the bone is a much more absorbing material against the soft tissue. For this reason, the segmentation of the bone in the  $\mu\text{CT}$  data is done using simple global thresholding method. Thanks to this, the detection procedure and the consequent analysis are very short time processes. Once the objects are segmented and recorded like individual particles, the morphological parameters like their volume, surface, center of gravity, position, and so on can be obtained.

The benefit of  $\mu\text{CT}$  technique is to examine the whole object in one measurement which can take a half or up to 1 h. However, the size of the sample influences the resulting voxel resolution as the  $\mu\text{CT}$  systems use the cone geometry of the X-ray beam for a magnification (Lim and Barigou 2004). That means a smaller object can be measured with higher resolution than the bigger one (typically object 10 mm in a diameter is possible to get with 10  $\mu\text{m}$  voxel resolution). It is always aimed to find a compromise between computing time and the accuracy of the results (Schoeman et al. 2016).

The measurement of ROI in twice better resolution (22  $\mu\text{m}$ ) proved that detectability of bone fragments was increased (160.18) in comparison with half of the sample (81.11) in lower resolution (42  $\mu\text{m}$ ). The total volume of bone fragments in the entire salami would not be significantly changed. It is also known that comparison of  $\mu\text{CT}$  measurement with the same settings is unable to give exactly the same results (result fluctuation can occur), which also applies to voxel resolution (Zatočilová et al. 2016). In comparison with histological section, we found several bright small regions in  $\mu\text{CT}$  data which were not detected as their brightness was not as high as that of a bone. This can mean that the fragment size is under the voxel size or it can be a piece of cartilage.

Application  $\mu\text{CT}$  analysis to different ingredients of meat products has already been validated in numerous studies. Especially for fat analysis where Frisullo et al. (2009) did not demonstrate a statistically significant difference between the  $\mu\text{CT}$  analysis and soxlet extraction, and in their subsequent study, Frisullo et al. (2010) and also Santos-Garcés et al. (2014) confirmed a strong correlation between these two

**Fig. 3** Falling out of bone fragments in histological analysis. A fragmentation and displacement; B size difference of bone fragments; C bone fragments missed in a histological section; D deformed zone of the original occurrence of bone fragment. 1 Histological analysis section thickness 4  $\mu\text{m}$ ; 2  $\mu\text{CT}$  analysis slice thickness 22  $\mu\text{m}$

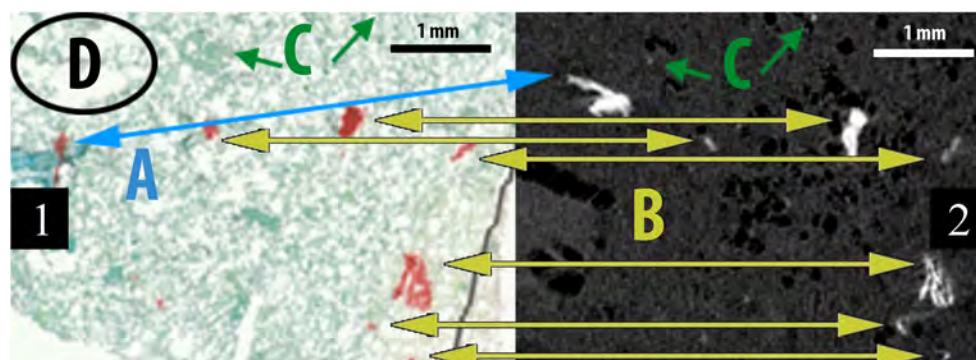


**Table 1** Number of bone fragments in product sections, comparison of methods

Analyzed section and corresponding slice	$\mu$ CT analysis			Histological analysis			Image analysis		
	Area [cm <sup>2</sup> ]	Number of bone fragments	Analyzed depth of slice [ $\mu$ m]	Area [cm <sup>2</sup> ]	Number of bone fragments	Analyzed depth of section [ $\mu$ m]	Area [cm <sup>2</sup> ]	Number of bone fragments	Analyzed depth of section [ $\mu$ m]
1.	3.8	54	22	3.36	47	4	4.01	53	4
2.				3.36	70	4	3.85	54	4
3.				3.36	55	4	4.17	55	4
4.				3.36	67	4	3.8	65	4
Sum			22			24			24
Average	3.80	54.00		3.60	59.75		3.98	56.75	
SD	0.00	0.00	0.00	0.00	9.26	0.00	0.16	4.82	0.00
Number of bone fragments/cm <sup>2</sup>		14.21			16.60			14.26	
MSM detection		Positive			Positive			Positive	

Note: bone fragment in quantity: 0–0.2 negative, 0.2–1.5 doubtful, and more than 1.5 positive (Ketteritzsch 2007)

methods. In the case of meat or meat product components, the advantage of  $\mu$ CT analysis is also its lower impact on the environment and human health, excluding organic solvents (Frisullo et al. 2010). Moreover, the  $\mu$ CT method used in the study provides additional information about bone fragments. Within MSM demonstration, parameters of individual bone fragments, such as volume, length, circumference, diameter, and surface area can be detected without any additional costs and sample processing, which can be used also for setting the conditions for use of MSM or appropriate setting of separators. This could be used, e.g., to check the maximum size of bone fragments stipulated in the United States of America (U.S.) provisions (Food Safety and Inspection Service, USDA 2003b). U.S. legislation specifies more requirements on qualitative parameters of MSM than EU legislation. US Department of Agriculture (USDA) sets the following limits. The maximum allowed amount of bone fragments in MSM is 3% and also imposes requirements on the size of the bone fragments. Ninety-eight percent of bone fragments in MSM must be smaller than 0.5 mm and the maximum width must not exceed 0.85 mm (Food Safety and Inspection Service, USDA 2003a).

In case of implementation, the method into the production line, it would be possible to evaluate other parameters of the meat product as well. Such as air volume, surface-to-volume ratio, connectivity, cell wall thickness and degree of anisotropy (Lim and Barigou 2004). Ultrafast  $\mu$ CT was confirmed for fresh agricultural products. The same author mentioned that high cost of performing is restricted for  $\mu$ CT. Nevertheless, X-ray  $\mu$ CT can serve as a valuable technique for the development of future prediction models for internal quality (Donis-González et al. 2014).

Currently, the  $\mu$ CT method is the only method applicable for MSM detection in product line system. Present-day MSM

detection methods used for bone calcium content determination (Branscheid and Troeger 2012) are time consuming. Moreover, some of the MSM detection methods used for bone or other accompanying compound analysis, use hazardous organic solvents with negative impact on the environment and on human health (Pickering et al. 1995; Branscheid and Troeger 2012, Zarkadas et al. 1995, Tremlová et al. 2006). On the other hand, histological methods (Pickering et al. 1995, Tremlová et al. 2006) achieve higher resolution. In case there is a need to obtain more precise morphological parameters of bone fragment, the other option is to use a smaller sample for higher resolution  $\mu$ CT evaluation. Furthermore, the  $\mu$ CT methods have economic benefit for the producers because in comparison with chemical methods, they are undestructible, except for the high resolution analysis, where the sample has to be resized to a small one.

## Conclusion

The  $\mu$ CT method was verified as a method suitable for analysis of bone fragments in meat products. Its comparison with histological analysis also confirmed the non-destructive nature of the  $\mu$ CT method and achievement of sufficient resolution for the analysis of a small sample of ROI (22  $\mu$ m) as well as the entire meat product (42  $\mu$ m). Size and shape parameters of bone fragments were comparable for both resolutions applied. The  $\mu$ CT method can thus be used to detect the number, volume, or other shape parameters which can be used to determine the use of MSM in meat products. Another positive factor is that the current  $\mu$ CT systems are able to non-destructively examine rather large numbers of samples against the standard histological examination. In practice, the large number of inspected samples can minimize sampling errors

and the short measurement time allows to compose this system in the production lines to examine final products.

**Funding information** This work was supported by the project of CEITEC 2020 (LQ1601) with financial support from the Ministry of Education, Youth and Sports of the Czech Republic under the National Sustainability Programme II and CEITEC Nano Research Infrastructure (MEYS CR, 2016-2019).

## Compliance with Ethical Standards

**Conflict of Interest** Matej Pospiech declares that he has no conflict of interest. Tomas Zikmund declares that he has no conflict of interest. Zdeňka Javůrková declares that she has no conflict of interest. Jazef Kaser declares that he has no conflict of interest. Bohuslava Tremlová declares that she has no conflict of interest.

**Human and Animal Studies** This article does not contain any studies with human participants or animal performed by any of the authors.

**Informed Consent** Not applicable.

## References

- Branscheid W, Troeger K (2012) Mechanical recovery of meat and residual meat in poultry. *Fleischwirtschaft* 92(1):98–105
- Donis-González IR, Guyer DE, Pease A, Barthel F (2014) Internal characterisation of fresh agricultural products using traditional and ultrafast electron beam X-ray computed tomography imaging. *Biosyst Eng* 117:104–113
- EFSA Panel on Biological Hazards (BIOHAZ) (2013) Scientific opinion on the public health risks related to mechanically separated meat (MSM) derived from poultry and swine. *European Food Safety Authority*, p 11
- European Union. Regulation of the European Parliament and of the council no. 1169/2011 of 25 October 2011, on the provision of food information to consumers, amending Regulations (EC) No 1924/2006 and (EC) No 1925/2006 of the European Parliament and of the Council, and repealing Commission Directive 87/250/EEC, Council Directive 90/496/EEC, Commission Directive 1999/10/EC, Directive 2000/13/EC of the European Parliament and of the Council, Commission Directives 2002/67/EC and 2008/5/EC and Commission Regulation (EC) No 608/2004. In: *Official Journal of the European Union* L No. 304, 22/11/2011, p 18–63
- Field RA (2000) Ash and calcium as measures of bone in meat and bone mixtures. *Meat Sci* 55(3):255–264. [https://doi.org/10.1016/S0309-1740\(99\)00147-3](https://doi.org/10.1016/S0309-1740(99)00147-3)
- Food Safety and Inspection Service, USDA (2003a) Mechanically separated (species). Office of the Federal Register, MD, Title 9, Section 319. 5:295–296
- Food Safety and Inspection Service, USDA (2003b) Limitations with respect to use of Mechanically Separated (Species). Office of the Federal Register, MD, Title 9, Section 319.6, p 297. <https://www.law.cornell.edu/cfr/text/9/319.6>. Accessed 20 July 2018
- Frisullo P, Laverse J, Marino R, Del Nobile MA (2009) X-ray computed tomography to study processed meat microstructure. *J Food Eng* 94(3):283–289. <https://doi.org/10.1016/j.jfoodeng.2009.03.020>
- Frisullo P, Marino R, Laverse J, Albenzio M, Del Nobile MA (2010) Assessment of intramuscular fat level and distribution in beef muscles using X-ray microcomputed tomography. *Meat Sci* 85(2):250–255. <https://doi.org/10.1016/j.meatsci.2010.01.008>
- Haff RP, Toyofuku N (2008) X-ray detection of defects and contaminants in the food industry. *Sens & Instrumen Food Qual* 2(4):262–273. <https://doi.org/10.1016/j.biosystemseng.2013.07.002>
- Josefowitz VP, Hildebrandt G, Islam R, Mare HJ (2007) Characteristics of the quality of mechanically separated turkey meat. *Fleischwirtschaft* 87(11):122–126
- Ketteritzsch K (2007) Berichte für Schwerpunktaufgaben, Nachweis von Separatorenfleisch in Würsten und Fleischerzeugnissen mittels Ca-Bestimmung und histologischer Untersuchung. *Landesamt für Verbraucherschutz Sachsen-Anhalt*, p 1–2
- Léonard A, Blacher S, Nimmol C, Devahastin S (2008) Effect of far-infrared radiation assisted drying on microstructure of banana slices: An illustrative use of X-ray microtomography in microstructural evaluation of a food product. *Journal of Food Engineering*, 85(1): 154–162. <https://doi.org/10.1016/j.jfoodeng.2007.07.01>
- Lim KS, Barigou M (2004) X-ray micro-computed tomography of cellular food products. *Food Res Int* 37(10):1001–1012. <https://doi.org/10.1016/j.foodres.2004.06.010>
- Pickering K, Evans CL, Hargin KD, Stewart CA (1995) Investigation of methods to detect mechanically recovered meat in meat products—III: microscopy. *Meat Sci* 40(3):319–326. [https://doi.org/10.1016/0309-1740\(94\)00062-C](https://doi.org/10.1016/0309-1740(94)00062-C)
- Santos-Garcés E, Muñoz I, Gou P, Garcia-Gil N, Fulladosa E (2014) Including estimated intramuscular fat content from computed tomography images improves prediction accuracy of dry-cured ham composition. *Meat Sci* 96(2):943–947. <https://doi.org/10.1016/j.meatsci.2013.09.018>
- Schoeman L, Williams P, du Plessis A, Manley M (2016) X-ray micro-computed tomography ( $\mu$ CT) for non-destructive characterisation of food microstructure. *Trends Food Sci Technol* 47:10–24. <https://doi.org/10.1016/j.tifs.2015.10.016>
- Tao Y, Ibarra JG (2000) Thickness-compensated X-ray imaging detection of bone fragments in deboned poultry—model analysis. *Trans ASAE* 43(2):453–459
- Toldrá F, Aristoy MC, Mora L, Reig M (2012) Innovations in value-addition of edible meat by-products. *Meat Sci* 92(3):290–296. <https://doi.org/10.1016/j.meatsci.2012.04.004>
- Tremlová B, Sarha P, Pospiech M, Buchtová H, Randulová Z (2006) Histological analysis of different kinds of mechanically recovered meat. *J Food Saf Food Qual* 57(3):85
- Zarkadas CG, Yu Z, Zarkadas GC, Minero-Amador A (1995) Assessment of the protein quality of beefstock bone isolates for use as an ingredient in meat and poultry products. *J Agric Food Chem* 43(1):77–83. <https://doi.org/10.1021/jf00049a015>
- Zatočilová A, Zikmund T, Kaiser J, Paloušek D, Kutný D (2016) Measurement of the porosity of additive-manufactured Al-Cu alloy using X-ray computed tomography. *Solid State Phenom* 258(1): 448–451

PAPER [XXII]

Article

# Selective Laser Melting Strategy for Fabrication of Thin Struts Usable in Lattice Structures

Radek Vrána <sup>1,\*</sup>, Daniel Koutný <sup>1</sup>, David Paloušek <sup>1</sup>, Libor Pantělejev <sup>2</sup>, Jan Jaroš <sup>1</sup>, Tomáš Zikmund <sup>3</sup> and Jozef Kaiser <sup>3</sup>

<sup>1</sup> Brno University of Technology, Faculty of Mechanical Engineering, Institute of Machine and Industrial Design, Technická 2896/2, 616 69 Brno, Czech Republic; Daniel.Koutny@vut.cz (D.K.); David.Palousek@vut.cz (D.P.); Jan.Jaros@vut.cz (J.J.)

<sup>2</sup> Brno University of Technology, Faculty of Mechanical Engineering, Institute of Materials Science and Engineering, Technická 2896/2, 616 69 Brno, Czech Republic; Libor.Pantelejev@vut.cz

<sup>3</sup> Brno University of Technology, Central European Institute of technology BUT, Purkyňova 123, 612 00 Brno, Czech Republic; Tomas.Zikmund@vut.cz (T.Z.); Jozef.Kaiser@vut.cz (J.K.)

\* Correspondence: Radek.Vrana@vut.cz; Tel.: +420-541-144-927

Received: 30 August 2018; Accepted: 12 September 2018; Published: 18 September 2018



**Abstract:** This paper deals with the selective laser melting (SLM) processing strategy for strut-lattice structure production which uses only contour lines and allows the porosity and roughness level to be managed based on combination of the input and linear energy parameters. To evaluate the influence of a laser scanning strategy on material properties and surface roughness a set of experiments was performed. The single welds test was used to find the appropriate processing parameters to achieve continuous welds with known width. Strut samples were used to find a suitable value of weld overlapping and to clarify the influence of input and linear laser energy on the strut porosity and surface roughness. The samples of inclined hollow struts were used to compare the wall thickness with single welds width; the results showed about 25% wider welds in the case of a hollow strut. Using the proposed SLM strategy it is possible to reach a significantly lower porosity and surface roughness of the struts. The best results for struts with an inclination of 35.26° were achieved with 25% track overlapping, input energy in the range from 9 J to 10.5 J and linear energy  $E_{lin}$  from 0.25 to 0.4 J/mm; in particular, the relative density of 99.83% and the surface roughness on the side of the strut of Ra 14.6 μm in an as-built state was achieved.

**Keywords:** selective laser melting (SLM); AlSi10Mg aluminum alloy; scanning strategy; porosity; roughness; contour strategy; melt-pool size; linear energy; input energy

## 1. Introduction

Nowadays, metallic porous materials such as cellular structures or foams have a wide range of applications. Metal foams are mostly used for energy-absorbing applications or as filling material of the conventionally produced profiles for weight reduction. Their most significant advantage is relatively cheap mass production. However, the regularity and shape of the foam structure cannot be precisely controlled [1–5]. On the other hand, the additively manufactured cellular lattice structures are mostly used for special parts in aerospace, space, cooling or biomedical applications [6–8]. The most important advantages of the lattice structure are their shape regularity and a wide range of possible materials that can be used [9,10]. One of the suitable additive technologies for lattice structure production is selective laser melting (SLM).

SLM is a layer-based metal additive technology allowing for rapid fabrication of prototypes and lightweight components with complex geometry [11–14]. Fabrication, using SLM, is affected by many

process parameters which have a significant effect on the final material properties. The main SLM process parameters are laser power (*LP*), laser speed (*LS*), thickness of the applied powder layer, distance between laser tracks, diameter of the laser beam, and scanning direction [15]. Its influence on the final mechanical properties was examined, especially for solid-based production; however, for lattice structures, this has not been well investigated.

Qiu et al. [8] investigated the influence of the laser power (*LP*) and the scanning (*LS*) speed on the diameter, shape and porosity of the struts made of AlSi10Mg material. The linear dependence between the strut diameter and the increasing *LP* was found. The authors used *LS* of 3500 mm/s while the *LP* was changed in the range from 150 W to 400 W. The diameter of strut changed from 260  $\mu\text{m}$  to 500  $\mu\text{m}$  for the nominal diameter of 300  $\mu\text{m}$ . Due to the number of struts in the lattice structure, the mechanical properties can significantly change. The dependence of the main process parameters on the strut porosity was evaluated, but only for one *LP* and *LS* level. Abele et al. [16] dealt with dimensional accuracy of the strut structure. The authors tested a laser strategy for lattice structure production focused on high dimensional accuracy of very thin struts ( $d = 0.2 \text{ mm}$ ). These struts were produced by only one laser path, and therefore the authors investigated primarily the offset of the laser contour paths. The linear energy  $E_{lin}$  (J/mm) and laser spot diameter were used as the main parameters. The authors defined the struts' size limitation as two times laser spot diameter. Leary et al. [17] investigated a manufacturability and surface roughness of the struts with the orientation typical for struts–lattice structures. They found that the surface roughness on the strut down-skin surface is significantly higher due to a heat transfer and sticking of the surrounding powder on the strut down-skin. The surface roughness is strongly dependent on the strut orientation which was also described by other authors [10,16,17]. Yan et al. [10] explained the higher surface roughness on the down-skin surface by the “stair effect” after slicing of the strut to the single layers. This effect increases at a lower strut inclination, where a greater part of the layer is produced directly on the powder. However, a lower height of layer thickness could decrease this effect. Koutný et al. [18] examined the influence of the strut orientation on the strut size. The samples were measured by a 3D optical scanner and evaluated by maximum inscribed cylinders inside the struts. Correction parameters for the struts' production with the accurate size were proposed.

Yu et al. [19,20] investigated the influence of the laser power and the scanning speed on the width of the single track. The scanning speed was found to be more influential in relation to the final width than the laser power. Samples fabricated with high energy density had a high porosity in the upper layers because the previous layers were re-melted and gas pores moved up to the current layer. Parts with full density were produced with high laser energy density. Wei et al. [21] showed that the weld samples produced in the linear energy density range of 1.5–1.875 J/cm had a continuous scan track with a relatively smooth surface without intertrack pores. Delroisse et al. [22] studied the influence of strut orientation on the microstructure. They found a heterogenous microstructure in case of inclined struts, while the vertical struts had a fully homogenous structure. The differences were explained by worse heat transfer in the bottom zone of the strut caused by strut orientation.

Koutný et al. [18] also examined the influence of the strut orientation on the strut size for samples made of stainless steel (*SS*) material. The results of *SS* material were different compared to aluminum alloy; while the samples of *SS* material had the diameter smaller than nominal, the samples of aluminum alloy had a larger diameter. Attar et al. [23] examined commercially pure titanium alloy (CP-Ti) from powder with a wide grain size range up to 100  $\mu\text{m}$ . The authors experimentally investigated the SLM process parameter to produce nearly full dense (>99.5%) CP-Ti cylindrical samples with diameter  $d = 4 \text{ mm}$  without any post-treatment.

The present study deals with SLM scanning strategy for struts fabrication using concentric contour laser paths in the entire strut cross-section instead of volume strategy [16]. The main aim is to allow for fabrication of struts–lattice structures with expected mechanical and material properties with high repeatability. This is very important for designing components for aerospace or space industries using finite element method (FEM) analysis [24] and topology optimization with great strength to weight

ratio. Due to a large number of the struts in the lattice structure, even a low increase in the single strut dimension can significantly change the mechanical properties of the lattice structure [8,25–28]. Also, the influence of the *LS* and *LP* process parameters on the struts' surface roughness and porosity are described.

## 2. Materials and Methods

### 2.1. Metal Powder Analysis

The AlSi10Mg aluminum alloy metal powder (TLS Technik GmbH, Bitterfeld, Germany) was used in all experiments. The metal powder was produced using a gas atomization in nitrogen atmosphere and its particles were almost spherical in shape (Figure 1b). A particle size distribution was analyzed (Horiba LA-960, Horiba, Kyoto, Japan) for powder quality verification. The results can be seen in the chart (Figure 1a). The particle mean size was 41.41  $\mu\text{m}$ , median size was 40.7  $\mu\text{m}$  and standard deviation was 12.9  $\mu\text{m}$ . The particle size up to 25.2  $\mu\text{m}$  represents 10% and the particle size up to 58  $\mu\text{m}$  represents 90% of particle size distribution. Depending on the particle size distribution, a 50  $\mu\text{m}$  layer was applied.

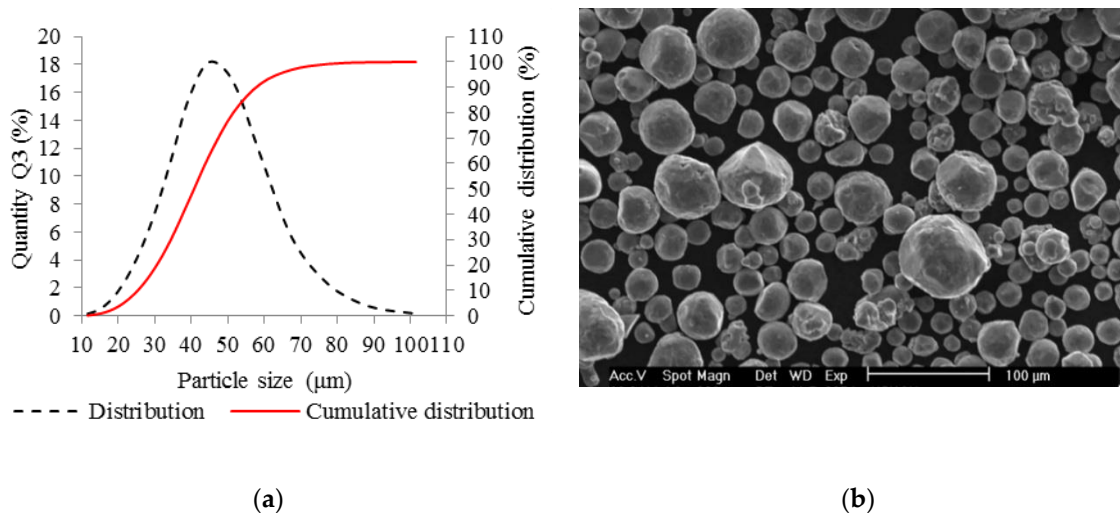


**Figure 1.** Selective laser melting (SLM) powder characteristics; (a) chart of particle size distribution; (b) shape of powder particles (scanning electron microscopy (SEM)).

### 2.2. Roughness Analysis

The struts samples were digitized by the optical measurement system (Atos Triple Scan III, GOM GmbH, Braunschweig, Germany) to find out the surface roughness on the strut side. The optical system was equipped with two 8 Mpx cameras and MV60 lens (resolution 17  $\mu\text{m}$ ). The samples were coated with a thin layer of  $\text{TiO}_2$  powder (thickness of around 3  $\mu\text{m}$ ) [29] before the scanning process and digitized separately one by one for a more detailed measurement. After digitization, the data were polygonised using a “more detailed” option in GOM Atos software. With the optical measurement, the down-skin surface cannot be sufficiently digitized. Therefore, data of micro-computed tomography were used.

The GOM Inspect software was employed to evaluate the surface roughness by comparing the section line of digitized strut surface and the best-fitted computer-aided design (CAD). (Figure 3a). Obtained values were used for calculation of the  $R_a$  surface roughness according to Equation (1).

$$Ra = \frac{1}{n} \sum_{i=1}^n |z_i| = \frac{|z_1| + |z_2| + \dots + |z_n|}{n} (\mu\text{m}) \quad (1)$$

### 2.3. Porosity Analysis

Software Image J was used for the initial porosity analysis of the top view sample images (8-bites) after basic grinding with the use a hand grinder (GP-2 Grinder, Sinowon, Dongguan, China). The image area for the analysis was cropped out using the rectangle window without inclusion of the rough border of the strut. Then, the colors were converted to black and white using the automatic threshold to reach a repeatability for all samples. The results of the porosity were evaluated as the percentage of black in the color white (Figure 2).

Internal porosity was also analyzed using the micro-computed tomography ( $\mu$ CT, GE phoenix v|tome|x L240, GE, Wunstorf, Germany). The main parameters of the X-ray tube used were the voltage of 130 kV, current of 100  $\mu$ A, and filter of 0.5 mm copper plate. Within two  $\mu$ CT measurements, two groups of four samples were jointly analyzed (Figure 3b). The measured data were obtained with the 15  $\mu$ m linear voxel size resolution and were reconstructed (using the back-projection algorithm) in the Datos reconstruction software. All subsequent post-processing was performed in the software VGStudio MAX 3.1.

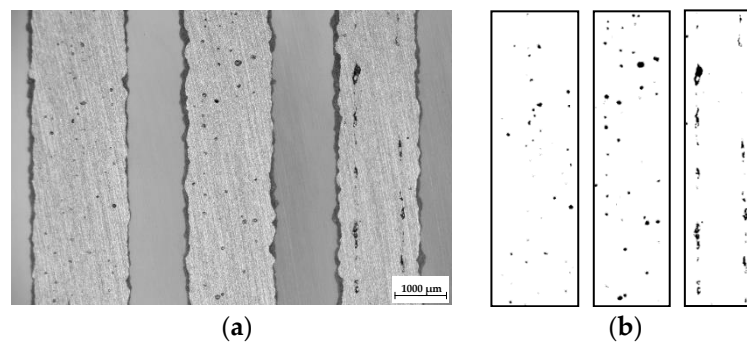


**Figure 2.** The samples after basic grinding to the struts mid-plane; (a) the top view images captured by light microscope; (b) three areas of the struts after converting of the colors in ImageJ software.

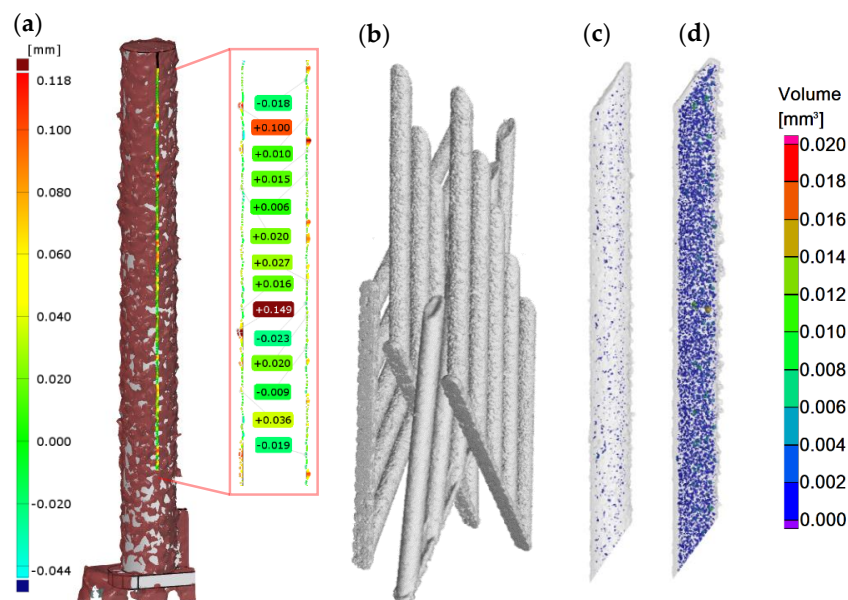


**Figure 3.** Struts analysis—(a) surface roughness evaluation in GOM Inspect software after optical measurement; (b) group of four samples measured together in VGStudio MAX software; (c) transparent 3D render of the strut with the lowest porosity 0.17% (d) transparent 3D render of the strut with the highest porosity 2.93%.

During the software analysis, the reconstructed data were divided into single struts and then each sample was independently analyzed in the porosity analysis module. The software detection of the air pores is based on the thresholding method that determines the boundary between the material and the air (background). This threshold was calculated automatically by software to reach comparability between both measurements. The results of the porosity analysis were between 0.17 and 2.93% (Figure 3c,d).

#### 2.4. Input Energy Calculation

The input energy to the current layer ( $E_{in}$ ) was obtained by Equation (2). It is based on the real laser paths in the actual layer, and on beam compensation and hatch distance parameters, which depended on actual process parameters and their single welds. The total length of the laser paths in the layer  $l$  was calculated based on the ellipse circumference  $o$  and the numbers of laser tracks  $N$  (Equation (3), Table 1),  $LS$  and  $LP$  were the main laser parameters.

$$E_{in} = \frac{LP}{LS} \cdot (J) \quad (2)$$

$$l = \sum_{i=1}^n o_1 + o_2 + \dots + o_n \text{ (mm)} \quad (3)$$

$$o \approx \frac{\pi}{2} \left[ a + b + \sqrt{2(a^2 + b^2)} \right] \text{ (mm)} \quad (4)$$

$$a = \frac{d}{2}; b = \left( \frac{d}{2} \right) \cdot \cos(54,74^\circ) \text{ (mm)} \quad (5)$$

#### 2.5. Samples Fabrication

All samples were manufactured using a SLM machine (SLM 280<sup>HL</sup>, Lübeck, Germany) equipped with 400 W Ytterbium fiber lasers (YLR) laser. The laser beam was focused to the diameter of 82  $\mu\text{m}$  and had a Gaussian shape. Laser scanning speed may reach up to 10,000 mm/s. During the production process,  $\text{N}_2$  atmosphere was used in the chamber and the oxygen level was kept under 0.2%. The platform temperature was 150  $^\circ\text{C}$ .

To find the most suitable material and surface properties of AlSi10Mg struts produced by SLM, several tests were used:

- Single welds test;
- Struts test;
- Struts test II;
- Hollow struts test.

##### 2.5.1. Single Welds Test

The aim of the single welds experiment was to find a suitable combination of the main process parameters ( $LP$ ,  $LS$ ) for the production of consistent single welds and to find out the width of single welds for a specific combination of process parameters.

To prepare the real condition during layer by layer production, single welds were produced on the top of 5 mm solid material block (Figure 4a). The influence of the laser direction on the single welds condition was also observed; therefore, all single welds were produced in and against atmosphere flow direction (Figure 4b). Images of the welds from the top view were captured by light microscope (Olympus SZX7, Olympus, Tokyo, Japan) and used for width measuring and a visual evaluation of the continuity and uniformity (Figure 4c). Their width was measured in six points along each single weld and one average value for both directions was used. For the experiment, the following process parameters were changed— $LP$  in the range between 175 and 400 W in steps 25 W and  $LS$  in the range between 200 and 2000 mm/s in steps 100 mm/s.

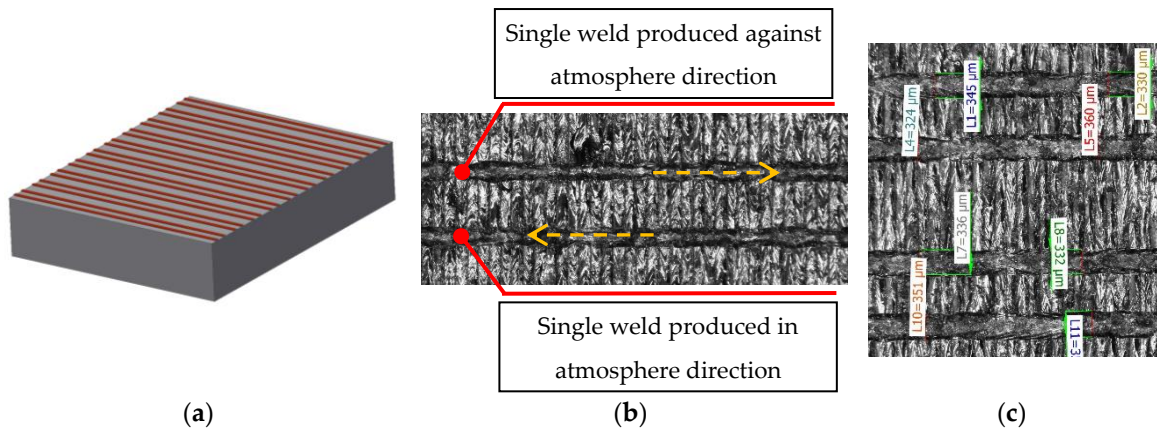


**Figure 4.** (a) Shape of the single welds samples; (b) one combination of process parameters produced in and against the atmosphere flow; (c) measurement of width of the single welds.

2.5.2. Strut Test

The aim of the test was to narrow the process parameter window of the single weld test depending on the porosity and surface roughness of the struts and to find the most suitable overlap (*OL*) parameter from the porosity point of view. The samples consisted of five struts with diameter  $d = 2$  mm were produced in two orientations (*OR*) compared to the platform *OR* 90 and *OR* 35.26°. The strut diameter was chosen to be sufficiently large to set *OL* in the range from *OL*-50% to *OL* 50% of the weld width (Figure 5b). The beam compensation parameter (*BC*, a distance between the strut surface and the first laser path) was applied as a half of the weld width. Laser process parameters were changed as follows—*LP* in the range from 225 to 350 W, and *LS* in the range from 400 to 2000 mm/s.

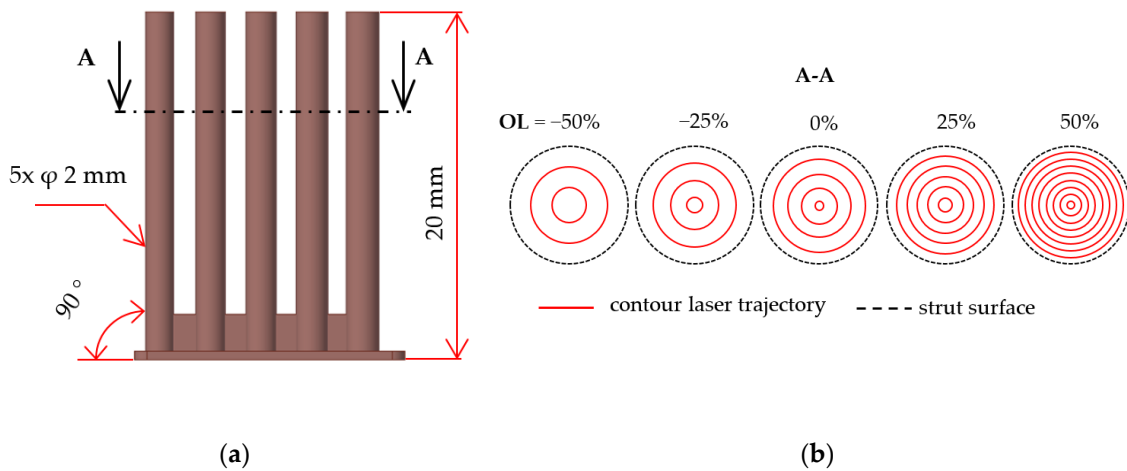


**Figure 5.** (a) Shape of the samples with inclination of 90°; (b) contour strategy with different overlap parameter.

In this experiment, the laser strategy for lattice structure production created only by contour lines was tested (Table 1). The main idea is the possibility to produce fine lattice structure using various combinations of the process parameters (low/high energy) to manage surface roughness or internal porosity and to allow for production of very thin struts. An advantage is an easy optimization of the strategy for the elimination of non-melted or over-melted areas in struts and for improving dimension accuracy.

**Table 1.** Laser strategies of the strut with inclination of 35.26° (orientation in body centered cubic (BBC) lattice structure).

Strategy/d (mm)	0.5 mm	0.6 mm	0.7 mm	0.8 mm	0.9 mm
Contour					
Standard					

After fabrication, samples were ground to the mid-plane of the struts using a hand metallographic grinder (GP-2 Grinder, Sinowon, Dongguan, China), and the images of the samples from the top view were taken by light microscope (Olympus SZX7, Tokyo, Japan). For the initial porosity analysis ImageJ software was used. Porosity was analyzed only on the samples with *OL* 0%, 25% and 50%.

### 2.5.3. Strut Test II

The aim of the experiment was to find the influence of *LP* and *LS* on the internal porosity and surface roughness. The following process parameters were selected: *LP* in the range between 225 W and 400 W and *LS* in the range between 500 mm/s and 2000 mm/s with respect to the perspective area of previous strut test. The strut samples with *OR* 35.26° only were used in the experiment. The samples were analyzed using  $\mu$ CT to obtain more accurate results of porosity and full surface data for down-skin roughness evaluation.

### 2.5.4. Hollow Struts Test

Samples of hollow strut shape; created with only one single weld in each layer, were produced (Figure 6). The cross-section of the hollow strut sample was designed to ensure evaluation of correct width of the wall without distortion caused by grinding in the inclined plane. The primary aim of the hollow strut test was to compare the width of the single welds on the solid block and the width of the wall of hollow struts (the shape close to the real strut). The combinations of the process parameters were selected also to obtain the influence of the width of wall on *LP* and *LS*. For this experiment, the following process parameters were changed—*LP* (225, 250, 275, 300, 350, 400 W); *LS* (500, 900, 1400 mm/s). After fabrication, the 37 samples were ground to the mid-plane of the struts using a hand metallographic grinder (GP-2 Grinder, Sinowon, Dongguan, China) and the images of the ground surface from the top view were captured by light microscope (Olympus SZX7, Olympus, Tokyo, Japan).

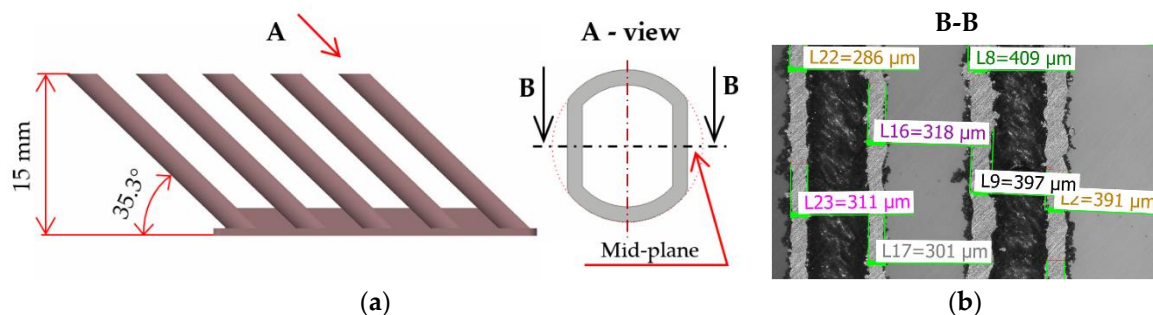


**Figure 6.** (a) A special shape of strut designed for evaluation of the width of hollow strut walls without distortion caused by inclined grinding plane; (b) wall width measurement using macro images captured by the light microscope.

### 3. Results

#### 3.1. Single Welds Test

The results of the width of single welds are shown in Figure 7. The final values were averaged from six measurements against and six measurements in the atmosphere flow direction. The values marked in red color were excluded due the worse quality of the welds (non-uniformity of width and bad continuity). For the input linear energy calculation, Equation (6) was used and the limit value of around 0.25 J/mm was found for continuous welds.

$$E_{lin} = LP/LS \quad (\text{J/mm}) \tag{6}$$

w (μm)		Laser speed (mm/s)																				
E <sub>lin</sub> (J/mm)		200	300	400	500	600	700	800	900	1000	1100	1200	1300	1400	1500	1600	1700	1800	1900	2000		
Laser power (W)	175	354	310	261	290	246	221	214	199	223												
		0.88	0.58	0.44	0.35	0.29	0.25	0.22	0.19	0.18												
	200	401	343	303	286	317	271	240	210	201	210											
		1.00	0.67	0.50	0.40	0.33	0.29	0.25	0.22	0.20	0.18											
	225		374	309	271	255	214	203	199	174	163	145										
			0.75	0.56	0.45	0.38	0.32	0.28	0.25	0.23	0.20	0.19										
	250		344	314	270	253	233	223	201	180	161	163	159									
			0.83	0.63	0.50	0.42	0.36	0.31	0.28	0.25	0.23	0.21	0.19									
	275			380	346	332	289	262	277	235	227	221	201	149								
				0.69	0.55	0.46	0.39	0.34	0.31	0.28	0.25	0.23	0.21	0.20								
	300				305	325	308	267	260	232	223	202	211	193	183	192	186					
					0.75	0.60	0.50	0.43	0.38	0.33	0.30	0.27	0.25	0.23	0.21	0.20	0.19					
	325					333	316	275	274	262	258	207	199	200	196	189	176	145				
						0.65	0.54	0.46	0.41	0.36	0.33	0.30	0.27	0.25	0.23	0.22	0.20	0.19				
	350						358	336	328	317	300	261	259	205	200	199	209	205	352			
							0.70	0.58	0.50	0.44	0.39	0.35	0.32	0.29	0.27	0.25	0.23	0.22	0.21	0.19		
375							317	308	201	372	370	272	267	250	287	230	237	239	223	217		
							0.63	0.54	0.47	0.42	0.38	0.34	0.31	0.29	0.27	0.25	0.23	0.22	0.21	0.20		
400								357	332	358	301	273	234	236	223	214	206	223	216	212	201	210
								0.67	0.57	0.50	0.44	0.40	0.36	0.33	0.31	0.29	0.27	0.25	0.24	0.22	0.21	0.20

Figure 7. The average width of the single welds in and against atmosphere flow (colored cells); line energy (color free cells).

Figure 8a shows the frequency of the continuous single welds widths from 145 μm to 401 μm in all tested process window. Different widths of single welds are useful for ensuring the dimension accuracy and material properties during production of the struts using a contour line strategy (especially thin struts). Therefore, for the next experiments, the welds across the entire perspective process window were selected as follows—the consistent welds were categorized into 11 classes according to weld widths. From each class, one combination of process parameters was chosen depending on the amount of linear energy  $E_{lin}$  in the (Equation (6)). The combination of  $LP$  and  $LS$  with the linear energy level closest to the average energy level of the class was selected. A few more combinations, e.g., laser parameters corresponding with standard process parameters or the parameters from previous studies, were chosen. Finally, 16 combinations of  $LS$  and  $LP$  were tested.

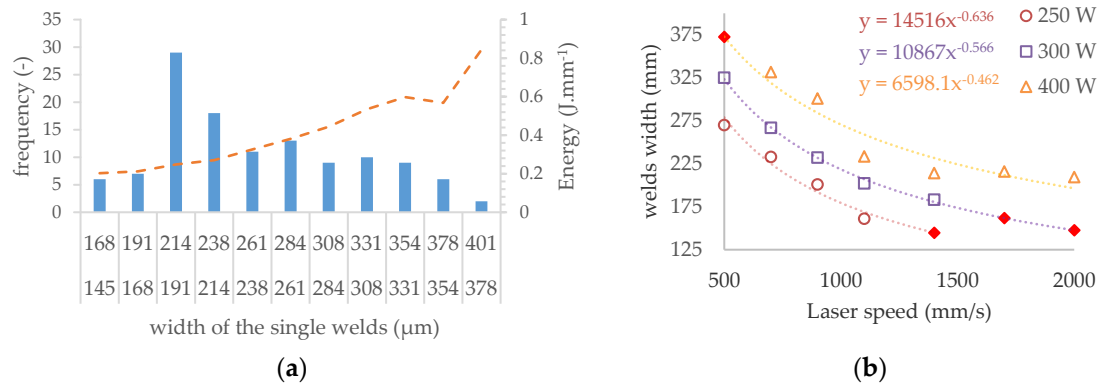


**Figure 8.** The results of the single welds test (a) histogram of the width frequency of single welds, (b) the prediction of weld width for non-tested combinations of process parameters.

### 3.2. Struts Test

#### 3.2.1. Determining the Overlap Parameter

The samples were ground to the mid-plane of the struts to measure the internal porosity and to check the weld overlap (*OL*). The internal porosity was analyzed on the struts with *OL* from 50% to 0% to prevent distortion of the results due to a disconnection between the neighboring single welds. For evaluation of the most suitable *OL* value, a dependence of the porosity vs. input energy  $E_{in}$  was used (Figure 9a,b).

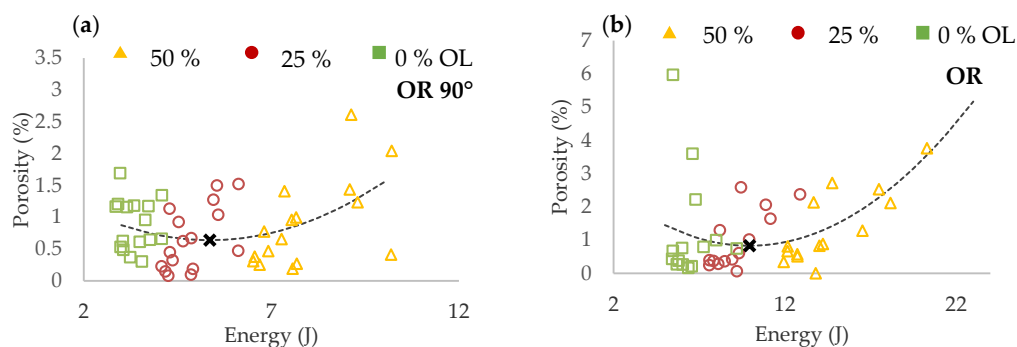


**Figure 9.** Porosity vs. input energy dependence (a) for inclination 90°; (b) for inclination 35.26°.

In the charts, three groups of porosity regarding the *OL* parameter were identified in both cases of struts inclination. To find out the *OL* parameter with the lowest porosity level, the results were interpolated with quadratic polynomial function and the minimum of the function was determined (black cross in Figure 9).

In the results of both strut inclination, the overlap *OL* 50% shows a higher porosity level. It occurs due to a large overlap area where the material is overheated. Higher porosity level is also at *OL* 0% where it could be caused by theoretically no overlap and insufficient connection between the neighboring welds. The lowest porosity level was reached at *OL* 25% in both orientations; therefore, for the next experiments, the *OL* 25% was selected as the most suitable. In the case of *OR* 35.26°, higher porosity values were identified compared to *OR* 90°.

#### 3.2.2. Initial Roughness Analysis

Results of surface roughness on the strut side show different trends based on struts inclination (Figure 10). For the struts of *OR* 90°, roughness decreases with higher  $E_{in}$  while for *OR* 35.26°, roughness significantly increases with higher  $E_{in}$ . The worse surface quality at *OR* 35.26° is caused by

approximately 40% higher  $E_{in}$  and heat transfer to the surrounding powder particles and caused by strut inclination.

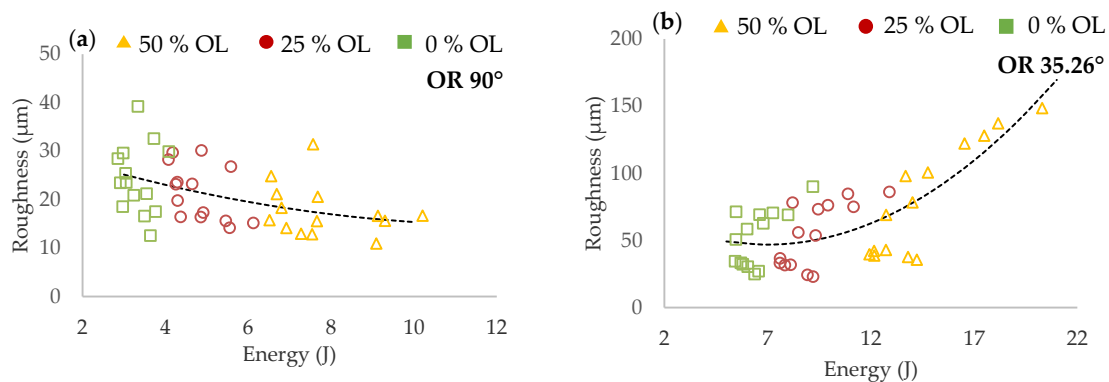


**Figure 10.** Surface roughness vs. input energy dependence (a) for inclination of 90°; (b) for inclination of 35.26°.

The images captured by light microscope (Olympus SZX7, Tokyo, Japan) confirm the previous results. Figure 11 shows two combinations of process parameter. The former with high  $E_{in}$ — $LP$  275 W,  $LS$  400 mm/s (Figure 11a,b), and the latter with low  $E_{in}$ — $LP$  300 W,  $LS$  1400 mm/s (Figure 11c,d). In the case of the struts at  $OR$  90° produced with higher  $E_{in}$ , the surface quality was smooth, with no partially melted powder (Figure 11b). The struts produced with lower  $E_{in}$  were characterized by visually rough struts surface (Figure 11d). In the case of the struts at  $OR$  35.26° produced with higher  $E_{in}$ , the top surface also seems to be smooth; however, a lot of partially melted powder appeared on the strut down-skin surface (Figure 11a). The struts produced with lower  $E_{in}$  had a significantly smaller amount of partially melted powder on the strut down-skin surface (Figure 11c).

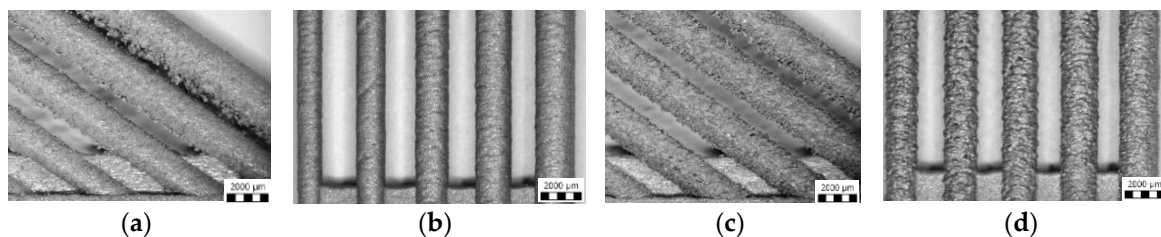


**Figure 11.** Struts surface quality—produced with higher  $E_{in}$  (a) at orientation ( $OR$ ) 36.26°; (b) at  $OR$  90°; produced with lower  $E_{in}$  (c) at  $OR$  36.26°; (d) at  $OR$  90°.

The results of porosity and surface roughness were jointly used to narrow the perspective area of the process parameters for struts production in 3D contour graph (Statistica software). Based on the results, the laser parameters were narrowed as follows— $LP$  between 225 W and 300 W,  $LS$  over 1000 mm/s.

### 3.3. Struts Test II

#### 3.3.1. Interpolation of Welds Width

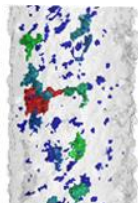
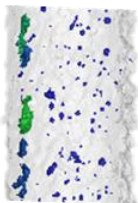
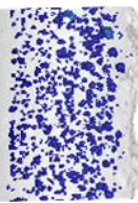
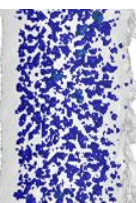
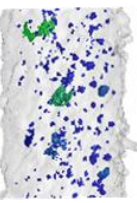
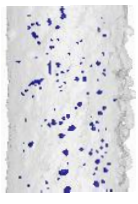
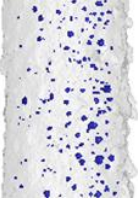
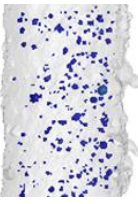
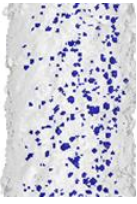
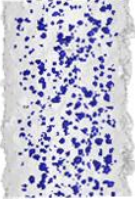
The aim of the struts test II mainly was to determining the effects of individual parameters on surface roughness and internal porosity. In order to obtain dependencies on  $LP$  and  $LS$ , the parameters were selected with respect to perspective area of the previous strut test. Some combinations of  $LP$  and  $LS$  were not included in the single welds test and their widths were not known. To find them, the dependence between  $LS$  and width of the single weld was used for prediction (Figure 8b).

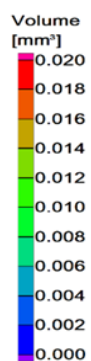
Figure 8b shows the curves of *LS* vs. welds width curves for *LP* 400, 300 and 250 W. From the results of *LP* 400 W, it is obvious that the dependence is not linear; therefore, the power functions, which best correspond to the measured data, were used for interpolation. This is also confirmed by the results for *LP* 300 W and *LP* 350 W. The calculated values are marked red.

### 3.3.2. Porosity Analysis

The porosity results were obtained by a micro-computed tomography ( $\mu$ CT) device with voxel size of 15  $\mu$ m. The struts were individually analyzed to find out the porosity level for each combination of process parameters. However, the shape and the size of pores is also important. Table 2 shows the images of the  $\mu$ CT analysis with various shapes of pores and porosity level. Based on the results, the required minimum values of linear energy  $E_{lin}$  0.25 J/mm and input energy  $E_{in}$  8 J were identified for strut production without creating large irregular pores.

**Table 2.** The porosity level of the strut samples—3D renders with pores shape; the pores in the entire volume were projected to the plane of the view; all images have the same pores scale bar.

	<i>LP</i> 225 W	<i>LP</i> 250 W	<i>LP</i> 300 W	<i>LP</i> 350 W	<i>LP</i> 400 W
	<i>LS</i> 1200 mm/s; $E_{in}$ 7.28 J; $E_{lin}$ 0.19 J/mm	<i>LS</i> 1400 mm/s; $E_{in}$ 9.17 J; $E_{lin}$ 0.18 J/mm	<i>LS</i> 500 mm/s; $E_{in}$ 13.54 J; $E_{lin}$ 0.6 J/mm	<i>LS</i> 500 mm/s; $E_{in}$ 15.43 J; $E_{lin}$ 0.7 J/mm	<i>LS</i> 1700 mm/s; $E_{in}$ 7.56 J; $E_{lin}$ 0.24 J/mm
					
	Por. -0.17%	Por. -0.27%	Por. -1.38%	Por. -2.26%	Por. -0.63%
	<i>LS</i> 700 mm/s; $E_{in}$ 9.02 J; $E_{lin}$ 0.32 J/mm	<i>LS</i> 700 mm/s; $E_{in}$ 9.84 J; $E_{lin}$ 0.36 J/mm	<i>LS</i> 900 mm/s; $E_{in}$ 9.37 J; $E_{lin}$ 0.33 J/mm	<i>LS</i> 1100 mm/s; $E_{in}$ 8.91 J; $E_{lin}$ 0.32 J/mm	<i>LS</i> 900 mm/s; $E_{in}$ 10.17 J; $E_{lin}$ 0.44 J/mm
					
	Por. -0.17%	Por. -0.31%	Por. -0.42%	Por. -0.43%	Por. -0.81%



### 3.3.3. Evaluation of Perspective Laser Parameters

The results of porosity levels generally show a similar trend as in the initial results of the previous test. However, in this case, the significant accumulation of results at the porosity level 0.4% occurs for  $E_{in}$  of 8 ÷ 10 J and for  $E_{lin}$  of 0.15 ÷ 0.4 J/mm (Figure 12a,b). However, the porosity level of linear energy  $E_{lin}$  in range 0.15 ÷ 0.25 J/mm is very low, and the porosity is created with a small number of large irregular pores. It can significantly decrease the mechanical properties; therefore, this area is unsuitable for the production of the struts. Regarding the charts, which show the influence of *LS* and *LP* on the porosity (Figure 13a,b) and the previous porosity analysis, the parameters *LP* of 225 ÷ 275 W, *LS* of 900 ÷ 1400 mm/s with  $E_{in}$  of 8 ÷ 10.5 J,  $E_{lin}$  of 0.25 ÷ 0.4 J/mm, and *OL* 25% were selected as the perspective for struts production from the porosity point of view.

The results of surface roughness were obtained by  $\mu$ CT measurement in this experiment; therefore, it was possible to analyze the results on the side and also down-skin strut surface (Figure 12c,d).

The results show a similar trend as the results of porosity except for the pronounced linear dependence of as-built surface roughness on linear energy  $E_{lin}$ . The best results were accumulated between  $E_{in}$   $8 \div 10$  J and  $E_{lin}$  of  $0.15 \div 0.4$  J/mm with the level of about Ra 30  $\mu\text{m}$  on the strut-side surface and about Ra 40  $\mu\text{m}$  on the down-skin surface.

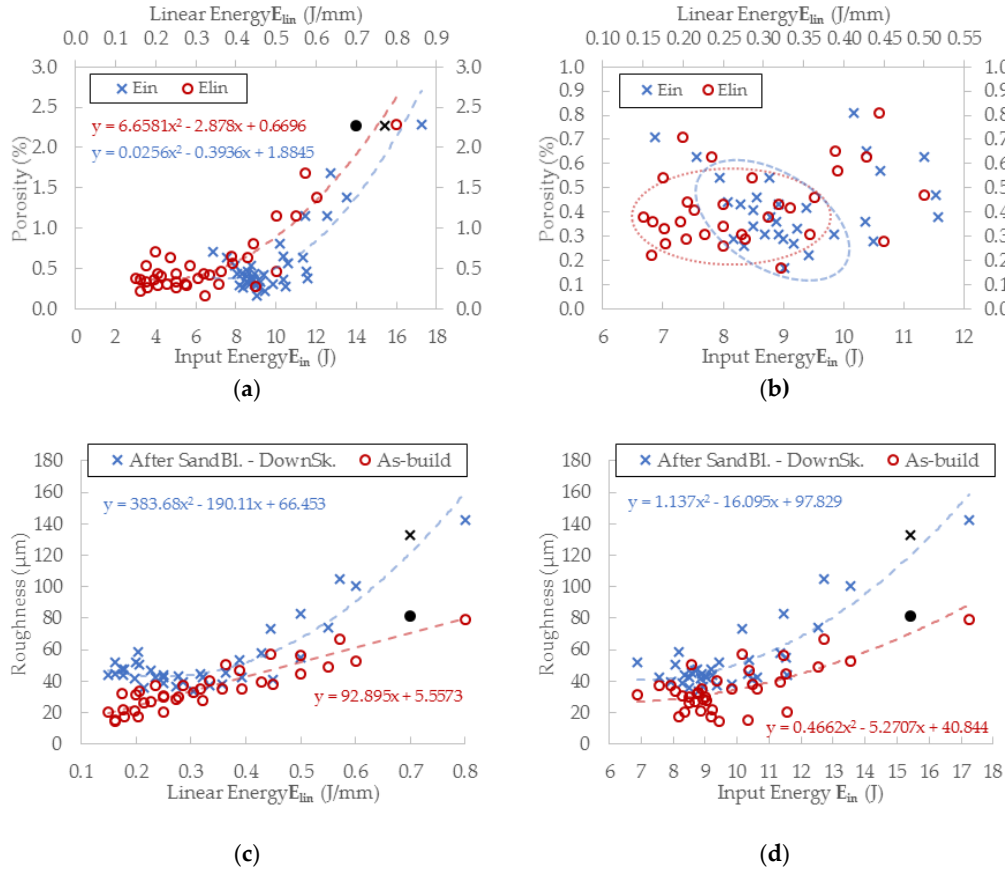


**Figure 12.** (a)  $\mu\text{CT}$  porosity vs. input and linear energy dependences, black mark represents the universal SLM process parameters; (b) focused results area up to 1% porosity level with marked perspective areas; (c) surface roughness vs. linear energy dependence—on the side and down-skin struts surface, black marks represent the universal SLM process parameters.; (d) surface roughness vs. input energy dependence.

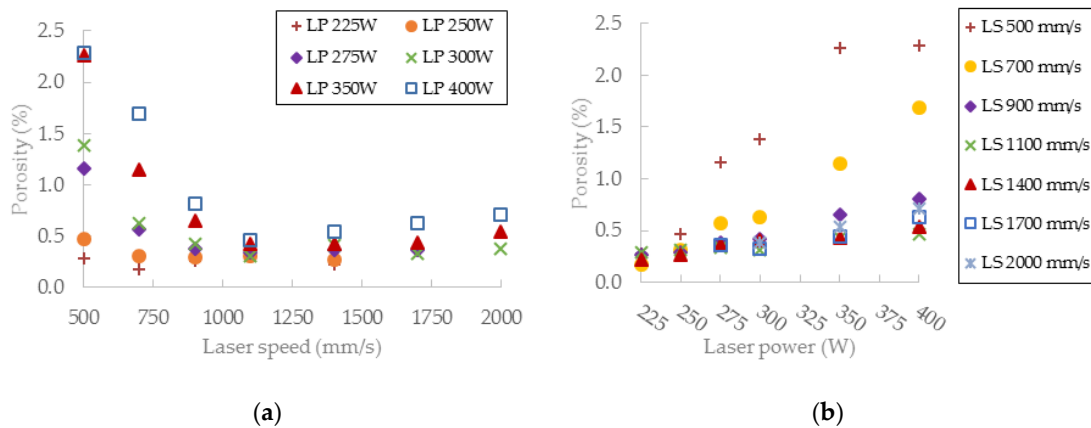


**Figure 13.** Cont.

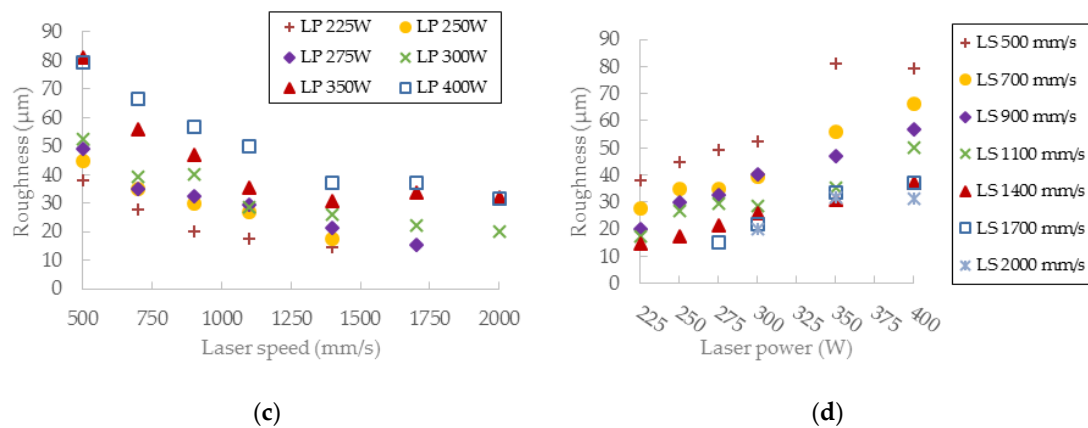


**Figure 13.** (a) The influence of various laser speed (LS) levels on porosity; (b) the influence of various laser power (LP) levels on porosity; (c) the influence of various LS levels on surface roughness; (d) the influence of various LP levels on surface roughness.

Regarding the charts, which show the influence of LS and LP on the roughness (Figure 13c,d), parameters LP in the range of 225 ÷ 300 W, LS in the range of 900 ÷ 2000 mm/s with  $E_{in}$  of 8 ÷ 10 J, Elin of 0.15 ÷ 0.4 J/mm and OL 25% were selected as the perspective for lattice structure production with a low roughness level.

### 3.4. Wall Width Analysis

Simultaneously with the strut samples, hollow strut samples were fabricated. The hollow strut shape was used because of similar heat transfer conditions as those in the case of struts production. The width of the wall at  $OR\ 35.26^\circ$  was of about 25% higher on average than that in the case of the single welds on a solid block (Figure 14). The results confirm the trends of the weld widths from a single weld test. The influence of LP seems to be more linear than that of LS.

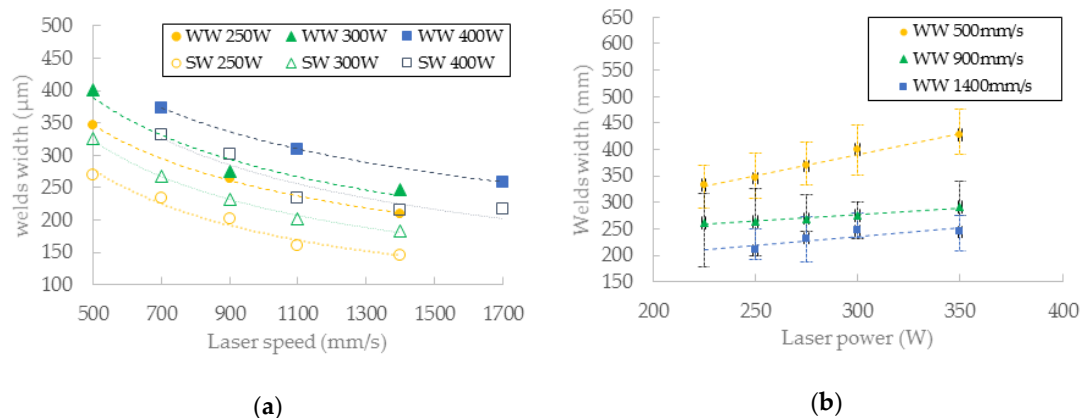


**Figure 14.** (a) Comparison of single welds and walls width according to LS—in chart (SW) single weld width; (WW) wall width; (b) the wall width according to LP.

### 3.5. Metallographic Analysis

A metallographic analysis for evaluation of the microstructure was performed. Standard methods were used for metallographic sample preparation, i.e., wet grinding and polishing with use of diamond pastes. A microstructure of the struts was analyzed in an etched state (Fuss etchant) and evaluated by metallographic light microscope (Olympus GX 51, Tokyo, Japan). Orientation of the micrographs is parallel to the strut axis (Figure 15a). The microstructure of the struts is inhomogeneous, consisting of single welds separated by fusion boundaries. Differences in the microstructure can be seen in the

layers close to the down-skin surface of the struts (B area in Figure 15a) in comparison with the up-skin surface (A area). Different shapes of porosity depend on the  $E_{in}$  parameter. Due to overheating of the material, gas pores with a spherical shape were created (Figure 15b,c). No cracks were found in the microstructure of the evaluated samples.

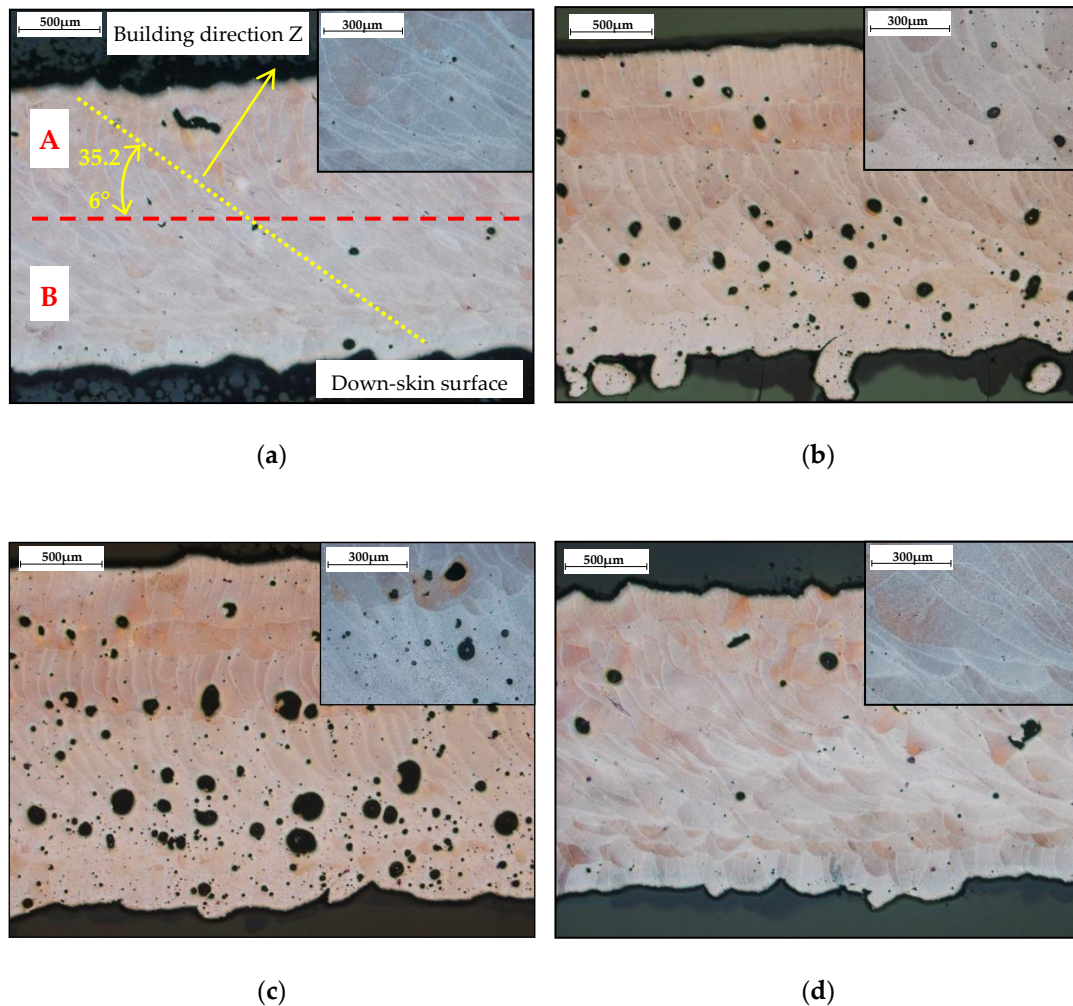


**Figure 15.** Microstructure of the struts (a) LP 250 W, LS 1400 mm/s,  $E_{in}$  9.17 J,  $E_{lin}$  0.18 J/mm with description common for all pictures; (b) LP 300 W, LS 500 mm/s,  $E_{in}$  13.54 J,  $E_{lin}$  0.6 J/mm (c) LP 350 W, LS 500 mm/s,  $E_{in}$  15.43 J,  $E_{lin}$  0.7 J/mm; (d) LP 400 W, LS 1700 mm/s,  $E_{in}$  7.56 J,  $E_{lin}$  0.24 J/mm.

## 4. Discussion

### 4.1. Comparison of the Linear Energy Needed for Consistent Single Weld

The results of the single welds experiment show as a limit value  $E_{lin}$  0.25 J/mm for consistent welds. The value is higher than that in the case of [21], where the determined limit was 1.5 J/cm. The difference is caused by the shape of the used sample. In [21], the single welds were fabricated directly on the platform. In the present study, the sample, which simulates real production and the increase of thickness of the deposited powder during the first few layers, was used. After melting, the produced layer has a height usually lower than that of the originally spread layer of 50  $\mu$ m. Then, the next deposited layer has higher thickness and a quality of weld and the required linear energy  $E_{lin}$  can be changed [30].

#### 4.2. Benefits of Contour Lines Laser Strategy

The state that led to the design of a contour scanning strategy is shown in Figure 16. There are examples of the laser strategy internally developed by SLM Solutions universal process parameters. In the cases of diameters of 0.5 and 0.6 mm, only one contour line was generated while in the case of 0.7 mm diameter, one more fill contour line was generated. Using the results of the single weld test, it is possible to calculate the theoretical dimensional accuracy and re-melting area.

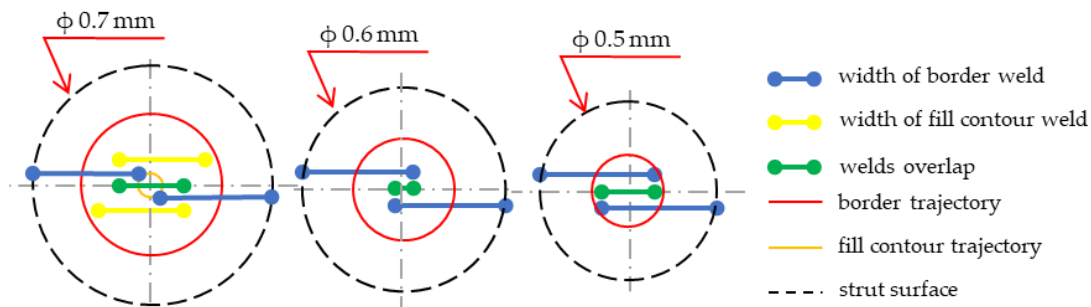


Figure 16. SLM Solutions universal struts laser strategy.

The laser parameters of universal process parameters are as follows: contour line **LP** 350 W, **LS** 500 mm/s; fill contour offset **LP** 250 W, **LS** 555 mm/s, and **LF** = -4). During production of a 0.5 mm strut, the diameter will be theoretically about 0.116 mm (23%) larger because of a combination of the beam compensation parameter of 0.15 mm and the weld width of 0.358 mm. A theoretical overlap area is 0.158 mm (44% of the weld width). In the case of a 0.6 mm strut, the diameter will also be larger (about  $d = 0.116$  mm; 19%) and a theoretical overlap area is 0.058 mm (16% of the weld width). The diameter of 0.7 mm will also be about 0.116 mm larger; as can be seen in Figure 16, from the contour line, no overlap area is created. Therefore, a fill contour track in the distance of 0.17 mm from the contour line is added. Due to the fill contour line and its distance from the contour path, an unfavorable state with large overlap of 0.31 mm (87% of the weld width) is created in the center of the strut. Its trajectory is also on the already produced contour weld and thus the material is re-melted, which can cause internal defects in the struts (Figure 16;  $d = 0.7$  mm). The aim of the proposed contour strategy is to create uniform conditions for different strut diameters and improve the dimension accuracy using single welds results.

Using the previous results of the single welds experiment, the hollow strut experiment and a designed script in Excel, the contour strategy for production of the struts with low porosity, and surface roughness, were designed (Table 3). The obtained weld widths from the single weld experiment which meet the required linear energy  $E_{lin}$  and input energy  $E_{in}$  were used only (Figure 19a). These values were increased by about 25% (parameter from the hollow strut test, Figure 19b) and then used to define the beam compensation **BC** parameter ( $(\text{single width} \times 1.25)/2$ ). The goal of the Excel script was to find a suitable combination of laser parameters which achieve the overlap in the center of the struts as close as possible to the value around **OL** 25%. The results are shown in Table 3. For the diameters of 0.5 and 0.6 mm, the combinations with the required **OL** parameter have been found. In the case of the diameter 0.7 mm, the best results were obtained with **LP** 225 W, **LS** 900 mm/s and **LP** 250 W, **LS** 1000 mm/s, however the **OL** parameter between neighboring welds must increase to 29% and 34%. For values closer to **OL** 25%, it would be necessary to discover other combinations of parameters around these two; however, the expected levels of porosity and roughness using these combinations will be significantly lower compared to standard SLM strategy (Figure 12).

**Table 3.** Various suitable combination of process parameters for production of the struts with diameters 0.5–0.7 mm, ( $N$  (-) is number of the used contour,  $w$  ( $\mu\text{m}$ ) is single width  $\times 1.25$ ).

d (mm)	OL (%)	LP (W)	LS (mm/s)	w ( $\mu\text{m}$ )	BC ( $\mu\text{m}$ )	N (-)	OL in Center ( $\mu\text{m}$ )	OL in Center (%)
0.5	-	225	600	295	147	1	89	30%
	-	325	1000	293	147	1	86	29%
	-	350	1300	285	143	1	70	25%
	-	375	1200	294	147	1	88	30%
0.6	-	400	1000	339	170	1	78	23%
0.7	34%	225	900	236	118	2	84	36%
	29%	250	1000	224	112	2	67	30%

#### 4.3. The Heat Transfer during Strut Fabrication

The first strut experiment in this study was also designed for comparison of the conditions during production the struts with  $OR$   $90^\circ$  and  $OR$   $35.26^\circ$ . The difference is caused by worse heat transfer in the inclined strut. It can lead to wider single welds than expected; therefore, the successful results of porosity at  $OL$  0% were discovered (Figure 9, Figure 18b). This was verified by the hollow struts experiment which confirmed this hypothesis. The width of the wall was increased on average by about 25% (Figure 14a). At higher energy levels (over 0.5 J/mm), the effect of the wider bottom part of the wall also appeared (Figure 17). It was caused by the thermal gradient during SLM production of struts with inclination and shows the heat energy transfer well. To describe the energy conditions during the struts' production, this must be considered:

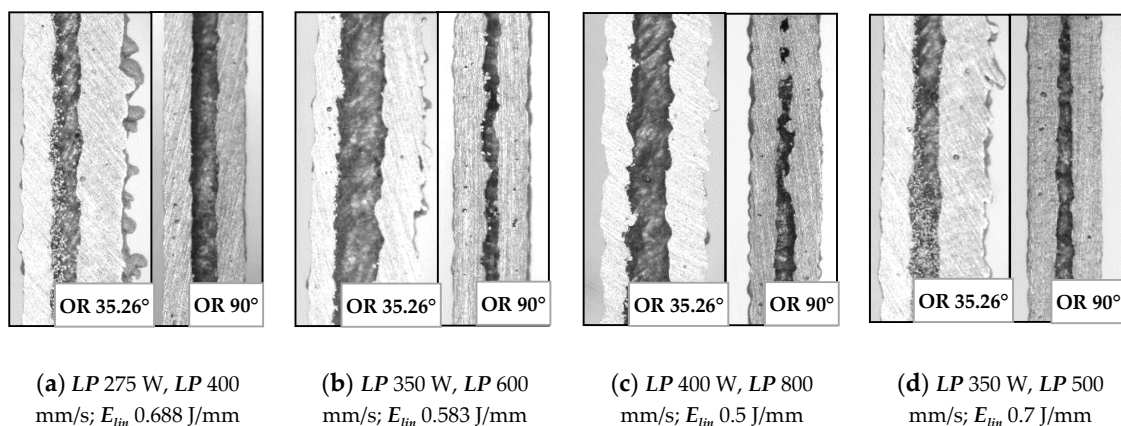


**Figure 17.** Comparison of inclined and perpendicular strut (a) for parameters LP 275 W, LP 400 mm/s; (b) LP 350 W, LP 600 mm/s; (c) LP 400 W, LP 800 mm/s; (d) LP 350 W, LP 500 mm/s.

- (1) Due to the point contact of the powder particles between themselves, the metal powder has much lower heat conductive performance and works as an insulator compared to the solid material.
- (2) Due to the strut inclination, the cross-section with a higher area occurs in every layer. Using the energy calculation in Equation (2), it is possible to calculate the increase of the input energy  $E_{in}$  and compare  $OR$   $35.26^\circ$  and  $OR$   $90^\circ$ ; it is about 40% higher in the case of  $OR$   $35.26^\circ$ .
- (3) The thermal gradient points in the direction  $-Z$ . Due to the inclination of the struts, the heat transfer is slower than in the case of the strut with the axis directed in thermal gradient direction.

After melting of each layer of the strut, the heat energy flows straight down in thermal gradient direction. There are two parts of each produced layer with different energy transmission, the part produced on the previous layer and overhanging part produced on the powder (Figure 18). In the former case of the part on the previous layer, the energy flows through the strut. Because the thermal gradient has a different direction than the strut, heat transfer is slower compared to the strut with  $OR$   $90^\circ$ .

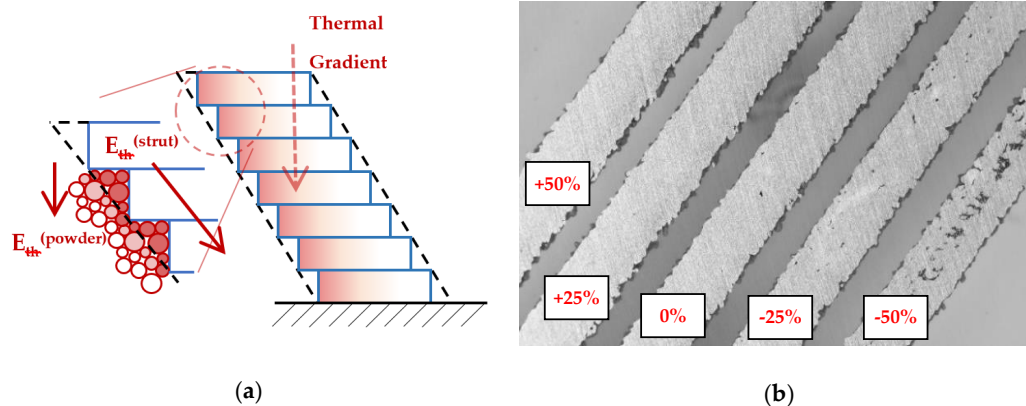


**Figure 18.** (a) Scheme of the heat transfer during SLM additive manufacturing; (b) The ground sample to the mid-plane of the struts.

In the latter, the thermal energy flows to the powder which is in contact with the strut down-skin surface and the powder particles are overheated because there is only a point contact between neighboring powder particles, and only poor heat transmission to the powder bed. Affected particles are melted on the down-skin surface which causes larger dimensions of the struts [8,18] or a wider bottom part of the hollow struts samples, as well as a higher surface roughness on the down-skin surface of the strut (Figure 17). The heat energy is also accumulated in overhanging part of the layer and the material structure is changed [22] (Figure 15).

#### 4.4. Porosity and Roughness Analysis

The results of  $\mu$ CT show a different shape and level of porosity according to the input energy  $E_{in}$  and the linear energy  $E_{lin}$ . The porosity in the struts with the lowest porosity level is often formed by a small number of larger pores which are located close to the top surface (Table 2). Formation of the large irregular pores is related to the heat transfer in the inclined struts where more heat energy is accumulated at the bottom part of the strut. Due to the low linear energy, there is no overheating area in the bottom part of the strut (the spherical porosity is very small); however, on the upper side, the state is an unstable because of a lack of linear energy. This causes the occasional disconnection of neighboring welds and formation of larger pores. The minimum value  $E_{lin}$  0.25 J/mm was determined; it is in line with the results of single welds.

A lack of  $E_{in}$  causes porosity in the center of the struts. During production of the laser tracks close to the strut surface, heat transfer is lower due to the surrounding powder. During production of single welds in the center of the strut, heat transfer is higher due to the neighboring welds; an unstable state occurs with occasional disconnection of the welds and formation of larger pores. The minimum value  $E_{in}$  9 J was determined. Also, the inside-out order of single welds production is recommended.

#### 4.5. Porosity and Roughness

The current results of strut experiments clearly show that the porosity and surface roughness is affected by the input energy  $E_{in}$  as well as linear energy  $E_{lin}$ ; these both include the laser power  $LP$  and the laser speed  $LS$ . It follows that for strut production free of internal defects and a rough surface, appropriate laser process parameters must be chosen. The charts of the dependences of  $LP$  and  $LS$  on the porosity (Figure 13) demonstrate a different influence of the parameters on porosity forming. The chart shows that the porosity increases with higher  $LP$  at all  $LS$  levels linearly, except for  $LS$  level of 500 mm/s, which shows unstable results. The  $LS$  parameter shows non-linear results with the lowest porosity in the range of 1000 ÷ 1250 mm/s. With higher  $LS$ , the porosity seems to be stable and at the constant level, except for  $LP$  400W where the porosity increases.  $LS$ s up to 1000 mm/s are

unstable and the porosity significantly increases. It could be caused by too high  $E_{in}$  and formation of gas pores in the material due to its overheating material (Figure 15c).

The influence of  $LS$  and  $LP$  on the surface roughness has a similar character as that on the porosity in case of input energy  $E_{in}$ . Linear energy  $E_{lin}$  dependence shows the pronounced linear dependence of as-built surface roughness. In Figure 13c, it is possible to find two approximately linear areas. The first area, up to 1400 mm/s, where there are significant changes in roughness values, and the other one, between 1400 mm/s and 2000 mm/s, where there is a significantly lower and stable roughness level. The dependence of  $LP$  vs. roughness is linear for all tested laser speeds. Generally, the results show a low surface roughness with lower  $E_{in}$  and  $E_{lin}$ .

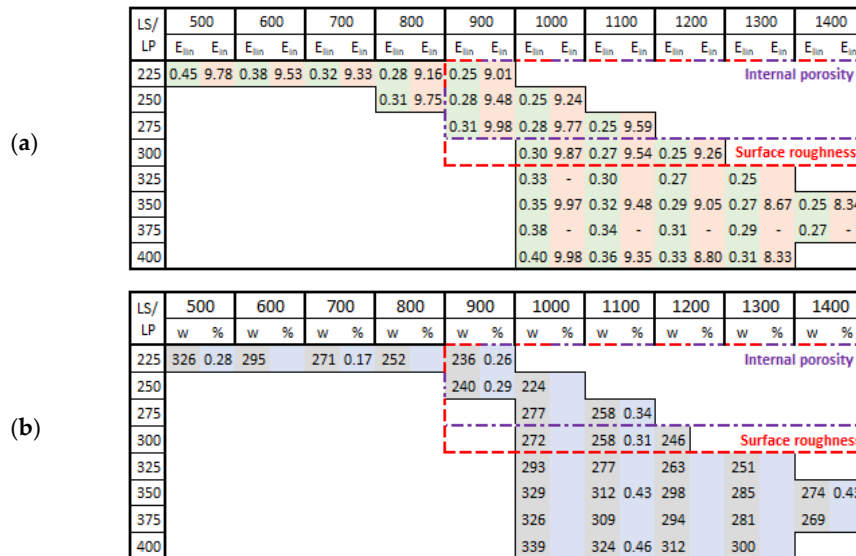


**Figure 19.** The perspective area (a) linear energy  $E_{lin}$  (J/mm) (green cells) and input energy to the layer  $E_{in}$  (J) (red cells); (b) width of single welds in ( $\mu\text{m}$ ) multiplied  $\times 1.25$  (parameter from hollow strut test) (grey cells) and porosity level (blue cells).

### 5. Conclusions

In this article, an experimental study was conducted to investigate the influence of a proposed contour line laser strategy for an SLM lattice structure on internal porosity and surface roughness of the single struts, which significantly affects the mechanical properties of the lattice structure. Based on the dependence of porosity vs. input  $E_{in}$  and linear energy  $E_{lin}$ , the influence of the laser speed  $LS$  and laser power  $LP$  was found and the perspective areas of suitable process parameters for the struts–lattice structure were defined. In the present study, the main conclusions are as follows:

- For the production of the struts–lattice structure, the contour strategy seems to be perspective, mainly because of the possibility to use various laser process combinations based on the required width of single welds of the different strut dimensions to achieve a fully melted strut with a constant  $OL$  25% parameter.
- The heat transfer condition in the inclined struts significantly influences all material and shape parameters of the struts (lattice structure). During the strut production with high  $E_{in}$ , heat energy is accumulated in the down-skin part of the strut and higher roughness, higher porosity and change of the material microstructure occur. Therefore, the production at lower  $E_{in}$  levels leads to more stable results with lower porosity and roughness.
- $E_{in}$  calculated based on the real laser trajectory in the strut describes the amount of the porosity ( $P$ ) and roughness ( $R$ ) in the strut samples ( $d = 2$  mm) well. Another necessary condition for struts production without large and irregular internal pores is the minimum level of linear energy  $E_{lin}$  0.25 J/mm. The perspective areas of process parameters based on  $P$  and  $R$  were defined as

follows— $E_{in}$  of  $8 \div 10$  J;  $E_{lin}$  of  $0.25 \div 0.4$  J/mm,  $LP$  of  $225 \div 300$  W,  $LS$  of  $1250 \div 1750$  mm/s and  $OL$   $20\% \div 30\%$ . Figure 19 shows the perspective area which meets all conditions for low porosity and surface roughness levels. The presented weld widths are combinations of single weld values multiplied by the parameter obtained from the hollow strut test ( $\times 1.25$ ).

**Author Contributions:** Conceptualization, R.V. and D.K.; Data curation, R.V.; Formal analysis, R.V.; Funding acquisition, D.P. and J.K.; Investigation, R.V., L.P., J.J. and T.Z.; Methodology, R.V. and D.K.; Project administration, R.V.; Resources, D.P. and J.K.; Supervision, D.K. and D.P.; Validation, R.V., D.K., D.P., L.P. and T.Z.; Visualization, R.V.; Writing—original draft, R.V., D.K. and L.P.; Writing—review and editing, R.V., D.K. and L.P.

**Funding:** This research was funded by [NETME Centre] grant number [CZ.1.05/2.1.00/01.0002], [NETME Centre Plus] grant number [LO1202], [Architected materials designed for additive manufacturing] grant number [CZ.02.1.01/0.0/0.0/16\_025/0007304], [BUT] grant number [FSI-S-17-4144], [CEITEC 2020] grant number [LQ1601] and the APC was funded by [BUT open access fund].

**Acknowledgments:** This work is an output of research and scientific activities of the NETME Centre, the regional R&D centre built with the financial support from the Operational Programme Research and Development for Innovations within the project NETME Centre (New Technologies for Mechanical Engineering), Reg. No. CZ.1.05/2.1.00/01.0002 and, in the follow-up sustainability stage, supported through NETME CENTRE PLUS (LO1202) by financial means from the Ministry of Education, Youth and Sports under the “National Sustainability Programme I”. The study was further supported by the ESIF, EU Operational Programme Research, Development and Education within the research project “Architected materials designed for additive manufacturing”, Reg. No.: CZ.02.1.01/0.0/0.0/16\_025/0007304, by the project FSI-S-17-4144 and by the Ministry of Education, Youth and Sports of the Czech Republic under the project CEITEC 2020 (LQ1601).

**Conflicts of Interest:** The authors declare no conflict of interest. The founding sponsors had no role in the design of the study; in the collection, analyses, or interpretation of data; in the writing of the manuscript, and in the decision to publish the results.

## References

- Kopanidis, A.; Theodorakakos, A.; Gavaises, E.; Bouris, D. 3D numerical simulation of flow and conjugate heat transfer through a pore scale model of high porosity open cell metal foam. *Int. J. Heat Mass Transf.* **2010**, *53*, 2539–2550. [[CrossRef](#)]
- Mohammed, R.; Ahmed, A.; Elgalib, M.A.; Ali, H. Low Velocity Impact Properties of Foam Sandwich Composites: A Brief Review. *Int. J. Eng. Sci. Innov. Technol.* **2014**, *3*, 579–591.
- Mohammed, R.; Zhang, F.; Sun, B.; Gu, B. Finite element analyses of low-velocity impact damage of foam sandwiched composites with different ply angles face sheets. *Mater. Des.* **2013**, *47*, 189–199. [[CrossRef](#)]
- Shimizu, T.; Matsuzaki, K.; Nagai, H.; Kanetake, N. Production of high porosity metal foams using EPS beads as space holders. *Mater. Sci. Eng. A* **2012**, *558*, 343–348. [[CrossRef](#)]
- Zhu, L.; Guo, K.; Li, Y.; Yu, T.X.; Zhou, Q. Experimental study on the dynamic behaviour of aluminium foam sandwich plates under single and repeated impacts at low temperature. *Int. J. Impact Eng.* **2018**, *114*, 123–132. [[CrossRef](#)]
- Harris, J.A.; Winter, R.E.; McShane, G.J. Impact response of additively manufactured metallic hybrid lattice materials. *Int. J. Impact Eng.* **2017**, *104*, 177–191. [[CrossRef](#)]
- Mines, R.A.W.; Tsopanos, S.; Shen, Y.; Hasan, R.; McKown, S.T. Drop weight impact behaviour of sandwich panels with metallic micro lattice cores. *Int. J. Impact Eng.* **2013**, *60*, 120–132. [[CrossRef](#)]
- Qiu, C.; Yue, S.; Adkins, N.J.E.; Ward, M.; Hassanin, H.; Lee, P.D.; Withers, P.J.; Attallah, M.M. Influence of processing conditions on strut structure and compressive properties of cellular lattice structures fabricated by selective laser melting. *Mater. Sci. Eng. A* **2015**, *628*, 188–197. [[CrossRef](#)]
- Attar, H.; Ehtemam-Haghighia, S.; Kent, D.; Dargusch, M.S. Recent developments and opportunities in additive manufacturing of titanium-based matrix composites: A review. *Int. J. Mach. Tools Manuf.* **2018**, *133*, 85–102. [[CrossRef](#)]
- Yan, C.; Hao, L.; Hussein, A.; Young, P.; Raymont, D. Advanced lightweight 316L stainless steel cellular lattice structures fabricated via selective laser melting. *J. Mater. Des.* **2014**, *55*, 533–541. [[CrossRef](#)]
- Brandl, E.; Heckenberger, U.; Holzinger, V.; Buchbinder, D. Additive manufactured AlSi10Mg samples using Selective Laser Melting (SLM): Microstructure, high cycle fatigue, and fracture behavior. *J. Mater. Des.* **2012**, *34*, 159–169. [[CrossRef](#)]

12. Kempen, K.; Thijs, L.; van Humbeeck, J.; Kruth, J.-P. Mechanical Properties of AlSi10Mg Produced by Selective Laser Melting. *Phys. Procedia* **2012**, *39*, 439–446. [[CrossRef](#)]
13. Thijs, L.; Kempen, K.; Kruth, J.-P.; van Humbeeck, J. Fine-structured aluminium products with controllable texture by selective laser melting of pre-alloyed AlSi10Mg powder. *Acta Mater.* **2013**, *61*, 1809–1819. [[CrossRef](#)]
14. Yadroitsev, I. *Selective Laser Melting: Direct Manufacturing of 3D-Objects by Selective Laser Melting of Metal Powders*; LAP Lambert: Saarbrücken, Germany, 2009; ISBN 3838317947.
15. Koutny, D.; Palousek, D.; Pantelejev, L.; Hoeller, C.; Pichler, R.; Tesicky, L.; Kaiser, J. Influence of scanning strategies on processing of aluminum alloy EN AW 2618 using selective laser melting. *Materials* **2018**, *11*, 298. [[CrossRef](#)] [[PubMed](#)]
16. Abele, E.; Stoffregen, H.A.; Klimkeit, K.; Hoche, H.; Oechsner, M. Optimisation of process parameters for lattice structures. *Rapid Prototyp. J.* **2015**, *21*, 117–127. [[CrossRef](#)]
17. Leary, M.; Mazur, M.; Elambasseril, J.; McMillan, M.; Chirent, T.; Sun, Y.; Qian, M.; Easton, M.; Brandt, M. Selective laser melting (SLM) of AlSi12Mg lattice structures. *Mater. Des.* **2016**, *98*, 344–357. [[CrossRef](#)]
18. Koutny, D.; Vrana, R.; Paloušek, D. Dimensional accuracy of single beams of AlSi10Mg alloy and 316L stainless steel manufactured by SLM. In Proceedings of the 5th International Conference on Additive Technologies iCAT2014, Vienna, Austria, 16–17 October 2014; pp. 142–147.
19. Yu, G.; Gu, D.; Dai, D.; Xia, M.; Ma, C.; Shi, Q. On the role of processing parameters in thermal behavior, surface morphology and accuracy during laser 3D printing of aluminum alloy. *J. Phys. D Appl. Phys.* **2016**, *1*–15. [[CrossRef](#)]
20. Yu, G.; Gu, D.; Dai, D.; Xia, M.; Ma, C.; Chang, K. Influence of processing parameters on laser penetration depth and melting/re-melting densification during selective laser melting of aluminum alloy. *Appl. Phys. A* **2016**, *122*, 1–12. [[CrossRef](#)]
21. Wei, P.; Wei, Z. The AlSi10Mg samples produced by selective laser melting: Single track, densification, microstructure and mechanical behavior. *Appl. Surf. Sci.* **2017**, *408*, 38–50. [[CrossRef](#)]
22. Delroisse, P.; Jacques, P.J.; Maire, E.; Rigo, O.; Simar, A. Effect of strut orientation on the microstructure heterogeneities in AlSi10Mg lattices processed by selective laser melting. *Scr. Mater.* **2017**, *141*, 32–35. [[CrossRef](#)]
23. Attar, H.; Calin, M.; Zhang, L.C.; Scudino, S.; Eckert, J. Manufacture by selective laser melting and mechanical behavior of commercially pure titanium. *Mater. Sci. Eng. A* **2014**, *593*, 170–177. [[CrossRef](#)]
24. Vrana, R.; Vosynek, P.; Koutny, D.; Navrat, T.; Palousek, D. Evaluation of mechanical behavior of 3D printed lattice structure by SLM: Experiment and FEA. In Proceedings of the Engineering Mechanics 2018 24th International Conference, Svratka, The Czech Republic, 14–17 May 2018; pp. 897–900.
25. Vrana, R.; Koutny, D.; Paloušek, D.; Zikmund, T. Influence of selective laser melting process parameters on impact resistance of lattice structure made from AlSi10Mg. In Proceedings of the World PM 2016 Congress and Exhibition, Hamburg, Germany, 9–13 October 2016; ISBN 978-189-907-248-4.
26. Vrana, R.; Koutny, D.; Paloušek, D. Impact Resistance of Different Types of Lattice Structures Manufactured by SLM. *MM Sci. J.* **2016**, *2016*, 1579–1585. [[CrossRef](#)]
27. Vrana, R.; Koutny, D.; Paloušek, D.; Zikmund, T. Impact resistance of lattice structure made by selective laser melting from AlSi12 alloy. *MM Sci. J.* **2015**, *2015*, 1579–1585. [[CrossRef](#)]
28. Vrana, R.; Koutny, D.; Paloušek, D.; Koukal, O.; Zikmund, T.; Krejci, P. Impact resistance of lattice structure made by selective laser melting technology. In Proceedings of the Euro PM 2015: International Power Metallurgy Congress and Exhibition, Reims, France, 4–7 September 2015; ISBN 978-189-907-247-7.
29. Palousek, D.; Omasta, M.; Koutny, D.; Bednar, J.; Koutecky, T.; Dokoupil, F. Effect of matte coating on 3D optical measurement accuracy. *Opt. Mater.* **2015**, *40*, 1–9. [[CrossRef](#)]
30. Aboulkhair, N.T.; Everitt, N.M.; Ashcroft, I.; Tuck, C. Reducing porosity in AlSi10Mg parts processed by selective laser melting. *Addit. Manuf.* **2014**, *1*, 77–86. [[CrossRef](#)]



PAPER [XXIII]

## ORIGINAL ARTICLE

# Epoxy-based gelcasting of machinable hydroxyapatite foams for medical applications

Premysl Stastny<sup>1</sup> | Zdenek Chlup<sup>2</sup> | Dominika Kalasova<sup>1</sup> | Tomas Zikmund<sup>1</sup> |  
 Jozef Kaiser<sup>1</sup> | Martin Trunec<sup>1,3</sup> 

<sup>1</sup>CEITEC BUT, Brno University of Technology, Brno, Czech Republic

<sup>2</sup>CEITEC IPM, Institute of Physics of Materials, Academy of Sciences of the Czech Republic, Brno, Czech Republic

<sup>3</sup>Department of Materials Science and Engineering, Brno University of Technology, Brno, Czech Republic

## Correspondence

Martin Trunec, CEITEC BUT, Brno University of Technology, Brno, Czech Republic.

Email: trunec@fme.vutbr.cz

## Funding information

CEITEC Nano Research Infrastructure; Vysoké Učení Technické v Brně, Grant/Award Number: STI-J-17-4305; Czech Health Research Council, Grant/Award Number: 17-31276A

## Abstract

Machinable hydroxyapatite foams for subtractive manufacturing of customized bone scaffolds have been developed. The foams were prepared by direct foaming of water-based hydroxyapatite suspension with dissolved epoxy resin. The foams were consolidated by gelation of the epoxy-based suspension in air atmosphere. The effect of processing conditions on the foam structure was investigated. The foams had a cellular-like structure with interconnected pores. The sintered foam with 78% open porosity, the most frequent pore size 430  $\mu\text{m}$ , and the most frequent interconnecting pore window size 150  $\mu\text{m}$ , has been chosen as the foam with the optimal structure from the viewpoint of an application in bone regeneration. The compressive strength of this sintered foam reached 3.3 MPa. The machinability of the optimal foam was investigated using computer numerical controlled (CNC) milling of a test pattern. The milling tests were carried out with the foam at different processing stages and after impregnation with paraffin wax. The best milling result was obtained for a dried foam impregnated with paraffin. The applicability of the whole processing chain was demonstrated and a customized scaffold was manufactured.

## KEYWORDS

foams, gelcasting, hydroxyapatite, mills/milling, scaffold

## 1 | INTRODUCTION

Pores have traditionally been avoided in ceramic parts because they reduce mechanical properties. However, porous ceramics with tailored porosity exhibit many unique properties that cannot be achieved in dense ceramic bodies. Therefore, advanced porous ceramics have been developed and the interest in porous ceramics is steadily increasing.<sup>1-3</sup> One of the important applications of macroporous ceramics has arisen in medicine. The porous 3-dimensional ceramic structures for bone regeneration, called scaffolds, support the newly developing tissue and often supply the building and stimulating substances to the cells through controlled degradation. They have to fulfill many demanding material

and geometrical requirements.<sup>4-6</sup> The material requirements include full biocompatibility. Ideal scaffolds must be osteoconductive to allow the attachment, growth, and formation of bone tissue on their surface, and osteoinductive to stimulate new bone formation through molecular signaling and recruiting of osteoprogenitor cells.<sup>4,5</sup> Furthermore, it is necessary for the scaffold to promote vascularization of the new tissue through new blood vessel formation.<sup>4,6</sup> The scaffold material should be bioresorbable with controlled degradation and drug-releasing kinetics that match the new tissue growth.<sup>5</sup> The geometrical requirements include interconnected macroporosity with pores of at least 100  $\mu\text{m}$  in diameter (with an optimum pore size in the range of 300-500  $\mu\text{m}$ ) for optimum tissue in-growth, and the supply of

essential nutrients and oxygen<sup>4,5,7</sup> as well as a mesoporosity with pores  $<10\ \mu\text{m}$  for protein adsorption and cell attachment.<sup>6</sup> Another requirement the scaffold must fulfill is sufficient mechanical strength for scaffold handling as well as for survival through physical forces *in vivo*.<sup>7</sup> Calcium phosphates (CaPs) are the first-choice ceramic materials for rigid and relatively strong scaffolds. CaPs are inherent to the human body and they show promising biological properties such as biodegradability, osteoconductivity, and in some cases even osteoinductivity.<sup>8-10</sup> Hydroxyapatite ( $\text{Ca}_{10}(\text{PO}_4)_6(\text{OH})_2$ ), tricalcium phosphates ( $\alpha\text{-Ca}_3\text{PO}_4$  and  $\beta\text{-Ca}_3\text{PO}_4$  phases), and their biphasic mixtures are the most frequently studied ceramics from the CaPs family for bone tissue engineering<sup>7,11-15</sup> and are frequently used in commercially available scaffold materials.<sup>6,8,16</sup>

The personalized medicine developing in the area of bone regeneration is based on progress in digital imaging of damaged bone tissue and requires customized scaffolds perfectly matching the defect in order to improve the healing process, including optimal aesthetic results.<sup>17</sup> Rapid prototyping methods based on the additive manufacturing approach seem to be the optimal processing methods for ceramic scaffold manufacturing. These methods can prepare a scaffold with customized shape as well as with complex pre-defined internal pore structure according to a digital model using the CAD/CAM processes, without any need for molds or other shaping tools.<sup>18-20</sup> The methods most frequently employed for ceramic scaffold manufacturing include different variants of stereolithography,<sup>21,22</sup> 3D printing,<sup>23,24</sup> robocasting,<sup>25,26</sup> fused deposition,<sup>27,28</sup> and selective laser sintering.<sup>29,30</sup> Despite the enormous progress in the last 2 decades these methods still suffer from some disadvantages related to scaffold production. Some of the additive methods of manufacturing ceramic scaffolds are time-consuming processes that take several days to deliver the required scaffold. Furthermore, the rapid prototyping methods are rather complex processes that require a specialized ceramic laboratory. These features can be inconsistent with some medical treatments requiring a quick and preferably in-house supply of scaffolds. Recently, Trunec and Chlup<sup>31</sup> have reported a simple alternative to rapid prototyping of scaffolds, based on computer numerical controlled (CNC) milling of ceramic foam. The proposed method is based on direct foaming of a hydroxyapatite suspension that is consolidated using the gelcasting method. After drying, the foam is presintered, milled to the required shape, and finally sintered. Ceramic foam blocks with suitable pore structure can be kept in stock and subsequently customized via milling into the final scaffold in  $<1$  day. The finalization of a scaffold (CNC milling, sintering, coating, etc.) can be performed in a common hospital or central laboratories. Unfortunately, the above-mentioned

processing chain exhibits several drawbacks. The gelcasting consolidation is based on acrylamide monomers that undergo radical polymerization. In that process, oxygen inhibits polymerization by free radicals, and thus the foaming and consolidation must be performed under an inert atmosphere. Although milling of presintered foams provides satisfactory results, there is still a need for an improvement of the milling precision.

The aim of the investigation presented here was an optimization of this recently proposed method for scaffold manufacturing. A novel gelcasting process for direct foaming of a hydroxyapatite suspension based on epoxy resin was investigated in order to simplify the process and improve the milling precision and quality of final scaffolds.

## 2 | EXPERIMENTAL PROCEDURE

### 2.1 | Materials and scaffold preparation

Figure 1 shows the flowchart of a scaffold manufacturing method. Hydroxyapatite nanopowder (tri-calcium phosphate, extra pure, Riedel-de Haen, Seelze, Germany) was calcined at  $1000^\circ\text{C}$  for 3 hours before use. The calcined hydroxyapatite powder was then dispersed in the premix

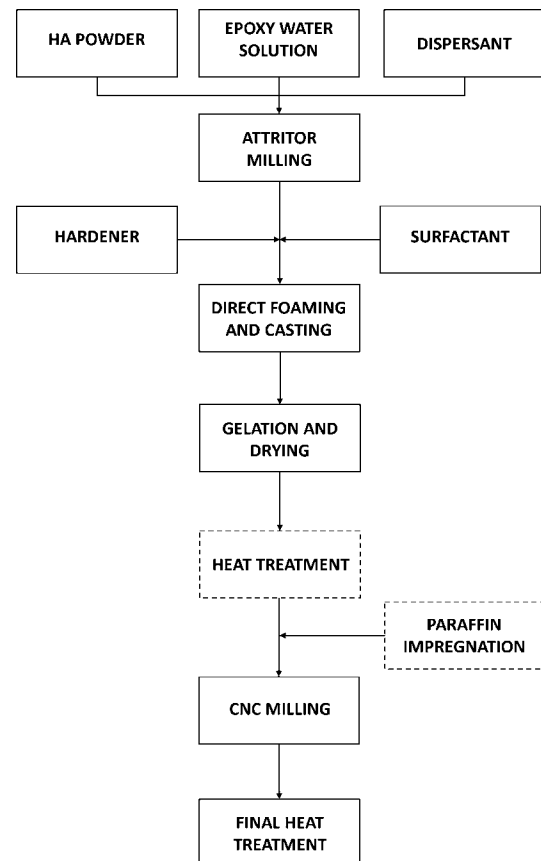


FIGURE 1 Flowchart of the scaffold preparation

solution of an epoxy resin with a dispersant and then attritor-milled (HD-01, Union Process, Akron, OH) for 3 hours with 1 mm zirconia balls to obtain a fine and narrow particle size distribution with a median particle size of 130 nm.<sup>31</sup> The premix epoxy solution was prepared by dissolving 16 wt% of ethylene glycol diglycidyl ether (Quetol 651, Electron Microscopy Sciences, Hatfield, PA, USA) in deionized water. The ceramic suspension was stabilized using a dispersant based on ammonium polyacrylate (Darvan 821A, R.T. Vanderbilt Co., Norwalk, CT, USA). The optimum amount of the dispersant was found by steady-shear rheological measurements at 1.2 wt% of solids. The hydroxyapatite water-based colloidal suspension was directly foamed using a mixer (Bamix Swiss Line, ESGE, Switzerland) for an optimum time of 3 minutes.<sup>31</sup> A suitable surfactant (Triton X-100, Sigma-Aldrich, Saint Louis, MO, USA) was added to the suspension prior to foaming to stabilize the foam until consolidation. Bis(3-aminodipropyl)amine (Sigma-Aldrich, Steinheim, Germany), also referred to as dipropylentriamine (DPTA), was added in a stoichiometric ratio to the suspension prior to foaming as a hardener for ethylene glycol diglycidyl ether (EGDGE), and the resulting polymer gel consolidated the ceramic foam. Based on previous experiments<sup>31</sup> a suspension with a solid loading of 31.8 vol% was chosen for all tests. The final composition of the ceramic suspension is given in Table 1. Prior to gelation, the foamed suspension was cast in plastic molds and sealed to obtain porous preforms (blanks) with a diameter of 40 and 100 mm and a thickness of 30 and 15 mm, respectively. The polymerization process of the suspensions was carried out at different temperatures (23–50°C) in order to optimize foam consolidation. Consolidated ceramic foams were dried under controlled temperature (20°C) and relative humidity (98% and 80%) until water loss ceased below 40%–45%, and then left to dry completely under laboratory conditions. 3D milling tests of porous foam were performed using a high-speed (28 000 min<sup>-1</sup>) CNC milling machine (Ultrasonic, Sauer, Stipshausen, Germany) equipped with a diamond-coated milling tool with a diameter of 1 mm. The finishing cutting speed was set at 2000 mm min<sup>-1</sup>, the depth and width of cuts were 0.13 and 0.08 mm, respectively. The milling of hydroxyapatite foams was tested in dried as well as presintered or sintered states. To improve the precision

of milling, the foams were impregnated with paraffin wax by dipping into molten paraffin at 90°C for 15 minutes. The paraffin wax and in the case of dried samples also the epoxy gel were removed from the impregnated and milled samples by heating to a temperature of 500°C at a rate of 50°C h<sup>-1</sup>, followed by heating to the sintering temperature at a rate of 120°C h<sup>-1</sup>. The final sintering of ceramic foams at 1250°C for 2 hours was used to maximize the strength of the scaffolds and keep the single-phase hydroxyapatite structure.<sup>31</sup>

## 2.2 | Evaluation methods

The gelation process in the suspension was monitored by small-strain oscillatory shear measurements performed on a rotational rheometer (HAKE MARS II, Thermo Scientific, Karlsruhe, Germany) equipped with parallel plate geometry.<sup>32</sup> The distribution of pore and pore window sizes in sintered foams was investigated manually from at least 3 scanning electron microscopy (SEM) images of a fracture surface, and compared with results obtained from computed tomography (phoenix v|tome|x L240, GE Sensing & Inspection Technologies, Huerth, Germany) of a test body. During the manual two-dimensional SEM image analysis, the largest dimension of a pore (expected to be spherical) or a pore window (expected to be circular) was always taken and no correction factor for the average pore and window diameters was applied. The 3-dimensional CT scan was carried out with a voxel resolution of 20 μm, that is, the smallest distinguishable volume element was 20 × 20 × 20 μm<sup>3</sup>. The CT structure data were processed using an analyzing software for the CT data (VGStudio MAX 3.0, Volume Graphics, Heidelberg, Germany) to find pore and pore window sizes. For porosity analysis, the software uses the watershed algorithm. This algorithm created a gradient parametric map on which it searched for local extrema. The local extrema corresponded with places determined as air pores in the original image. The open porosity of sintered scaffolds was also determined in water by the Archimedes method, using the value 3.16 g cm<sup>-3</sup> for the theoretical density of hydroxyapatite. The compressive strength was measured using a universal testing machine (8862, Instron, Norwood, MA, USA) on cylindrical samples (with a diameter of 14.5 mm and a height of 21–22 mm). The samples were prepared in the same way as the disc for milling. A cross-head speed of 0.5 mm min<sup>-1</sup> was applied and force-deflection traces were recorded. The compressive strength was calculated from the first maximum on the loading curve before the sample rupture. Work of fracture was calculated as the integral of the load-displacement curve (up to the fracture) divided by the cross-section of the sample. The parameters of the Weibull strength distribution were calculated numerically, using the

**TABLE 1** Composition of hydroxyapatite suspension

	HA powder	Water	EGDGE	DPTA	Darvan 821A	Triton ×-100
wt%	58.5	31.0	6.0	1.8	0.3	2.4
vol%	31.8	53.3	8.9	3.3	0.5	2.2

EGDGE, ethylene glycol diglycidyl ether; DPTA, dipropylentriamine.

maximum likelihood method, in accordance with the EN 843-5 Standard.

### 3 | RESULTS AND DISCUSSION

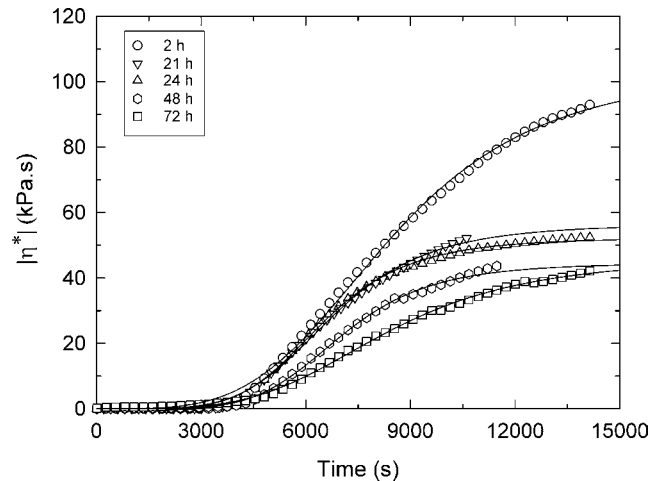
#### 3.1 | Gelation of epoxy based suspensions

Figure 2A schematically shows the epoxy-amine cross-linking, which occurs in the ceramic suspension through the reaction of the epoxy groups in EGDGE and the amine groups in DPTA. The gel (polymer network) formed by these reactions consolidates the ceramic foam and prevents any further foam degradation during drying. Epoxy-based gelcasting suspensions can be polymerized in air atmosphere. This is a clear advantage compared with polyacrylamide systems.<sup>31</sup> In the water suspension, however, the epoxy ring can be cleaved even under basic conditions, which is the case of our hydroxyapatite suspension (pH of the suspension stabilized with Darvan 821A dispersant was about 9). The hydrolysis of the epoxy resin resulted in the formation of alcohols<sup>33</sup> (Figure 2B) and the reduced number of epoxy groups lowered the density of the polymerized gel network. Figure 3 shows the time dependence of the absolute value of complex viscosity during polymerization of ceramic suspensions that were aged for different times before polymerization. The experimental viscosity data in Figure 3 were fitted to the Hill equation:

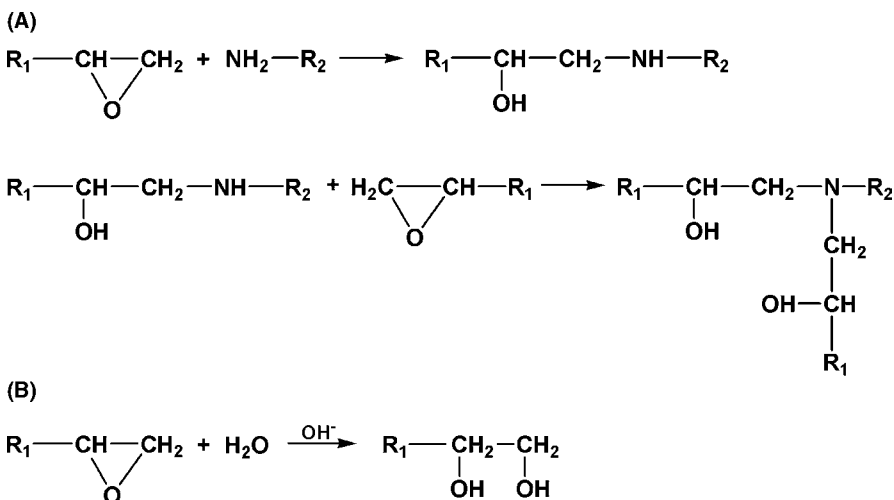
$$|\eta^*(t)| = |\eta^*(\infty)| \frac{t^n}{t^n + \theta^n} \quad (1)$$

where  $\eta^*(\infty)$  is the final equilibrium complex viscosity of the gel,  $\theta$  is the half-gelation time, and  $n$  is a coefficient relative to the asymptotic slope at the half-gelation time  $\theta$ . This phenomenological model yields parameters that can be used to determine the final (equilibrium) viscosity of the gelled ceramic body and the total gelation time (defined as

the time necessary to reach 95% of the final viscosity). For more details on the Hill equation and its use in the modeling of polymerization kinetics,<sup>31,32</sup> The calculated parameters are shown in Table 2. It can be seen in Figure 3 and Table 2 that the decrease in final viscosity was steep in the first 24 hours of aging and then slowed down. In order to minimize the changes in gel properties with processing time variations, the 24-hour-old suspension was used in all the following experiments. Despite its degradation, this 24-hour-old epoxy-based suspension still reached a final viscosity higher than the polyacrylamide-based hydroxyapatite gel did (51 vs. 44 kPa s).<sup>31</sup> The above-mentioned cross-linking reaction was temperature-dependent, and increasing temperature speeded up the polymerization reaction in the suspension and decreased the idle time (i.e., the time before the suspension viscosity started to grow). Sufficient idle time after hardener addition is necessary for foaming the suspension and casting the foam. Figure 4 shows the onset



**FIGURE 3** Time dependence of complex viscosity during gelation at a temperature of 25°C for hydroxyapatite suspensions after different aging

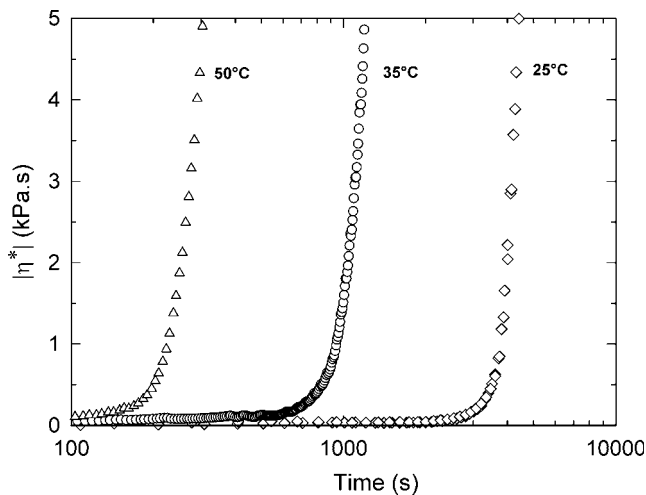


**FIGURE 2** Chemical reactions of (A) epoxy groups with amine groups resulting in polymer network, (B) the epoxy group with water

**TABLE 2** Gelation parameters of hydroxyapatite suspensions

Suspension	Temperature (°C)	Aging time (h)	Idle time (s)	Total gelation time (s)	Final viscosity (kPa s)
HA 25/2	25	2	3150	18 330	104.4
HA 25/21	25	21	3050	12 340	56.6
HA 25/24	25	24	3200	11 400	51.3
HA 25/48	25	48	3490	12 120	44.7
HA 25/72	25	72	3490	17 270	46.3
HA 35/24	35	24	910	2180	56.2
HA 50/24	50	24	230	N/A	N/A

Values not available due to rapid water evaporation during rheological testing.

**FIGURE 4** Time dependence of complex viscosity for a hydroxyapatite suspension at different gelation temperatures. The suspension was aged for 24 h before gelation

of the polymerization of ceramic suspensions at different temperatures. The idle time (determined as a time point where the tangent to the viscosity curve in logarithmic coordinates changed at the highest rate) as well as the other parameters of suspensions polymerized at different temperatures are given in Table 2. It follows from the rheological experiments that the idle time for the suspension polymerized at 50°C (~4 minutes) was too short for foaming and

casting into molds. On the other hand, the suspension treated at 25°C exhibited a long idle time of over 50 minutes. The idle time reached for the suspension treated at 35°C seemed to be optimal but there could be unexpected processing results with slight time and temperature deviations during the treatment. Therefore, we investigated a method working with a suspension at room temperature (25°C) that was heated to 35°C or 50°C only after foaming to quickly consolidate the foam structure. This approach was easy to apply because the effect of gelling temperature on the final viscosity of epoxy-based ceramic gel seemed to be insignificant.

### 3.2 | Structure of hydroxyapatite foams

The structure of the hydroxyapatite foams prepared depended strongly on the temperature of the suspension treatment. Table 3 gives variants of the foaming temperature,  $T_{\text{foam}}$ , and gelation temperature,  $T_{\text{gel}}$ , used in our investigation. The hardener was added to the suspension at the foaming temperature, and foaming and casting were also performed at this temperature. Immediately after foaming and casting, the temperature was changed to the gelation temperature. The processing time,  $t_{\text{process}}$ , between the hardener addition and the temperature change to the gelation temperature varied from 4 minutes (a minimum for foaming and casting) up to 16 minutes. Figure 5 shows

**TABLE 3** Porosity and average pore and window sizes of sintered foams prepared at different processing conditions

Foam structure	$T_{\text{foam}}$ (°C)	$T_{\text{gel}}$ (°C)	$t_{\text{process}}$ (s)	Open porosity <sup>a</sup> (%)	Pore size (μm)	Window size (μm)
A	35	50	540	76.1 ± 1.2	214	46
B	35	35	540	74.2 ± 4.0	172	48
C	25	50	240	82.1 ± 4.2	644	135
D	25	35	360	78.1 ± 0.9 (65.8) <sup>b</sup>	317 (260) <sup>b</sup>	78 (79) <sup>b</sup>
E	25	35	660	82.4 ± 1.0	464	117
F	25	35	960	73.2 ± 0.9	287	73

<sup>a</sup>Sample mean is given with 95% confidence interval.

<sup>b</sup>Values determined by CT analysis.

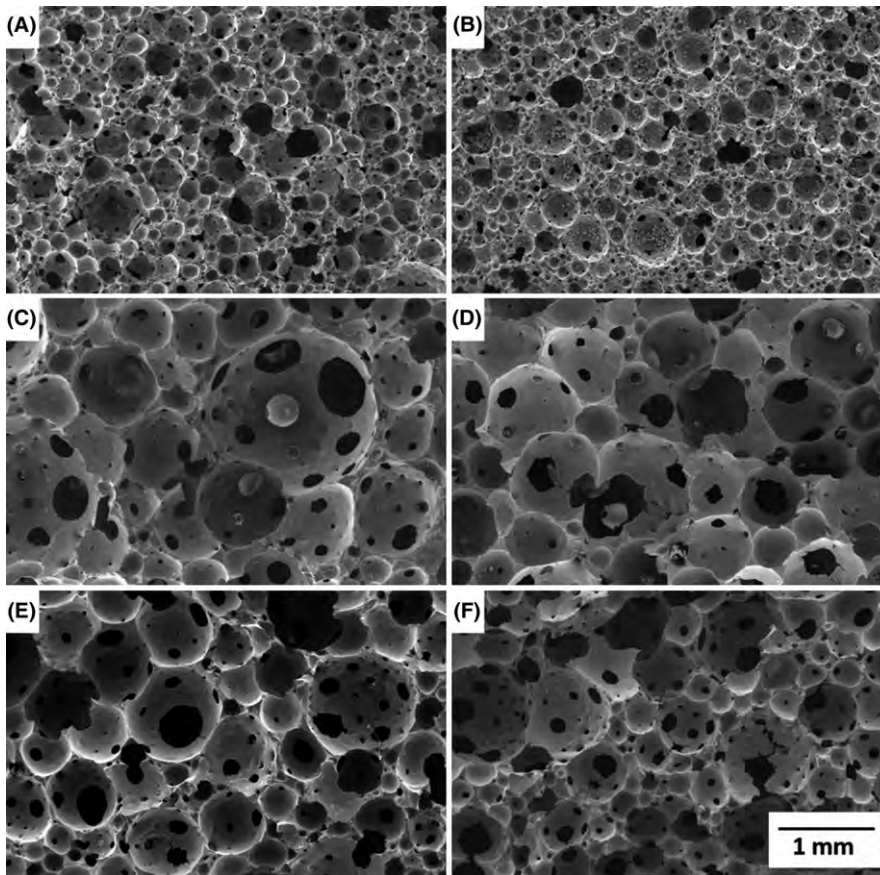


**FIGURE 5** SEM images of sintered foam structures prepared with different processing parameters; A, foam temperature  $T_{\text{foam}} = 35^{\circ}\text{C}$ , gelation temperature  $T_{\text{gel}} = 50^{\circ}\text{C}$ , and processing time  $t_{\text{process}} = 540$  s; B,  $T_{\text{foam}} = 35^{\circ}\text{C}$ ,  $T_{\text{gel}} = 35^{\circ}\text{C}$ ,  $t_{\text{process}} = 540$  s; C,  $T_{\text{foam}} = 25^{\circ}\text{C}$ ,  $T_{\text{gel}} = 50^{\circ}\text{C}$ ,  $t_{\text{process}} = 240$  s; D,  $T_{\text{foam}} = 25^{\circ}\text{C}$ ,  $T_{\text{gel}} = 35^{\circ}\text{C}$ ,  $t_{\text{process}} = 360$  s; E,  $T_{\text{foam}} = 25^{\circ}\text{C}$ ,  $T_{\text{gel}} = 35^{\circ}\text{C}$ ,  $t_{\text{process}} = 660$  s; F,  $T_{\text{foam}} = 25^{\circ}\text{C}$ ,  $T_{\text{gel}} = 35^{\circ}\text{C}$ ,  $t_{\text{process}} = 960$  s

SEM images of sintered foam structures prepared at different temperatures and processing times. The sintered foams had spherical interconnected pores with an open porosity that varied from 73% to 82%. The preheated suspensions, foamed at  $35^{\circ}\text{C}$ , polymerized quickly, which resulted in a very fine pore structure. On the other hand, the structure of the suspension foamed at  $25^{\circ}\text{C}$  and gelled at  $50^{\circ}\text{C}$  exhibited a coarse structure due to air expansion in the foam bubbles during heating from  $25^{\circ}\text{C}$  to  $50^{\circ}\text{C}$ . The most suitable pore structure from the viewpoint of bone scaffolds was obtained after foaming at  $25^{\circ}\text{C}$  and gelling at  $35^{\circ}\text{C}$ . The optimum pore structure was found in samples (D) prepared with a processing time of 6 minutes. Open porosity, average pore size and pore window size (i.e., the size of open interconnections between pores) of sintered structures are given in Table 3. The structural parameters of the optimal sample (D) were also investigated by computed tomography. Figure 6 shows the CT image and the way the evaluating software identified and analyzed the pore windows (Figure 6C) and pores (Figure 6D). The analysis of the CT image underestimated the porosity (67% from CT vs. 78% from the Archimedes method), most probably because of the limited scanning resolution (with a voxel volume of  $20\ \mu\text{m}^3$ ), which omitted mesoporous voids in the sample. On the other hand, the pore size distributions determined by SEM and CT image analyses (Figure 7)

matched well. The most frequent volume-based pore size was in both analyses similar, with a value of  $430\ \mu\text{m}$ . The window size distribution determined by CT image analysis showed the most frequent area-based window size to be  $150\ \mu\text{m}$ . The SEM analysis provided a slightly shifted distribution, with the most frequent window size of  $130\ \mu\text{m}$  (Figure 8). This shift was caused probably by a skewed projection of the pore windows during the SEM analysis. Nevertheless, this quite well-matching comparison justifies the utilization of the relatively simple SEM method to evaluate cellular-like porous structures.

### 3.3 | Strength and 3D milling of scaffolds

The milling tests were performed using a milling pattern (Figure 9A). This milling pattern allowed us to evaluate the important features of milled scaffolds, namely surface smoothness, sharpness and continuity of edges, and quality of tiny object and details. Only the optimal foam with the structure D (Table 3) was tested. The foam blanks were milled at different processing stages (dried, presintered, and fully sintered). The foam blanks impregnated with paraffin wax were also examined. In these cases, molten paraffin wax was used to infiltrate into the foam, where it finally solidified as a thick layer on the ceramic walls. Table 4 summarizes the treatment of the foams tested and gives a

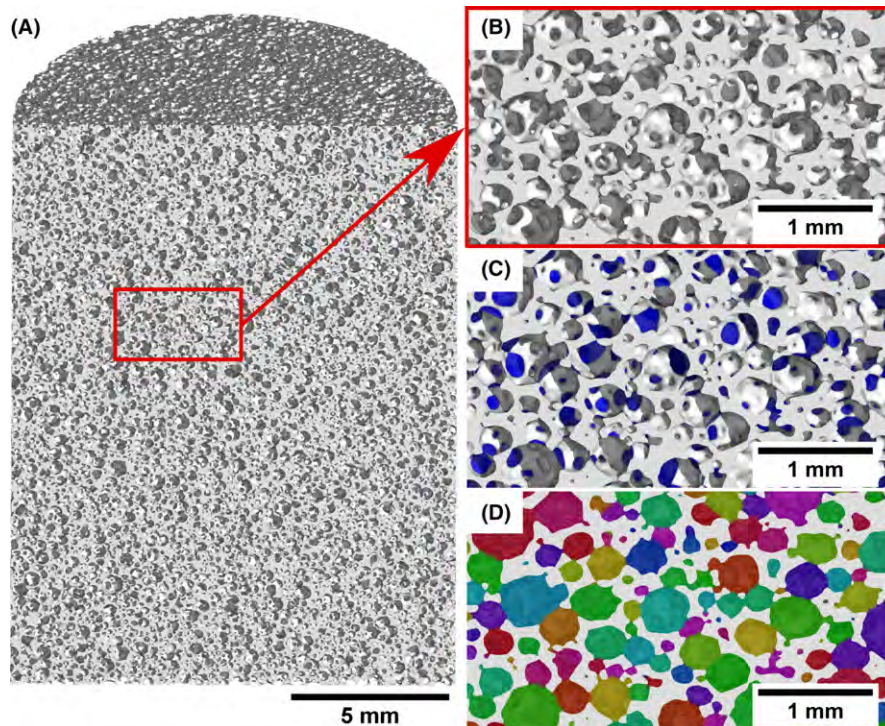


**FIGURE 6** CT images and pore structure analysis of sintered foam with structure D; A, cross section of the tested foam, B, detail of the foam structure, C, pore windows analysis, D, pore size analysis [Color figure can be viewed at wileyonlinelibrary.com]

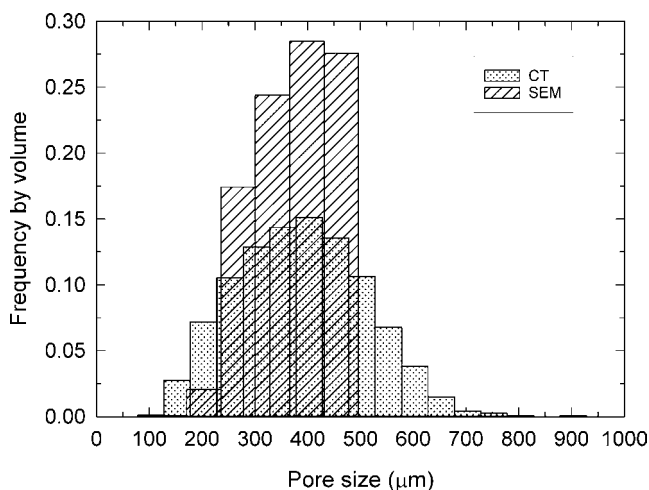


**FIGURE 7** Pore size distribution in a sintered foam with the structure D. SEM and CT analyses are compared

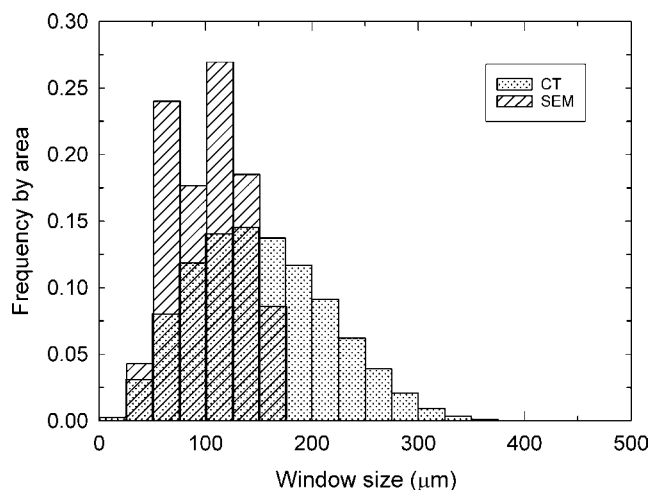


**FIGURE 8** Window size distribution in a sintered foam with the structure D. SEM and CT analyses are compared

qualitative evaluation of the milled parts. The milled parts after final sintering are shown in Figure 9B-F. The best milling results were obtained with dried foam impregnated with paraffin wax. All the evaluated features (surfaces, edges, tiny objects) were perfectly reproduced. The dried foam (not impregnated) still provided satisfactory milling results but a little bit rougher surfaces and edges. Good milling results were obtained even with impregnated sintered foam, but the tiny pin was broken, which could be connected with the brittle nature of sintered hydroxyapatite ceramics. The other variants of foam treatment exhibited unsatisfactory milling results. The results showed that

impregnation with paraffin wax improved the milling performance through improving the mechanical properties of the foam. Table 5 gives average values and the Weibull parameters of compressive strength of hydroxyapatite foams at different processing stages. The Weibull plots of compressive strength are shown in Figure 10. It is obvious that paraffin wax considerably improved the strength of the dried foam. The paraffin also acted as a toughening agent. The work of fracture of the dried foam increased from 0.33 to 0.74 mJ mm<sup>-2</sup> as a result of wax impregnation. Moreover, there is another important benefit of impregnation of dried foams. The average strength of the sintered foam was

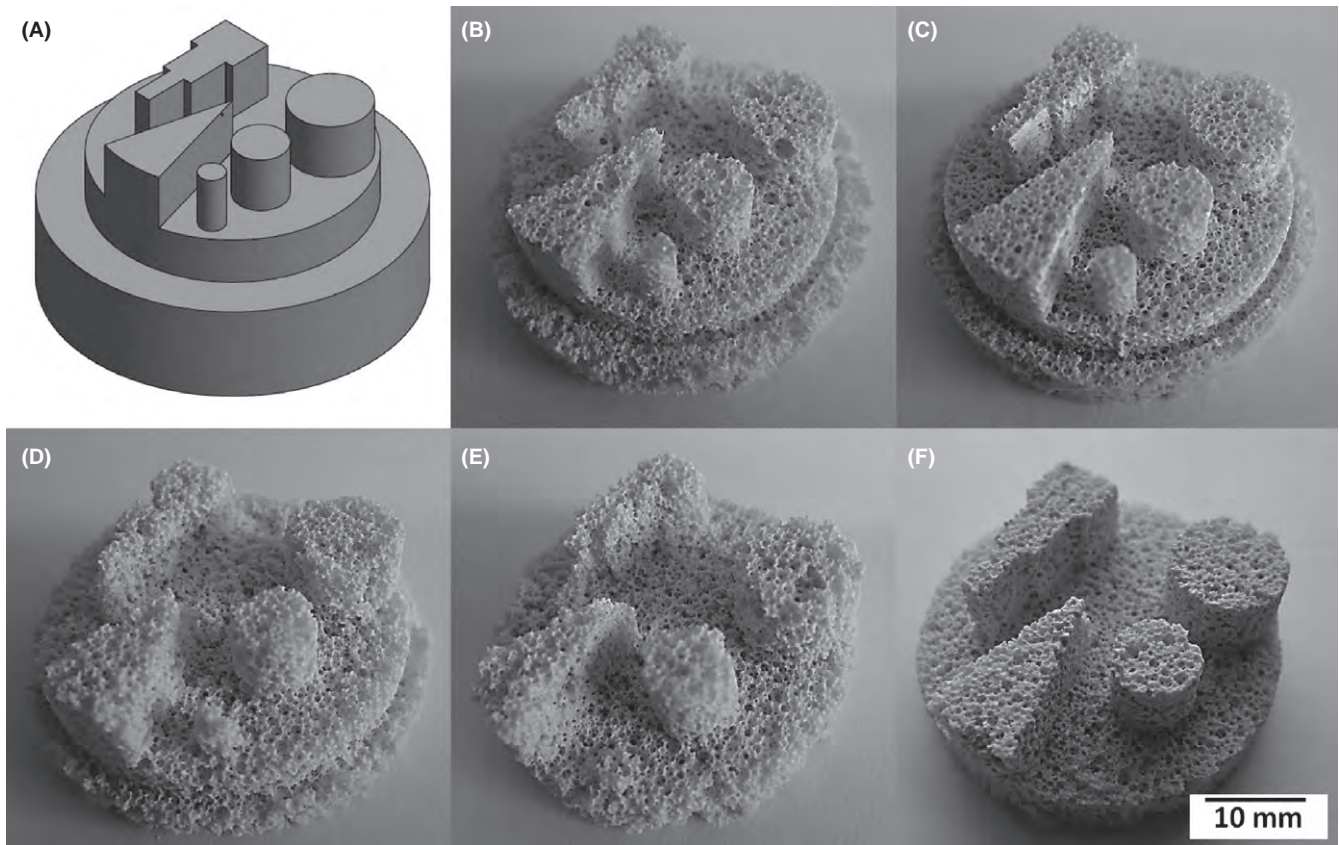


**FIGURE 9** Milling pattern and milled foam blanks with different treatments; A, milling pattern, B, dried foam, C, dried foam impregnated with paraffin wax, D, presintered foam at 1150°C/2 h, E, sintered foam at 1250°C/2 h, F, sintered foam at 1250°C/2 h and impregnated with paraffin wax

**TABLE 4** Evaluation of milling tests

Foam structure	Thermal treatment	Impregnation	Milling results	Notes
D	Dried	—	Good	Rough edges and surfaces, tiny parts ok
D	Dried	Paraffin wax	Excellent	Sharp edges, smooth surfaces, tiny parts ok
D	1150°C/2 h	—	Bad	Jagged edges, very rough surfaces, tiny parts broken
D	1150°C/2 h	Paraffin wax	N/A	Disintegrated during dewaxing
D	1250°C/2 h	—	Bad	Jagged edges, very rough surfaces, tiny part broken
D	1250°C/2 h	Paraffin wax	Good	Sharp edges, smooth surfaces, tiny pin broken

**TABLE 5** Compressive strength of hydroxyapatite foams tested at different processing stages

Sample	Average strength (MPa)	Number of samples	Weibull strength <sup>a</sup> (MPa)	Weibull modulus <sup>a</sup>
Dried	0.38	10	0.38 <sup>+0.01</sup> <sub>-0.01</sub>	25.2 <sup>+18.2</sup> <sub>-11.0</sub>
Dried + impregnated	1.64	10	1.77 <sup>+0.26</sup> <sub>-0.22</sub>	5.47 <sup>+3.95</sup> <sub>-2.40</sub>
Sintered (dried only)	1.59	32 <sup>b</sup>	1.07 <sup>+0.17<sup>b</sup></sup> <sub>-0.15</sub>	2.61 <sup>+0.76<sup>b</sup></sup> <sub>-0.79</sub>
		13 <sup>c</sup>	3.37 <sup>+0.34<sup>c</sup></sup> <sub>-0.31</sub>	6.59 <sup>+3.12<sup>c</sup></sup> <sub>-3.35</sub>
Sintered (dried + impregnated)	3.32	36	3.58 <sup>+0.23</sup> <sub>-0.22</sub>	5.85 <sup>+1.59</sup> <sub>-1.66</sub>

<sup>a</sup>Weibull parameters were determined with the confidence interval at a significance level of .05.

<sup>b</sup>Low strength population of samples.

<sup>c</sup>High strength population of samples.

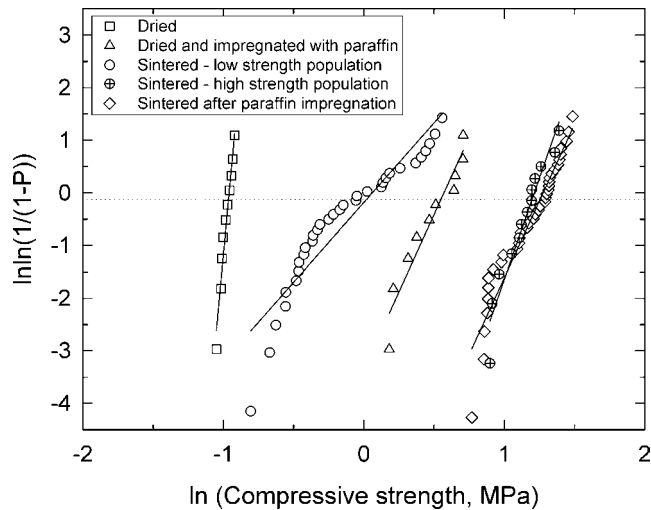


**FIGURE 10** Weibull plots of compressive strength of the optimal hydroxyapatite foam at different processing stages

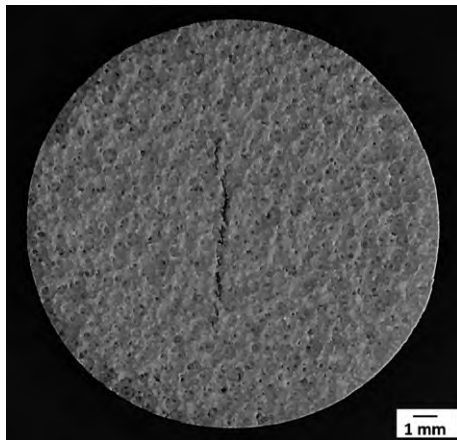


**FIGURE 11** Image of the cross-section of a debinded test body with an internal crack

1.59 MPa and increased to 3.32 MPa when impregnated with paraffin in the dried state. It can be seen in Figure 9 that the strength values of sintered foam (without impregnation in the dried state) can be divided into 2 groups. The Weibull analysis showed that there were 2 populations of samples with a different type of critical defects responsible for the rupture during the compressive test. The high strength population (13 out of a total of 45 samples) exhibited the Weibull parameters comparable to the sintered foam after paraffin impregnation (see Figure 10 and Table 5). This means that the low strength values of sintered bodies were eliminated when the foam was impregnated in the dried state. To explain this effect, it is necessary to observe the foam structure after debinding. The dried test bodies often exhibited a central crack (Figure 11). This is a common drying defect that can be seen after

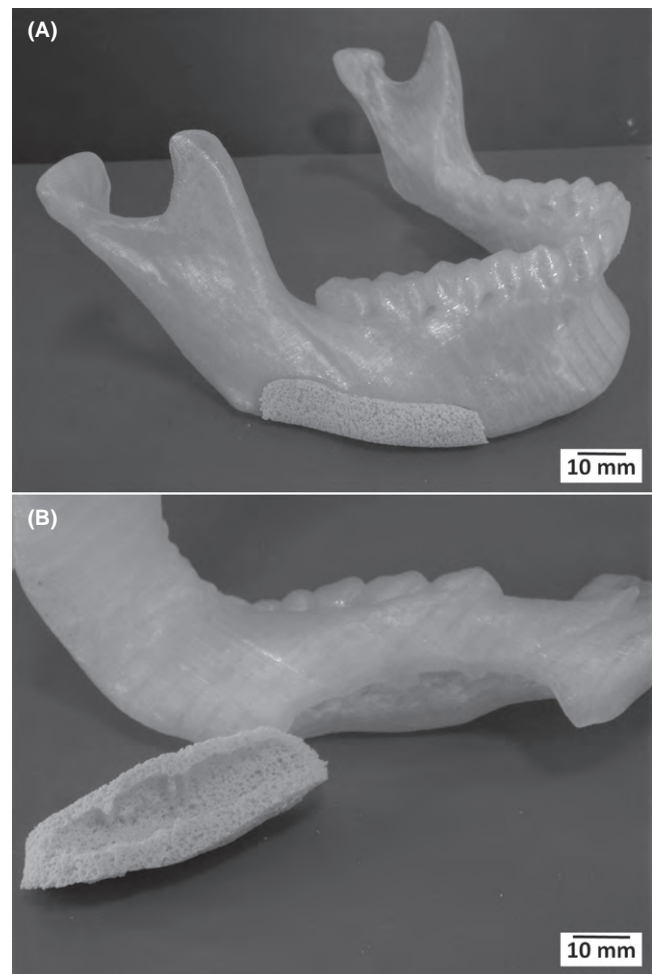


**FIGURE 12** Photographs showing (A) a model of human mandible with a defect filled with the customized hydroxyapatite scaffold, (B) a detail of the mandibular defect and the internal shape of the scaffold

debinding in large bodies<sup>34</sup> and these cracks were responsible for the low strength values. Thermal analysis showed that the infiltrated paraffin got melted during debinding and affected the degradation and removal of the epoxy-based gel in a temperature range from 200°C to 350°C, when paraffin evaporated and finally burned out. Within this temperature range, about 80% of the epoxy gel was also removed. We hypothesize that the capillary forces of the molten paraffin may have rearranged the ceramic particles during gel removal and thus eliminated particle inhomogeneity in the ceramic foam. It is believed that inhomogeneous particle packing and the resulting inhomogeneous shrinkage during debinding were responsible for the crack formation.

The above results show considerable progress in the preparation of customized hydroxyapatite scaffolds compared with previously reported processes.<sup>31</sup> The present process simplifies the foam preparation, increases the foam strength with similar pore structure, and provides more

precise milling of a scaffold. Figure 12 shows a customized scaffold for a large mandibular defect, prepared according to 3D digital data of a real patient. The images show a perfect fit of the ceramic scaffold in a model of damaged mandible (Figure 12A) and the internal structure of the scaffold (Figure 12B).

## 4 | CONCLUSIONS

A machinable hydroxyapatite foam for application in bone regeneration was prepared by direct foaming of a water-based hydroxyapatite suspension with a dissolved epoxy resin. The foam was consolidated by gelling the epoxy-based suspension in air atmosphere. The sintered foam with the optimal structure had a cellular-like structure with an open porosity of 78%. The most frequent pore size of the foam was 420  $\mu\text{m}$  while the most frequent interconnecting window size was 150  $\mu\text{m}$ . The compressive strength of the sintered foam reached an average value of 3.3 MPa with a Weibull modulus of 5.85. The developed foam could be precisely machined by CNC milling to complex shapes. The best milling results were obtained with the foam in dried state, impregnated with paraffin wax. The whole manufacturing process was successfully demonstrated by manufacturing a customized scaffold for a large mandibular defect.

## ACKNOWLEDGMENTS

This research was financially supported by Ministry of Health of the Czech Republic under the grant 17-31276A and by CEITEC BUT, Brno University of Technology, under the grant STI-J-17-4305. Part of the work was carried out with the support of CEITEC Nano Research Infrastructure (MEYS CR, 2016-2019).

## ORCID

Martin Trunec  <http://orcid.org/0000-0001-6402-7518>

## REFERENCES

1. Studart AR, Gonzenbach UT, Tervoort E, Gauckler LJ. Processing routes to macroporous ceramics: a review. *J Am Ceram Soc.* 2006;89:1771-1789.
2. Colombo P. Conventional and novel processing methods for cellular ceramics. *Philos Trans A Math Phys Eng Sci.* 2006;364:109-124.
3. Hammel EC, Ighodaro OLR, Okoli OI. Processing and properties of advanced porous ceramics: an application based review. *Ceram Int.* 2014;40:15351-15370.
4. Bose S, Roy M, Bandyopadhyay A. Recent advances in bone tissue engineering scaffolds. *Trends Biotechnol.* 2012;30:546-554.
5. Li JJ, Kaplan DL, Zreiqat H. Scaffold-based regeneration of skeletal tissues to meet clinical challenges. *J Mater Chem B.* 2014;2:7272.
6. Liu Y, Lim J, Teoh S-H. Review: development of clinically relevant scaffolds for vascularised bone tissue engineering. *Biotechnol Adv.* 2013;31:688-705.
7. Karageorgiou V, Kaplan D. Porosity of 3D biomaterial scaffolds and osteogenesis. *Biomaterials.* 2005;26:5474-5491.
8. Dorozhkin SV. Calcium orthophosphate-based bioceramics. *Materials.* 2013;6:3840-3942.
9. Debruijn JD, Vanblitterswijk CA, Davies JE. Initial bone matrix formation at the hydroxyapatite interface in-vivo. *J Biomed Mater Res.* 1995;29:89-99.
10. Muller WEG, Tolba E, Schroder HC, Munoz-Espi R, Diehl-Seifert B, Wang X. Amorphous polyphosphate-hydroxyapatite: a morphogenetically active substrate for bone-related SaOS-2 cells in vitro. *Acta Biomater.* 2016;31:358-367.
11. Ebrahimi M, Botelho MG, Dorozhkin SV. Biphasic calcium phosphates bioceramics (HA/TCP): concept, physicochemical properties and the impact of standardization of study protocols in biomaterials research. *Mater Sci Eng C.* 2017;71:1293-1312.
12. Cihlar J, Buchal A, Trunec M. Kinetics of thermal decomposition of hydroxyapatite bioceramics. *J Mater Sci.* 1999;34:6121-6131.
13. Cihlar J, Trunec M. Injection moulded hydroxyapatite ceramics. *Biomaterials.* 1996;17:1905-1911.
14. Habibovic P, Kruyt MC, Juhl MV, et al. Comparative in vivo study of six hydroxyapatite-based bone graft substitutes. *J Orthop Res.* 2008;26:1363-1370.
15. Wang X, Wang S, He F, et al. Polyphosphate as a bioactive and biodegradable implant material: induction of bone regeneration in rats. *Adv Eng Mater.* 2016;18:1406-1417.
16. Dorozhkin SV. Multiphasic calcium orthophosphate ( $\text{CaPO}_4$ ) bioceramics and their biomedical applications. *Ceram Int.* 2016;42:6529-6554.
17. Forrestal DP, Klein TJ, Woodruff MA. Challenges in engineering large customized bone constructs. *Biotechnol Bioeng.* 2017;114:1129-1139.
18. Gmeiner R, Deisinger U, Schonherr J, et al. Additive manufacturing of bioactive glasses and silicate bioceramics. *J Ceram Sci Technol.* 2015;6:75-86.
19. Mota C, Puppi D, Chiellini F, Chiellini E. Additive manufacturing techniques for the production of tissue engineering constructs. *J Tissue Eng Regen Med.* 2015;9:174-190.
20. Seol YJ, Kang TY, Cho DW. Solid freeform fabrication technology applied to tissue engineering with various biomaterials. *Soft Matter.* 2012;8:1730-1735.
21. Chartier T, Dupas C, Lasgorceix M, et al. Additive manufacturing to produce complex 3D ceramic parts. *J Ceram Sci Technol.* 2015;6:95-104.
22. Melchels FPW, Feijen J, Grijpma DW. A review on stereolithography and its applications in biomedical engineering. *Biomaterials.* 2010;31:6121-6130.
23. Bergmann C, Lindner M, Zhang W, et al. 3D printing of bone substitute implants using calcium phosphate and bioactive glasses. *J Eur Ceram Soc.* 2010;30:2563-2567.
24. Cox SC, Thornby JA, Gibbons GJ, Williams MA, Mallick KK. 3D printing of porous hydroxyapatite scaffolds intended for use in bone tissue engineering applications. *Mater Sci Eng C Mater Biol Appl.* 2015;47:237-247.

25. Cesarano J, Dellinger JG, Saavedra MP, et al. Customization of load-bearing hydroxyapatite lattice scaffolds. *Int J Appl Ceram Technol.* 2005;2:212-220.
26. Miranda P, Saiz E, Gryn K, Tomsia AP. Sintering and robocasting of beta-tricalcium phosphate scaffolds for orthopaedic applications. *Acta Biomater.* 2006;2:457-466.
27. Kim J, McBride S, Tellis B, et al. Rapid-prototyped PLGA/beta-TCP/hydroxyapatite nanocomposite scaffolds in a rabbit femoral defect model. *Biofabrication.* 2012;4:025003.
28. Zein I, Hutmacher DW, Tan KC, Teoh SH. Fused deposition modeling of novel scaffold architectures for tissue engineering applications. *Biomaterials.* 2002;23:1169-1185.
29. Chung H, Jee H, Das S. Selective laser sintering of PCL/TCP composites for tissue engineering scaffolds. *J Mech Sci Technol.* 2010;24:241-244.
30. Shuai C, Li P, Liu J, Peng S. Optimization of TCP/HAP ratio for better properties of calcium phosphate scaffold via selective laser sintering. *Mater Charact.* 2013;77:23-31.
31. Trunec M, Chlup Z. Subtractive manufacturing of customized hydroxyapatite scaffolds for bone regeneration. *Ceram Int.* 2017;43:11265-11273.
32. Bera O, Trunec M. Optimization of fine alumina gelcasting using in situ dynamic rheology. *J Am Ceram Soc.* 2012;95:2849-2856.
33. Mori AL, Porzio MA, Schalege LL. Kinetics and mechanism of epoxy ether hydrolysis. I. Mechanism of hydrolysis of an acyclic hemiacetal intermediate. *J Am Chem Soc.* 1972;94:5034-5039.
34. Trunec M, Cihlar J. Thermal removal of multicomponent binder from ceramic injection mouldings. *J Eur Ceram Soc.* 2002;22:2231-2241.

**How to cite this article:** Stastny P, Chlup Z, Kalasova D, Zikmund T, Kaiser J, Trunec M. Epoxy-based gelcasting of machinable hydroxyapatite foams for medical applications. *J Am Ceram Soc.* 2018;101:3317–3327. <https://doi.org/10.1111/jace.15523>

PAPER [XXIV]

## Article

# Lyophilized Polyvinylpyrrolidone Hydrogel for Culture of Human Oral Mucosa Stem Cells

Carolina Oliver-Urrutia <sup>1,2,\*</sup> , Raúl Rosales Ibañez <sup>3</sup>, Miriam V. Flores-Merino <sup>1</sup> , Lucy Vojtova <sup>2</sup>,  
Jakub Salplachta <sup>2,\*</sup> , Ladislav Čelko <sup>2</sup>, Jozef Kaiser <sup>2</sup>  and Edgar B. Montufar <sup>2</sup> 

<sup>1</sup> Faculty of Chemistry, Autonomous University of the State of Mexico, Paseo Colon S/N, Toluca 50120, Mexico; mv.flores.merino@gmail.com

<sup>2</sup> Central European Institute of Technology, Brno University of Technology, Purkynova 123, 61200 Brno, Czech Republic; lucy.vojtova@ceitec.vutbr.cz (L.V.); ladislav.celko@ceitec.vutbr.cz (L.Č.); jozef.kaiser@ceitec.vutbr.cz (J.K.); eb.montufar@ceitec.vutbr.cz (E.B.M.)

<sup>3</sup> Faculty of Higher Studies Iztacala, National Autonomous University of Mexico, Los Reyes Iztacala 1, Mexico City 54090, Mexico; dr.raul.rosales@gmail.com

\* Correspondence: oliver@vutbr.cz (C.O.-U.); jakub.salplachta@ceitec.vutbr.cz (J.S.); Tel.: +420-54114-9284 (J.S.)

**Abstract:** This work shows the synthesis of a polyvinylpyrrolidone (PVP) hydrogel by heat-activated polymerization and explores the production of hydrogels with an open porous network by lyophilisation to allow the three-dimensional culture of human oral mucosa stem cells (hOMSCs). The swollen hydrogel showed a storage modulus similar to oral mucosa and elastic solid rheological behaviour without sol transition. A comprehensive characterization of porosity by scanning electron microscopy, mercury intrusion porosimetry and nano-computed tomography (with spatial resolution below 1 µm) showed that lyophilisation resulted in the heterogeneous incorporation of closed oval-like pores in the hydrogel with broad size distribution (5 to 180 µm,  $d_{50} = 65$  µm). human oral mucosa biopsies were used to isolate hOMSCs, expressing typical markers of mesenchymal stem cells in more than 95% of the cell population. Direct contact cytotoxicity assay demonstrated that PVP hydrogel have no negative effect on cell metabolic activity, allowing the culture of hOMSCs with normal fusiform morphology. Pore connectivity should be improved in future to allow cell growth in the bulk of the PVP hydrogel.

**Keywords:** polyvinylpyrrolidone; hydrogel; lyophilisation; nano-computed tomography; porosity; oral mucosa; stem cell



**Citation:** Oliver-Urrutia, C.; Rosales Ibañez, R.; Flores-Merino, M.V.; Vojtova, L.; Salplachta, J.; Čelko, L.; Kaiser, J.; Montufar, E.B. Lyophilized Polyvinylpyrrolidone Hydrogel for Culture of Human Oral Mucosa Stem Cells. *Materials* **2021**, *14*, 227. <https://doi.org/10.3390/ma14010227>

Received: 24 November 2020

Accepted: 23 December 2020

Published: 5 January 2021

**Publisher's Note:** MDPI stays neutral with regard to jurisdictional claims in published maps and institutional affiliations.



**Copyright:** © 2021 by the authors. Licensee MDPI, Basel, Switzerland. This article is an open access article distributed under the terms and conditions of the Creative Commons Attribution (CC BY) license (<https://creativecommons.org/licenses/by/4.0/>).

## 1. Introduction

Polyvinylpyrrolidone (PVP) is a synthetic and hydrosoluble polymer produced by free radical polymerization [1,2]. The hydrophilic and hydrophobic functional groups allow PVP solubility in water and in several organic solvents, such as methanol, ethanol, chloroform, or propanol [1–3]. PVP is chemically inert and suitable as a stable biomaterial in numerous medical applications [2,4]. For instance, in the pharmaceutical industry, it is used as a carrier of some hydrophilic and hydrophobic drugs [1,3]. Moreover, PVP can encapsulate DNA to protect it from intracellular degradation [5]. One advantage of PVP is that it can be processed to obtain hydrogels [4,6,7]. hydrogels are three-dimensional (3D) polymeric networks that can mimic both the biological and the mechanical properties of extracellular matrix [7–9]. Therefore, hydrogels can act as a cell-supporting material for cell encapsulation and delivery [7,8]. Furthermore, the porous network in the hydrogels is controlled in a variety of pore sizes and shapes that allow the exchange of nutrients and signalling molecules [9,10]. An optimal combination of porosity, pore size, pore connectivity and pore spatial distribution is a critical requirement for proper cell seeding and further homogeneous cell growth in the bulk of the hydrogel [11]. It has been demonstrated that the space between hydrogel polymeric molecules is not suitable for cell migration, leading

to heterogeneous distributions of cells [12]. hence, bigger pores are required for homogeneous cell ingrowth [11,13]. There are several methods for the production of structures with an open porous network in the scale of few hundreds of micrometres, including phase separation [14], porogen leaching [15], gas foaming [16], freeze-thawing [17,18], lyophilisation [19], and cryogelation [20]. Among them, lyophilisation is a process where ice crystals are formed and then removed through sublimation under vacuum [12,21]. Since hydrogels contain more than 50% of water, the frozen water acts as a green and safety porogen for the formation of porous structures (i.e., scaffolds) [12,19,21].

One possible use of PVP scaffolds is in the regeneration of tooth supporting structures (i.e., cementum, periodontal ligament and bone). The scaffold can be used for the transport and delivery of stem cells that promote healing and repair of oral tissues damaged by inflammatory diseases, such as periodontitis, which worldwide is the leading cause of tooth loss. Although blends of PVP with other polymers revealed no toxic effects on fibroblast and endothelial cells [22,23], the encapsulation of stem cells in PVP hydrogels requires further investigation. A variety of post-natal tissues have reservoirs of stem cells that contribute to the maintenance, development, homeostasis, and tissue regeneration [24–26]. In past, the stem cell harvesting required invasive procedures that limited their clinical utility. This limitation was reduced when stem cells started to be isolated from orofacial tissues, which are much more accessible [24]. The first stem cells isolated from the oral cavity were the dental pulp stem cells (DPSCs) [25]. Nowadays, more oral sites with stem cell reservoirs have been discovered, leading to the isolation of periodontal ligament stem cells (PDLSCs), gingiva-derived mesenchymal stem cells (GMSCs), dental follicle progenitor cells (DFPCs), and stem cells from apical papilla (SCAP) [26–28]. All these cells have the potential to differentiate in osteogenic and chondrogenic lineages, representing a suitable source of stem cells for therapeutic applications [24,29]. Moreover, the mesenchymal stem cells (MSCs) of dental origin showed immunosuppressive properties and an anti-inflammatory function [30,31] that may aid in tissue repair related to oral inflammatory infections.

The aim of this work was to explore heat-activated polymerization process to synthesize a crosslinked PVP hydrogel with storage modulus similar to oral mucosa stroma. In addition, pores with size in the scale of tens of micrometres were incorporated by lyophilisation to allow the 3D culture of human oral mucosa stem cells (hOMSCs). As prove in this study, hOMSCs were easily isolated from the retromolar region and expressed MSCs markers in more than 95% of the cell population. The cytocompatibility of the PVP hydrogel was shown for the first time in direct contact with hOMSCs. As the cell response depends on the mechanical microenvironment and porosity, the stiffness of the hydrogel was determined by rheological test and the porosity generated by lyophilisation was studied by X-ray nano-computed tomography (nano-CT), acquiring information about pore size distribution and connectivity with a spatial resolution below 1  $\mu\text{m}$ . The results are encouraging to continue exploring PVP as a promising alternative to natural (alginate, collagen, agarose, chitosan) and synthetic (poly(ethylene glycol)) hydrogels for the encapsulation and delivery of stem cells.

## 2. Materials and Methods

### 2.1. Synthesis of Poly (N-vinylpyrrolidone) Hydrogel

Polymeric hydrogel networks were obtained by a sequential method previously described [32,33]. First, 1-vinyl-2-pyrrolidone (NVP; Sigma-Aldrich, St. Louis, MS, USA) was solubilized in distilled water (70 wt.%). Then, di-ethylene glycol bis-allyl carbonate (DEGBAC; Sigma-Aldrich, St. Louis, MS, USA) and azobisisobutyronitrile (AIBN; Sigma-Aldrich, St. Louis, MS, USA) were added (0.4 wt.% in 1:1 ratio). Polymerization of the solution was performed at  $50 \pm 2$  °C for 24 h in glass beakers, sealed with aluminium foil inside an oven (Blue-M, TPS, Riverside, MI, USA). Subsequently, the hydrogel was placed in an ethanol/water (70%/30% *v/v*) solution for 48 h in order to remove any unreacted reagents. Finally, PVP hydrogel network was embedded in a 0.1 M phosphate buffer

solution (PBS; pH = 7.4, Sigma Aldrich, St. Louis, MS, USA) until swollen equilibrium was reached. Finally, samples were stored at 4 °C until characterization.

### 2.2. Infrared Spectroscopic Analysis

For Fourier-transform infrared spectroscopy (FTIR) analysis (Hyperion 3000/Vertex, Bruker, Billerica, MA, USA) the PVP hydrogel was dried in vacuum and grinded in a mortar and pestle. Transmittance was measured in the wavenumber range between 4000 and 800  $\text{cm}^{-1}$  with 32 scans per sample.

### 2.3. Raman Spectroscopy Analysis

Similar to FTIR analysis, ground and dry hydrogel powder was analysed by Raman spectroscopy (Confocal Raman Imaging system WITec alpha 300R, WITec, Ulm, BW, Germany). Raman scattering was excited using 352 and 440 nm wavelengths lasers. The laser power of 5 mW together with a 40 $\times$  objective lens were used.

### 2.4. Rheological Measurement

The mechanical properties (storage ( $G'$ ) and loss ( $G''$ ) modulus) of the swollen hydrogel were measured by oscillatory frequency sweep rheological test (ARES-G2 rheometer, New Castle, DE, USA). Water saturated hydrogel films with 5 mm of thickness were cut into disks (diameter of 22 mm) to match the diameter of the parallel-plates of the rheometer (gap width of 5 mm). Three independent samples were analysed in a frequency range from 0.1 to 100 rad/s at a constant temperature of 25 °C.

### 2.5. Fabrication and Characterization of Porous Samples

The porous samples for cell culture were fabricated by lyophilisation process (Martin Christ Epsilon 2-10D lyophilizer, Osterode am Harz, Germany) as previously described [19]. Swollen hydrogels were frozen in 24-well cell culture plates at  $-35$  °C under 100 Pa for 15 h, afterwards, lyophilized at 25 °C under 1 Pa for 24 h.

The porosity and pore size distribution of lyophilized hydrogels were analysed by mercury intrusion porosimetry (MIP, Poremaster Quantachrome, Boynton Beach, FL, USA) in the range between 0.009 and 150  $\mu\text{m}$ . Scanning electron microscopy (SEM, Lyra 3 Tescan, Brno, Czech Republic) was employed to examine the morphology of lyophilized hydrogels. Samples were fixed on metal stubs by employing double-sided electrical conductive adhesive tapes and were coated with a 20 nm layer of carbon. The external surface and the longitudinal cross-sections of the hydrogel were observed. The pore size was determined using Image J 1.52a software (National Institutes of Health, Bethesda, MD, USA). Values were determined from three independently prepared samples. Furthermore, the total porosity of the hydrogel was determined by the hydrodynamic method in water at a constant temperature. The PVP hydrogel was weighed in a dry, immersed and wet state (maximum swelling). The percentage of porosity was obtained by the following equation,

$$\% \text{ Porosity} = (W_w - W_d) / (W_w - W_i) \quad (1)$$

where,  $W_w$  and  $W_d$  represent the wet and dry weight of the material, respectively. Whereas,  $W_i$  is the weight of maximum swelled hydrogels immersed.

The 3D structure of lyophilized hydrogels was analysed by X-ray nano-CT (RIGAKU Nano3DX, Shibuya, Tokyo, Japan). Employed Nano3DX device was equipped with a  $3300 \times 2500$  pixel<sup>2</sup> X-ray CCD camera and a Cu rotatory target, working at an accelerating voltage of 40 kV and a current of 30 mA. An optical head with 20 $\times$  magnification was chosen to reach the field of view at  $700 \times 900$   $\mu\text{m}^2$ . The sample to detector distance was set to minimum, i.e., 0 mm. Binning 2  $\times$  2 was used. All determining the linear voxel size of the resulting data at 0.54  $\mu\text{m}$ . The size of sample was restricted to  $800 \times 400 \times 300$   $\mu\text{m}^3$  to achieve such resolution. A total of 800 projections were taken with an exposure time of 12 s. The contrast between the material and the background was further increased using custom-written phase-retrieval software based on Paganin phase-retrieval algorithm [34].

Subsequently, tomographic data was reconstructed using ASTRA Tomography Toolbox (CWI, Amsterdam, The Netherlands) [35]. Visualization of the samples and quantifications of structural parameters were performed using VG Studio MAX 3.3 software (Volume Graphics GmbH, heidelberg, Germany). A cuboid region of interest that fitted a representative volume of the scaffold was manually created. The surface determination tool was used to estimate the sample porosity and the foam structure analysis module was used to determine volumetric pore size distribution.

#### 2.6. Isolation of Primary human Oral Mucosa Cells

Primary human oral mucosa specimens were obtained in accordance with the Ethical Committee of the Medical Sciences Research Center, Autonomous University of the State of Mexico (authorization CEI CICMED 2019/01). All human donors were informed about the procedure and provided consent for biopsy and cell harvest. Samples were obtained from healthy human oral mucosa (retromolar region and maxillary tuberosity) through oral surgeries for clinical reasons. The oral mucosa samples were placed in 3 mL of transport medium consisting of 100 µm/mL streptomycin, 100 IU/mL penicillin, and 10 µm/mL amphotericin B in PBS (all from Sigma-Aldrich, St. Louis, MS, USA). Oral mucosa cells were obtained by the explant technique. Briefly, the epithelium was removed with a scalpel and the remaining connective tissue was aseptically cut into pieces of 1 mm<sup>3</sup>. The fragments were plated in 25 cm<sup>2</sup> culture dishes and cultivated for 5 min at 37 °C, with 5% CO<sub>2</sub> and 85% humidity. After the time, Dulbecco's Modified Eagle Medium (DMEM, Biowest, Nuaille, Pays de la Loire, France) supplemented with 10% fetal bovine serum (FBS, Sigma Aldrich, St. Louis, MS, USA), penicillin and streptomycin (100 mg/mL, both from Sigma-Aldrich, St. Louis, MS, USA) was added and the fragments cultured at 37 °C, 5% CO<sub>2</sub> and 85% humidity. After 14 days of culture the isolated cells were expanded in a new culture plate. Briefly, upon reaching 80% confluence, the cells were digested with 0.05% trypsin containing 1 mM EDTA (Sigma-Aldrich, St. Louis, MS, USA), and passaged. Cells on the third passage were used for the biological assays presented in this study. The culture medium was replaced every three days.

#### 2.7. Flow Cytometry Analysis of Isolated human Oral Mucosa Cells

Mesenchymal stem cells derived from human oral mucosa were analysed for cell surface markers expression (Cluster differentiation; CD) using a flow cytometer (CytoFLEX LX, Beckman Coulter, Indianapolis, IN, USA). Briefly, after three passages the cells were trypsinized, collected, and washed twice with PBS. The cell density was adjusted to 1 × 10<sup>5</sup> cells/mL of PBS and 100 µL of the suspension was transferred into a fresh Eppendorf tube. The cells were incubated in dark with CD90 (Thy-1/Thy-1.1; FITC conjugated), CD73 (ecto-5'-nucleotidase; PECY7 conjugated) and CD105 (Endoglin; VB421 conjugated) for 30 min at 4 °C. All the antibodies were purchased from Abcam plc, Cambridge, UK. The cells were washed twice with PBS. Labelled cells were measured by flow cytometer using CytExpert software (Beckman Coulter, Indianapolis, IN, USA).

#### 2.8. Immunocytochemical Analysis

Oral mucosa cells were seeded at a density of 8 × 10<sup>4</sup> cells/well in a 96-well cell culture plate. After 24 h of culture, the cells were fixed in 10% formalin (Sigma-Aldrich, St. Louis, MS, USA) for 20 min and permeabilized in 0.025% Triton X-100 (Sigma-Aldrich, St. Louis, MS, USA) for 20 min. Subsequently, inhibition in 1% bovine serum albumin (BSA, Sigma-Aldrich, St. Louis, MS, USA) for 30 min was done. Cells were labelled independently with anti-human monoclonal primary antibodies CD29, CD90, and Stro-1 (1:100, Santa Cruz Biotechnology, Dallas, TX, USA). As a secondary antibody, Alexa Fluor 488 (Anti-Rabbit IgG polyclonal, Invitrogen, Waltham, MA, USA) was used. The primary antibodies and the secondary antibodies were incubated for 2 h under dark at room temperature, performing three rinses with PBS between the two steps. Fluorescent images were captured with a fluorescence microscope (Zeiss hXP 120 C, Zeiss, Oberkochen, Germany) using a

proper set of filters and ZEN LITE 201 Software (Zeiss, Oberkochen, Germany) was used for image acquisition.

### 2.9. Cytotoxicity Assay

The hOMSCs ( $8 \times 10^4$  cells/well) were seeded in direct contact with fully-swollen PVP hydrogels (4 mm in diameter by 6 mm in height) in a 96-well cell culture plate. The cells and the PVP hydrogel were incubated together in 300  $\mu$ L of supplemented DMEM for 3, 7 and 10 days at 37 °C, under 5% CO<sub>2</sub> and 85% humidity. At such time points, the cells were washed twice with 100  $\mu$ L of PBS. Then, 300  $\mu$ L of phenol red-free medium (Biowest, Nuaille, Pays de la Loire, France) containing 10% AlamarBlue™ reagent (Thermo Fisher Scientific Inc., Waltham, MA, USA) were added to each well and further incubated overnight, protected from light. Afterward, 150  $\mu$ L of the reacted mixture per sample were transferred to a new 96-well plate and fluorescence (excitation at 560 nm, emission at 590 nm) was measured using a microplate reader (Elx808, Biotek, Winooski, VT, USA). Cells cultured without hydrogel under the same conditions were used as control.

### 2.10. Statistical Analysis

Statistical analysis was performed by two-way analyses of variance (ANOVA) using GraphPad Prism 4 software (GraphPad, San Diego, CA, USA). Differences were considered statistically significant when  $p < 0.05$ . The results are shown as mean  $\pm$  standard deviation (SD), where  $n$  represents the number of experimental samples.

## 3. Results

### 3.1. Chemical Composition of PVP Hydrogel

The FTIR spectrum of the PVP hydrogel is shown in Figure 1A. The vibration of the methylene group (CH<sub>2</sub>) is observed at 2953 and 2875 cm<sup>-1</sup>. A strong peak corresponding to carbonyl stretching (C=O) is found at 1660 cm<sup>-1</sup>. Medium bands are shown at 1496, 1461, and 1425 cm<sup>-1</sup> corresponding to CH<sub>2</sub> scissoring vibrations. C-N vibration is presented at 1288 cm<sup>-1</sup>. The peak at 1226 cm<sup>-1</sup> is due to the CH<sub>2</sub> vibration.

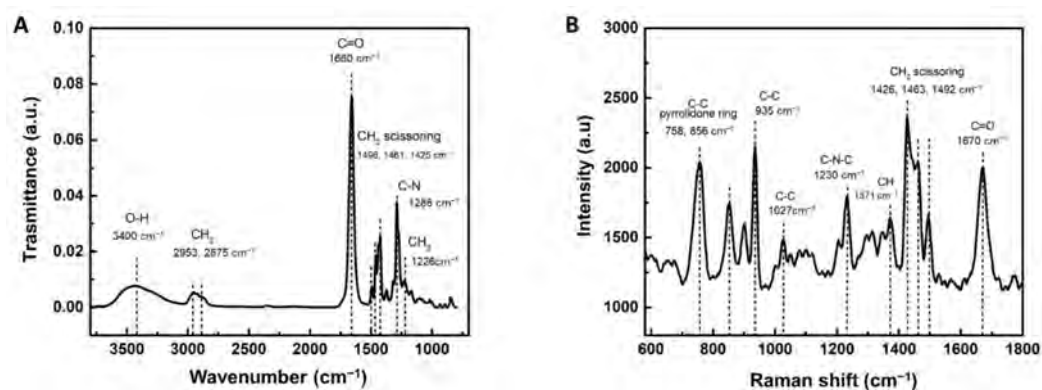


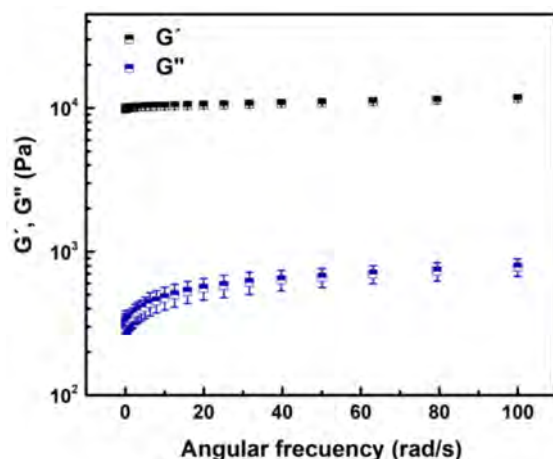
**Figure 1.** Chemical analysis of PVP hydrogel by (A) FTIR and (B) Raman spectroscopies.

Raman spectrum of PVP hydrogel is shown in Figure 1B. The intense band of carbonyl group vibration (C=O) is observed at 1670 cm<sup>-1</sup>. The peaks at 1492, 1463, 1426 cm<sup>-1</sup> are assigned to CH<sub>2</sub> scissoring vibration. While the peak at 1371 cm<sup>-1</sup> is assigned to CH group vibration. The C-N-C and C-C bands are presented at 1230 cm<sup>-1</sup> and 1027 cm<sup>-1</sup>, respectively. The peak at 935 cm<sup>-1</sup> is ascribed to C-C ring breathing. Also, 856 and 758 cm<sup>-1</sup> peaks corresponded to C-C vibrations of pyrrolidone ring.

### 3.2. Oscillatory Frequency Sweep

Figure 2 shows that the loss modulus ( $G''$ ) increases while the storage modulus ( $G'$ ) was constant with the frequency of oscillation, suggesting a moderated time-dependent rheological behaviour. Storage modulus ( $11.04 \pm 0.36$  kPa) was always 1 to 2 orders of

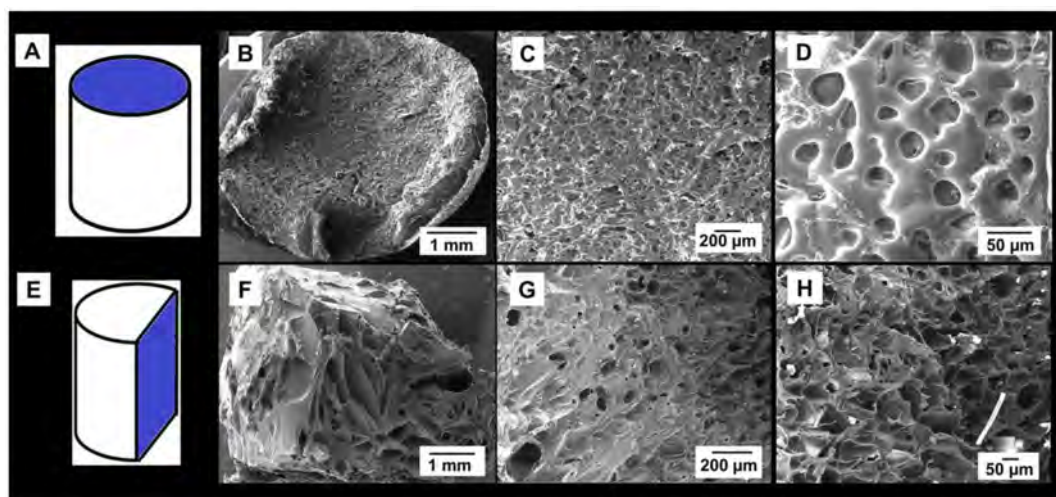
magnitude greater than loss modulus ( $0.73 \pm 0.04$  kPa). Therefore, according to rheological principles [36–38], PVP is in gel form (solid-like), it does not show sol transition and is mechanically strong.



**Figure 2.** The relationship of storage ( $G'$ ) and loss ( $G''$ ) modulus with angular frequency of oscillation for PVP hydrogel at 25 °C. Results are expressed as the mean and standard deviation of the three independent measurements.

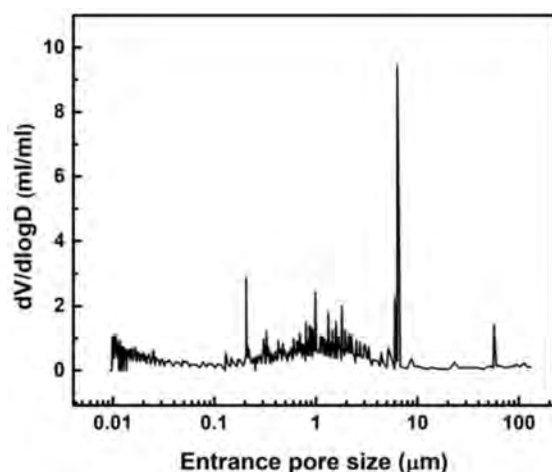
### 3.3. Porosity Analyses of Lyophilized hydrogel

Figure 3 shows the porous structure of the lyophilized hydrogel. The surface of the sample showed an equiaxed open cell pore morphology with an average pore size of around  $40 \mu\text{m}$  and low dispersion ( $\pm 7 \mu\text{m}$ ) (Figure 3A–D). In contrast, the interior of the sample presented pores with heterogeneous size and complex morphology (Figure 3E–H).



**Figure 3.** Representative secondary electron—SEM images of the microstructure of lyophilized PVP hydrogel: (A–D) top surface and (E–H) longitudinal cross-section.

The MIP analysis revealed a multimodal pore size distribution with well-defined peaks at 0.2, 6.3, and  $60 \mu\text{m}$ ; and a broad hump in the range from 0.1 to  $6 \mu\text{m}$  (Figure 4). The larger pores detected by MIP corresponded to the open pores observed by SEM at the sample surface. In fact, the pore size is in good correlation between the two techniques, differences attributed to the principle of pore size measurement of MIP. MIP also showed smaller pores inside the samples (below  $10 \mu\text{m}$ ) and confirms the heterogeneity of their size. The open porosity determined by MIP was 65%, while the total porosity, determined by the hydrodynamic method, was 86%. The difference attributed to the range of analysis of MIP (from 0.009 to  $150 \mu\text{m}$  in this study) and the presence of closed pores.



**Figure 4.** Entrance pore size distribution of lyophilized PVP hydrogel obtained by MIP.

The porosity determined by nano-CT was 43%. Figures 5 and 6 show the 3D virtual reconstruction of the lyophilized hydrogel (the material is presented in grey colour). The volumetric size distribution of the pores is visualized by a colour scale in the Figure 5B–F. Moreover, in order to have a better perspective of the pore morphology and distribution, the material was set transparent in the visualizations shown in Figure 5C,F. The presence of a large number of pores implies that they are not connected, at least by apertures bigger than 1.5  $\mu\text{m}$  (size of the smallest detectable feature). If the pores were open they would appear in one single colour self-connected and running continuously along the sample. Furthermore, the hydrogel presented heterogeneity in the spatial distribution of pores. The smooth surfaces of the material at the edges of the reconstruction appeared due to the cutting planes virtually applied to define the region of interest.

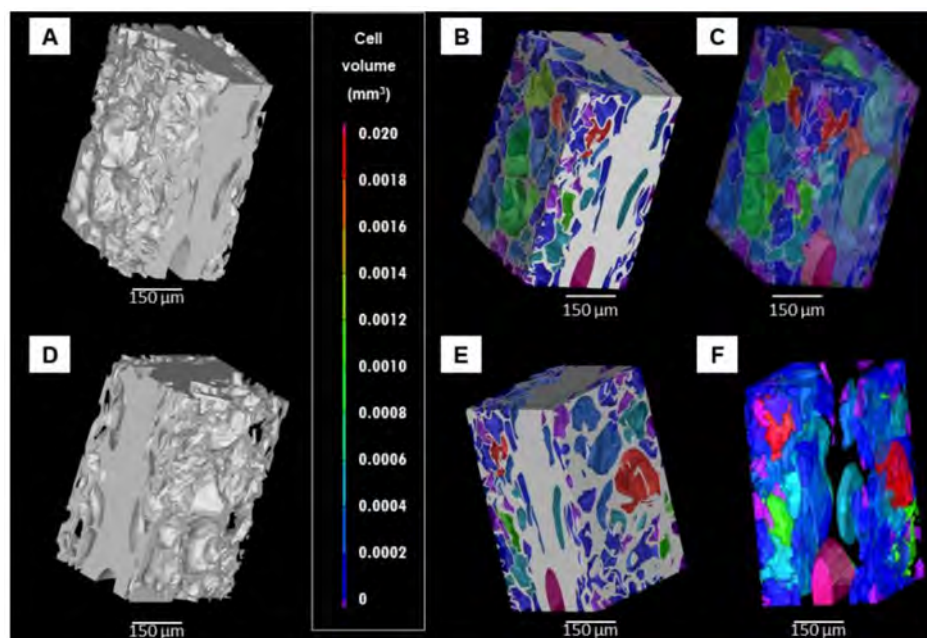


**Figure 5.** Three-dimensional (3D) virtual reconstructions of a lyophilized PVP hydrogel obtained by nano-CT. (A,D) Two different views of the material. (B,C,E,F) Pore volume distribution in colour-scale, images C and F are the same than images B and E, respectively, but the material was defined transparent for better observation of the pore morphology and distribution.

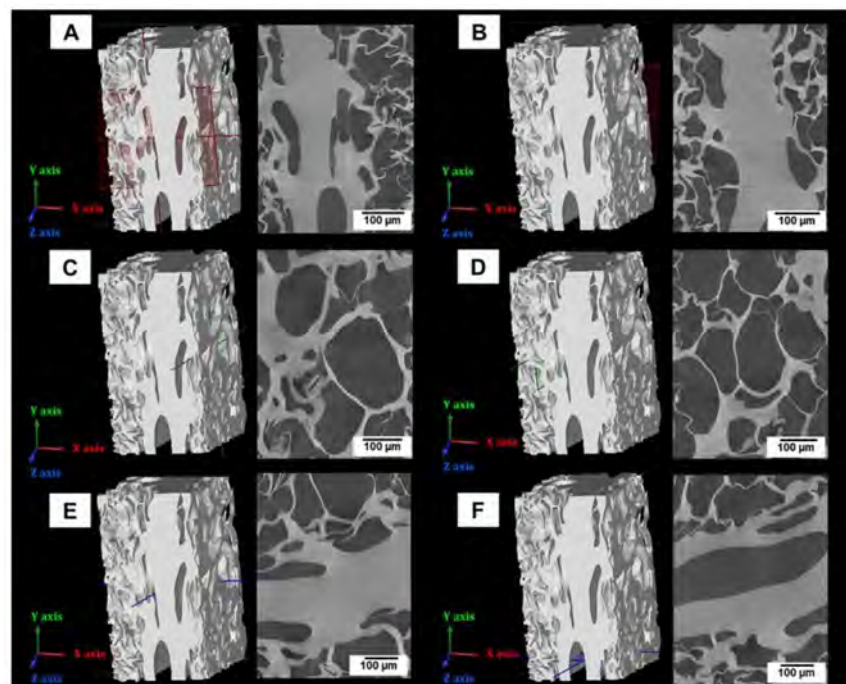


**Figure 6.** Representative images of orthogonal planes of the lyophilized PVP hydrogel obtained by nano-CT. The images (right side) were acquired in orthogonal planes of the virtual reconstruction (left side): (A,B) XY-plane in red colour, (C,D) YZ plain in green colour and (E,F) XZ-plane in blue colour.

Orthogonal cross-sections of the sample show that in general the pores had an oval-like morphology (Figure 6). The pores had a broad size distribution (Figure 7), the smallest pores had an equivalent spherical diameter of around 5 µm, while the largest pores presented an equivalent spherical diameter of around 180 µm. The median diameter of the pores ( $d_{50}$ ) was 65 µm, whereas the average diameter was  $67 \pm 29$  µm.

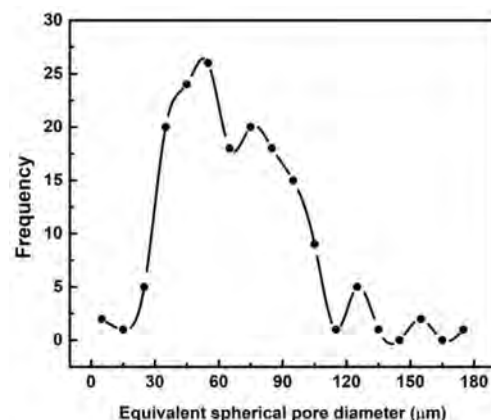


**Figure 7.** Histogram of the pore size distribution of the lyophilized PVP hydrogel determined by nano-CT analysis. Pore size is indicated as the equivalent spherical diameter of the pores observed in Figure 5.

### 3.4. Primary Human Oral Mucosa Stem Cells

Isolated human oral mucosa cells grew in clusters and exhibited fusiform fibroblast-like morphology after 14 days of culture (Figure 8A). The cells showed 96.04% positivity towards CD90 and CD105, 97.74% positivity towards CD90 and CD73, and 95.37% positivity towards CD73 and CD105 (Figure 8B). Moreover, the immunostaining showed the presence of CD29, CD90, and Stro-1 proteins on the cell membrane (Figure 8C). All

of them membrane markers of MSCs according to the International Society for Cellular Therapy [27,28,39].

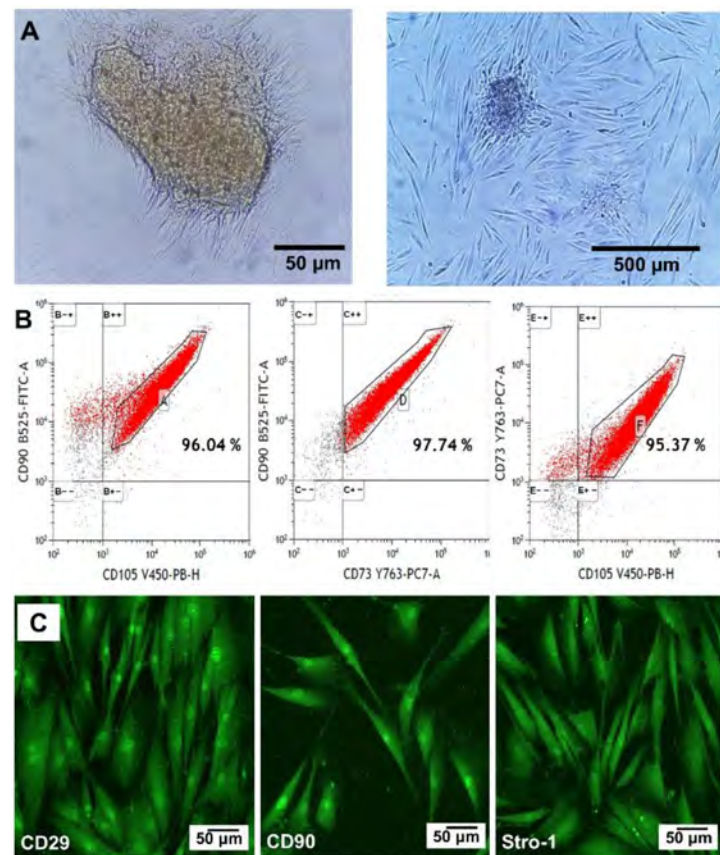


**Figure 8.** Characterization of human oral mucosa stem cells (hOMSCs). (A) Optical microscope images of the cells isolated from tissue explant after 14 days of culture. (B) Flow cytometry profiles and percentage of cells expressing CD90, CD105 and CD73, among the population of cells. (C) Fluorescence microscopy of selected mesenchymal stem cell markers (CD29, CD90 and Stro-1).

### 3.5. Hydrogel Cytotoxicity

A fusiform shape of the cells in direct contact with the hydrogel was observed on day 3 and 7 (Figure 9A,B). The cell metabolic activity in the control group (without hydrogel) did not have a statistically significant variation over the time (Figure 9C). The hydrogel generated a reduction ( $p < 0.05$ ) of the cell metabolic activity after 3 days, showing 68.4% of activity respect to the control group (Figure 9C). Therefore, according with the ISO standard 10993-5, the hydrogel is 2% below the threshold to be consider cytocompatible. After this lag phase, the cell metabolic activity recovered a value close to the control group (93.8%), with no statistically significant differences in comparison to the control group at day 7 and 10 (Figure 9C). Therefore, the hydrogel did not exhibit a sustained cytotoxic effect on the primary hOMSCs.

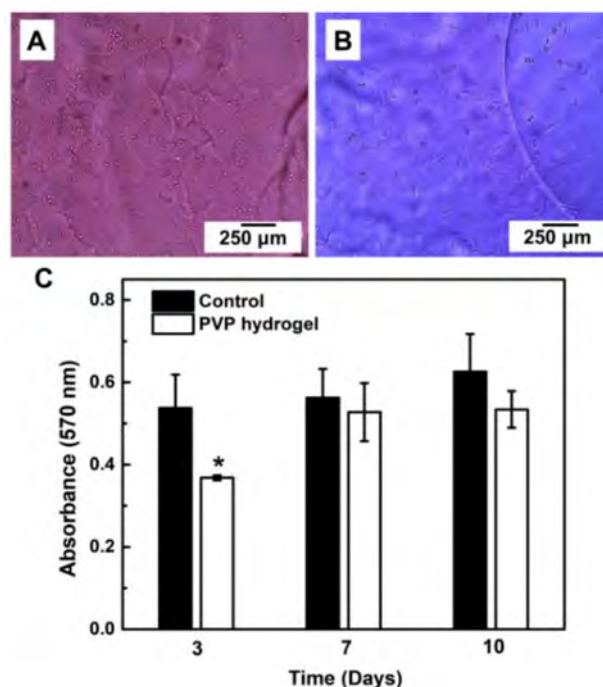


**Figure 9.** Hydrogel's cytotoxicity against human oral mucosa stem cells (hOMSCs). (A,B) Optical microscope images of the cells in direct contact with PVP hydrogel at day 3 and 7, respectively. (C) Cell metabolic activity, results expressed as mean  $\pm$  SD, (\*) represents significant difference ( $p < 0.05$ ) between groups and throughout days ( $n = 3$ ; two-way ANOVA, Bonferroni).

#### 4. Discussion

Heat-activated polymerization was used to fabricate a PVP hydrogel. This method is widely used in polymer network synthesis [3,6,12]. It is driven by the homolytic thermal dissociation of the initiator to create free radicals, allowing the formation of covalent bonds between the polymer chains. The chemical composition of PVP determined by FTIR and Raman spectroscopies was in agreement with previous reports where it was polymerized by different routes [3,4,18,40]. Furthermore, heat-activated polymerization produced a stable PVP hydrogel with clear elastic solid behaviour able to recover stored energy. In general, similar solid behaviour is reported for a wide range of PVP formulations and oscillation frequencies [4,37,38]. In particular, the PVP hydrogel developed in this work presented a storage modulus between keratinized gingiva (20 kPa) and tongue and soft palate (2.5 kPa) [41,42], the main tissues forming the oral mucosa, which is the target of this study to culture and retain undifferentiated the hOMSCs. Moreover, the processing conditions, such as cross-linker content, monomer concentration, amount of initiator, or increasing number of ionic groups, can be adjusted to approach even more the storage modulus to the specific site of the oral mucosa of interest. This is important since the mechanical properties are known to greatly influence cell fate. For example, Cameron et al. showed that increasing the loss moduli of polyacrylamide gels from 1 Pa to 130 Pa increases human MSCs spread area and proliferation [43]. Other works demonstrated different cell growth rates in response to stiffness. In general, stiffer hydrogels promote stem cell proliferation compared to softer gels [44].

In addition to the mechanical properties, porosity regulates cell attachment, cell interactions, cell migration, and differentiation [11,29,45]. Moreover, porosity affects the mechanical behaviour of the hydrogels. It was demonstrated that Young's modulus of hydrogels with low porosity (60%) and small pore size (40  $\mu\text{m}$ ) was more than three times higher than Young's modulus of hydrogels with 89% of porosity and higher pore size (125  $\mu\text{m}$ ) [46]. In this study, lyophilisation allowed the production of porous structures. During freezing, the water in the hydrogel form ice crystals that became pores after drying [12,21]. Under the optimal conditions, the drying of the sample by sublimation does not change the morphol-

ogy of the ice crystals [12,21]. Therefore, freezing is the most important step to control the size and shape of pores. In this study, the freeze-drying conditions were selected according to the optimal parameters set to obtain collagen scaffolds [19]. It was found that the pore size distribution for the PVP (5 to 180  $\mu\text{m}$ ) differed from the pore size observed before in collagen (70 to 110  $\mu\text{m}$ ), indicating that the freeze-drying conditions cannot be generalized. There is not information about the optimum pore size to restore all the tooth supporting structures. Moreover, the optimum pore size may vary between the different oral tissues, but the lyophilized PVP may allow the regeneration of skin that grows in pores between 20 and 125  $\mu\text{m}$  [47], being the tissue that most resembles the oral mucosa. It was also observed that scaffolds with a diverse pore size (50 to 100  $\mu\text{m}$ ) promoted stem cell growth with a significantly lower level of differentiation compared with scaffolds with a narrow pores size distribution, either with bigger (125  $\mu\text{m}$ ) or smaller (40  $\mu\text{m}$ ) pores [46]. Furthermore, unequally pore size distribution may provide an environment for MSC adhesion and invasion promoting viability and metabolism [45].

A comprehensive characterization of porosity was performed in this study. In addition to MIP and SEM, nano-CT was used to characterize the pore size distribution and morphology with submicron spatial resolution in 3D, providing additional information not obtained with SEM and MIP. Specifically, the achieved linear voxel size of the nano-CT data was 0.54  $\mu\text{m}$ , when normally the CT data have voxel size values around tens of  $\mu\text{m}$ . The improved resolution was a clear advantage of the nano-CT analysis, since the size of the smallest feature detectable in the virtual reconstruction is around 1.5  $\mu\text{m}$ . The most frequent pores detected by nano-CT had an equivalent sphere diameter of 65  $\mu\text{m}$  (Figure 7), a value in very good agreement with the highest entrance pore size detected by MIP (60  $\mu\text{m}$ , Figure 4). Moreover, these values are close to the pore size measured by SEM image analysis at the surface of the material (40  $\mu\text{m}$ ). Unlike MIP and SEM, nano-CT uncovered that lyophilisation produced a heterogeneous spatial distribution of pores, with some fractions of the sample free of pores. This may be due to the gradients of temperature during freezing and the physical interactions between the PVP molecules [19]. Furthermore, nano-CT detected only closed pores, meaning that the open pores detected by MIP at the sample surface corresponded to blind pores. The presence of closed pores explains the difference between the total porosity measured by the hydrodynamic method (86%) and the porosity detected by MIP (65%). Or in other words, the material has around 20% of closed pores. There is also a significant difference between the porosity determined by MIP (65%) and nano-CT (43%). This difference is attributed to submicrometric channels linking the micrometric pores, likely between the molecules of PVP. It should bear in mind that the quantity of submicrometric channels does not correspond to the difference between the porosity detected by MIP and nano-CT, due to the bottleneck effect related to the MIP principle of measurement [48]. Though the pores are connected by submicrometric channels, the size of such channels is not suitable to allow cell migration and colonization of the scaffold. Therefore, other lyophilisation conditions (speed, temperature, pressure) that result in open pores must be required.

This work demonstrates a simple method for the isolation of hOMSCs, expressing the membrane markers that characterize the MSCs. Furthermore, the results uncover that heat-activated polymerization produced a cytocompatible PVP hydrogel, which only produced a transient reduction of cell metabolic activity on day 3, recovering normal activity after 7 and 10 days of culture. The short-term reduction of the cell metabolic activity may be explained by the mechanical adaptation of the stem cells to the hydrogel [49]. In fact, the stiffness of polystyrene is eight orders of magnitude higher than the one of the PVP hydrogel. The cytocompatibility of PVP was in agreement with previous results, where PVP networks did not show toxic effects on mouse subconjunctival tissue cells, human dermal fibroblasts, and monocytes [22,23,32,38]. Similarly, poly ( $\epsilon$ -caprolactone) and PVP networks did not show cytotoxicity, allowing the proliferation of MSCs [50]. The long term purpose of culturing hOMSCs in the PVP hydrogel is to use it as cell delivery system to restore periodontally damaged tooth supporting structures. Oral mucosa grafts have been suc-

cessfully used in urethral and spinal cord reconstruction, as well as repair of calvarial and mandibular defects [51–54]. Oral mucosa is a less invasive source for MSCs harvesting than bone marrow or even tooth pulp. In general, oral stem cells have higher proliferation rate than bone marrow MSCs, allowing faster expansion [27]. These cells can differentiate into osteoblasts, adipocytes, chondrocytes and astrocytes [28,54], and have immunomodulatory and anti-inflammatory properties [27,30,54]. Further experiments will be performed to improve pore connectivity in PVP, allowing the evaluation of cell proliferation, migration, phenotype, and differentiation in 3D.

## 5. Conclusions

Heat-activated polymerization produced a PVP hydrogel with clear elastic solid behaviour in a wide range of oscillation frequencies and storage modulus similar to oral mucosa stroma. The rheological behaviour of the hydrogel was independent of time, did not show sol transition, and PVP chemical composition was in agreement with previous reports. The porosity analysis showed that lyophilisation resulted in the heterogeneous incorporation of 43% of closed pores in the hydrogel with a median equivalent spherical diameter of 65  $\mu\text{m}$ . Therefore, the freeze-drying conditions should be optimized to promote pore connectivity through big apertures that allow cell colonization. Cytotoxicity assay demonstrated the ability of PVP hydrogel to support hOMSCs culture for up to 10 days, suggesting that the lyophilized hydrogel may provide a favourable environment for cells to adhere and proliferate. The optimal parameters for the 3D culture of the hOMSCs have to be elucidated in future.

**Author Contributions:** Conceptualization, C.O.-U., R.R.I., M.V.F.-M. and E.B.M.; investigation, C.O.-U., R.R.I., L.V. and J.S.; validation, C.O.-U. and J.S.; formal analysis, C.O.-U., J.S., L.Č., J.K. and E.B.M.; resources, R.R.I., M.V.F.-M., L.Č. and J.K.; funding acquisition, R.R.I., M.V.F.-M., J.K. and E.B.M. All authors have read and agreed to the published version of the manuscript.

**Funding:** The authors acknowledge the financial support from UAEMex (project: 4993/2020/CIB) and CONACYT. Part of the research was carried out under the project CEITEC 2020 (LQ1601) with financial support from the Ministry of Education, Youth and Sports of the Czech Republic under the National Sustainability Programme II and CzechNanoLab Research Infrastructure supported by MEYS CR (LM2018110). C.O.U. and E.B.M. acknowledge the CONACYT grants 2020-000021-01EXTV-00235 and 2019-000029-01EXTV-00070, respectively.

**Institutional Review Board Statement:** The study was conducted according to the guidelines of the Declaration of Helsinki, and approved by the Medical Sciences Research Center of Autonomous University of the State of Mexico (authorization CEI CICMED 2019/01).

**Informed Consent Statement:** Informed consent was obtained from all subjects involved in the study.

**Data Availability Statement:** The data that support the findings of this study are contained within the article.

**Acknowledgments:** Special thanks to K. Valová from CEITEC-BUT for her assistance in rheological measurements and A. González from UNAM for her participation in biological analysis.

**Conflicts of Interest:** The authors declared no conflict of interest with the present research, authorship or publication of this article.

## References

1. Teodorescu, M.; Bercea, M. Poly(vinylpyrrolidone) A Versatile Polymer for Biomedical and Beyond Medical Applications. *Polym. Plast. Technol. Eng.* **2015**, *54*, 923–943. [[CrossRef](#)]
2. Lim, J.I.; Im, H.; Lee, W.K. Fabrication of porous chitosan-polyvinyl pyrrolidone scaffolds from a quaternary system via phase separation. *J. Biomater. Sci. Polym. Ed.* **2015**, *26*, 32–41. [[CrossRef](#)]
3. Anwar, M.; Pervaiz, F.; Shoukat, H.; Noreen, S.; Shabbir, K.; Majeed, A.; Ijaz, S. Formulation and evaluation of interpenetrating network of xanthan gum and polyvinylpyrrolidone as a hydrophilic matrix for controlled drug delivery system. *Polym. Bull.* **2020**. [[CrossRef](#)]

4. Huang, M.; Hou, Y.; Li, Y.; Wang, D.; Zhang, L. High performances of dual network PVA hydrogel modified by PVP using borax as the structure forming accelerator. *Des. Monomers Polym.* **2017**, *20*, 505–513. [[CrossRef](#)]
5. Ng, S.L.; Such, G.K.; Johnston, A.P.R.; Antequera-García, G.; Caruso, F. Controlled release of DNA from poly (vinylpyrrolidone) capsules using cleavable linkers. *Biomaterials* **2011**, *32*, 6277–6284. [[CrossRef](#)]
6. Hu, W.; Wang, Z.; Xiao, Y.; Zhang, S.; Wang, J. Advances in crosslinking strategies of biomedical hydrogels. *Biomater. Sci.* **2019**, *7*, 843–855. [[CrossRef](#)]
7. Archana, D.; Singh, B.K.; Dutta, J.; Dutta, P.K. Chitosan-PVP-nano silver oxide wound dressing: In vitro and in vivo evaluation. *Int. J. Biol. Macromol.* **2015**, *73*, 49–57. [[CrossRef](#)]
8. Akhmanova, M.; Osidak, E.; Domogatsky, S.; Rodin, S.; Domogatskaya, A. Physical, Spatial, and Molecular Aspects of Extracellular Matrix of In Vivo Niches and Artificial Scaffolds Relevant to Stem Cells Research. *Stem Cells Int.* **2015**, *2015*, 67025. [[CrossRef](#)]
9. Ghosh, M.; Halperin-Sternfeld, M.; Adler-Abramovich, L. Bio mimicking of extracellular matrix. *Adv. Exp. Med. Biol.* **2019**, *1174*, 371–399.
10. Catoira, M.C.; Fusaro, L.; Di Francesco, D.; Ramella, M.; Boccafroschi, F. Overview of natural hydrogels for regenerative medicine. *J. Mater. Sci. Mater. Med.* **2019**, *30*, 115–125. [[CrossRef](#)]
11. Perez, R.A.; Mestres, G. Role of pore size and morphology in musculo-skeletal tissue regeneration. *Mater. Sci. Eng. C* **2016**, *61*, 922–939. [[CrossRef](#)]
12. Autissier, A.; Le Visage, C.; Pouzet, C.; Chaubet, F.; Letourneur, D. Fabrication of porous polysaccharide-based scaffolds using a combined freeze-drying/cross-linking process. *Acta Biomater.* **2010**, *6*, 3640–3648. [[CrossRef](#)]
13. Caballé-Serrano, J.; Zhang, S.; Ferrantino, L.; Simion, R.; Chappuis, V.; Bosshardt, D.D. Tissue Response to a Porous Collagen Matrix Used for Soft Tissue Augmentation. *Materials* **2019**, *12*, 3721. [[CrossRef](#)]
14. Li, X.; Rombouts, W.; Van der Gucht, J.; De Vries, R.; Dijkssam, J.A. Mechanics of composite hydrogels approaching phase separation. *PLoS ONE* **2019**, *14*, e0211059. [[CrossRef](#)]
15. Wu, Y.; Chen, Y.X.; Yan, J.; Yang, S.; Dong, P.; Soman, P. Fabrication of conductive polyaniline hydrogel using porogen leaching and projection micro-stereolithography. *J. Mater. Chem. B* **2015**, *3*, 5352–5360. [[CrossRef](#)]
16. Tang, Y.; Lin, S.; Yin, S.; Jiang, F.; Zhou, M.; Yang, G.; Sun, N.; Zhang, W.; Jiang, X. In situ gas foaming based on magnesium particle degradation: A novel approach to fabricate injectable macroporous hydrogels. *Biomaterials* **2020**, *232*, 119727. [[CrossRef](#)]
17. Hassan, C.M.; Peppas, N.A. Structure and morphology of freeze/thawed PVA hydrogels. *Macromolecules* **2000**, *33*, 2472–2479. [[CrossRef](#)]
18. Morariu, S.; Bercea, M.; Teodorescu, M.; Avadanei, M. Tailoring the properties of poly(vinyl alcohol)/poly(vinylpyrrolidone) hydrogels for biomedical applications. *Eur. Polym. J.* **2016**, *84*, 313–325. [[CrossRef](#)]
19. Babrnáková, J.; Pavliňáková, V.; Brtníková, J.; Sedláček, P.; Prosecká, E.; Rampichová, M.; Filová, E.; Hearn, V.; Vojtová, L. Synergistic effect of bovine platelet lysate and various polysaccharides on the biological properties of collagen-based scaffolds for tissue engineering: Scaffold preparation, chemo-physical characterization, in vitro and ex ovo evaluation. *Mater. Sci. Eng. C* **2019**, *100*, 236246. [[CrossRef](#)]
20. Savina, I.; Ingavle, G.; Cundy, A.; Mikhalovsky, S.V. A simple method for the production of large volume 3D macroporous hydrogels for advanced biotechnological, medical and environmental applications. *Sci. Rep.* **2016**, *6*, 21154. [[CrossRef](#)]
21. Grenier, J.; Duval, H.; Barou, F.; Lv, P.; David, B.; Letourneur, D. Mechanisms of pore formation in hydrogel scaffolds textured by freeze-drying. *Acta Biomater.* **2019**, *94*, 195–203. [[CrossRef](#)]
22. Teixeira, M.A.; Amorim, M.; Felgueiras, H.P. Poly(Vinyl Alcohol)-Based Nanofibrous Electrospun Scaffolds for Tissue Engineering Applications. *Polymers* **2019**, *12*, 7. [[CrossRef](#)]
23. Risbud, M.V.; Bionde, M.R.; Bionde, R.R. Effect of chitosan-polyvinyl pyrrolidone hydrogel on proliferation and cytokine expression of endothelial cells: Implications in islet immunoisolation. *J. Biomed. Mater. Res.* **2001**, *57*, 300–305. [[CrossRef](#)]
24. Wang, F.; Yu, M.; Yan, X.; Wen, Y.; Zeng, Q.; Yue, W.; Yang, P.; Pei, X. Gingiva-derived mesenchymal stem cell-mediated therapeutic approach for bone tissue regeneration. *Stem Cells Dev.* **2011**, *20*, 2093–2102. [[CrossRef](#)]
25. Han, J.; Menicanin, D.; Marino, V.; Ge, S.; Mroczek, K.; Gronthos, S.; Bartold, P.M. Assessment of the regenerative potential of allogeneic periodontal ligament stem cells in a rodent periodontal defect model. *J. Periodontol.* **2014**, *49*, 333–345. [[CrossRef](#)]
26. Diomedea, F.; Gugliandolo, A.; Cardelli, P. Three-dimensional printed PLA scaffold and human gingival stem cell-derived extracellular vesicles: A new tool for bone defect repair. *Stem Cell Res. Ther.* **2018**, *9*, 104. [[CrossRef](#)]
27. Zhang, Q.Z.; Nguyen, A.L.; Yu, W.H.; Le, A.D. Human oral mucosa and gingiva: A unique reservoir for mesenchymal stem cells. *J. Dent. Res.* **2012**, *91*, 1011–1018. [[CrossRef](#)]
28. Marynka-Kalmani, K.; Treves, S.; Yafee, M.; Rachima, H.; Gafni, Y.; Cohen, M.A.; Pitaru, S. The Lamina Propria of Adult human Oral Mucosa harbors a Novel Stem Cell Population. *Stem Cells* **2010**, *28*, 984–995. [[CrossRef](#)]
29. Schmelzer, E.; McKeel, D.; Jörg, G. Characterization of human Mesenchymal Stem Cells from Different Tissues and Their Membrane Encasement for Prospective Transplantation Therapies. *BioMed Res. Int.* **2019**, *5*, 1–13. [[CrossRef](#)]
30. Hernández-Monjaraz, B.; Santiago-Osorio, E.; Monroy-García, A.; Ledesma-Martínez, E.; Mendoza-Núñez, V.M. Mesenchymal Stem Cells of Dental Origin for Inducing Tissue Regeneration in Periodontitis: A Mini-Review. *Int. J. Mol. Sci.* **2018**, *19*, 944. [[CrossRef](#)]

31. Schop, D.; Janssen, F.W.; van Rijn, L.; Fernandes, H.; Bloem, R.M.; De Bruijn, J.D.; Van Dijkhuizen-Radersma, R. Growth, Metabolism, and Growth Inhibitors of Mesenchymal Stem Cells. *Tissue Eng. Part A* **2009**, *15*, 1877–1886. [[CrossRef](#)]
32. Oliver-Urrutia, C.; Rosales-Ibañez, R.; Domínguez-García, M.V.; Flores-Estrada, J.; Flores-Merino, M.V. Synthesis and evaluation of poly acrylic acid/polyvinylpyrrolidone interpenetrating network as a matrix for oral mucosa cells. *J. Biomater. Appl.* **2020**, *34*, 998–1008. [[CrossRef](#)]
33. Flores-Merino, M.V.; Chirasatitsin, S.; Lo Presti, C. Nanoscopic mechanical anisotropy in hydrogel surfaces. *Soft Matter* **2010**, *6*, 4466–4470. [[CrossRef](#)]
34. Paganin, D.; Mayo, S.C.; Gureyev, T.E.; Miller, P.R.; Wilkins, S.W. Simultaneous phase and amplitude extraction from a single defocused image of a homogeneous object. *J. Microsc.* **2002**, *206*, 33–40. [[CrossRef](#)]
35. Van Aarle, W.; Palenstijn, W.J.; Cant, J.; Janssens, E.; Bleichrodt, F.; Dabravolski, A.; De Beenhouwer, J.; Batenburg, K.J.; Sijbers, J. Fast and flexible X-ray tomography using the ASTRA toolbox. *Opt. Express* **2016**, *24*, 25129–25147. [[CrossRef](#)]
36. Shi, Y.; Xiong, D.; Liu, Y.; Wang, N.; Zhao, X. Swelling, mechanical and friction properties of PVA/PVP hydrogels after swelling in osmotic pressure solution. *Mater. Sci. Eng. C* **2016**, *65*, 172–180. [[CrossRef](#)]
37. Fanesi, G.; Abrami, M.; Zecchin, F.; Giassi, I.; Dal Ferro, E.; Boisen, A.; Grassi, G.; Bertocin, P.; Grassi, M.; Marizza, P. Combined Use of Rheology and LF-NMR for the Characterization of PVP-Alginates Gels Containing Liposomes. *Pharm. Res.* **2018**, *35*, 171. [[CrossRef](#)]
38. Alsarra, I.A.; Hamed, A.Y.; Alanazi, F.K.; Neau, S.H. Rheological and mucoadhesive characterization of poly (vinylpyrrolidone) hydrogels designed for nasal mucosal drug. *Arch. Pharm. Res.* **2011**, *34*, 573–582. [[CrossRef](#)]
39. El-Sayed, K.M.F.; Paris, S.; Becker, S.; Kaseem, N.; Ungefroren, H.; Fändrich, F.; Wiltfang, J.; Dörfer, C. Isolation and characterization of multipotent postnatal stem/progenitor cells from human alveolar bone proper. *J. Craniomaxillofac. Surg.* **2012**, *40*, 735–742. [[CrossRef](#)]
40. Lopérgolo, L.C.; Lugao, A.B.; Catalini, L.H. Direct UV photocrosslinking of poly (N-vinyl-2-pyrrolidone) (PVP) to produce hydrogels. *Polymer* **2003**, *44*, 6217–6222. [[CrossRef](#)]
41. Cheng, S.; Gandevia, S.C.; Green, M.; Sinkus, R.; Bilston, L.E. Viscoelastic properties of the tongue and soft palate using MR elastography. *J. Biomech.* **2011**, *44*, 450–454. [[CrossRef](#)]
42. Chen, J.; Ahmad, R.; Li, W.; Swain, M.; Ki, Q. Biomechanics of oral mucosa. *J. R. Soc. Interface* **2015**, *12*, 20150325. [[CrossRef](#)]
43. Cameron, A.R.; Frith, J.E.; Cooper-White, J.J. The influence of substrate creep on mesenchymal stem cell behaviour and phenotype. *Biomaterials* **2011**, *32*, 5979–5993. [[CrossRef](#)]
44. Barber-Pérez, N.; Georgiadou, M.; Guzmán, C.; Isomursu, A.; hamidi, H.; Ivaska, J. Mechano-responsiveness of Fibrillar Adhesions on Stiffness-Gradient Gels. *J. Cell Sci.* **2020**, *133*, 242909. [[CrossRef](#)]
45. Das, P.; Salerno, S.; Remigy, J.C.; Lahitte, J.F.; Bacchin, P.; De Bartolo, L. Double porous poly ( $\epsilon$ -caprolactone)/chitosan membrane scaffolds as niches for human mesenchymal stem cells. *Colloids Surf. B* **2019**, *184*, 110493. [[CrossRef](#)]
46. Bonartsev, A.P.; Zharkova, I.I.; Voinova, V.V.; Kuznetsova, E.S.; Zhuikov, V.A.; Makhina, T.K.; Myshkina, V.L.; Potashnikova, D.M.; Chesnokova, D.V.; Khaydapova, D.D.; et al. Poly (3-hydroxybutyrate)/poly(ethylene glycol) scaffolds with different microstructure: The effect on growth of mesenchymal stem cells. *3 Biotech* **2018**, *8*, 328. [[CrossRef](#)]
47. Annabi, N.; Nichol, J.W.; Zhong, X.; Ji, C.; Koshy, S.; Khademhosseini, A.; Dehghani, F. Controlling the porosity and microarchitecture of hydrogels for tissue engineering. *Tissue Eng. Part B* **2010**, *16*, 371–383. [[CrossRef](#)]
48. Romero, E.; Simms, P.H. Microstructure investigation in unsaturated soils: A Review with special attention to contribution of mercury intrusion porosimetry and environmental scanning electron microscopy. *Geotech. Geol. Eng.* **2008**, *26*, 705–727. [[CrossRef](#)]
49. Lawyer, T.; McIntosh, K.; Clavijo, C.; Potekhina, L.; Mann, B.K. Formulation Changes Affect Material Properties and Cell Behavior in hA-Based hydrogels. *Int. J. Cell Biol.* **2012**, *2012*, 1–9. [[CrossRef](#)]
50. Izgordu, M.S.; Uzgur, E.I.; Ulag, S.; Sahin, A.; Yilmaz, B.K.; Kilic, B.; Ekren, N.; Oktar, F.N.; Gunduz, O. Investigation of 3D-Printed Polycaprolactone-/Polyvinylpyrrolidone-Based Constructs. *Cartilage* **2019**, *1*, 1–10. [[CrossRef](#)]
51. Xiong, S.; Wang, J.; Zhu, W.; Yang, K.; Ding, G.; Li, X.; Eun, D.D. Onlay repair technique for the management of ureteral strictures: A comprehensive review. *Biomed Res. Int.* **2020**, *27*, 6178286. [[CrossRef](#)]
52. Ganz, J.; Shor, E.; Guo, S.; Sheinin, A.; Arie, I.; Michaelievski, I.; Pitaru, S.; Offen, D.; Levenberg, S. Implantation of 3D Constructs Embedded with Oral Mucosa-Derived Cells Induces Functional Recovery in Rats with Complete Spinal Cord Transection. *Front. Neurosci.* **2017**, *11*, 589. [[CrossRef](#)]
53. Egusa, H.; Sonoyama, W.; Nishimura, M.; Atsuta, I.; Akiyama, K. Stem cells in dentistry-part I: Stem cell sources. *J. Prosthodont Res.* **2012**, *56*, 151–165. [[CrossRef](#)]
54. Abou-Neel, E.A.; Chrzanowski, W.; Salih, V.M.; Kim, H.W.; Knowles, J.C. Tissue engineering in dentistry. *J. Dent.* **2014**, *42*, 915–928. [[CrossRef](#)]

PAPER [XXV]



Cite this: DOI: 10.1039/c7sm02074k

# Chondrogenic potential of macroporous biodegradable cryogels based on synthetic poly( $\alpha$ -amino acids)<sup>†</sup>

T. Sedlačik,<sup>a</sup> O. K. Acar,<sup>b</sup> H. Studenovská,<sup>a</sup> I. Kotelnikov,<sup>a</sup> J. Kučka,<sup>a</sup> Z. Konečná,<sup>c</sup> T. Zikmund,<sup>c</sup> J. Kaiser,<sup>c</sup> G. T. Kose<sup>bd</sup> and F. Rypáček<sup>a</sup>

In this study, the potential of highly porous hydrogels based on biodegradable synthetic poly( $\alpha$ -amino acids) to support proliferation and chondrogenesis of human dental pulp stem cells (hDPSCs) was investigated. Covalently crosslinked gels with permanent pores were formed under cryogenic conditions by free-radical copolymerization of poly[*N*<sup>5</sup>-(2-hydroxyethyl)-L-glutamine-*stat*-*N*<sup>5</sup>-(2-methacryloyl-oxyethyl)-L-glutamine] (PHEG-MA) with 2-hydroxyethyl methacrylate (HEMA) and *N*-propargyl methacrylamide (PrMAAm) as minor co-monomers. PrMAAm provided alkyne groups for modifying the gels with cell-supporting moieties (RGDS peptides) by the azide–alkyne “click”-reaction. Two types of gels with different compressive moduli were prepared. Each type was modified with two different concentrations of RGDS peptide. X-ray computed nanotomography (nanoCT) was used to visualize and analyze the 3D-structure of the cryogels. It was shown that modifying the PHEG-MA cryogels within the range of RGDS concentrations examined here had a positive effect on the proliferation of hDPSCs. Immunofluorescence staining for collagen type 2 and aggrecan proved that there was differentiation of hDPSCs into chondrocytes.

Received 20th October 2017,  
Accepted 30th November 2017

DOI: 10.1039/c7sm02074k

rsc.li/soft-matter-journal

## Introduction

### State-of-the-art in cartilage regeneration

Articular cartilage is an avascular tissue with a complex structure that has only a limited capacity for self-repair, depending on the type and size of the defect and also on the patient's age. Severe focal injuries in cartilage are currently treated by one of the three main types of arthroscopic surgery: bone marrow stimulating techniques, mosaicplasty (an autogenous osteochondral grafting system clinically used since 1992), and cell-based therapies.<sup>1</sup> The cell-based therapy approach was introduced by autologous chondrocyte implantation in 1987, and resulted in the first commercial product, ChondroCelect, in 2009. Several matrix-assisted cell therapies have also been developed and are currently under clinical trials.<sup>1</sup> Matrix-assisted autologous cell transplantation is considered to be one of the most promising techniques in

cartilage regeneration. This concept utilizes complex temporary cell-supporting materials (scaffolds), which can mimic both the biological properties and the mechanical properties of the original extracellular matrix (ECM). As far as tissue-engineered scaffolds are concerned, soft porous hydrogels can offer similar properties to the ECM from the mechanical and structural point of view.<sup>2,3</sup>

### Biodegradable cryogels

An adequate pore structure of the scaffold is a critical requirement in tissue engineering applications.<sup>2–7</sup> However, preparing porous hydrogels with an open-cell structure and suitable mechanical strength can be a complicated process.<sup>8</sup> A promising method, in terms of the mechanical properties of the resulting porous hydrogels, is based on cryogelation.<sup>9–11</sup> The so-called cryogels are gels formed below the freezing point of the solvent. While the sample is frozen macroscopically, the crosslinking reaction leading to gelation takes place in the concentrated liquid microphase that remains in the interstitial spaces between crystals of the frozen solvent. This specific mechanism allows the preparation of hydrogels with an open-cell morphology and interesting mechanical and swelling behaviour, despite their high pore volume and water content.

Scaffolds designed for tissue engineering applications should fulfil the requirements not only for a suitable porous morphology, but also for biocompatibility and degradability in a biological environment.<sup>2,3</sup> Biodegradable cryogels have been

<sup>a</sup> Institute of Macromolecular Chemistry, Academy of Sciences of the Czech Republic, Prague, Department of Biomaterials and Bioanalogous Systems, Heyrovsky sq. 2, 162 06 – Prague 6, Czech Republic. E-mail: sedlacik@imc.cas.cz

<sup>b</sup> Department of Genetics and Bioengineering, Yeditepe University, 26 Ağustos Campus, Kayışdağı Cad., 34755 Istanbul, Turkey

<sup>c</sup> CEITEC – Central European Institute of Technology, Brno University of Technology, Purkynova 123, 612 00 Brno, Czech Republic

<sup>d</sup> Center of Excellence in Biomaterials and Tissue Engineering, BIOMATEN, METU, Ankara, Turkey

<sup>†</sup> Electronic supplementary information (ESI) available. See DOI: 10.1039/c7sm02074k

synthesized from both natural and synthetic polymers.<sup>12</sup> Cryogels from natural polymers intended for application in tissue engineering have been made of proteins such as collagen,<sup>13</sup> gelatin,<sup>14,15</sup> casein,<sup>15</sup> ovalbumin<sup>15</sup> or fibroin,<sup>16</sup> and of polysaccharides such as agarose,<sup>17</sup> dextran<sup>18</sup> or chitosan.<sup>19</sup> Several hybrid systems based on a combination of natural and synthetic polymers,<sup>20–24</sup> or combined with inorganic compounds,<sup>25,26</sup> have been introduced. Although natural polymers and their derivatives may offer biodegradability, they exhibit some specific drawbacks, *e.g.* inadequate mechanical properties, dependence of the properties on the source, a potential immune reaction, or solubility problems.<sup>2,3</sup> An advantage of scaffolds based on synthetic polymers is that they allow for biomaterials with controllable and reproducible chemistry and properties. However, only a few biodegradable cryogels based on synthetic polymers have been presented, for example, cryogels based on *N*-vinylcaprolactam,<sup>27</sup> which are degradable by hydrolysis, and cryogels based on vinyllic monomers and disulfide- or peptide-cross-linkers.<sup>28–30</sup> The latter cryogels are bioresorbable by enzymatic hydrolysis.

### Cryogels of synthetic poly( $\alpha$ -amino acids)

An alternative for preparing synthetic biodegradable cryogels is to use synthetic poly(amino acids) (pAAs) as gel precursors. Synthetic pAAs are an important group of biocompatible and biodegradable synthetic polymers, which have been studied for use in biomedical applications in many fields.<sup>31–33</sup> Recently, we have introduced cryogels based on synthetic poly( $\alpha$ -amino acids) (pAAs), poly(*N*<sup>5</sup>-(2-hydroxyethyl)-L-glutamine) (PHEG), and *N*-propargyl acrylamide comonomers carrying alkyne groups, which can be modified easily and efficiently by biomimetic groups. We demonstrated that these porous gels can be well designed in terms of morphology and mechanical properties.<sup>8</sup> Shirbin *et al.* have developed cryogels based on random copolymers of L-glutamic acid and L-lysine.<sup>34</sup>

The use of pAAs to form degradable scaffolds provides a unique opportunity to combine the merits of both synthetic degradable and natural polymers. Due to their polypeptide backbone, synthetic pAAs exhibit the inherent potential to be degraded by a range of proteases and peptidases.<sup>35–38</sup> In earlier studies, we have demonstrated that the rate and enzyme specificity of PHEG degradation can be considerably modified by side chain modification or by the addition of minor amino acids into the polymer chain by copolymerization.<sup>39–41</sup>

### Dental pulp stem cells

Numerous types of human dental tissue-derived mesenchymal stem cells (MSCs) have recently been isolated and characterized, including dental pulp stem cells (DPSCs).<sup>42</sup> MSC-like cells exhibit self-renewal, multi-lineage differentiation potential, and immunomodulatory properties. Several studies have demonstrated some advantages of DPSC-based approaches for regenerative treatments and immunotherapies. Among other dental stem cells, DPSCs can be easily and efficiently isolated, and they exhibit a fast population doubling time.<sup>43</sup> Their potential to differentiate into various cell types, such as adipocytes, osteoblasts or chondrocytes, has already been demonstrated.<sup>44</sup>

DPSCs appear to be a promising source of cells for the treatment of various health complications, including some challenging degenerative diseases and injuries.<sup>42</sup> Efforts are therefore being made to personalize the medicine by using patients' own stem cells. Dental stem cells, dental tissues and also extracted teeth can be cryopreserved for many years to retain their regenerative potential for use in future regenerative therapies.

## Results and discussion

In this study, we have focused on evaluating the potential of biomimetic cryogels based on a synthetic poly( $\alpha$ -amino acid) derivative to support chondrogenesis of human dental pulp stem cells (hDPSCs). Poly[*N*<sup>5</sup>-(2-hydroxyethyl)-L-glutamine] (PHEG) is a synthetic polymer with a polypeptide chain which, as in natural proteins, is enzymatically degradable.<sup>35–41</sup> The synthesized linear hydrophilic polymer (PHEG) was methacryloylated in order to provide a polymerizable water-soluble gel precursor (PHEG-MA). The respective covalently crosslinked macroporous hydrogels were prepared by radical copolymerization of PHEG-MA with a minor amount of (meth)acrylic co-monomers (HEMA and PrMAAm) in a moderately frozen solution. PrMAAm structural units of the polymer chain carry alkyne groups, which can subsequently be used to bind any bioactive substance to the cryogel surface (the gel walls of macropores). We modified cryogels with RGDS peptide moieties to promote cell adhesion, proliferation and differentiation. The potential of macroporous biomimetic hydrogels to support the proliferation and chondrogenesis of hDPSCs was evaluated by LIVE/DEAD<sup>®</sup> viability tests, by an MTS assay (see the Experimental section) to follow up the cell proliferation activity, and by immunofluorescence staining of protein expression.

### Preparation of polymeric precursors

The general features of polymeric precursor preparation (PHEG-MA) have been described elsewhere.<sup>8</sup> The characteristics of specific PHEG-MA samples used in this work were as follows:  $\bar{M}_w = 27\,700$ ;  $\bar{M}_n = 20\,500$ ;  $D = 1.35$ ; MA% = 9.0, where  $\bar{M}_w$  is the weight average molecular weight and  $\bar{M}_n$  is the number average molecular weight (as polyethyleneoxide equivalents) from size exclusion chromatography,  $D$  is the dispersity ( $\bar{M}_w/\bar{M}_n$ ), and MA% is the degree of methacryloylation, determined by <sup>1</sup>H NMR.<sup>8</sup>

### Preparation and characterization of cryogels

The cryogels that were prepared, together with their mechanical and swelling properties and their porosity, are listed in Table 1. We prepared two types of gels, coded as samples C4 and C10 (the number in the code corresponds to the total amount – in wt% – of gel precursors at gel formation; for the molar ratios of the precursors, see the Experimental section). The samples have a similar pore architecture but significantly different mechanical properties expressed as the compressive moduli ( $1.7 \pm 0.4$  and  $20.9 \pm 3.8$  kPa, details are provided below). These gels were loaded with various concentrations of RGDS peptide

**Table 1** The mechanical and swelling properties and the porosity of the cryogels

Sample ID	Gel yield <sup>a</sup> [%]	Compressive modulus <sup>b</sup> [kPa]	Porosity (Hg) <sup>c</sup> [%]	Porosity (CH) <sup>d</sup> [%]	Equilibrium water regain <sup>e</sup> [g g <sup>-1</sup> ]
C4	89 ± 3	1.7 ± 0.4	93.6	96.5 ± 0.2	37.7 ± 2.0
C10	83 ± 3	20.9 ± 3.8	88.3	89.7 ± 0.3	16.2 ± 1.1

<sup>a</sup> The gel yield represents the conversion of monomers into an insoluble gel, determined gravimetrically after soluble products of crosslinking polymerization are washed out by dialysis against water. <sup>b</sup> The moduli of the cryogels represent the overall moduli of the porous hydrogels (bulk moduli). <sup>c</sup> Determined by mercury porosimetry (Hg). <sup>d</sup> Determined by cyclohexane (CH) uptake. <sup>e</sup> The equilibrium water regain represents the total water content in the gel, including the polymer bound water and also the free water present in the macropores, expressed as the weight of water per gram of freeze-dried gel; see the ESI for respective equations.

(see the Experimental section), using the azide-alkyne “click”-reaction two different concentrations for each type of cryogel (C4 and C10), plus blank samples without the peptide (Table 2), in order to observe the influence of the material stiffness and also of the biomimetic features of the gels upon the differentiation of hDPSCs into chondrocytes. Both cryogel samples contained more than 90% water (the values of the equilibrium water regain in Table 1 correspond to 97.4% and 94.2% of water content, respectively), while the equilibrium swelling regain was several times higher for sample C4 than for sample C10 (Table 1). The porosity of the cryogels, determined by the cyclohexane uptake method, was 96.5 vol% for sample C4 and 89.7 vol% for sample C10, and just slightly lower when determined by mercury porosimetry (Table 1). These results were also in good agreement with the nanoCT data (in comparison with the wall volume in Table 2). Both the higher equilibrium swelling regain and the higher pore volume fraction of sample C4 were due to the lower concentration of the gel precursors used in the preparation of the gels. The morphology of the cryogels was observed by nanoCT and scanning electron microscopy (SEM) (Fig. 1–3). The images acquired from nanoCT measurements show the delicate interconnective porous structure of both cryogels (C4 and C10). This corresponds well with the structure revealed by SEM.

Both samples show a well-developed pore architecture with an open-cell morphology. The mean pore diameter, as obtained from an analysis of the nanoCT data (Table 2), was 55 μm and 83 μm, for samples C4 and C10, respectively, with a very small portion of the pores smaller than 20 μm (Fig. 2). The pores in both samples thus provide ample space for cell migration and spreading.<sup>4,5</sup> The mean pore diameter, as obtained from mercury porosimetry (see the ESI,† Fig. S1 and Table S1), was

several times smaller and did not correspond with the SEM and tomographic images. We therefore consider this method to be inappropriate for determining the pore size of cryogels, while nanotomography can be used to obtain accurate data. However, the shape of the distribution curves was similar for the two methods, indicating that the calculation model used for mercury porosimetry can be inappropriate for cryogels. Sample C10 shows a well-developed pore architecture with a narrower pore-size distribution than sample C4 (Fig. 2).

This feature makes sample C10 stiffer and more fragile than sample C4, which shows a similar but less developed regular pore architecture and exhibits higher equilibrium water regain. The compression curves for the two samples (measured up to 90% strain) are shown in Fig. 4. Both samples showed mechanical behaviour typical for hydrogels with an open-cell morphology, especially for cryogels. The samples reached a plateau in the region of 20–60/80% strain, and then became stiffer as the water present in the pores was squeezed out and the cryogels began to behave like gels without macropores. This stage occurred at higher compression for sample C4, because of the higher volume fraction of the pores. The cryogels can be repeatedly squeezed and soaked again without damaging the structure. There was no change in the stress–strain waveform for sample C4, and just a small change was observed for sample C10, when they were compressed to 90% up to a compression strain close to their porosity, both in percentage terms.

The nanoCT technique provides an advanced analysis of the gel structure in comparison with common microCT techniques<sup>7</sup> (Table 2 and Fig. 3): (A) the wall thickness distribution was calculated and is presented in Fig. 3. Greater thickness (2.16 vs. 1.64 μm) is shown for sample C10, which was prepared from a more concentrated solution of gel precursors (10 wt% vs. 4 wt% for sample C4).

**Table 2** Results of a nanoCT analysis of the cryogels, and the amount of bound RGDS peptide determined by radioassay and related to the nanoCT analysis

Sample ID	Average pore diameter [μm]	Wall surface <sup>a</sup> [cm <sup>2</sup> cm <sup>-3</sup> ]	Wall volume <sup>b</sup> [%]	Average wall thickness [μm]	RGDS-density [pmol cm <sup>-2</sup> ]
C4-Blank	55 ± 25	767	4.77	1.64 ± 0.69	—
C4-Low					5.4
C4-High					31.2
C10-Blank	83 ± 19	619	9.06	2.16 ± 1.07	—
C10-Low					6.1
C10-High					38.7

<sup>a</sup> The wall surface represents the total surface area of a freeze-dried porous sample divided by its volume. <sup>b</sup> The wall volume represents the total volume of the gel walls of the macropores in the sample (the volume of the freeze-dried sample, excluding the free space of the macropores), expressed here as a percentage of the total volume of the sample.

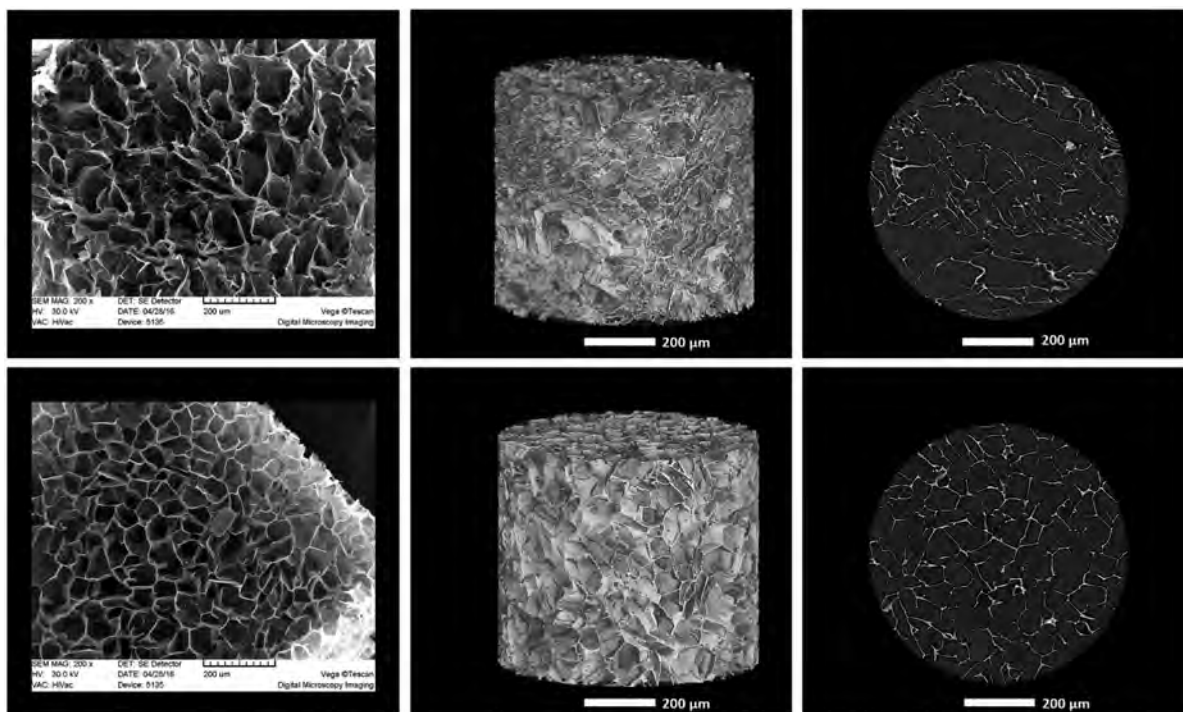


Fig. 1 Morphology of the cryogels observed using SEM (left – scale bar: 200 μm) and using nanoCT (centre – 3D render, and right – cross-sections). The upper row represents sample C4, and the lower row represents sample C10.

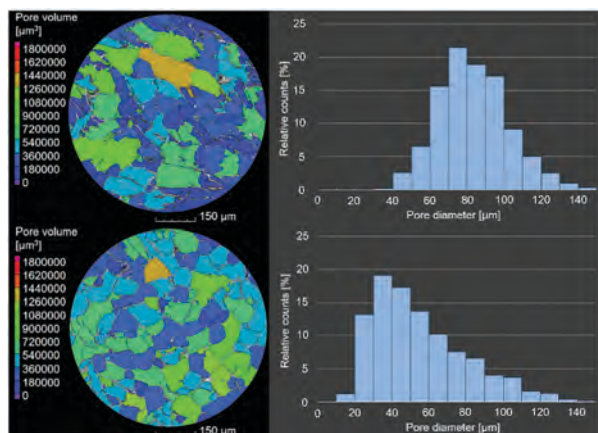


Fig. 2 Pore volume analysis of the cryogels provided by nanoCT data; the upper picture represents the cross section of cryogel C4, and the lower picture represents the cross section of cryogel C10. The pores are color-coded by their volume. The plots are the respective pore size distributions. The pore diameters are calculated as the diameters of spheres corresponding to the pore volumes.

Clearly, the more developed pore architecture together with the greater wall thickness of the macropores resulted in greater stiffness of the cryogels; (B) the calculation of the wall surface area of the cryogels showed a high wall surface area for both samples (C4 and C10). The slightly smaller wall surface area of the C10 samples corresponds well with the lower volume fraction of the pores and the greater wall thickness of the pores in these samples.

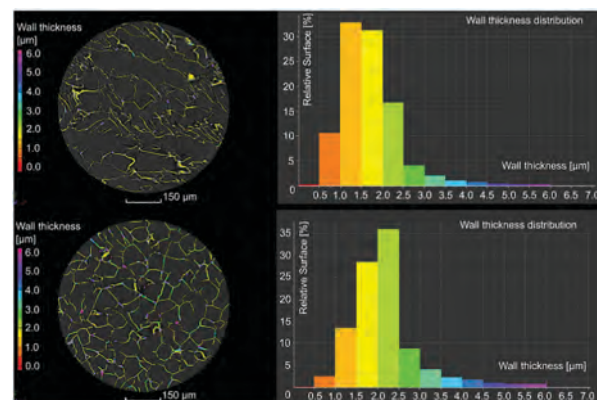


Fig. 3 Wall thickness analysis of the cryogel provided by nanoCT data; the upper pictures represent cryogel C4, and the lower pictures represent cryogel C10.

The calculated areas of the wall surfaces were used for estimating the RGDS surface density in the samples:

$$\text{RGDS-density} = \frac{c \cdot k}{M \cdot W \cdot s^2},$$

where  $c$  is the weight concentration of N3-peptide in the reaction mixture,  $k$  is the yield of the “click”-reaction determined by the radioassay,  $M$  is the molecular weight of the RGDS peptide analogue,  $W$  is the wall surface area of the freeze-dried sample provided by nanoCT measurements, and  $s$  is the shrinking ratio resulting from freeze-drying ( $s \sim 0.9$ ). The detailed results of the radioassay (yields of the “click”-reaction being between 50 and 65%)

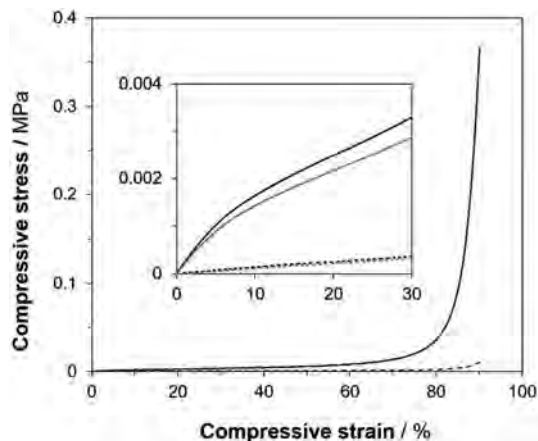


Fig. 4 Typical compression curves of cryogels C4 and C10 measured up to 90% strain; full line – sample C10, dashed line – sample C4; the smaller window shows a detail of the beginning of the compression. The 1st run (black) and the 2nd run (gray) for each sample are shown here.

are provided in the ESI† (Fig. S2). The surface concentration of biomimetic groups in porous hydrogel systems is generally very complicated to quantify. We assumed that the wall surface area obtained from nanoCT on the submicrometer scale represents the surface that is well-accessible to the cell receptors, and is therefore more relevant than the wall surface area provided by the nitrogen adsorption method.<sup>8</sup> According to our previous experience, the wall surface area provided by the nitrogen adsorption method can be biased for weaker gels because of damage to the microstructure. The calculated surface density of RGDS peptide is still only approximate, as reactants of the “click”-reaction can also partly diffuse into the dense gel phase (gel walls of macropores). Nevertheless, this method is suitable for comparing the RGDS surface density of samples with different pore architectures.

#### *In vitro* cell culture studies on cryogels

**Cell viability.** The viability of hDPSCs cultivated on the cryogel samples was analyzed by the LIVE/DEAD<sup>®</sup> assay (Fig. 5). High cell viability was observed, reaching a maximum of 85–95% for all samples throughout 20 days of incubation, followed by a slight decrease (about 75%) on day 30. Relevant pictures are provided in the ESI† (Fig. S4 and S5). The predominant presence of live cells indicated that the PHEG-MA based scaffolds were not cytotoxic, and had good biocompatibility. With increasing time of incubation,

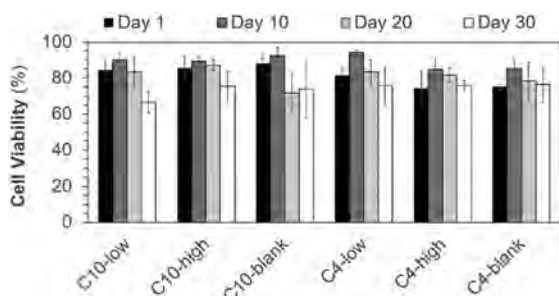


Fig. 5 Cell viability of hDPSCs on the cryogels throughout 1, 10, 20 and 30 days of incubation via the LIVE/DEAD<sup>®</sup> assay.

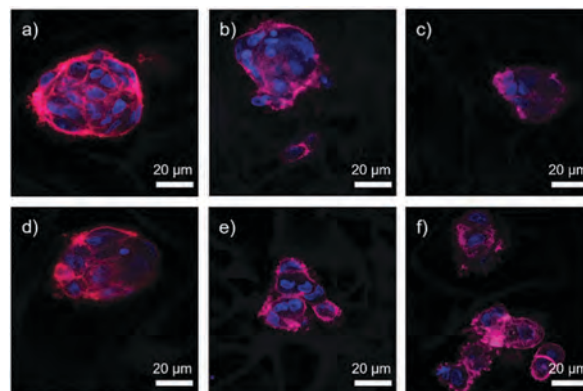


Fig. 6 Morphology of hDPSCs on day 1 of incubation (63× magnification, 20 μm): (a) sample C4-blank, (b) C4-low RGDS, (c) C4-high RGDS, (d) sample C10-blank, (e) C10-low RGDS, and (f) C10-high RGDS.

the cells not only proliferated on the cryogels but also spread inside the pores.

**Morphology of the cells.** The morphology of the seeded hDPSCs on the cryogels was visualized by staining with phalloidin/DAPI (see the Experimental section), using confocal microscopy. Fig. 6 shows the initial attachment of the seeded cells on the first day of incubation. It was observed that the cells had an intact plasma membrane and were viable in all samples. Though there was no significant spreading pattern between the groups, the cells seeded on the RGDS-containing cryogels seem to have a slightly greater tendency to spread, while the cells seeded on the blank cryogels had a strong cell–cell interaction rather than a cell–substrate interaction (Fig. 6a and b).<sup>45,46</sup> Similarly, the hDPSCs seemed to anchor a little bit more strongly on the RGDS-modified samples with a higher modulus (Fig. 6e and f) than on the RGDS-modified samples with a lower modulus (Fig. 6b and c).

**Cell growth determination by MTS assay and chondrogenic differentiation by immunofluorescence staining.** The results of the MTS assay are depicted in Fig. 7. On the first day of incubation, only the cells seeded on the TPP<sup>®</sup> tissue culture flasks showed significant proliferation. It should be noted that the tested hydrogels made from flexible hydrophilic precursors were extremely hydrophilic with a high water content. They exhibited very low adsorption of proteins and, as a consequence, the spontaneous adhesion of the cells was expected to be very low, unless it was facilitated by the introduction of cell-adhesion units. The effect of cell-adhesion motifs (RGDS peptides) became apparent after 10 days of incubation, showing that the cell proliferation on the cryogels was equal to the cell proliferation on the TPP<sup>®</sup>. After 10 days of incubation, there was a significant increase in the proliferation of cells on the RGDS-modified cryogels, in comparison with the proliferation of the blank cryogels. There was a slight tendency towards better cell proliferation on cryogels with a higher RGDS density.

The decrease in the cell number as revealed by the MTS assay on all cryogel samples after 20 days of cultivation (day 20) can be explained by the diminished growth of the hDPSCs due to their incipient differentiation to chondrocytes, as the viability of

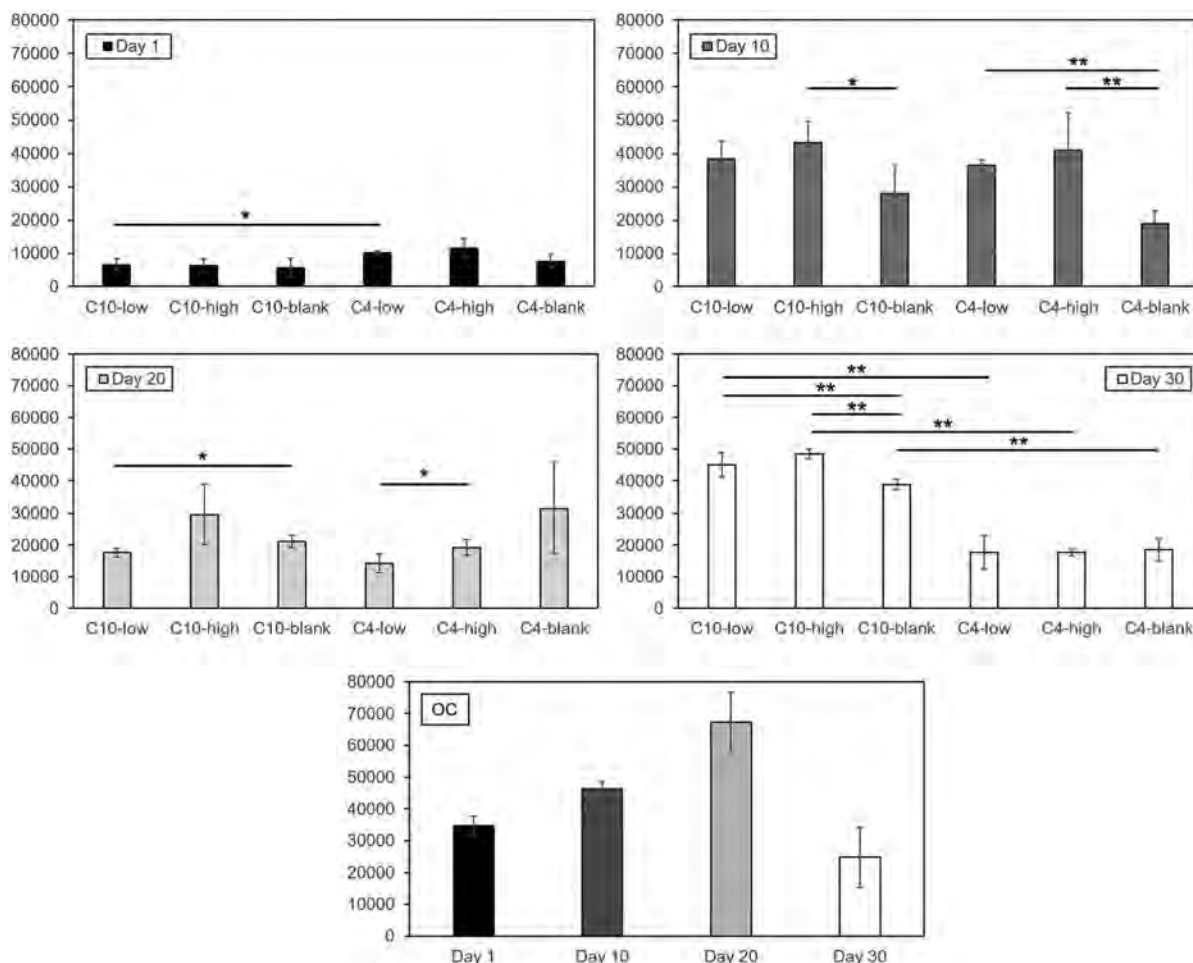


Fig. 7 The proliferation of the hDPSCs seeded on the cryogels after 1, 10, 20 and 30 days of culture using the MTS assay. OC – cells seeded on the TPP<sup>®</sup> tissue culture flasks. The data represent the standard error of the mean;  $n = 3$ . (\* $p < 0.05$ ; \*\* $p < 0.01$ ).

the hDPSCs has been shown to be constant or not significantly decreasing. The effects of both RGDS density and gel stiffness were not clearly pronounced at this stage of cultivation, probably because they were combined with different degrees of cell differentiation.

An additional increase in the cell number can be clearly observed in all C10 samples after 30 days of incubation. This increase may reflect the proliferation of differentiated cells. The differentiation was confirmed by immunofluorescence staining of collagen type 2 and aggrecan proteins, which are considered to be differentiation markers in the later stage of chondrogenesis (Fig. 8).<sup>47</sup> The expression of these markers for the C10 sample with higher concentration of RGDS (C10-high) began sooner, on day 20, (Fig. 8a–c) in comparison with the C-10 sample with lower concentration of RGDS and with the blank sample (C10-low and C10-blank), where aggrecan was confirmed later, on day 30 (Fig. 8d and e). These results confirmed that a higher concentration of RGDS was more efficient at chondrogenic differentiation of hDPSCs on cryogels with a higher modulus (C10 samples).

For low modulus cryogels (C4 samples), RGDS modification made no considerable difference in the initial attachment (day 1) in comparison with the blank sample. An increase in

the cell number was observed for all C4 samples after 10 days of incubation (Fig. 7). The cryogels with a high concentration of RGDS modifications (C4-high) showed a significantly higher cell number (proliferation) than the blank sample. After 20 days, a decrease in the cell number was observed for both of the low modulus samples with RGDS (C4-low and C4-high). This can be explained by the differentiation of hDPSCs. The differentiation was confirmed by immunofluorescence staining of collagen type 2 and aggrecan proteins after 20 days of incubation (Fig. 9a–c). After 30 days of incubation, higher expression of these markers on the low modulus blank sample (C4-blank) was also observed (Fig. 9d–f).

It is known that the stiffness of the scaffold plays a significant role in stem cell differentiation. Soft matrices that mimic the brain are neurogenic, stiffer matrices that mimic muscles are myogenic, and comparatively rigid matrices that mimic collagenous bones prove to be osteogenic.<sup>48,49</sup> With respect to the stiffness of the cryogels, greater cell proliferation activity was detected on the high modulus samples on day 30. This can be attributed to the proliferation of already differentiated cells.

The compressive moduli of the cryogels in our work represent the overall moduli of the porous hydrogels (bulk moduli) and are

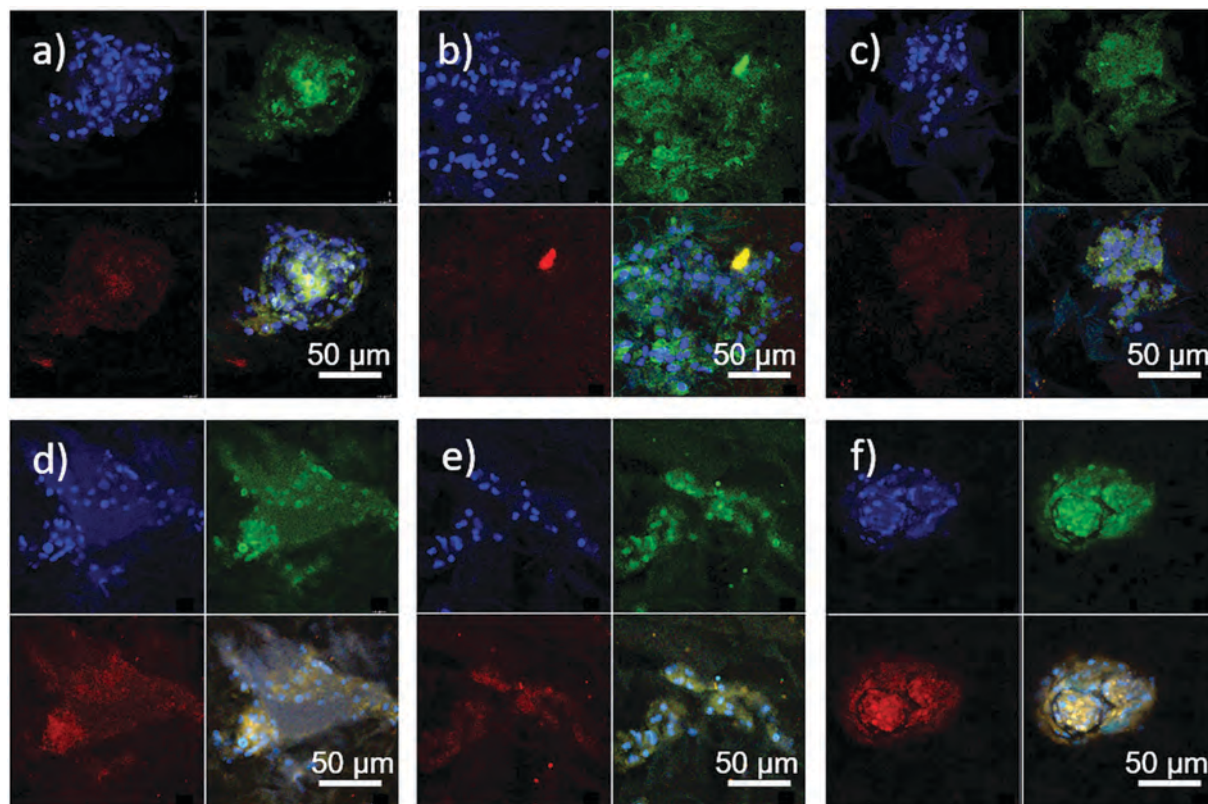


Fig. 8 Chondrogenic differentiation by immunofluorescence staining (40 $\times$  magnification, 50  $\mu$ m): blue – nucleus by DAPI, green – collagen type 2, red – aggrecan, bottom right in each picture – merged; (a–c) day 20; (d–f) day 30; (a and d) C10-blank; (b and e) C10-low RGDS; (c and f) C10-high RGDS. See the ESI<sup>†</sup> for detailed pictures.

assumed to be lower than the moduli of the polymeric walls of the macropores (moduli of the gel phase), due to the high fraction of macropores. According to Welzel *et al.*,<sup>50</sup> the modulus of the gel phase of the cryogels measured by atomic force microscopy nano-indentation is almost constant with the concentration of the polymeric precursors when the crosslinking density is the same. This corresponds with our assumption that the difference in the bulk modulus of the two samples is due to the difference in morphology. The greater proliferation activity on higher modulus samples could therefore be rather due to the different morphologies of the samples.

As concerns the RGDS concentration in the samples, the addition of RGDS had almost no influence on the initial attachment of the seeded cells. However, it is clear that after 10 days of cultivation, cell proliferation was favored on the RGDS-containing scaffolds and a higher number of cells were detected in all the samples than in the blanks. There was no significant difference between the samples with a low concentration and a high concentration of RGDS for the initial attachment, but a higher concentration seemed to provide more support for the proliferation and differentiation of hDPSCs.

## Experimental

### Materials

Reagents and solvents for synthesizing polymeric precursors and for preparing cryogels: acetonitrile (for HPLC), ammonium

acetate, copper(II) sulfate, cyclohexane, glycerin and pyridine were of analytical grade, and were purchased from Lach-Ner, Czech Republic. Ammonium persulfate (APS,  $\geq 98\%$  for electrophoresis), ethanol (absolute), and methacryloyl chloride (MA-Cl, 97%) were purchased from Sigma-Aldrich. (+)-Sodium L-ascorbate ( $\geq 98\%$ , crystalline) was purchased from Sigma-Aldrich. Bis(trichloromethyl)carbonate (triphosgene,  $> 98\%$ ) was purchased from TCI Europe, N.V., Belgium. 2-Hydroxyethyl methacrylate (HEMA) was purchased from Rohm GmbH, Germany. Polyethylene-oxide standards (PEO) were purchased from Polymer Standard Service, Germany. All chemicals listed above were used as received.  $\gamma$ -Benzyl-L-glutamate (BLG), 99% was purchased from Emmennar Bio-Tech, India, and was recrystallized from hot water. Lithium chloride ( $\geq 98\%$ ) was purchased from Sigma-Aldrich, and was dried under vacuum at 30  $^{\circ}$ C. *N,N*-Dimethylacetamide (DMA), 1,4-dioxane, chloroform, and tetrahydrofuran (THF) were purchased from Lach-Ner, and were redistilled and dried over molecular sieves. 2-Aminoethanol ( $\geq 99\%$ ) was purchased from Sigma-Aldrich and was redistilled. *N*-Propargyl methacrylamide (PrMAAm) was synthesized by analogy with *N*-propargyl acrylamide according to Macková *et al.*<sup>51</sup> Azidopentanoyl-GGGRGDSGGGY-NH<sub>2</sub> (N3-peptide) and its radiolabelled analogue N3-peptide-<sup>125</sup>I were prepared according to Proks *et al.*<sup>52</sup> Deionized ultrapure water (Milli-Q<sup>®</sup>) was used in all experiments where water was a solvent.

Materials for cell cultivations: L-ascorbic acid (cell culture grade) primary antibodies: collagen type2 and aggrecan were

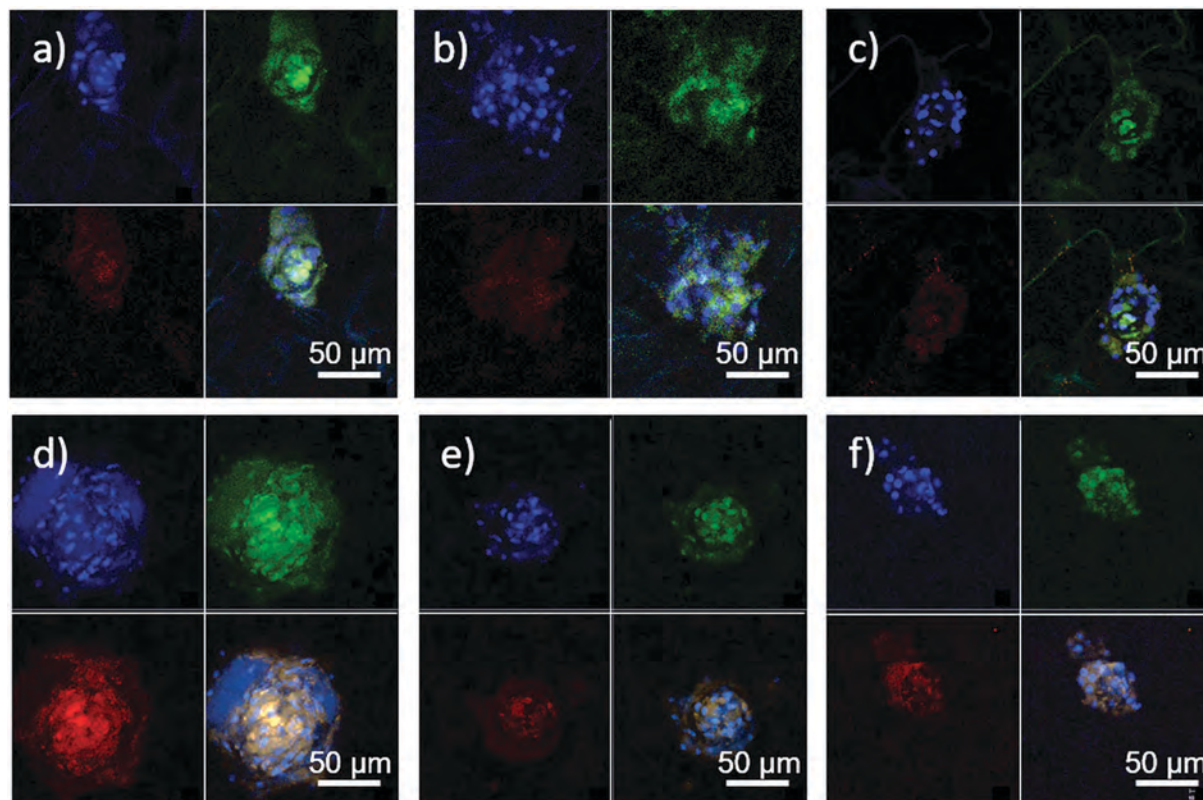


Fig. 9 Chondrogenic differentiation by immunofluorescence staining (40 $\times$  magnification, 50  $\mu$ m): blue – nucleus by DAPI, green – collagen type 2, red – aggrecan, bottom right in each picture – merged; (a–c) day 20; (d–f) day 30; (a and d) C4-blank; (b and e) C4-low RGDS; (c and f) C4-high RGDS. See the ESI† for detailed pictures.

purchased from Santa Cruz Biotechnology Inc., USA. CellTiter 96<sup>®</sup> Aqueous One Solution Cell Proliferation Assay (CellTiter 96<sup>®</sup>) was purchased from Promega, USA. Dexamethasone ( $\geq 98\%$  for HPLC, powder), L-proline (ReagentPlus<sup>®</sup>,  $\geq 99\%$ , HPLC) and sodium pyruvate (ReagentPlus<sup>®</sup>,  $\geq 99\%$ ) were purchased from Sigma-Aldrich. 4',6-Diamine-2-phenylindol (DAPI), 1 $\times$  Dulbecco's Modified Eagle Medium (DMEM), fetal bovine serum (FBS), Penicillin/Streptomycin, ProLong<sup>®</sup> Gold Antifade Mountant, secondary antibodies (anti-mouse and anti-rabbit), Trypsin-EDTA (0.25%) and a Viability/Cytotoxicity Kit for mammalian cells (LIVE/DEAD<sup>®</sup> assay) were purchased from Thermo Fisher Scientific, USA. FITC anti-human CD24, PE anti-human CD45, FITC anti-human CD44, PE anti-human CD90, and PE anti-human CD117 antibodies were purchased from BD Biosciences. ITS+ Premix Tissue Culture Supplement (ITS+ Premix) was purchased from Corning, USA. Phosphate buffered saline (PBS, 500 mM, pH 7.4) was purchased from Lonza, Switzerland. Recombinant human transforming growth factor-beta 1 (rhTGF- $\beta$ 1) was purchased from R&D Systems, USA.

### Synthesis of the polymeric precursor

The polymeric precursor for the preparation of biodegradable hydrogels was synthesized as described previously.<sup>8</sup> In the first step, N-carboxyanhydride of  $\gamma$ -benzyl-L-glutamate (NCA-BLG) was prepared by reacting  $\gamma$ -benzyl-L-glutamate (BLG) with triphosgene in THF. In the next step, NCA-BLG was polymerized

in 1,4-dioxane, using sodium methanolate as the initiator. The resulting polymer, poly( $\gamma$ -benzyl-L-glutamate) (PBLG), was precipitated in ethanol, dried and aminolyzed with excess of 2-aminoethanol to obtain a water-soluble polymer, poly[N<sup>5</sup>-(2-hydroxyethyl)-L-glutamine] (PHEG), which was purified by dialysis against water and was freeze-dried. To obtain a cross-linkable polymeric precursor, PHEG was reacted with methacryloyl chloride in DMA in the presence of pyridine and lithium chloride. The product, *i.e.*, the statistical copolymer poly[N<sup>5</sup>-(2-hydroxyethyl)-L-glutamine-*stat*-N<sup>5</sup>-(2-methacryloyl-oxy-ethyl)-L-glutamine] (PHEG-MA), was freeze-dried and was stored over a drying agent in the freezer.

The weight and number average molecular weights of the water-soluble polymers (PHEG and PHEG-MA) were determined by size-exclusion chromatography (SEC) on a system consisting of a PolySep-GFC-P Linear column, a Knauer gradient solvent-delivery system with diode array detection and an Alltech 3300 evaporative light scattering detector (Grace, USA). The system was calibrated with PEO standards.<sup>8</sup>

The degree of methacryloylation of the polymeric precursor was determined by <sup>1</sup>H NMR spectroscopy in D<sub>2</sub>O at 30 °C (Bruker Avance DPX 300).<sup>8</sup>

### Preparation of cryogels

Cryogels based on PHEG-MA were prepared by radical copolymerization of PHEG-MA with HEMA (mole ratio of HEMA to

HEG units of PHEG-MA: 0.11) and PrMAAm (mole ratio to HEG units of PHEG-MA: 0.03) as comonomers.<sup>8</sup> Polymerization was carried out in 2 mL glass ampoules (10.5 mm in inner diameter) at  $-15\text{ }^{\circ}\text{C}$  for 40 hours. APS and sodium sulfite were used as initiators. Sodium sulfite was used as the co-initiator instead of widely-used TEMED, which has been reported to be ineffective under acidic conditions.<sup>55</sup> *N*-propargyl acrylamide is an acidic monomer (the proton of the alkyne group can be removed by a strong base) and, moreover, the pH of a solution of it is expected to decrease after cryoconcentration of the reactants. According to our experience, the reaction with sulfite as the co-initiator of radical polymerization can provide higher gel yields within a reasonable reaction time when acidic monomers are used. The gels were washed thoroughly with water and were swollen in water to equilibrium.

The functional alkyne groups of the cryogels (introduced by copolymerization of PHEG-MA with PrMAAm) were used for binding the bioactive component, *i.e.* N3-RGDS peptide, by Cu(I)-catalyzed Huisgen azide-alkyne 1,3-dipolar cycloaddition.<sup>53,54</sup> The procedure for the modification reaction was described in detail in our previous work.<sup>8</sup>

### Characterization of cryogels

The amount of RGDS peptide covalently bound to the cryogel-carrying the alkyne groups was determined by radioassay analysis, with the use of a  $^{125}\text{I}$ -radiolabelled peptide analogue. The radioactivities of the solutions and samples were measured in a Bqmetr 4 ionization chamber (Empos, Czech Rep.) with an NaI/TlSpectroAnalyzerTM scintillation detector (AccuSync Medical Research Corporation, USA).

The X-ray nanocomputed tomography measurements (nanoCT) were performed on the freeze-dried samples of the gels, using a RIGAKU nano3DX system (Rigaku Corporation, Japan). Details of the measurement and data analysis are given in the ESI.†

The scanning electron microscopy (SEM) studies were carried out using a Vega microscope (Tescan, Czech Republic). The freeze-dried samples identical to those used for the nanoCT measurements were provided, and were sputter-coated with platinum (SCD050, Leica Microsystems, Germany) before scanning.

The swelling properties and the porosity of the gels were determined, and are presented in the ESI.† The porosity was measured by mercury intrusion porosimetry, and by cyclohexane uptake on the dried samples.<sup>8</sup>

The mechanical compression tests were performed on an Instron 6025 (Instron, USA). The swollen cylindrical samples approx. 5 mm in height were compressed in a solvent trap at a rate of  $1\text{ mm min}^{-1}$ . The compressive moduli of the cryogels were calculated from the slope of the compression curves (0.5–3.0% strain).

### *In vitro* evaluation of cell attachment, morphology, viability and chondrogenesis on the cryogels

**Preparation of cryogel samples for cell culture studies.** Cryogels polymerized in the form of cylinders were cut into 2 mm slices and were kept in PBS. All the samples were sterilized by autoclaving at  $121\text{ }^{\circ}\text{C}$  for 15 min (autoclave Tuttnauer, the

Netherlands). Afterwards, the cryogel slices were transferred to 24-well plates with the cultivation medium (DMEM supplemented with 10% FBS,  $100\text{ U mL}^{-1}$  penicillin and  $100\text{ mg mL}^{-1}$  streptomycin) for 24 hours at  $37\text{ }^{\circ}\text{C}$  in a  $\text{CO}_2$  incubator (Steri-Cycle™  $\text{CO}_2$  Incubator HEPA Class100, Thermo Fisher Scientific, USA).

**Isolation, culture, characterisation and seeding of dental pulp stem cells.** Human dental pulp stem cells (hDPSCs) were collected from human permanent teeth of healthy patients (11–18 years of age). The teeth were immediately placed in sterilized physiological saline and were transferred to the laboratory. The procedure for isolating and characterizing the cells is described in detail in the ESI.† The human DPSCs were seeded onto sterilized cryogel scaffolds with initial cell seeding concentrations of 50 000 cells for each sample. The cultivation medium was replaced by a chondrogenic medium (DMEM-high glucose,  $4.5\text{ g L}^{-1}$ ) supplemented with 100 unit per mL of penicillin/streptomycin, 1% ITS+ Premix, 1% FBS,  $40\text{ }\mu\text{g mL}^{-1}$  of L-proline, 2 mM of sodium pyruvate,  $50\text{ }\mu\text{g mL}^{-1}$  of L-ascorbic acid, 100 nM of dexamethasone and  $10\text{ ng mL}^{-1}$  of rhTGF- $\beta$ 1 on the third day of incubation. The culture medium was changed every 48 h.

**Cell viability assay.** A LIVE/DEAD<sup>®</sup> assay reagent was prepared with the addition of  $4\text{ }\mu\text{M}$  EthD-1 and  $2\text{ }\mu\text{M}$  calcein-AM in PBS. The cryogels seeded with the cells were washed with PBS twice before adding the assay reagent. They were then incubated at room temperature for 30–45 minutes in the dark. The reagents were removed, and a washing step with PBS was performed twice. This procedure was applied for 1, 10, 20 and 30 days of incubation. The samples were maintained in PBS until imaging with the use of a fluorescent microscope. To assess the cell viability, three different zones were processed, using the ImageJ software, to calculate the number of green and red spots. The ratio (cell-viability percentage) of the number of live cells to the number of total cells was calculated.

**Immunofluorescence staining of hDPSCs.** Cell seeded cryogel samples were washed twice with PBS between each addition of the solution. The samples were first fixed in a solution of 3.7% formaldehyde for 30 minutes at room temperature (RT), then permeabilized in 0.1% Triton X-100 for 5 minutes at RT, and incubated in 3% FBS for 10 minutes at RT to block non-specific binding. For morphological analysis (F-actin staining), the samples were incubated in phalloidin solution (1:100 dilution) at RT in the dark for 1 hour, and were then stained in DAPI solution (1:1000 dilution) at RT in the dark for 15 minutes. They were transferred to empty wells and then ProLong<sup>®</sup> Gold Antifade Mountant was added. For differentiation, the samples were incubated with a primary antibody against collagen type 2 (COL2A1) and aggrecan (AGC) (1:500 dilution) for 1 hour at RT, and were then incubated with secondary antibodies conjugated to Alexa Fluor<sup>®</sup> 488 and Alexa Fluor<sup>®</sup> 647 for 1 hour at RT. Between each addition of antibodies, the samples were washed twice with PBS. Finally, the samples were stained in DAPI solution and were stored at  $4\text{ }^{\circ}\text{C}$  until they were examined *via* confocal microscopy (ZEISS LSM 700, Germany).

**hDPSC proliferation by the MTS assay.** Following cell seeding, the number of living cells on the scaffolds throughout 30 days of

incubation was determined by the MTS assay (CellTiter 96<sup>®</sup>). The cell seeded cryogel samples were transferred into a new 24-well plate and were washed with PBS (pH = 7.4). Low glucose DMEM was mixed with the MTS assay reagent at a ratio of 5:1. The mixture was added to each scaffold in equal amounts and was incubated at 37 °C in a CO<sub>2</sub> incubator. After 2 h of incubation, the absorbance was measured at 490 nm using an Elisa Plate Reader (Bio-Tek Elx800, USA). The absorbance values were converted to the number of cells, using the slope of the calibration curve (Fig. S3, ESI†).

**Statistical analysis.** In the MTS assay, at least triplicate cell experiments were performed. One-way analysis of variance followed by Tukey's HSD multiple comparison tests was used to compare more than two groups. Probability  $P < 0.05$  was considered significant. All the values are reported as the mean and standard error of the mean.

## Conclusions

Two types of cryogels based on a synthetic poly( $\alpha$ -amino acid), namely poly[N<sup>5</sup>-(2-hydroxyethyl)-L-glutamine-*stat*-N<sup>5</sup>-(2-methacryloyloxy-ethyl)-L-glutamine] (PHEG-MA), were prepared with a similar morphology of the interconnected macropores, but with a significant difference in the compressive moduli (1.7 vs. 20.9 kPa). These gels were modified with a cell-adhesion peptide sequence, RGDS, using the azid-alkyne "click"-reaction. The gels were subjected to a biological evaluation of their potential to support the proliferation and chondrogenic differentiation of human dental pulp stem cells (hDPSCs). It was shown that the RGDS modification of the cryogels had a moderate influence on the initial attachment of the hDPSCs on the first day of incubation, and had a progressive influence on their proliferation after 10 days of incubation. Immunofluorescence staining for collagen type 2 and aggrecan proved that p(AA)-based cryogels supported the differentiation of the hDPSC into chondrocytes. Better cell proliferation was detected on the high modulus samples than on the low modulus samples at a later stage of incubation, already reflecting the progress of differentiation. The PHEG-based hydrogels were found to have good biocompatibility and also potential for supporting the chondrogenesis of hDPSCs.

## Conflicts of interest

There are no conflicts to declare.

## Acknowledgements

The *in vitro* studies were funded by Yeditepe University, Istanbul, Turkey. Part of this research was carried out within the framework of the CEITEC 2020 (LQ1601) project, with financial support from the Ministry of Education, Youth and Sports of the Czech Republic under the National Sustainability Programme II. We would also like to thank Dr V. Proks for determining the average molecular weight of the polymeric precursor of the gels, Ms D. Kalasová and Mr J. Dvořák for their help with the analysis

of the nanotomography data, Ms H. Hlídková for analysing the samples by mercury intrusion porosimetry, Mr Z. Tesař for technical support, and Mr J. Hodan for his help with the measurements of the compression moduli of the cryogels.

## Notes and references

- 1 C. Madeira, A. Santhagunam, J. B. Salgueiro and J. M. S. Cabral, *Trends Biotechnol.*, 2015, **33**, 35.
- 2 K. Y. Lee and D. J. Mooney, *Chem. Rev.*, 2001, **101**, 1869.
- 3 J. L. Drury and D. J. Mooney, *Biomaterials*, 2003, **24**, 4337.
- 4 N. Annabi, J. W. Nichol, X. Zhong, Ch. Ji, S. Koshy, A. Khademhosseini and F. Dehghani, *Tissue Eng., Part B*, 2010, **16**, 371.
- 5 K. Whang, K. E. Healy, D. R. Elenz, E. K. Nam, D. C. Tsai, C. H. Thomas, G. W. Nuber, F. H. Glorieux, R. Travers and S. M. Sprague, *Tissue Eng.*, 1999, **5**, 35.
- 6 M. C. Wake, C. W. Patrick Jr. and A. G. Mikos, *Cell Transplant.*, 1994, **3**, 339.
- 7 Y.-Ch. Chiu, M.-H. Cheng, H. Engel, S.-W. Kao, J. C. Larson, S. Gupta and E. M. Brey, *Biomaterials*, 2011, **32**, 6045.
- 8 T. Sedlacik, V. Proks, M. Slouf, M. Duskova-Smrckova, H. Studenovska and F. Rypacek, *Biomacromolecules*, 2015, **16**, 3455.
- 9 V. I. Lozinsky, Russ, *Chem. Rev.*, 2002, **71**, 489.
- 10 F. M. Plieva, A. Kumar, Y. I. Galaev and B. Mattiasson, in *Advanced Biomaterials: Fundamentals, Processing and Applications*, ed. B. Basu, D. S. Katti and A. Kumar, John Wiley & Sons, Inc., Hoboken, NJ, 1st edn, 2009, p. 499.
- 11 V. I. Lozinsky and O. Okay, in *Polymeric Cryogels, Macroporous Gels with Remarkable Properties*, Advances in Polymer Science, ed. O. Okay, Springer: Switzerland, 1st edn, 2014, vol. 263, p. 49.
- 12 K. R. Hixon, T. L. Scott and A. Sell, *Acta Biomater.*, 2017, **62**, 29–41.
- 13 C. Mu, F. Liu, Q. Chen, H. Li, B. Wu, G. Zhang and W. Lin, *Macromol. Mater. Eng.*, 2010, **295**, 100–107.
- 14 S. Van Vlierberghe, V. Cnudde, P. Dubrue, B. Masschaele, A. Cosijns, I. De Paepe, P. J. S. Jacobs, L. Van Hoorebeke, J. P. Remon and E. Schacht, *Biomacromolecules*, 2007, **8**, 331–337.
- 15 L. Elowsson, H. Kirsebom, V. Carmignac, M. Durbeej-Hjalt and B. Mattiasson, *J. Mater. Sci.: Mater. Med.*, 2012, **23**, 2489–2498.
- 16 F. Ak, Z. Oztoprak, I. Karakutuk and O. Okay, *Biomacromolecules*, 2013, **14**, 719–727.
- 17 V. I. Lozinsky, M. D. Damshkaln, K. O. Bloch, P. Vardi, N. V. Grinberg, T. V. Burova and V. I. Grinberg, *J. Appl. Polym. Sci.*, 2008, **108**, 3046–3062.
- 18 G. L. Georgiev, B. Trzebicka, B. Kostova and P. D. Petrov, *Polym. Int.*, 2017, **66**, 1306–1311.
- 19 H. Kirsebom, M. R. Aguilar, J. San Roman, M. Fernandez, M. A. Prieto and B. Bondar, *J. Bioact. Compat. Polym.*, 2007, **22**, 621–636.
- 20 J. Wu, Q. Zhao, Ch. Lian and T. Xie, *Soft Matter*, 2013, **9**, 11136–11142.

- 21 S. Bhat, A. Tripathi and A. Kumar, *J. R. Soc., Interface*, 2011, **8**, 540–554.
- 22 N. Bölgen, Y. Yang, P. Korkusuz, E. Güzel, A. J. El Haj and E. Pişkin, *J. Tissue Eng. Regener. Med.*, 2011, **5**, 770–779.
- 23 D. Singh, A. Tripathi, V. Nayak and A. Kumar, *J. Biomater. Sci., Polym. Ed.*, 2011, **22**, 1733–1751.
- 24 D. Zhou, S. Shen, J. Yun, K. Yao and D. Q. Lin, *Front. Chem. Sci. Eng.*, 2012, **6**, 339–347.
- 25 T. Kutlusoy, B. Oktay, N. K. Apohan, M. Süleymanoğlu and S. E. Kuruca, *Int. J. Biol. Macromol.*, 2017, **103**, 366–378.
- 26 M. V. Konovalova, P. A. Markov, E. A. Durnev, D. V. Kurek, S. V. Popov and V. P. Varlamov, *J. Biomed. Mater. Res., Part A*, 2017, **105A**, 547–556.
- 27 A. Srivastava and A. Kumar, *J. Mater. Sci.: Mater. Med.*, 2010, **21**, 2937–2945.
- 28 M. Andac, F. M. Plieva, A. Denizli, I. Y. Galaev and B. Mattiasson, *Macromol. Chem. Phys.*, 2008, **209**, 577–584.
- 29 X.-L. Sun, W.-D. He, J. Li, L.-Y. Li, B.-Y. Zhang and T.-T. Pan, *J. Polym. Sci., Part A: Polym. Chem.*, 2009, **47**, 6863–6872.
- 30 P. Perez, F. Plieva, A. Gallardo, J. S. Roman, M. R. Aguilar, I. Morfin, F. Ehrburger-Dolle, F. Bley, S. Mikhailovsky, I. Y. Galaev and B. Mattiasson, *Biomacromolecules*, 2008, **9**, 66–74.
- 31 H. Studenovska, P. Vodicka, V. Proks, J. Hlucilova, J. Motlik and F. Rypacek, *J. Tissue Eng. Regener. Med.*, 2010, **4**, 454.
- 32 T. J. Deming, *Wiley Interdiscip. Rev.: Nanomed. Nanobiotechnol.*, 2014, **6**, 283.
- 33 J. Svobodova, V. Proks, O. Karabiyik, A. C. C. Koyuncu, G. T. Kose, F. Rypacek and H. Studenovska, *J. Tissue Eng. Regener. Med.*, 2015, **11**, 831–842.
- 34 S. J. Shirbin, F. Karimi, N. J.-A. Chan, D. E. Heath and G. G. Qiao, *Biomacromolecules*, 2016, **17**, 2981.
- 35 H. R. Dickinson, A. Hiltner, D. F. Gibbons and J. M. Anderson, *J. Biomed. Mater. Res.*, 1981, **15**, 577.
- 36 H. R. Dickinson and A. Hiltner, *J. Biomed. Mater. Res.*, 1981, **15**, 591.
- 37 T. Hayashi, Y. Tabata and A. Nakajima, *Polym. J.*, 1985, **17**, 463.
- 38 H. C. Chiu, P. Kopeckova, S. S. Deshmane and J. Kopecek, *J. Biomed. Mater. Res.*, 1997, **34**, 381.
- 39 J. Pytela, V. Saudek, J. Drobnik and F. Rypacek, *J. Controlled Release*, 1989, **10**, 17.
- 40 J. Pytela, J. Jakes and F. Rypacek, *Int. J. Biol. Macromol.*, 1994, **16**, 15.
- 41 T. Sedlacik, H. Studenovska and F. Rypacek, *J. Mater. Sci.: Mater. Med.*, 2011, **22**, 781.
- 42 M. Tatullo, M. Marrelli, K. M. Shakesheff and L. J. White, *J. Tissue Eng. Regener. Med.*, 2015, **9**, 1205.
- 43 J. Liu, F. Yu, Y. Sun, B. Jiang, W. Zhang, J. Yang, G.-T. Xu, A. Liang and S. Liu, *Stem Cells*, 2015, **33**, 627.
- 44 R. Patil, B. M. Kumar, W.-J. Lee, R.-H. Jeon, S.-J. Jang, Y.-M. Lee, B.-W. Park, J.-H. Byun, Ch.-S. Ahn, J.-W. Kim and G.-J. Rho, *Exp. Cell Res.*, 2014, **320**, 92.
- 45 M. Akhmanova, E. Osidak, S. Domogatsky, S. Rodin and A. Domogatskaya, *Stem Cells Int.*, 2015, **15**, 167025.
- 46 P. A. Kenny, Y. L. Lee, C. A. Myers, R. M. Neve, J. R. Semeiks, P. T. Spellman, K. Lorenz, A. H. Lee, M. H. Barcellos-Hoff, O. W. Petersen, J. W. Gray and M. J. Bissell, *Mol. Oncol.*, 2007, **1**, 84.
- 47 R. Delaine-Smith and G. Reilly, Stem Cell Regulators, in *Vitamins & Hormones 87*, ed. G. Litwack, Academic Press, 1st edn, 2011, p. 417.
- 48 A. J. Engler, S. Sen, H. L. Sweeney and D. E. Discher, *Cell*, 2006, **126**, 677.
- 49 H. Lv, L. Lisha Li, M. Sun, Y. Zhang, L. Chen, Y. Rong and Y. Li, *Stem Cell Res. Ther.*, 2015, **6**, 103.
- 50 P. B. Welzel, J. Friedrichs, M. Grimmer, S. Vogler, U. Freudenberg and C. Werner, *Adv. Healthcare Mater.*, 2014, **3**, 1849.
- 51 H. Mackova, V. Proks, D. Horak, J. Kucka and M. Trchova, *J. Polym. Sci., Part A: Polym. Chem.*, 2011, **49**, 4820.
- 52 V. Proks, J. Jaros, O. Pop-Georgievski, J. Kucka, S. Popelka, P. Dvorak, A. Hampl and F. Rypacek, *Macromol. Biosci.*, 2012, **12**, 1232.
- 53 Ch. W. Tornøe, C. Christensen and M. Meldal, *J. Org. Chem.*, 2002, **67**, 3057.
- 54 V. V. Rostovtsev, L. G. Green, V. V. Fokin and K. B. Sharpless, *Angew. Chem.*, 2002, **114**, 2708.
- 55 S. Caglio and P. G. Righetti, *Electrophoresis*, 1993, **14**, 554–558.

PAPER [XXVI]

# The 3D imaging of mesenchymal stem cells on porous scaffolds using high-contrasted x-ray computed nanotomography

L. VOJTOVÁ\*, T. ZIKMUND\*, V. PAVLIŇÁKOVÁ\* , J. ŠALPLACHTA\*, D. KALASOVÁ\*, E. PROSECKÁ†, J. BRTNÍKOVÁ\*, J. ŽÍDEK\*, D. PAVLIŇÁK‡ & J. KAISER\*

\*CEITEC, Brno University of Technology, Brno, Czech Republic

†Institute of Experimental Medicine ASCR v.v.i., Prague, Czech Republic

‡CEPLANT, Department of Physical Electronics, Masaryk University, Brno, Czech Republic

**Key words.** Biopolymeric scaffold, mesenchymal stem cells, SEM/EDX, tissue engineering, X-ray computed nanotomography.

## Summary

This study presents an X-ray computed nanotomography (nano-CT) based, high-resolution imaging technique. Thanks to a voxel resolution of 540 nm, this novel technique is suitable for observing the 3D morphology of soft biopolymeric scaffolds seeded with stem cells. A sample of highly porous collagen scaffold seeded with contrasted mesenchymal stem cells (MSC) was investigated by using lab-based nano-CT. The whole volume of the sample was analysed without its destruction. To evaluate the potential of nano-CT, a comparison measurement was done using a standard microscopy technique. Scanning electron microscopy (SEM) combined with energy dispersive X-ray analysis (EDX) established an extension and local accumulation of the contrasting agent – heavy metallic osmium tetroxide. The presented imaging technique is novel as it will help to understand better the behaviour of cells while interacting with three-dimensional biomaterials. This is crucial for both experimental and clinical tissue engineering applications in order to limit the risk of uncontrolled cell growth, and potentially tumour formation.

## Introduction

In recent years, some resorbable porous cell and drug carriers, generally named scaffolds, which are based on biopolymer composites, have been developed. These scaffolds are used with successful preclinical results for a treatment of bone and cartilage by applying tissue engineering methods (Prosecká *et al.*, 2011; Prosecká *et al.*, 2015). It has been confirmed that namely collagen-based 3D porous scaffolds represent an ideal matrix for the deposition of cells such as mesenchymal stem cells (MSC) or already differentiated chondrocytes. Even

though the scaffolds were implanted into a damaged tissue, cell growth continued as in common living tissue (Van der Rest & Garrone, 1991; Jančář *et al.*, 2009; Nečas *et al.*, 2010).

The morphology of porous biopolymer scaffolds is usually observed using scanning electron microscopy (SEM); however, SEM micrographs enable to visualise only two-dimensional (2D) images of fractured surfaces. The real three-dimensional (3D) shape and connectivity of pores cannot be imaged or quantified without using stereology. Despite the steady progress in the field of electron microscopy, polymeric and ceramic scaffolds have to be coated with an electric conductive layer, which make the technique destructive especially if high beam intensity is needed. However, for both *in vitro* and *in vivo* tests or for clinical trials it is necessary to know the exact structure of pore network before and also after the implantation within the responses of living cells. Therefore, a nondestructive characterisation technique is required for a quantification. Moreover, 3D imaging and quantification of tissue regeneration using degradable polymer scaffolds is a useful and desirable part of every bio-technological research.

The most common 3D imaging method used for examining cells proliferated in the artificially created scaffolds is confocal reflection fluorescence microscopy (Moore *et al.*, 2004; Oliveira *et al.*, 2007; Oliveira *et al.*, 2010). However, a limited depth resolution of about 300  $\mu\text{m}$ , cell's invasive staining and a requirement of substrate transparency prevent from using this method for larger opaque tissue engineering constructs. Other common methods for measuring the cell presence include the colorimetric and fluorometric assays for enzymes (dehydrogenase), proteins (BCA), RNA or DNA (PicoGreen assay). The main disadvantage of these assays is the missing information about the cell distribution in the whole volume of the sample. The 3D real-time observation of live cells' properties in scaffold's microenvironments, such as morphology, motility and migration using multimodal holographic microscopy

Correspondence to: T. Zikmund, CEITEC, Brno University of Technology, Purkyňova 656/123, 612 00 Brno, Czech Republic. Tel: +420 541 142 846; email: tomas.zikmund@ceitec.vutbr.cz

(Q-Phase microscope), enable a quantitative measurement of cell mass movement (Collaková *et al.*, 2015, Kollarova *et al.*, 2015). The 3D real time observation methods are less known but very advanced. There is no need of the cell contrasting; however, the scaffold has to be transparent. Moreover, the method does not provide any information about the scaffolds' structure.

Due to the recent progress in the 3D imaging methods and image analysis strategies, X-ray high-resolution micro focus computed tomography (micro-CT) has been commonly applied as a nondestructive technique for visualising the scaffolds' interior by providing quantitative information of scaffolds' 3D morphology as well as of bone ingrowth after in vivo scaffold implantation (Yang *et al.*, 2008; Komlev *et al.*, 2009; Cedola *et al.*, 2014; Sun *et al.*, 2014). CT has been used to scan hard tissues (Taboas *et al.*, 2003; Hofmann *et al.*, 2007; Mather *et al.*, 2008). As for soft tissues and tissue replacements, their scanning of soft tissues and tissue replacements is more complex, due to their low linear attenuation coefficient (Momose *et al.*, 1996). In comparison with hard tissue objects, the weak contrast of soft biological materials in CT has contributed to the phase contrast imaging technique development (Bech *et al.*, 2009; Kalasová *et al.*, 2016). Synchrotron radiation-based CT systems provide better phase contrast because the synchrotron source generates an X-ray with high spatial coherence and high flux, which has been used for an investigation of cells in the extracellular matrix (Albertini *et al.*, 2009; Giuliani *et al.*, 2014). Gros *et al.* (2005) compared various types of X-ray microscopes for synchrotron radiation which could be used for an imaging of, for example, yeast or *Escherichia coli*. Schneider *et al.* (2002) focused on the visualisation of immune-gold labelled *Drosophila melanogaster* cells using cooling capillary for the sample. A study published by Larabell & Gross (2004) describes 3D reconstructions of *Saccharomyces cerevisiae* using photon energies just below the oxygen edge (i.e. 517 eV). Synchrotron-based nano-CT has been used for a calcium distribution in coccolithophores (Sun *et al.*, 2014). The synchrotron imaging quality is exceptional; however, the method's availability is restricted. Along with the recent development of X-ray micro and nanofocus tubes and X-ray detectors, tomographic imaging of biomaterials becomes available also with laboratory sources. Lab-based CT enables an observation of structures with a voxel resolution from micron (micro-CT) to submicron (nano-CT). The phase contrast effect might be observed also with laboratory nano-CT devices (Kaiser *et al.*, 2011). Khoury *et al.* (2015) compared two tomographic lab-based systems, micro-CT and nano-CT. Among others, they showed that these systems enable measurements with various resolutions implemented on object size in the range coming from mouse organ down to cellular level. Nano-CT technique was also utilised for the visualisation of cell-free soft collagen-based scaffolds (Židek *et al.*, 2016) or hard titanium alloy scaffolds with periosteum-derived cells (Papantoniou *et al.*, 2014).

Unfortunately, the aforementioned studies did not provide a simultaneous visualisation of both soft scaffold environment and MSC due to their small size in the range from 10 to 35  $\mu\text{m}$  (Ge *et al.*, 2014; Kampschulte *et al.*, 2016). Moreover, a 3D visualisation of MSC seeded on collagen-based scaffolds done by using CT imaging methods depends on choosing the most suitable contrast agent. The reason is that some of the agents, such as collagen and fibrin, are specifically bonded to connective (Balint *et al.*, 2000; Metscher, 2009; Herzog *et al.*, 2013; Tesařová *et al.*, 2016).

In this study, we used a high-resolution, high-contrast X-ray microscope Rigaku Nano3DX with an ability to deliver 3D nano-CT images of relatively large samples at a high voxel resolution down to 270 nm. The Nano3DX enables to change the target, meaning the X-ray wavelength, and sample-detector distance. Thanks to this variability it is possible to some extent to make an experimental setup suitable for phase contrast imaging. However, the following conditions must be fulfilled: avoiding geometrical unsharpness due to the finite focal spot size of the X-ray tube (Lubberts & Rossmann, 1967), imaging in an edge-detection regime (Baruchel, 2000), maintaining a sufficient degree of X-ray tube coherency (Wu & Liu, 2007). Phase contrast imaging is a CT imaging method suitable for light biological materials which do not have a sufficient absorption contrast. However, in this work osmium tetroxide X-ray opaque staining (Hildore *et al.*, 2007) has to be used in order to visualise MSCs seeded on porous collagen scaffold. Experimental conditions were set to meet the conditions' requirements necessary for phase contrast imaging. The phase contrast effects were utilised for edge-enhancement. This novel 3D imaging method helps to understand the biomaterial/cell interactions in the whole volume, which is applicable in cell biology, tissue engineering and modern medicine.

## Results

Prior to the nano-CT visualisation using X-ray microscope, the SEM equipped with an energy dispersive X-ray (EDX) for the elemental analysis was used to characterise MSCs proliferated on collagen scaffolds (Fig. 1A). To enhance the contrast and MSCs distinction from the collagen matrix in the nano-CT scan, the cells seeded on collagen scaffold were fixed at day 21. Consequently, their continuous proliferation throughout the scaffold followed by staining with  $\text{OsO}_4$  was seen. Elemental distribution of osmium confirmed our first hypothesis that osmium is spread not only on the MSCs surface but also partly on the entire scaffold surface as it can be seen in Figure 1. However, the increased osmium concentration was predominantly detected on cells' surface (Figs. 1B and C, respectively). Different concentration of  $\text{OsO}_4$  (0.1, 0.5 and 1.0 wt %) led to different absorbing properties of MSCs and scaffolds in nano-CT. In this paper we present the optimal  $\text{OsO}_4$  concentration equal to 1 wt %.

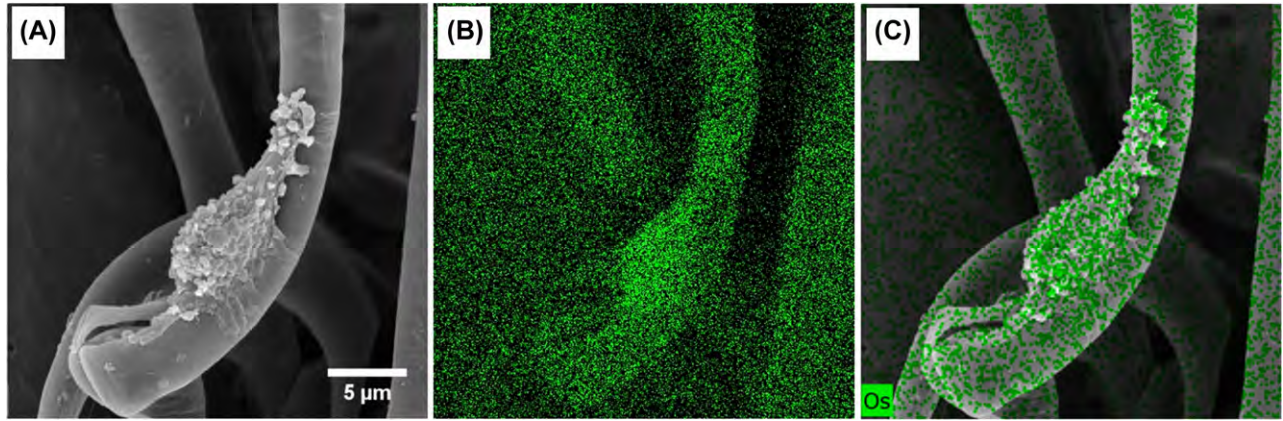


**Fig. 1.** (A) 2D SEM image of collagen fibre in scaffold with adhered MSC, (B) EDX mapping analysis of osmium distribution in the surface of the specimen, (C) EDX mapping analysis of osmium distribution in the surface of the specimen merged with SEM image as a substrate.

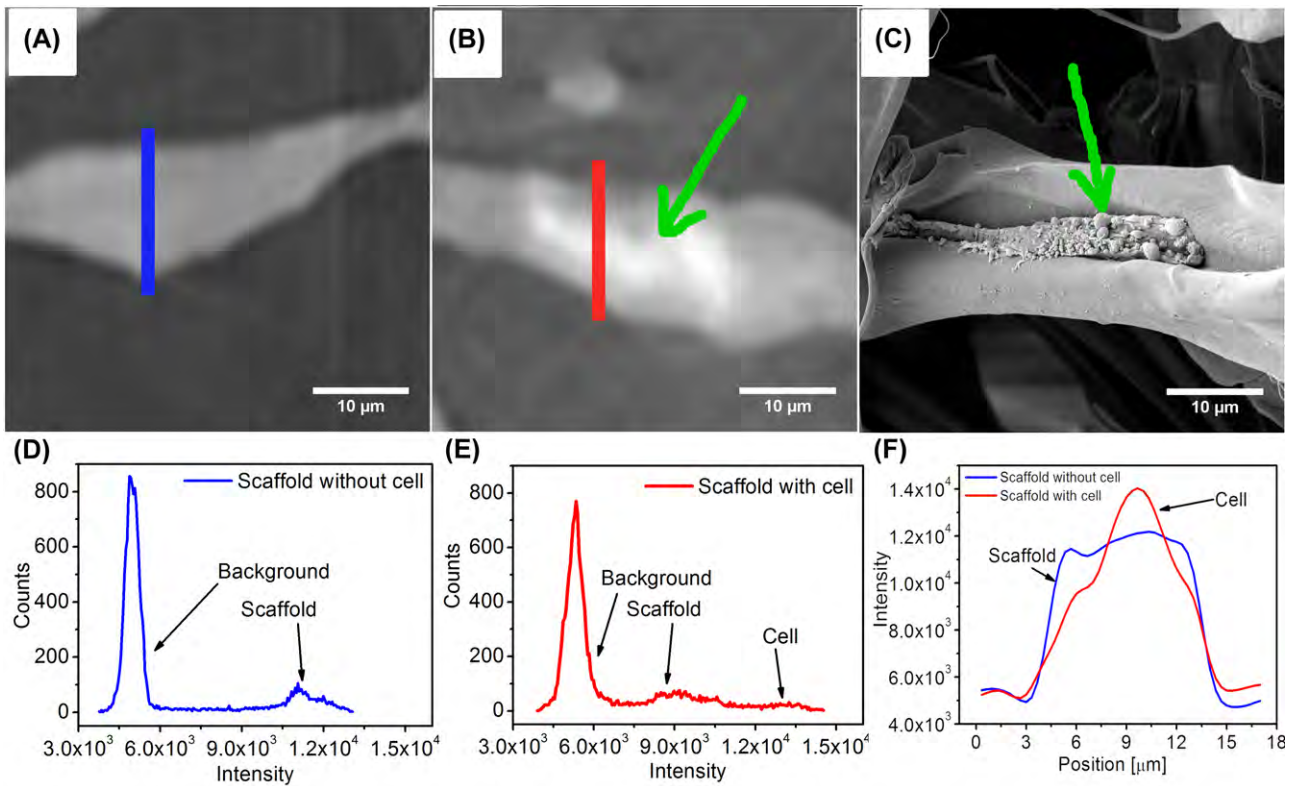


**Fig. 2.** Collagen scaffold seeded with MSCs integrated inside of the collagen scaffold structure: (A) selected nano-CT slice of collagen fibre without cell presence with labelled blue area for line profile analysis – intersection from CT slice with scaffold structure without cells, (B) a slice from nano-CT including MSCs (light area) inside the scaffold structure with labelled red area for line profile analysis – intersection from CT slice with scaffold structure with cells, (C) an appropriate image from scanning electron microscopy. Green arrow shows the cell. CT images were magnified according to SEM scale. (D) Histogram of grey levels for Figure 2(A), (E) a histogram of grey levels for Figure 2(B) and (F) result of line profile analysis.

Thanks to the increased osmium concentration on the MSC surface, we detected higher intensities of the MSCs compared to collagen scaffold in nano-CT data (Figs. 2A, B). As it is obvious, reference sample was homogeneously visualised by grayscale through its volume (Fig. 2A). The sample showed a contour of

collagen fibril. In comparison with the reference sample, the tomographic slice of the seeded scaffold included light areas inside the scaffold structure (Fig. 2B). The brighter area (green arrow) represents a cell separated from the collagen scaffold. These areas were caused by an increased  $\text{OsO}_4$  concentration

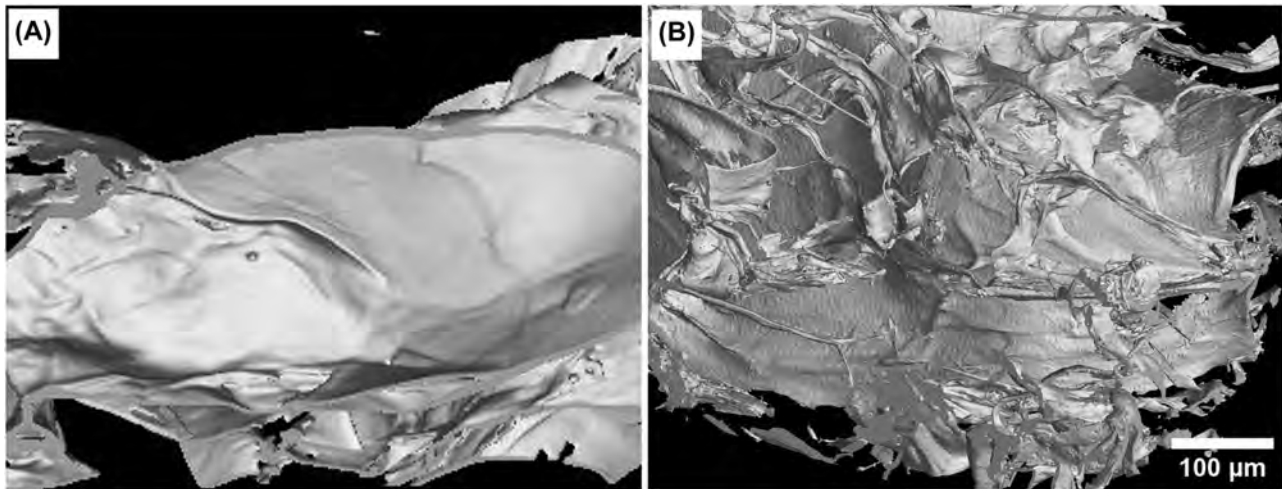


Fig. 3. The comparison of the pure collagen scaffold without MSCs (A) and the collagen scaffold seeded with MSCs at the same magnification (B).

in MSCs. Both SEM and EDX confirmed that the MSC adherent on the fibre inside the collagen scaffold (see supplementary material S1) corresponded with the light area of tomographic slice. A cell from the same sample was visualised by using scanning electron microscopy with a fine resolution (Fig. 2C). The shape and size of the cell detected in Figure 2(B) is similar to the cell obtained from SEM. Figures 2(D)–2(F) represent histograms of gray levels and intensity profile to better visualise the  $\text{OsO}_4$  presence in cells.

The Figure 2 also compares visualisations of 2D projection of samples scanned by nano-CT and SEM. The quality of SEM visualisation is given by high resolution which cannot be reached by nano-CT. On the other hand, the nano-CT scan contains information about 3D structure of the sample. The reconstruction of object from 3D data enables us to improve the visualisation from Figure 2(B) (presented below).

The advantage of SEM is a possibility to visualise the cell structure details. Contrary to this, at nano-CT visualisation results in the cell shape as well as the volume information of cell morphology and the cell distribution within the scaffold. This is important for the investigation of cell growth and proliferation at different time intervals or changes in the scaffold morphology after certain time exposed to the cells. An accurate 3D image of biopolymeric scaffold seeded with MSCs can be reached by a volume reconstruction of nano-CT data (Fig. 3).

In order to confirm the correct distinction of MSCs from the collagen scaffold, we compared the 3D visualisation of the pure collagen cell-free scaffold (Fig. 3A) with the 3D visualisation of the scaffold seeded with MSCs (Fig. 3B). The nano-CT image of pure collagen scaffold exhibited smooth surface without any visible clusters. On the contrary, the surface of the scaffold seeded with the MSCs exhibited uneven morphology consisting of cell arrangements with an average size of around  $20 \mu\text{m}$ .

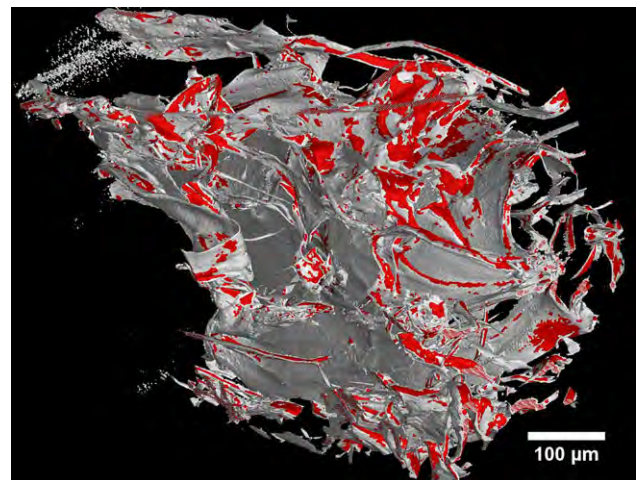


Fig. 4. 3D rendering of MSCs (red colour) proliferated on scaffold surface (grey area). Cells are segmented by simple thresholding method and cover approximately 60% of the visualised object (calculated without air volume).

Based on the previous results showed in Figure 2(B), high intensities of the visualisation in the CT data representing cells were coloured red. The resulting 3D visualisation of the scaffold seeded with MSCs is given in Figure 4 where cells can be recognised more accurately than in the case of 2D slice in Figure 2(B). Therefore, the distribution of cells both within the scaffold volume and on its surface is clearly visible. Based on the 3D rendering it is possible to make the decision whether cells are homogeneously dispersed throughout the scaffold proving their migration and proliferation abilities on a 3D biomaterial substrate.

A more detailed 3D image of the scaffold after the volume rendering exhibited a good adhesion of MSCs to the scaffold surface (Fig. 5). The Figure 5(B) represents the zoomed

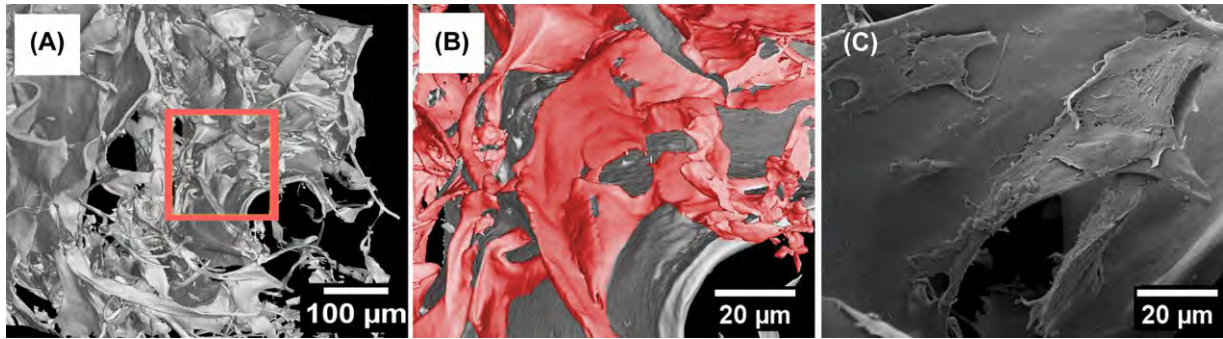


Fig. 5. 3D visualisation of MSCs seeded on the collagen porous scaffold 3D rendering of nano-CT data, (B) detail on the red labelled area from the (A). Cells are manually visualised by red colour. (C) SEM visualisation of MSCs on the collagen scaffold.

rectangle area from Figure 5(A). For a better representation, MSCs were highlighted in red colour (Fig. 5B). Similar MSC size and shape adhering to the scaffold surface were also established by SEM (Fig. 5C).

## Discussion

Nowadays, a simultaneous imaging of 3D substrate structure together with incorporated cells is a great challenge in the field of tissue engineering and cell biology. As we previously proved (Židek *et al.*, 2016), biopolymeric scaffolds could be visualised by a nondestructive 3D nanofocus X-ray CT. However, by this method, we were not able to visualise both biopolymeric scaffold and seeded MSC due to a relatively low voxel resolution of approx.  $4\ \mu\text{m}$ . In this paper, we proposed Nano3DX as a novel 3D nano-CT imaging technique to visualise the whole volume of porous collagen scaffold seeded with MSC stained by osmium with a voxel resolution of about  $540\ \text{nm}$ .

Based on our previous experience from visualising osmium-stained adipose cells on nanofocus CT (unpublished results), we used  $\text{OsO}_4$  to stain MSCs in order to increase their contrast on a novel Rigaku Nano3DX nano-CT and to separate them better from the collagen scaffold image. Similarly to Scheller *et al.* (Scheller *et al.*, 2014) who used osmium tetroxide to stain bone marrow adipose tissue for micro-CT visualisation, we reasoned to stain MSCs by osmium to make cells radio dense and therefore visible on nano-CT.  $\text{OsO}_4$  was firstly introduced in 1952 (Palade, 1952) to identify the structure and function of cell organelles using the electron microscope. Since  $\text{OsO}_4$  is one of the oldest fat stains, unsaturated fat acids like oleic acid (content of phospholipid membranes) are considered to be responsible for the reduction reaction. By an addition of  $\text{OsO}_4$  to the double carbon-to-carbon bonds (contained in fats), osmium becomes soluble and forms a black hydrated reduced osmium dioxide compound (Riemersma, 1968). Moreover, osmium is a heavy metal and is radiodense, which shows a higher contrast while using CT. Thanks to this fact it is possible to visualise stained cells. If a polar group as well as double bonds play a part in the reactions, this might explain some

electron microscopic findings suggesting that during osmium fixation the deposition of osmium dioxide probably occurs at the polar ends of the organic molecules (Riemersma, 1968). Starborg *et al.* (2013) determined collagen fibril size and its self-assembly by TEM 3D images from embryonic tendon prepared by the reduced osmium staining protocol. 3D images have a sufficient contrast to identify individual collagen fibrils and to obtain quantitative information about the cell number, cell shape, cell-cell interactions and collagen fibril number. The contrast is also sufficient to identify collagen fibrils in cell surface fibroblasts.

However, the MSCs seeded the collagen scaffold were difficult to identify because the thickness of flat cells is supposed to be low, depending on the cell adhesion on scaffold, and because the size of a cell is approx. between  $10$  and  $30\ \mu\text{m}$ . Moreover, well-adhered cells appeared to be well attached to the scaffold surface. We distinguished the cells from the collagen matrix based on following criteria. The first criterion was a high osmium concentration inside the cells because  $\text{OsO}_4$  binds better to the cell membrane than to the collagen scaffold during the staining process (Bahr, 1954; Hayes *et al.*, 1963). Moreover, our collagen scaffold is chemically cross-linked via polar end-groups ( $-\text{COOH}$  and  $-\text{NH}_2$ ) resulting in nonpolar amide bond ( $-\text{CONH}$ ) thus limiting active sites for  $\text{OsO}_4$  binding. Obtained results were confirmed by the elemental analysis and tomographic data. From the tomographic slices and 3D rendering, it was evident that cells were well distributed both on the surface and within the scaffold.

The segmentation of scaffold and cells from the background of CT data is sensitive to the selection of optimal threshold value, which make the quantitative analysis still challenging. The application of the phase retrieval algorithm and denoising filter was crucial improvement leading to achieve a high CT data quality. Moreover, as mentioned above, cells exhibited a higher intensity thanks to the higher concentration of osmium in comparison to pure collagen scaffold (Fig. 2). Other criteria for the segmentation of cells were their size and shape. As it has been revealed by both tomographic data and 3D rendering, the MSCs appeared elongated with the average size of around

20  $\mu\text{m}$  that is in a good acceptance with the study reported by Ge *et al.* (2014).

The presented study demonstrated that the nano-CT is a suitable imaging method for observing cells seeded on scaffold through its entire volume. The 3D nano-CT imaging pictures also enable to separate cells from the scaffold which help to understand better following: the methods of seeding 3D porous scaffolds by cells; the behaviour of cells within the scaffold (their adhesion, migration, proliferation and differentiation at different time intervals); changes in the scaffold morphology after certain time exposed to the cells. These issues are essential in the cell biology and modern tissue engineering concept allowing regeneration of both soft and hard tissue (e.g. skin, cartilage or bone) as well as organs (heart, kidney, liver, lung etc.).

## Experimental procedures

### Materials

For the scaffold preparation: certified bovine collagen type I was obtained in a freeze-dried form from VUP medical, Ltd. (Czech Republic). *N*-(3-Dimethylaminopropyl)-*N'*-ethylcarbodiimide hydrochloride (EDC), *N*-hydroxysuccinimide (NHS) (Sigma Aldrich, Germany) and  $\text{Na}_2\text{HPO}_4 \cdot 12\text{H}_2\text{O}$  (Sigma Aldrich) were used as received for scaffold' cross-linking. For the cell culture: Dulbecco's phosphate-buffered saline and heparin were obtained from Zentiva (Czech Republic), Gelofusine from B-Braun (Czech Republic), l-glutamine from PAA (Czech Republic), dexamethasone, ascorbic acid-2-phosphate, and glycerol 2-phosphate disodium salt hydrate from Sigma Aldrich. Fetal bovine serum and penicillin/streptomycin were used as the culture medium.

### Scaffold preparation

Collagen porous scaffolds were prepared with slight modification according to the method developed by our group (Sloviková *et al.*, 2008). Briefly, a 0.5 wt % collagen aqueous solution was prepared by disintegration at 8000 rpm. The solution was subsequently centrifuged for 5 min at  $2879 \times g$  in order to remove air bubbles. Subsequently, a primary freeze-drying process was applied using Martin Christ Epsilon 2–10D lyophilizator at 35°C under 1 mBar for 15 h followed by secondary drying process at 25°C under 0.01 mBar until decreasing  $\Delta p$  up to 10 %. Dry foamed scaffolds were stabilised by treating with EDC/NHS in ethanol solution, washed with  $\text{Na}_2\text{HPO}_4 \cdot 12\text{H}_2\text{O}$ , flushed with distilled water and freeze-dried again. Prepared collagen scaffolds were sterilised using ethylene oxide gas.

### Cell seeding

Our previous study (Prosecká *et al.*, 2015) described an isolation of MSCs from rabbits (age 3 months). The autologous cells in the culture medium were trypsinated, and in the

second passage were seeded on the scaffolds at a density of  $2 \times 10^6 \text{ cm}^{-2}$  in a cultivated 24-well plate modified with the culture medium. The plate was centrifuged at 7G for 20 min and cultured at 37°C in a humidified atmosphere with 5%  $\text{CO}_2$ . MSCs were cultivated on collagen scaffolds for 21 days, fixed and stained. The Ethical Principles and Guidelines for Scientific Experiments on Animals were respected throughout this study. The maintenance and handling of the experimental animals followed EU Council Group Description Directive (2010/63/EU), and the animals were treated in accordance with the principles of Care and Use of Animals.

### Staining

Seeded scaffolds were subsequently rinsed with phosphate-buffered saline (PBS) and transferred to a glutaraldehyde solution (Sigma Aldrich) to fix the cells. Consequently, the cells fixed in scaffolds were stained by immersing in a PBS solution of staining agents, specifically  $\text{OsO}_4$  (Sigma Aldrich). For the purpose of a nano-CT comparative study, cell-free crosslinked collagen scaffolds were also stained with osmium.

### X-ray computed nanotomography

The nano-CT measurement of scaffolds was performed on a RIGAKU Nano3DX device. This machine is equipped with a  $3300 \times 2500 \text{ pixel}^2$  X-ray CCD camera and a Cu rotatory target working at an accelerating voltage of 40 kV and a current of 30 mA. An optical head with  $20\times$  magnification was chosen to reach the field of view at  $0.7 \times 0.9 \text{ mm}^2$ . The sample-detector distance was set to 1.5 mm. This is a satisfactory distance for the X-rays to have a sufficient degree of coherence and to exhibit phase contrast. Binning 2 was set due to a low signal. This determined the linear voxel size of the resulting CT data at  $0.54 \mu\text{m}$ . A total of 800 projections were taken with an exposure time of 10 s.

### Image data analysis

In order to increase the image quality and data utilisation for the subsequent analysis the acquired tomographic projections were processed by the series of image analysis techniques before applying the filtered back projection based tomographic reconstruction process. The projections were filtered using an optimised block wise nonlocal means (NLM) denoising filter (Coupe *et al.*, 2008) and movement artefacts were reduced using a custom developed movement correction technique based on the phase correlation. This resulted in an increase of SNR (signal-to-noise ratio) from 41 to 89 and from 59 to 72 in tomogram domain (data after tomographic reconstruction). An application of phase retrieval algorithm increased the contrast between cell and scaffold structure (see Supplementary material S2) having a positive effect on the subsequent cell segmentation. Nano3DX

generates sufficiently coherent X-rays to observe the phase contrast effects via edge-enhancement (Kaiser *et al.*, 2011). The phase retrieval algorithm was applied on filtered and corrected projections using an ANKPhase (Weitkamp *et al.*, 2011) plugin for ImageJ (Rasband, 2017), which implements algorithm by Paganin (Paganin *et al.*, 2002). Then the projections were reconstructed with the ASTRA Toolbox (Aarle *et al.*, 2016; Aarle *et al.*, 2015). The final analysis and visualisation of scaffold structures with MSCs based on surface determination and global thresholding was accomplished using VGStudio MAX software (Palenstijn *et al.*, 2011), where the volume reconstruction of nano-CT data was done by applying the isosurface volume rendering method. Global thresholding with use of manual selected threshold was applied to carry out a quantitative analysis of cell volume.

#### Scanning electron microscopy (SEM) and elemental analysis (EDX)

Scaffold morphology was investigated employing a scanning electron microscope Tescan Mira 3 (Tescan, Czech Republic). If not specified otherwise, the secondary electron emission mode at 15 kV acceleration voltages was used for all observations. In order to achieve a better resolution, samples were coated with a 20 nm of gold layer. The surface elemental analysis was determined by Energy Dispersive X-ray Spectroscopy (EDX) (Oxford Instruments) and evaluated by Aztec 2.1a software.

#### Author contributions

LV, TZ, VP, DK the interpretation of results; VP, LV, TZ writing the manuscript; VP collagen scaffold preparation; EP cell seeding; JB, DP SEM and EDX analysis; DK nano-CT measurement; JŠ, DK, DP, JŽ image analysis; JK supervisor of the project. All authors read and approved the final manuscript.

#### Acknowledgements

This research was carried out under the project CEITEC 2020 (LQ1601) with financial support from the Ministry of Education, Youth and Sports of the Czech Republic under the National Sustainability Programme II. This research has been also supported by the project CZ.1.05/2.1.00/03.0086 funded by European Regional Development Fund and project LO1411 (NPU I) funded by Ministry of Education, Youth and Sports of Czech Republic as well as support from the Ministry of Health of the Czech Republic under grant number 17–31276A.

#### References

Albertini, G., Giuliani, A., Komlev V., *et al.* (2009) Organization of extracellular matrix fibers within polyglycolic acid-polylactic acid scaffolds analyzed using X-ray synchrotron-radiation phase-contrast micro computed tomography. *Tissue Eng. Part C Methods* **15**, 403–411. <https://doi.org/10.1089/ten.tec.2008.0270>.

Bahr, G.F. (1954) Osmium tetroxide and ruthenium tetroxide and their reactions with biologically important substances: electron stains III. *Exp. Cell Res.* **7**, 457–479. [https://doi.org/10.1016/S0014-4827\(54\)80091-7](https://doi.org/10.1016/S0014-4827(54)80091-7).

Balint, R., Lowe, T. & Shearer, T. (2000) Optimal contrast agent staining of ligaments and tendons for X-ray computed tomography. *PLOS ONE* **11**, e0153552. <https://doi.org/10.1371/journal.pone.0153552>.

Baruchel, J. (2000) *X-Ray Tomography in Material Science*. Hermes Science, Paris. ISBN: 978-2-7462-0115-6.

Bech, M., Jensen, T.H., Feidenhans, R., Bunk, O., David, C. & Pfeiffer, F. (2009) Soft-tissue phase-contrast tomography with an x-ray tube source. *Phys. Med. Biol.* **54**, 2747–2753. <https://doi.org/10.1088/0031-9155/54/9/010>.

Cedola, A., Campi, G., Pelliccia, D., *et al.* (2014) Three dimensional visualization of engineered bone and soft tissue by combined X-ray micro-diffraction and phase contrast tomography. *Phys. Med. Biol.* **59**, 189–201. <https://doi.org/10.1088/0031-9155/59/1/189>.

Collaková, J., Křížová, A., Kollarová, V., Dostál, Z., Slabá, M., Veselý, P. & Chmelík, R. (2015) Coherence-controlled holographic microscopy enabled recognition of necrosis as the mechanism of cancer cells death after exposure to cytopathic turbid emulsion. *J. Biomed. Opt.* **20**, 111213. <https://doi.org/10.1117/1.JBO.20.11.111213>.

Coupe, P., Yger, P., Prima, S., Hellier, P., Kervrann, C. & Barillot, C. (2008) An optimized blockwise nonlocal means denoising filter for 3D magnetic resonance images. *IEEE Trans. Med. Imaging* **27**, 425–441. <https://doi.org/10.1109/TMI.2007.906087>.

Ge, J., Guo, L., Wang, S., Zhang, Y., Cai, T., Zhao, R.C. & Wu, Y. (2014) The size of mesenchymal stem cells is a significant cause of vascular obstructions and stroke. *Stem Cell Rev.* **10**, 295–303. <https://doi.org/10.1007/s12015-013-9492-x>.

Giuliani A., Moroncini, F., Mazzoni, S., *et al.* (2014) Polyglycolic acid-polylactide acid scaffold response to different progenitor cell *in vitro* cultures: A demonstrative and comparative X-ray synchrotron radiation phase-contrast microtomography study. *Tissue Eng. Part C Methods* **20**, 308–316. <https://doi.org/10.1089/ten.TEC.2013.0213>.

Hayes, T.L., Lindgren, F.T. & Gofman, J.W. (1963) A quantitative determination of the osmium tetroxide-lipoprotein interaction. *J. Cell Biol.* **19**, 251–255. <https://doi.org/10.1083/jcb.19.1.251>.

Herzog, F., Clift, M.J.D., Piccapietra, F., Behra, R., Schmid, O., Petri-Fink, A. & Rothen-Rutishauser, B. (2013). Exposure of silver-nanoparticles and silver-ions to lung cells *in vitro* at the air-liquid interface. *Part Fibre Toxicol.* **10**, 1–14. <https://doi.org/10.1186/1743-8977-10-11>.

Hildore, A., Wojtowicz, A. & Johnson, A.W. (2007) Micro-CT based quantification of non-mineralized tissue on cultured hydroxyapatite scaffolds. *J. Biomed. Mater. Res. Part A* **82A**, 1012–1021. <https://doi.org/10.1002/jbm.a.31264>.

Hofmann, S., Hagenmüller, H., Koch, A.M., Müller, R., Vunjak-Novakovic, G., Kaplan, D.L., Merkle, H.P. & Meinel, L. (2007) Control of *in vitro* tissue-engineered bone-like structures using human mesenchymal stem cells and porous silk scaffolds: the origin, evolution, and impact of doi moi. *Biomaterials* **28**, 1152–1162. <https://doi.org/10.1016/j.biomaterials.2006.10.019>.

Jančář, J., Vojtová, L., Nečas, A., Srnc, R., Urbanová, L. & Crha, M. (2009) Stability of collagen scaffold implants for animals with iatrogenic articular cartilage defects. *Acta Vet. Brno* **78**, 643–648. <https://doi.org/10.2754/avb200978040643>.

Kaiser, J., Holá, M., Galiová, M., *et al.* (2011) Investigation of the microstructure and mineralogical composition of urinary calculi fragments by synchrotron radiation X-ray microtomography:

- a feasibility study. *Urol. Res.* **39**, 259–267. <https://doi.org/10.1007/s00240-010-0343-9>.
- Kalasová, D., Zikmund, T. & Kaiser, J. (2016) Phase contrast tomographic imaging of polymer composites. *Materials Structure in Chemistry, Biology, Physics and Technology. Materials Structure*, Vol. **23**, pp. 304–305. Czech and Slovak Crystallographic Association, Czech Republic. ISSN: 1211–5894. <http://www.xray.cz/ms/>
- Kampschulte, M., Langheinrich, A.C., Sender, J., et al. (2016). Nano-computed tomography: technique and applications. *Fortschr Röntgenstr.* **188**, 146–154. <https://doi.org/10.1055/s-0041-106541>.
- Khoury, B.M., Bigelow, E.M., Smith, L.M., Schlecht, S.H., Scheller, E.L., Andarawis-Puri, N. & Jepsen, K.J. (2015) The use of nano-computed tomography to enhance musculoskeletal research. *Connect Tissue Res.* **56**, 106–119. <https://doi.org/10.3109/03008207.2015.1005211>.
- Kollarová, V., Collaková, J., Dostál, Z., Veselý, P. & Chmelík, R. (2015) Quantitative phase imaging through scattering media by means of coherence-controlled holographic microscope. *J. Biomed. Opt.* **20**, 111206. <https://doi.org/10.1117/1.JBO.20.11.111206>.
- Komlev, V.S., Mastrogiacommo, M., Peyrin, F., Cancedda, R. & Rustichelli, F. (2009) X-ray synchrotron radiation pseudo-holotomography as a new imaging technique to investigate angio- and microvasculogenesis with no usage of contrast agents. *Tissue Eng. Part C Methods* **15**, 425–430. <https://doi.org/10.1089/ten.tec.2008.0428>.
- Larabell, C.A. & Legros, M.A. (2004) X-ray tomography generates 3D reconstructions of the yeast, *Saccharomyces cerevisiae*, at 60-nm resolution. *Mol. Biol. Cell* **15**, 957–962. <https://doi.org/10.1091/mbc.E03-07-0522>.
- Le Gros, M.A., Mcdermott, G. & Larabell, C.A. (2005) X-ray tomography of whole cells. *Curr. Opin. Struct. Biol.* **15**, 593–600. <https://doi.org/10.1016/j.sbi.2005.08.008>.
- Lubberts, G. & Rossmann, K. (1967) Modulation transfer function associated with geometrical unsharpness in medical radiography. *Phys. Med. Biol.* **12**, 65–77. <https://doi.org/10.1088/0031-9155/12/1/307>.
- Mather, M.L., Morgan, S.P., White, L.J., Tai, H., Kockenberger, W., Howdle, S.M., Shakesheff, K.M. & Crowe, J.A. (2008). Image-based characterization of foamed polymeric tissue scaffolds. *Biomed. Mater.* **3**, 015011. <https://doi.org/10.1088/1748-6041/3/1/015011>.
- Metscher, B.D. (2009) MicroCT for comparative morphology: simple staining methods allow high-contrast 3D imaging of diverse non-mineralized animal tissues. *BMC Physiol.* **9**, 11–25. <https://doi.org/10.1186/1472-6793-9-11>.
- Momose, A., Takeda, T., Itai, Y. & Hirano, K. (1996) Phase-contrast X-ray computed tomography for observing biological soft tissues. *Nat. Med.* **2**, 473–475. <https://doi.org/10.1038/nm0496-473>.
- Moore, M.J., Jabbari, E., Ritman, E.L., Lu, L., Currier, B.L., Windbank, A.J. & Yaszemski, M.J. (2004) Quantitative analysis of interconnectivity of porous biodegradable scaffolds with micro-computed tomography. *J. Biomed. Mater. Res. A* **71A**, 258–267. <https://doi.org/10.1002/jbm.a.30138>.
- Nečas, A., Plánka, L., Srnec, R., et al. (2010) Quality of newly formed cartilaginous tissue in defects of articular surface after transplantation of mesenchymal stem cells in a composite scaffold based on collagen I with chitosan micro- and nanofibers. *Physiol. Res.* **59**, 605–614. ISSN: 1802–9973.
- Oliveira, A.L., Malafaya, P.B., Costa, S.A., Sousa, R.A. & Reis, R.L. (2007) Micro-computed tomography ( $\mu$ -CT) as a potential tool to assess the effect of dynamic coating routes on the formation of biomimetic apatite layers on 3D-plotted biodegradable polymeric scaffolds. *J. Mater. Sci. Mater. Med.* **18**, 211–223. <https://doi.org/10.1007/s10856-006-0683-8>.
- Oliveira, S.M., Ringshia, R.A., Legeros, R.Z., Clark, E., Yost, M.J., Terracio, L., & Teixeira, C.C. (2010) An improved collagen scaffold for skeletal regeneration. *J. Biomed. Mater. Res. A* **94A**, 371–379. <https://doi.org/10.1002/jbm.a.32694>.
- Paganin, D., Mayo, S.C., Gureyev, T.E. Miller P.R. & Willkins, S.W. (2002) Simultaneous phase and amplitude extraction from a single defocused image of a homogeneous object. *J. Microsc.* **206**, 33–40. <https://doi.org/10.1046/j.1365-2818.2002.01010.x>. ISSN 0022–2720.
- Palade, G.E. (1952) A study of fixation for electron microscopy. *J. Exp. Med.* **95**, 285–298. <https://doi.org/10.1084/jem.95.3.285>.
- Palenstijn, W.J., Batenburg, K.J. & Sijbers, J. (2011) Performance improvements for iterative electron tomography reconstruction using graphics processing units (GPUs). *J. Struct. Biol.* **176**, 250–253. <https://doi.org/10.1016/j.jsb.2011.07.017>.
- Papantoniou, I., Sonnaert, M., Geris, L., Luyten, F.P., Schrooten, J. & Kerckhofs, G. (2014) Three-dimensional characterization of tissue-engineered constructs by contrast-enhanced nanofocus computed tomography. *Tissue Eng. Part C Methods* **20**, 177–187. <https://doi.org/10.1089/ten.tec.2013.0041>.
- Prosecká, E., Rampichová, M., Litvinec, A., et al. (2015) Collagen/hydroxyapatite scaffold enriched with polycaprolactone nanofibers, thrombocyte-rich solution and mesenchymal stem cells promotes regeneration in large bone defect in vivo. *J. Biomed. Mater. Res. A* **103**, 671–682. <https://doi.org/10.1002/jbm.a.35216>.
- Prosecká, E., Rampichová, M., Vojtová, L., et al. (2011) Optimized conditions for mesenchymal stem cells to differentiate into osteoblasts on a collagen/hydroxyapatite matrix. *J. Biomed. Mater. Res.* **99**, 307–315. <https://doi.org/10.1002/jbm.a.33189>.
- Rasband, W.S. (1997–2017) *ImageJ*, U. S. National Institutes of Health. Bethesda, Maryland, USA, <http://imagej.nih.gov/ij/>.
- Riemersma, J.C. (1968) Osmium tetroxide fixation of lipids for electron microscopy. A possible reaction mechanism. *Biochem. Biophys. Acta* **152**, 718–727. [https://doi.org/10.1016/0005-2760\(68\)90118-5](https://doi.org/10.1016/0005-2760(68)90118-5).
- Scheller, E.L., Troiano, N., Vanhoutan, J.N., et al. (2014) Use of osmium tetroxide staining with microcomputerized tomography to visualize and quantify bone marrow adipose tissue *in vivo*. *Methods in Enzymology* (ed. by A. Ormond Macdougald), Vol. **537**, pp. 123–139. Academic Press, Elsevier. ISSN 0076–6879; ISBN 9780124116191.
- Schneider, G., Anderson, E., Vogt, S., Knöchel, C., Weiss, D., Legros, M., & Larabell, C. (2002) Computed tomography of cryogenic cells. *Surf. Rev. Lett.* **9**, 177–183. <https://doi.org/10.1142/S0218625X02001914>.
- Sloviková, A., Vojtová, L. & Jančář, J. (2008) Preparation and modification of collagen-based porous scaffold for tissue engineering. *Chem. Pap.* **62**, 417–422. ISSN: 0366–6352.
- Starborg, T., Kalson, N.S., Lu, Y., Mironov, A., Cootes, T.F., Holmes, D.F. & Kadler, K.E. (2013) Using transmission electron microscopy and 3View to determine collagen fibril size and three-dimensional organization. *Nat. Protoc.* **8**, 433–448. <https://doi.org/10.1038/nprot.2013.086>.
- Sun, S., Yao, Y., Zou, X., et al. (2014) Nano-scale spatial assessment of calcium distribution in coccolithophores using synchrotron-based nano-CT and STXM-NEXAFS. *Int. J. Mol. Sci.* **15**, 23604–23615. <https://doi.org/10.3390/ijms151223604>.
- Taboas, J.M., Maddox, R.D., Krebsbach, P.H. & Hollister, S.J. (2003) Indirect solid free form fabrication of local and global porous, biomimetic

- and composite 3D polymer-ceramic scaffolds. *Biomaterials* **24**, 181–194. [https://doi.org/10.1016/S0142-9612\(02\)00276-4](https://doi.org/10.1016/S0142-9612(02)00276-4).
- Tesařová, M., Zikmund, T., Kaucká, M., Adameyko, I., Jaroš, J., Paloušek, D., Škaroupka, D. & Kaiser, J. (2016) Use of micro computed-tomography and 3D printing for reverse engineering of mouse embryo nasal capsule. *J. Instrum.* **11**, C03006. <https://doi.org/10.1088/1748-0221/11/03/C03006>.
- Van Aarle, W., Palenstijn, W.J., Cant, J., *et al.* (2016) Fast and flexible X-ray tomography using the ASTRA toolbox. *Opt. Express* **24**, 25129–25147. <https://doi.org/10.1364/OE.24.025129>.
- Van Aarle, W., Palenstijn, W.J., De Beenhouwer, J., Altantzis, T.A., Bals, S., Batenburg, K.J. & Sijbers, J. (2015) The ASTRA Toolbox: a platform for advanced algorithm development in electron tomography. *Ultramicroscopy* **157**, 35–47. <https://doi.org/10.1016/j.ultramic.2015.05.002>.
- Van der Rest, M. & Garrone, R. (1991) Collagen family of proteins. *FASEB J.* **5**, 2814–2823.
- Weitkamp, T., Haas, D., Wegrzynek, D. & Rack, A. (2011) ANKAphase: software for single-distance phase retrieval from inline X-ray phase-contrast radiographs. *J. Synchrotron Radiat.* **18**, 617–629. <https://doi.org/10.1107/S0909049511002895>.
- Wu, X. & Liu, H. (2007) Clarification of aspects in in-line phase sensitive X-ray imaging. *Med. Phys.* **34**, 737–743. <https://doi.org/10.1118/1.2431475>.
- Yang, Y., Dorsey, S.M., Becker, M.L., Lin-Gibson, S., Schumacher, G.E., Flaim, G.M., Kohn, J. & Simon, C.G.J. (2008) X-ray imaging optimization of 3D tissue engineering scaffolds via combinatorial fabrication methods. *Biomaterials* **29**, 1901–1911. <https://doi.org/10.1016/j.biomaterials.2007.12.042>.
- Židek, J., Vojtová, L., Abdel-Mohsen, A.M., *et al.* (2016) Accurate micro-computed tomography imaging of pore spaces in collagen-based scaffold. *J. Mater. Sci. Mater. Med.* **27**, 1–18. <https://doi.org/10.1007/s10856-016-5717-2>.

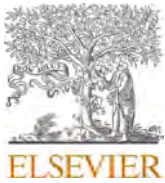
### Supporting Information

Additional supporting information may be found online in the Supporting Information section at the end of the article.

**Supplementary material S1:** (A) Detail of SEM image of MSC adhering on collagen fibre in scaffold (B) EDX mapping analysis of osmium (green colour) and carbon (red colour) in the surface of the sample. Osmium has origin from the contrast agent and carbon comes from the collagen scaffold.

**Supplementary material S2:** A part of CT slice of collagen porous scaffold seeded with MSCs, (A) original data (B) after filtration and application of phase retrieval algorithm.

PAPER [XXVII]



Contents lists available at ScienceDirect

Journal of the Mechanical Behavior of Biomedical Materials

journal homepage: <http://www.elsevier.com/locate/jmbbm>

## On the limits of finite element models created from (micro)CT datasets and used in studies of bone-implant-related biomechanical problems

Petr Marcián<sup>a</sup>, Libor Borák<sup>a,\*</sup>, Tomáš Zikmund<sup>b</sup>, Ladislava Horáčková<sup>c</sup>, Jozef Kaiser<sup>b</sup>, Marek Joukal<sup>c</sup>, Jan Wolff<sup>d,e</sup>

<sup>a</sup> Institute of Solid Mechanics, Mechatronics and Biomechanics, Faculty of Mechanical Engineering, Brno University of Technology, Brno, Czech Republic

<sup>b</sup> CEITEC - Central European Institute of Technology, Brno University of Technology, Czech Republic

<sup>c</sup> Department of Anatomy, Faculty of Medicine, Masaryk University, Brno, Czech Republic

<sup>d</sup> Department of Oral and Maxillofacial Surgery, Division for Regenerative Orofacial Medicine, University Hospital Hamburg-Eppendorf, Hamburg, Germany

<sup>e</sup> Fraunhofer Research Institution for Additive Manufacturing Technologies IAPT, Hamburg, Germany

### ARTICLE INFO

#### Keywords:

Finite element method  
Computational modeling  
Computed tomography  
Image resolution  
Bone tissue  
Mechanical strain

### ABSTRACT

Patient-specific approach is gaining a wide popularity in computational simulations of biomechanical systems. Simulations (most often based on the finite element method) are to date routinely created using data from imaging devices such as computed tomography which makes the models seemingly very complex and sophisticated. However, using a computed tomography in finite element calculations does not necessarily enhance the quality or even credibility of the models as these depend on the quality of the input images. Low-resolution (medical-)CT datasets do not always offer detailed representation of trabecular bone in FE models and thus might lead to incorrect calculation of mechanical response to external loading. The effect of image resolution on mechanical simulations of bone-implant interaction has not been thoroughly studied yet. In this study, the effect of image resolution on the modeling procedure and resulting mechanical strains in bone was analyzed on the example of cranial implant. For this purpose, several finite element models of bone interacting with fixation-screws were generated using seven computed tomography datasets of a bone specimen but with different image resolutions (ranging from micro-CT resolution of 25  $\mu\text{m}$  to medical-CT resolution of 1250  $\mu\text{m}$ ). The comparative analysis revealed that FE models created from images of low resolution (obtained from medical computed tomography) can produce biased results. There are two main reasons: 1. Medical computed tomography images do not allow generating models with complex trabecular architecture which leads to substituting of the intertrabecular pores with a fictitious mass; 2. Image gray value distribution can be distorted resulting in incorrect mechanical properties of the bone and thus in unrealistic or even completely fictitious mechanical strains. The biased results of calculated mechanical strains can lead to incorrect conclusion, especially when bone-implant interaction is investigated. The image resolution was observed not to significantly affect stresses in the fixation screw itself; however, selection of bone material representation might result in significantly different stresses in the screw.

### 1. Introduction

Currently, patient-specific constructs are gaining in popularity, especially in the field of craniomaxillofacial surgery. For instance, in patients undergoing cranioplasty the treatment planning involves thorough clinical diagnostic procedures, 3D tomographic imaging, designing of the patient-specific cranial implant and lastly the fabrication of the implant using additive manufacturing. To date most cranial implants are made of Polyether ether ketone (PEEK) or Polymethyl

methacrylate (PMMA). The implants are initially stabilized using fixation plates and fixation-screws which are typically made of a titanium alloy. The clinical success of such cranial implants depends significantly on the biomechanical performance of the implant fixation. Major role plays the osseointegration of fixation-screws which is histologically similar to that occurring in dental implants (Bolind et al., 2000) and has also similar success rates (>90%), (Miles et al., 2006; Sinn et al., 2011). However, as in dental implants, the loading conditions are crucial in the overall survival rate of cranial implants. Under external loading

\* Corresponding author.

E-mail address: [liborborak@seznam.cz](mailto:liborborak@seznam.cz) (L. Borák).

<https://doi.org/10.1016/j.jmbbm.2021.104393>

Received 23 July 2020; Received in revised form 12 January 2021; Accepted 10 February 2021

Available online 18 February 2021

1751-6161/© 2021 Elsevier Ltd. All rights reserved.

conditions, forces are usually transmitted into the skull bone via the fixation plates and corresponding fixation-screws. A pathological overloading can lead to fixation screw loosening and plate damage and implant loss (Miles et al., 2006). It is extremely difficult to assess the effect of the bone overload and to predict the overall survival rate of such implants. However, this problem can be partially overcome by using finite-element-method-based computational simulations. Such simulations can help clinicians assess the risks associated with bone overloading and furthermore estimate the long-term success rate of patient-specific cranial implants.

The finite element method (FEM) has been used in biomechanics since the 1970's and has ever since proven to be a powerful tool for solving various biomechanical problems (Achour et al., 2011; Wirth et al., 2012). FEM has become the basis of *in silico* trials and its popularity and significance has increased rapidly with the advent of the new millennium (Pappalardo et al., 2018). The reason for this breakthrough can be attributed to the unprecedented computational power which has become available. Furthermore, FEM offers the unique possibility to investigate complex biomechanical systems in ways that are difficult or impossible to do *in vivo* or *in vitro*. Computational models in biomechanics are commonly created using data acquired from X-ray (micro-) computed tomography (micro-CT, CT) scanners or magnetic resonance imaging (MRI). It must be noted that the rapid development of imaging technologies has also greatly contributed to the quality and range of computational simulations. These developments have been pivotal in creating personalized FEM models and for the fabrication of patient-specific implants (Zadpoor and Weinans, 2015). This novel approach is however still in its infancy and despite general optimism one should still bear in mind that computational simulations have limitations that should be recognized and understood. George Box famously expressed these concerns by saying: "All models are wrong, but some are useful." (Box, 1979). This is also true for patient-specific FEM models that are only as good as the input data and assumptions allow them to be.

FEM models are routinely based on data acquired from the imaging devices. The acquired images are subsequently processed in order to obtain 3D surface models in a suitable digital format, e.g. in the standard tessellation language (STL) format. These 3D surface models are further processed to obtain a finite element mesh; sometimes, information about elastic properties of the bone was determined from the very same images using empirical relationships. The final FEM model is then mathematically solved adopting several other simplifying assumptions. Considering that each of these steps depends on many variables that each carry some degree of uncertainty, it is easy to comprehend the concerns about the FEM model credibility outlined above. It has been reported, for instance, that significant differences in the final geometrical accuracy can occur depending on the image processing software used (Huotilainen et al., 2014; Matsiushevich et al., 2018). Besides, the accuracy of the final geometry and thus the computational simulation itself can be affected by the imaging resolution. Another issue associated with the credibility of the FEM models arises in cases where bone to implant interactions are assessed. For instance, in case of cranial implants, the fixation-screws are embedded in the skull and their performance strongly depends on the local quality of the surrounding bone. A knowledge of the bone properties is crucial. More importantly, omission of the trabecular bone architecture in FEM-based computational models can significantly affect simulations of bone-implant performances (Limbert et al., 2010; Marcián et al., 2014; P. Marcián et al., 2018; Wirth et al., 2012; Wolff et al., 2014) and can lead to biased results. Since current medical-CT devices used in clinical settings do not provide images with sufficient resolution to create detailed computational models including the trabecular architecture, simplified computational models without trabeculae are still widely used (Borges Radaelli et al., 2018; Cinel et al., 2018; Korabi et al., 2017; Lee et al., 2018; Pellizzer et al., 2018). However, credibility of such models is questionable.

Although micro-CT images are to date commonly used for FEM

simulations and corresponding micro-FE models are considered to be a "gold standard" for comparisons (Alsayednoor et al., 2018), medical-CT outputs are still taken as input data for clinically-oriented computational models. Therefore, there are two approaches in computational biomechanics: 1. Some studies are carried out using micro-CT-based models that can be experimentally validated with satisfactory results but are somewhat detached from specific clinical problems; 2. Other studies are carried out using medical-CT-based models whose credibility might be challenged due to low resolution of input images and a lack of experimental data. Patient-specific micro-CT cannot be obtained in the clinical studies and, therefore, cannot be compared with medical-CT. However, it can be assumed, that the different resolutions of micro-CT and medical-CT images might lead to different biomechanical assessments of the identical bone-implant system. The impact of the image quality and image data processing on the accuracy of computational simulations has not yet been thoroughly studied. We hypothesize that CT resolution has a significant effect on the outcome of mechanical simulations and might lead to biased biomechanical assessments due to misrepresentation of some specifics of modelled bone. This effect was investigated on the example of a cranial implant fixation. For this purpose, a series of FEM-based computational models of bone-implant assemblies were created using medical-CT and micro-CT images with different resolutions. The models were subsequently used to calculate mechanical quantities in the surrounding bone. Another aim of this study is to point out the limits of the computational models created using the data from medical-CT devices.

## 2. Materials and methods

### 2.1. Tissue sample

The sample of the human tissue was acquired from the Department of Anatomy, Faculty of Medicine, Masaryk University Brno, Czech Republic in full accordance with relevant institutional and legislative requirements (the donor agreed with using of the body for scientific purpose in full accordance with Articles 81(2) and 81(5) of the Act no. 372/2011 Coll., on Health Services valid in the Czech Republic). An approximately  $25 \times 25 \times 10$  mm sample of the bone with adjacent soft tissues (skin, subcutaneous tissue, galea aponeurotica, subgaleal tissue and dura mater) was removed from the parietal region of an 83-year-old deceased male 12 h after death and immediately frozen ( $-18^\circ\text{C}$ ) for 12 h.

The sample included adjacent soft tissue intentionally to better capture the boundaries of bone tissue in subsequent micro-CT scanning (see Fig. 1a). Due to presence of the soft tissues, the contrast between the bone and the surrounding is lower which might enhance the accuracy of the micro-CT-based models.

### 2.2. Micro-CT scanning

12 h after the autopsy, the sample was imaged using a micro-computed tomography scanner (GE phoenix v|tome|x L240, GE Sensing & Inspection Technologies GmbH, Wunstorf, Germany) with a voxel size of  $25 \mu\text{m} \times 25 \mu\text{m} \times 25 \mu\text{m}$  using accelerating voltage at 85 kV, current of microfocus X-ray tube at 150  $\mu\text{A}$  and 400 ms of detector exposure time in each 2700 positions over  $360^\circ$  rotation. A hydroxyapatite phantom (MicroCT-HA D20, © QRM GmbH, Moehrendorf, Germany) consisting of five calibration cylinders of various densities (0, 50, 200, 800, 1200  $\text{mg}/\text{cm}^3$ ; see Fig. 1a) was simultaneously imaged along with the sample. In total, 1500 DICOM (Digital Imaging and Communications in Medicine) images were obtained with a resolution of  $1500 \times 1500$  pixels (see Fig. 1b). The micro-CT phantom images were used to determine the bone mineral density (BMD) in accordance with the standard procedure based on the linear relationship between the hydroxyapatite density and the corresponding CT image gray values (see Fig. 1c) (Sekhon et al., 2009).

All micro-CT images (labeled also as the "original dataset"

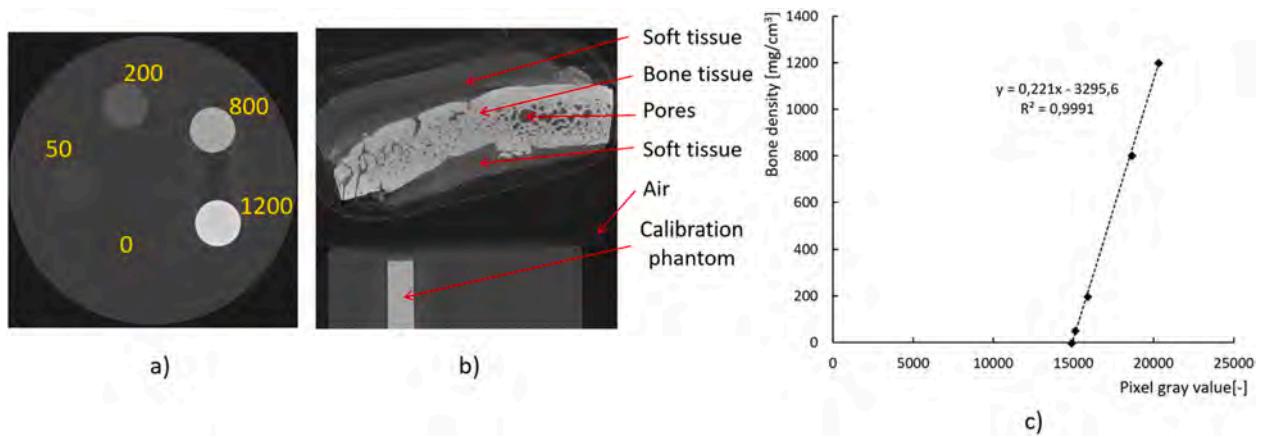


**Fig. 1.** Typical micro-CT-scanning output: a) Transversal view of the hydroxyapatite phantom blocks; b) Sagittal view of the cranial sample (soft tissue represents skin, subcutaneous tissue, galea aponeurotica, subgaleal tissue and dura mater); c) Linear relationship between the BMD of hydroxyapatite samples and the image-pixel gray values.

throughout this paper) were subsequently imported into ImageJ software (Schneider et al., 2012) in order to resize the images using a bicubic interpolation. The aim of this procedure (which preceded the actual construction of computational models) was to intentionally degrade the micro-CT image resolution to mimic image quality of the medical-CT devices. For the purpose of this study, the resize was done 6-times to obtain 6 additional sets of images with pixel sizes of 50  $\mu\text{m}$ , 100  $\mu\text{m}$ , 250  $\mu\text{m}$ , 500  $\mu\text{m}$  and 1250  $\mu\text{m}$  (see Fig. 2). These sizes were selected to be multiples of 25 in order to minimize rounding errors in the subsequent modeling procedures. In total, 7 datasets with different image resolutions were used to generate FE models of the cranial sample with titanium fixation-screw. The key point of this image-degradation process was to guarantee the precision of fixation-screw positioning within various FE models created from images with different resolutions. Results obtained from the original-dataset-based FE models were intended to be used as reference for comparisons of results obtained from models based on lower-resolution images.

All 7 image datasets were reviewed for the BMD in the region of

interest (ROI); specifically, in the region where the fixation-screw was to be inserted ( $4 \times 4 \times 6 \text{ mm}$ ; see Fig. 3a). It was assumed throughout the study, that a qualitative threshold between the bone tissue and soft tissues/pores was represented by pixels with a gray value approaching 17000, i.e. the bone mass was defined in the study by corresponding pixels with a gray value above 17000 (see Fig. 3b).

### 2.3. Models of geometry

The acquired micro-CT dataset as well as the artificially degraded datasets were processed to obtain digitized geometries of various precision. Specifically, image processing was performed using an application programmed in a numerical computing environment Matlab 2012 (Math Works, Natick MA, USA) (Marcián et al., 2011) to generate 3-dimensional STL models of the ROI including the detailed trabecular architecture. The segmentations of the bone tissues were performed using the methodology described by Minnema et al. (Minnema et al., 2018; van Eijnatten et al., 2018). A threshold value of 17000 was used to

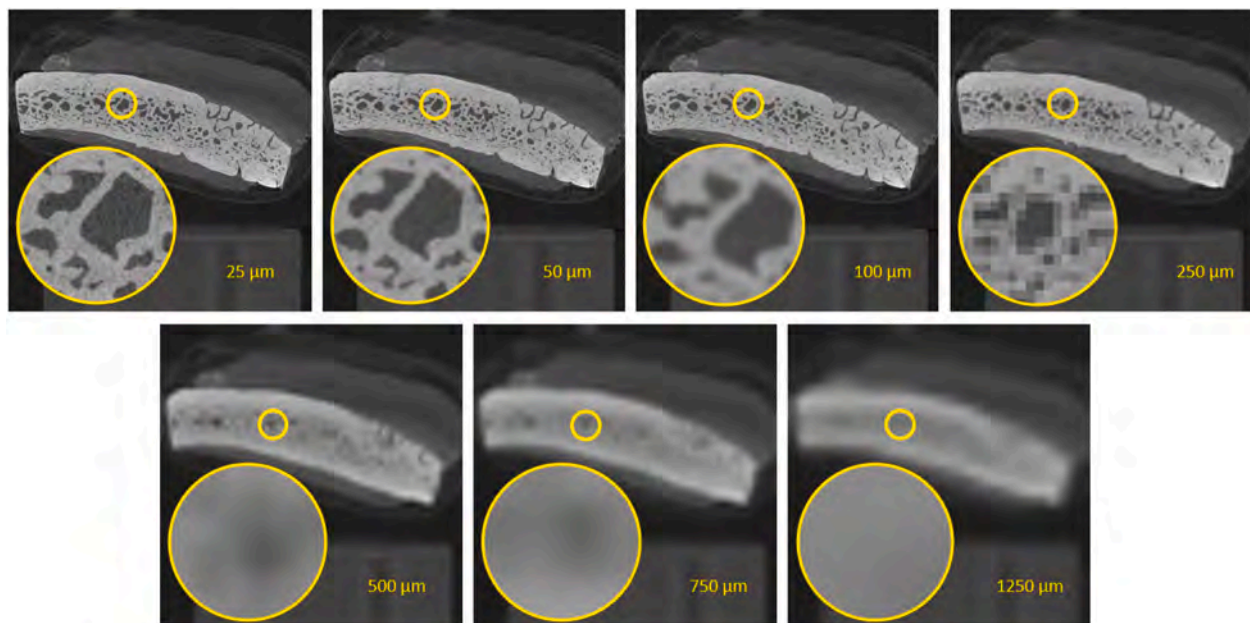


**Fig. 2.** Overview of 7 (micro)CT datasets with different image resolutions: The leftmost image in upper row presents a typical image obtained from a micro-CT scanner (i.e. a typical image from the original dataset). The other images show intentionally degraded images. The circles indicate in more detail how the image resolution affects visibility of individual trabeculae. The image resolution is defined by the value in micro-meters ( $\mu\text{m}$ ).

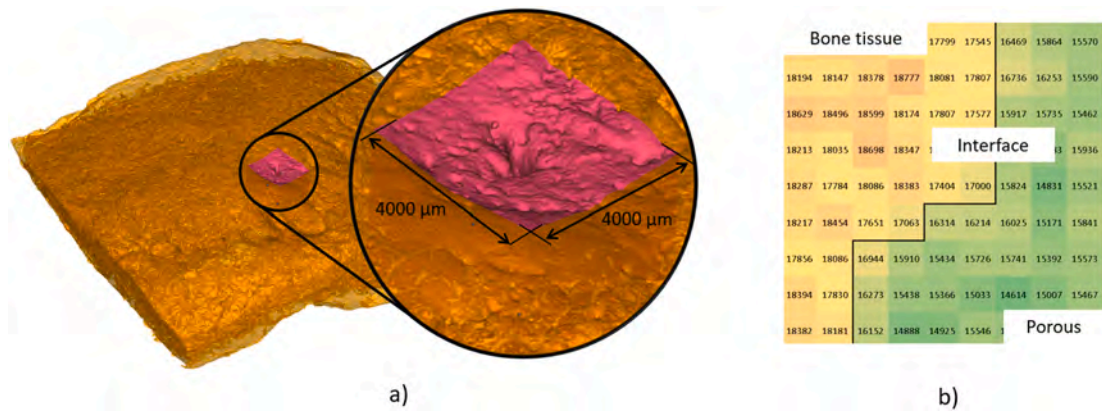


Fig. 3. Cranial sample: a) The region of interest (ROI) defined for the assessment of bone mineral density (BMD) and for the FE analysis (the square area of  $4 \times 4$  mm with a thickness of 6 mm); b) Typical example of gray value distribution at the interface between bone tissue and a pore (a threshold of 17000 is considered between hard and soft tissues).

distinguish between hard and soft tissues/pores (see Fig. 3b). In total, 7 STL models of the ROIs were generated. Furthermore, one STL model of a fixation-screw (KLS Martin, MICROPL.,  $\varnothing 1$  mm, L = 5 mm) was generated in Solid Works (2012) (Dassault Systèmes, Vélizy-Villacoublay, France).

#### 2.4. Finite element model

The bone and fixation-screw STL models (see Fig. 4) were solidified and assembled in a finite element environment using ANSYS® Academic Research Mechanical, Release 19.0 (Swanson Analysis, Inc., Houston, PA, USA). Both components were discretized using 10-node higher-order element SOLID187 with a global size of 25  $\mu\text{m}$  (the sample) and 25–100  $\mu\text{m}$  (the fixation-screw). The element size at the bone-screw interface was set to 10  $\mu\text{m}$  to capture the jaggedness of the thread surface. Interaction between the bone and the fixation-screw was modelled

using standard contact elements CONTA174 and TARGE170. The fixation-screw was assumed to be fully osseointegrated; therefore, the contact was bonded (i.e. with no relative movement at the interface) (Korabi et al., 2017; Marcián et al., 2014; Wirth et al., 2012). The element sizes were based on results of preliminary tests and sensitivity calculations. The finite element mesh consisted of 29–32 million nodes and 11–12 million elements, depending on the dataset-based variant (see Fig. 5 for the FE mesh demonstration).

#### 2.5. Boundary conditions and loads

The fixation-screw was loaded with a force of 11.54 N and a moment of 5.45 Nmm, as depicted in Fig. 5. The magnitudes of the loading force and moment were obtained from a preliminary coarse FEM model of a skull mimicking the mechanical loading of a typical cranial implant by a force of 50 N (Ridwan-Pramana et al., 2016, 2017; Yoganandan et al.,

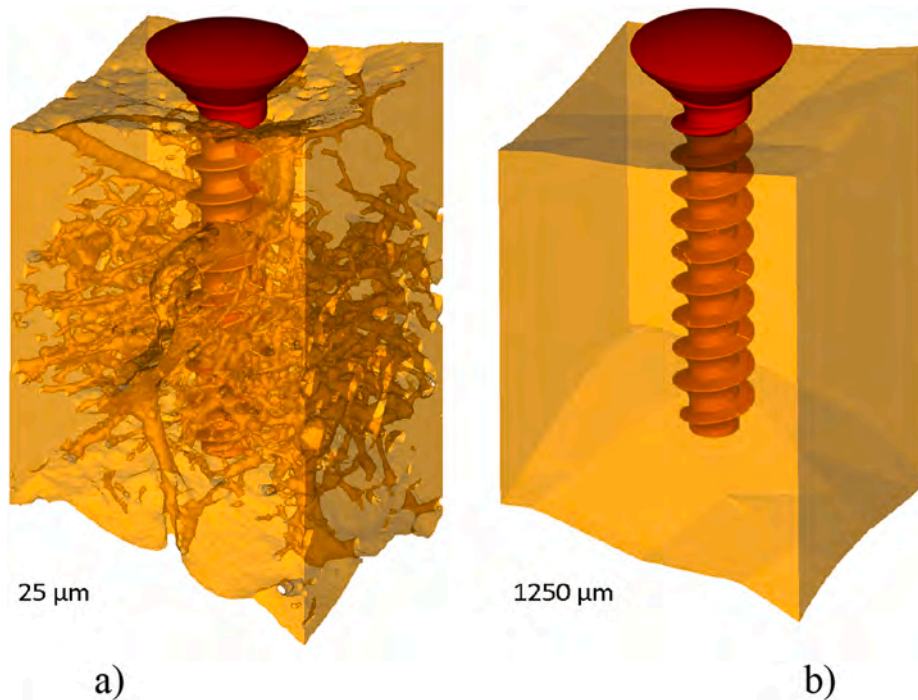


Fig. 4. Two examples of bone and fixation-screw STL models created from different (micro)CT datasets. The fixation-screw was placed in the exact same position in all dataset-variants: a) Highly-detailed geometry including complex trabecular architecture (based on the original micro-CT dataset, pixel size 25  $\mu\text{m}$ ); b) Non-trabecular geometry (based on dataset with the most degraded image quality, pixel size 1250  $\mu\text{m}$ ).

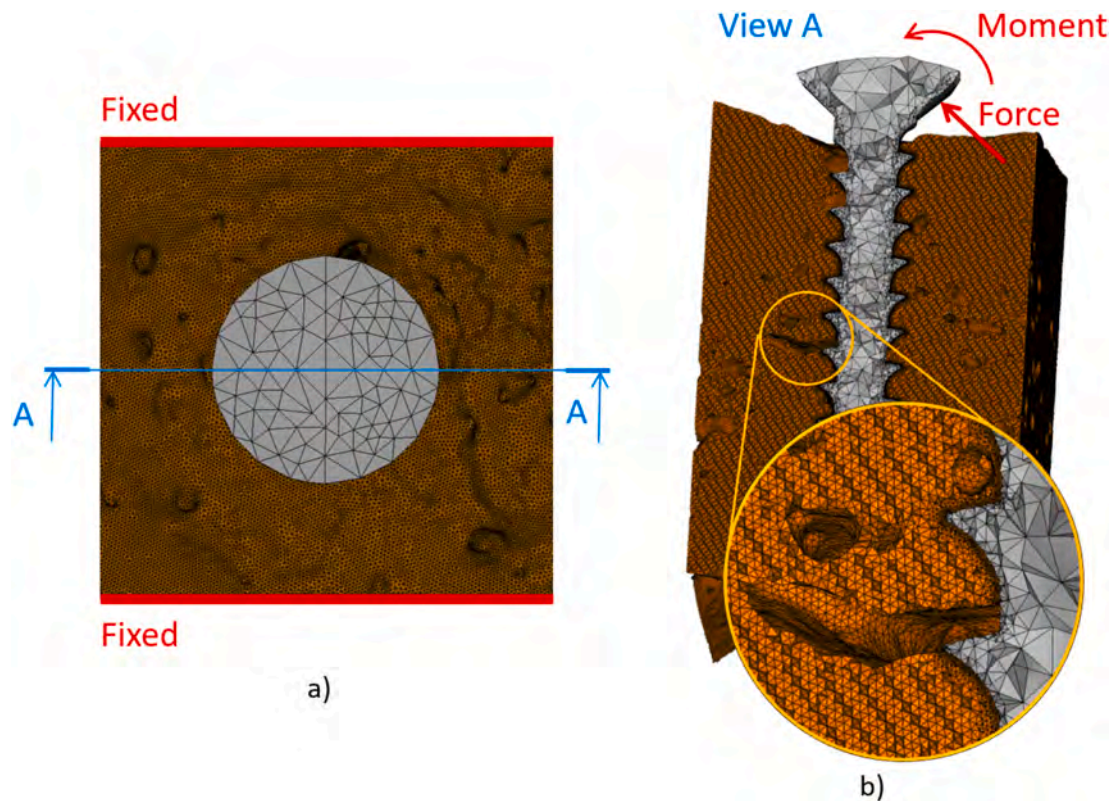


Fig. 5. Example of the finite element mesh (based on the original micro-CT dataset, pixel size 25  $\mu\text{m}$ ): a) Upper view of the model (coarse mesh = fixation-screw head, fine mesh = bone segment). Thick red lines indicate the boundary conditions applied to the bone segment; b) Section view with a detail of the bone-screw interface mesh. The red arrows indicate the loading force and moment.

2009) and intracranial pressure of 15 mmHg (Czosnyka, 2004). See Appendix A for more details. The samples were fixed on their boundaries to prevent movement in all three directions (see Fig. 5).

### 2.6. Material model

The FE models consisted of two parts: bone segment and titanium alloy fixation-screw. The fixation-screw material was represented adopting a homogeneous, isotropic and linear-elastic model with typical values of the Young's modulus  $E = 110 \text{ GPa}$  and the Poisson's ratio  $\mu = 0.3$  (Kayabaşı et al., 2006; Natali et al., 2008). While there is a wide consensus on the material behavior of titanium alloys, many uncertainties prevail in the realm of mechanical simulations of living tissues. For the purpose of this study, two basic and widely accepted assumptions were adopted: 1. From a microscopic viewpoint, the material properties of the cancellous bone as well as cortical bone were considered identical (Bayraktar et al., 2004; Rho et al., 1997; Turner et al., 1999); 2. An isotropic and linear-elastic model is sufficient to describe the behavior of bones in most situations (Viceconti, 2011). Based on these assumptions, two elastic constants ( $E, \mu$ ) are needed. While there is a general agreement on the Poisson's ratio of bone tissues ( $\mu = 0.3$  (Kayabaşı et al., 2006; Natali et al., 2008);), the value of the Young's modulus is much less clear, ranging from 5 to 30 GPa (Daoui et al., 2017; Dowson, 1992; Motherway et al., 2009; Shibata et al., 2015; van Rietbergen et al., 1995). Moreover, homogeneity of material distribution within the bones might be an issue. According to the level of bone mineralization (which is detectable better in images with high resolution), bone can be modelled as a homogeneous (Limbert et al., 2010; Marcián et al., 2014; P. Marcián et al., 2018; Wirth et al., 2012; Wolff et al., 2014) or inhomogeneous (Inagawa et al., 2018; Keller, 1994; Mao et al., 2019; Shefelbine et al., 2005; Snyder and Schneider, 1991) material. To cover the uncertainty regarding the bone material

properties, several scenarios were adopted in this study as follows:

#### 1. Homogeneous distribution of Young's modulus in bone:

a) "High modulus" (Boruah et al., 2017; Motherway et al., 2009; Shefelbine et al., 2005)

$$E = 15$$

b) "Low modulus" (Costa et al., 2017; Rahmoun et al., 2014)

$$E = 5$$

#### 2. Inhomogeneous distribution of Young's modulus in bone:

a) "Shefelbine's model" (Shefelbine et al., 2005)

$$E = \begin{cases} 0.050 & \text{for } CT < 17000 \\ 13.636 \cdot (CT \cdot 2.21 \times 10^{-4} - 3.30) & \text{for } CT \geq 17000 \end{cases}$$

b) "Keller's model" (Keller, 1994; Shefelbine et al., 2005)

$$E = \begin{cases} 0.050 & \text{for } CT < 17000 \\ 10.5 \cdot (CT \cdot 2.21 \times 10^{-4} - 3.30)^{2.39} & \text{for } CT \geq 17000 \end{cases}$$

c) "Snyder's model" (Shefelbine et al., 2005; Snyder and Schneider, 1991)

$$E = \begin{cases} 0.050 & \text{for } CT < 17000 \\ 3.891 \cdot (CT \cdot 2.21 \times 10^{-4} - 3.30)^{2.39} & \text{for } CT \geq 17000 \end{cases}$$

d) "Inagawa's model" (Inagawa et al., 2018; Shefelbine et al., 2005)

$$E = \begin{cases} 0.050 & \text{for } CT < 17000 \\ 17.486 \cdot (CT \cdot 2.21 \times 10^{-4} - 3.30)^{1.596} & \text{for } CT \geq 17000 \end{cases}$$

where CT is a unitless gray value (pixel intensity) obtained from the

image datasets and  $E$  is Young's modulus in GPa. In case of inhomogeneous distribution (Scenarios 2a through 2d), the Young's moduli were calculated for each pixel of all seven datasets and were mapped onto the corresponding FE meshes. In those scenarios, the soft tissues ( $CT < 17000$ ) were assumed to have a modulus of  $E = 0.05$  GPa according to (Shefelbine et al., 2005). Typical distribution of the gray values within the bone is illustrated in Fig. 6. This figure also demonstrates the effect of image quality (resolution) on the gray value distribution and on the bone geometry reconstruction.

### 2.7. Simulations overview

As was discussed in the previous sections, 7 geometries (consisting of bone segment + fixation-screws) were constructed based on 7 (micro)CT datasets (1 original dataset + 6 degraded datasets). Each geometry was investigated for 6 variants of bone material (scenarios labeled as 1a, 1b, 2a, 2b, 2c, and 2d). Therefore, there were 6 different material assignments to 7 different finite element meshes making in total 42 variants/computational models. These models were used for evaluations of maximum shearing strain (defined as the difference between the maximum and the minimum principal strain and called "strain intensity" throughout the paper) in the bone and for equivalent (von Mises) stress in the fixation-screw. These evaluations follow the common practice used in musculoskeletal computational biomechanics (Bujtár et al., 2010; Frost, 2004; Fujiki et al., 2013; Lekadir et al., 2016; Liu et al., 2013; Marcián et al., 2014; Narra et al., 2014; Sarrafpour et al., 2012; Chileo et al., 2008; Suzuki et al., 2016; Wolff et al., 2014).

## 3. Results

### 3.1. Finite element analysis: equivalent stress in fixation-screw

Equivalent (von Mises) stress distributions in the fixation-screw inserted in the model based on the original dataset and considering different scenarios of bone material behavior are presented in Fig. 7. In all the variants based on the original dataset, the maximum stresses were always located in the first micro-thread under the fixation-screw head. The specific values in these variants ranged from 65 to 176 MPa indicating that the selection of bone material scenario is crucial for calculating stresses in the fixation-screw. Fig. 8 shows the mean maximum stresses in the fixation-screw for various material scenarios. The small variabilities of the stress peaks within models of the same material scenario ( $\pm 8$  MPa) suggest that the (micro)CT dataset resolution has a

limited impact on the stresses in the fixation-screw.

### 3.2. Finite element analysis: strain intensity in bone

Strain intensity distributions in the bone segment modelled based on different (micro)CT datasets and with one material scenario (2a) are presented in Fig. 9. The figure demonstrates that the strains strongly depend on geometrical nuances of the models caused by (micro)CT dataset resolution. This observation is supported also by the comparison of results from various material scenarios documented in Fig. 10. For more comprehensive comparison, strain intensities from two linear paths of interest (POI) located 0.6 mm from fixation-screw axis (as indicated in Fig. 11) were retrieved. Strain intensities along those paths are shown in Fig. 12 and Fig. 13.

## 4. Discussion

The stable attachment of cranial implants to bone is pivotal in clinical settings and plays a significant role in the functionality of the implant (Marcián et al., 2019). To date many publications dealing with craniomaxillofacial biomechanics either omit or oversimplify the mechanical interaction between bone, cranial implants and corresponding fixation-screws. The mechanical interaction between bone and implant is dependent primarily on geometrical configuration, loading conditions and material properties of the interacting components (Mao et al., 2019; Marcián et al., 2014; Petr Marcián et al., 2018; Wee et al., 2015). While the loading scenarios can be predicted and simulated with sufficient reliability, the structural properties inside the human body are often a matter of guesswork. Subsequently, the assessment of biomechanical performances is dependent on the quality of the data used to generate computational (FEM) models.

To date, it is a common clinical practice to obtain information concerning the geometry and material properties of bones from CT or MRI (Zadpoor and Weinans, 2015). However, it must be noted that the accuracy of such data can have a significant effect on the quality of FEM models used for biomechanical simulations. More specifically, the image resolution of medical-CT devices is often not sufficient for constructing complex computational models of trabecular bone. Therefore, CT and MRI are currently only used for capturing outer surfaces of bones and for implementing inhomogeneous (or homogenized) distributions of elastic material properties into the computational models (often assuming that the latter is a sufficient substitution for the omitted trabecular architecture). Questioning the results of biomechanical assessments in such

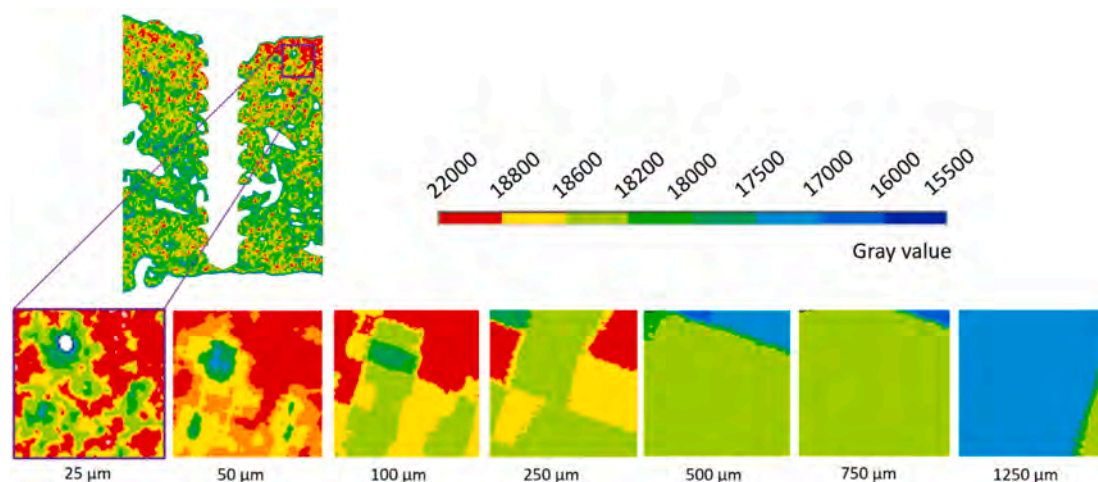


Fig. 6. Gray value distribution within an arbitrary section of the bone model: A comparison of the distributions among the dataset-based variants. The leftmost detail shows a pore inside the bone (see the white spot inside the square) and a strong inhomogeneity caused by a high image resolution (25  $\mu\text{m}$ ). As the pixel size of the input image grows ( $\rightarrow 1250$   $\mu\text{m}$ ), the distribution is more and more homogenized, and the pore thus diminishes (in FE models is substituted by finite elements of non-zero Young's moduli). In the FE models, the gray values are converted into Young's moduli using a linear relationship between gray values and BMD.

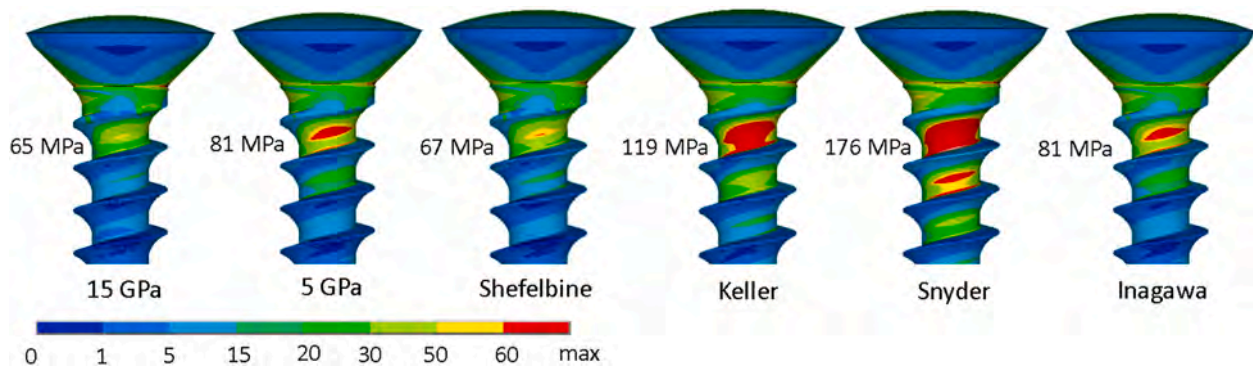


Fig. 7. Equivalent (von Mises) stress distribution in the fixation-screw: Comparison of results from the original-dataset-based models (pixel size 25  $\mu\text{m}$ ) of different bone material scenarios. The values on the left of the fixation-screws indicate the maximum stress.

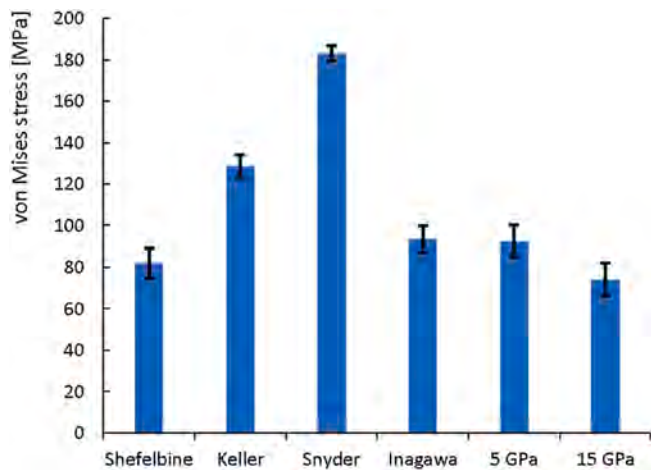


Fig. 8. Equivalent (von Mises) stress peaks in the fixation-screw: Mean values and standard deviations of maximum values obtained from all dataset-based models (i.e. pixels 25–1250  $\mu\text{m}$ ) with the same bone material scenario.

cases is therefore legitimate because the omission of trabeculae interacting with the fine threads of the fixation-screws might lead to incorrect or biased conclusions of analyses that are focused specifically to biomechanical performance of implants. Obtaining more accurate micro-CT data could be a solution to the aforementioned problem as intertrabecular pores would be modelled more realistically as void spaces. However, micro-CT scanning cannot be carried out on living patients due to high-dose radiation exposure.

The differences of micro-CT-based and medical-CT-based FEM models and the effects of corresponding methodological nuances on the accuracy of biomechanical response of bone-implant interaction have not, to the best of authors' knowledge, been thoroughly investigated. Therefore, the present study focused on developing computational models of one particular biomechanical system using different image resolutions. This approach allowed the authors to compare FEM calculations based on medical-CT datasets with micro-CT datasets. The results of this study clearly demonstrate that medical-CT image data generates less detailed model of trabecular architecture compared to micro-CT datasets. Moreover, from a certain resolution on (pixel size > 1000  $\mu\text{m}$ ) there was no trabecular architecture present in the CT-generated model whatsoever. As a consequence of this phenomenon, pores that exist within the trabecular architecture of real bone can be represented in FEM models in three different ways depending on the quality of the input image data: 1. Pores are modelled realistically as a void space surrounded by finite elements representing the bone mass (see Detail A in Fig. 9); 2. Pores are modelled by finite elements with a low value of Young's modulus attributed (see Detail B in Fig. 9); 3. Pores are

completely neglected in the FE model and the Young's modulus attributed to the finite elements in that location is a result of a local homogenization due to poor resolution of the input images (see Detail C in Fig. 9). From a mechanical viewpoint, pore representations defined by these three categories behave differently. This can markedly affect results of the bone-implant biomechanical interaction.

Biomechanical performance of bone tissue is usually assessed based on the distribution and magnitude levels of mechanical strains (Frost, 2004; Fujiki et al., 2013; Lekadir et al., 2016; Limbert et al., 2010; Suzuki et al., 2016). The strain evaluations, however, strongly depend on geometry, mass distribution, material characteristics and the level of porosity. The present study confirms that the local strains in highly porous models (based on image resolution  $\leq 250 \mu\text{m}$ ; pore category 1) are affected by a strong local stiffness variability due to bone scaffolding. However, the highest strain intensity values were observed in models with a few or no pores, i.e. in the models that were classified as category 2 or 3 (see above). While in the cases of correctly modelled trabecular architecture the pores have no capability of the load transmission (see Fig. 14a), models based on coarser image data contain pore-substitutes (i.e. finite elements) of a non-zero modulus of elasticity that have capability to transfer loads (see Fig. 14b) and, therefore, produce non-zero strains. Young's moduli of those pore-substitutes are usually very low (e.g. 0.05 GPa in models of category 2) or similar to those of the surrounding bone (5–15 GPa in models of category 3). In other words, while there are no strains in the pores of category 1 (because no mass = no strains) and the strain energy is distributed exclusively within the trabeculae, an extreme ductility of pore elements in category 2 leads to high strains that are entirely fictitious. Models that include pore element of category 3 are stiffer and do not evince signs typical for singularities but, at the same time, they prevent from a credible assessment of the interaction with fixation-screws because strains in those elements are fictitious as well. The above discussed differences in strain evaluations are clearly visible in Figs. 12 and 13 depicting results along the POIs. In addition to the resolution-based phenomenon, there can be sudden swings in the strain distribution along the POI in models with inhomogeneous distribution of material properties (see detail "swing" in Fig. 12a). Those swings are caused by step changes in Young's moduli at the boundaries of regions of significantly different BMDs and, therefore, strains in those locations can also be considered as fictitious. Observations regarding the strain results in bone models created from image data can have significant consequences for bone/implant performance assessments. For instance, strain-governed bone remodeling algorithms (Rungsiyakull et al., 2015; Yoda et al., 2017) used for predictions of bone structure evolution in various biomechanical environment can lead to biased results when the initial state is based on CT images of insufficient resolution. The specific effects of intertrabecular pore (mis)representation and/or material assumptions on predictions of implant life or bone remodeling estimations would depend on the specific patient, site, type of implant, and other factors. Such a thorough analysis would

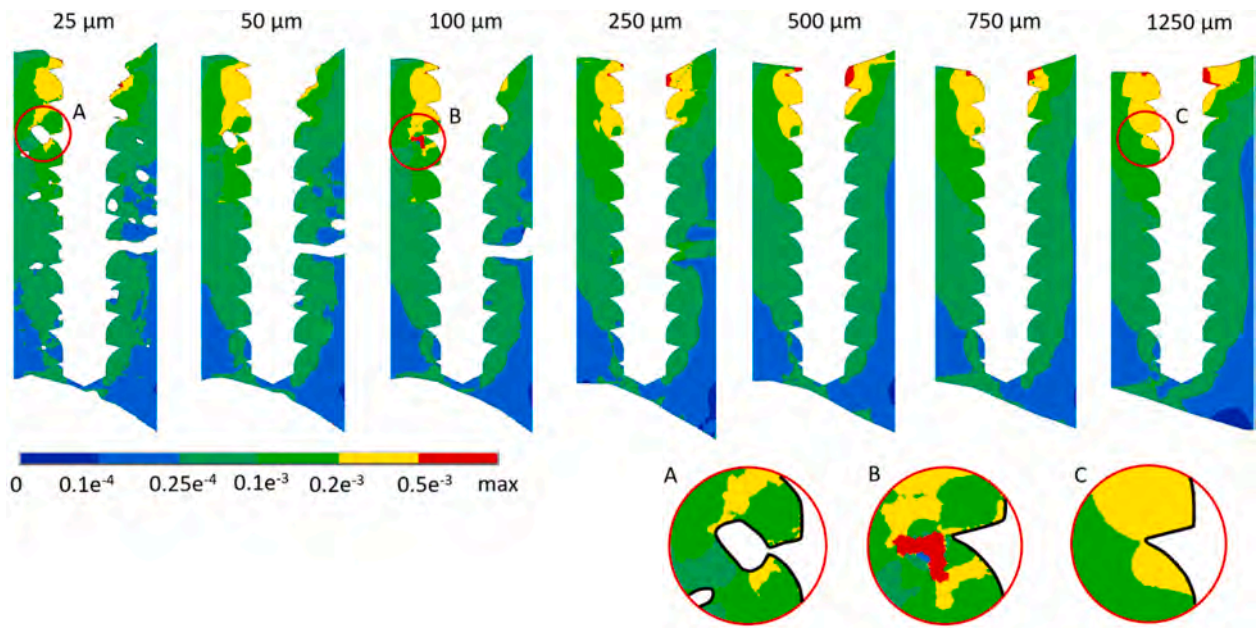


**Fig. 9.** Strain intensity distribution in bone: Results for all dataset-based variants with Shefelbine’s material model (scenario 2a). The red circles indicate significantly different strains in a pore location modelled differently depending on the micro-CT dataset resolution. A - The high resolution of the original dataset enabled modelling of the pore realistically (resulting in no significant strain intensity concentrations; “Pore category 1”); B - Coarser images prevented from modelling the pore realistically as a void space. Instead, bone tissue of low Young’s modulus was detected and subsequently modelled in that location resulting in unrealistically high (fictitious) strain intensity (“Pore category 2”); C - Images of the lowest resolution prevented from detecting the pore; moreover, the gray values distribution in that location were too homogenized to show satisfactorily accurate values of BMD and strain intensity (“Pore category 3”).

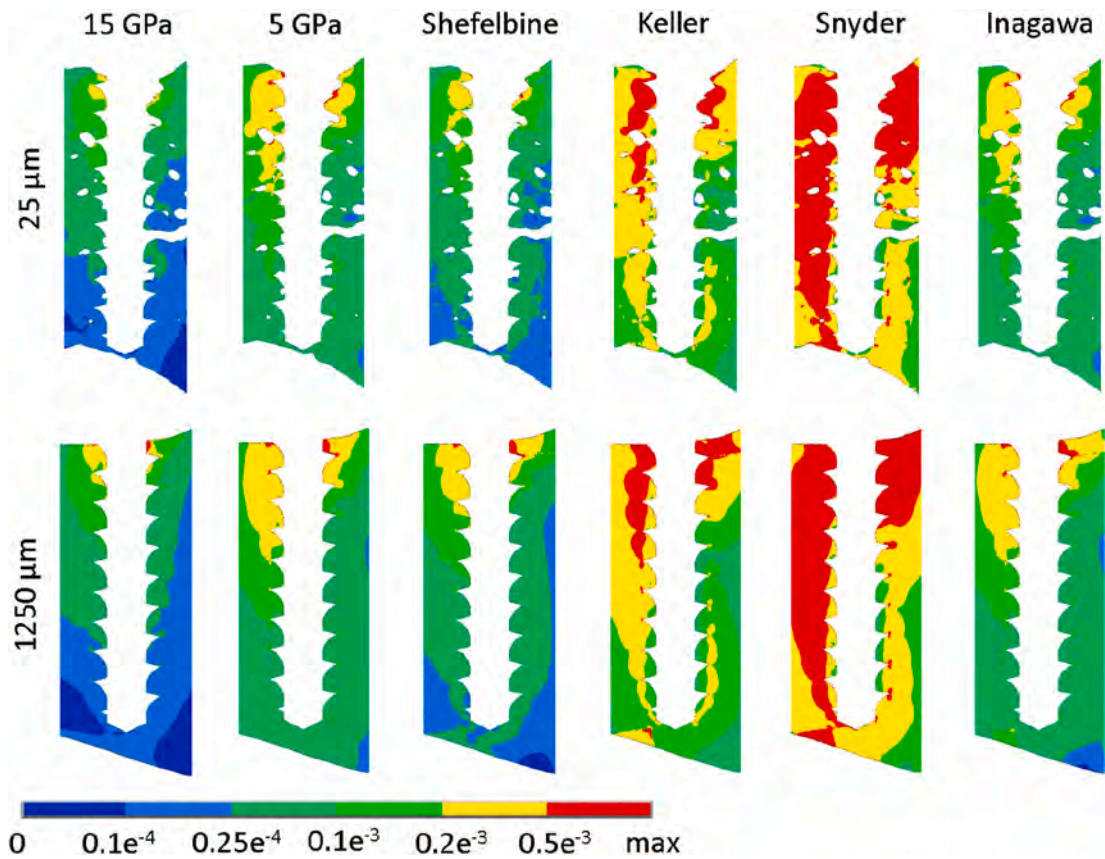


**Fig. 10.** Strain intensity distribution in bone: Results for all bone material scenarios and two extreme datasets (25 μm and 1250 μm).

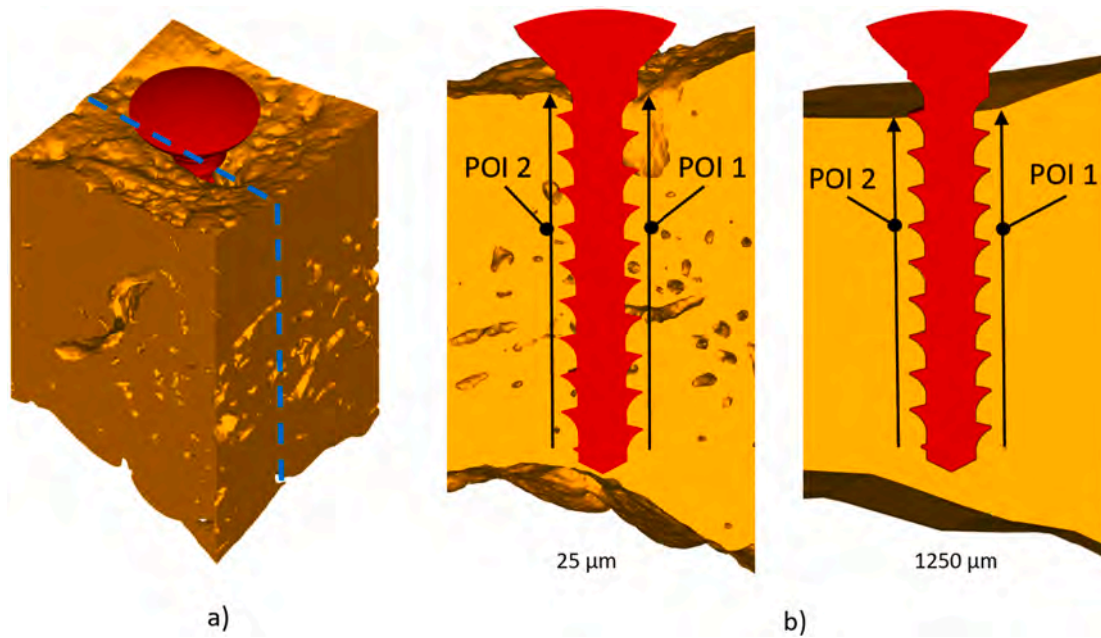


Fig. 11. Region and paths of interest (abbreviated as ROI and POI): a) Definition of the section for strain intensity visualization; b) Location of POI 1 and POI 2. Location of the POIs are identical for all analyzed variants.

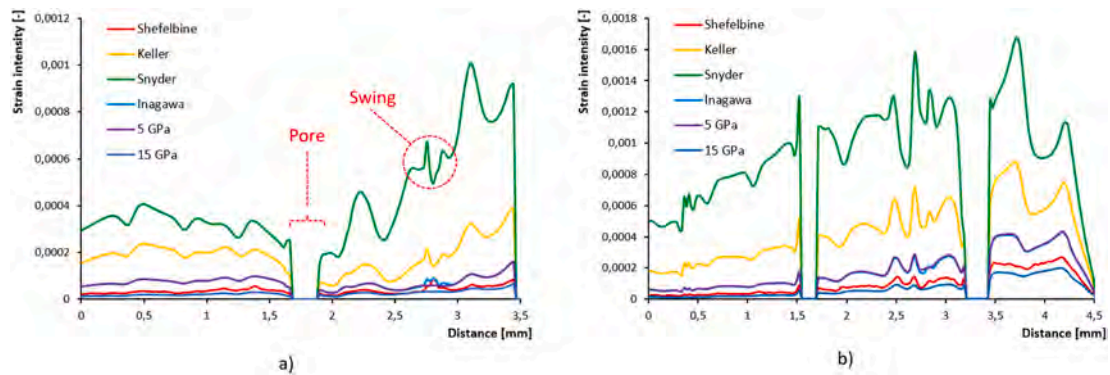


Fig. 12. Strain intensity distribution along the paths of interest: Comparison of results from original-dataset-based models (pixel size 25 µm) with different bone material scenarios: a) POI 1; b) POI 2.

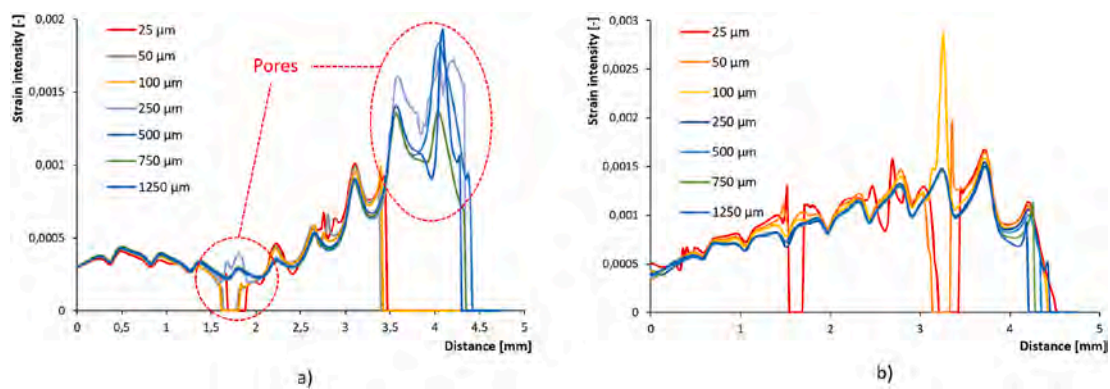
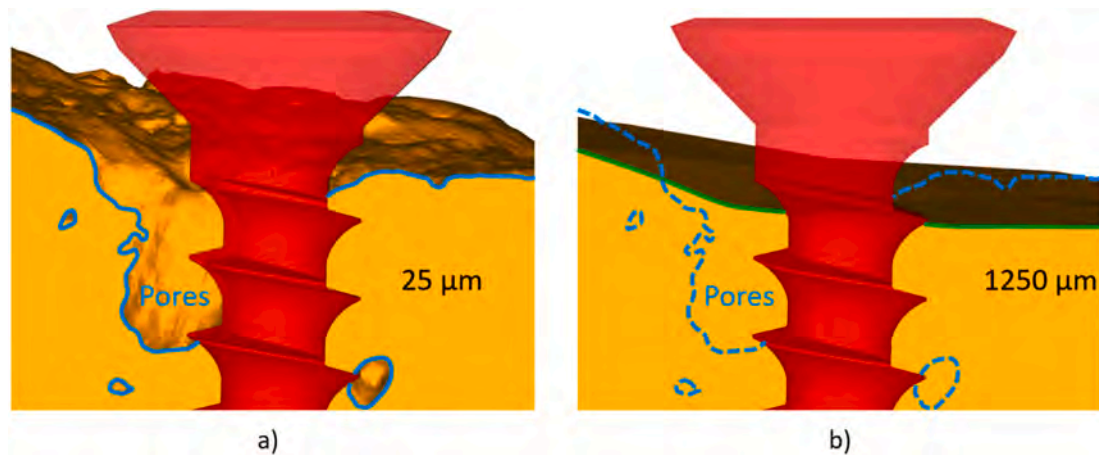


Fig. 13. Strain intensity distribution along the paths of interest: Comparison of results from different dataset-based models with Shefelbine's material (bone material scenario 2a). In variants based on coarse images (pixel size >100 µm), high strain values are detected in locations where in reality there are pores and voids: a) POI 1; b) POI 2.



**Fig. 14.** Differences in bone mass representation based on different (micro)CT dataset: a) Model contains realistic pores (delimited by solid blue lines); b) Model neglects the pores (dashed blue lines) geometrically. The pores are substituted by bone mass of degraded or homogenized Young's moduli instead (delimited by solid green line).

be, however, beyond the scope of the present study. Nevertheless, as indicated in Fig. 13, calculated mechanical strains might locally differ by tens of percent depending on the quality of the input images. Such a difference might affect bone remodeling prediction significantly (i.e. completely different density distribution or/and trabecular architecture might be predicted).

As demonstrated in the present study, maximum equivalent (von Mises) stress in the fixation-screw is located in the first thread under the screw head regardless the image dataset variant. However, the specific value of the stress peak is dependent dominantly on the selection of the bone material scenario. The difference between the lowest (scenario 1a) and highest (scenario 2c) stress peaks exceeds 100 MPa which is a significant discrepancy that might affect reliability and credibility of the implant performance assessment. In other words, the selection of appropriate bone material scenario is a crucial step for subsequent correct evaluation of fixation-screw stresses. Regarding the effect of image resolution, the original-dataset-based models provided lower stress peaks in the screw than models created from degraded datasets. However, the stress peak differences in extreme cases ranged only from 13 to 21 MPa (depending on the material scenario used). Therefore, in contrast to strains in surrounding bone, the effect of the image resolution on stresses in fixation-screw is much smaller than that of material specifics. The differences in stresses within the fixation screw might have consequences on prediction/estimation of the fixation screw life. Computationally, the life is usually determined using fatigue life analysis. In cases of high-cycle fatigue, calculated stresses are compared to an endurance limit or the number of cycles is determined using an appropriate cumulative damage rule. Based on the input quality/accuracy, the stresses used in the fatigue life analysis might be over- or underestimated and, correspondingly, the estimation of the fatigue life might be over- or underestimated. The results of the current study suggest that the fixation screw life might not be significantly affected by the quality of the images since only relatively small stress peak differences were observed in models based on micro- and medical-CT data (there might be no effect at all when the stresses are well below the endurance limit which is over  $\sim 600$  MPa for titanium alloys (Niinomi, 1998)). On the contrary, selection of bone material scenario for the calculations is much more crucial factor as the observed stress peak differences of up to 100 MPa (Fig. 8) might be decisive in terms of fatigue damage initiation. However, the specific quantification of the influence of the input data quality on the life prediction is beyond the scope of this study as it is subject- and object-specific.

One drawback of this study was that the study was limited to a completely osseointegrated fixation-screw; however, in cases of imperfect osseointegration, the principles described above would still apply.

Moreover, it might be assumed that the observed discrepancies between low- and high-resolution image datasets would be even higher in such cases. Similarly, the study was also limited to one bone specimen with one type of fixation-screw. Although trabecular architecture of two individuals can differ significantly producing different mechanical response to implant loading, the aim of this study was not a thorough analysis of a specific type of implant or estimation of biomechanical response of a specific patient; rather, a certain phenomenon and methodological features were investigated in order to demonstrate how a specific trabecular morphology is represented in the FE models when using different ( $\mu$ )CT resolutions and how the results of those representations might lead to different interpretations of the mechanical response. For this purpose, one typical representative of bone-screw interaction scenario was considered to be satisfactory for proving the existence of the hypothesized phenomenon.

The same reasoning as used in the previous paragraph applies to the specific material characterization as well. Since the study objective was not to examine the specific response of a specific subject but rather to investigate a certain methodological features associated with CT-based finite element models, there is no need for having experimentally validated subject-specific material data. Moreover, the observed phenomenon – which is related exclusively to the FE-modelling procedure – depends on the mechanical properties of bones (density-modulus relationship) only indirectly. If an experimentally validated subject-specific density-modulus curve was at disposal, the same phenomenon would still be observed because the misrepresentation of the intertrabecular pore in clinical-CT-based FE models is usually caused by blurring of the ROI in the images of lower resolution. It does not depend on the specific density-modulus curve; rather, it is caused by local homogenization of the material data within the ROI (as indicated in Fig. 13).

At the beginning we hypothesized that there were significant differences in the mechanical performance of bone near the bone-implant interface when (micro)CT datasets of different image resolutions were used for creation of the computational model. Results of this study strongly support this hypothesis.

## 5. Conclusion

Nowadays, the patient-specific approach in FEA-based computational simulations is gaining a wide popularity in craniomaxillofacial biomechanics. Such models are now routinely created using data from imaging devices. However, the present study shows that the quality of (micro)CT-based input data plays a huge role in the assessment of bone-implant biomechanical interaction performance and its influence on the calculation results should not be overlooked or underestimated.

Specifically, computational simulations of problems involving bone-implant biomechanical interaction requires high-resolution micro-CT images to avoid misrepresentation of intertrabecular pores and thus obtain reliable strain results. CT image resolution has much smaller effect on the stress results in the implant parts than on the strains in bone; the stresses in fixation-screw are much more affected by a selection of correct bone material representation. Though medical-CT images with standard resolution can provide conservative results of mechanical stress in the fixation-screws attaching implants to the bone, strains in bone in such cases might be highly biased. In the view of the fact that the bone performance (resorption, formation etc.) is believed to be governed by mechanical strains (or strain energy density etc.), a special attention should be paid to a proper level of model quality and using micro-FEA should be preferred where possible. Though the simulation within this study was carried out on the cranial bone interacting with cranial-implant-fixation-screw, it can be expected that the findings of the present study are not inherent only to cranial biomechanics. The problems of trabecular pore misrepresentation in FE models due to insufficient CT

data are closely associated with the general methodology of FEA-oriented biomechanics.

#### Declaration of competing interest

The authors declare that they have no known competing financial interests or personal relationships that could have appeared to influence the work reported in this paper.

#### Acknowledgment

The work was supported by the Czech Science Foundation by Grant No. 16-08944S. This research was carried out under the project CEITEC 2020 (LQ1601) with financial support from the Ministry of Education, Youth and Sports of the Czech Republic under the National Sustainability Programme II and CzechNanoLab Research Infrastructure supported by MEYS CR (LM2018110).

## Appendix A

The loading condition used in the present study was based on a preliminary calculation using a coarse FE model of a skull with cranial implant covering a typical large-scale cranial defect (Marcián et al., 2019). In this model, the implant was fixed to the bone by means of micro-plates and fixation-screws placed in typical positions for this type of cranial defect (see Figure A1). The skull model was fixed to prevent from any movement at its caudal boundary in transverse plane. The implant was loaded by intracranial pressure of 15 mmHg and by a concentrated external force of 50 N acting on the center of the implant in a normal direction (Marcián et al., 2019). The model was meshed by 10-node higher-order finite elements. All participating parts (skull, implant, fixation-screw and micro-plate) were interconnected using appropriate contact elements assuming a friction in all pairs except for the interfaces between the fixation-screw and bone where a bonded contact mimicked the perfect osseointegration (Marcián et al., 2018). All materials were assumed to be homogeneous, isotropic and linearly-elastic with following values of Young's modulus ( $E$ ) and Poisson's ratio ( $\mu$ ):

$$\begin{aligned} E_{\text{bone}} &= 5000 \text{ MPa} \\ \mu_{\text{bone}} &= 0.3 \\ E_{\text{PMMA}} &= 3000 \text{ MPa} \\ \mu_{\text{PMMA}} &= 0.38 \end{aligned}$$

Finally, a static structural calculation was performed using ANSYS® software to obtain forces acting on the individual fixation-screw which were to be used in the sub-model of the main study. It was concluded that a force  $F = 11.54 \text{ N}$  and a moment  $M = 5.45 \text{ Nmm}$  acting on the fixation-screw head as indicated in Fig. 5 are a sufficient substitution of the global model behavior for the purpose of the sub-model analysis used in the main study.

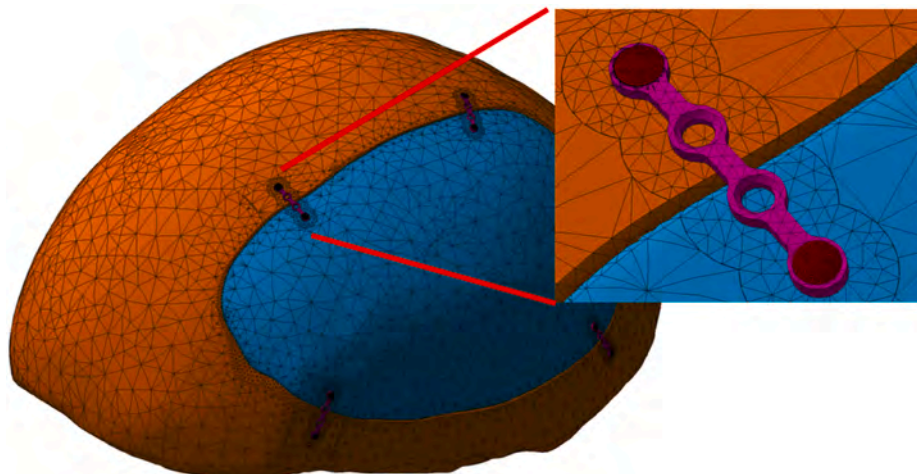


Fig. A1. Coarse model of skull with cranial implant used for the determination of the fixation-screw loading.

#### Author statement

Petr Marcián: Conceptualization, Writing - original draft, Investigation, Visualization, Methodology, Writing - review & editing, Funding acquisition. Libor Borák: Conceptualization, Investigation, Visualization, Methodology, Writing - review & editing. Tomáš Zikmund: Conceptualization,

Performed micro-CT images, Writing - review & editing. Ladislava Horáčková: Contributed bone sample, Jozef Kaiser: Supervision, Performed micro-CT images, Funding acquisition. Marek Joukal: Supervision, Contributed bone sample, Writing - review & editing. Jan Wolff: Conceptualization, Methodology, Supervision, Writing - review & editing.

## References

- Achour, T., Merdji, A., Bachir Bouaidja, B., Serier, B., Djebbar, N., 2011. Stress distribution in dental implant with elastomeric stress barrier. *Mater. Des.* 32, 282–290. <https://doi.org/10.1016/j.matdes.2010.05.053>.
- Alsayednoor, J., Metcalf, L., Rochester, J., Dall'Ara, E., McCloskey, E., Lacroix, D., 2018. Comparison of HR-pQCT- and microCT-based finite element models for the estimation of the mechanical properties of the calcaneus trabecular bone. *Biomech. Model. Mechanobiol.* 17, 1715–1730. <https://doi.org/10.1007/s10237-018-1051-6>.
- Bayraktar, H.H., Morgan, E.F., Niebur, G.L., Morris, G.E., Wong, E.K., Keaveny, T.M., 2004. Comparison of the elastic and yield properties of human femoral trabecular and cortical bone tissue. *J. Biomech.* 37, 27–35.
- Bolind, P., Acton, C., Albrektsson, T., Bonding, P., Granström, G., Johansson, C., Lindeman, P., Mühlbauer, W., Tjellström, A., 2000. Histologic evaluation of retrieved craniofacial implants. *Otolaryngol. Neck Surg* 123, 140–146. <https://doi.org/10.1067/mhn.2000.104667>.
- Borges Radaelli, M.T., Idogava, H.T., Spazzin, A.O., Noritomi, P.Y., Boscato, N., 2018. Parafunctional loading and occlusal device on stress distribution around implants: a 3D finite element analysis. *J. Prosthet. Dent* 120, 565–572. <https://doi.org/10.1016/j.prosdent.2017.12.023>.
- Boruah, S., Subit, D.L., Paskoff, G.R., Shender, B.S., Crandall, J.R., Salzar, R.S., 2017. Influence of bone microstructure on the mechanical properties of skull cortical bone – a combined experimental and computational approach. *J. Mech. Behav. Biomed. Mater.* 65, 688–704. <https://doi.org/10.1016/j.jmbm.2016.09.041>.
- Box, G.E.P., 1979. Robustness in the strategy of scientific model building. *Robust. Stat.* 201–236. <https://doi.org/10.1016/B978-0-12-438150-6.50018-2>.
- Bujtár, P., Sándor, G.K.B., Bojtos, A., Szűcs, A., Barabás, J., 2010. Finite element analysis of the human mandible at 3 different stages of life. *Oral Surgery. Oral Med. Oral Pathol. Oral Radiol. Endodontol.* 110, 301–309. <https://doi.org/10.1016/j.tripleo.2010.01.025>.
- Cinel, S., Celik, E., Sagirkaya, E., Sahin, O., 2018. Experimental evaluation of stress distribution with narrow diameter implants: a finite element analysis. *J. Prosthet. Dent* 119, 417–425. <https://doi.org/10.1016/j.prosdent.2017.04.024>.
- Costa, M.C., Tozzi, G., Cristofolini, L., Danesi, V., Viceconti, M., Dall'Ara, E., 2017. Micro Finite Element models of the vertebral body: validation of local displacement predictions. *PLoS One* 12, e0180151. <https://doi.org/10.1371/journal.pone.0180151>.
- Czosnyka, M., 2004. Monitoring and interpretation of intracranial pressure. *J. Neurol. Neurosurg. Psychiatry* 75, 813–821. <https://doi.org/10.1136/jnnp.2003.033126>.
- Daoui, H., Cai, X., Boubenider, F., Laugier, P., Grimal, Q., 2017. Assessment of trabecular bone tissue elasticity with resonant ultrasound spectroscopy. *J. Mech. Behav. Biomed. Mater.* 74, 106–110. <https://doi.org/10.1016/j.jmbm.2017.05.037>.
- Dowson, D., 1992. Bio-tribology of natural and replacement synovial joints. In: Mow, V., Ratcliffe, A., Woo, S.L.-Y. (Eds.), *Biomechanics of Diarthrodial Joints*. Springer, New York, pp. 305–345.
- Frost, H.M., 2004. A 2003 update of bone physiology and Wolff's Law for clinicians. *Angle Orthod.* 74, 3–15. [https://doi.org/10.1043/0003-3219\(2004\)074<0003:AUOBPA>2.0.CO;2](https://doi.org/10.1043/0003-3219(2004)074<0003:AUOBPA>2.0.CO;2).
- Fujiki, K., Aoki, K., Marcián, P., Borák, L., Hudieb, M., Ohya, K., Igarashi, Y., Wakabayashi, N., 2013. The influence of mechanical stimulation on osteoclast localization in the mouse maxilla: bone histomorphometry and finite element analysis. *Biomech. Model. Mechanobiol.* 12 <https://doi.org/10.1007/s10237-012-0401-z>.
- Huotilainen, E., Jaanimets, R., Valášek, J., Marcián, P., Salmi, M., Tuomi, J., Mäkitie, A., Wolff, J., 2014. Inaccuracies in additive manufactured medical skull models caused by the DICOM to STL conversion process. *J. Cranio-Maxillofacial Surg.* 42 <https://doi.org/10.1016/j.jcms.2013.10.001>.
- Inagawa, H., Suzuki, N., Aoki, K., Wakabayashi, N., 2018. Potential for estimation of Young's modulus based on computed tomography numbers in bone: a validation study using a nano-indentation test on murine maxilla. *Dent. Oral Craniofacial Res.* 4 <https://doi.org/10.15761/DOCR.1000254>.
- Kayabaşı, O., Yüzbasoğlu, E., Erzincanlı, F., 2006. Static, dynamic and fatigue behaviors of dental implant using finite element method. *Adv. Eng. Software* 37, 649–658. <https://doi.org/10.1016/j.advengsoft.2006.02.004>.
- Keller, T.S., 1994. Predicting the compressive mechanical behavior of bone. *J. Biomech.* 27, 1159–1168.
- Korabi, R., Shemtov-Yona, K., Dorogoy, A., Rittel, D., 2017. The failure envelope concept applied to the bone-dental implant system. *Sci. Rep.* 7, 2051. <https://doi.org/10.1038/s41598-017-02282-2>.
- Lee, H., Park, S., Noh, G., 2018. Biomechanical analysis of 4 types of short dental implants in a resorbed mandible. *J. Prosthet. Dent.* <https://doi.org/10.1016/j.prosdent.2018.07.013>.
- Lekadir, K., Noble, C., Hazrati-Marangalou, J., Hoogendoorn, C., van Rietbergen, B., Taylor, Z.A., Frangi, A.F., 2016. Patient-specific biomechanical modeling of bone strength using statistically-derived fabric tensors. *Ann. Biomed. Eng.* 44, 234–246. <https://doi.org/10.1007/s10439-015-1432-2>.
- Limbert, G., van Lierde, C., Muraru, O.L., Walboomers, X.F., Frank, M., Hansson, S., Middleton, J., Jaecques, S., 2010. Trabecular bone strains around a dental implant and associated micromotions—a micro-CT-based three-dimensional finite element study. *J. Biomech.* 43, 1251–1261. <https://doi.org/10.1016/j.jbiomech.2010.01.003>.
- Liu, J., Pan, S., Dong, J., Mo, Z., Fan, Y., Feng, H., 2013. Influence of implant number on the biomechanical behaviour of mandibular implant-retained/supported overdentures: a three-dimensional finite element analysis. *J. Dent.* 41, 241–249. <https://doi.org/10.1016/j.jdent.2012.11.008>.
- Mao, Q., Su, K., Zhou, Y., Hossaini-Zadeh, M., Lewis, G.S., Du, J., 2019. Voxel-based micro-finite element analysis of dental implants in a human cadaveric mandible: tissue modulus assignment and sensitivity analyses. *J. Mech. Behav. Biomed. Mater.* 94, 229–237. <https://doi.org/10.1016/j.jmbm.2019.03.008>.
- Marcián, P., Borák, L., Valášek, J., Kaiser, J., Florian, Z., Wolff, J., 2014. Finite element analysis of dental implant loading on atrophic and non-atrophic cancellous and cortical mandibular bone - a feasibility study. *J. Biomech.* 47 <https://doi.org/10.1016/j.jbiomech.2014.10.019>.
- Marcián, P., Konečný, O., Borák, L., Valášek, J., Řehák, K., Krpálek, D., Florian, Z., 2011. On the level of computational models in biomechanics depending on gained data from CT/MRI and micro-CT. In: *Mendel*.
- Marcián, P., Narra, N., Borák, L., Chamrad, J., Wolff, J., 2019. Biomechanical performance of cranial implants with different thicknesses and material properties: a finite element study. *Comput. Biol. Med.* 109, 43–52. <https://doi.org/10.1016/j.compbmed.2019.04.016>.
- Marcián, P., Wolff, J., Horáčková, L., Kaiser, J., Zikmund, T., Borák, L., 2018a. Micro finite element analysis of dental implants under different loading conditions. *Comput. Biol. Med.* 96 <https://doi.org/10.1016/j.compbmed.2018.03.012>.
- Marcián, Petr, Wolff, J., Horáčková, L., Kaiser, J., Zikmund, T., Borák, L., 2018b. Micro finite element analysis of dental implants under different loading conditions. *Comput. Biol. Med.* <https://doi.org/10.1016/j.compbmed.2018.03.012>.
- Matsiushevich, K., Belvedere, C., Leardini, A., Durante, S., 2018. Quantitative comparison of freeware software for bone mesh from DICOM files. *J. Biomech.* <https://doi.org/10.1016/j.jbiomech.2018.12.031>.
- Miles, B.A., Sinn, D.P., Gion, G.G., 2006. Experience with cranial implant-based prosthetic reconstruction. *J. Craniofac. Surg.* 17, 889–897. <https://doi.org/10.1097/01.scs.0000230614.72141.b9>.
- Minnema, J., van Eijnatten, M., Kouw, W., Diblen, F., Mendrik, A., Wolff, J., 2018. CT image segmentation of bone for medical additive manufacturing using a convolutional neural network. *Comput. Biol. Med.* 103, 130–139. <https://doi.org/10.1016/j.compbmed.2018.10.012>.
- Motherway, J.A., Verschuere, P., Van der Perre, G., Vander Sloten, J., Gilchrist, M.D., 2009. The mechanical properties of cranial bone: the effect of loading rate and cranial sampling position. *J. Biomech.* 42, 2129–2135. <https://doi.org/10.1016/j.jbiomech.2009.05.030>.
- Narra, N., Valášek, J., Hannula, M., Marcián, P., Sándor, G.K., Hyttinen, J., Wolff, J., 2014. Finite element analysis of customized reconstruction plates for mandibular continuity defect therapy. *J. Biomech.* 47 <https://doi.org/10.1016/j.jbiomech.2013.11.016>.
- Natali, A.N., Carniel, E.L., Pavan, P.G., 2008. Investigation of bone inelastic response in interaction phenomena with dental implants. *Dent. Mater.* 24, 561–569. <https://doi.org/10.1016/j.dental.2007.11.024>.
- Niinomi, M., 1998. Mechanical properties of biomedical titanium alloys. *Mater. Sci. Eng., A* 243, 231–236. [https://doi.org/10.1016/S0921-5093\(97\)00806-X](https://doi.org/10.1016/S0921-5093(97)00806-X).
- Pappalardo, F., Russo, G., Tshinanu, F.M., Viceconti, M., 2018. In Silico Clinical Trials: Concepts and Early Adoptions. *Bioinform. Brief.* <https://doi.org/10.1093/bib/bby043>.
- Pellizzer, E.P., Lemos, C.A.A., Almeida, D.A.F., de Souza Batista, V.E., Santiago Júnior, J. F., Verri, F.R., 2018. Biomechanical analysis of different implant-abutments interfaces in different bone types: an in silico analysis. *Mater. Sci. Eng. C* 90, 645–650. <https://doi.org/10.1016/j.msec.2018.05.012>.
- Rahmoun, J., Auperrin, A., Delille, R., Naceur, H., Drazetic, P., 2014. Characterization and micromechanical modeling of the human cranial bone elastic properties. *Mech. Res. Commun.* 60, 7–14. <https://doi.org/10.1016/j.mechrescom.2014.04.001>.
- Rho, J.Y., Tsui, T.Y., Pharr, G.M., 1997. Elastic properties of human cortical and trabecular lamellar bone measured by nanoindentation. *Biomaterials* 18, 1325–1330.
- Ridwan-Pramana, A., Marcián, P., Borák, L., Narra, N., Forouzanfar, T., Wolff, J., 2017. Finite element analysis of 6 large PMMA skull reconstructions: a multi-criteria evaluation approach. *PLoS One* 12. <https://doi.org/10.1371/journal.pone.0179325>.
- Ridwan-Pramana, A., Marcián, P., Borák, L., Narra, N., Forouzanfar, T., Wolff, J., 2016. Structural and mechanical implications of PMMA implant shape and interface geometry in cranioplasty - a finite element study. *J. Cranio-Maxillofacial Surg.* 44 <https://doi.org/10.1016/j.jcms.2015.10.014>.
- Rungsiyakull, C., Chen, J., Rungsiyakull, P., Li, W., Swain, M., Li, Q., 2015. Bone's responses to different designs of implant-supported fixed partial dentures. *Biomech. Model. Mechanobiol.* 14, 403–411. <https://doi.org/10.1007/s10237-014-0612-6>.
- Sarrafpour, B., Rungsiyakull, C., Swain, M., Li, Q., Zoellner, H., 2012. Finite element analysis suggests functional bone strain accounts for continuous post-eruptive emergence of teeth. *Arch. Oral Biol.* 57, 1070–1078. <https://doi.org/10.1016/j.archoralbio.2012.05.001>.
- Schileo, E., Taddei, F., Cristofolini, L., Viceconti, M., 2008. Subject-specific finite element models implementing a maximum principal strain criterion are able to estimate

- failure risk and fracture location on human femurs tested in vitro. *J. Biomech.* 41, 356–367. <https://doi.org/10.1016/j.jbiomech.2007.09.009>.
- Schneider, C.A., Rasband, W.S., Eliceiri, K.W., 2012. NIH Image to ImageJ: 25 years of image analysis. *Nat. Methods* 9, 671–675. <https://doi.org/10.1038/nmeth.2089>.
- Sekhon, K., Kazakia, G.J., Burghardt, A.J., Hermannsson, B., Majumdar, S., 2009. Accuracy of volumetric bone mineral density measurement in high-resolution peripheral quantitative computed tomography. *Bone* 45, 473–479. <https://doi.org/10.1016/j.bone.2009.05.023>.
- Shelfelbine, S.J., Simon, U., Claes, L., Gold, A., Gabet, Y., Bab, I., Müller, R., Augat, P., 2005. Prediction of fracture callus mechanical properties using micro-CT images and voxel-based finite element analysis. *Bone* 36, 480–488. <https://doi.org/10.1016/j.bone.2004.11.007>.
- Shibata, Y., Tanimoto, Y., Maruyama, N., Nagakura, M., 2015. A review of improved fixation methods for dental implants. Part II: biomechanical integrity at bone-implant interface. *J. Prosthodont. Res.* 59, 84–95. <https://doi.org/10.1016/j.jpor.2015.01.003>.
- Sinn, D.P., Bedrosian, E., Vest, A., 2011. Craniofacial implant surgery. In: Miloro, M. (Ed.), *Peterson's Principles of Oral & Maxillofacial Surgery*. People's Medical Publishing House-USA.
- Snyder, S.M., Schneider, E., 1991. Estimation of mechanical properties of cortical bone by computed tomography. *J. Orthop. Res.* 9, 422–431. <https://doi.org/10.1002/jor.1100090315>.
- Suzuki, N., Aoki, K., Marcián, P., Borák, L., Wakabayashi, N., 2016. A threshold of mechanical strain intensity for the direct activation of osteoblast function exists in a murine maxilla loading model. *Biomech. Model. Mechanobiol.* 15 <https://doi.org/10.1007/s10237-015-0746-1>.
- Turner, C.H., Rho, J., Takano, Y., Tsui, T.Y., Pharr, G.M., 1999. The elastic properties of trabecular and cortical bone tissues are similar: results from two microscopic measurement techniques. *J. Biomech.* 32, 437–441.
- van Eijnatten, M., van Dijk, R., Dobbe, J., Streekstra, G., Koivisto, J., Wolff, J., 2018. CT image segmentation methods for bone used in medical additive manufacturing. *Med. Eng. Phys.* 51, 6–16. <https://doi.org/10.1016/j.medengphy.2017.10.008>.
- van Rietbergen, B., Weinans, H., Huiskes, R., Odgaard, A., 1995. A new method to determine trabecular bone elastic properties and loading using micromechanical finite-element models. *J. Biomech.* 28, 69–81.
- Viceconti, M., 2011. *Multiscale Modeling of the Skeletal System*. Cambridge University Press, Cambridge. <https://doi.org/10.1017/CBO9781139049627>.
- Wee, H., Armstrong, A.D., Flint, W.W., Kunselman, A.R., Lewis, G.S., 2015. Peri-implant stress correlates with bone and cement morphology: micro-FE modeling of implanted cadaveric glenoids. *J. Orthop. Res.* 33, 1671–1679. <https://doi.org/10.1002/jor.22933>.
- Wirth, A.J., Müller, R., van Lenthe, G.H., 2012. The discrete nature of trabecular bone microarchitecture affects implant stability. *J. Biomech.* 45, 1060–1067. <https://doi.org/10.1016/j.jbiomech.2011.12.024>.
- Wolff, J., Narra, N., Antalainen, A.-K., Valásek, J., Kaiser, J., Sándor, G.K., Marcián, P., 2014. Finite element analysis of bone loss around failing implants. *Mater. Des.* 61 <https://doi.org/10.1016/j.matdes.2014.04.080>.
- Yoda, N., Zheng, K., Chen, J., Li, W., Swain, M., Sasaki, K., Li, Q., 2017. Bone morphological effects on post-implantation remodeling of maxillary anterior buccal bone: a clinical and biomechanical study. *J. Prosthodont. Res.* 61, 393–402. <https://doi.org/10.1016/j.jpor.2016.12.010>.
- Yoganandan, N., Pintar, F.A., Zhang, J., Baisden, J.L., 2009. Physical properties of the human head: mass, center of gravity and moment of inertia. *J. Biomech.* 42, 1177–1192. <https://doi.org/10.1016/j.jbiomech.2009.03.029>.
- Zadpoor, A.A., Weinans, H., 2015. Patient-specific bone modeling and analysis: the role of integration and automation in clinical adoption. *J. Biomech.* 48, 750–760. <https://doi.org/10.1016/j.jbiomech.2014.12.018>.

PAPER [XXVIII]

# Effect of deriving periosteal and endosteal contours from microCT scans on computation of cross-sectional properties in non-adults: the femur

Vladimír Sládek,<sup>1</sup>  Veronika Sabolová,<sup>1</sup> Ondřej Šebesta,<sup>1</sup> Tomáš Zikmund,<sup>2</sup> Jozef Kaiser<sup>2</sup> and Simona Čerevková<sup>1</sup>

<sup>1</sup>Faculty of Science, Charles University, Prague 2, Czech Republic

<sup>2</sup>Central European Institute of Technology, Brno University of Technology, Brno, Czech Republic

## Abstract

Derivation of periosteal and endosteal contours taken from transversal long bone cross-sections limits the accuracy of calculated biomechanical properties. Although several techniques are available for deriving both contours, the effect of these techniques on accuracy of calculated cross-sectional properties in non-adults is unknown. We examine a sample of 86 non-adult femora from birth to 12 years of age to estimate the effect of error in deriving periosteal and endosteal contours on cross-sectional properties. Midshaft cross-sections were taken from microCT scans and contours were derived using manual, fully automatic, spline, and ellipse techniques. Agreement between techniques was assessed against manually traced periosteal and endosteal contours using percent prediction error (%PE), reduced major axis analysis, and limits of agreement. The %PEs were highest in the medullary area and lowest in the total area. Mean %PEs were sufficiently below the 5% level of acceptable error, except for medullary areas, but individual values can greatly exceed this 5% boundary given the high standard deviation of %PE means and wide minimum–maximum range of %PEs. Automatic processing produces greater errors than does combination with manual, spline, and ellipse processing. Although periosteal contour is estimated with stronger agreement compared with endosteal contour, error in deriving periosteal contour has a substantially greater effect on calculated section moduli than does error in deriving endosteal contours. We observed no size effect on the resulting bias. Nevertheless, cross-sectional properties in a younger age category may be estimated with greater error compared with in an older age category. We conclude that non-adult midshaft cross-sectional properties can be derived from microCT scans of femoral diaphyses with mean error of < 5% and that derivation of endosteal contour can be simplified by the ellipse technique because fully automatic derivation of endosteal contour may increase the resulting error, especially in small samples.

**Key words:** biomechanics; EPmAcROJ; femora; IMAGEJ; microCT.

## Introduction

Biomechanical analysis of long bone cross-sections provides important insight into the functional anatomy of adult and non-adult human skeletons (Ruff, 2008; Skedros, 2011). Although cross-sectional analysis is becoming a standard tool and analyses of large datasets are already available for adults (Ruff et al. 2015; Sládek et al. 2016), cross-sectional analysis of non-adults remains rare. This is partly because the smaller size of non-adult diaphyses limits application of

the techniques elaborated for adults. Thus, any improvement in the technique for obtaining cross-sectional properties for non-adults would increase the availability of datasets and improve our knowledge of human postcranial ontogeny.

Biomechanical analysis of diaphyses employs properties estimating diaphyseal strength and rigidity such as cross-sectional areas, second moments of areas, and section moduli (Biewener, 1992). All of these properties are calculated from periosteal and endosteal contours utilizing the engineering beam model (Huiskes, 1982). Thus, estimation of both contours is the most important step influencing the final accuracy.

Cross-sectional contours can be obtained by direct sectioning of diaphyses (DSM; Kimura, 1971; Takahashi, 1982) and using natural breaks (Lovejoy & Trinkaus, 1980; Di Vincenzo et al. 2015). Cross-sectional contours can also be

### Correspondence

Vladimír Sládek, Faculty of Science, Charles University, Viničná 7, 128 43 Prague 2, Czech Republic. E: sladekv@yahoo.fr

Accepted for publication 3 May 2018

Article published online 31 May 2018

estimated either by the molding of periosteal contours and using indirectly estimated endosteal contours from biplanar radiographs, such as in the latex cast method (LCM; Trinkaus & Ruff, 1989), or by fitting ellipses without attempting to reconstruct the true shape, using the ellipse model method (EMM; Runestad et al. 1993; Ohman, 1993). Finally, contours can be taken from CT images (CTSM; Sumner et al. 1985). None of these techniques provides an ideal solution for deriving cross-sectional properties in non-adults, but CTSM seems to be a better solution because it enables a combination of techniques for deriving contours (Sylvester et al. 2010). Standard CT scans do not achieve sufficient resolution in non-adults, and the processing of images may be limited by the more irregular shape of the non-adult endosteal contour. However, higher resolution can be obtained by microCT scanning, and it is therefore not necessary to also reject automatic and semi-automatic processing of microCT images in non-adults. It has been shown on adult cross-sections that the estimation of the periosteal contour shows strong agreement (Stock, 2002; O'Neill & Ruff, 2004), and we may expect that this will also be true for non-adults. In contrast, estimation of the endosteal contour is subject to greater error in adults, especially for cross-sections with thinner cortices and less circular shapes (Stock, 2002; O'Neill & Ruff, 2004). Nevertheless, the error in estimated endosteal contours may have a low impact on biomechanical properties because the endosteal contour is less relevant in the calculation (Stock, 2002; O'Neill & Ruff, 2004). This assumption follows the prediction that mechanical rigidity increases from the centroid (Martin et al. 1998) and that the tissue situated near the periosteal contour is mechanically more relevant. Thus, we may expect that automatic processing of the endosteal contour may have a greater impact on the medullary area than on other properties and that accuracy in the endosteal contour can be increased by a semi-automatic technique approaching the endosteal boundary by fitting an ellipse, similarly to the LCM method.

The main goal of this paper is to establish an image processing protocol for derivation of cross-sectional contours that is as accurate as possible while also employing automatization to the maximum extent. We concentrate on microCT images of non-adult femora between birth and 12 years of age. We analyze agreement between the manually estimated contours, used in this study as the 'true' values, and automatically and semi-automatically derived properties.

## Materials and methods

The total sample consisted of 86 non-adult femoral diaphyses selected from the Early Medieval sites Pohansko and Mikulčice (Czech Republic; Sládek & Macháček, 2017; Poláček, 2008). Pohansko and Mikulčice belong to the main centers of the Great Moravian Empire dated between the 9th and 10th centuries A.D. (Macháček, 2010) and are characterized by excellent preservation of

non-adult skeletons (Sládek & Makajevová, 2017). All individuals were pooled without respect to sex because no effect of sexual dimorphism on the accuracy of cross-sectional properties has been observed, even among adults (O'Neill & Ruff, 2004). The selected individuals also had well-preserved diaphyses without any substantial damage. Given that the asymmetry in femoral length in our sample was near zero, we preferred the more preserved left side (only six femora were from the right side).

We used three age-at-death categories, *Infans* Ia, Ib, and II (Table 1), following the general division of the non-adult period of Knussmann (1988). We narrowed Knussmann's age category Ia up to 0.99 year to avoid the larger variability caused by mixing of perinatal and early postnatal individuals (see details about definition of age categories and age-at-death estimation in Sládek et al. 2017). The age-at-death was estimated using crown and root formation following the technique of Ubelaker (1989) with high agreement with calendar age (Smith, 2005; AlQahtani et al. 2014). The age-at-death for 12 individuals was estimated by the technique of Stloukal & Hanáková using the length of the diaphysis (1978), presenting the best agreement with dental age in the Early Medieval samples (Sládek et al. 2017).

Femoral diaphyses were imaged using a microCT station of the GE PHOENIX V|TOME|x L240 equipped with a 240 kV/320 W micro-focus X-ray tube. The parameters of tomographic measurements were set according to the bone thickness. The accelerating voltage of the X-ray tube was set to 70–100 kV and filtered through a 1-mm-thick aluminum plate. An exposure time of 400 ms was used in every position of the 360° rotation (Hsieh, 2003). The resolution was set with a voxel size between 0.05 and 0.186 mm, depending upon the age category and diaphysis size (Table 1). Diaphyses were imaged either individually or as a group of four to six bones mounted in a thin-walled paper tube. The tomographic reconstruction was carried out using the GE PHOENIX DATOS|x 2.0 software. Image data were further reconstructed using DATOS and then visualized and rendered in VGSTUDIO v2.2 and v3.0. Each image was oriented using the digital tools available in VGSTUDIO (Bouxsein et al. 2010). The bone was oriented with the longitudinal axis connecting the midpoints on the anterior side of the proximal and distal ends. The second axis connected the midpoints on the lateral side of the diaphyseal ends. The third axis connected the lateral and medial midpoints on the metaphyseal surfaces. Sections were taken in the transversal plane perpendicular to our coordinate system. We used cross-sections at 50% of the maximum femoral diaphyseal length taken parallel to its longitudinal axis. Given that studied individuals lacked fused epiphyses and that the potential error in the midshaft location between the total and diaphyseal length was relatively small (i.e. 1.75% distally; Gosman et al. 2013), no adjustment was made for midshaft location.

Derivation of contours and calculation of cross-sectional properties were performed using `FUI` (Schindelin et al. 2012) and our newly developed `EPmacroJ` (v1) implementation (see <https://github.com/Schebique/EPmacroJ> for the most recent version of the macro). `EPmacroJ` enables cross-sectional properties to be derived from different protocols used for estimating periosteal and endosteal contours. `EPmacroJ` has been further enhanced by implementing the script from the `MOMENTmacroJ` used for calculating cross-sectional properties (see details about `MOMENTmacroJ` v1.4B at <http://www.hopkinsmedicine.org/fae/mmacro.html>).

Contours were determined on each cross-section using manual, automatic, and semi-automatic processing (Fig. 1). Periosteal contours were determined manually (m) and automatically (a). Endosteal contours were estimated manually (m), automatically (a), and

**Table 1** Studied sample descriptive statistics.

	Total (n = 86)			Age category Ia (n = 9)			Age category Ib (n = 55)			Age category II (n = 22)		
	Mean	SD	Range	Mean	SD	Range	Mean	SD	Range	Mean	SD	Range
Age	4.3	2.93	0–12	0.6	0.41	0–1	3.2	1.46	1.2–6.5	8.5	1.21	7–12
Pixel size	0.119	0.0238	0.05–0.186	0.083	0.0226	0.05–0.103	0.117	0.0183	0.09–0.186	0.139	0.016	0.13–0.186
Femoral length	191.1	52.88	77–324	104.1	22.79	77–124	172.1	27.73	122–234	259.2	29.77	224–324
A-P diameter	12.6	3.03	5.7–20.6	7.6	1.71	5.7–9.8	11.9	1.55	8.6–15.7	16.3	1.95	13.3–20.6
M-L diameter	12.8	2.75	6–18.9	8.3	1.98	6–10.9	12.2	1.33	9.4–15	16.2	1.65	14–18.9
TA <sub>m</sub>	128.2	55.71	25.1–291.5	50.7	22.54	25.1–78.7	111.7	25.15	63.3–170.4	201.2	43.22	137.3–291.5
CA <sub>m</sub>	79.7	39.2	20.8–187.7	35.5	12.32	20.8–52.5	65	17.43	30.6–100.6	134.4	29.02	94.1–187.7
MA <sub>m</sub>	48.6	20.93	4.4–127.7	15.2	10.63	4.4–29.3	46.7	13.05	19.2–76.6	66.8	21.4	31.7–127.7
Zx <sub>m</sub>	176.6	123.63	15.3–569.9	44.3	25.45	15.3–75.2	130.8	48.32	46–250.2	345.2	113.4	199.5–569.9
Zy <sub>m</sub>	185.2	124.26	17.5–572.1	50.2	30.01	17.5–95.6	138.7	47.69	55.9–259.3	356.6	109.67	214.3–572.1
Zp <sub>m</sub>	346.2	239.81	31.7–1066.2	88.1	51.27	31.7–159.2	257	93.4	96.8–505.7	674.8	216.43	389.6–1066.2

CA, cortical area; MA, medullary area; TA, total area; Zp, polar section modulus (areas in mm<sup>2</sup>, section moduli in mm<sup>3</sup>); Zx, A-P section modulus; Zy, M-L section modulus. Age category Ia: birth to 0.99 year, age category Ib: 1–6.99 years, age category II: 7–12 years. Pixel size in mm. Femoral length taken as diaphyseal length between the most proximal and distal points parallel to longitudinal axis (mm). A-P diameter: anterior-posterior diameter; M-L diameter: medial-lateral diameter; taken at 50% of diaphyseal length (mm). Statistics for areas and section moduli are computed from manually traced periosteal and endosteal contours at 50% of femoral diaphyseal length. All studied properties are significantly different between age categories at *P* < 0.001.

by spline curve (s) and ellipse (e). Automatic processing was based on the histogram-derived 'minimum' thresholding method (Prewitt & Mendelsohn, 1966). The spline curve method estimates the endosteal boundary using four points manually placed on the endosteal boundary at the intersection points between the endosteal boundary and the axis of the maximum and minimum second moments of area. The resulting endosteal contour was then computed using IMAGEJ tool Convex Hull to connect the points and, subsequently, to fit a spline curve using the built-in Fit Spline-in function. The ellipse technique estimated the endosteal contour using the same four points as in the spline technique. The endosteal contour was then estimated by fitting an ellipse into the four selected points using the built-in Fit Ellipse function. The IMAGEJ Fit Ellipse algorithm fits an ellipse with the most similar area to that provided by the initial selection.

Special attention was given to the manual processing of contours. The contours were defined on microCT scans using points placed manually using digital tools in IMAGEJ. Points were placed on contours in gray scale between the minimum density (i.e. air) and maximum density (i.e. cortical bone tissue). The distance between the selected points was in the range of 3–10 pixels, depending upon the irregularity of the estimated shape and age category. The resulting contours were estimated from approximately 50 points for age Ia, 70 points for age Ib, and 85 points for age II. The presence of trabecular bone and poor development of a clear endosteal boundary made estimation of endosteal contour particularly difficult. When trabecular bone was present, we followed the recommendation of Ruff & Hayes (1983) while trying to include only cortical bone into the final endosteal contour.

Cross-sectional areas were estimated as the total area (TA), cortical area (CA), and medullary area (MA). The total area is the measure of the subperiosteal area, the medullary area is the subendosteal area, and the cortical area is the area between the periosteal and endosteal contours. Section moduli were

estimated with respect to anterior–posterior ( $Z_x$ ) and medial–lateral axes ( $Z_y$ ) and as polar section modulus ( $Z_p$ ) (for further details see Ruff, 2008).

Cross-sectional properties were calculated to assess all possible combinations between manual (m) and automatic (a), periosteal and manual (m), automatic (a), spline (s), and ellipse (e) methods for endosteal contour processing. We analyzed two estimates of the total area (manual: TA\_m; automatic: TA\_a) and four estimates of the medullary area (manual: MA\_m; automatic: MA\_a; spline: MA\_s; ellipse: MA\_e). The cortical area and section moduli combined two options for periosteal contour and four options for endosteal contour processing. For example, we analyzed CA estimated from four options for endosteal contour processing with manual periosteal contour processing (CA\_mm, CA\_ma, CA\_ms, and CA\_me) and four options for endosteal contour processing with automatic periosteal contour (CA\_am, CA\_aa, CA\_as, and CA\_ae) processing. The first lowercase letter indicates the method of processing the periosteal contour and the second indicates the method used for the endosteal contour.

We evaluated the overall accuracy as the agreement between properties calculated from manually traced contours and those calculated from other techniques. It was expected that manually traced contours give or would give results nearest to the true biomechanical properties, even though the actual accuracy of the manually traced contours against the true values is unknown. Agreement between the studied techniques was further specified by an acceptable error at 5%, which is widely used in studies of cross-sectional geometry (Trinkaus & Ruff, 1989; Stock, 2002; O'Neill & Ruff, 2004). We are aware, however, that the magnitude of the acceptable error may differ based on the settings for a particular analysis. Therefore, we also provide details about the range of agreement (i.e. limits of agreement; see below) to specify the practical impact of the observed error for further applications.

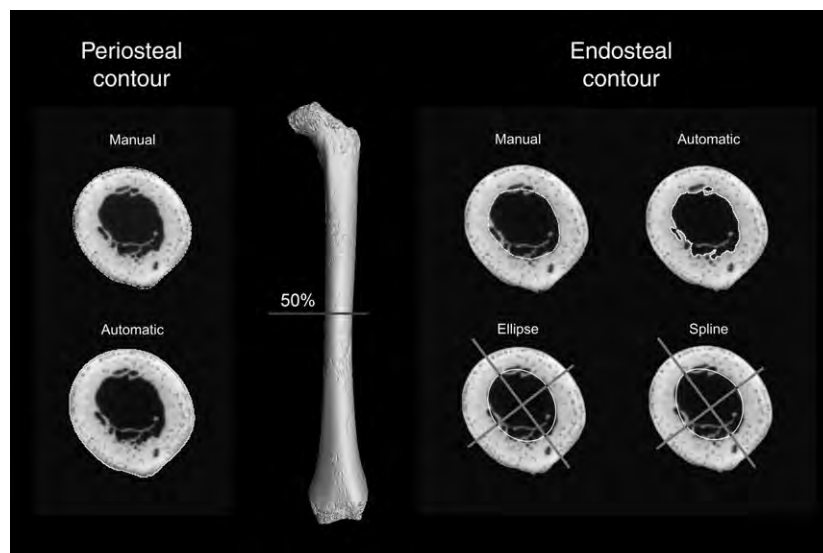


**Fig. 1** Techniques used for deriving periosteal and endosteal contours: manual, automatic, ellipse, and spline. The gray lines on ellipse and spline endosteal contour derivation represent  $I_x$  and  $I_y$  axes used for manual placement of points of intersection with endosteal contours. Note that manual contours were derived using manually placed points (each point is presented on the manually derived contour), whereas automatic contours were derived only by automatic algorithms (i.e. no points are presented on the contour). Automatic contours derived on the endosteal boundary also each follow the marginal projection of the trabecular bone, including small holes due to rough surfaces.

Directional bias was estimated using the percent prediction error: %PE = [(true – estimated)/estimated] × 100 where ‘true’ is a property obtained by manual processing and ‘estimated’ is a property estimated by some combination of manual, automatic, spline, and ellipse processing. Percent PEs between manual and other techniques were analyzed by repeated-measures ANOVA with Tukey’s *post-hoc* test. Systematic bias was assessed by the slope of the reduced major axis (RMA). Manually determined values were used as the baseline from which to develop RMA equations for cross-sectional properties obtained by other techniques. Only log-transformed data were used for RMA analysis. The effect of size on accuracy was specified as a test of RMA slopes against isometry (i.e. slope = 1).

Because correlation and regression analysis may provide misleading results when analyzing accuracy, an alternative approach using the limits of agreement was also applied (see details in Bland & Altman, 1986). We computed the individual differences between manually determined values and values obtained by other techniques as Diff = (true – estimated), where ‘true’ is the value obtained by manual processing and ‘estimated’ is the value obtained by combination with other techniques. We also calculated the mean Diff and standard deviation of Diff (SD<sub>diff</sub>) to compute ±95% limits of agreement (±95%LA) according to the equation ±95%LA = mean Diff ± 1.96 × SD<sub>diff</sub>. Limits of agreement were computed from log-transformed data and are presented in figures. The limits of agreement are also presented as raw data in a table. This may help to compute limits of agreement in a practical application when the error in accuracy must be specified as an acceptable error other than 5%.

The data were prepared and limits of agreement were calculated in Microsoft EXCEL 2010 (2010 Microsoft Corporation). In addition, statistical analysis was carried out using STATISTICA 12 for Windows (2013 StatSoft). The RMA regressions were computed using RMA software v1.14 (Bohonak, 2002).

**Results**

The mean statistics for diaphyseal and manually obtained cross-sectional properties are shown in Table 1. As expected, there was a significant increase in the mean diaphyseal and cross-sectional properties from younger (Ia) to older (II) age groups at *P* < 0.001. Cross-sectional properties also showed an increase in standard deviation and minimum–maximum range between younger and older age categories.

The mean directional %PEs for estimated cross-sectional properties are shown in Tables 2 and 3. The mean %PEs were highest in MA (2.5–6%) and lowest in TA (–0.25%) in the total sample. Although this trend was also present among age groups, the effect of periosteal and endosteal processing on MA and TA diminished between age categories Ia and II. The MA estimated by automatic processing in age group Ia was particularly sensitive, with a %PE of approximately 16% compared with the %PE of 3.5% obtained for age II.

The mean %PEs for CA and section moduli ranged between 0.1 and 2.5% in the total sample. Although this

**Table 2** Percent prediction error (%PE) in cross-sectional properties: total sample.

		Total (n = 86)			
	Tech	Mean	SD	Range	ANOVA
TA	a	–0.25	1.028	–3.24–2.85	n.s.
CA	ma	–2.23	5.291	–19.55–17.27	*
	ms	–1.28	2.369	–7.04–7.11	*
	me	–1.33	2.347	–6.99–6.89	*
	aa	–2.48	5.947	–19.01–23.2	*
	am	–0.30	1.717	–4.35–6.19	
	as	–1.58	2.646	–6.92–6.6	*
	ae	–1.63	2.622	–6.86–6.38	*
MA	a	5.76	12.246	–20.47–56.36	<i>P</i> < 0.01
	s	2.34	4.284	–14.77–12.32	*
	e	2.40	4.242	–14.41–12.2	*
Zx	ma	–0.96	4.014	–13.83–17.97	<i>P</i> < 0.01
	ms	–1.79	2.714	–8.13–6.65	*
	me	–1.48	2.655	–7.61–6.13	*
	aa	–1.31	5.071	–13.72–22.58	
	am	–0.48	2.51	–6.90–7.65	
	as	–2.12	3.526	–10.33–7.58	*
	ae	–1.97	3.476	–10.35–7.3	*
Zy	ma	–1.06	3.259	–10.01–17.14	<i>P</i> < 0.01
	ms	–0.37	2.371	–5.65–6.95	*
	me	–0.11	2.452	–6.16–6.92	
	aa	–1.41	4.217	–9.23–22.59	*
	am	–0.43	2.121	–6.61–5.61	
	as	–1.04	2.998	–9.12–7.2	
	ae	–0.85	3.036	–8.9–7.99	
Zp	ma	–1.06	3.612	–10.86–17.07	<i>P</i> < 0.01
	ms	–0.87	2.048	–6.47–5.18	*
	me	–0.47	2.011	–5.36–4.77	
	aa	–1.30	4.643	–11.17–23.56	*
	am	–0.30	2.09	–5.29–6.67	
	as	–1.12	2.601	–7.03–4.77	*
	ae	–0.75	2.596	–6.76–6.55	

%PE = [(true – estimated)/estimated × 100], where ‘true’ indicates manually traced contours and estimated indicates compared techniques. Tech: technique (a – automatic, m – manual, s – spline, and e – ellipse processing of periosteal and endosteal contours). First letter under technique indicates processing of periosteal contour and second letter represents processing of endosteal contour. The technique used was periosteal contour for TA and endosteal contour for MA. Range: minimum–maximum range. ANOVA: significances from repeated-measures ANOVA for overall test, *post-hoc* comparison with factor ‘Technique’ (i.e. between manually obtained cross-sectional property and other compared technique).

\*Significant at *P* < 0.05, n.s.: not significant. (See Table 1 for further abbreviations).

**Table 3** Percent prediction error (%PE) in cross-sectional properties according to age.

	Tech	Age category Ia (n = 9)					Age category Ib (n = 55)					Age category II (n = 22)				
		Mean	SD	Range	ANOVA	Mean	SD	Range	ANOVA	Mean	SD	Range	ANOVA			
TA	a	-1.26	1.544	-3.24-0.82	P = 0.049	-0.12	1.025	-2.51-2.85	n.s.	-0.14	0.421	-0.95-0.84	n.s.			
	ma	-2.58	4.382	-8.84-5.04	*	-2.47	6.301	-19.55-17.27	*	-1.48	1.760	-5.19-1.28	*			
	ms	-0.83	2.206	-3.71-4.38	n.s.	-1.33	2.773	-7.04-7.11	*	-1.37	0.997	-3.60-1.70	*			
	me	-0.83	2.210	-3.67-4.41		-1.38	2.74	-6.99-6.89		-1.43	1.004	-3.68-1.64	*			
	aa	-4.14	5.162	-11.89-5.02		-2.50	7.042	-19.01-23.2	*	-1.72	1.920	-6.16-0.98	*			
	am	-1.69	2.064	-4.35-0.89		-0.09	1.868	-3.88-6.19		-0.26	0.624	-1.13-1.39	*			
	as	-2.49	3.003	-6.01-4.36		-1.42	3.001	-6.92-6.6		-1.61	1.152	-3.74-1.03	*			
	ae	-2.49	2.976	-5.81-4.39		-1.47	2.973	-6.86-6.38		-1.68	1.152	-3.82-0.94	*			
MA	a	15.64	22.075	-8.91-52.4	n.s.	5.06	11.785	-20.47-56.36	*	3.45	3.938	-3.17-11.96	*			
	s	3.31	5.165	-7.88-8.70		1.88	4.678	-14.77-12.32		3.09	2.513	-4.14-8.44	*			
	e	3.24	5.100	-7.93-9.05		1.93	4.632	-14.41-12.20		3.22	2.488	-4.01-8.65	*			
	Zx				P < 0.01				P < 0.01				P < 0.01			
Zy	ma	-1.40	2.456	-6.61-1.4		-1.11	4.883	-13.83-17.97		-0.41	1.076	-2.33-2.17	*			
	ms	-1.56	2.531	-7.64-0.69		-2.09	3.056	-8.13-6.65	*	-1.16	1.642	-5.60-1.51	*			
	me	-1.08	2.301	-6.64-1.12		-1.66	3.007	-7.61-6.13	*	-1.19	1.742	-6.01-2.09	*			
	aa	-4.13	2.407	-6.85-0.78		-1.31	6.047	-13.72-22.58		-0.16	1.744	-3.22-3.34	*			
	am	-3.00	2.163	-6.9-0.60		-0.35	2.65	-5.38-7.65		0.25	1.528	-3.47-3.32	*			
	as	-4.51	2.665	-8.47-1.06	*	-2.26	3.908	-10.33-7.58	*	-0.80	1.995	-5.87-2.31	*			
	ae	-4.26	2.374	-7.46-1.22	*	-2.01	3.919	-10.35-7.3	*	-0.94	1.978	-6.28-1.86	*			
	Zy				P < 0.01				n.s.				n.s.			
Zp	ma	-1.15	1.829	-3.8-2.77		-1.14	3.957	-10.01-17.14		-0.83	1.171	-4.13-1.19	*			
	ms	-0.98	2.058	-4.28-2.99		-0.29	2.725	-5.65-6.95		-0.33	1.365	-3.02-1.96	*			
	me	-0.80	1.775	-3.40-2.32		0.04	2.846	-6.16-6.92		-0.18	1.434	-2.48-2.39	*			
	aa	-3.91	2.601	-7.49-1.84	*	-1.28	4.934	-9.23-22.59	*	-0.70	1.881	-5.17-1.83	*			
	am	-2.94	2.052	-6.61-0.69		-0.23	2.189	-4.12-5.61		0.13	1.072	-2.10-2.35	*			
	as	-3.44	3.211	-6.57-3.86	*	-0.93	3.206	-9.12-7.2	*	-0.32	1.725	-3.10-4.38	*			
	ae	-3.30	2.863	-5.94-3.22	*	-0.71	3.322	-8.90-7.99	*	-0.19	1.656	-2.44-4.50	*			
	Zp				n.s.				n.s.				P < 0.01			
	ma	-1.33	1.729	-4.23-1.86		-1.19	4.433	-10.86-17.07		-0.64	0.942	-2.62-1.14	*			
	ms	-0.93	2.408	-6.47-2.32		-0.89	2.34	-5.51-5.18		-0.79	0.817	-3.20-0.70	*			
	me	-0.82	2.052	-5.36-1.70		-0.41	2.32	-5.34-4.77		-0.48	0.934	-2.85-1.55	*			
	aa	-3.43	2.786	-6.46-2.35		-1.22	5.579	-11.17-23.56		-0.64	1.357	-2.71-2.00	*			
	am	-2.02	2.864	-5.29-2.35		-0.14	2.18	-3.76-6.67		-0.01	0.959	-1.74-2.12	*			
	as	-3.01	2.859	-5.91-1.86		-0.97	2.878	-7.03-4.77		-0.71	1.096	-3.54-1.66	*			
	ae	-2.90	2.751	-5.47-1.61		-0.49	2.863	-6.76-6.55		-0.52	1.047	-2.85-2.32	*			

See Tables 1 and 2 for details about computation and abbreviations.

error was sufficiently smaller than our acceptable error of 5%, the standard deviation of %PEs and the minimum–maximum range indicated that individual values could greatly exceed the 5% boundary, especially in combination with automatic processing. Therefore, if means computed from larger samples are compared, the effect of processing on accuracy will be less significant than in cases of analyzing small samples or individual values.

Combinations with automatic processing produced the largest error and widest minimum–maximum range compared with manual and semi-automatic processing. The effect of automatic processing differed between periosteal and endosteal contours. Automatic processing of periosteal contour influenced the mean %PEs less than did automatic processing of the endosteal contour. This observation was supported by the lower mean %PE in the estimations for TA and a higher mean %PE in MA, as well as by differences in the %PE between CA<sub>am</sub> (−0.3%) and CA<sub>ma</sub> (−2.23%). On the other hand, automatic processing of the periosteal contour had a greater effect on section moduli than on CA. While the mean %PEs in automatically estimated periosteal contours (i.e. <sub>am</sub>) for CA and section moduli were in a similar range of between −0.3 and −0.5% in the total sample, the automatically estimated endosteal contour (i.e. <sub>ma</sub>) had only about half as great an effect on section moduli (range of mean %PE being −0.96 to −1.06) as on cortical area (%PE = −2.23%). The effect of periosteal automatic processing on section moduli also changed with age and was particularly large for age category Ia. For example, the automatically estimated periosteal contour produced a decrease in the mean %PE of Zp<sub>am</sub> from −2.02% in age category Ia to −0.14% for age Ib and −0.01% for age II, and automatically estimated endosteal contour decreased the %PE of Zp<sub>ma</sub> from −1.33% in age Ia to −1.19% in age Ib and −0.64% in age II. Thus, even though the periosteal contour can be estimated with better agreement between manual and automatic techniques, the effect of estimation error in the periosteal contour is greater on section moduli than on CA.

Combinations using spline and ellipse methods for estimating the endosteal contour showed similar mean %PE values and minimum–maximum ranges. The ellipse technique estimated section moduli with slightly lower mean %PEs, whereas the spline technique estimated MA and CA with slightly lower mean %PEs. However, the most important observation was that semi-automatic techniques may also narrow the minimum–maximum range of the %PEs. For example, the combination of manually estimated periosteal contour and endosteal contour estimated by the ellipse technique showed a mean %PE for Zy of near 0 (−0.11%) with a minimum–maximum range close to our acceptable error of 5% (−6.16 to 6.92%) in the total sample. This smaller error was also seen among the age categories. The combination of manually estimated periosteal contour with endosteal contour estimation by the ellipse

technique could decrease the bias in estimating the cortical area by as much as −0.8% and in estimating section moduli by between −1 and −0.8%. Moreover, the ellipse technique also decreased the error in medullary area by as much as 3.2%.

Correlation coefficients and RMA slopes are shown in Table 4. Only log data were used. Regression slopes were consistently close to 1, and this was also observed in the case of slopes significantly deviated from isometry. This indicates that size had little practical effect on the resulting bias. The only larger deviation from isometry was observed in the case of automatically estimated MA in the Ia age group (slope = 0.85).

Bias and precision ( $\pm 95\%$  LA) are summarized in Table 5 and Figs 2 and 3. Table 5 summarizes non-transformed (raw) data. The figures show log-transformed data free from the effect of increasing diaphyseal size. The overall results of  $\pm 95\%$  LAs highlight patterns observed in %PE and RMA. All mean differences between manual and compared properties were negative, except those for MA. TA was the best estimated among areas, whereas Zy was the best estimated property among moduli. The fully automatic technique had the greatest impact on error in the case of MA but only a modest effect in relation to CA, and a low impact on the error in TA. The ellipse technique performed slightly better than did the spline technique, but that improvement was seen mainly in section moduli. The  $\pm 95\%$  LA also supports the results obtained by RMA analysis, such as the low impact of size on bias and precision. Regression coefficients calculated for relations between average size and difference were close to zero for the ellipse technique (Fig. 3) and low for automatic processing (Fig. 2). The  $\pm 95\%$  LA did show, however, that the minimum–maximum range was partly sensitive to age. Consistently wider ranges were found in age category Ib. Differences between age groups concerning the range of estimated cross-sectional properties were diminished somewhat when the ellipse technique was used in estimating the endosteal contour.

## Discussion

The main conclusion is that the majority of the studied techniques estimate non-adult femoral midshaft cross-sectional properties from microCT scan images with mean %PEs below the 5% level. In fact, only the mean %PEs of automatically estimated MA exceeded the 5% boundary. However, evaluation of the minimum–maximum range of %PE indicated that individual values may substantially exceed the 5% acceptable error in a majority of the studied properties. This conclusion is based on the evidence that the majority of the techniques produced %PEs with minimum–maximum ranges larger than 5%, and in some cases, even larger than  $\pm 20\%$  (e.g. for CA<sub>aa</sub> the range was −19 to 23%).

**Table 4** Regression coefficients and analysis of isometry.

Tech	Total (n = 86)				Age category Ia (n = 9)				Age category Ib (n = 55)				Age category II (n = 22)			
	r	Slope	95% CI	r	Slope	95% CI	r	Slope	95% CI	r	Slope	95% CI	r	Slope	95% CI	
	TA	0.99	1.0066*	1.0021–1.0111	0.99	1.0134	0.9859–1.0415	0.99	1.0041	0.9919–1.0165	0.99	0.9995	0.9902–1.0089	0.99	0.9995	0.9902–1.0089
CA	0.99	1.0154	0.9908–1.0406	0.97	1.0853	0.9924–1.1869	0.99	1.0144	0.9468–1.0869	0.99	1.0082	0.9696–1.0482	0.99	1.0082	0.9696–1.0482	
	0.99	0.9992	0.9887–1.0098	0.99	1.0134	0.9608–1.0689	0.99	1.0027	0.9746–1.0317	0.99	0.9952	0.9730–1.0170	0.99	0.9952	0.9730–1.0170	
	0.99	0.9989	0.9886–1.0094	0.99	1.0122	0.9594–1.0679	0.99	1.0028	0.9750–1.0315	0.99	0.9964	0.9748–1.0184	0.99	0.9964	0.9748–1.0184	
	0.99	1.0174	0.9903–1.0453	0.99	1.1077	0.9977–1.2299	0.96	0.9989	0.9265–1.0768	0.99	1.0070	0.9648–1.0509	0.99	1.0070	0.9648–1.0509	
	0.99	1.0033	0.9957–1.0109	0.99	1.0201	0.9711–1.0717	0.99	0.9896	0.9713–1.0083	0.99	0.9992	0.9858–1.0128	0.99	0.9992	0.9858–1.0128	
	0.99	1.0028	0.9910–1.0147	0.99	1.0341	0.9641–1.1091	0.99	0.9938	0.9636–1.0249	0.99	0.9944	0.9698–1.0196	0.99	0.9944	0.9698–1.0196	
	0.99	1.0025	0.9908–1.0144	0.99	1.0329	0.9635–1.1074	0.99	0.9939	0.9639–1.0248	0.99	0.9955	0.9708–1.0209	0.99	0.9955	0.9708–1.0209	
MA	0.98	0.9253*	0.8952–0.9564	0.98	0.8524*	0.7494–0.9695	0.94	0.9179	0.8370–1.0060	0.99	0.9787	0.9249–1.0356	0.99	0.9787	0.9249–1.0356	
	0.99	0.9965	0.9810–1.0122	0.99	0.9683	0.9207–1.0182	0.98	1.0286	0.9847–1.0744	0.99	0.9847	0.9492–1.0216	0.99	0.9847	0.9492–1.0216	
	0.99	0.9976	0.9823–1.0133	0.99	0.9700	0.9222–1.0202	0.98	1.0295	0.9861–1.0748	0.99	0.9860	0.9507–1.0227	0.99	0.9860	0.9507–1.0227	
Zx	0.99	1.0058	0.9939–1.0178	0.99	1.0132	0.9807–1.0468	0.99	1.0032	0.9670–1.0407	0.99	1.0089	0.9939–1.0242	0.99	1.0089	0.9939–1.0242	
	0.99	1.0009	0.9927–1.0091	0.99	0.9859	0.9537–1.0193	0.99	0.9954	0.9728–1.0186	0.99	1.0024	0.9786–1.0268	0.99	1.0024	0.9786–1.0268	
	0.99	0.9978	0.9899–1.0057	0.99	0.9876	0.9583–1.0178	0.99	0.9888	0.9669–1.0112	0.99	1.0013	0.9760–1.0272	0.99	1.0013	0.9760–1.0272	
	0.99	1.0158*	1.0012–1.0307	0.99	1.0165	0.9856–1.0483	0.98	1.0074	0.9632–1.0536	0.99	1.0129	0.9884–1.0381	0.99	1.0129	0.9884–1.0381	
	0.99	1.0121*	1.0050–1.0192	0.99	1.0046	0.9745–1.0356	0.99	1.0121	0.9925–1.0321	0.99	1.0038	0.9820–1.0262	0.99	1.0038	0.9820–1.0262	
	0.99	1.0134*	1.0030–1.0239	0.99	0.9921	0.9557–1.0298	0.99	1.0073	0.9777–1.0377	0.99	1.0083	0.9790–1.0380	0.99	1.0083	0.9790–1.0380	
	0.99	1.0107*	1.0004–1.0211	0.99	0.9938	0.9612–1.0274	0.99	1.0010	0.9717–1.0313	0.99	1.0068	0.9780–1.0364	0.99	1.0068	0.9780–1.0364	
Zy	0.99	1.0022	0.9923–1.0121	0.99	1.0071	0.9831–1.0318	0.99	0.9979	0.9674–1.0294	0.99	1.0088	0.9907–1.0272	0.99	1.0088	0.9907–1.0272	
	0.99	1.0009	0.9937–1.0083	0.99	0.9988	0.9712–1.0272	0.99	0.9999	0.9785–1.0219	0.99	0.9844	0.9650–1.0040	0.99	0.9844	0.9650–1.0040	
	0.99	0.9998	0.9923–1.0074	0.99	0.9988	0.9750–1.0233	0.99	0.9961	0.9739–1.0189	0.99	0.9805	0.9610–1.0004	0.99	0.9805	0.9610–1.0004	
	0.99	1.0133*	1.0008–1.0259	0.99	1.0173	0.9841–1.0515	0.99	1.0062	0.9684–1.0456	0.99	1.0184	0.9890–1.0480	0.99	1.0184	0.9890–1.0480	
	0.99	1.0116*	1.0055–1.0178	0.99	1.0124	0.9856–1.0398	0.99	1.0074	0.9900–1.0250	0.99	1.0086	0.9924–1.0251	0.99	1.0086	0.9924–1.0251	
	0.99	1.0116*	1.0025–1.0207	0.99	1.0100	0.9670–1.0549	0.99	1.0095	0.9839–1.0357	0.99	0.9890	0.9635–1.0151	0.99	0.9890	0.9635–1.0151	
	0.99	1.0104*	1.0012–1.0197	0.99	1.0106	0.9725–1.0502	0.99	1.0042	0.9779–1.0313	0.99	0.9857	0.9619–1.0101	0.99	0.9857	0.9619–1.0101	
Zp	0.99	1.0045	0.9938–1.0153	0.99	1.0066	0.9832–1.0306	0.99	1.0038	0.9706–1.0381	0.99	1.0113	0.9982–1.0246	0.99	1.0113	0.9982–1.0246	
	0.99	0.9997	0.9936–1.0059	0.99	0.9942	0.9613–1.0282	0.99	0.9970	0.9795–1.0149	0.99	0.9990	0.9870–1.0112	0.99	0.9990	0.9870–1.0112	
	0.99	0.9988	0.9928–1.0049	0.99	0.9919	0.9647–1.0199	0.99	0.9937	0.9765–1.0113	0.99	0.9916	0.9786–1.0047	0.99	0.9916	0.9786–1.0047	
	0.99	1.0109	0.9975–1.0246	0.99	1.0248	0.9912–1.0595	0.98	0.9987	0.9583–1.0408	0.99	1.0133	0.9940–1.0330	0.99	1.0133	0.9940–1.0330	
	0.99	1.0066*	1.0005–1.0127	0.99	1.0151	0.9769–1.0547	0.99	0.9981	0.9819–1.0146	0.99	1.0025	0.9885–1.0167	0.99	1.0025	0.9885–1.0167	
	0.99	1.0068	0.9990–1.0146	0.99	1.0066	0.9671–1.0478	0.99	0.9967	0.9752–1.0187	0.99	1.0018	0.9857–1.0183	0.99	1.0018	0.9857–1.0183	
	0.99	1.0055	0.9978–1.0133	0.99	1.0043	0.9662–1.0439	0.99	0.9939	0.9727–1.0156	0.99	0.9951	0.9801–1.0105	0.99	0.9951	0.9801–1.0105	

See Tables 1 and 2 for abbreviations.  
\*Indicates significant deviation from isometry at  $P < 0.05$ .

**Table 5** Mean difference and limits of agreement.

Tech	Total (n = 86)			Age category Ia (n = 9)			Age category Ib (n = 55)			Age category II (n = 22)		
	Diff	+95%LA	-95%LA	Diff	+95%LA	-95%LA	Diff	+95%LA	-95%LA	Diff	+95%LA	-95%LA
TA	a	-0.20 (1)	1.76	-2.16	0.78	-0.51 (0.66)	-0.12 (1.11)	2.06	-2.30	-0.28 (0.79)	1.27	-1.83
CA	ma	-1.64 (3.12)	4.48	-7.76	2.56	-0.65 (1.64)	-1.66 (3.53)	5.26	-8.58	-1.99 (2.44)	2.79	-6.77
	ms	-1.08 (1.85)	2.55	-4.71	1.85	-0.25 (1.07)	-0.89 (1.96)	2.95	-4.73	-1.89 (1.56)	1.17	-4.95
	me	-1.12 (1.85)	2.51	-4.75	1.86	-0.26 (1.08)	-0.92 (1.95)	2.90	-4.74	-1.98 (1.58)	1.12	-5.08
	aa	-1.84 (3.34)	4.71	-8.39	2.61	-1.17 (1.93)	-1.76 (3.77)	5.63	-9.15	-2.33 (2.59)	2.75	-7.41
MA	am	-0.21 (1.01)	1.77	-2.19	0.80	-0.53 (0.68)	-0.10 (1.12)	3.10	-2.30	-0.34 (0.79)	1.21	-1.89
	as	-1.29 (1.96)	2.55	-5.13	1.69	-0.78 (1.26)	-0.99 (2.07)	3.07	-5.05	-2.23 (1.63)	0.96	-5.42
	ae	-1.33 (1.96)	2.51	-5.17	1.69	-0.78 (1.26)	-1.02 (2.06)	3.02	-5.06	-2.32 (1.63)	0.87	-5.51
	a	1.64 (3.12)	7.76	-4.48	3.86	0.65 (1.64)	1.66 (3.53)	8.58	-5.26	1.99 (2.44)	6.77	-2.79
Zx	s	1.08 (1.85)	4.71	-2.55	2.35	0.25 (1.07)	0.89 (1.96)	4.73	-2.95	1.89 (1.56)	4.95	-1.17
	e	1.12 (1.85)	4.75	-2.51	2.38	0.26 (1.08)	0.92 (1.95)	4.74	-2.90	1.98 (1.58)	5.08	-1.12
	ma	-1.20 (4.65)	7.91	-10.31	1.56	-0.46 (1.03)	-1.37 (5.06)	8.55	-11.29	-1.08 (4.58)	7.90	-10.06
	ms	-2.91 (4.42)	5.75	-11.57	3.05	-0.99 (2.06)	-2.80 (4.11)	5.26	-10.86	-3.97 (5.59)	6.99	-14.93
Zy	me	-2.63 (4.33)	5.86	-11.12	2.81	-0.74 (1.81)	-2.33 (3.89)	5.29	-9.95	-4.15 (5.62)	6.87	-15.17
	aa	-1.17 (6.12)	10.83	-13.17	1.16	-1.62 (1.42)	-1.56 (6.47)	11.12	-14.24	-0.02 (6.43)	12.58	-12.62
	am	-0.02 (3.89)	7.60	-7.64	1.04	-1.25 (1.17)	-0.24 (3.70)	7.01	-7.49	1.03 (4.86)	10.56	-8.50
	as	-2.67 (5.71)	8.52	-13.86	2.37	-2.22 (2.34)	-2.83 (5.49)	7.93	-13.59	-2.46 (7.21)	11.67	-16.59
Zp	ae	-2.64 (5.59)	8.32	-13.60	1.94	-2.06 (2.04)	-2.58 (5.42)	8.04	-13.20	-3.03 (7.01)	10.71	-16.77
	ma	-1.74 (3.65)	5.41	-8.89	2.35	-0.43 (1.42)	-1.58 (3.73)	5.73	-8.89	-2.69 (3.96)	5.07	-10.45
	ms	-0.82 (4.45)	7.90	-9.54	2.91	-0.52 (1.75)	-0.53 (4.15)	7.60	-8.66	-1.69 (5.79)	9.66	-13.04
	me	-0.46 (4.6)	8.56	-9.48	2.36	-0.42 (1.42)	-0.15 (4.41)	8.49	-8.79	-1.24 (5.81)	10.15	-12.63
Zp	aa	-1.75 (4.84)	7.74	-11.24	1.65	-1.68 (1.70)	-1.67 (4.64)	7.42	-10.76	-1.96 (6.20)	10.19	-14.11
	am	-0.08 (2.92)	5.64	-5.80	0.54	-1.28 (0.93)	-0.20 (2.77)	5.23	-5.63	0.73 (3.62)	7.83	-6.37
	as	-1.35 (4.56)	7.59	-10.29	3.32	-1.56 (2.49)	-1.26 (4.26)	7.09	-9.61	-1.49 (5.91)	10.09	-13.07
	ae	-1.10 (4.58)	7.88	-10.08	2.72	-1.47 (2.14)	-1.02 (4.49)	7.78	-9.82	-1.14 (5.60)	9.84	-12.12
Zp	ma	-2.84 (7.43)	11.72	-17.40	3.35	-0.98 (2.21)	-2.87 (8.34)	13.48	-19.22	-3.53 (6.37)	8.96	-16.02
	ms	-3.04 (6.33)	9.37	-15.45	6.15	-1.04 (3.67)	-2.42 (6.75)	10.81	-15.65	-5.41 (5.62)	5.61	-16.43
	me	-1.91 (6.40)	10.63	-14.45	4.77	-0.99 (2.94)	-1.28 (6.63)	11.71	-14.27	-3.87 (6.64)	9.14	-16.88
	aa	-3.12 (9.62)	15.74	-21.98	3.18	-2.31 (2.8)	-3.16 (10.51)	17.44	-23.76	-3.36 (9.33)	14.93	-21.65
Zp	am	-0.35 (5.48)	10.39	-11.09	2.74	-1.30 (2.06)	-0.43 (5.47)	10.29	-11.15	0.22 (6.50)	12.96	-12.52
	as	-3.11 (7.19)	10.98	-17.20	4.00	-2.47 (3.3)	-2.62 (7.66)	12.39	-17.63	-4.61 (7.16)	9.42	-18.64
	ae	-2.14 (7.00)	11.58	-15.86	3.17	-2.42 (2.85)	-1.43 (7.42)	13.11	-15.97	-3.81 (7.03)	9.97	-17.59

Diff: mean difference and standard deviation between manual (mm) and compared techniques [mean (SD)]; ±95%LA: ±95% limits of agreement (Bland & Altman, 1986). (See Tables 1 and 2 for further abbreviations).

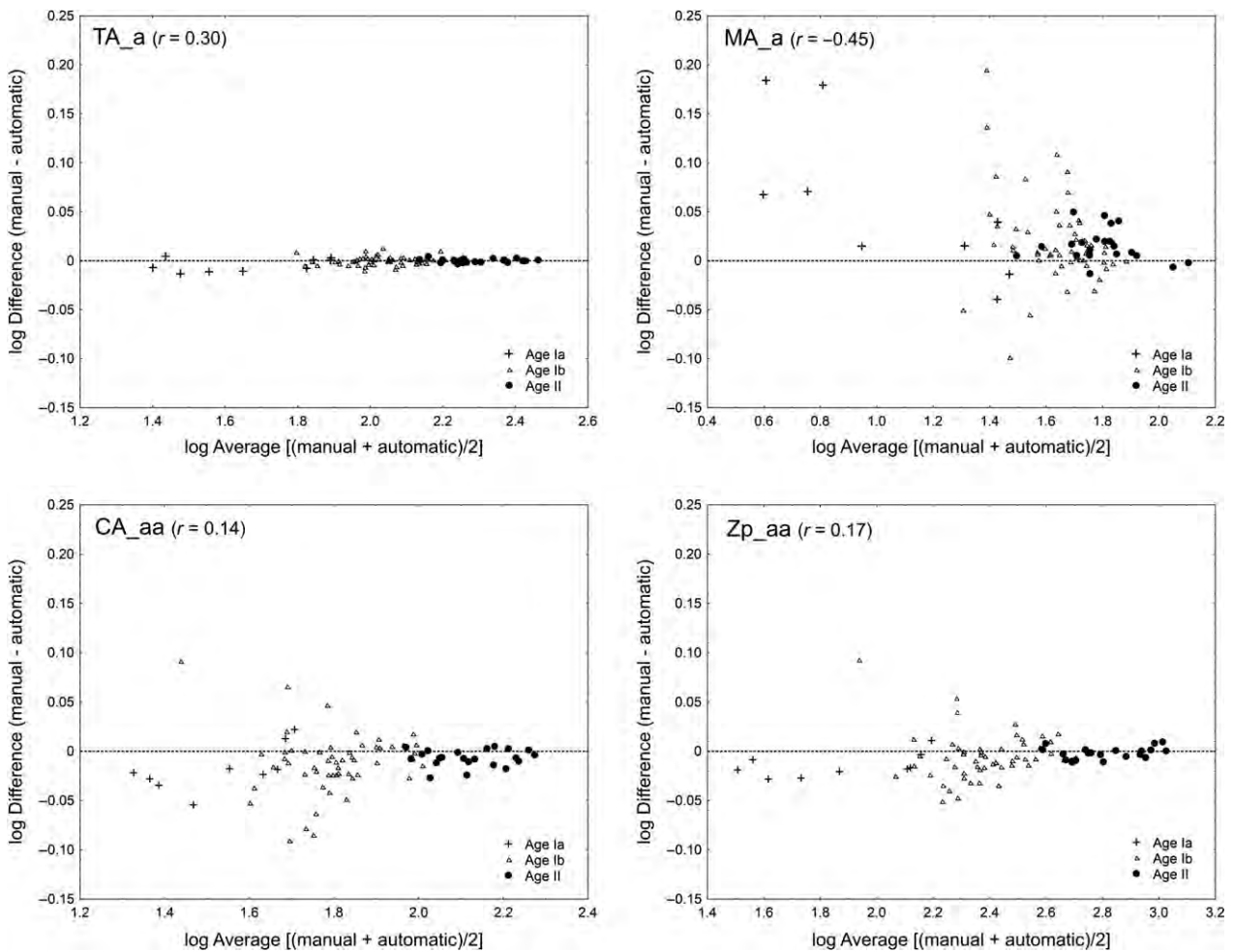


**Fig. 2** Limits of agreement ( $\pm 95\%$  LA) for cross-sectional properties estimated by automatic processing of periosteal and endosteal contours. Log-transformed data are shown. TA shows  $\pm 95\%$  LA for automatic processing of periosteal contour and MA shows  $\pm 95\%$  LA for automatic processing of endosteal contour. CA and Zp summarize  $\pm 95\%$  LA for processing of both contours. (See Table 2 for abbreviations).

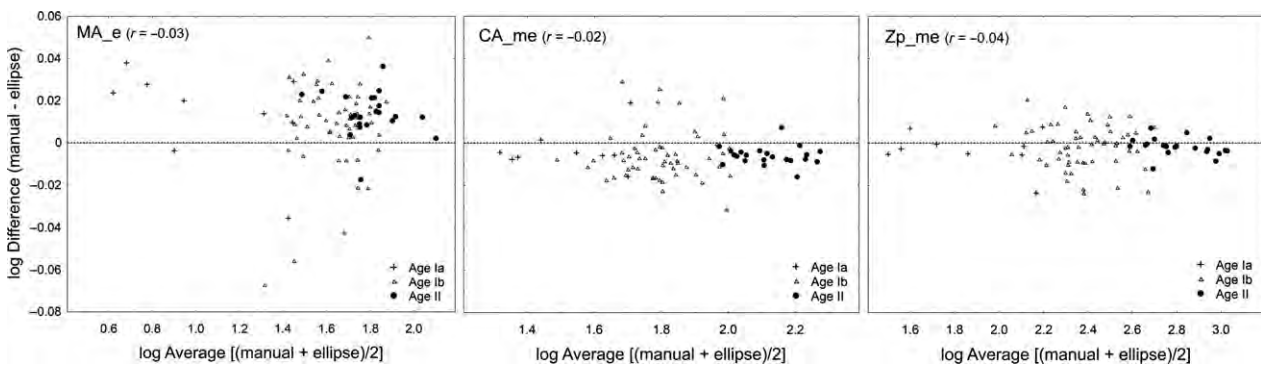


**Fig. 3** Effect of ellipse technique used for deriving endosteal contour on  $\pm 95\%$  limits of agreement for medullary area (MA), cortical area (CA), and polar section modulus (Zp). Log-transformed data are shown. (See Table 2 for further abbreviations).

Our results reinforce the view that processing of endosteal contours has weaker agreement among applied techniques than does the processing of periosteal contours

(O'Neill & Ruff, 2004). This conclusion is particularly supported by the observed agreement among techniques applied in deriving MA (i.e. derived entirely from endosteal

contours) and TA (i.e. derived entirely from periosteal contours) values. MA consistently showed the weakest agreement in non-adults among all studied femoral midshaft properties, with a particularly large error occurring in fully automatic processing (%PE = 3.5–15.5%). By contrast, TA showed the strongest agreement with reference values, even for automatic processing (%PE = –1.26 to –0.12%). Thus, although an automatic protocol can well be used to simplify derivation of the periosteal contour, this is not true for deriving endosteal contours. Our results indicate that error in deriving the endosteal contour can be reduced through semi-automatic processing. This is supported by the observation that semi-automatic processing can substantially reduce the error in estimated MA values to below the 5% acceptable level of error.

Our results also indicate that non-adult femoral midshaft properties can be estimated with a measurement error comparable to that reported for adults (Stock, 2002; O'Neill & Ruff, 2004). For example, agreement of the adult LCM technique shows a mean directional error in a range between –4.2 and 0.5% (O'Neill & Ruff, 2004), and the mean %PEs observed for techniques for automatic periosteal contour and ellipse endosteal contour in our total non-adult sample ranged between 2.1 and 0.8% (%PE was recalculated as %PE = [(estimated – true)/true] × 100 used in O'Neill & Ruff, 2004).

We observed strengthening of the agreement between ages Ia and II. The stronger agreement was probably not associated simply with the effect of allometry because the RMA axis slopes did not deviate from isometry. This could indicate that error in the estimated properties may be partly sensitive to changes with age in the circularity of the midshaft femoral cross-section, as observed for adults (O'Neill & Ruff, 2004). This is supported, too, by the observation that the mean shape ratio comparing the anterior–posterior and medial–lateral second moments of area ( $I_x/I_y$  ratio) increased in our non-adult age samples from 0.82 observed for age Ia to a more circular shape of 0.98 observed for age II. However, the decrease of the mean %PEs between ages Ia and II may be explained by developmental changes in the endosteal contours. The effect of trabecular structures on endosteal surfaces especially needs to be further examined in the future to elucidate the effect on reconstruction of cross-sectional contours.

Our results showed that semi-automatic processing offers a viable option for automatization in estimating cross-sectional properties. In fact, semi-automatic techniques strongly reduced error in estimated MA and, especially, for age categories Ia and Ib. Moreover, semi-automatic processing is particularly advantageous in estimating section moduli in age category II, where section moduli estimated by semi-automatic processing had mean errors similar to those obtained for manually estimated endosteal contours. Moreover, the minimum–maximum %PE range was within –5 to 5%. Both the ellipse and spline curve techniques estimated

cross-sectional properties with similar mean %PEs and minimum–maximum ranges. Given that the most biomechanically relevant cross-sectional properties (i.e. section moduli) were estimated with lower error by the ellipse technique, we recommend preferring the ellipse fitting technique over spline curve endosteal reconstruction. The ellipse technique may, however, be limited by the circular shape of endosteal contours, as seen from our observations (see Discussion above) and observations on adult cross-sections (O'Neill & Ruff, 2004). It may be, therefore, that the ellipse technique could be favored in non-adult femoral cross-sectional processing near the midshaft but not in proximal and distal segments of femoral diaphyses, because in the proximal and distal directions, femoral cross-sections significantly deviate from circular shape (Gosman et al. 2013).

Our results also reinforce the view that accuracy in periosteal contour estimation has more effect on accuracy in section moduli than does accuracy of the estimation of endosteal contours. The unequal effect of periosteal and endosteal contour estimation on the calculation of section moduli was observed for each age category and each section moduli (although a slightly weaker effect was observed in the case of  $Z_x$ ). Thus, a special effort must be made during the processing of non-adult cross-sectional contours, particularly for periosteal contour derivation. If necessary, the error in accuracy can be reduced more by manually determining the periosteal contour than by using special care during endosteal contour processing.

## Conclusions

Our results have shown that the majority of non-adult cross-sectional properties can be taken from microCT scans with an acceptable error of < 5%. Individual values, however, may significantly exceed the defined error. Although we observed increasing agreement between techniques with age, the mean %PE values obtained across age categories were similar to those observed in adults. Weak agreement was observed in estimating endosteal contours. This weak agreement mainly affected the derivation of MA. Processing of endosteal contours can be simplified by semi-automatic techniques, mainly by using ellipse techniques for femora. On the other hand, although the periosteal contour can also be derived with strong agreement using automatic processing, the potential error in deriving the periosteal contour has a greater effect on calculated cross-sectional properties than does the error in the endosteal contour.

We can recommend several steps to improve the accuracy in estimating non-adult midshaft femoral cross-sectional properties from microCT images. We advise using digital tools in PHOTOSHOP or IMAGEJ to correct any damage on contours prior to processing. It is particularly important to correct the periosteal contour because this contour has a stronger effect on the resulting accuracy. Fully automatic

processing can be favored for deriving the periosteal contour, whereas semi-automatic processing (ellipse technique) is preferred for deriving endosteal contours. When estimating individual cross-sections or in the case of small samples, we recommend using automatic processing only for the periosteal contour and estimating the endosteal contour manually. If needed, the presented  $\pm 95\%$  LA can be used to specify error in estimated non-adult femoral midshaft cross-sectional properties.

## Acknowledgements

We thank Kristýna Farkašová and the researchers from the Centre of Excellence in Telč for their help with data for the Pohansko sample. We thank Jiří Macháček and Petr Velemínský for their assistance with skeletal collections. We thank to Eliška Makajevová, Martin Hora, and students from Charles University for their technical support. This research was carried out under the Grant Agency of Charles University (No. 1506314; Cortical bone tissue ontogeny), the Grant Agency of the Czech Republic (18-154805; Death, burials, and skeletons), and the project under the Ministry of Education, Youth, and Sports of the Czech Republic (CEITEC 2020, LQ 1601 and CEITEC Nano Res. Inf., MEYS CR, 2016–2019).

## Funding

Czech Science Foundation (GAČR: 18-154805); Grant Agency of Charles University (No. 1506314); National Sustainability Programme II (CEITEC 2020; LQ1601).

## Author contributions

Vladimír Sládek: planning and design of the study, design of data acquisition and IMAGEJ analysis, EPmACROJ development, statistical analysis, draft of the manuscript, final approval. Veronika Sabolová: design of IMAGEJ analysis, EPmACROJ development, participation in data acquisition. O.Š.: design of IMAGEJ analysis, EPmACROJ development. T.Z.: design and data acquisition. J.K.: data acquisition. S.Č.: design of IMAGEJ analysis, data acquisition. All authors contributed to the final revision of the manuscript. No authors have any conflict of interest.

## References

AlQahtani S, Hector M, Liversidge H (2014) Accuracy of dental age estimation charts: Schour and Massler, Ubelaker and the London Atlas. *Am J Phys Anthropol* **154**, 70–78.

Biewener AA (1992) *Biomechanics-Structures and Systems: A Practical Approach*. Oxford: Oxford University Press.

Bland JM, Altman DG (1986) Statistical methods for assessing agreement between two methods of clinical measurement. *Lancet* **327**, 307–310.

Bohonak AJ (2002) *RMA: Software for Reduced Major Axis Regression (v. 1.14)*. San Diego: San Diego State University.

Bouxsein ML, Boyd SK, Christiansen BA, et al. (2010) Guidelines for assessment of bone microstructure in rodents using micro-computed tomography. *J Bone Miner Res* **25**, 1468–1486.

Di Vincenzo F, Rodriguez L, Carretero JM, et al. (2015) The massive fossil humerus from the Oldowan horizon of Gombore I, Melka Kunture (Ethiopia, >1.39 Ma). *Quat Sci Rev* **122**, 207–221.

Gosman JH, Hubbell ZR, Shaw CN, et al. (2013) Development of cortical bone geometry in the human femoral and tibial diaphysis. *Anat Rec* **296**, 774–787.

Hsieh J (2003) *Computed Tomography: Principles, Design, Artifacts, and Recent Advances*. New York: John Wiley & Sons.

Huiskes R (1982) On the modeling of long bones in structural analyses. *J Biomech* **15**, 65–69.

Kimura T (1971) Cross-section of human lower leg bones viewed from strength of materials. *J Anthropol Soc Nip* **79**, 323–336.

Knussmann R (1988) *Anthropologie, Handbuch der vergleichenden Biologie des Menschen (Band I)*. New York: Gustav Fisher Verlag.

Lovejoy CO, Trinkaus E (1980) Strength and robusticity of the Neandertal tibia. *Am J Phys Anthropol* **53**, 465–470.

Macháček J (2010) *The Rise of Medieval Towns and States in East Central Europe: Early Medieval Centres as Social and Economic Systems*. Leiden: Brill.

Martin RB, Bur DB, Sharkey NA (1998) *Skeletal Tissue Mechanics*. New York: Springer Verlag.

Ohman JC (1993) Computer software for estimating cross-sectional geometric properties of long bones with concentric and eccentric elliptical models. *J Hum Evol* **25**, 217–227.

O'Neill MC, Ruff CB (2004) Estimating human long bone cross-sectional geometric properties: a comparison of noninvasive methods. *J Hum Evol* **47**, 221–235.

Poláček L (2008) Great Moravia, the power centre at Mikulčice and the issue of the socio-economic structure. In: *Studien zum Burgwall von Mikulčice VIII* (eds Velemínský P, Poláček L), pp. 11–44. Brno: Archeologický ústav.

Prewitt J, Mendelsohn ML (1966) The analysis of cell images. *Ann N Y Acad Sci* **128**, 1035–1053.

Ruff CB (2008) Biomechanical analysis of archaeological human skeletons. In: *Biological Anthropology of the Human Skeleton* (eds Katzenberg MA, Saunders SR), pp. 183–206. Hoboken: Wiley-Liss Inc.

Ruff CB, Hayes WC (1983) Cross-sectional geometry of Pecos Pueblo femora and tibiae: a biomechanical investigation. I. Method and general patterns of variation. *Am J Phys Anthropol* **60**, 359–381.

Ruff CB, Holt B, Niskanen M, et al. (2015) Gradual decline in mobility with adoption of food production in Europe. *PNAS* **112**, 7147–7152.

Runestad JA, Ruff CB, Nieh JC, et al. (1993) Radiographic estimation of long bone cross-sectional geometric properties. *Am J Phys Anthropol* **90**, 207–213.

Schindelin J, Arganda-Carreras I, Frise E, et al. (2012) Fiji: an open-source platform for biological-image analysis. *Nat Methods* **9**, 676–682.

Skedros JG (2011) Interpreting load history in limb-bone diaphyses: important considerations and their biomechanical foundations. In: *Bone Histology: An Anthropological Perspective* (eds Crowder CM, Stout SD), pp. 153–220. New York: CRC Press.

Sládek V, Macháček J (2017) *At the End of Great Moravia: Skeletons from the Second Church Cemetery at Pohansko-Břeclav (9th–10th Century A.D.)*. Oxford: British Archaeological Reports (International Series).

Sládek V, Makajevová E (2017) The assessment of preservation of a skeletal sample excavated from the Pohansko second church cemetery. In: *At the End of Great Moravia: Skeletons from the Second Church Cemetery at Pohansko-Břeclav*

- (9th–10th century A.D.) (eds Sládek V, Macháček J), pp. 19–34. Oxford: British Archaeological Reports (International Series).
- Sládek V, Ruff C, Berner M, et al.** (2016) The impact of subsistence changes on humeral bilateral asymmetry in Terminal Pleistocene and Holocene Europe. *J Hum Evol* **92**, 37–49.
- Sládek V, Makajevová E, Berner M** (2017) Dental and skeletal age-at-death for non-adult and adult individuals from the Pohansko second church cemetery. In: *At the End of Great Moravia: Skeletons from the Second Church Cemetery at Pohansko-Břeclav (9th–10th Century A.D.)* (eds Sládek V, Macháček J), pp. 35–50. Oxford: British Archaeological Reports (International Series).
- Smith EL** (2005) *A Test of Ubelaker's Method of Estimating Sub-adult Age from the Dentition*. Thesis. Indianapolis: University of Indianapolis.
- Stloukal M, Hanáková H** (1978) The length of long bones in ancient Slavonic populations with particular consideration to the questions of growth. *Homo* **29**, 53–69.
- Stock JT** (2002) A test of two methods of radiographically deriving long bone cross-sectional properties compared to direct sectioning of the diaphysis. *Int J Osteoarchaeol* **12**, 335–342.
- Sumner DR, Mockbee B, Morse K, et al.** (1985) Computed tomography and automated image analysis of prehistoric femora. *Am J Phys Anthropol* **68**, 225–232.
- Sylvester AD, Garofalo E, Ruff C** (2010) Technical note: an R program for automating bone cross-section reconstruction. *Am J Phys Anthropol* **142**, 665–669.
- Takahashi H** (1982) Geometrical properties of the femur shaft. *Biomechanism* **6**, 17–25.
- Trinkaus E, Ruff CB** (1989) Diaphyseal cross-sectional morphology and biomechanics of the Fond-de-Forêt 1 femur and the Spy 2 femur and tibia. *Bull Soc R Belge Anthropol Prehist* **100**, 33–42.
- Ubelaker DH** (1989) *Human Skeletal Remains: Excavation, Analysis, Interpretation*. Washington, DC: Taraxacum.